Lecture Notes in Electrical Engineering 237

Wego Wang
Editor

Mechatronics and Automatic Control Systems

Proceedings of the 2013 International Conference on Mechatronics and Automatic Control Systems (ICMS2013)

Springer

For further volumes:
http://www.springer.com/series/7818

Wego Wang
Editor

Mechatronics and Automatic Control Systems

Proceedings of the 2013 International Conference on Mechatronics and Automatic Control Systems (ICMS2013)

Springer

Editor
Wego Wang
University of Massachusetts Lowell
Wellesley, MA, USA

ISSN 1876-1100 ISSN 1876-1119 (electronic)
ISBN 978-3-319-01272-8 ISBN 978-3-319-01273-5 (eBook)
DOI 10.1007/978-3-319-01273-5
Springer Cham Heidelberg New York Dordrecht London

Library of Congress Control Number: 2013950379

Printed on acid-free paper

Springer is part of Springer Science+Business Media (www.springer.com)

Preface

This book contains papers accepted by the 2013 International Conference on Mechatronics and Automatic Control Systems (ICMS), which was held on 10 and 11 August, 2013, in Hangzhou, China.

It covers emerging technologies in a timely manner for two important subjects: mechatronics and automatic control systems. In particular, it allows researchers and students to become familiar with state-of-the-art developments in the field, and it also helps engineers and practitioners enhance their productivity with the latest technology.

The book is composed of two volumes. The first volume has 64 papers focusing on Advanced Mechanics and Mechatronics (Part I), Intelligent Systems and Algorithms (Part II), and Manufacturing Engineering and Engineering Systems (Part III); the second includes 56 papers in the areas of Control Theory and Application (Part IV), Data Mining and Application (Part V), Sensing Control Theory (Part VI), and Signal Processing and Control (Part VII). Both volumes will serve as references for practitioners, faculty, and students to help them quickly incorporate into their work the most recent advancements in these fields and state-of-the-practice of mechanics, electronics, and computing, to efficiently and effectively improve the reliability and feasibility of high-traffic and mission-critical systems.

We extend our gratitude not only to the authors for contributing their ideas, works, and experiences but also to the reviewers for guiding the evaluation and selection of high-quality papers – this book would not have been possible without them. Special thanks also to Mr. Brett Kurzman and Miss Rebecca Hytowitz at Springer US for their valuable assistance with logistical issues throughout the publication process.

Wellesley, MA, USA Wego Wang

ICMS2013 Committee

Advisory Chair	
Andrew Lu	U.S. Jiangsu Economy, Trade and Culture Association, USA
Aniruddha Bhattacharjya	CSE Department, Amrita School of Engineering, Amrita University, Bangalore, India
Jiaxi Hu	Corporate-Social-Responsibility Zhuzhou Institute Co. Ltd, China
Rakesh Kumar Tripathi	Devi Ahilya university Indore, India
General Chair	
Wego Wang	University of Massachusetts Lowell
Yudong Zhao	Columbia University, USA
Zhanming Wei	Fortinet Technologies Inc, Sunnyvale, USA
Program Chair	
PakKin Wong	Macau University, China
Shu-lung Wang	Taoyuan Innovation Institute of Technology, Taiwan, China
Tianhong Yan	China Jiliang University, China
Program Committee	
Abdalhossein Rezai	Academic Center for Education, Culture and Research and Semnan University, Iran
Aihua Mao	South China University of Technology, China
Amitabha Chanda	University Collage of Science, Technology & Agriculture, University of Calcutta, India
Andres Ivan Oliva Arias	Cinvestav IPN Unidad Mérida, Spain
Ashwini Kumar	Institute for Education by Radio-Television Allahabad, India
Baiqiang You	Xiamen University, China
Caihua Kang	National Chiao Tung University, Taiwan, China
Chadwick Carreto Arellano	National Polytechnic Institute Interpenetrating Polymer Network, México
Denis V. Bogdanovich	Moscow State Technical University, Russia
Dongliang Wang	Army Aviation Institute, China
Fuli Zhao	Sun Yat-Sen University, China
Guojie Qin	Beijing Institute of Technology, China
Hong Hu	Harbin Institute of Technology, China

José RAGOT	Université de Lorraine, France
Kleanthis Thramboulidis	University of Patras, Greece
Kumar Dookhitram	University of Technology, Mauritius
Kuswara Setiawan	UPH Surabaya, Indonesia
Long Zhang	University of Science & Technology Beijing, China
Marco Ivan Ramirez Sosa Moran	Instituto Tecnologico de Nuevo Leon, México
Mohamed Chtourou	National School of Engineering, Sfax-Tunisia
Muhammad Naufal Bin Mansor	University Malaysia Perlis
Rajiv Kumar Chechi	Haryana College of Technology and Management Technical campus, India
Reggie C. Gustilo	De La Salle University Manila, Philippines
Sabina Jeschke	Rheinisch-Westfaelische Technische Hochschule Aachen University, Germany
Taiwo	Obafemi Awolowo University, Nigeria
Tao Li	Institute of Electrical Engineering Chinese Academy of Sciences, China
Tiecheng Xia	Shanghai University, China
Tse-Chen Yeh	Academia Sinica, Taiwan, China
Wenbang Sun	The Airforce and Aeronautical University of the People's Liberation Army, China
Wenyong Gong	Jilin University, China
Wenzheng Lai	Ming Chi University Of Technology, Taiwan, China
Xianqiang Yan	University of Science & Technology, Beijing, China
Xiaobing Sun	Southeast University, China
Xiaoshan Chen	Naval Engineering University of the People's Liberation Army, China
Xingfei Yuan	Zhejiang University, China
Yanbo Zhang	Henan University, China
Yang Zhang	Emhiser Research, Inc., USA
Yi Li	Hefei Nova Institute of Technology, China
Yudong Gao	National University of Defense Technology, China
Yu-ying Shi	North China Electric Power University, China
Yuxia Sun	Jinan University, China
Zielinska Teresa	Warsaw University of Technology, Poland

Contents

Part I
Advanced Mechanics and Mechatronics

Multi-point Pitting Corrosion Fault Diagnosis on Rolling Element Bearing of Vibrating Machine

Xuanming Zhao, Baoliang Guo, and Zhishan Duan

Abstract According to the mechanical vibration of rolling element bearing multi-point pitting fault diagnosis problems, the vibration model of the multi-point pitting corrosion fault was built in the vibrating machine rolling element bearing with inner ring and outer ring based on Hertz contact theory. We proposed a criterion of multi-point pitting failure, simulated the theoretical model, and did some research on the vibrant screen. There is an obvious phenomenon of amplitude modulation when vibrating machine rolling element bearing has an outer ring pitting fault, but the phenomenon of amplitude modulation was shown when rotating machine rolling element bearing has an outer ring pitting fault, which was shown by theoretical analysis and experimental results. There is a slight amplitude modulation phenomenon when vibrating machine rolling element bearing has an inner ring pitting fault, and there is phenomenal of amplitude modulation when rotating machine rolling element bearing has an inner ring pitting fault.

Keywords Fault diagnosis • Discrimination criterion • Vibrating machine • Rolling element bearing • Multi-point pitting corrosion

X. Zhao (✉)
College of Energy Engineering, Yulin University, Yulin, China

School of Mechanical and Electrical Engineering, Xi'an University of Architecture and Technology, Xi'an, China
e-mail: gamezxm@163.com

B. Guo • Z. Duan
School of Mechanical and Electrical Engineering, Xi'an University of Architecture and Technology, Xi'an, China

W. Wang (ed.), *Mechatronics and Automatic Control Systems*, Lecture Notes in Electrical Engineering 237, DOI 10.1007/978-3-319-01273-5_1,

1 Introduction

Vibration method can diagnose the majority of rolling element bearing fault. There are many kinds of methods to diagnose the rolling element bearing fault using the vibration signal. The envelope demodulation analysis method can separate the vibration shock feature information from complex modulation vibration signal. Modulation theory and envelope demodulation method is always the focus of attention of many scholars. The envelope demodulation analysis method is the one of the most successful methods of bearing fault diagnosis [1]. McFadden and Smith [2, 3] first put forward that theory and establish a rolling element bearing inner ring local single-point and multi-point pitting failure vibration model. TANDON and Choudhury [4, 5] popularized this method which can use for the rolling element bearing element single-point of pitting fault diagnosis. Yang Jiang-xin et al. [6, 7] further refinements of the method by added the system noise into the rolling element bearing inner and outer rings of single point pitting corrosion fault diagnosis model. Kiral and Karagulle [8] established the finite element analysis of vibration model to simulate each component of rolling element bearing single-point or multi-point pitting fault, and using the envelope demodulation analysis method to analyze the fault characteristic frequency in the end. The above theory research also yielded consistent results on rotating machinery in the static radial load bearing pitting fault diagnosis. However, vibrating machine is a kind of machine which working applied the principle of vibration. That's ball bearing radial load is dynamic load which amplitude and direction is changing. But the rotor balancing of rotating machinery's rolling element bearing radial load amplitude and direction is constant. The work principle and structure are very different between these two kinds of machine. Therefore, the bearing fault model that established by former can't be directly used for vibration fault diagnosis of rolling element bearing.

This paper based on the analysis of mechanical vibration on rolling element bearing working state, and it improved the pulse impact model of envelope demodulation theory analysis method, which is suitable for vibration machine. And then proposes the distinguish basis of vibration machine rolling element bearing inner ring and outer ring pitting fault.

2 Establish a Vibration Model of Rolling Element Bearing Inner Ring and Outer Ring Multi-Point Pitting Fault

I take a two-point pitting fault as example. If the rolling element bearing inner-outer ring raceway and rolling body has no relative sliding in the running process. The inner ring is fixed to the rotating shaft and rotates along with the shaft to rotate together. The outer ring is fixed to the bearing seat. We only consider about the undamped case. Rolling element bearings during operation under external loading conditions was shown in Fig. 1. The inner or outer ring has two pitting faults. In

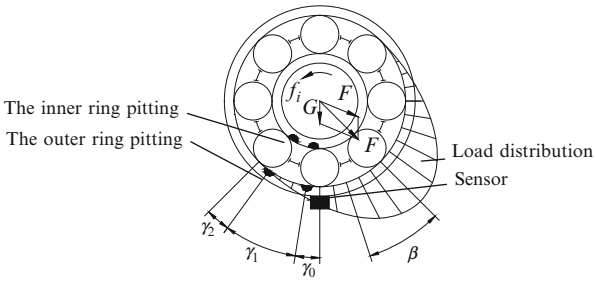

Fig. 1 Rolling element bearing of vibrating machine two-point pitting diagram

order to facilitate analysis, a sensor is mounted under the bearing, the angle of the sensor and the first pitting failure is γ_0, the angle of two pitting failure is γ_1, The angle of second pitting failure and rotating direction adjacent the rolling body is γ_2.

In diagram: F_r – radial load; F – exciting force; G – shafting gravity; β – azimuth; f_i – rotation frequency of the inner ring.

$$\begin{cases} F_r \cos\alpha = G + F\cos\varphi \\ F_r \sin\alpha = F sin\varphi \end{cases} \tag{1}$$

In formula: α – angle of F_r and G, $\alpha \in (0, \pi/2)$; φ – angle of F and G, $\varphi = 2\pi f_i t$

From the formula (1), we can obtain as follows

$$\begin{cases} F_r = \sqrt{G^2 + F^2 + 2GF\cos\varphi} \\ \alpha = \arcsin\left(\dfrac{F\sin\varphi}{F_r}\right) \end{cases} \tag{2}$$

From the formula (2), we can learn that radial load F_r along with the rotation of the rotating shaft whose amplitude and direction are constantly changing.

$$\gamma_2 = k\frac{2\pi}{Z} - \gamma_1 - \gamma_0, k = 1,2,\ldots \tag{3}$$

In formula: k—second pitting of the rolling body interval number

According to the classical Hertz theory, The relationship between single ruling body of the bearing and the inner, outer ring raceway generated by nonlinear contact deformation δ and the rolling body load relationship Q [9, 10].

$$Q = K\delta^{3/2} \tag{4}$$

where K – load – displacement coefficient

Radial load F_r is equal to the sum of load of rolling element components:

$$F_r = ZQ_{\max}(\varphi)J_r(\varepsilon) \tag{5}$$

$$J_r(\varepsilon) = \frac{1}{2\pi}\int_{-\beta_L}^{\beta_L}\left[1-\frac{1}{2\varepsilon(\varphi)}(1-\cos\beta)\right]^{\frac{3}{2}}\cos\beta d\beta \tag{6}$$

From the formulas (4) and (5), we can obtain as follows

$$\delta_{\max}(\varphi) = \left(\frac{F_r(\varphi)}{ZKJ_r(\varepsilon)}\right)^{\frac{2}{3}} \tag{7}$$

where ε – load distribution coefficient;

$$\varepsilon(\varphi) = \frac{1}{2}\left(1-\frac{P_d}{P_d+2\delta_{\max}(\varphi)}\right) \tag{8}$$

where P_d – radial clearance;

The angular range of load area which was determined by radial clearance is

$$\beta_L(\varphi) = \arccos\left(\frac{P_d}{P_d+2\delta_{\max}(\varphi)}\right) \tag{9}$$

From the formula (4), we can obtain as follows

$$Q_{\max}(\varphi) = K\delta_{\max}(\varphi)^{3/2} \tag{10}$$

Load distribution function $Q(\beta)$ is

$$Q(\beta) = \begin{cases} Q_{\max}(\varphi)\left[1-\frac{1}{2\varepsilon(\varphi)}(1-\cos\beta)\right]^{\frac{3}{2}} & |\beta| \le \beta_L \\ 0 & |\beta| > \beta_L \end{cases} \tag{11}$$

From the formula (11), we can learn that load distribution curve is a dynamic curve. The amplitude and direction are constantly changing.

In the unit load, The first roller body through the first pitting fault instantaneous impact force generated by the contact is $d_1(t)$, The rotation direction of a ruling body through second pitting fault transient impact force for contact is $d_2(t)$. It can be approximated as two cycles as T_d. Amplitude rectangular pulse with the width of T_v. The relation between these can be expressed as

$$d_1(t) = \begin{cases} d(m\cdot T_d + t), m = 1, 2\ldots & \\ A & 0 < t < T_v \\ 0 & T_v < t < T_d \end{cases}. \tag{12}$$

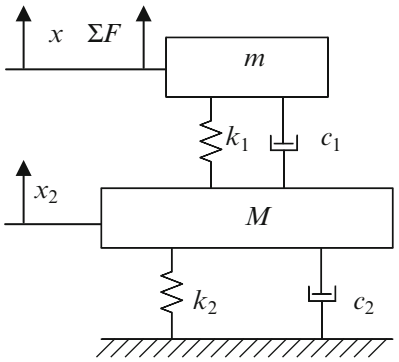

Fig. 2 Vibration mode of vibration machine rolling element bearing

$$d_2(t) = \begin{cases} d(m \cdot T_d + t + tc), m = 1, 2 \ldots \\ A \qquad\qquad\qquad 0 < t < T_v \\ 0 \qquad\qquad\qquad T_v < t < T_d \end{cases} . \tag{13}$$

In formula: A – two pulse amplitude; tc – Time interval; $tc = \gamma_2/2\pi f_i$.

Sequence cycle T_d related with pitting fault location, is the reciprocal of fault frequency. Pulse width T_v shows the time which rolling bodies through pitting fault position.

When the bearing rotates, the rolling body through multi-pitting failure generates a sequence of pulses is $d(t)$, show as:

$$d(t) = d_1(t) + d_2(t) \tag{14}$$

Under distributed load, the pulse force which generated by the rolling body through the inner or outer ring pitting failure is F_{mc}, it can be expressed as

$$F_{mc} = d(t) \times Q(\beta) \tag{15}$$

The mechanical vibration of rolling element bearing system is simplified as two order of two degree of freedom spring damping system. The basic model was shown in Fig. 2. In figure, k_1 is bearing equivalent stiffness, c_1 is bearing equivalent damping, m is bearing equivalent mass, k_2 is spring element stiffness of vibration machine. c_2 is the damping element's damping of vibration machine. M is participating mass. In order to establish the differential equations of system, set the system static equilibrium position as the zero of the system.

$$\begin{pmatrix} m & \\ & M \end{pmatrix} \begin{pmatrix} \ddot{x}_1 \\ \ddot{x}_2 \end{pmatrix} + \begin{pmatrix} c_1 & -c_1 \\ -c_1 & c_1 + c_2 \end{pmatrix} \begin{pmatrix} \dot{x}_1 \\ \dot{x}_2 \end{pmatrix} + \begin{pmatrix} k_1 & -k_1 \\ -k_1 & k_1 + k_2 \end{pmatrix} \begin{pmatrix} x_1 \\ x_2 \end{pmatrix} = \begin{pmatrix} \sum F \\ 0 \end{pmatrix} \tag{16}$$

For inner ring pitting corrosion condition,

$$F = F_r(\varphi)\cos\alpha + F_{mcin1}\cos(\gamma_0 + \varphi) + F_{mcin2}\cos(\gamma_0 + \gamma_1 + \varphi) \tag{17}$$

In formula: F_{mcw1} — the outer ring first pitting pulse impact force, F_{mcw2} — the outer ring second pitting pulse impact force;

$$F = F_r(\varphi)\cos\alpha + F_{mcw1}\cos\gamma_0 + F_{_{mcw2}}\cos(\gamma_0 + \gamma_1) \tag{18}$$

Put formula (17) and formula (18) into the formula (16), we can get the vibration machine rolling element bearing inner ring and outer ring multi-point pitting pulse shock model.

3 Model Simulation Analysis and Experimental Research

The test of vibrating screen model is SDM00, is double-shaft motor multifunctional vibration screen. The model of two motors both is Y90S-6. Synchronous speed is 1,000 rpm, same as 16.67 Hz. The model of rolling element bearing is 1,308, with double line, each line has 15 rolling bodies. Theoretical calculation of outer race fault characteristic frequencies is 104.18 Hz, Inner race fault characteristic frequency is 145.82 Hz. The rolling body revolution frequency is 6.95 Hz, $\gamma_0 = 0°$, $\gamma_1 = 2°$, $\gamma_2 = 10°$. Due to the actual bearing manufacturing, installation and motor speed, load change caused the actual bearing fault frequency and calculation of fault frequency have deviation.

The inner two-point pitting failure simulation results were shown in Fig. 3. The measured results were shown in Fig. 4. Figure 5 is the measured time domain waveform and envelope spectrum of the inner single pitting. Figures 2 and 3 show that, the amplitude of the response was showed slight modulation phenomenon. There are amplitude relatively large inner fault frequency f_{bpi} and frequency doubling appeared in its' fault feature spectrum. Theoretical simulation is coincident with experimental results at amplitude smaller side frequency $nf_{bpi} \pm f_i (n = 1,2,\ldots)$ and modulation frequency f_i. For example, large amplitude as 145.7, 291.4 Hz are inner fault frequency and frequency doubling in Fig. 3c. Frequency as 129.1 and 162.1 Hz are the inner ring fault frequency 145.7 Hz's side frequency. Frequency as 275 and 308.2 Hz are the inner ring fault frequency 291.4 Hz's side frequency etc. Large amplitude as 144.96, 289.92 Hz are inner fault frequency and frequency doubling in Fig. 4b. Frequency as 273.51 and 306.7 Hz are the inner ring fault frequency 289.92 Hz's side frequency. Frequency as 418.47 and 451.66 Hz are the inner ring fault frequency 435.26 Hz's side frequency etc. The frequency distribution in Figs. 4b and 5b

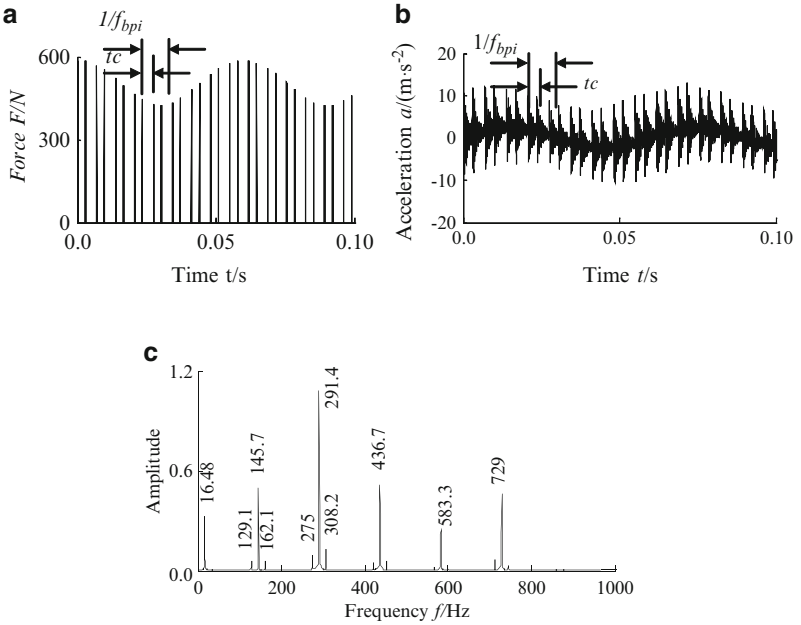

Fig. 3 The inner two-point pitting failure simulation (**a**) pulse impact force (**b**) time domain waveform (**c**) frequency spectrum of fault characteristic

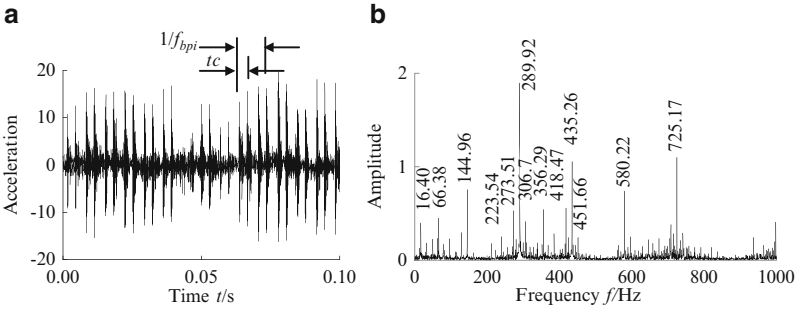

Fig. 4 The inner two-point pitting failure (**a**) time domain waveform (**b**) frequency spectrum of fault characteristic

are the same. Figures 3c, 4b, and 5b show that fault characteristic frequency in two-point pitting and single point pitting are the same. But in the selected parameters, two-point pitting failure characteristic spectrum of 2 f_{bpi} was higher than that of f_{bpi}. In the single point pitting failure feature spectrum is exactly the opposite. Two-point pitting fault waveform in Figs. 3b and 4a is obviously

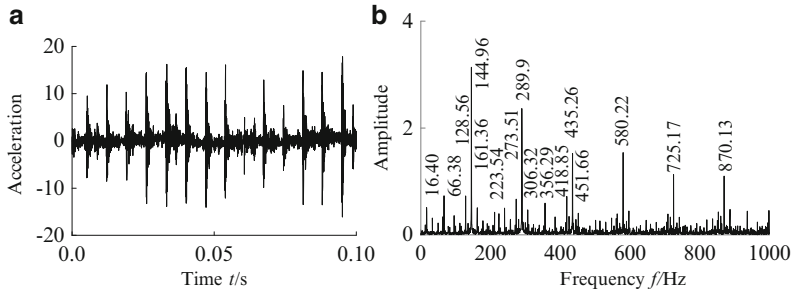

Fig. 5 The inner single point pitting failure (**a**) time domain waveform (**b**) frequency spectrum of fault characteristic

different with the single pitting failure time domain wave in Fig. 5a. It can be clearly distinguished two-point pitting and single point pitting.

The outer ring two-point pitting failure simulation results were shown in Fig. 6. The measured results were shown in Fig. 7. Figure 8 is the measured time domain waveform and envelope spectrum of the outer ring single pitting. Figures 6 and 7 show that, the amplitude of the response was showed significant modulation phenomenon. There are amplitude relatively large outer fault frequency f_{bpi} and frequency doubling appeared in its' fault feature spectrum. Theoretical simulation is coincident with experimental results at obviously amplitude side frequency $nf_{bpi} \pm f_i (n = 1,2,\ldots)$ and modulation frequency mf_i. For example, Frequency as 104.4, 208.8, 312.2 Hz etc. are outer fault frequency and frequency doubling in Fig. 6e. There is obvious side frequency distributed around this frequency. For example, Frequency as 103.39, 206.76, 310.52 Hz etc. are outer fault frequency and frequency doubling in Fig. 7b. There is big amplitude side frequency distributed around this frequency. For example, frequency as 173.57, 190.35, 223.54, 239.94 Hz is 206.76 Hz's side frequency. Frequency as 293.73, 326.92 Hz is 310.52 Hz's side frequency. Side frequency is very obvious, distribution regularity. The obvious spectral line in low frequency part is 33.19 Hz, It is the frequency doubling of the inner ring frequency f_i, obvious amplitude, the system has obvious modulation phenomenon. he frequency distribution in Figs. 7b and 8b are the same. Figures 6e, 7b, and 8b show that fault characteristic frequency in rolling element bearing two-point pitting and single point pitting are the same. But in the selected parameters, two-point pitting failure characteristic spectrum of 2 f_{bpi} was higher than that of f_{bpi}. In the single point pitting failure feature spectrum is exactly the opposite. Two-point pitting fault waveform in Figs. 6d and 7a is obviously different with the single pitting failure time domain wave in Fig. 8a. It can be clearly distinguished two-point pitting and single point pitting.

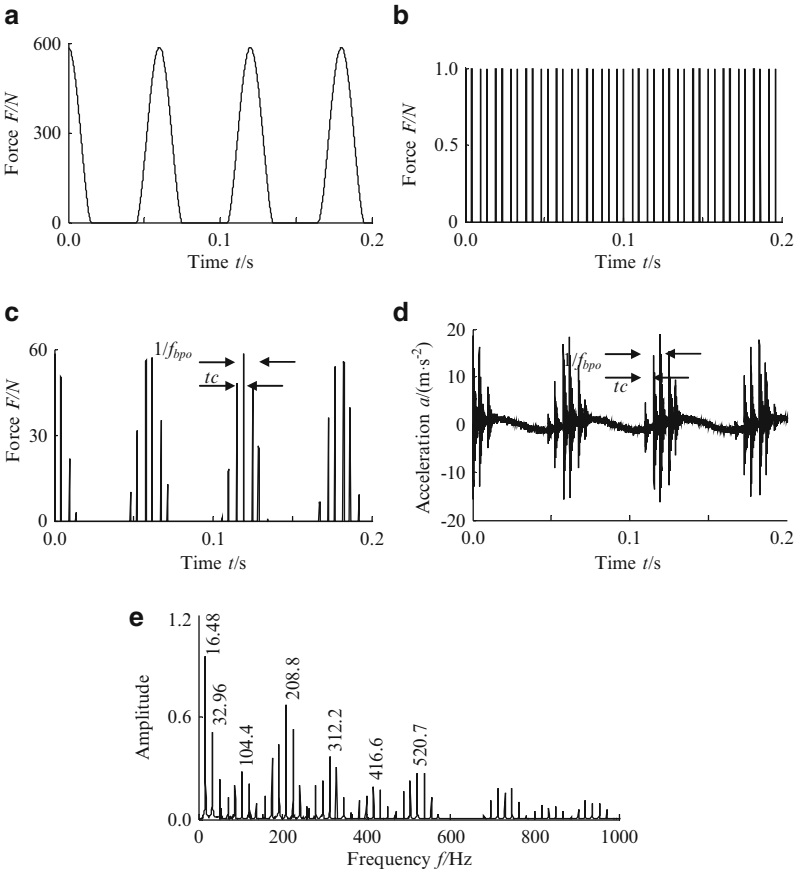

Fig. 6 The outer ring two pitting failure simulation (**a**) load distribution function (**b**) unit impulse force series (**c**) pulse impact force (**d**) time domain waveform (**e**) frequency spectrum of fault characteristic

4 Conclusion

Based on the mechanical vibration of rolling element bearing multi-point pitting fault diagnosis problems, this article built the vibration model of the multi-point pitting corrosion fault in the vibrating machine rolling element bearing with inner ring and outer ring based on Hertz contact theory. We proposed a criterion of multi-point pitting failure, simulated the theoretical model, and did some research on the vibrant screen. We get the following conclusions.

I establish multi-point pitting failure vibration model of vibration machine, and the simulation analysis is carried out.

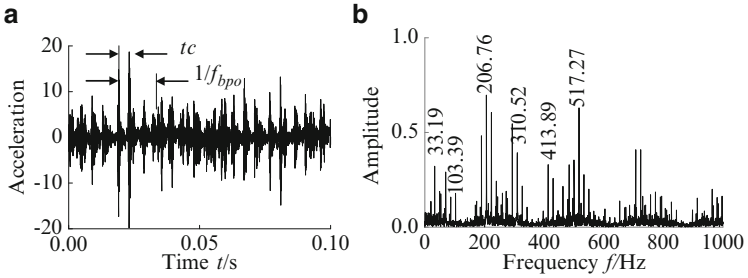

Fig. 7 The outer two-point pitting failure (**a**) time domain waveform (**b**) frequency spectrum of fault characteristic

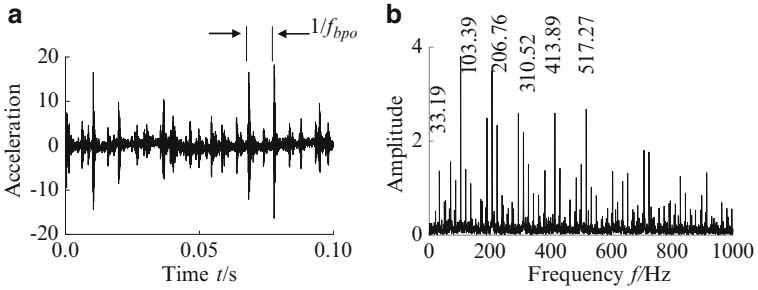

Fig. 8 The outer single point pitting failure (**a**) time domain waveform (**b**) frequency spectrum of fault characteristic

1. When the outer ring of the rolling element bearing of vibration machine has multi-point pitting failure, there is an apparent modulation phenomenon at the response amplitude. There is an apparent amplitude side frequency around the outer ring of the fault characteristic frequency, and rotation machine didn't have modulation phenomenon.
2. When the inner ring of the rolling element bearing of vibration machine has multi-point pitting failure, there is a slight modulation phenomenon at the response amplitude. There is a slight amplitude side frequency around the outer ring of the fault characteristic frequency, and rotation machine has apparent modulation phenomenon.
3. Multi-point pitting and single point fault characteristic frequency of rolling element bearing of vibration machine are same.

References

1. Zhefei Hou (2010) Research on key techniques for fault diagnosis of rolling element bearing in heavy noise. Wuhan University of Technology, Wuhan, In Chinese
2. McFadden PD, Smith JD (1984) Model for the vibration produced by a single point defect in a rolling element bearing. J Sound Vib 96(1):69–82
3. McFadden PD, Smith JD (1985) The vibration produced by multiple point defects in a rolling element bearing. J Sound Vib 98(2):263–273
4. Tandon N, Choudhury A (1997) An analytical model for the prediction of the vibration response of rolling element bearings due to a localized defect. J Sound Vib 205(3):164–181
5. Zhongmin Zhang, Wenxiang Lu, Shuzi Yang et al (1997) A model for the vibration produced by local faults in roller bearing and its application. J Huazhong Univ Sci Technol 25(3):50–53, In Chinese
6. Jiangxin Yang, Chongfeng Cao, Yanlong Cao et al (2007) Model for dynamic characteristics produced by inner race local defect in ball bearing system and its simulation. J Zhejiang Univ (Eng Sci) 41(4):551–555, In Chinese
7. Chongfeng Cao, Jingwei Song, Qiuhong Wang (2005) Dynamic characteristics for the part fault of outer race in ball bearing and computer simulation. J East China Jiaotong Univ 22 (2):123–126, In Chinese
8. Kiral Z, Karagulle H (2006) Vibration analysis of rolling element bearings with various defects under the action of an unbalanced force. Mech Syst Signal Process 20(8):1967–1991
9. Harris TA, Kotzalas MN (2009) Rolling bearing analysis. In: Luo Jiwei, et al Transfer. China Machine Press, Beijing, pp 82–85 (In Chinese)
10. Jiwei Luo, Tianyu Luo (2009) Rolling bearing analysis calculation and application. China Machine Press, Beijing, pp 45–62, In Chinese

Finite Element Analysis on Internal Locking Device of Switch Machines and Design of Profiled Pin Hole

Yuguang Liu, Long Wang, and Lichen Shi

Abstract In order to solve the stress concentration in a pinhole, which is caused by the bending deformation, a kind of Noncircular Pin Hole Technology is used in this paper. The locking mechanism of switch machine is used as an example. The manuscript deduced the deflection curve equations of the pin hole. And a designed hole model according to the equations is generated by Abaqus software. The analysis of the FEA results shows that, the maximum stress of the pinhole is reduced to 53.95 MPa from 117.2 MPa, and there is no stress concentration. The noncircular pinhole designed based on the reflection curve can effectively solve the stress concentration.

Keywords Noncircular pinhole • Switch machine • Locking mechanism • Stress concentration • Abaqus • Bending deformation

1 Introduction

With the development of railway transportation, switch machine's locking mechanism plays an important role on safety and reliability of the train. We made finite element analysis of the main parts of an internal locking mechanism – the action rod and the locking shaft. At the same time we try to solve the stress concentration and stress excessive of action rod pin hole by using abnormal pin hole.

Cylinder pin hole concludes oval pin hole, unloading chamber pin hole and the inner cone pin hole. Many foreign companies such as BO-HAI in the US, WWY of the British, already use this technology in their production. But this technology is confidential to some degree. In domestic China little research could be found, and the research mostly was focused on the design of the engine piston profiled pin hole

Y. Liu (✉) • L. Wang • L. Shi
College of Mechanical and Electrical Engineering, Xi'an University of Architecture and Technology, Xi'an, China
e-mail: ly041@163.com; 1052771244@qq.com; 35531342@qq.com

W. Wang (ed.), *Mechatronics and Automatic Control Systems*, Lecture Notes in Electrical Engineering 237, DOI 10.1007/978-3-319-01273-5_2,

(the pin is the type of both ends fixed and force in the middle) [1]. In this paper, we made a model of a kind of common general pin hole pin structure (pin one end fixed and the other one end of the force), and proposed a method to design its cylinder pin hole.

2 The Principle of Switch Machine's Internal Locking Device

The working principle of the locking mechanism is shown in Fig. 1. The locking block and the actuating rod are connected by a locking shaft and a sliding bearing. At the beginning, the mechanism is in left locked state, the operation rod cannot move to the left, while locking block 2 cannot be rotated (as shown in Fig. 1a) because of the limitation of supporting iron connected to the screw nut. The locking block 1 and action rod will move to the left together while the supporting iron connected on the screw nut clash locking block 1 during the screw moved leftward drive screw nut. And at the same time, the locking block 2 rotates counterclockwise, which lead to revoking lateral constraint (shown in Fig. 1a, b) between the locking block 2 and the locking iron. When the actuating rod moves to the desired position (shown in Fig. 1c), the locking block 1 rotates counterclockwise, and creates a lateral constrain with the locking iron. As a result the action rod can't move to the right. At the same time the supporting iron has limited the rotation of the rotation of the locking block 1. The mechanism is in the right latching state after the rotation of the action is completed. The left locking action process is similar to the above, but in the opposite direction.

3 Finite Element Analysis of Key Parts

This paper focuses on the force situation of the locking shaft and the action rod. According to the drawings provided by the factory, by using Abaqus software, we established the finite element model of the action rod, locking shaft and sliding

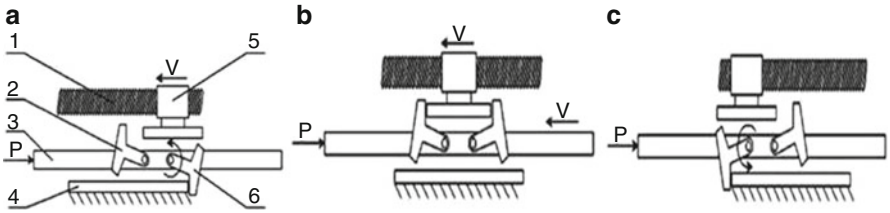

(1-screw; 2-locking block; 3-action rod;
4-locked iron; 5-screw nut; 6-locking block2)

Fig. 1 The working principle of the locking mechanism

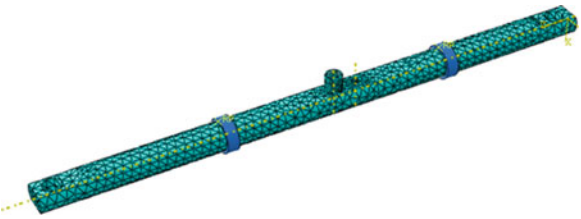

Fig. 2 The finite element model of the action rod and locking shaft

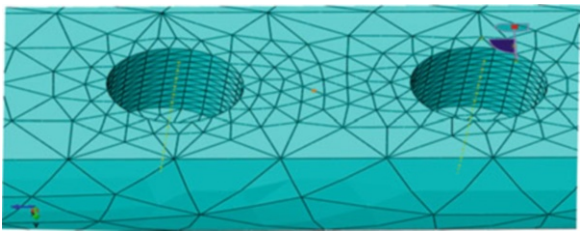

Fig. 3 The refinement of the grid

bearings. The material of action rod and locking block is steel 45, locking shaft is 40Cr, and sliding bar is lead bronze. To be similar to the real situation, at both ends of the action rod a rigid body ring is used to analog the support and constraint of the chassis to the action rod. Tetrahedral free meshing is used. Meshing unit property is C3D10. The whole model is shown in Fig. 2. And refinement of the grid is carried out in the contact portion and in the places where the stress concentration may occur, as shown in Fig. 3.

Contact constraints on the model are established. There are seven pairs of contact surfaces. According to the experimental data, suppose that the sliding bearings and supporting solid on both ends are fixed, 4.49 Mpa surface loads are applied. After calculation, the stress cloud is as Fig. 4.

As we can see, the maximum stress occurs in the contact part between the pinhole opening and the locking shaft. The maximum equivalent stress of action rod pin hole is 117.2 Mpa. The stress concentration phenomenon in the pin hole opening part is very obvious, which will bring out obvious impact on the fatigue life of the parts.

4 General Cylinder Pin Hole and Pin Shaft Statically Indeterminate Model and Amount Deformation Calculation

The profiled pin hole usually reduced pressure arc (the unloading chamber) pin hole, oval pin hole, the inner cone pinhole three kinds, which the best of pin hole is the inner cone [1–3]. In this article, the research object is calculated based on the inner cone pinhole, the design method of the special-shaped pin holes [1], and

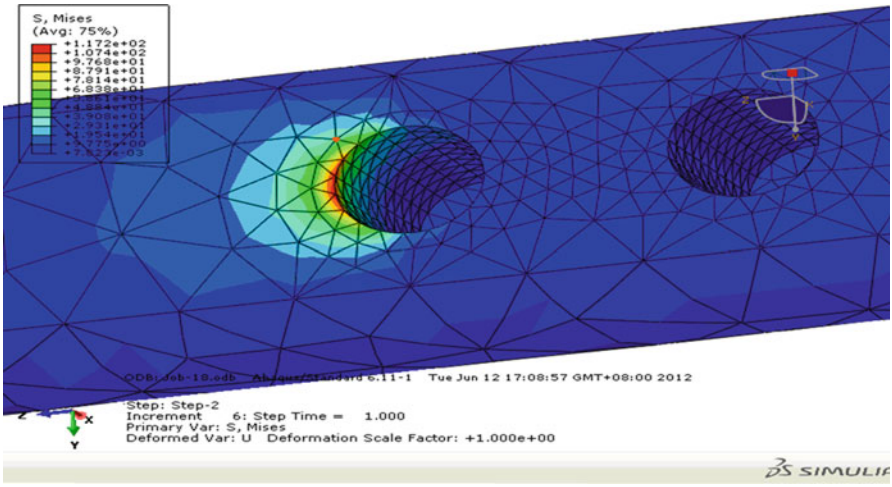

Fig. 4 The stress cloud

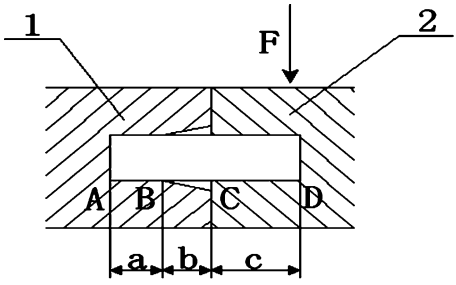

Fig. 5 General cone shaped pin holes of the structure

planetary reducer coupling pin deformation calculation method [4, 5], proposed general pin connection pin deflection curve equation and shaped pin hole design method.

General cone shaped pin holes of the structure is shown in Fig. 5. Part 1 is fixed, while the stress on part 2 is F. The contract length of the cylinder pin hole with pin shaft is AB, its value is a. The tapered surface length of the cylinder pin hole is BC, its value is b. The contract length of pin hole two and pin shaft is CD, its value is c.

According to the result of the amount of the finite element calculation and the analysis of pin shaft deformation we can see that the pin shaft force is mainly concentrated on pin hole opening and the contact points between the bottom and pin shaft, as shown in Fig. 6. Then pin shaft can be simplified to statically indeterminate beam as shown in Fig. 7.

After analyzing, we can see that the reaction force of point C and point D are the forces pin hole two exerts to pin shaft, respectively represented by F_1 and F_2, as shown in Fig. 8. The pin shaft deformation is a tiny deformation, so the Deformed Superposition Principle can be applied [6]. Suppose that the upward direction of

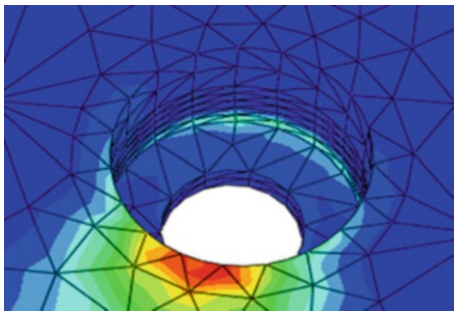

Fig. 6 The pin shaft force

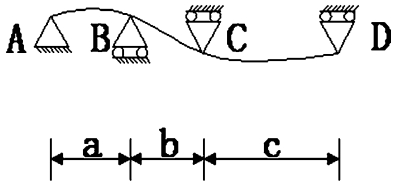

Fig. 7 The pin shaft mechanical model

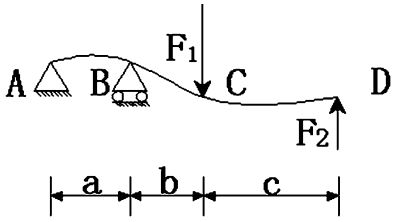

Fig. 8 The pinhole mechanical model

force F is positive, and that downward is negative. Assume that the clockwise direction of Me is positive, and that counterclockwise is negative.

Acted only by F_1, part AB is equivalent to a simply supported beam, which finish B is applied by $Me_1 = -F_1 b$. Sectional twist angle of end B is $\theta_{B-1} = \frac{F_1 ba}{3EI}$. BD can be simplified to a cantilever beam that θ_{B-1} rotating in the roots [6].

Only F_1 applies, the pin shaft deflection curve equation is:

$$\omega_1 = \begin{cases} -\dfrac{F_1 bx}{6EIa}(a^2 - x^2) & ;0 \le x \le a \\ \dfrac{F_1 (x-a)^2}{6EI}(3b - x + a) + \dfrac{F_1 ba}{3EI}(x-a) & ;a \le x \le a + b \\ \dfrac{F_1 b^2}{6EI}(3x - 3a - b) + \dfrac{F_1 ba}{3EI}(x-a) & ;a + b \le x \le a + b + c \end{cases} . \quad (1)$$

The deflection of point C: $\omega_{C-1} = \frac{F_1 b^2}{3EI}(a+b)$

The deflection of D point: $\omega_{D-1} = \frac{F_1 b}{6EI}(2b^2 + 3bc + 2ab + 2ac)$

Similarly, acted only by F_2, part AB is equivalent to a simply supported beam, which finish B is applied by $Me_2 = -F_2(b+c)$. Sectional twist angle of end B is $\theta_{B-2} = \frac{F_2(b+c)a}{3EI}$. BD can be simplified to a cantilever beam that θ_{B-2} rotating in the roots.

Only F_2 applies, the pin shaft deflection curve equation is:

$$\omega_2 = \begin{cases} -\dfrac{F_2(b+c)x}{6EIa}(a^2 - x^2) & ;0 \le x \le a \\ \dfrac{F_2(x-a)^2}{6EI}(3a+3b+3c-x) + \dfrac{F_2 a(b+c)(x-a)}{3EI} & ;a \le x \le a+b+c \end{cases} \cdot \tag{2}$$

The deflection of point C: $\omega_{C-2} = \frac{F_2 b}{6EI}(4ab + 2b^2 + 3bc + 2ac)$

The deflection of point D: $\omega_{D-2} = \frac{F_2(b+c)^2}{3EI}(2a+b+c)$

Due to the limitations of the pin hole two, point C and point D has same deflection, and the deformation coordination equation is: $\omega_{C-1} + \omega_{C-2} = \omega_{D-1} + \omega_{D-2}$

We can get: $\dfrac{F_2}{F_1} = \lambda = -\dfrac{3b^2 + 2ab}{3b^2 + 6ab + 4ac + 6bc + 2c^2}$

In addition, the force on component two can be approximated considered as $F - F_1 - F_2 = 0$

So: $F_1 = \frac{1}{1+\lambda}F$, $F_2 = \frac{\lambda}{1+\lambda}F$

While F_1 and F_2 act together, according to the deformation of the principle of superposition we can know: $\omega = \omega_1 + \omega_2$. The final deflection curve equation can be obtained:

$$\omega = \begin{cases} -\dfrac{Fx(a^2-x^2)}{6EIa(1+\lambda)}(b + \lambda b + \lambda c) & ;0 \le x \le a \\ \dfrac{F(x-a)^2}{6EI(1+\lambda)}[(3b - x + a) + \lambda(3a+3b+3c-x)] + \dfrac{Fa(x-a)}{3EI(1+\lambda)}[b + \lambda(b+c)] & ;a \le x \le a+b \\ \dfrac{F}{6EI(1+\lambda)}\left[b^2(3x-3a-b) + \lambda(x-a)^2(3a+3b+3c-x)\right] + \dfrac{Fa(x-a)}{3EI(1+\lambda)}[b + \lambda(b+c)] & ;a+b \le x \le a+b+c \end{cases} \cdot \tag{3}$$

5 The Design of the Shaped Pin Hole of Action Rod

Inner cone shaped tapered section length of the pin hole is generally about the pin hole length of 1/2, the shortest length is about 1/3 [7].

To inner locking system of switch machine in this article, $F = -4,500$ N, $E = 2$ 10, 000 MPa, $I = \frac{\pi d^4}{64} = 5,153$ mm^4, $a = 15$ mm, $b = 16$ mm, $c = 25$ mm.

According to the deflection curve equation, after the calculation of the Matlab software, the pin deflection curve can be obtained as shown in Fig. 9.

The deflection of the shaped pin hole openings, whose position is $x = 31$ mm, is $\omega_c \approx 0.006$ mm. According to the above results, action rod cylinder pin hole finite element model is established. A decompression arc $R = 1$ mm is taken in the opening. The result of finite element calculation is shown in Fig. 10.

As we can see, the max stress value is 53.95 MPa, which is reduced a lot compared with that of before. Meanwhile, there is an even distribution of stress

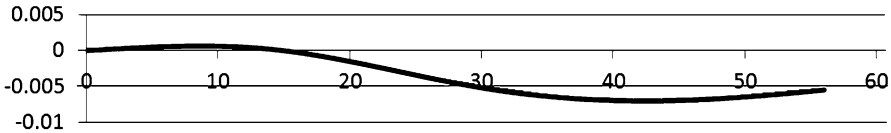

Fig. 9 The pin shaft deflection curve

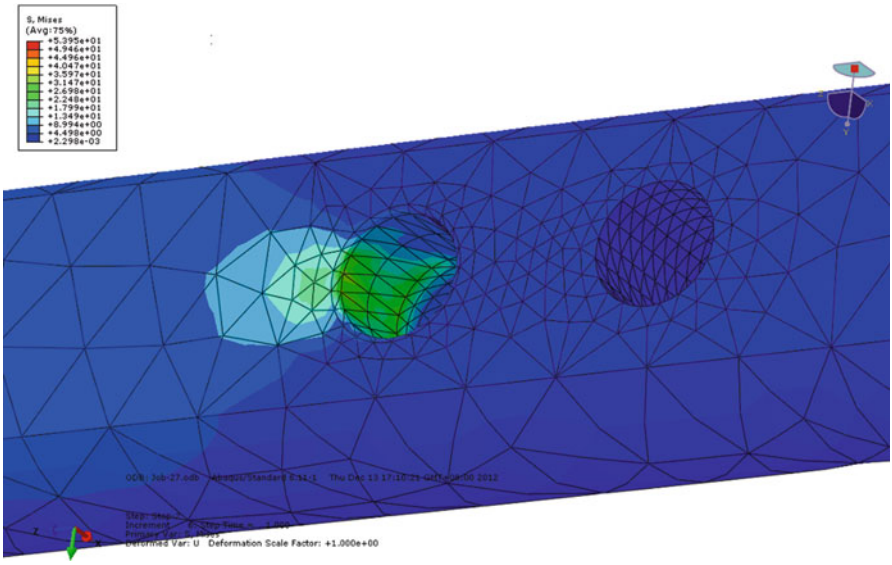

Fig. 10 The shaped pin hole stress cloud

on the cone of pin hole, and not obvious stress concentration. The analysis proves that it is possible to design pin hole by using the deflection curve we deduced above.

6 Conclusion

This paper explained the work principle of a switch machine's internal locking mechanism. A finite element model of the key parts is set up and is analyzed. The statically indeterminate models of general profiled pin hole with the pin shaft are established, and the pin shaft deflection curve equations are derived. A design theory of the cylinder pin hole is put forward. All of these are used in the design of the profiled pin hole. The results show that the above theoretical method is feasible.

Acknowledgements The paper is supported by Scientific research plan projects of Shaanxi Education Department (2010JK619) and Foundation research of Xi'an University of Architecture and Technology (JC1013).

References

1. Jinsong Wu, Shengzhen Wu (1994) Non-cylinder pin hole of piston study. Shijiazhuang Intern Combust Accessories 4:7–13, In Chinese
2. Shiying Liu (2007) Internal combustion engine piston mechanical fatigue damage and reliability research. Shandong University, Jinan
3. Shiying Liu, FengHua Lin, Youzhi Qing et al (2007) Pin hole structure design on the piston effect reliability. Jinan Intern Combus Engine Eng 28(1):46–50, In Chinese
4. Lin Mou (2005) Planetary reducer support plate hole pin type output mechanism of stress and deformation calculation. Zibo Mech Des Res 6:69–71, In Chinese
5. Peng Shan, Wanlu Tian, Jinhai Wen (2003) Less tooth differenced planetary reducer pin shaft type W mechanism pin shaft force analysis. Anshan Mech Design 9:48–50, In Chinese
6. Hongwen Liu (2004) Material mechanics. J 4th edn. Higher Education Press, Beijing, pp 176–197
7. Fangtai Li (2002) Railway switch the locking device strength analysis. Tsinghua University, Beijing

A Calculation Approach to Complete Profile of Noncircular Gear Teeth

Hua Qiu and Gang Deng

Abstract In this paper, the authors propose a practical approach for calculating the complete tooth profile of a noncircular gear based on the fundamental laws of plane gearing and the offset theory of planar curve, together with all details contained in algorithm and numerical solution process. The algorithm not only has a simpler construction and higher calculation efficiency than other published approaches but also no special limitation imposed upon the types of the gear to be dealt with. The approach is explained referring to a machining model using a rack cutter with straight tooth profile to machine the gears; however, it is also applicable to other machining models such as employing a pinion cutter if performing some minor modifications in the algorithm. The effectiveness of the approach is illustrated through a practical example of design and manufacturing for a pair of noncircular gears.

Keywords Noncircular gear • Complete tooth profile • Plane gearing • Offset curve

1 Introduction

As a variable transmission ratio mechanism, noncircular gears have early been researched [1]. However, the difficulties in manufacturing significantly restrict the applications. In most of practical utilizations up to now, elliptical gears are employed since the tooth profile machining is relatively easy.

H. Qiu (✉)
Department of Mechanical Engineering, Kyushu Sangyo University, Fukuoka 813-8503, Japan
e-mail: chiu@ip.kyusan-u.ac.jp

G. Deng
Department of Mechanical Systems Engineering, University of Miyazaki, Miyazaki, Japan

W. Wang (ed.), *Mechatronics and Automatic Control Systems*, Lecture Notes in Electrical Engineering 237, DOI 10.1007/978-3-319-01273-5_3,

With the advances of NC machining technology, in recent years, the circumstance of noncircular gear manufacture is being improved [2]. Thus, in addition to elliptical gears, the noncircular gear transmissions with more general characteristics attract the attentions of researchers and engineers again. Many new applications of noncircular gears have been reported, for example, a planetary gear train built in high performance bicycle [3], a mechanical hinge with variable stiffness applicable to robot [4], a ratio variation system to transmit power and motion continuously [5], and so on. As an unfortunate fact, however, nowadays only a few makers deal with the noncircular gear manufacturing.

Different from circular gears, the tooth profile of a noncircular gear is generated based on the tooth cutting method, the gear pitch curve type and the cutter tooth profile, and thus it is possible that every tooth has a profile distinct from the others. Most of the published analysis approaches provide a calculation method on the profile belong to the working part, in general, but does not deal with the profile of the root fillet, tip and bottom land of the gear tooth [2, 6]. Only a few published calculation models carry out the whole profile of gear teeth but almost limited to elliptical gears, and the authors hardly explained the necessary details contained in the complex numerical solutions, especially, no model gives the method to calculate the tip land profile of the gear tooth [7–9]. Taking the further research and development of noncircular gear transmissions into consideration, for example, manufacturing a mold to mass-produce gears utilized in small devices or analysing the stress and dynamic characteristic in gear meshing [10], the precise and complete profile date of each tooth is required.

This study aims at developing a practical and efficient calculation approach for the complete profile of all teeth of a noncircular gear that possesses a pre-specified pitch curve and is machined by a rack cutter. The approach with a detailed algorithm is expressed in Chap. 2. Moreover, a practical example of design and manufacturing for a noncircular gear pair is presented in Chap. 3 to demonstrate the effectiveness of the proposed approach. Finally, the main conclusions are summarized in Chap. 4.

2 Calculation Method

2.1 Pitch Curves of Noncircular Gears

Figure 1 shows pitch curves of a noncircular gear pair in meshing. Here, θ and r_θ, ϕ and r_ϕ respectively indicate the rotation angle and pitch curve radius for driving and driven gear, and a is the central distance. The values of θ and ϕ are assigned as positive when the driving gear rotates in clockwise direction and the driven gear in counter clockwise direction; otherwise, assigned as negative. If the angular velocity ratio of both gears, $\mathrm{d}\phi/\mathrm{d}\theta$, has been pre-specified in a form of function on θ, r_θ and r_ϕ can be defined as the functions of θ and calculated from the following equation.

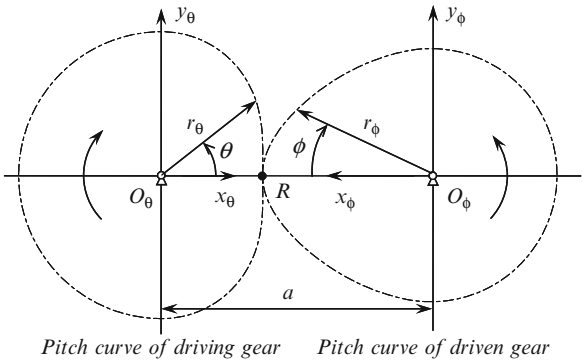

Fig. 1 Pitch curves of noncircular gear pair

$$\boldsymbol{r}_\theta = \frac{\mathrm{d}\phi/\mathrm{d}\theta}{1+\mathrm{d}\phi/\mathrm{d}\theta}a \equiv r_\theta(\theta), \quad r_\phi = \frac{1}{1+\mathrm{d}\phi/\mathrm{d}\theta}a \equiv r_\phi(\theta) \tag{1}$$

For such the pitch curves, it is readily to confirm whether tooth undercutting occurs [7–9]. It should be mentioned that the pitch curve of a gear must be convex if the tooth profile of the gear is machined by a rack cutter, i.e. $\mathrm{d}^2 r_\theta/\mathrm{d}\theta^2 > 0$ and $\mathrm{d}^2 r_\phi/\mathrm{d}\theta^2 > 0$.

In Fig. 1, coordinate frames O_θ -x_θ y_θ and O_ϕ -x_ϕ y_ϕ are respectively fixed on the driving and driven gear, whose origins are set at the rotation center of the gears. Point R is a reference position, where $\theta = 0$ and $\phi = 0$, to measure the rotation angles. The lengths of pitch curve from Point R, S_θ and S_ϕ, can be obtained as follows:

$$\begin{aligned} S_\theta &= \int_0^\theta \sqrt{r_\theta^2 + (\mathrm{d}r_\theta/\mathrm{d}\theta)^2}\,\mathrm{d}\theta = \int_0^\phi \sqrt{r_\phi^2 + \left(\mathrm{d}r_\phi/\mathrm{d}\phi\right)^2}\,\mathrm{d}\phi = S_\phi, \\ \phi &= \int_0^\theta (\mathrm{d}\phi/\mathrm{d}\theta)\mathrm{d}\theta \end{aligned} \tag{2}$$

2.2 Tooth Profiles of Rack Cutter and Gear

In Fig. 2, the graph (a) illustrates the tooth profile of a rack cutter and the graph (b) the tooth profile of the gear to be machined, where m is the module and α_0 is the pressure angle of the cutter tooth. In (a), T_a–T_a' is straight line that generates the bottom land curve of the gear, G_a–G_a' in (b); T_a–T_b and T_a'–T_b' are circular arcs that generate the root fillet curves of the gear tooth, G_a–G_b and G_a'–G_b' in (b); T_b–T_c and T_b'–T_c' are straight lines to generate the working parts of the gear tooth, G_b–G_E and G_b'–G_E' in (b); and T_c–T_d and T_c'–T_d' are circular arcs that do not cut gear blanks in general. The tip land curve, G_E–G_E' in (b), is an offset curve of the gear pitch curve,

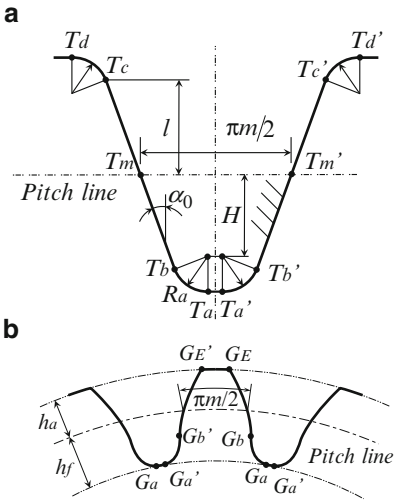

Fig. 2 Tooth profiles of rack cutter and gear

as well as the bottom land curves. In actual noncircular gear manufacturing, the tip land contour has been pre- worked on the blank so this part is not necessary to be cut in tooth profile machining.

2.3 *Profile Calculation of Tip Land and Bottom Land of Gear Tooth*

For a planar parametric curve $\boldsymbol{r}_1(t) = \{x(t), y(t)\}$as shown in Fig. 3, an offset curve $\boldsymbol{r}_2(t)$ that moves through a normal distance h from $\boldsymbol{r}_1(t)$ can be expressed as follows [11]:

$$\boldsymbol{r}_2(t) = \left\{ x(t) \mp \frac{hy'(t)}{\sqrt{x'^2(t) + y'^2(t)}},\ y(t) \pm \frac{hx'(t)}{\sqrt{x'^2(t) + y'^2(t)}} \right\} \tag{3}$$

where the symbol $'$ indicates a differential on t, the upper sign is for an offset having the same direction and the lower sign for an offset along the opposite direction with respect to the unit normal vector $\boldsymbol{n}$ of $\boldsymbol{r}_1(t)$. Therefore, substituting the pitch curve, i.e. Eq. 1 that is defined by the rotation angle θ of the driving gear, together with the addendum value h_a or dedendum value h_f into Eq. 3, the profiles of the tip land and bottom land of the gear tooth can be readily calculated, respectively.

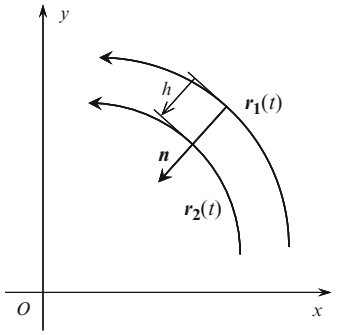

Fig. 3 Offset curve of a planar curve

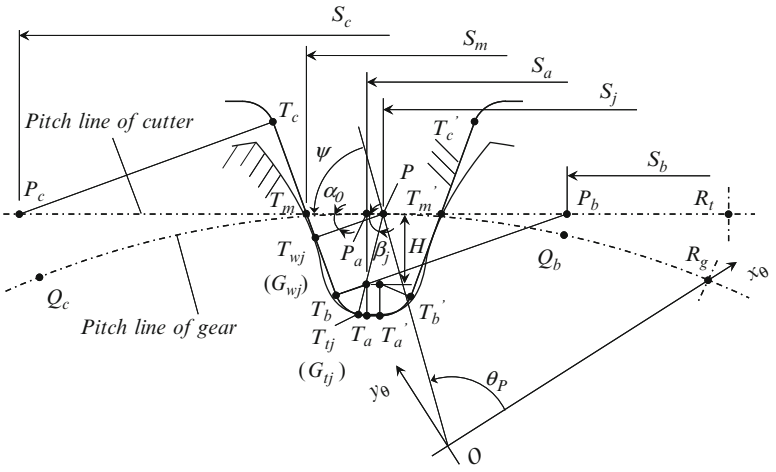

Fig. 4 Generation of tooth profile within working and root fillet areas

2.4 *Profile Calculation of Working Part and Root Fillet of Gear Tooth*

While using a rack cutter to machine a noncircular gear, the pitch line of the cutter (PLC) performs a pure roll without sliding on the pitch curve of the gear (PCG) and the envelope of movement loci of the cutter teeth forms the tooth profile of the gear. At the same time, the normal line at a contact point of the cutter tooth profile with the gear tooth profile must passes through the pitch point of action. Based on these fundamental laws of plane gearing, we can readily derive the analysis relations for calculating the working part and root fillet profile of machined gear tooth.

Figure 4 illustrates the situation of the i-th tooth of cutter machining the i-th tooth space of gear. We set a reference position on the PLC and PCG, Point R_t and Point R_g, for measuring the rolling distance of both the curves. At this position, the PLC starts to roll on the PCG and the rotation angle θ of the gear is set as 0. At a

contact point between both pitch curves, indicated as Point P that corresponds to a gear rotation angle θ_P, the length from Point R_g along the PCG is always equal to that from Point R_t along the PLC. Points P_b, P_c and P_a indicate the intersection points of the PLC with the normal lines at Points T_b, T_c and T_a on the left side of the cutter tooth, which have been defined in Fig. 2. When the gear respectively rotates an angle, θ_b, θ_c or θ_a, Points P_b, P_c or P_a will contact with Point Q_b, Q_c or Q_a on the PCG. Therefore, through substituting the lengths of the points P_b, P_c and P_a along the PLC from Point R_t into Eq. 2 and solving this equation, the values of θ_b, θ_c and θ_a that define the positions of Points Q_b, Q_c and Q_a on the PCG can be obtained.

Moreover, as shown in Fig. 4, the normal line of Point T_{wj} belong to the profile T_b–T_c of cutter tooth passes through the pitch point of action, Point P, so that the position of Point T_{wj} in the gear coordinate frame O-$x_\theta\, y_\theta$ is just the point generated by Point T_{wj} on the working part of the gear tooth, indicated Point G_{wj}. Similarly, in O-$x_\theta\, y_\theta$, a point on the root fillet of gear tooth, Point G_{tj}, is also located at the same position with its generating point T_{tj} on the tip fillet of cutter tooth, if the normal line of Point T_{tj} just passes through Point P. Therefore, writing the position vector of Point P as $\boldsymbol{r}_\theta(\theta_P) = \{r_\theta(\theta_P), \theta_P\}$ in O-$x_\theta\, y_\theta$, the coordinates of the points G_{wj} and G_{tj} can be determined from the following equations.

$$\begin{cases} x_{gwj} = r_\theta(\theta_P)\cos\theta_P + L_{wj}\cos(\theta_P + \alpha_0 + \psi) \\ y_{gwj} = r_\theta(\theta_P)\sin\theta_P + L_{wj}\sin(\theta_P + \alpha_0 + \psi) \end{cases} \tag{4}$$

$$\begin{cases} x_{gtj} = r_\theta(\theta_P)\cos\theta_P + (L_{tj} + R_a)\cos(\theta_P + \beta_j + \psi) \\ y_{gtj} = r_\theta(\theta_P)\sin\theta_P + (L_{tj} + R_a)\sin(\theta_P + \beta_j + \psi) \end{cases} \tag{5}$$

where ψ is the angle of tangential vector of the PCG at $\boldsymbol{r}_\theta(\theta_P)$ and the value is given by Eq. 6.

$$\tan\psi = r_\theta(\theta_P)/\left(\frac{\mathrm{d}r_\theta}{d\theta}\,|_{\theta=\theta_P}\right) \tag{6}$$

Furthermore, from Fig. 4, the values of L_{wj} and L_{tj} in Eqs. 4 and 5 can be obtained as follows:

$$L_{wj} = (S_m - S_j)\cos\alpha_0, \quad L_{tj} = H/\sin\beta_j, \quad \tan\beta_j = H/(S_a - S_j) \tag{7}$$

As shown in Fig. 5, on the other hand, if the normal line of the upper end G_E of the working part of gear tooth corresponds to a pitch point of action, Point P_E, the length from Point R_t to Point P_E along the PLC, S_E, satisfies (8).

$$S_E = \int_0^{\theta_E} \sqrt{r_\theta(\theta)^2 + (\mathrm{d}r_\theta/\mathrm{d}\theta)^2}\,\mathrm{d}\theta \tag{8}$$

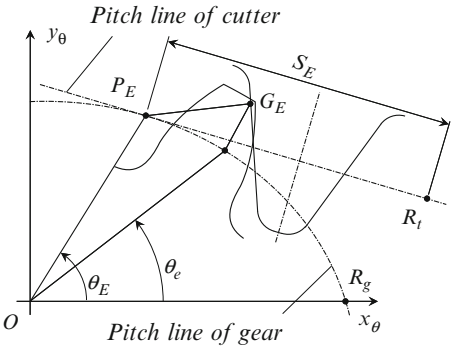

Fig. 5 Determination of apex position of tooth working part

Instituting the gear rotation angle θ_E, which corresponds to Point P_E, into Eq. 4 instead of θ_P, the coordinates of Point G_E, (x_{GE}, y_{GE}) on the frame O-x_θ y_θ, are obtained. At the same time, Point G_E also lies on the tip land of gear, thus (x_{GE}, y_{GE}) satisfy the following equation.

$$\begin{cases} x_{GE}(\theta_E) = x_\theta(\theta_e) + \dfrac{h_a y'_e}{\sqrt{x'^2_e + y'^2_e}}, \quad y_{GE}(\theta_E) = y_\theta(\theta_e) - \dfrac{h_a x'_e}{\sqrt{x'^2_e + y'^2_e}}, \\ x'_e = \dfrac{\mathrm{d}x_\theta}{\mathrm{d}\theta}\Big|_{\theta=\theta_e}, \quad y'_e = \dfrac{\mathrm{d}y_\theta}{\mathrm{d}\theta}\Big|_{\theta=\theta_e} \end{cases} . \tag{9}$$

Therefore, solving Eq. 9 together with Eqs. 4, 6, 7, and 8, the values of the rotation angles θ_E and θ_e that determine the position of Point G_E on the PCG can be obtained.

In the above, we have expressed the calculation method on the profile of the left side of a gear tooth space. Using the similar method, the profile of the right side can be calculated, too.

2.5 *Calculation Algorithm for Complete profile of Gear Teeth*

Under a condition that the central line of the first tooth of rack cutter passes through the reference position on the PLC, the algorithm to calculate the whole profile for all teeth of a driving gear to be machined can be summarized as follows:

(a) Determine the lengths along the PLC, S_{a0}, S_{b0}, S_{a0}' and S_{b0}', corresponding to the characterizing points on the first cutter tooth, i.e. Points T_a, T_b, T_a' and T_b' shown in Figs. 2 and 4. Set the cutter tooth number i as 1.

(b) Let $S_a = S_{a0}+\Delta$, $S_b = S_{b0}+\Delta$, $S_a' = S_{a0}'+\Delta$ and $S_b' = S_{b0}'+\Delta$ with $\Delta = (i-1)\pi m$. By instituting these pitch line lengths into Eq. 2 and solving this

equation, determine the parameter values of corresponding points on the PCG, θ_a, θ_b, θ_a' and θ_b'. Moreover, solve Eq. 9 to determine the values of parameters θ_E, θ_e, θ_E' and θ_e' with respect to the upper ends of the working part of tooth profile.

(c) Properly divide the parameter intervals $[\theta_b, \theta_a]$ and $[\theta_a', \theta_b']$ of the PCG, institute the values θ_{tj}, θ_{tj}' of each dividing point into Eq. 2 to calculate the corresponding lengths S_{tj} and S_{tj}' along the PCG, and finally calculate the coordinates of Point G_{tj} and G_{tj}' belong to the root fillet of the tooth profile with Eq. 5.

(d) Properly divide the parameter intervals $[\theta_b, \theta_E]$ and $[\theta_E', \theta_b']$ of the PCG, institute the values θ_{wj}, θ_{wj}' of each dividing point into Eq. 2 to calculate the corresponding lengths S_{wj} and S_{wj}' along the PCG, and finally calculate the coordinates of Point G_{wj} and G_{wj}' belong to the working part of the tooth profile from Eq. 4.

(e) Properly divide the parameter interval $[\theta_a', \theta_a]$ of the PCG, institute the values θ_{rj} of each dividing point into Eq. 3 to calculate the coordinates of Point G_{rj} belong to the bottom land of the tooth profile. Furthermore, record θ_e as $\theta_{i,L}$, θ_e' as $\theta_{i,R}$.

(f) If $i \geq z$, go to Step (g); otherwise reset $i = i + 1$ then go back to Step (b). Here z is the tooth number of the gear.

(g) Following to the turn of $i = 1, 2, \ldots, z$, properly divide the parameter interval $[\theta_{i-1,L}, \theta_{i,R}]$ of the PCG, institute the values θ_{sj} of each dividing point into Eq. 3 to calculate the coordinates of Point G_{sj} belong to the tip land of the tooth profile but use $\theta_{z,L}$ instead of $\theta_{0,L}$ in the calculation.

(h) Stop.

In Step (b), the Newton–Raphson method is used for numerically solving Eqs. 2 and 9. The Simpson's rule is applied to calculate the integrations of Eqs. 2 and 8.

On the other hand, if we set the central line of the first tooth space of the cutter passing over the reference position of the PLC and employ $r_\phi(\theta)$ instead of $r_\theta(\theta)$, the above algorithm can be also used to calculate the tooth profiles for the corresponding driven gear.

It should be mentioned that, in the proposed algorithm, an iterative numerical solution process is not necessary for calculating the tip land and bottom land profile of gear tooth, and thus the algorithm is more efficient than other approaches published; at the same time, the programming operation can be completed more readily, too. Moreover, the proposed algorithm is also applicable to calculating the tooth profile of a noncircular gear machined by other types of cutter such as a pinion cutter or a cutter with different tooth profile [12]. In such the situation, only some minor modifications according to the pitch curve or tooth profile of the cutter are required to the algorithm.

3 Practical Example

In order to illustrate the application and effectiveness of the proposed approach, a noncircular gear pair was designed and the complete profiles of both driving and driven gears were machined by a wire electric discharge machine based on the calculated profile data.

In this example, the module is 2.5 mm, the tooth number 42 and the central distance 104.637 mm. In the design, a standard tooth profile was employed for rack cutter, the rate of proportional portion and variable portion in angular velocity ratio was set at 1:0.8833, and a modified constant velocity cam curve [13] was adopted to define the angular velocity in the variable portion. The final angular velocity ratio is shown in Fig. 6. As the profile date, 390 points, 20 points for tip land, 10 points for bottom land, 300 points for working part and 60 points for root fillet, were calculated and recorded for each tooth.

Figure 7 illustrates the driving and driven gears meshed at the start position of $\theta = 0$ and $\phi = 0$. Figure 8 is a photograph of the machined gears. Through a simple test, it has been confirmed that both gears rotate and mesh very smoothly under a condition of exactly keeping the designed central distance.

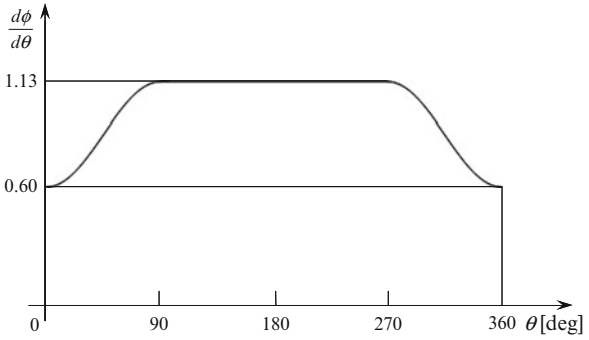

Fig. 6 Angular velocity ratio curve used in the example

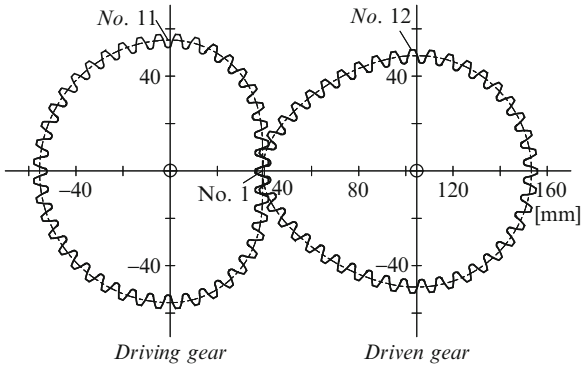

Fig. 7 Contours of noncircular gears in the example

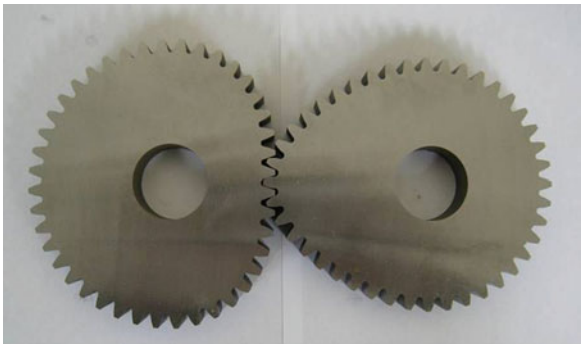

Fig. 8 Photograph of machined gears

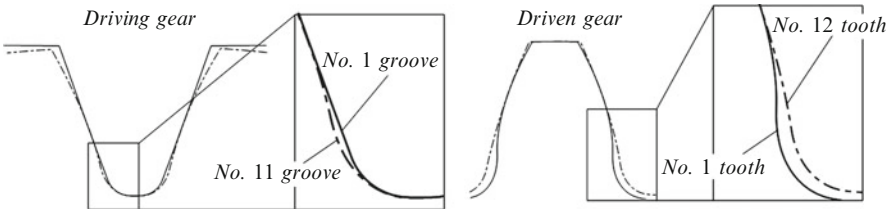

Fig. 9 Comparison of tooth profiles located at different positions

In addition, Fig. 9 shows two comparisons of tooth profile, the first and the eleventh tooth space for the driving gear, and the first and the twelfth tooth for the driven gear. This result sufficiently illustrates that, for a noncircular gear, the profile may remarkably vary at the different positions of the tooth. Therefore, in order to obtain a correct result, the precise and complete profile date is necessary in an analysis of stress and dynamic characteristic for noncircular gear meshing.

4 Concluding Remarks

In this paper, based on the fundamental laws of plane gearing and the offset theory of planar curve, the authors proposed an efficient approach for calculating the precise and complete profile of each tooth of a noncircular gear machined by a rack cutter; at the same time, also provided necessary explanations for the calculation details contained in algorithm and numerical solutions. The proposed algorithm not only has a simpler construction and requires less calculation than other published approaches but also no special limitation imposed upon the types of the noncircular gear to be dealt with. This approach is also applicable to calculating the tooth profile of a noncircular gear machined by other types of cutter such as a pinion cutter or a cutter with different tooth profile, if some corresponding minor

modifications are performed in the algorithm. The effectiveness and applications of the proposed approach has been demonstrated through a practical example of design and machining for a noncircular gear pair.

References

1. Olsson U (1953) Non-circular cylindrical gears, ACTA Polytechnica. Mech Eng Ser 2 (10):1–216
2. Katori H (2001) Design, manufacturing and applications of noncircular gears. The Nikkan Kogyo Shimbun LTD, Tokyo, pp 35–115, in Japanese
3. Mundo D (2006) Geometric design of a planetary gear train with non-circular gears. Mech Mech Theory 41(4):456–472
4. Matsuda T, Murata S (2007) Variable stiffness hinge using non-circular gears. J Robot Soc Jpn 25(3):429–439, in Japanese
5. Komori M et al (2010) Study on the ratio variable system to transmit power and motion continuously. J Jpn Soc Des Eng 45(10):512–519, in Japanese
6. Litvin FL, Fuentes A (2004) Gear geometry and applied theory, 2nd edn. Cambridge University Press, Cambridge, pp 318–349
7. Chang S, Tsay C (1996) Mathematical model and undercutting analysis of elliptical gears generated by rack cutters. Mech Mach Theory 31(7):879–890
8. Bair B (2002) Computer aided design of elliptical gears. Trans ASME, J Mech Des 124 (4):787–793
9. Tsay M, Fong Z (2005) Study on the generalized mathematical model of noncircular gears. Math Comput Model 41(4/5):555–569
10. Barkah D et al (2002) 3D mesh generation for static stress determination in spiral noncircular gears used for torque balancing. Trans ASME, J Mech Des 124(2):313–319
11. Chiu H et al (1993) An analysis using offset curves for profiles, manufacturing and errors of plane cams. JSME Int J, Ser C 36(1):110–118
12. Bair B et al (2007) Mathematical model and characteristic analysis of elliptical gears manufactured by circular-arc shaper cutters. Trans ASME, J Mech Des 129(1):210–217
13. Makino H (1976) Mechanisms of automatic machines. The Nikkan Kogyo Shimbun Ltd, Tokyo, pp 29–31, in Japanese

Modeling and Simulation of Short Circuit Faults in Stator Coils of Brushless DC Motor

Kang Xiangli, Ruiqing Ma, Qingchao Zhang, and Wei Wang

Abstract In order to study inter-turn short circuit and inter-phase short circuit fault more effectively, improved mathematical models of brushless DC motor (BLDCM) with faults in stator coil are built up. To reflect the faults state more accurately, a mathematic formula of self-inductance and mutual-inductance between two windings is presented utilizing waveform analysis of magnetic induction intensity. Based on the mathematical model, simulation waveforms under the two kinds of faults have been obtained in Matlab/Simulink. Through simulation analysis, both inter-turn and inter-phase short circuit faults have concealment and continuing faults will accelerate damage level of motor. The model provides a convenient and economical method for the study of short circuit faults.

Keywords BLDCM • Inter-turn short circuit fault • Inter-phase short circuit fault • Modelling • Simulation

1 Introduction

With speed control superior performance, long service life, high efficiency, and good maintainability, BLDCM has obtained considerable international recognition of electric fields. BLDCM is often used in such systems that need long time continuous stable operation, such as fuel pumps, electric steering gears, etc. On that account, any faults can cause greater effect. Fault detection in electric motors and drive system is a high-profile hot research topic. Correct diagnosis, precise location, and isolation of incipient faults will help to avoid harmful, even devastative consequences to the system [1, 2]. Short circuit faults in stator coils have the characteristics of high concealment which is difficult to detect. However, when

K. Xiangli (✉) • R. Ma • Q. Zhang • W. Wang
School of Automation, Northwestern Polytechnical University, Xi'an, China
e-mail: xiangli@mail.nwpu.edu.cn

W. Wang (ed.), *Mechatronics and Automatic Control Systems*, Lecture Notes in Electrical Engineering 237, DOI 10.1007/978-3-319-01273-5_4,

windings insulation damage leads to short circuit, the temperature of short circuit will rise up. With long-term development, it will aggravate the damage and even lead to single-phase ground short circuit faults and other more serious faults. Therefore, the research of short circuit faults is necessary.

Swarnakar et al. introduced a simple mathematical model, which simply assumed that the mutual-inductance is proportional to the number of short circuit turns, while the self-inductance is proportional to the square of the number, but didn't specify the model basis [3]. Yang Fang et al. simply quoted the conclusion and even ignored the mutual inductance between the short circuit winding and the remaining winding [4–6].

This paper builds up the mathematical model of a BLDCM with inter-turn short circuit fault and inter-phase short circuit fault. With the waveform analysis of magnetic induction intensity, the mathematic formula of self-inductance and mutual-inductance between two phases has been presented under slot number $q = 1$. In matlab/simulink environment, the dynamic parameters simulation curves of bus bar current, phase current, motor speed and line voltage have been obtained. At last, this paper analyzes the system operation performance under two different short circuit faults.

2 Mathematical Model

2.1 Mathematical Model of Inter-turn Short Circuit Fault

It is assumed that three phase stator windings of BLDCM adopt Y-shaped connection and concentrative fully pitched winding. If inter-turn short circuit fault happens in phase A, short circuit formed a current circulation, as is shown in Fig. 1. Three phases are not symmetrical any more, as is shown in Fig. 2. After inter-turn short circuit fault happened, the short winding would form a closed loop. No matter whether the fault phase was conducted, the closed loop would produce an induced electromotive force with the rotation of the rotor poles, and form a current circulation. This fault current in the circuit flowed to the opposite direction to the normal phase current, and produced resisting force. This paper assumes that current flowing into the neutral point is positive.

Regardless of the eddy current and hysteresis losses, with unsaturated magnetic circuit and ideal power switching device, three-phase winding completely symmetrical, the voltage balance equation with inter-turn circuit fault is as follows.

$$U = RI + Q\frac{dI}{dt} + E \tag{1}$$

Where $U = [\,u_{a'} \quad u_b \quad u_c \quad 0\,]^T$; $R = diag[\,r_{a'} \quad r \quad r \quad r_s\,]$; $I = [\,i_{a'} \quad i_b \quad i_c \quad i_s\,]^T$; $E = [\,e_{a'} \quad e_b \quad e_c \quad e_s\,]^T$;

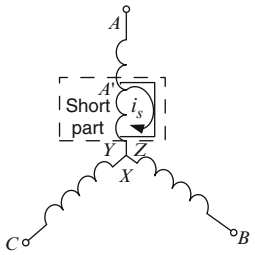

Fig. 1 One phase inter-turn short circuit fault indicator diagram

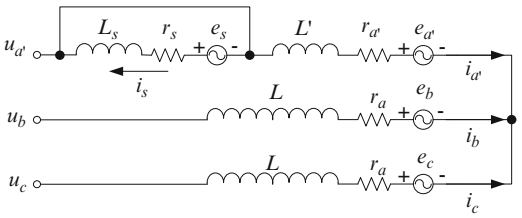

Fig. 2 One phase inter-turn short circuit fault analysis diagram

$Q = \begin{bmatrix} L' & M_{a'b} & M_{a'c} & M_{a's} \\ M_{a'b} & L & M_{bc} & M_{sb} \\ M_{a'c} & M_{bc} & L & M_{sc} \\ M_{a's} & M_{sb} & M_{sc} & L_s \end{bmatrix}$; r, L and K_e are resistance, induction and back-EMF(electromotive force) constant of normal phase respectively. Parameters U, I, E are phase variable matrixes of voltage, current and back-EMF. R is diagonal matrix. Q is induction matrix, and matrix elements subscript a' and s are the rest windings and the short windings of phase A. Because winding resistance, back-EMF constant are proportional to the number of short turns, $r_{a'} = (1 - S_t)r$, $r_{as} = S_t \cdot r$, $K_{e_{a'}} = (1 - S_t)K_e$, $K_{e_{as}} = S_t \cdot K_e$ can be obtained. S_t is the percentage of short turns to total turns in phase A. L' and L_s are the self-induction of the rest winding and the short winding in phase A. M is a mutual-inductance, and its subscript is a pair of winding that produce it.

Based on Kirchhoff's current law (KCL), $i_{a'} + i_b + i_c = 0$. The mutual-inductance between A and B is equal to that between A and C, which is $M_{sb} = M_{sc}$ and $M_{a'b} = M_{a'c}$, so matrix Q can be simplified as

$$Q = \begin{bmatrix} L' - M_{a'b} & 0 & 0 & M_{a's} \\ 0 & L - M_{a'b} & M_{bc} - M_{a'b} & M_{sb} \\ 0 & M_{bc} - M_{a'b} & L - M_{a'b} & M_{sc} \\ M_{a's} - M_{sb} & 0 & 0 & L_s \end{bmatrix} \tag{2}$$

Due to the short circuit, motor torque equation turn into

$$T_e = \frac{1}{\omega}(e_{a'}i_{a'} + e_b i_b + e_c i_c + e_s i_s) \tag{3}$$

Mechanical motion equation is as follows.

$$T_e - T_L = J\frac{d\omega}{dt} + B\omega \tag{4}$$

Where T_e is the electromagnetic torque and unit is $\mathrm{N}\cdot\mathrm{m}$, T_L is the load torque and unit is $\mathrm{N}\cdot\mathrm{m}$, J is the rotational inertia and unit is $\mathrm{kg}\cdot\mathrm{m}^2$, B is the damping coefficient and unit is $\mathrm{N}\cdot\mathrm{m}\cdot\mathrm{s}$, ω is the angular velocity and unit is $\mathrm{rad/s}$.

2.2 Inductance Calculation Method

BLDCM generally adopts fully pitched winding. Suppose that winding coefficient $K_w = 1$, slot number $q = 1$ in each phase per pole, drive current is 120° square wave. When the rotor adopts tiles form permanent magnet steel, within the limits of electrical angle of a pair of poles, three-phase winding distribution is as shown in Fig. 3 below [7]. The waveform of magnetic flux intensity under normal condition is as shown in Fig. 4. The waveform of magnetic flux intensity of the rest winding under inter-turn short circuit fault is as shown in Fig. 5. According to the waveform analysis of magnetic induction intensity, Inductance calculation formula can be obtained by the following analysis.

When pole-pairs is one, the self-induction of phase A is

$$L_a = \frac{\Psi_a}{I_a} = \frac{\pi\mu_0 W^2 l_d r_d}{2\delta_i} = L$$

The mutual-induction between phase A and phase B is

$$M_{ab} = \frac{\Psi_{ba}}{I_a} = -\frac{1}{3}\frac{\pi\mu_0 W^2 l_d r_d}{2\delta_i} = -\frac{1}{3}L = M_{bc}$$

Where $\mu_0 = 4\pi \times 10^{-7}$ is the air permeability and unit is H/m, δ_i is the air gap width and unit is m, r_d is the armature radius and unit is m, I_d is armature length, unit is m [7].

When inter-turn short circuit happened in phase A, the magnetic potential of the rest winding in phase A is $F_{a'} = (1 - S_t)WI_{a'}$, where $I_{a'}$ is the current flowing through the rest winding in phase A. The air gap magnetic induction intensity is $B_{a'} = \mu_0 F_{a'}/2\delta_i$.

The self-inductance magnetic linkage of the rest winding in phase A is

$$\Psi_{a'} = (1 - S_t)Wl_d r_d \pi B_{a'} = \frac{\pi\mu_0(1 - S_t)^2 W^2 l_d r_d}{2\delta_i} I_a$$

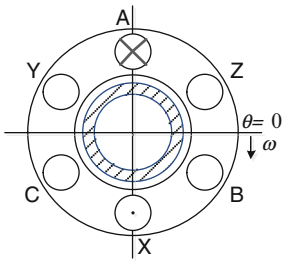

Fig. 3 Three-phase winding distribution diagram

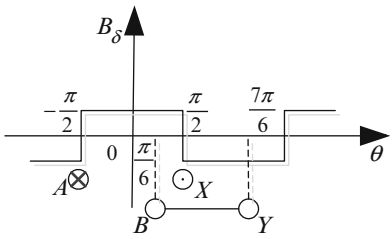

Fig. 4 Magnetic induction waveform of normal phase A winding

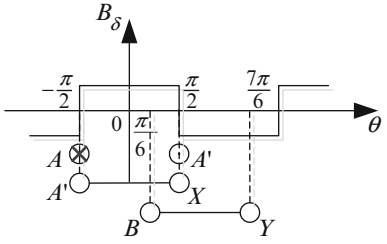

Fig. 5 Magnetic induction waveform of the rest winding of faulty phase A

So the self-inductance of the rest winding in phase A is

$$L_{a'} = \frac{\Psi_{a'}}{I_{a'}} = \frac{\pi\mu_0(1-S_t)^2W^2l_dr_d}{2\delta_i} = (1-S_t)^2L$$

Similarly, the self-inductance of the short winding in phase A is

$$L_s = \frac{\Psi_s}{I_s} = \frac{\pi\mu_0{S_t}^2W^2l_dr_d}{2\delta_i} = {S_t}^2L$$

The mutual-inductance between the rest and the short winding in phase A is

$$M_{a's} = \frac{\Psi_{a's}}{I_{a'}} = \frac{\pi\mu_0S_t(1-S_t)W^2l_dr_d}{2\delta_i} = S_t(1-S_t)L$$

The ramp angle between the rest winding in phase A and the winding in phase B is 120°, so the mutual-inductance between them is

$$M_{a'b} = \frac{\Psi_{a'b}}{I_{a'}} = -\frac{1}{3}\frac{\pi\mu_0(1-S_t)W^2 l_d r_d}{2\delta_i} = -\frac{1}{3}(1-S_t)L$$

Similarly, the mutual-inductance between the short winding in phase A and the winding in phase B is

$$M_{sb} = \frac{\Psi_{sb}}{I_s} = -\frac{1}{3}\frac{\pi\mu_0 S_t W^2 l_s r_d}{2\delta_i} = -\frac{1}{3}S_t L$$

According to the method, the following matrix can be obtained.

$$Q = \begin{bmatrix} {S_t}^2 - \frac{7}{3}S_t + \frac{4}{3} & 0 & 0 & S_t - {S_t}^2 \\ 0 & \frac{4}{3} - \frac{S_t}{3} & -\frac{S_t}{3} & -\frac{S_t}{3} \\ 0 & -\frac{S_t}{3} & \frac{4}{3} - \frac{S_t}{3} & -\frac{S_t}{3} \\ -{S_t}^2 + \frac{4}{3}S_t & 0 & 0 & {S_t}^2 \end{bmatrix} L \tag{5}$$

2.3 Mathematic Model of Inter-phase Short Circuit Fault

Assuming that inter-phase short circuit fault occurs between phase A and phase B, short circuit formed circulation, as shown in Fig. 6. When phase A and phase B conduct, current in circulation is generated by the back-EMF of the short winding. Currents flowing through the short windings in phase A and B are equal in amplitude but opposite in direction as shown in Fig. 7. When phase C and phase B conduct, currents flowing through the short windings are not equal in amplitude, because that them contain components of current in phase C, as shown in Fig. 8. So currents flowing through short windings can't be regard as one parameter.

Voltage balance equation is as follows.

$$U = RI + Q\frac{dI}{dt} + E \tag{6}$$

Where $U = [\,u_{a'} \quad u_{b'} \quad u_c \quad u_{a_s} \quad u_{b_s}\,]^T$; $R = diag[\,r_{a'} \quad r_{b'} \quad r \quad r_{a_s} \quad r_{b_s}\,]$; $I = [\,i_{a'} \quad i_{b'} \quad i_c \quad i_{a_s} \quad i_{b_s}\,]^T$;

$$E = [\,e_{a'} \quad e_{b'} \quad e_c \quad e_{a_s} \quad e_{b_s}\,]^T Q = \begin{bmatrix} L_{a'} & M_{a'b'} & M_{a'c} & M_{a'a_s} & M_{a'b_s} \\ M_{a'b'} & L_{b'} & M_{b'c} & M_{b'a_s} & M_{b'b_s} \\ M_{a'c} & M_{b'c} & L & M_{ca_s} & M_{cb_s} \\ M_{a'a_s} & M_{b'a_s} & M_{ca_s} & L_{a_s} & M_{a_sb_s} \\ M_{a'b_s} & M_{b'b_s} & M_{cb_s} & M_{a_sb_s} & L_{b_s} \end{bmatrix};$$

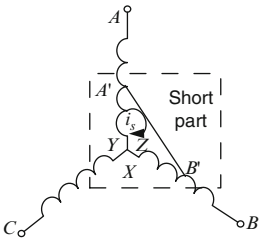

Fig. 6 Inter-turn short circuit fault indicator diagram

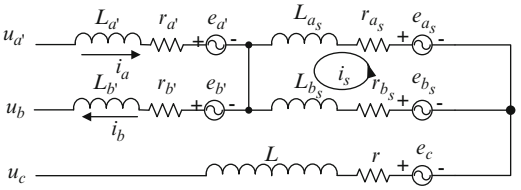

Fig. 7 Inter-phase short circuit fault analysis diagram when phase A and B conduct

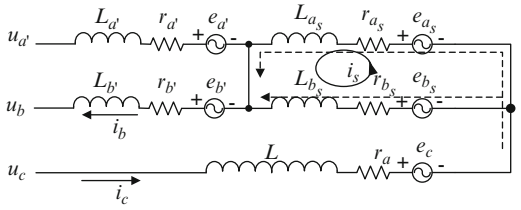

Fig. 8 Inter-phase short circuit fault analysis diagram when phase C and B conduct

Subscripts as a', b', a_s, b_s represent the rest winding and the short winding in phase A and phase B. Subscripts of M are a pair of windings which produce mutual-induction.

Because that the phase resistance and back-EMF constant are proportional to the number of short turns, $r_{a'} = (1 - S_a)r$, $r_{b'} = (1 - S_b)r$, $r_{a_s} = S_a \cdot r$, $r_{b_s} = S_b \cdot r$ can be obtained. Where S_a and S_b are the percentage of short turns to total turns in phase A and B.

According to the method given in 2.2, self-induction and mutual-induction of different windings can be obtained. Based on Kirchhoff's current law (KCL) $i_{a'} + i_{b'} + i_c = 0$, so

$$Q = \begin{bmatrix} 1 - S_a \\ 1 - S_b \\ 1 \\ S_a \\ S_b \end{bmatrix}^T \begin{bmatrix} \frac{4}{3} - S_a & \frac{S_b}{3} & 0 & S_a & -\frac{S_b}{3} \\ \frac{S_a}{3} & \frac{4}{3} - S_b & 0 & -\frac{S_a}{3} & S_b \\ 0 & \frac{S_b - S_a}{3} & \frac{4 - S_a}{3} & -\frac{S_a}{3} & -\frac{S_b}{3} \\ \frac{4}{3} - S_a & \frac{S_b}{3} & 0 & S_a & -\frac{S_b}{3} \\ \frac{S_a}{3} & \frac{4}{3} - S_b & 0 & S_b & -\frac{S_b}{3} \end{bmatrix} L \tag{7}$$

Based on Kirchhoff's voltage law (KVL) $u_{a_s} - u_{b_s} = 0$.
Because of the short circuit, motor torque equation turns into

$$T_e = \frac{1}{\omega}(e_{a'}i_{a'} + e_{b'}i_{b'} + e_c i_c + e_{a_s}i_{a_s} + e_{b_s}i_{b_s}) \tag{8}$$

Mechanical motion equation is as follows.

$$T_e - T_L = J\frac{d\omega}{dt} + B\omega \tag{9}$$

3 Simulation

Through the above mathematical model, the simulation model can be obtained in Matlab/Simulink environment, with the method that sine-wave shaven top substitutes back-EMF [7]. This paper adopts the open loop simulation model to analyze primitive traits of BLDCM with short circuit fault. Simulation parameters are rated voltage $U_N = 27$ V, rated torque $T_e = 0.1$ N · m, stator winding resistance $r_a = 0.33\Omega$, self-induction $L = 0.108mH$, rotary inertia $J = 0.56 \times 10^{-3}$ kg · m^2, polepairs $p = 2$, damping coefficient $B = 0.002$ N · m · s, EMF coefficient K_e =0.0185 V/(rad · s^{-1}).

To compare the static and dynamic characteristics of BLDCM before and after faults, motor starts with rated torque and PWM wave of 80 % duty cycle, and joins 20 % inter-turn short circuit fault and inter-phase short circuit with 20 % short turns in phase A and B at 0.06 s. Simulation curves of bus bar current, phase current, motor speed and line voltage are shown in Figs. 9, 10, 11, and 12.

Observing from Figs. 9 and 10, every line voltage has little change before and after faults. Though the motor speed has a little drop, it is difficult to been discovered. By the analysis of the above that inter-turn short circuit have the characteristics of high concealment which is difficult to detect.

Observing from Fig. 11, every phase current has great change before and after inter-turn short circuit fault. Current in faulty phase A increases in amplitude, while currents in phase B and phase C has distortion. When conducted with phase A, the current increases. Every phase current also increases in different forms after inter-phase short circuit fault, as shown in Fig. 12. Due to the increasing of current, the temperatures of BLDCM accelerates rising, which will reduce the efficiency and reliability of motor. Meanwhile fault will bring in short circuit currents, which are five times more than the normal phase current in amplitude, as shown in Figs. 11 and 12. It will accelerate the fever of the short windings and aggravate the faults. Shown in Figs. 11 and 12, Bus bar currents both have obvious changes. Through testing them, inter-turn short circuit faults can be detected timely.

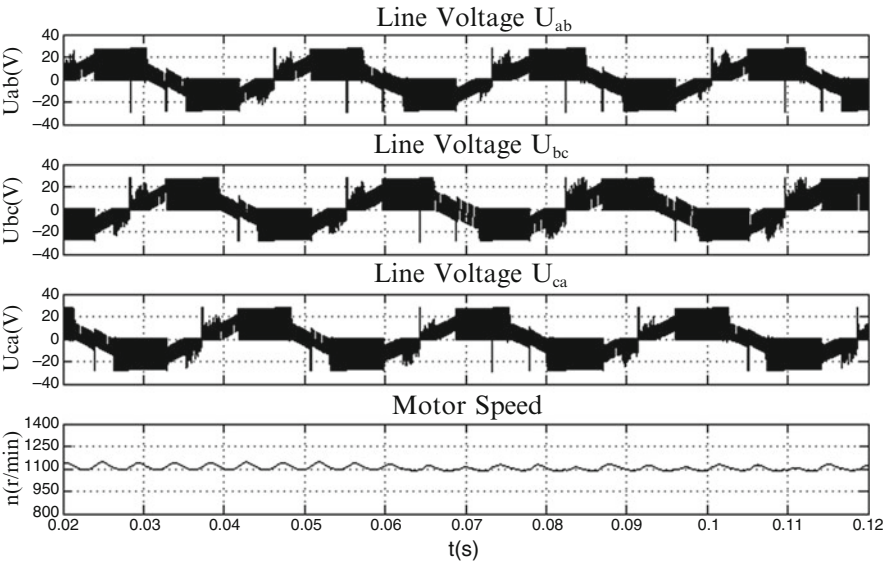

Fig. 9 Line voltages and motor speed before and after interphase short circuit fault

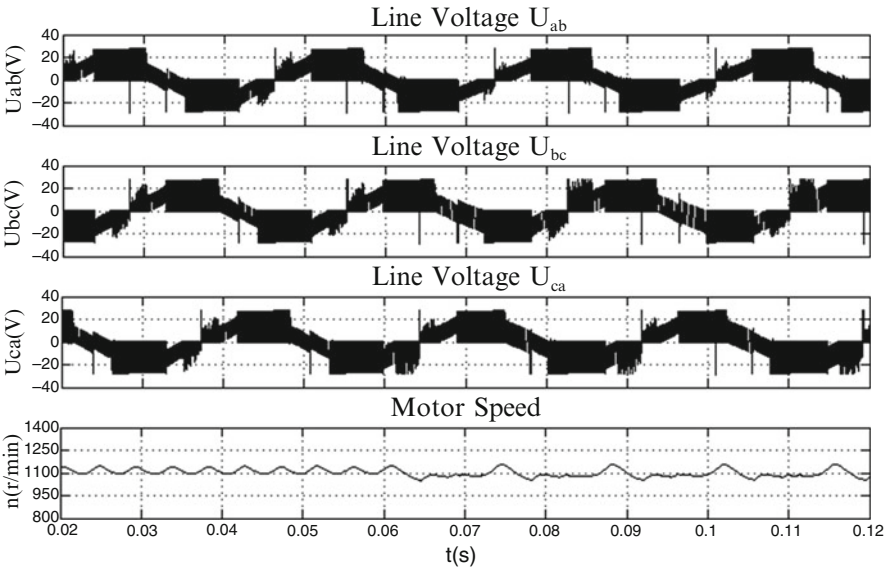

Fig. 10 Line voltages and motor speed before and after interphase short circuit fault

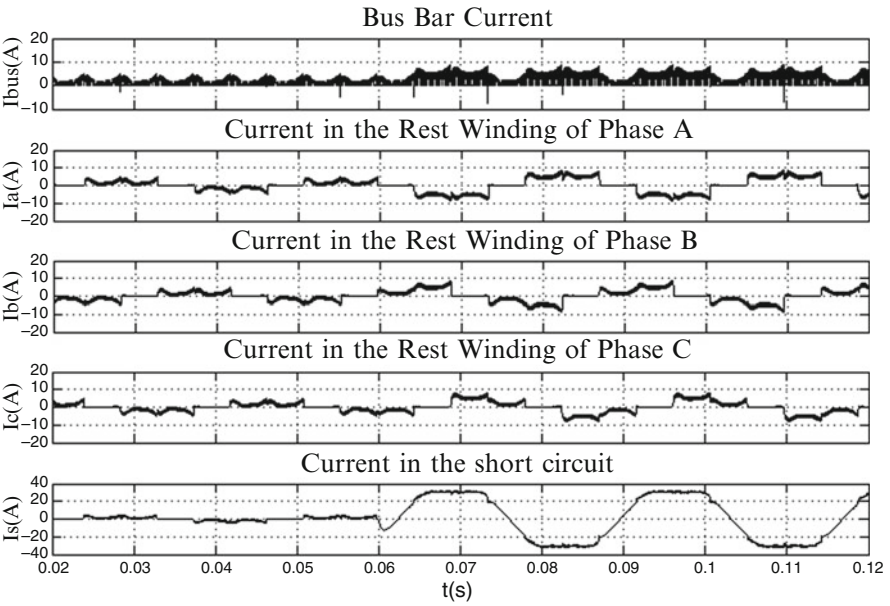

Fig. 11 Bus bar current and every winding current before and after inter-turn short circuit fault

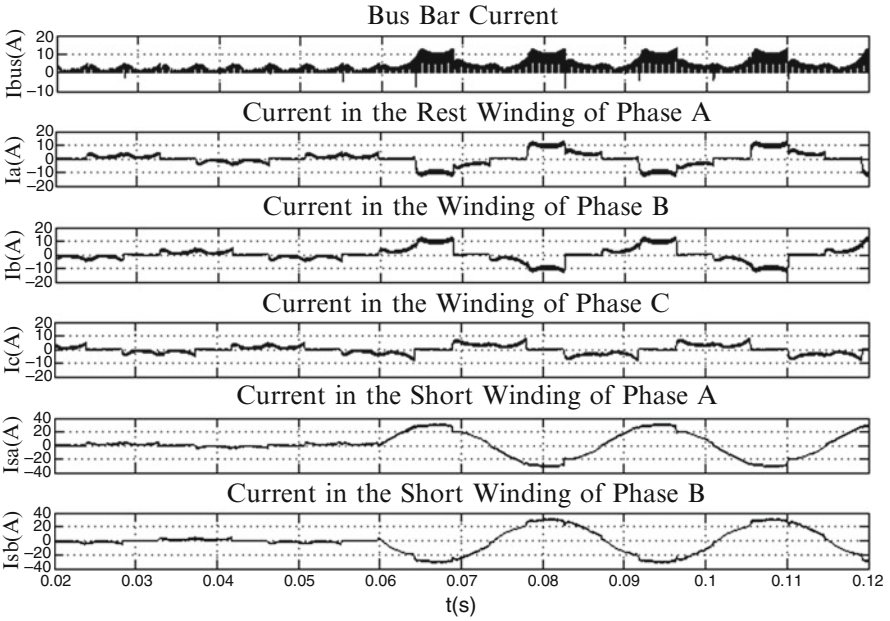

Fig. 12 Bus bar current and every winding current before and after inter-phase short circuit fault

When inter-turn short circuit fault happens, back-EMF of short winding still exist, which produces the short current. Not affected by the switch tube, the current waveform does not exist big chopper, while, because of the existence of mutual-inductance, there is still a small harmonic, which can be verified in Fig. 11.

When inter-phase short circuit fault happens, the above situation also exists. Meanwhile, when phase A and B conduct, current flowing through short windings in them, has equal amplitude and opposite direction. When phase C conducts, these current's amplitudes are not equal because of the existence of component of current in phase C, which can be verified in Fig. 12.

4 Conclusion

The mathematical model of BLDCM with inter-turn short circuit fault and inter-phase short circuit fault are built up. The mathematic formulas of self-inductance and mutual-inductance between two phases have been presented under $q = 1$ in each phase per pole. The corresponding simulation model is obtained under Matlab/Simulink environment. Through the open loop simulation analysis, the following conclusion can be obtained. Both inter-turn and inter-phase short circuit faults have concealment. The short currents accelerate motor fever and reduce the efficiency and reliability of BLDCM. Continuing inter-turn short circuit and inter-phase short circuit fault will accelerate damage level of motor.

References

1. Awadallah MA, Morcos MM, Gopalakrishnan S, Nehl TW (2006) Detection of stator short circuits in VSI-fed brushless DC motors using wavelet transform. IEEE Trans Energy Convers 21(1):1–8
2. Awadallah MA, Morcos MM (2004) Anfis-based diagnosis and location of stator interturn faults in PM brushless DC motors. IEEE Trans Energy Convers 19(4):795–796
3. Swarnakar S, Mukhopadhyay S, Kastha D (2005) Fault detection and remedial strategies for inter-turn short circuit faults in a permanent magnet brushless DC motor. IEEE Indicon Conference, Chennaim, India. pp 492–496
4. Zhao Kun, Li Yinghui, Yang Pengsong (2009) Feature extraction of BLDC inter-turn short circuit faults based on wavelet packet. Large Electric Mach Hydraulic Turbine (4):20–23, (In Chinese)
5. Yang Fang, Yu Kaiping, Guo Hong, Wang Wei (2008) Simulation research of fault detection method on brushless DC motor system. J Syst Simul 20(22):6268–6272, In Chinese
6. Wang Wei, Guo Hong, Li Yanming (2010) Analysis of winding short-circuit in electrical/mechanical hybrid 4-redundancy brushless DC torque motor. Acta Aeronautica ET Astronautica Sinica 31(5):975–982, In Chinese
7. Ma Ruiqing, Liu Weiguo, Xie En (2008) Simulation and test of position servo system based on dual-redundancy BLDCM. Proc CSEE 28(18):98–103, In Chinese

Space-Vector Modulation Based on Advanced RISC Machine for Single-Phase Induction Motor

Mingyue Ma and Ding Wang

Abstract The space-vector pulsewidth-modulation (SVPWM) technique is a most important technique in motor drive. Its realization is more important for applications of motor drives. For single-phase induction motors, realizations of SVPWM have a few of applications. Especially, the papers with software levels of their realizations are not seen. Space-vector modulation based on ARM (Advanced RISC Machine) for single-phase induction motor is presented. The system configuration, synthesis principle of SVPWM and the software design of the system are discussed in detail. The experiment prototype is built up and proved the feasibility of them.

Keywords Single-phase induction motor • Space-vector pulsewidth-modulation (SVPWM) • ARM • Frequency control

1 Introduction

Single-phase induction motors have advantages of single-phase power supply and small power application. The single-phase induction motors have been widely employed in low or middle power level fields, especially in households where a three-phase supply is not available.

The single-phase induction motor requires the auxiliary winding to produce the starting torque in early application [1]. For example, the capacitor-starting motor produces the starting torque with the aid of the auxiliary winding and series-connected capacitor. Accordingly, it operates as the asymmetrical two-phase induc-

M. Ma • D. Wang (✉)
Provincial Key Disciplines for Control Science and Engineering,
Heilongjiang University, Heilongjiang, China
e-mail: 316933876@qq.com; climbing200310@aliyun.com

W. Wang (ed.), *Mechatronics and Automatic Control Systems*, Lecture Notes in Electrical Engineering 237, DOI 10.1007/978-3-319-01273-5_5,

tion motor at starting, but operates as a pure single-phase induction motor during running after a centrifugal switch is opened.

The single-phase induction motor is unsuitable for adjustable-speed control because of poor speed characteristic. Traditionally, speed operation of the single-phase induction motors has been obtained through voltage control using a triacor back-to-back thyristors [2]. Accordingly, the harmonic content of the output voltage becomes larger, and the frequency range is narrower. Therefore, low-cost static converters which can improve the quality are required in single-phase induction motor drives [3–5].

The variable frequency speed regulation technology in induction motor speed control systems with its high speed and start-up performance, high power factor and power saving effect was made using more and more extensive in the motor control. But at present the most research of variable frequency control mainly focus on three-phase motor, the single-phase motor research is not enough, makes it less maturing than three-phase motor control technique. SVPWM techniques for the single-phase inverter-fed symmetrical single-phase induction motors are proposed [6, 7]. Its realization is more important for applications of motor drives. Space-vector modulation based on ARM for single-phase induction motor is presented. The system configuration and synthesis principle of SVPWM are described in Sect. 2. And the software design of the system is discussed in Sect. 3. Experiments are introduced in Sect. 4.

2 The Design of System

2.1 System Configuration

Considering that the single-phase induction motor requires speed control, a set of high-precision ac speed regulation system is designed and implemented based on ARM. The whole system consists of three phase IGBT inverter, angle sensor, single-phase induction AC motor, rectifier power supply, Samsung S3C2440 as the main chip. The main work includes: system initialization, read key state, change the motor speed. Figure 1 shows the block diagram of system.

In above system, the single-phase induction motor has characteristics of time-varying and nonlinear and coupling, and can be expressed in a state equation of two state variables [6]. The inverter of SVPWM is used for controlling it. In front of inverter, there is a controller. With a encoder on the motor, control diagram is shown in Fig. 2. But for this paper, the technologies on SVPWM are described detail.

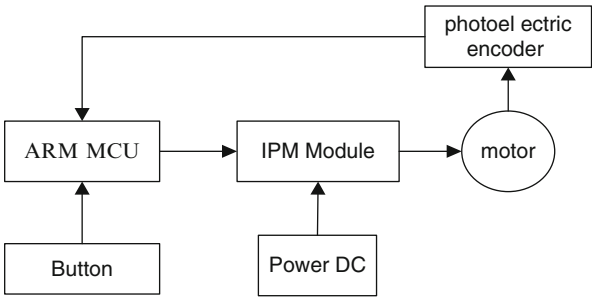

Fig. 1 Block diagram of hardware of system

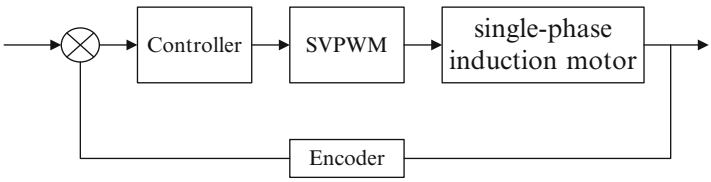

Fig. 2 Control diagram of system

2.2 The Synthesis Principle of SVPWM

Six switches can form eight allowed switch combinations in the three-phase inverter bridge, as shown in Fig. 3. There are eight kinds of conducting situation, which is T1, T4, T6 conduction, T1, T3, T6 conduction, T2, T3, T6 conduction, T2, T3, T5 conduction, T2, T4, T5 conduction, T1, T4, T5 conduction, T1, T3, T5 conduction and T2, T4, T6 conduction. It is defined that the upper arm device conduction use one described, the next bridge arm device conduction uses 0 described. The above eight kinds of condition is arranged in turn. There are 100,110,010,011,001,101,000 and 111 according to ABC phase sequence. From the normal working of the inverter, the first six kinds of working condition is effective, the last two states is invalid.

For the output of each complete cycle in the inverter there were six kinds of effective working state, and appears only once. So inverter transform an effectively work state every $2\pi/6$, but the phase remained in $2\pi/6$ moment of time. Set working from the state of 100 to begin, then VT1, VT4, VT6 conduction, the potential respective to point A is positive, B and C point is negative. Follow the transition of inverter effective working states, the amplitude of voltage space vector is not changed, and phase changes $2\pi/6$ each time, until a complete conversion cycle is over, six space vector just linked end to end, so that the six voltage space vector rotate 2π radian in a complete conversion cycle, then formed a closed hexagon graphics. 111 and 000 are invalid working condition, their amplitude and phase is

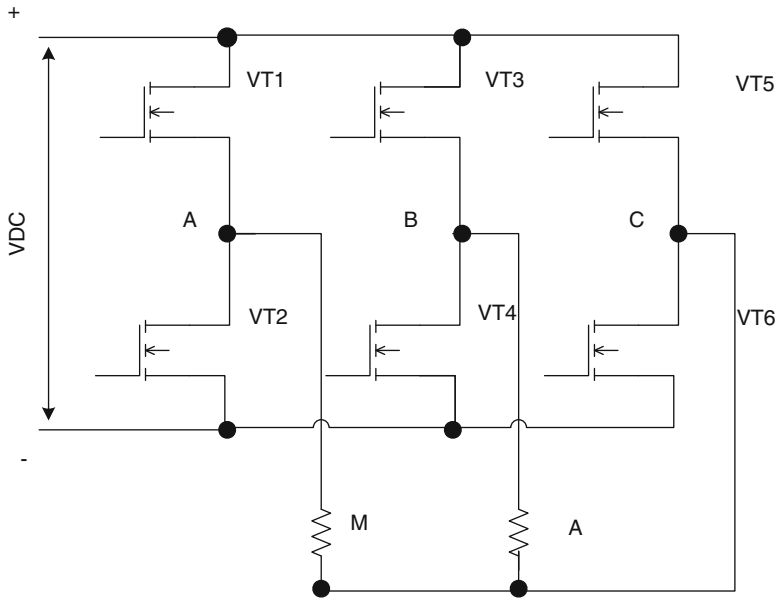

Fig. 3 Space voltage vector and inverter circuit of voltage source type

Fig. 4 The track of space vector

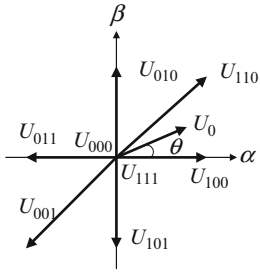

zero, which is called zero vector value, but we could think they exist in center of hexagon graphics, shown in Fig. 4.

The objective of SVPWM is to approximate the reference voltage vector U_0 by a combination of the eight switching patterns. One simple means of approximation is to require the average output of the inverter (in a small period T_{PWM}) to be the same as the average of U_0 in the same period. Supposing that U_0 is located in the sector formed by U_1 and U_2, we can get

$$T_{PWM}U_0 = T_1U_1 + T_2U_2 \tag{1}$$

where T_1 and T_2 are the respective durations in time for which switching patterns U_1 and U_2 are applied within period T_{PWM}.

From Eq. 1, we can say that for every PWM period, the desired reference voltage U_0 can be approximated by switching patterns U_1 and U_2 for T_1 and T_2 durations

of time, respectively. Since the sum of T_1 and T_2 is less than or equal to T_{PWM}, the rest of the switching period is occupied by the zero switching state. Therefore, we define T_0 as

$$T_0 = T_{PWM} - T_1 - T_2 \tag{2}$$

We can define that

$$U_1 = W_1 e^{j\theta_1} \tag{3}$$

$$U_2 = W_2 e^{j\theta_2} \tag{4}$$

Where W_1 and W_2 stand for the magnitudes of the resulting switching state vectors and θ_1 and θ_2 are their angles measured in a clockwise direction with respect to the real axis α.

Supposing $U = We^{j\theta}$ and substituting Eqs. 3 and 4 into Eq. 1, we can get

$$T_1 = T_{PWM} M W_1 \cos\theta \tag{5}$$

$$T_2 = T_{PWM} M W_2 \sin\theta \tag{6}$$

Where

$$M = \begin{bmatrix} W_1 \cos\theta_1, W_2 \cos\theta_2 \\ W_1 \sin\theta_1, W_2 \sin\theta_2 \end{bmatrix}^{-1}$$

Once the sector of reference U_0 is determined, we can compute the matrix M. The actual values of the components of matrix M are either 1, 1, or 0. After M is known, T_1 and T_2 can be easily calculated by using Eqs. 5 and 6. Figures 5, 6, 7, 8, 9, and 10 shows the switching time of T_1 and T_2 in any period of six periods in which the switching frequency is set at 10 kHz. Thus, when designing these kinds of inverters, the rated current of the insulated gate bipolar transistors (IGBTs)in the return bridge should be higher.

3 The Software Design of the System

This controller is designed basing on the embedded processor; the software of system is also based on embedded operating system, as is shown in Fig. 10. The controller could ensure the experimental control object is rapid, accurate and stability. This software design of topic mainly includes two aspects: first is the main interface driver program of the basic peripheral circuit, second is the application. In the LINUX operating system, every hardware equipment can drive on the basis of the driver program, so the hardware equipment of system determines how

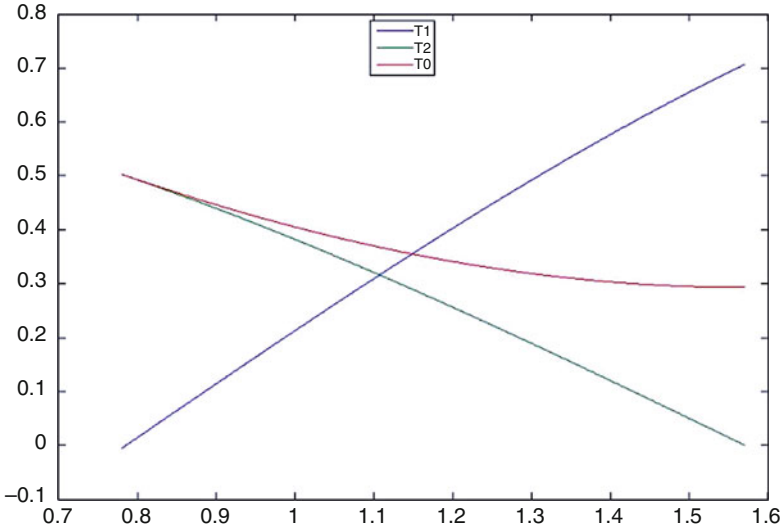

Fig. 5 The modulation ratio is 0.707 of the first period

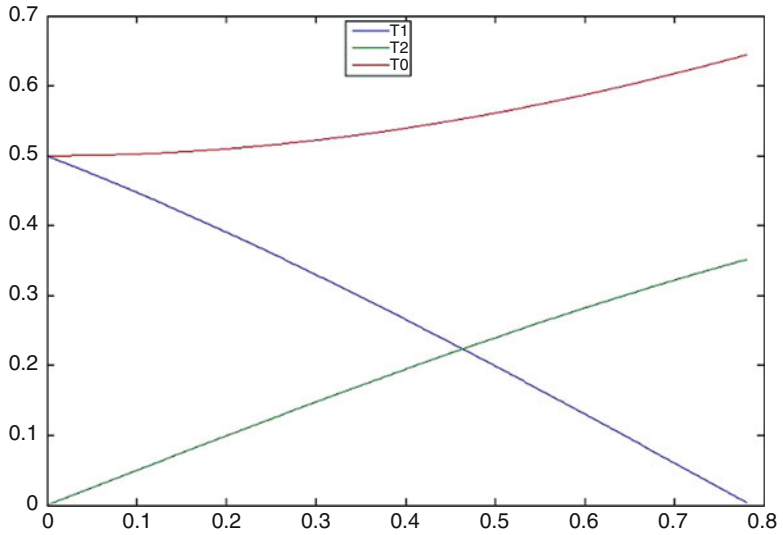

Fig. 6 The modulation ratio is 0.707 of the second period

much driver program of device. There are several of the bottom drive programs, the drive of PWM, the drive of photoelectric encoder, the drive of D/A; applications mainly include the man–machine interface program, the control algorithm and program. Hierarchical relationship of LINUX software system in Fig. 11.

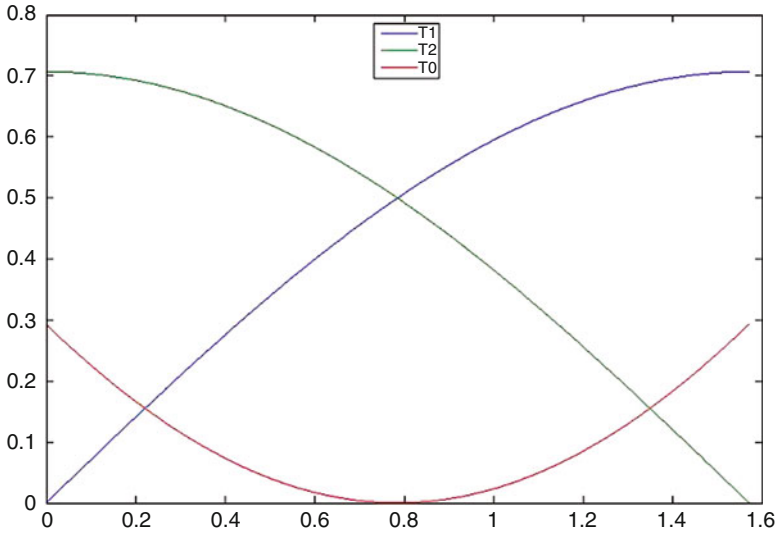

Fig. 7 The modulation ratio is 0.707 of the third period

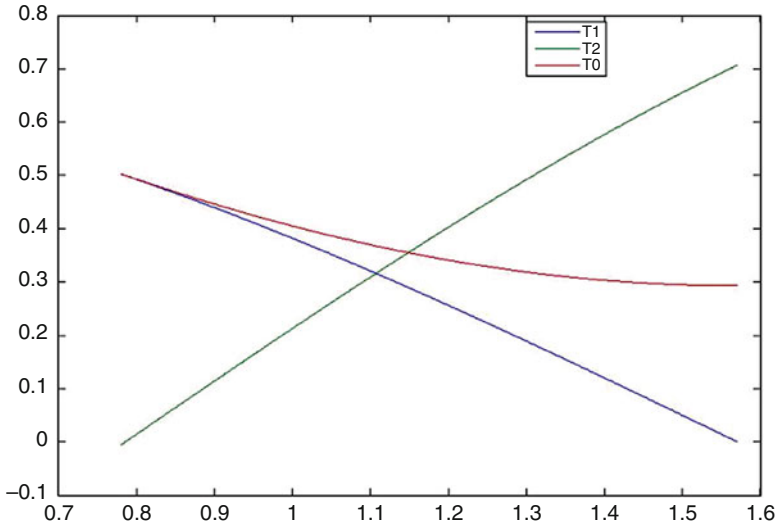

Fig. 8 The modulation ratio is 0.707 of the fourth period

A given speed acquisition compared with the real-time speed collected by encoder. Control program transmit output message to space vector program through the named pipe. Space vector procedure called I/O port driver to control six I/O port. The system will produce SVPWM waveform. The flow chart of main program is shown in Fig. 12.

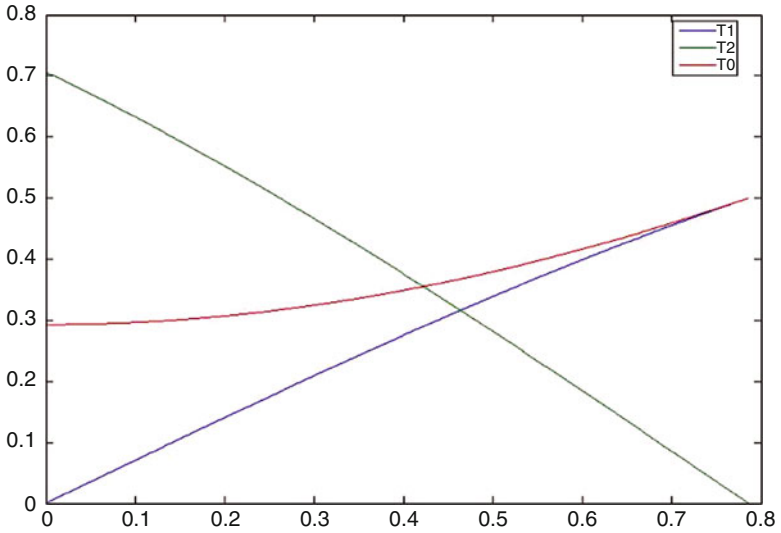

Fig. 9 The modulation ratio is 0.707 of The fifth period

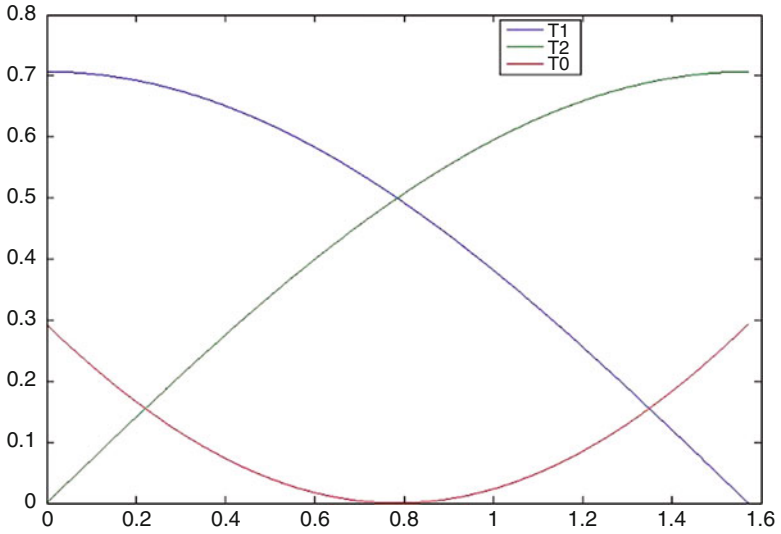

Fig. 10 The modulation ratio is 0.707 of the sixth period

4 Experiments

This system uses ARM9 as the control core, the type of shingle-phase induction motor is D5022, The rated power of motor is 60 W, the rated voltage is 220 V, the rated current is 0.6A, and the model of photoelectric coupler is TLP250. The motor

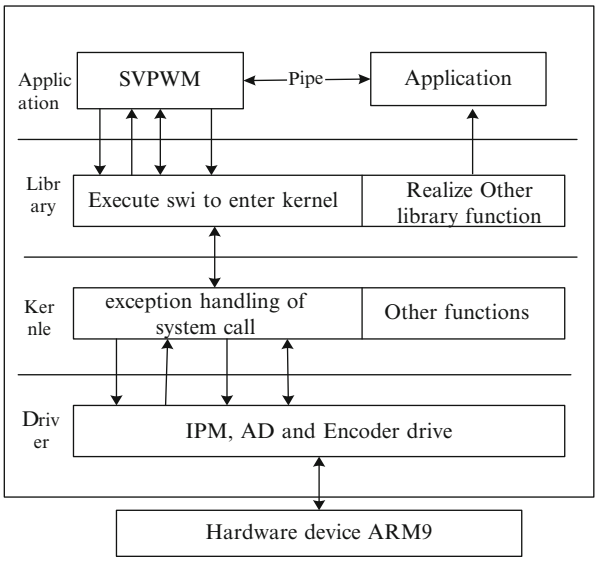

Fig. 11 Hierarchical relationship of LINUX

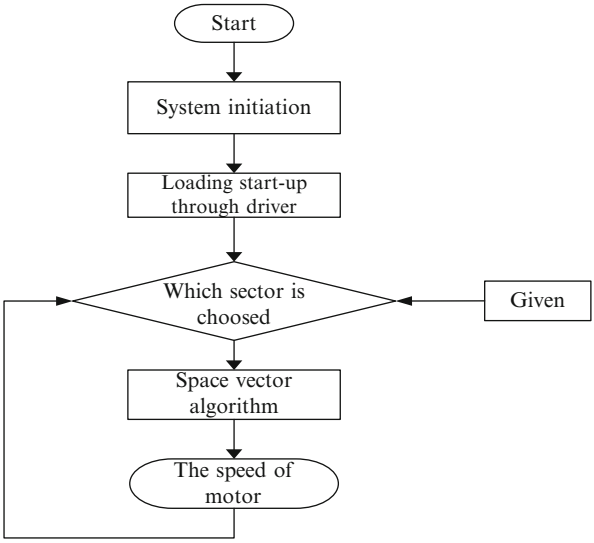

Fig. 12 The flow chart of main program

and its load of experiments are shown in Fig. 13. After built the hardware system, software program is on according to the system structure and control algorithm. After application of cross compile tools to software program and download into the system, the main debugging process to modify the program is completed until the output is satisfied.

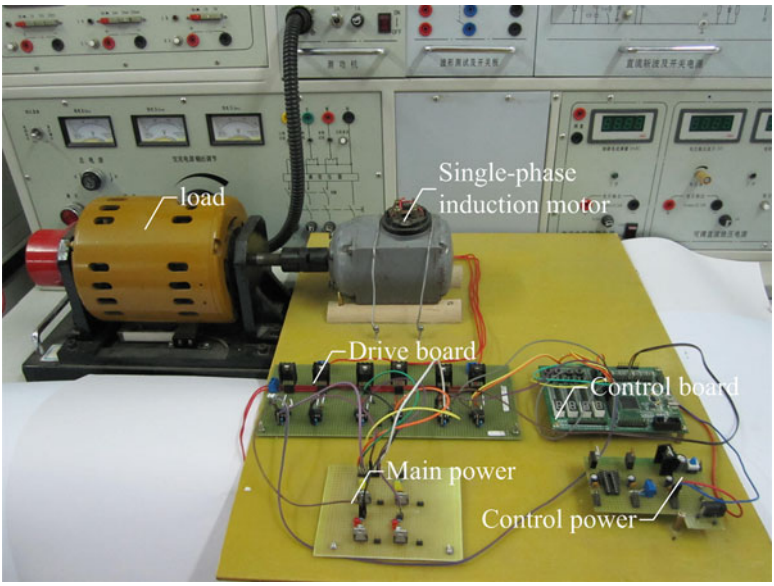

Fig. 13 Motor and its load of experiments

Fig. 14 Wave forms of SVPWM in experiments

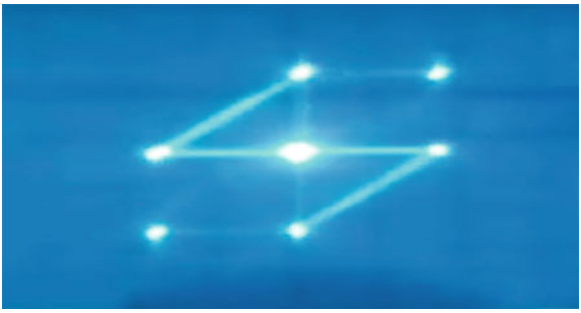

The wave forms of SVPWM in experiments are shown in Fig. 14. U_{100} and U_{011} are same like them in Fig. 4, U_{010} and U_{101} a are also same like them in Fig. 4, but their colors are a little light. It is note that U_{110} and U_{001} are a horizontal space from them in Fig. 4 because there are change of reference level in IGBT bridge. Therefore, usages of SMPWM are correct, and further studies are necessary.

5 Conclusion

According to the rotation situation of motor, the SVPWM technique is proposed for single-phase induction motor. There are six space voltage vectors and no zero vectors in two-phase inverters. A reference voltage vector is realized by adjusting six space vectors without zero space vectors. A three-phase inverter topology with SVPWM was used to produce higher output voltage with lower distortion as compared to an H-bridge inverter. Hence, this method is simple and cost efficient. The method is should applied to practical productions in the future.

Acknowledgements This work was supported by the Scientific and Technological Project of Education Bureau of Heilongjiang Province (Grant No: 12521419), P. R. China.

References

1. Walls TA, Sudho SD (1996) Analysis of a single-phase induction machine with a shifted auxiliary winding. IEEE Trans Energy Convers 11:681–687
2. Jawad Faiz, Jafarian A, Neekzad M (2003) PSPICE simulation of a capacitor start and triac start single phase induction motor during steady state and transient operations and its experimental verification. Energy Convers Manage 44:479–495
3. Makky A-RAM, Nabil Abd El-Latif (1997) Integral-cycle control with a d.c. chopper controller for single-phase induction motor. Electr Power Syst Res 40:91–98
4. Nabil A. Ahmed, Kenji Amei, Masaaki Sakui (2000) AC chopper voltage controller-fed single-phase induction motor employing symmetrical PWM control technique. Electr Power Syst Res 55:15–25
5. Jawad Faiz, Kasebi F, Pillay P (2004) Design and testing of an integrated electronically controlled capacitor for integral and fractional horse power single phase induction motor. Energy Convers Manage 45:2989–3001
6. Ding Wang (2010) Hybrid fuzzy vector control for single phase induction motor. In: 2010 international conference on computing, control and industrial engineering, IEEE Computer Society, Los Alamitos, vol 2. pp 122–125
7. Ding Wang (2012) Hybrid adaptive fuzzy vector control for single-phase induction motors. Lect Notes Electr Eng 135:257–262

Analysis on the Error Caused by Working Frequency Drift for the Silicon Micromechanical Gyroscope

Pu-hua Wang, Bing Luo, An-cheng Wang, Ming-ming Jiang, and Dong-feng Song

Abstract The Silicon Micromechanical Gyroscope (SMG) has broad application in various fields, but its development is badly restricted by the error caused by temperature drift. The temperature drift will lead to the change of working frequency, and it is one of the main factors which caused the drift error. Presently, fewer researchers focus on how the working frequency affects the scale factor and bias of the gyroscope. In this paper, the effects of the working frequency drift on the scale factor and bias of the gyroscope will be analyzed in theory and simulation, in terms of the dynamics equations and the process of signal detection of SMG. The results show that, the working frequency drift has a significant impact on the performance of the gyroscope, and typically, considering 1 Hz working frequency drift, the relative variation of scale factor is up to the order of 10,000 ppm, and the variation of bias is up to the order of $10^2(^\circ/\mathrm{h})$. The conclusions of this paper provide a basis for the further research on the temperature error models and compensations for SMG.

Keywords Silicon micromechanical gyroscope • Working frequency drift • Scale factor • Bias

1 Introduction

Silicon micromechanical gyroscopes are widely used in a various fields such as inertial navigation system, dexterous bomb, car manufacture and so on, for its advantages of small size, light weight, low cost and high reliability. The error caused by temperature drift is one of the main factors which restrict the

P.-h. Wang • B. Luo (✉) • A.-c. Wang • M.-m. Jiang • D.-f. Song
College of Mechatronic Engineering and Automation, National University of Defense Technology, Changsha, China
e-mail: ruobing@nudt.edu.cn

W. Wang (ed.), *Mechatronics and Automatic Control Systems*, Lecture Notes in Electrical Engineering 237, DOI 10.1007/978-3-319-01273-5_6,

development of SMG [1]. Man Hai-ou points out that, the fluctuation of the environment temperature will lead to change of the structure spring modulus of gyroscope, then the working frequency will drift, and the experiment shows that the drive mode resonance frequency will drift about 8 Hz while the temperature changes from −40 °C to 60 °C [2]. Chihwan Jeong and Liu Xiao-wei also study on the working frequency drift features caused by temperature, and get similar conclusions [3, 4]. Experiment results of Man Hai-ou show that there is a strict relativity between the bias of gyroscope and the working frequency [5].

It is thus clear that, the working frequency drift caused by temperature is a significant factor of the error caused by temperature of SMG. Presently, the research on this issue mostly focus on the temperature features of mode frequency, but the mechanism of how the working frequency affects the scale factor and bias of gyroscope are rarely reported. Focusing on this question, this paper starts from the dynamic equations of silicon micromechanical gyroscope, combines with the process of signal detection, analyses the effect of the working frequency drift to the scale factor and bias of gyroscope, and evaluates the relevant error quantitatively with simulation.

2 The Fundamental Operation of SMG

SMG has two orthogonal modes which are drive mode and sense mode. Both of them can be regarding as a second-order oscillating system. By disregarding the external influences of gravity and acceleration of reference frame, the dynamic equations of SMG can be expressed as follow ([6], pp. 10–19):

$$\begin{cases} \ddot{x} + (\omega_d/Q_d)\dot{x} + \omega_d^2 x = f_d/m \\ \ddot{y} + (\omega_s/Q_s)\dot{y} + \omega_s^2 y = -2\Omega\dot{x} \end{cases}$$

Where, ω_d is the resonance frequency of drive mode; Q_d is the quality factor of drive mode; ω_s is the resonance frequency of sense mode; Q_s is the quality factor of sense mode; f_d is the drive force; Ω is the input angular velocity.

Generally, the drive mode is operating in resonant state with constant amplitude through feedback controlling [7]. Suppose the movement displacement of drive mode is $x(t) = A_0 sin\omega_d t$, where, A_0 is the amplitude of displacement, ω_d is the drive frequency, which is equal to the resonance frequency of drive mode, and also is the frequency of output signal, named as working frequency in this paper. With the constant angular velocity input, the dynamic equation of sense mode can be written as:

$$\ddot{y} + \frac{\omega_s}{Q_s}\dot{y} + \omega_s^2 y = -2\Omega\dot{x} = C_0\omega_d x \tag{1}$$

Where C_0 is a constant related to the amplitude of angular velocity, and is considered as 1 in the following analysis.

According to Eq. 1, the output of sense mode can be worked out:

$$y(t) = G(\omega_d)\cos(\omega_d t + \Phi(\omega_d)) \tag{2}$$

Where $G(\omega_d)$, $\Phi(\omega_d)$ are the gain and phase shift of the output signal of sense mode relative to reference signal x respectively,

$$G(\omega_d) = \frac{\omega_d}{\sqrt{\left(\omega_d^2 - \omega_s^2\right)^2 + \left(\omega_d\omega_s/Q_s\right)^2}} \tag{3}$$

$$\Phi(\omega_d) = \frac{\pi}{2} - atan\left(\frac{\omega_d\omega_s}{(\omega_d^2 - \omega_s^2)Q_s}\right) \tag{4}$$

Equations 2, 3, and 4 show that, the gain and phase of the displacement output signal of sense mode are all related to mode frequency ω_d, and the output signal contains the angular velocity which is needed to measure, thus the working frequency drift will have an effect on performance of gyroscope finally.

3 The Effects of Working Frequency Drift on the Performance of the Gyroscope

3.1 The Effects of Working Frequency Drift on the Gain and Phase of Output Signal of Sense Mode

Assume that besides the drive resonance frequency, the other operating parameter of gyroscope, such as sense mode resonance frequency, Q-factor of both the drive mode and sense mode all remain constants. Considering of the typical mode parameters of a gyroscope, generally, the mode frequency is about 4 KHz, the difference of the resonance frequency of the two mode is about 50 Hz, the quality factor of sense mode is about 1,000, that is to say, the magnitude of ω_d, ω_s are in the order of $10^4(2\pi \cdot 4$ KHz),and the magnitude of $\omega_d - \omega_s$ (assume $\omega_d > \omega_s$)is in the order of $10^2(2\pi^*50$ Hz), Q_s is in the order of 10^3, then

$$\left(\omega_d^2 - \omega_s^2\right)^2 = (\omega_d + \omega_s)^2(\omega_d - \omega_s)^2 > 4\omega_s^2(\omega_d - \omega_s)^2 >> (\omega_d\omega_s/Q_s)^2$$

Here, two reasonable approximations are given as follow:

- Approximation 1:

$$\omega_d^2 - \omega_s^2 = (\omega_d + \omega_s)(\omega_d - \omega_s) \approx 2\omega_d(\omega_d - \omega_s) \approx 2\omega_s(\omega_d - \omega_s) \tag{5}$$

- Approximation 2:

$$(\omega_d^2 - \omega_s^2)^2 + (\omega_d\omega_s/Q_s)^2 \approx (\omega_d^2 - \omega_s^2)^2 \tag{6}$$

3.1.1 The Relation Between the Output Gain of Sense Mode and Working Frequency

Differentiating G in Eq. 3 with respect to ω_d yields:

$$\frac{\partial G}{\partial \omega_d} = \left(-\frac{1}{2}\right)[(\omega_d^2 - \omega_s^2)^2/\omega_d^2 + (\omega_s/Q_s)^2]^{-\frac{3}{2}}\left(\frac{2(\omega_d^4 - \omega_s^4)}{\omega_d^3}\right)$$

According to the approximation 1, it can be simplified to,

$$\frac{\partial G}{\partial \omega_d} \approx \frac{\omega_d^2 + \omega_s^2}{(\omega_d^2 - \omega_s^2)^2}$$

Then the relative variation of gain is,

$$\delta_{\omega_d}^G = \frac{\frac{\partial G}{\partial \omega_d}}{G} \approx \frac{\omega_d^2 + \omega_s^2}{(\omega_d^2 - \omega_s^2)\omega_d} \approx \frac{1}{(\omega_d - \omega_s)}$$

The magnitude of $\delta_{\omega_d}^G$ is in the order of 10^{-3}, which means the relative variation of gain is in the order of 10^{-2} when the drive frequency changes 1 Hz (ω_d changes 2π).

3.1.2 The Relation Between the Output Phase Shift of Sense Mode and Working Frequency

Differentiating Φ in Eq. 4 with respect to ω_d yields:

$$\delta_{\omega_d}^P = \frac{\partial \Phi}{\partial \omega_d} = \frac{\omega_s Q_s(\omega_d^2 + \omega_s^2)}{(\omega_d^2 - \omega_s^2)^2 Q_s^2 + \omega_d^2\omega_s^2}$$

According to the Approximation 1and Approximation 2, it can be simplified to:

$$\delta_{\omega_d}^\Phi = \frac{\partial \Phi}{\partial \omega_d} = \frac{\omega_s}{2Q_s(\omega_d - \omega_s)^2}$$

The magnitude of $\delta_{\omega_d}^{\Phi}$ is in the order of $10^{-4,}$ that's to say the relative variation of phase shift is in the order of 10^{-2} (degree) when the drive frequency changes 1 Hz (ω_d changes 2π).

3.2 The Effects of the Gain Error and the Phase Shift Error of Sense Mode on the Scale Factor and Bias of the Gyroscope

By considering of the in-phase error and quadrature error, the output of the sense mode of silicon micromechanical gyroscope can be described as ([6], pp. 147–149):

$$V_{out} = (K\mu + V_i)cos(\omega_d t + \theta) + V_q sin(\omega_d t + \theta)$$

Where, K is the scale factor, μ is the input angular velocity, V_i is the amplitude of in-phase error, V_q is the amplitude of quadrature error, θ is the phase shift of mode.

Assuming φ as the reference phase of the demodulation signal, the output of in-phase and quadrature respective is,

$$I_{out} = (K\mu + V_i)cos(\theta - \varphi) + V_q sin(\theta - \varphi)$$

$$Q_{out} = -(K\mu + V_i)sin(\theta - \varphi) + V_q cos(\theta - \varphi)$$

After proper calibration, $\varphi = \theta$ and V_i, V_q and K are think as known constants. Taking I_{out} as the effective output y, then

$$y = K\mu + V_i$$

Defined the relative error of gain as ε, and the phase shift error as α, with the effects of ε and α, the output y' turns to

$$y' = (1 + \varepsilon) \cdot cos\alpha \cdot K\mu + (1 + \varepsilon) \cdot cos\alpha \cdot V_i + (1 + \varepsilon) \cdot sin\alpha \cdot V_q$$

The relative variation of scale factor is

$$\delta K = |(1 + \varepsilon) \cdot cos\alpha - 1| \tag{7}$$

The variation of bias is

$$\Delta B = ((1 + \varepsilon) \cdot cos\alpha - 1)V_i + (1 + \varepsilon)V_q \cdot sin\alpha \tag{8}$$

The Eqs. 7 and 8 show that, the gain error and phase shift will all lead to the change of scale factor and bias, and the variation of bias is related to the variation of in-phase error and quadrature error of gyroscope as well.

4 Simulations

Some real parameters of a certain type of gyroscope are used in the simulation, shown in Table 1.

4.1 The Simulation of Gain Error and Phase Shift of Sense Mode

According to the parameters in Table 1, the relative variations of gain error and phase shift respect to the working frequency are simulated in the whole temperature range ($-40 \sim 60\ ^\circ\mathrm{C}$). As shown in Fig. 1, in the whole temperature range, the gain will change about 160,000 ppm, and the phase will shift about 0.4°.

4.2 The Simulation of the Relative Variation of Scale Factor and the Variation of Bias

According to the results of Sect. 4.1, when the resonance frequency drifts for 1 Hz, the relative error of gain $\varepsilon \in [0, 0.02]$, and phase shift $\alpha \in [-0.05^\circ, 0]$. Based on these results and the parameters in Table 1, the variation of scale factor and bias can be easily gotten, as shown in Fig. 2.

Simulation results can be concluded as Table 2. The results show that, relatively, in the same conditions, the variation of scale factor caused by gain error is more significant while the variation of bias caused by phase shift is more significant when the resonance frequency of drive mode is drift. Particularly, when the frequency drifts 1 Hz, the relative variation of scale factor caused by gain error is about 20,000 ppm, and the variation of bias caused by phase shift is about $8 \cdot 10^{-4}$ V. The

Table 1 Parameters used in simulation

ω_d (rad/s)	ω_s (rad/s)	Q_s	V_i (V)	V_q (V)	K (mV/°/s)
$2\pi \cdot (4,000 + [-4, 4])$	$2\pi \cdot 4,050$	1,000	0.0034	0.8722	15

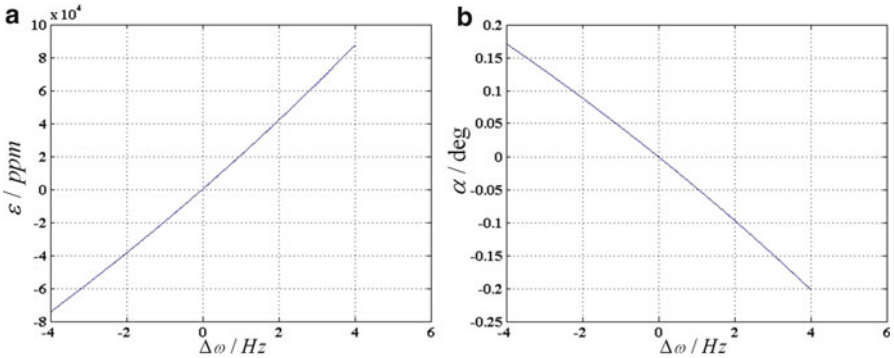

Fig. 1 Graphs of gain error (ε) and phase shift (α) respect to the working frequency drift ($\Delta\omega$) (**a**) Gain error (**b**) Phase shift

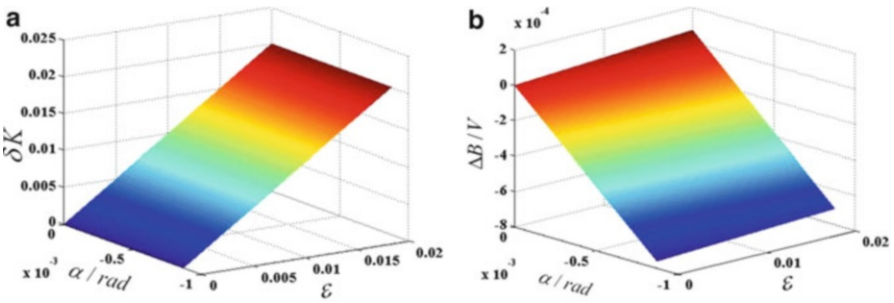

Fig. 2 Graphs of the relative variation of scale factor (δK) and the variation of bias (ΔB) respect to the gain error (ε) and phase shift (α) (**a**) The relative variation of scale factor (**b**) The variation of bias

Table 2 The simulation results of the relative variation of scale factor and the variation of bias

$\Delta\omega$	The features of sense mode	δK	ΔB
1 Hz	$\alpha = 0.05°$	0.38 ppm	$8 \cdot 10^{-4}$ V
	$\varepsilon = 20,000$ ppm	20,000 ppm	$8 \cdot 10^{-5}$ V

measured scale factor of this gyroscope is about 15 mV/°/s, and then the bias can be converted to angular velocity,

$$Bias = \frac{8 \cdot 10^{-4}}{15 \cdot 10^{-3}} \cdot 3,600 = 192°/\text{h}$$

5 Conclusion

In this paper, the relations between the working frequency and the scale factor and bias of the gyroscope are analyzed, in terms of the dynamics equations and the process of signal detection of SMG. The results of theoretical analysis and simulation show that, the working frequency drift has a significant impact on the performance of the gyroscope, and typically, considering 1 Hz working frequency drift, the relative variation of scale factor is up to the order of 10,000 ppm, and the variation of bias is up to the order of $10^2(^\circ/\mathrm{h})$. The conclusions of this paper provide a basis for the further research on the temperature error models and compensations of the gyroscope.

Acknowledgements This work was supported by the National University of Defense Technology Innovation Foundation For Postgraduate (Grant No. 4345111141N)

References

1. Chen Shu-ling (2010) Research on the temperature stability of silicon micromachined vibratory gyroscope. A dissertation submitted to Southeast University for the Academic Degree of Master of Engineering, Nan Jing (In Chinese)
2. Man Hai-ou, Xiao Ding-bang, Wu Xue-zhong (2009) Research on temperature characteristic of mode frequency of silicon micro-gyroscope. Chin J Sensor Actuator 22(8):1117–1121 (In Chinese)
3. Chihwan Jeong, Seonho Seok, Byeungleul Lee (2004) A study on resonant frequency and Q factor tunings for MEMS vibratory gyroscopes. J Micromech Microeng 14:1530–1536
4. Liu Xiao-wei, Chen Hong, Chen Wei-ping (2006) Frequency and damping characteristics of micro-machined gyroscope working at atmospheric pressure. Chin J Sensor Actuator 19 (5):2268–2271 (In Chinese)
5. Man Hai-ou, Xiao Ding-bang, Wu Xue-zhong (2012) Research on the closed-loop driving method of the silicon micro-machined gyroscope. Chin J Sensor Actuator 25(5):624–627 (In Chinese)
6. Saukoski M (2008) System and circuit design for a capacitive MEMS gyroscope. Doctoral dissertation, Helsinki University of Technology, Finland
7. Wang An-cheng, Luo Bing, Wu Mei-ping, Yu Hua-peng (2010) Digital double-closed-loop drive control method for silicon microgyroscope. J Chin Inert Technol 18(6):210–214 (In Chinese)

The Analysis of Coating Quality of Thin Copper Film Prepared by Wire Exploding Spray Coating Method

Jiazhi Yang, Cunbo Jiang, Xingming Fan, Fei Yang, Shengli Yi, and Fan Yang

Abstract Wire Exploding Spray Coating (WESC) technology is capable to prepare metal coating on nonmetal surface, such as glass, ceramic, etc. In order to determine the relationship between the technological parameters and the coating quality, experimental samples of WESC under different technological parameters are measured and analyzed in this paper. The results demonstrate that, during the WESC process, when the initial capacitor voltage increases from 10 to 20 kV, the metal wire diameter decreases from 1 to 0.5 mm, the circuit conductance decreases from 10.8 to 3.9 μH, the wire is heated up more sufficient, the mean diameter of metal micro-particle generated by the exploding is smaller, and the temperature and speed of the particles are higher, and the prepared coating is more compact, dense and even.

Keywords Wire exploding spray coating • Technological parameter • Coating quality • SEM

1 Introduction

It has a significant application value to prepare a metal film onto nonmetal material's surface, such as glass and ceramic [1]. But because the glass and ceramic are frangible, cannot be heating up for a relatively long time, it is very difficult to

J. Yang (✉) • C. Jiang • F. Yang • S. Yi
Department of Information Science & Engineering, Guilin University of Technology, Guilin, China
e-mail: jiazhi_yang@126.com

X. Fan
Department of Mechanical and Electrical Engineering, Guilin University of Electronic Technology, Guilin, China

F. Yang
Henan Xinyang Power Supply Company, Xinyang, China

W. Wang (ed.), *Mechatronics and Automatic Control Systems*, Lecture Notes in Electrical Engineering 237, DOI 10.1007/978-3-319-01273-5_7,

prepare a coating on the surface on these nonmetals, especially the inner surface of the nonmetal tube [2, 3].

Wire exploding spray coating (WESC) is one of thermal spray methods; it featured with a fast and controllable spray process, metal or nonmetal substrate material, and less heating up process affecting. The WESC method is suitable for preparing thin film on nonmetal surface, and will have a bright application foreground [4].

On the other hand, the WESC process is very complicated; the process is affected by many technological parameters. The WESC process is comprised of deeply coupled electrical process and physical process [5, 6]. In order to unveil the relationship between technological parameters (namely, the initial voltage of the capacitor, the inductance of the circuit, the diameter of the metal wire, and so on) and the electrical and physical process, and finally, how the technological parameters affecting the prepared film quality, a few experiments are carried out in this paper.

The electrical and physical process under different technological parameters has been analyzed in our former work [7]; and the instructions for WESC film preparing have also been proposed. In this paper, the WESC method is conducted to prepare copper film on the glass and ceramic surface; the samples prepared under different technological parameters are measured and analyzed; and the relationship between the technological parameters and the film quality is researched.

2 Experiment

2.1 Experimental Conditions

The WESC experiment is conducted under the WESC equipment whose schematic diagram is shown in Fig. 1. The WESC equipment is composed of energy storage unit, pulse formation unit, and spraying chamber.

The initial voltage of the capacitor applied in the experiment is 10, 12.5, 15, 17.5, and 20 kV respectively; the circuit conductance is 3.9, 6.5 and 10.8 μH; The capacitance of the capacitor is 14 μF, and the circuit resistance is 20.8 mΩ.

Copper wire is selected as spraying material; and whose length is 120 mm, diameter is 0.5, 0.75 and 1 mm. The substrate material is flat glass (which consists mainly of CaSiO3), with a dimension of 80 mm (length)*50 mm (width), 5 mm (thickness). The spraying distance is 10, 20 and 30 mm, respectively.

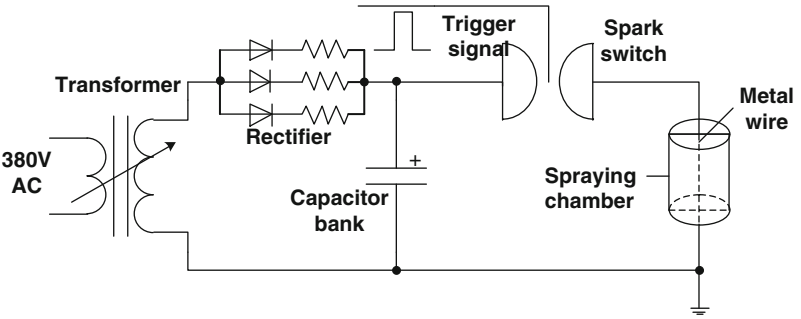

Fig. 1 Schematic diagram of the wire exploding spray coating equipment

2.2 Evaluation Method of the Experiment Result

In order to analyze the spaying quality under different technological parameters, and then unveil the optimal technological parameters for metal film preparing, a set of experiment result evaluation method must be established.

Effective spraying width means the maximum distance between two boundaries of the prepared film which are parallel with the long side of the substrate. The effective spraying width of the film is related to the efficiency of the spraying. Wider effective spraying width means less spraying processes.

Resistance of the film is the concentrated reflection of the thickness, effective spraying width, oxidation rate of the film.

Surface topography of the film is one of the most important criterions for the spraying quality. Such conditions of the film could be determined through the analysis of the surface topography, which are size distribution and inter combination of the particles, uniformity and void fraction of the film.

2.3 Measurement of the Experiment Samples

According to the evaluation method of the experiment result, the measurement methods are applied as below:

The film resistance is measured by QJ44 portable DC Kelvin Bridge. The measurement range of the bridge is 10-4 ~ 11 Ω. If the film resistance is above 11 Ω, the resistance is measured by multimeter. During the measurement, the long side of the substrate is assumed as the length of the conductor.

The surface topography of the film is analyzed by JSM-5600 LV SEM which is manufactured by JEOL.

3 Analysis of the Experimental Results

3.1 Experimental Results Under Different Initial Capacitor Voltage

In the experiment, the initial capacitor voltage is 10 kV (#01), 12.5 kV (#02), 15 kV (#03), 17.5 kV (#04) and 20 kV (#05), respectively. The diameter of the copper wire is 0.5 mm, the circuit conductance is 3.9 μH, and the spraying distance between the wire and the substrate is 20 mm.

The SEM micrographs of the film under different initial capacitor voltage are shown in Fig. 2. The SEM micrographs are 500× magnified. Through the topography, it shows that, accompany with the increase of initial capacitor voltage, the surface of the film is more even and neat, with less void fraction, the particles are shaped from oblate to spheroidal, the film covering surface over the substrate is increasing too.

Some detailed parameters of the WESC process is listed in Table 1. It can be indicated from the table that the weight of the film decreasing from 0.1571 to 0.0176 g with the initial capacitor voltage increasing from 10 to 20 kV. However, the resistance of the prepared film has its own variation method, when the initial capacitor voltage is 10 kV, the resistance of the film is out of range of the electric

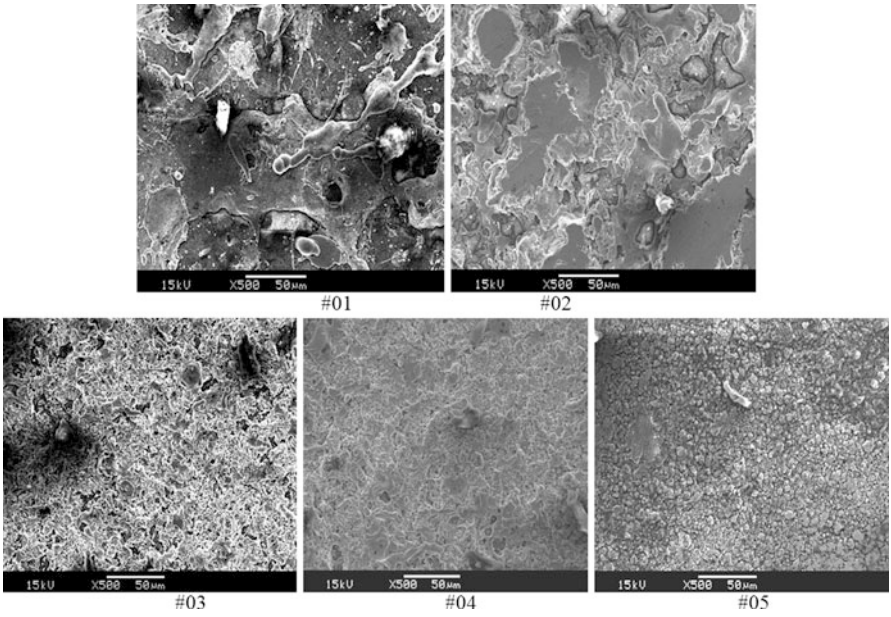

Fig. 2 Surface topography of the coating under initial capacitor voltage of 10 kV (#01), 12.5 kV (#02), 15 kV (#03), 17.5 kV (#04) and 20 kV (#05)

Table 1 The parameters of the substrate under different initial capacitor voltage

No.	Weight before spraying (g)	Weight after spraying (g)	Weight of the film (g)	Average width (mm)	Resistance of the film (Ω)
#01	53.1749	53.3320	0.1571	20	very great
#02	53.2022	53.2673	0.0651	25	very great
#03	52.7266	52.7544	0.0278	26	1.14
#04	52.5245	52.5470	0.0225	30	1.55
#05	53.6290	53.6466	0.0176	31	21.51

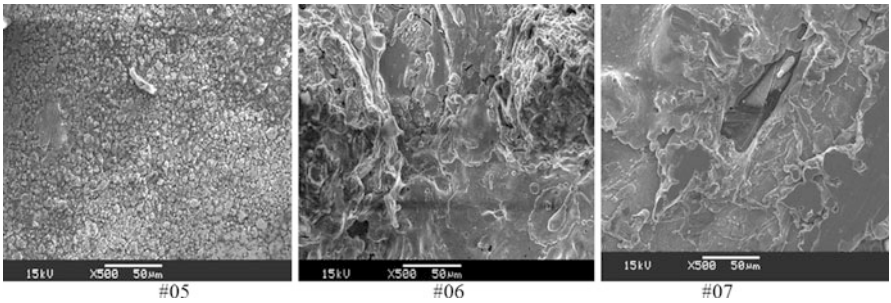

Fig. 3 Surface topography of the coating under wire diameter of 0.5 mm (#05), 0.75 mm(#06), and 1 mm(#07)

bridge; when the initial capacitor voltage increases to 15 kV, the resistance is 1.14 Ω; and the resistance increases again with the rise of the initial capacitor voltage.

3.2 Experimental Results Under Different Wire Diameter

Experiment #05, #06 and #07 is conducted under the wire diameter of 0.5, 0.75, and 1 mm, respectively. The initial capacitor voltage is 20 kV, circuit inductance is 3.9 μH, and spraying distance is 20 mm.

The SEM micrographs of the film under different wire diameter are shown in Fig. 3.

The film surface is magnified by 500× in Fig. 3. It can be told from the micrograph #5 that the surface of the film is neat; the particles are even, and without sandwich structure. But with the increasing of wire diameter, sandwich structure is more obvious, the film has more holes in it, and the substrate can be seen in certain places.

The detail of experimental results under different wire diameter is shown in Table 2. The result shows that film is more even with a smaller wire diameter. Smaller wire diameter means that the wire will be heated up fast, and the generated particles are small, and move fast toward the substrate, from an even film.

Table 2 The parameters of the substrate under different wire diameter

No.	Weight before spraying (g)	Weight after spraying (g)	Weight of the film (g)	Average width (mm)	Resistance of the film (Ω)
#05	53.6290	53.6466	0.0176	31	21.51
#06	52.4189	52.8150	0.3961	31	0.589
#07	52.3282	52.9813	0.6531	33	very great

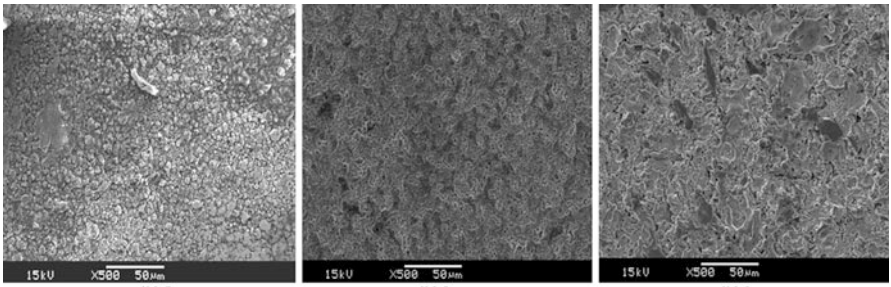

Fig. 4 Surface topography of the coating under different circuit inductance

Table 3 The parameters of the substrate under different circuit inductance

No.	Weight before spraying (g)	Weight after spraying (g)	Weight of the film (g)	Average width (mm)	Resistance of the film (Ω)
#05	53.6290	53.6466	0.0176	31	21.51
#08	53.2831	53.3906	0.1075	28	0.965
#09	53.0782	53.173	0.0948	21	0.235

3.3 Experimental Results Under Different Circuit Inductance

Experiment #05, #08 and #09 are conducted under the circuit inductance is 3.9, 6.5 and 10.8 μH, respectively. The initial capacitor voltage is 20 kV, wire diameter is 0.5 mm, and spraying distance is 20 mm.

The SEM micrographs of the film under different circuit inductance are shown in Fig. 4.

The film surface is magnified by 500× in Fig. 4. The SEM micrographs tell that the film surface topography of the film is influenced by the circuit inductance strongly. When the circuit inductance is small, the film surface is neat, even; but with the increasing of the inductance, the surface of the film is irregular, and has more holes in it.

The detail of experimental results under different circuit inductance is shown in Table 3. Smaller circuit distance means the energy stored in the pulsed capacitors can be deposited into the wire faster and more efficient, and thus, the wire is heated up faster and evener, forms a neater, evener film surface.

4 Conclusion

The WESC experiment for preparing copper film on glass substrate was conducted under different initial capacitor voltage, wire diameter, circuit conductance in this paper. The result showed that, higher initial capacitor voltage, smaller circuit conductance and wire diameter were conducive to the fast energy depositing into the copper wire, and then decrease the influence of the uneven heating up process. The thin film prepared under this condition has a more even and neat surface.

Acknowledgments This paper is supported by Supported by National Natural Science Foundation of China (Grant No. 51167004, 51067002), and Guangxi Natural Science Foundation (Grant No. 2013GXNSFBA019250).

References

1. Das R, Das BK, Shyam A (2012) Synthesis and characterization of copper nanoparticles by using the exploding wire method. J Korean Phys Soc 61(5):710–712
2. Snitka V et al (2007) Structural and optical properties of zinc oxide films deposited by wire explosion technique. Phys Stat Sol (b) 244(5):1504–1511
3. Zhao Hongsheng, Chen Wei, Wong Dan et al (2004) The development of functional thin film on glass surface. Mat Rev 18:1–4 (in Chinese)
4. Moosman B (1999) Diagnostics for exploding wires. Rev Sci Instrum 70:671
5. Yang Jiazhi, Liu Zhongyang, Xu Dongwei et al (2009) Wire resistance variation during its electrical explosion. Explo Shock Waves 29:205–208 (in Chinese)
6. Yang Jiazhi, Liu Zhongyang, Niu Qinzhou et al (2010) Simulation of wire resistance in variation explosion. J Guilin Univ Technol 30:300–304 (in Chinese)
7. Briand D, Weber P, de Rooij NF (2004) Bonding properties of metals anodically bonded to glass. Sensor Actuator A Phys 114:543–549

Separation Criterion Based on Apparent Impedance Angle

Chunjie Chen, Zhonglei Chen, Danzhen Gu, and Xiu Yang

Abstract In order to improve the criterion based on apparent impedance angle, the electrical parameters in the process of asynchronous oscillation based on the two-machine equivalent system are analyzed, and oscillation center is studied in the paper. In order to detect oscillation period correctly, the voltage and the active power is utilized. Moreover, the integration of reactive power is used to determine oscillation center. The simulation of New England 10 machine system shows that the criterion based on apparent impedance angle can distinguish asynchronous oscillation effectively, and oscillation period can be detected by voltage and active power. Also, the simulation indicates that oscillation center can be captured by reactive power.

Keywords Asynchronous oscillation • Apparent impedance angle • Oscillation center

1 Introduction

Power system stability is the key to the safe operation of power grid. With the continuous development of power network, the security of power system has been greatly improved. But natural disasters and unpredictable accidental factors still can cause the instability of the system [1–3]. Out of step splitting as the last line of defense ensures that the grid will not completely collapse, has been widely used [4, 5]. The accurate judgement of asynchronous oscillation is the basis of splitting.

C. Chen (✉) • D. Gu • X. Yang
Electric Power and Automation Engineering, Shanghai University of Electric Power, Shanghai, China
e-mail: ccj19890126@126.com

Z. Chen
Guizhou Liupanshui Power Supply Bureau, Guizhou, China

W. Wang (ed.), *Mechatronics and Automatic Control Systems*, Lecture Notes in Electrical Engineering 237, DOI 10.1007/978-3-319-01273-5_8,

Now separation criterion used in power system are mainly [6, 7]: the principle based on impedance track, the principle based on three-phase current, the principle based on apparent impedance angle, the principle based on $u\cos\varphi$, etc.

The principle based on impedance track can distinguish synchronous oscillation and asynchronous oscillation, but it is vulnerable to the influence of power system operation mode and network structure, and it is quite difficult for device setting [8]. The principle based on three-phase current can overcome the influence of load and operation mode, but it cannot distinguish the direction of current [9]. The principle based on $u\cos\varphi$ can accurately estimate the time when power angle reaches180°, but it cannot judge the location of oscillation center [10]. In this paper, the principle based on apparent impedance angle is studied. This separation criterion determines the state of system by utilizing the variation of phase different between voltage and current, and this criterion can effectively distinguish the direction of oscillation center. In order to distinguish oscillation period correctly, the voltage and the active power are utilized. In addition, the integration of reactive power is used to determine whether the oscillation center lies in this line.

2 The Characteristics of Apparent Impedance Angle in the Process of Asynchronous Oscillation

All units are usually divided into two coherent generator groups when the power system is in the process of out of step. So the two-machine equivalent system can be used to analyze the characteristic of electrical parameters [11], as shown in Fig. 1. The equivalent impedance of the system is $\dot{Z}_{eq}$, and the impedance angle is φ_{eq}. M is oscillation center.

It is assumed that the electric potential amplitudes of $\dot{E}_1$ and $\dot{E}_2$ are equal, and deemed that the impedance angle of the system is the same. $\dot{E}_1$ is referenced vector, and the angle between $\dot{E}_1$ and $\dot{E}_2$ is δ.

The apparent impedance angle of measuring point O1 in the process of asynchronous oscillation is:

$$\theta_{o1} = \arctan\frac{n\sin\delta}{1+n\cos\delta} - \frac{\delta}{2} - \frac{\pi}{2} + \varphi_{eq} \tag{1}$$

$$n = (Z_{eq}/2 + Z_{om})/(Z_{eq}/2 - Z_{om}) \tag{2}$$

The variation of apparent impedance angle is different when oscillation center is in the different position of measuring device. It is assumed that the power flows from bus to line as the positive direction. When the power flows to oscillation center, the oscillation center is located in the positive direction of measuring point. On the contrary, oscillation center is located in the negative direction of measuring point [12].

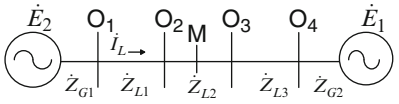

Fig. 1 Diagram of two-machine equivalent system

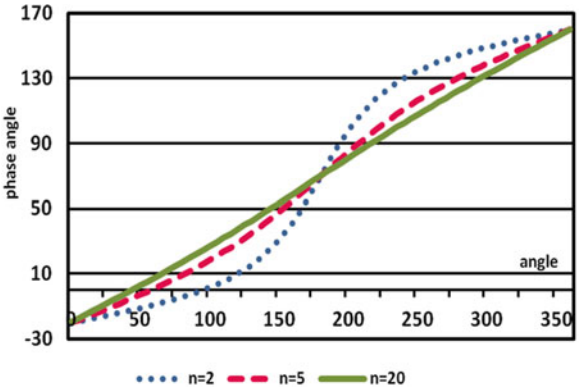

Fig. 2 The curve of impedance angle as $n > 1$

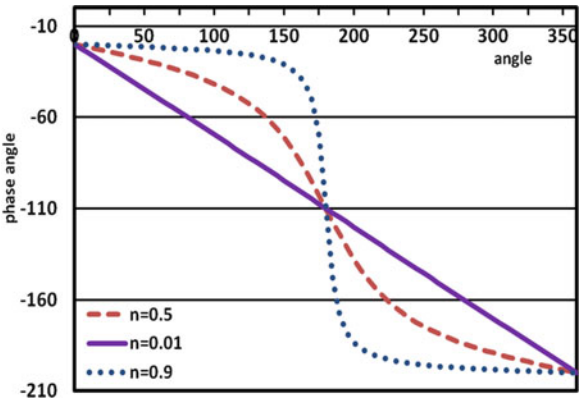

Fig. 3 The curve of impedance angle as $0 < n < 1$

1. When oscillation center is located in the positive direction of measuring point and measuring point is sending end ($Z_{om} > 0$ then $n > 1$), the change curve of apparent impedance angle is shown in Fig. 2 when n takes different values. It is shown that the apparent impedance angle increases when the angle δ changes from 0° to 360°.
2. When oscillation center is located in the negative direction of measuring point and measuring point is receiving end ($Z_{om} < 0$ then $0 < 1$), the change curve of apparent impedance angle is shown in Fig. 3 when n takes different values. It is shown that the apparent impedance angle decreases when the angle δ changes from 0° to 360°.

Also, the variation of apparent impedance angle in other positions can be obtained by the same theory.

3 The Out-of-Step Criterion of Apparent Impedance Angle

There is certain function relation between apparent impedance angle and angle δ according to the above analysis. Therefore, apparent impedance angle can be used to distinguish asynchronous oscillation, synchronous oscillation and short circuit faults.

The impedance plane is divided into six parts, as shown in Fig. 4 [13, 14]: the range from φ_1 to φ_2 is part I; the range from φ_2 to 90° is part II; the range from 90° to φ_3 is part III; the range from φ_3 to φ_4 is part IV; the range from φ_4 to 270° is part V; the range from 270° to φ_1 is part VI.

In the process of asynchronous oscillation, the change law of apparent impedance angle is:

1. When measuring point is sending end and oscillation center is in the positive direction of measuring point, the change law of impedance angle is: I-II-III-IV.
2. When measuring point is sending end and oscillation center is in the negative direction of measuring point, the change law of impedance angle is: IV-V-VI-I.
3. When measuring point is receiving end and oscillation center is in the positive direction of measuring point, the change law of impedance angle is: IV-III-II-I.
4. When measuring point is receiving end and oscillation center is in the negative direction of measuring point, the change law of impedance angle is: I-VI-V-IV.
5. When oscillation center is located in measuring point, the change law of impedance angle is: IV-I or I-IV.

When the system is subjected to a large disturbance, the reactive power will over zero repeatedly, so the principle based on apparent impedance angle will misjudge the number of oscillations easily [15].

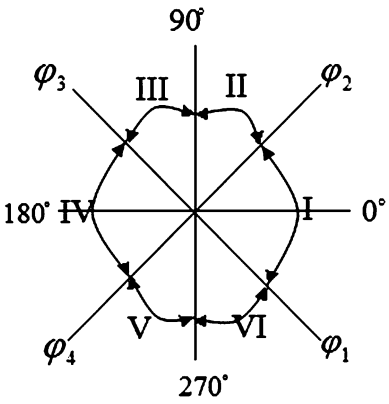

Fig. 4 The division of impedance plane

Without considering the losses of lines, meaning that line impedance is represented by reactance, the active power of measuring point O1 is:

$$P = \mathrm{Re}[\dot{U} \cdot \hat{I}_L] = 2\frac{{E_1}^2}{X_{eq}} \sin\frac{\delta}{2} \cos\frac{\delta}{2} = \frac{{E_1}^2}{X_{eq}} \sin\delta \tag{3}$$

It shows that the active power is over zero periodically in the process of asynchronous oscillation, and the period is 2π. Therefore, the active power can be used to detect the out of step oscillation period. When the active power cross zero two times, it can be determined as an out-of-step period [16].

So, when both of the following conditions happened, it can be determined as an out-of-step period

1. Apparent impedance angle accords with the change law of asynchronous oscillation.
2. The active power is crossing zero two times.

Oscillation center is mainly determined by the minimum value of apparent impedance or by the minimum value of voltage, but this method cannot determine the direction of oscillation center [17]. Because of the strong coupling relation between reactive power and voltage [18], the integration of reactive power is used to distinguish the direction of oscillation center in this paper.

The reactive power of bus O1 is:

$$Q = \frac{E_1^2}{Z_{eq}}\{[\sin\varphi_{eq} - \sin(\varphi_{eq} + \delta)] - k(2 - 2\cos\delta)^* \sin\varphi_{eq}\} \tag{4}$$

Where, $k = Z_{om}/Z_{eq}$.

The integration of reactive power in an oscillation period is:

$$f(k) = \int_0^{2\pi} Q d\delta = 2\pi\frac{E_1^2}{Z_{eq}}(1 - 2k)\sin\varphi_{eq} \tag{5}$$

$f(k)$ is positive when $k < 0.5$, and $f(k)$ is negative when $k > 0.5$. So the integrations of reactive power at each end can be used to determine oscillation center. If the integrations of reactive power at each end are positive and negative respectively, it is determined that oscillation center is in this line.

4 Simulation Example

The system of New England 10 machine [19] is simulated in this paper, as shown in Fig. 5. The PSD-BPA program is used for time-domain simulation.

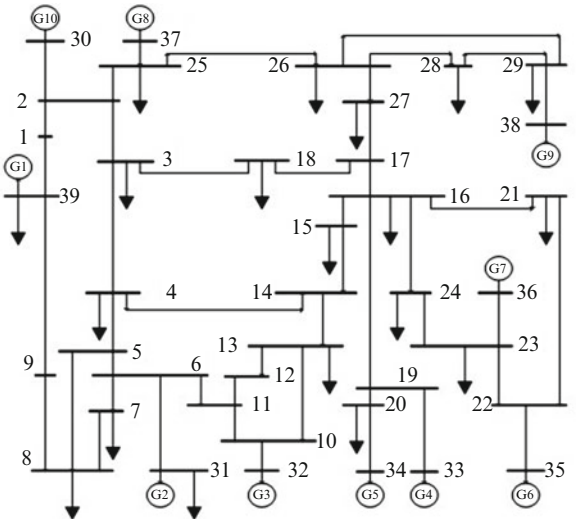

Fig. 5 The diagram of New England 10 machine system

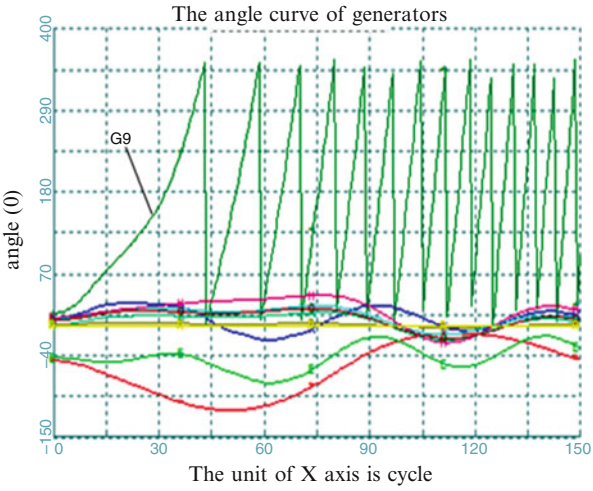

Fig. 6 The angle curves of all generators

Assuming that the generator G2 is referenced unit, when three-phase short circuit fault occurs at line 26–27 and the fault is removed at 0.2 s, the angle curves of all generators are shown in Fig. 6.

As shown in Fig. 6, relative to other generators, the unit G9 is instability. The line 26–28 is discussed in this paper. The change law of apparent impedance angle at bus 26 is shown in Fig. 7.

As shown in Fig. 7, the change law of apparent impedance angle at bus 26 is IV-III-II-I, and it meets the law of the criterion based on apparent impedance angle. So it can be determine that the system is in the state of asynchronous oscillation.

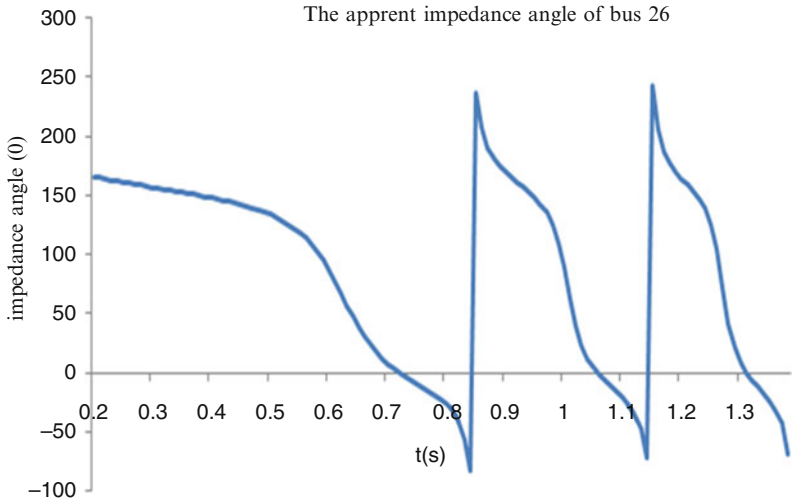

Fig. 7 The change curve of apparent impedance angle at bus 26

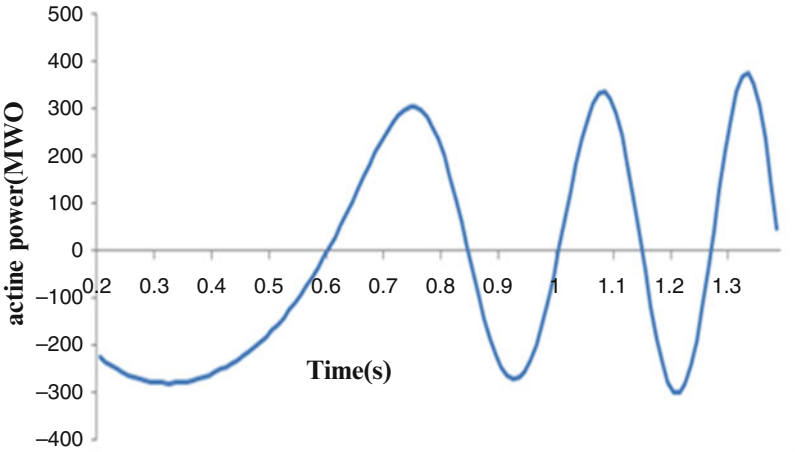

Fig. 8 The curves of active power in line 26–28

In order to distinguish oscillation period correctly, the active power of line 26–28 is need to discuss, and the result is shown in the Fig. 8.

As shown in Fig. 8, the active power of line 26–28 is over zero two times at 0.84 s. So, according to the change law of apparent impedance angle, it is confirmed that 0.2 ~ 0.84 s is the first out-of-step oscillation period.

The integration of reactive power of line 26–28 is calculated, and the result is shown in Table 1.

Table 1 The integration of reactive power in line 26–28

Time (s)	The location of device	The integration of reactive power (Mvar)	Time (s)	The location of device
0.85–1.15	Bus 26	736.1	0.85–1.15	Bus 26
0.85–1.15	Bus 28	−855.8	0.85–1.15	Bus 28

The integration of reactive power at bus 26 is positive, and it is negative at bus 28. So it is confirmed that oscillation center is located in line 26–28. The line 26–29 is studied according to the above analysis, and it also determined that oscillation center is located in line 26–29.

5 Conclusion

The separation criterion based on apparent impedance angle can distinguish the asynchronous oscillation, synchronous oscillation and short-circuit faults. And it also can tell the direction of oscillation center effectively. When the system is subjected to a large disturbance, this criterion tends to misjudge the number of oscillations. If the voltage falls down to the lowest and the active power is over zero at the same time, it is determined as an out-of-step period. Oscillation center was captured by the integration of reactive power in this paper. If the integrations of reactive power at each end are positive and negative respectively, it can be confirmed that oscillation center is in this line. The correctness of this criterion is verified by the analysis of New England 10 machine system.

Acknowledgments Supported by National Natural Science Foundation of China (50977055), Key technology R&D program of Shanghai(09160501600, 10dz1203100), Project Sunburst (10SG51), Shanghai Higher Education '085' engineering construction program.

References

1. Shen Gen-cai (2004) Recognizing power oscillations in depth to improve network configuration and splitting arrangement of a grid rationally. Int Electr Power China 8:4–6 (In Chinese)
2. Andersson G, Donalek P, Farmer R et al (2005) Causes of the 2003 major grid blackouts in North America and Europe and recommended means to improve system dynamic performance. IEEE Trans Power Syst 20(4):1922–1928
3. Yuan Ji-xiu (1999) Emergency control for prevent widespread blackout of power system the third line of defence. Power Syst Technol 23(4):1–4 (In Chinese)
4. Ren Jian-feng, Ding Ya-wei, Fu Lei, Chen Xiong, Li Xue-ming (2011) An improved strategy for out-of-step separation based on phase angle principle for 1000kv ultra-high voltage AC power grids. Autom Electr Power Syst 35(10):104–107 (In Chinese)

5. Lu Fang, Yu Ji-lai (2011) A method of power system out-of step separation based on network energy. J Harbin Eng Univ 32(6):780–785 (In Chinese)
6. Gao Peng, Wang Jian-quan, Gan De-qiang, Hang Zhen-xiang (2005) Review on power system out-of-step separation. Autom Electr Power Syst 29(9):90–96 (In Chinese)
7. Fan Jin (2011) A review on the studies on power system islanding. J Xi'an Univ Posts Telecommun 16(3):56–60 (In Chinese)
8. Taylor CW, Haner JM et al (1983) A new out-of-step relay with the rate of resistance augmentation. IEEE Trans Power Ap Syst PAS 102(3):631–639
9. Lei Xiao-peng (2008) The research and analysis on out-of-step separation of large-scale interconnection power system. Xi'an University of Technology, Xi'an (In Chinese)
10. Zong Hong-liang, Ren Zu-yi, Zheng Yu-ping et al (2003) An out-of- step splitting device based on the changing track of the voltage of oscillation center. Autom Electr Power Syst 27 (19):83–85 (In Chinese)
11. Sui Yong-zheng (1997) Distinguishing method of coherency set group in electric power system. Heilongjiang Electr Power Technol 19(6):325–327 (In Chinese)
12. Dong Xi-jian, Zhao Jie, Ling Chao, Li Xue-ming, Li Hui-jun, Zhang Zheng-qin, Zhang Chang-yin (2010) Research on out-of-step oscillation criterion mechanism based on principle of phase angle. Power Syst Prot Control 38(7):1–6 (In Chinese)
13. Dong Xuan (2007) The research of large power system out-of-step separation. Nanjing University of Science & Technology, Nanjing (In Chinese)
14. Liu Ping (2004) Study on principle of power system separation device based on local electrical parameter. North China Electric Power University, Beijing (In Chinese)
15. Gao Peng, Wang Jian-quan, Zhou Wen-Ping (2004) Improvement of the apparent impedance separation criterion. Autom Electr Power Syst 28(24):36–40 (In Chinese)
16. Zhang Bao-hui, Zhang Yi-gang, Liu Hai-tao (2001) Study on principle of power system separation device based on local electrical parameter. Proc CSEE 21(12):67–72
17. Li Li (2009) Studies on out-of-step splitting criterion and control scheme based on wide area measurements. Shandong University, Shandong (In Chinese)
18. Gao Peng, Yang Mei-qiang, Ren Zu-yi (2006) A new method of capturing the out-of-step central location. Jiangsu Electr Eng 25(3):7–10 (In Chinese)
19. Wang Yi-xuan (2011) Study on the out-of-step identification and islanding strategy based on PMU data. North China Electric Power University, Beijing (In Chinese)

The Design for Photoelectric Graphics Generator of Small Arms Sights

Qiushui Yu, Hui Guo, Jinzhi Sun, Bing Liu, and Ruining Yang

Abstract In order to simulate infinite far targets in the testing system of small arms sights, improve the test efficiency and accuracy, this paper designed a set of photoelectric graphics generator based on the collimator and DLP technology. The photoelectric graphics generator uses a computer and a modified DLP to replace the traditional reticule. It is controlled by a computer and automatically generates a variety of graphics according to our needs. These graphics are reflected onto the beam splitter through the reflector, and are reflected onto the collimator collimating objective through the beam splitter again, and finally, generate an infinite far target. Experiment results show that the photoelectric graphics generator not only simulates the infinite far targets, but also reduces tedious work of component replacement reticule and overcome the influence of human factors. It can improve the test accuracy of testing system, and meet the testing requirements of performance parameters of light weapons sights.

Keywords Light weapons sights • DLP • Collimator • Photoelectric graphics generator

1 Introduction

The sight is an important part of the light weapons. The optical sights, which is composed of visible light photoelectric sensors, laser photoelectric sensors, low light level photoelectric sensors, infrared photoelectric sensors, used to the gun is playing an important role in modern warfare. So the world's major countries are

Q. Yu (✉) • H. Guo • J. Sun • B. Liu
Fundamental Department, Aviation University of Air Force, ChangChun, China
e-mail: yuqiushui123@126.com

R. Yang
Linyi Normal University, Linyi, China

W. Wang (ed.), *Mechatronics and Automatic Control Systems*, Lecture Notes in Electrical Engineering 237, DOI 10.1007/978-3-319-01273-5_9,

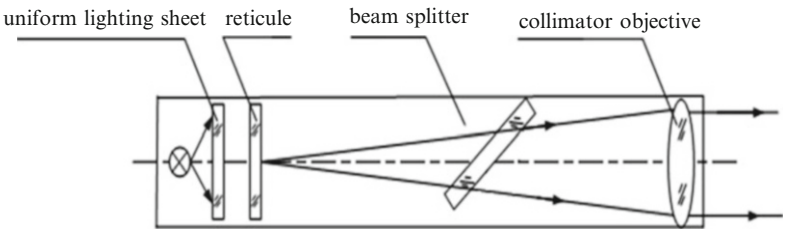

Fig. 1 Traditional photoelectric graphics generator

strongly to develop photovoltaic technology, research and manufacturing new type optical sights. In the process of research and manufacturing of optical sights, the performance parameters of optical system affect the overall performance of light weapons sights directly. Therefore, its quality must be fully tested after designing, processing and assembly, accordingly understand the quality of performance parameters on the overall performance, further adjustment and correction, and achieve the best extent [1].

Conventional test of optical sights performance parameters basically uses classical optical testing techniques. These techniques are more mature and standardized. The test instruments used universal optical measuring instruments (See Fig. 1). In order to simulate an infinite target, to meet the requirements of the different parameters test, which need to produce the reticule components of a variety of different patterns, mainly include: framed cross and circle reticule (3), the framed perot board (1), star point board with a box (1 set), a frame resolution board, 1 set (No. 1 ~ No.5) and framed frosted glass, opal glass, evenly-rays, polarizer (1 set).

These reticules, when the components are testing in simulation infinity goals, not only troubled for replacing them and also influenced by the human factors. In order to facilitate to generate the various reticule patterns that we need and reduce the influence of human factors to meet the objective test of image surface stability of zoom white sights, low light sights, on the basis of the collimator, combined with DLP technology, we designed a set of photoelectric graphics generator. The photoelectric graphics generator can be controlled by a computer and generated a variety of reticule graphics according to our needs automatically. These graphics are located in the focal plane of collimator lens, and simulated infinity goals.

2 The Design of Photoelectric Graphics Generator

The photoelectric graphics generator uses a kind of new generative technology of graphics – Photoelectric Digital Light Processing (DLP) technology. It can auto-generate all kinds of reticule graphics we need by a computer controlled, so the selection of DLP is essential.

2.1 Selection of DLP

DLP is an abbreviation for Digital Light Processing. This technique need to convert image signal into digital signal through the digital processing firstly, then the light projected. It is a technology based on Deyi company developed a digital micromirror device – DMD to complete the digital visual information display, and it is an unique, using an optical semiconductor to produce digital multiple light sources display solutions. It is a highly reliable all-digital display technology, can provide the best image results in all kinds of products.

DMD is the abbreviation for Digital Micromirror Device, it is the core of DLP technology [2]. A DMD can be simply described as a semiconductor light switch, composed of hundreds of thousands or even millions of micro-lenses [3]. A micro-lens represents a pixel; the transformation rate is 1,000 times/second or faster [4]. Each lens size is 14 × 14 μm (or 16 × 16 μm), and below it has a hinge-like rotation of the role of device is easy to adjust the direction and angle. Each lens can pass or cut off a pixel's light, the hinge allows the lens to tilt between two states, +10° is "on", −10° is "off", When the lens is not working, they are "parked" state of 0°. Under the "On" state, the reflected incident light projected the image onto the screen through the projection lens; while under the "off" state, the incident light reflected in the micro-lens was absorbed by absorber [5]. DLP projection technology use digital micromirror device to realize digital optical processing.

The principle of DLP projection technology is homogenizing the light source by an integrator, through a color wheel of three primary colors, the light is divided into R, G, B three-color, and then make the color imaging in the DMD through the lens. Use the method of Sync signal, convert the electric signal of digital rotating lens into grayscale, shown colors coordinate with the R, G, B three colors, the last projection imaging through lens. Working principle [6] see Fig. 2.

Because the qualification requirements of the photoelectric graphics generator can display the computer VXGA signal, resolution (pixels) is 1024 × 768, Pixel size is 16 × 16 μm, Uniformity is ≤10 %, therefore, we selected DLPTM projectors of PLUS company produced, its model number is U3-1100WZ/C. DLP installation structure diagram shown in Fig. 3.

2.2 Schematic Diagram of Photoelectric Graphics Generator

In order to facilitate to generate the various reticule patterns that we need and reduce the influence of human factors, we used a computer and a modified DLP to instead of the reticule. In order to simulate an infinite far target, we carried out transformation for DLP projector, removed the projection lens out of the DLP itself, and placed the DMD in the focal plane of the collimating lens. In order to control the illumination of light source, and prevent CCD supersaturation, the Polaroid was

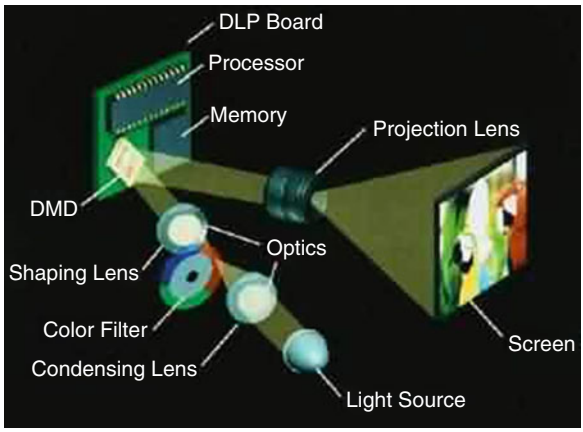

Fig. 2 DLP working principle schematic

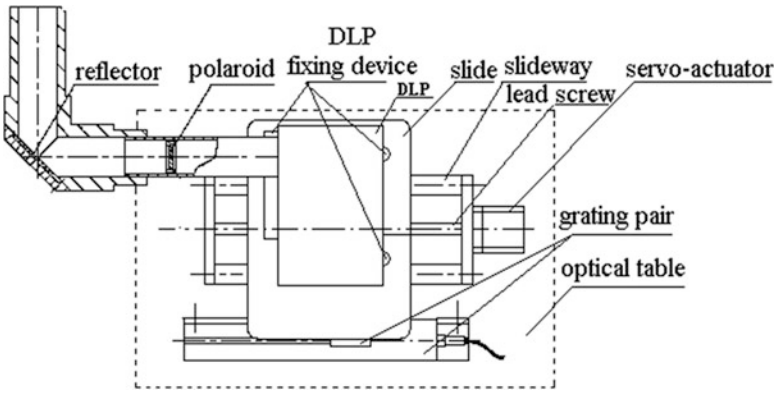

Fig. 3 DLP installation schematic

joined in the optical path, to meet the qualification requirements of the area CCD devices, and easy to display and process image. The principle of photoelectric graphics generator are shown in Fig. 4.

3 The Testing Experiment of Photoelectric Graphics Generator

First, using the VC++ 6.0 programming techniques to generate a variety of reticule graphics that we need. Then, making required graphic image on the digital micromirror device in the DLP by a computer. Now, the DMD in the focal plane of the collimator collimating lens, which achieve infinity far target simulation, shown in Figs. 5, 6, 7, and 8.

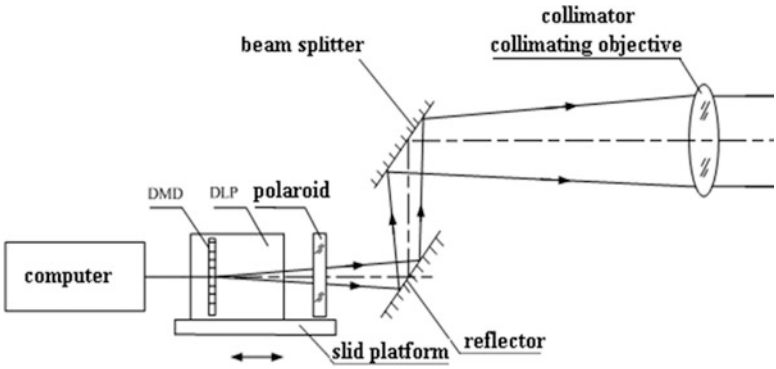

Fig. 4 The photoelectric graphics generator schematic diagram

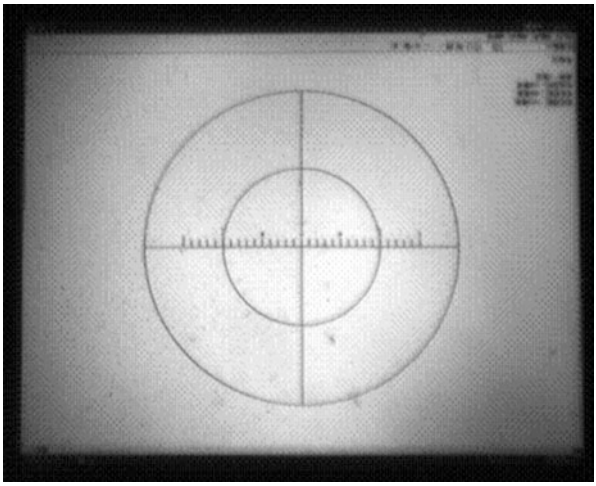

Fig. 5 DLP generated cross division image

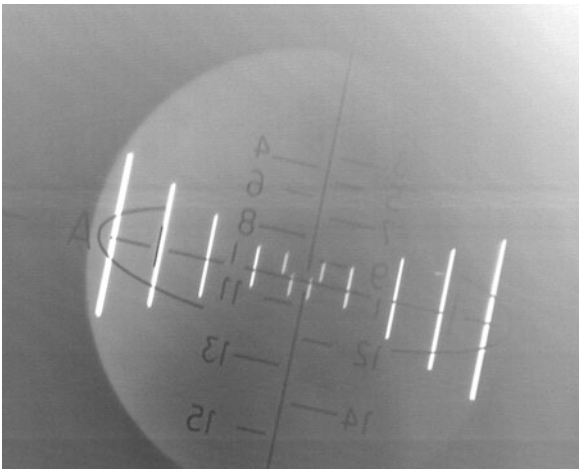

Fig. 6 DLP generated perot board image

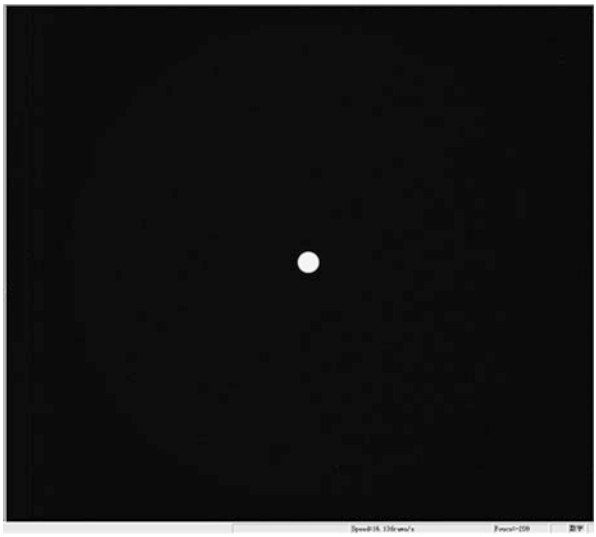

Fig. 7 DLP generated star image

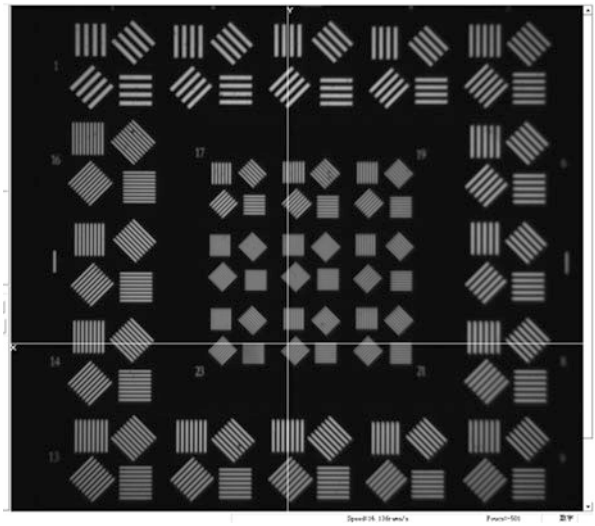

Fig. 8 DLP generated $2^{\#}$ resolving power test target

When the testing, in order to make DMD can be accurate in the focal plane of the collimating lens, we used the photoelectric automatic focusing technology to make CCD camera system uptake the clear image of collimator reticule firstly; then, switched to the optical path of automatically generate optical graphics through the beam splitter, uptake the image formation in DMD by the CCD camera system. And finally, combined the computer image processing technology, through the control system to control DLP real-time micro drive to determine the focal plane position.

4 Conclusion

This study used the technology of DLP and collimator combination to develop an infinity optical pattern generator successfully for the first time. The experiments showed that the pattern generator not only reduced the tedious work of replacing the components of the reticule, but also overcame the influence of human factors, which met the requirements of objective test of the performance parameters of the light weapons sights optical system.

References

1. Yu Qiushui, An Zhiyong, Yang Ruining et al (2010) Test of parallax parameters for optoelectronic sights in small arms. Opt Precis Eng 18(8):1732–1737
2. Jing-xian Zhou, Rong-zhi Wu (2003) Digital micromirror device. Chin J Liq Cryst Displays 18 (6):445–449
3. Hong-Zhou Zhai (2000) Imaging principle of the DLP projector. Motion Pict Video Technol 8 (5):8–10
4. http://www.dlp.com/technology/how-dlp-works/
5. Feng-he Yang, Dong-hui Lan (2005) Special techniques in DLP-based projection display. Video Eng 17(4):39–42
6. http://en.wikipedia.org/wiki/Digital_Light_Processing

The Fluid Flow Investigation of the Compact Motor with Medium-Size and High-Voltage in YJKK Series

Dawei Meng, Jinze He, and Yongming Xu

Abstract According to the asymmetry characteristics of the fluid flow in YJKK serious compact motor, a motor of YJKK500-4,2500 kW was taken as an example, 3D physical and mathematical models for the ventilation system in the motor were established. The boundary conditions and assumptions for solving domain were given. According to the computational theory of hydromechanics, some useful conclusion can be drawn based on the calculation of the stable global fluid field of a YJKK compact box-type motor at rated operation state, the performance curve of the fan in motor was given, the improments of the stator ventilating channel steel, wind shield at fan sides and inner baffles of coolers were put forward. The results obtained was consistent with the actual operating condition, which proved the feasibility of the global fluid model.

Keywords Motor • 3D fluid field • Fan • Ventilation • Cooling system

1 Introduction

With the improvement of correlative technology in the field of motors, high-efficiency motors with high power density has become the future development trend. However, cooling problems have thereupon become the bottleneck of the development of such motor technology. Rational use of forced ventilation and proper cooling medium to take away the motor internal loss can effectively reduce localized excessive temperature rise. In recent years, experts and scholars at home and abroad have done some research on fluid field and fluid temperature coupling

D. Meng • J. He (✉) • Y. Xu
Department of Electrical Engineering, Harbin University of Science and Technology, Harbin, China
e-mail: arthurhjz0452@163.com

W. Wang (ed.), *Mechatronics and Automatic Control Systems*, Lecture Notes in Electrical Engineering 237, DOI 10.1007/978-3-319-01273-5_10,

field of high-efficiency motors with high power density [1], but only a few studies have been published referring to the analysis on global fluid distribution of internal motors.

The YJKK series motors is a new product developed based on the original the YKK series medium-sized high-voltage motor. Compared with original the YKK series motor, its center high is two levels' lower on average in the case of the same capacity while its power density is increased. According to the geometry similarity law of the motor [2], along with the increase in power density, the internal heat dissipation problem is bound to become increasingly prominent, therefore, it is necessary to improve the cooling system to ensure motors operate safely and reliably.

In the past, usually only the analysis model of certain parts of the region is established and afterwards some estimates are carried out on the fluid flow characteristics of the overall model when the distribution of cooling gas parameters within high-voltage motors are calculated. In that case, the empirical formula and test need to be fitting if boundary conditions are to be applied [3]. Therefore, existing research results are not fully applicable for the motor with new structure. In order to describe the fluid flow and pressure distribution of the internal motor, so as to lay the foundation for solving the temperature field of the motor, this paper take a YJKK500-4,2500 kW compact motor with medium-sized and high-voltage as an example, established global fluid model, analysed the fluid distribution and flow characteristics of the motor.

2 Establishment of the Model for Global Fluid

2.1 The Physical Model of the Global Fluid Analysis

The ventilation structure of the YJKK serious compact motor with medium-sized and high-voltage is shown in Fig. 1, the motor adopts new mixed-flow ventilation system which consists of two parts as a whole. The overall trend of fluid flow can be seen from the internal motor ventilation structure. Some air enters the end of internal cooling windings of motors via inlets while the majority enters into the gap between the rotating shaft welding reinforcing plates which play a supporting role in the motor structure and act as fan blades to blow away the air between plates through radial ventilating ducts. The pressure difference generated by rotation of centrifugal fan makes the fluid at the back of the stator core enter outlets via wind shield and then discharge into the cooler.

Main dimensions and parameters related to ventilation system are as follows: the core of motor model length is 900 mm; stator outer diameter is 900 mm and stator inner diameter is 560 mm; rotor outer diameter is 553.6 mm and rotor inner diameter is 310 mm; axis outer diameter is 210 mm; the number of rows of radial ventilating ducts of stator and rotor is 14 and the width of each duct is 8 mm;

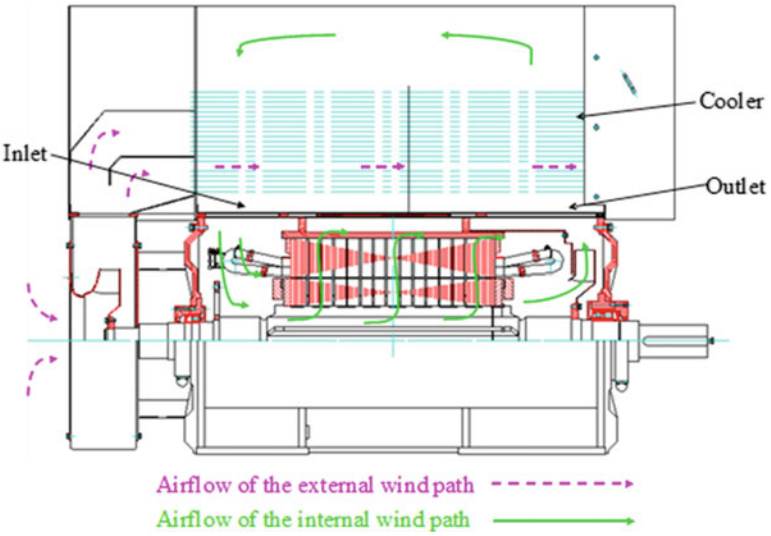

Fig. 1 The structure of YJKK mixed ventilation

60 pieces of ventilation channel steel, whose shape is 4 * 8 * 160 mm, are distributed evenly in each row of ventilation channel of stator and rotor; inside the motor, the inlet area of ventilation circuit is 920 * 400 mm^2, and the outlet area of it is 920 * 299 mm^2.

Due to the asymmetry of the fluid flow area of the ventilation circuit inside motor, overall modeling is required in calculation [4]. In view of the rotation of fan and rotor when the motor is running, the whole model is partitioned into three parts: fan, rotor and overall static flow channel including stator. All flow areas are connected to each other. The end region of the stator winding of the motor is not taken into account in overall modeling because it has little effect on fluid. The cross-section view of 3D model of the ventilation system and the fan is shown in Fig. 2. Due to the fan section is important in the fluid calculation, Fig. 3 shows a 3D model of the fan. The model shows that the centrifugal fan is equipped with 9 blades evenly. It is a backward inclined fan with entry angle $\beta_1 = 18^\circ$ and exit angle $\beta_2 = 18^\circ$.

2.2 The Mathematical Model of the Global Fluid Analysis

3D turbulence flow of fluid satisfies the mass conservation equation, the momentum conservation equation [5] and the standard $k - \varepsilon$ turbulence equation [6].

The basic assumptions of fluid flow calculation are:

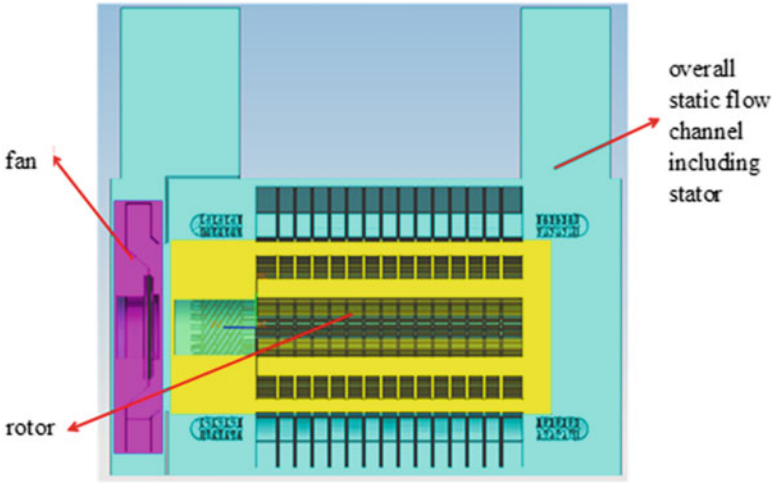

Fig. 2 Cross-section view of 3D model

Fig. 3 Fan model the ventilation system

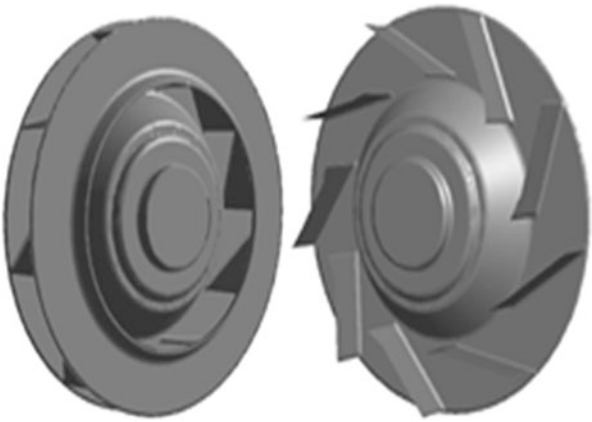

1. The Reynolds number of flow inside the motor is great and it is turbulent flow, hence turbulence model is used for the solution.
2. The affection of buoyancy and gravity of air fluid in the motor is ignored under standard atmospheric pressure.
3. The fluid velocity in the motor is less than sound velocity, which means low Mach number; hence it cannot be treated as compressed fluid [7].
4. There is no gap between stator slots as they are fully filled with windings.
5. Assume the end face of the stator slot wedge close to air gap and the inner surface of the stator core is coplanar, which means the air gap is treated as smooth torus [8].

The boundary conditions in calculating fluid flow of the motor are:

1. Inlet and outlet boundary conditions under standard atmospheric pressure are used for the calculation, thus, inlet and outlet pressures are both zero. The flow rate inside the motor can be calculated by solving the inner ventilation circuit.
2. All the surfaces contacted with air all use no-slip boundary condition.
3. The components of the rotor use rotating wall surface boundary condition and multi-reference frame to simulate; air gap, stator and the air behind stator core are treated as static part to simulate.
4. The rated speed of the motor is 1,490 r/min.

3 Finite Element Calculation and Result Analysis of Ventilation Systems

In accordance with finite-volume method, the continuous space is decomposed into a number of discrete points, using unstructured grid to begin mesh subdivision on the model, the global mess is subdivided into 2.2 million units, 10.8 million nodes.

The global fluid distribution is obtained though numerical calculation. The fan vector speed is shown in Fig. 4. The fan performance curve is shown in Fig. 5 When the fan works under rated condition, the flow rate from simulation is 1.95 kg/s while that from experiment is 1.87 kg/s with the error of 4.56 %. Because the slight larger wind resistance caused by the complex environmental factors in practical operation of the motor is ignored and the influence of the winding in end region to flow resistance is ignored, the calculation flow rate is slightly larger than that from actual measurement. This proves the model that created using global fluid field in this paper is rational. Figure 6 is the velocity vector diagram of the middle section of fan blades along z axis and the fluid path line graph. As shown in the picture, the fluid shape on both sides of the fan is of asymmetric distribution, which is because of the centrifugal fan used as the inner fan of the motor. It rotated counterclockwise at run time and its outlet is at the upper end of the fan, so the velocity of fluid at upper left of the fan is higher than that of other parts and the highest fluid velocity exists at the fan. Meanwhile, the fluid flow is quite regular observed from the fluid path line graph, which illustrates that the design of the engine base and the fan is more reasonable (Fig. 7).

Number the 14 radial ventilating ducts of stator and rotor core, the one at inlet side is No. 1, the one at outlet side is No. 14. The flow distribution of each ventilation channel is shown in Fig. 8.

In the prototype experiment, imbed three platinum thermal resistances in the inlet, the outlet of the fluid model and the middle of stator core. The stable temperature value is as follow: 42 °C at the inlet, 70 °C at the middle and the outlet is 82 °C. Therefore, the temperature of fluid rises along with the increase of ventilating duct number. But the flow increases correspondingly so that it can take away more heat, so it is consistent with original design intention of the ventilation and cooling system.

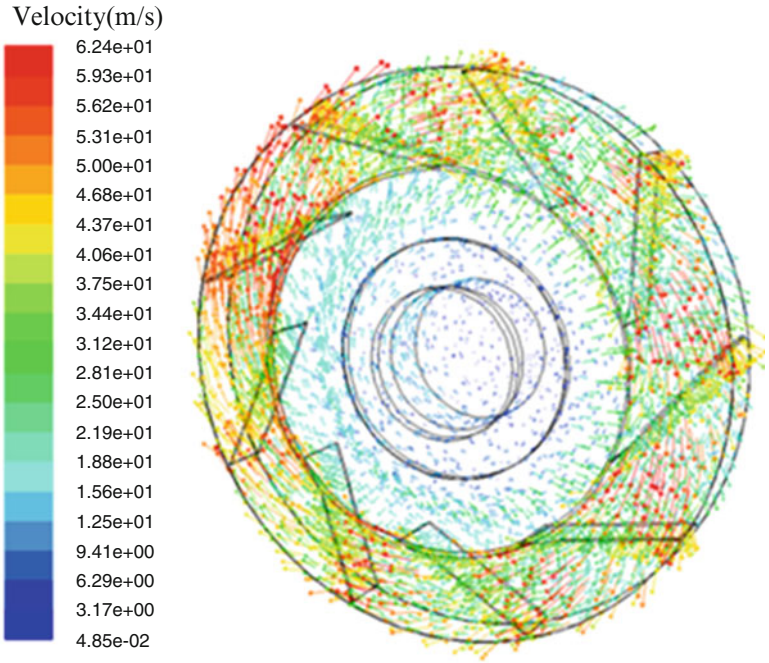

Fig. 4 Picture of fan vector speed

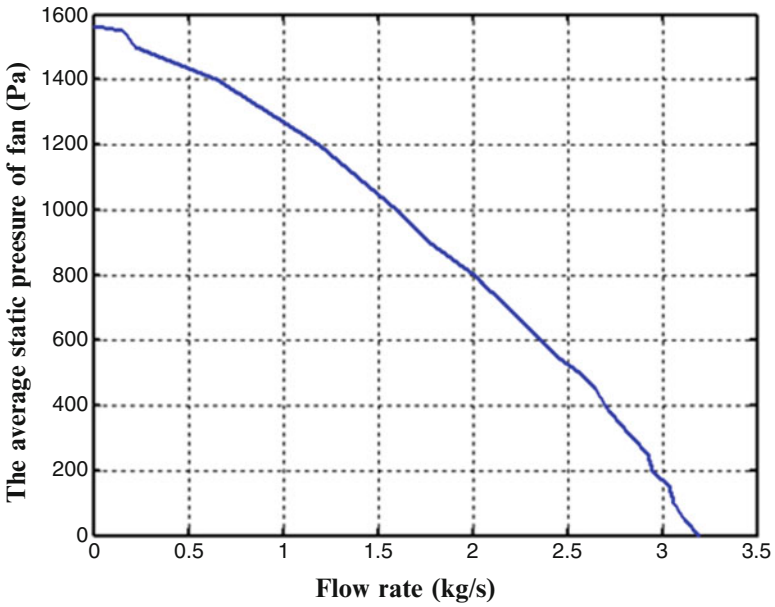

Fig. 5 Fan characteristic curve

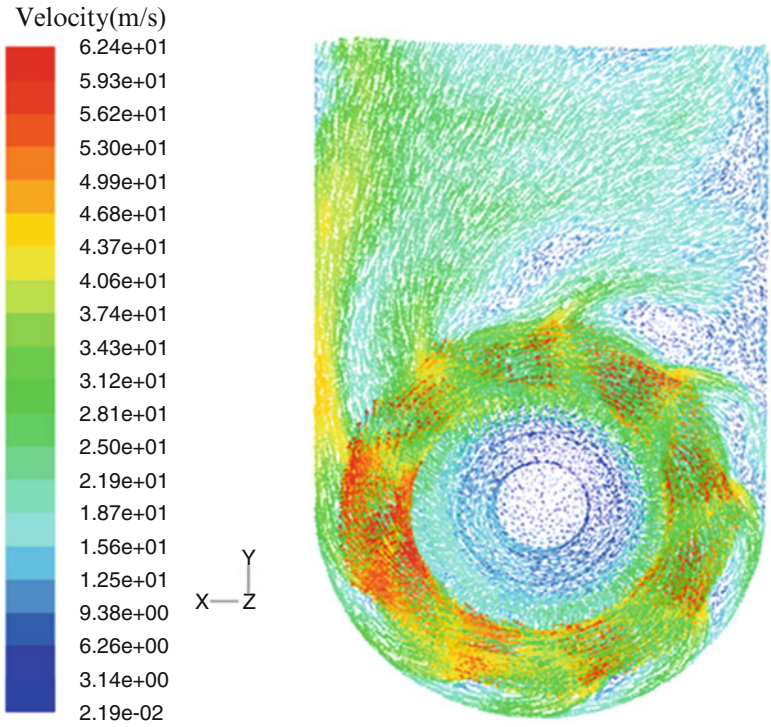

Fig. 6 The velocity vector nearby the fan

The schematic of stator ventilation channel is shown in Fig. 9. In Fig. 9, R_t (Unit: mm) represents the radius from ventilation to the geometric center of the core. The velocity vector of number 8 ventilation duct section is shown in Fig. 10. It is observed that both the radial distributions of fluid velocity along stator and slot are uneven or asymmetric; eddy flows emerge near all the stator windings inside ventilating ducts, and there are some air flowing back into the air-gap. The analysis shows that the generation of eddy flows depends on the installation position of air ducts. $R_t = 288.5$ mm in the original motor design scheme is redefined as $R_t = 283.5$ mm in position after optimum calculation and analysis, and the recalculation result of new model is as shown in Fig. 11. The comparison between Figs. 10 and 11 suggests internal swirls in ducts is decreasing greatly, thus reducing the energy loss.

The fluid velocity contour of internal neutral surface and fan and rotor is shown in Fig. 12. Figure 13 shows the fluid trace map of internal motor. The wind velocity at the left side of motor is lower and its path line of fluid is scanty. Due to the sudden decrease of fluid flow area of the fan side at wind shield and fan-ring-collector, the velocity is higher with the maximum of 62.4 m/s. It can be observed clearly from Fig. 13 that greater eddy flows are generated near the end of fan sides mainly

Fig. 7 The fluid trace map nearby the fan section

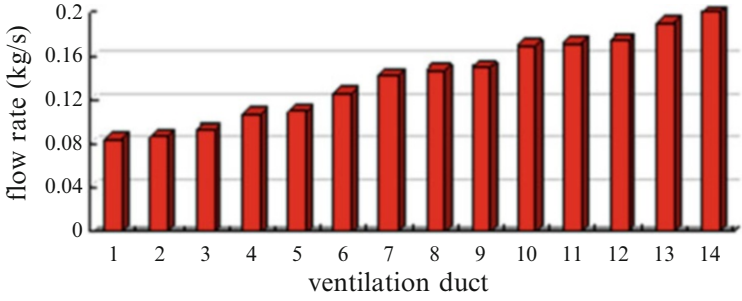

Fig. 8 Flow distribution of each ventilation channel

because of the right angle used in design of wind shield. Proper improvement can be made there and the chamfer can be considered in design of wind shield to avoid the generation of eddy flows.

4 Conclusion

By the calculation and analysis of the fluid fields of YJKK500-4,2500 kW compact motor with medium-size high-voltage, the following conclusions are acquired:

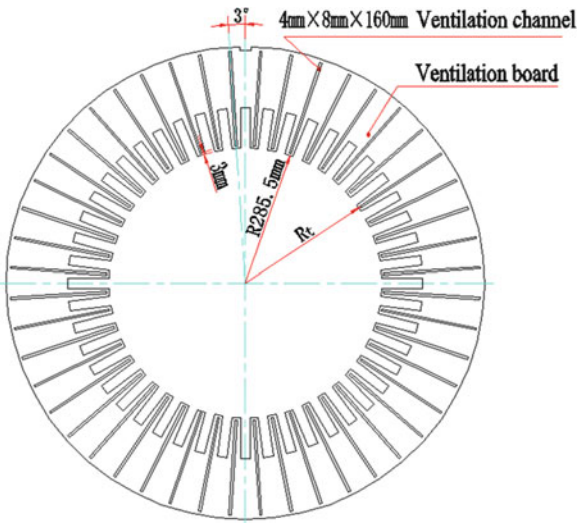

Fig. 9 Schematic of stator ventilation channel

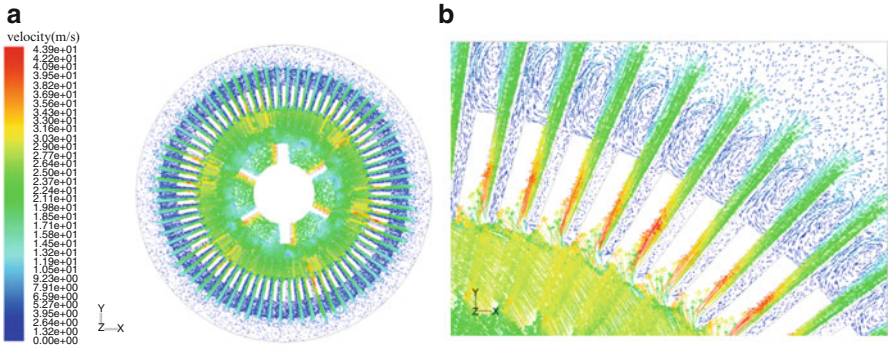

Fig. 10 Velocity vector of number 8 ventilation duct section (**a**) Overall effect of the velocity vector (**b**) Partial view of the velocity vector

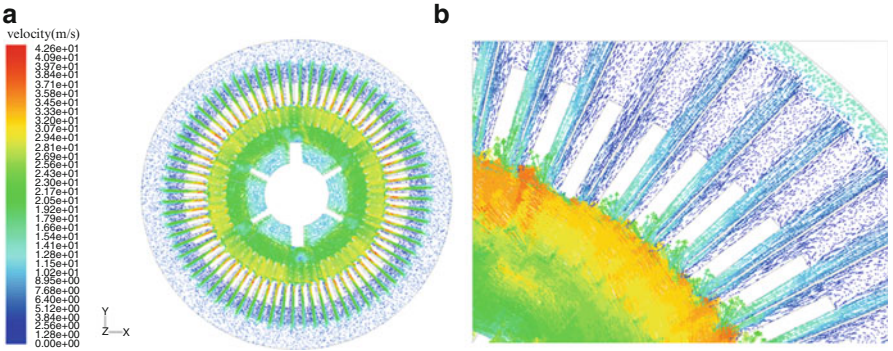

Fig. 11 Velocity vector of the improved number 8 ventilation duct (**a**) Overall effect of the velocity vector (**b**) Partial view of the velocity vector

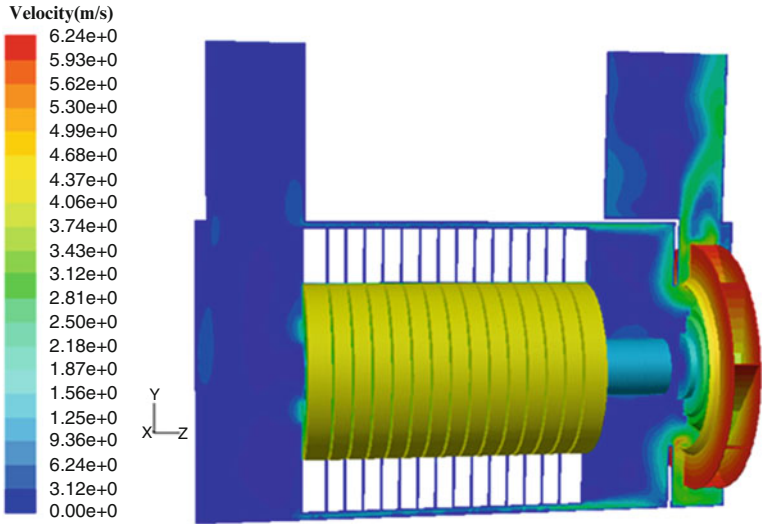

Fig. 12 The fluid velocity contour of internal neutral surface and fan and rotor

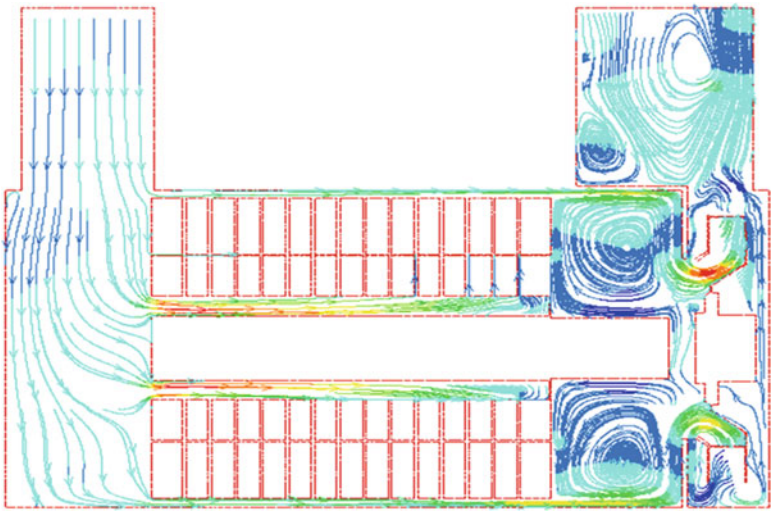

Fig. 13 The fluid trace map of internal motor

1. The global analysis result on 3D fluid field inside motor coincides with the measured value, which shows that the computational model established is feasible, fundamental assumption and boundary conditions are reasonable.
2. The performance curve between pressure and flow of the fan is obtained. It provides theoretical basis for selecting fan design and calculating temperature field.

3. This paper indicates the obvious phenomenon of fluid eddy flow near the stator winding inside ventilating ducts through relevant analysis, and optimizes the R_t value of ventilating channel steel of stators, which can effectively reduce the phenomenon of eddy flow in ventilating ducts.

References

1. Li Weili, Yang Xuefeng et al (2009) Influence of air current flow change on fluid flow and heat transfer of air-cooled turbo-generator with multipath ventilation. Proc CSEE 21(29):53–54
2. Chen Shikun (2008) Motor design. China Machine Press, Beijing, pp 12–13
3. Lu Yiping, Li Weil, Ma Xianhao et al (2007) Numerical simulation of temperature field in rotor of large turbo generator with air-coolant. Proc CSEE 12(27):7–9
4. Xia Haixia, Li Tao, Ni Zhengguang (2007) Analysis of ventilation fluid field and rotor temperature field of a generator. Electr Mach Control 5(11):472–473
5. Wang Fujun (2004) Computational fluid dynamics analysis – the principle and application of CFD. Tsinghua University Press, Beijing, pp 7–8
6. Huo Feiyang, Li Yong et al (2010) Calculation and analysis on stator ventilation structure of different optimum proposal in air-cooled turbogeneator. Proc CSEE 6(30):69–74
7. Li Weili, Yang Xuefeng, Gu Debao et al (2009) Calculation and analysis of fluid flow and heat transfer of air-cooled turbo-generator with multipath ventilation. Tran China Electrotech Soc 12 (24):24–31
8. Li Junqing, Hu Jiwei (2010) 3D fluid field calculation and analysis in stator radial ventilation ducts of turbogenerators. Large Electr Mach Hydraul Turb 1:19–22

Part II
Intelligent Systems and Algorithms

Parametric Identification of Ship's Maneuvering Motion Based on Kalman Filter Algorithm

Yugang Qin and Liang Zhang

Abstract In order to solve the identification problem for ship response model parameters, the method using Kalman filter algorithm was developed. Firstly, the first order linear, first order nonlinear and second order linear models were established. Then they were dispersed, and the parameters of the models were identified using Kalman filter algorithm. At last, simulation experiment was carried out. The simulation results show that the algorithm is able to identify the ship motion parameters online accurately and efficiently, and it is feasible and effective.

Keywords Maneuvering motion • Response model • Parametric identification • Kalman filter

1 Introduction

Ship maneuverability is one of the important ship hydrodynamic performances, and is closely related to the security of the ship's navigation. With the development of modern shipbuilding industry and shipping business, as well as people improve safety awareness,ship maneuverability is taken seriously more and more [1]. Especially the IMO (International Maritime Organization, IMO) has issued provisional standards and formal standards for ship maneuverability in 1993 and 2002 [2]. It puts forward the specific requirements to the maneuvering forecast and the maneuverability index which ships should meet during the ship design phase. And it greatly promotes the ship maneuverability prediction research.

Simulation using ship maneuvering motion mathematical model on the computer is the most practical and effective method for the prediction and assessment of maneuverability in ship design phase [3, 4]. The premise of this method is modeling

Y. Qin (✉) • L. Zhang
College of Shipbuilding Engineering, Harbin Engineering University, Harbin, China
e-mail: e_work_heu@126.com

W. Wang (ed.), *Mechatronics and Automatic Control Systems*, Lecture Notes in Electrical Engineering 237, DOI 10.1007/978-3-319-01273-5_11,

the ship in mathematic, and determine the hydrodynamic derivatives of mathematical model is the key step. At present, there are two major kinds of mathematical models of ship maneuvering [5]: one is hydrodynamic model, including the integrated model and separate model; and the other is responding model, including maneuverability index K, T which may be obtained by linear hydrodynamic parameters. The hydrodynamic parameters of ship maneuvering motion equations can be obtained using system identification. This method is simple and effective, and can be directly used in the analysis of the test results of the real ship [6]. This can avoid 'the scale effect' brought by the different Reynolds number between model and real ship [7].

Kalman filtering theory has been widely used in many fields, and has become one of the basic methods of state estimation [8, 9]. It is not only used for dynamic system state estimation, but also can be used for dynamic system parameters estimated online. Under certain assumptions, the results got by the Kalman filter algorithm are optimal.

In this paper, motion parameters of Ship response model are identified using Kalman filter algorithm online. The simulation results show that this algorithm can identify the ship motion parameters online effectively, and it has an important signification for the ship parameters identification.

2 Establishment of the Ship Motion Equations

In this paper, the classical KT equations are used as the ship mathematical model for the ship maneuverability identification research.

First-order linear response model is

$$T\dot{r} + r = K\delta \tag{1}$$

First-order nonlinear response model is

$$T\dot{r} + r + \alpha r^3 = K\delta \tag{2}$$

Second-order linear response model is

$$T_1T_2\ddot{r} + (T_1 + T_2)\dot{r} + r = K\delta + KT_3\dot{\delta} \tag{3}$$

In the formulas, r is the angular velocity of the turn bow, δ is rudder angle, K, T, T_1, T_2 and T_3 are maneuverability index, α is nonlinear coefficient.

Forward difference discrimination equations of formulas (1) and (2) are

$$r(k+1) = \left(1 - \frac{\Delta t}{T}\right) r(k) + \frac{K\Delta t}{T}\delta(k) \tag{4}$$

$$r(k+1) = \left(1 - \frac{\Delta t}{T}\right) r(k) + \frac{K\Delta t}{T}\delta(k) - \frac{\alpha \Delta t}{T} r^3(k) \tag{5}$$

Where, Δt is the sampling interval.

When $T_1 T_2 = h$, $T_1 + T_2 = g$, forward difference discrimination equation of formulas (3) is

$$r(k+1) = a_1 r(k) + a_2 r(k-1) + b_1 \delta(k) + b_2 \delta(k-1) \tag{6}$$

In the formulas, a_1, a_2, b_1, and b_2 are identification parameters. The relationship between them and ship maneuverability parameters are as follows:

$$\begin{cases} h = \dfrac{\Delta t^2}{1 - a_1 - a_2}, & g = \dfrac{(2 - a_1)\Delta t}{1 - a_1 - a_2} \\ K = \dfrac{b_1 + b_2}{1 - a_1 - a_2}, & T_1 = \dfrac{g + \sqrt{g^2 - 4h2}}{} \\ T_2 = g - T_1, & T_3 = \dfrac{b_1 \Delta t}{b_1 + b_2} \end{cases} \tag{7}$$

From Eqs. 4, 5, 6, and 7, first-order linear response model of training samples are

$$\begin{cases} x(k) = [r(k), \delta(k)]^T \\ y(k) = r(k+1) \end{cases}. \tag{8}$$

First-order nonlinear response model of training samples are

$$\begin{cases} x(k) = [r(k), \delta(k), r^3(k)]^T \\ y(k) = r(k+1) \end{cases}. \tag{9}$$

Second-order nonlinear response model of training samples are

$$\begin{cases} x(k) = [r(k), r(k-1), \delta(k), \delta(k-1)]^T \\ y(k) = r(k+1) \end{cases}. \tag{10}$$

3 Parameter Identification Based on Kalman Filter Method

Assuming that the system can be identified with the following difference equation:

$$\begin{aligned} &y(k) + a_1 y(k-1) + \cdots + a_n y(k-n) \\ &= b_1 u(k-1) + \cdots + b_m u(k-m) + v(k) \end{aligned} \tag{11}$$

Where $u(k)$ and $y(k)$ are the system inputs, and the output sequence. a_i $(i = 1,2,\ldots,n)$ and b_j $(j = 1,2,\ldots,m)$ are the unknown parameters of the system. $\{v(k)\}$ are zero-mean Gaussian white noise sequence, and

$$E\{v(k)v^T(j)\} = R_k\delta_{kj} \tag{12}$$

When using Kalman filter algorithm to estimate system parameters, first the unknown parameters of the system should be seen as unknown states, and then the system dynamic differential equation 8 is transformed into the state-space equations. Therefore,

$$\begin{cases} x_1(k) = a_1(k) \\ \cdots \\ x_n(k) = a_n(k) \\ x_{n+1}(k) = b_1(k) \\ \cdots \\ x_{n+m}(k) = b_m(k) \end{cases} \tag{13}$$

$$\begin{cases} x_1(k+1) = a_1(k) + w_1(k) \\ \cdots \\ x_n(k+1) = a_n(k) + w_n(k) \\ x_{n+1}(k+1) = b_1(k) + w_{n+1}(k) \\ \cdots \\ x_{n+m}(k+1) = b_m(k) + w_{n+m}(k) \end{cases} \tag{14}$$

Where in Eq. 11, $\{w_i(k)\}$ $(i = 1,2,\ldots,n+m)$ are the noise component of the parameters, assuming that they are zero-mean Gaussian white noise sequence, and independent with $\{v(k)\}$. The system state equation can be got:

$$X(k+1) = \phi(k+1,k)X(k) + \Gamma(k)W(k) \tag{15}$$

Wherein: $\phi(k+1,k) = I$, $\Gamma(k) = I$, $W(k)$ are vector s consisting of $\{w_i(k)\}$ $(i = 1,2,\ldots,n+m)$, and $E\{W(k)W^T(j)\} = Q_k\delta_{kj}$.

When let:

$$C(k) = [-y(k-1),\cdots -y(k-n), u(k-1)\cdots u(k-m)] \tag{16}$$

We can get the observation equation from the system state equation:

$$y(k) = C(k)X(k) + v(k) \tag{17}$$

Getting the state space equation

$$\begin{cases} X(k) = \phi(k, k-1)X(k-1) + \Gamma(k-1)W(k-1) \\ y(k) = C(k)X(k) + v(k) \end{cases} \tag{18}$$

If the coefficient matrixes $\phi(k, k-1), \Gamma(k), C(k)$ are determined, we can directly estimate parameter by using the Kalman filter equations.

Kalman filter's recursive algorithm is as follows:

Basing on the previous filtered value $\hat{X}(k-1|k-1)$ calculate state one-step prediction

$$\hat{X}(k|k-1) = \phi(k, k-1)\hat{X}(k-1|k-1) \tag{19}$$

State estimation equation is:

$$\hat{X}(k|k) = \hat{X}(k|k-1) + K(k)[y(k) - C(k)\hat{X}(k|k-1)] \tag{20}$$

Then calculating the forecast error variance matrix:

$$\begin{aligned} P(k|k-1) = \phi(k|k-1)P(k-1|k-1)\phi^T(k|k-1) \\ + \Gamma(k-1)Q(k-1)\Gamma^T(k-1) \end{aligned} \tag{21}$$

Calculating the Kalman gain:

$$K(k) = P(k|k-1)C^T(k)[C(k)P(k|k-1)C^T(k) + R(k)]^{-1} \tag{22}$$

Calculating filtering error matrix:

$$P(k|k) = [I - K(k)C(k)]P(k|k-1) \tag{23}$$

4 Simulation Experiment

The simulation is a numerical simulation of a certain type of ship, including the first-order linear, first-order nonlinear and second-order linear model. In the simulation experiments, the ship response model integrates using the 4-order Runge–Kutta method, and sampling interval is 1. The initial values of the first-order linear response model are $K = 0, T = 1$. The initial value of the first-order nonlinear response model is $K = 0, T = 0, \alpha = 0$. The initial values of the second order linear model are $K = 1, T_1 = 100, T_2 = 0.5, T_3 = 0.7$.

The comparison results in simulation are shown in Tables 1, 2, and 3, the courses of the individual identification parameters curve are shown in Figs. 1, 2, and 3.

Table 1 First-order linear simulation data table

	Setting	Identification	Error(%)
K	0.233	0.2328	0.09
T	16.700	16.6682	0.19

Table 2 First-order nonlinear simulation data table

	Setting	Identification	Error(%)
K	0.216	0.2158	0.09
T	13.514	13.4997	0.11
α	258.405	257.8405	0.22

Table 3 Second-order nonlinear simulation data table

	Setting	Identification	Error(%)
K	0.231	0.2310	0.00
T1	18.921	18.9246	0.02
T2	0.915	0.9153	0.03
T3	0.500	0.5021	0.42

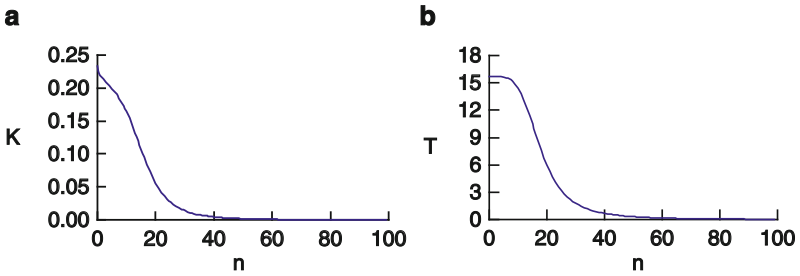

Fig. 1 Curves of first-order linear simulation (**a**) the error curve of K, (**b**) the error curve of T

(a) Comparison of first-order linear simulation
(b) Comparison of first-order nonlinear simulation
(c) Comparison of second-order linear simulation

Figures 1, 2, and 3 show that the various parameters reach the true value in about 40 steps. When choose a suitable initial value, the algorithms has a greater converge speed. It is known that the maximum error of parameters using Kalman filter algorithm is less than 0.5 % from Tables 1, 2, and 3. And it proves that the algorithm can identify the parameters of ship response model online fast and accurately.

5 Conclusion

The method is reached to identify the parameters of ship response model online using Kalman fitter algorithm beginning in the ship response model in this paper. The simulation results show that the method can identify the parameters of ship response model fast and accurately online. And it has great significance on the simulation of ship maneuverability.

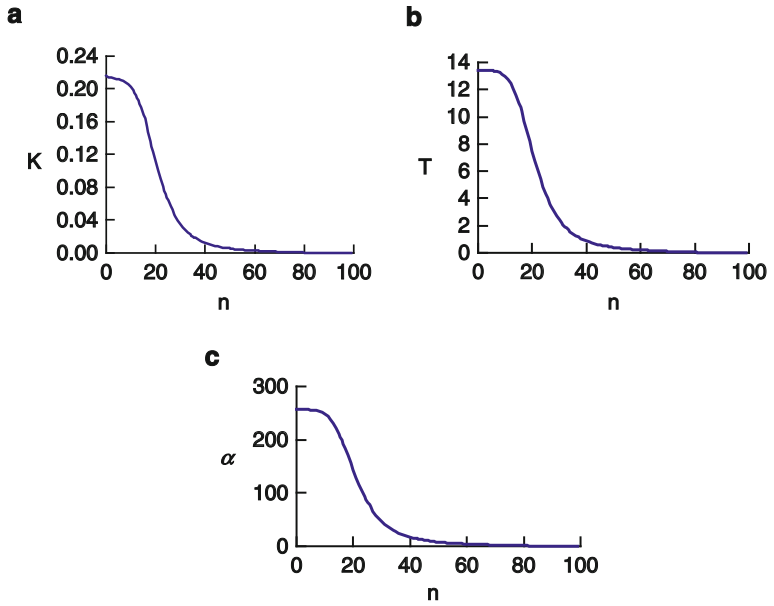

Fig. 2 Curves of first-order nonlinear simulation (**a**) the error curve of K, (**b**) the error curve of T, (**c**) the error curve of α

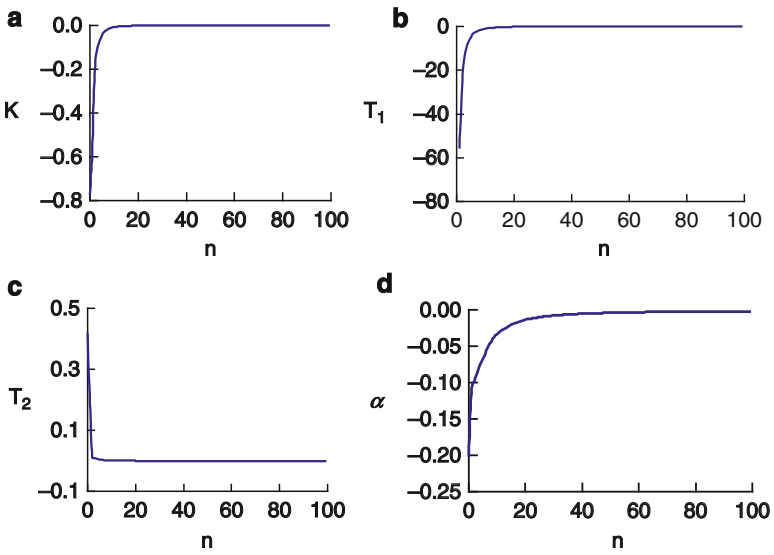

Fig. 3 Curves of second-order linear simulation (**a**) the error curve of K, (**b**) the error curve of T1, (**c**) the error curve of T_2, (**d**) the error curve of T_3

References

1. Li Guanglei, Zang Tao, Fan Zhou, Han Bing (2011) Application of parameter identification to ship motion control. Mar Electr Electron Technol 31:46–50,54 (in Chinese)
2. Chen Weiqi, Yan Kai, Wang Baoshou (2011) Intelligent identification of Hydrodynamic parameters of navigating body. J Ship Mech 15:359–363, in Chinese
3. Xu Feng, Zou Zaojian, Song Xin (2011) Parametric identification of AUV's maneuvering motion based on support vector machines. J Ship Mech 15:981–987
4. Wang Bo (2009) Research on motion simulation of a small underwater vehicle. Harbin Engineering University, Harbin (in Chinese)
5. Xu Feng, Zou Zaojian, Yin Jianchuan (2012) On-line modeling of ship maneuvering motion based on support vector machines. J Ship Mech 16:218–225
6. Haddara MR, WangY (1999) Parametric identification of maneuvering models for ships. International Shipbuilding Progress 46:5–27
7. Zhang Xinguang, Zou Zaojian (2011) Identification of response models of ship manoeuvring motion using support vector regression. J Shang Hai Jiaotong Univ 45:501–504 (in Chinese)
8. Wan EA, van der Merwe R (2000) The unscented Kalman filter for nonlinear estimation. Proc Symp Adaptive Syst Signal Process Commun Control 1:153–158
9. Grewal MS, Andrews AP (1993) Kalman filtering: theory and practice. Englewood Cliffs, New Jersey

LMI Approach for Stability of Cohen-Grossberg Neural Networks with Multi-delay and Distributed Delays

Junfeng Cui and Haijian Shao

Abstract In this paper, stability of periodic solutions of the Cohen-Grossberg neural network with time delays and higher-order terms is investigated. Some sufficient conditions for global stability of periodic solutions are provided by employing Lyapunov-Krasovskii function and linear matrix inequality (LMI) approach. Simulation results show the feasibility and effectiveness of the proposed method.

Keywords Cohen-Grossberg neural network • Lyapunov-Krasovskii functional • Linear matrix inequality • Multi-delay and distributed delay

1 Introduction

In 1983, Cohen and Grossberg proposed a class artificial neural network described by:

$$\frac{\mathrm{d}u_i(t)}{\mathrm{d}t} = -a_i(u_i(t))\Big[b_i(u_i(t)) - \sum\nolimits_{j=1}^{n} T_{ij} f_j(u_j(t))\Big], \quad i = 1, \ldots, n,$$

where u_i is the neural state variables, a_i and f_i are amplification function and activation function respectively, and $b_i(u_i(t))$ is continuous differentiable function, and $b_i\ (u_i) \in \mathrm{C}^1[R,R]$. The symmetric real matrix $T \triangleq (T_{ij})_{n\times n}$ is the connections between neurons. Cohen-Grossberg neural networks [1, 2] have many important

J. Cui (✉)
College of Mathematics and Physics, Huaiyin Institute of Technology, Huaian, China
e-mail: cjfxxm@yahoo.com.cn

H. Shao
Department of automation, Southeast University, Nanjing, China
e-mail: shaohaijian2012@gmail.com

W. Wang (ed.), *Mechatronics and Automatic Control Systems*, Lecture Notes in Electrical Engineering 237, DOI 10.1007/978-3-319-01273-5_12,

applications in various fields such as parallel computation, biological systems, information science and optimization problems, even in the neurobiology, population biology [3] and evolutionary theory.

In fact, a real system is usually affected by external perturbations [4], and due to the finite speeds of the switching and transmission of signals in a network, time delays do exist in a working network and thus should be incorporated into the model equations of the network [5]. It was observed both experimentally and numerically in that time delay could induce instability [6], causing sustained oscillations which may be harmful to a system. These papers study the lag inherent characteristics and higher-order term in the practical application, focus on the stability of periodic solutions of the Cohen-Grossberg neural network with time delays and higher-order terms [7].

Based on the above discussions, the purpose of this paper is to study the dynamic behavior of the generalized Cohen–Grossberg neural network with variable coefficients, multi-delays, distributed delays and time-varying delays. Sufficient conditions for the global stability of periodic solutions of the Cohen-Grossberg neural network with time delays and higher-order terms by employing Lyapunov function and LMI approach are presented.

The paper is organized as follows: In Sect. 2, System Description and Preliminaries are stated and some definitions and lemmas are listed. Based on the Lyapunov stability theory and LMI approach, and the conditions ensuring the global stability of the Cohen–Grossberg neural network with time delays and higher-order terms are obtained in Sect. 3. Some illustrative examples and their numerical simulations are provided to confirm our analysis in the Sect. 4, and we conclude this paper in Sect. 5.

2 Problem Description and Preliminaries

Consider the following Cohen-Grossberg neural networks with multi-delay and distributed delays:

$$\begin{aligned}\dot{x}_i(t) = -a_i(x_i(t))\Big[b_i(x_i(t)) - \sum\nolimits_{j=1}^{n}\sum\nolimits_{k=1}^{n} d_{ijk} f_j(x_j(t-\tau_j)) f_k(x_k(t-\tau_k)) \\ - \sum\nolimits_{j=1}^{n} c_{ij} f_j(x_j(t-\eta_j)) - \sum\nolimits_{j=1}^{n} g_{ij}\int_{-\infty}^{t} K_{ij}(t-s) h_j(x_j(s))\mathrm{d}s + I_i(t)\Big], i \\ = 1, 2, \ldots, n\end{aligned} \tag{1}$$

where $x(t) = (x_1(t), x_2(t), \ldots, x_n(t))^{\mathrm{T}}$ is the neuron state vector, $a(x) = diag\,(a_1(x_1), \ldots, a_n(x_n))$ represents an amplification function, $b(x(t)) = (b(x_1(t)), \ldots, b(x_n(t)))^{\mathrm{T}}$ is the

behaved function, $f_i(\cdot)$ and $h_i(\cdot)$ $(j = 1,\ldots, n)$ denote the neuron activation, c_{ij}, d_{ijk} represent the right of first order and the right of second order of the neuron network respectively, $\tau_j, \eta_j\,(j = 1,\ldots, n)$ represent the transmission delay with $0 \le \tau_j, \tau_k \le \tau$, $\dot{\tau}_k \le \rho_1 < 1,\ (j = 1,\ldots,n)$, g_{ij} denote the distributive delayed connection weighted, the kernel function K_{ij}: $[0,\infty) \to [0,\infty)$ is continuous in the sub$[0,\infty)$, and satisfies $\int_0^\infty K_{ij}(s)\mathrm{d}s = k_{ij}, i,j = 1,2,\ldots,n,$ the initial conditions for system (1) is $x(t) = \psi(t), \mathrm{t} \le 0, \psi(t) \in C([-T, 0], R^{\mathrm{n}})$.

In this paper, the following useful definitions, assumptions and lemmas throughout this manuscript are addressed.

Definition 1 For any $\phi(\theta) \in C([-\rho, 0], R^n)$, let $|\phi| = \max\{\|\phi(\theta)\| : \theta \in [-\rho, 0]\}$, the norm $\|\cdot\|_r^r$ is defined as $\|\phi - x^*\|_r^r = \sup_{-\infty\le\theta\le 0} \sum_{i=1}^n \left|\phi_i(\theta) - x_i^*\right|^r,$ for $r > 1$.

Definition 2 The periodic solution $x^* = (x_1^*, x_2^*, \ldots, x_n^*)^T$ of the system (1) is said to be global stable if there is positive constant $\mu > 0$ such that $\left|x_i(t) - x_i^*\right| \le \mu \sup_{-\rho\le\theta\le 0} \left|\phi_i(\theta) - x_i^*\right|,\ t > 0.$

Assumption 1 **(A1)** For $i = 1, 2, \ldots, n$, the neuron activation functions in (1) satisfy $\left|f_j(s_1) - f_j(s_2)\right| \le \alpha_j^+|s_1 - s_2|, \left|h_j(s_1) - h_j(s_2)\right| \le \beta_j^+ |s_1 - s_2|, \forall\, s_1 \ne s_2.$ where $\alpha_j^+,\ \beta_j^+$ are positive constants.

Assumption 2 **(A2)** Neuron activation functions $f_j(x_j(t))$, $h_j(x_j(t))$ $j = 1,\ldots,n$ are bounded.

Assumption 3 **(A3)** Function $\alpha_{\mathrm{i}}(x_{\mathrm{i}})$ $(i = 1,\ldots,n)$ is positive bounded, continuously differentiable and satisfies $\underline{\alpha_i} \le \alpha_i(t) \le \bar{\alpha}_i$, where $\underline{\alpha_i}$ $(i = 1,\ldots,n)$ are some positive constants,

$$|\alpha_i(x) - \alpha_i(y)| \le H_i|x - y|,\ \text{for any } x, y \in R,$$

where H_{i} $(i = 1,\ldots, n)$ is a positive constant.

Assumption 4 **(A4)** γ_{i} $(i = 1,\ldots,n)$ is a positive constant, the function $b_i^{-1}(\cdot)$ is Lipschitz continuous, and $b'_i \ge \gamma_i,\ (i = 1,\ldots,n).$

Remark 1 The constants $\alpha_j^+,\ \beta_j^+$ in Assumption 1 are allowed to be positive or zero. thus, the resulting activation functions could be non-monotonic, and more general than the usual sigmoid functions.

Lemma 1 *(Schur complement) For a given matrix*

$$S = \begin{pmatrix} S_{11} & S_{12} \\ S_{21} & S_{22} \end{pmatrix} > 0,$$

where $S_{11}^T = S_{11},\ S_{22}^T = S_{22},$ is equivalent to any one of the following
(1) $S_{22} > 0,\ S_{11} - S_{12}S_{22}^{-1}S_{12}^T > 0$; *(2)* $S_{11} > 0,\ S_{22} - S_{12}^T S_{11}^{-1} S_{12} > 0.$

Lemma 2 *[8] For any constant matrix* $\Delta = \Delta^T \in R^{n\times n}$, *scalar* a *and* b *with* a $<$ b, *vector function* $\delta(t) : [a, b] \to R^n,$ *such that the integrations concerned are well defined, then* $\left(\int_a^b \delta(s)\mathrm{d}s\right)^T \Delta\left(\int_a^b \delta(s)ds\right) \le (b-a)\int_a^b \delta^T(s)\Delta\delta(s)\mathrm{d}s.$

Lemma 3 *[9] For any vector* x, y$\in$R$^{\mathrm{n}}$, *and positive definite* Q$\in$R$^{\mathrm{n}\times\mathrm{n}}$, *the following matrix inequality holds:* $2x^Ty \le x^TQx + y^TQ^{-1}y.$

3 Main Results

In this section, based on the Lyapunov-Krasovskii functionals and LMI approach, we will investigate the global stability of periodic solutions of the model (1), and the main results of this manuscript are specified as follows:

Theorem 3.1 *Assume that*:

1. *Assumption* (A1–A4) *hold.*
2. *The equilibrium point of the system* (1) *is globally stable if there diagonal matrices* $p_i > 0,\ W_i > 0, q_i^{(j)} > 0,\ i = 1,\ldots,n, j = 1,\ldots,6,$ *satisfy the following condition*

$$\Xi = \begin{pmatrix} \Xi_{11}^{(0)} & * & * & * & * & \Xi_{15}^{(0)} & * \\ 0 & \Xi_{22}^{(0)} & * & * & * & * & * \\ 0 & 0 & \Xi_{33}^{(0)} & * & * & * & * \\ 0 & 0 & 0 & \Xi_{44}^{(0)} & * & * & * \\ 0 & 0 & 0 & 0 & \Xi_{55}^{(0)} & * & * \\ \Xi_{61}^{(0)} & \Xi_{62}^{(0)} & 0 & 0 & 0 & \Xi_{66}^{(0)} & * \\ 0 & 0 & 0 & 0 & 0 & 0 & \Xi_{77}^{(0)} \end{pmatrix} < 0,$$

where H_{i}, $\tilde{m}_i$ $(i = 1,\ldots, n)$ *are positive constants, and*

$$\Xi_{11}^{(0)} = \begin{pmatrix} \Xi_{11} & \cdots & p_1 g_{1n} k_{1n} \beta_n^+ \\ \vdots & \ddots & \vdots \\ p_n g_{n1} k_{n1} \beta_1^+ & \cdots & \Xi_{nn} \end{pmatrix}, \Xi_{15}^{(0)} = \begin{pmatrix} p_1 c_{11} & \ldots & p_1 c_{1n} \\ \vdots & \ddots & \vdots \\ p_n c_{n1} & \cdots & p_n c_{nn} \end{pmatrix},$$

$$\Xi_{61}^{(0)} = \begin{pmatrix} q_1^{(1)} g_{11} k_{11} \beta_1^+ & \ldots & q_1^{(1)} g_{1n} k_{1n} \beta_1^+ \\ \vdots & \ddots & \vdots \\ q_n^{(1)} g_{n1} k_{n1} \beta_n^+ & \cdots & q_n^{(1)} g_{nn} k_{nn} \beta_n^+ \end{pmatrix},$$

$$\Xi_{11} = -\Big[p_1\gamma_1 + \bar{\alpha}_1 p_1 H_1 \tilde{m}_1 + q_1^{(2)} + \frac{1}{2} W_1^{-1} q_1^{(1)} \bar{\alpha}_1 H_1 \tilde{m}_1 + q_1^{(5)} + \left|\alpha_1^+\right|^2 \Big(q_1^{(6)} + q_1^{(3)} + q_1^{(4)} \tau_1^2 + \frac{1}{2} W_1 q_1^{(1)} \bar{\alpha}_1 H_1 \tilde{m}_1\Big) - p_1 g_{11} k_{11} \beta_1^+\Big],$$

$$\Xi_{nn} = -\Big[p_n\gamma_n + \bar{\alpha}_n p_n H_n \tilde{m}_n + q_n^{(2)} + \frac{1}{2} W_n^{-1} q_n^{(1)} \bar{\alpha}_n H_n \tilde{m}_n + q_n^{(5)} + \left|\alpha_n^+\right|^2 \Big(q_n^{(6)} + q_n^{(3)} + q_n^{(4)} \tau_n^2 + \frac{1}{2} W_n q_n^{(1)} \bar{\alpha}_n H_n \tilde{m}_n\Big) - p_n g_{nn} k_{nn} \beta_n^+\Big],$$

$$\Xi_{22}^{(0)} = diag\Big\{-q_1^{(5)}(1-\rho_1), \ldots, -q_n^{(5)}(1-\rho_n)\Big\},$$

$$\Xi_{33}^{(0)} = \Big\{-q_1^{(2)}(1-\rho_1), \ldots, -q_n^{(2)}(1-\rho_n)\Big\},$$

$$\Xi_{44}^{(0)} = diag\Big\{-q_1^{(3)}(1-\rho_1), \ldots, -q_n^{(3)}(1-\rho_n)\Big\},$$

$$\Xi_{55}^{(0)} = diag\Big\{-q_1^{(6)}(1-\rho_1), \ldots, -q_n^{(6)}(1-\rho_n)\Big\},$$

$$\Xi_{66}^{(0)} = diag\Big\{-q_1^{(1)}\gamma_1\big(\beta_1^+\big)^{-1}, \ldots, -q_n^{(1)}\gamma_n\big(\beta_n^+\big)^{-1}\Big\}, \Xi_{77}^{(0)} = diag\Big\{-nq_1^{(4)}, \ldots, -nq_n^{(4)}\Big\},$$

$$\Xi_{62}^{(0)} = \begin{pmatrix} p_1 \sum_{k=1}^{n} (d_{11k} + d_{1k1}) f_k^M \alpha_1^+ & \ldots & p_1 \sum_{k=1}^{n} (d_{1nk} + d_{1kn}) f_k^M \alpha_1^+ \\ \vdots & \ddots & \vdots \\ p_n \sum_{k=1}^{n} (d_{n1k} + d_{nk1}) f_k^M \alpha_n^+ & \cdots & p_n \sum_{k=1}^{n} (d_{nnk} + d_{nkn}) f_k^M \alpha_n^+ \end{pmatrix}_{n\times n}.$$

Proof We shift the equilibrium point $x^* = (x_1^*, x_2^*, \ldots, x_n^*)^{\mathrm{T}}$ of (1) to the equation

$$u(t) = x(t) - x^* = [u_1(t), u_2(t), \ldots, u_n(t)]^{\mathrm{T}},$$

Then the following equation is obtained,

$$\begin{aligned}\dot{u}_i(t) = -a_i(x_i(t))\Big\{ & b_i(x_i(t)) - b_i(x_i^*) - \sum_{j=1}^{n} c_{ij}[f_j(x_j(t-\eta_j)) - f_j(x_j^*)] \\ & - \sum_{j=1}^{n} g_{ij} \int_{-\infty}^{t} K_{ij}(t-s)[h_j(x_j(s)) - h_j(x_j^*)]\mathrm{d}s \\ & - \sum_{j=1}^{n}\sum_{k=1}^{n} d_{ijk}[f_j(x_j(t-\tau_j))f_k(x_k(t-\tau_k)) \\ & - f_j(x_j^*)f_k(x_j^*)]\Big\} - [\alpha_i(x_i(t)) - \alpha_i(x_i^*)] \cdot \Delta_i^{x^*}(t)\end{aligned} \tag{2}$$

where $\Delta_i^{x^*}(t) = b_i(x_i^*) - \sum_{j=1}^{n} c_{ij} f_j(x_j^*) - \sum_{j=1}^{n}\sum_{k=1}^{n} d_{ijk} f_j(x_j^*) f_k(x_k^*) + I_i(t)$.

The model (1) has periodic solutions and satisfies $\left|\Delta_i^{x^*}(t)\right| \le \tilde{m}_i,\ i = 1, \ldots, n$, by the reference [7]

$$\begin{aligned}& \sum_{j=1}^{n}\sum_{k=1}^{n} d_{ijk}[f_j(x_j(t-\tau_j))f_k(x_k(t-\tau_k)) - f_j(x_j^*)f_k(x_k^*)] \\ & = \sum_{j=1}^{n}\sum_{k=1}^{n} d_{ijk}[(f_j(x_j(t-\tau_j)) - f_j(x_j^*))(f_k(x_k(t-\tau_k)) - f_k(x_k^*)) \\ & \quad + (f_j(x_j(t-\tau_j)) - f_j(x_j^*))f_k(x_k^*) \\ & \quad + (f_k(x_k(t-\tau_k)) - f_k(x_k^*))f_j(x_j^*)]\end{aligned}$$

Thus, the system (2) is described as the following,

$$\begin{aligned}\dot{u}_i(t) = -\alpha_i(u_i(t))\Big[& \beta_i(u_i(t)) - \sum_{j=1}^{n} c_{ij}\varphi_j(u_j(t-\eta_j)) \\ & - \sum_{j=1}^{n} g_{ij} \int_{-\infty}^{t} K_{ij}(t-s)\phi_j(u_j(s))\mathrm{d}s \\ & - \sum_{j=1}^{n}\sum_{k=1}^{n} (d_{ijk} + d_{ikj})\xi^{f_k}\varphi_j(u_j(t-\tau_j))\Big] \\ & - [\alpha_i(u_i(t) + x_i^*) - \alpha_i(x_i^*)] \cdot \Delta_i^{x^*}(t), \quad i = 1, \ldots, n\end{aligned} \tag{3}$$

where $\alpha_i(u_i(t)) = \alpha_i(u_i(t) + x_i^*),\ \beta_i(u_i(t)) = b_i(u_i(t) + x_i^*) - b_i(x_i^*),\ \varphi_j(u_j(t)) = f_j(u_i(t) + x_i^*) - f_j(x_i^*), \phi_j(t) = h_j(x_j(t)) - h_j(x_j^*),\ \xi^{f_k} = \frac{1}{2}[f_k(x_k(t-\tau_k)) + f_k(x_k^*)]$, and the initial condition of $u_i(t)$ is $u_i(t) = \psi_i(t) = x_i^0(t) - x_i^*(t)$, thus $C([-T, 0], R^n)$ with norm $|\cdot|_0$ is a Banach Space. Then, consider the following Lyapunov-Krasovskii functional for model (3):

$$V(t, u_t) = V_1 + V_2 + V_3 + V_4,$$

where

$$V_1 = \sum_{i=1}^{n} p_i \int_0^{u_i(t)} \frac{s}{\alpha_i(s)} \mathrm{d}s + \sum_{i=1}^{n} q_i^{(1)} \int_0^{u_i(t)} \frac{\varphi_i(s)}{\alpha_i(s)} \mathrm{d}s,$$

$$V_2 = \sum_{i=1}^{n} \int_{t-\eta_i(t)}^{t} u_i^{\mathrm{T}}(s) q_i^{(2)} u_i(s) \mathrm{d}s + \sum_{i=1}^{n} \int_{t-\eta_i(t)}^{t} \varphi_i^{\mathrm{T}}(s) q_i^{(3)} \varphi_i(s) \mathrm{d}s,$$

$$V_3 = \sum_{i=1}^{n} \sum_{j=1}^{n} q_i^{(4)} \tau_j \int_{-\tau_j(t)}^{0} \int_{t+v}^{t} \varphi_j^{\mathrm{T}}(u_j(s)) \varphi_j(u_j(s)) \mathrm{d}s \mathrm{d}v,$$

$$V_4 = \sum_{i=1}^{n} \int_{t-\tau_i(t)}^{t} u_i^{\mathrm{T}}(s) q_i^{(5)} u_i(s) ds + \sum_{i=1}^{n} \int_{t-\eta_i(t)}^{t} \varphi_i^{\mathrm{T}}(u_i(s)) q_i^{(6)} \varphi_i(u_i(s)) ds,$$

Then, $\dot{V}_i$ $(i = 1, 2, 3, 4)$ along the trajectories of the model (3) is calculated as following, respectively,

$$\begin{aligned}
\dot{V}_1 < & \sum_{i=1}^{n} \Big\{ -u_i^{\mathrm{T}}(t) p_i \gamma_i u_i(t) + u_i^{\mathrm{T}}(t) p_i \sum_{j=1}^{n} c_{ij} \varphi_j(u_j(t-\eta_j)) \\
& + u_i^{\mathrm{T}}(t) p_i \sum_{j=1}^{n} g_{ij} k_{ij} \beta_j^{+} u_j(t) \\
& + u_i^{\mathrm{T}}(t) p_i \sum_{j=1}^{n} \sum_{k=1}^{n} (d_{ijk} + d_{ikj}) f_k^{M} \alpha_i^{+} u_j(t-\tau_j) + u_i^{\mathrm{T}}(t) \bar{\alpha}_i p_i H_i \tilde{m}_i u_i(t) \Big\} \\
& + \sum_{i=1}^{n} \Big\{ -\varphi_i^{\mathrm{T}}(u_i(t)) q_i^{(1)} \gamma_i u_i(t) + \varphi_i^{\mathrm{T}}(u_i(t)) q_i^{(1)} \sum_{j=1}^{n} c_{ij} \varphi_j(u_j(t-\eta_j)) \\
& + \varphi_i^{\mathrm{T}}(u_i(t)) q_i^{(1)} \sum_{j=1}^{n} g_{ij} k_{ij} \beta_j^{+} u_j(t) + \varphi_i^{\mathrm{T}}(u_i(t)) q_i^{(1)} \\
& \times \sum_{j=1}^{n} \sum_{k=1}^{n} (d_{ijk} + d_{ikj}) f_k^{M} \alpha_i^{+} u_j(t-\tau_j) + \varphi_i^{\mathrm{T}}(u_i(t)) q_i^{(1)} \bar{\alpha}_i H_i \tilde{m}_i u_i(t) \Big\}
\end{aligned} \tag{4}$$

$$\begin{aligned}
\dot{V}_2 < & \sum_{i=1}^{n} \Big\{ u_i^{\mathrm{T}}(t) q_i^{(2)} u_i(t) - u_i^{\mathrm{T}}(t-\eta_i) q_i^{(2)} u_i(t-\eta_i)(1-\rho_i) + \varphi_i^{\mathrm{T}}(t) q_i^{(3)} \varphi_i(t) \\
& - \varphi_i^{\mathrm{T}}(t-\eta_i) q_i^{(3)} \varphi_i(t-\eta_i)(1-\dot{\eta}_i) \Big\}
\end{aligned} \tag{5}$$

By utilizing the Lemma 2 and the fact $\dot{\tau}_k \le \rho < 1, j = 1, \ldots, n,$ the following inequality is derived:

$$\begin{aligned}
\dot{V}_3 = & \sum_{i=1}^{n} \sum_{j=1}^{n} \left\{ q_i^{(4)} \tau_j^2 \varphi_j^{\mathrm{T}}(u_j(t)) \varphi_j(u_j(t)) - q_i^{(4)} \tau_j \int_{t-\tau_j}^{t} \varphi_j^{\mathrm{T}}(u_j(s)) \varphi_j(u_j(s)) \mathrm{d}s \right\} \\
\le & \sum_{i=1}^{n} \sum_{j=1}^{n} \left\{ q_i^{(4)} \tau_j^2 \varphi_j^{\mathrm{T}}(u_j(t)) \varphi_j(u_j(t)) - \left(\int_{t-\tau_j}^{t} \varphi_j(u_j(s)) \mathrm{d}s \right)^{\mathrm{T}} \right. \\
& \left. \times q_i^{(4)} \left(\int_{t-\tau_j}^{t} \varphi_j(u_j(s)) \mathrm{d}s \right) \right\}
\end{aligned} \tag{6}$$

and

$$\dot{V}_4 \leq \sum_{i=1}^{n} \left\{ u_i^{\mathrm{T}}(t) q_i^{(5)} u_i(t) - u_i^{\mathrm{T}}(t-\tau_i) q_i^{(5)} u_i(t-\tau_i)(1-\rho_i) \right\} + \sum_{i=1}^{n} \left\{ \varphi_i^{\mathrm{T}}(u_i(t)) q_i^{(6)} \varphi_i(u_i(t)) - \varphi_i^{\mathrm{T}}(u_i(t-\eta_i)) q_i^{(6)} \varphi_i(u_i(t-\eta_i))(1-\rho_i) \right\} \tag{7}$$

Combining the Eqs. 4, 5, 6, and 7 and Lemma 3, the following result is specified,

$$\begin{aligned}
\dot{V}(t) =& \dot{V}_1(t) + \dot{V}_2(t) + \dot{V}_3(t) + \dot{V}_4(t) \\
\leq & \sum_{i=1}^{n} \Bigg\{ -u_i^{\mathrm{T}}(t)(p_i\gamma_i + \bar{\alpha}_i p_i H_i \tilde{m}_i + q_i^{(2)} + \frac{1}{2} W_i^{-1} q_i^{(1)} \bar{\alpha}_i H_i \tilde{m}_i + q_i^{(5)} \\
& + \left|\alpha_i^{+}\right|^2 q_i^{(3)} + \left|\alpha_i^{+}\right|^2 q_i^{(4)} \tau_i^2 + \left|\alpha_i^{+}\right|^2 \frac{1}{2} W_i q_i^{(1)} \bar{\alpha}_i H_i \tilde{m}_i + \left|\alpha_i^{+}\right|^2 q_i^{(6)}) u_i(t) \\
& + u_i^{\mathrm{T}}(t) p_i \sum_{j=1}^{n} g_{ij} k_{ij} \beta_j^{+} u_j(t) + u_i^{\mathrm{T}}(t) p_i \sum_{j=1}^{n} c_{ij} \varphi_j(u_j(t-\eta_j)) \\
& + u_i^{\mathrm{T}}(t) p_i \sum_{j=1}^{n} \sum_{k=1}^{n} (d_{ijk} + d_{ikj}) f_k^{M} \alpha_i^{+} u_j(t-\tau_j) \\
& - \varphi_i^{\mathrm{T}}(t-\eta_i) q_i^{(3)} \varphi_i(t-\eta_i)(1-\rho_i) - u_i^{\mathrm{T}}(t-\eta_i) q_i^{(2)} u_i(t-\eta_i)(1-\rho_i) \\
& - \varphi_i^{\mathrm{T}}(u_i(t)) q_i^{(1)} \gamma_i \left(\beta_j^{+}\right)^{-1} \varphi(u_i(t)) + \varphi_i^{\mathrm{T}}(u_i(t)) q_i^{(1)} \sum_{j=1}^{n} c_{ij} \varphi_j(u_j(t-\eta_j)) \\
& + \varphi_i^{\mathrm{T}}(u_i(t)) q_i^{(1)} \sum_{j=1}^{n} g_{ij} k_{ij} \beta_j^{+} u_j(t) + \varphi_i^{\mathrm{T}}(u_i(t)) q_i^{(1)} \\
& \times \sum_{j=1}^{n} \sum_{k=1}^{n} (d_{ijk} + d_{ikj}) f_k^{M} \alpha_i^{+} u_j(t-\tau_j) - u_i^{\mathrm{T}}(t-\tau_i) q_i^{(5)} u_i(t-\tau_i)(1-\rho_i) \\
& - \varphi_i^{\mathrm{T}}(u_i(t-\eta_i)) q_i^{(6)} \varphi_i(u_i(t-\eta_i))(1-\rho_i) \\
& - \sum_{j=1}^{n} \left(\int_{t-\tau_j}^{t} \varphi_j(u_j(s)) ds \right)^{\mathrm{T}} q_i^{(4)} \left(\int_{t-\tau_j}^{t} \varphi_j(u_j(s)) ds \right) \Bigg\} = \xi^{\mathrm{T}}(t) \Xi \xi(t) < 0,
\end{aligned}$$

where $\xi^{\mathrm{T}}(t) = \big(u_1^{\mathrm{T}}(t), \ldots, u_n^{\mathrm{T}}(t),\ u_1^{\mathrm{T}}(t-\tau_1(t)), \ldots, u_n^{\mathrm{T}}(t-\tau_n(t)), u_1^{\mathrm{T}}(t-\eta_1(t)), \ldots, u_n^{\mathrm{T}}(t-\eta_n(t)), .\varphi_1^{\mathrm{T}}(t-\eta_1(t)), \ldots,$

$$\varphi_n^{\mathrm{T}}(t-\eta_n(t)), \varphi_1^{\mathrm{T}}(u_1(t-\eta_1(t))), \ldots, \varphi_n^{\mathrm{T}}(u_n(t-\eta_n(t))), \varphi_1^{\mathrm{T}}(u_1(t)), \ldots, \varphi_n^{\mathrm{T}} \times (u_n(t)), \left(\int_{t-\tau_1}^{t} \varphi_1(u_1(s)) ds \right)^{\mathrm{T}}, \ldots, \left(\int_{t-\tau_n}^{t} \varphi_n(u_n(s)) ds \right)^{\mathrm{T}} \Bigg)^{\mathrm{T}}.$$

Thus, $\frac{dV}{dt} \leq \xi^{T}(t) \Xi \xi(t) < 0$, this completes the proof of the Theorem 3.1.

4 Numerical Simulation

In this section, we will give some examples to illustrate and confirm the effectiveness of the obtained results.

Example 4.1 We consider the following Cohen-Grossberg neural networks with multi-delay and distributed delays:

$$\dot{x}_i(t) = -a_i(x_i(t))\Big[b_i(x_i(t)) - \sum_{j=1}^{2}\sum_{k=1}^{2} d_{ijk} f_j(x_j(t-\tau_j)) f_k(x_k(t-\tau_k)) - \sum_{j=1}^{2} c_{ij} f_j(x_j(t-\eta_j)) - \sum_{j=1}^{2} g_{ij}\int_{-\infty}^{t} K_{ij}(t-s) h_j(x_j(s))ds + I_i(t)\Big], \quad i = 1,2,$$

where the activation function is described by $f_1(x) = \sin(x)$, $f_2 = \tanh(x)$, $h_i(s) = \tanh(s)$, $i = 1,2$,

$$\left|\alpha_j^+\right| = \left|\beta_j^+\right| = 1, j = 1,2, a_1(t) = 1, a_2(t) = 3, b_1(x) = 7x - \sin x,$$
$$b_2(x) = 16x - \cos x, \eta_1(t) = 0.6 - 0.5\sin(t), \eta_2(t) = 0.06 + 0.04\cos(t),$$
$$\tau_1(t) = 0.2|\cos(t)|, \tau_2(t) = 0.5|\sin(t)|, I_1(t) = -36\sin\left(\frac{2\pi}{3}t\right),$$
$$I_2(t) = 36\cos\left(\frac{2\pi}{3}t\right), K = \left\{k_{ij}\left|e^{-t}\right.\right\}_{2\times 2},$$

$\int_0^\infty e^{\lambda t} K_{ij}(t)dt = k_{ij} < \infty$, λ is an exponential convergence rate estimate, and $\omega = 3$, $\rho = \min\{\rho_1, \rho_2\} < 1$ the parameter matrices are respectively given by $W_i = q_i^{(j)} = I_2$, $i = 1,2$, $j = 1,2,3,4,6$,

$$C = diag\{-0.5, 2\}, G = I_2, D_1 = \begin{pmatrix} -0.5 & 0 \\ 2 & 0 \end{pmatrix}, D_2 = \begin{pmatrix} 0 & 0.5 \\ 0 & -1 \end{pmatrix},$$

$$p_1 = diag\{1.0530, 1.0427\}, q_1^{(5)} = diag\{1.0536, 1.0439\} > 0, q_2^{(5)} = diag\{1.0530, 1.0437\} > 0,$$

Furthermore, the initial condition of the $x(t) = (-5,6)$, thus it is easy to verify the given condition are satisfied the assumptions A1–A4, then the state trajectories of the neurons $x_1(t)$ and $x_2(t)$ is shown in the Fig. 1.

We can learn that the solution with respect to the Eq. 1 is a global exponential stability from the Fig. 1 and convergence to one third periodic solution.

Example 4.2 If $a_1(t) = \frac{1}{1+t^2}, a_2(t) = \frac{2}{1+t^2}, \eta_1(t) = \tau_1(-t) = \frac{e^t}{1+e^t}, \eta_2(t) = 0.06 - 0.04\cos(t), \tau_2(t) = 0.08 - 0.5|\sin(t)|$, the state trajectories of the neurons $x_1(t)$ and $x_2(t)$ is shown in the Fig. 2. The solution with respect to the Eq. 1 is a global stability from the Fig. 2.

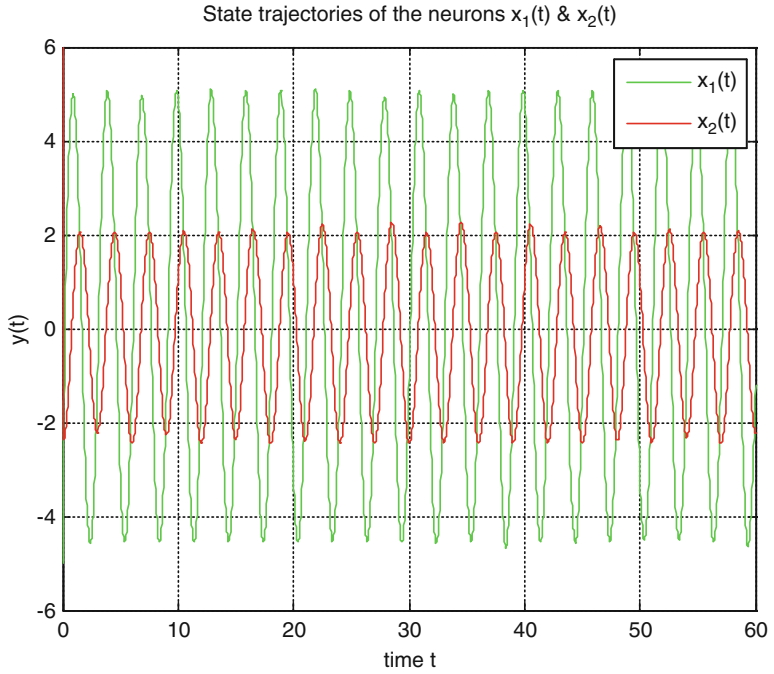

Fig. 1 State trajectories of neurons $x_1(t)$ & $x_2(t)$

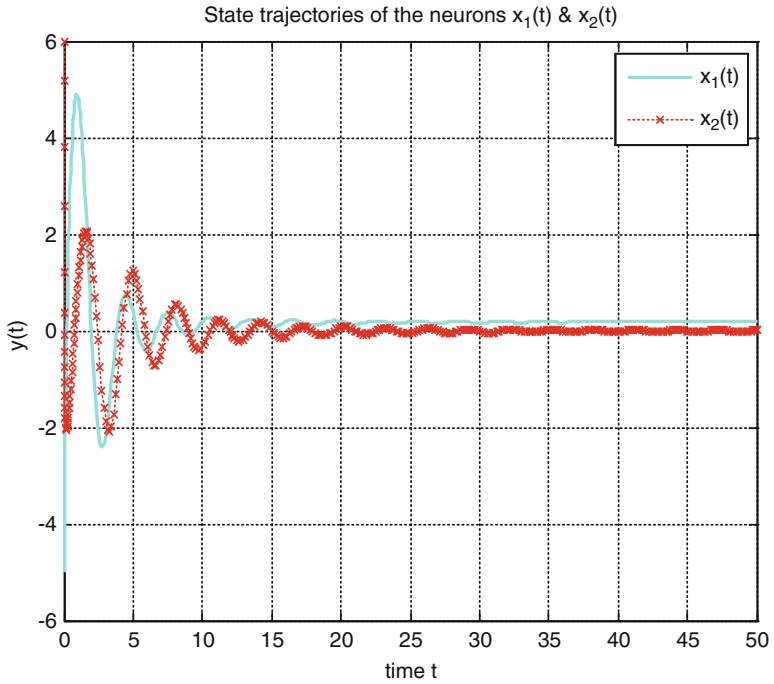

Fig. 2 State trajectories of neurons x1(t) & $x2$(t)

5 Conclusion

The dynamics of the Cohen–Grossberg neural network with time delays and higher-order terms is investigated by employing Lyapunov function and LMI approach. Some new sufficient conditions ensuring the model to be globally stable are derived. Moreover, the obtained results of this paper are delay-independent, which implies the strong self-regulation is dominant in the networks. We believe that the proposed results of this paper may be extended for the similarities even more complex system.

Acknowledgements The authors thank the reviewers and the editor for their helpful comments and constructive suggestions, and the authors Cao J, Xilin Fu,Wu chen et al.

References

1. Balasubramaniam P, Samath JA, Kumaresan N, Kumar VAA (2006) Solution of matrix Riccati differential equation for the linear quadratic singular system using neural networks. Appl Math Comput 182:1832–1839
2. Balasubramaniam P, Abdul Samath J, Kumaresan N (2007) Optimal control for nonlinear singular systems with quadratic performance using neural networks. Appl Math Comput 187:1535–1543
3. Cao J, Feng G, Wang Y (2008) Multistability and multiperiodicity of delayed Cohen–Grossberg neural networks with a general class of activation functions. Phys D 237:34–49
4. Xilin Fu, Xiaodi Li (2011) LMI conditions for stability of impulsive stochastic Cohen–Grossberg neural networks with mixed delays. Commun Nonlinear Sci Num Simul 16:435–454
5. Cao J, Liang J (2004) Boundedness and stability for Cohen–Grossberg neural network with time-varying delays. J Math Anal Appl 296:665–685
6. Marcus C, Westervelt R (1989) Stability of analog neural networks with delay. Phys Rev A 39:347–359
7. Chen Wu, Dong Ruan (2006) Dynamics of some neural networks and the research on chaos theory (in Chinese). Ph.D. thesis, Fudan University, pp 46–47
8. Rakkiyappan R, Balasubramaniam P, Lakshmanan S (2008) Robust stability results for uncertain stochastic neural networks with discrete interval and distributed time-varying delays. Phys Lett A 372:5290–5298
9. Jinde Cao (2007) Synchronization-based approach for parameters identification in delayed chaotic neural networks. Phys A Statis Mech Appl 382:672–682

The Temperature/Humidity Control System of Equipment Warehouse Based on Fuzzy Control Algorithm

Jinhua Liu, Guoquan Ren, Guang Tian, and Yunguang Qi

Abstract In order to solve the problem of temperature and humidity strong coupling, and improve the control precision of equipment warehouse, fuzzy control algorithm is used to solve the strong coupling between temperature and humidity that effects on the control process and control precision. Based on the fuzzification of the measured environmental parameters, the formation of fuzzy control rules according to expert experience, the fuzzy matrix reasoning, and the decoupling control of temperature and humidity, the effect of coupling in process of the temperature and humidity control is effectively solved. For illustration, a result of equipment warehouse temperature and humidity control is utilized to shows the effectiveness of the fuzzy control algorithm. The application results show that fuzzy control algorithm can reduce the overshoot of the temperature and humidity control and short the transition time of control process. The fuzzy control can satisfy the requirements of equipment warehouse temperature and humidity control. Applicating fuzzy control algorithm in the temperature and humidity control system, the adverse effect of strong coupling and large time-delay on control process is effectively solved, and the control accuracy of the system is improved.

Keywords Equipment warehouse • Control system • Fuzzy control algorithm

1 Introduction

The moistureproof, anti-corrosion and temperature control are the important contents of equipment warehouse daily management. Temperature and humidity is the important parameters of equipment warehouse environment that directly affect the storage equipment life and working reliability. Today the traditional

J. Liu (✉) • G. Ren • G. Tian • Y. Qi
Shijiazhuang Mechanical Engineering College, Shijiazhuang, China
e-mail: liuhequngao@sina.com

W. Wang (ed.), *Mechatronics and Automatic Control Systems*, Lecture Notes in Electrical Engineering 237, DOI 10.1007/978-3-319-01273-5_13,

method is manual testing by temperature and humidity meter. If the temperature and humidity is not in conformity with the requirements of the warehouse, the operator need timely operation control equipment to control temperature and humidity. The traditional manual test methods need more staff, the error of control result is big, and the process of control has great randomness. The temperature and humidity control has strongly nonlinear and big-lag characteristics. Meanwhile Temperature and humidity has strongly cross coupling characteristic. So the traditional artificial detection and control is not appropriate.

Many researchers have done work on the warehouse and greenhouse environment control, which has the characteristics of large time delay, nonlinear and uncertain, adopting fuzzy control. On the basis of analysis warehouse/greenhouse characteristics, Li Xiuhua puts forward a new control method, in which control system is divided into common controller and fuzzy inferior. The method simplifies the design and realization of the control system, and meanwhile, it takes full advantage of fuzzy inferior and common control method [1]. Yang Weizhong designs a greenhouse temperature fuzzy controller with on-line self-tuning parameters, that automatically adjusts the quantization factor according to the knowledge base of rules, optimizes the system response, and can automatically detect the global system response performance. But the controller only studies the temperature parameters in the environment [2]. Li Hui and Cai Min design the adjusting system of storehouse temperature by use of the theory of faintly controling, and emulate the faint controller on base of MATLAB. The result of computer simulation demonstrates the effectiveness of the fuzzy control algorithm, but the system is not actually using in warehouse [3]. Although there are many existing fuzzy control methods for the warehouse/greenhouse environment control, most of them study fuzzy control algorithm only for the single factor in the environment. For the control process has characteristics of multi-factor coupling, the study is less. the existing warehouse/greenhouse control system either steady-state error, overshoot or de-couple effect is not satisfactory [4–6].

Current research and practice show that fuzzy control algorithm can get satisfactory control effect if the controlled system is hard to build up the accurate mathematic model. Aiming at temperature and humidity control system of equipment warehouse, This paper draws up the fuzzy control rules, and puts forward the temperature and humidity decoupling method. Based on the temperature and humidity fuzzy control algorithm of equipment warehouse, a temperature and humidity automatic detection and control equipment is developed.

2 The Structure of Control System

Two parts are designed in the system, one is to monitor temperature and humidity, the other is to control them through turning on/off the executive device.

The first step of system working is temperature and humidity signals are collect by temperature/humidity sensor Installed in equipment warehouse. Then by the

signal conditioning circuit, the signal will be amplification, filter and regulate etc. The next the temperature and humidity signal is transmitted to data acquisition board (DAQ). After analog-digital conversion (A/D) by DAQ, the signal is transmitted to computer. The collected temperature/humidity data is analyzed, processed and displayed through the software platform of computer. According to the current value of the Equipment Warehouse temperature/humidity and the control algorithm of software, the computer outputs the temperature and humidity control signal to the temperature/humidity control equipment. Finally the controlling signal controls the executive device turning on/off to adjust the temperature and humidity of storehouse in order to keep relative stability of the environment parameters.

3 Fuzzy Controller Design

In the equipment warehouse temperature and humidity control system, the controlled parameters are temperature and humidity. The temperature/humidity sensor output corresponding signal, and the signal is processed by the signal conditioning circuit and A/D conversion circuit, then is inputted into computer fuzzy controller. According to the temperature/humidity deviation and deviation rate, and using the fuzzy control algorithm, controller outputs corresponding control value. Through the decoupling of software, the fuzzy controller outputs temperature/humidity accurate control signal. Through the drive circuit, the control signal realizes controlling temperature/humidity control equipment, operating alarm equipment etc.

Based on summarizing the actual operating experience and using fuzzy conditional statement, the fuzzy temperature/humidity controller constitutes a set of control rules and obtains the fuzzy control model. The design of the fuzzy controller has three key steps, one is accurate amount of fuzzification, the second is fuzzy control rules, the last is the formation of fuzzy reasoning.

3.1 Fuzzy Variable

In order to improve the control precision and speed, the system adopts two-dimensional fuzzy controller. Because there are two control signals, two fuzzy controller are correspondingly designed. The fuzzy variables are E_t-temperature deviation, E_h-humidity deviation, EC_t- temperature deviation rate, EC_h- humidity deviation rate, C_t- temperature control quantity, and C_h- humidity control quantity.

Table 1 Value assignments of fuzzy variable E_h and EC_h

	−3	−2	−1	0	1	2	3
PB	0	0	0	0	0.3	0.5	1
PS	0	0	0	0.5	1	0.5	0
Z	0	0.5	0.5	1	0.5	0	0
NS	0	0.5	1	0.5	0	0	0
NB	1	0.5	0.3	0	0	0	0

Table 2 Value assignments of fuzzy variable C_h

	−3	−2	−1	0	1	2	3
PB	0	0	0	0	0	0.3	1
PS	0	0	0	0	0.5	0.8	0
Z	0	0	0.5	1	0.5	0	0
NS	0	0.8	0.5	0	0	0	0
NB	1	0.3	0	0	0	0	0

3.2 The Fuzzification of Accurate Amount

The domain of E_t is {−3, −2, −1, −0, 0, +1, +2, +3}, fuzzy language variables are divided into: negative big(NB), negative small (NS), negative zero (NZ), positive zero(PZ), positive small (PS), positive big (PB). The domain of EC_t is {−3, −2, −1, 0, +1, +2, +3}, fuzzy language variables are divided into: {NB, NS, Z, PS, PB}. The domain of C_t is {−4, −3, −2, −1, 0, +1, +2, +3, +4}, fuzzy language variables are divided into: {NB, NS, Z, PS, PB}. Considering the specific environment of warehouse equipment, to ensure the system control characteristic is gentle and the control stability is good, the membership function curve changing slow need to be select. According to the principle of membership function selection, the Gaussian shape normal membership function is chosed. In the paper E_t, EC_t and C_t are calculated by normal distribution type membership function.

The domain of E_h, EC_h, C_h is same as {−3, −2, −1, 0, 1, 2, 3}, fuzzy language variables are divided into: {NB, NS, Z, PS, PB}, Value assignments of fuzzy variable E_h and EC_h are shown in Table 1. Value assignments of fuzzy variable C_h are shown in Table 2.

3.3 The Formation of the Fuzzy Control Rules

In the temperature/humidity fuzzy control system, the model of "*IF* A_i *and* B_j *Then* C_{ij}" is adopted as fuzzy control rules. In the rules A_i is error fuzzy subset, B_j is error rate fuzzy subset, and C_{ij} is control quantity of fuzzy subset. Supposed the number of such rules is k, then

$$R_l = A_i \cdot B_j \cdot C_{ij}$$
$$(\lambda = 1, 2, \ldots, k;\ i = 1, 2, \ldots, n;\ j = 1, 2, \ldots, m)$$

Table 3 Fuzzy control rule base of temperature

	EC_t				
E_t	PB	PS	Z	NS	NB
PB	NB	NB	NB	NS	Z
PS	NB	NS	NS	Z	PS
PZ	NB	NS	Z	Z	PB
NZ	NB	Z	Z	PS	PB
NS	NS	Z	PS	PS	PB
NB	Z	PS	PB	PB	PB

Table 4 Fuzzy control rule base of humidity

	EC_h				
E_h	PB	PS	Z	NS	NB
PB	NB	NB	NS	Z	PS
PS	NB	NS	Z	PS	PS
Z	NS	Z	PS	PS	PS
NS	Z	PS	PS	PB	PB
NB	PS	PS	PB	PB	PB

According to the actual operating experience the fuzzy control rules is summed up, summarized and determined. The fuzzy control rules are shown in Table 3 and 4.

3.4 Fuzzy Reasoning

The control rules shown in Table 3 or Table 4 can be expressed in a general fuzzy relation R, namely

$$R = K \bullet A\_\{i\} \bullet B\_\{j\} \bullet C\_\{ij\}$$

The membership function of R is

$$\mu_R(x, y, z) = \bigvee_{i=1,j=1}^{i=n,j=m} (\mu_{A\_\{i\}}(x) \wedge \mu_{B\_\{j\}}(y) \wedge \mu_{C\_\{ij\}}(z));$$

In the formula: $x \in X, y \in Y, z \in Z$.

When the error, error rate are taken fuzzy set A_i *and* B_j, according to the fuzzy reasoning rules the output control quantity U_{ij} is:

$$U_{ij} = \left(A_i \bullet B_j \right) \circ R;$$

The membership function of U is:

Table 5 Temperature control table

	−3	−2	−1	−0	0	1	2	3
−3	4	3	2	2	1	1	0	0
−2	4	3	2	2	1	1	0	0
−1	4	3	2	1	1	1	0	0
0	4	2	1	0	0	−1	−2	−4
1	2	1	0	−1	−1	−3	−3	−4
2	0	0	−1	−1	−2	−2	−3	−4
3	0	0	−1	−1	−2	−2	−3	−4

Table 6 Humidity control table

	−3	−2	−1	0	1	2	3
−3	3	3	3	3	2	1	0
−2	3	3	3	2	1	0	−1
−1	3	3	2	1	0	−1	−2
0	3	2	1	0	−1	−2	−2
1	2	1	0	−1	−2	−2	−3
2	2	0	−1	−2	−2	−3	−3
3	0	−1	−2	−3	−3	−3	−3

$$\mu_U(z) = \bigvee_{x \in X, y \in Y} (\mu_R(x, y, z) \wedge \mu_A(x) \wedge \mu_B(y));$$

According to each pair of input fuzzy quantity, the corresponding output fuzzy vector is calculated. Adopted the maximum membership degree method, the fuzzy control table is deduced. The table is shown in Table 5 and 6. The fuzzy control system calculate input variable of temperature/humidity error and their error rate online, then fuzzificates the input variable. After inquires the fuzzy control table, According to the Control decision, the control system runs defuzzication processing.

3.5 The Decoupling of Temperature/Humidity Control Value

Due to the temperature and humidity control of equipment warehouse has cross coupling phenomenon, the control value of temperature/humidity must be decouplied in order to obtain the good control effect. The decoupling method in the paper is introducing the decoupling parameters P1 and P2. the method make the temperature/humidity control separate into:

Temperature output: $V_t = K_t[(1-P_1)*C_t + P_1*C_h]$;
Humidity output: $V_h = K_h[(1-P_2)*C_h + P_2*C_t]$.

In the formula K_t and K_h is system coefficient in order to improve the control accuracy. The actual value of P_1/P_2 is 0 ~ 1. Different warehouse environment has different coupling degree. In order to better control the environment temperature

and humidity parameters, the operator can adjust the numerical P_1/P_2 respectively. When the control system adjusting, the operator can set $P_1 = P_2 = 0$. The control equipment start or stop will cause the larger change of the temperature and humidity in this state. After P_1 and P_2 are gradually increased, the change is gradually decreased, and the purpose of decoupling is achieved. In the testing warehouse, Owing to the effect of temperature on humidity is big, and The effect of humidity on temperature is small, so $P_1 = 0.8$, $P_2 = 0.3$ is set, and the decoupling effect of the control system is good.

4 Experiment Analysis

This temperature and humidity fuzzy control system has been applied in a large equipment warehouse. In the warehouse, the original environment temperature is 10°C, and the original environment humidity is 40 %. During the control system running, the system initial temperature is set for 20°C and initial humidity is set for 25 %RH, and the real-time changing of temperature and humidity is shown in Fig. 1. The Trial result shows that the temperature and humidity fuzzy control system has small control overshoot and has steady control performance. Meanwhile the control transition time of system is less than 20 min, the warehouse temperature control error is less than ±2°C, and relative humidity error is less than ±7 % RH. The working performance of the system is satisfactory.

Compared with traditional control method, such as PID control, fuzzy control is very suitable for non-line control of the equipment warehouse, as the accurate mathematics model is unnecessary. and it has the advantage of well robust, insensitivity of the parameter change, the easily realization of the control arithmetic, and the well control effect.

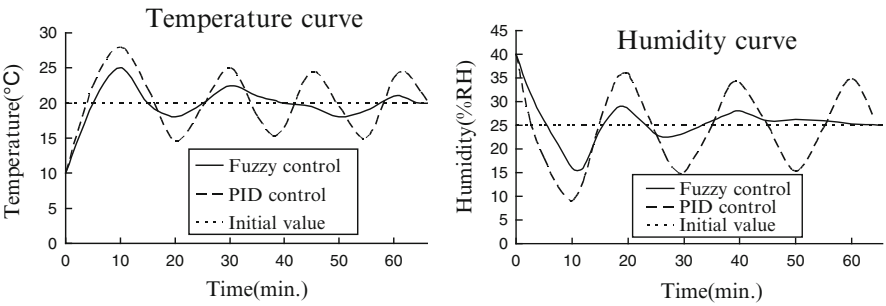

Fig. 1 Measurement and control curve of temperature/humidity

5 Conclusion

The temperature and humidity of the Equipment warehouse change has strong time-lag characteristics. In order to improve robustness of the detection and control system, fuzzy control technology is introduced into the control of temperature and humidity in equipment warehouse. In the process of the fuzzy controller design, the temperature and humidity control characteristics and mutual coupling relationship are fully studied. Testing result confirms that temperature and humidity controller has good decoupling effect, and has small overshoot. This system has virtues of quick convergence, high precision and high stability contrast to conventional system. Using this system to control the temperature and humidity of the warehouse equipment, the transition time of control is short. Meanwhile adopting fuzzy control technology improves the efficiency of the warehouse environmental measure and control.

References

1. Li X (2006) Multi-variable fuzzy control system in greenhouse. J Liaoning Tech Univ 25 (4):582–584 (In Chinese)
2. Weizhong Y, Yiming W and Haijian Li (2005) Study on greenhouse environmental temperature fuzzy controller with on-line self-tuning parameters. Trans Chin Soc Agric Mach 36(9): 79–82 115 (In Chinese)
3. Hui L, Min C (2009) Emulation of the adjusting system of storehouse temperature faintly controled on base of MATLAB. Chin New Telecommun 13:61–64 (In Chinese)
4. Shungeng Hu (1997) A study of the algorithms of fuzzy controllers. J Chongqing Univ Posts Telecommun 2:57–60 (In Chinese)
5. Xuguang Z, Jianhui LIU (2005) Temperature and humidity control for agriculture-greenhouses. Tech Autom Appl 24(2):45–47 (In Chinese)
6. Congquan Z, Zheng X, Suying Y (2001) The design of intelligent temperature control meter based on fuzzy control. Electr Meas Instrum 38(4):23–26 (In Chinese)

A Node Localization Algorithm for Wireless Sensor Network Based on Improved Particle Swarm Optimization

Qing-guo Zhang and Meng Cheng

Abstract In order to solve the problem that the positioning results of DV-hop algorithm are greatly affected by distance estimation errors, a new localization algorithm for wireless sensor network by combining DV-Hop algorithm and extremum disturbed and simple particle swarm optimization (tsPSO) is proposed in this paper. The proposed algorithm iteratively searches for the location of unknown nodes with the distance information received from anchor nodes to suppress the effect of the distance estimation error on positioning accuracy. The simulation results indicate that the proposed algorithm can achieve higher positioning accuracy than that of DV-Hop algorithm and that of DV-Hop algorithm based on standard PSO optimized.

Keywords Wireless sensor network • Particle swarm optimization • Node localization • DV-Hop • Disturbed extremum

1 Introduction

Wireless Sensor Network (WSN) is a multi-hop self-organizing network which formed by a large number of low-cost, low-power micro sensor nodes through wireless communication and nodes deployed in a target area. Wireless sensor network has a wide range of applications in various fields such as environmental monitoring, medical care, military field, target tracking and so on. For most applications, the perceived data is meaningless when the position of sensor is unknown [1]. By deploying nodes artificially or installing the GPS locator for

Q.-g. Zhang (✉) • M. Cheng
School of Computer, Central China Normal University, Wuhan, China
e-mail: zqglaowu@163.com; chriseagle@163.com

W. Wang (ed.), *Mechatronics and Automatic Control Systems*, Lecture Notes in Electrical Engineering 237, DOI 10.1007/978-3-319-01273-5_14,

each node is restricted by WSN application environment, cost and energy consumption and so on. Therefore, it is very necessary to find an algorithm to let WSN nodes locate themselves [2].

Wireless sensor network localization algorithm can be divided into two categories: range-based and range-free. The range-based algorithms require nodes with units for measuring distances between any pairs of nodes, and then the position of nodes can be calculated according to these distances. They have higher location accuracy than range-free algorithms, but also require more energy consumption and cost. RSSI [3], TOA [4], TDOA [5], AOA [6] are typical range-based algorithms; Range-free algorithms estimate the distance by just relying on the communication between nodes. Then the approximate location of nodes can be calculated with the estimated distance (Because location errors will not have much influence on routing performance and accuracy of target tracking when the positioning error is less than 40 % of the node communication radius) [7]. Centroid algorithm [8], Convex positioning algorithm [9], DV-Hop algorithm [10] are all typical range-free location algorithms. The DV-Hop algorithm is drawn the greatest attention among them. In DV-Hop algorithm, the product of hops between an unknown node and an anchor node and the average size for one hop will be as estimated distance between them. The estimated distance error is large influenced by the network topology and the WSN node density, so the localization error is high when node's density is low in the network. In recent years, the DV-Hop algorithm with heuristic algorithm is optimized such as genetic algorithm, simulated annealing algorithm and so on. These algorithms calculate the unknown node's position by iterative refinement. Then the influence of the accumulated error in distance estimation on the precision of localization can be suppressed. In this paper, a localization algorithm which combine DV-Hop algorithm and extremum disturbed and simple particle swarm optimization is presented. The new algorithm significantly improves the positioning accuracy of the DV-Hop algorithm.

2 DV-HOP Algorithm

The algorithm requires some nodes which are called anchor nodes equipped with GPS positioning equipment. The algorithm has three steps:

Step 1: Each node maintains a table $\{x_i, y_i, h_i\}$ and exchanges updates only with its neighbors. The neighbor nodes which receive information add 1 to h_i and continue to broadcast. In the table, the minimum value of h_i from the node to the anchor node i is always saved.

Step 2: Each anchor node calculates an average size for one hop as a correction. It is obtained by Eq. 1, in which node i and node j are anchor node.

$$HopSize_i = \sum_{i \neq j} \sqrt{(x_i - x_j)^2 + (y_i - y_j)^2} \Big/ \sum_{i \neq j} h_i \tag{1}$$

Then the corrections of anchor nodes will be broadcasted in the entire network. Each unknown node only gets and forwards the first received correction value to ensure that the correction value is obtained from the nearest anchor node.

Step 3: With the distance information obtained under the second phase, the position of the unknown nodes can be evaluated by maximum likelihood estimation method.

3 Particle Swarm Algorithm

Particle Swarm Optimization (PSO) [11] is a stochastic algorithm based on collective intelligence developed by Dr. Eberhart and Dr. Kennedy in 1995, inspired by social behavior of bird flocking [12].

First, the algorithm needs to initialize a population randomly. Each particle is a candidate solution of the problem in the population, while initialize a velocity for each particle to determine the flight of the particle. Particles according to the flying experience of themselves and the social behavior of the whole population to adjust the next flight in optimization process. In the population, the i-th particle will be described as $X_i = (x_{i1}, x_{i2}, \cdots, x_{iD})$ and the best position of particle i can be expressed as $pBest_i = (p_{i1}, p_{i2}, \cdots, p_{iD})$ in the optimization process, meanwhile gBest record the index of the best particle which algorithm obtained so far. Particle velocity can be described as $V_i = (v_{i1}, v_{i2}, \cdots, v_{iD})$. Particles update their velocity and positions iteratively according to the formula (2) and formula (3).

$$v_{id}^{k+1} = \omega \bullet v_{id}^{k} + c_1 \bullet r_1 \bullet (p_{id} - x_{id}^{k}) + c_2 \bullet r_2 \bullet (p_{gBestd} - x_{id}^{k}) \tag{2}$$

$$x_{id}^{k+1} = x_{id}^{k} + v_{id}^{k+1} \tag{3}$$

Where c_1 and c_2 are positive learning factors. The r_1 and r_2 are random number between 0 and 1. The ω is the inertia weight. v_{id}^{k} and x_{id}^{k} respectively describe velocity and position of the d-th dimension of particle i in k-th iteration. P_i is the best position of particle i until now. P_{gBest} shows the best particle of the population so far. The algorithm will terminate when iterations run to a pre-set number or the fitness value be optimized to a predetermined level. The particle which is expressed by $pBest_{gBest}$ will be the optimal solution of the objective function.

4 Extremum Disturbed and Simple Particle Swarm Optimization

PSO algorithm has some disadvantages such as slow convergence, low precision in the late evolutionary. And the algorithm ignores the effect of time on the course of campaign in the physics which add the position and velocity directly. For these

reasons, Hu Wang et al. [13]. build a new particle swarm optimization equation to achieve the evolutionary process of particles without speed item by simplifying the PSO algorithm. The simplified equation is as follows:

$$x_{id}^{k+1} = \omega \bullet x_{id}^{k} + c_1 \bullet r_1 \bullet (p_{id} - x_{id}^{k}) + c_2 \bullet r_2 \bullet (p_{gBestd} - x_{id}^{k}) \tag{4}$$

The first item stands for the influence which was brought by the past position of particle, and the extent of the influence will be adjusted by ω. The others have the same meaning as their counterpart in the original velocity equations.

Meanwhile, the literature [13] proposes a method which put an extremum disturbed into the algorithm in order to overcome the shortcoming of PSO algorithm which is easy to fall into the local extrema. By recording steps of evolutionary stagnation as t, the Algorithm will randomly churn the individual extrema p_0 and the global extrema p_g respectively when t achieves a pre-set threshold value. The operators of extremal perturbation are:

$$p_0 = r_3^{t_0 > T_0} p_0;\ p_g = r_4^{t_g > T_g} p_g$$

Where t_0 is evolutionary stagnation iterations of the individual extrema, and t_g express the evolutionary stagnation iterations of the global extrema; T_0 and T_g are their pre-set threshold values of the individual extrema and the global extrema; $r_3^{t_0 > T_0}$ and $r_4^{t_g > T_g}$ need to meet the following conditions:

$$r_3^{t_0 > T_0} = \begin{cases} 1 \\ U(0,1), \quad t_0 > T_0 \end{cases};\ r_4^{t_g > T_g} = \begin{cases} 1 \\ U(0,1), \quad t_g > T_g \end{cases}$$

$U(0,1)$ is a random number between 0 and 1 who satisfies uniformly distribution. Equation 5 can be obtained by putting extremum perturbation operator is in Eq. 4:

$$x_{id}^{k+1} = \omega \bullet x_{id}^{k} + c_1 \bullet r_1 \bullet (r_3^{t_0 > T_0} \bullet p_{id} - x_{id}^{k}) + c_2 \bullet r_2 \bullet (r_4^{t_g > T_g} \bullet p_{gBestd} - x_{id}^{k}) \tag{5}$$

This is the formula of extremum disturbed and simple particle swarm optimization.

5 DV-Hop Localization Algorithm Based on tsPSO Optimization

It can be seen from the first item of the Eq. 5 that Particles always move along the direction which slope is 1 in the process of iterative evolution. The ω just controls the magnitude of the change of particle's position. In order to make the algorithm

convergence fast, the variable d which controls the direction of particle's movement will be added to Eq. 5 as follow:

$$x_{id}^{k+1} = d_i \bullet \omega \bullet x_{id}^{k} + c_1 \bullet r_1 \bullet (r_3^{t_0 > T_0} \bullet p_{id} - x_{id}^{k}) + c_2 \bullet r_2 \bullet (r_4^{t_g > T_g} \bullet p_{gBestd} - x_{id}^{k}) \tag{6}$$

Where the d can be calculated by Eq. 7:

$$d_i = (x_i - p_{gBest}) / \left\| x_i - p_{gBest} \right\| \tag{7}$$

The distance from an unknown node to an anchor node is based on the product of the hops between them and average size for one hop of the anchor node, so the results' error is inevitably. The problem of optimization locations of the unknown nodes substantially converted to evaluate minimum of Eq. 8:

$$f_i(\hat{x}, \hat{y}) = \left| d_i - \sqrt{(x - x_i)^2 + (y - y_i)^2} \right| \tag{8}$$

Where $(\hat{x}, \hat{y})$ is the estimated coordinates of a unknown node, and (x_i, y_i) is the coordinates of anchor node *i*. So the fitness function of particles can be expressed as:

$$fitness(\hat{x}, \hat{y}) = \sum_{i=1}^{n} (f_i(\hat{x}, \hat{y}) / h_i)^2 \tag{9}$$

h_i is the hops between the unknown node and anchor node *i* which was obtained in first step of DV-Hop algorithm.

6 Simulation Experiments and Analysis of Effects

In order to verify the effectiveness and availability of tsPSO algorithm in the WSN node localization, the DV-Hop algorithm, DV-Hop algorithm based on standard PSO optimized and DV-Hop algorithm based on tsPSO optimized are all implemented and simulated by Matlab version 7.0. One hundred nodes are distributed in the region of 300*300 m as grid and the anchor nodes are evenly distributed on the boundary of the area. The communication radius of nodes is 50 m. Here are the settings of other parameters of PSO algorithm: the population size is 20; the maximum evolution generation, $Maxgen$, is 300; ω decreases linearly according to Eq. 10, $c_1 = c_2 = 2$; The threshold values of the individual extrema, $T_0 = 3$; the threshold values of the global extrema, $T_g = 5$;

$$\omega = \omega Max - (\omega Max - \omega Min) \times i / Maxgen \tag{10}$$

$\omega Max = 0.9$, $\omega Min = 0.4$ in the formula, i is the current number of iterations.

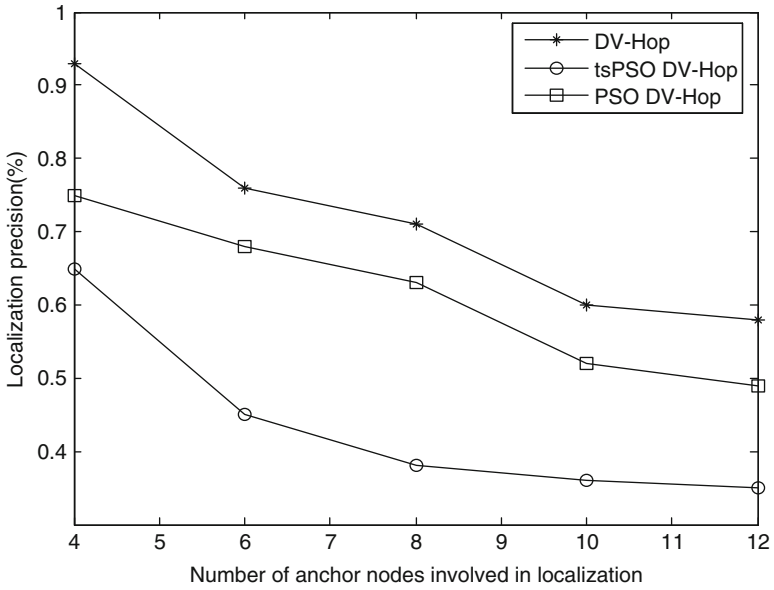

Fig. 1 Average of localization error with different number of beacons

Average localization error is generally used as the evaluation criteria of the localization algorithm; the average localization error is calculated as follows:

$$AveragError = \sum_{i=1}^{N} \sqrt{(\hat{x}_i - x_i)^2 + (\hat{y}_i - y_i)^2} \times 100\%/N \times R \tag{11}$$

N is the number of unknown nodes; $(\hat{x}_i, \hat{y}_i)$ is the estimated coordinates of the unknown node i; (x_i, y_i) is the real coordinates of the unknown node i; R is communication radius.

Figure 1 shows the influence of different number of beacon on average localization errors. DV-Hop algorithm, DV-Hop algorithm based on standard PSO optimized and DV-Hop algorithm based on tsPSO optimized are ran 10 times and averaged respectively.

It was known from Fig. 1 that the more beacon nodes involved in localization, the higher the localization accuracy is. Because of the simulation is performed in the case of a relatively small proportion of anchor nodes, DV-Hop's localization error decrease from 93 % to 57 % when the number of anchor node increases from 4 to 10; DV-Hop algorithm based on standard PSO optimized converges slowly with fewer anchor nodes and the localization error varies between 75 % and 49 %; DV-Hop algorithm based on tsPSO optimized has a faster convergence speed and higher localization accuracy when the number of anchor node is very small. The localization error decreases from 59 % to 30 %.

Table 1 The convergence rate of algorithms with different number of beacons

Number of anchor nodes		4	6	8	10	12
DV-Hop based PSO	Localization precision	75 %	68 %	63 %	52 %	49 %
	Number of iteration	306	297	295	291	293
DV-Hop based tsPSO	Localization precision	65 %	45 %	38 %	36 %	35 %
	Number of iteration	256	254	259	251	257
DV-Hop based tsPSO with d	Localization precision	65 %	45 %	38 %	36 %	35 %
	Number of iteration	164	166	158	170	166

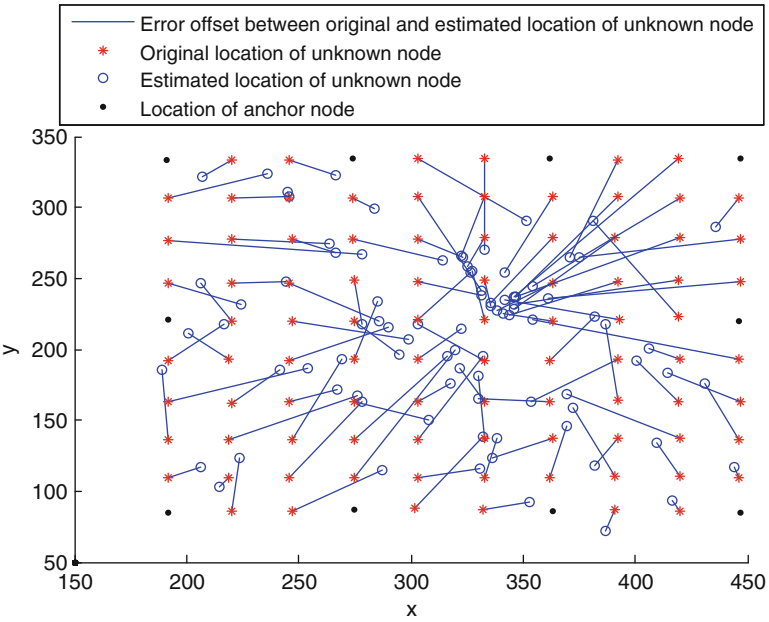

Fig. 2 The results of DV-Hop algorithm

DV-Hop algorithm based on tsPSO optimized has more obvious advantages on no matter localization accuracy or convergence speed among the above three location algorithms when proportion of the anchor node is small.

As can be seen from Table 1, the tsPSO algorithm is convergence faster than that of PSO, and the tsPSO algorithm which is added the direction variable d is convergent fastest. In the Figs. 2, 3, and 4, the solid circles represent the position of the anchor nodes; the asterisks are the actual location of unknown nodes; and hollow circles represent the estimated position of the unknown node. As can be seen from Fig. 2, because the anchor node is evenly distributed on the boundary, the results of DV-Hop algorithm tend to the regional centers excessively and the error is higher, at 58.47 %.

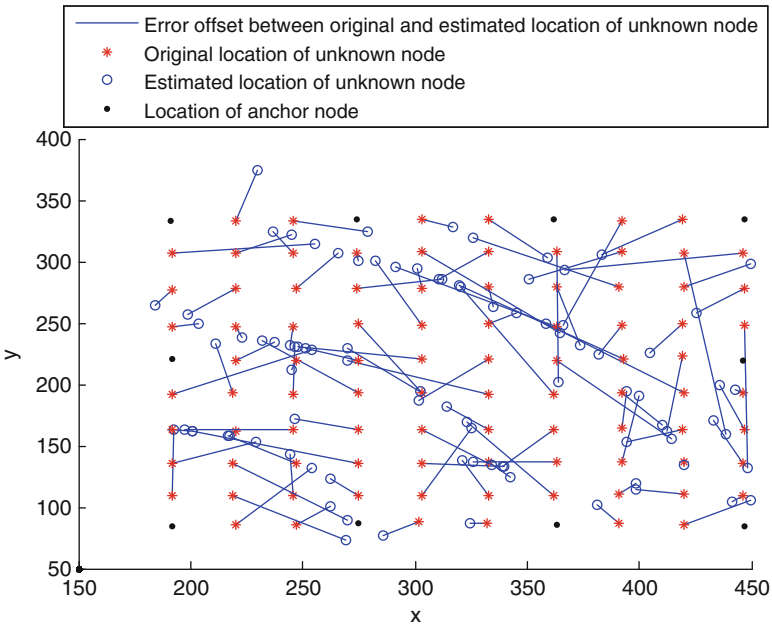

Fig. 3 The results of DV-Hop algorithm based on standard PSO optimize

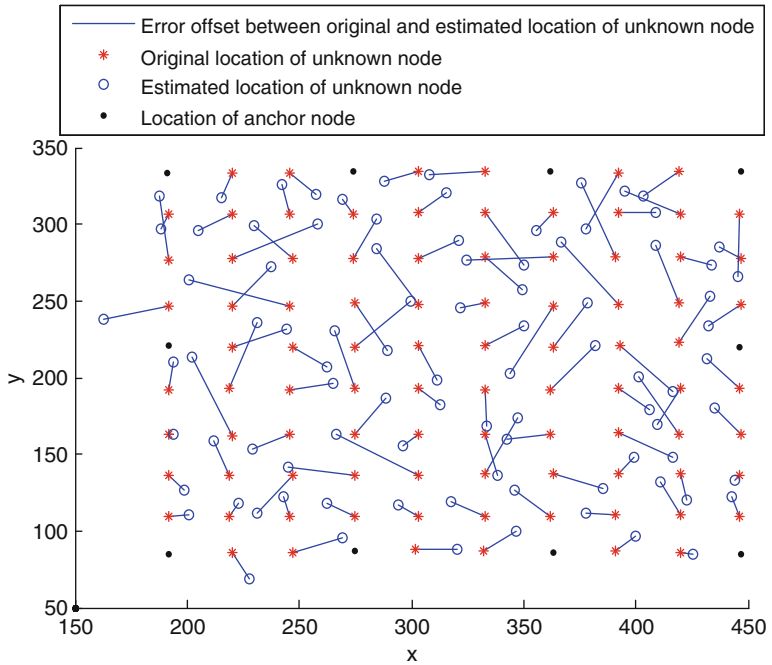

Fig. 4 The results of DV-Hop algorithm based on tsPSO optimized

It was known from Fig. 3 that localization results of DV-Hop algorithm based on standard PSO optimized constitute three arc-shaped areas nearly; the localization error is 49.01 %.

The results of DV-Hop algorithm based on tsPSO optimized are more in accordance with the nodes' actual distribution characteristics and positioning error, 30.35 %, is also better than the first two algorithms. They are shown in the Fig. 4.

7 Conclusion

In order to solve the problem of low localization accuracy of standard DV-Hop algorithm, in this paper a improved DV-Hop localization algorithm based on extremum disturbed and simple particle swarm optimization is proposed. Simulation results indicates that the localization accuracy is much higher than that of DV-Hop algorithm and that of DV-Hop algorithm based on standard PSO optimized. And the new algorithm is convergent faster than that of DV-Hop algorithm based on standard PSO optimized. The effect is more obvious when the anchor node ratio is low.

Then there are still many issues to be resolved around WSN applications such as energy consumption and stability of algorithm. Further work is necessary in these areas.

References

1. Rabaey JM, Ammer MJ, da Silva JL Jr, Patel D, Roundy S (2000) PicoRadio supports ad hoc ultra-low power wireless networking. Computer 33(7):42–48
2. Wang FB, Shi L, Ren FY (2005) Self-localization systems and algorithms for wireless sensor networks. Ruan Jian Xue Bao(J Softw) 16(5):857–868 (In Chinese)
3. Bahl P, Padmanabhan VN (2000) RADAR: an in-building RF-based user location and tracking system. In: INFOCOM 2000. Nineteenth annual joint conference of the IEEE computer and communications societies. Proceedings, IEEE, Tel Aviv, (2), pp 775–784
4. Cheung KW, So HC (2005) A multidimensional scaling framework for mobile location using time-of-arrival measurements. Signal Process IEEE Trans 53(2):460–470
5. Cheng X, Thaeler A, Xue G, Chen D (2004) TPS: a time-based positioning scheme for outdoor wireless sensor networks. In: INFOCOM 2004. Twenty-third annual joint conference of the IEEE computer and communications societies, IEEE, Hong Kong, (4), pp 2685–2696
6. Niculescu D, Nath B (2003) Ad hoc positioning system (APS) using AOA. In: INFOCOM 2003. Twenty-second annual joint conference of the IEEE computer and communications. IEEE Societies, San Francisco, California, (3), pp 1734–1743
7. He T, Huang C, Blum BM, Stankovic JA, Abdelzaher T (2003) Range-free localization schemes for large scale sensor networks. In: Proceedings of the 9th annual international conference on Mobile computing and networking, ACM, San Diego, California, pp 81–95
8. Bulusu N, Heidemann J, Estrin D (2000) GPS-less low-cost outdoor localization for very small devices. Pers Commun IEEE 7(5):28–34

9. Doherty L & El Ghaoui L (2001) Convex position estimation in wireless sensor networks. In: INFOCOM 2001. Twentieth annual joint conference of the IEEE computer and communications societies. Proceedings, IEEE, Anchorage, AK, (3), pp 1655–1663
10. Niculescu D, Nath B (2001) Ad hoc positioning system (APS). In: Global telecommunications conference, 2001. GLOBECOM'01, IEEE, San Antonio, Texas, (5), pp 2926–2931
11. Kennedy J, Eberhart R (1995) Particle swarm optimization. In: Neural networks, 1995. proceedings., IEEE international conference, Perth, WA, (4), pp 1942–1948
12. Namin PH, Tinati MA (2011) Node localization using Particle Swarm Optimization. In: Intelligent sensors, sensor networks and information processing (ISSNIP), 2011 seventh international conference, Adelaide, SA, pp 288–293
13. Hu W, Li ZS (2007) Simpler and more effective particle swarm optimization algorithm. Ruan Jian Xue Bao (J Softw) 18(4):861–868 (In Chinese)

Stochastic Stabilizing Control of Networked Control System with Markovian Parameters

Ying Wu, Yanpeng Wu, and Lei Guo

Abstract In order to solve the potential issues caused by network induced delays and dropouts which could arise the performance degradation and system instability, this paper studies the stochastic stability problem of Networked control systems (NCSs) with arbitrary time delays and packet dropouts by using an active time-varying sampling method. The random time delays and successive packet dropouts are driven by two separately Markov chains and NCSs are modelled as a discrete time Markovian jump linear systems. Based on Lyapunov approach, sufficient conditions for the stochastic stability of the networked control system are derived and stabilization controller is designed in terms of linear matrix inequalities (LMIs) correspondingly. Gridding approach is introduced to guarantee the solvability of the LMIs with finite jump modes. A numerical example is given to illustrate the effectiveness of the proposed method which stabilizes the NCS with random time delays and packet dropouts.

Keywords Networked control system • Stochastic stability • Markov chain • Linear matrix inequality • Time delay • Packet dropouts

1 Introduction

Due to the advantages of low installation cost, reduced wiring, easy maintenance and good system flexibility, NCSs have been widely used in manufacturing systems, monitoring system and vehicle highway systems. Despite lots of

Y. Wu (✉) • Y. Wu
Department of Automation, Northwestern Polytechnical University, Xi'an, China
e-mail: wuyg1226@hotmail.com; wu.yanpeng@hotmail.com

L. Guo
China Petroleum Pipeline Engineering Corporation, Langfang, Hebei, China
e-mail: guolei2140@cnpc.com.cn

W. Wang (ed.), *Mechatronics and Automatic Control Systems*, Lecture Notes in Electrical Engineering 237, DOI 10.1007/978-3-319-01273-5_15,

advantages and potentials network brings to the control system, potential issues arise to degrade a system's performance and even cause system instability, such as delays and packet dropouts [1].

Many researchers have studied stability criteria and stabilizing controller design for networked control systems with delays and packet dropouts. Time-based time-delay analysis of the NCS is provided to explain how it affects network systems and an adaptive Smith predictor control scheme is designed [2]. A switched system approach was used to study the stability of networked control systems and optimal gain is calculated for stabilizing controller design [3]. The network-induced random delays are modelled as Markov chains such that the closed-loop system is a jump linear system with one mode [4, 5]. NSCs with packet dropouts are modelled as discrete Markov jump system [6, 7]. So far, the stability synthesis for the NCSs with time delays and packet dropouts as a Markovian jump system with two Markov chains has not been fully investigated.

In this paper, the stochastic stability problem of NCSs with random time delays and packet dropouts is investigated. The closed-loop NCS is modelled as a discrete-time jump system characterized by driving two separately Markov chains. An active time-varying sampling method is proposed to make sure time delay always less than one sampling period [8]. Based on the Lyapunov stability theory, sufficient conditions for the stochastic stabilization of the NCS are obtained and the mode-dependent stabilizing controller for the closed-loop NCS is designed in the linear matrix inequalities (LMIs) formulation via the Shur complement theory. A "gridding" approach is introduced to obtain the finite combination of time delays and packet dropouts which ensures the feasibility of the constructed LMIs [9].

Notation: The notation used throughout the paper is fairly standard. A^T represents the transpose of matrix A, the notation $P > 0$ means that P is positive definite, $\lambda_{\max}(P)(\lambda_{\min}(P))$ denotes the maximal (minimal) eigenvalue of matrix P; $diag\{\cdots\}$ stands for a block-diagonal matrix; $E[\bullet]$ stands for the mathematical expectation; $\|\bullet\|$ denotes the standard norm.

2 Problem Formulation

Consider a linear time-invariant plant described by

$$\dot{x}(t) = Ax(t) + Bu(t) \tag{1}$$

where $x(t) \in \mathbb{R}^n$ is the state vector, $u(t) \in \mathbb{R}^p$ is the input vector. A, B are constant matrices of appropriate dimensions.

In this paper, the sampling period will be set time varying to make sure time delay is less than one sampling period. In order to achieve this goal, sensor is assumed both time-driven and event-driven. Actuator and controller are event-driven. Suppose time axis is partitioned into equidistant small intervals and the

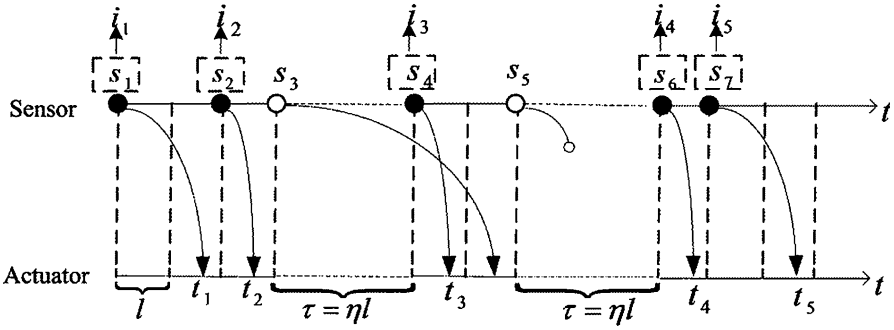

Fig. 1 Sampling and updating conditions of NCS

length of each interval is l. Define t_k as the kth updating instant of actuator, and assume that total transmission delay from sensor to actuator of the updating signal at the instant t_k is τ_k. Then the next sampling instant can be selected as

$$s_{k+1} = \begin{cases} s_k + al & t_k \in [s_k + (a-1)l,\ \ s_k + al) \\ s_k + \tau & t_k \geq s_k + \tau \end{cases} \tag{2}$$

where s_k is the kth sampling instant, τ is the allowable maximum delay from sensor to actuator ($\tau = \eta l$, η is the bound positive integer of delay), a is a positive integer and $0 < a < \eta$.

Figure 1 shows the sampling and updating conditions of NCS. if the transmission time of sampled signal at time s_k is less than τ, the actuator will be updated by the signal and the sensor will be driven to do the next sampling, which is called an effective sampling instant because the signal at this sampling instant is successfully transmitted from sensor to actuator, such as s_1 and s_2 marked in Fig. 1; if the signal sampled at time s_k has not arrived before the maximal allowable updating time $s_k + \tau$, which means the total transmission delay is out of τ, the signal will be discarded and the sensor will adopt time-driven mode, such as s_3 marked in Fig. 1; if packet dropout happened to the sampled signal, which can be seen as a long delay packet, the time-driven mode will adopted by sensor to do the next sampling, such as s_6 marked in Fig. 1.

Suppose h_k as the length of interval between two successive effective sampling instants i_k and i_{k+1}, the discrete time representation of Eq. 1 can be described as

$$x(i_{k+1}) = \Phi_k x(i_k) + \Gamma_0(\tau_k, h_k)u(i_k) + \Gamma_1(\tau_k, h_k)u(i_{k-1}) \tag{3}$$

where $\Phi_k = e^{Ah_k}$, $\Gamma_0(\tau_k, h_k) = \int_0^{h_k - \tau_k} e^{As} B ds$, $\Gamma_1(\tau_k, h_k) = \int_{h_k - \tau_k}^{h_k} e^{As} B ds$

Let us introduce a new augmented state $z(k) = [\, x(i_k)\ u(i_{k-1})\,]^T$. Therefore, we can get the following augmented closed-loop system

$$z(k+1) = \Psi_k z(k) \tag{4}$$

where $\Psi_k = \begin{bmatrix} \Phi_k + \Gamma_0(\tau_k, h_k)K(i_k) & \Gamma_1(\tau_k, h_k) \\ K(i_k) & 0 \end{bmatrix}$

3 Stochastic Stability Analysis and Controller Design

Define d_k as the number of dropped packet between two successive *effective updating instants* i_k and i_{k+1}, then we can get $i_{k+1} - i_k = d_k + 1$, $i_k \in I = \{i_1, i_2, i_3, \ldots\}$. If assume the bound of consecutive dropped packets is d, we can conclude that d_k takes value from a finite set $\Omega = \{0, 1, \cdots, d\}$.

In Sect. 2, we defined the bound of τ_k ($\tau = al$) is τ ($\tau = \eta l$) and a takes value from a finite set $M = \{1, 2, \cdots, \eta\}$, and then τ_k takes value from the finite set $T = \{1l, 2l, \cdots, \eta l\}$.

In this paper, we assume that random delays τ_k and packet dropouts d_k are two independent Markov chains that take values in Ω and M with the following transition probabilities

$$\begin{aligned} \omega_{mi} &= \Pr(\tau_{k+1} = il | \tau_k = ml), \quad \forall i, m \in \mathrm{M} := \{1, 2, \cdots, \eta\} \\ \lambda_{nj} &= \Pr(d_{k+1} = j | d_k = n), \quad \forall j, n \in \Omega := \{0, 1, \cdots, d\} \end{aligned} \tag{5}$$

where $\omega_{mi}, \lambda_{nj} \geq 0$, and $\sum_{i=1}^{\eta} \omega_{mi} = 1$, $\sum_{j=0}^{d} \lambda_{nj} = 1$

The transition probability matrixes are defined by Υ and Π.

Based on the above assumptions, the e*ffective sampling period* h_k can be written into: $h_k = \tau_k + \tau d_k$

Therefore, the values of $\Phi_k, \Gamma_0(\tau_k, h_k)$ and $\Gamma_1(\tau_k, h_k)$ are finally determined by τ_k and d_k, system (4) can be seen as a discrete-time Markovian jump linear system with finite jump modes varying in a finite set which is combined by sets T and Ω. Define $\hat{A}(m, n)$ as the jump modes determined by $\tau_k = m$ and $d_k = n$, $K(m, n)$ as the mode-dependent state feedback controller gain, then augmented system (4) can be written into

$$z(k+1) = \hat{A}(m, n) z(k), \quad \forall m \in \mathrm{M}, n \in \Omega \tag{6}$$

where

$$\hat{A}(m, n) = \begin{bmatrix} \Phi(m, n) + \Gamma_0(m, n)K(m, n) & \Gamma_1(m, n) \\ K(m, n) & 0 \end{bmatrix} \tag{7}$$

Definition 1 The system (6) is stochastically stable if for every initial state $z_0 = z(0)$ and initial distributions $\tau_0 = \tau(0) \in \mathrm{T}$ and $d_0 = d(0) \in \Omega$, there exists a finite matrix $Q > 0$ such that $E(\sum_{k=0}^{\infty} \|z(k)\|^2 | z_0, \tau_0, d_0) < z_0^T Q z_0$ holds.

Theorem 1 *If there exists symmetric positive definite matrices $X(m,n) > 0, m \in M$, $n \in \Omega$ satisfying*

$$\begin{bmatrix} X(m,n) & * & \cdots & * \\ \Xi_{01} & \omega_{m0}^{-1}\lambda_{n0}^{-1}X(0,0) & & \\ \vdots & & \ddots & \\ \Xi_{(\eta d)1} & 0 & \cdots & \omega_{m\eta}^{-1}\lambda_{nd}^{-1}X(\eta,d) \end{bmatrix} > 0, \quad m = 1,2,\ldots,\eta,\ n = 0,1,2,\ldots,d \tag{8}$$

where $\Xi_{01} = \Xi_{21} = \cdots = \Xi_{(\eta d)1} = A(m,n)X(m,n)$

Then the system (6) is stochastically stable.

Proof Consider the following form of the Lyapunov function:

$$V(k) = z^T(k)P(m,n)z(k) \tag{9}$$

where $P(m,n) = X^{-1}(m,n) > 0$

Then we have

$$\begin{aligned} E(\Delta V) &= E(V(k+1) - V(k)) \\ &= \sum_{j=0}^{d}\sum_{i=0}^{\tau} \lambda_{nj}\omega_{mi} z^T(k)\hat{A}^T(m,n)P(m,n)\hat{A}(m,n)z(k) - z^T(k)P(m,n)z(k) \\ &= z^T(k)V(m,n)z(k) \end{aligned} \tag{10}$$

where $V(m,n) = \sum_{j=0}^{d}\sum_{i=0}^{\eta} \lambda_{nj}\omega_{mi}\hat{A}^T(m,n)P(i,j)\hat{A}(m,n) - P(m,n)$

Define $H(m,n) = diag\{P(m,n), I_{00}, \ldots, I_{\eta d}\}$, and pre-multiply and post-multiply Eq. 8 by $H(m,n)$, we get

$$\begin{bmatrix} P(m,n) & * & \cdots & * \\ A(m,n) & \omega_{m0}^{-1}\lambda_{n0}^{-1}P^{-1}(0,0) & & \\ \vdots & & \ddots & \\ A(m,n) & 0 & \cdots & \omega_{m\eta}^{-1}\lambda_{nd}^{-1}P^{-1}(\eta,d) \end{bmatrix} > 0, \quad m = 0,1,2,\ldots,\eta,\ n = 0,1,2,\ldots,d \tag{11}$$

By Schur complement, we can get $V(m,n) < 0$.since $V(m,n) < 0$, then

$$\begin{aligned} E(\Delta V(k)) &= E(V(k+1) - V(k)) \\ &\le -\lambda_{\min}(-V(m,n))\|z(k)\|^2 < 0 \end{aligned} \tag{12}$$

For any integer $M \ge 1$, we have

$$E(V(z(M+1)) - E(V(z_0)) \le -\lambda_{\min}(-V(m,n))E\left\{\sum_{k=0}^{M}\|z(k)\|\right\}$$

Thus, from Definition 1, if $V(m,n) < 0$, the system (6) is stochastically stable.

Theorem 2 *If there exists symmetric positive definite matrices $G(m,n)$ and $V(m,n)$, matrices $R(m,n)$ ($\forall m \in M, n \in \Omega$) satisfying*

$$\begin{bmatrix} G(m,n) & * & * & * & \cdots & * & \\ 0 & V(m,n) & * & * & \cdots & * & \\ \Pi_0 & \Lambda_0 & \omega_{m0}^{-1}\lambda_{n0}^{-1}G(0,0) & * & \cdots & * & \\ R(m,n) & 0 & 0 & \omega_{m0}^{-1}\lambda_{n0}^{-1}V(0,0) & \cdots & * & \\ \vdots & \vdots & \vdots & \vdots & \ddots & * & \\ \Pi_{(\eta d)} & \Lambda_{(\eta d)} & 0 & 0 & \cdots & \omega_{m\eta}^{-1}\lambda_{nd}^{-1}G(\eta,d) & \\ R(m,n) & 0 & 0 & 0 & \cdots & 0 & \omega_{m\eta}^{-1}\lambda_{nd}^{-1}V(\eta,d) \end{bmatrix} > 0, \forall m \in M, n \in \Omega \tag{13}$$

where

$$\begin{aligned} \Pi_0 = \Pi_1 = \cdots = \Pi_{(\eta d)} &= \Phi(m,n)G(m,n) + \Gamma_0(m,n)R(m,n) \\ \Lambda_0 = \Lambda_1 = \cdots = \Lambda_{(\eta d)} &= \Gamma_1(m,n)V(m,n) \end{aligned}$$

Then the system (4) is stochastically stable and the mode-dependent state feedback controller is given by

$$K(m,n) = R(m,n)G^{-1}(m,n), \quad m \in M, n \in \Omega \tag{14}$$

Proof Denote the following matrixes:

$$\begin{aligned} \tilde{A}(m,n) &= \begin{bmatrix} \Phi(m,n) & \Gamma_1(m,n) \\ 0 & 0 \end{bmatrix}, \quad \tilde{B}(m,n) = \begin{bmatrix} \Gamma_0(m,n) \\ I \end{bmatrix}, \\ \tilde{K}(m,n) &= [K(m,n) \quad 0] \end{aligned} \tag{15}$$

Rewrite system (6) into: $z(k+1) = [\tilde{A}(m,n) + \tilde{B}(m,n)\tilde{K}(m,n)]z(k)$, then by applying Theorem 1, we can easy proof this theorem.

4 Numerical Example

Consider the following system

$$\dot{x} = \begin{bmatrix} 0 & 1 \\ -2 & -3 \end{bmatrix} x + \begin{bmatrix} 0 \\ 1 \end{bmatrix} u \tag{16}$$

where u is the control input for the continuous-time linear plant. According to the driven mode and active time-varying sampling method proposed in this paper, the state feedback controller for discrete-time plant in the NCS should be $u(t) = u(i_k) = K(i_k)x(i_k), t_k \leq t < t_{k+1}$

Suppose the length of gridded equidistant small interval l is 0.05 ms, $\tau_k = \{0.05$ ms, 0.1 ms, 0.15 ms$\}$, $d_k \in \{0, 1, 2\}$, the transition probability matrices are given by

$$\Upsilon = \begin{bmatrix} 0.6 & 0.3 & 0.1 \\ 0.5 & 0.3 & 0.2 \\ 0.7 & 0.2 & 0.1 \end{bmatrix}, \quad \Pi = \begin{bmatrix} 0.2 & 0.5 & 0.3 \\ 0.5 & 0.4 & 0.1 \\ 0.6 & 0.3 & 0.1 \end{bmatrix} \tag{17}$$

The state feedback controller gains will be calculated by Matlab LMI Control Toolbox, the results are as follows:

$$\begin{aligned} K(1,\ 0) &= [\text{-}3.9926 \quad \text{-}4.1845]; K(2,0) = [\text{-}4.5639 \quad \text{-}4.9267]; K(3,0) = [\text{-}5.3038 \quad \text{-}5.9421]; \\ K(1,\ 1) &= [\text{-}2.4297 \quad \text{-}2.8355]; K(2,1) = [\text{-}2.4823 \quad \text{-}3.0359]; K(3,1) = [\text{-}2.5342 \quad \text{-}3.2598]; \\ K(1,\ 2) &= [\text{-}1.5838 \quad \text{-}2.1412]; K(2,2) = [\text{-}1.5801 \quad \text{-}2.2609]; K(3,2) = [\text{-}1.5824 \quad \text{-}2.3977]; \end{aligned} \tag{18}$$

The state trajectories of NCS with the feedback control law are proposed in Fig. 2, which shows the networked control system is stochastically stable even if there exist time delays and packet dropouts.

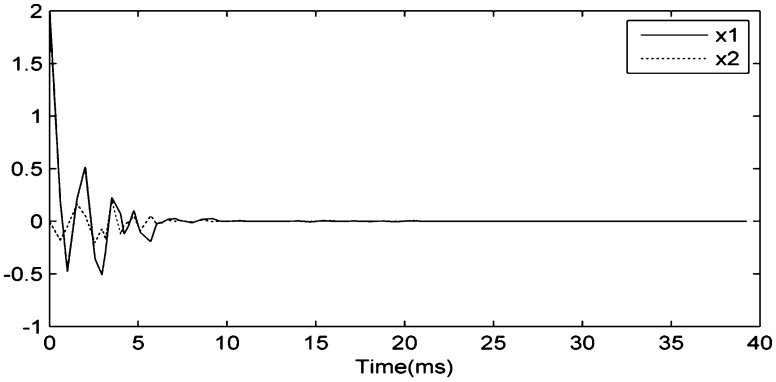

Fig. 2 States trajectory of NCS

5 Conclusion

This paper studies the stochastic stability problem of networked control systems by modeling NCS as a two mode Markovian jump linear system. The random time delays and packet dropouts are driven by two Markov chains. Sufficient conditions of stochastic stability for the jump linear systems are given in terms of a set of LMIs. To solve the LMIs for obtaining feedback gains, the "gridding approach" is adopted to guarantee the LMIs set for the jump linear systems with finite jump modes. Numerical examples illustrate the effectiveness of the proposed strategy for the stochastic stabilizing controller over NCS.

References

1. Tipsuwan Y, Chow MY (2003) Control methodologies in networked control systems. Control Eng Pract 11:1099–1111
2. Lai CL, Hsu PL (2010) Design the remote control system with the time-delay estimator and the adaptive Smith predictor. IEEE Trans Ind Inform 6:73–80
3. Li HB et al (2009) Optimal stabilizing gain selection for networked control systems with time delays and packet losses. IEEE Trans Control Syst Technol 17:1154–1162
4. Yu B et al (2011) Discrete-time H-2 output tracking control of wireless networked control systems with Markov communication models. Wirel Commun Mobile Comput 11:1107–1116
5. Liu M et al (2009) Stabilization of Markovian jump linear system over networks with random communication delay. Automatica 45:416–421
6. Ye X et al (2010) Modelling and stabilisation of networked control system with packet loss and time-varying delays. IET Control Theory Appl 4:1094–1100
7. Wan X et al (2010) Fault detection for networked systems subject to access constraints and packet dropouts. J Syst Eng Electron 22:127–134
8. Wu Y, Yuan ZH et al (2012) Lmi-based tracking control for networked control systems with random time delay and packet dropout. JDCTA 6:364–373
9. Sala A (2005) Computer control under time-varying sampling period: an LMI gridding approach. Automatica 41:2077–2082

An Automatic Clutch Engagement Strategy for Electric Vehicle Based on Fuzzy Control

Rui Hou, Cheng Lin, and Lingling Zhang

Abstract In order to solve the deterioration problem of synchronizer for no clutch automated mechanical transmission (AMT) technology, an automatic clutch actuator was developed for a light electric vehicle which is driven by a single traction motor. By introducing an automatic clutch engagement-schedule and thereof the fuzzy control strategy which simulate the experienced manual process of clutch, a double variables fuzzy controller (DVFC) is designed with the speed signals of clutch driving and driven discs as input parameters and the pulse width modulation (PWM) signal of the automatic clutch actuate motor as output parameter. By using MATLAB/Simulink software, off-line simulation model of AMT system is created. The simulation results show that the automatic clutch fuzzy control strategy can realize the "quick-slow-quick" engagement schedule at clutch sliding stage and it can simulate the experienced manual clutch with greatest degree. The friction work and degree of shock has been controlled effectively and thus the problem for AMT system is solved.

Keywords Electric vehicle • AMT • Automatic clutch • Fuzzy control

1 Introduction

Application for no clutch AMT technology is an important trend of development for the electric vehicle driveline technology. A variety of electric vehicles in China had adopted this technology, cumulative operated more than ten millions of kilometers, and got good overall results. However, the system performance and reliability about these applications remain to be further improved. The disadvantages are manifested

R. Hou (✉) • C. Lin • L. Zhang
National Engineering Laboratory for Electric Vehicle, Beijing Institute of Technology, Beijing, China
e-mail: ruicostaacm@163.com

W. Wang (ed.), *Mechatronics and Automatic Control Systems*, Lecture Notes in Electrical Engineering 237, DOI 10.1007/978-3-319-01273-5_16,

in: motor speed adjustment time and the total vehicle shifting time are affected by the inappropriate control of shifting forces or motor speed while shifting. The wear of synchronizer will deteriorate the shifting process and make the shifting less soft, even being unable to shift [1].

In order to covering the shortage of the no clutch shifting technology, and avoiding the inaccuracy of motor speed control and the synchronizer frequently wear, a new AMT shifting technology is created to improve the vehicle shifting reliability. The system consists of a 100 kW of permanent magnet synchronous traction motor, an automatic clutch, and a three gears manual transmission with an automatic shifting actuator. The automatic clutch will be introduced in the next Section. In Sect. 3, an automatic clutch engagement schedule is discussed. An automatic clutch fuzzy control strategy is presented in Sect. 4 to simulate the experienced manual process of clutch. Simulation results are analyzed in Sect. 5.

2 Automatic Clutch Actuator

An electric clutch actuator where is shown in Fig. 1 has been used for the system. Outside condition are sampled and identified by sensors, and the signals from the controller make the actuator work. Actuator driven by a brushless direct current (BLDC) motor makes the screw rotate; the nut turns rotary motion into linear motion, it means that the nut will reciprocates in the axial and realizes engagement or disengagement of the clutch. In this system, ball screw nut pair is the key device which can turn rotary motion into linear motion; it has the advantages of lower drive torque, micro speed-feed and high speed-feed abilities.

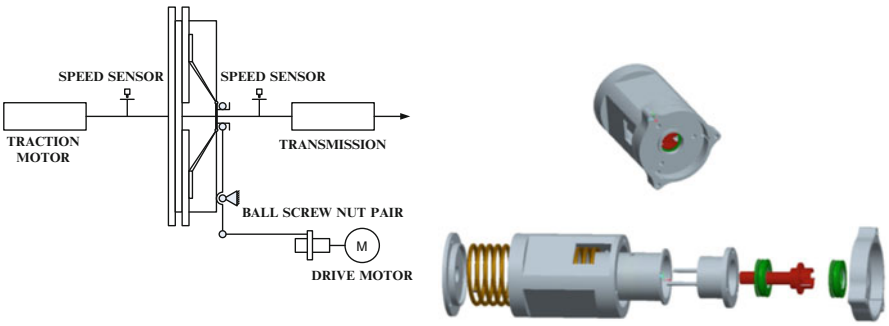

Fig. 1 Automatic clutch system is shown on the *left*, assembly drawing is shown on the *upper right*, parts drawing is shown on the *lower right*

3 Analysis of Automatic Clutch Engagement Schedule

Although several researches had been focused on automatic clutch control technology, such as an innovative power-split device for a hybrid powertrain system [2], the impedance control of a single shaft-type clutch using homogeneous electrorheological fluid [3], and the clutch control for a novel dual-belt continuously variable transmission [4], there were little achievements for AMT or pure electric vehicles which have the advantages of wide speed range for traction motor, high instantaneous power and overload capability. So for the EVs, the clutch can be engaged at the start-up state, and start the vehicle by taking full advantage of low speed and high torque characteristics of the traction motor at its constant torque area. Then, the key and difficult point for electric clutch control turns to engagement control during shifting process [5, 6]. This paper applies a new clutch control technique to simulate the experienced manual process of clutch by using a fuzzy controller.

The shifting evaluation indexes for AMT include shifting time t, degree of shock j, and clutch sliding friction work W_C. The proposes for automatic clutch engagement control are same as AMT shifting control, the shifting time must be shorten, the clutch sliding friction work must be lower and the degree of shock during shifting process must be reduced. Automatic clutch engagement processes include complete disengagement stage, sliding stage, and complete engagement stage, corresponding to "quick-slow-quick" engagement control schedule.

4 Fuzzy Controller Design

Based on the characteristics of nonlinear and time varying for automatic clutch, on the other hand, based on the automatic clutch engagement schedule, this paper design a DVFC with double input variables and single output variable to realize engagement process control for automatic clutch, its principle is shown in Fig. 2, speed difference for clutch driving and driven discs and its rate of change are using as input parameters of the controller, expressed as ω_{cd} and $\dot{\omega}_{cd}$, respectively; PWM signal of the automatic clutch actuate motor is using as output controlling parameter, expressed as α_E. Speed control for automatic clutch engagement will be realized by changing PWM signals of the actuator. As shown in Fig. 2, ω_{Egoal} is the target speed for actuate motor.

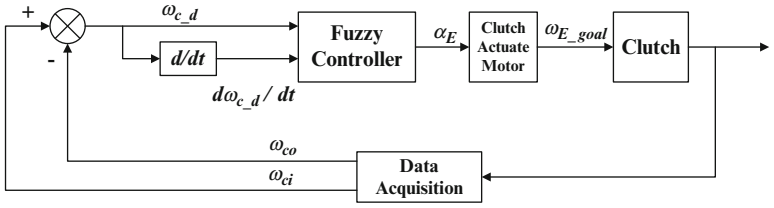

Fig. 2 Fuzzy engagement control principle of automatic clutch

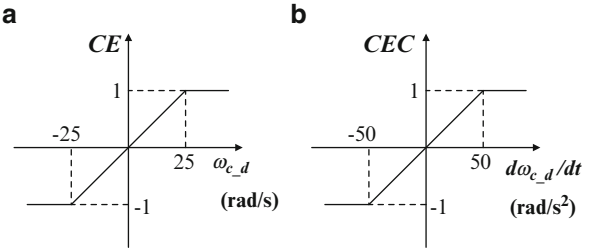

Fig. 3 Normalization of input parameters, (**a**) Normalization for ωcd (**b**) Normalization for $\dot{\omega}_{cd}$

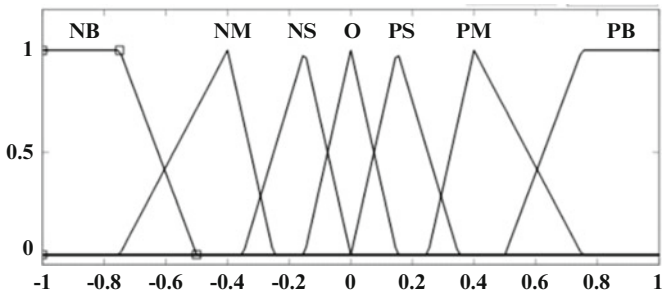

Fig. 4 Membership function for clutch driving and driven speed difference ***CE*** and for rate of change of clutch driving and driven speed difference ***CEC***

Functions for fuzzy controller consist of input variables normalization, fuzzification, fuzzy control rules, fuzzy reasoning, decision making and clear output variables. The normalization for input variables ω_{cd} and $\dot{\omega}_{cd}$ can put them to precise values *CE* and *CEC* which range from −1 to 1. The processes of normalization are shown in Fig. 3 [7].

Membership function of *CE*, *CEC*, *and* α_E can be obtained by fuzzification, as shown in Figs. 4 and 5. Fuzzy subsets for *CE* and *CEC* are {*NB,NM,NS,O,PS,PM, PB*}, denote the fuzzy state value for speed difference of clutch driving and driven discs and fuzzy state value for rate of change of the speed difference, respectively. In order to control the power output tube of automatic clutch actuate motor by using PWM, the controller needs not only to change the PWM signals but also to change the direction of current in the power tube, so the fuzzy subset of α_E is defined as {*N, O, PS, PM, PB*}, in which a negative value indicates a change of the actuate motor work direction. In the fuzzy subsets where *NB, NM, NS, N, O, PS, PM, PB* stand for Negative Big, Negative Medium, Negative Small, Negative, Zero, Positive Small, Positive Medium and Positive Big respectively [8].

On the basis of reduce wear and degree of shock during the automatic clutch engagement, at the same time, in order to simulate the experiential manual process of clutch, the fuzzy control rules for automatic clutch engage speed α_E is developed, as shown in Table 1, where *N* denotes the clutch disengage quickly, *O* denotes the clutch hold its position, *PS* denotes the clutch engage slowly, *PM* denotes the clutch engage in a middle speed, *PB* denotes the clutch engage quickly.

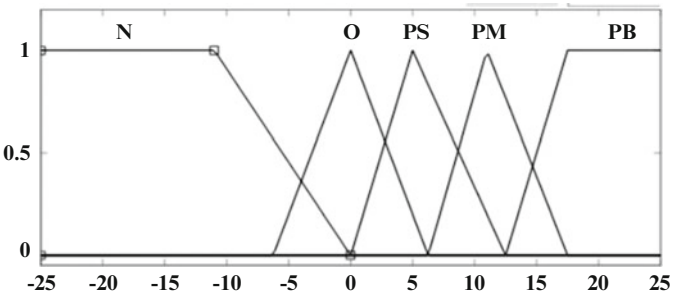

Fig. 5 Membership function for PWM signals of the automatic clutch actuate motor

Table 1 Fuzzy control rules of automatic clutch engagement speed

	CE						
CEC	NB	NM	NS	O	PS	PM	PB
NB	N	O	PS	PS	PS	O	N
NM	O	PS	PS	PM	PS	PS	O
NS	PM	PM	PB	PB	PB	PM	PM
O	PM	PM	PB	PB	PB	PM	PM
PS	PM	PM	PB	PB	PB	PM	PM
PM	O	PS	PS	PM	PS	PS	O
PB	N	O	PS	PS	PS	O	N

Clear for the output of the fuzzy controller is using by methods of weighted averages [9]:

$$\alpha_E = \frac{\sum_{i=1}^{n} \varepsilon_i \prod_{j=1}^{m} \mu_{ij}(\alpha_E)}{\sum_{i=1}^{n} \prod_{j=1}^{m} \mu_{ij}(\alpha_E)} \tag{1}$$

where $\boldsymbol{n}$ stand for rules number; $\boldsymbol{m}$ stand for input variables number, $\boldsymbol{\varepsilon_i}$ stand for weighted average vector of the membership function for $\boldsymbol{\alpha_E}$, $\boldsymbol{\mu_{ij}}$ stand for the membership function for ***CE*** and ***CEC***.

Output surface characteristics were shown in Fig. 6, it's clear to observe the nonlinear characteristic of control for automatic clutch.

5 Model Simulation and Results Analysis

Automatic clutch fuzzy control this paper presented and the traction motor speed control [10] could be combined to simulate based on shifting evaluation indexes of AMT with automatic clutch. Based on vehicle driveline dynamic and clutch characteristic, system simulation model was created by using MATLAB/Simulink software. The model is consists of motor, clutch, transmission, vehicle longitudinal

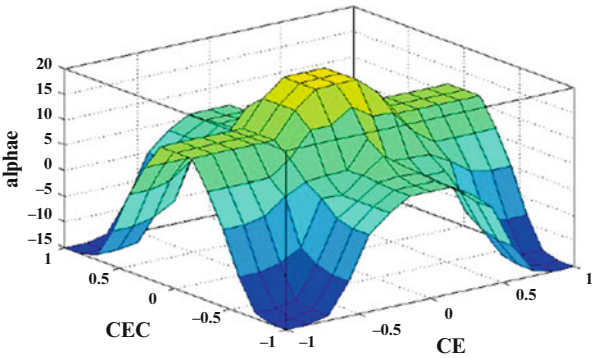

Fig. 6 Inferred surface for the fuzzy control rules

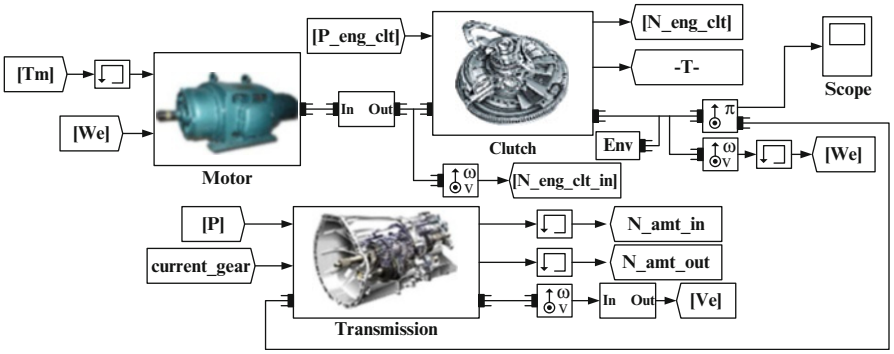

Fig. 7 System simulation models

dynamics and controller, as shown in Fig. 7. The simulation was based on up-shift process.

During the up-shift process, clutch disengaged at first, due to the speed weren't equal before the synchronization of the clutch driving and driven discs, the friction work increased nonlinearly with time, it grown to maximum when the two discs synchronized, and no longer changed after the synchronization due to the friction work no longer existed, as shown in Fig. 8a.

The maximum degree of shock was 7.23 m/s^3 which reasonable and less than the recommendation [11]. In the moment of clutch driving and driven discs engaged, the degree of shock was much more than others due to the torque delivered by the clutch changed suddenly at the two moments, as shown in Fig. 8b.

As shown in Fig. 9a, clutch driving and driven discs hadn't engaged at the complete disengagement stage, their speeds' difference was too little to consider them worked at a constant speed by controlling the traction motor speed. At clutch sliding stage, the two clutch discs just came into contact with each other. While the engagement went on, the clutch driven disc's speed began to rise, and the driving disc's speed began to decline, until the driving and driven discs' speeds synchronized. At complete engagement stage, clutch engaged quickly, the driving and driven discs' speeds rose synchronously.

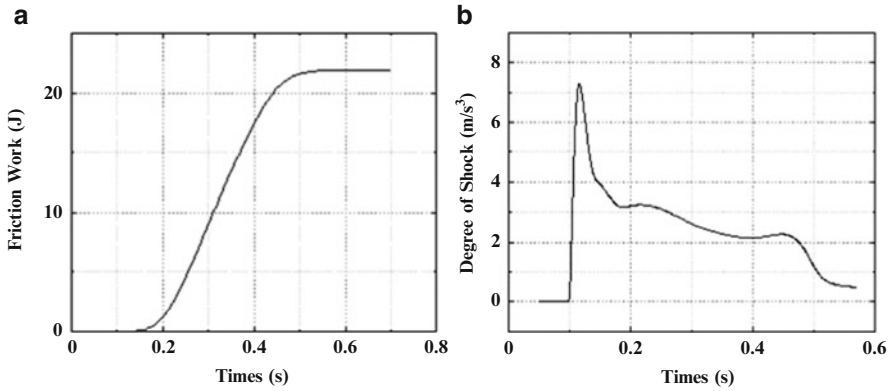

Fig. 8 (**a**) Friction work changes (**b**) Degree of shock changes

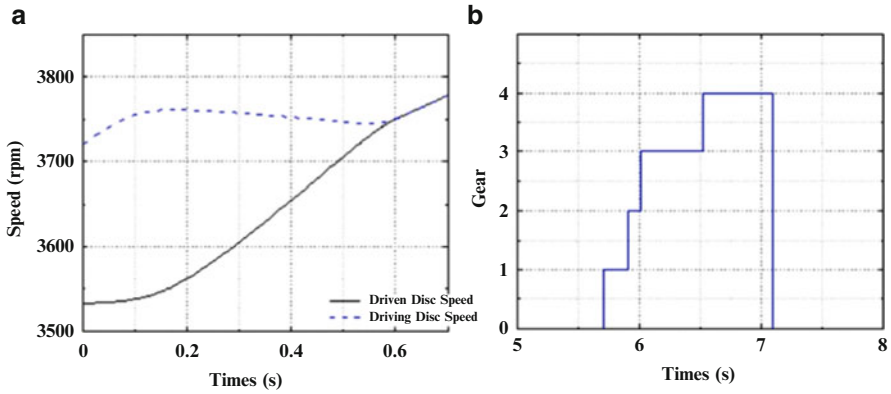

Fig. 9 (**a**) Driving and driven discs speeds changes (**b**) Shifting time distribution

AMT up-shift process gone though several stage such as clutch disengage, pick-up shift, select shift, up-shift and clutch engage. Figure 9b is the shifting time distribution, it was essential to see the shift time concentrated in up-shift stage and clutch engage stage. The total clutch work time was 0.8 s and less than the recommendation [11].

6 Conclusion

The up-shifting simulation and analysis could prove the automatic clutch fuzzy control strategy presented this paper was practicable and possible. It could realize the "quick-slow-quick" engagement schedule at clutch sliding stage. The degree of

shock and friction work had been controlled effectively. The strategy simulated the experienced manual clutch with greatest degree. This fuzzy control strategy may apply in electric drive clutch system.

References

1. Cheng Z, Cheng L, Fengchun S (2008) Dynamic modeling and analysis of AMT shifting process for EV-BUS. IEEE vehicle power and propulsion conference, Published by IEEE pp 1203–1205
2. Mashadi B, Emadi SAM (2010) Dual-mode power-split transmission for hybrid electric vehicles. IEEE Trans Veh Technol, Published by IEEE 59(7): 3223–3232
3. Nakamura T, Saga N, Nakazawa M (2002) Impedance control of a single shaft-type clutch using homogeneous electrorheological fluid. J Intell Mater Syst Struct 13(7–8):465–469
4. Chen YQ, Wong PK, Xie ZC, Wu HW, Chan KU, Huang JL (2012) Modelling of a novel dual-belt continuously variable transmission for automobiles. World Acad Sci Eng Technol 70:1157–1161
5. Liu Jinlong (2005) Simulation study on dynamic characteristic of AMT electromechanic clutch actor. Unpublished M.E. dissertation, Jilin University, Jilin University Press, Changchun(In Chinese)
6. Moon SE, Kim MS, Yeo H, Kim HS, Hwang SH, Song HL, Han KS (2004) Design and implementation of clutch-by-wire system for automated manual transmissions. Int J Veh Des 35(1):83–100
7. Gu Yanchun (2006) Gear shift schedule and gearshift control for AMT in hybrid electric vehicle. Unpublished M.E. dissertation, Shanghai Jiao Tong University, Shanghai Jiao Tong University Press, Shanghai(In Chinese)
8. Wong Pak-kin, Xie Zhengchao, Wong Hang-cheong, Huang Xinzheng (2011) Design of a fuzzy preview active suspension system for automobiles. In: Proceedings of 2011 international conference on system science and engineering (ICSSE 2011), Published by IEEE pp 525–529
9. Zhao Yongsheng, Ren weiqun, Zhang Yunqin, Chen Liping (2007) Region-wise linear fuzzy sliding mode controller for the automated clutch of AMT vehicle. Trans Chin Soc Agric Mach 38(1):17–21 (In Chinese)
10. Zhang Lingling (2012) Study on AMT shifting process control strategy for pure electric vehicles. Unpublished M.E. dissertation, Beijing Institute of Technology, Beijing Institute of Technology Press, Beijing(In Chinese)
11. Guo Lishu (2003) AMT shift process control. Trans Chin Soc Agric Mach 34(2):1–10 (In Chinese)

Application of Twin Support Vector Machine for Fault Diagnosis of Rolling Bearing

Zhongjie Shen, Ningping Yao, Hongbo Dong, and Yafeng Yao

Abstract The number of fault samples is only the small portion in the whole sample set. How to diagnose the rolling bearing fault accurately becomes a challenge in the unbalance sample set. Twin Support Vector machine (TWSVM) is applied into the bearing fault diagnosis in the study. It aims at generating two nonparallel planes in which each plane is closer to one of the two classes and is as far as possible from the other. The fault diagnosis experiments verify that TWSVM has higher accuracy and faster speed than Support Vector Machine, and identify the bearing fault well.

Keywords Fault diagnosis • TWSVM • Nonparallel plane • Rolling bearing

1 Introduction

Rolling bearing is one of the most precise components in rotating machine. It not only transmits the motion but also supports the load. The operation condition of the rolling bearing directly affects the whole performance of the equipment. An unexpected fault of bearing may cause huge economic losses, even personal injury [1]. Thereby it is necessary to detect faults of rolling bearing effectively as early as possible.

There are insufficient of the typical fault samples that may result in the low diagnosis accuracy. The fault diagnosis with limited samples has become a problem of industry. Support vector machine (SVM) proposed by Vapnik is an efficient classification method for small samples [2]. Aiming at the binary classification, SVM constructs a hyperplane and two parallel planes to separate the two types of samples with the maximum margin. The hyperplane classification principle makes

Z. Shen • N. Yao • H. Dong (✉) • Y. Yao
Xi'an Research Institute of China Coal Technology & Engineering Group, Xi'an, China
e-mail: donghongbo@cctegxian.com

W. Wang (ed.), *Mechatronics and Automatic Control Systems*, Lecture Notes in Electrical Engineering 237, DOI 10.1007/978-3-319-01273-5_17,

SVM remarkable in the equivalence or approximate equivalence data classification [3]. However, the fault diagnosis of rolling bearing is usually the unbalanced data classification in which the fault samples are the small portion of the whole sample set. And we need to discriminate the fault samples accurately from a large number of unknown state samples. The difficulty of the unbalanced data classification is that the fault samples are not able to reflect the sample distribution of the whole sample set. In SVM classification with the unbalanced data, the whole classification accuracy may be high but the recognition accuracy of fault samples may be low. SVM have some difficulties in the unbalanced data classification.

How to diagnose the rolling bearing fault well becomes a challenge in the unbalance sample set. Twin support vector machine (TWSVM) proposed by Jayadeva et al. can deal with the unbalanced data classification well [4]. Unlike SVM, it aim at generating two nonparallel planes such that each plane is closer to one of the two classes and is as far as possible from the other. TWSVM is not affected by the sample proportion. Moreover, TWSVM works faster than SVM in that TWSVM solves two smaller quadratic programming problems instead of solving larger one as in a classical SVM. We applied TWSVM into the fault diagnosis of rolling bearing in the study.

Now, the research of TSVM mainly concentrates in the improved algorithm and the computer simulation [5, 6], and there are few applications of TWSVM for the other fields. Thereby it is an application innovation to diagnose the bearing faults using TWSVM. TWSVM may identify the fault samples well from large number of unknown state samples.

2 Twin Support Vector Machine

2.1 Support Vector Machine

Given a sample set $S = \{\boldsymbol{X}_i, \boldsymbol{Y}_i\}_{i=1}^{l}$, where $\boldsymbol{X}_i \in \Re^n$, and corresponding binary class labels $\boldsymbol{Y}_i \in \{-1, +1\}$, where $\boldsymbol{X}$, $\boldsymbol{Y}$ are the matrixes. An optimal separating hyperplane is computed in the feature space to construct SVM which classifies training samples correctly or basically correctly. The SVM find the optimal separating hyperplane by resolving the following optimization problem,

$$\begin{aligned} \min \quad & \frac{1}{2}\|\boldsymbol{w}\|_2^2 + C\mathbf{e}^T\boldsymbol{\xi} \\ \text{s.t.} \quad & \begin{cases} \boldsymbol{Y}(\boldsymbol{w}\cdot\boldsymbol{X} + \boldsymbol{e}b) \geq \boldsymbol{e} - \boldsymbol{\xi} \\ C \geq 0, \qquad\qquad \boldsymbol{\xi} \geq 0 \end{cases} \end{aligned} \tag{1}$$

where $\|\|_2$ denotes the L_2-norm, C is a penalty constant, $\boldsymbol{\xi}$ is a slack variable, b is a threshold and $\boldsymbol{e}$ is a vector of one of l dimensions. The dual quadratic programming problem of the problem (1) is

$$\begin{aligned} &\max \quad \boldsymbol{e}^T\boldsymbol{\alpha} - \frac{1}{2}\boldsymbol{\alpha}^T\boldsymbol{Y}\boldsymbol{X}\boldsymbol{X}^T\boldsymbol{Y}\boldsymbol{\alpha} \\ &\text{s.t.} \quad \begin{cases} \boldsymbol{e}^T\boldsymbol{Y}\boldsymbol{\alpha} = 0 \\ \boldsymbol{0} \le \boldsymbol{\alpha} \le C\boldsymbol{e} \end{cases} \end{aligned} \tag{2}$$

where $\boldsymbol{\alpha} = (\alpha_1, \alpha_2, \ldots, \alpha_l)^T$ is the Lagrangian vector. In the decision phase, SVM predicts the labels of the testing samples according to the optimal separating hyperplane. The decision function is given by

$$f(x) = \text{sign}(\boldsymbol{w} \cdot \boldsymbol{x} + b) \tag{3}$$

2.2 Twin Support Vector Machine

In TWSVM, the training samples with the positive labels, $\boldsymbol{X}_+$, construct the matrix $\boldsymbol{A}$ while the training samples with the negative labels, $\boldsymbol{X}_-$, construct the matrix $\boldsymbol{B}$. The TWSVM classifier is obtained by solving the following pair of quadratic programming problems

$$\begin{aligned} &(\text{TWSVM1}) \min_{\boldsymbol{w}_1, b_1, \boldsymbol{\xi}} \frac{1}{2}\|\boldsymbol{A}\boldsymbol{w}_1 + \boldsymbol{e}_1 b_1\|_2^2 + C_1 \boldsymbol{e}_2^{\mathrm{T}}\boldsymbol{\xi} \\ &\qquad \text{s.t.} \quad -(\boldsymbol{B}\boldsymbol{w}_1 + \boldsymbol{e}_2 b_1) + \boldsymbol{\xi} \ge \boldsymbol{e}_2, \boldsymbol{\xi} \ge 0 \\ &(\text{TWSVM2}) \min_{\boldsymbol{w}_2, b_2, \boldsymbol{\eta}} \frac{1}{2}\|\boldsymbol{B}\boldsymbol{w}_2 + \boldsymbol{e}_2 b_2\|_2^2 + C_2 \boldsymbol{e}_1^{\mathrm{T}}\boldsymbol{\eta} \\ &\qquad \text{s.t.} \quad (\boldsymbol{A}\boldsymbol{w}_2 + \boldsymbol{e}_1 b_2) + \boldsymbol{\eta} \ge \boldsymbol{e}_1, \boldsymbol{\eta} \ge 0 \end{aligned} \tag{4}$$

where C_1, C_2 are the penalty constants, $\boldsymbol{\xi}$, $\boldsymbol{\eta}$ are the slack variables, b_1, b_2 are the thresholds, $\boldsymbol{e}_1$ is a vector of one of l_+ dimensions and $\boldsymbol{e}_2$ is a vector of one of l_- dimensions.

Using the K.K.T. conditions, we obtain the dual quadratic programming problem of TWSVM1 as follows:

$$\begin{aligned} &(\text{DTWSVM1}) \max_{\alpha} \ \boldsymbol{e}_2^{\mathrm{T}}\boldsymbol{\alpha} - \frac{1}{2}\boldsymbol{\alpha}^{\mathrm{T}}\boldsymbol{G}\left(\boldsymbol{H}^{\mathrm{T}}\boldsymbol{H}\right)^{-1}\boldsymbol{G}^{\mathrm{T}}\boldsymbol{\alpha} \\ &\qquad \text{s.t. } 0 \le \boldsymbol{\alpha} \le C_1 \end{aligned} \tag{5}$$

where $\boldsymbol{H} = [\boldsymbol{A} \quad \boldsymbol{e}_1], \boldsymbol{G} = [\boldsymbol{B} \quad \boldsymbol{e}_2]$. Similarly, we consider TWSVM2 and obtain its dual as

$$\begin{aligned} &(\text{DTWSVM2}) \max_{\alpha} \ \boldsymbol{e}_1^{\mathrm{T}}\boldsymbol{\gamma} - \frac{1}{2}\boldsymbol{\gamma}^{\mathrm{T}}\boldsymbol{H}\left(\boldsymbol{G}^{\mathrm{T}}\boldsymbol{G}\right)^{-1}\boldsymbol{H}^{\mathrm{T}}\boldsymbol{\gamma} \\ &\qquad \text{s.t. } 0 \le \boldsymbol{\gamma} \le C_2 \end{aligned} \tag{6}$$

Finally, the decision function is given by

$$f(\boldsymbol{x}) = \boldsymbol{x}^{\mathrm{T}}\boldsymbol{w} + b = \min_{l=1,2} \left| \boldsymbol{x}^{\mathrm{T}}\boldsymbol{w}_l + b_l \right| \tag{7}$$

where $||$ is the perpendicular distance of point x from the plane $x^T w^{(k)} + b^{(k)} = 0$, $k = 1, 2$.

3 Experiment Verifications

3.1 Bearing Fault Diagnosis Experiment

The bearing fault diagnosis experiments were performed to validate the effectiveness of TWSVM. The experimental data were downloaded from Prognostics Center of Excellence (PCoE) through prognostic data repository contributed by Intelligent Maintenance System (IMS), University of Cincinnati [7]. The bearing test rig contains four bearings on one shaft as described in Fig. 1. The rotation speed is kept constant at 2,000 r/min and a radial load of 26.67 kN was placed onto each bearing. All the bearings were force lubricated. The testing bearing is Rexnord ZA-2115 double row bearing with 16 rollers in each row. It has a pitch diameter of 71.5 mm, a roller diameter of 8.4 mm and a tapered contact angle of 15.17°. The vibration signals are acquired with a sampling frequency of 20 kHz per channel by a National Instruments DAQCard-6062E data acquisition card. The data recorder is equipped with low-pass filters at the input stage for anti-aliasing. Each sample with 20,480 points data is collected every 20 min. The acceleration sensor is the PCB 353B33 High Sensitivity ICP accelerometer and installed on the bearing housing.

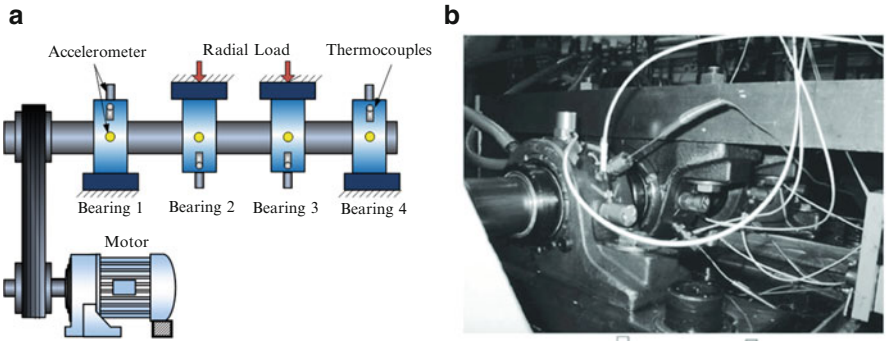

Fig. 1 Bearing test rig (**a**) Integrated framework (**b**) Sensors installation

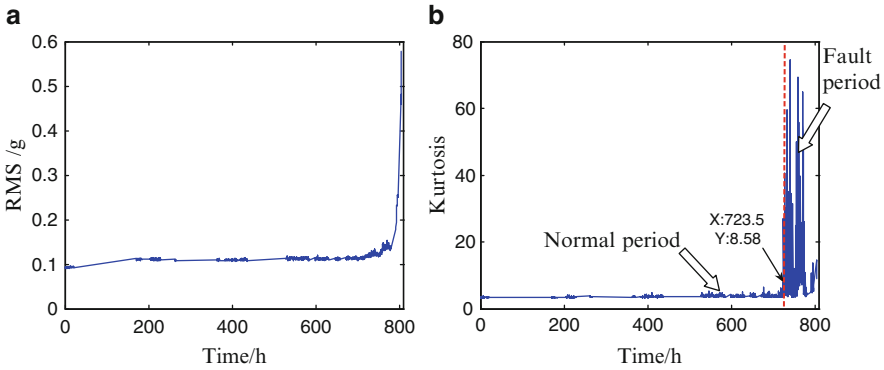

Fig. 2 Time statistics feature (**a**) RMS (**b**) Kurtosis

Table 1 Comparison of the bearing fault diagnosis in SVM and TWSVM

	Accuracy (%)		Time(s)	
Sample number	SVM	TWSVM	SVM	TWSVM
$n = 20; f = 20$	87.5	100	0.4840	0.1664
$n = 100; f = 100$	85.5	99.5	0.6568	0.1708
$n = 20; f = 100$	81.33	100	0.5904	0.1687
$n = 50; f = 100$	82.67	99.33	0.6287	0.1695
$n = 200; f = 100$	87.67	97.0	0.7355	0.2365
$n = 500; f = 100$	91.83	93.83	0.9074	0.2975

3.2 Experimental Results Analysis

Test 1 includes four bearings in the collected vibration data [8]. Bearing three of test 1 finally fails with the serious inner-race fault. The time-domain features, namely Root Mean Square (RMS) and Kurtosis, are calculated as shown in Fig. 2. Kurtosis shows that the initial defect occurs at 723.5 h. The bearing is normally working before the moment while it enters into the fault state after 723.5 h. The bearing life is divided into two parts by the red dotted line in Fig. 2: normal period and fault period [9]. We choose 20 normal training samples from 605.2 to ~608.6 h and 20 fault training samples from 748.3 to ~753.6 h. The normal training samples and the fault training samples construct the training sample set. Then 500 normal testing samples are selected from 608.6 to ~719.3 h while 100 fault testing samples are chose from 731.5 to ~748.3 h. The testing sample set is made up of normal testing samples and fault testing samples. What's more, the training samples are at both ends and the testing samples are in the middle, which increased the difficulty of the classification. The diagnosis difficulty is rising as the number of the testing samples increases. A comparison of SVM and TWSVM is performed with the equal proportion testing sample set, the fault samples dominant testing sample set and the normal samples dominant testing sample set, as described in Tables 1 and 2, in which 'n' and 'f' represent the number of normal samples and fault samples.

Table 2 Comparison of the bearing fault diagnosis with normal samples and fault samples

	Accuracy of normal samples (%)		Accuracy of fault samples (%)	
Sample number	SVM	TWSVM	SVM	TWSVM
$n = 20; f = 20$	100	100	75.0	100
$n = 100; f = 100$	98.0	99.0	73.0	100
$n = 20; f = 100$	98.0	100	78.0	100
$n = 50; f = 100$	96.0	98.0	76.0	100
$n = 200; f = 100$	95.5	95.5	72.0	100
$n = 500; f = 100$	96.6	92.6	68.0	100

First of all, the equal proportion testing sample set is inputted into SVM and TWSVM for classification. The diagnosis accuracies of SVM are 87.5 %, 85.5 % while those of TWSVM are 100 %, 99.5 % when 'n = 20, f = 20' and 'n = 100, f = 100'. The calculation times of SVM are 0.4840 s, 0.6568 s while those of TWSVM are 0.1664 and 0.1708 s. TWSVM has higher diagnosis accuracy and faster computing speed than SVM. What's more, Table 2 shows that the accuracy of normal samples precedes that of fault samples in SVM and TWSVM has the approximate diagnosis results for the normal samples and the fault samples.

Secondly, the fault samples dominant testing sample set is used to examine the performance of the two classifiers in the unbalance samples classification. The classification results of SVM and TWSVM with 'n = 20, f = 100' and 'n = 50, f = 100' are described in Tables 1 and 2. TWSVM gains the higher diagnosis accuracy and the faster computing speed again. The diagnosis accuracy of normal samples decreases but that of fault samples increases in SVM as compared with the equal proportion testing sample set. The diagnosis accuracy of TWSVM changes subtly, especially the fault samples. The change means that SVM may be biased towards the majority class.

Finally, we use SVM and TWSVM to diagnose the normal samples dominant testing sample set which is common in industry. The diagnosis demand discriminates the fault well and reduces the missing report rate. From Table 1, the diagnosis accuracy of SVM increases with the more normal samples, but its accuracy of fault samples decreases. It may lead to the serious consequences with big missing report rate. Meanwhile, TWSVM has the high diagnosis accuracy for the fault samples though its accuracy of all samples decreases. TWSVM is able to diagnose the bearing fault well, even if the fault samples are insufficient.

Above all, the diagnosis accuracy of TWSVM is not affected by the sample proportion. TWSVM can diagnose the bearing fault accurately, no matter what proportion of the sample set.

4 Conclusion

In the study, Twin Support Vector Machine is applied into the fault diagnosis of the rolling bearing. Unlike SVM, it aims at generating two nonparallel planes in which each plane is closer to one of the two classes and is as far as possible from the other.

TWSVM has higher accuracy and faster speed than SVM, especially in the unbalance samples classification. The fault diagnosis experiments verify that TWSVM diagnoses the bearing fault well and is not affected by the proportion of the sample set.

Acknowledgements This work is supported by the Youth Foundation of Xi'an Research Institute of China Coal Technology & Engineering Group (No. 2011XAYQN007).

References

1. Lei YG, He ZJ, Zi YY (2011) EEMD method and WNN for fault diagnosis of locomotive roller bearings. Expert Syst Appl 38(6):7334–7341
2. Vapnik VN (1998) Statistical learning theory. Wiley, New York, pp 1–740
3. Peng XJ (2011) TPMSVM: a novel twin parametric-margin support vector machine for pattern recognition. Pattern Recognit 44:2678–2692
4. Jayadeva KR, Chandra S (2007) Twin support vector machines for pattern classification. IEEE Trans Pattern Anal Mach Intell 29(5):905–910
5. Singh M, Chadha J, Ahuja P, Jayadeva CS (2011) Reduced twin support vector regression. Neurocomputing 74:1474–1477
6. Zhong P, Xu YT, Zhao YH (2012) Training twin support vector regression via linear programming. Neural Comput Appl 21(2):399–407
7. Lee J, Qiu H, Yu G, Lin J (2007) Rexnord Technical Services, 'Bearing Data Set', IMS, University of Cincinnati, NASA Ames Prognostics Data Repository, http://ti.arc.nasa.gov/project/prognostics-data-repository, NASA Ames, Moffett Field
8. Qiu H, Lee J, Lin J, Yu G (2006) Wavelet filter-based weak signature detection method and its application on rolling element bearing prognostics. J Sound Vib 289:1066–1090
9. Caesarendra W, Widodo A, Yang BS (2010) Application of relevance vector machine and logistic regression for machine degradation assessment. Mech Syst Signal Process 24:1161–1171

Mid-term Load Forecasting Based on Modified Grey Model

Haijiang Wang and Shanlin Yang

Abstract The construction of smart grid put forward higher requirements on deployment accuracy of the energy. Power generation and electricity sectors have carried out more accurate data analysis and forecasting. In this context, we provide a Gauss-Chebyshev GM(1,1) model, This model could overcome the lack of traditional grey model and made accurate forecasting of electricity consumption in smart grid, Finally, numerical examples demonstrate that this method can efficiently improve the prediction accuracy.

Keywords Smart grid • Load forecasting • GM (1,1) model

1 Introduction

The short-term electricity load is the focus of the competitive electricity market. How to make an accurate prediction of electricity load is the crucial task for all participants in market. Electricity load varies a lot, and peaks appear frequently. Electricity load forecasting, according to the length of time, can be divided into the long-term forecasting and short-term forecasting. Medium-and-long term forecast is used to predict the annual and monthly electricity load. While short-term electricity load forecast includes daily load forecasting and hourly load forecasting.

H. Wang (✉)
Key Lab of Process Optimization and Intelligent Decision-making,
Hefei University of Technology, Hefei, China
e-mail: tonysun800@sina.com

S. Yang
School of Management, Hefei University of Technology, Hefei, China
e-mail: hgdysl@gmail.com

W. Wang (ed.), *Mechatronics and Automatic Control Systems*, Lecture Notes in Electrical Engineering 237, DOI 10.1007/978-3-319-01273-5_18,

Data prediction ability determines the quality of smart grid. As for electricity consumption, low prediction will cause power cut due to lack of allocated electricity, while high prediction will bring unnecessary generation cost and energy waste. Therefore, it is essential to predict the electricity consumption accurately. One of the commonest electricity consumption prediction models is grey model- GM (1, 1) [1]. GM (1, 1) model can play a greater role in data forecast of electrical grid. By use of its theory, prediction data accuracy can be improved to meet the requirement for data with high quality in smart grid.

After 20 years of development, grey system theory has been widely applied in many areas, including social science and economics. Deng [1]created the grey sys-tem theory and system described the principle of grey system, the applications of grey system in many different fields, such as science and economy; Wang et al. [2] used cubic spline formula to improve the background value, and constructed a novel grey forecasting model, they used this new model to forecast electricity consumption and obtained high predict accuracy; Hsu and Wang [3, 4] applied the grey prediction model to the global integrated circuit industry and obtained a good prediction effect; Shen, Chung and Chen [5] introduced a novel application of grey system theory to information security, expanded the application field of grey system; Chang and Tsai [6] used neural network adaptation to support vector regression grey model, obtained effect forecasting results, the grey system and artificial intelligence method are combined well; Chen [7] combined the grey system with Bernoulli model, constructed a new grey forecasting model NGBM (1,1), use this NGBM(1,1) model to forecast the foreign exchange rates of Taiwan's major trading partners, and receive good effect; Huang [8] use a hybrid grey model to forecast the stock market also achieved good results. But the GM (1, 1) model is ineffective in predicting non-stationary time series, however, mainly because the sequence computed by the GM (1, 1) model is monotonic and be-cause the inverted sequence is also monotonic. Based on these previous studies, this paper aims to find the appropriate treatment to turn a non-stationary sequence into a sequence suitable for the GM (1, 1) model and then to create the GM (1, 1) model to improve modelling and prediction accuracy.

These methods can improve prediction accuracy indeed, but in order to place undue emphasis on accuracy, these methods also add nodes, which lead a vibration-Runge phenomenon that causes decrease in model applicability or even make the model cannot be used.

Based on literature mentioned above, this paper first proposes combination interpolation method combining piecewise linear interpolation with Lagrange interpolation, and constructs interpolation function $P(t)$ on condition of convergence as the background value in the new state, which is approximate to the background value $z^{(1)}(k+1)$ in the interval $[k, k+1]$. Compared with previous interpolation methods, this method is high in algebraic precision and has small error. In addition, it overcomes the problems in single interpolation methods, avoids distortion, improves theory depth of the model and increases stability in application. It is of simple calculation and easy to program and is beneficial to promote the prediction technology in smart grid.

2 Modeling Idea of Conventional GM (1, 1) Model

First, we introduce the modeling mechanism of traditional GM (1, 1) model.

Let $X^{(0)} = \{x^{(0)}(1), x^{(0)}(2), \cdots, x^{(0)}(n)\}$ be the original series. Make one-accumulation:

$$X^{(1)} = \{x^{(1)}(1), x^{(1)}(2), \cdots, x^{(1)}(n)\}$$

where $X^{(1)}(k) = \sum_{i=1}^{k} x^{(0)}(i)$ $(k = 1, 2, \cdots, n)$, $X^{(1)}(k)$ is the one-accumulation series of $X^{(0)}(k)$, denoted as $1 - AGO.x^{(1)}$ satisfies the following grey differential equation

$$\frac{dx^{(1)}}{dt} + ax^{(1)} = b \tag{1}$$

where a, b are parameters. a is developing coefficient, and b is grey input.

In order to estimate a, b, discretely process Eq. 1, we have:

$$\Delta\left(x^{(1)}(k+1) + aX^{(1)}(k+1)\right) = b \; k = 1, 2, \cdots, n-1 \tag{2}$$

where $\Delta(x^{(1)}(k+1))$ is inverse accumulated generated on $(k+1)th$ and

$$\Delta\left(x^{(1)}(k+1)\right) = x^{(1)}(k+1) - x^{(1)}(k) = x^{(0)}(k+1) \tag{3}$$

In grey prediction, $x^{(1)}(k+1)$ in Eq. 2 is the background value of $dx^{(1)}/dt$ on $(k+1)th$, generally,

$$z^{(1)}(k+1) = \frac{1}{2}[x^{(1)}(k) + x^{(1)}(k+1)], (k = 1, 2, \cdots, n-1) \tag{4}$$

Induce Eqs. 3 and 4 into the following equations and get:

$$\begin{cases} z^{(1)}(2) = a\left[-\frac{1}{2}\left(x^{(1)}(1) + x^{(1)}(2)\right)\right] + b \\ z^{(1)}(3) = a\left[-\frac{1}{2}\left(x^{(1)}(2) + x^{(1)}(3)\right)\right] + b \\ \qquad\qquad \vdots \\ z^{(1)}(n) = a\left[-\frac{1}{2}\left(x^{(1)}(n-1) + x^{(1)}(n)\right)\right] + b \end{cases} \tag{5}$$

$$B = \begin{bmatrix} -z^{(1)}(2) & 1 \\ -z^{(1)}(3) & 1 \\ \vdots & \vdots \\ -z^{(1)}(n) & 1 \end{bmatrix},$$

$$Y_n = [x^{(0)}(2), x^{(0)}(3), \cdots, x^{(0)}(n)]^T, \boldsymbol{\alpha} = (a, b)^T$$

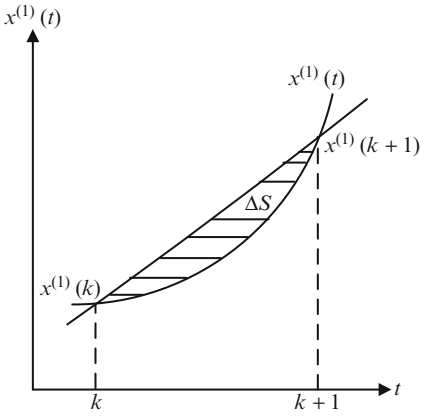

Fig. 1 Prediction deviation of GM (1, 1)

Then Eq. 5 can be simplified as the linear model $Y = B\boldsymbol{\alpha}$. Using least square estimation approach, we have

$$\boldsymbol{\alpha} = \left(B^T B\right)^{-1} B^T Y \tag{6}$$

Induce Eq. 6 into Eq. 1, we obtain the discrete solution:

$$\hat{x}^{(1)}(k+1) = \left(x^{(0)}(1) - \frac{b}{a}\right) \cdot e^{-ak} + \frac{b}{a} \tag{7}$$

Then, we get the prediction series:

$$\hat{x}^{(0)}(k+1) = \hat{x}^{(1)}(k+1) - \hat{x}^{(1)}(k) = (1 - e^{a})\left(x^{(0)}(1) - \frac{b}{a}\right) \cdot e^{-ak} \tag{8}$$

and $k = 1, 2, \cdots, n$.

From Eq. 4, we know the exploit trapezoid area is

$$S(k \cdot x^{(1)}(k) \cdot x^{(1)}(k+1) \cdot (k+1))$$

When we replace the area by curve $x^{(1)}(t)$, we find the conventional GM model has some defects. As shown in Fig. 1, with the index growing, data sequence changes intensify and the prediction deviation will be enlarged (ΔS), that affect the suitability of the model to some extent.

To overcome this deficiency, We use Gauss-Chebyshev formula to reconstruct the background value.

Firstly, we change the form of whiten differentiation Eq. 1.

Do the integral operation on both sides of Eq. 1 in the interval [k,k + 1], we obtain:

$$\int_k^{k+1} \frac{dx^{(1)}}{dt} dt + a \int_k^{k+1} x^{(1)} dt = b$$

That is

$$x^{(1)}(k+1) - x^{(1)}(k) + a \int_k^{k+1} x^{(1)} dt = b.$$

Namely,

$$x^{(1)}(k+1) + a \int_k^{k+1} x^{(1)} dt = b \tag{9}$$

From Eq. 2 we know, the background value is

$$z^{(1)}(k+1) = \int_k^{k+1} x^{(1)} dt \tag{10}$$

3 Data Simulation and Accuracy Comparison

Now using the residual GM(1,1) model forecasting the electricity consumption and C# program to realize the forecast data. Next, we also apply the traditional GM(1,1) model for comparison purposes. First, we give the trends of original data in Fig. 2. Secondly, the comparison results are show in Table 1 and Fig. 3.

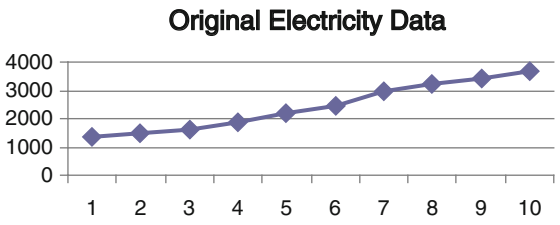

Fig. 2 Trends of original electricity load data

Table 1 Prediction and relative error comparison

Original data	Research model	RE (%)	Traditional GM model	RE (%)
1,346.62	1,283.549	4.68	1,435.28	6.58
1,468.25	1,404.6689	4.33	1,553.87	5.83
1,638.62	1,560.8704	4.74	1,740.65	6.22
1,889.12	1,877.8124	0.59	1,949.87	3.21
2,176.13	2,263.1869	4.00	2,184.24	0.37
2,468.85	2,660.8946	7.77	2,446.78	0.89
2,936.82	3,072.6476	4.62	2,740.87	6.67
3,245.84	3,192.2110	1.65	3,070.32	5.40
3,426.85	3,247.8194	5.22	3,439.37	0.36
3,659.53	3,611.2760	1.31	3,852.77	5.28

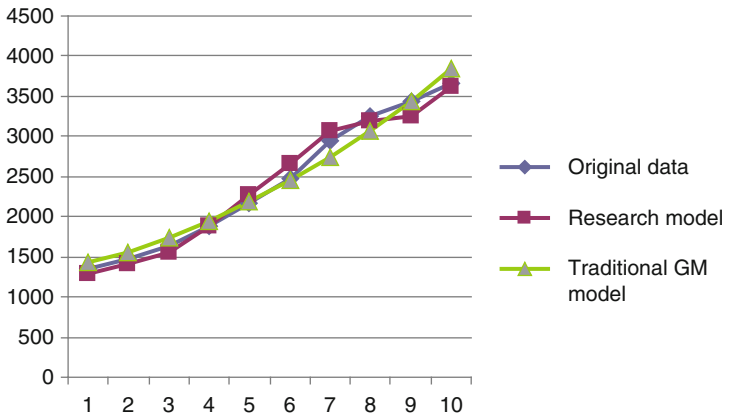

Fig. 3 Comparison chart of prediction accuracy

4 Conclusion and Future Work

This paper introduced a residual GM(1,1) model to forecast the electricity load. Simulation example shows that the residual GM(1,1) model can more accurately make prediction than the traditional GM(1,1) method. The result showed that the proposed method can be effective for electricity load forecasting in smart grid.

Acknowledgements This research was partially supported by National Natural Science Foundation of China, grant No.71101041, National 863 Project, grant No. 2011AA05A116, Foundation of Higher School Outstanding Talents Grant No. 2012SQRL009 and National Innovative Experiment Program No.111035954.

References

1. Deng Julong (1985) Gray system: social and economics. National Defence Industry Press, Beijing, pp 24–76
2. Wang Xiaojia, Yang Shanlin, Wang Haijiang et al (2010) Dynamic GM(1,1) model based on cubic spline for electricity consumption prediction in smart grid. China Commun 7(4):83–88
3. Hsu LiChang (2003) Applying the gray prediction model to the global integrated circuit industry. Technol Forecast Soc Change 70(6):563–574
4. Hsu Lichang, Wang Chaohung (2009) Forecasting integrated circuit output using multivariate gray model and gray relational analysis. Expert Syst Appl 36(5):1403–1409
5. Victor.R.L. Shen, Chung Yufang, Chen Teshong (2009) A novel application of gray system theory to information security(Part I). Comp Stand Interface 31(1):277–281
6. Chang Baorong, Hsiu Fen Tsai (2008) Forecast approach using neural network adaptation to support vector regression gray model and generalized auto-regressive conditional heteroscedasticity. Expert Syst Appl 34(2):925–934
7. Chen Chun, Chen Hong Long, Chen Shuo-Pei (2008) Forecasting of foreign exchange rates of Taiwan's major trading partners by novel nonlinear gray Bernoulli model NGBM(1,1). Commun Nonlinear Sci Numer Simul 13:1194–1204
8. Huang KuangYu, Jane CJ (2009) A hybrid model for stock market forecasting and portfolio selection based on ARX, gray system and RS theories. Expert Syst Appl 36(5):5387–5392

The Application of Fuzzy Predictive Control in Lime Production

Haijian Zhuo, Jiayan Zhang, and Xugang Feng

Abstract In the process of lime production, controlling temperature of kiln is crucial to the quality and energy saving. However, as limekiln is a delayed, inertia and nonlinear object, it is hard to get a satisfied control effect via traditional control arithmetic method. Based on the mathematical model study on gas-burning lime-kiln control system, this paper brings up a fuzzy predictive controlling method, which well combines the predictive function of predictive control with the rapid reaction of fuzzy control in a big deviation range. The simulation on Matlab proves that not only the controlling effect of fuzzy predictive control is superior to fuzzy or predictive controlling method, but also the speed and constancy are improved as well.

Keywords Lime production • Limekiln • Fuzzy controlling • Burning controlling

1 Introduction

Active lime is a light burning lime with high-quality. It has small grains (0.1~3 μm), highly porosity (50 %), small volume density (1.5~1.7 g/cm^3), highly specific surface area (1.5~2.0 m^2/kg), highly active degree (300 ml) and low residual content of carbon dioxide (2 % or lower) and so on. Active lime is used to converter steelmaking. It can shorten the time, improve purity of liquid steel and its yield and reduce the consumption of lime and fluorite. Lime production is a complicated physical and chemical process, which has characteristics of large delay, large inertia and nonlinearity. Traditional controlling method is far from a satisfied

H. Zhuo (✉) • J. Zhang • X. Feng
Department of Electrical and Information Engineering, Anhui University of Technology, Maanshan, china
e-mail: jianjian1222@126.com

W. Wang (ed.), *Mechatronics and Automatic Control Systems*, Lecture Notes in Electrical Engineering 237, DOI 10.1007/978-3-319-01273-5_19,

control method. So based on the mathematical model study on gas-burning limekiln control system, this paper brings up a fuzzy predictive control method, which well combines the predictive function of predictive control with the rapid reaction of fuzzy control in a big deviation range and better solves the temperature reaction of fuzzy control in a big deviation range and better solves the temperature controlling problem of traditional method.

2 Lime Calcinations and Controlling Requirements

The new gas-burning limekiln is used to product high quality and high activity degree lime products whose main composition is calcium oxide. In this process, lime with calcium carbonate goes through heating, flaming, cooling, and other physical and chemical reactions. The whole procedures are showed in Fig. 1.

In general, limekiln is made up of kiln body, loading device, distributing gear, burning device, the dust equipment, electrical instrument device and dust removal equipment etc. Weighed in weighing hopper, lime comes to the top of kiln. And then goes through down-spouting to distributing gear, when rotating to different points, the bell opens, and the limestone begins a second cloth in kiln crown, and last gets to the body. With the stones slow down, the body can be divided into

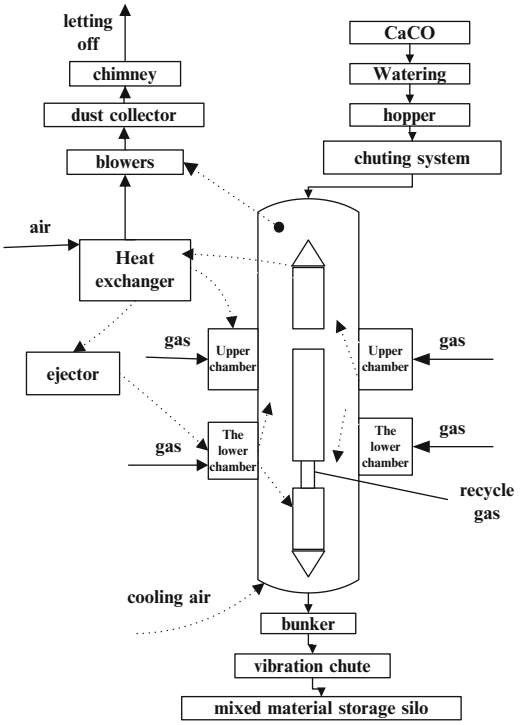

Fig. 1 Process flow diagram of producing lime

preheating zone, the upper reflux burning zone, the central reflux burning zone, and the bottom reflux burning zone. It is called preheating zone before upper reflux burning zone and cooling zone after it. The waste gas from the preheating zone converges with the waste gas from heat exchanger through circular channels. Then they formed waste gas goes through dust removal equipment to chimney with the help of pump fan.

After the analysis of lime process, its mechanism in new gas-burning limekiln, and according to operators' experience it is found that temperature has great effects on lime's quality and yield. In normal circumstances, the quantity of lime rate and the quantity of ventilation rate are relatively stable. But the mixed gas ratio of blast furnace gas, converter gas and coke oven gas is changed with time, which affects temperature in a great deal. Ventilation rate is controlled by valve, so we can take lime quantity and ventilation rate as interference factors, and keep the temperature within a prescribed scope by adjust the gas valve to control the coal gas amount, i.e. to control the temperature of kiln [1].

3 The Design of Fuzzy Predictive Control System

The temperature of limekiln is mainly influenced by the changes of wind, gas and materials. But in normal circumstances, the quantity of lime rate and the quantity of ventilation rate are relatively stable. And then the gas amount is of great influence on temperature. Fuzzy predictive control system aims to control the temperature of limekiln by changing the gas amount through burner [2].

The fuzzy predictive system mainly consists of prediction model, fuzzy control and model correction, as showed in Fig. 2.

3.1 Predicting Model

Supposing limekiln predicting model is based on step response and the vector of it is $a = [a_1, a_2, \ldots, a_N]$, N is modeling time domain. If considering the number of

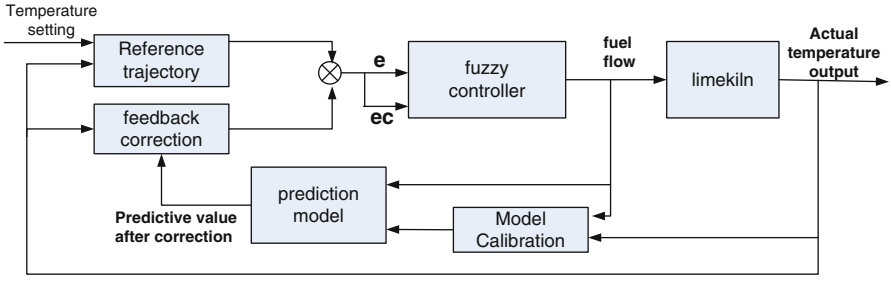

Fig. 2 Control system diagram

time domain is M at present and in the future, and under the action of $\Delta u(k),\ldots, \Delta u(k + M - 1)$ in the time domain of K, we can get the corresponding result $y_m(k) = y_0(k) + a^* \Delta u(k)$ in the future. $y_0(k)$ refers to the P times output of limekiln control system if time domain K is the predictive moment without controlling. $y_m(k)$ refers to the P times output of limekiln control system under the action of $\Delta u(k),\ldots, \Delta u(k + M - 1)$ in the time domain of K. $\Delta u(k)$ is the increment of M from now on. A is dynamic matrix, whose elements are used to describe the dynamic characteristics of limekiln step response coefficient [3].

3.2 Feedback and Correction

We can get the future output $y_m(k)$ by means of the predictive model when we put u (k) on combustion control system. But because of the model error, the nonlinear features and the uncertainty factors in the actual process, the predicative output will deviate from the practice one. So we need to use y(k + 1) to feedback and correct the output online at k + 1:

$$y_p(k) = y_m(k) + h^*[y(k+1) - y_m(k+1|k)] \tag{1}$$

$h = [h_1, h_2, \ldots, h_N]$, h is the revising vector of N. and usually makes $h_1 = 1.0$, $h_i = 0.9$, $i = 2,3,\ldots,N$. $y_p(k) = [y_p(k + 1|k),\ldots, y_p(k + N|k)]$, $y_p(k)$ is the predicative output after adjustment. And after shift, it can be taken as the initial predictable output of k + 1. The vector is $y_{p0}(k + 1) = s^* y_p(k)$. In the form, s is the shift matrix [4].

3.3 Fuzzy Control

In combustion control loop, the fuzzy controller is a control system with two-input and single-output. The input is predicting error E and predicted error variation EC, and the output is controlling increment U. It achieves continuous adjustment by using online calculating [5].

Set scope of error e as [−1 MPa, 1 MPa], and the domain of fuzzy variation e is [−8, 8], then $k_e = 8$. Set the scope of error ratio as [−0.1 MPa, 0.1 MPa], and then domain of its fuzzy variation EC is [−8, 8], $k_{ec} = 80$. The scope of controlled variable u is [−48, 48], and its fuzzy domain of U is [−8, 8], then $k_u = 6$. The subsets of E, EC and U are E,EC,U = {NB,NM,NS,ZO,PS,PM,PB}.

The shape of membership functions has a great effect on fuzzy controller's functions. The narrower the membership functions' variable scope is, the more sensitive the controller is. Conversely, the controller is not accurate. Usually when the error is tiny, membership functions can be a narrow one, and when bigger,

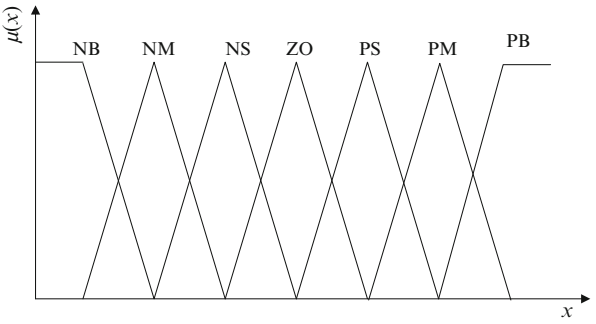

Fig. 3 Membership functions

membership functions can be a wider one. The degree of E, EC and U are upon the triangle membership functions. Membership functions are showed in Fig. 3.

The selection of control rules is a revised outcome based on the theory knowledge and the summary of operators' practice experience. The 49 rules are showed in the Table 1:

We can get the system output in the future time K, and then the predictable error p_e and the predictable error variation p_{ec} are

$$p_e = y_r(\,k + p \mid k) - y_m(\,k + p \mid k) \tag{2}$$

$$p_{ec} = y_m(\,k + p - 1 \mid k) - y_m(k + p \mid k) \tag{3}$$

Multiplied by factors K_e and K_{ec}, p_e and p_{ec} get the domain $[-8, 8]$ of E and EC, then according to the table and using Zadeh reasoning theory and weighted average fuzzy method, we can get the accurate value of variation U during $[-8, 8]$. And multiplied by Ku factors get $\Delta u(k)$. The size of K_e, K_{ec}, Ku can become the best value by manual adjustment online [6].

3.4 Model Self-Adjustment

The model self-adjustment is an online parameter adjustment mainly directed against the phase step vector of a. Having considered the N steps, step response has been closed to the steady-state value, so we can set the desirable step response as

$$\overline{a_i} = \begin{cases} a_i & i \le N \\ a_N & i > N \end{cases} \tag{4}$$

Then with any input, the output in the k moment of limekiln combustion control system is

$$y(k) = \sum_{i=1}^{\infty} \overline{a_i} \cdot \Delta u(k - i) \tag{5}$$

Table 1 Control rules

E / EC	NB	NM	NS	ZE	PS	PM	PB
NB	NB	NB	NB	NB	NM	NS	ZE
NM	NB	NB	NM	NM	NS	ZE	ZE
NS	NB	NM	NS	NS	ZE	ZE	PS
ZE	NM	NM	NS	ZE	PS	PM	PB
PS	NM	ZE	ZE	PS	PM	PM	PB
PM	ZE	ZE	PS	PM	PM	PB	PB
PB	ZE	PS	PM	PB	PB	PB	PB

Similarly, in the k − 1 moment, the combustion control system output is [7]:

$$\mathrm{y}(k-1) = \sum_{i=1}^{\infty} \overline{a_i} \cdot \Delta u(k-i-1) \tag{6}$$

The subtracting result of the two is:

$$\Delta \mathrm{y}(k) = \sum_{i=1}^{N} \mathrm{g}_i \cdot \Delta u(k-i) = \Delta u^T(k-1) \cdot g \tag{7}$$

$$\Delta \mathrm{u}(k-1) = \left[\, \Delta u(k-1), \quad \Delta u(k-2), \quad \cdots, \quad \Delta u(k-N) \,\right]^T \tag{8}$$

$$\mathrm{g} = \left[\, \mathrm{g}_1, \quad g_2, \quad \cdots, \quad g_N \,\right]^T \tag{9}$$

$$\mathrm{a}_i = \sum_{j=1}^{i} g_i \tag{10}$$

This can be got by using the Recursive Least Square (RLS) method with forgetting factor to estimate parameters online. The calculation formula is

$$\hat{\mathrm{g}}(\mathrm{k}) = \hat{\mathrm{g}}(\mathrm{k}-1) + \mathrm{K}(\mathrm{k})\left[\Delta \mathrm{y}(\mathrm{k}) - \Delta \mathrm{u}^{\mathrm{T}}(k-1)\hat{\mathrm{g}}(\mathrm{K}-1)\right] \tag{11}$$

$$K(k) = P(k-1)\Delta u(k-1) \times \left[\lambda + \Delta u^T(k-1)P(k-1)\Delta u(k-1)\right]^{-1} \tag{12}$$

$$P(\mathrm{k}) = \frac{1}{\lambda}\left[I - K(k)\Delta u^T(k-1)\right]P(k-1) \tag{13}$$

In it, we can get the initial value $\hat{g}(0)$ from $P(0) = \alpha I, \alpha = 10^5 \tilde{} 10^6$. The forgetting factor λ usually selects from $0.95 \leq \lambda \leq 0.995$, and a(k) can be got by the above formula [8].

4 Simulation Analyses

4.1 Parameter Design of Combustion Control System

The approximation model of the whole limekiln temperature control system can be expressed as

$$G(s) == \frac{K_1 K_2 e^{-\tau s}}{Ts + 1} \tag{14}$$

The increment can be estimated after adding practical system with incremental step representation, $K_1K_2 = 2\sim3$, delayed time $\tau = 13\sim16$ s, time constant $T = 140\sim150$ s. Take sampling period as $Ts = 1$ s, model domain as $N = 100$. So the simulation model is [9]:

$$G(s) = \frac{2.48}{147.5s + 1} e^{-15s} \tag{15}$$

4.2 Analysis of Application Results

The following Fig. 4 is experimental curves in Matlab of fuzzy control strategy, predictive control strategy and fuzzy predictive control strategy.

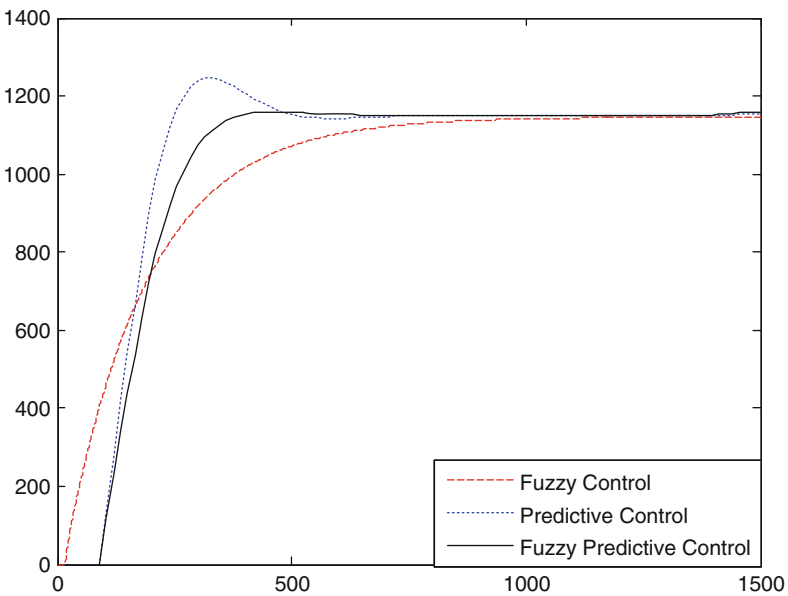

Fig. 4 Simulation curve

5 Conclusion

Traditional control arithmetic method is far from a satisfied control method in lime production. So this paper introduced fuzzy predictive control method, which well combines the predictive function of predictive control with the rapid reaction of fuzzy control in a wide deviation range. From the comparison curves in Matlab of the three control strategy, the following conclusions can be obtained: on the one hand, compared with fuzzy control and predictive control the fuzzy predictive control has quicker response speed, smaller overstrike, smaller temperature fluctuations, and better control effect; on the other hand, the fuzzy predictive control theory is simple and easy to be applied to delayed, inert process controlling system.

References

1. Han Tailun (2004) The latest practices encyclopedia of lime production technology management and pollution prevention measures. Jilin Electronic Press, Beijing, pp 192–232, In Chinese
2. Ćojbašić Ž, Stephan V, Gross HM et al (2003) Intelligent control of complex combustion processes. Mech Eng 1(10):1393–1406
3. Havlena V, Findejs J (2005) Application of model predictive control to advanced combustion control. Control Eng Pract 13(6):671–680
4. Richalet J (1993) Industrial application of model based predictive control. Automatic 29(10):1251–1274
5. Guo Feng, Liu Bin, Hao Xiaochen, Gao Peng (2010) Research on the fuzzy predictive control for calcining temperature of the rotary cement kiln. In: Signal processing (ICSP), IEEE press, Beijing, pp 2568–2571
6. Li Gongfa, Kong Jianyi, Jiang Guozhang, Yang Jintang, Xiang Hegen, Hou Yu (2007) Temperature predictive fuzzy control of coke oven. In: Control conference, IEEE press, Los Alamitos, CA, USA, pp 434–436
7. Xi Yugong, Li Dewei (2008) The basic ideas and comprehensive research status of predictive control theory. Acta Autom Sin 34(10):1225–1234, In Chinese
8. Li Shaoyuan, Li Ning (2003) Fuzzy predictive control and its application of complex system. Science Press, Beijing, pp 32–98, In Chinese
9. Rao CV, Rawlings JB (1999) Steady states and constraints in model predictive control. AIChE J 45(6):1266–1278

Application of Fuzzy Neural-PID Controller in the Static Inverter's Simulation

Bo Fan, Jialiang Wu, Jiangchuan Niu, Antang Zhang, and Jianshe Liu

Abstract This article proposes Fuzzy Neural PID controller plan to increase the quality of the Static Inverter output voltage. This strategy has advantages of fuzzy logic and neural network. This plan is combined with the steady performance advantages of PID control, so that it adjusts controlled variable in real time. The system is simulated under the circumstance of the Static Inverter. Compared with the fuzzy PID control, the analysis of the fuzzy neural PID controller simulation result shows that the control system has good performance of auto-adaptive capacity and it meets the requirements of the high robustness and quickness in the system.

Keywords Static inverter • Fuzzy neural network • PID control • Simulation

1 Introduction

In recent years, with the power electronic technology developing, the static inverter is widely used in industry, military, medical treatment, aerospace and other fields. The static inverter, one of the major parts of certain ground-to-air missile weapon systems, is the power supply of the whole system. Whether the power supply is reliable or uninterrupted has a directly impact on the performance of weapon system. The high performance of the static inverter mainly displays in the good steady voltage function, high quality of the output voltage waveform, stronger load adaptability, and good dynamic state characteristic. In order to obtain high-quality sinusoidal output voltage waveform, the modern control theories have been applied

B. Fan (✉) • J. Wu • A. Zhang • J. Liu
The Missile Institute of Air Force Engineering University, Xi'an, China
e-mail: fanbo2000@163.com

J. Niu
Launch and Test Station of 63723 Troops, KeLan Shanxi, China

W. Wang (ed.), *Mechatronics and Automatic Control Systems*, Lecture Notes in Electrical Engineering 237, DOI 10.1007/978-3-319-01273-5_20,

in the control of the static inverter power system, and a lot of control methods based on these modulation strategies have been put forward [1, 2].

The PID controller has an extensive application at steady state currently because it is robust and it has a simple structure. But the result of the traditional PID control cannot get better along with the technique progress and the control objects become more complicated. In order to improve the traditional PID control effect and strengthening the system adaptability, this article designs a fuzzy PID controller which can adjust the system control quantity. This fuzzy controller has certain advantages in overcoming the non-linearity and time-varying of the system. But the performance is not really perfect because the weakness of its 'membership and control rules can't be changed once determined'. The paper combines the characteristics of the static inverter control system, introduces the BP neural network into the fuzzy module of the controller to improve the quality of the static inverter output voltage waveform, and to make the system have both good dynamic and static performance.

2 The Design of Fuzzy Neural Network PID Controller

2.1 The Strategy of the Fuzzy PID Control

Based on previous experience, the quality of the static inverter output voltage waveform is closely related to the modulate signal, the control performance of the traditional PID controller would become bad or even unsteady if the output voltage varies greatly. Therefore, to realize the auto-adaptive of the controller, the direct voltage control method of the static inverter based on fuzzy PID algorithm is carried out [3].

The principle of the static inverter fuzzy PID control is shown in Fig. 1. The modulate signal is produced after the error signal of the expectations and the actual output value regulated by the fuzzy PID controller, which produces PWM signal through the triangle signal to control the inverter bridge, so that the output signal approaches to the expectations. The principle of the fuzzy PID control is shown in Fig. 2.

The static inverter uses two-dimensional on fuzzy control, and there are three domains need to be taken into consideration: the voltage error e, the error change

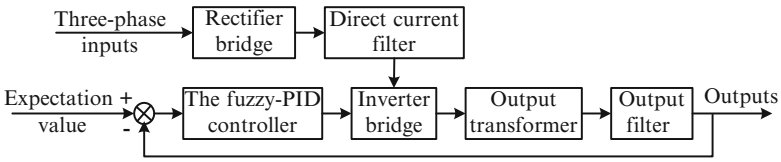

Fig. 1 The principle of the static inverter fuzzy PID control

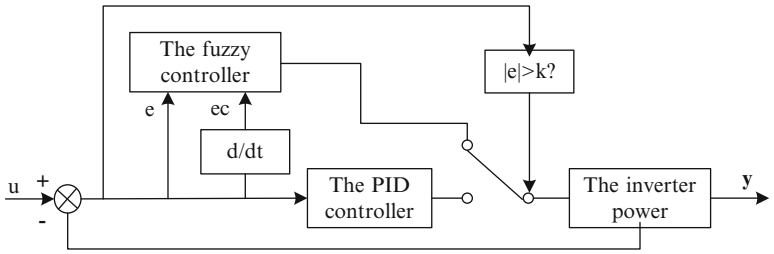

Fig. 2 The principle of the fuzzy PID control

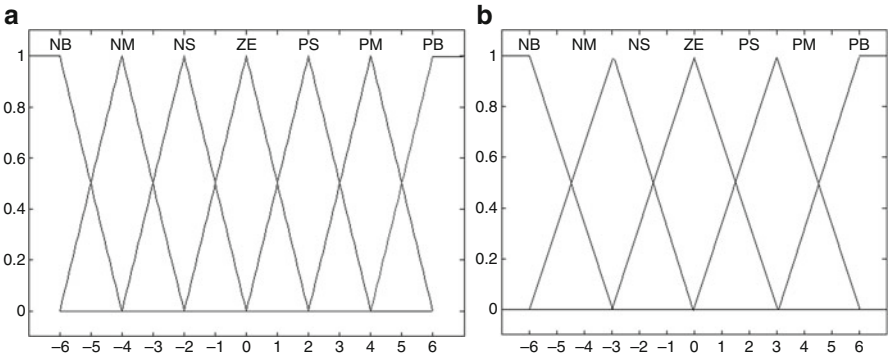

Fig. 3 The principle of the fuzzy PID control. (**a**) The voltage error e and error change rate e_c. (**b**) The controlled variable u

rate e_c and the controlled variable u; and the voltage error and the error change rate are chosen to be the input.

At first the domains of the input need to be fuzzified, and the output needs to be ascertained. Using the standardize design method putting forward by Mamdani, this three domains can be separated into thirteen ranks in the voltage error controlling, they are $[-6, -5, -4, -3, -2, -1, 0, 1, 2, 3, 4, 5, 6]$, e and e_c will change in both positive and negative directions, then $[-6, 6]$ is divided into seven language variable value, they are NB, NM, NS, ZO, PS, PM, PB.

Based on previous experience knowledge and repeated experiments, the voltage error e, the error change rate e_c and the controlled variable u are shown as triangle membership function in Fig. 3. Therefore, the functioning control rules of the domains are made certain, and the fuzzy control state form is shown as Table 1.

The characteristic of the fuzzy PID controller is that, using the fuzzy reasoning method to adjust the system control quantity based on the input of maximum range of deviation, then convert into PID control in the minimum deviation range. This conversion realize automatically based on the pre-given deviation, in order to achieve automatic adjustment of the amount of system control.

Table 1 The fuzzy control rule of e, e_c, u

	NB	NM	NS	ZO	PS	PM	PB
NB	PB	PB	PB	PB	PM	PS	ZO
NM	PB	PB	PB	PB	PS	ZO	ZO
NS	PB	PM	PM	PM	ZO	ZO	NS
ZO	PM	PS	PS	ZO	NS	NS	NM
PS	PS	ZO	ZO	NS	NM	NM	NB
PM	ZO	ZO	NS	NM	NB	NB	NB
PB	ZO	NS	NM	NB	NB	NB	NB

2.2 *The Realization of the Fuzzy Neural Network PID Controller*

In this design, the T-S fuzzy neural network controller is established based on the improved fuzzy control module which has been mentioned before, the precision of the system control will be advanced through the self-learning ability of the neural network which can increase and improve the fuzzy control rules. Moreover, the self-learning ability of the neural network has good fault-tolerance function. The neural network can also reduce the conflict between each other and the wrong fuzzy control rules automatically, ensure and improve the completeness and consistency of fuzzy control rules, and reduce the interaction among the fuzzy control rules [4, 5]. Then combined with the PID method, the output voltage of static inverter will be controlled.

(a) The structure of the fuzzy neural network

The structure of the fuzzy neural network is shown in Fig. 4, the network has five layer structures, which were used to match the fuzzy rules and generate fuzzy rules.

Layer 1, the input layer, inputs the voltage error and the voltage error change rate.

Layer 2, the input membership function layer, each node represents a language variable value, which computes each input vector that belong to the membership function u_i^j of the language variable value fuzzy sets,

$$u_i{}^j = u_{Ai}{}^j(x_i)\ i = 1, 2, \ldots, n;\ j = 1, 2, \ldots, m_i \tag{1}$$

Where, n is the dimension of input, m_i is the fuzzy partitions of x_i. In this system, $n = 2$; x_1 =E; x_2 =EC; m_1 =7; m_2 =7; the membership function as follows:

$$u_i^j = e^{-\frac{(x_R - c_i^j)}{\sigma_{ij}}} \tag{2}$$

Where, c_{ij} is the center point and σ_{ij} is the width of the membership function.

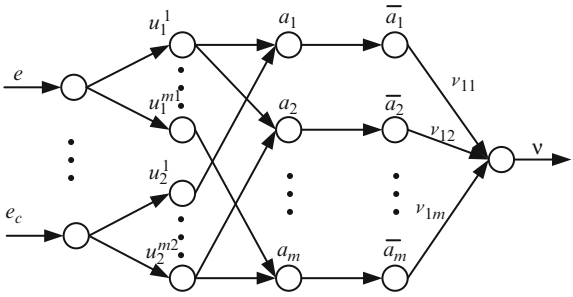

Fig. 4 The structure of the fuzzy neural network

Each node in layer 3 represents a fuzzy rule, which is used to match the antecedent network of the fuzzy rule and calculate the firing strength of each fuzzy rule, as follows:

$$a_j = \min\left\{u_1^{i1}, u_2^{i2}\right\} \tag{3}$$

Where, $i_1 \in \{1, 2, \ldots, m_i\}$; $i_2 \in \left\{1, 2, \ldots, m_j\right\}$; $j = 1, 2, \ldots, m$, $m = \prod_{i=1}^{n} m_i$

The number of the node in layer 3 is $N_3 = m = 49$, the membership value is bigger only when the language variable is around the input. Otherwise the membership value is smaller or 0. When the degree of membership is very small (e.g. less than 0.05), it will be considered as 0.

The number of the node in layer 4 is the same to layer 3, it is $N_4 = N_3 = m = 49$. It is the normalized layer to calculate the normalized firing strength of corresponding rules, it can be described as

The number of the node in layer 4 is the same as layer 3, it is $N_4 = N_3 = m = 49$. It is the normalized layer, it can be described as

$$\bar{a}_j = a_j / \sum_{i=1}^{m} a_i,\ j = 1, 2, \ldots, m \tag{4}$$

Layer 5 is the consequent network, which is the function layer to calculate the consequent parameters of every rule. The liner relationship between input and output in every layer can be describe as

$$v_{ij} = p_{j0}^i + p_{j1}^i x_1 + \ldots p_{jn}^i x_n = \sum_{k=0}^{n} p_{jk}^i x_k \tag{5}$$

Where, $i = 1, 2, \ldots, r$; $j = 1, 2, \ldots, m$. The consequent network of each rule represents the weight of the last layer.

The output of the system is as follows:

$$v_i = \sum_{j=1}^{m} \bar{a}_j v_{ij},\ i = 1, 2, \ldots, r \tag{6}$$

(b) The adjustment of the consequent network parameters

As shown before, the initial value of c_{ij} and σ_{ij} are given, because the output v_i is the linear function of p_{ij}^k, and all training samples are expressed as the Eq. 6, AX = B is the problem of the standard minimum two multiplications. The expression of X is:

$$X = (A^T A)^{-1} A^T B \tag{7}$$

The total error function of the output is:

$$E = \frac{1}{2} \sum_{i=1}^{r} (v_{di} - v_i)^2 \tag{8}$$

Where, v_{di} and v_i are the expect output voltage and actual output voltage, respectively. The learning algorithm of the parameters is:

$$\frac{\partial E}{\partial p_{ij}^k} = \frac{\partial E}{\partial v_k} \frac{\partial v_k}{\partial v_{kj}} \frac{\partial v_{kj}}{\partial p_{ij}^k} = -(v_{di} - v_k)\, \bar{a_j}\, x_i \tag{9}$$

$$p_{ij}^k(l+1) = p_{ij}^k(l) + \beta (v_{di} - v_k)\, a_j \bar{x}_i \tag{10}$$

Where, $i = 1, 2, \ldots, n$; $j = 1, 2, \ldots, m$; $k = 1, 2, \ldots, r$.

The parameter p_{ij}^k can be selected at this time, $\frac{\partial E}{\partial c_{ij}}$ and $\frac{\partial E}{\partial \sigma_{ij}}$ are calculated by adopting BP algorithm, then c_{ij} and σ_{ij} are adjusted through the gradient search algorithm, and the formula of first-order gradient is:

$$\frac{\partial E}{\partial c_{ij}} = \frac{\partial E}{\partial f_{ij}^{(2)}} \frac{\partial f_{ij}^{(2)}}{\partial c_{ij}} = -\delta_{ij}^{(2)} \frac{2(x_i - c_{ij})}{\sigma_{ij}^2} \tag{11}$$

$$\frac{\partial E}{\partial \sigma_{ij}} = \frac{\partial E}{\partial f_{ij}^{(2)}} \frac{\partial f_{ij}^{(2)}}{\partial \sigma_{ij}} = -\delta_{ij}^{(2)} \frac{2(x_i - c_{ij})^2}{\sigma_{ij}^3} \tag{12}$$

At last the learning algorithm of the parameters adjustment is:

$$c_{ij}(k+1) = c_{ij}(k) - \beta \frac{\partial E}{\partial c_{ij}},\ \sigma_{ij}(k+1) = \sigma_{ij}(k) - \beta \frac{\partial E}{\partial \sigma_{ij}}$$

Where, β is the learning rate, $\beta > 0$; $i = 1, 2, \ldots, n$; $j = 1, 2, \ldots, m_i$.

3 The Simulation and Analysis of the System

In this part, the T-S fuzzy neural network is carried on off-line training with the input and output sample data obtained from the fuzzy PID control based on MATLAB/Simulink7.1; the control model is shown in Fig. 5, the trained fuzzy neural network has been embedded into the analog circuits to realize the concurrent control. In the model, the sampling period T is 0.001, the domain of the error is $[-35, 35]$, the domain of the error changing rate is $[-5, 5]$, the domain of the output is $[-40, 40]$; the reasoning fuzzy factor are $k_e = 0.2$, $k_{ec} = 0.02$, $k_u = 6.5$, and the parameters of the PID controller are $K_p = 1.2$, $K_i = 10$, $K_d = 0.0005$; the switch frequency is 3 KHz, the input AC voltage is 380 V, the output AC voltage 220 V, the power is 12 WKVA, the output filter capacitance and inductance

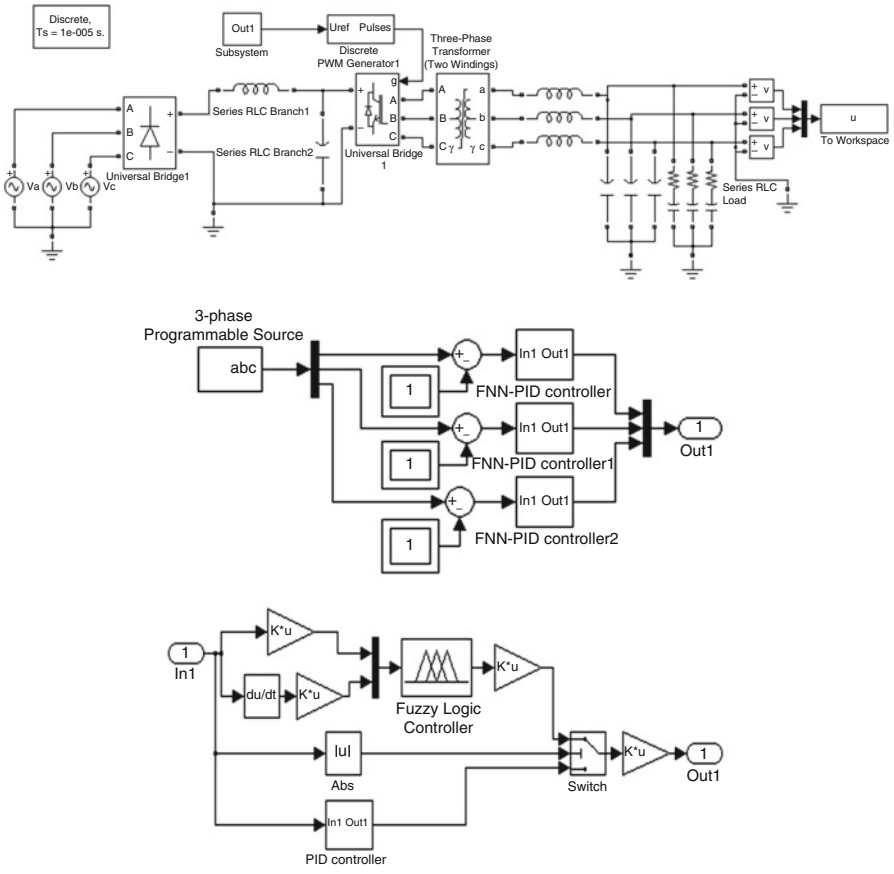

Fig. 5 The circuit of the fuzzy neural network PID control system (1) The main circuit of the fuzzy neural network PID control system (2) The model of the modulate wave (3) The model of the fuzzy neural network PID control

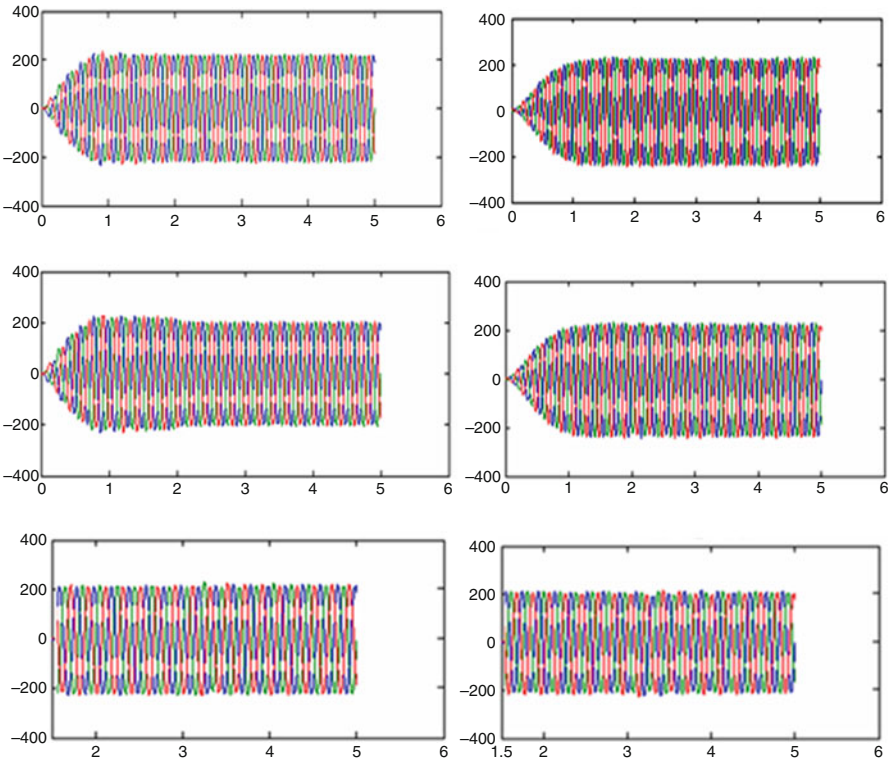

Fig. 6 The result of the system simulation (The x, y-axis are time t(/0.1 s) and voltage (/v); (1), (3), (5) are the output voltage of the normal condition, connect the load and disconnect the load based on the fuzzy PID controller; (2), (4), (6) are the output voltage of the normal condition, connect the load and disconnect the load based on the fuzzy neural PID controller)

are 5000 μF and 3 mH, the parameters of the output transformer are 380 V/120 V, 25 WKVA, 50 Hz.

In the simulation, the fuzzy PID controller and the fuzzy neural network PID controller are used in the static inverter circuit, respectively. The switch threshold is 5 V; the three voltmeters measure corresponding phase ABC output voltages, respectively. The simulation time is 0.5 s, and the result of the simulation is shown in Fig. 6.

According to the result of the simulation, from the static inverter started up to the voltage stability, the control performance of the fuzzy neural network PID controller is better than the fuzzy PID controller. The performance of the voltage recover stability is also better when the system is connected the load at 0.2 s and disconnected the load at 0.3 s. The step signal response cure of the controller is shown in Fig. 7, the overshoot and steady-state time of the fuzzy neural network PID controller is reduced. In conclusion, the strategies of the static inverter both have the advantages of the dynamic characteristics of fuzzy neural network control and

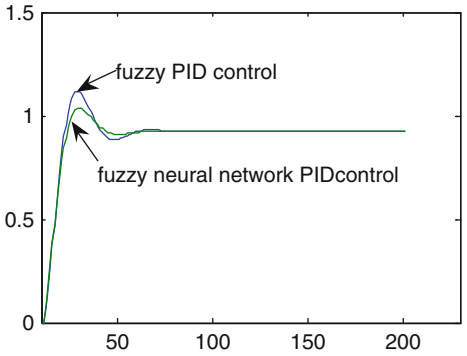

Fig. 7 The step signal response cure of the controller

the steady-state performance of the PID control. So that the stability, the overshoot, the precision of the control, and the learning efficiency of the static inverter have been improved greatly.

4 Conclusion

The neural network is brought in the fuzzy PID controller, which may solve the problems of low-precision control and the limited auto-adaptive capability. The simulation result showed that the fuzzy neural network PID controller had better performance, and it met the requirements of the system. The result also showed that the fuzzy neural network PID control way to control the static inverter is valid and possible.

References

1. XiaoHuan Wang, ChunJiang Zhang, Feng Ding (2010) Design and implementation of three-phase inverter controller with double mode of grid-connection and stand-alone [J]. Power Electron 12(44):82–84 (In Chinese)
2. Yanfeng Li, Guanlu Yang, Nianzhi Lv, Yadong Li (2009) Fuzzy proportion-integral-derivative controller for power inverter [J]. J Detect Control 3(31):35–38
3. Qingjie Yang, Guohou Li, Xusheng Kang (2008) Application of fuzzy PID control in the heating system [C]. Chinese control and decision conference, IEEE Computer Society, Washington DC, USA, pp 2686–2690
4. Yanfei Liu, Qi'an Wang (2009) Direct torque control of induction motor based on fuzzy neural network [J]. Proc CSU EPSA 12(26):86–89 (In Chinese)
5. Honglin Ouyang, Lanxian Cheng (2007) Multiple phase permanent synchronous motor speed control system based on fuzzy neural network control [J]. J Mot Control 2(11):111–115 (In Chinese)

Calculation of Impulse Grounding Resistance of Extended Grounding Electrode

Anqi Shangguan

Abstract In order to calculate the impulse grounding resistance of extended grounding electrode accurately, this paper introduces a method for computing the impulse grounding resistance based on the spark discharge characteristic of the earth, using a nonlinear differential circuit model. The relation curves of impulse grounding resistance with the current peak value and the electrode length are acquired. Then the results are compared with the national standard, real model testing results and simulated testing results, which shows that the proposed method can be used in practice.

Keywords Impulse grounding resistance • Extended grounding electrode • Differential circuit

1 Introduction

To calculate the impulse grounding resistance of transmission line, we usually multiply frequency grounding resistance by the impulse coefficient. But the impulse coefficient is determined by the simulation test [1], which is difficult to truly reflect the process of the spark discharge of grounding electrode. The field test of impulse grounding resistance provides some results which is in condition of low lightning current [2], but this method is difficult to reflect the results in high lightning current condition and is inconvenient to operate. This paper is based on the true test of the impact properties of extended grounding electrode of unit length, and use nonlinear differential circuit model to calculate the impulse grounding resistance of extended grounding electrode, which can truly reflect the process of the spark discharge without using large-capacity impulse generator.

A. Shangguan (✉)
School of Electrical Engineering, Wuhan University, Wuhan, China
e-mail: shumoshangguan@126.com

W. Wang (ed.), *Mechatronics and Automatic Control Systems*, Lecture Notes in Electrical Engineering 237, DOI 10.1007/978-3-319-01273-5_21,

2 Nonlinear Differential Circuit Model

Split the extended grounding electrode to N equal parts, each long as Δx. Strike the parameters of different parts of the extended grounding electrode based on soil impulse discharge voltage characteristics and the spark discharge characteristics [3]. Put N into infinity, then we can acquire the nonlinear distributed parameter circuit of the extended grounding electrode and nonlinear partial differential equations of the impulse discharge . But this kind of equations can be worked out only by numerical methods [4]. So we need to build finite partition numerical circuit. If the lightning current flows into the grounding electrode from the first end when t = 0, and flows by the cell circuit in Δt, the voltage、 current on $j\Delta t$ in $k\Delta x$ will be:

$$u(k,j) = u(k\Delta x, j\Delta t), i(k,j) = i(k\Delta x, j\Delta t) \tag{1}$$

Compare the result in Figs. 1 and 2, we find the conductance and capacitance of the unit grounding in the Fig. 1 is:

$$\begin{aligned} G(k,j) &= G(u(k\Delta x, j\Delta t)), \\ C(k,j) &= C(u(k\Delta x, j\Delta t)). \end{aligned} \tag{2}$$

They are function of voltage in the corresponding location, the conductance of unit grounding is:

$$G = 2\pi/\rho \ln\left(l^2/2hr\right), \tag{3}$$

ρ is the soil resistivity h, l and r is the depth of the grounding, the length and the radius. Because spark discharge increase the diameter of the grounding electrode, r should be the equivalent radius which has considered impact of the spark discharge characteristics [5]. It can be acquired by impact test.

The capacitance of unit grounding is:

$$C = 2\pi\varepsilon/\ln\left(l^2/2hr\right) \tag{4}$$

ε is the soil permittivity. There will be errors when we make r the equivalent radius. But in general, $\rho = 10\tilde{}1000\Omega \cdot m$, the influence of C, the displacement current of C can be ignored. Though it is necessary to take capacitance effects into account when ρ is large, the error of using equivalent radius is very low [6].

Because the length of the grounding charging dynamic changes with the propagation time. So it's not good to calculate it by the actual grounding length directly. We can consider the impact of the wave process by using wave propagation distance as the equivalent length.

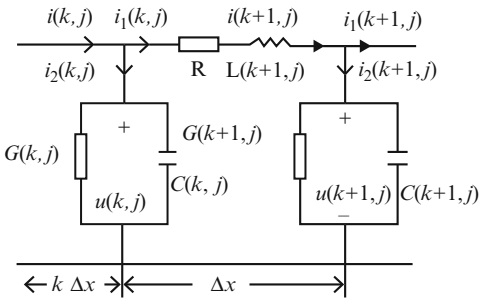

Fig. 1 Nonlinear differential circuit model

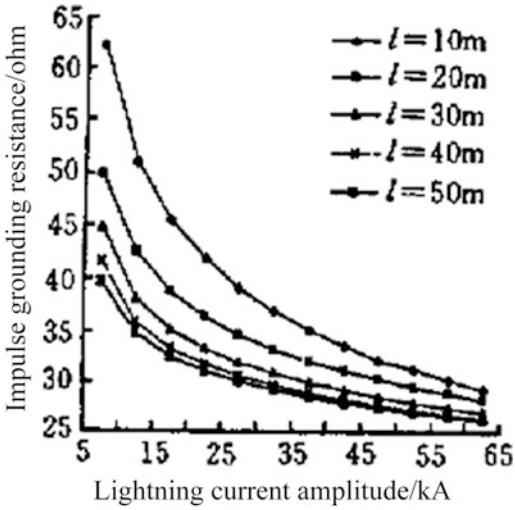

Fig. 2 Nonlinear differential circuit model

The resistance of unit grounding has nothing to do with the spark discharge and the wave process but is related with the skin effect, and is decided by the parameter of grounding, the magnitude of the lightning current and the equivalent frequency of the wave head of the lightning current [7]. R can be ignored when $\rho = 10\tilde{}1250$ $0\Omega \cdot m$. So R should be considered when ρ is high and treat it as constant.

Spark discharge does not increase the conductivity of the grounding in the direction of its length, and has nothing to do with the calculation of the inductance. L (k, j) is the function of spatial location and the propagation time of the wave [8], and is called dynamic inductance. It is necessary to consider the change of flux during the wave process. Each unit circuit has a certain length in the differential circuit, which is not like that in the distributed parameter circuit. There will be some delay when the current flows by and the current of the end of the inductive branch is the result of the transmission of the first terminal current in Δt. Distribution of current in the inductive branch is approximated as a continuous linear distribution. Its distribution curve is a segment which connects the first and the end of the current. So we define $i_1(k\Delta x, j\Delta t)$ and $i((k+1)\Delta x, j\Delta t)$ in the first end of the inductive branch of the nonlinear difference circuit. And we define

$$i((k+1)\Delta x, j\Delta t) = i_1(k\Delta x, (j-1)\Delta t) \tag{5}$$

And the nonlinear difference equations can be:

$$\begin{aligned} i(k,j) &= i_1(k,j) + i_2(k,j) \\ u(k,j) &= u((k+1),j) + \overline{i(k,j)}R\Delta x \\ &\quad + \mathrm{L}(k,j)\Delta x \frac{\overline{i(k,j)} - \overline{i(k,j-1)}}{\Delta t} \\ i_2(k,j) &= G(k,j)u(k,j)\Delta x \\ &\quad + \mathrm{C}(k,j)\Delta x \frac{u(k,j) - u(k,j-1)}{\Delta t} \end{aligned} \tag{6}$$

$i(k,j) = (i_1(k,j) + i_2(k+1,j))/2$ is the average current which flows by the inductive branch from $(j-1)\Delta t$ to $j\Delta t$.

3 Dynamic Boundary Conditions and the Solving of Difference Equation

Electrode $i(0,j) = i_s(j)$ is decided by the lightning current. The influence of the change of the first side of the wave should be considered in the other side of the grounding electrode. Its boundary conditions are dynamic. And two conditions should be considered.

3.1 Boundary Conditions When $j \leq N$

$$\begin{aligned} i(j,j) &= i_1(j,j) = i_2(j,j) = 0 \\ u(j,j) &= 0 \end{aligned} \tag{7}$$

3.2 Boundary Conditions When $j > N$

$$\begin{aligned} i_1(N,j) &= 0 \\ i(N,j) &= i_2(N,j) = i_1(N-1,j-1) \\ i_2(N,j) &= G(N,j)u(N,j)\Delta x \\ &\quad + \mathrm{C}(N,j)\Delta x \frac{u(N,j) - u(N,j-1)}{\Delta t} \end{aligned} \tag{8}$$

This condition just adapts to finite length horizontal grounding. The wave reflection in the end can be approximately seen as the end is open. Three unknowns of the nonlinear differential equation can be worked out from the boundary conditions:

$$\begin{aligned}
&i_1(k,j) = \{i_1(k-1,j-1) - [G(k,j)\Delta x + C(k,j)\Delta x/\Delta t] \cdot [u(k+1,j) \\
&+ (i_1(k,j-1)/2)\cdot \\
&R\Delta x - i(k+1,j-1)L(k,j)\Delta x/2\Delta t] + C(k,j) \cdot u(k,j-1)\Delta x/\Delta t\} \\
&\div [1 + \left(\Delta x^2/2\right)(R + L(k,j)/\Delta t) \\
&(G(k,j) + C(k,j)/\Delta t)] \\
&i_2(k,j) = i_1(k-1,j-1) - i_1(k,j) \\
&u(k,j) = (i_1(k,j)/2 + i_1(k,j-1)/2)R\Delta x \\
&\qquad + u(k+1,j) + L(k,j)\Delta x\cdot \\
&\qquad (i_1(k,j) - i(k+1,j-1))/2\Delta t
\end{aligned} \tag{9}$$

Based on the above three type and boundary conditions, adopt the retrogression algorithm from the end of the grounding to the beginning, we can directly calculate the current, voltage distribution and the impulse grounding resistance after several cycles.

4 Results of the Comparison Between Our Example and Other Examples

Take computing conditions for: $h = 0.6m, \rho = 1000\Omega \cdot m,$ r = 0.005 m, soil $\varepsilon = 9 \times 8.86 \times 10^{-12}$ soil permeability $\mu = 4\pi \times 10^{-7}$, the injected lightning current waveforms in the beginning of the grounding $i_s = I_m(e^{-0.019j\Delta t} - e^{-1.89j\Delta t})$. In C、G、R、L, $R = 0.05\Omega/m$, the rest can be worked out by dynamic calculation.

According to the results of the discharge test of the true grounding of unit length, using the computational model in this paper, we can get the impulse grounding resistance curve of 10~50 m long extended grounding when one of its ending is injected with 5~60 kA lightning current, which is shown in Fig. 2. Figure 3 shows the comparison of results between literature and this paper [9], proving that it is very close to the field measurement result and the power line standard.

5 Conclusion

Nonlinear differential circuit model and its corresponding algorithms, which are based on the true type test results of impulse characteristics of extended grounding electrode of unit length, take into account spark effect of the impulse discharge

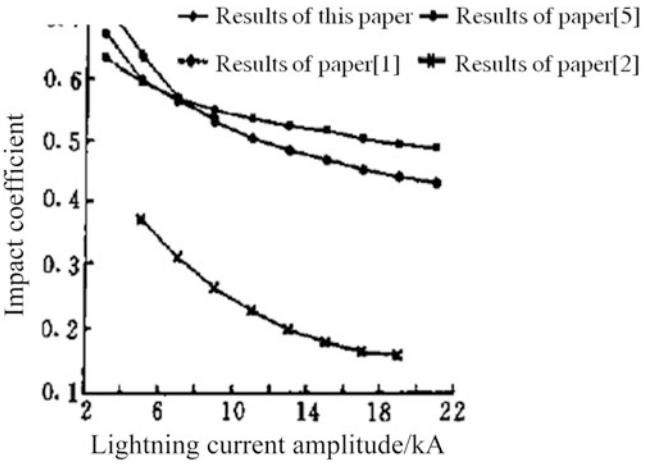

Fig. 3 The impact coefficients obtained by different methods

process and the dynamic characteristics of the inductance and capacitance during the propagation of the lightning current. It is a true reflection of lightning current drain diffusion process of the extended grounding and is very reliable.

The true type test of impulse characteristics of extended grounding electrode of unit length can be conducted by using the impulse generator of smaller capacity in the laboratory. This method can easily replace the electrode and dielectric and has good application prospects, which provides a reference for the amendment of "The Technical Regulations of Grounding".

References

1. Xianlu Chen (1996) The formula of impulse grounding resistance of transmission line tower grounding device. Power Syst Technol 20(6):9
2. Wen Cheng (1962) Test of grounding impulse characteristics in high-resistivity soil. Electr Power Technol 12(6):30
3. Changzheng Xia, Cixuan Chen (2001) The true type test of the impact properties of the extended grounding of unit length. High-Volt Eng 27(3):34
4. Shu Xiang, Wen Xishan, Zhang Yunjian, Peng Ningyun (2004) Development of test device for tower impulse grounding resistance. High Volt Eng 30(10):9
5. Ye Haifeng, Liu Xun (2007) Research of lightning impulse characteristics of horizontal grounding electrode. Water Resour Power 49(1):15
6. Xiong Jun (2005) Research on the impulsive characteristics of grounding resistance of transmission-line towers. Insul Surge Arresters 11(6):8
7. Guoqiang Zhang, Boming Zhang (2008) Study of wind power prediction based on neural networks and combinatorial prediction of the similarity of samples. 2008 National PhD Academic Forum – electrical engineering papers, pp 441–446
8. Changzheng Xia (2001) Study of the impact properties of the extended grounding. Ph.D. thesis of Wuhan University, Wuhan
9. DL/T621-1997. The grounding of AC electrical installations

Dual-Array Tracking Algorithm for Underwater Bearing-Only Target Tracking Based on EKF

Xiaohua Li, Ya'an Li, Wangsheng Liu, and Xiaojuan Bai

Abstract In this paper, according to the characteristics of underwater target tracking, extended Kalman filter (EKF) algorithm was applied to address underwater bearing-only non-maneuverable target tracking problem. To ensure the observability in bearing-only passive target tracking, we use two sensor arrays in uniform rectilinear motion to track the single target. EKF is recursive Bayesian filter algorithm based on the linearization of the nonlinearities in the state and the measurement system. And the simulation experiment shows that, to the constant velocity single target, the bearings-only EKF algorithm with dual-array has good results, also the EKF has lower computation complexity than unscented Kalman filter and particle filter. It confirms the effectiveness of the EKF algorithm in solving the underwater bearing-only target tracking problem.

Keywords Bearing-only targets tracking • Extended Kalman filter • Dual-array • Underwater target

1 Introduction

Because of the extensive application on military and civil industries, target tracking has gained more and more attention by many experts and scholars all over the world [1, 2]. In a variety of radar and sonar applications, the bearings-only tracking problems, in other words, passive localization and tracking problems, has been broadly welcomed by researchers [3]. Two-dimensional bearings-only target

X. Li (✉) • Y. Li • X. Bai
College of Marine Engineering, Northwestern Polytechnical University, Xi'an, China
e-mail: lxhxy2009@163.com

W. Liu
School of Mechanical Engineering and Automation, Zhejiang Sci-Tech University, Hangzhou, China

W. Wang (ed.), *Mechatronics and Automatic Control Systems*, Lecture Notes in Electrical Engineering 237, DOI 10.1007/978-3-319-01273-5_22,

tracking technical were generally used in the underwater environment [4, 5]. And there are numerous solutions have been proposed until recently. One of the most important parts in target tracking is the filtering algorithm. The typical Kalman filter can get the recursive minimum mean-square estimation (MMSE) under the linear and write Gaussian noise circumstance. However, usually the systems are nonlinear and non-Gaussian in practice for which Kalman filter may not be suitable and cannot track the targets with effect, especially in highly nonlinear non-Gaussian conditions when the target and sensor are close [6]. Therefore, the nonlinear filtering becomes a very hotspot research in target tracking. The method extended Kalman filter (EKF) has shown promise outperforming.

It is well known that the difficult problem for bearings-only tracking is that only using bearings measurements, a single sensor cannot track targets, particularly when the sensor is static. There are two main issues which contribute to making this problem hard. The first is that the measurement process is high degree of nonlinearity [7]. The second is that we cannot observe the target state fully, that is the sensor cannot have accurate information about the targets' range unless the sensor platform exerts to out maneuver the target [8, 9].

The observability issue can be solved by using two or more sensors (static or maneuver) [10, 11]. In this paper, we consider a scenario with two sensors tracking one target. The applied methodology for tracking is extended Kalman filter, which is a linearization technique using linear transformation of first order Taylor series expansion to approximate the nonlinear system.

In Sect. 2, we introduce the problem of bearings-only process model. Section 3 explains the bearings-only tracking problem based on EKF. Finally, we provide the simulation results and analysis in Sect. 4 and conclusions are outlined in Sect. 5.

2 Bearings-Only Process Model

The bearing-only target tracking problem can be expressed by a linear state model and a nonlinear scalar measurement equation of the form. Consider the two-dimensional (2D) dual-array tracking problem depicted in Fig. 1.

We assume the single target located at the coordinates system (r_{Tx} r_{Ty}) with constant velocities (v_{Tx} v_{Ty}) and is defined to have the state vector

$$X_T = \left[r_{Tx}\ r_{Ty}\ v_{Tx}\ v_{Ty}\right]^T \tag{1}$$

The observer state measurement equation is similarly defined as

$$X_O = \left[r_{ox}\ r_{oy}\ v_{ox}\ v_{oy}\right]^T \tag{2}$$

where the velocity may be varied. And the relative state vector can be defined by

$$X = X_T - X_O = \left[r_x\ r_y\ v_x\ v_y\right]^T \tag{3}$$

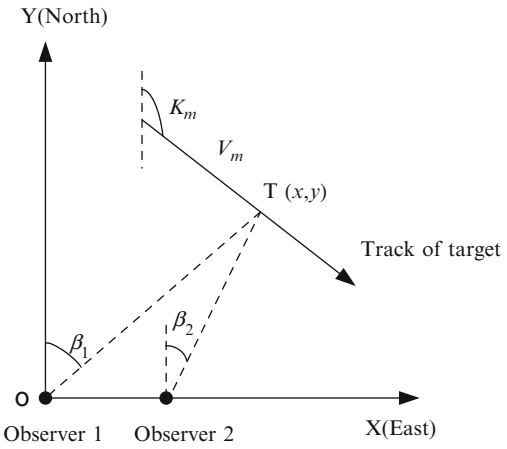

Fig. 1 Typical two-dimensional (2D) dual-array tracking problem

As we known, targets have only one dynamic motion models at a time. Typically for a non-maneuvering period target, the constant velocity model is appropriate under underwater target tracking scenarios. For maneuvering targets period, we can use the coordinate turn models or coordinate uncoupled models [12]. We only consider the linear dynamic constant velocity models with process noise in this paper.

Consider the target is moving parallel in constant velocity in the horizontal plane, the discrete-time state equation is

$$\mathrm{X}(t_k) = \Phi(t_k, t_{k-1})X(t_{k-1}) + \Gamma(t_k, t_{k-1})w(t_{k-1}) \tag{4}$$

where t_k is the time at the kth sample, and the $w(t_{k-1})$ is zero mean white process noise with variance Q, and $\Phi(t_k, t_{k-1})$ is a 4×4 deterministic transition matrix,

$$\begin{aligned} \Phi(t_k, t_{k-1}) &= \begin{bmatrix} I & (t_k - t_{k-1})I \\ 0 & I \end{bmatrix} \\ \Gamma(t_k, t_{k-1}) &= \begin{bmatrix} \frac{1}{2}(t_k - t_{k-1})^2\mathrm{I} \\ (t_k - t_{k-1})\mathrm{I} \end{bmatrix}, \; I = \begin{bmatrix} 1 & 0 \\ 0 & 1 \end{bmatrix} \end{aligned} \tag{5}$$

It should be noted that the state vector's initial state estimates and associated error covariance matrix are assumed to be known.

The available measurement is the angle between the observer's sensor and the target, referenced clockwise-positive to the y-axis, and is defined by

$$Z(k) = \begin{bmatrix} \beta_1(k) \\ \beta_2(k) \end{bmatrix} = h[X[k]] + V(k) = H(k)X(k) + v(k) \tag{6}$$

where $v(k)$ is zero-mean independent Gaussian noise with variance R, and $\beta_1(k)$, $\beta_2(k)$ are the noise-free bearings between the sensor and the target,

$$\beta_1(k) = \tan^{-1}\left[r_{x1}/r_{y1}\right],\ \beta_2(k) = \tan^{-1}\left[r_{x2}/r_{y2}\right] \tag{7}$$

We assume the sensor noise is independent to the perturbations of sensor platform.

The bearings-only target tracking analysis problem are defined by the four-dimensional state Eq. 4 and the nonlinear measurement of Eqs. 6 and 7.

Especially for EKF,

$$H(k) = \frac{\partial h(X_k)}{\partial X_k} = \begin{bmatrix} \frac{\partial \beta_1}{\partial r_x} & \frac{\partial \beta_1}{\partial r_y} & \frac{\partial \beta_1}{\partial v_x} & \frac{\partial \beta_1}{\partial v_y} \\ \frac{\partial \beta_2}{\partial r_x} & \frac{\partial \beta_2}{\partial r_y} & \frac{\partial \beta_2}{\partial v_x} & \frac{\partial \beta_2}{\partial v_y} \end{bmatrix} \tag{8}$$

3 Basic Principle of Extended Kalman Filter Algorithm

Based on the principle of Bayesian filtering method, Kalman filtering algorithm proposed by Kalman in 1960 [13] is one of the most well-known and often-used tools for stochastic estimation from noisy sensor measurements. It is one of the common recursive target state filtering algorithms, and is the theoretically best stationary targets' state estimation under the minimum mean square error. However, it is not possible to direct apply the conventional Kalman filter to nonlinear system. To deal with nonlinear problems, we usually use the classic approximate algorithms, such as the extended Kalman filter [14] and unscented Kalman filter (UKF).

The EKF algorithm is simply a publicly used state estimator which linearizes the nonlinear system (the current mean and covariance). It is well to known that EKF algorithm only approximates the Bayesian statistics by linearization the nonlinear state equation and measured equation, and remains the linear items and omit the more than two orders' parts.

To the bearing-only problem in the present case, the target states are linear in Cartesian coordinates, while the measurements are modeled in polar coordinates. So the EKF is implemented in mixed coordinates: the Cartesian coordinates for target's states, and polar coordinate for the measurements.

For the problem under consideration, we summarize the implementation of EKF in the following equations.

Lets define the initial estimate of the state vector as X(0|0), and initial estimate of the state vector error covariance matrix P(0|0).

State prediction:

$$\hat{\mathrm{X}}(k+1|k) = \Phi(k)\hat{X}(k|k) \tag{9}$$

Covariance matrix of state prediction:

$$\mathrm{P}(k+1|k) = \Phi(k)P(k|k)\Phi^T(k) + Q(k) \tag{10}$$

Measurement matrix (linearized):

$$\mathrm{H}(k+1) = \frac{\partial h}{\partial X|_{X=\hat{X}(k+1|k)}} \tag{11}$$

Measurement residual:

$$\varepsilon(k+1) = \beta(k) - h[X(k+1|k)] \tag{12}$$

Predicted measurement covariance:

$$\mathrm{S}(k+1|k) = H(k+1)P(k+1|k)H^T(k+1) + R(k+1) \tag{13}$$

Gain matrix computation:

$$\mathrm{G}(k+1) = P(k+1|k)H^T(k+1)S(k+1)^{-1} \tag{14}$$

Updated state:

$$\mathrm{X}(k+1|k+1) = X(k+1|k) + G(k+1)\varepsilon(k+1) \tag{15}$$

Updated state covariance matrix:

$$\mathrm{P}(k+1|k+1) = \mathrm{P}(k+1|k) - G(k+1)H(k+1)\mathrm{P}(k+1|k) \tag{16}$$

where the "prime" symbol ($^{\mathrm{T}}$) denotes matrix transposition.

4 Simulation and Analysis

To demonstrate the effectiveness of the EKF algorithm in underwater bearings-only target tracking using two observers sensors, we set the conditions of simulation as follows.

The initial distance from target to origin of coordinate is 1,000 m with the origin of target bearing 30°, and the origin of target speed and target course are 40 kn

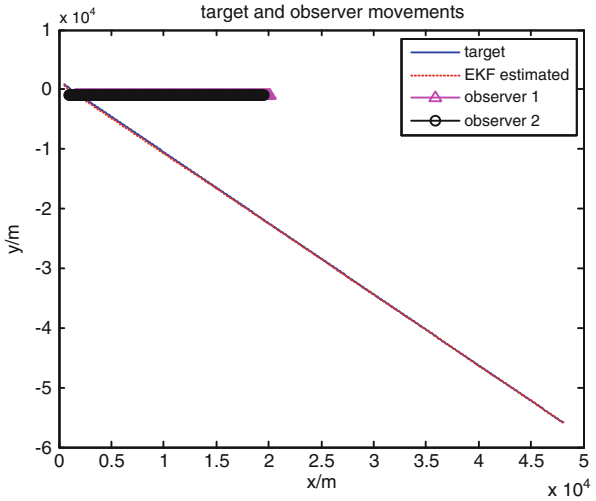

Fig. 2 Observers and target moments

and 140°, respectively. The locations of two arrays are (1600, −1000) m and (1000, −1000) m with the velocity (10, 0 kn).

The measurement noise and process noise were modeled as Gaussian distributions. The measurement noise covariance matrix is:

$$R = \begin{bmatrix} 0.1 & 0 \\ 0 & 0.1 \end{bmatrix}$$

Process noise covariance matrix is:

$$Q = \begin{bmatrix} 0.01 & 0 \\ 0 & 0.01 \end{bmatrix}$$

Initial estimate of the state vector error covariance matrix is:

$$P = \begin{bmatrix} 10 & 0 & 0 & 0 \\ 0 & 10 & 0 & 0 \\ 0 & 0 & 1 & 0 \\ 0 & 0 & 0 & 1 \end{bmatrix}$$

In the simulation, we set the period of the system 1,800 s, the measurement interval 2 s, and the Monte-Carlo simulation100 times. Here all angles are clockwise positive with respect to True North 0–360°. The simulation results are as follows:

As is shown from Figs. 2, 3, 4, and 5, we can see clearly that the relative error of range and velocity are less than 10 %, the RMS error of x axis and y axis are approximate to 300 m and the RMS error of x axis velocity and y axis velocity are

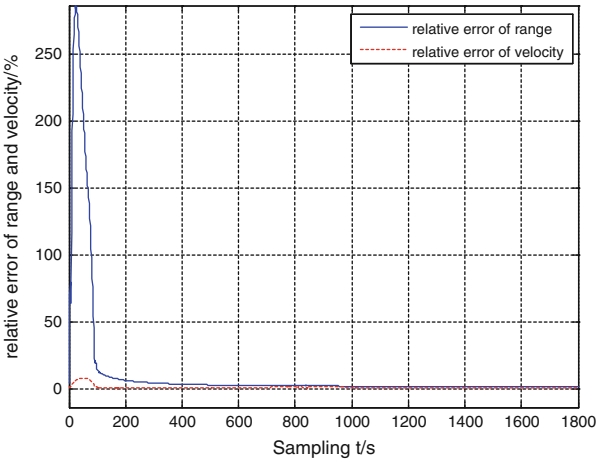

Fig. 3 Relative error of range and velocity

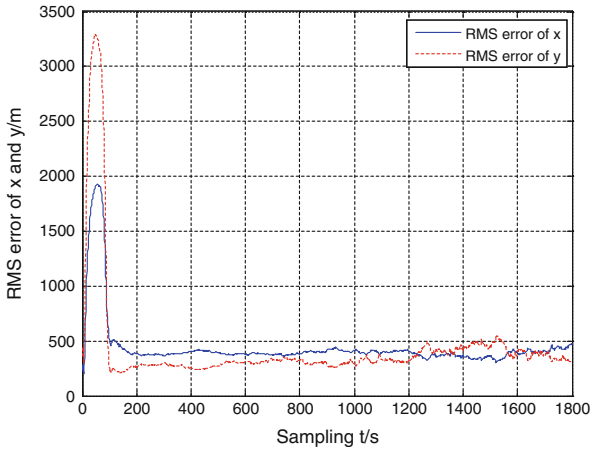

Fig. 4 RMS error of x and y

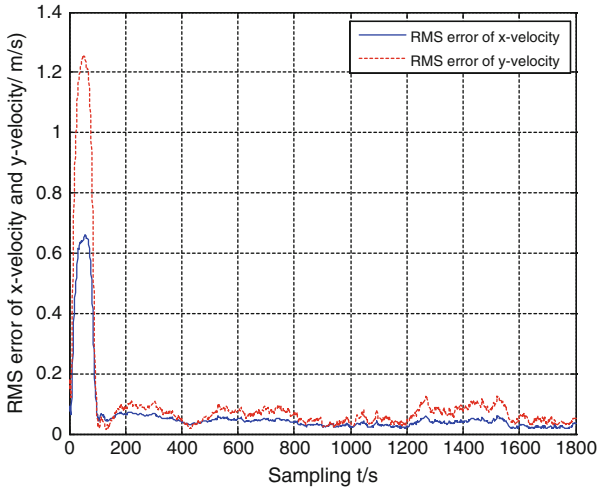

Fig. 5 RMS error of x velocity and y velocity

approximate to 0.07 m/s. It reveals that over the simulation period, the EKF algorithm has good tracking performance on the condition of underwater bearing-only dual-array target tracking, and sensor platform propagation conditions are satisfactory during this target tracking period. This means that EKF estimated moments can track the target moments accurately.

In addition, the whole simulation time is 5.5457 s, it means that the computational load of the EKF algorithm is small. EKF algorithm is the best choice if when the initial estimation errors are not very large.

5 Conclusion

To ensure the observability in bearing-only target tracking, in this paper, we proposed the dual-array algorithm for solving the underwater bearings-only target tracking problem, and extended Kalman filter algorithm was used for this problem. The computer simulations revealed that the EKF estimate yields good results and confirmed the effectiveness of the EKF in the tracking of underwater target under two sensors scenarios. Also the extended Kalman filter has lower computation complexity than other nonlinear and non-Gaussian filter algorithms, such as unscented Kalman filter (UKF), particle filter (PF) and other improved PF, so it is more suitable for addressing bearing-only target tracking problem and has high theoretical value and broad application prospects in practice.

Acknowledgements We would like to thank my tutor Ya'an Li for giving me many comments and all the friends who helped me. Also, many thanks to the sponsor of the National Natural Science Foundation of China (under 51179157 and 51179158) who has supported the research.

References

1. Foy WH (1976) Position-location solutions by Taylor series estimation. IEEE Trans Aerosp Electron Syst AES-12:187–194
2. Hassab JC (1976) Passive tracking of a moving source by a single observer in shadow water. J Sound Vib 44:127–145
3. Poirot JL, McWilliams GV (1976) Navigation by back triangulation. IEEE Trans Aerosp Electron Syst AES-12:270–274
4. Kolb RC, Hollister FH (1967) Bearings-only target motion estimation. In: Proceedings of the 1st Asilomar conference on circuits systems, pp 935–946
5. Murphy DJ (1970) Noisy bearings-only target motion analysis. Ph.D. Dissertation, Northeastern University, Boston, pp 25–29
6. Ristic B, Arulampalam S, Gordon N (2004) Beyond the Kalman filter: particle filters for tracking applications. Artech House, Boston/London, pp 103–108
7. La Scala BF, Mallick M, Arulampalam S (2007) Differential geometry measures of nonlinearity for filtering with nonlinear dynamic and linear measurement models. In: SPIE conference on signal and data processing of small targets, SPIE digital library, San Diego, California, USA, pp 28–30

8. Blackman S, Popoli R (1999) Design and analysis of modern tracking systems. Artech House, Boston/London, pp 30–36
9. Song TL (1996) Observability of target tracking with bearings only measurements. IEEE Trans Aerosp Electron Syst 32:1468–1471
10. Jauffret C, Pillon D (1996) Observability in passive target motion analysis. IEEE Trans Aerosp Electron Syst 32:1290–1300
11. Shar P, Li XR (1999) A practical approach to observability of bearings-only target tracking. In: Proceedings of SPIE. SPIE digital library, vol 3809, Denver, Colorado, USA, pp 514–520
12. Li XR, Jilkov VP (2003) A survey of maneuvering target tracking-part I: dynamic models. IEEE Trans Aerosp Electron Syst 39(4):1333–1364
13. Kalman RE (1960) A new approach to linear filtering and prediction problems. Trans ASME-J Basic Eng Autom Control 82:35–45
14. Julier S, Uhlmalll J, Durrant-Whyte HE (2000) A new method for the nonlinear transformation of means and covariant in filters and estimators. IEEE Trans Autom Control 45(3):477–482

Online Voltage Stability Prediction Based on Wide Area Measurement System

Qian Miao, Dun-wen Song, Feng Yan, Ya-nan Liu, and Shi-ying Ma

Abstract In order to do online voltage monitoring and stability margin judgment, a second exponential smoothing method is used in this paper to predict the node voltage amplitude. By using improved second exponential smoothing method and introducing the method of accumulated generating operation (AGO) to deal the date, to get a more accurate prediction result. For illustration, three disturbance examples in IEEE9 system are used to show the feasibility of the method. Empirical results show that the improved model with AGO can get a more accurate prediction result and can be used in the voltage amplitude prediction. And by introducing the prediction error feedback part make it correspond to the engineering application. Second exponential smoothing method using the wide area measurement system (WAMS) data can effectively predict the node voltage amplitude to help online voltage monitoring and stability margin judgment.

Keywords WAMS • Voltage amplitude prediction • Second exponential smoothing method • AGO. prediction feedback

1 Introduction

The expanding scale of the power grid and the increasing load brought a lot of problems, some of them imperil the security of power system. One of the most prominent one was the large area black out caused by voltage instability [1].

Q. Miao (✉) • F. Yan • Y.-n. Liu
Department of Electrical Engineering, North China Electric Power University, Bao Ding, China
e-mail: miaoqian126@126.com

D.-w. Song • S.-y. Ma
China Electric Power Research Institute, Beijing, China

W. Wang (ed.), *Mechatronics and Automatic Control Systems*, Lecture Notes in Electrical Engineering 237, DOI 10.1007/978-3-319-01273-5_23,

Because of the large amount of calculation and analysis and gradually not adapt to the development trend of modern power system, we should consider the online voltage stability control from the whole system. There were more scholars paid attention to online voltage stability monitoring after the year 2000 because of the several large area black out global happened. Online voltage stability index based on WAMS would gradually replace offline calculation and become the main method of power system dynamic monitoring. Under the electric power market mechanism, users put forward high demand of power quality also made it a must effectively solved problem [2].

In order to improve safety, reliability and flexibility, it is necessary to give online voltage monitoring and stability margin judgment. This paper used improved second exponential smoothing to give real-time online prediction of node voltage amplitude, adding the feedback part in the prediction process, make it correspond to the engineering application. It testified the precision of the reliable and practical value through the simulation in IEEE9 system.

2 The Application of WAMS in Voltage Stability Control

With the development of the extra-high voltage and national network interconnection project in China, the network of power system becoming larger and complex which make it more necessary to reinforce the reliability of power system, the dispatching institutions urgently need a way of reflecting dynamic behaviours of the large power grid.

WAMS was matching of available technology to dynamic information needs. It was a template for dynamic information, which provided a framework and testbed for associated efforts in which the WAMS participants drew together and refined a suite of information tools which meet the need to reinforce the reliability of power system.

2.1 Online Voltage Stability Monitoring and Prediction Based on WAMS

The voltage stability analysis method could be divided into two methods: static analysis method based on flow equation and dynamic analysis method based on state equation. At present, many scholars have focused on the commonly used method improved with synchronous phasor measuring unit, using the simplified two nodes equivalent system to estimate voltage stability [3]. It used π equivalent model and set the online voltage stability index and bus bar voltage stability monitoring index [4].

There were still not many references that did voltage stability prediction so far. It put forward to give the key node voltage surveillance, it was based on prior knowledge and experience, worth attention [5]. It deduced the voltage correlation form between the nodes through PQ decomposition method, so as to estimate the whole system node voltage based on the nodes installed PMU but the system was not completely observable [6].

2.2 *Node Voltage Amplitude Prediction Ideas*

If we could promptly forecast the development situation by using the real-time measurement information provided via WAMS and foresee potential risk, we could bring forward prevention and online control to prevent power system development deteriorating effectively [7]. Send the real-time data to computer center recorded by PMU, and then input data to a fixed width time window after the pre-treatment. Use data in the time window to do T steps voltage amplitude prediction. Add the feedback part in the prediction process, and give a error analysis between the prediction results and the new collected data before the T step time. When the prediction error met the accuracy requirement, outputting prediction results and considered that the prediction result is credible and could provide support for the voltage stability control, or shutting prediction results output link, then switching to the conventional voltage control process without the prediction. Here shutting prediction results output link was not mean to stop predict but still carry on the prediction, when prediction error reach the requirement unlocking the output function, provided prediction results. The premise of using feedback part was that the error analysis result output time must before the T step time points, otherwise the prediction lost its significance. The application of node voltage amplitude prediction process was shown in Fig. 1.

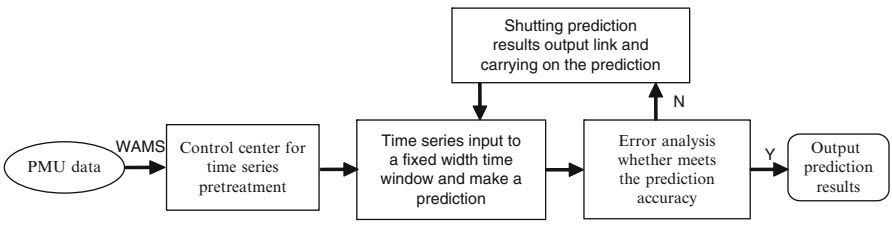

Fig. 1 The application process of node voltage amplitude prediction

3 Improved Exponential Smoothing Model

Second exponential smoothing method was appropriate for time series data that had the linear trend, its smoothing formula were [8]

$$S_t^{(1)} = \alpha y_t + (1-\alpha) S_{t-1}^{(1)} \tag{1}$$

$$S_t^{(2)} = \alpha S_t^{(1)} + (1-\alpha) S_{t-1}^{(2)} \tag{2}$$

Here $S_t^{(1)}$ was the first exponential smoothing value at the t time point; $S_t^{(2)}$ was the second exponential smoothing value; $S_{t-1}^{(2)}$ was the second exponential smoothing value at the t-1 time point; α was exponential smoothing coefficient; y_t was time series.

Its prediction expression was

$$\hat{Y}_{t+T} = a_t + b_t T \quad (T = 1, 2, \ldots) \tag{3}$$

$$a_t = 2S_t^{(1)} - S_t^{(2)} \tag{4}$$

$$b_t = \frac{\alpha}{1-\alpha}(S_t^{(1)} - S_t^{(2)}) \tag{5}$$

Here $\hat{Y}_{t+T}$ was the prediction value at the t + T time point.

In the traditional exponential smoothing method α was static. It put forward the exponential smoothing considered lag deviation and had the dynamic characteristics and could predict many steps [9]. This paper used this method and introduce the method of AGO to improve the prediction accuracy. Recursive expanding the exponential smoothing model [10].

$$\begin{aligned} S_t &= \alpha y_t + (1-\alpha) S_{t-1} \\ &= \alpha y_t + (1-\alpha)[\alpha y_{t-1} + (1-\alpha) S_{t-2}] \\ &= \alpha y_t + \alpha(1-\alpha) y_{t-1} \\ &\quad + (1-\alpha)^2 [\alpha y_{t-2} + (1-\alpha) S_{t-3}] \\ &= \cdots \\ &= \sum_{i=1}^{t} \alpha(1-\alpha)^{t-i} y_i + (1-\alpha)^t S_0 \end{aligned} \tag{6}$$

Supposing the time series had linear characteristics $y_t = a + bt$, substituted Eq. 6, could get

$$S_t^{(1)} = a + bt - \frac{1-\alpha}{\alpha} b + \frac{(1-\alpha)^{t+1}}{\alpha} b \tag{7}$$

$$S_t^{(2)} = a + bt - 2\frac{1-\alpha}{\alpha}b + 2\frac{(1-\alpha)^{t+1}}{\alpha} + bt(1-\alpha)^{t+1} \tag{8}$$

Then put them into a_t, b_t,

$$a_t = a + bt - bt(1-\alpha)^{t+1} \tag{9}$$

$$b_t = b - b(1-\alpha)^t(1+\alpha t) \tag{10}$$

So the prediction expression was Eq. 11

$$\hat{Y}_{t+T} = a + b(t+T) - b(1-\alpha)^t[(t+T) + (T-1)\alpha t] \tag{11}$$

4 Accumulated Generating Operation

The AGO came from the grey system theory was a basic method of data processing. It used "generation method" to get a new data sequence with randomness weakened and regularity enhanced characteristics.

Supposing $y^{(0)}$ was the original time series

$$y^{(0)} = \{y^{(0)}(1), y^{(0)}(2), \ldots, y^{(0)}(n)\},\ \forall y^{(0)}(i) \in R^+\ i \in [1,n]\ n \in N$$

Its first accumulated generating operation could be expressed as

$$y^{(1)} = \{y^{(1)}(1), y^{(1)}(2), \ldots, y^{(1)}(n)\},\ y^{(1)}(k) = \sum_{i=1}^{k} y^{(0)}(i)$$

Here k = 1,2,. . .,n, $y^{(1)}(1) = y^{(0)}(1)$.

The output data used AGO were not the true prediction results, we need a inverse accumulated generating operation to get the true results.

5 Simulation Analysis

Using IEEE9 to simulate voltage amplitude prediction, building the simulation model with PSD-BPA, using BPA simulation data instead of the data collected from WAMS, the simulation step was one cycle and simulation time length was 300 cycle.

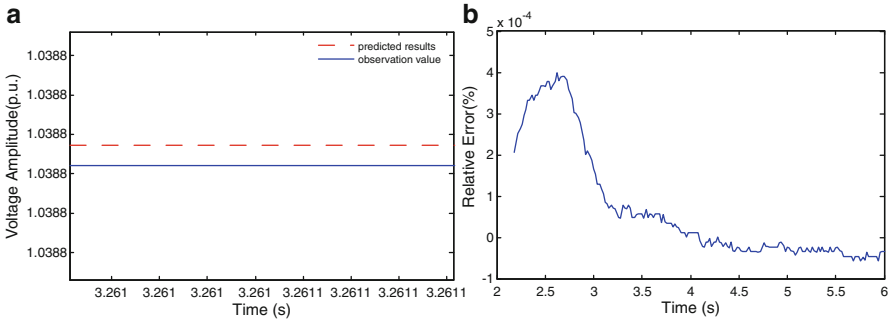

Fig. 2 Predicted values and observed value curve (**a**) and relative error curve (**b**)

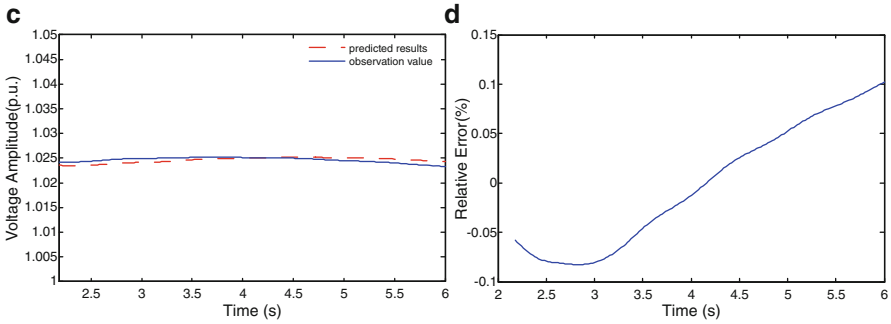

Fig. 3 Predicted values and observed value curve (**c**) and relative error curve (**d**)

5.1 Case 1

Simulating in stable state (case 1), predicted results curve and the observation value curve is shown in Fig. 2. Due to the two curves almost overlap, here (a) had given the partial enlargement figure.

Figure 2b shows that the relative error is very small, the orders of magnitude in 10^{-4}, so prediction result was accurate.

5.2 Case 2

Assume that the load of bus bar A increased (case 2), constant impedance active change the volume for A 25 MW, constant impedance load reactive change 14 MW, the operation time in the fifth cycle, output the bus bar 1 voltage amplitude prediction.

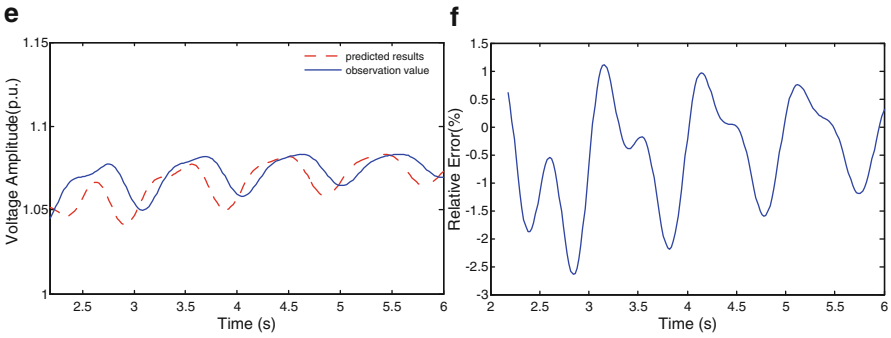

Fig. 4 Predicted values and observed value curve (**e**) and relative error curve (**f**)

Table 1 Prediction results analysis

Index	ME	MAD	MPE	MAPE	MSE	SDE
case 1*10-5	−0.0712	0.1025	−0.0685	0.0987	0.0000	0.1613
case 2*10-3	0.0260	0.5744	0.0252	0.0004	0.5607	0.6381
case 3	0.0054	0.0088	0.0050	0.0082	0.0001	0.0113
case 4	0.0021	0.0021	0.0020	0.0020	0.0000	0.0026
case 5	0.0034	0.0052	0.0034	0.0051	0.0001	0.0072
case 6	0.0032	0.0048	0.0032	0.0048	0.0000	0.0063
case 7*10-3	0.2574	0.2574	0.2474	0.2474	0.0001	0.2984

From Fig. 3d we could find the two tip relative errors were bigger than middle period, so it was necessary to shut prediction results output link and output voltage stability control only when the prediction error met the accuracy requirement. Under this occurs the largest relative error is 0.11 % and was a higher accuracy, so output the prediction results. When the system occurred serious fault, supposing there was a three-phase short-circuit (case 3) near bus bar A between bus bar A and bus bar 1, fault time at the fifth cycle, fault eliminated time at the tenth cycle, output the bus bar 1 voltage amplitude prediction as shown in Fig. 4e.

Because of bus bar 1 close to bus bar A, its voltage sharply fluctuated and made the prediction accuracy low. We could see the relative error curve in Fig. 4f that the lowest point reached 2.6 %, at this time shutting prediction results output link, then switching to the conventional voltage control process without the prediction.

In addition, simulating two phase short-circuit (case 4), single phase miss trip in three phase short-circuit (case 5), Single phase short-circuit permanent fault (case 6), three phase short-circuit temporary fault (case 7). Due to the limited of the article length did not show every fault curve and relative error curve, only listing the prediction results Analysis in Table.1. We could find that its various indexes were excellent.

6 Conclusion

This paper uses the improved second exponential smoothing method and introduces the method of AGO to deal the date. The improved exponential smoothing considered lag deviation, it had the dynamic characteristics and could predict many steps, improved forecasting precision. The AGO method can make the irregular sequence have a monotone trend, it increased the smoothness of the sequence, which made the prediction results more accurate.

The combination of the two methods made prediction accuracy greatly improved. Beside, considering the prediction failure, in order to avoid the error guidance to voltage control adding the feedback part in the prediction process, make it correspond to the engineering application.

References

1. Li Peng, Zhang Baohui, Hao Zhiguo, Shu Jin (2011) Voltage control based on power system equivalent model[J]. Electr Power Autom Equip 31(3):52–56, 61, In Chinese
2. Jia Xiu-fang, Zhao Xia (2007) Synthesis evaluating index of voltage quality in electricity market environment[J]. Power Syst Technol 31(11):59, 62, 68 (In Chinese)
3. Li Xing-yuan, Wang Xiu-ying (2003) Fast voltage stability analysis methods based on static equivalence and singular value resolution[J]. Proc CSEE 23(4):l–5 (In Chinese)
4. Gan Lei, Kang He-wen, He Min (2010) The dynamic monitoring of voltage stability based on wide-area measurement system[J]. Power Syst Prot Control 38(21):152–161 (In Chinese)
5. Duan Jun-dong, Sun Yan-kai, Yin Xiu-gang (2009) Voltage stability's online prediction using WAMS[J]. High Volt Eng 35(7):1748–1752 (In Chinese)
6. Deng Ji-yu, Liu Jun-yong (2011) A real-time voltage monitoring method based on hybrid SCADA/PMU system[J]. East China Electr Power 39(2):0226–0230 (In Chinese)
7. Yang Fang, Sun Yuan-zhang, Cheng Lin (2010) Real-time iteration based on-line coordinated voltage control[J]. Autom Electr Power Syst 34(7):6–10 (In Chinese)
8. Wu De-hui (2008) Dynamic exponential smoothing method and its applications[J]. J Syst Manage 17(2):151–155 (In Chinese)
9. Li Guang-jiu (1993) Linear model secondary exponential smoothing prediction method research[J]. Forecasting 6:53–54 (In Chinese)
10. Li Suo-ping, Liu Kun-hui (2003) Optimized dynamic exponential smoothing model and its applications. J Syst Eng[J] 18(2):163–167 (In Chinese)

A Multi-sensor Data Fusion Algorithm Based on Improved Kalman Filter

Changchun Tang, Zhigang Ao, Kangyi Zhang, and Youcheng Wang

Abstract Aiming to the handling issue of the multi-source information of joint training, a multi-sensor data fusion algorithm applicable for monitoring joint training is designed. On the basis of Kalman filter, this paper proposed an improved filtering algorithm which takes the quality of measurement data into consideration, a framework of data fusion system is provided based on the needs of algorithm, and this paper also improves the strategy of getting the weights for data fusion. The result of simulation shows that more accurate data can be achieved than any other single sensor measurements after fusing the multi-sensor data through this method.

Keywords Dada fusion • Oint training • Kalman filter • Correction coefficient

1 Introduction

During the joint training, sensor and any other monitoring equipment track and monitor the training process at the same time so as to obtain the multidimensional and panoramic situation data. These data are transferred to guidance and control centre of joint training for analysis and integration to form consistent description about target, thus providing strategic bases for guidance and control of situation analysis and training process. The process of conducting automatic detection, association, relevance, estimation and combination is called data fusion (DF) [1].

Kalman filter (KF) is one of the most widely applied methods for data fusion, which is minimum variance estimation, adopting state space to describe the system and recursive form to simplify calculation, while the data storage is small

C. Tang (✉) • Z. Ao • K. Zhang • Y. Wang
Engineering Institute of Corps of Engineers, People's Liberation Army University of Science and Technology, Nanjing, China
e-mail: 357502975@qq.com

W. Wang (ed.), *Mechatronics and Automatic Control Systems*, Lecture Notes in Electrical Engineering 237, DOI 10.1007/978-3-319-01273-5_24,

[2, 3]. Classic KF algorithm cannot adjust the affection degree of relevant information based on the quality of measurement data, as it does not consider the impact of time varying factors such as environment and technical conditions on the measurement accuracy of sensor, which influences the fidelity of data fusion to a certain degree. In the same time, adopting classic KF algorithm can easily get divergent because of the inaccurate system model, accumulation of round-off error, the deviation of interfering noise from white Gaussian noise, etc. This paper proposed an improved KF algorithm that is similar to attenuated memory filter by adding correction coefficient to filter gain, which is called SMAKF. Although SMAKF algorithm may reduce the optimal of filtering estimation, it makes the result of data fusion more close to the real value and restrains the divergence effectively. By combining the characteristics and needs of algorithm, this paper designs a system structure of multi-sensor data fusion based on SMAKF filter, and it also gives a formula to strike the weight of local estimation in the data fusion procedure, thus increasing the accuracy of data fusion.

2 System Model

As to the joint training of information system, it needs to conduct real-time monitoring on the state of trained objects, such as the precise location of personnel and equipment. The state of certain equipment at time k can be expressed as $X_k = (x_1(k), x_2(k), ..., x_m(k))^T$, during which each component represents the state information at the time of k, such as location, velocity and fault conditions and so on. The state of equipment involved in joint training can be controlled under the command of guidance and control centre, therefore the state transition process of equipment can be considered as a discrete system, where a deterministic control input exists. In brief, this paper assumes that this system is linear and expanded Karman Filter can be adopted for nonlinear system, and the system model is as follows [3]:

$$X_k = \Phi_{k\,|k-1} X_{k-1} + \Psi_{k\,|k-1} U_{k-1} + \Gamma_{k\,|k-1} W_{k-1} \tag{1}$$

Where $\Phi_{k\,|k-1}$ is $m \times m$ dimensional state transition matrix of the system, W_k is a p-dimensional systematic procedure noise sequence, $\{U_k\}$ is known non-random sequence, $\Psi_{k\,|k-1}$ and $\Gamma_{k\,|k-1}$ are respectively input matrixes of deterministic control and noise.

Assuming that n sensors or other monitoring equipments conduct monitor to certain equipment in joint training simultaneously and that all the sensors are controlled under the guidance and control centre of joint training. The measurement equation of sensor i can be expressed as:

$$Z^{(i)}{}_k = H^{(i)}{}_k X_k + M^{(i)}{}_k + V^{(i)}{}_k \tag{2}$$

Where ${Z^{(i)}}_k$ is n dimensional observation sequence of sensor i to system, ${H^{(i)}}_k$ is $n \times m$ dimensional observation matrix of sensor i, ${V^{(i)}}_k$ is a n dimensional measurement noise sequence and $\{{M^{(i)}}_k\}$ is known non-random sequence.

Assuming that both W_k and ${V^{(i)}}_k$ are noise sequences which possessing the distribution characteristics of white Gaussian noise and they satisfy the following relations:

$$E[W_k] = 0, \qquad E[W_k W_i^T] = Q_k \delta_{kj}; \qquad E[{V^{(i)}}_k] = 0;$$
$$E[{V^{(i)}}_k ({V^{(i)}}_j)^T] = {R^{(i)}}_k \delta_{kj}; \qquad E[W_k ({V^{(i)}}_j)^T] = 0.$$

During which δ_{kj} is the function of $Kronec\,\ker -\delta$, Q_k is non-negative variance matrix of W_k and ${R^{(i)}}_k$ is positive definite variance matrix of ${V^{(i)}}_k$.

3 The SMAKF Algorithm

The measuring accuracy of sensors may be affected by the environmental factors such as weather condition and terrain and human factors like technical conditions; accordingly, the contribution degree of measurement data to equipment state shall be adjusted. Meanwhile, in order to restrain the accumulation of round-off error, deviation of statistic property of noise and inaccurate model when using the filtering diffuse phenomenon by the use of classic KF algorithm, which draws on the algorithm property of attenuated memory filter and adjust the function of present measurement during the filtering process. This paper proposed an improved KF algorithm that is similar to attenuated memory filter by adding correction coefficient to filter gain (namely weighting of information) and taking overall consideration of relevant time varying factors on measurement accuracy of sensors, thus inhibiting the filtering divergence effectively [4, 5].

3.1 The Solution Process of SMAKF

With regard to linear discrete system with determinate control input described in the formula (1) and (2), the iteration solution procedure of SMAKF algorithm can be expressed as follows [6]:

Time update equations (prediction):

Project the state ahead:

$${\hat{X}^{(i)}}_{k|k-1} = \Phi_{k|k-1} \hat{X}_{k-1|k-1} + \Psi_{k|k-1} U_{k-1} \tag{3a}$$

Project the error covariance ahead:

$$P^{(i)}{}_{k\,|k-1} = \Phi_{k\,|k-1} P_{k-1\,|k-1} \Phi^{T}{}_{k|k-1} + \Gamma_{k\,|k-1} Q_{k-1} \Gamma^{T}{}_{k\,|k-1} \tag{3b}$$

Measurement update equations (correction):

Compute the innovation sequence:

$$\tilde{Z}^{(i)}{}_{k|k-1} = Z^{(i)}{}_{k} - M^{(i)}{}_{K} - H^{(i)}{}_{K} \hat{X}^{(i)}{}_{k\,|k-1} \tag{3c}$$

Compute the filtering gain:

$$G^{(i)}{}_{k} = S^{(i)}{}_{k} P^{(i)}{}_{k\,|k-1} (H^{(i)}{}_{k})^{T} [H^{(i)}{}_{k} P^{(i)}{}_{k\,|k-1} (H^{(i)}{}_{k})^{T} + R^{(i)}{}_{k}]^{-1} \tag{3d}$$

Update estimate with $\tilde{Z}^{(i)}{}_{k|k-1}$:

$$X^{(i)}{}_{k\,|k} = \hat{X}^{(i)}{}_{k\,|k-1} + G^{(i)}{}_{k} \tilde{Z}^{(i)}{}_{k\,|k-1} \tag{3e}$$

Update the error covariance:

$$\begin{aligned} P^{(i)}{}_{k\,|k} = {} & [I - [S^{(i)}{}_{k}]^{-1} G^{(i)}{}_{k} H^{(i)}{}_{k}] P^{(i)}{}_{k\,|k-1} + [I + H^{(i)}{}_{k} P^{(i)}{}_{k\,|k-1} (H^{(i)}{}_{k})^{T} \\ & + R^{(i)}{}_{k}] G^{(i)}{}_{k} [I - [S^{(i)}{}_{k}]^{-1}] \end{aligned} \tag{3f}$$

In the equation group (3a, 3b, 3c, 3d, 3e, and 3f), those symbols with superscript (i) refer to the local parameters of sensor i, and the others that without superscript (i) are overall parameters of the system. It can be observed that the major difference between classic KF algorithm and SMAKF algorithm is the way to strike the filtering gain. As shown in Eq. 3d, SMAKF give the gain ($G^{(i)}{}_{k}$) a correction coefficient $S^{(i)}{}_{k}$,it forwardly take the cost of increasing the filtering variance compare to classic KF, to restrain the filtering divergence and obtain the overall estimation that most close to the real value. When $S^{(i)}{}_{k}$ equate to I, the SMAKF algorithm degenerate into KF algorithm, and the error covariance become:

$$P^{(i)*}{}_{k\,|k} = [I - G^{(i)}{}_{k} H^{(i)}{}_{k}] P^{(i)}{}_{k\,|k-1} \tag{4}$$

3.2 The Correction Coefficient $S^{(i)}{}_k$

The role of correction factor $S^{(i)}{}_k$ is similar to the attenuation factor in attenuated memory KF, and the distinction between them is that attenuation factor refrain the filtering diffusion by artificially reducing the function of previous data, while the correction factor $S^{(i)}{}_k$ is amending the filter gain based on the advantages of present measurement value so as to increase the accuracy of data. In the existing related literature, the major method to strike the attenuation factor is from the perspective of restraining filtering diffusion and decreasing filter estimation variance, which lacks too much consideration on the actual and physical significance of filter estimation. This paper will strike $S^{(i)}{}_k$ based on the advantages and disadvantages of sensor measurement value and history of filtering process.

It only takes monitoring value of one single state (e.g. location) of the equipment through sensor for convenient narration. Providing $Z_k = (z^{(1)}{}_k, z^{(2)}{}_k, \ldots, z^{(n)}{}_k)$ is the set of measurement value under n sensors to one equipment at the time k, the expectation of Z_k ($E(Z_k)$ is the average of n measurement values, and the variance $\mathrm{var}(Z_k)$ can be obtained from formula (5):

$$\mathrm{var}(Z_k) = \frac{1}{n}\sum_{i=1}^{n}\left[z^{(i)}{}_k - E(Z_k)\right]^2 \tag{5}$$

The value of $\mathrm{var}(Z_k)$ differs from each other under different sampling times, depending on environment condition and other time-varying factors. $\mathrm{var}(Z_k)$ reflects the advantages of overall measurement value of n sensors, meanwhile, the larger the value, the more difficult to determine the accuracy of each sensor and achieve the consistent description of target state through Z_k. Therefore, in order to increase the accuracy of data fusion result, the weight of measurement value in filtering process shall be adjusted accordingly through $\mathrm{var}(Z_k)$, namely amending the filter gain. Obviously, correction filter $S^{(i)}{}_k$ has negative correlation with $\mathrm{var}(Z_k)$, and the complex mapping relation can be established as follows:

$$S^{(i)}{}_k \sim F(\mathrm{var}(Z_k), f_k{}^{(i)}(\cdot), k) \tag{6}$$

The composite mapping of formula (6) includes an unknown mapping $f_k{}^{(i)}(\cdot)$, which can be analyzed from various angles, if it is given by:

$$f_k{}^{(i)}(Z^{(i)}, \hat{X}) = \frac{1}{k-1}\sum_{t=1}^{k-1}\left[z^{(i)}{}_t - \hat{X}_{t|t}\right]^2 \tag{7a}$$

$$f_1{}^{(i)}(Z^{(i)}, \hat{X}) = \left[z^{(i)}{}_1 - \hat{X}_0\right]^2 \tag{7b}$$

Where $\hat{X} = \{\hat{X}_{t\,|t} | t = 1, 2, \ldots, k-1\}$ shows the overall filtering estimation of multi-sensors under the k situation, and the calculation method will be given below, and $\hat{X}_0$ is given initial filtering value; $Z^{(i)} = \{z^{(i)}{}_t | t = 1, 2, \ldots, k-1\}$ refers to the collection of measurement data of sensor i under the k situation. Therefore, the value of $f_k{}^{(i)}(Z^{(i)}, \hat{X})$ represents the measurement accuracy of sensor i, and the smaller the $f_k{}^{(i)}(Z^{(i)}, \hat{X})$, the more accurate of measurement value will be. It is easy to understand that the measurement value with higher accuracy should be given a greater weight value in the filtering process, namely that the filter gain shall be increased though correction factor.

In order to keep the optimality of filtering estimation, the value of $S^{(i)}{}_k$ shall be close to1 under the satisfied conditions. To sum up, the formula (6) can be adapted as follows:

$$\begin{aligned} S^{(i)}{}_k &\sim F(\mathrm{var}(Z_k), f_k{}^{(i)}(Z^{(i)}, \hat{X}), k) \\ &= 1 + \lambda \exp\left[\mathrm{var}(Z_k)^* f_k{}^{(i)}(Z^{(i)}, \hat{X})\right]^{-1} \end{aligned} \tag{8}$$

Where λ is characteristic parameter related with the value of $\mathrm{var}(Z_k) * f_k{}^{(i)}(Z^{(i)}, \hat{X})$.

4 The Multi-sensor Data Fusion Algorithm Based on SMAKF

SMAKF is an improved KF algorithm, which is designed for handling with the multi-sensor data fusion [7], and the measurement data of each sensor is filtered by the use of this algorithm, thus the local optimal estimation of target is obtained. Meanwhile, the optimal consistent description of overall information can be formed by using certain regulation to fuse it.

4.1 Architecture for Multi-sensor Data Fusion System Based on SMAKF

The measurement data of each sensor is filtered through SMAKF algorithm, which requires the overall parameters of multi-sensor data fusion system. In order to solve the information exchange matter during the algorithm implementation process, this paper designs one new multi-sensor data fusion architecture (as shown Fig. 1) based on SMAKF filtering, which lays foundation on the study of literature 6 and 7. This architecture is divided into three layers: perception layer, filter layer and fusion centre layer. In the perception layer, the original monitoring data collected through multi-sensors deliver to filter layer as well as data fusion centre. In the filter layer,

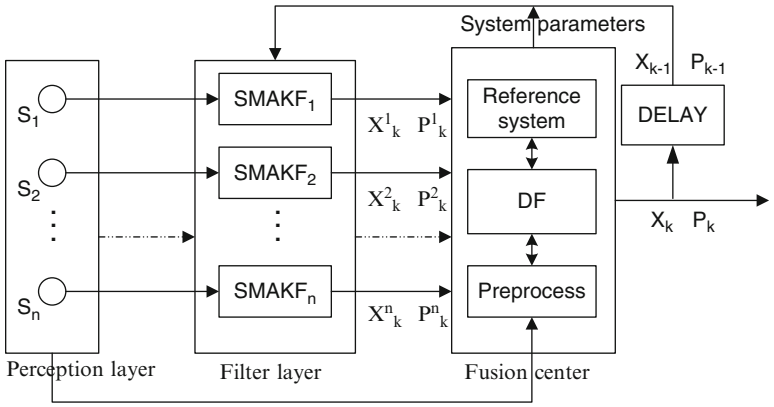

Fig. 1 Architecture for multi-sensor data fusion system based on SMAKF

each sensor has a local SMAKF sub-filter and the measurement data of every sensor is parallel processed to obtain a series of local optimal estimation. In the data fusion centre, the overall optimal estimation of measured object can be obtained based on certain rules and algorithm. In the mean time, fusion centre sends the global processing parameters to filter layer and provides necessary information parameter to SMAKF filter. This multi-sensor data fusion architecture with feedback makes full use of the information in each link and layer, and increases the accuracy of data fusion.

4.2 The Fusion Algorithm

The measurement data of each sensor is processed through local SMAKF filter, thus obtaining the local optimal estimation of measured target situation $\hat{X}^{(i)}{}_{k\,|k}$, and the error variance is $P^{(i)}{}_{k\,|k}$, the global estimation $\hat{X}^{(i)}{}_{k\,|k}$ is the result of weighted fusion for the local optimal estimation by giving each $\hat{X}^{(i)}{}_{k\,|k}$ a weight value $w^{(i)}{}_k$. Providing $P_{\max}(k) = \max\{P^{(i)}{}_{k\,|k}\ |i = 1, 2 \ldots n\}$, $P_{\min}(k) = \min\{P^{(i)}{}_{k\,|k}\ |i = 1, 2 \ldots n\}$, and define the formula (9) as follows [8]:

$$t_k(i) = [1 + P^{(i)}{}_{k\,|k} - P_{\min}(k)]^{-1} P_{\min}(k) \tag{9a}$$

$$h_k(i) = [1 + P_{\max}(k) - P^{(i)}{}_{k\,|k}]^{-1} P_{\max}(k) \tag{9b}$$

It is known that $t_k(i),\ h_k(i) \in (0, 1]$ refers to the error variance of sensor i filtering estimation, which is the appropriation degree between $P_{\min}(k)$ and $P_{\max}(k)$. Error variance reflects the accuracy of filtering estimation, and obviously the

filtering estimated value with higher accuracy can be offered with larger weight. Therefore, the value of ${w^{(i)}}_k$ shall increase with the value of $t_k(i)$ and decreases with the value of $h_k(i)$. Using the formula (10) to combine $t_k(i)$ with $h_k(i)$ 8 to obtain the weight value from the normalization of ${\gamma^{(i)}}_k$:

$$ {\gamma^{(i)}}_k = (t_k(i) + 1 - h_k(i))/2 \tag{10} $$

The weight value ${w^{(i)}}_k$ of weight fusion of ${\hat{X}^{(i)}}_{k\,|k}$ can be obtained from the normalization of ${\gamma^{(i)}}_k$:

$$ {w^{(i)}}_k = {\gamma^{(i)}}_k / \left(\sum_{j=1}^{n} {\gamma^{(j)}}_k \right) \tag{11} $$

The global estimation value of multi-sensor data fusion system can be described as follows:

$$ \hat{X}_{k\,|k} = \sum_{i=1}^{n} {w^{(i)}}_k {\hat{X}^{(i)}}_{k\,|k} \tag{12} $$

Providing the true value of measured target situation as X_k, and the error of global estimation is as follows [9]:

$$ \begin{aligned} \tilde{X}_k &= X_k - \hat{X}_{k\,|k} = X_k - \sum_{i=1}^{n} {w^{(i)}}_k {\hat{X}^{(i)}}_{k\,|k} \\ &= \sum_{i=1}^{n} {w^{(i)}}_k (X_k - {\hat{X}^{(i)}}_{k\,|k}) + \left(1 - \sum_{i=1}^{n} {w^{(i)}}_k \right) X_k \end{aligned} \tag{13} $$

Providing $\sum_{i=1}^{n} {w^{(i)}}_k = 1$, and then $\tilde{X}_k = \sum_{i=1}^{n} {w^{(i)}}_k (X_k - {\hat{X}^{(i)}}_{k\,|k})$. In general, ${\tilde{X}^{(i)}}_k = X_k - {\hat{X}^{(i)}}_{k\,|k}$ complies with normal distribution during several measurements or testing, the error is ${P^{(i)}}_{k\,|k}$, thus the error variance of global estimation is:

$$ P_{k\,|k} = \sum_{i=1}^{n} [({w^{(i)}}_k)^2 {P^{(i)}}_{k\,|k}] \tag{14} $$

5 Simulation and Analysis

The joint training is usually developed based on the fixed scheme, and the equipment situation shall be controlled by the previewed scheme and command centre, while the changing process is similar to the system mode of formula (1). Given the difficulty of collecting data, this paper simulates the conversion process of situation and measurement data of several sensors by the use of MATLAB process simulation. In order to simplify the procedure, the velocity change of equipment is only selected as object of study. Assuming that the equipment is on the complex terrain and designed with constant power control, and the initial velocity is 0; meanwhile assuming that ten sensors track and monitor the equipment, and that the data collection time is 10 min and sample interval is 6 s. Figure 2 shows the velocity changing process of simulated equipment, the original measurement data of sensor 2 and sensor 6, and it can be observed that the measurement error between these two sensors is large. Figure 3 reflects the result of data fusion by using KF and SMAKF filtering method respectively.

The simulation result shows that the measurement data is more accurate with the use of multi-sensor fusion data than adopting any other kinds of sensors. Considering the influence of relevant factors on measuring property of sensors, SMAKF can amend the filtering gain adaptively, thus the accuracy of handling data is higher than KF filtering algorithm. The Fig. 4 makes a comparison for the error of data fusion, reflecting that the average error is lower by using the method adopted by this paper.

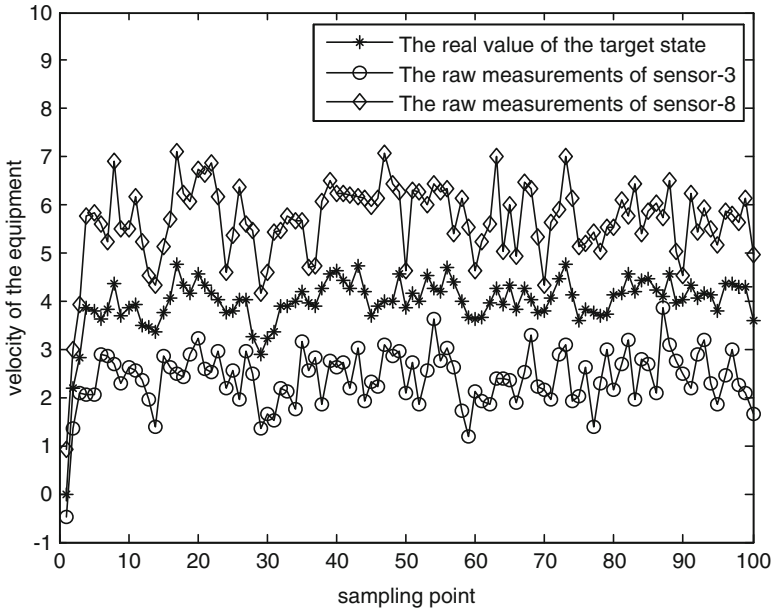

Fig. 2 The real value of the simulated equipment velocity and the raw measurement of sensor 3 and 8

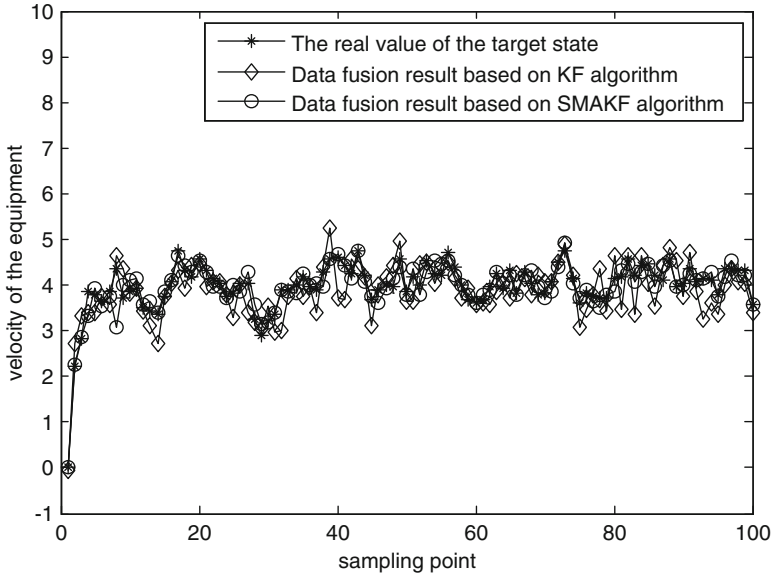

Fig. 3 The multi-sensor data fusion result

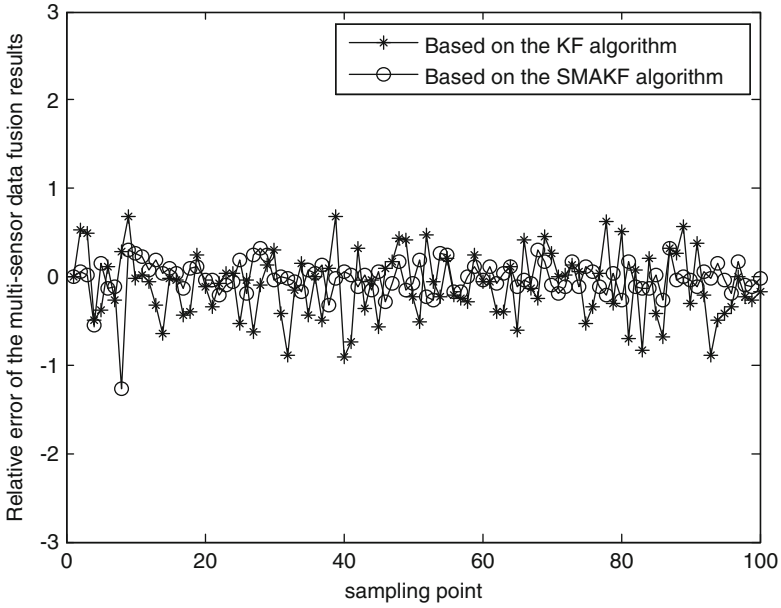

Fig. 4 The relative error comparison

6 Conclusion

With the development of Beidou navigation system and various sensor technologies, the monitoring devices of joint training also increase. In order to apply the collected multi-source situation information accurately, this paper proposes a set of multi-sensor data fusion algorithm that is suitable for monitoring joint training. This is an improved filtering algorithm based on KF algorithm, which is called SMAKF. In order to solve the matter of information exchange during the implementation of algorithm, a multi-sensor data fusion architecture based on SMAKF filter is designed. Besides, it also provides a formula to strike the weight value of local filtering estimation. The methods that this paper adopts can adjust the function of relevant information in the filtering estimation based on the quality of measurement data, make full use of the information in each link and increase the accuracy of data fusion. However, it is observed that this methods is not extremely stable mainly because the measuring way of correction factor is not accurate enough, which needs to be studied more deeply in the next step.

References

1. Varshney PK (1997) Multisensor data fusion. Electron Commun Eng J 9(6):245–253
2. Li HY, Li WJ, Huang YB (2011) Mulsensor measured data fusion based on Kalman filtering. Eng J Wuhan Univ 44(4):521–525
3. Fu MY, Deng ZH, Zhang JW (2003) Kalman filter theory and application in the navigation system. Science Publishing House, Beijing
4. Liu SJ, Guo L, Liu CJ, Zhu JZ (2004) Multiple hypothesis tracking algorithm based on memory atenuated filter. Signal Process 20(4):346–349
5. Ning XL, Li WB, Chen LH (2011) Multi-sensor information fusion based on federate particle filter. J Projectiles Rocket Missiles Guid 31(4):45–52
6. Al-Dhaher AHG, Mackesy D (2004) Multi-sensor data fusion architecture. In: HAVE 2004. Proceedings. The 3rd IEEE international workshop on haptic, audio and visual environments and their applications, Los Alamitos, CA, USA, pp 159–163
7. Li XR (2001) Comparison of two measurement fusion methods for Kalman-filter-based multi-sensory data fusion. IEEE Trans Aerospace Electron Syst 37(1):273–280
8. Guo Q, Yu SN (2006) Distributed multisensor data fusion based on Kalman filtering and the parallel implementation. J Shanghai Univ (English Edition) 10(2):118–122
9. Zhou XG, Zhang Q (2005) Comparison and improvement on similarity measures between vague sets and between elements. J Syst Eng 20(6):613–619

Heuristic Algorithm for the Ribonucleic Acid Pseudoknotted Structure Prediction

Zhendong Liu, Xuemei Hu, Zhipeng Zhang, Yuejun Li, and Hongluan Zhao

Abstract The paper further investigates the computational problem and complexity of predicting Ribonucleic Acid structure in order to find a way to optimize the Ribonucleic Acid pseudoknotted structure in electronics engineering. We investigate the Ribonucleic Acid pseudoknotted structure based on thermal dynamic model, computational methods and models with minimum free energy are adopted to predict Ribonucleic Acid structure. The contribution of this paper is to obtain an efficient algorithm for finding RNA pseudoknotted structure. Compared with other algorithms, the heuristic algorithm takes $O(n^3)$ time and $O(n^2)$ space. The experimental test in PseudoBase shows that the algorithm is more effective and exact than other algorithms, and the algorithm can predict arbitrary pseudoknots.

Keywords Pseudoknotted structure • Minimum free energy • Stem • Heuristic algorithm

1 Introduction

Molecular computing can be designed in integrated circuit. Ribonucleic Acid (RNA) is an important biomacromolecule which performs a wide range of function in biological system. RNAs are three-dimensional molecules, an RNA folds into a three-dimensional structure by forming pairs of bases, pseudoknots

Z. Liu (✉) • X. Hu • Y. Li • H. Zhao
School of Computer Science and Technology, Shandong Jianzhu University & Shandong University, Jinan, China
e-mail: liuzd2000@126.com

Z. Zhang
LuoNing Tobacco Monopoly Bureau, Luoning, China

W. Wang (ed.), *Mechatronics and Automatic Control Systems*, Lecture Notes in Electrical Engineering 237, DOI 10.1007/978-3-319-01273-5_25,

are known to exist in some RNAs. For predicting secondary structures with pseudoknots, Nussinov et al. (1978) have studied the case where the energy function is minimized when the number of basepairs is maximized and have obtained an $O(n^3)$ time algorithm for predicting RNA secondary structures [1], but Nussinov algorithm cannot predict pseudoknotted structure. Algebraic dynamic programming algorithm for finding RNA pseudoknotted structure with simple planar pseudoknots was proposed by Jens and Robert, the algorithm takes $O(n^4)$ time and $O(n^2)$ space [2]. Efficient algorithms for finding optimal foldings of an RNA structure have been known first by Michael Zuker [3]. Pknots algorithm for RNA pseudoknotted structure of predigesting model based on minimum free energy have presented by Rivas and Eddy, whose time complexity and space complexity are $O(n^6)$ and $O(n^4)$ respectively [4]. The problem for predicting RNA secondary structure including pseudoknots is NP-complete [5], and predicting RNA pseudoknotted structure with arbitrary pseudoknots is a NP-hard problem [6].in mimic RNA structure, pseudoknots are apparently exist [7]. A heuristic algorithm including pseudoknots for finding RNA pseudoknotted structures Jihong Ren [8].

The paper presents a new efficient algorithm including pseudoknots with thermal dynamic model and stable stems, and implement the algorithm in VC++ to complete the computation.

2 Heuristic Algorithm

2.1 Terminology

1. RNA: Ribonucleic Acid.
2. Let $S = s_1 s_2 \ldots s_i \ldots s_n$ be an RNA sequence, base $s_i \in \{A, U, C, G\}$, $1 \leq i \leq n$. The subsequence $s_{i,j} = s_i\, s_{i+1} \ldots s_j$ is a segment of S, $1 \leq i \leq j \leq n$.
3. MFE: Minimum Free Energy.
4. Stem: the RNA structure closed by base pairs (i, j) and $(k, l) \in S$, (i, j), (i + 1, j-1), . . ., (k, l) are base pairs, $i \leq k < l \leq j$.

2.2 The Dynamic Programming Algorithm

1. Given $s = s_1 s_2 \ldots s_n$, $s_{ij} = s_i \ldots s_j$, V(i,j) and W(i,j) can be computed, $1 \leq i < j \leq n$ (Fig. 1).

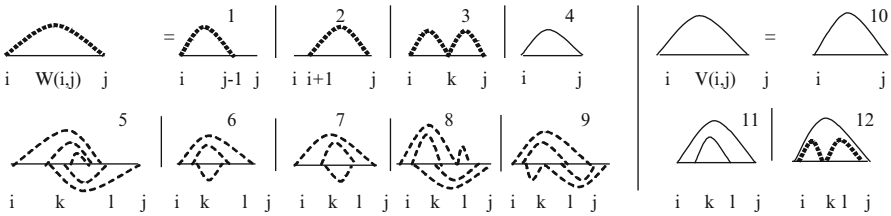

Fig. 1 The representation of W and V

$$V(i,j) = \min \begin{cases} E_1(i,j) \\ \min\{E_2(i,k:lj) + V(k.l)\}, i < k < l < j, u = (k-i+j-l) - 2 < U \\ \min\{W_M(i+1,h) + W_M(h+1j-1) + M + P\}, i < h < j < -1 \end{cases}$$

$$W_M(i,j) = \min \begin{cases} V(ij) + P, W(i+1j) + Q, W(ij-1) + Q \\ \min\limits_{i<k<j-1} \{W_M(i,k) + (j-k)Q, (k-i+1)Q + W_M(k+1,j), W_M(i,k) \\ + W_M(k+1,j)\} \end{cases}$$

$$W(i,j) = \min \left\{ V(i,j), W(i+1,j), W(i,j-1), \min_{i<k<j-1} (W(i,k) + W(k+1,j)) \right\}$$

Based on method of minimum free energy use the thermodynamic parameters of Turner, the algorithm can output the pseudoknotted structure.

3 Heuristic Algorithm

3.1 Algorithmic Design

1. Definition

$$E_p = M_1 S_b + M_2 P_b + M_3 N_b + M_4 + M_5$$

E_p is the total energy of an RNA pseudoknotted sequences. S_b is the total number of RNA pseudoknots, P_b is the total number of bases for RNA pseudoknotted sequences, N_b is the no base number of RNA pseudoknotted sequences, M_1 is the weight of RNA pseudoknots, M_2 is the weight of P_b, M_3 is the weight of N_b, M_4 is the weight of coaxial stack, M_5 is the weight of dangles bases (Figs. 2 and 3).

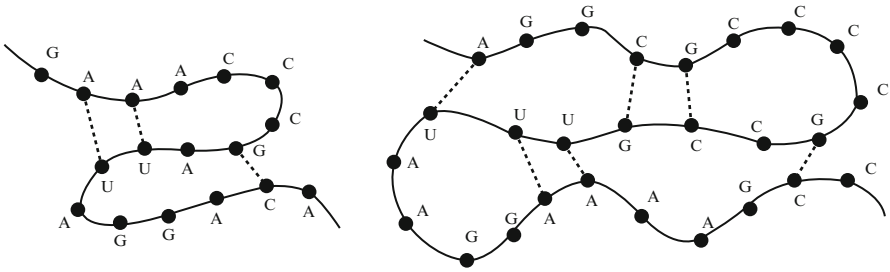

Fig. 2 Examples of pseudoknots

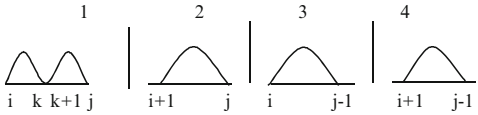

Fig. 3 The representation of dangle bases and coaxial stack

2. Heuristic Algorithm

Step 1 Calculate energy E of RNA sequence, $E = E_n + E_p$. E_n is the energy value of RNA nest structure, E_p is the energy of RNA pseudoknotted folding sequence.

Fill entry of A[i, j] to save energy value E and stems.

Step 2 S$\leftarrow \phi$, Va$\leftarrow \phi$, Pe $\leftarrow$ 0.

Define S as the m-stems which is finded in RNA structure, Define Va as the energy value in m-stems structure, structure Pe as the amount of RNA pseudoknots of E_{pseu}.

Step 3.1 For (i= 1; i $<=$ m;i++) (m = 36)

Find the prefix of i-stem.

For (j= 1; j $<=$ m;j++)

Find the suffix of j-stem.

Seek i-stem s_i which is relative maximum in RNA molecule according to the MFE.

Step 3.2 $v_i = \min \{v_0, v_1, v_2, \ldots, v_{n-1}\}$, the i-stem which is relative maximum is s_i, S $\leftarrow$ S$\cup\{s_i\}$, Va $\leftarrow$ Va$\cup\{v_i\}$.

Step 3.3 while (fd = 1) do

Mark the i-stem s_i which is relative maximum in RNA structure Seq, Seq $\leftarrow$ Seq -$\{s_i\}$.

Step 3.4 To search the stem s_j which is hypo-maximum in RNA structure Seq except the marked i-stem s_i which is relative maximum, S $\leftarrow$ S$\cup\{s_j\}$, Va $\leftarrow$ Va$\cup\{v_j\}$, until without i-stem in Seq.

Step 4 $S = \{s_0, s_1, s_2, \ldots, s_{n-1}\}$,$Va = \{v_0, v_1, v_2, \ldots, v_{n-1}\}$.

Step 5 Calculate the number P_n of pseudoknots in Seq.

Table 1 The comparison of HeuSearch algorithm and Pknots algorithm

	HeuSearch algorithm		Pknots algorithm	
Sequence	Specificity	Sensitivity	Specificity	Sensitivity
Mottle virus	98 %	100 %	95 %	100 %
Mosaic virus	97 %	89 %	96 %	90 %
Ringspot virus	93 %	91 %	88 %	86 %
Sapiens mRNA	76 %	71 %	67 %	63 %
Time complexity	$O(n^3)$		$O(n^6)$	
Space complexity	$O(n^2)$		$O(n^4)$	

The algorithm is called HeurSearch algorithm

Table 2 The comparison of algorithm HeuSearch and Pknots, MWM, ILM

	ILM		MWM		Pknots		HeuSearch	
Sequence	SN %	SP %	SN %	SP %	SN %	SP %	SN %	SP %
TYMV	100	82.9	100	63.3	100	96	97.9	98.6
DR7741	94.5	96.8	91.2	84.5	100	100	98.2	97.9
HIV-1-RT	100	100	100	92.7	100	95.5	100	96.7
BMV1	85.4	84.6	87.8	85.4	84.2	80.4	95.3	96.5
TMV-3′-up	81.3	83.9	68.1	41.6	52.1	59.2	87.6	88.3
TMV-3′-down	76.6	68.5	73.6	51.1	97.1	97.1	90.8	89.6
HDV	100	82.5	67.9	45.3	85.8	75.0	96.8	92.5
Anti-HDV	100	66.8	70.9	38.5	95.9	69.8	98.3	84.3
Average	93.8	82.5	83.2	53.6	87.1	84.6	95.2	90.1

Step 6 Calculate the energy value E_n and E_p
Step 7 Calculate the energy E according to E_{nest} and E_{pseu}.
Step 8 Save and Output S, E and P_n.

3.2 Experimental Analysis

In the experiment, we compute and analysis the energy value of i-stem with pseudoknots, refers to the energy parameters [9, 10]. Our algorithm can compute RNA pseudoknotted structure and stems in RNA sequences; we use the RNA sub-sequence in the PseudoBase and Rfam10.1 to compute experiment [11–13]. A much larger number of experiments on RNA pseudoknotted structure, our algorithm has above 88.5 % predicting accuracy. The heuristic algorithm may predict more than 1,700 nucleotides of RNA sequences. Possible effective ways to improve the prediction accuracy for long sequences are to be design, The prediction accuracy for long sequences descends with the increasing of the RNA bases (Tables 1 and 2).

We also performed experiments on reconstruction. Four RNA molecule experiments can be computed less than 50 s. accuracy of experiments is valuable, the prediction accuracy outperforms other algorithms, such as ILM algorithm [14],

MWM algorithm and PKNOTS algorithm etc. The RNA structural alignment is proved to be an efficient technique [15, 16] in the experiments.

The result of research in the paper has the engineering significance in biological pharmaceutical field. The stability of your algorithm is better than the related algorithm.

4 Conclusion

In order to realize the algorithm in the electronic circuit, the algorithm should reduce the time complexity and space complexity. HeurSearch algorithm can be completed with $O(n^3)$ time and $O(n^2)$ space. $O(n^4)$ time and $O(n^2)$ space are required in ILM Algorithm, with RNA pseudoknotted structure. The heuristic algorithm outperforms existing algorithms in sensitivity and specificity. The algorithm can compute arbitrary nested pseudoknots, and it can also compute crossed pseudoknots. The algorithm can compute nested structures and more complex pseudoknotted structures.

Acknowledgements Our work was supported by the NNSF of China under Grant No. 61272431, 61070019, 60970003 and the Natural Science Foundation of Shandong Province under Grant No. ZR2012GQ010.

References

1. Nussinov R, Pieczenik G, Griggs JR, Kleitman DJ (1978) Algorithms for loop matchings. SIAM J Appl Math 35(1):68–82
2. Reeder J, Giegerich R (2004) Design, implementation and evaluation of a practical pseudoknot folding algorithm based on thermodynamics. BMC Bioinformatics 5:104
3. Zuker M (1989) On finding all suboptimal foldings of an RNA molecule. Science 244:48–52
4. Rivals E, Eddy SR (1999) A dynamic programming algorithm for RNA structure prediction including pseudoknots. J Mol Biol 285:2053–2068
5. Lyngsø RB, Christian NS (2000) Pseudoknots in RNA pseudoknotted structure. In: Proceedings of Recomb, Tokyo Publishing, Tokyo, Japan, pp 201–209
6. Ieong S, Kao MY, Lam TW et al (2003) Prediction RNA pseudoknotted structures with arbitrary pseudoknots by maximizing the number of stacking pairs. J Comput Biol 6:981–995
7. Kolk MH, vanderGraff M, Wijmenga S et al (1998) NMR structure of a classical pseudoknots: interplay of single and double-stranded RNA. Science 280:434–438
8. Jihong R, Baharak R, Anne C et al (2005) HotKnots: heuristic prediction of RNA pseudoknotted structures including pseudoknots. RNA 11:1494–1504
9. Turner DH, Sugimoto N, Freier SM (1998) RNA structure prediction. Ann Rev Biophys Chem 17:167–192
10. Jaeger JA, Turner DH, Zuker M (1989) Improved predictions of pseudoknotted structures for RNA[J]. Proc Natl Acad Sci 86:7706–7710
11. Ruan J, Stormo GD, Zhang W (2004) An iterated loop matching approach to the prediction of RNA pseudoknott-ed structures with pseudoknots. Bioinformatics 20:58–66
12. http://www.bio.leidenuniv.nl/~Batenburg/PKBGet.html

13. Zhengdong Liu, Hengwu Li, Damig Zhu (2005) The predicting algorithm of RNA pseudoknotted structure for computing maximum stacking. J Nanjing Univ 41:532–537
14. Zhengdong Liu, Hengwu Li, Damig Zhu (2010) A predicting algorithm of RNA pseudoknotted structure based on stems. Kybernetes 39:1050–1057
15. Han B (2008) Structural alignment of pseudoknotted RNA. J Comput Biol 15:489–500
16. Wong TK (2011) Structural alignment of RNA with complex pseudoknot structure. J Comput Biol 18:97–108

An Advanced Method to Calculate Parameters of PSS Using the State Model

Wei Wang, Chongru Liu, Pengfei Tian, Zuowei Chen, and Haifeng Li

Abstract Low Frequency Oscillation (LFO) problems are caused by the lack of sufficient damping torque. Power System Stabilizer (PSS) is recognized as a practical and economical solution to eliminate the LFO. The phase compensation characteristics of the PSS are necessary to design the parameters of PSS properly. A method to obtain the parameters of PSS by using the information of the state-space matrix is proposed in this paper. The small signal model is used to provide the information to design the parameters of PSS. By using the left and right eigenvectors as well as the participation factors, the parameters of PSS can be calculated easily and fast. In this way, the parameters of PSS are calculated by linearization of the state model of power system. Simulation results show that the method provided in this paper is effective.

Keywords PSS • Low frequency oscillation • State model

1 Introduction

Recently, the fast controllable exciter is widely used in modern power plants. Therefore, time constants of its regulator decreases from tens of second to tens of millisecond. The responses of fast exciters to a disturbance are rapid to keep the generator voltage stable. However, the fast exciters weaken the small signal stability of power systems, especially the LFO problems. Practically, the oscillations always divide an inter-connected system into several independent parts, even with

W. Wang (✉) • C. Liu • P. Tian • Z. Chen • H. Li
State Key Laboratory for Alternate Electrical Power System with Renewable Energy Sources, North China Electric Power University, Beijing, China
e-mail: w.wei.ncepu@gmail.com

W. Wang (ed.), *Mechatronics and Automatic Control Systems*, Lecture Notes in Electrical Engineering 237, DOI 10.1007/978-3-319-01273-5_26,

the blackouts of the large-scale systems. The PSS has been widely used to solve the LFO problems by enhancing damping torque of the system [1–3]. The classic approach to design the parameters of PSS is a two-step procedure. At the first step, the value of the compensation phase is calculated; at the second step, parameters of each block of PSS are determined by using the method of modern control theory. There are many achievements on the determination of the parameters. A functional index considering the non-linearity of the power system is presented to optimize the parameters of PSS [4]. The PSS designed by this way can not only enhance the damping ratio under small-signal disturbance but also increase the stability under large disturbance. An approach to optimize parameters of PSS [5, 6] is introduced, which requires real-time data of generators. In another aspect, the prediction of the compensation phase is useful for the detection of the parameters of PSS. However, the research on the calculation of the value of the phase compensation is not sufficient yet.

An effective and fast calculation method to calculate the value of the compensation phase is proposed in this paper. Based on the linear state-space equations at the operating point, the value of the compensation phase could be calculated fast by using a basis of the eigenvector space. It is unnecessary to design an accurate value at each frequency point. PSS is only needed to work well at the specified frequency which associates with the LFO problem.

2 General Description of the State Model

The differential equations to represent the dynamic behaviour of the power system are highly nonlinear. The problem is very hard to solve. In order to represent the power system in linear state model form, it is necessary to establish the linear differential algebraic equations (DAE). After linearization, the linear DAE of the power system could be written as the following form,

$$\begin{cases} \dfrac{dx}{dt} = Ax + Bu \\ y = Cx + Du \end{cases} \tag{1}$$

where x is the vector of state variables, u is the vector of input variables and y is the vector of the output. The output in Eq. 1 is represented from the dynamic device side. In another hand, the output can also expressed by x and u from the network side, without considering its dynamic behaviors [7]. Linear algebraic equations for the network would be,

$$y = Ex + Fu \tag{2}$$

Submitting Eqs. 1 with 2, we have,

$$\begin{cases} \dfrac{dx}{dt} = Ax + Bu \\ 0 = C'x + D'u \end{cases} \tag{3}$$

where, $C' = C - E$ and $D' = D - F$. If the square matrix D' is invertible, vector x can be expressed by vector u, and the dynamic equations in Eq. 2 become,

$$\frac{dx}{dt} = \left[A - B\left(D'^{-1}\right)C'\right]x = A'x \tag{4}$$

where A' is the linear system matrix which reflects the interactions between elements in vector x.

According to the Lyapunov's law and the practical requirements of power system, the criterion to judge the small signal stability by eigenvalues of A' is:

(a) If all the eigenvalues have negative real parts (positive damping), the related system is stable under small disturbance;
(b) If there are more than one eigenvalues with positive real parts (negative damping), the related system is unstable under small disturbance;

3 The Relationship Between the Transfer Functions and the Eigenvectors

Define z as,

$$x = \Phi z \tag{5}$$

where $\Phi = [\varphi_1, \varphi_2, \ldots, \varphi_n]^{\mathrm{T}}$ is the right eigenvector matrix of the system and φ_1, $\varphi_2, \ldots, \varphi_n$ are the right eigenvectors corresponding to each eigenvalues. Assuming $\Lambda = \Phi^{-1}A'\Phi$, Λ is a diagonal matrix.

For a nth order system, the s-domain block diagram, which is one of the implementations of the nth state model described by Eq. 4, is shown in Fig. 1.

Assuming $T_{ik}(s)$ is the transfer function with x_k as motivation and x_i as response, the value of $T_{ik}(s)$ can be calculated by Eq. 6,

$$T_{ik}(s) = X_i(s)/X_k(s) \tag{6}$$

Assuming λ_l is the lth eigenvalue of the state mode; ϕ_{il} and ϕ_{kl} are the lth components of eigenvector φ_i and φ_k. $T_{ik}(\lambda_l)$ can be figured out by,

$$T_{ik}(\lambda_l) = \phi_{il}/\phi_{kl} \tag{7}$$

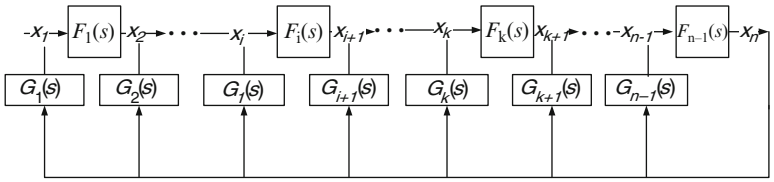

Fig. 1 Block diagram of *n*th system

4 The Calculation of Compensation Phase

Deficient damping usually causes LFO problems and PSS is an effective way to enhance the damping torque of the system. The measurements, representing the motion of rotors, are used as the input of the PSS. However, the PSS could not provide the damping torque itself, for it does not connect with rotor directly. Practically, an auxiliary input signal is added to the exciter by PSS to enhance the damping torque. According to the characteristics of generators, a phase shift between the output of exciter and the damping torque is caused because of the compensation of the PSS. To keep the damping torque provided by PSS and the speed of the generator in phase, a phase compensation block has to be included in PSS [8]. Figure 2 draws the structure of a typical excitation system with PSS,

According to the input signal of the PSS, there are several types of PSS with the input as the angular speed of rotors, the system frequency measured at the power plants and the electric magnetic power measured at the joint bus [9]. Figure 3 shows a transfer function block diagram of the PSS1A type, in which the input is the speed of generators.

In order to avoid the effects on the electric magnetic transient features of PSS, only the time constant of the phase compensation block is regulated to produce a desired compensation phase.

Assuming there are n generators in a power system, and the mth generator is related greatly to a LFO problem, which can be identified by lth eigenvalue λ_l. The mth generator is presented by a 4th state model. The electric magnetic torque $T^m{}_e$ can be calculated by Eq. 8.

$$\begin{aligned} T_e^m &= P_e^m = U_d^m I_d^m + U_q^m I_q^m \\ &= E_d^{m\prime} I_d^m + E_q^{m\prime} I_q^m - (X_d^{m\prime} - X_q^{m\prime}) I_d^m I_q^m \end{aligned} \tag{8}$$

where P_e^m is the electric magnetic power. By using Taylor expansion method, we know,

$$T_e^m \Big/ E_q^{m\prime} = K^m \tag{9}$$

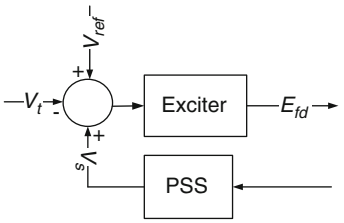

Fig. 2 Excitation system with PSS

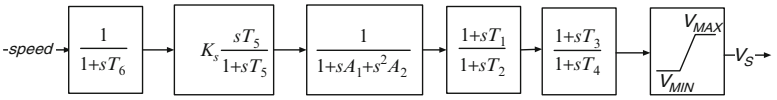

Fig. 3 Transfer functions of PSS1A

Since there is no phase shift between $T^m{}_e$ and $E^m{}_q'$, a damping torque can be introduced by components of $E^m{}_q'$. It is learned from the 4th state model of generator that $E^m{}_q'$ can be affected by the output of the exciter $E^m{}_f$. The transfer function $M^m{}_{q\text{-}fd}$ can be defined by,

$$M^m_{q-fd}(s) = E^{m\prime}_q \Big/ E^{m\prime}_f \tag{10}$$

Assuming $\alpha^m{}_{ex}$ is the phase shift that the output of exciter leads the input, $\alpha^m{}_{PSS}$ is the phase shift that the output of PSS leads the input, and $\alpha^m{}_{torque}$ is the phase shift that $T^m{}_e$ leads $E^m{}_f$. If Eq. 11 satisfied, PSS can provide a pure damping torque at the complex frequency identified by the eigenvalue λ_l.

$$\alpha^m_{\text{ex}}(\lambda_i) + \alpha^m_{\text{PSS}}(\lambda_i) + \alpha^m_{\text{torque}}(\lambda_i) = 0 \tag{11}$$

The value of a transfer function $T_{ik}(\lambda_l)$ between two arbitrary state variables can be calculated by Eq. 12. The $\alpha^m{}_{\text{torque}}$ of mth generator would be,

$$\alpha_{\text{torque}}(\lambda_i) = angle\left(\phi_{E'_q,i}(\lambda_i) \Big/ \phi_{E_f,i}(\lambda_i)\right) \tag{12}$$

where $\phi_{E^m{}_{q'},i}$ and $\phi_{E^m{}_{fd},i}$ represent the components of the eigenvector responding to eigenvalue λ_l, and $angle(X)$ is a function to find the phase of a complex number X. Therefore, the ideal compensation phase can be calculated by Eq. 14,

$$\alpha_{\text{PSS}} = -\alpha_{\text{torque}}(\lambda_i) - \alpha_{\text{ex}}(\lambda_i) \tag{13}$$

5 Applications and Validation

A single machine infinite bus system in PSCAD, shown in Fig. 4, is used to verify the effectiveness of the approach. The Timed Breaker Logic is used to implement a small disturbance at t = 1.0 *s* (parts of load cut from the system) in the model.

Parameters of the system are:

Generator:

$X_{\mathrm{d}} = 1.81\ pu, X_q = 1.76\ pu, X'_d = 0.3\ pu, X'_{\mathrm{q}} = 0.3\ pu, T'_d = 6\ s, T'_q = 6\ s$

Exciter (AC exciter with silicon controlled) (Fig. 5):

where $K_a = 200\ pu$, $T_a = 0.02\ s$, $T_B = 0\ s$, $T_C = 0\ s$

Network:

$X_{T1} = 0.1\ pu, X_{T2} = 0.25\ pu, X_{line} = 0.3\ pu$

Operating condition:

$V_t = 1.00(36\ ^\circ), P_G = 0.86\ pu, Q_G = 0.35\ pu$

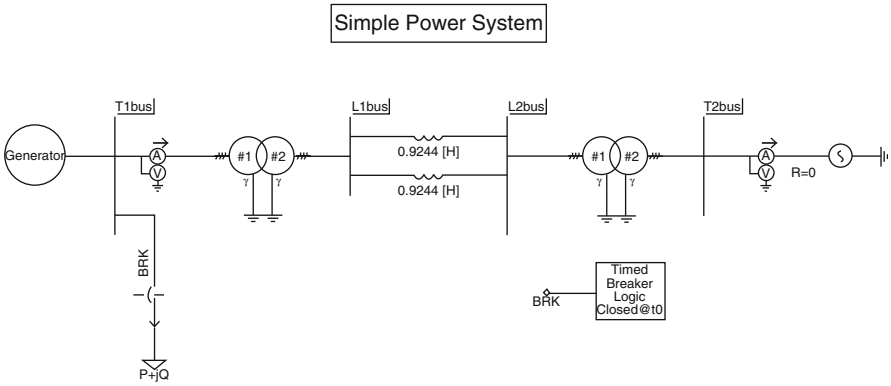

Fig. 4 The single machine infinite bus system

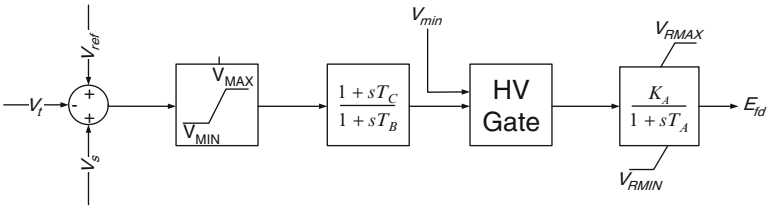

Fig. 5 The AC exciter model

Table 1 The eigenvalues associated with oscillation mode

Num	Eigenvalue	Mode	Damping ratio	Frequency (*Hz*)
1	0.547451 + j7.22642	1	−0.0755	1.1501
2	0.547451−j7.22642			
3	−25.1554 + j15.3856	2	0.8531	2.4487
4	−25.1554−j15.3856			

Base MVA:

$$S_{base} = 100\ MVA$$

In order to form the state model, the vector x is chosen to be $[\delta\ \omega\ E_q'\ E_d'\ E_{fd}]^{\mathrm{T}}$, in which δ is the angular position of the rotor, ω is the angular speed of the rotor, E_q' and E_d' are electromotive force associated with q- and d-axes and E_{fd} is the excitation voltage.

The result of the eigenvalues figures out that there exist two oscillation modes listed in Table 1. The frequencies of the two modes are 1.1501 and 2.4487 Hz, respectively. Further information about the small signal stability can be found by calculating the right and left eigenvectors, and participation factors, listed in Table 2.

The participation factors of δ and ω are much greater than others for mode 1. That is, only the mode 1 has strong relationship with the angle and velocity of generators. Hence, the mode 1 is related with LFO, while mode 2 does not. The damping ratio of mode 1 is negative. Therefore, the amplitude of the oscillation will increase, which will leads to the instability. Figure 6 proves the conclusion in PSCAD simulation.

According to Eq. 13, the $\alpha^m{}_{\text{torque}}$ is calculated when $s = 0.547451 + \text{j}7.22642$,

$$\begin{aligned}\alpha_{\text{torque}}(0.547451 + \text{j}7.22642) &= \frac{\phi_{E'_{q},i}(0.547451 + \text{j}7.22642)}{\phi_{E_{fd},i}(0.547451 + \text{j}7.22642)} \\ &= \frac{0.0047 - 0.0210\text{i}}{0.9974} = 0.0216\angle -77.3846^\circ \end{aligned} \quad (14)$$

The α_{ex} is calculated by parameters of the exciter, depicted by Fig. 5,

$$\alpha_{ex}(0.547451 + \text{j}7.22642) = 7.25\angle 8.22^\circ \quad (15)$$

Finally, the compensation phase of PSS is calculated below,

$$\alpha_{\text{PSS}}(0.547451 + \text{j}7.22642) = 77.3846^\circ - 8.22^\circ = 69.1646^\circ \quad (16)$$

The remaining work is to set the parameter of each part in Fig. 3. The design can be done with the method proposed. Hence, the parameters of the PSS1A are listed as follow:

Table 2 The participation factors of state variables

Mode	Freq (Hz)	δ	ω	E_q'	E_d'	E_{fd}
1	1.1501	*0.4788 ± 0.0362i*	*0.4788 ± 0.0362i*	0.0479 ± 0.0578i	0.0001 ± 0.0047i	0.0056 ± 0.0099i
2	2.4487	0.0214 ± 0.0020i	0.0214 ± 0.0020i	*0.4514 ± 0.7836i*	0.0001 ± 0.0000i	*0.5056 ± 0.7875i*

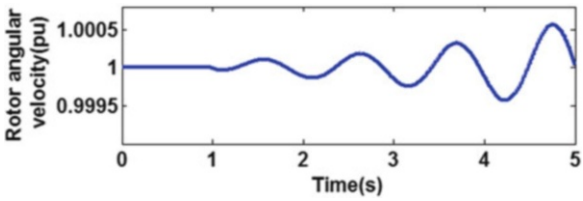

Fig. 6 The oscillation of ω without PSS

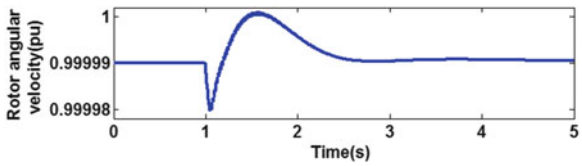

Fig. 7 The oscillation of ω with PSS

T1 = 0.05 s, T2 = 0.01 s, T3 = 0.3 s, T4 = 0.01 s, T5 = 10 s, T6 = 2 s, Ks = 5 pu, A1 = A2 = 0 s

Figure 7 shows the PSS obviously increases damping torque of the system and the maximum amplitude of the oscillation is halved.

6 Conclusion

An approach to calculate the compensation phase of PSS was proposed in the paper. The information of the power system at an operating point is necessary, which can be obtained from the linear system matrix. Generally, the LFO is always detected by using small signal analysis. Therefore, the method provided in this paper to calculate the compensation phase can be very convenient and efficient with linear system matrix of small signal analysis. The value of the compensation phase could be given directly by following the small signal analysis. A single machine infinite bus system is used to validate the approach. The time-domain simulation results showed that the PSS can damp the unstable oscillation mode well.

Acknowledgements This work was supported by National Natural Science Foundation of China (50807013), the Fundamental Research Funds for the Central Universities (10ZG02) and partially supported by "111" Project (B08013) of China.

References

1. ZHU Lian-li (2008) Application and designation of power system stabilizer (PSS)[J]. Xinjiang Elec Power Technol 4(1):9–11 (In Chinese)
2. CHEN Jun (2008) Experiments on power system stabilizer[J]. Xinjiang Elec Power Technol 3 (1):1–3 (In Chinese)

3. Xue Zhen-Yu, Fang Da-zhong, Yuan Shi-qiang (2011) Parameter optimization design of PSS based on functional sensitivity[J]. J South China Univ Technol 39(8):140–149 (In Chinese)
4. MAO Xiao-ming, CAI Yong-zhi, ZHAO Yong (2011) PSS parameter tuning based on phase characteristics of site measurements[J]. Elec Power Automat Equip 31(10):56–60 (In Chinese)
5. Chen Gang, Cheng Lin, Sun Yuanzhang (2011) Small signal excitation based online closed-loop setting method to multi-PSS parameters. Automat Elec Power Syst 35(5):5–9 (In Chinese)
6. Karawita C, Annakkage UD (2010) A hybrid network model for small signal stability analysis of power systems[J]. IEEE Trans Power Syst 25(1):443–451
7. Kundur P (1994) Power system stability and control[M]. McGraw Hill, New York, pp 699–822
8. https://www.pti-us.com/pti/software/psse/
9. SUN Yang-sheng (2007) The theory of automatic control, 4th edn. China Electric Power Press, Beijing, pp 156–186 (In Chinese)

Influence of Photovoltaic Random Output on Distribution Networks Node Voltage

Zhiqiang Li, Jianbing Meng, Shuqiang Li, Yazhou Zhang, and Zhenhua Kang

Abstract The output of photovoltaic power generator is constrained by the illumination time and intensity. According to the photovoltaic grid model, the PI and Photovoltaic system of photovoltaic power were handled by negative injection current law and the superposition of the compensation current law, at last using forward/backward substitution method to simulate the impact of photovoltaic power grid under different weather conditions on the system node's voltage. The algorithm can provide a basis for improving the quality of distribution network voltage, an effective reference and guidance in the actual running of the photovoltaic power system. Using IEEE 33 node system to build a simulation model, and analyzing simulation results, and results demonstrates the effectiveness and practicality.

Keywords Photovoltaic • Distributed generation • Back/forward sweep algorithm

Z. Li (✉)
Hebi Power Supply Company of Henan Provincial Electric Power Corporation, Henan, China
e-mail: kqiangren1@163.com

J. Meng
Puyang Longyuan electric design Corporation, Puyang Power Supply Company, Puyang, China

S. Li
School of Electrical Engineering, Zhengzhou University of Light Industry, Zhengzhou, China

Y. Zhang
Hefei Power Supply Company, Hefei, China

Z. Kang
Guodian Zhumadian Thermal & Power Co., Ltd, Zhumadian, China

W. Wang (ed.), *Mechatronics and Automatic Control Systems*, Lecture Notes in Electrical Engineering 237, DOI 10.1007/978-3-319-01273-5_27,

1 Introduction

For the contradiction between energy development and environmental protection has become increasingly prominent, the PV (Photovoltaic) system which can take into account as a strategic emerging industries of energy demand while avoiding environmental pollution has obtained a rapid development. After a mass of PV power or PV power with larger capacity were installed to the distribution network, the topology of the distribution network will change, and this leads to the traditional "passive" network to become an "active" network. Power flow is not necessarily only from the substation bus flow to the load, there may be against the tide and complexity of change in voltage. Besides the output power of photovoltaic power generation system is constrained by the light irradiation intensity and irradiation time, and this will impact distribution network node voltages further [1].

A paper described using numerical simulation techniques and modular design a numerical simulation system, which links the PV power to the distribution network, and refers the PV power to PQ node, and last it simulates the influence of the photovoltaic power to the distribution network's voltage under sunny condition, and makes corresponding analysis. But in the actual grid, node which connects photovoltaic power types need to be considered [2]. Another described the influence of distributed photovoltaic power on network, but it did not carry out the simulation analysis, and its conclusion can't be effective [3].

According to the random variation of characteristics of the photovoltaic power, this paper consider the photovoltaic power nodes as PV (constant active and voltage) or PI (constant active and current), and build the power flow calculation program of the weakly meshed distribution network containing photovoltaic powers, at last simulate the influence of PV power to system node under different weather conditions. Through the study of these new problems, it has important significance to improve the construction of photovoltaic power generation system, and expand its application in distribution network, and the study of the reliability of the entire distribution network.

2 The Influence of Light Intensity on the Photovoltaic

The photovoltaic cells are subject to the natural conditions [4], and the light condition affects the power output of photovoltaic cells directly. While light intensity due to rain, clouds, dust and other factors' influence, the power output has a certain random variation. Stochastic model of a photovoltaic cell can be established: in a period of time, light intensity is meet the Beta distribution, and the output of the photovoltaic cells is directly proportional to the light intensity, therefore, the output power of photovoltaic cells is meet the Beta distribution:

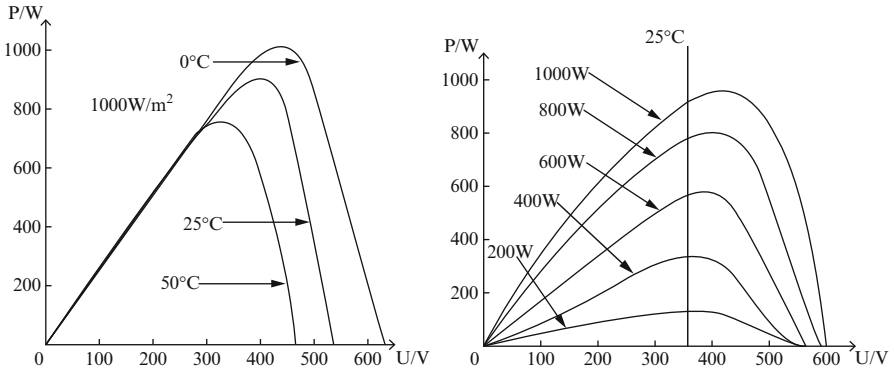

Fig. 1 Photovoltaic battery output performance (Under different temperature with same sunshine, Under normal temperature with different sunshine)

$$f(P_M) = \frac{\Gamma(\alpha+\beta)}{\Gamma(\alpha)\Gamma(\beta)}\left(\frac{P_M}{R_M}\right)^{\alpha-1}\left(1-\frac{P_M}{R_M}\right)^{\beta-1} \tag{1}$$

Where P_M and R_M are the actual output power and maximum output power, Γ is the Gamma function, α and β are Beta-distributed shape parameter, which can derivate from the average intensity μ and variance σ:

$$\alpha = \mu^*\left[\frac{\mu^*(1-\mu)}{\sigma^2} - 1\right] \tag{2}$$

$$\beta = (1-\mu)\left[\frac{\mu^*(1-\mu)}{\sigma^2} - 1\right] \tag{3}$$

The Volt-watt characteristic of typical photovoltaic is shown in Fig. 1.

From Fig. 1, we can get a conclusion that light intensity and temperature have a huge impact on photovoltaic cells' output, and the relation between of them is non-linear. The power generation is almost totally dependent on weather conditions, so the photovoltaic power's injection power is uncertainty. And the weather condition is the main reason of the distribution system voltage fluctuations.

3 Power Flow's Calculation with Photovoltaic Power

3.1 Equivalent Model of the Photovoltaic Power

When connects the Photovoltaic cells to the network, it can always run in the case of a power factor of 1[5], and can run in loss of part of the active power in distribution network, which is used to reactive power compensation by controlling

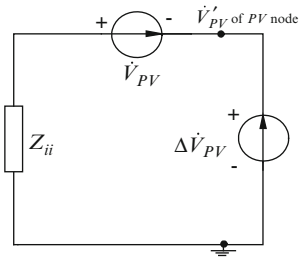

Fig. 2 Calculating I_{PV} equivalent circuit diagram

the inverter, to make the grid more stable and economic. So, the photovoltaic cells can be modeled by the inverter with a limited output. According to difference of control type, the inverter is divided into the current control and voltage control.

1. If the inverter is the current control type, the node is PI node with constant active power and constant current. In this condition, the injection power is:

$$Q = \sqrt{|I^2|(e^2 + f^2) - P^2} \tag{4}$$

   Thus, photovoltaic power can be taken as PQ node, which can be handled by the distribution network, by the formula (4). During flow calculation it is considered as load with the same power level and opposite direction, so its apparent power is $S = -P - jQ$, we get the injected current:

$$\dot{I} = [(-P - jQ)/(e + jf)]^* \tag{5}$$

   In formula (4) and (5), e and f are the real and imaginary part of the photovoltaic power supply voltage respectively.
2. For voltage-controlled inverter, the node is PV node with constant active power and voltage, the treatment of constant PV system is:

   In order to ensure that the PV node voltage amplitude and the active power of PV node unchanged during iteration, a voltage source could be added to PV nodes by injecting a certain current to make sure the value of PV node voltage amplitude equal to the set voltage amplitude, as shown in Fig. 2, if the node i is PV node, the calculations are as follows:

$$\Delta\dot{I}^{\mathrm{i}}_{PV} = Z^{-1}_{\mathrm{ii}} \times \Delta V_{PV} \tag{6}$$

$\Delta V_{PV} = V'_{PV} - |V_{PV}|$. $Z_{ii} = R_{ii} + jX_{ii}$. Where $\Delta\dot{I}^{\mathrm{i}}_{PV}$ is injected compensating current vector of PV node, ΔV_{PV} is the change of voltage amplitude of PV node, V'_{PV} is set value of voltage amplitude of PV node, V_{PV} is voltage vector of PV node, and Z_{ii} is the self-impedance of PV node. When the network has more than one PV node, Z_{ii} is an impedance matrix, the diagonal elements are the self-impedance of PV nodes, non-diagonal elements are the mutual impedance of PV nodes.

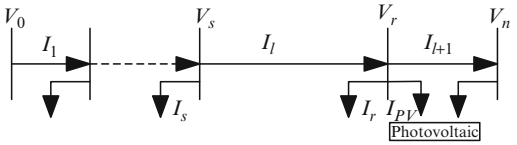

Fig. 3 Backward and forward sweep power flow calculation

3.2 Distribution Power Flow Calculation Method with PV System

Forward and backward substitution method is very useful in distribution network power flow calculation. This algorithm assumes that each node voltage is the root node voltage firstly, and then calculating the current or the beginning power of each branch in the radiation network, according to load power and the node voltage as known, from the end node. Then according to the root node voltage and obtained current or the beginning power to calculate the each branch's voltage form the first node to the end, the process is repeated until the iteration is convergence. Figure 3 is schematic with PV system by forward and backward substitution algorithm.

The specific process of distribution power flow with PV system using forward and backward substitution method is as follows:

1. Calculate the projected current

$$\dot{I}_i = \left(S_i/\dot{V}_i\right)^* \tag{7}$$

In the formula, $\dot{I}_i$ is projected current of the i node, S_i is projected power, and $\dot{V}_i$ is node voltage.

If this node is a photovoltaic power, the injection current is calculated as follows:

If the node's P and I is constant, then according to the formula (5) to solve the injection current; If the node's P and V is constant, then according to the formula (6) to solve the compensation current;

2. Calculate the current of each branch

Update the branch current using injection current: advancing to the root from the main trunk or branch lines, by assuming that the current is from the substation to the load, the branch current is just the simple sum of the branch current behind, as in Fig. 2, the current slip I:

$$\dot{I}_l = \dot{I}_{l+1} + \dot{I}_r + \dot{I}_{PV} \tag{8}$$

In the formula, $\dot{I}_l$ is the current of brunch l, $\dot{I}_{l+1}$ is the current of brunch $l+1$, $\dot{I}_r$ is the injected current of the r-node, and $\dot{I}_{PV}$ is the injected current of PV system.

3. Update the node's voltage with forward method
   When branch current calculation is finished, the forward method is to calculate the node's voltages. Starting from the root node, forward to the end of the main trunk and branch lines, and the voltage of substation power-saving is known, in Fig. 2, the voltage of the node r is:

$$\dot{V}_r = \dot{V}_s - Z_l \dot{I}_l \tag{9}$$

   In the formula, $\dot{V}_r$ is the voltage of the node r, $\dot{V}_s$ is the voltage of node s, and Z_l is the impedance of branch l.

4 The Influence of PV System on Distributed Network

After the PV system being connected to distribution network, the weather condition is an important factor that affects the distribution network node voltage. If a sudden decrease in proportion to the total load of photovoltaic generating capacity, the grid will appear power shortfall. If the shortfall exceeds a certain limit, it will have an adverse impact on voltage stability. When it is cloudy, the PV power output can be affected greatly, and generating power will appear rapid and dramatic changes. To illustrate the impact of random output of photovoltaic power systems to distributed network, the IEEE 33 node distribution system was tested. And the system network is as shown in Fig. 4; it contains 37 branches and five loops in total [6].

4.1 Verify the Correctness of the Algorithm

Program was developed by MATLAB to calculate the IEEE 33 node system, and its convergence precision is $\varepsilon = 10^{-6}$. The value of voltage reference is taken as 12.66 kV and power reference value is taken as 10 MVA. Figure 5 shows the simulation results of voltage. After comparing the value of each node voltage of the final iteration of the algorithm to other algorithm, it verifies that the proposed algorithm is correct.

4.2 Analysis of Flow Calculation Results

In order to simulate the randomness of the photovoltaic output influence on the distribution network, this article assumes that the network structure is fixed; the load size is also constant. Photovoltaic power capacity and type are shown in Table 1.

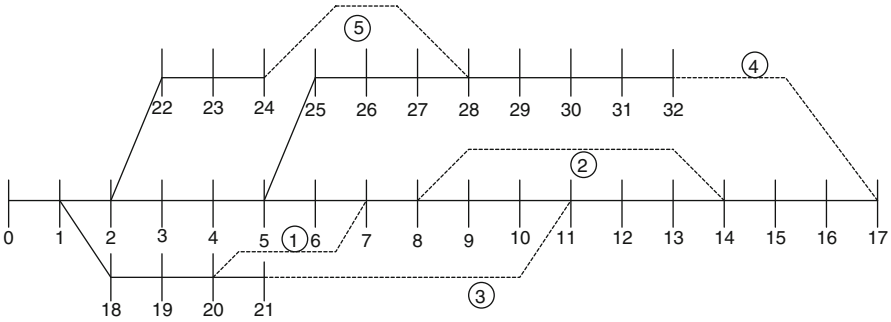

Fig. 4 The 33-bus distribution network system

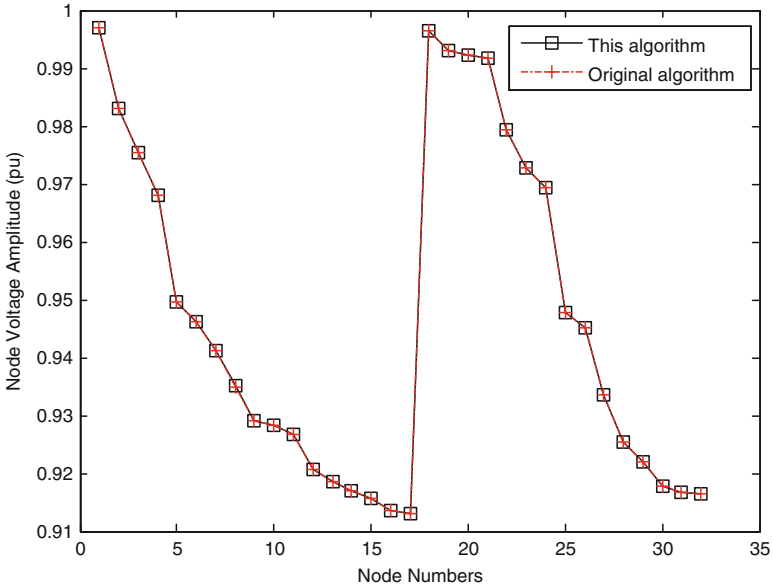

Fig. 5 Check the correctness of the algorithm

Table 1 The capacity and type of the photovoltaic

Case	Location	Weather	Parameter of photovoltaic power	Type
1.	9	Sunny	P = 100 kW, I = 50A	PI
2.	9	Cloudy	P = 100 kW, I = 50A	PI
3.	9	The night	P = 100 kW, I = 50A	PI
4.	9	Sunny	P = 100 kW, V = 12.66 kV	PV
5.	9	Cloudy	P = 100 kW, V = 12.66 kV	PV
6.	9	The night	P = 100 kW, V = 12.66 kV	PV

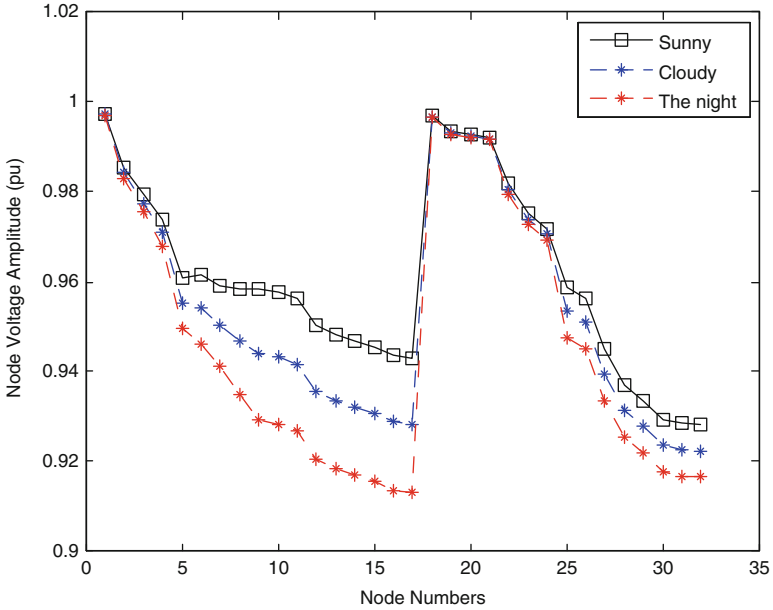

Fig. 6 Comparison of PI in different weather situation

Situation 1: the impact on the voltage of grid nodes in different weather conditions when photovoltaic power's P and I are constant

Figure 6 shows the simulation result of case1, case2, and case3. The voltage of the access point in case1 is 0.9586, and the lowest node voltage is 0.92816; the voltage of the access point in case2 is 0.9441, and the lowest node voltage is 0.9223; the voltage of the access point in case3 is 0.9292, and the lowest node voltage is 0.913.

Situation 2: the impact on the voltage of grid nodes in different weather conditions when photovoltaic power's P and U is constant

Figure 7 shows the simulation result of case4, case5, and case6. The voltage of the access point in case4 is 1.0014, and the lowest node voltage is 0.9645; the voltage of the access point in case5 is 0.9317, and the lowest node voltage is 0.92533; the voltage of the access point in case6 is 0.9292, and the lowest node voltage is 0.91.

5 Conclusion

This paper analyzes and builds the PI and PV mathematical models of photovoltaic power supply, at the same time, applies back/forward sweep algorithm with IEEE 33 test system to calculate power flow. The main conclusions are:

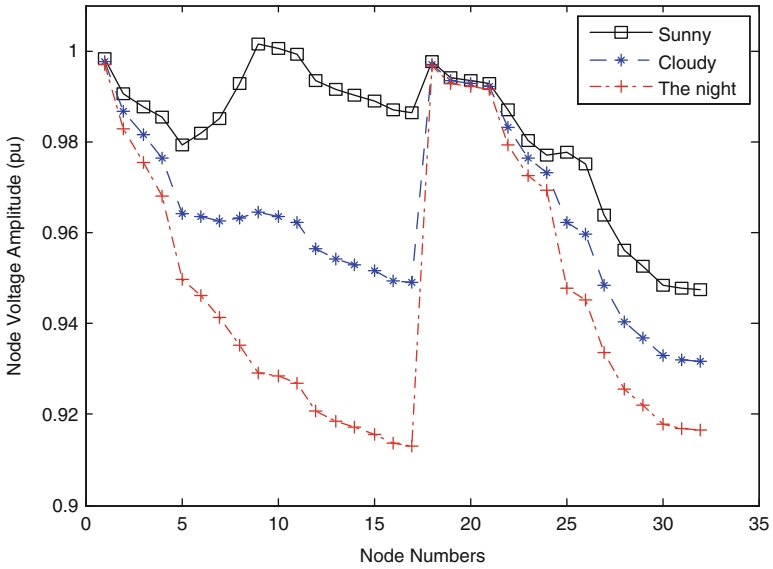

Fig. 7 Comparison of PV in different weather situation

1. Both PI type and PV type of photovoltaic power supply connection with grid will push up the Node voltage of access point and improve power supply quality of the whole network.
2. Different weather situation has different influence on photovoltaic power supply network. When the sun is enough, Photovoltaic power output is the largest; it will obviously improve the access point voltage. In the cloudy or sunshine mutations, Photovoltaic power output usually can only achieve the half of its rated output to support access point voltage. At night, photovoltaic power supply usually has no output and influence on the system.
3. Comparing Case 1 and Case 2, PV type is obviously better than the PI type in promoting node voltage effect, and the further the distance to the access point, the little influence to the node voltage.

References

1. Chen Cheng (2011) Analysis of impact of photovoltaic-connected on distribution system voltage profile[D]. North China Electr Power Univ, BaoDing
2. Fenghai Kou, Xiaorong Zhu, Xiaobo Duan et al (2011) Hourly simulation of distribution network voltage influenced by PV power sources[J]. Electr Power Sci Eng 27(3):5–9
3. Bo Zhao (2010) A study on the impact of the large-scale distributed photovoltaic power on the distribution grid system[J]. Zhejiang Electr Power 29(6):5–8

4. Abouzahr I, Ramakumar R (1993) An approach to assess the performance of utility-interactive photovoltaic systems[J]. IEEE Trans Energ Convers 8(2):145–153
5. Xin Li, Yi Peng, Jingjing Zhao et al (2009) Power flow calculation of distribution network with distributed generation[J]. Power Syst Prot Control 37(17):78–81
6. Shouxiang W, Chengshan W (2007) Modern distribution system analysis[M]. Higher education press, Beijing, pp 110–150

Cubature Particle Filter Algorithm Base on Integrated Navigation System

Qiurong Li and Feng Sun

Abstract In this research work, we study on the Cubature Particle filter (CPF) algorithm to calculate the estimate value of GPS/INS integrated navigation system. The error model of the GPS/INS integrated navigation system is nonlinear. CPF is the algorithm built on Cubature Kalman filter (CKF) and Particle filter (PF), which has the advantages of both. CPF may therefore provide a systematic solution for high-dimensional nonlinear filter problems. CPF is presented for simulation. Simulation results show the superior performance of this approach when compared with suboptimal techniques such as Cubature Kalman filter (CKF) in cases of large initial misalignment. The results of simulation demonstrate the improved performance of the CPF over conventional nonlinear filters. The research provides theoretical support for engineering design and modification.

Keywords Cubature rule • Cubature Kalman Filter(CKF) • Cubature Particle filter (CPF) • Integrated navigation

1 Introduction

Filter plays a very important role in the actual systems. In the real world, almost all systems have nonlinear characteristics. Deeply understand the essence of the nonlinear system, reasonably establishes the system model, the nonlinear filtering method effectively helps to analyze and solve all kinds of problems encountered in engineering practice.

Q. Li (✉)
College of National Defense Education, Harbin Engineering University, Harbin, China
e-mail: liqiurongrong@163.com

F. Sun
College of Automation Harbin Engineering University, Harbin, China

W. Wang (ed.), *Mechatronics and Automatic Control Systems*, Lecture Notes in Electrical Engineering 237, DOI 10.1007/978-3-319-01273-5_28,

Kalman filter (KF) is the optimal filter used to estimate linear system [1]. The GPS/INS navigation system usually uses the Kalman filter to estimate the state of the system [2, 3]. The simple calculation, recursive structure, and mathematical rigour of the derivation of the Kalman filter make it suitable and attractive for use in plenty of practical applications. However, lots of real-world systems are nonlinear in nature. The extended Kalman filter (EKF) is developed to help account for these nonlinearities. But EKF is a suboptimal nonlinear filter due to the truncation of the higher-order terms when linearizing the system [4, 5]. The computational time of the EKF is similar to that of the Kalman filter [6].

Cubature Kalman filter (CKF) is a nonlinear filtering method without linearization of nonlinear model [7]. The CKF algorithm is unbiased and minimum variance, which is better than the EKF method in GPS/INS dynamic system [8]. The CKF is suggested for debasing lineariation bias for the nonlinear measurement eqziations [9]. Physical systems are often subjected to unexpected deviations or failures [10]. As a result, it is important to have a method in order to maintain an accurate and reliable solution [11]. Cubature Kalman Filter (CKF) algorithm is introduced into the particle filter (PF) framework in papers [12].

Inertial navigation system (INS) is one kind of autonomous navigation system. It can supply not only continuous vehicle position and velocity information but also three axes attitude. Global Position System (GPS), which was developed in 1980s, can supply accurate position and velocity information at any time in any place. Its characters lead itself to be more and more widely used for vehicles navigation in air, sea and land. By integrating the merits of GPS and INS, the GPS/INS integration system will improve navigation accuracy and reliability.

2 Cubature Particle Filter

The dynamic state space model of discrete form can be expressed as [7]:

Process equation:

$$\boldsymbol{x}_{k+1} = \boldsymbol{f}_k(\boldsymbol{x}_k, \boldsymbol{u}_k) + \boldsymbol{w}_k \tag{1}$$

Measurement equation:

$$\boldsymbol{z}_k = \boldsymbol{h}_k(\boldsymbol{x}_k) + \boldsymbol{v}_k \tag{2}$$

Where $\boldsymbol{x}_k$ is the state of the dynamic system at discrete time k; $\boldsymbol{f}_k(\bullet)$ and $\boldsymbol{h}_k(\bullet)$ are some known functions; $\boldsymbol{u}_k$ is the known control input; $\boldsymbol{z}_k$ is the measurement; $\boldsymbol{w}_k$ and $\boldsymbol{v}_k$ are independent process and measurement Gaussian noise sequences with zero rueans and covariances, respectively.

In the Bayesian filtering paradigm, the posterior density of the state provides a complete statistical description of the state at that time. On the receipt of a new measurement at time k, we update the old posterior density of the state at time $(k-1)$ in two basic steps: time update and measurement update.

Consider a multiple integral of the following form

$$I(f) = \int_{R^n} f(x)w(x)dx \tag{3}$$

Where $f(\bullet)$ is arbitrary function, $w(x) \geq 0$ $(x \in R^n)$. Usually the analytical value of above integral cannot be obtained and need to get the approximate value by numerical integration. We can select a set of points with weights (ξ_i, ω_i) to approximate the integral $I(f)$

$$I(f) \approx \sum_{i=1}^{m} \omega_i f(\xi_i) \tag{4}$$

Recently, Canadian scholars [7] proposed CKF based on spherical-radial criterion to choose the above point set, the specific derivation process can be reference [7]. CPF choose 2n (n stands for state dimension) cubature points with the same weights through spherical-radial criterion.

$$\xi_i = \sqrt{\frac{2n}{2}}[1]_i \tag{5}$$

$$\omega_i = \frac{1}{2n}, i = 1, 2, \ldots, 2n \tag{6}$$

Where $[1]_i$ shows the i column of set $[1]$. For the two dimensional, namely $n = 2$:

$$[1] = \left\{[1,0]^T, [-1.0]^T, [0,-1]^T [0,1]^T\right\} \tag{7}$$

After calculating point set (ξ_i, ω_i), CPF algorithm can be acquired through time updating and measurement updating.

The pseudo-code for the CPF is summarized as follows:

1. Initialization:

$$\begin{cases} \hat{\boldsymbol{x}}_0 = \mathrm{E}(\boldsymbol{x}_0) \\ \boldsymbol{P}_0 = \mathrm{Cov}\left(\boldsymbol{x}_0, \boldsymbol{x}_0^{\mathrm{T}}\right) = \mathrm{E}\left[(\boldsymbol{x}_0 - \hat{\boldsymbol{x}}_0)(\boldsymbol{x}_0 - \hat{\boldsymbol{x}}_0)^{\mathrm{T}}\right] \end{cases}. \tag{8}$$

2. Time Update:

$$\boldsymbol{P}_{k-1} = S_{k-1}S_{k-1}^{T} \ (k = 1, 2, \ldots, \infty) \tag{9}$$

$$\chi_{i,k-1} = S_{k-1}\xi_i + \hat{x}_{k-1} \tag{10}$$

$$\chi_{i,k|k-1} = f\left(\chi_{i,k-1}\right) \tag{11}$$

$$\hat{\boldsymbol{x}}_{k|k-1} = \sum_{i=1}^{m} \chi_{i,k|k-1}/m \tag{12}$$

$$P_{k|k-1} = \sum_{i=1}^{m} \chi_{i,k|k-1}\chi^{T}{}_{i,k|k-1}/m - \hat{\boldsymbol{x}}_{k|k-1}\hat{\boldsymbol{x}}_{k|k-1}^{T} + Q_{k-1} \tag{13}$$

3. Measurement Update:

$$P_{k|k-1} = S_{k|k-1}S_{k|k-1}^{T} \tag{14}$$

$$\chi^{*}{}_{i,k|k-1} = S_{k|k-1}\xi_i + \hat{x}_{k|k-1} \tag{15}$$

$$Z_{i,k} = h\left(\chi^{*}{}_{i,k|k-1}\right) \tag{16}$$

$$\hat{z}_k = \sum_{i=1}^{m} Z_{i,k}/m \tag{17}$$

$$P_{zz} = \sum_{i=1}^{m} Z_{i,k}Z^{T}{}_{i,k}/m - \hat{\boldsymbol{z}}_k\hat{\boldsymbol{z}}_k^{T} + R_k \tag{18}$$

$$P_{xz} = \sum_{i=1}^{m} \chi^{*}{}_{i,k|k-1}Z^{T}{}_{i,k}/m - \hat{\boldsymbol{x}}_{k|k-1}\hat{\boldsymbol{z}}_k^{T} \tag{19}$$

$$W_k = P_{xz}P^{-1}{}_{zz} \tag{20}$$

$$\hat{\boldsymbol{x}}_k = \hat{\boldsymbol{x}}_{k|k-1} + W_k(z_k - \hat{\boldsymbol{z}}_k) \tag{21}$$

4. Filter Update:

$$\begin{cases} \hat{\boldsymbol{x}}_{k+1} = \hat{\boldsymbol{x}}_{k+1|k} + \boldsymbol{K}_{k+1}\left(\boldsymbol{z}_{k+1} - \hat{\boldsymbol{z}}_{k+1|k}\right) \\ \boldsymbol{K}_{k+1} = \boldsymbol{P}_{\tilde{\boldsymbol{x}}_{k+1}\tilde{\boldsymbol{z}}_{k+1}} \boldsymbol{P}_{\tilde{\boldsymbol{z}}_{k+1}}^{-1} \\ \boldsymbol{P}_{k+1} = \boldsymbol{P}_{k+1|k} - \boldsymbol{K}_{k+1} \boldsymbol{P}_{\tilde{\boldsymbol{z}}_{k+1}} \boldsymbol{K}_{k+1}^{T} \end{cases}. \tag{22}$$

3 System Model

In the east-north-up navigation reference frame,

$$\begin{aligned} \boldsymbol{x}(t) = &[\varphi_{\mathrm{E}}\ \varphi_{\mathrm{N}}\ \varphi_{\mathrm{U}}\ \delta V_{\mathrm{E}}\ \delta V_{\mathrm{N}}\ \delta V_{\mathrm{U}}\ \delta L\ \delta\lambda\ \delta H \\ &\varepsilon_x\ \varepsilon_y\ \varepsilon_z\ \boldsymbol{\Delta}_x\ \boldsymbol{\Delta}_y\ \boldsymbol{\Delta}_z]^{\mathrm{T}} \end{aligned}$$

where $\boldsymbol{x}(\boldsymbol{t})$ is an 15-dimensional system state vector; $\varphi_{\mathrm{E}}, \varphi_{\mathrm{N}}, \varphi_{\mathrm{U}}$ are vehicle's attitude rotation vector errors; $\delta V_{\mathrm{E}}, \delta V_{\mathrm{N}}, \delta V_{\mathrm{U}}$ are velocity errors; $\delta L, \delta\lambda, \delta H$ are latitude error, longitude error and height error separately; $\varepsilon_x, \varepsilon_y, \varepsilon_z$ are gyro constant drifts; and $\boldsymbol{\Delta}_x$, $\boldsymbol{\Delta}_y, \boldsymbol{\Delta}_z$ are accelerometer zero errors .

The system state error model can be described as follows.

(a) Attitude error equations can be determined by

$$\dot{\boldsymbol{\varphi}} = \boldsymbol{\delta\omega}_{ie}^{t} + \boldsymbol{\delta\omega}_{et}^{t} + (\boldsymbol{I} - \boldsymbol{C}_{t}^{p})(\boldsymbol{\omega}_{ie}^{t} + \boldsymbol{\omega}_{et}^{t}) + \hat{\boldsymbol{C}}_{b}^{t}\boldsymbol{\varepsilon}^{b} \tag{23}$$

(b) Velocity error equations can be described as

$$\delta\dot{V}^{t} = C_{t}^{p}\hat{f}^{b} - (2\delta\boldsymbol{\omega}_{ie}^{t} + \delta\boldsymbol{\omega}_{et}^{t}) \times V^{t} - (2\boldsymbol{\omega}_{ie}^{t} + \boldsymbol{\omega}_{et}^{t}) \times \delta V^{t} + C_{p}^{t}\hat{C}_{b}^{t}\Delta^{b} \tag{24}$$

(c) Position elTor equations can be described as

$$\begin{cases} \delta\dot{L} = -\dfrac{\delta V_{\mathrm{N}}}{R_{\mathrm{M}} + H} \\ \delta\dot{\lambda} = \dfrac{\delta V_{\mathrm{E}}}{R_{\mathrm{N}} + H}\sec L - \dfrac{V_{\mathrm{E}}\sec L}{R_{\mathrm{N}} + H}\boldsymbol{tan}L\delta L \\ \delta\dot{H} = \delta V_{\mathrm{U}} \end{cases}. \tag{25}$$

(d) Error equations can be described as

$$\begin{cases} \boldsymbol{\varepsilon}^{b} = \boldsymbol{\varepsilon} + \boldsymbol{\omega}_{\varepsilon} \\ \boldsymbol{\Delta}^{b} = \boldsymbol{\Delta} + \boldsymbol{\omega}_{\Delta} \end{cases}. \tag{26}$$

where $\boldsymbol{\omega}_{\varepsilon}$ and $\boldsymbol{\omega}_{\Delta}$ are zero-mean Gauss white noises.

(e) Velocity measurement equations are determined by

$$Z_v(t) = \begin{bmatrix} V_{\mathrm{E}}^{c\_SINS} - V_{\mathrm{E}}^{c\_GPS} \\ V_{\mathrm{N}}^{c\_SINS} - V_{\mathrm{N}}^{c\_GPS} \\ V_{\mathrm{U}}^{c\_SINS} - V_{\mathrm{U}}^{c\_GPS} \end{bmatrix} = \begin{bmatrix} \delta V_x + M_x \\ \delta V_y + M_y \\ \delta V_z + M_z \end{bmatrix} \tag{27}$$

(f) Position measurement equations are determined by

$$Z_p(t) = \begin{bmatrix} L_{c\_SINS} - L_{c\_GPS} \\ \lambda_{c\_SINS} - \lambda_{c\_GPS} \\ h_{c\_SINS} - h_{c\_GPS} \end{bmatrix} = \begin{bmatrix} \delta L + N_x \\ \delta \lambda + N_y \\ \delta h + N_z \end{bmatrix} \tag{28}$$

where M_x, M_y, M_z are the velocity errors of GPS receiver; and N_x, N_y, N_z are the position errors of GPS receiver.

4 Simulation

Conditions as follows.

Initial position: Latitude is 34.1 deg, longitude is 108.7 deg and height is 378.0 m. Both initial velocity and attitude are 0. Gyro constant drift is 10.0 deg/h. Random drift is 1.0 deg/h. Accelerometer constant bias is 1,000.0ug. Random bias is 100.0 ug. GPS horizontal position error is 10.0 m. Height error is 10.0 m. Velocity error is 0.01 m/s. Initial attitude error: 1.5, 1.5, 10.0 deg.

Simulation time is 500 s, the figure consists of the east velocity estimation error, the north velocity estimation error and the vertical velocity estimation error.

In simulation, we use CPF and CKF on vehicle navigation error estimation, output after correction of velocity error simulation of Fig. 1 is shown as follows.

As seen in the Fig. 1, the estimation errors of CPF is less than that of CKF about the estimation of speed errors in the GPS/INS. The error of the east velocity from 0.207 to 0.155 m/s, the error of the north velocity from 0.248 to 0.186 m/s, and the error of the vertical velocity from 0.373 to 0.364 m/s. Thus, CPF improves the performance of the filter and the estimation accuracy of the navigation parameters.

It can be seen from the above figures that CPF is more accurate than CKF. CPF precision is slightly higher than that of CKF, and CPF curve relative to the CKF smoother.

CPF positioning accuracy is higher than that of CKF, this is because when the azimuth error is large INS/GPS integrated navigation system for strong nonlinear, nonlinear state UT to the posterior distribution of the approximation precision is higher than that of CKF in first-order linear approximation.

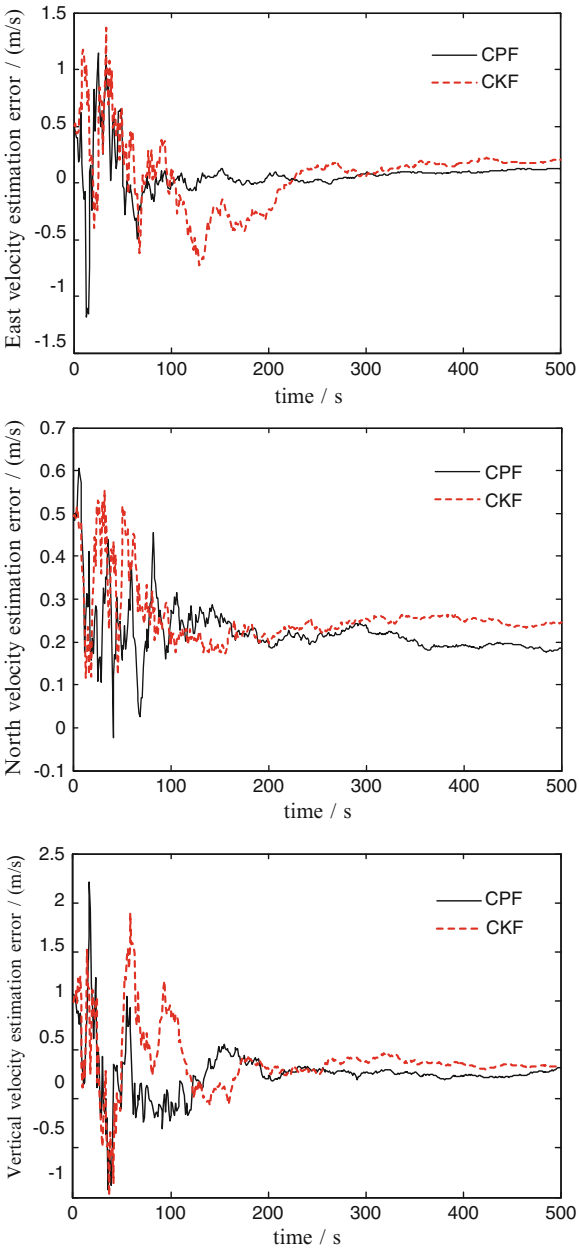

Fig. 1 Speed estimation error chart

5 Conclusion

This paper presented a method (Cubature Particle filter) for GPS/INS integrated navigation system based on CKF and PF. The simulation results showed the performance of the CPF is slightly better than that of the CKF, and the computational time of the CPF is less than that of the CKF. The CPF can provide superior performance over the CKF, by better accounting for nonlinearities. The computational complexity of the CPF is equivalent to that of the EKF. This study might provide theoretical support for engineering design and modification.

Acknowledgements This paper is supported by the National Natural Science Foundation of China (Grant No. 60834005 and 60775001) and the International Exchange Program of Harbin Engineering University for Innovation-oriented Talents Cultivation.

References

1. Kalman RE (1960) A new approach to linear filtering and prediction problem[J]. Trans ASME Ser D J Basic Eng 82(3):34–45
2. Crassidis JL (2006) Sigma-point Kalman filtering for integrated GPS and inertial navigation. IEEE Trans Aerospace Electron Syst 42:750–756
3. Chhetri AS, Morrell D, Papandreou-Suppappola A (2004) The use of particle filtering with the unscented transform to schedule sensors multiple steps ahead[C]. In: IEEE international conference aconstics, speech, and signal, Montreal, Quebec, Canada. Processing vol 2, pp 301–304
4. Julier SJ, Uhlman JK (2004) Unscented filtering and nonlinear estimation. Proc IEEE 92 (3):401–422
5. Julier SJ, Uhlman JK (1997) A new extension of the Kalman filter to nonlinear systems [J]. Proc Soc Photo-Opt Instrum Eng 3068:182–193
6. Crassidis JL, Markley FL (2003) Unscented for spacecraft attitude estimation[J]. J Guid Control Dyn 26(4):536–542
7. Ienkaran A, Simon H (2009) Cubature Kalman filters. IEEE Trans Automat Control 54(6):1254–1269
8. Kotecha JH, Djuric PM (2003) Gaussian particle filtering[J]. IEEE Trans Signal Process 51(10):2592–2601
9. Farina A, Ristic B, Benvenuti D (2002) Tracking a ballistic target: comparison of several nonlinear filters[J]. IEEE Trans Aerospace Electron Syst 38(3):854–867
10. Gordon NJ, Salmond DJ, Smith AFM (1993) Novel approach to nonlinear/non-Gaussian Bayesian state estimation. IEEE Proc Radar Signal Process 140:107–113
11. Carpenter J, Clifford P, Feamhead P (1999) Improved particle filter for nonlinear problem. IEEE Proc Radar Son Nav 146:2–7
12. Gustafsson F, Gunnarsson F, Bergman N et al (2002) Particle filters for positioning, navigation, and tracking. IEEE Trans Signal Process 50:425–437

Unequal Clustering Algorithm for WSNs Using Particle Swarm Optimization

Ruihua Zhang, Heyou Cheng, and Zhiping Jia

Abstract An important issue in wireless sensor networks (WSNs) is how to balance the entire network energy consumption and prolong its lifetime. To address the problem, this paper proposes an Unequal Clustering Algorithm (UCA-PSO) using Particle Swarm Optimization (PSO) for wireless sensor networks, which considers nodes' residual energy and position by grouping them into clusters of unequal sizes. First, the sink selects a set of cluster heads and groups all nodes into initial clusters according to clustering radius. Second, PSO algorithm selects the optimal cluster-head in each initial cluster. Simulation results show that the UCA-PSO well balanced nodes' energy consumption and improved the network lifetime.

Keywords WSNs • Unequal clustering • PSO

1 Introduction

In recent years, the application and demand of wireless sensor networks are more and more, but nodes' energy makes its application is restricted. How to balance nodes' energy consumption and prolong its lifetime has an important application foreground.

Clustering and multi-hop routing can reduce energy consumption. Therefore, many cluster-based routing algorithms have been proposed [1]. EEUC [2] proposes an energy efficient unequal clustering algorithm for wireless sensor networks. This

R. Zhang (✉) • Z. Jia
School of Computer Science and Technology, Shandong University, Jinan, China
e-mail: ruihua_zhang@sdu.edu.cn

H. Cheng
Shandong Second Light Industry Economic and Technologic Information Department, Jinan, China

W. Wang (ed.), *Mechatronics and Automatic Control Systems*, Lecture Notes in Electrical Engineering 237, DOI 10.1007/978-3-319-01273-5_29,

algorithm selects the optimal cluster head by localized competition among tentative cluster heads. EEUC takes into account the energy balance of intra-clusters and cluster heads, but it has great randomness.

PSO is an iteration-based optimization algorithm. A set of random solutions are initialized, then find the optimal solution through many iterations. The best evaluation of a given fitness function is this optimal solution. In the process of iterations, each particle adjusts its position using previous best individual position and global best position information, so as to find the optimal solution [3]. When both the optimal value are find, the particle update its velocity and position according to the following equations:

$$V_{id}(t) = WV_{id}(t-1) + c_1\alpha(P_{id} - X_{id}(t-1)) + c_2\beta(P_{gd} - X_{id}(t-1)) \quad (1)$$

$$X_{id}(t) = X_{id}(t-1) + V_{id}(t) \quad (2)$$

Where, V_{id} and X_{id} are the velocity and position vector for particle i respectively, t is the number of iterations. c_1 and c_2 are learning factors, α and β are random numbers uniformly distributed in 0 and 1, P_{id} and P_{gd} are the best position of particle i and the global best position respectively, and W is the inertia weight.

Based on EEUC, this paper proposes an unequal clustering algorithm (UCA-PSO) using PSO. In this algorithm, the sink first initializes a set of the cluster heads, and forms clusters. In each cluster, the optimal cluster head is found using PSO. Then, each cluster-head receives and aggregates its members data, and transmit them to the sink by multi-hop communication.

2 System Model

A sink and many nodes are uniformly distributed in monitoring area, and they are static after deployment. It is assumed that all node knows its own position by localization techniques [4].

Following a free space model [5], energy $E_{Tx}(k,d)$ is for transmitting a l-bit packet over distance d,

$$E_{Tx}(l,d) = le_{te} + le_{ta}d^2 \quad (3)$$

Where, e_{te} is the energy dissipated per bit to operate the transmitter circuit, e_{ta} is the energy dissipated by transmitter amplification. To receive this message, the radio expends energy is:

$$E_{Rx}(l) = l \cdot e_{rx} \quad (4)$$

3 The UCA-PSO Mechanism

The UCA-PSO consists of four parts: clustering initialization, unequal clustering radius, fitness function, and PSO algorithm.

3.1 Clustering Initialization

After the nodes are deployed, each node sends its position and energy information to the sink. The sink receives this information and selects a set of initial cluster heads using the simulated annealing algorithm [6]. During the choice of cluster heads, the sink considers their energy and location.

The sink calculates the distance to each node according to their position, and broadcasts a message to all sensor nodes. The message includes the parameter d_{max}, d_{min}, and the position of cluster heads and sink. d_{max} and d_{min} are the maximum and minimum distance between sensor nodes to the sink, respectively.

3.2 Unequal Clustering Radius

In WSNs, many-to-one communication pattern makes cluster heads nearer the sink relay more data pockets. So cluster heads nearer the sink have smaller cluster sizes, and its clustering radius is smaller. Suppose predefined constant R_{max} is the maximum clustering radius. Clustering radius R_i of node i is the following equations [2]:

$$R_i = \left(1 - c \times \frac{d_{\max} - d(i, \text{sink})}{d_{\max} - d_{\min}}\right) R_{\max} \tag{5}$$

Where, $d(i, \text{sink})$ is the distance of node i and the sink, c is a constant coefficient in [0,1].

3.3 Fitness Function

In PSO, fitness function definition is a major issue. Cluster-head selection in WSNs should consider its energy and location. The optimal cluster-head selection uses PSO algorithm. So the fitness function f is defined:

$$f(k) = \varepsilon \times f_1(k) + (1 - \varepsilon) f_2(k) \tag{6}$$

$$f_1(k) = E(k) \Big/ \sum_{i=1}^{m} E(i) \tag{7}$$

$$f_2(k) = (m-1) \Big/ \sum_{i=1}^{m} d(i,k) \tag{8}$$

During each generation, $E(i)$ is the energy of particle i, and $E(k)$ is the energy of the particle k, and m is the number of nodes in the initial cluster, and $d(i,k)$ is the distance of particle i and k, and ε is a predefined constant between 0 and 1. So each iteration chooses the particle with the maximum fitness value of f as global best position. Function f_1 optimizes the network energy efficiency, and f_2 minimizes the intra-cluster distance of nodes and their candidate cluster-head.

3.4 PSO Algorithm

PSO algorithm needs to group the network into initial clusters, and chooses the optimal cluster-head using PSO for each cluster. Process of this specific steps is as follows:

1. According to clustering initialization, the sink selects a set of cluster heads. Each cluster-head broadcast a message to its neighbor nodes in clustering radius, and ordinary nodes join the nearest cluster-head by sending a message. This message contains its current energy and position. So the network set up initial clusters.
2. For each initial cluster, PSO selects the optimal cluster head.

   Step1: Initialize m particles, and m is the number of nodes in the initial cluster.
   Step2: For each particle i, initial operation is as follows:

   1. Randomly initialize each particle's position and velocity, and correct its position to map the nearest node.
   2. Calculate each particle's fitness value using formula (6, 7, and 8), and

   $$P_{id} = f(i), \quad P_{gd} = \underbrace{\max f(i)}_{i=1,2,\ldots,m}$$

   Step3: Repeat the following steps until the maximum number of iterations or the specific conditions are reached.

   1. Update the position of each particle using formula (1) and (2), and correct its position to map the nearest node. So each particle identifies a node in the initial cluster.
   2. Calculate each particle's fitness value using formula (6, 7, and 8), and

   $$P_{id} = f(i), \quad P_{gd} = \underbrace{\max f(i)}_{i=1,2,\ldots,m}$$

Step4: Select the particle with the maximum fitness value as the cluster-head, and it is the optimal cluster head. Cluster head broadcast a message across the cluster.

3. Set up the optimal clusters in WSNs.

4 Simulations

In this section, several simulations are carried out to evaluate the performance of the proposed UCA-PSO using network simulator OMNET++. For simulation environment, 100 static nodes are uniformly distributed in a 200 m × 200 m monitoring area, and sink is located at position (100,250). In implementing PSO, the search is terminated within 40 iterations. Table 1 is the simulation parameters [5]. The average of 200 independent experiments is each simulation result.

4.1 Clustering Characteristics

According to data transmission in the hierarchical WSNs, cluster-head consumes more energy relative to member node, and number of cluster heads directly affects network lifetime. So we analyze the performance of clustering characteristics about UCA-PSO, and the UCA-PSO and EEUC in different scenarios are run.

Figure 1 shows the average clusters number trends based on R_{max} when c in Eq. 5 is difference. Their change trend for UCA-PSO and EEUC is the same. This is because they all are unequal clustering and clustering radius function Eq. 5 is the same. When R_{max} and c is fixed, UCA-PSO generate less clusters than EEUC. This is due to the difference in cluster-head selection strategy for two algorithms. In UCA-PSO, cluster-head selection considers nodes' residual energy and position within its clustering radius. In EEUC, final cluster head selection considers their residual energy within tentative cluster-heads that are randomly selected according to a constant T.

Table 1 Parameters

Parameter	Value	Parameter	Value
Monitoring area	200 m × 200 m	c	0.4
Sink position	(100, 250)m	N	100
R_{max}	50 m	Data packet	128 bytes
Transmitter circuitry, e_{te}	50nJ/bit	Control packet	10 bytes
Receiver circuitry, e_{rx}	50nJ/bit	TD_MAX	70 m
e_{ta}	10 pJ/bit/m2	c1 and c2	2
Initial energy	0.5 J		

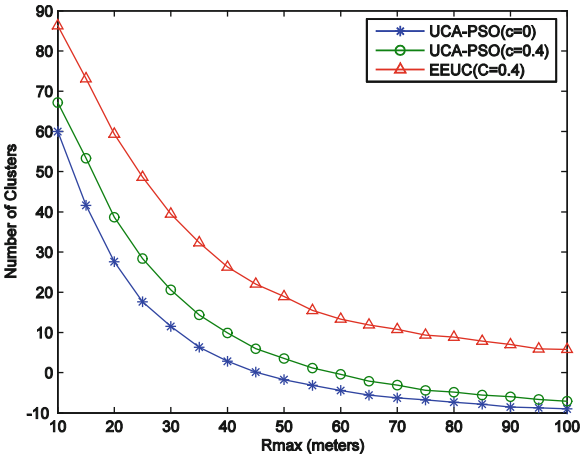

Fig. 1 The average number of clusters generated by unequal clustering

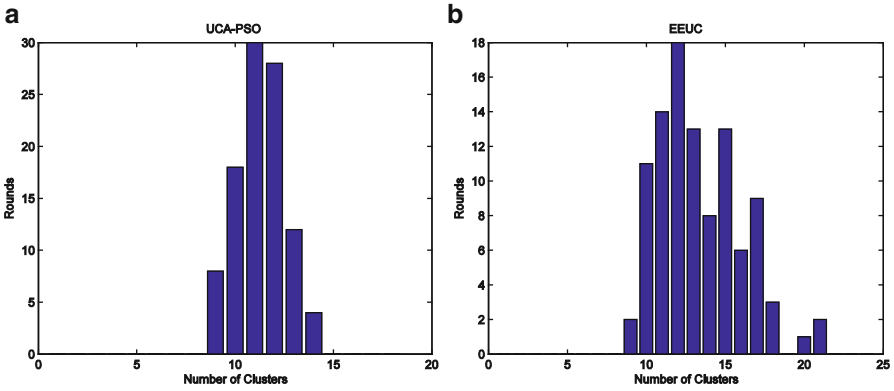

Fig. 2 Distribution of clustering in 100 round (**a**) UCA-PSO (**b**) EEUC

The clustering algorithm stability is studied in the section. Figure 2 illuminates the distribution of the clustering for UCA-PSO and EEUC. It is statistics from randomly selected 100 experiments. Clustering number for UCA-PSO is more steadier than that for EEUC. This is because EEUC randomly selects a set of tentative cluster-heads, and they rely on the constant T. In UCA-PSO, position and residual energy become the two primary factors in selecting cluster-heads. So UCA-PSO gets a steady clustering.

4.2 Network Lifetime

In this section, the network lifetime for both UCA-PSO and EEUC algorithms is compared. The network lifetime is defined as rounds until the first node dies.

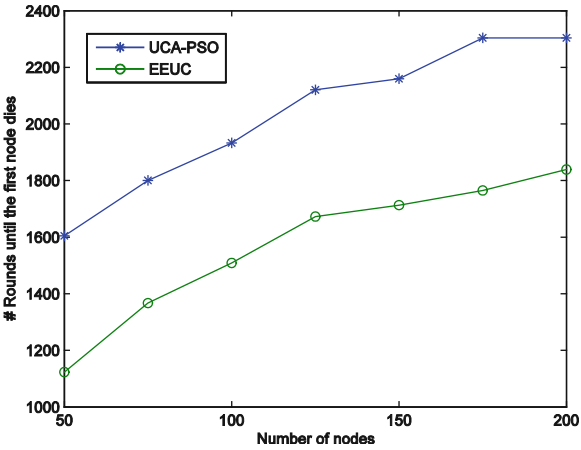

Fig. 3 Network lifetime

Figure 3 shows the network lifetime for both UCA-PSO and EEUC based on the number of nodes when R_{max} is 50 m. As seen in Fig. 3, the network lifetime for EEUC algorithm is shorter than that for UCA-PSO algorithm. This is because of the generated more clusters and its instability of the clustering mechanism for EEUC algorithm. It shows UCA-PSO achieves 11.8 % improvement over EEUC in the network lifetime.

5 Conclusion

This paper proposed an unequal clustering algorithm (UCA-PSO) for WSNs using PSO to improve the network lifetime. The clustering radius was given that should decrease as the distance to the sink decreases. The sink selected a set of cluster heads and set up initial unequal clusters according to clustering radius. A new fitness function was defined that considers nodes' energy and location. The optimal cluster-head was selected by PSO algorithm in each initial cluster. Simulation results showed that UCA-PSO achieves 11.8 % improvement over EEUC in the network lifetime, and clearly improved the network lifetime.

Acknowledgements This research is supported by the Natural Science Foundation of China (No. 61070022) and the Independent Innovation Foundation of Shandong University (No.2012ZD011).

References

1. Akkaya K, Younis M (2005) A survey on routing protocols for wireless sensor networks. Ad Hoc Netw 3(3):325–349

2. Chengfa Li, Mao Ye, Guihai Chen, Jie Wu (2005) An energy-efficient unequal clustering mechanism for wireless sensor networks. In: Proceedings of the IEEE international conference on mobile adhoc and sensor systems. Institute of Electrical and Electronics Engineers Computer Society, Washington DC, USA, pp 597–604
3. Raghavendra VK, Raghavendra VK (2011) Particle swarm optimization in wireless-sensor networks: a brief survey. IEEE Trans Syst Man Cybern – PART C: Appl Rev 41(2):262–267
4. Gracioli G, Frohlich AA, Pires RP, Wanner L (2011) Evaluation of an RSSI-based location algorithm for wireless sensor networks. IEEE Lat Am Trans 9(1):96–101
5. Younis O, Fahmy S (2004) HEED: a hybrid energy-efficient distributed clustering approach for ad Hoc sensor networks. IEEE Trans Mobile Comput 3(4):366–379
6. Shekofteh SK, Khalkhali MB, Yaghmaee MH, Deldar H (2010) Localization in wireless sensor networks using tabu search and simulated annealing. In: Proceedings of the 2nd international conference on computer and automation engineering (ICCAE). IEEE Computer Society, Singapore, pp 752–757

A New Protection Algorithm for Distribution Network with Distributed Generation Based on Intelligent Electronic Device Information

Wentao Ruan and Hongxia Zhan

Abstract With multiple distributed generation (DG) connected to the distribution network, the original protection of the distribution network is no longer adaptable. A new protection algorithm based on intelligent electronic (IED) information is presented. The algorithm firstly determines which feeder the fault is located by comparing with the fault current size of the relative IED department, then it finds out the fault area by simple vector operations and synthetic analysis. At the same time, it forms fault trip information vector and sends trip instruction for fault isolation. This algorithm is clear and its vector operations and processing are simple and small. It can find out the fault section exactly. Through some case analysis of different faults, the validity of the algorithm was verified.

Keywords Distributed generation • Distribution network • Intelligent electric device • Protection algorithm • Vector

1 Introduction

With the rapid development of distributed power generation technology, DG penetration levels increase in the distribution network. The traditional power distribution system of radiation is from a single supply network into multiple power supply network, and the environment of protection has undergone great changes [1]. The current protection based on radiation network is difficult to meet changing requirements of distribution networks with DG. In order to meet the compatibility of smart grid, ensuring safe and stable operation for the new distribution network, the new protection strategy must be developed. A paper proposed a simple fault location algorithm of multiple power [2], but it ignored the issue of the

W. Ruan (✉) • H. Zhan
School of Electrical & Information, Xihua University, Chengdu, China
e-mail: winter327@qq.com

W. Wang (ed.), *Mechatronics and Automatic Control Systems*, Lecture Notes in Electrical Engineering 237, DOI 10.1007/978-3-319-01273-5_30,

fault location of the end. A paper proposed a fault location algorithm, which determined the fault section by network structure matrix and fault information matrix [3]. But the fault section is divided into "between the FTU" and "between nodes", increasing the complexity of this algorithm and is not adaptive to changes in the structure of the network. A algorithm in a paper solved the problem of the protection selection [4], but it needs to install PT for solving the problem of direction distinguishing. As PT is not installed on the feeder, its application field is limited. Another paper has proposed a fault location algorithm without PT channel [5], but all nodes information of the network needs to be collected, so the amount of information processing and computing is too large. With the development of modern measurement technology and communications technology, a wide area protection is appearing. It can attain much information of the power system and make use of the information for developing protection strategy [6]. Based on this thought, the paper proposed a protection algorithm based on IED information: First, it determines which feeder the fault is located by comparing with the fault current size of the beginning's IED of the feeders. Then it forms power path vector and fault information vector according to the network structure and IED's fault direction information of the fault feeder, finding out the fault area by simple vector operations and analysis. At the same time, it forms fault trip information vector and sends trip instructions to related IED for fault isolation.

2 Implementation of the Protection Algorithm

This algorithm is implemented in two steps. The first step is to distinguish fault feeder, that is, it determines which feeder the fault is located. The second step is to distinguish fault zone, that is, it determines the specific fault area from the fault feeder.

2.1 System Structure and Configuration of Protection

Figure 1 is a distribution network with DGs. In order to take full advantage of DG and ensure island or micro-grid operation in the fault event, each DG is accessible to the system from section bus. Both ends of the line and the access port of DG are equipped with circuit breaker or switch. Additionally, each breaker has a corresponding IED. The protection system consists of the main station of protection, the breakers, their corresponding IEDs and communication network. IED is responsible for collecting and processing information(size, direction of the fault current) of its installation point. In addition the IED has the ability to communicate with the station of distribution network automation and perform action commands [7]. When a failure occurs, related IEDs send fault information to main station through communication network, then the main station calls protection algorithm

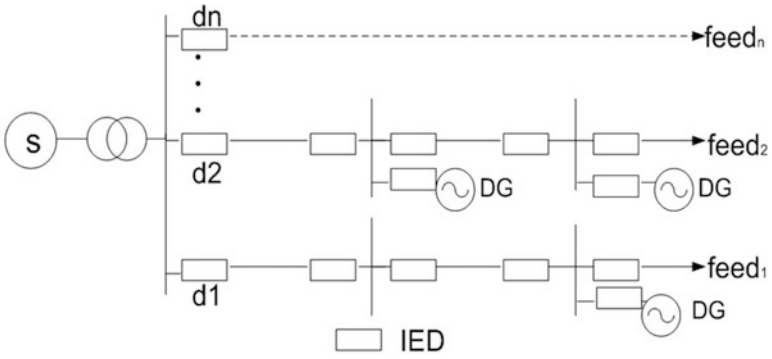

Fig. 1 The structure of distribution network with DGs

for comprehensive judgment to find fault area and sends tripping commands to relevant IED for fault isolation. As the DGs access to system, the fault current is no longer just provided by the system power. Therefore, the protection algorithm regulates that the positive direction is from the system power to the load or DG.

2.2 Fault Feeder Detection

As we know, the fault current is provided by the system power and DGs in the distribution network with DGs. If a fault occurs in the feeder 2 as shown in Fig. 1, the following equation can be obtained by the KCL:

$$I_{d2} = I_s + \sum I_{dn} \tag{1}$$

Here,"I_{d2}" is the current detected by the IED of feed$_2$. "I_s" is the fault current provided by system power. "$\sum I_{dn}$" is the current flowing through beginning's IEDs of the other feeders and provided by DGs.

In the current distribution network, the capacity of DG connected to the user side is between KW and MW, but the capacity of main transformer in the substation is relatively large. We can approximatively take the short-circuit capacity of system power as the main transformer's [8]. Because there is a huge difference in the short-circuit capacity, the size of fault current provided by system power is much larger than the one provided by DG on the other feeders and they are not an order of magnitude. That is, $I_s \gg \sum I_{dn}$, thereby, $I_{d2} \gg \sum I_{dn}$. That is to say, the fault current detected by the beginning's IED on the fault feeder is much larger than any one on non-fault feeder. (We can attain the result by transient simulation in MATLAB software).

Therefore, the searching criterion of fault feeder is:

$$I_d = \max\{I_{dn}\} \tag{2}$$

After the fault, the system station will compare with the size of "I_{dn}" to find out the maximal one, which is on the fault feeder.

2.3 Location and Isolation of Fault Section

After detecting which feeder the fault is in, protection algorithm will be further carried out in the fault feeder.

2.3.1 Network Path Vector and Fault Direction Vector

The topology of feeder$_2$ is shown in Fig. 2 according to positive direction. It takes each IED on the feeder as a node and it gives each node a number. Additionally, the sections between the adjacent nodes are also numbered and each section number is the same as the node number of the upstream which is directly connected to. Assume that the system network is in normal state and all circuit breakers are in the closed state. According to the circulation path of the current in the feeder, we can identify all of the power supply path in the feeder. There are three power supply paths in the feeder$_2$. If each path is represented by the nodes which contains, the paths are as follows: $L_1(1 \to 2 \to 6)$, $L_2(1 \to 2 \to 3 \to 4 \to 7)$, $L_3(1 \to 2 \to 3 \to 4 \to 5)$. The power supply path of one feeder can also be represented by the vector of L,

$$L = (L_1, L_2 \ldots L_i \ldots L_n) \tag{3}$$

(i = 1,2. . .n, "n" is the number of power supply path, L_i is the corresponding row vector of a path).

This article provides that if a node belongs to the path, it is marked with "1", if not, it is marked with "0". Therefore, the corresponding vectors of three paths in the feeder$_2$ are as follows: $L_1 = (1\ 1\ 0\ 0\ 0\ 1\ 0)$; $L_2 = (1\ 1\ 1\ 1\ 0\ 0\ 1)$; $L_3 = (1\ 1\ 1\ 1\ 1\ 0\ 0)$. That is, $L = (L_1, L_2, L_3)$. When a fault occurs, each IED on the feeder detects its direction and uploads the information to the master side. Thus a fault direction vector is formed, which is represented by "F". Element in F is the fault direction information of each node. Its elements are defined as follows:

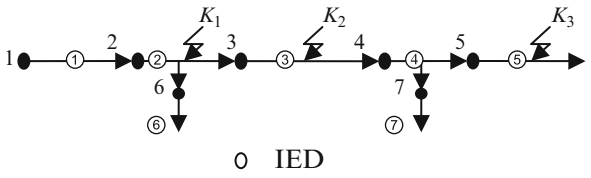

Fig. 2 The topology of feeder 2

$$f_j = \begin{cases} 1 & \textit{fault current flowing through ``j'' and it's positive} \\ 0 & \textit{``j'' is negative fault current or no fault current flowing} \end{cases} \tag{4}$$

Suppose a fault occurred in region"②", only node "1"and "2" are flowed through the positive fault current. Thus the direction vector of fault current was " $F = (1\ \ 1\ \ 0\ \ 0\ \ 0\ \ 0\ \ 0)$".

2.3.2 The Steps of Location and Isolation

① The first step is to determine which path the fault section belongs to. if path vector "L"and vector "$digF$" meet the flowing condition:

$$L \bullet digF = (M_1, M_2 \cdots M_i \cdots M_n)^T = M \text{ and } M_i = L_i \tag{5}$$

the fault is located in the path of L_i.
② The second step is to find out the out-point of the fault section and determine the fault section. (the "out-point" is a node directly connected to the fault section and the fault current flow out of it). "P_i" is the judging vector, which is equal to "F" minus "L_i", that is, "$P_i = L_i - F$" . Then it begins to query (from the left to the right) the first element in "P_i"whose value is "1". If "P_i" is not "0", the corresponding node of that element is the out-point, the section in the upstream of the out-point and which is directly connected to is the fault section. If "P_i" is "0", the fault section is at the end of path"L_i".
③ The third step is fault isolation. After finding the fault section, tripping vector "T "is formed. The element "t_j" in "T"is defined as follows:

$$t_j = \begin{cases} 1 & \textit{node ``j'' is the out} - \textit{point or its number is the same} \\ & \textit{as fault section's} \\ 0 & \textit{other cases} \end{cases} \tag{6}$$

The main station will send tripping commands to the nodes in "T" whose value is "1" for fault isolation.

3 Analysis of Fault Example

Take the fault in feeder$_2$ for example. After the fault, the protection algorithm starts to search fault feeder. According to the searching criterion of fault feeder, "I_{d2}" is maximum in "I_{dn}", so feeder 2 is the fault feeder. Now We analyze the fault in sectionalized busbars, middle of the feeder and end of the feeder.

① A fault of "K_1" is in sectionalized busbars. At this moment, $F = (1\ 1\ 0\ 0\ 0\ 0\ 0)$. According to the step "①" above, we make a simple multiplication. We can get the result that the path vector L_1、L_2 and L_3 meet the condition, then they respectively make subtraction with "F". We can get the judging vector: $P_1 = (0\ 0\ 0\ 0\ 0\ 1\ 0)$, $P_2 = (0\ 0\ 1\ 1\ 0\ 0\ 1)$, $P_3 = (0\ 0\ 1\ 1\ 1\ 0\ 0)$. The first element in "$P_1$" whose value is "1" is node "6". Similarly, node "3" is the first element in "P_2" and "P_3". So the node "6"and node "3"are the out-points. Obviously, the fault section is "②". According to step "③", we can get the results: $t_2 = 1, t_3 = 1, t_6 = 1$. Then the tripping vector is formed : $T = (0\ 1\ 1\ 0\ 0\ 1\ 0)$.Finally the main station would send tripping commands to the breaker of node "2", node "3" and node "6" for fault isolation.

② A fault of "K_2" is in the middle of feeder. According to the steps of the protection algorithm, we can get the flowing vector: $F = (1\ 1\ 1\ 0\ 0\ 0\ 0)$, $P_2 = (0\ 0\ 0\ 1\ 0\ 0\ 1)$, $P_3 = (0\ 0\ 0\ 1\ 1\ 0\ 0)$, $T = (0\ 0\ 1\ 1\ 0\ 0\ 0)$. So the fault section is "③" and tripping commands would be sent to the node "2", node "3" for isolation.

③ A fault of "K_3" is in the end of feeder. Similarly, we can get the result: $F = (1\ 1\ 1\ 1\ 1\ 0\ 0)$, $P_3 = 0$, $T = (0\ 0\ 0\ 0\ 1\ 0\ 0)$. The fault section is "⑤". Then the main station would send tripping command to the node "5" for isolation.

4 The Instructions of the Protection Algorithm

From Sect. 3, we can know that the faults were all found out exactly. The fault examples verified the validity of the protection algorithm. Simultaneously, it didn't need PT to collect voltage information and only some relevant nodes information of fault current should be collected. The algorithm reduced the amount of processing information and computation. In the distribution network, the DG switching is determined by the operator of the DG, it has the characteristics of random variability. But the DG switching would inevitably lead to the changes of feeder network topology and the network power supply path and the node on feeder will change. Therefore, once the DG in operation or decommissioning, the master side amended the power supply path vector accordingly (only operational DG corresponding to the IED as a node).

The details discussed above shows that the fault current information is the basis of the protection algorithm. The algorithm detects the size of fault current by installing CT on corresponding IED. The detection of the fault direction can use the method which makes use of the phase changes of positive sequence current to detect the direction [9]. In addition, we must rely on a strong and reliable communication network to ensure the accuracy and rapidity of information transmission. The standard of IEC61850 made hierarchical and distributed standardized modeling and configuration for power system. It can achieve seamless connectivity between

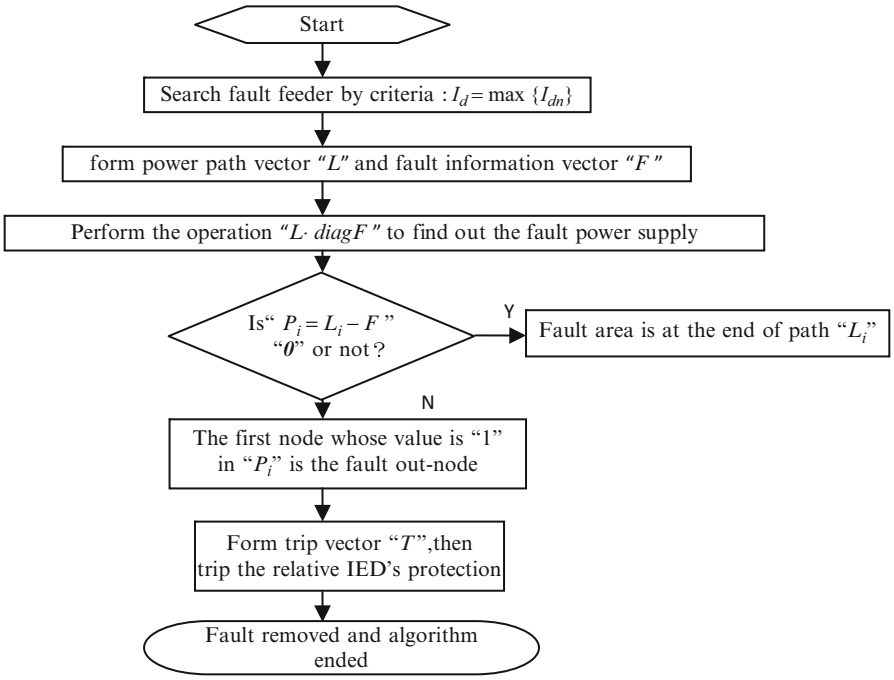

Fig. 3 Flowchart of the protection algorithm

different systems and achieve interoperability between different devices. According to the standard's definition, when several data upload to a server platform, it can guarantee that the operating time of the protection is about 4 ms [10]. Therefore, we can apply the IEC61850 technology to the protection algorithm.

Flowchart of the protection algorithm is as follows (Fig. 3):

5 Conclusion

① According to the characteristics of fault current and network structure, this paper proposed a protection algorithm based on IED information. This algorithm was implemented following two steps, which are detection of fault feeder, location and isolation of fault section. The algorithm can be deemed as clear and reliable.

② The protection algorithm narrows the fault scope to a specific feeder, simplifying the network structure and excluding a lot of unrelated nodes. Thereby, it can reduce the amount of processing information and computation. In the computing process, there are only vector multiplication and addition operations, which are much simpler than the matrix algorithm of the past. So it can greatly accelerate the processing speed of the computer program.

③ The protection algorithm can clearly distinguish the fault of each section. In addition, it is adaptable to the changes of network structure and it can be amended accordingly.
④ The protection algorithm does not require collecting the information of voltage, so it needn't to install PT device. Thus the configuration of protection and investment costs can be reduced.

Acknowledgements The paper is Supported by the innovation Found of Postgraduate (ycjj201255), Xihua University.

References

1. De Britto TM,Morais DR, Marin MA (2004) Distributed generation impacts on the coordination of protection systems in distribution networks. In: IEEE transmission and distribution conference and exposition. Latin (America), pp 16–21
2. Wei Zhinong, He Hua, Zheng Yuping (2001) A novel algorithm for fault location in power distribution network. Autom Electr Power Syst 25(14):48–50
3. Yao Cheng, Liu xingdong, Zheng Bing (2010) A new fault locating algorithm for distribution network with distributed generations. Mod Electr Pow 27(3):54–56
4. Wang Fei, Sun Ying (2003) An improved matrix algorithm for fault location in distribution network of power systems. Autom Electr Pow Syst 27(24):45–47
5. Lin Xia, Lu Yuping, Wang Lianhe (2008) New fault region location scheme in distribution system with DGs. Trans China Electrotech Soc 23(11):139–145
6. Yang Shirong (2006) A research on wide-area protection based on wide-area measurement information of grid. College of Electrical & Electronic Engineering/Huazhong University of Science and Technology, Wuhan
7. Cong Wei, Pan Zhencun, Zhao Jianguo (2006) A wide-area relaying protection algorithm based on longitudinal comparison principle. Proc CSEE 26(21):8–14
8. Wu Ning, Xu Yang, Lu Yuping (2009) New fault section location algorithm for distribution network with DG. Autom Electr Power Syst 33(14):77–82
9. Shen Binbin (2010) New method to determine fault direction with phase change of positive sequence current. Sci Technol Inf 35:41–42
10. Wu Ning (2009) Research on protection IED of distribution line with DGS based on IEC 61850). Southeast University, Nanjing

The Day-Ahead Neural Network Wind Power Prediction Method in Wind Farms

Wen-hui Zhao, Jin Ma, and Zheng-zhong Zhang

Abstract When the proportion of the wind energy is more and more in the word energy, the large scale of wind power grid has great influence on the power system scheduling and the safe operation. Because the day-ahead wind power prediction can help the scheduling department make electricity generation plan, it is very necessary for the wind farms. Now the wind power prediction method is mainly based on the short-term prediction. The prediction method expounded by this paper, is the application of the BP network to forecast the wind power in the wind farms, and improves the forecast model and day-ahead the prediction results.

Keywords Wind power • Prediction method • Day-ahead forecast • Neural network

1 Introduction

Since the global oil, coal and other fossil resources become increasingly scarce, wind and other renewable energy development and application has been paid great attention all over the world. After the large scale wind power connection with power grid, lots of experts devote to studying the wind power forecast method all over the world.

At present most mature wind power forecast system is mainly developed by Europe, the United States and other developed countries. For example, the Prediction system which is developed by Danish national laboratory uses the physical model [1];The Prediction system which is developed by German Walden university uses the combination forecast method, and can give 2 days of wind power prediction on large area [2];The ANMOS project, which is jointly developed by France,

W.-h. Zhao (✉) • J. Ma • Z.-z. Zhang
North China Electric Power University, Beijing, China
e-mail: zhaowh19861105@163.com

W. Wang (ed.), *Mechatronics and Automatic Control Systems*, Lecture Notes in Electrical Engineering 237, DOI 10.1007/978-3-319-01273-5_31,

Ireland, Spain, German, Greece, Denmark and England, uses the combination forecast model and can be applied to both land and sea wind farms; In addition, there are also the EWind system which is developed by the United States TrueWind company and the GH-FORECASTER system which is developed by Garrad Hassan company. The forecast system which is designed by china electrical science institute has been put into application; its RMS error is about 15 % [3].

2 Wind Power Prediction Principle

According to different time scale [4], the wind power prediction can be divided into three kinds: one is the short-term prediction (a few minutes), mainly applied in the wind generator control; Another is medium-term prediction (hours to days), mainly used in wind power grid-connected and grid dispatching; The last one is long-term prediction (weeks and months), mainly used in wind farms and grid maintenance plan. According to the different needs for operation mode of the power system scheduling department arrangement, the wind power prediction can be divided into day-ahead prediction and real-time prediction, day-ahead prediction is the forecast ahead 24 h. Real-time prediction is the rolling forecast to each point. According to the different prediction model, the wind power prediction method can generally be divided into physical method and statistics method.

2.1 Physical Method

The physical methods essence is that using the wind speed, wind direction, temperature, humidity and other weather information to forecast. According to the wind farms geographic information and physical information to calculate the wind speed, wind direction, temperature, pressure and so on. The physical method does not require a lot of long measure data and applies to the complex terrain, but the researchers must have abundant weather knowledge to build an accurate model. When the model is rough, the prediction accuracy is poor. Figure 1 shows the physical prediction method.

2.2 Statistical Method

The statistical methods essence is that, building a mapping relationship between the system input (NWP, historical data, and the measured data) and wind power. The commonly used methods have duration method, stochastic time series method [5], support vector machine (SVM) method [6], artificial neural network method [7] and so on. In the wind power prediction, the input of the model is usually several

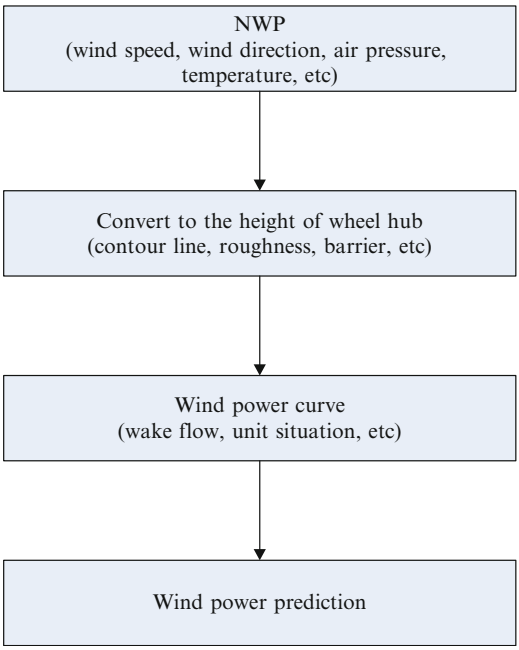

Fig. 1 Prediction flowchart of the physical method

historical data, the real-time data SCADA (supervisory control and data acquisition) system and digital meteorological forecast (NWP) data.

3 Neural Network Methods

Using the traditional statistics methods to predict the wind power has the characteristics of the model simple and speed fast, but in the face of complex nonlinear wind speed and wind power the prediction accuracy certainly will be affected. The advantage of Neural network is not needed to ensure the accurate mathematical model.

3.1 BP Neural Network

The BP neural network is a kind of the most commonly used neural network method, based on the error back propagation algorithm of artificial neural network includes the input layer, interface layer (hidden) and output layer. The BP neural network learning process is divided into positive spread and back propagation, namely the information positive dissemination and the error back propagation two processes are made up. In the process of positive transmission, the neurons of the

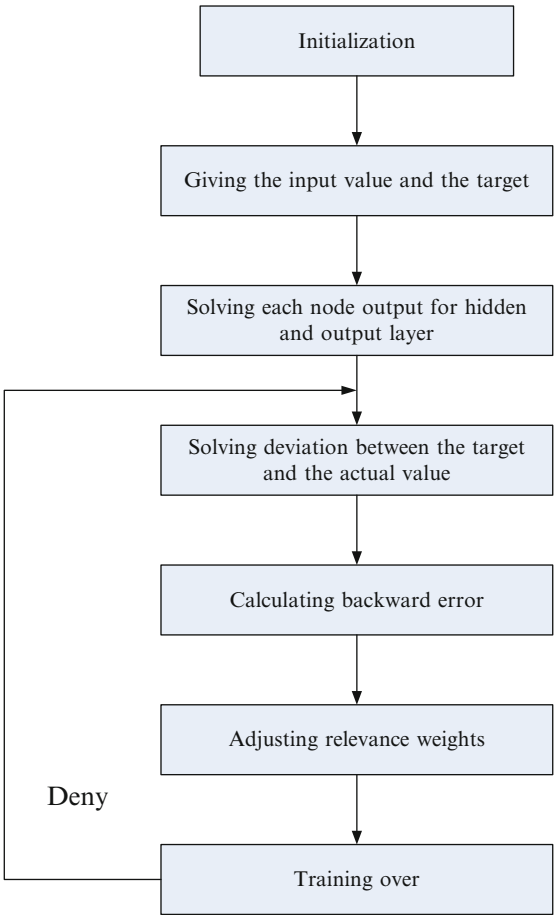

Fig. 2 Flow chart of BP network learning

input layer is responsible for receiving the information from outside, and pass the information to the neurons of the interface layer; Interface layer is the internal information processing layer, which is responsible for information transformation, according to the demand for information change capacity, interface layer can also be designed to single hidden layer or more hidden layer structure; Finally the hidden layer transfer the each neuron information to output layer, after the further processing completing a learning process is spread. Then the output layer output information processing results to the outside world. When output does not agree with output, it is time to turn into the error back propagation process. Through the network will return the error signal through the original connecting path, meanwhile modifying every layer neurons weights until it reaches the desired objective. In constant positive spread and error back propagation process, the model adjusts the weights of each layer, until the network error output reduced to the desired value, or the pre-set number of learning. Figure 2 shows the learning process.

3.2 Used for the Wind Power Prediction and the BP Neural Network Model

This paper uses the BP neural network model with the wind speed, wind direction sine, wind direction cosine, temperature as input parameters, and the wind power as the output.

In order to improve the prediction precision, firstly needing to input data optimized.

1. To calibrate the data of the numerical weather prediction system
   Using linear regression method. The correction model is that:

$$v_{NMP.t}^{r} = v_{NMP.t} - e_{NMP.t} \tag{1}$$

   Where $v_{NMP.t}$ is the wind speed of numerical weather prediction system at time t before the correction $v_{NMP.t}^{r}$ is the wind speed at time t after the correction.

$$e_{NMP.t} = a + b \cdot v_{NMP.t} \tag{2}$$

$$a = \overline{e}_{NMP} - \overline{b}_{NMP} \tag{3}$$

$$b = \frac{N_c \sum_{i=1}^{N_c} e_{NMP,i}\ v_{NMP,t} - \sum_{i=1}^{N_c} e_{NMP,i} \sum_{i=1}^{N_c} e_{NMP,i} \sum_{i=1}^{N_c} v_{NMP,i}}{N_c \sum_{i=1}^{N_C} v_{NMP,i}^{2} - \left(\sum_{i=1}^{N_c} v_{NMP,i}\right)^{2}} \tag{4}$$

$$e_{NMP,i} = v_{NMP,i} - v_{means,i} \tag{5}$$

   Where the number of samples is N_c, $v_{means,i}$ is wind electric field measured wind speed.
2. Data normalization
   In order to be beneficial to the neural network training for the local minimum and as far as possible to train converge, the data initial selection cannot be ignored. In this paper, each input individually normalized in the interval [−1, 1], the normalization formula is that:

$$y_i = \frac{x_i - \min\{x_i\}}{\max\{x_i\} - \min\{x_i\}} \tag{6}$$

   Where $\{x_i\}$ is the sequence normalized before, $\{y_i\}$ is the sequence after normalized. The other input parameters are the same normalization method.

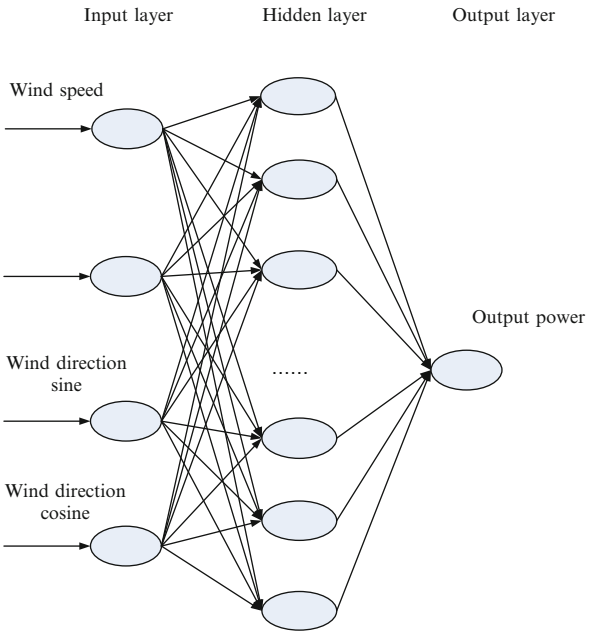

Fig. 3 Structure chart of BP neural network

3. BP neural network parameters
   According to the literature [8], the hidden layer node is selected as 9, transfer function uses the sigmoid function and linear function, hidden layer transfer function uses the tansig function, the output layer uses the purelin transfer function, training algorithm uses L-M algorithm. Figure 3 shows the BP neural network model.

4 Forecast Instance and Analysis

Figure 4 is the results of wind power prediction 24 h before, the abscissa has 96 time points and each point represents the interval of 15 min. Figure 5 is the results of wind power prediction 48 h before, the abscissa has 192 time points. Figure 6 is the results of wind power prediction 72 h before; the abscissa has 288 time points. In all figures the blue solid line is the real value which is collected by the wind farm SCADA system, the red dotted line is the forecast value of the BP neural network.

In the common, using two prediction errors of the common international indicators to analysis the predict results: one is the mean absolute error (MAE); the other is the normalized root mean square error (NRMSE). The mean absolute error is defined as:

$$MAE = \frac{1}{N}\sum_{n=1}^{N}\left|P_{measure} - P_{forecast}\right| \tag{7}$$

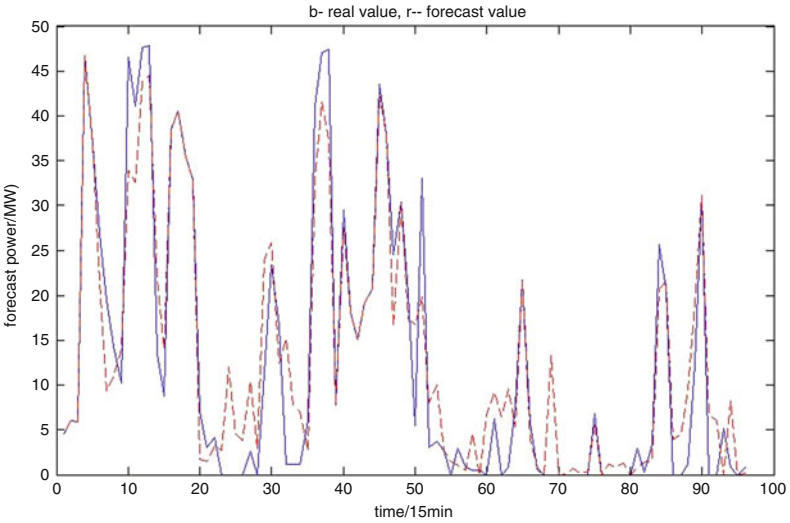

Fig. 4 Wind power prediction results of 24 h before

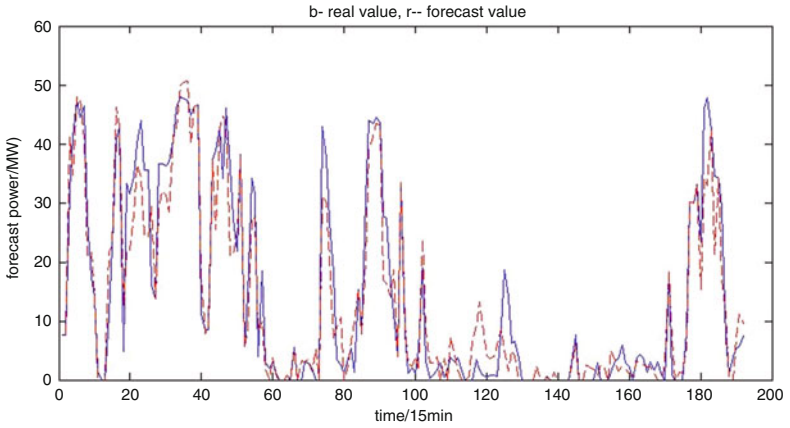

Fig. 5 Wind power prediction results of 48 h before

The normalized root mean square error is defined as:

$$NRMSE = \frac{1}{N}\sum_{n=1}^{N}\left(\frac{P_{measure} - P_{forecast}}{P_{rated}}\right)^2 \tag{8}$$

Where $P_{measure}$, $P_{forecast}$, P_{rated} represent the real wind power value, BP neural network forecast value and the rated power of prediction wind generator, N is the number of forecast data.

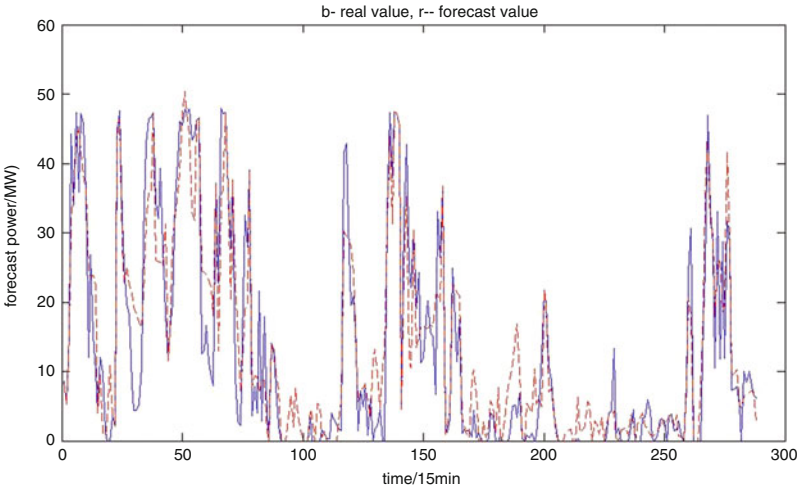

Fig. 6 Wind power prediction results of 72 h before

Table 1 The contrast of different time neural network prediction results

Predict ahead of time	MAE/MW	NRMSE/%
24 h	4.1690	12.26
48 h	5.4414	16.75
72 h	5.7333	18.15

Shown in Figs. 4, 5, 6 and Table 1, BP neural network is more accurate prediction of wind power results in 24 h before. More than 24 h after 48 h in advance and 72 h in advance of regularization of the root mean square error (NRMSE), but the average absolute error (MAE) changes in the rate of change of more than 30 % 48 h in advance and 72 h in advance, the average absolute error (MAE) rate of change of 5.36 %. This study shows that the BP neural network more accurate results in 24 h in advance of the wind power forecast from the formal rms error of about 12 %, more than 24 h after the prediction error will increase significantly, and the average absolute error changes, indicating that neural network on the recently predicted that the results were quite good, more than 24 h in advance accuracy will be significantly decreased. MAE and NRMSE of 48 h in advance and 72 h in advance or less, explain or less 48 h in advance and 72 h in advance of forecast accuracy.

5 Conclusion

By analyzing the result from the wind farm which is 49.5 MW rate power in 6 months, it is shown that the BP neural network can be very good at predicting the day-ahead forecast wind farm output power. Using wind speeds, wind direction

sine, wind direction cosine and temperature as input variables and the network structure 4-9-1, the mean absolute error of 24 h in advance day-ahead prediction is 4.169 MW; its numerical root mean square error is 12.26 %. In this paper using the linear regression calibration to calibrate the numerical weather prediction system data and optimize the input parameters, thus improving the day-ahead wind power prediction accuracy of the BP neural network. It provides the scheduling department to design a power generation plan, improving the impact of wind power grid-connected.

References

1. Landberg L, Prediktor (2000) An on-line prediction system. In: Wind Power for the 21st Century, EUWEC Special Topic Conference, Kassel 4(7):31–37
2. Lange M, Focken U, Heinemann D (2002) Previento-regional wind power prediction with risk control. In: Proceedings of the World Wind Energy Conference, Berlin 13(3):54–61
3. FAN Gao-feng, WANG Wei-sheng, LIU Chun (2008) Artificial neural network based wind power short term prediction system. Power Syst Technol 32(22):72–76
4. Billinton R, HUA Chen, Ghajar R (1996) A sequential simulation technique for adequacy evaluation of generating systems including wind energy. IEEE Trans Energy Convers 11 (4):728–734
5. El-Fouly THM, El-Saadany EF, Salama MMA (2007) Improved grey predictor rolling models for wind power prediction. IEEE Proc Gener Transm Distrib 1(6):928–937
6. Lange B, Rohrig K, Ernst B et al (2006) Wind power prediction in Germany: recent advances and future challenges. In: European Wind Energy Conference, Athens 1(5):73–81
7. Bechrakis DA, Sparis PD (1998) Wind speed prediction using artificial neural networks. Wind Eng 22(6):287–295
8. Peng Huai-wu, L Iu Fang-rui, Yang Xiao-feng (2009) Study of short-term wind power prediction based on artificial neural networks. East China Electr Power 11(11):1918–1921

Blind Single-Image Super Resolution Reconstruction with Gaussian Blur

Fengqing Qin

Abstract To enhance the resolution of image, a framework of a blind single-image super resolution reconstruction method with Gaussian blur is proposed. In the low resolution imaging model, the processes of Gaussian blur, down-sampling and noise are considered. Through an error-parameter analyzing method, Gaussian point spread function is estimated automatically. Super resolution image is reconstructed through iterative back projection algorithm. Experiment is performed on a simulated low resolution image. The results show that the parameters of Gaussian point spread function are accurately estimated. The influence of Gaussian blur estimation on blind single-image super resolution reconstruction is also justified in an experimental way. The more accurate the Gaussian blur is estimated, the better quality of the SR image will be achieved.

Keywords Gaussian blur • Super resolution • Single-image • Low resolution • Iterative back projection

1 Introduction

High resolution (HR) image is required in many areas, such as medical imaging, satellite imaging, and video surveillance [1]. Due to the limitations of imaging system and imaging process, the commonly acquired image is low resolution. To resolve this problem, hardware method is a direct way by enhancing the precision with expensive cost and some limitations. Software method is considered and researched with lower cost. Among them, super resolution (SR) reconstruction method is an efficient way to produce a HR image from one or multiple low resolution (LR) images.

F. Qin (✉)
Institute of Computer Science and Technology, College of Computer and Information Engineering in Yibin University, Yibin, China
e-mail: qinfengqing@163.com

W. Wang (ed.), *Mechatronics and Automatic Control Systems*, Lecture Notes in Electrical Engineering 237, DOI 10.1007/978-3-319-01273-5_32,

According to the used LR images, image SR mainly includes multi-image SR and single-image SR [2]. Multi-image SR is commonly researched, in which the movement with sub-pixel precision is estimated and utilized to reconstruct a HR image. Image registration is very important in this multi-image SR. If the movement between the LR images is estimated with low accuracy, the misregistration phenomenon will be very obvious, and the SR reconstruction quality will degrade greatly [3]. However, in some cases, multiple image of the same scene cannot be acquired. HR image should be reconstructed from a single LR image. Thus, single-image SR is proposed naturally [4].

As the second generation of image restoration technology, image SR reconstruction is also a blind problem, which means the blur process of the imaging system should be estimated to obtain the HR image. However, the estimation of blur function has always been the difficult problem in image processing area, which has not been well resolved yet. Thus, in many papers, the blur function is given with a supposed Gaussian PSF or not considered at all, which does not conform to the true imaging process of optical devices and limits the SR reconstruction quality. Blind image SR reconstruction is still a difficult and hot discussed issue in image processing [5].

A framework of blind sing-image SR reconstruction method with is researched. In the LR imaging model, the processes of Gaussian blur, down-sampling, as well as noise are considered. The Gaussian PSF is estimated automatically and its role on SR blind single-image SR reconstruction is justified.

2 The Framework of Blind Single-Image SR Reconstruction

2.1 LR Imaging Model

In the LR imaging model, the degrading processes of blurring, down-sampling and noise are all considered, as shown in Fig. 1. Firstly, the real scene is blurred. The blurring process (B) may be denoted by point spread function (PSF). The blurred image is gained by the convolution of HR image (F) and PSF. The blur mainly

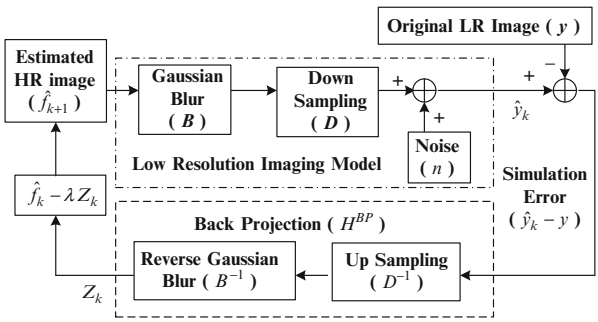

Fig. 1 Framework of single-image SR reconstruction

includes the Gaussian blur induced by the optical devices of the imaging system, the motion blur caused by the movement of the scene or the camera, as well as the defocus blur bringing by the false focus while imaging, etc. Among them, Gaussian blur is the most common, and the support of PSF is larger than the LR pixel size [6, 7]. Secondly, the down-sampling process (D) is performed on the blurred image. Here, the down-sampling factor is taken as an integer value. The down-sampled image is gained by taking the neighborhood averaging of the blurred image. Thirdly, the final LR image (Y) is generated by adding noise (N) to the down-sampled image. Here, the noise is assumed to be the white noise with zero means.

According to the above analysis, the mathematical description of LR imaging model of single-image SR can be expressed as follows:

$$Y = DBF + N \tag{1}$$

Where, Y represents the LR image, which is gained by the following steps. The HR image (F) is convolved with a blurring function (B). Then, the blurred image is down-sampled (D) with a given factor. Finally, noise is added to the down-sampled image.

2.2 *Framework of the Single-Image SR Reconstruction*

Among the current SR reconstruction approaches, iterative back projection (IBP) method has the advantages of small computation, fast convergence rate, good reconstruction effect, etc. The estimated information about the LR imaging model can be well utilized in the IBP algorithm. If the LR imaging model is estimated accurately, the SR reconstructed image will achieve quality.

In IBP algorithm, by back projecting the error of the estimated LR image and the original image onto the HR image grid, the estimation error is gained to modify to estimated HR image. Repeating the above process until the iteration time is greater than a given number or the estimation error is less than a threshold, the SR image will be gained.

According to the LR imaging model proposed in this paper and the idea of IBP algorithm, the framework of the single-image SR reconstruction method is shown in Fig. 1. Here, k is the iteration time; $\hat{f}$ is the estimated SR image; y is the observed LR image; $\hat{y}$ is the simulated LR images of $\hat{f}$ passed through the LR imaging model; B and D are the matrix forms of the motion blur and down-sampling respectively; B^{-1} and D^{-1} denote the inverse operation of B and D; n is the system noise; H^{BP} is the back projection operation; $\hat{y} - y$ is the difference of simulated LR image and the practical LR image; λ is the gradient step.

The IBP algorithm may be expressed as follows:

$$\hat{f}_{k+1} = \hat{f}_k - \lambda H^{BP}(\hat{y}_k - y). \tag{2}$$

Here, the initial value of the estimated HR image is the Bilinear interpolated image of the LR image. In some cases, the gray levels at some pixels in the estimated image may be beyond the boundary. In to make sure that the gray levels at each pixel are in the range of [0, 255], gray level correction is performed on the estimated SR image. Namely, the gray levels beyond 255 are taken as 255, and the gray levels below 0 are taken as 0. In this way, the artifact caused by excessively iterating may be decreased.

3 Gaussian Blur Estimation Method

Gaussian blur is very common in imaging systems, which may be expressed by the Gaussian PSF as follows:

$$h(m,n) = \begin{cases} \frac{1}{\sqrt{2\pi}\sigma} \exp\{-\frac{1}{2\sigma^2}(m^2+n^2)\} & (m,n) \in R \\ 0 & \text{others} \end{cases}. \tag{3}$$

Here, σ and R are the standard deviation and the supporting region of Gaussian PSF respectively. R is often indicated by a $K \times K$ matrix, and K is taken as an odd number. Thus, K and σ should be estimated for the Gaussian PSF.

In order to estimate these two parameters of Gaussian PSF, error-parameter analysis algorithm is used [8]. For a given size (K_i) and standard deviation (σ_i), according to equation (3), a Gaussian PSF (h_i) is gained. Using Wiener filter algorithm, a restoration error (E_i) is generated. Here, the range of K is [3, 11] with an increment of 2, and the range of σ is [0.5, 2] with and increment of 0.1. In this way, one error-parameter curve will be gained for a given K and differentσ, and multiple error-parameter curves will be generated at different K and differentσ. By analyzing the relationship between these curves, the size and the standard deviation of Gaussian PSF will be estimated.

In addition, to estimate the Gaussian PSF automatically, distance threshold (T_1) and slop threshold (T_2) are set. For and given estimation error, with the increasing of K, the size where once the distance between the curves is less than T_1 is the estimated size ($\hat{K}$). In this estimated curve, with the increasing ofσ, the standard deviation where once the slop is greater than T_2 is the estimated deviation ($\hat{\sigma}$).

4 Experiments

4.1 Generation of Simulated LR Image

Experiments are performed on simulated LR image to test the algorithm objectively and subjectively. The HR image 'lena.bmp' with size 256 $\times$ 256 as shown in Fig. 2 is passed through the LR imaging model as shown in Fig. 1. Firstly, the HR image is

Fig. 2 The HR image

Fig. 3 The LR image

convolved with a Gaussian PSF. Here, the original size (K_0) and standard deviation (σ_0) are taken as 7 and 1respectively. Secondly, the blurred image is down-sampled by 2 times. Finally, white Gaussian noise is added, and the standard deviation is taken as 1. The generated LR image with size 128 $\times$ 128 is shown in Fig. 3. Namely, the LR image in Fig. 3 is the blurred, down-sampled and noised image of the HR image in Fig. 2.

4.2 Gaussian PSF Estimation

The size (K) is taken from 3 to 11 with an increment of 2, and the standard deviation (σ) is taken from 0.5 to 2 with and increment of 0.1. The researching time is 50. The distance threshold (T_1) is 3, and the slop threshold (T_2) is 0.5. The generated error-parameter curves are drawn in Fig. 4.

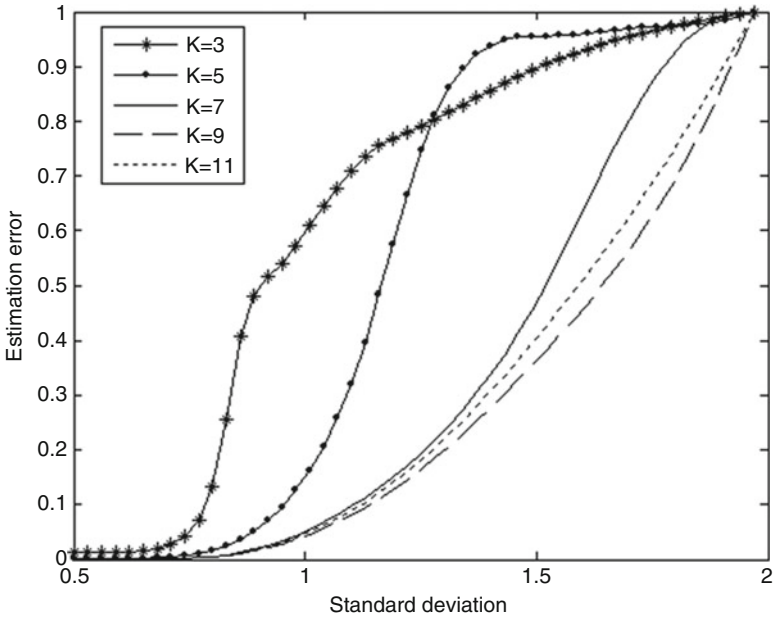

Fig. 4 The generated error-parameter curves

Using the error parameter analysis method, the estimated parameters of Gaussian PSF are $\hat{K} = 7$ and $\hat{\sigma} = 1.07$. The relative estimation errors are as follows respectively:

$$\left|K_0 - \hat{K}\right|/K_0 = |7 - 7|/7 = 0; |\sigma_0 - \hat{\sigma}|/\sigma_0 = |1 - 1.07|/1 = 0.07 \quad (4)$$

4.3 Blind Single-Image SR Reconstruction

Utilizing the estimated Gaussian PSF, when the up-sampling factor is taken as 2, SR image is reconstructed through the proposed framework. Here, in IBP algorithm, the maximum iteration time is 30, and the relative iteration error is 10^{-6}. The SR reconstructed image is shown in Fig. 5a, and PSNR = 35.4693 dB. The Bilinear interpolated image is shown in Fig. 5b, and PSNR = 33.5442 dB. From the experimental results, we can see that the SR image has higher PSNR and better quality.

4.4 Impact of Blur Estimation on SR Reconstructed Image

In order to justify the impact of Gaussian PSF estimation on blind single-image SR reconstruction, when the estimated size ($\hat{K}$) of Gaussian PSF is 7, and the estimated standard deviation ($\hat{\sigma}$) is from 0.5 to 3 with an increment of 0.1, SR images are

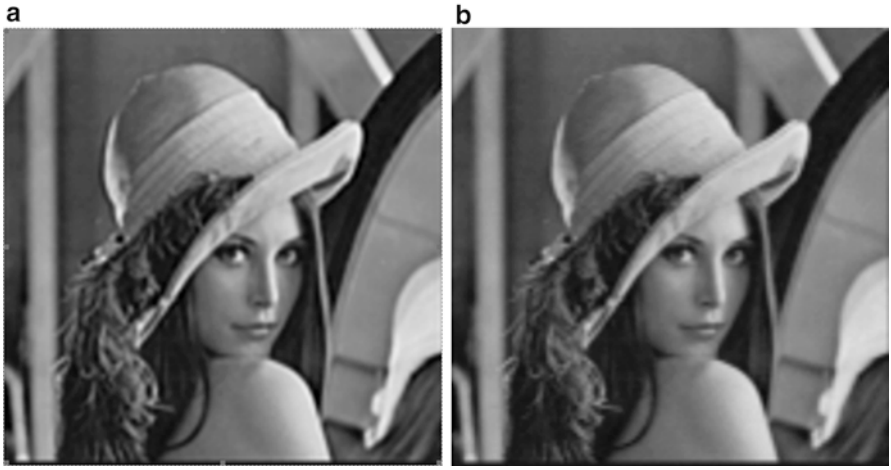

Fig. 5 The SR image and the Bilinear interpolated image. (**a**) SR image ($\hat{\sigma}$ =1.07) (PSNR = 35.4693 dB) (**b**) Bilinear interpolated image (PSNR = 33.5442 dB)

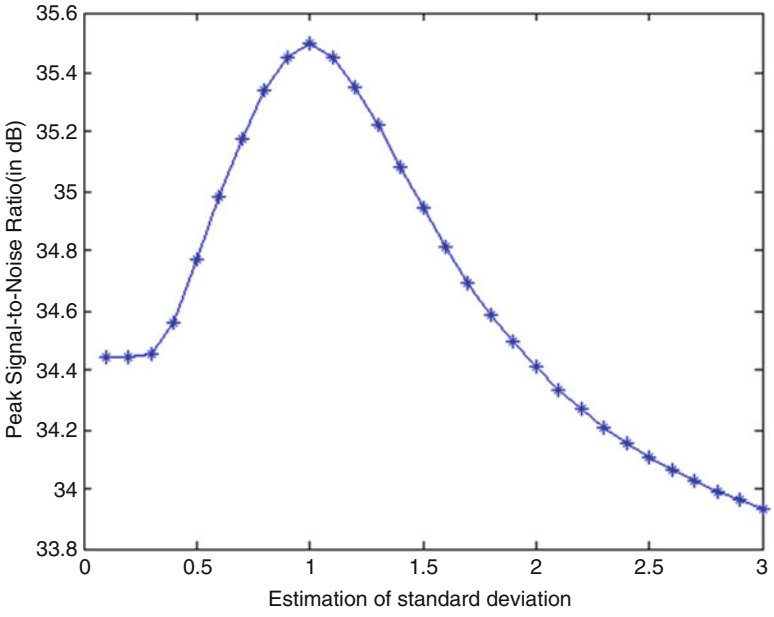

Fig. 6 The PSNRs of SR images at different $\hat{\sigma}$

reconstructed. The corresponding PSNRs at different $\hat{\sigma}$ is shown in Fig. 6. The SR images when $\hat{\sigma}$ are taken as 0.5 and 2 are shown in Fig. 7.

Comparing the experimental results, we can see that when the estimated Gaussian PSF is close to the actual value, the SR image has higher PSNR and

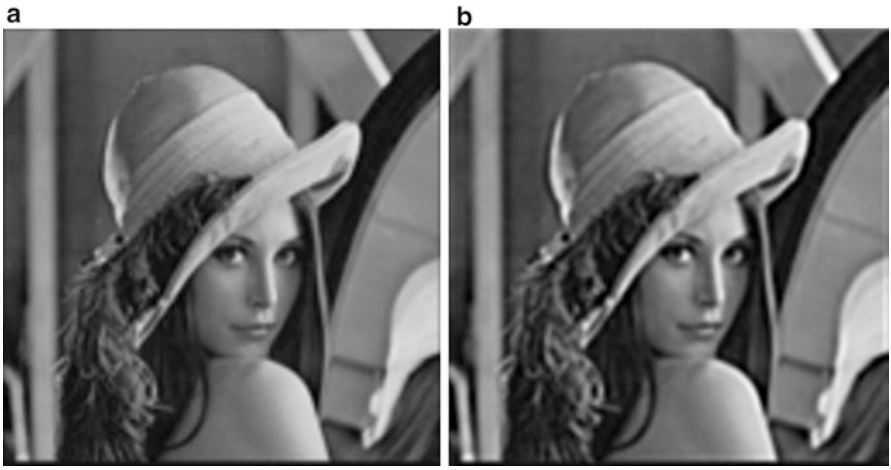

Fig. 7 The SR images when $\hat{\sigma}$ are 0.5 and 2 respectively (**a**) SR image ($\hat{\sigma} = 0.5$) (PSNR = 34.7696 dB) (**b**) SR image ($\hat{\sigma} = 2$) (PSNR = 34.4112 dB)

better resolution ability. If the Gaussian PSF is far away from the actual value, the PSNR decreases, and ringing effect appears in the SR reconstructed image.

5 Conclusion

Blind single-image SR reconstruction is a difficult and hot problem in image processing. A framework of blind single-image SR reconstruction was proposed. The processes in LR imaging model were sufficiently considered. Utilizing error-parameter analyzing method, the Gaussian PSF was accurately estimated. The SR image was reconstructed though IBP algorithm. The experimental results showed that Gaussian PSF estimation can play an important role in blind single-image SR reconstruction. The proposed method may be applied to restore the Gaussian blurred and slightly noised image. In future work, how to restore the degraded image with low SNR is a challenge problem. The de-noise process should be added.

Acknowledgements This paper is supported by the National Nature Science Foundation of China (61202195), the Sichuan Provincial Education Department project (11ZA174), the Application Fundamental Research Project of Sichuan Provincial Scientific and Technology Department (2011JY0139), the key project of Yibin Science and Technology Bureau (2011SF016).

References

1. Yuan Q, Zhang L, Shen H, Li P (2010) Adaptive multiple-frame image super-resolution based on U-curve[J]. IEEE Trans Image Process 19(12):126–141
2. Xiong Z, Sun X, Wu F (2010) Robust web image/video super-resolution[J]. IEEE Trans Image Process 19(8):2017–2028
3. Qin FQ, He XH, Chen WL, Yang XM, Wu W (2009) Video super-resolution reconstruction based on sub-pixel registration and iterative back projection[J]. J Electr Imaging 18(1):1–11
4. Kim KI, Kwon Y (2010) Single-image super-resolution using sparse regression and natural image prior [J]. IEEE Trans Pattern Anal Mach Intell 32(6):1127–1133
5. Ali MD (2009) Super-resolution: a short review, a new method based on hidden Markov modeling of HR image and future challenges[J]. The Comput J 52(1):126–141
6. He Y, Yap KH, Chen L (2009) A soft MAP framework for blind super-resolution image reconstruction[J]. Image Vis Comput 27(4):364–373
7. Giannoula A (2011) Classification-based adaptive filtering for multiframe blind image restoration[J]. IEEE Trans Image Process 20:382–390
8. Zou MY (2004) Deconvolution and signal recovery[M]. Defence Industry, Beijing, pp 184–214

Research on the Detection Method of Power Quality Based on Phase-Locked Loop

Zhixia Zhang and Xin Zhang

Abstract This paper uses a power quality disturbance detection method based on improved phase-locked loop (IPLL) system. The IPLL is a closed-loop phase feedback control system, which can track the instantaneous phase and instantaneous amplitude of the input fundamental in real-time. The generated output signal can be used for the detection of a variety of power quality disturbances. Moreover, the internal parameters of the detection system and the change of power system's frequency are robust. The use of the MATLAB/Simulink can study power quality problems, such as harmonics, frequency deviation, voltage swells, voltage interruptions, transient pulse, transient oscillation and voltage gap. Simulation results showed that the detection method had better accuracy and instantaneity.

Keywords Power quality • The improved phase-locked loop • MATLAB

1 Introduction

In recent years, with the extensive use of nonlinear, the impact load in the grid and the promote use of sensitive electronic equipment; power quality issues have become increasingly prominent. In order to ensure the normal operation of various equipments, measures must be taken to improve the power quality. Effective way to maintain high-quality electricity is that rapid detection for power quality; therefore power quality disturbance detection is very important [1–3].

Z. Zhang (✉) • X. Zhang
Shenyang Agricultural University, Shenyang, China
e-mail: syzzx7@163.com

W. Wang (ed.), *Mechatronics and Automatic Control Systems*, Lecture Notes in Electrical Engineering 237, DOI 10.1007/978-3-319-01273-5_33,

2 The Basic Principles of Detection Based on IPLL

In this paper, power quality detection method is carried out on the basis of improving PLL system [4, 5]. The IPLL system structure is shown in Fig. 1. Such as the traditional PLL, it consists of three basic components: phase detection (PD), loop filter (LF), and voltage controlled oscillator (VCO). The three parts form a closed loop phase feedback control system. The different between IPLL and traditional PLL are: the PD of traditional PLL is generally a multiplier, but the PD of IPLL consists of three multipliers, an integrator, a 90° phase shifter and a subtractor; IPLL has a number of useful output signals, including the fundamental component of output signal y (t), fundamental component of the amplitude A (t), phase U (t), instantaneous angular frequency ω (t) and the error signal e (t). Its biggest feature is y (t) and u (t) consistent. And both are synchronized, there is no phase difference between them. Using this feature, the ideal sinusoidal and interference components in the signal can be detected. In addition, using A (t) and ω (t), the disturbance of the fundamental amplitude and frequency of detection signal can be obtained respectively. This is the basic principle of the IPLL system which can detect power quality disturbances. The IPLL system is also characterized by the detection system of internal parameters and the input signal frequency changes is robust. And the IPLL system is stable. Therefore it is ideally suited for a wide range of power quality disturbances detection.

3 Simulations

We use the Matlab/Simulink simulation for a variety of power quality disturbances detection of IPLL system. The system simulation diagram is shown in Fig. 2. Input signal used in the paper is written in the M-file. To make the simulation results graphics visualization, a number of power quality disturbances are made by a certain degree of amplification. This may larger than the actual power quality disturbance amplitude in power system operation process. But these do not affect

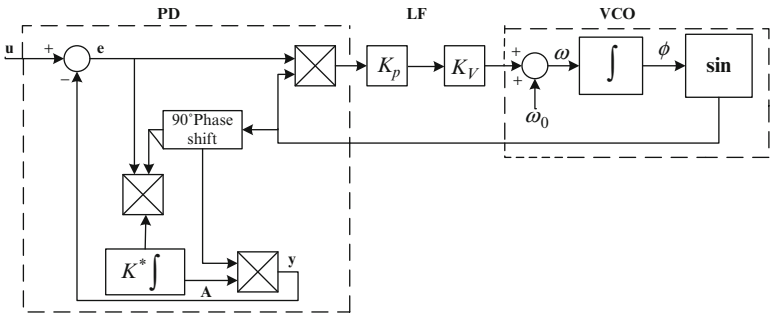

Fig. 1 Improved phase-locked loop system block diagram

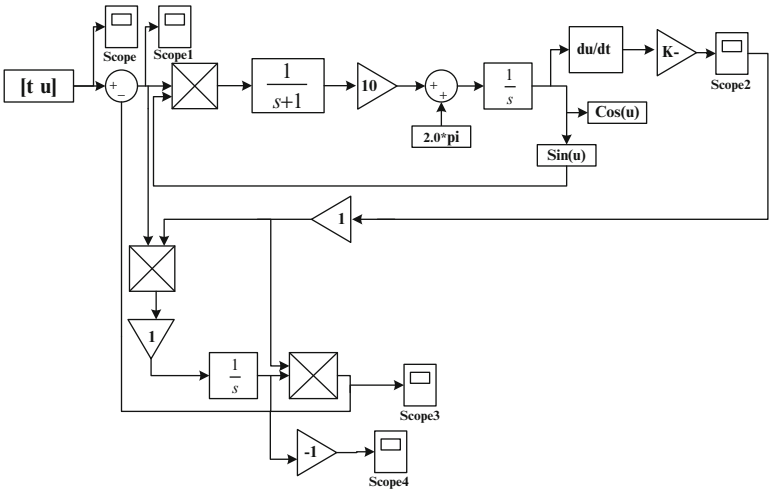

Fig. 2 IPLL system simulation diagram

the IPLL system is also suitable for the actual existence of power quality disturbance detection. The simulation results can estimate to the detection performance of the IPLL system on a variety of power quality disturbances.

3.1 Harmonic Detections

1. Square Wave Detection

```
M-file
clear all; t=(0:0.005:50)';
for c=1:50
  for m=(200*(c-1)+1):(200*c-100)
    u1(m)=1;
  end;
  for m=(200*(c-1)+1+100):(200*c)
    u1(m)=-1;
  end;
end;
u1(10001)=1; u=u1'; plot(t',u'); axis([0 55 -1.5 1.5])
grid on;
```

2. Dynamic Harmonic Detection

```
M-file
clear all;t=(0:0.005:50)';
for m=1:10001
  u2(m)=sin(2*pi*(m-1)*0.005);
end;
```

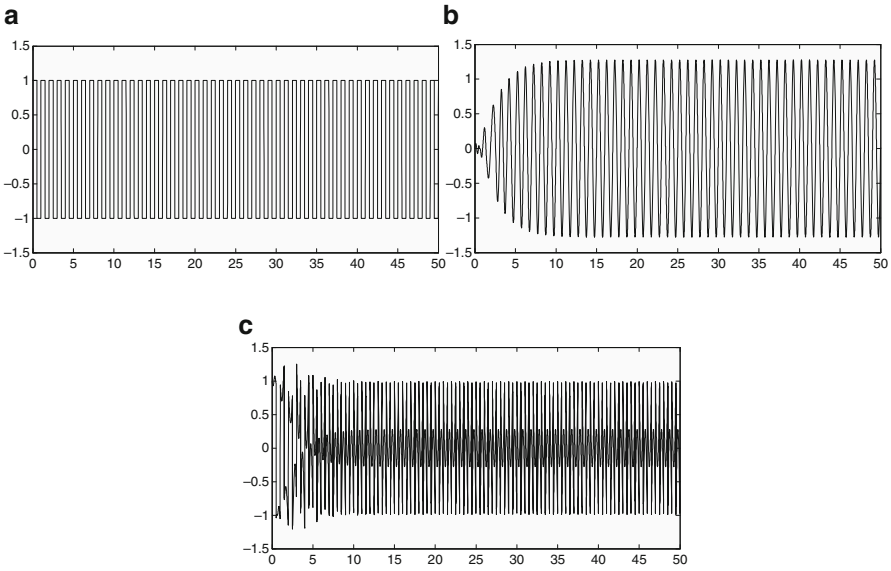

Fig. 3 Square-wave detection (**a**) square wave (**b**) the fundamental signal (**c**) square-wave total harmonic output

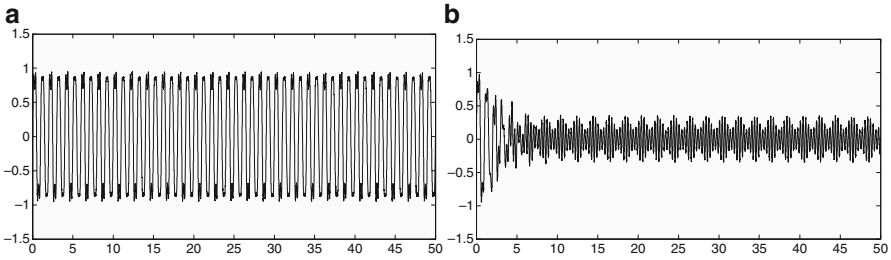

Fig. 4 Dynamic harmonic detection (**a**) dynamic harmonics (**b**) total harmonic output waveform

```
for m=1:10001
  u3(m)=(0.1*sin(pi*(m-1)*0.005)+0.2+0.05*rand(1))
  *sin(3*2*pi*(m-1)*0.005);
end;
  u=(u2+u3)'; %plot(t',u3'); plot(t',u'); axis([7 16
  -1.5 1.5]) grid on;
```

Figures 3 and 4 simulation results indicate that for two kinds of typical contain harmonics of the input signal on the above, IPLL system can effectively detect isolated from its fundamental components and total harmonic distortion component. And it can output its value in five cycles.

3.2 Frequency Deviation Detections

Using the output of the instantaneous angular frequency of the fundamental component to IPLL system ω(t), after transformation (/2π), can detect the fundamental frequency of the power system, then get the system frequency deviation. Set the input signal:u(t) = 1*sin(a*2πt) + 0.3*sin(a*6πt),where a = 0.95.

```
M-file
clear all; t=(0:0.005:50)';
for m=1:10001
  u2(m)=sin(0.95*2*pi*(m-1)*0.005)+0.3*sin(0.95*6*pi*
  (m-1)*0.005);
end;
u=u2'; plot(t',u'); axis([0 20 -1.5 1.5]) grid on;
```

Detection of the simulation results shown in Fig. 5, according to the fundamental frequency of the output of the system, the system frequency deviation is 5 %. The simulation results show that the IPLL systems can more accurate real-time detection system frequency deviation.

3.3 Detections of Voltage Swells and Voltage Interruptions

Using the amplitude of the output of the fundamental component, we get amplitude of the disturbance of the detected signal fundamental. It not only can detect the voltage fluctuation also can detect the voltage drop, the voltage rise and voltage interruptions disturbance [6, 7].

In which take the voltage swells disturbance signal is normal when 0–25 cycles; there is a 30 % voltage swells when 25–40 cycles; finally the voltage is restored to normal. M-file is as follows (Fig. 6).

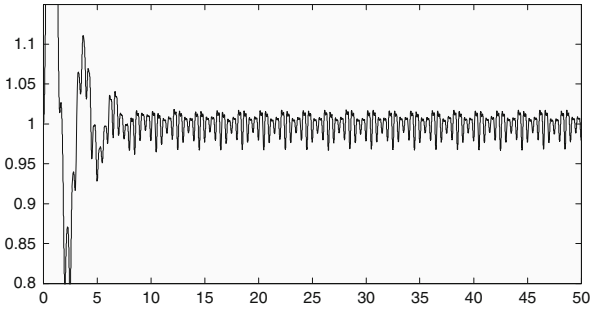

Fig. 5 Frequency deviation detection

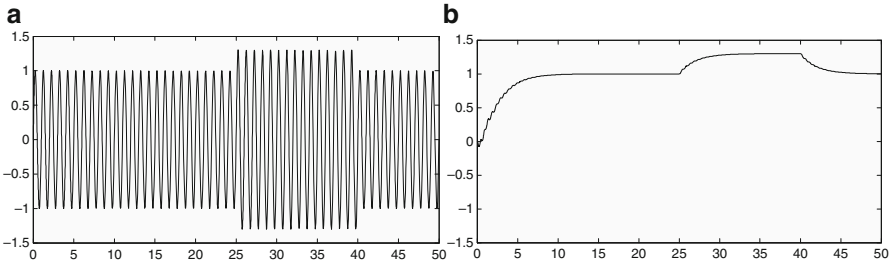

Fig. 6 Detection of voltage swells (**a**) a 30 % voltage swells (**b**) the detected voltage swells

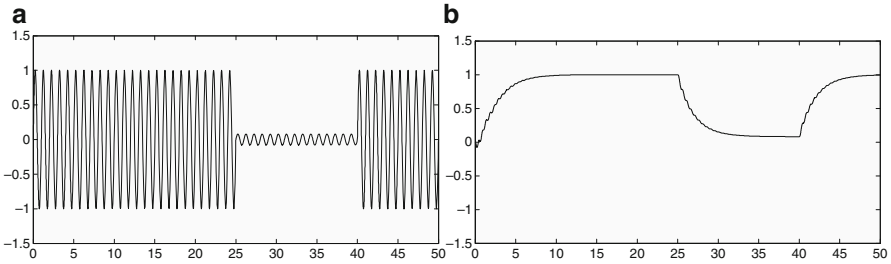

Fig. 7 Detection of voltage interruption (**a**) a voltage interruption (**b**) the detected voltage interruption

```
clear all; t=(0:0.005:50)';
for m=1:5000
  u2(m)=sin(2*pi*(m-1)*0.005);
end;
for m=5001:8000
  u2(m)=1.3*sin(2*pi*(m-1)*0.005);
end;
for m=8001:10001
  u2(m)=sin(2*pi*(m-1)*0.005);
end;
u=u2'; plot(t',u'); axis([0 50 -1.5 1.5]) grid on;
```

In which take the voltage interruption disturbance signal is normal when 0–25 cycles; there is a voltage interruption when 25–40 cycles; Finally the voltage is restored to normal.

The m-file of voltage interruption is similar to voltage swells (Fig. 7).

Simulation results show that IPLL system can instantaneous detect voltage swells and voltage interruptions disturbance. It can output its value in five cycles.

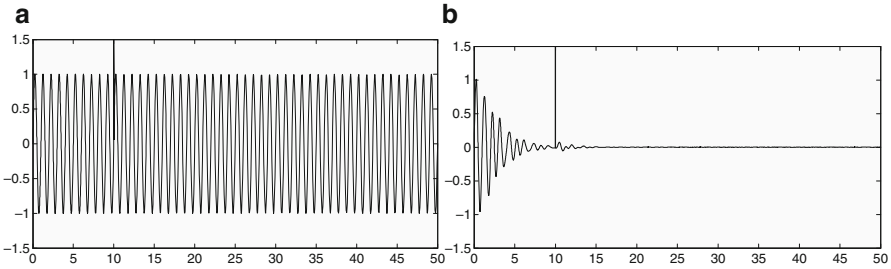

Fig. 8 Detection of transient pulse (**a**) input signal with transient pulse (**b**) the detected transient pulse

3.4 Transient Pulse Detections

Transient pulse is the natural frequency of the power grid incentives arising from the oscillation transient phenomena. It is caused by the line being struck by lightning or inductive circuit division. There is a pulse in the 10th cycle. M-file as follows [8–10] (Fig. 8).

```
clear all; t=(0:0.005:50)';
for m=1:2000
  u2(m)=sin(2*pi*(m-1)*0.005);
end;
for m=2001:2002
  u2(m)=2;
end;
for m=2003:10001
  u2(m)=sin(2*pi*(m-1)*0.005);
end;
u=(u2)'; plot(t',u'); axis([0 50 -1.5 3]) grid on;
```

Simulation results show that IPLL system can effectively detect the fundamental component and the total disturbance composition of the transient pulse signal.

4 Conclusion

Power quality disturbances detection methods based on IPLL system is an ideal method. It can more accurately detect a variety of power quality disturbances. It has strong robustness for the internal parameters of the detection system and the power system frequency changes. The method also has good instantaneity and stability, which is unmatched by many other detection methods. In addition, the output signal

of the IPLL system can track of the fundamental component of the external input signal in real-time.

The next task is to improve specific performance of the IPLL system based on disturbance characteristics of the detected signal and to make a more accurate simulation model, thus further improving the system so that it can accurately detect disturbance signal.

References

1. Mao Niankui, Zhang Xuefeng (2010) Power quality signal disturbance detection and location. J Huainan Vocat Techn Coll 10(1):22–27
2. Zhao Jing, Qian Qingquan, He Zhengyou (2011) A way to identify of hybrid power quality disturbances. Autom Electr Power Syst 35(3):71–76
3. Wang Lixia, He Zhengyou, Dai Ming, Zhao Jing, Qian Qingquan (2009) A new power quality disturbance signal hierarchical identification method. Autom Electr Power Syst 33(24):65–69
4. Ge Naicheng, Cheng Haozhong, Lv Ganyun (2004) The power quality detection based on Matlab/Simulink simulation. For Electr 21(6):29–32
5. Lv Ganyun, Ding Qifeng, Ge Naicheng (2004) Detection method of power quality disturbance based on an improved PLL system. Proc CSU-EPSA 16(5):20–25
6. Lv Ganyun, Cheng Haozhong, Wang Xiaodong, Zhang Haoran (2006) Phase-shift of power quality detection method. Relay 43(3):60–62
7. Zhan Yong, Cheng Haozhong, Ding Yifeng, Lv Ganyun, Sun Yibin (2005) S-transform-based classification of power quality disturbance signals by support vector machines. Proc CSEE 25(4):51–56
8. Fang Guozhi, Hu Bingfang, Song Guoyi (2008) Three classes of grid disturbance signal detection method. Electr Power Autom Equip 28(6):74–76
9. Gong Jing (2009) The use of wavelet modulus maximum principle in the detection of disturbance signal for transient power quality. Northeast Electr Power Technol 20(5):10–13
10. Quan Huimin, Dai Yuxing (2007) Detection and localization of power quality disturbances based on S-transform module matrixes. Trans China Electrotechn soc 22(8):119–126

A Discriminant Analysis Method for Power System Small Signal Based on Matrix Norm

Qi-rong Qiu, Jianlei Shi, and Mengdi Wang

Abstract As we all know, the analysis of small signal stability plays an important role in power system stability. This paper presents a new discriminant analysis method for power system small signal based on the norm of matrix, that is, estimate the system stability according to the norm of matrix S. Comparing with traditional methods, there is no need to compute the eigenvalue of the matrix and the choice of the parameters has little effect on the problem. The analysis of typical problems showed that the proposed method solve perfectly the slow convergence problem of power method, which is used to calculate the principal eigenvalue, when the separated eigenvalue became a "cluster".

Keywords Small perturbation • Stability • S-matrix • Norm • Eigenvalue

1 Introduction

With the construction of the large-capacity long-distance transmission system and the interconnection of large power systems [1, 2], whose purpose is to improve the economy and reliability of generation and transmission, the size of the power system is constantly expanding. However, multiple interconnections between different grids induce much new problem on power system stability, which make the

Q.-r. Qiu
School of Mathematics and Physics, North China Electric Power University, Beijing, China

J. Shi (✉)
State Grid Jibei Electric Power Company Limited, Economic Research Institute, Beijing 100070, China
e-mail: 2002sjl2908@sina.com

M. Wang
Faculty of Mechanical and Electronic Information, China University of Geosciences, Wuhan, China

W. Wang (ed.), *Mechatronics and Automatic Control Systems*, Lecture Notes in Electrical Engineering 237, DOI 10.1007/978-3-319-01273-5_34,

power system easier to loss stability. At the same time, the problems such as the fast excitation system, high voltage direct current (HVDC) [3], A Nonlinear thyristor controlled series compensation (TCSC) [4], as well as the adoption of new technology in new energy generation make the power system more random and complex. Therefore, the study of small signal stability has been brought to the forefront in power system stability.

Small signal stability analysis method is based on state equation, which is a nonlinear differential equations and algebraic equations of power system. And the equation described the dynamic behavior of power system and was linearized at the operating point. Discriminant of system stability depends on the positions of eigenvalues of the state-describing matrix in the complex plane (i.e., the real part of characteristic root is less than zero).

Quick Response(QR) method-calculation of all the matrix eigenvalues used to be a very effective method to study power system small signal stability. However, as the increase of dimension of the system, its limitations become increasingly apparent. As for the small signal stability, QR method has inadequacies in unacceptable computation time needed by the large-scale systems. In addition, while the dimension is very high, "forward instability" may occur sometimes [5], namely the so-called "pathological" problem, which can't obtain the characteristic value.

Since the 1980s, many of the partial eigenvalue analysis methods began to be used in power system small signal stability analysis. These methods computed a part of the principle eigenvalue-the largest eigenvalues of the real part, in order to reduce calculation amount. An Evolutionary System for Online Processing (AESOP) algorithm, which is proposed by Byerly [6] and similar to frequency response method, transformed the eigenvalue problem into the problem of finding roots of nonlinear equations. However, it is difficult to the chose initial value. What's more, the method couldn't predict which eigenvalue can be converged. Angelidis [7] proposed a two-step method based on fractional transformer, which use the simultaneous iteration method to calculate the estimated eigenvalue near the displacement point, then use these estimates values as the initial ones to calculate the exact values with Newton method. However, in order to guarantee not to lose principal eigenvalues, this approach must select multiple displacement points, and thus to conduct several fractional transformations and several rounds of iterations. Uchida [8] proposed S-matrix method-calculating the some of the principal eigenvalue of the original system with matrix transformation, which estimate the system stability through the principal eigenvalue of the S matrix. However, with S-matrix method, the parameters selected from the matrix transformations have large effect on the convergence speed, and may converge to a non-main eigenvalue. Xiaopeng [9] proposed a triple Cayley transformation method, and make the parameters $d = 7 + j10$ and $h = 6$, to avoid the difficulty in choosing parameters with S-matrix. However, this method using a triple Cayley transformation, which the computing amount of each Diegothe generation is about five times as the S-matrix method.

Set $\lambda_{s,1}, \lambda_{s,2},\ldots, \lambda_{s,n}$ is eigenvalues of matrix S and $|\lambda_{s,1}| \geq |\lambda_{s,2}| \geq \cdots |\lambda_{s,n}|$. To calculate $|\lambda_{s,1}|$ by power method, the convergence speed depends on $\lambda_{s,2}/\lambda_{s,1}$. Set λ_A is the eigenvalue of matrix A. If the real part of λ_A is not only less than 0 but also quite large, the mode of the corresponding eigenvalue of conversed S closes to 1. In order to find the principle eigenvalue as soon as possible, Zhengchun [10] presented an explicit restarted Arnodli-Chebyshev algorithm to calculate directly the real-part-diminished feature subset of large scale power system. The method constructed Low dimensional Krylov subspace by Arnoldi decomposition so that the subspace contains the information of real-part-diminished feature subset. Chebyshev acceleration technology speeded up the convergence of the method. However the technology is not good at solving the problem of clustered principle eigenvalues of matrix s.

This paper presents a new estimate method of the small signal stability based on the norm of matrix. It estimates the system stability by spectral radius of matrix S according to the norm of matrix S. It means to compare $\|S^{2m}\|_1$ with 1. As $\|A^{2m}\|_1 \sim (\rho(A))^{2m}$, the speed of drop (growth) is fast and there's almost no difference to solve the original problem by different parameter s. The proposed method solved the slow convergence problem of power method perfectly, which is used to calculate the principal eigenvalue, when the separated eigenvalue became a "cluster". The analysis of some typical problems showed that the proposed method is able to estimate the stability of power systems by small signal.

2 The Mathematical Model of Small Signal Stability Analysis

The mathematical model of small signal stability analysis for electric power system can be described by Equation (1) which is linear differential-algebraic equations [11].

$$\begin{pmatrix} \Delta\dot{x} \\ 0 \end{pmatrix} = \begin{pmatrix} \tilde{A} & \tilde{B} \\ \tilde{C} & \tilde{D} \end{pmatrix} \begin{pmatrix} \Delta x \\ \Delta y \end{pmatrix} \tag{1}$$

Set m equal to the amount of network nodes, n equal to the amount of state variables. Then, there are $\tilde{A} \in R^{n\times n}, \tilde{B} \in R^{n\times 2m}, \tilde{C} \in R^{2m\times n}, \tilde{D} \in R^{2m\times 2m}$. Cancelling the parameter vector Δy, we obtain Eq. 2

$$\Delta\dot{x} = A\Delta x \tag{2}$$

where

$$A = \tilde{A} - \tilde{B}\tilde{D}^{-1}\tilde{C} \tag{3}$$

3 The Criterion of Stability Based on the Norm of Matrix

The matrix transform is described by Eq. 4:

$$S = (sE + A)(sE - A)^{-1} \tag{4}$$

Theorem 1 could be testified according to the matrix theory [12]:

Theorem 1 *$f(A)$ is the matrix function, where $A \in C^{n\times n}$. If λ is the eigenvalue of matrix A and v is the eigenvector corresponding to λ, $f(\lambda)$ is the eigenvalue of $f(A)$ and v is the eigenvector of $f(A)$ corresponding to $f(\lambda)$.*

Corollary 1 *λ is the eigenvalue of matrix* A, *where $S = (sE + A)(sE - A)^{-1}$ and $A \in C^{n\times n}$, then*

(a) $\frac{\lambda+s}{s-\lambda}$ is the eigenvalue of matrix S;
(b) The real part of λ equals to one. $\Leftrightarrow$ The spectral radius of the matrix S equals to 1.
(c) 0 is the eigenvalue of matrix A $\Leftrightarrow$ 1 is the eigenvalue of matrix S .

Corollary 2 *If λ is the eigenvalue of matrix A, λ^k is the eigenvalue of matrix A^k.*

Theorem 2 *The necessary and sufficient condition of the real part of eigenvector of matrix A is negative is that $sE - A$ is nonsingular and the spectral radius of* S *is less than 1 for any $s > 0$, where $S = (sE - A)^{-1}(sE + A)$.*

Based on theorem 2, in order to estimate the ability of the system, we only need to prove whether the spectral radius of S is less than 1 or not. If the spectral radius of the matrix S is less than 1, the system is stability. If the spectral radius of the matrix S equals to 1, the system is in critical condition. If the spectral radius of the matrix S is larger than 1, the system is not stability.

According to the matrix theory[12], get the theorem 3.

Theorem 3 *If λ is the eigenvalue of matrix* A, *$|\lambda| \le \|A\|$ is true for any $\|\cdot\|$; Any two matrix norms are equivalent; For any $\varepsilon > 0$, there exists $\|\cdot\|_*$, such that $\| A \|_* \le \rho(A) + \varepsilon$;*

By theorem 3, we can conduct theorem 4 easily.

Theorem 4 *μ is a positive constant which is independent with the matrix* S, *then $\rho(S)/\mu \le \|S\| \le \mu\rho(S)$, where $\rho(S)$ is the spectral radius of the matrix* S.

We know that if $S \in C^{n\times n}$, then $\|S\|_1 = \max\limits_{1\le j\le 1} \sum\limits_{i=1}^{n} |S_{ij}|$. Noticing $\rho(S^{2m}) = (\rho(S))^{2m}$, we can conclude that $\left\|S^{2m}\right\|_1$ will quickly tend to be 0 when $\rho(S) < 1$; while it will quickly tend to be $+\infty$ when $\rho(S) > 1$. So this paper proposed the new estimate method of the small signal stability based on the norm of matrix, algorithm steps are shown as following:

(a) Get a number M which is large enough, set m equal to 0 and S_0 equal to S;
(b) Calculate S_{m+1} and $\|S_{m+1}\|_1$, where $S_{m+1} = S_m \cdot S_m$;
(c) If $\|S_{m+1}\|_1 < 1$, then the system is stability, and the calculation ends. Otherwise turn to step 4
(d) If $\|S_{m+1}\|_1 = 1$, then the system is in critical condition, and the calculation ends. Otherwise turn to step 5
(e) If $\|S_{m+1}\|_1$ then the system is not stability, and the calculation ends. Otherwise turn to step 2 after $m = m + 1$.

4 The Analysis of Typical Problems

In order to test the effect of the proposed discriminant analysis method, this paper analyzed three typical problems.

4.1 Two Area and Four Machine System

Figure 1 showed the typical two-area and four-machine system [13]. Power system simulation software PSS/E is used to calculate the state matrix of power systems in a certain operating condition. Set S equal to the state matrix of the two areas and four-machine system.

Set $M = 10000\|S\|_1$, get $\left\|S^{2^{18}}\right\| > M$ after calculation, that is to estimate that the power systems is not stability by small signal.

4.2 Network for Subsynchronous Resonance Studies

Figures 2 and 3 is the first benchmark model for computer simulation of subsynchronous resonance [14]. Figure 2 shows the network for subsynchronous resonance studies. Figure 3 shows rotor model for transient studies. The shaft of the generator is composed by HP,IP,LPA,LPB,GEN and EXC [15]. The active

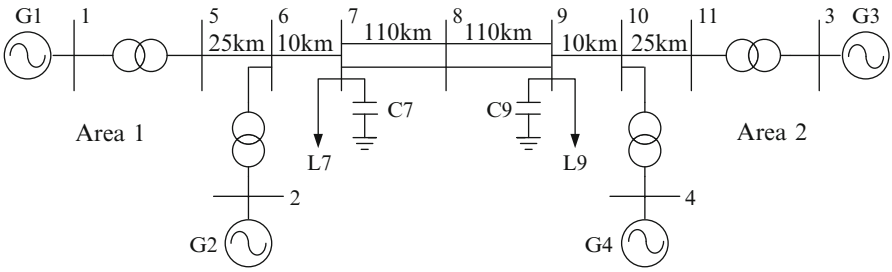

Fig. 1 Test system of four-machine eleven-bus

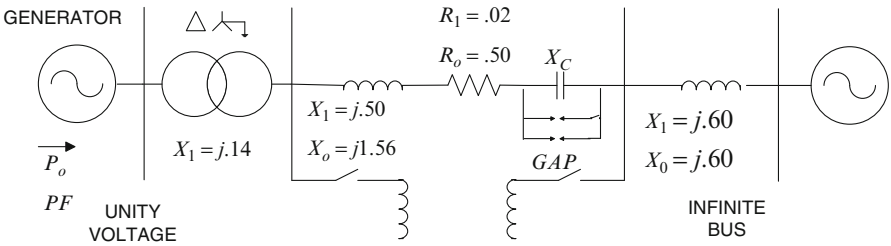

Fig. 2 Network for subsynchronous resonance studies

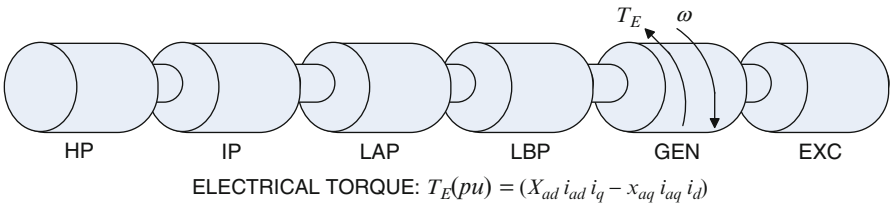

Fig. 3 Rotor model for transient studies

power is 0.8, and power factor is 0.9, system voltage is 1 (per-unit value). Set S equal to the state matrix of the first benchmark model for computer simulation of subsynchronous resonance of IEEE.

Set $M = 10000\|S\|_1$, get $\left\|S^{2^3}\right\| > M$ after calculation of three steps, that is to estimate that the power systems is stability by small signal based on $\|S_3\|$.

4.3 IEEE 3 Generators and 9 Nodes

Figure 4 showed IEEE 3 generators and 9 nodes [13] including 3 generators, 9 nodes and 3 loads. Kundur [13] shows detailed data, parameters and the matrix S. The parameter s in Eq. 4 is equal to 1. Set $M = 10000\|S\|_1$, get $\left\|S^{2^{11}}\right\| < 1$, that is to estimate that the power systems is stability by small signal based on $\|S_{11}\|$.

4.4 The Effect of Parameter Selection on the Algorithm Efficiency

There is little effect of parameter M on the algorithm efficiency, because $\|S_{m+1}\|_1 = O(\|S_m\|^2)$. Set m be the calculation steps. Table 1 showed the value of m in the three typical problems when parameter s is diverse after estimating the stability of systems.

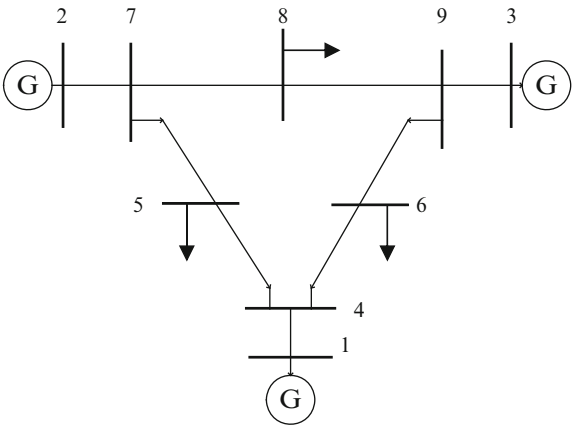

Fig. 4 IEEE 3 generators and 9 nodes

Table 1 Number of calculation steps

s	0.01	0.1	0.5	1	1.5	2	4	0
Two area and four machine system	5	4	4	3	3	3	4	6
First benchmark model for computer simulation of subsynchronous resonace	24	21	19	18	17	7	6	5
IEEE 3 generators and 9 nodes	17	14	12	11	11	10	11	12

5 Conclusion

It is necessary to estimate matrix eigenvalues of the system state in small signal stability analysis. The traditional QR method fails when the system size is large. Because the separated eigenvalue may become a "cluster", the convergence speed Cayley converter technique is slow when calculate the principle eigenvalue by power method, furthermore, the choice of the parameter s has big effect on the problem. This paper presents a new estimate method of the small signal stability based on the norm of matrix, that is, estimate the system stability according to $\left\|S^{2^m}\right\|_1$. The analysis of typical problems showed that the proposed method solve perfectly the slow convergence problem of power method, which is used to calculate the principal eigenvalue, when the separated eigenvalue became a "cluster". When the system is not stable, $\left\|\lambda_{S,\max}\right\|$ can be estimated by $\sqrt{[2^m]}$ $\|S_{m+1}\|_1/\|S_m\|_1$. However, there should be another way to calculate the specific eigenvalue. And this is the disadvantage of the method.

References

1. Zhou Xiaoxin (1997) To develop power system technology suitable to the need in 21st century. Power Syst Technol 21(11):11–15
2. Ding Gongyang (2000) Features and characteristics of three gorges plant and its position and effect in three gorges power system. Power Syst Technol 24(8):1–4
3. Arabi S, Rogers GJ, Wong DY (1991) Small signal stability program analysis of SVC and HVDC in AC power systems. IEEE Trans Power Syst 6(3):1147–1153
4. Jiang D, Lei X (2000) A nonlinear TCSC control strategy for power system stability enhancement. In: APSCOM 2000 – 5th international conference on advances in power System Control, Operation and Management, Hong Kong, pp 576–581
5. Watkins DS (1995) Forward stability and transmission of shifts in the QR algorithm. SIAM 16(2):469–487
6. Byerly RT, Bennon RJ, Sherman DE (1982) Eigenvalue analysis of synchronizing power flow oscillations in large electric power systems. IEEE Trans PAS 101(1):235–243
7. Angelidis G, Semlyen A (1995) Efficient calculation of critical eigenvalue clusters in the small signal stability analysis of large power systems. IEEE Trans PWRS 10(1):427–432
8. Uchida N, Nagao T (1988) A new eigen-analysis method of steady-state stability studies for large power systems: S-matrix method. IEEE Trans PWRS 3(2):706–714
9. Liu Xiaopeng, Lu Shirong, Guo Qiang, Xia Daozhi (1998) A multiple cayley transformation method for analysing partial eigenvalues of power system small signal stability. Autom Electr Power Syst 22(9):38–42
10. Du Zhengchun, Liu Wei, Fang Wanliang, Xia Daozhi (2004) Calculation of critical eigenvalues in large-scale power systems using Arnoldi-Chebyshev Method. J XI'AN Jiaotong Univ 38(10):995–999
11. Xifan Wang, Wanliang Fang, Zhengchun Du (2003) Modern power system analysis. Science Press, Beijing, pp 122–143
12. Qiu Qirong (2008) Matrix theory and its application. China Power Press, Beijing, pp 17–28
13. Kundur P (1994) Power system stability and control. McGraw-Hill, New York
14. (1977) IEEE subsynchronous resonance task force of the dynamic system performance working group power system engineering committee, first Benchark model for computer simulation of subsynchronous resonance. IEEE Transactions on Power Apparatus and Systems (5), PAS-96
15. Zheng Xiang (2011) Research on subsynchronous oscillation suppression devices and their control strategies. Zhejiang University, Zhejiang

Bandwidth Enhancement for Planar Inverted F Antenna

Eng Gee Lim, Zhao Wang, Xiang Li, Ka Lok Man, Nan Zhang, and Kaiyu Wan

Abstract Planar Inverted F Antenna (PIFA) is popular and widely used in hand-held wireless devices because of several significant advantages. However, PIFA also has many shortages that become big limitations for its commercial application, such as narrow bandwidth. Therefore, it is a great challenge to design a PIFA with good performance. In this paper, a conventional PIFA working on GSM dual-band system (GSM 900: 900 MHz and GSM 1800: 1800 MHz) was investigated first. Then, by adding a stub on the feed line, the narrow bandwidth problem of this PIFA was well solved. By this method, no additional cost is needed, and also it is easy to manufacture.

Keywords Planar inverted F antenna • Dual-band • Bandwidth

1 Introduction

Planar Inverted F Antenna (PIFA) is very popular and widely used in portable wireless devices because of several significant advantages. The first one is that PIFA has a small size and can be fitted into the housing of a mobile phone compared to other types of antenna. Second, PIFA can reduce backward radiation toward to the user's body, which minimized the electromagnetic power absorption and maximized the antenna performances. Third advantage is that PIFA performs moderate to high gain in both horizontal and vertical states of polarization (near omnidirectional), which is very useful in some particular wireless communications where the antenna orientation is random and the reflections are present from the

E.G. Lim (✉) • Z. Wang • X. Li • K.L. Man • N. Zhang • K. Wan
Xi'an Jiaotong-Liverpool University, Suzhou, China
e-mail: enggee.lim@xjtlu.edu.cn

W. Wang (ed.), *Mechatronics and Automatic Control Systems*, Lecture Notes in Electrical Engineering 237, DOI 10.1007/978-3-319-01273-5_35,

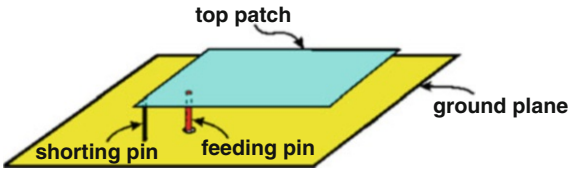

Fig. 1 A basic PIFA

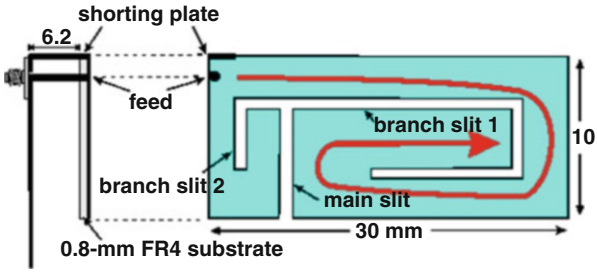

Fig. 2 Embedded PIFA designed for mobile phone

different directions of the environment [1]. The other advantages are its low profile, easy fabrication, low cost for manufacturing and simple structure [2]. Also, PIFA is embedded into the phone circuitry and the space within the mobile phone can be reused for other needs [3].

Narrow-bandwidth characteristic of PIFA is one of the limitations for its commercial application for mobile phone. The shorting pin near the feed probe location of usual PIFA types is good technique for reducing the antenna size, but consequently this will cause narrow impedance bandwidth [1].

A basic PIFA contains a top plate element, a feed tab feeding the resonating top plate, a ground plane and a DC-shorting tab which connects the ground plane with the top plate. Figure 1 shows a basic PIFA [4]. The top patch is attached above the ground plane the supports of the shorting pin and feeding pin, which is connected to the top patch at designed positions, have the same length as the distance between the top patch and the bottom ground.

There are some basic rules for design PIFA. For an inverted F antenna, the total length of the antenna should be approximately close to a quarter-wavelength. Figure 2 shows an Embedded PIFA designed for mobile phone [4]. From the figure, there are two branch slit on the top patch, which are designed for two working band of the antenna (900 and 1800 MHz). Therefore, this is a dual-band PIFA.

In this paper, a brief introduction of PIFA and the investigation of a conventional PIFA that works on dual-band (GSM 900: 900 MHz and GSM 1800: 1800 MHz) system will be introduced first. In addition, the optimization of this conventional PIFA and final discussion of the results will be given based on the simulation. Conventional PIFA with Feed Stub is added to enhance the operating bandwidth.

2 Antenna Designs

2.1 Conventional PIFA

Figure 3 shows the layout of a conventional PIFA (dimensions in mm) [5]. The antenna is designed on a 100 × 40 × 0.8 mm GETEKML200M with a permittivity of 3.8. It is connected through a microstrip line that runs from the center of the ground plane connecting to a typical 50 Ω coaxial cable at the back of the ground plane, as shown in Fig. 3. The width of the microstrip line is set to 2.02 mm to match the antenna to the 50 Ω coaxial cable. This dual-band PIFA is designed to work on GSM 900: 880–960 MHz and GSM 1800: 1710–1880 MHz.

2.2 Conventional PIFA with Feed Stub

To solve the narrow band problem of PIFA, changes need to be done to the antenna. Many researches have been done on PIFA broad banding, such as [5] and [6]. However, in these researches, capacitors, dual feed or even integrated match circuit are used. In this proposed paper, a very simple method, adding feed stub has been used to extend the narrow band of PIFA to achieve the bandwidth requirement of both GSM 900 and GSM 1800. In Fig. 4a stub (in the red circle) is added on the feed line of the conventional design. It has a length of 3.5 mm and a width of 3.125 mm. It is 5 mm away from the centerline.

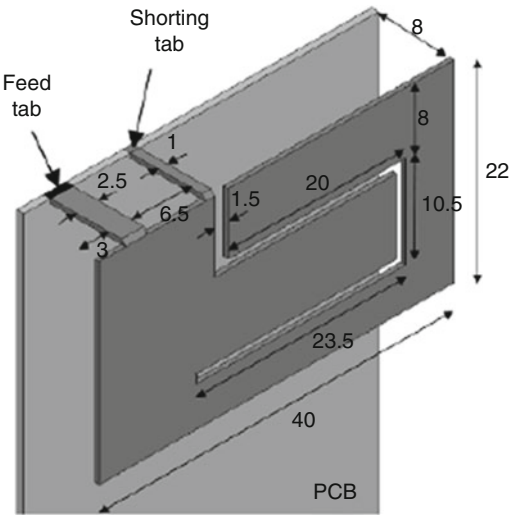

Fig. 3 Conventional PIFA

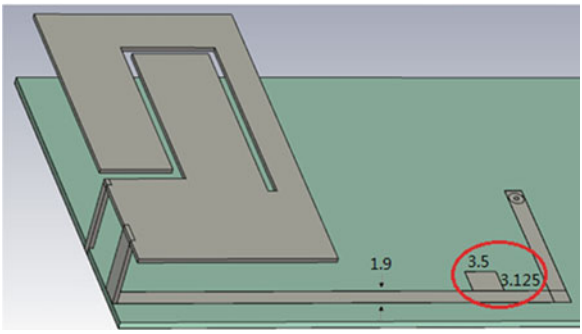

Fig. 4 Conventional PIFA with added stub

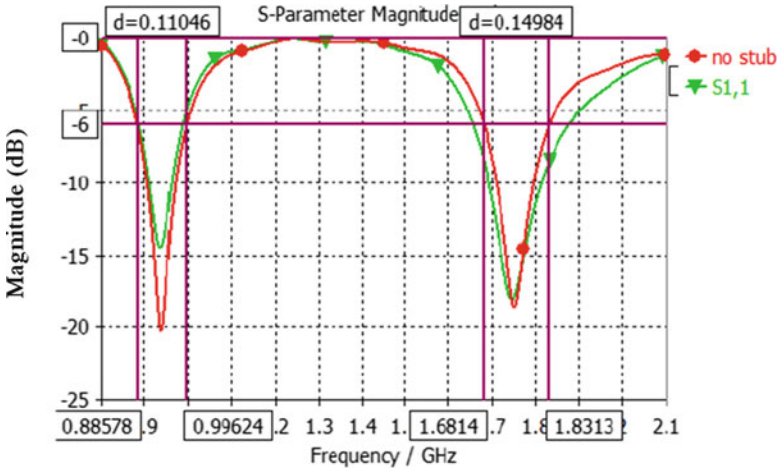

Fig. 5 Return loss of the PIFA

3 Results

The return loss of the proposed design is shown in Fig. 5 below. The green line with dot is the return loss of the conventional PIFA without stub, and the red one with triangle stands for the return loss with stub added to the feed line.

As is shown in the Fig. 5, there are two resonant bands: one is approximately resonant at 910 MHz and another is resonant at 1,750 MHz. As mobile phone antennas are normally designed to give a return loss of 6 dB or better, in this design -6 dB will be assumed as a satisfactory level. Therefore, the bandwidth of GSM 900is measured as 110.46 MHz (from 885.78 to 996.24 MHz)and for GSM 1800 the bandwidth is 149.85 MHz (from 1681.4 to 1831.3 MHz). However, compared with the typical requirement mentioned above, the bandwidth of GSM 1800 is too narrow (GSM 1800: 1,710–1,880 MHz(170 MHz)). To improve this problem, the

design in Fig. 2 has used complicated dual-feed system with capacitor [4]. However, in this proposed design, only a small microstrip stub is added on the feed line as shown in Fig. 4. Furthermore, in this proposed design no additional cost and no soldering will be required in manufacturing. By the effect of this stub, the GSM 1800 band is broadened effectively. The detail is shown in Fig. 5. As shown in the Fig. 5, the band is extended to 219.7 MHz, which is from 1656.4to 1876.1 MHz. This bandwidth is wide enough to reach the requirement of GSM 1800.

4 Conclusion

In this project, a conventional PIFA working on GSM dual-band system (GSM 900: 880–960 MHz and GSM 1800: 1710–1880 MHz) was investigated, especially on return loss performance. To solve the narrow bandwidth problem of this PIFA, a feed stub was added on the feed line. By this optimization, the bandwidth of GSM 1800 of the PIFA was extended greatly. Thus this conventional PIFA can work properly on GSM dual-band system. Compared with the previous designs that aim at improving the bandwidth performance of PIFA using capacitors or integrated match circuit, the method introduced in this project is simpler and easier for manufacturing by the current printed circuit technique without additional cost. It is a big advantage of this design.

Acknowledgements This work is partially supported by the Natural Science Foundation of Jiangsu province (No. BK2010251 and BK2011352), Suzhou Science and Technology Bureau (No.SYG201011 and SYG201211), and XJTLU Research Development Fund (No.10-03-16).

References

1. PIFA Planar Inverted F Antenna, Available via webpage. http://www.qsl.net/va3iul/Antenna/PIFA/PIFA_Planar_Inverted_F_Antenna.pdf
2. Wang F, Du Z, Wang Q, Gong K (2004) Enhanced-bandwidth PIFA with T-shaped ground plane. Electr Lett 40(23):1504–1505
3. Yarman BS (2007) Design of ultra wideband antenna matching networks. In: Proceeding applied electromagnetics conference, IEEE Press, Kolkata, India, pp 1–4
4. Wong KL (2010) EMC and Thin Internal Planar Antennas for Mobile Devices. ANSYS Product Suite, Oct 2010. http://www.ansoft.com/leadinginsight/pdf/High Performance Microwave and RF Design/EMC And Thin Internal Planar Antennas For Mobile Device-NSYSU.pdf
5. Boyle K, Udink M, de Graauw A, Ligthart LP (2007) A Dual-Fed, self-diplexing PIFA and RF front-end. IEEE Trans AP 55:373–382
6. Ollikainen J, Kivekas O, Ichein C, Vainikainen P (2003) Internal multiband handset antenna realized with an integrated matching circuit. In: Proceeding 12th international conference on antennas and propagation, vol 2. IEEE Press, Exeter, UK, pp 629–632

The Application of Improved Genetic Algorithm Optimized by Radial Basis Function in Electric Power System

Yuhong Zhao, Heguo Hu, and Yunhui Zhang

Abstract This paper is concerned with the short-term load forecasting (STLF) in power system operations. It provides load prediction for generation scheduling and unit commitment decisions; therefore precise load forecasting plays an important role in reducing the generation cost and the spinning reserve capacity. In order to improve the precision of electric power system load forecasting, the hybrid algorithm which combines improved genetic algorithm with radial basis function (RBF) neural network is used in short-term load forecasting of electric power system in this paper. In the model, disruptive selection strategy, adaptive crossover and mutation probability were adopted to improve population diversity during iterative process and prevent premature convergence. The improved genetic algorithm and gradient descent method were mixed for interactive computing, and the hybrid algorithm was used for RBF learning. The model was applied to the actual system. The results were compared with traditional RBP algorithm and offered a high forecasting precision.

Keywords Radial basis function • Genetic algorithm • Electric power system • Load forecasting

Y. Zhao (✉)
School of Electric Engineering, University of south China, Hunan, China
e-mail: gsxl666@163.com

H. Hu
Statistical Bureau of Hengyang City, Hunan, China
e-mail: hhg.hy.hn@sohu.com

Y. Zhang
Eastern Boiler Control company Limited, Shenzhen, China
e-mail: zhangyunhui1106@163.com

W. Wang (ed.), *Mechatronics and Automatic Control Systems*, Lecture Notes in Electrical Engineering 237, DOI 10.1007/978-3-319-01273-5_36,

1 Introduction

STLF is a very important part of power system operation, and it is also an integral part of the energy management system (EMS). STLF is the basis of optimal operation for power system. Prediction accuracy has a significant impact on safety, quality, and economic performance of the power system. Therefore, it is very important to search more suitable STLF method in order to maximize the prediction accuracy.

On the one hand, the power system load relates to many complex factors, and it is non-linear, uncertain and random. On the other hand, RBF neural network has the abilities of strong self-learning and complex non-linear function fitting, so it is suitable for load forecasting problems. But studies show that there are still many problems to be solved on the RBF neural network algorithm, particularly the parameters identify of RBF network, such as the number of hidden layer nodes, the center and width value in the RBF activation function for each node, and connection weights between the hidden layer nodes and output layer node. These parameters have great impact on the RBF network learning speed and performance. If improper parameters are selected, network convergence will slow, or even result in the network does not converge. In this paper, an improved genetic algorithm is used to optimize the RBF network, and the optimized network is used to forecast power load. Case analysis and calculation show that the method has high accuracy and good applicability.

2 Radial Basis Function Neural Network

2.1 RBF Network Structure

Radial basis function network is a local approximation network, generally including three layers (n inputs, m hidden node, p output). The structure is shown in Fig. 1.

Basis function of RBF network is commonly used Gaussian function, which can be expressed as

$$\phi_i(x) = \exp\left[\frac{-\left\|X - c_i\right\|^2}{2\sigma_i^2}\right], i = 1, 2 \cdots, m \tag{1}$$

Where: $\phi_i(x)$ is the output of the i-th hidden layer node; X is the input sample, $x = (x_1, x_2, \ldots, x_n)^T$; c_i is the center of the Gaussian kernel function of the i-th hidden layer node, having the same number of dimensions with X; σ_i is a variable for the i-th hidden layer node, called normalization constant or the base width [1, 2]. RBF network output is a linear combination of the output of hidden layer nodes.

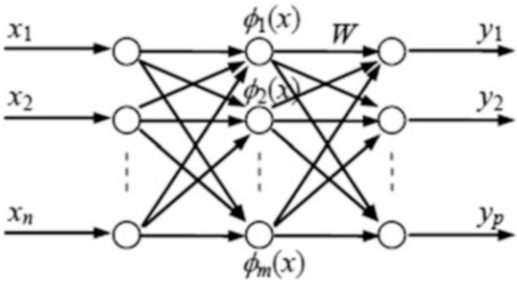

Fig. 1 Radial Gaussian function network topology

$$y_k = \sum_{i=1}^{m} w_{ik}\phi_i(x), k = 1, 2, \cdots, p \tag{2}$$

2.2 The Learning Algorithm of Network Parameters

In the section, Gradient descent method is used to study the center c_i and the width parameters σ_i of RBF network. For the convenience of discussion, consider the case that the output layer has only one node. Substitute Eq. 1 into Eq. 2:

$$f(x) = \sum_{i=1}^{m} w_i \exp\left[\frac{-\left\|X - c_i\right\|^2}{2\sigma_i^2}\right] \tag{3}$$

Let the network desired output is $y^d(x)$, the network energy function can be expressed as:

$$E = \frac{1}{2}\sum_{j=1}^{n}\left(y^d(x^j) - f(x^d)\right)^2 \tag{4}$$

Let $f(x^j)$ substitute into Eq. 4, we can get:

$$E = \frac{1}{2}\sum_{j=1}^{n}\left(y^d(x^j) - \sum_{i=1}^{m} w_i \exp\left[\frac{-\left\|x^j - c_i\right\|^2}{2\sigma_i^2}\right]\right)^2 \tag{5}$$

Let the sample size is L, then

$$E = \frac{1}{2}\sum_{j=1}^{n}\sum_{l=1}^{L}\left(y^d(x_l^j) - \sum_{i=1}^{m} w_i \exp\left[\frac{-\left\|x_l^j - c_i\right\|^2}{2\sigma_i^2}\right]\right)^2 \tag{6}$$

Remember

$$\xi\left(x_l^j, c_i, \sigma_i\right) = \frac{1}{2}\sum_{j=1}^{n}\sum_{l=1}^{L}\left(y^d(x_l^j) - \sum_{i=1}^{m} w_i \exp\left[\frac{-\left\|x_l^j - c_i\right\|^2}{2\sigma_i^2}\right]\right)^2 \tag{7}$$

Then Eq. 6 becomes

$$E = \frac{1}{2}\sum_{j=1}^{n}\sum_{l=1}^{L}\left(\xi(x_l^j, c_i, \sigma_i)\right)^2 \tag{8}$$

w_i is consider as a constant when you learn center values and width parameters, and you can get the central value and width parameter updating formula which can be represented by:

$$\begin{aligned} c_i(t+1) &= c_i(t) - \lambda\frac{\partial E}{\partial c_i}, \\ \sigma_i(t+1) &= \sigma_i(t) - \beta\frac{\partial E}{\partial c_i} \end{aligned} \tag{9}$$

In Eqs. 9 and 10, λ, β are the learning efficiency of the central value and width parameters. If the formula (8) is substituted into the formula (9) and formula (10), we can get:

$$c_i(t+1) = c_i(t) - \frac{\lambda}{2\sigma_i^2}\sum_{j=1}^{n}\sum_{l=1}^{L}\xi(x_l^j, c_i, \sigma_i)\cdot\exp\left[\frac{-\left\|x^j - c_i\right\|^2}{2\sigma_i^2}\right](x_l^j - c_i) \tag{10}$$

$$\sigma_i(t+1) = \sigma_i(t) - \frac{\lambda}{2\sigma_i^3}\sum_{j=1}^{n}\sum_{l=1}^{L}\xi(x_l^j, c_i, \sigma_i)\cdot\exp\left[\frac{-\left\|x^j - c_i\right\|^2}{2\sigma_i^2}\right](x_l^j - c_i)^2 \tag{11}$$

According to the input samples, weights of the output layer can be calculated by using the least squares algorithm of system identification theory. In this paper, the learning algorithm for connection weights between the hidden layer and output layer can be expressed as:

$$w_{ik}(l+1) = w_{ik}(l) + \eta[y_k^d - y_k(l)]\phi_i(x) \tag{12}$$

In the formula: y_k^d is the output to expect; l is the number of iterations; η is the learning rate, general $0 < \eta < 2$, to ensure iterative convergence.

3 RBF Network Training Based on Improved Genetic Algorithm

The core of RBF network design is to determine the number of hidden nodes and the central values, and other parameters of basis functions. We will design a neural network to meet the target error as small as possible to ensure that the generalization ability of neural networks. Genetic algorithm (GA) is a randomized search method which simulates biological evolution. This paper presents an improved genetic algorithm (IGA) [3]; the starting point for the algorithm is described as follows. First: to maintain population diversity and prevent premature; second: to improve local search ability of GA; Third: speed up the search; Fourth: to reduce the chance of getting into local extreme value.

3.1 Encoding and Initial Population Generation

That is to say, the RBF network hidden nodes number m, each hidden node center parameters c_i and the width parameters σ_i are compiled chromosome, and the collection of these parameters for the network are treated as an individual. In the initialization phase, initial population is generated by completely random method.

3.2 Select Options

Based on the deviation degree of this population, this article defines a selection operator which can bring a diversity of species, which is described as follows:

For a given fitness measure f, so

$$U(X_j) = \left| f(X_j) - \bar{f}(X) \right| \tag{13}$$

Among them, $\bar{f}(X) = \frac{1}{N}\sum_{k=1}^{N} f(X_k)$ is the population average fitness; N is the population size, $f(X_j)$ is the j-th individual's fitness value in the group, $U(X_j)$ is the

deviation degree between individual j and the group mean fitness. Disruptive selection chooses each individual according to the following probability formula:

$$P\{Y_i = X_j\} = \frac{U(X_j)}{\sum_{k=1}^{N} U(X_k)}, i = 1, 2, \cdots, M \tag{14}$$

From geometry, this means that the farther away from the average individual fitness, the higher the chance to be selected, thus corresponding with the fitness of the individual does not have a monotonic, can bring a greater diversity of species.

3.3 Cross Operating

The algorithm uses real number coding, therefore, the corresponding intersection operation can be realized by arithmetic crossover. Arithmetic crossover is defined as a linear combination of two individuals to generate a new breed of individual operations. We can set:

$$C(X_1, X_2) = \mu X_1 + (1 - \mu) X_2 \tag{15}$$

Among them, X_1, X_2 are two different individuals of the populations. We can take:

$$\mu = \left\{ \begin{array}{ll} \xi > 1, & F(X_1) \geq F(X_2) \\ \xi < 0, & F(X_1) < F(X_2) \end{array} \right\} \tag{16}$$

3.4 Mutation Operating

The adaptive mutation operator is used in this paper, and the specific description is as follows: First, if we randomly choose a component in the parent body vector $x = (x_1, x_2, \cdots, x_n)$, assumption it is the k-th, and then we randomly choose a number x'_k instead of x_k in its definition interval $[a_k, b_k]$ to get mutated individuals y, That is $y = (x_1, x_2, \cdots x'_k, \cdots, x_n)$, among them,

$$x'_k = \left\{ \begin{array}{ll} x_k + \Delta(T, b_k - x_k), & if \ \ random\ (0,1) = 0 \\ x_k - \Delta(T, b_k - x_k), & if \ \ random\ (0,1) = 1 \end{array} \right\} \tag{17}$$

Where $random(0, 1)$ is the random number in the interval (0,1); $\Delta(T, y) \in [0, y]$ is a random number obeying uniform distribution. As T decreases, the greater the likelihood $\Delta(T, y)$ tends to 0. So that the algorithm searches large fitness individual

in a small range and the small fitness individual in a large range, which makes the variation according to solution quality adaptively adjust the search area, which can obviously improve search capabilities [4].

The specific expression of the function $\Delta(T, y)$ can be taken as:

$$\Delta(T, y) = y \cdot (1 - r^{T\lambda}) \tag{18}$$

$$T = 1 - \frac{f(x)}{f_{\max}} \tag{19}$$

Where r is random number of the interval [0, 1], λ plays a regulatory role of the local search area, and its value is generally 2–5. $f(x)$ represents fitness of the individual $x, f_{\max}$ is the biggest fitness value of problem to be solved; Due to $f_{\max}$ is difficult to determine in many problems, we can use rough upper or the largest fitness value of the current population.

3.5 Algorithm Realization

The RBF network structure optimization and parameter learning are carried out in two phases, namely training and evolution. First, randomly generate N individuals to form groups, We use a gradient descent to learn the center c_i and width parameters σ_i corresponding to each individual hidden nodes chromosomes in the network, and use the least squares to learn linear weight value w_i of the network; Secondly, We use genetic evolutionary algorithm to optimize hidden nodes, by alternating these two processes to obtain the minimum number of hidden nodes required to meet the error basis functions and have different width parameter of RBF network [5].

In order to use genetic algorithms to solve optimization problems for RBF network structure, Boolean vectors $U^T = (u_{1,}u_{2,} \ldots, u_{M,}) u_i = \{0, 1\}$ is introduced. $u_i = 1$ represents the corresponding hidden node exists; $u_i = 0$ represents the corresponding hidden node does not exist. Each Boolean vectors U^T generate two chromosomes: one center parameters chromosomes, one width parameter chromosomes. Center parameters chromosome U_c^T and width parameters chromosome U_σ^T are coded by real number.

3.6 Example Application

In this paper, to predict the region May 12, 2005 24-point load, we uses 3 months the historical load data of the region Power Grid in 2005, The prediction results are shown in Table 1:

Table 1 The result of load forecasting

		Algorithm of this paper		RBF algorithm	
Time/h	Actual value/MW	Predictive value/MW	Relative error/%	Predictive value/MW	Relative error/%
01:00	435.1	428.18	1.59	421.35	3.16
03:00	461.4	448.94	2.7	440.59	4.51
05:00	415.9	414.44	0.35	410.99	1.18
07:00	433.3	429.66	0.84	428.79	1.04
09:00	453.6	442.17	2.52	433.55	4.42
11:00	435.5	431.71	0.87	428.44	1.62
13:00	438.7	432.60	1.39	421.28	3.97
15:00	439.6	435.42	0.95	431.60	1.82
17:00	438.6	436.14	0.56	430.79	1.78
19:00	400.7	400.18	0.13	397.21	0.87
21:00	414.9	410.00	1.18	404.28	2.56
23:00	416.2	413.54	0.64	404.84	2.73

It can be seen from the table, the maximum relative error of the short-term load forecasting model based algorithm which proposed in this paper is 2.7, and the minimum relative error of it is 0.13. While the maximum relative error of prediction model based on RBF algorithm is 4.51, the minimum relative error is 0.87. It can be seen that the prediction model built in this article can better fit the mapping relationship between the loads; it has better prediction accuracy.

4 Conclusion

According to the deficiencies of RBF neural network and the premature shortcoming of genetic algorithm, this paper presented a radial basis function (RBF) neural network short term load forecasting model based on improved genetic algorithm. The model introduces the real-coded adaptive mechanism for the genetic algorithm. The selection strategy, adaptive crossover and mutation were improved, and its interaction with the gradient descent hybrid operation was used as the RBF network learning algorithm. The experimental results showed that the method can effectively improve the accuracy of load forecasting with good applicability.

Acknowledgements A Project Supported by Scientific Research Fund of Hunan Provincial Science and Technology Programme, Project Number [2010FJ3157]

References

1. Park J, Sandberg IW (1991) Universal approximation using radial basis-function networks [J]. Neural Comput 3(2):246–257
2. Roopesh R, Kumar Reddy, Ranjan Ganguli (2003) Structural damage detection in a helicopter rotor blade using radial basis function neural networks [J]. Smart Mater Struct 12(1):232–241
3. Stones J, Collinson A (2001) Power quality [J]. Power Eng J 15(2):58–64
4. Kandil MS, El Debeiky SM, Hasanien NE (2001) Overview and comparison of long term forecasting techniques for a fast developing [J]. Electr Power Syst Res 58(1):11–17
5. Zhang L, Bai YF (2005) Genetic algorithm trained radial basis function neural networks for modeling photovoltaic panels [J]. Eng Appl Artif Intel 18(7):833–844

Anisotropic Nonconforming Mixed Element Method for Maxwell's Equations

Lifang Pei and Chao Xu

Abstract In order to get numerical solution of Maxwell's equations which plays an important role in the electric-magnetic fields, a new anisotropic nonconforming mixed finite element method is presented. Based on special construction of the element pair and some novel techniques, error estimates of electric and magnetic fields in L^2 norm are obtained under anisotropic meshes. The convergence results demonstrate the validity of the anisotropic nonconforming mixed element method for solving Maxwell's equations.

Keywords Maxwell's equations • Low order nonconforming element • Error estimates • Anisotropic meshes

1 Introduction

Maxwell's equations is the most important equations in the electromagnetic fields. The study on its numerical solution is a hot and difficult topic in both numerical analysis and engineering calculations. Finite element method is an effective method to solve this problem. Monk presented a mixed finite element method and provided convergence analysis [1]. Lin and Yan obtained superconvergence with the integral identity technique in three dimensions [2]. Brandts and Lin et al. focused on the transverse electric model, which is the formulation of Maxwell's equations in two dimensions [3, 4].

However, it is not difficult to find that almost all results in previous literature only concentrated on conforming elements and demanded the meshes satisfying the classical regularity condition [5]. These requires are deficient in applications of

L. Pei (✉) • C. Xu
Department of Mathematics and Physics, Luoyang Institute of Science and Technology, Luoyang 471023, China
e-mail: plf5801@126.com; xc-lyct@126.com

W. Wang (ed.), *Mechatronics and Automatic Control Systems*, Lecture Notes in Electrical Engineering 237, DOI 10.1007/978-3-319-01273-5_37,

finite element methods. On one hand, nonconforming elements are more effective than conforming elements in some aspect. On the other hand, anisotropic meshes have advantages over regular meshes in narrow domain and solutions with anisotropic behavior [6]. Therefore, employing anisotropic nonconforming element scheme to approximate Maxwell's equations is meaningful. Recently, Shi and Pei discussed some nonconforming finite element methods for Maxwell's equations in two and three dimensions, and obtained convergence results under anisotropic meshes [7, 8].

In this paper, we propose a new anisotropic nonconforming mixed finite element scheme of Maxwell's equations in two dimensions. The constrained ${Q_1}^{rot}$ finite element space is used in the scheme. The total degrees of freedom is lowest on rectangular meshes. By use of the special property of the element and some new approaches, we get error estimates with order $O(h)$ under anisotropic meshes.

2 Nonconforming Mixed Finite Element Scheme

Consider the following Maxwell's equations:

$$\begin{cases} \varepsilon \mathbf{E}_t + \sigma \mathbf{E} - rotH = \mathbf{J}, & in \ \ \Omega \times (0,T), \\ \mu H_t + curl\mathbf{E} = 0, & in \ \ \Omega \times (0,T), \\ \mathbf{n} \times \mathbf{E} = 0, & on \quad \partial\Omega \times (0,T), \\ \mathbf{E}(0) = \mathbf{E}_0, H(0) = H_0, \end{cases} \tag{1}$$

where $\Omega \subset R^2$ is a bounded convex domain, $\mathbf{E} = (E_1, E_2)$ and H are electric and magnetic fields, ε, σ and μ are the dielectric constant, the conductivity of the medium and the magnetic permeability, respectively. $\mathbf{J} = (J_1, J_2)$, $\mathbf{E}_0$ and H_0 are given functions. $0 < \ \varepsilon_{min} \le \varepsilon, \quad 0 < \ \mu_{min} \le \mu$, where ε_{min} and μ_{min} are constants. σ is nonnegative and bounded on $\overline{\Omega}$. $rotH = \left(\dfrac{\partial H}{\partial y}, -\dfrac{\partial H}{\partial x}\right), curl\mathbf{E} = \dfrac{\partial E_2}{\partial x} - \dfrac{\partial E_1}{\partial y}$ and $\mathbf{n} \times \mathbf{E} = E_1 n_2 - E_2 n_1$, where $\mathbf{n} = (n_1, n_2)$ is the unit outward norm of $\partial\ \Omega$.

The variational form of problem (1) is: find $(\mathbf{E}, H) \in (L^2(\Omega))^2 \times H(\mathbf{curl}; \Omega)$, such that for all $(\mathbf{Q}, \Psi) \in (L^2(\Omega))^2 \times H(\mathbf{curl}; \Omega)$

$$\begin{cases} (\varepsilon \mathbf{E}_t, \mathbf{Q}) + (\sigma \mathbf{E}, \mathbf{Q}) - (rotH, \mathbf{Q}) = (\mathbf{J}, \mathbf{Q}), \\ (\mu H_t, \Psi) + (\mathbf{E}, rot\Psi) = 0, \end{cases} \tag{2}$$

where $H(\mathbf{curl}; \Omega) = \{v \in L^2(\Omega); rotv \in (L^2(\Omega))^2\}$, $(\cdot, \cdot)$ is the $L^2(\Omega)$ or $(L^2(\Omega))^2$ inner product.

Suppose T^h is an anisotropic rectangular decomposition of Ω, the edges of $T \in T^h$ are parallel to axes of coordinates. Denote the center and edge lengths of T are (x_T, y_T), $2h_x$ and $2h_y$ respectively, $h_T = \max\{h_x, h_y\}$, $h = \max_{K \in T^h} h_T$. Let the

reference element $\hat{T} = [-1, 1] \times [-1, 1]$, $\hat{d}_i$ and $\hat{l}_i = \overline{\hat{d}_i \hat{d}_{i+1}}$ $(i = 1 \cdots, 4)$ be vertices and edges of $\hat{T}$. The affine mapping $F_T : \hat{T} \to T$ is define by

$$\begin{cases} x = x_T + h_x \xi, \\ y = y_T + h_y \eta. \end{cases} \tag{3}$$

To begin with, we describe the $Q_1{}^{rot}$ finite element space [9].

Let

$$\hat{\Sigma} = \{\hat{v}^1, \hat{v}^2, \hat{v}^3, \hat{v}^4\}, \hat{P} = span\{1, \xi, \eta, \xi^2 - \eta^2\},$$

where $\hat{v}^i = \frac{1}{|\hat{l}_i|} \int_{\hat{l}_i} \hat{v} ds$ $(i = 1, 2, 3, 4)$. The $Q_1{}^{rot}$ finite element space is

$$NR = \left\{ v; \hat{v}|_{\hat{T}} = v|_T \circ F_T \in \hat{P}, \int_l [v] ds = 0, l \subset \partial T, \forall T \in T^h \right\}, \tag{4}$$

where $[v]$ denotes the jump of v across the internal edge l and $[v] = 0$ on $\partial \Omega$.

Then the constrained $Q_1{}^{rot}$ finite element space [10] can be defined as

$$CNR = \{v;\ v \in NR,\ \int_{l_1 + l_3} v ds = \int_{l_2 + l_4} v ds, l_i \subset \partial T, i = 1, 2, 3, 4, \forall T \in T^h\}.$$

Denote the associated interpolation operator by I. It has been shown that I has the anisotropic interpolation property [11].

Moreover, let

$$W^h = \{\mathbf{w} \in (L^2(\Omega))^2, \mathbf{w}|_T \in P_0(T) \times P_0(T), \forall T \in T^h, \mathbf{n} \times \mathbf{w}\ |_{\partial\Omega} = 0\}, \tag{5}$$

where $P_0(T)$ is a constant space on T. For $\mathbf{w} \in (L^2(\Omega))^2$, the interpolation $R\mathbf{w} \in W^h$ on T is defined as follows

$$\int_T (\mathbf{w} - R\mathbf{w}) dx dy = 0. \tag{6}$$

Now, for the magnetic H and electric $\mathbf{E}$, we choose $V^h = CNR$ and W^h as the finite element approximate spaces, respectively.

Then the mixed element approximation of (2) is to find $(\mathbf{E}^h, H^h) \in W^h \times V^h$, such that for all $(\mathbf{Q}, \Psi) \in W^h \times V^h$

$$\begin{cases} (\varepsilon \mathbf{E}_t^h, \mathbf{Q})_h + (\sigma \mathbf{E}^h, \mathbf{Q})_h - (rot H^h, \mathbf{Q})_h = (\mathbf{J}, \mathbf{Q})_h, \\ (\mu H_t^h, \Psi)_h + (\mathbf{E}^h, rot \Psi)_h = 0, \\ \mathbf{E}^h(0) = R\mathbf{E}_0,\ H^h(0) = IH_0, \end{cases} \tag{7}$$

where $(p, q)_h = \sum_{T \in T^h} \int_T pq dx dy$.

3 Convergence Analysis

The main results will be derived in this section. We give some important lemmas firstly.

Lemma 1 *For all* $v_t \in H^1(\Omega)$, *we have*

$$\| v_t - Iv_t \|_{0h} \leq Ch|v_t|_1, \tag{8}$$

here and later, the positive constant C is independent of the mesh parameter h and may be different at each appearance, $\| v \|_{0h} = (v, v)_h = (\sum_{T \in T^h} \| v \|^2_{0,T})^{\frac{1}{2}}$.

Proof By the anisotropic interpolation theorem [6], it is easy to derive (8). □

Lemma 2 *For all* $\mathbf{v} \in (L^2(\boldsymbol{\Omega}))^2$, *we have*

$$(\mathbf{v} - R\mathbf{v}, rot\boldsymbol{\Psi})_h = 0, \qquad \forall \boldsymbol{\Psi} \in V^h. \tag{9}$$

Proof Since for all $\Psi \in V^h$, $rot\ \Psi|_K$ is a constant, by the definition of R, we have

$$(\mathbf{v} - R\mathbf{v}, rot\boldsymbol{\Psi})_h = 0, \qquad \forall \boldsymbol{\Psi} \in V^h. \quad \square$$

Lemma 3 *For all* $\mathbf{E} \in (H^2(\boldsymbol{\Omega}))^2$, *there holds*

$$\sum_{T \in T^h} \int_{\partial T} \boldsymbol{\Psi}\ \mathbf{n} \times \mathbf{E} ds \leq Ch|\mathbf{E}|_2 \| \boldsymbol{\Psi} \|_{0h}, \quad \forall \boldsymbol{\Psi} \in V^h. \tag{10}$$

Proof Using the similar arguments as Zhu et al. [11], the proof can be completed. In fact, we only need to check that V^h satisfies the following properties: for all $\Psi \in V^h$, there holds

$$(i) \int_l [\boldsymbol{\Psi}] ds = 0, \quad \forall l \subset \partial T_1 \cap \partial T_2, T_1, T_2 \in T_h.$$

$$(ii)\ \frac{\partial \boldsymbol{\Psi}}{\partial x}|_T \in span\{1, x\}, \quad \frac{\partial \boldsymbol{\Psi}}{\partial y}|_T \in span\{1, y\}, \quad \forall T \in T_h. \quad \square$$

For simplicity, let $\varepsilon = \mu = 1$ and $\sigma = 0$, we can obtain the following theorem.

Theorem 1 *Assume that* $(\mathbf{E},H)\in(L^2(\boldsymbol{\Omega}))^2\times H(\mathbf{curl};\boldsymbol{\Omega})$, $(\mathbf{E}^h,H^h)\in W^h\times V^h$ *are the solutions of* (2) and (7), *respectively,* $\mathbf{E}\in(H^2(\boldsymbol{\Omega}))^2, H\in H^2(\boldsymbol{\Omega}), H_t\in H^1(\boldsymbol{\Omega})$. *Then we have*

$$\| \mathbf{E}^h - R\mathbf{E} \|_{0h} + \| H^h - IH \|_{0h} \leq Ch\left(\int_0^t (|H|_1^2 + |H|_2^2 + |\mathbf{E}|_2^2)d\tau\right)^{\frac{1}{2}}, \tag{11}$$

$$\| \mathbf{E} - \mathbf{E}^h \|_{0h} + \| H - H^h \|_{0h} \leq Ch[|\mathbf{E}|_1 + |H|_1^2 + \left(\int_0^t (|H|_1^2 + |H|_2^2 + |\mathbf{E}|_2^2)d\tau\right)^{\frac{1}{2}}]. \tag{12}$$

Proof Define

$$D((\mathbf{E},H);(\mathbf{Q},\boldsymbol{\Psi})) = (\mathbf{E}_t,\mathbf{Q}) - (rotH,\mathbf{Q}) + (H_t,\boldsymbol{\Psi}) + (\mathbf{E},rot\boldsymbol{\Psi}), \tag{13}$$

and

$$D_h((\mathbf{E},H);(\mathbf{Q},\boldsymbol{\Psi})) = (\mathbf{E}_t,\mathbf{Q})_h - (rotH,\mathbf{Q})_h + (H_t,\boldsymbol{\Psi})_h + (\mathbf{E},rot\boldsymbol{\Psi})_h. \tag{14}$$

Then there holds

$$D((\mathbf{E},H);(\mathbf{E},H)) = (\mathbf{E}_t,\mathbf{E}) + (H_t,H) = \frac{1}{2}\frac{d}{dt}(\| \mathbf{E} \|_0^2 + \| H \|_0^2).$$

For any $(\mathbf{Q},\boldsymbol{\Psi})\in W^h\times V^h$, it follows from (1) and (7) that

$$D_h((\mathbf{E}-\mathbf{E}^h,H-H^h);(\mathbf{Q},\boldsymbol{\Psi})) = \sum_{T\in T^h}\int_{\partial T}\boldsymbol{\Psi}\ \mathbf{n}\times\mathbf{E}ds.$$

By using of (8)–(10), we have

$$\begin{aligned}
&D_h((\mathbf{E}^h - R\mathbf{E}, H^h - IH);(\mathbf{Q},\boldsymbol{\Psi}))\\
&\quad = D_h((\mathbf{E}-R\mathbf{E},H-IH);(\mathbf{Q},\boldsymbol{\Psi})) + D_h((\mathbf{E}^h-\mathbf{E},H^h-H);(\mathbf{Q},\boldsymbol{\Psi}))\\
&\quad = ((\mathbf{E}-R\mathbf{E})_t,\mathbf{Q})_h - (rot(H-IH),\mathbf{Q})_h + (H_t - IH_t,\boldsymbol{\Psi})_h\\
&\qquad + ((\mathbf{E}-R\mathbf{E}),rot\boldsymbol{\Psi})_h - \sum_{T\in T^h}\int_{\partial T}\boldsymbol{\Psi}\ \mathbf{n}\times\mathbf{E}ds\\
&\qquad \leq Ch|H|_2 \| \mathbf{Q} \|_{0h} + Ch(|H_t|_1 + |\mathbf{E}|_2) \| \Psi \|_{0h}\ .
\end{aligned} \tag{15}$$

Taking $(\mathbf{Q},\Psi) = (\mathbf{E}^h - R\mathbf{E}, H^h - IH)$ in (15) and applying Schwarz inequality, there yields

$$\frac{1}{2}\frac{d}{dt}(\| \mathbf{E}^h - R\mathbf{E} \|_{0h}^2 + \| H^h - IH \|_{0h}^2)$$
$$\leq Ch^2(|H_t|_1^2 + |H|_2^2 + |\mathbf{E}|_2^2) + \frac{1}{2}\| \mathbf{E}^h - R\mathbf{E} \|_{0h}^2 + \frac{1}{2}\| H^h - IH \|_{0h}^2 . \quad (16)$$

Integrating (16) for t, by use of $\mathbf{E}^h(0) - R\mathbf{E}(0) = (0,0), H^h(0) - IH(0) = 0$ and Gronwall inequality, we can obtain (11).

By triangle inequality it follows that

$$\begin{aligned} &\| \mathbf{E} - \mathbf{E}^h \|_{0h} + \| H - H^h \|_{0h} \\ &\leq \| \mathbf{E} - R\mathbf{E} \|_{0h} + \| R\mathbf{E} - \mathbf{E}^h \|_{0h} + \| H - IH \|_{0h} + \| IH - H^h \|_{0h} \\ &\leq Ch[|\mathbf{E}|_1 + |H|_1^2 + \left(\int_0^t (|H_t|_1^2 + |H|_2^2 + |\mathbf{E}|_2^2)d\tau\right)^{\frac{1}{2}}]. \end{aligned} \quad (17)$$

The proof is completed. □

Remark 1 We point out that the results in this paper are no longer valid for some popular elements, such as Q_1^{rot} element [9], $E\,Q_1^{rot}$ element [12] and low order triangular C-R element [13] and so on. This means that it is not easy to construct a suitable anisotropic nonconforming mixed element scheme for approximating Maxwell's equations.

4 Conclusion

In this paper, we discussed a nonconforming mixed finite element method for approximating Maxwell's equations. Convergence results are obtained for anisotropic meshes, which are the same as those in the previous literature for conforming elements for regular meshes. The study shows that the nonconforming mixed finite element method is effective for solving Maxwell's equations.

References

1. Monk P (1991) A mixed method for approximating Maxwell's equations. SIAM J Numer Anal 28(6):1610–1634
2. Lin Q, Yan NN (1999) Global superconvergence for Maxwell's equations. Math Comput Am Math Soc 69(229):159–176
3. Brandts JH (1999) Superconvergence of mixed finite element semi-discretizations of two time-dependent problems. Appl Math 44(1):43–53
4. Lin Q, Lin JF (2003) High accuracy approximation of mixed finite element for 2-D Maxwell equations. Acta Math Sci A 23(4):499–503 (in Chinese)

5. Ciarlet PG (1978) The finite element method for elliptic problems. North-Holland, New York, pp 1–80
6. Chen SC, Shi DY, Zhao YC (2004) Anisotropic interpolations and quasi-Wilson element for narrow quadrilateral meshes. IMA J Numer Anal 24(1):77–95
7. Shi DY, Pei LF (2008) Low order Crouzeix-Raviart type nonconforming finite element methods for approximating Maxwell's equations. Int J Numer Anal Model 5(3):373–385
8. Shi DY, Pei LF (2009) Low order Crouzeix-Raviart type nonconforming finite element methods for the 3D time-dependent Maxwell's equations. Appl Math Comput 211(1):1–9
9. Rannacher R, Turek S (1992) Simple nonconforming quadrilateral Stokes element. Numer Methods PDEs 8(2):97–111
10. Hu J, Shi ZC (2005) Constrained quadrilateral nonconforming rotated Q_1 element. J Comput Math 23(5):561–586
11. Zhu GQ, Shi DY, Chen SC (2007) Superconvergence analysis of a low order anisotropic finite element. Appl Math Mech 28(8):1119–1130
12. Lin Q, Tobiska L, Zhou AH (2005) Superconvergence and extrapolation of non-conforming low order finite elements applied to the Poisson equation. IMA J Numer Anal 25(1):160–181
13. Apel T, Nicaise S, Schöberl J (2001) Crouzeix-Raviart type finite elements on anisotropic meshes. Numer Math 89(2):193–223

New Back-Up Protection Principle and Its Modeling Based on IEC 61850

Zheng-tuo Zhang, Jing Li, Zeng-ping Wang, and Li-ming Tu

Abstract The traditional protection only uses the information of the places where protection installs to make judgments. This limitation leads to that protection becomes increasingly unsuited to the requirements of the modern grid. This paper proposes a multi-information back-up protection principle that makes use of the corresponding relationship between the fault location and fault output data. The logical model and communication model were established following IEC 61850. The model establishes a multi-information protection logic node and describes the information flow among LNs in the station. Finally, a strategy table was put forward and a logic simulation was set up in PSCAD. Analysis shows that the program can make the protection configuration more flexible and more effective.

Keywords IEC 61850 • Multi-information • Back-up protection • Modeling

1 Introduction

Traditional protection has some natural technical defects which can make power system a lot of faults. The root cause is that the sampling information used for protection decision is all collected from the local transformer [1]. From the multi-information technology consideration, the amount of information can affect the protection performance. When it comes to the SAS, we should collect more information from the bay level and process level and exchange status messages and trip Goose messages among IEDs of each level.

Z.-t. Zhang (✉) • J. Li • Z.-p. Wang
State Key Laboratory for Alternate Electrical Power System with Renewable Energy Sources, North China Electric Power University, Beijing, China
e-mail: nceputuo@sina.com

L.-m. Tu
State Key Laboratory for Alternate Electrical Power System with Renewable Energy Sources, Beijing Sifang Automation Co. Ltd, Beijing, China

W. Wang (ed.), *Mechatronics and Automatic Control Systems*, Lecture Notes in Electrical Engineering 237, DOI 10.1007/978-3-319-01273-5_38,

IEC 61850 solves some problems that large amount of information is transformed and secondary wiring is so complex for a lot of information channel. It makes it become reality that optical fiber is used in the substation communication. The physical world is described as a abstract and virtual system. This advanced mechanism fully resolves the interoperability among IEDs of different companies and brings a huge change to substation communication system [2, 3]. What this paper researches is a distributed backup protection system based on IEC 61850. Its concept comes from wide-area protection. Multi-information fusion technology [4, 5] is used in the issue. It is a deep application of IEC 61850 in substation. Traditional single-point protection is gradually replaced by multi-information protection and then this scheme makes protection configuration more flexible and more effective.

2 The Distributed Backup Protection Principle

Figure 1 shows a typical substation wiring diagram, we use a multi-information backup protection algorithm to realize a backup protection system based on IEC 61850. This scheme defines three levels in a substation: incoming line level, transformer level, outgoing line. Each level contains one or more interval. Three levels have three judging units and these units collect information together to calculate the result, then we can initially determine the failure location. Finally the information collected from each level and the initial calculation result will be sent to coordination unit to make final analysis. F1-F9 in Fig. 1 mean any faults in the station. D1-D11 mean direction components and the RB mean bus differential protection components. The output value of Di and RBn can be defined as follows.

$$Di = \begin{cases} 0 & \text{Positive direction components act} \\ 0 & \text{direction component still} \\ 1 & \text{opposite direction components act} \end{cases}$$

$$\mathrm{RB_n} = \begin{cases} 1 & \text{bus differential components act} \\ 0 & \text{bus differential components still} \end{cases}$$

For example, in the transformer level, the values of D3, D4, D5 and D6 can only be what occurs in this table below when the failure occurs at F2 and F3 (Table 1).

The above relationships can obtain two sets of data (0,0,0,1) and (0,0,1,0), corresponding to the D3-D6 values when the F2 and F3 failure occurs. When the actual fault occurs, the output data XOR two sets of data. If the result obtained is (0,0,0,0), it can be determine that the fault location is located in this place corresponding to the fault. The method of the line layer and outlet layer judgement are the same. Taking into account the big amount of information, the inaccuracies of judgment and the results, a decision-making coordination unit is increased, the judgment results of the three layers and the collected direction information are

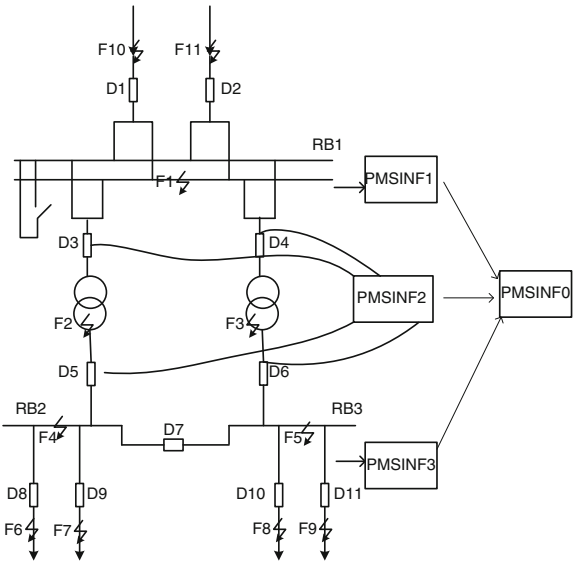

Fig. 1 The distribute construct of faults in the substation

Table 1 Relationships of fault location and transformer level output

	D3	D4	D5	D6
F2	0	0	0	1
F3	0	0	1	0

Table 2 Relationships of fault location and information output in the whole station

	D1	D2	D3	D4	D5	D6	D7	D8	D9	D10	D11	RB1	RB2	RB3
F1	1	1	1	1	0	0	0	1	1	1	1	1	0	0
F2	1	1	0	0	0	0	1	1	1	1	1	0	0	0
F3	1	1	0	0	0	0	0	1	1	1	1	0	0	0
F4	1	1	0	0	1	1	1	1	1	1	1	0	1	0
F5	1	1	0	0	1	1	0	1	1	1	1	0	0	1
F6	1	1	0	0	1	1	1	0	1	1	1	0	0	0
F7	1	1	0	0	1	1	1	1	0	1	1	0	0	0
F8	1	1	0	0	1	1	0	1	1	0	1	0	0	0
F9	1	1	0	0	1	1	0	1	1	1	0	0	0	0
F10	0	1	1	1	0	0	0	1	1	1	1	0	0	0
F11	1	0	1	1	0	0	0	1	1	1	1	0	0	0

consolidated into the coordination unit and then by relationship matrix method a global judgment will be made. The relationship matrix is shown in Table 2.

This method, not only can guarantee the reliability and fast backup protection, the protection principle of using single information is changed to the principle of using multi-information. In IEC 61850 substation, the networking and intelligent is better achieved.

3 The Establishment of Station Backup Protection Modeling Based on IEC 61850

3.1 Extension of Protection LN Class

Compared with traditional protection, multi-information relay protection based on IEC 61850 is a new kind of protection type. In order to make sure to build modeling smoothly and establish such a protection system, creating a logic node of multi-information protection is necessary and it should observe the rules which are regulated in IEC 61850 [6]. According to the rules, the new logical node "multi-information protection" is defined in Table 3:

The function of PMSINF is to integrate information from everywhere in the station to achieve logical judgment, which includes direction information, sampling information from the electronic transformer, protection tripping messages PTRC sends, acting signal of the protection node and XCBR status information (Fig. 2).

3.2 The Protection Logic Device Modeling

Throughout the station protection, this paper uses traditional protection as the main protection of the substation and multi-information protection as backup protection.

Table 3 Naming "multi-information protection"

First word	Second word	Third word	LN
P	MS	Inf	PMSINF
Protection	Multi-source	Information	Multi-source information protection

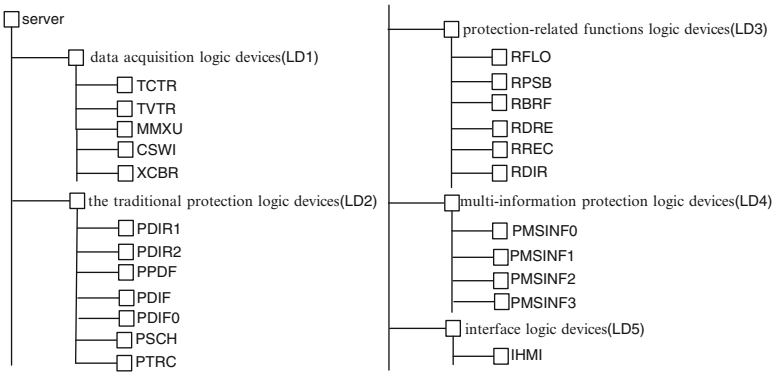

Fig. 2 Logical modeling

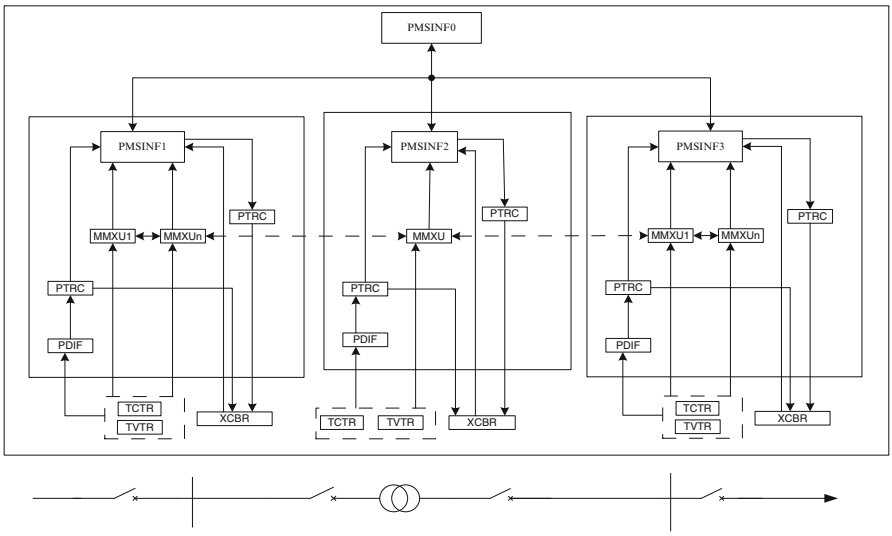

Fig. 3 The information exchange modeling

We set five logical device LDs, data acquisition logic devices, traditional protection logic devices, protection-related functions logic devices, multi-information protection logic devices and interface logic devices [7, 8].

3.3 Information Exchange Model

In the station distributed protection information model includes traditional main protection information model, protecting related function model, multi-information protection logic equipment model and message exchange service among other IED. To set up message service model, we should know how content of datas among each other exchange. Document [9] introduce message exchange model among the traditional protection IED and this article adds multi-message protection logic nodes based on it, the function of model is mainly to reflect distributed backup protection function. For simplicity, it only mentions the logic nodes which are relevant to this function. The man – machine interface logic node inside substation and protection-related function nodes are not marked, but in practical modeling it should include all the function nodes (Fig. 3).

The collaboration process of LNs is following:

- After PDIF tests out the fault, the value of the status message Str becomes 1 and trip message Op becomes 1. These two changes will be passed to PTRC. After analysis, PTRC sends tripout GOOSE message to XCBR and RREC. Meanwhile GOOSE messages are sent to PMSINF1-3 to prepare to realize backup protection function. XCBR receives tripout message and then jumps breaker after

additional process. When the state of breaker changes from on to off. XCBR sends new state to PTRC and RREC via GOOSE message at once. Send the change message of breaker to PMSINF1-3.

- RREC receives GOOSE messages from XCBR and then decides to reclose the breaker, while sending GOOSE message with value to XCBR.
- XCBR receives GOOSE message with value and closes the breaker after processing. Then it sends GOOSE packets with new status of breaker to PTRC、RREC and PMSINF1-3.
- PMSINF1-3 receive direction information, tripping message and status message and then make the initial judgment. The results and other information needed will be sent to PMSINF0 to make the final decision. When the main protection is broken, PMSINF1-3 will send GOOSE trip messages to XCBR and RREC.

3.4 Model Mapping

The most prominent feature of IEC 61850 is model and communication. The application of the model should implemented in the actual communication service. The model of services defined in IEC 61850 have the same function in ACSI and MMS, while relating to different specific model which requires mutual conversion between models.

Entities in the mode communication process is data model and related services. In IEC 61850 data model is mapped to the MMS via the SCSM services and IEC 61850 is also scalable. When the communication service agreement updates, it maps new communication protocols by SCSM in order to achieve a global update. Therefore, the communication model is the most important in IEC 61850. The model is fixed but the communication protocol is changing. For distributed multi-information backup protection, the communication model has a very important meaning for a specific communication network.

4 Scheme Analyses

According to the verification and analysis in IEC 61850–5, the loading of communication network with a process samples is 750–1,200 kBytes. LAN simulation analysis of communication performance when substation fault happens shows that all critical circuit breakers receive a trip command in less than 4 ms using special broadcast messages mapped on MMS/OSI protocol. In the traditional hard-wired mode, the time from giving power to the device contact to reach the threshold is about 8–20 ms. The protection system based on IEC 61850 has a distinct advantage regardless of point of view from the communication channel or reaction time.

The scheme in Fig. 1 uses a lot of directional information. On the basis of the existing microprocessor-based protection, as long as using the directional element

Table 4 Strategy table for determining the fault location

Fault position		F10	F11	F1	F2	F3	F4	F5	F6	F7	F8	F9
Incoming line level	F10	0	1	1	1	1	1	1	1	1	1	1
	F11	1	0	1	1	1	1	1	1	1	1	1
	F1	1	1	0	1	1	1	1	1	1	1	1
transformer level	F2	1	1	1	0	1	1	1	1	1	1	1
	F3	1	1	1	1	0	1	1	1	1	1	1
outgoing line	F4	1	1	1	1	1	0	1	1	1	1	1
	F5	1	1	1	1	1	1	0	1	1	1	1
	F6	1	1	1	1	1	1	1	0	1	1	1
	F7	1	1	1	1	1	1	1	1	0	1	1
	F8	1	1	1	1	1	1	1	1	1	0	1
	F9	1	1	1	1	1	1	1	1	1	1	0

Fig. 4 Output data at F3 and output data at other places

component in a correct way, the direction can be determined correctly. In this scheme we use positive sequence directional component. Do some XOR calculations between the real output data of the directional component and the fixed value in the database and then do OR calculation for each data of each result. Thus, the fault location can be determined by simple binary number 0 and 1. A strategy table is generated through analysis and calculation in Table 4. It can be the basis for determining the fault location.

Use logical-mathematical components to perform simple logic operations for the algorithm in PSCAD. If fault happens at F3, the output data of F3 and of other places are shown in Fig. 4.

It can be seen from Fig. 4 that the output data at F3 is 0 and the output data at other places are 1. Make a comparison between the data and the strategy table and it can be determined that fault location is at F3. Then PMSINF0 sends trip message to the breaker. The program is very easy to extend. If a new transmission line is added, we can add a new directional component at the corresponding location and add all output data in Table 2 when fault happens at this line. After analysis, the back-up protection scheme based on IEC 61850 has good reliability and also improves the speed. It is a effective scheme.

The simulation of the network delay in this system is as below in Fig. 5. Through the simulation we can know the scheme is reasonable for commutation demand.

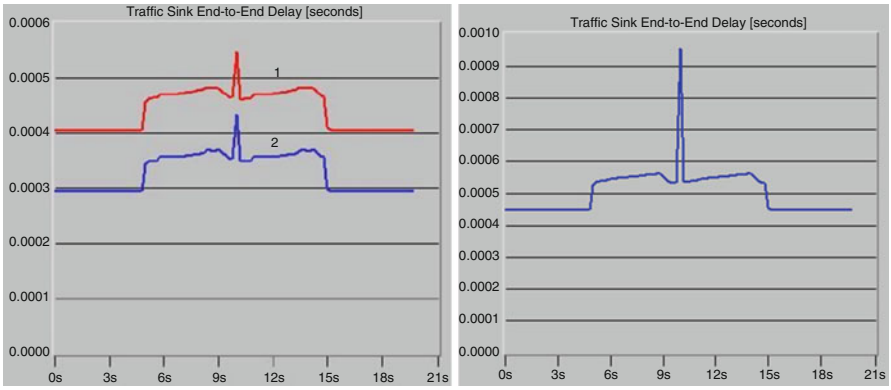

Fig. 5 Communication simulation in OPNET

5 Conclusion

This paper presented a back-up protection algorithm based on IEC 61850 which makes full use of the relationship between the fault position and fault output data to decide the fault location and achieve rapid and effective back-up protection. It can effectively solve the problems caused by traditional backup protection whose acting time is too long. This paper also established the logic modeling and information exchange modeling, while describing the principle of modeling mapping. The program is an organic integration of the protection theory and computer science communication theory, which turns out to be more effective and practical.

References

1. YI Jun, ZHOU Xiao-xin (2006) A survey on power system wide-area protection and control. Power Syst Technol 30:7–12, In Chinese
2. Hu Yu feng, Yin Xiang gen, Chen De shu, Zhang Zhe (2002) The application study of information fusion in power system ─basic theory and method. Relay 30:1–5 (In Chinese)
3. Hu Yu feng, Yin Xiang gen, Chen De shu, Zhang Zhe (2002) The application study of information fusion in power system -development activity and applying foreground. Relay 31:17–22 (In Chinese)
4. Ma Lei, Wang Zeng-ping, Ma Jing (2006) Study on local multi-information backup protection. Relay 34:6–9 (In Chinese)
5. He Wei, Tang Chenghong, Zhang Xiangwen (2007) Design of data structure for IED based on IEC 61850. Autom Electr Power Syst 31:57–60, In Chinese
6. Zhang Jie, Hou Si-zu, Chen Xiao-qian, Zhang Ke-gang (2011) Research on data modeling method based on IEC 61850. Telecommun Electr Power Syst 32:31–35 (In Chinese)
7. Wang Li-hua, Ma Jun-hua, Wang Chuan-qi (2006) Research on application of substation configuration description language. Power Syst Technol 30:93–96 (In Chinese)

8. IEC 61850-7-4-2003 Communication networks and systems in substations: Part 7–4 basic communication structure for substation and feeder equipment compatible logical node classes and data classes. Switzerland (2003)
9. Tong Xiaoyang, Li Yingchuan, Zhang Li, Xu Kelai (2008) Interaction model of protection functions based on IEC 61850. Autom Electr Power Syst 32:41–45 (In Chinese)

A Novel Approach to Deploying High Performance Computing Applications on Cloud Platform

Jinyong Yin, Li Yuan, Zhenpeng Xu, and Weini Zeng

Abstract Now people can run HPC applications on cloud platform and they do not need to own or maintain physical infrastructure. However, they have the burden of managing large pools of virtual machines (VMs), because cloud users today must manually instantiate, configure and maintain the virtual hosts. In this paper, a novel approach is proposed to deploy HPC applications on cloud platform easily which integrates a message passing interface (MPI) based simple programming model and single system image (SSI) technology. By hiding the details of MPI applications and VMs cluster, the approach allows cloud users to execute MPI applications on VMs cluster as normal multi-process applications on a single machine. So cloud users are promised to create and maintain a single VM only to deploy and execute HPC applications on hundreds of VMs. The experimental results show that the approach can reduce the burden of deploying HPC applications on cloud platform greatly.

Keywords Message passing interface (MPI) • Single system image (SSI) • High performance computing (HPC) • Cloud computing

1 Introduction

Nowadays some HPC applications are too small for supercomputers like IBM Blue Gene series, but too big for PC or workstation. Traditional solution to implement these type applications is to adopt PC or workstation cluster as physical infrastructure and MPI standard as communication mechanism, but this solution can not satisfy HPC users' needs mostly due to programming model, installation processes and high maintenance cost.

J. Yin (✉) • L. Yuan • Z. Xu • W. Zeng
Jiangsu Automation Research Institute, Lianyungang, China
e-mail: yinjinyong@yahoo.com

W. Wang (ed.), *Mechatronics and Automatic Control Systems*, Lecture Notes in Electrical Engineering 237, DOI 10.1007/978-3-319-01273-5_39,

Cloud computing [1] is an alternative computing platform to bridge the gap between HPC users' computational demands and their local computing capabilities. Recent years have seen an increasing adoption of cloud computing in a wide range of computing intensive domains, such as high-energy, nuclear physics, bioinformatics, astronomy and climate research [2]. Cloud computing is also an excellent collaboration tool that allows users to share information globally, and replicate others' work in the cloud that contains identical application, datasets and environmental settings.

MPI provides APIs to simplify the message passing inter-process, and provides a process management environment to launch parallel application across hosts in the cluster. In fact, MPI has become an IPC standard in HPC applications domain. However, in a cloud environment, users must set up their cluster of VMs and MPI process management environment by managing the instantiation, configuration and maintenance of the cluster members, which increases the management burden of running HPC applications on cloud platform.

To reduce the cloud users' management burden, we propose a MPI based programming model which eliminates MPI commands and parallel environment so that executing MPI application is as the same as normal application. The programmer can write parallel programs in a more natural and simple way. SSI technology make cluster as a high performance machine. By integrating the programming model and SSI, cloud users can execute MPI application on VMs cluster as on single machine.

This paper is organized as follows: in Sect. 2, we introduce some related works; in Sect. 3, we detail the cloud platform; Sect. 4 is the main part of the paper including the SSI-MPI programming model and its implementation; in Sect. 5, we conclude this paper with some forward-looking remarks.

2 Related Works

In recent years, a lot of projects have explored the areas of MPI, VM replication and feasibility studies of HPC applications on cloud platform.

Youseff et al. [3] have explored the suitability of virtualization for applications MPI-based and demonstrated that MPI applications can run in Xen platform with a little of overhead. Beyond MPICH, there are several other implementations of MPI including Open MPI [4] and LAM MPI [5] and other parallel programming frameworks such as the Parallel Virtual Machine (PVM) [6], which provides a message passing model very similar to that of MPI, OpenMP [7], which targets parallel computing in a shared memory multiprocessor and MapReduce [8], which targets the large parallel data intensive computations.

Cloud user can quickly replicate virtual machines by adopting SnowFlock [9], but they have to address issues related to parallel APIs. The Potemkin project [10] implements a honeypot. Honeypot machines are lightweight VMs which are cloned with memory copy-on-write techniques from a static template in the same physical

machine. Remus provides fault-tolerance of VM by keeping an up-to-date replica a separate host. Denali focus on security and isolation in a web-server by dynamically multiplexing VMs executing user-provided code.

3 Cloud Platform Overview

As mentioned in above sections, we intend to provide a transparent programming model similar to the single machine platform for the designers. For this reason, we adopt SSI technology to image VMs cluster to a high performance SMP VM in operation system layer and improve MPI implementation to suit for the SSI platform i.e. the MPI applications can be written and executed as the same way as single machine applications.

As shown in Fig. 1, the platform proposed has the hierarchy as follows:

- Physical layer: Provides hardware infrastructures such as processor, memory, disk, network, etc.
- Virtualization layer: Provides resource partition and management service; in the case, KVM hypervisor is adopted because KVM is included in the standard linux kernel and can be used conveniently.
- SSI layer: Image VMs cluster to a single VM, where kerrighed (a popular SSI system) is adopted because it is implemented in kernel level and more transparent to programmers.
- MPI layer: By improving MPICH (a popular MPI implementation), MPI layer can run MPI applications on cluster platform with SSI as a single machine.
- Parallel algorithm library layer: Provides some general MPI library functions such as FFT and can be called transparently.
- Application layer: Provides special software service which can call MPI library functions or MPI APIs directly.

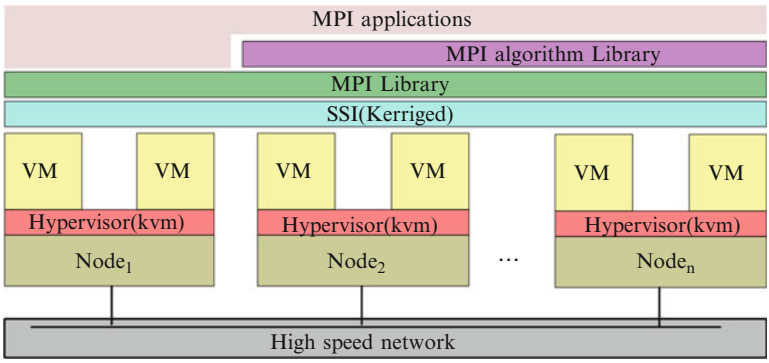

Fig. 1 The architecture of cloud platform

4 SSI Based Programming Model and Its Implementation

The MPI architecture and the changes that are more suitable for SSI platform are described in this section. Our works are based on the MPICH2 which is an efficient implementation of MPI developed by the Argonne National Laboratory (Fig. 2).

4.1 Programming Model

Users must set up a management daemon on each machine to launch standard MPI application. This daemons form a one-way ring topology to communicate each other. Users must use **mpirun** program to run MPI applications and initiate the execution as follows:

mpirun -n numofprocs programname args

where **numofprocs** is the number of MPI processes, **programname** is the name of the program, and **args** are arguments passed to the program.

The standard MPI architecture involves a persistent one-way ring of management processes (mpd), and another one-way ring that manages each application run (mpdman). Control messages travel through the rings, while workers exchange application messages point-to-point.

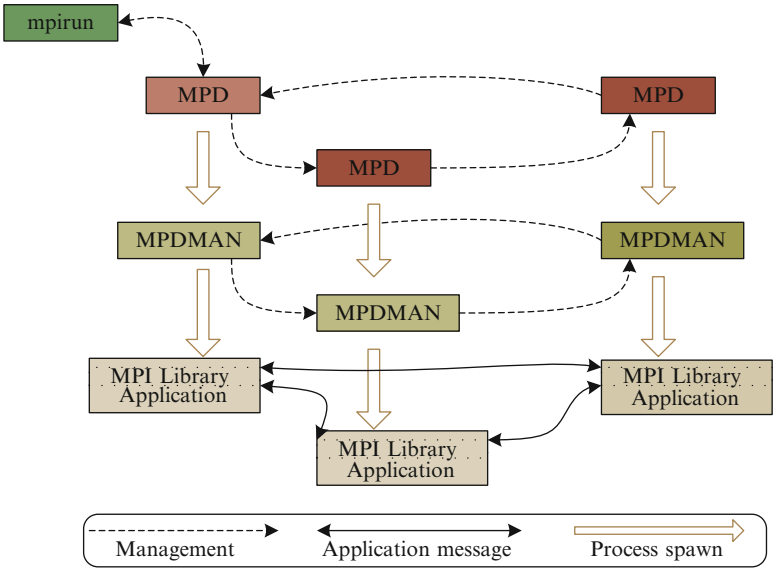

Fig. 2 Standard MPI architecture

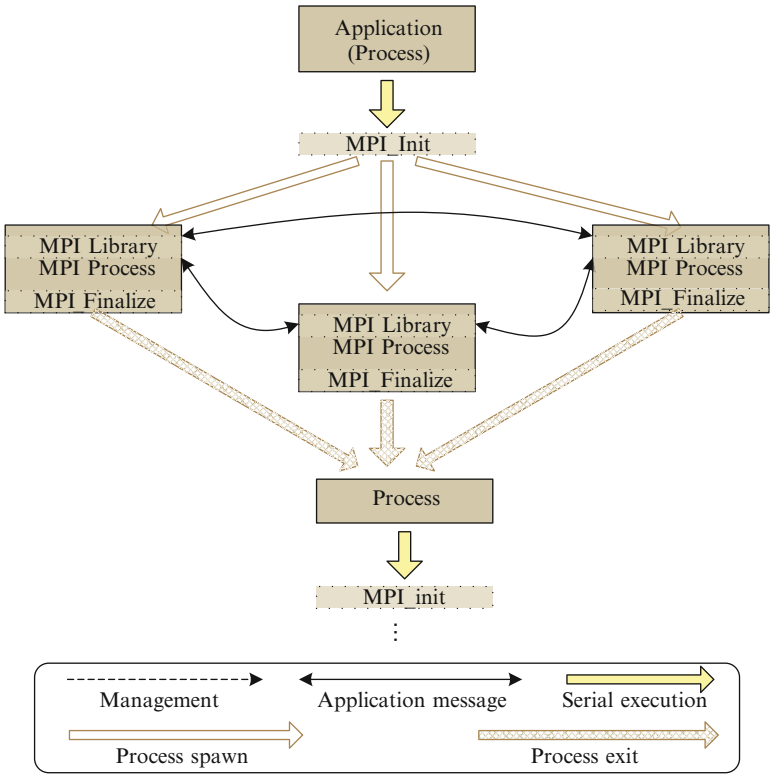

Fig. 3 The SSI-MPI architecture

To make MPI architecture more suitable for SSI platform, that is running MPI applications on cluster as normal multi-process applications on a single machine, we modified MPICH architecture as shown in Fig. 3 (SSI-MPI)and the details of implementation will be shown below.

SSI-MPI eliminates standard MPI's commands and parallel environment such as mpd and mpdman processes. The SSI-MPI application can be started by the shell immediately. The SSI-MPI application runs as a single process. When parallel computing is needed, SSI-MPI application calls MPI_Init function to fork as many processes as required and the new processed are migrated to other node by the SSI transparently. When SSI-MPI application calls MPI_Finalize function, the parallel computing is finished. The parallel computing procedure can be repeated when needed in the same application.

Furthermore, unlike standard MPI needing many application binary copies, the SSI-MPI can completely encapsulates the parallel computing procedure in a library function which can be called as a normal library function. So SSI-MPI can increase the reusability of parallel codes and make the programmer write MPI application in a more natural and simple way.

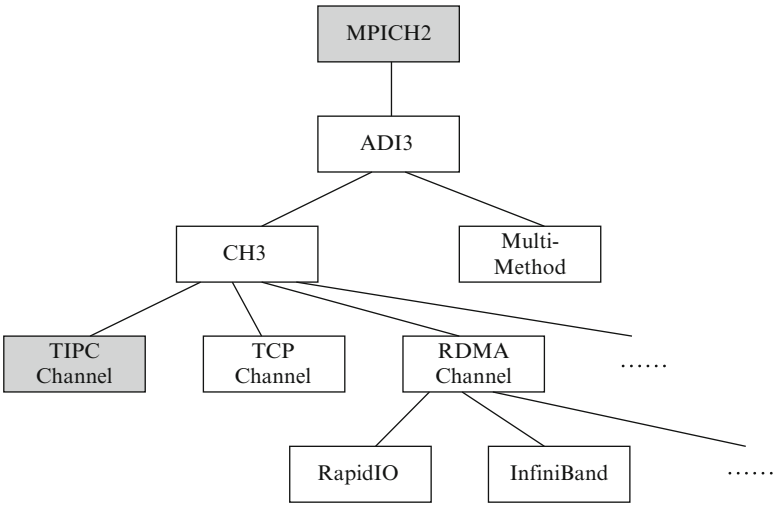

Fig. 4 The modified MPICH2 architecture

As shown in Fig. 3, the SSI-MPI implementation doesn't need mpirun to start MPI application which hides details of MPI applications. The MPI application starts and executes as normal application before it calls MPI_Init function. When it calls MPI_Init function it forks multi processes called MPI processes. The MPI processes communicate each other by calling MPI library functions and after calling MPI_Finalize function, the MPI application executes as normal application again. It can launch a new parallel procedure when needed.

4.2 The Implementation Way

We are going to implement the SSI-MPI through modifying MPICH2 which is a efficient and matured implementation of MPI. The main modified parts include TIPC channel, MPI_Init function and MPI_Finalize function as shadows in Fig. 4.

MPICH2 uses ADI3 as a portability layer to facilitate porting from one platform to another. Because ADI3 is abstract devices interface with full-featured, it has many functions to be implemented for porting to a new channel. CH3 is introduced to reduce the porting effort.

As shown in Fig. 4, there have been several channels for TCP, RDMA, etc. different communication architectures. Because functions associated with each channel interface are fewer that associated with ADI3, it is easier to implement a channel than the ADI3 device. We implement a TIPC channel in SSI-MPI. TIPC is a standard protocol with low overhead and satisfies the special needs of application working within dynamic cluster environments. Its name service supports communication inter

processes after migrating which are what SSI-MPI needs because SSI-MPI forks many processes and migrates them to other node for load balancing.

The main differences between SSI-MPI and MPICH are the implementation of MPI_Init function and MPI_Finalize function. Because MPICH has mpirun tool, mpd and mpdman process demons which can launch MPI application and setup environment variables, MPI_Init can parse the environment variables set up by mpdman. But in SSI-MPI, these works must be done in MPI_Init function.

In SSI-MPI, MPI_Init function and MPI_Finalize functions work as follows: firstly, MPI_Init function initializes the global variable pUniv and Set a default for the universe size; secondly, MPI_Init forks processes according to parameter passed from user and migrates them to other nodes; finally, MPI_Finalize function waits for the forked processes to exit and resets global variables so that the application can call MPI library next time.

4.3 A Programming Example

In this section, we show how to use SSI-MPI to write parallel application by an example.

Figure 5 is a Fast Fourier Transform (FFT) algorithm written in SSI-MPI, from which we can see that all the parallel computing are encapsulated in MPI_fft function and the MPI_fft function can be called as a general function in main function.

The procedure is same as standard MPI. Firstly, MPI_fft calls MPI_Init to setup environment variables and initializes worker processes; in this instance, eight worker processed are initialized. Secondly, MPI_fft perform calls such as MPI_Comm_rank to determine its rank, or MPI_Comm_size to find out about the total number of workers spawned. Throughout execution, workers transmit information to one another via the MPI_Send and MPI_Recv calls. Finally, MPI_Finalize is called to finish the parallel procedure.

Except for MPI_Init, all the APIs accord with MPI specification. Because MPI_Init can parse the environment variables set up by mpdman in standard MPI, however there is no mpdman in SSI-MPI, the parameters such as worker process number must be passed to MPI_Init.

4.4 Discussion

SSI-MPI eliminates MPI's commands and the maintenance of management daemons. It can reduce the difficulty of writing MPI application and increase utilization of parallel codes greatly. It allows parallel programmer to write MPI application in a more natural and simple way and is more transparent to

```
void MPI_fft(double [] Time_commn , double [] Frequency _commn , int Points,
                int Process _num)
{
   int ProcRank,Size ;

   MPI_Init(Process _num);        // Create Process _num processes
   MPI_Comm_rank(MPI_COMM_WORLD,&ProcRank);
    MPI_Comm_size (MPI_COMM_WORLD,&Size );

// Parallel computing
   if(ProcRank==0)
   {
       //do something
   }

   if(ProcRank==1)
   {
      //do something
   }
              .
              .
              .

   MPI_Finalize();
   return;
}
void main()
{
   double  Time_commn [1024 ],Frequency _commn [1024 ];

   MPI_fft(Time_commn ,Frequency _commn ,1024 ,8);
   // do something else

   return;
}
```

Fig. 5 The parallel FFT algorithm

programmer and users. One drawback of SSI-MPI is that it needs SSI's supports. On the other hand, if SSI-MPI itself implements process migration, it can run on normal cluster platform.

5 Conclusion

In this paper, an approach was proposed to reduce the burden of deploying HPC applications on cloud platform by integrating SSI and MPI. It can allow the cloud users to deploy HPC applications on cloud platform only to configure and interact with a single VM.

This study mainly focused on SSI and MPI on cloud platform and there still are much deserving exploitations. The future works include the implementation of process migration in MPI and the exploitation of management tools that allow cloud users to create and manage their high performance VM.

Acknowledgements This work was supported by Natural Science Foundation for Young Scholars of Jiangsu Province of China (BK2012237).

References

1. Armbrust M, Fox A, Grith R et al (2009) Above the clouds: a Berkeley view of cloud computing. Technical report. UC Berkeley
2. Ostermann S, Yigitbasi M, Prodan R et al (2011) Performance analysis of cloud computing services for many-tasks scientific computing [J]. IEEE Trans Parallel Distrib Syst 22 (6):931–945
3. Youseff L, Wolski R, Krintz C (2006) Evaluating the performance impact of Xen on MPI and process execution for HPC systems [C]. The first international workshop on Virtualization Technology in Distributed Computing (VTDC), p 1
4. Gabriel E, Fagg E, Bosilca G et al (2004) Open MPI: goals, concept, and design of a next generation MPI implementation [C]. 11th European PVM/MPI users' group meeting, pp 97–104
5. Chase J, Irwin D, Grit LE et al (2003) Dynamic virtual clusters in a grid site manager. In: Proceeding 12th IEEE international symposium on High Performance Distributed Computing (HPDC), IEEE, Berlin, Germany, pp 90–100
6. Clark C, Fraser K, Hand S et al (2005) Live migration of virtual machines. In: Proceeding 2nd symposium on Networked Systems Design and Implementation (NSDI), ACM, vol 2. Washington DC, USA, pp 273–286
7. Lagar-Cavilla H, Whitney J, Scannell A et al (2009) SnowFlock: rapid virtual machine cloning for cloud computing. In: Proceeding of Eurosys 2009, ACM, Boston, MA, USA, pp 1–12
8. Vrable M, Ma J, Chen J et al (2005) Scalability, fidelity and containment in the potemkin virtual honeyfarm. In: Proceeding 20th Symposium on Operating Systems Principles (SOSP), ACM, Nüremberg, Germany, 39(5):148–162
9. Dean J, Ghemawat S (2004) MapReduce: simplified data processing on large clusters. In: Proceeding 6th symposium on Operating System Design and Implementation (OSDI), ACM, New York, USA, pp 137–149
10. Whitaker A, Shaw M, Gribble S (2002) Scale and performance in the Denali Isolation Kernel. In: Proceeding 5th symposium on Operating System Design and Implementation (OSDI), ACM, New York, USA, pp 195–209

Parallelization of Characteristic Series

Jiamei Liu, Suping Wu, Hongbo Li, Xinbo Yao, and Fang Du

Abstract The algorithm of computing characteristic series is the core of Wu elimination method and its computation is very huge, so the common serial program usually cannot meet the speed requirement. To solve this problem, parallel computing is introduced. In this paper, the algorithm of computing characteristic sets is analyzed, firstly, and then the parallelization of computing characteristic series, which is implemented with distributed computing environment in Maple, is given. The experimental results verify the performance and the acceleration effect of the parallel algorithm.

Keywords Wu elimination method • Parallel algorithm • Characteristic set • Maple

1 Introduction

Wu elimination method supplies an integrated theory and efficient method for solving non-linear algebraic equations [1]. Solving non-linear algebraic equations is a basic and most difficult problem. With the rapid development of the Wu's method, it is used more and more [2–4]. The mechanical algorithm of characteristic series is the core of Wu's method and its computation complexity is very high. However, those serial computing process cannot meet the current speed requirement of specific applications usually. To improve the computing efficiency and to tackle much more complex non-linear algebraic equations, parallel computing using Grid Computing Toolbox in Maple is introduced.

Some achievements have been made in the research of parallelization for computing characteristic set based on different mathematic computing software.

J. Liu • S. Wu (✉) • H. Li • X. Yao • F. Du
School of Mathematics and Computer Science Ningxia University, Yinchuan, China
e-mail: wspg123@163.com

W. Wang (ed.), *Mechatronics and Automatic Control Systems*, Lecture Notes in Electrical Engineering 237, DOI 10.1007/978-3-319-01273-5_40,

Such as Ajwa I. et al. [5] implemented a specific package of parallelizing the computation of characteristic set in the environment of PVM and SACLIB; Wang D. M. [6] researched on the parallelism of Computing characteristic set in Maple system using distributed workstation connected by a local network; Wu Y. W. et al. [7] designed a distributed computing environment for the parallelization of Wu's method by combining different techniques including ELIMINO [8], MPI and Globus Toolkits 3, which get a preferable speedup ratio of about 2. The paper [9] gives the parallelization of Wu's method on multi-core platform with the multithreading model in Maple.

This paper tries to parallelize the computation of calculating characteristic series which is very time-consuming, and develop the corresponding parallel program with distributed computing environment in Maple. The experimental result shows a satisfactory acceleration.

2 The Main Theorems and Sequential Algorithm

A solution of a given polynomial equation system is called a zero point where the value of each polynomial is zero. Given a polynomial set PS, we get a polynomial equation system $PS = 0$. Then the process of solving this polynomial equation system is the same to find out all of the corresponding zero points. These zero points constitute a set and we call this zero set of PS, denoted by $Zero\ (PS)$.

During the process of solving polynomial equations by elimination method, the polynomial equation system of triangular form is very important. The goal of Wu's method is just to use the polynomial equation system of triangular form to describe exactly the zero set of the given polynomial equation system. To be more specific, characteristic series, a set of characteristic sets, is just the polynomial equations of triangular form. The algorithm of computing characteristic series is extremely critical to Wu's method.

Definition 1 (Characteristic set) [1]. Given a polynomial equation system $PS = \{P_1(x), P_2(x),\ldots, P_m(x)\}$, where $P_i(x_1, x_2,\ldots, x_n) \in K[x_1, x_2,\ldots, x_n], i = 1, 2, \ldots, m$. Ascending set $CS = \{C_1(x), C_2(x),\ldots, C_r(x)\}$, where $C_i(x_1, x_2,\ldots, x_i) \in K[x_1, x_2,\ldots, x_i], i = 1, 2, \ldots, r$, is called the characteristic set of PS, if it satisfies the following two conditions:

1. The pseudo remainder of each polynomial P_i in PS with respect to CS is zero, i.e.

$$Rem(P_i/CS) = 0,\ i = 1,\ 2,\ldots,\ m.$$

2. The polynomial equation system PS and ascending set CS satisfy

$$Zero(PS)\ \subset Zero(CS).$$

Theorem 1 (Well Ordering Principle) [1]. *Given a finite, non-empty set PS of non-zero polynomials, PS = {P1, P2, …, Pm}, Pi∈K[X], i = 1, 2, …, m, there certainly exists a mechanized algorithm, with which follows limited steps of computation a basic set of PS, denoted by BS, can be computed, which satisfies that the pseudo remainder of each polynomial in PS with respect to BS is zero. If this BS is non-contradictory, then it is the characteristic set of PS, denoted by CS.*

Theorem 2 (Zero Set Structure Theorem) [1]. *Given the characteristic series CS, CS = {C1, C2, …, Cr}, of polynomial set PS, PS = {P1, P2, …, Pm}. The initial of Ci is Ii, i = 1, 2, …, r. The zero set of PS, denoted by Zero(PS) has this structure:*

$$Zero(PS) = Zero(CS/I)\bigcup\bigcup_{i=1}^{r} Zero(PS, I_i),\ I = \prod_{i=1}^{r} I_i.$$

Theorem 3 (Zero Set Decomposition Theorem) [1]. *Given the polynomial sets PS, PS = {P1, P2, …, Pm}, whose zero set can be decomposed into a set, union of a series of characteristic sets' zero sets:*

$$Zero(PS) = \bigcup_j Zero(CS_j/I_j),$$

The set of index j in this equation is finite, Ij represents the product of all the initials in CSj.

The well ordering principle is applied in the process of computing characteristic set, the zero set structure theorem and the zero set decomposition theorem describe the constructive description of zero set. The definition and theorems can be found and proved in [1].

In the elimination process the selection of basic sets is not sole and in practice it has great flexibility. So the characteristic set is not one and only either. As described before, we call the combination of all the characteristic sets characteristic series. According to the constructive description of zero set indicated by Theorem 2 and 3 and referring to the Wsolve package in Maple designed by Wang D. K. [10], the serial algorithm of computing characteristic series can be extracted. The algorithm of computing characteristic series consists of several important parts: calculating basic sets, pseudo division of polynomials, factorization, calculating characteristic sets, decomposition for computing characteristic series. For the sake of simplicity and basis for parallel algorithm description that followed, the last part is given only. Its sequential algorithm is put as follows.

```
Wusolve ( Input: PS; Output: CSS )
Begin
// Decomposing PS into many independent polynomial sets,
QS is a set of sets
QS := Factorization (PS)
for i in QS do
```

```
  CSS:= CSS∪CharacteristicSetSeries(i)
    od
  End
  // Computing the characteristic series of PS
  CharacteristicSetSeries( Input: PS; Output: CSS )
  Begin
    QS := PS
    CS := CharacteristicSet(PS)
    // The difference set between CS and constant set
    IS := init(CS) −{constant}
    for I in IS do
      // CharacteristicSet: computing CS
      CSS := CS∪CharacteristicSet(QS∪{I})
    od
  End
```

3 Parallel Algorithm

In order to realize parallel programming, two different kinds of parallel programming forms are developed in Maple. The first one is the multithreading programming model. The other one is the distributed computing model, depending on Grid Computing Toolbox. The distributed computing model uses multiple process parallelism, each process has its own independent memory. The Maple Grid Computing Toolbox enables you to run Maple computations in parallel, taking advantage of all your hardware resources, cutting down on processing time, and enabling applications that were not possible before. It allows you to deploy your parallel programs to large-scale compute cluster and supercomputer, making full use of all processing power available to tackle very large problems [11].

The Grid Computing Toolbox is very easy to set up. It can connect directly into your existing Windows HPC Server cluster without the need to set up services on each node. You can also start a server process on each computer on a network and the grid will self-assemble as each node automatically detects other nodes that are present. The Grid Computing Toolbox also integrates into existing job scheduling systems such as PBS. Maple includes the ability to easily set up multi-process computations on a single computer. The Maple Grid Computing Toolbox extends this power to multi-machine or cluster parallelism. The two versions, Personal Edition and Cluster Edition, are fully compatible, so that an algorithm can be created and fully tested by using the local implementation inside Maple, and then deployed to the full cluster using the toolbox, without changes to the algorithm [11].

In this paper, Personal Edition on a system with multi-core processor is chosen to perform an experiment. In this situation parallelism is implemented by creating a certain number of virtual nodes, which is realized by creating a certain number of processes to simulate a Grid Computing Environment.

Factorization plays an important role in solving polynomial equation system. In the process of solving polynomial equation systems, it is a common phenomenon that there are usually polynomials can be factorized. So if some polynomials can be factorized into several polynomials with lower degree and fewer terms, it will facilitate the computation to a great extent. Based on this notion, the best way to compute characteristic series is to factorize the polynomial set firstly in this way the zero set of original polynomial equation system can be converted into a series of polynomial equation systems' zero sets.

For example, given polynomial set *(R, S)*, if R can be factorized in this way: $R = R_1 \times R_2$, then the original zero set could be decomposed into two zero sets as follows:

$$Zero(R, S) = Zero(R_1, S) \bigcup Zero(R_2, S)$$

In addition, due to the independence among the processes of solving these newly generated polynomial equation systems, parallelization on this part can accelerate the computing process obviously. Parallel algorithm is described as follows.

```
PWusolve ( Input: PS,ORD; Output: CSS )
Begin
    QS := Factorization (PS)
    for i in QS parallel-do
    CSS:= CSS∪CharacteristicSetSeries(i)
  od
End
```

This algorithm is grounded on data-parallel method, i.e. each node executes the same code, but with different data. Hereon, several critical steps to implement parallelization with Grid Computing Toolbox in Maple are put due emphasis. These critical steps can be listed as follows.

1. A sever is established. The simplest way to start a sever is to use personal grid server worksheet, an interactive Maple document that can start a personal server with many nodes, we start a personal server with seven nodes. The alternative method is to use Maple commands to configure your computer as personal server.
2. The mode of operation for parallel computation using the Grid package is designated. This step can be realized by calling Grid[Setup] command. The specific call is given as follows. In this call, the mode is not designated obviously and the default value and local mode are used. By setting *host = "localhost"*, *port = "2000"*, the location of the running Grid Server, is known by Maple and the master server whose port number is 2,000 is designated. *Grid*[*Setup*] ("localhost", 2000):
3. A parallel computation can be launched by calling *Grid[Launch]* command. The specific call is given below. the list includes expressions which are used in *CssGrid* or its subprograms and imported from the current Maple session to each of the nodes.

Grid[Launch](N, CssGrid, printf, proc () false end proc, ["psets", "ords", "nonzeros", "ascs", "Css", "Degenerate", "Cs_c", "Cs_b", "Cs_a", "Inits1", "Inits", "Init", "Emptyset", "Nums", "Nrs", "LProduct", "Produce", "Factorlist", "Premas_a", "Premas", "NPrem", "Basicset", "Reducedset", "Reducedp", "Least", "Lessp", "Initial", "Mainvar", "dIndets", "Class", "Nonumber", "Remset"]);

4. Because of *psets* in a group of polynomial set and we need to compute each polynomial set's characteristic series independently, a mapping operation in *CssGrid*. *Grid[Util][Map]* command can be used, whose specific call is given below. Here we focus on the first two parameters: *Css* is the true procedure computing characteristic series; *psets* is the set union of newly generated polynomial sets gained by factorizing the original polynomial set. So we come to know that we can apply *Css* to each element in *psets.CssGrid:=proc() Grid [Util][Map](Css,psets,ords,nonzeros,ascs):end proc:*
5. To gather the results returned by each node to get the final result.

4 Experimental Results and Analysis

Experiments have been performed on the computer with a dual-core processor with different number of virtual nodes. Sequential program is the Wsolve package created by Wang D. K. and parallel program is modified based on this package.

Software environment: Windows XP, Maple 14. Hardware platform: CPU, Intel (R) Core(TM) 2 Duo CPU T6570 @ 2.10GHz 2.10GHz; Memory capacity, 2G.

Experimental results are shown in Table 1, in Table 1, serial time and parallel time with different number of nodes are shown, one node represents serial environment, two nodes represent on platform with two nodes, and so on. Execution time is given in seconds.

In order to contrast the accelerating effect of the parallel algorithm, the speedups of the parallel algorithm are given in Fig. 1, in this figure, the horizontal axis represents the number of nodes, and the vertical axis represents the speedup.

Based on the above experimental results, some phenomena can be concluded. (1) The computing efficiency of the parallel algorithm for all the given instances is obviously much higher than that of serial method. (2) With the increase of the number of nodes, in addition to the problems of small scale, such as instances 1, the best speedups of other instances are also getting bigger. The speedup we get is

Table 1 Serial time and parallel time with different number of nodes

Example	1 node	2 nodes	3 nodes	4 nodes	5 nodes	6 nodes	7 nodes	8 nodes
1	78.777	40.263	32.885	39.764	38.952	37.753	42.337	40.092
2	198.715	94.146	93.101	89.419	96.034	90.589	86.158	84.022
3	252.626	131.867	136.291	143.738	132.366	126.533	124.005	131.196
4	262.194	163.407	157.990	144.740	146.174	147.412	127.748	133.092

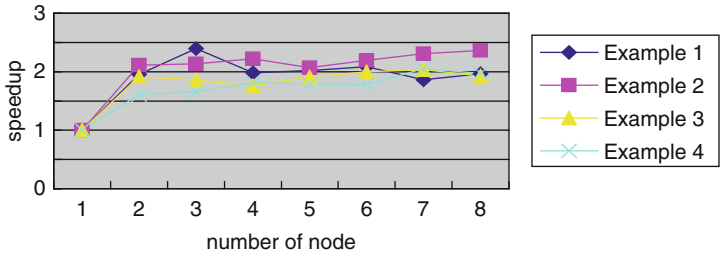

Fig. 1 Comparison of speedup with different number of nodes

determined by the ratio of overhead in total time, parallelization overhead is also increased with the number of nodes increases, but as the number of node increases and the problem scale accordingly do too, the speedups become stable rise in fluctuation gradually. Due to that ratio of overhead is getting large, when the number of nodes increases, so if advancing speedup, the problem scale must be enlarged. Due to that absolute load balancing cannot be reached, the fluctuation cannot be avoided in the converging process. If the example can be factorized into many independent problems the number of which is much bigger than the number of nodes, under this situation there are enough tasks, parallel effect will be good. (3) The distributed computing model performs stably in the experiment and it achieves a preferable accelerating effect.

5 Conclusion

This paper tries to parallelize the algorithm of computing characteristic series and implements the parallelization with the distributed computing model in Maple, and the high efficiency of parallel algorithm was proved. But there is a problem here, in the situation that the number of factorable polynomials is very small this parallel algorithm will fail to meet its high performance. The difficulty of getting a good workload balance and the limitation of memory capacity resulted in the inability to make full use of the computing power offered by this model. So in the future it needs to take into consideration of two directions to further enhance the computing efficiency. Firstly, it is recommended to optimize the serial program and the parallel part. Next, more effort should be poured into combining different parallel programming methods – the multithreading model and the distributed computing model, the utilization of computing resources can be promoted much higher, which leads to a much higher computing efficiency.

Acknowledgements This paper is funded by the National Natural Science Foundation of China (No. 60963004), and National Xinghuo project of China (No. 2011GA880001). We would like to express our sincere gratitude to the National Natural Science Foundation of China and National Xinghuo project of China for the financial support.

References

1. Shi H (1988) Introduction to mechanized mathematics[M]. Hunan Education Press, Changsha, pp 5–46 (in Chinese)
2. Wu TJ (2007) On applications of Wu's method in bilevel-programming problems[J]. Acta Math Sci 27A(1):176–183
3. Lü SZ, Zhang DW, Liu HN (2010) Solution of screw equation for inverse kinematics of 6R Robot based on Wu's method[J]. J Mech Eng 46(17):35–41 (in Chinese)
4. Chai F, Gao XS, Yuan C (2008) A characteristic set method for solving Boolean equations and applications in cryptanalysis of stream ciphers[J]. J Syst Sci Complex 21(2):191–208 (in Chinese)
5. Ajwa I, Wang P (1997) Applying parallel/distributed computing to advanced algebraic computations. In: Proceeding of the 1997 I.E. national aerospace and electronics conference, IEEE Press, Washington, pp 156–164
6. Wang DM (1991) On the parallelization of characteristic-set-based algorithms. In: Proceedings of the 1st international conference ACPC, Salzburg, pp 338–349
7. Wu YW, Yang GW, Yang H, Zheng WM, Lin DD (2005) A distributed computing model for Wu's method[J]. J Softw 16(3):384–391 (in Chinese)
8. Lin DD, Liu J, Liu ZJ (1998) Mathematical research software: ELIMINO. In: Li ZB (ed) Proceeding of theACM'98, Lanzhou University Press, Lanzhou, pp 107–114
9. Li HB, Wu SP, Liu R, Yang J (2012) Improved parallel algorithm of solving characteristic sets [J]. Comput Simul 29(11):189–193 (in Chinese)
10. Wang DK (1993) A maple package for solving system of polynomial equations[M]. Math-Mech Res Prepr 10:11–14 (in Chinese)
11. Maplesoft Online Help (2011) http://www.maplesoft.com/support/help

Part III
Manufacturing Engineering and Engineering Systems

Wireless Monitoring System for Elevator on Android Platform

Hang Xu and Guo-jun Zhao

Abstract This paper introduces and presents an Android based remote monitoring system for elevator which can connect the elevator controller with Wi-Fi or GPRS network. The system provides friendly interfaces for users to get monitoring information about the elevator. Compared with existing elevator monitoring systems, this system runs on a smartphone with Android O.S rather than the expensive PC platform and there is no need to write before installing the system. The user could achieve the lift monitoring at anywhere and anytime.

Keywords Android • Elevator monitoring system • Wireless communication

1 Introduction

Nowadays elevators in our environment are gaining popularity, but the accidents are still common. Elevators are expected to run safety, reliability and repair efficiency and timeliness. In order to meet the set of requirements, elevator maintenance staffs should access real-time information and learn about the running states of the elevator. Elevator monitoring system is designed for the elevator remote data maintenance, remote fault diagnosis and statistical analysis. But most existing elevator monitoring systems are wired elevator controller and PC platforms [1]. This method has some issues that have to be considered and addressed:

- It is difficult and expensive to wire between PC platforms and elevator controller.
- The maintenance staffs have to stay at the control room day and night to prevent unexpected events.

H. Xu (✉) • G.-j. Zhao
Key Laboratory of E&M, Ministry of Education & Zhejiang Province,
Zhejiang University of Technology, Hangzhou, China
e-mail: johnhill87@yahoo.cn; cnzgj@163.com

W. Wang (ed.), *Mechatronics and Automatic Control Systems*, Lecture Notes in Electrical Engineering 237, DOI 10.1007/978-3-319-01273-5_41,

- It is difficult to find the point of fault if the communication faults of the monitoring system occurred.

To solve these issues, an Android based wireless monitoring system was used which could allow maintenance staffs use Android smartphone with wireless network to solve the above problems and to simplifies the install process of monitoring system.

2 Structure of the System

BÖHNKE+PARTNER BP304 elevator controller [2] was used as experimental platform, BP304 is a high-end product, its control system used three 32 industrial microprocessors, and enhanced the operation speed and performance. It supports 64 floors at most, up to eight sets of elevator group control and supports for remote monitoring, the structure of BP304 is shown in Fig. 1.

The system is designed as the Client/Server communication model [3, 4]. By installing a IEEE802.11 b/g protocol wireless module [5], Elevator controller acting as a server and achieves wireless communication with smartphone which acts as a client. Users can have three methods to implement a connection with the elevator controller, as shown in Fig. 2:

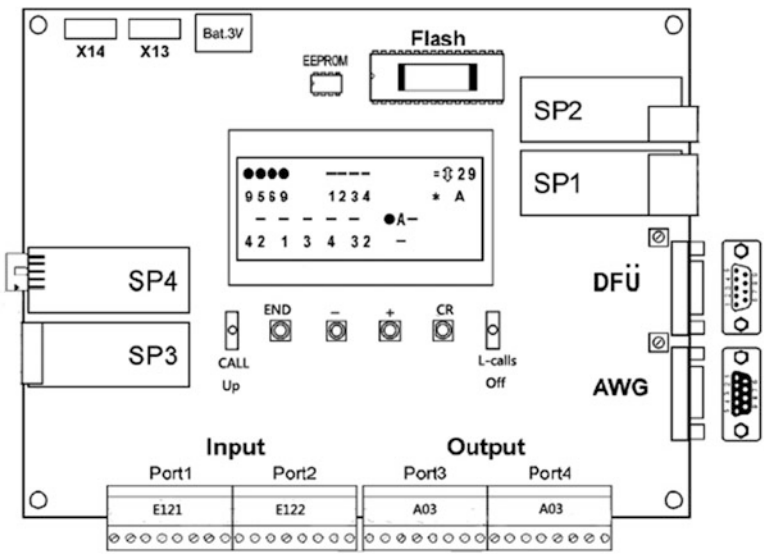

Fig. 1 Structure of BP304 elevator controller

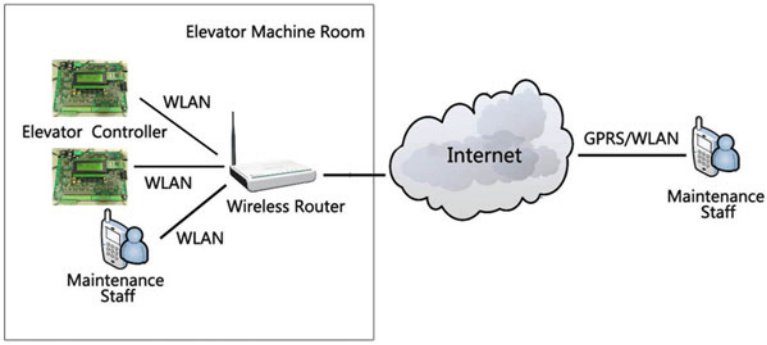

Fig. 2 The network structure of the system

2.1 LAN Connection Through a Wireless Router

If user located in the elevator machine room, LAN connection method is the best choice. Before using this method, we need to access configuration interface of the wireless router and arrange a static IP address and port number for the wireless module of the elevator controller. It's called DHCP (Dynamic Host Configuration Protocol). DHCP has three methods to allocate IP address: Manual Allocation, Automatic Allocation, and Dynamic Allocation. Normally, and DHCP will allocate an IP address using Dynamic Allocation method, but in this method every time the wireless module connect to the wireless router the IP address is different. It brings difficulty for the smartphone to connect to the wireless module. For this situation, we use Manual Allocation. In this case, DHCP will allocate a static IP address and port number manually by the MAC address which is set in the wireless device uniquely. By DHCP, the smartphone can build a LAN connection with the elevator controller through the static IP address and port number of the wireless module.

With the help of the wireless router, the system will not be influenced by the network bandwidth and can be carried out with a minimum of delay and the best stability.

2.2 WAN Connection with WLAN Network

This method is designed for the situation where the user could access the WAN by Wi-Fi network, for example, in the control room.

User should register DDNS (Dynamic Domain Name Server) for elevator controllers first. Due to the shortage of the IPv4, we can only connect to the Internet with dynamic IP address. In this case, each time our equipments access the WAN, they will get different WAN IPs and we call it dynamic IP address. It makes difficult to access a network host. DDNS technology maps user's dynamic IP address to a

fixed DNS service. Each time a user connect to the network, the program will send the information to the DNS service and allow us access a host with a domain name provided by the DNS server. With this function, the user just needs to set the DDNS configuration of the wireless router, and input the domain name to the system to implement connection.

In fact, with the development of the Wi-Fi technology, now we can find WLAN access points not only in the buildings but also at the outdoor in some modern cities. It provides us convenience to access the WAN. Meanwhile, because of the fast speed, user also can enjoy the best performance of the system.

2.3 WAN Connection with GPRS Network

This method allows user access WAN almost everywhere where there is cell phone signal.

In order to access the wireless router, user also should register the DDNS first. Data access function of the smartphone also need to be open before the connection.

Due to the limited speed of GPRS network which is no more than 300 kbps in ordinary, the system communication will not be so fluent. But after testing, the system delay is acceptable.

From the above, we can conclude that using this system, staffs could implement the real-time monitoring of the elevator almost at anywhere and anytime.

3 Software Design Flow

As previously mentioned, the system aims to build Elevator Remote Monitoring System on the smart phones to implement wireless LAN/WAN connection, remote monitoring, operate elevator, manage elevator database. For this, the system will have the features as shown in Fig. 3.

The system is divided into two parts: presentation layer and logic layer. The presentation layer is designed to displays and updates the user's interface and the logic layer implements data transmission and information processing, such as messages decoding, data storage, database processing. Logic layer provide data for presentation layer.

3.1 Account Module

Account Module consists of three parts including Login, Password Retrieve and Register. For safety consideration, user can register a personal account only in the initial use of the software. Otherwise, if users forget the password, Password

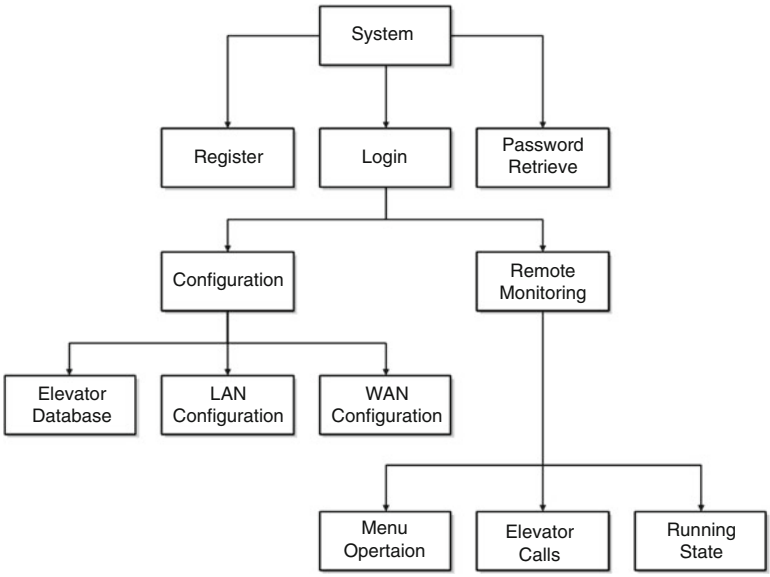

Fig. 3 System features

Retrieve function can be used to reset password after the user provide the account name and E-mail address. At the logic layer, A SQLite database [6] is designed to store the account information.

As special equipment, Elevator has a high requirement on the safety, in order to prevent non-staff log in to the system through illegal means, all account information is encrypted by DES encryption algorithm. Furthermore, we use the IMEI (International Mobile Equipment Identity) number of the smartphone as operate to avoid to log in by copying the database file of the other users. DES algorithm as a high level of security encryption algorithm, it can effectively protect data security.

3.2 Configuration Module

Because of kinds of site conditions, the system uses three kinds of connection methods to communicate with the elevator controller. In order to provide a good user experience, a database is designed to save the lift network information, called elevator database. It provides information including SSID and password of the wireless router, IP address, port number and domain if necessary.

1. LAN Configuration. To configure LAN connection, Firstly user has to connect to the Wi-Fi network. In this module, WifiManager [7] class is called to offer a range of methods to deal with Wi-Fi related issues. Here we design a spinner widget to list all AP names which can be found by the WifiManager. After

choosing an AP name form the spinner, system will pop-up an AlertDialog. It will guide the user to complete a Wi-Fi connection. Then, system will search the elevator database to find out all elevator name connected to the AP, and list them in a spinner. If users choose an elevator name, the system will open a socket connection. By now, it's ready to connect the elevator.

2. WAN Configuration. The WAN Configuration guides user through GPRS or WAN Wi-Fi network to connect to the elevator controller.

Here we register a handler to realize Try to Connect function. After inputting the target domain, the system will call new Socket(domain, port) to open a socket connection as well as a timer. If the connection is established successfully, the system will display all details of the connection, otherwise it will pop-ups a AlertDialog to warn user what happened. To avoid the system run into an infinite wait, the timer will interrupt to cancel the connection.

3.3 Remote Monitoring Module

As the core module of the system, Remote monitoring module is used to realize communication between the client and the elevator controller. We use stop-and-wait protocol [8] to ensure the stability during the communication. Stop-and-wait protocol has two basic mechanisms to implement the above requirements: acknowledgement and timeout. After sending a data, the sender will wait until it receives an ACK frame.

If there is no ACK frame in a while or receive NACK frame, the sender will resend this frame data. By using this structure, the possibility of packet error reduces greatly.

The wireless remote monitoring system developed with Android-ADT plug-in on the Eclipse platform. Because of the system. Due to the system is involved in network connectivity, in order to describe the system better an Android phone was used to implement functional testing. The test platform is shown in Fig. 4.

The Remote Monitoring Module consists of three parts, including Running State, Elevator Calls and Menu Operation.

1. Running State. Allow user to learn about the elevator car position, running direction, door state, elevator calling and car call signal. We design a simulation elevator hoistway to display this module, as shown in Fig. 5.

   In Fig. 5 we can see Running State Module running on real smartphone. It displays the real-time running state of the elevator. In the middle of the screen is the simulation elevator hoistway and up and down arrows tell user the elevator calling signals. If there is a car call signal on No. 19 floor, the color of the number will change just as shown in figure.

   Besides, Dynamic Data, Lift State and Error Stack Interface are designed with Tab widget to provide all monitoring information, user could scan this information by tapping the top column of the interface.

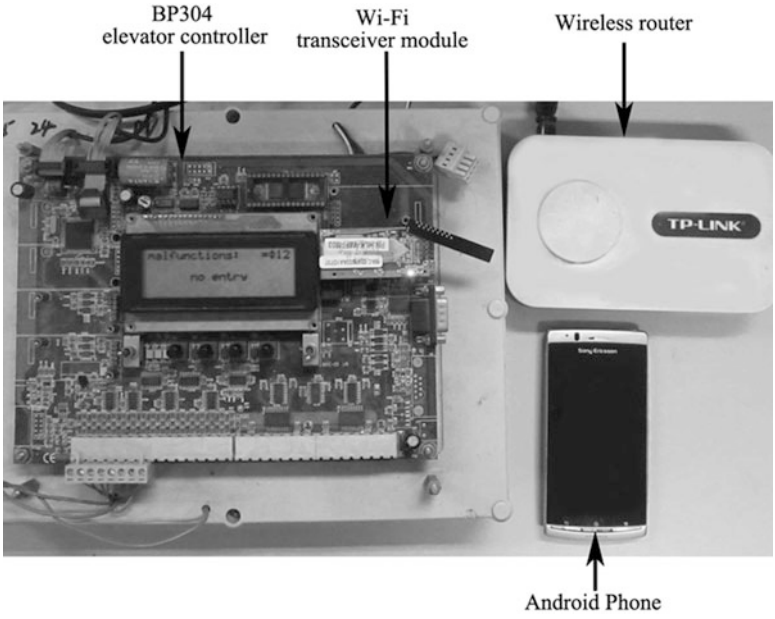

Fig. 4 Test platform

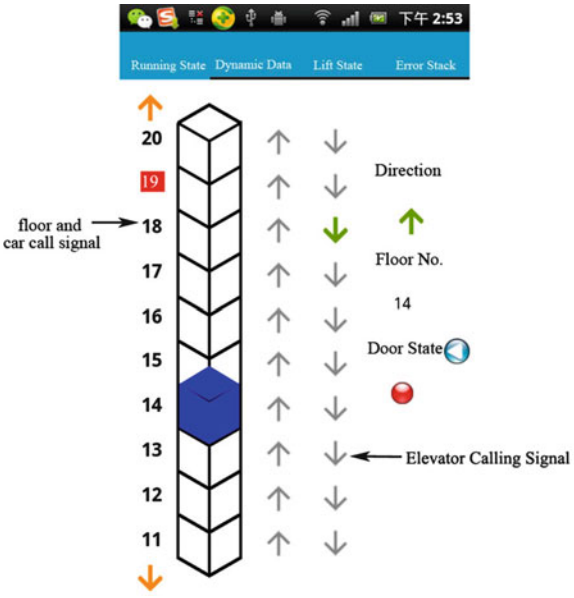

Fig. 5 Running state module

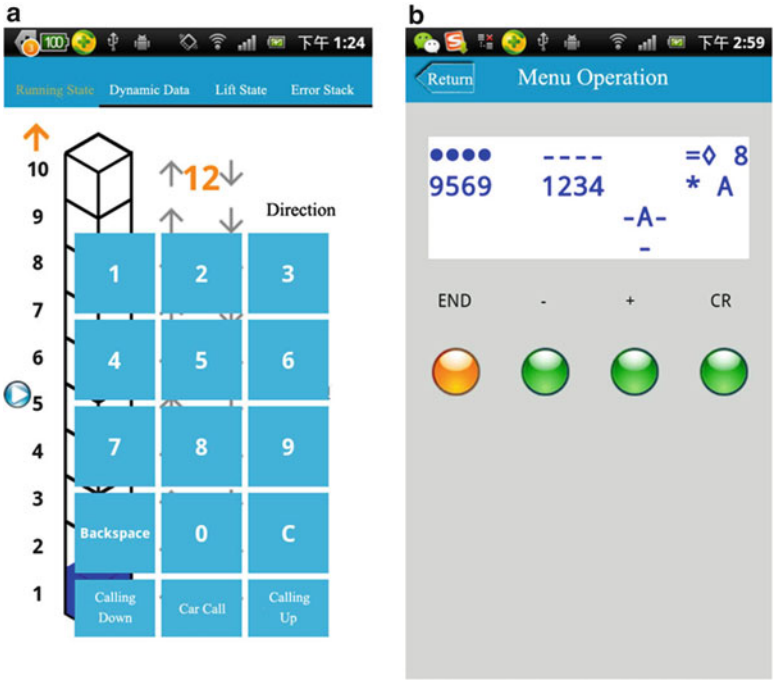

Fig. 6 Elevator calls module and menu operation module

2. Elevator Calls Module. Allow to simulate car call or elevator calling operation. It was designed with a SlidingDrawer widget. User could open the drawer from the right side of the screen. To provide good user experience, this module is displayed as a 15 grids interface, as shown in Fig. 6a.

   For this situation, the system use RelativeLayout place all Button widgets. Android provides a variety of layouts for developers to place widgets. But with the RelativeLayout, developers can place widgets with relative positions, which could finish a layout quickly and simply to similar interfaces. After typing the floor number, user can press "Calling Up", "Calling Down" or "Car Call" button to implement simulated call function which are listed at the bottom of the interface. This module also provides "C" and "Backspace" button to realize reset and backspace function. Once the user clicks the button, system will use the onClickListener() method, and complete all work in this method.
3. Menu Operation Module. Allow to scan the LCD display and operate the entity keys on the elevator controller, as shown in Fig. 6b. User can change the configuration remotely by using the system instead of standing before the elevator controller. In this module, we design four TextView widgets to simulate the $4^{*}20$ LCD of the controller. Once the system receives the relative message, all characters will be decoded and showed on these widgets. Meanwhile, we use the ImageButton widget to simulate the buttons on the controller. Users also can use the physical BACK button to turn back to the previous menu. The system uses the KeyEvent -KEYCODE_BACK method to realizes this function.

4 Conclusion

The wireless elevator monitoring system presented in this paper considers three methods to the connection that can be freely selected by the users. For doing this, we use the module that today's smartphones allow us to get through its connectivity. Meanwhile, friendly interfaces are provided to allow users access elevator information conveniently. The use of Android OS also makes the solution cost low and maintenance simple as compared to other existing solutions with PC platform and wiring method.

In the further research, we will improve the system concentrating on the multiple elevators monitoring, because in a subdistrict one maintenance staff should manage more than one elevator, so we will collect multiple elevators information and send short messages to the users to warn users if an error occurs. Otherwise, we will improve the stability of the system to avoid crash and other unexpected error.

References

1. Ju Rong (2006) Design of elevator monitoring system in intelligent building. Electrotech Mag 25(9):143–146
2. (2010) BÖHNKE+PARTNER: BP-Controllers
3. Aihua Xu, Shuhai Quan (2006) Research on the socket network communication and its application in the elevator control system. J WUT 28(11):56–59
4. (2010) Socket Communication between android and PC platform. URL: http://www.cnblogs.com/tt_mc/archive/2010/06/04/1751260.html
5. Naian Liu (2004) Wireless local area networks (WLAN). Xi'an Electronic and Science University Press, Xi'an, pp 152–160
6. ZhiWen Yang (2008) Google android programming guide. Beijing Electronic Industry Press, Beijing, pp 56–89
7. Yiming Liu (2011) Wifi Operation on Android. URL: http://www.eoeandroid.com/forum.php?mod=viewthread&tid=76196
8. Peterson LL, Davie BS (2000) Computer networks: a systems approach. Morgan Kaufmann, American

Air Cooling Equipment Health Status Prediction Techniques Based on Data-Driven Method

Bing Chen, Shimeng Cui, Haodong Ma, and Hongzheng Fang

Abstract In order to predict the future status of the fan of telecommunication and electronic equipments in practical application, and for the purpose of improvement of condition-based maintenance, a data-driven method is used in this paper. And the paper is mainly about the application research of health status prediction of brushless fan. According to the results of the fan structure and failure mode analyzing, the parameters of the acquisition are determined. Before the analysis of prediction, the raw data characteristics are extracted. Then the fan's health status is classified by K-Means clustering method. In the end, the fan status is estimated on the basis of comprehensive tests and fault symptoms monitoring. The validation results show that the proposed prediction method has higher precision, with a less-than 10%'s average relative error, and the efficiency of maintenance work is improved to reduce the waste of replacement parts, reduce costs, and has strong practical engineering value.

Keywords Air cooling equipment • Fan • FMMEA • Health status prediction

1 Introduction

Air cooling equipment (such as fan) is a key component of thermal management solutions for electronic equipment, and its performance directly affects the performance of expensive telecommunications equipments, powers and server equipments.

B. Chen
College of Electric Engineering, Navy Engineering University, Wuhan, China

S. Cui (✉) • H. Ma • H. Fang
Beijing Key Laboratory of High-Speed Transport Intelligent Diagnostics and Health Management, Beijing, China

Beijing Aerospace Measurement & Control Corp, Beijing, China
e-mail: smcui_2009@126.com

W. Wang (ed.), *Mechatronics and Automatic Control Systems*, Lecture Notes in Electrical Engineering 237, DOI 10.1007/978-3-319-01273-5_42,

The poor performance of the fan may cause intermittent or catastrophic failure of the target system, and a major loss to the system [1]. For this situation, the demand for air cooling equipment failure Prognostics and Health Management (PHM) growing in the industrial field.

There are some researches of fan life evaluation already, but most are from the point of reliability to assessment, which only for bulk rather than individual for device [2, 3]; also some fan failure mechanism analysis and estimates based on the physical failure model (PoF) have been carried out [4], but most are not combined with the actual working conditions and failure modes, so with limited engineering significance. This study is from the view of solution for practical engineering problem, and it makes an attempt of transforming the theoretical research into practical applications. On the basis of carrying out a large number of failure mode analysis and experiments, a more practical fan failure prediction method is studied, and the prediction accuracy of the method is verified.

2 Analysis of Fault Mode and Failure Mechanism for Fan Operation

Failure Mode, Mechanism and Effects Analysis (FMMEA) is a systematic method, it can identify all potential failure modes including failure mechanism and model, and make failure mechanism prioritization. FMMEA developed by CALCE Center of Maryland University, aimed at eradicating process defects of the traditional Failure Mode and Effects Analysis (FMEA), and Failure Modes, Effects and Criticality Analysis (FMECA).

The potential failure modes, causes and mechanism of brushless DC fan are analyzed according to FMMEA principle, as shown in Table 1.

The priority of potential failure mechanism of the fan is shown as in Table 2.

Based on the above results, it is possible to provide the basis for determining the parameters and developing fan life prediction methods. In this study, considering the combination of analysis of the results and the actual feasibility, current, voltage, speed and vibration signal are selected as the monitoring parameters.

3 Fan Fault Testing

In this study, fan data of sub-health to failure is obtained through the design of fault simulation test. Fan is accelerated to failure by making imbalance, wear, corrosion, and other initial defects in the trial. Fault simulation and the fan test running are shown as follows.

Table 1 Analysis of failure modes, causes and mechanism

Point of failure		Failure mode	The cause of the failure	Failure mechanism
Ball bearings		Stuck	Overheat	Lubricant degradation
		Hash	Rotary load	Fatigue
		Small cracks	Damp	Erosion
		Hardness mark	Mechanical overload	Vulnerable segments
Blades		Surface dirt	Dust	Adhesive
		Rupture	Rotary load	Fatigue
BLDC motors	BLDC drive	Short circuit, open circuit, transistor off	High temperature, high bias, power cycle	Scattering
	Fixed piece	Rupture, line film stripping	Overheat, mechanical overload	Isolated material thermal aging

Table 2 Potential failure mechanism priority analysis of brushless DC fan

Point of failure		Failure mechanism	Occurrence	Severity	Risk priority	Risk
Ball bearings		Lubricant degradation	5	3	15	High
		Fatigue	1		3	Low
		Erosion	2	3	6	Low
		Vulnerable segments	4	3	12	High
Blades		Adhesive	5	3	15	High
		Fatigue	3	3	9	Medium
BLDC motors	Scattering	Scattering	2	4	8	Medium
	Isolated material thermal aging	Isolated material thermal aging	2	4	8	Medium

Explanation
1. Occurrence standards: 5(Frequent occurrence), 4(Proper occurrence), 3(Accidental occurrence), 2(Small occurrence), 1(Very few occurrence)
2. Severity criteria: 5(Entire product failure), 4(Loss of function), 3(Run degradation), 2(Operating capacity reduction), 1(Small effectiveness)

The first picture of Fig. 1 from the left is imbalance imitation of fan, and a mass block is stick to one of the vanes, as shown with the red mark in picture. The second and third pictures are erosion and fatigue faults. The last picture shows the operation of acceleration tests. The entire test which collected fan life cycle related parameters lasted about 3 months.

Fig. 1 Fault simulation and fan test running

4 Health Status Prediction Based on Data-Driven Method

The fan data is preprocessed and feature processed after the whole life cycle data of fan is obtained, and followed by health status classification and state prediction. The whole health status prediction's processing chart is as follows (Fig. 2):

4.1 Feature Extraction

According to the acquired data, the relevant characteristic information is extracted to assess the health status of the equipment. There are two method of characteristic calculation in this study, the time domain statistical characteristics and frequency domain statistical characteristics.

The time domain statistical parameters can be divided into dimension parameters and dimensionless parameters. The so-called dimensionless parameters are the parameters which with all of the dimensionless index in zero, and do not vary with the amplitude of the signal, it means the parameters do not change in time with t the working conditions, and is only sensitive to the change of the shape of the probability density function. The parameters are shown in the following table (Table 3).

For the situation, this algorithm converts filtered current I, voltage U, and speed P into fan characteristic description parameter T ($T = \varepsilon UI/P$), where ε is a constant. Results are shown as follows (Fig. 3).

Then the process of normalizing is done for converted fan characteristic value, so time domain features are obtained, such as peak, average amplitude, variance, standard deviation, and the results are shown as below (Fig. 4).

- *Health status classification*
  Based on the extracted features, the method of K-Means clustering is used for classifying device health status. In the process of the practical application, fan health status classification is two parts:

  First part is the stage of model training. In this stage, existing data is used for getting the center point of the various types according to the method of K-means clustering.

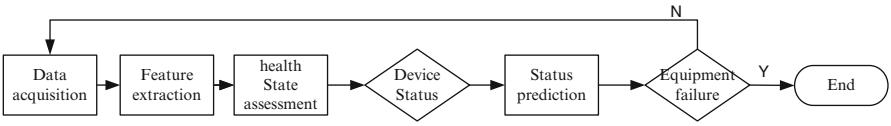

Fig. 2 Health status prediction processing chart

Table 3 Time domain characteristics

No.	Parameter	Type
1	Average amplitude	Dimension parameters
2	Variance	Dimension parameters
3	Mean square deviation	Dimension parameters
4	Peak	Dimension parameters
5	Kurtosis	Dimensionless parameters
6	Skewness	Dimensionless parameters
7	Pulse factor	Dimensionless parameters
8	Waveform indicators	Dimensionless parameters
9	Margin factor	Dimensionless parameters

Fig. 3 Fan characterization parameters transition diagram

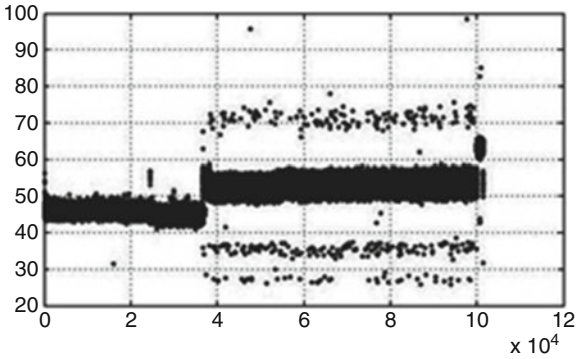

Second part is the stage of model application. In this stage, various types of center point and distance calculation (Euclidean distance) is used for classifying the existing samples.

The classification results are shown in Fig. 5, each sub-figure respectively corresponding to the classification result of the current, speed and torque. The black represents the status of normal situation, and the yellow represents the status of the abnormal situation, and red represents fan failure status.

- *Prediction of fan status*

For the mechanical equipment, generally the state which could be predicted must be a slowly varying state. So in a neighborhood interval, the health status of equipment can be expressed by the curve approximation. For different equipments and different periods, the parameters may be different; it needs an adaptive parameter estimation method. Therefore, for the algorithm of the study,

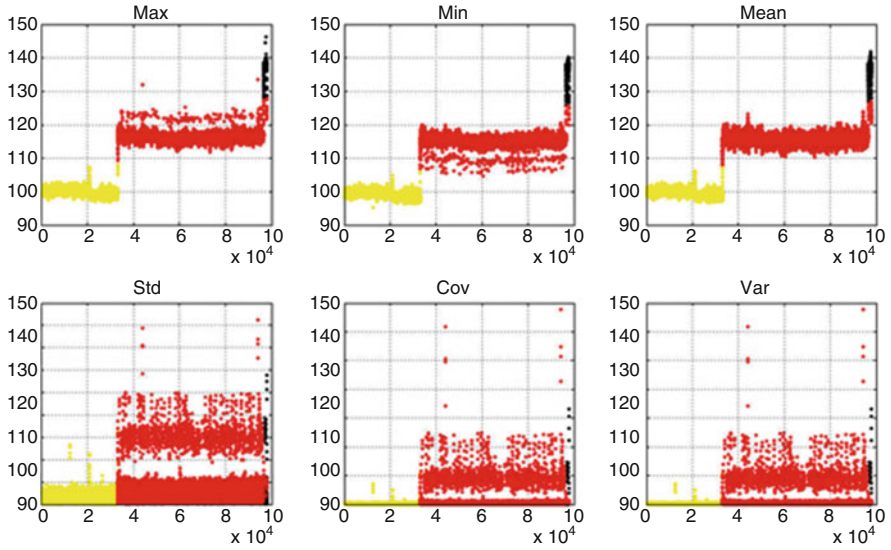

Fig. 4 Feature extraction and normalization

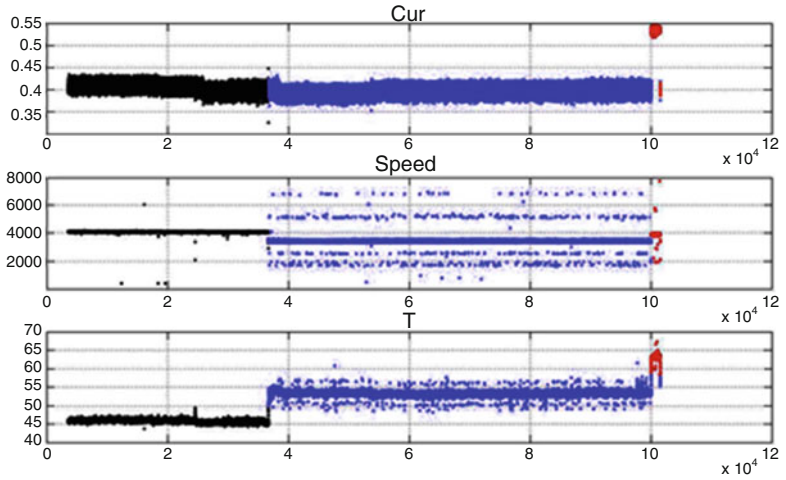

Fig. 5 The classification of equipment health status

the short-term prediction uses curve fitting with the method of combining AR model; medium predictions use recursive AR methods, model parameters are on-line updated; the long-term prediction method is based on the combination of the forecasting models. The above is described as follows:

The method of curve regression and dynamic adaptive fitting. In the study of the statistical methods of scientific experimentation, often from a set of test data

(x_i, y_i) (i = 0, 1, 2,... m), finding the functional relationship $y = F(x)$ between the independent variable x and variable y. The observational data are often inaccurate, it does not require, for all points (x_i, y_i), $y = F(x)$ is only required minimal according to some standard error on a given point x_i. If it is denoted $s = (s_o, s_1, \ldots, s_m)\,T$, to require the norm $\| s \|$ of the vector s is minimum. If S (x) is polynomials of degree n, in order to make the formulation of the problem more general, usually the $\| s \|^2$ in least squares method is considered the form of weighted average sum of squares, resulting the least squares solution of the function f (x) as Eq. 1:

$$S^*(x) = a_0{}^*\varphi_0(x) + a_1{}^*\varphi_1(x) + \ldots + a_n{}^*\varphi_n(x) \tag{1}$$

The method of time series parametric modeling. The most commonly used and effective prediction method in condition monitoring is the use of sequence model for state prediction. If the sequence for a change of state of the equipment is regarded as a random sequence, the existing data is seen as samples, then what needs to be done is to use sample data to establish the sequence model. Time series ARMA (Auto Regressive Moving Average) model, especially AR model, is the basic sequence analysis and the most widely used parameter model in the practical application:

$$x_i = \sum\nolimits_{i=1}^{n} \varphi_i x_{t-i} + a_t \tag{2}$$

Where $\{x_t\}$ is a series of signal observation (sampling) values by a certain "time" order, $\{a_t\}$ is corresponding noise sequence, $\{\varphi_i\}$ is the regression coefficients, n is model order, $i = 1, 2, \ldots, n$. Due to the complexity of the AR model order determination, the computing time of prediction is long, so here it is simplified to pseudo-model for AR, with the advantages of simple model and rapid calculation [5].

5 Validation of Health Status Estimation Results

When the fan is abnormal, model parameters needs to be corrected in real-time according to historical data in the prediction process, so the real value of the test data and the predictive value are used for validating the accuracy of the prediction model. The results are as follows: (Fig. 6)

From the health status estimated results, the average relative error is less than 10%, it meets the technical requirements. The results show that this method can predict the health status of the fan, and the accuracy meets the related requirements, so the prediction results can be used to guide the engineering maintenance work.

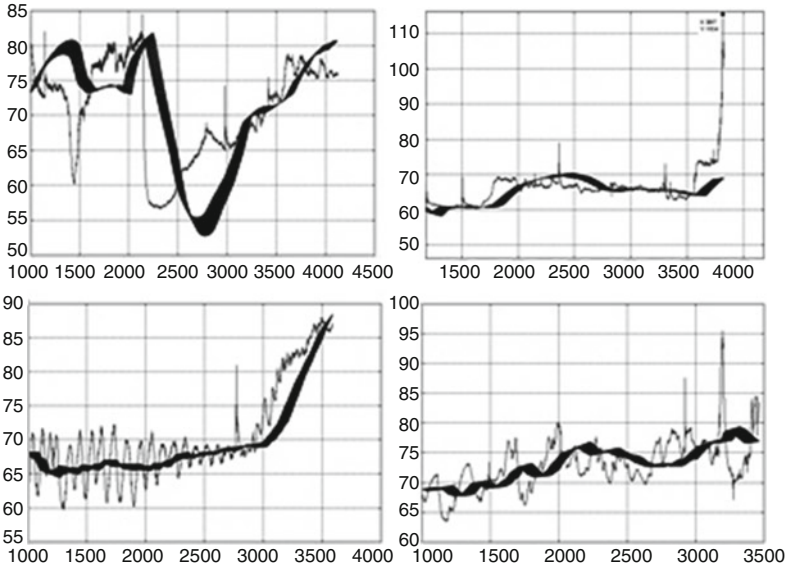

Fig. 6 Error analysis of health status estimation based on the data-driven (Fan 1 (average relative error: 8.74%, the maximum relative error: 42.5%), Fan 2 (average relative error: 3.18%, maximum relative error: 40.23%), Fan 3 (average relative error: 3.76%, maximum error:14.825%), Fan 4 (average relative error: 4.17% average relative error: 18.94%))

6 Health Status Prediction Software for Air Cooling Equipment

In order to achieve the goal of the fan PHM, a software is developed on the basis of the FMMEA and life tests. It can make an analysis and verification for the health management process of the fan. The present data such as voltage, current and speed signals can meet the basic needs of the project, and they can achieve the goal of classification and the remaining life prediction. As shown in Fig. 7.

The left figure is the window of data playback, which shows voltage, current, temperature and speed parameters. The middle figure is the result of characteristics extraction, and the right figure shows the calculation of life estimation. This system realizes the application for the fan health status prediction in physical engineering.

7 Conclusion

The health status prediction of air cooling equipment is an important part of the electronic equipment heat management solutions. The main process of the proposed method is to analyze the structural and failure modes of the fan, determining the

Fig. 7 Software of health status prediction

parameters to be collected. After that, according to the characteristics of the fan, the prognostic tests are carried out. On this basis, a prognostics method which based-on data-driven models is used for predicting the status of the fan. The validation results show that the proposed method has a strong practical value.

References

1. Kim S, Claassen A (1996) How to evaluate fan life, electronics Cooling. http://www.electronicscooling.com/1996/05/how-to-evaluate-fan-life
2. Xie L, Michael P (2012) Fan bearing fault diagnosis based on continuous wavelet transform and autocorrelation. In: 2012 prognostics and system health management conference, IEEE conference publications, Beijing, China, pp 105–109
3. Tian X (2006) Cooling fan reliability: failure criteria, accelerated life testing, modelling and qualification. In: Proceeding of the reliability and maintainability symposium, Newport Beach, pp 380–384
4. Jin XH, Azarian MH, Lau CP, Cheng LL, Pecht MG (2011) Physics-of-failure analysis of cooling fans. In: 2011 prognostics & system health management conference, IEEE conference publications, Shenzhen, China, pp 34–38
5. Gareth J, Louise S (1993) Time series, forecasting, simulation, application. Ellis Horwood Limited, New York, pp 96–102

The Application of i-bus Intelligent Lighting Control System in the Terminal of Wuhan Tianhe International Airport

Yongli Wang

Abstract This paper aims to present an implementation of advanced lighting control system in airport terminal. The lighting requirements of the terminal are fulfilled and regulated by an intelligent control system deployed with i-bus. The intelligent control system adjusts the lighting in terminal at different time according to the real-time requirements. Compared with conventional control system, this intelligent control system can control the lighting in time as long as the real-time requirements are shifted in a remote way. Besides, this new system can also save energy to a great extent.

Keywords Component • Intelligent lighting control system • i-bus • Terminal

1 Introduction

As an advanced lighting control system that meets the national standard, the Installation Bus (hereafter referred to as "the Installation Bus" or in short as "the i-bus") has been applied in more and more buildings, such as schools, residence, hotels, factories as well as hospitals. It aims to provide monitoring and control on many functions, such as lighting, heating, signalling etc. [1]. Designed as a management system, i-bus provides electrical installation for environmental control and security, and thus brings us convenience for the daily life and work. To our knowledge, there are fewer reports on the application of such systems in the airport terminal, where the systems can save large effort on the construction and utilization of the building, and also provide a significant approach on energy saving.

Y. Wang (✉)
Central Planning and Design Institute, China Airport Construction Group Corporation of Civil Aviation Administration of China, Beijing, China
e-mail: 706509122@qq.com

W. Wang (ed.), *Mechatronics and Automatic Control Systems*, Lecture Notes in Electrical Engineering 237, DOI 10.1007/978-3-319-01273-5_43,

2 Backgrounds

2.1 Overview of i-bus System

Bus system aims to apply the latest computer-controlled technology field bus technology to the conventional field of electrical installation [2–5]. Each component in this system has its own agent, and thus no central control unit, such as a PC, is needed [6, 7]. Therefore, the composition of i-bus system is extremely convenient, and thus can be applied to both small installation, such as floor, and large-scale projects i.e., airports, hotels, administrative offices, industrial buildings, etc. The components in i-bus can be divided into three categories according to its functionality: sensors, actuators and system components. As architected as a distributed system, the intelligent modules composing the system can work independently which improves the efficiency and safety as well.

2.2 Differences Between i-bus and Conventional Installation

Nowadays conventional electrical installation technology (Fig. 1) has been widely adopted. More specifically, the data acquisition and control of various systems and equipment in the building, e.g., power, lighting, drainage, fire fighting, air conditioning and ventilation, elevators etc., are usually accomplished by direct digital controller. And then control and alarm signals sent to a central host computer for dynamic graphics/event handling, control processing or other recording. In such systems, the products from different vendors are adopted and they cannot communicate with each other, therefore, a separate control line is needed. The disadvantage of such a structure lies as follows:

- Complexity in distribution lines and high amount of installation space;
- Large amount of cable required;
- Fire hazards;
- Fixed system and low flexibility;
- High operating costs and waste of energy

All the control signals in i-bus system (Fig. 2) are transmitted through a two-core control cable, thus it can reduce the usage of installation cable; the control lines and distribution lines unit are completely separated, thus, fire hazards are greatly reduced. In this way, i-bus is an implementation of two-wire electrical installation system, which meets the trends of future electrical installation technology in China. In addition, in i-bus system, not only the requirements in electrical installation are satisfied, but also the signals, such as alarm, status and centralized monitoring signal, are all connected to the system through the bus, as well as correlated systems, such as the telephone network, digital network, Internet, building control systems, with the communication interface. And with test components integrated,

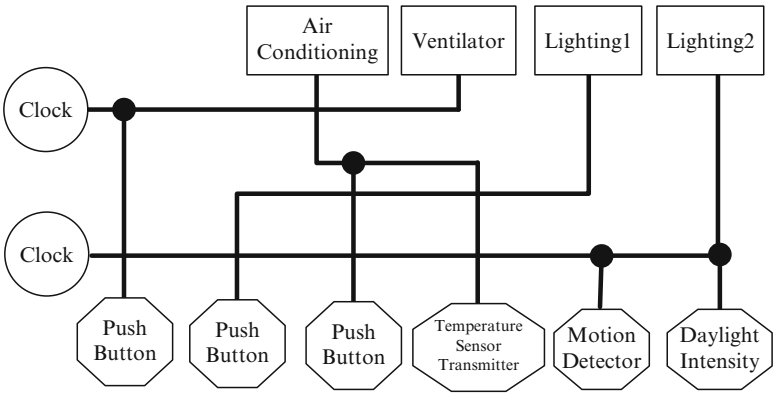

Fig. 1 Conventional electrical installation technology

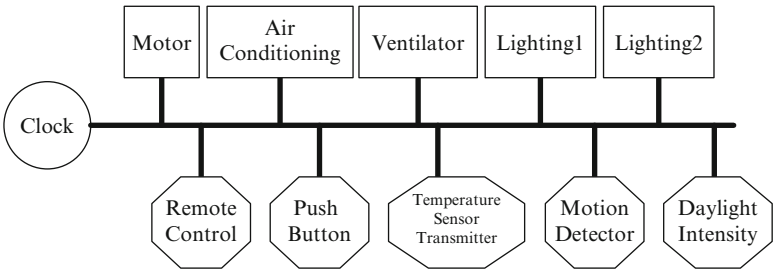

Fig. 2 i-bus system

a modern intelligent building system is constructed. The advantages of i-bus system are shown as follows:

- Reduces planning, installation and wiring costs.
- Can be expanded virtually without restriction and constantly adapted during the entire service life of the installation, and is therefore a secure investment in the future.
- Enables the integration of new functions at any time.
- Realizes intelligent automation, for example lighting and heating control during absence. This saves on energy costs and makes a significant contribution to environmental protection and our carbon footprint.
- Provides simple operation and monitoring thus forming the long-term basis for lower running costs, efficient facility management and optimum building maintenance.
- Offers a great deal of individual comfort, thereby increasing the value of the building for tenants and buyers.
- Increases safety and security for both people and the building, thus protecting the investment.

3 Applications of *i-bus* System in the Airport Terminal

ABB's i-bus Intelligent Building Control System allows for the centralized control of all electrical terminals (such as lighting and air conditioners). In China, i-bus system has been deployed in a number of landmark construction projects, such as the National Stadium (Bird's Nest), the National Swimming Center (Water Cube), Beijing Capital International Airport Terminal 3, Shanghai Pudong International Airport Terminal 2, and many other high-end residences and villas, receiving extensive recognition for its outstanding energy performance. The system of i-bus has helped Beijing Airport Terminal 3 cut the energy consumption of its lighting system by 20 %. An ABB i-bus® KNX lighting control solution for Terminal 3 at the Indira Gandhi International Airport in Delhi, India, has been named the largest and best of its kind in Asia. By providing precise demand related control of 11,000 electrical devices and 100,000 illumination points, the solution enables the airport to make considerable energy savings. The following section focuses on the application of i-bus in Wuhan Tianhe Airport.

3.1 Introduction to i-bus System in Terminal

Up to 2011, Terminal 2 at Wuhan Tianhe Airport, with a capacity of 13 million passengers a year, is reputed to be the fourteenth largest airport passenger terminal in China.

The huge 149,800 m^2 complex is arranged on four levels and has two piers, each of which is 258 m-long.

All of this requires lighting and illumination. Even though 80 % of the terminal's structure is made of glass, the airport's lighting system is huge.

It comprises more than 20,000 light fittings and illumination points, and some 10,000 or so electrical and electronic devices like actuators, dimmers and detectors.

The i-bus system control slighting in Wuhan Tianhe Airport. The lighting range includes the departure hall, arrival hall, baggage delivery area, underground garage and other large space.

There are several control methods including local panel control, timing control, centralized computer control, etc.

According to the number of locations and lighting control area, the whole system is divided into several feeders: concourse feeder, two feeders for underground garage, baggage delivery feeder, departure hall feeder and arrival hall feeder. Equipment in each feeder runs independently, and can be locally controlled. All feeders are connected to the bus to form a system, and this system can be controlled by the control center in the concourse, thus the lighting of entire terminal building is under centralized remote control, scene control and timing control.

Meanwhile, this system can also communicate with the building control system to ensure monitoring on the lights. Lighting of the entire terminal building is usually under timing control and scene control, and can also be switched to panel control in special scenarios, e.g., inspection and other special circumstances, to increase the flexibility and convenience.

Besides, in the office area and VIP reception area, i-bus system provides the corridor lighting control in this area, and also local control can be facilitate d by the intelligent control panel installed in the duty room or front desk position. Also, the computer in the control room can monitor the status of lighting in the above area.

3.2 Advantage of i-bus System in the Application of the Airport Terminal

3.2.1 Efficient Construction

The system uses the tree structure, and each bus device can be placed at any position in the system. It facilitates the construction process for deploying bus cables. No wall mounted panel control is required for each lighting loop, and this leads to significant savings in the construction of a strong electric cables and wiring tube, that is, not only saving in the material, but also avoidance of the wall-mounted panel. In this way, the failure rate of the system will be reduced, and it brings convenience to the property management.

3.2.2 Flexible Management

As the terminal building lighting control is undertaken by i-bus system, it is convenient to control different lights in different time periods through remote control, timing scene control. For example, the system automatically shuts down the lights in departure hall and departure corridors, at the end of the night flight; meanwhile the staff can check the scene lights in the control room. It is convenient for managers; and at the same time, it significantly improves the punctuality of turning off the lights which saves management costs and avoids energy waste.

3.2.3 Analysis on Energy Saving

The areas under the control of i-bus system include the departure hall with its corridor, arrival hall with its corridor, baggage delivery area and underground garage. Take the departure hall as example, the analysis of the energy-saving effect is shown as follows.

Table 1 The lamp working data for the manual control

Time	The ratio for working lamps	Hours for working
5:00–8:00 and 17:00–1:00	1	11
8:00–17:00	0.5	9
1:00–5:00	0	4

Table 2 The lamp working data of the i-bus system

Time	The ratio for working lamps	Hours for working
5:30–7:30 and 17:30–24:00	1	8.5
7:00–17:30	0.5	10
24:00–5:30	0	5.5

A total of 11 power distribution stations and 22 distribution boxes are adopted in the departure hall with its corridor, which reaches up to a total power of 498 kW. The manual control approach is indicated by the Table 1:

Note that the manual labor is involved in the control of the lighting, thus this kind of control cannot meet the need of real-time control. In such scenario, delay on the control of lighting is unavoidable. The total consumption by manual approach is:

$$11 \times 498 + 9 \times 0.5 \times 498 + 4 \times 0 = 7{,}719\ \text{kWh}.$$

While the i-bus solution is as the Table 2 shows:

In the i-bus system, the control of lighting is remote and real-time, thus some manual labor is saved. Moreover, this kind of save can reduce the consumption of unnecessary energy. Thus, in this scenario, the total consumption is:

$$8.5 \times 498 + 10 \times 0.5 \times 498 + 5.5 \times 0 = 6{,}723\,\text{kWh}.$$

The saving on energy for i-bus in each day is 996 kWh compared with manual approach. In this way, the total saving for 1 year can reach up to 363,540 kWh. Besides of saving on the energy, the utilization of i-bus can also lower the labor intensity of the staff.

The details of comparison between two approaches for the arrival hall with its corridor, baggage delivery area and underground garage are listed in the following Table 3.

The mode denotes how many lights are on during different time interval, e.g., "1" denotes all lights on, "1/2" denotes half lights on, "1/3" denotes a third of lights on and "0" denotes all lights off.

As the Table 3 indicates, a total saving of 7.479×10^5kWh every year can be achieved by the i-bus in the four major areas.

Table 3 Comparison between manual approach and i-bus

Area			Manual approach			i-bus		
	# of distribution boxes	Power	Time interval	Time length (h)	Mode	Time interval	Time length (h)	Mode
Arrival hall with its corridor	13	282.9	6:30–8:00	1.5	1	7:00–7:30	0.5	1
			8:00–17:00	9	1/3	7:30–17:30	10	1/3
			17:00–2:00	9	1	17:30–1:00	7.5	1
			2:00–6:30	4.5	0	1:00–7:00	6	0
	Consumption		3,819 kWh			3,197 kWh		
	Saving per day		622 kWh					
	Saving per year		227,169 kWh					
Underground garage	9	65.1	5:00–8:00	3	1	5:30–7:30	2	1
			8:00–17:00	9	1/2	7:30–17:30	10	1/2
			17:00–2:00	9	1	17:30–0:00	4.5	1
			2:00–5:00	3	0	0:00–5:30	5.5	0
	Consumption		1,074 kWh			749 kWh		
	Saving per day		326 kWh					
	Saving per year		118,808 kWh					
Baggage delivery area	4	42	5:00–8:00	3	1	6:00–7:30	1.5	1
			8:00–17:00	9	1/2	7:30–17:30	10	1/2
			17:00–2:00	9	1	17:30–1:00	7.5	1
			2:00–5:00	3	0	1:00–6:00	5	0
	Consumption		693 kWh			588 kWh		
	Saving per day		105 kWh					
	Saving per year		38,343 kWh					

4 Conclusion

The i-bus system for lighting control in the terminal of Wuhan Tianhe Airport brings great benefits. This kind of benefit lies in several folds: first, both the construction and the management for i-bus are much more convenient. As compared with i-bus systems the traditional approach involves much more components, such as switches for local control, fewer components lead to much save on the construction and management; secondly, according to the data of the traditional manual approach and the i-bus system, a large amount of energy per year in many places, such as the departure hall with its corridor, arrival hall with its corridor, baggage delivery area and underground garage can be saved by the i-bus; besides, this i-bus solution for lighting in airport terminal brings great convenience for the airport.

References

1. Neugschwandtner G, Kastner W (2009) Congestion control in building automation networks: considerations for KNX. In: Proceedings of the 35th annual conference of IEEE industrial electronics, IEEE Computer Society, Alfandega Congress Center, Porto, Portugal, pp 4149–4154
2. Kolokotsa D, Pouliezos A, Stavrakakis G, Lazos C (2009) Predictive control techniques for energy and indoor environmental quality management in buildings. Build Environ 44:1850–1863
3. Bujdei C, Moraru SA (2011) Ensuring comfort in office buildings: designing a KNX monitoring and control system. In: Proceedings of the 7th international conference on intelligent environments, IEEE Computer Society, Nottingham Trent University, United Kingdom, pp 222–229
4. Ruta M, Scioscia F, Sciascio ED, Loseto G (2011) Semantic-based enhancement of ISO/IEC 14543-3EIB/KNX standard for building automations. IEEE Trans Ind Inform 7(4):31–739
5. Matijevics E (2009) KNX based lighting control solutions with GIRA Home Server 3. In: Proceedings of the 7th international symposium on intelligent systems and informatics. IEEE Computer Society, Subotica, Serbia, pp 263–266
6. Shehata M, Eberlein A, Fapojuwo AO (2007) Managing policy interactions in KNX-based smart homes. In: Proceedings of 31st annual international IEEE computer software and applications conference, IEEE Computer Society, Beijing, China, pp 367–378
7. Kastner W, Neugschwandtner G, Soucek S, Newman HM (2005) Communication systems for building automation and control. Proc IEEE 93(6):1178–1203

Voltage Equalization in Super Capacitors Series

Weidong Ma

Abstract The problem that each cell's voltage is not equal in super capacitors series will affect the whole performance of series connected super capacitor strings. In order to solve this problem, an equalizing circuit is designed in this paper. This equalizing circuit uses inductances as energy storage elements, transfers energy from super capacitor with high voltage to the lower ones to achieve voltage balance. To prove the feasibility of this method, simulations and experiments have been done. The results show that this method can make each super capacitor's voltage tend to be equaled even when the discrepancy of the super capacitors' capacity is big. This method solves the voltage inequality in super capacitors series effectively and eliminates a difficult problem in engineering application.

Keywords Super capacitor • Series connection • Equalizing

1 Introduction

Super capacitor was developed in 1960s as a new-type of energy storage element. The super capacitor is classified into three types: Double layer capacitor, Pseudo-capacitor and Hybrid capacitor [1]. Its capacity can reach several farad or even several thousand farad comparing with a traditional one. Super capacitor working as an energy storage element was first put forward by an American named Becker in the year of 1957. As an ideal energy storage element, its energy density is close to a battery and it can be used in DC power supply system instead of battery [1]. In recent years super capacitors have been used in more and more engineering programs as a mature technology. But the capability and life of super capacitors, which are used in series, are badly restricted by cell to cell voltage imbalance.

W. Ma (✉)
Henan Electric Power Research Institute, Zhengzhou, China
e-mail: mwdong2000@163.com

W. Wang (ed.), *Mechatronics and Automatic Control Systems*, Lecture Notes in Electrical Engineering 237, DOI 10.1007/978-3-319-01273-5_44,

Generally dozens or hundreds of super capacitors are required to form series. Some capacitor cells charge or discharge not fully, or charge excessively. The reasons are as bellow [2].

1. *Effect of capacity deviation:* There is capacity deviation between nominal capacity and actual capacity of super capacitor. Some can be off by 20 %, as a result the charging time of each capacitor may be different though the charging current is the same. Those with smaller capacity may be charged full in a short time and those of larger capacity in a longer time.
2. *Effect of leakage current:* Leakage current exists in every super capacitors, it will affect the sustaining voltage (or charge) of per super capacitor unit. When a capacitor is placed for a long time, the one with lower leakage current can hold a higher voltage than the one with higher leakage current. For this reason, capacitor with lower leakage current first reach the rated voltage in charging and last reach the stop voltage in discharging.
3. *Effect of internal resistance:* The internal resistance of a capacitor rises with the increasing charging and discharging times. The one with higher internal resistance reaches the stop voltage in discharging earlier and the one with lower internal resistance can't be discharged fully.

Based on the above-mentioned reasons, equalizing problem must be solved when super capacitors are used in series. This paper conducts a study on this topic.

There is an equalizing method that it consumes the energy of super capacitors which have higher voltage than the average voltage of the whole super capacitor group to keep voltage balance [3, 4].

There is another method that it uses a common convert circuit through energy storage elements, transfer energy from super capacitor unit with higher voltage to lower, in either centralized or decentralized structure, to balance the voltage of each unit [5–7].

So the equalizing voltage schemes can be divided into two kinds roughly: Dissipative and Non-dissipative.

Problems still exist in both dissipative and non-dissipative methods which are given in the references. For example: the dissipative methods waste energy in working and cannot be used in discharging process. The non-dissipative methods have a too complicated circuit or low efficiency. This paper put forward a new method to solve all these problems.

2 Equalizing Voltage Technical Scheme

2.1 Dissipative Equalizing Scheme

Dissipative equalizing schemes have varied forms. Figure 1 shows the PWM shunting circuit. In this picture each super capacitor connects a parallel circuit: R denotes shunting resistance and *S* denotes MOSFET [3].

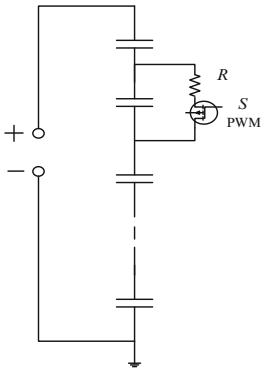

Fig. 1 The PWM shunting circuit diagram

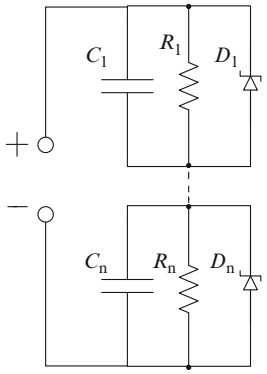

Fig. 2 No control voltage balancing circuit

The MOSFETs are controlled by PWM. Voltage value decreases by consuming energy through parallel circuit when some capacitor's voltage is above the average. The decrease value can be figured out by comparing with average voltage and be controlled by adjusting the duty cycle of MOSFET.

Another uncontrolled equalizing scheme is showed in Fig. 2. In this picture, C_i are super capacitors, R_i are equalizing resistances and D_i are Zener diodes. Every equalizing resistance's value and every Zener diode's parameters are required to be the same. The rated voltage of super capacitor is equal to Zener diode's breakdown voltage, so the diode can hold the voltage to be certain value by discharging when the capacitor's voltage exceeds the diode's breakdown voltage. Those Zener diodes are demanded to have features of short recovery time, low loss and high efficiency [4].

The Dissipative Equalizing Scheme has simple circuit and is easy to implement. Especially the circuit showed in Fig. 2 can achieve aim without control. But it has the problems of wasting energy, long equalizing time and heat emission. It is generally used in charging.

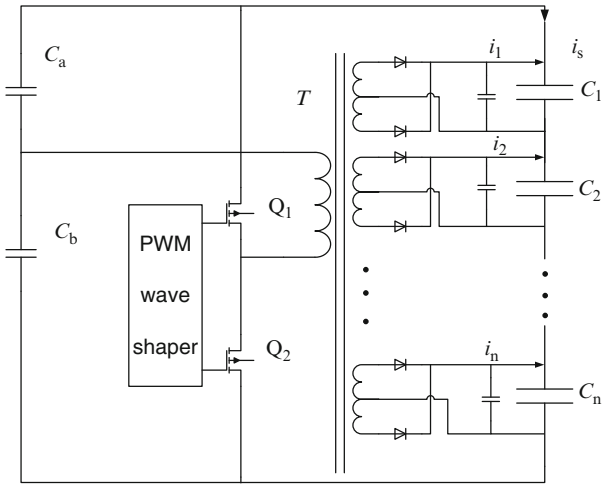

Fig. 3 Centralized equalizing charge schematic diagram

2.2 *Non-dissipative Equalizing Scheme*

For the flaws of dissipative equalizing scheme in energy utilization, non-dissipative equalizing scheme is invented. The non-dissipative equalizing scheme keeps voltage balanced by transferring energy with energy storage elements. It has big equalizing current and high efficiency on one hand, and complicated circuit and controlling system on the other hand. It can be divided into two kinds: centralized and decentralized equalizing methods.

The method called centralized equalizing in this paper means that the whole series use only one equalizer as shown in Fig. 3. In this picture, C_a, C_b are storage capacitor and C_1, $C_2 \ldots C_n$ are super capacitors. The core of the equalizer is a DC-DC converter composed with a PWM controller, FET Q_1, Q_2 and a high-frequency converter T. The converter has one input and n outputs that every output voltage is designed to be the same. The PWM controller keeps voltage by adjusting pulse width [5].

In this equalizing scheme, every capacitor has two charging currents: i_s and i_m ($m = 1, 2 \ldots n$). The i_s charges for every capacitor, and the value and existing time of i_m depend on super capacitor's specific conditions.

This method can transfer the power from higher voltage capacitors to lower ones without controller units, thus avoid energy loss. But its equalizing circuit is too complicated and the cost is too high.

The decentralized equalizing scheme usually uses inductance as an energy storage element. Figure 4 shows the currently popular bidirectional lossless equalizing charge and discharge diagram. C_1, C_2 are super capacitors; Q_1, Q_2 are two FETs; D_1, D_2 are two diodes and L is an inductance component. When the voltages of two adjacent capacitors are not equal, for example, $V_{C1} > V_{C2}$, then Q_1

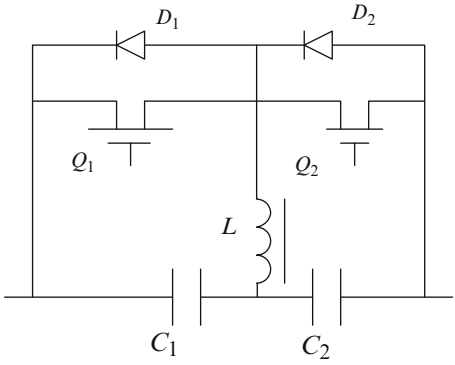

Fig. 4 Bidirectional lossless equalizing charge and discharge diagram

is triggered flow. L is charged by C_1. When Q_1 is stopped, (L, C_2, D_2) come into being a cycle circuit. Then C_2 is charged by L. In this way, the power is transferred from higher voltage capacitor to the lower one [6, 7].

This method has advantages of short equalizing time and high efficiency, commonly above 80 %. But the power transfer is restricted between two adjacent super capacitors. If two capacitors are not adjacent, the power needs to be transferred many times. Due to this reason, the transfer efficiency falls fast if the distance between capacitors is too far. So using this method must have a good Algorithm to avoid transfer power between two far-distance capacitors.

3 New Equalizing Scheme

The method main discussed in this paper belongs to non-dissipative equalizing scheme. It improves the original scheme, transfers power from one capacitor to the whole capacitor group. The schematic diagram is showed in Fig. 5.

In this picture, $C_1, C_2, C_3 \ldots C_n$ are super capacitors; $Q_1, Q_2 \ldots Q_n$ are MOSFETs; L_1, L_{i1}, L_{i2} and L_n are inductances as energy storage elements. The L fallow the equation $L_{i1} + L_{i2} = L_1 = L_n, L_{i1}/L_{i2} = (i - 1)/n - i)$. When some capacitor's voltage is above the rated voltage, for example C_2, then Q_2 is controlled to conduct, and L21, L22 and Q2 form to be splitting branch circuit. The charging current passes the way that from C1, L21, L22, D22 and C3 until Cn. At this time, C2 is discharging through the branch. When Q_2 is stopped, the energy in L_{21} flows back to C_1 through D_{21} and that in L_{22} back to all the super capacitors except C_1 and C_2. The rest capacitors' equalizing theory is the same as C_2.

This scheme solves the problem showed in Fig. 4. It could transfer the extra energy of one capacitor to all the others. In this way, it not only raises the energy-transfer speed but also enhance energy-transfer efficiency by avoiding energy flowing back and forth between two capacitors when they both reach the rated voltage [8].

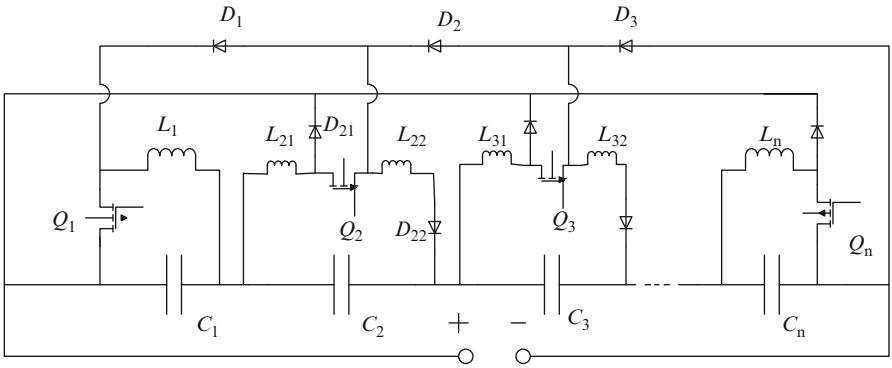

Fig. 5 Improved equalizing schematic diagram

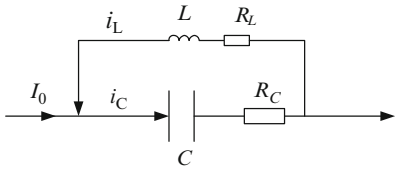

Fig. 6 Energy-transfer process schematic diagram

A control unit is needed in this scheme to monitor the voltage values of super capacitors. When some capacitor's voltage exceeds the rated voltage, the MOSFET is controlled to conduct to release energy. The released energy will be transferred to the rest super capacitors through storage elements.

In the energy transferring process, when the MOSFET is controlled off, the inductances can charge for specific capacitors as independent sources. Figure 6 is the schematic diagram.

In Fig. 6, I_0 is external charging current and constant; i_{L} is inductance current and $i_C = i_L + I_0$; R_{L} is internal resistance of L and R_{C} is internal resistance of C. When the MOSFFET is off, the voltage at the moment before L charge for C is

$$U_{\mathrm{c}} = V_{\mathrm{c}} + R_{\mathrm{c}} I_0 \tag{1}$$

In Eq. 1, V_{C} is the actual voltage of C and U_{C} is the measurement voltage. The value of I_0 is very small, as a result: $U_C \approx V_C$.

When L start charging for C, $U_{\mathrm{C}} = V_{\mathrm{C}} + R_{\mathrm{C}} i_{\mathrm{C}}$, namely

$$U_{\mathrm{c}} = V_{\mathrm{c}} + R_c (i_L + I_0) \tag{2}$$

In Eq. 2, the value of i_L is very big, so the value of $R_C i_C$ is very big too. If the actual voltage V_C is close to the rated voltage, the measurement voltage would

exceed the rated voltage that could cause misjudgment of the control unit. If the direction of i_C and i_L is opposite, it also could show the situation that the super capacitor discharges the extra energy. The measurement voltage is lower than the actual voltage at this time. Due to this reason, the judgment of control unit would be affected by the fluctuation of measurement voltage.

There are two solutions to solve the problem above. First, as i_L takes a short time to weaken to zero, so the wave crest of i_L can be avoided in voltage measurement. For example, it can be provided that only if the measurement voltage is higher than the rated voltage for a certain time can it be thought that the actual voltage of the super capacitor achieves its rated voltage. Second, lock the parallel MOSFET when the super capacitor is charged with inductance. Namely, the parallel MOSFET could conduct only if there is no inductance charging for the super capacitor. The first method is used in the following simulation and experiment in this paper.

4 Verification and Analysis

Simulations and experiments were done in this paper. The equivalent model of super capacitor in simulation is showed in Fig. 7. C is an ideal capacitor; r is the internal resistance of super capacitor and R is the equivalent parallel resistance representing the leakage [9].

In the simulation, three super capacitor units were connected in series and the equivalent model were used instead of the super capacitors. The parameters of super capacitor are fluctuating between 80 % and 120 % of the nominal value. Setting the nominal capacitance as 100 F and rated voltage 2.7 V, change the capacitance, internal resistance and equivalent parallel resistance values of super capacitors, and make the simulation separately. Each super capacitor's parameters are showed in Tables 1, 2, and 3. While the simulation waves are showed in Figs. 8 and 9.

In order to show the effect of internal resistance and leakage current on the charging balance of super capacitor series. This simulation presumed that the power supply is constant-current source with small current, and the charging time is long.

The first simulation data is showed in Table 1. The waves are showed in Fig. 8. From the simulation result, we can see that the capacitor with the smallest capacitance, namely C_1, first reaches the rated voltage. Then the extra power is transferred to the other two capacitors through equalizing circuit. Later, the C_2 reaches the rated voltage, and transfers power to the other capacitors. Finally, the C_3 reaches the rated voltage, and then the charging process ends.

The second and third simulation data are showed in Tables 2 and 3. The voltage waves of the two simulations are basically in coincidence. The voltage waves are showed in Fig. 9. So a conclusion can be concluded that the effect of internal resistance and leakage current is little in charging and can be neglected.

To prove the effectiveness of this new scheme, experiments were made. Three super capacitors with the same nominal parameters were used and experiments

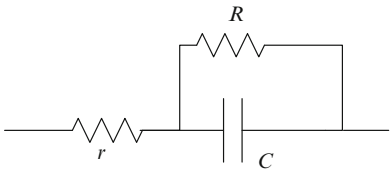

Fig. 7 The super capacitor equivalent model

Table 1 The first simulation data (different capacity value)

	C1	C2	C3
C (F)	80	100	120
R (ohm)	14,000	14,000	14,000
r (ohm)	0.015	0.015	0.015

Table 2 The second simulation data (different internal resistance)

	C1	C2	C3
C (F)	100	100	100
R (ohm)	14,000	14,000	14,000
r (ohm)	0.012	0.015	0.018

Table 3 The third simulation data (different leakage current)

	C1	C2	C3
C (F)	100	100	100
R (ohm)	11,200	14,000	16,800
r (ohm)	0.015	0.015	0.015

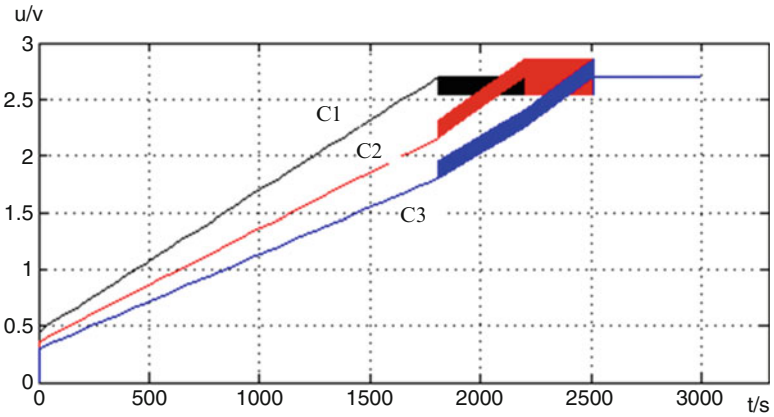

Fig. 8 Curve: each capacitor voltage with different capacitance values

were performed separately in both cases that there was an equalizing circuit or not. The results are showed in Tables 4 and 5.

The results show that this scheme has good performance and works well in equalizing voltage.

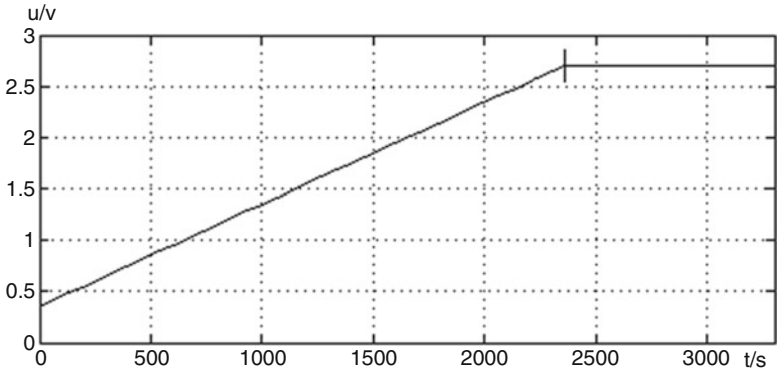

Fig. 9 Curve: each capacitor voltage with different internal resistance and different leakage current

Table 4 Experiment without equalizing circuit

	V1	V2	V3
U(V)	2.68	2.52	2.84

Table 5 Experiment with equalizing circuit

	V1	V2	V3
U(V)	2.69	2.69	2.69

This new equalizing scheme not only decrease the power loss, but also avoids the flaws of long equalizing time and short transferring distance in classic equalizing method. But this scheme needs a control unit to compare the actual and rated voltage of each capacitor in order to control the make and break of MOSFET.

This scheme can also be applied when the super capacitor group is used as power supply. Controlling the make and break of MOSFET by comparing the actual voltage and average voltage of each capacitor can also transfer power from the capacitor with high voltage to the lower one. But the output voltage would be unstable, as a result, current limiting and voltage stabilizing steps are needed at the output terminal.

Conclusions can be made that the new equalizing scheme can equalize voltage among capacitors by transferring power from capacitors with higher voltage to lower in the condition that the capacitance disparity of super capacitor are big.

5 Conclusion

This paper analyzes the problems exists when super capacitors are used in series and the influencing factors. After comparing the advantages and disadvantages between dissipative and non-dissipative equalizing schemes, a new equalizing scheme is put forward.

The new scheme uses inductances as energy storage elements, transfers energy from capacitor with high voltage to the lower ones. It avoids energy wasting in the dissipative equalizing schemes which are showed in Figs. 1 and 2. It can transfer one capacitor' extra energy to the whole strings except itself. In this way, the efficiency is raised and the cost is lower than the scheme showed in Fig. 3.

This scheme not only can be used in charging, but also can be used in the process that the super capacitor series is used as power supply. But current limiting and voltage stabilizing steps are needed at the output terminal to make the output voltage to be stable.

It solves the unequal voltage of single unit of a super capacitor group in charging and discharging, and the correctness and effectiveness are verified by simulations and experiments. It solves a difficult problem in engineering application of super capacitors and has practical significance.

References

1. Buhan Zhang, Yunling Wang, Jie Zeng (2006) Super capacitor energy storage technology and its application. Water Resour Power 24(5):50–52 (In Chinese)
2. Xiaonan Han (2010) Super capacitor series connection equalizing voltage research. J Northeast Dianli Univ 30(4):68–72 (In Chinese)
3. Haihong Huang, Zheyuan Zhao, He jin (2010) Research on having the function of active maintenance of distributed battery management system. J Electron Meas Instrum 24(3):283–288 (In Chinese)
4. Jingjing Lei, Qiuhong Li (2010) Research on power lithium ion battery management system. Chin J Power Source 34(11):1192–1195 (In Chinese)
5. Liang Tian (2007) Research on hybrid vehicle battery management system. Chin Battery Ind 11(5):330–332 (In Chinese)
6. Lingzhi Liu (2008) Study on Li-ion battery management system[J]. J Anqing Teach Coll 14(2):50–78 (In Chinese)
7. Haidong Li, Zhiyue Feng, Zhiping Qi (2006) A novel voltage balancing method for series connected supercapacitor strings. Chin J Power Source 30(6):499–503 (In Chinese)
8. Binqiang Ma, Hongwei Liu (2010) Electric vehicle battery management system research. J Henan Agric Univ 44(4):428–431 (In Chinese)
9. Liangjie Yu, Xin Qiao (2010) Battery management system in electric vehicle application. Shan Dong Sci 23(3):87–91 (In Chinese)

Mobile Robot Localization in Coal Mine Based on ZigBee

Quanxi Li and Lili Wu

Abstract Aiming at the issue of precise location for the mobile robot underground coal mine, propose three-point calculation of close distance and Gaussian filter, use the classical logarithmic distance attenuation model as a platform, create a node backstepping algorithm model. The main research of the algorithm is as follows: how to determine the reference node which is the closest to the mobile node and the parameters the closest to the mobile node; how the reference node to deal with the RSSI information received from the other reference nodes can obtain the best A, n value used for positioning.

Keywords Confined space • ZigBee • RSSI (Received Signal Strength Indicator) • Near distance three-point calculating method

1 Introduction

The coal mining industry is a kind of production industry with quite harsh working conditions, whose main performance are that the production environment has unsafe factors, such as coal dust, gas, roof caving and so on, these unsafe factors threaten the safety of mine workers greatly. Mining process is generally more complex, this complex work is hard to be completed by using the automated machinery in general, it is the best solution that using the robot with some intelligence and considerable flexibility to complete coal mining. In practice, the mobile communication and accurate positioning of the mobile robot is a key problem. There are much technologies can solve the positioning of the mobile robot under the

Q. Li (✉)
College of Computer Science and Technology, Henan Polytechnic University, Jiaozuo, China
e-mail: lqx427@163.com

L. Wu
China Water Power Press, Beijing, China

W. Wang (ed.), *Mechatronics and Automatic Control Systems*, Lecture Notes in Electrical Engineering 237, DOI 10.1007/978-3-319-01273-5_45,

limited space in coal mine, for example, the positioning technology based on infrared, such as the Active Badge Location System studied by Olivetti [1], but due to the infrared requires straight line sight, its application is very limited in the complex environment of the coal mine; DC magnetic field positioning, the positioning results of such equipment are more accurate, but the equipment is quite expensive, and difficult to promote; the radio frequency identification technology is widely used now, which use the method of radio frequency to realize exchange data by non-contact type bidirectional communication in order to achieve the purpose of identification and location, but distance range of the technique is short; with the development of wireless mobile devices and wireless LAN, the positioning technology using a wireless network is developing constantly, such as Wi-Fi positioning [2], ZigBee positioning [3–5], they mainly adopt TOA (time of arrival) [6] method, AOA (angle of arrival) [7] method and the method based on signal strength (received signal strength indicator, RSSI) for positioning.

The methods above, under conditions of the limited space in coal mine, due to the ZigBee technology has the following characteristics: low-power, low-cost, low-rate, short delay, high-capacity network, high reliability and high security, so we use ZigBee technology to locate, the positioning method based on the received signal strength ranging (RSSI) is worth studying. The focus of the study is how to improve the positioning accuracy [8, 9]. Localization method based on signal strength can be divided into two categories: the method of deterministic model and empirical model. Deterministic model uses electromagnetic principles to build a detailed model of specific environment, the modeling method based on geometrical optics and ray tracing technology is commonly used. The basic idea of the ray-tracing method is that taking emitting point as the point source of the emission lines, the wireless signal is regarded as the rays of the different directions, tracing for each ray, we assume ray generate a reflection, transmission, diffraction and then calculate the field strength according to this when meeting the obstacles, finally merge all the rays at the location of the target point, calculating the distribution of the wireless signal strength deterministically. Deterministic model has a large amount of computation, low efficiency and great error in a complex environment. Empirical model, also known as statistical model, which do not need to known the specific environment and the detailed structure of the building, it can derive the attenuation law of signal strength according to a lot of statistical data. We will focus on the study of improvement based on empirical model in order to improve positioning accuracy.

2 Empirical Model Ranging Method

This model is the mathematical model which uses the signal propagation model to convert the propagation loss into the distance by measuring the received signal strength in the case of the known transmitting power, also it is called the propagation attenuation model.

2.1 The Mathematical Model of Free Space

In free space, the signal strength received by the antenna whose distance is d from the launch point can be given by the following equation:

$$\frac{P_d}{P_T} = \frac{G_T G_d \lambda^2}{(4\pi)^2 d^2 L} \tag{1}$$

In this, P_T is the transmitting power, P_d is the receiving power whose distance is d from the transmitting point, G_T is the gain of transmitting antenna, G_d is the gain of receiving antenna, d is the distance from the transmitting node to the receiving node, the unit is meter, λ is the signal wavelength, the unit is also meter, L is the system loss.

By Eq. 1, the receiving power in free space attenuate with the square of the receiving distance, therefore, by measuring the strength of the received signal, using the formula (1) will be able to calculate the distance between the receiving node and the transmitting node. After getting the distance between the receiving node and the transmitting node, using the trilateration method can realize node localization. However, the formula above is only the mathematical model when the electromagnetic waves spread in the ideal free space, it will have a great error in the limited space of the actual coal mine, it's mainly because there are serious reflection, refraction, multipath propagation, non-line-of-sight (NLOS) phenomenon in the limit space of the coal mine, at this time, we need to study the mathematical model of the confined space. The main words in all headings (even run-in headings) begin with a capital letter. Articles, conjunctions and prepositions are the only words which should begin with a lower case letter.

2.2 The Mathematical Model of Limited Space

In case of limited space in the coal mine, signal propagation will be affected by reflection, refraction, diffraction and so on, the received signal is the superposition of all signals, sometimes the performance of the signal intensity is increased, sometimes weakened. Through a large number of engineering practices, we found that the received signal strength obeys the log-normal distribution, and summarized a signal propagation mode:

$$P_d = P_{d_0} - 10\mu \lg\left(\frac{d}{d_0}\right) + \chi_\sigma \tag{2}$$

In this, P_d is the received signal strength whose distance is d from the launch point, P_{d_0} is the received signal strength of the mobile node whose distance is d_0 from the launch point, d is the distance between the mobile node and the reference node,

μ is the path loss exponent, loss exponent μ depends on the surrounding environment and the type of building, represents the speed of path loss increase with distance increase; χ_σ is Gaussian random variable which obey that the mean value is *0*, standard deviation is *c,* and has nothing to do with the propagation distance, That is to say, the same propagation distance, the loss may be measured different completely, even a difference of several times. χ_σ is mainly used to reduce the error of the signal intensity, that is to reduce the positioning error. Through a lot of fast measurements and then calculate their average, we can basically eliminate the error brought by the Gaussian random variable χ_σ.

In practice, we found that the probability model of the Eq. 2 reflects the laws of limited space signal propagation precisely in coal mine than other models [10], and is simple to use. We use this model as the research base of signal propagation of limited space in coal mine and the positioning base of the mobile robot.

3 RSSI Ranging Research

Figure 1 is the ranging figure for ZigBee network nodes. In this, A is a mobile node, B1, B2, B3 are the closest three reference nodes to point A, The position of the reference node and the distance between them are known, that is, d_{12} and d_{13} are known, d is the measuring value of the distance.

Making reference distance d_{12} as calculating unit d_0 (calculation unit, that is provisionally designated unit), then by the formula (2), the signal strength of the node B1 received by the reference node B2 can be obtained:

$$P_{12} = P_{d_0} + \chi_\sigma \tag{3}$$

By the formula (3) obtained:

$$P_{d_0} = P_{12} + \chi_\sigma \tag{4}$$

In actual measurements, the P_{12} in formula (3) and (4) will do many fast measurements and calculate the average, at this time the average of χ_σ is

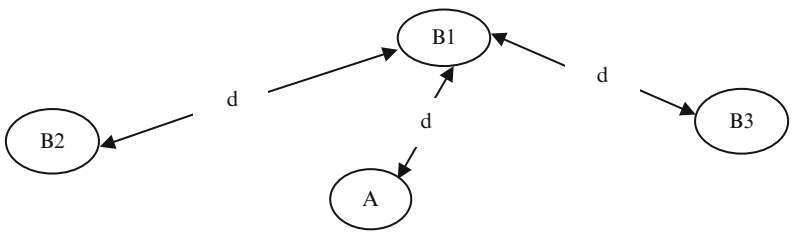

Fig. 1 Network nodes ranging figure

approximate to 0. Practice has proved that χ_σ is close to zero even disappearing when we use the Gaussian filter method mentioned later in this paper.

Making $P_{d_0} = P_{12} + \chi_\sigma = A_{12}, A_{12}$ *as* signal strength value which is at a computing unit of distance, then the formula (2) can be rewritten as:

$$P_d = A_{12} - 10\mu \lg\left(\frac{d}{d_{12}}\right) \tag{5}$$

By the formula (5), the signal strength of the node B1 received by the reference node B3 is:

$$P_{13} = A_{12} - 10\mu \lg\left(\frac{d_{13}}{d_{12}}\right) \tag{6}$$

In the case of P_{13}, A_{12}, d_{13}, d_{12} are known, μ value can be calculated:

$$\mu = \frac{A_{12} - P_{13}}{10 * \lg\left(\frac{d_{13}}{d_{12}}\right)} \tag{7}$$

Therefore, using the formula (5), the signal strength of B1 received by the mobile node A is:

$$P_d = A_{12} - 10\mu \lg(d/d_{12}) \tag{8}$$

Comprehensive formula (7) and (8), the distance between the mobile node A and the node B1 as follows:

$$d = d_{12} * 10^{\frac{(A_{12} - P_d) * \lg\left(\frac{d_{13}}{d_{12}}\right)}{A_{12} - P_{13}}} \tag{9}$$

By the formula (9), only to obtain accurate A_{12}, P_d and P_{13} values, the distance between the mobile node A and the reference node B1 can be calculated. Because B1, B2, B3 are the closest three reference nodes to point A, the formula (9) is known as the close three point calculating method. The following study is the filtering process problem of A_{12}, P_d and P_{13} values.

In the measured, we found that coordinate values measured when the mobile node is in a stationary case have drift phenomenon, drift may get worse when the environment changes (such as venue staff walking around), the drift problem can be solved from two aspects: Firstly, the mobile node calculates parameters A_{12}, P_d and P_{13}, as far as possible using the latest parameters obtained by the reference node the closest to node A; Secondly, the measured parameter values can be made reasonable filter processing. The study found that using the Gaussian filter is better.

Gaussian filter is a widely used probabilistic filtering method [11]. In this method, a node in the same location receives a number of signal strength P, in which inevitably there are small probability events, we can select signal intensity values with high probability through Gaussian filter, and then calculate the geometric mean. This practice reduces the interference to the overall measurement's results from the small probability events [12], enhances the positioning accuracy. The specific process of the algorithm is as follows: The P values measured by nodes in the same position are put into the corresponding R array, using Gaussian distribution function to deal with the data within the array, the density function of the received signal strength is shown in the following formula:

$$F(x) = \frac{1}{\sigma\sqrt{2\pi}} e^{-\frac{\left(x-\overline{P}\right)^2}{2\sigma^2}} \tag{10}$$

Where:

$$\sigma^2 = \frac{1}{n-1}\sum_{i=1}^{n}\left(P_i - \overline{P}\right)^2 \tag{11}$$

$$\overline{P} = \frac{1}{n}\sum_{i=1}^{n} P_i \tag{12}$$

The following can be obtained by calculation:

$$0.6 \leq \frac{1}{\sigma\sqrt{2\pi}} e^{-\frac{\left(x-\overline{P}\right)^2}{2\sigma^2}} \leq 1 \tag{13}$$

According to the experience of the existing literature [13], 0.6 is chosen to be the function distribution value of the critical point, when the Gaussian distribution function value is greater than 0.6, the P value is a high probability event, if less than 0.6, the P value can be seen as a small probability event. Using formula (13) to determine the range of P, in this range of the P values in the experimental data are put into the array $R_{Gauss}[i]$, the final optimization value can be obtained by formula (14). After the optimization processing, the A_{12}, P_d and P_{13} are put into Eq. 9 to calculate the value of d.

$$P = \frac{1}{n}\sum_{i=1}^{n} R_{Gauss}[i] \tag{14}$$

We could obtain the distances between the robot and near the three reference nodes by using near the distance three-point calculating method, practice shows that

the error of measurement is less than 0.5 m. All of the reference nodes' coordinates are known, we can use a variety of methods to obtain the coordinates of the mobile robot. At present there are three main kinds of calculation methods: trilateration method, triangulation method and the least square method. We used the trilateration method to complete the robot's location in actual measurements, specific algorithm is no longer discussed here.

4 Conclusion

In the study of mobile robot localization, measure the distance between the robot and nearby reference nodes is very important. In order to continue the Gaussian filter processing for A_{12}, P_d and P_{13} three values, the A_{12}, P_d and P_{13} three-value dynamic array can be established, this array should satisfy the principle of first-in and first-out to keep the length of the array is the same, sampling period is depended on signal change speed of the A_{12}, P_d, P_{13} and microprocessor running speed.

Acknowledgements This work was financially supported by Henan key scientific and technological (102102210032) and Opening Project of Key Laboratory of Mine Informationization, Henan Polytechnic University (KZ2012-04).

References

1. Hazas M, Hopper A (2006) Broadband ultrasonic location systems for improved indoor positioning. IEEE Trans Mobile Comput 5(5):536–547
2. Cheng Y, Chawathe Y, Lamarca A (2005) Accuracy characterization for metropolitan-scale Wi-Fi localization. In: Proceeding of MobiSys, ACM, Seattle, pp 233–245
3. Goncalo G, Helena S (2009) Indoor location system using ZigBee technology. In: Proceeding of international conference on sensor technologies and applications, IEEE, Washington DC, pp 152–157
4. CC2430 data sheet (rev.2.1) SWRS036F [EB/OL]. http://focus.ti.com/lit/ds/symlink/cc2430.pdf, 13 Aug 2010
5. CC2431 data sheet: system-on-chip for 2.4 GHz ZigBee/IEEE 802.15.4 with location engine [EB/OL]. http://focus.Ti.com/lit/ds/symlink/cc2431.pdf, 13 Aug 2010
6. Chehri A, Fortier F, Tardif PM (2007) On the TOA estimation for UWB ranging in complex confined area. In: Proceeding of international symposium on signals, systems and electronics [S.l.], IEEE, Seattle, USA, pp 533–536
7. Peng R, Sichitiu ML (2006) Angle of arrival localization for wireless sensor networks. In: Proceeding of IEEE communications society on sensor and Ad Hoc communications and networks [S.l.], IEEE, Washington DC, USA, pp 374–382
8. Yang Wei, Zhou Siyong, Qiao Hua (2007) Node localization in wireless sensor networks for coal mine security monitoring. J China Coal Soc 32(6):652–656 (In Chinese)
9. Yang Wei, Feng Xisheng, Cheng Shixin et al (2004) The theories and key technologies for the new generation mine wireless information system. J China Coal Soc 29(4):506–509 (In Chinese)

10. Cheng Zhang, Xuerui Song (2011) The study of RSSI ranging method accuracy based on the ZigBee. J Hunan Technol Univ 25(5):37–41 (In Chinese)
11. Xiaoling Wang, Jun Lu (2008) Optimization method and optimal control. Harbin Engineering University Press, Harbin, pp 40–56 (In Chinese)
12. An Xun, Jiang Ting (2007) Centroid localization algorithm for wireless sensor networks. Comput Eng Appl 43(20):136–138
13. Liyang He, Guohua Jiang, Ming Lv (2009) District vehicle management system based on ZigBee wireless location technology. Netw Secur Technol Appl 25(6): 68–69 (In Chinese)

Static Security Analysis of the Regional Power Grid Based on the Busbar Automatic Transfer Switch

Liang Zhao, Jian Zhang, He Zhu, Xiaoxiao Cheng, and Feifei Zhang

Abstract In order to solve the inapplicability of the transmission grid N-1 criterion in the regional power grid which is running with a large number of the BATS (busbar automatic transfer switch) devices, a new safety analysis criteria that taking the BATS devices into consideration has been proposed in this paper, namely N-1 + M. Through the twice topological analysis of two situations about whether to put the BATS device into use after the regional power grid failure, we come to the conclusion that it is of great significance for ensuring the normal operation of the grid to improve power supply reliability and reduce outage cost by inputting the BATS device. Take N-1 + M analysis on a regional power grid for example, it verifies the results of the static security analysis by the safety analysis criteria derived can better meet the actual situation of the regional power grid operation and prove the validity and practicality of the criteria.

Keywords Static security analysis • Busbar automatic transfer switch • N-1 + M criterion • Twice topological analysis

1 Introduction

With the rapid development of the national economy, the demand for electricity is growing and the requirements of the load on the power quality are also increasing, in order to ensure reliable power supply grid, the operation of the power system

L. Zhao (✉) • J. Zhang • F. Zhang
Zhengzhou Power Supply Bureau of Henan Province, Zhengzhou, China
e-mail: klosek@sina.com

H. Zhu
Xuchang Power Supply Bureau of Henan Province, Xuchang, China

X. Cheng
Henan Electric Power Research Institute, Zhengzhou, China

W. Wang (ed.), *Mechatronics and Automatic Control Systems*, Lecture Notes in Electrical Engineering 237, DOI 10.1007/978-3-319-01273-5_46,

needs an efficient, accurate security analysis software to analyze the current level of security of the grid operation mode as a preventive measure. With the continuous expansion of the grid size and continuing to open up the electricity market, the size of the transaction will continue to expand and the requirements of the corresponding grid static security analysis is also increasing.

In the past, people mainly focused on the transmission grid security analysis and put forward the transmission grid of the N-1 criterion [1, 2], and showed little concern about the safety analysis of the regional power grid. In terms of the regional power grid, we usually focus on the trend of the distribution of N-1 static security analysis, thermal stability analysis, and so on; among which static security analysis is the core issue.

Due to the significant differences between the regional power grid and the transmission grid in structure, for example, regional power grid is the closed-loop structure, open-loop operation, and mostly appears radial; any breaking of components on any path can cause grid splitting or lost load, lost power, etc. This is easy to form a number of island nodes, so lots of BATS device have been input in regional power grid to ensure the reliability of the power supply to users [3, 4]. When a fault occurs in a power system in bus result in load rejection, the BATS devices satisfying the investment conditions will automatically move on the electric bus power. At this time, the original grid structure will change and the system will turn to a new connection mode and running state [5]. Yet it has brought new problems to traditional power system static security analysis based on N-1 criterion just because of the change of the power grid structure [6].

2 Regional Power Grid Static Security Analysis

Considering the important role that the regional power grid played in the entire power supply, area power system static security analysis method, which is a necessary component of the DMS (Distribution Management System), has gained extensive attention. Many experts and scholars in this field have made a lot of beneficial exploration, and put forward some algorithm and security index applying to the areas of power system static security analysis. At present, it has been widely accepted in the industry that the distribution grid static state security analysis must take into account the action of the BATS device in order to simulate the grid wiring fault accurately. Otherwise, the result of the security analysis is often that direct load rejection and even electrical Island. This is not match with the actual operation result of the regional power grid, and the analysis results will be meaningless.

Because of the consideration of switch action and the BATS device action, the traditional N-1 safety analysis code will change to N-1 + M principle (N node number, 1 electric circuit, M inputs from the vote count), static security analysis software must be renewed by topology analysis, which requires a fast and effective method of topological analysis [7, 8], that is, taking topology analysis in terms of the failure of the power transmission grid and then calling flow module for

calculation; the advantage of this method is accurate and flexible, and it can handle arbitrary faulty equipment and simulation fault automatic device action. Besides, it is capable of processing multiple island flow calculation condition after fault.

3 Models for BATS

The action principle of BATS device is more complex and more ways, through the analysis and research into it, we have got the following four basic models, as it is shown in Fig. 1.

Finally, complete content and organizational editing before formatting. Please take note of the following items when proofreading spelling and grammar:

(a) Busbar sectionalizing switch as circuit breaker backup
During normal operation, two incoming line switch 1 and 2 will be closed, busbar sectionalizing switch 3 is regarded as the backup switch of switch 1, through which we will illustrate its principle of work: after the failure, the power in B bus will be lost, and the current of the switch 2 connected with it is 0. At the same time, the low voltage side bus and the medium voltage side bus of the transformer which connected with the B bus will also lose power, but another line A will be charged, so BATS will begin to act, breaking off switch 2 and closing switch 3, and providing the loss of electrical bus B with power supply. As shown in Fig. 1a.

(b) Three switches with each other as a backup.
During normal operation, any two of either the two incoming line switches or the busbar sectionalizing switch are closed, the other for standby. If the busbar sectionalizing switch is a backup switch, the operation principle is the same as that of the standby of the line busbar sectionalizing switch. On the contrary, it is divided into two types: (1) if only bus line B loses power while the incoming line switch 2 has electricity, then close the switch 2; at the same time, if the switch 1 and 3 are closed, then break off the incoming line switch 1. (2) if the bus A loses power, then the current of switch 1 is 0. In the transformer connected with the bus A, its low voltage side bus and medium voltage side

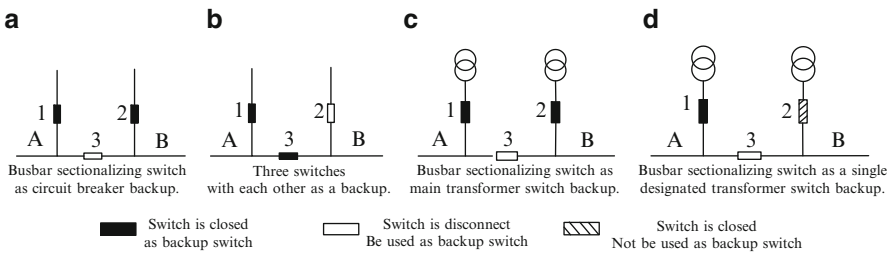

Fig. 1 Four basic models of BATS

bus will be both in power failure, but the line B is electric, so BATS begins to act, disconnecting switch 1, closing the standby switch 2 to supply the electric bus A with power. As shown in Fig. 1b.

(c) Busbar sectionalizing switch as main transformer switch backup
During normal operation, the switch 1 and 2 of the low voltage side of main transformer are closed, and as a backup switch for switch 1 and 2, the busbar sectionalizing switch 3 is disconnect. Take this for example, we will describe its working principle: after the failure, bus B will be in power failure, and the transformer switch 2 connected with the bus B is disconnected, then BATS starts to act, closing busbar sectionalizing switch 3 and supply power to the electric bus B. As shown in Fig. 1c.

(d) Busbar sectionalizing switch as a single designated transformer switch backup
The difference between its operating principle and main transformer bus sectionalizing switch used as a backup switch lies in: the busbar sectionalizing switch 3 will only be used for designated transformer as a backup switch, such as: busbar sectionalizing switch 3 only as a backup switch for switch 1, but not for transformer switch 2. As shown in Fig. 1d.

4 Twice Topology Analysis Method

This paper proposes a twice topology analysis method to analyse the static security of regional power grid. The topology analysis of power grid is to figure out the structure of the power grid based on the state of the grid switch, to present the grid, formed by the connection of all sorts of equipment (such as a generator, load, shunt reactor, transformers, transmission lines, etc.), as a node or a branch model, which can be calculated by power system analysis software, and to distinguish among the reciprocally isolated branch systems. Power grid topology analysis, on which the power system analysis and calculation are based, in essence, is a mathematical problem.

Figure 2 is an electrical hookup of a regional power grid. Take Huo Zhuang substation as an example, the direction of the power flow is from 220 to 110 kv. If Huo Zhuang substation bus malfunctions and loses of power, it will cause the following lines lose electric: Huo Yu 1, Huo Long 1, Huo Dian 1, Huo Yang 1, Huo Jian 1. Then part of the bus in YuTai substation, LongQuan substation, thermal power plant substation, YangZhuang substation, MoZhuang substation will be in power failure. Leave the BATS device out of accounts will lead to load rejection in above substations. Obviously, the results do not tally with the actual situation.

From this we can see, because the operating mode of the system is constantly changing, when a system component has power failure, which may lead to action of one or more BATS device. If we just analyse this matter using N-1 principle as we do with transmission grid, that is, the fault section is directly cut off when a

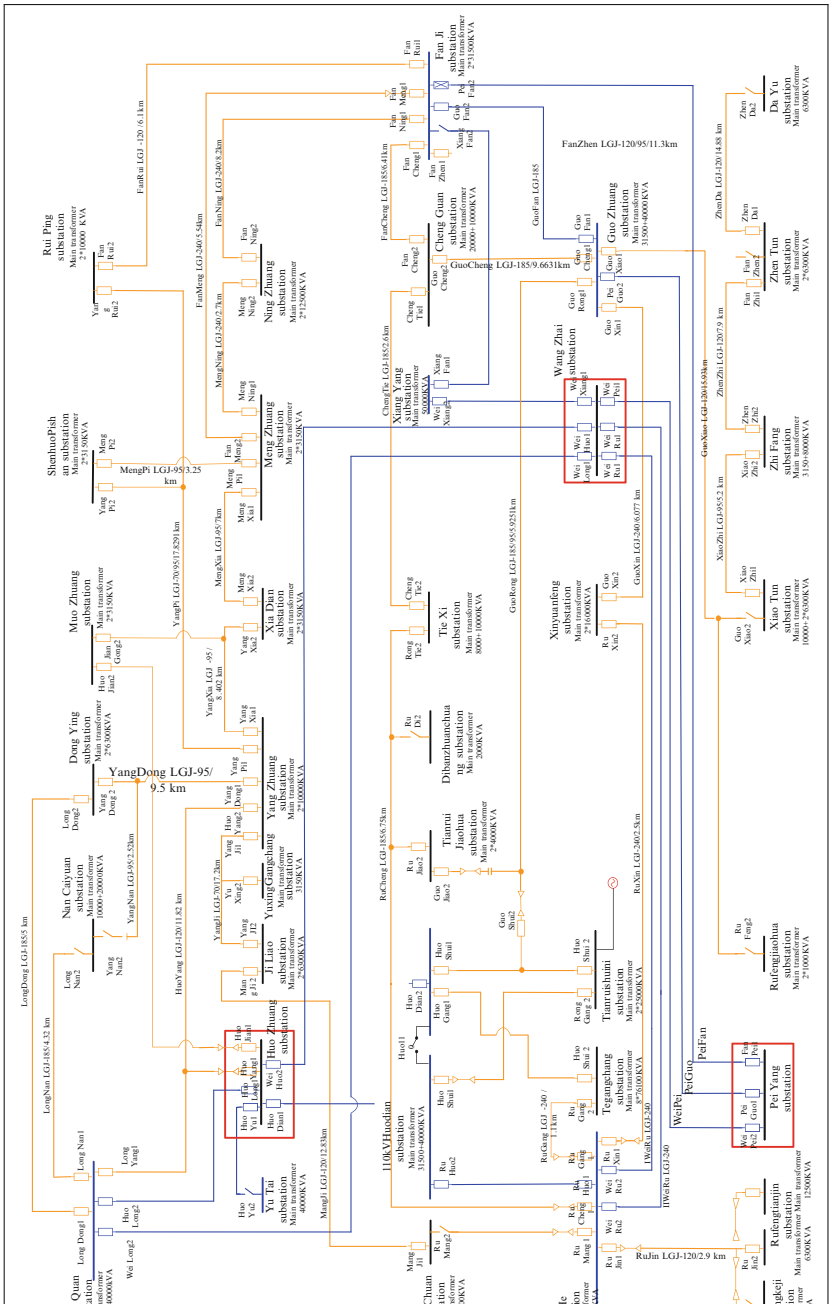

Fig. 2 A regional grid of electrical hookup

component has fault. Through topology analysis, we can find that the results of the analysis will be inconsistent with the actual situation, and no real significance and reference value to the operating personnel.

According to the analysis above, this paper uses the N-1 + M analysis to analyse the static security of regional power grid based on the twice topology analysis method. First, give each component a number, when a component breaks down, after considering the fault component's corresponding BATS device moves, the first topology analysis is used to judge whether other equipment will go from the charged state into a loss of power after the fault component is cut off; sum up all the fault components, and find out from the BATS device table how, in the current situation, the corresponding BATS will act in response to the state of power loss of the failing components, and then, all the results considered, topology analysis is used for the second time to go on the safety analysis. The introduction of the twice topology method can save work on analyzing the way the system works, because of which, it's no longer necessary to establish the corresponding BATS device action table when the next device fails under different operating modes. Not only is the process of establishing such a table complex, but lacking in flexibility; besides, it needs constant maintenance; the twice topology is a very flexible, convenient, and effective method, therefore it's really necessary to adopt the twice topology method in the static security analysis.

5 Example Analysis

5.1 The Introduction of the Calculation Process

The software development is based on the Visual Basic software of windows system. First of all, each component node of the regional power grid is being numbered, then disconnect any lines to judge whether it is connected or whether there are electrical islands. The first topology analysis is carried on the current state of the grid, and then operate the BATS device corresponding with the power failure node, flow calculation, to determine whether the system still exists load rejection or voltage limit condition, the software will give a second topological analysis. Flow chart is as Fig. 3.

5.2 The Analysis of the Result

Regional power grid operation mode is divided into do not consider BATS device (case 1) and consideration the BATS device (case 2) in two cases. After comparing the two kinds of operation modes of calculation results, as it is shown in Table 1,

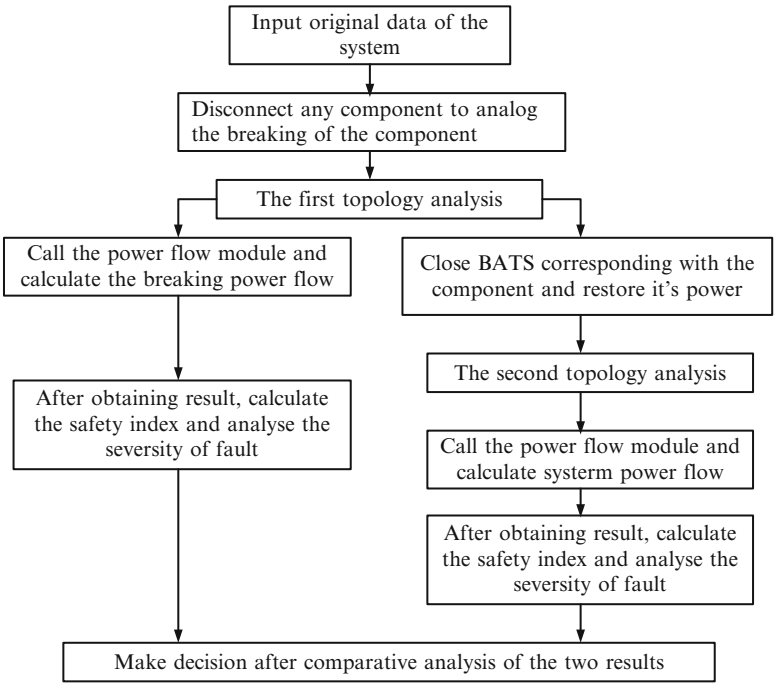

Fig. 3 Twice topological analysis flow chart

Table 1 Part of results of security analysis of equipments

Name of faulty equipment	The severity of fault		Number of power failure bus		Volume of load rejection/ MW		Number of the BATS	
	Case1	Case2	Case1	Case2	Case1	Case2	Case1	Case2
Guo Zhuang 1# transformer	Load rejection	Voltage limit	4	0	35.20	0	0	2
Ru He 1# transformer	Load rejection	Voltage limit	5	0	56.05	0	0	4
Long Quan 2# transformer	Load rejection	Voltage limit	3	0	22.97	0	0	2

we can find, if we do not consider the BATS device of power system, that can directly load rejection phenomenon when the system is in power failure, while inputting the BATS device, the number of power failure bus and the volume of load rejection decrease apparently which ensure the safety and reliability of the regional power grid operation.

6 Conclusion

Traditional regional power grid security analysis is based on the N-1 breaking mode without considering the changes of the grid topology structure caused by the BATS device and this way doesn't match with the operation way of the current regional power grid. This paper proposes a N-1 + M assumption considering that the BATS device has a great role in the safe operation of the power grid. According to the BATS information table illustrates, this paper simulates the actual situation of the corresponding BATS device after a component out of operation. Then through the double topology analysis and corresponding calculation, obtains the relevant information of overload lines and overload transformers. According to comparison the Line load flow table, the overload component statistical table is obtained. Finally, through the static security analysis and calculation of regional power, proved that the calculating results agree with the actual situation. This shows that the method has better practical application value.

References

1. Jishun Wu (1985) Static security analysis of power system. Shanghai Jiao Tong University Press, Shanghai, pp 1–65 (In Chinese)
2. Junwei Zhu (1995) The analysis of power system. Electric Power Press, Beijing, pp 1–32 (In Chinese)
3. LI Yong, Zhao Chuan, Pan Li et al (2006) Design and application of static security analysis in a regional power grid on twice topological analysis. Mod Electr Power 23(6):30–34 (In Chinese)
4. Chen Yong, Yubin Yao, Xia Xiang et al (2004) Design and application of static security analysis considering bats for a regional power grid. Autom Electr Power Syst 28(19):84–87 (In Chinese)
5. Feng Ling (2006) Practice on preventing overload after automatic closing emergency sources acting. North China Electr Power 8:19–20 (In Chinese)
6. Shuyan Pan, Liangjun Lu, Hongtao Zhou et al (2007) Automatic bus transfer equipment under safety and stability control system. Electr Power Automat Equip 27(2):4–7 (In Chinese)
7. Boming Zhang, Shousun Chen (1996) Advanced power system grid analysis. Tsinghua University Press, Beijing (In Chinese)
8. Youma Deng, Decheng Zhong, Boming Zhang (1998) Some problems should be concerned in implementing distribution automation project. Automat Electr Power Syst 22(12):37–48 (In Chinese)

The Space Distributed Power System: Power Generation, Power Distribution and Power Conversion

Lei Yu, Trillion Q. Zheng, Deying Yi, Zhiyong Li, and Cheng'an Wan

Abstract This paper focus on the space distributed power system, which contains distributed power generation system, distributed power distribution system and distributed voltage-convert system. This paper gives a distributed power generation system realized by voltage–current-regulator, and its working mechanism and test result are also given. This paper gives a distributed power distribution system structure constructed by SSPC, and its short-circuit protection, I^2T protection and loads characteristic test result is presented. For distributed voltage-convert technology, this paper gives the simulation results of the impedance matching affecting the system stability.

Keywords Space power system • Space distributed power system • Distributed generation system • Distributed power distribution system • Distributed voltage-convert system

L. Yu (✉)
School of Electrical Engineering, Beijing Jiaotong University, Beijing, China

China Academy of Space Technology, Institute of Manned Spacecraft System Engineering, Beijing, China
e-mail: yul529@yeah.net

T.Q. Zheng
School of Electrical Engineering, Beijing Jiaotong University, Beijing, China

D. Yi • C. Wan
China Academy of Space Technology, Beijing Spacecrafts, Beijing, China

Z. Li
China Academy of Space Technology, Institute of Manned Spacecraft System Engineering, Beijing, China

W. Wang (ed.), *Mechatronics and Automatic Control Systems*, Lecture Notes in Electrical Engineering 237, DOI 10.1007/978-3-319-01273-5_47,

1 Introduction

Space power system is to generate, store, regulate, control and distribute electrical energy. Space power system consists of power generation subsystem, power distribution subsystem and voltage-convert subsystem [1]. Power generation subsystem is generally a photovoltaic-battery system, which contains photovoltaic array, battery and PCU (power-control-unit). The power generation subsystem transforms solar energy to electrical energy, and generates a stable power bus. Power distribution subsystem contains DC/DC converter, power switch, wire and measure and monitor unit. The power distribution subsystem distributes main power to different loads and converts the main power bus to different voltage to suit load requirement.

For large-scale complicated assembled spacecrafts, distributed power system is meaningful for increase power system capacity, efficiency, reliability and intelligence. This paper focus on the space distributed generation technology, space distributed distribution technology and space distributed voltage-convert technology. For each part, the paper present the basic structure and principle, and simulation and experiment results are also been given (Fig. 1).

2 Distributed Power Generation System

Large-scale aircraft (e.g.: space station) usually has several modules. Each module has its own power system. When these modules combined to form a whole one, and influenced by the berthing position and the mutual shelter, some modules may not generate enough power, while other modules may have affluent power. By these single power systems combining to distributed power system, power can flow among different modules, system capacity and reliability are enhanced too [2].

Figure 2 shows the structure of a space distributed power system by the voltage–current-regulator. Every separate power system contains solar array, power shunt, battery, power charge–discharge unit and a S3R (sequential switching

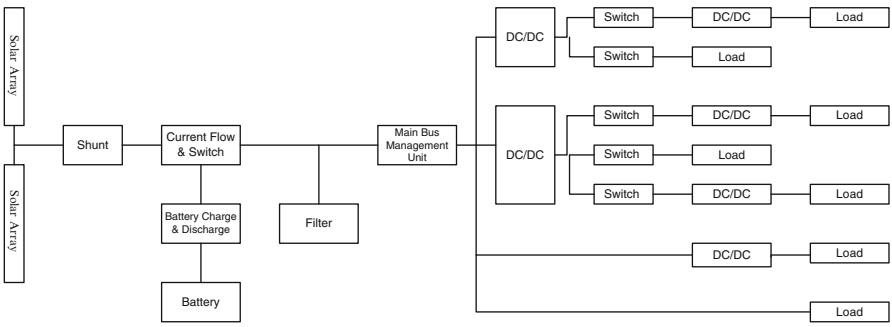

Fig. 1 The structure of space power system

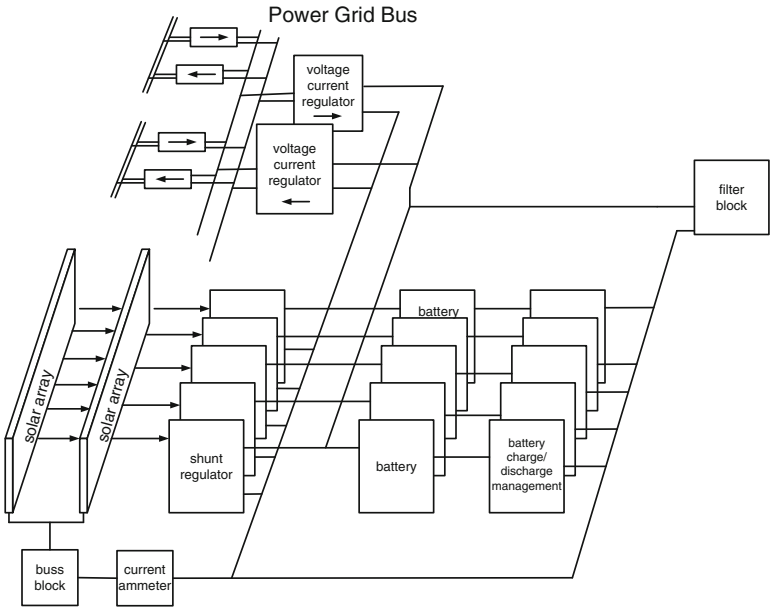

Fig. 2 Distributed generation structure

shunt regulator) power bus. Voltage–current-regulators among separate power systems accomplish power transition and regulation between each other.

The voltage–current-regulator has constant current and output-voltage-limitation function and constant current value can be regulated (current -variable). Figure 3 shows the power bus wave when voltage–current-regulator and power generation subsystem working together. The voltage of power bus is controlled by the voltage closed loop of power generation subsystem. During the orbit in sunlight, MEA (main error amplifier) sample power bus voltage and generate the shunt signal to control the shunt working. The power bus voltage is between V1–V2.During the shadow, MEA samples power bus voltage and generates the step-up signal to control the BDR (Battery Discharge Regulator) working. The power bus voltage is between V3–V4.V2–V3 is the transition region between the sunlight and the shadow. In normal load situation, the voltage–current-regulator works in constant current mode to provide the defined power together with the solar array. In heavy load situation, the voltage–current-regulator works in constant current mode to provide the defined power together with the solar array and the battery. In light load situation, the voltage–current-regulator works in output-voltage-limitation mode to afford the load supply alone and the voltage-limitation value is V5. According to the load power requirement, the voltage–current-regulator can be set in different constant current mode.

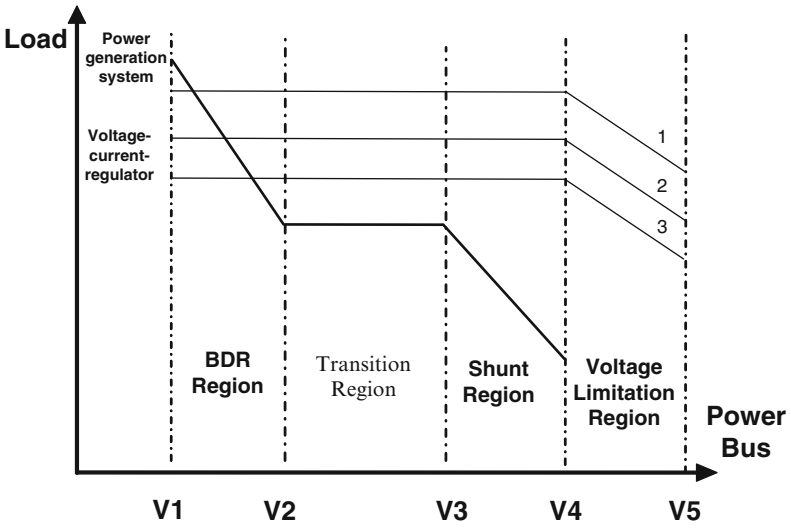

Fig. 3 Distributed generation system power bus

This method is based on current source (VCR output characteristics) and voltage source (power -receiving end power system output characteristic) parallel in the form of power grid and bus voltage depend entirely on the receiving end power system bus itself closed-loop control. There is no bus voltage control competition.

The ISS (International Space Station)'s method is "constant-voltage with current-limitation". This required the output voltage of VCR falls on the "Transition Region" of the power -receiving end power system. Considering the influence of the line resistance and the grid current, it makes more difficulty to design the VCR. Especially for S3R, S4R type full-regulated bus power system, which has a narrow region voltage (0.5 V or so). On the other hand, when we need to expand the grid system (such as multiple spacecrafts supply power to other one at the same time), current source type VCR module can be directly in parallel while voltage source type VCR is not easy to realize directly parallel.

In the Fig. 4: the left oscilloscope channel 1 is input voltage of VCR, channel 2 is input current of VCR, channel 3 is output voltage of VCR, channel 4 is output current of VCR. The right oscilloscope channel 1 is bus voltage of grid system, channel 2 is output current of power -receiving end power system. Power -receiving end power system output power is 2,500 w, while the VCR maximum output power is 2,000 W. Setting load from 2,200 w step to 5,200 w, the grid system work from "solar array + VCR " into" solar array + VCR + battery". The bus voltage cross domain from 101.25 V (V3–V4) to 98.89 V (V1–V2). The test proves that grid system work stably when load step.

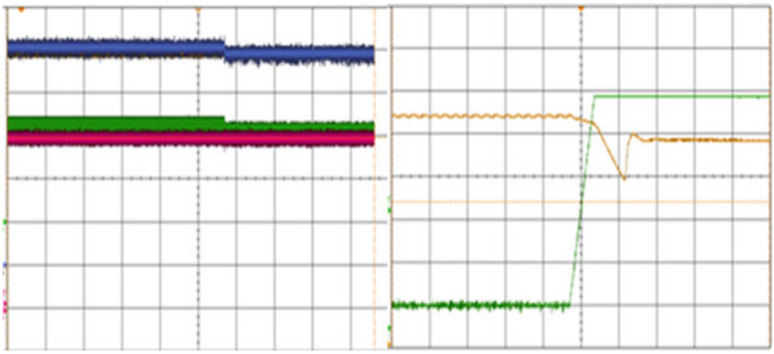

Fig. 4 The bus voltage test waveform when load step

3 Distributed Power Distribution System

Distributed power distribution subsystem contains power distribution, power control, information sampling, fault protection, hierarchical management, etc. [3]. Distributed power distribution subsystem is based on solid state power controller (SSPC). Fault detection and dispatch is accomplished by SSPC, and power supply will recover when fault eliminates. Distribution subsystem hierarchical management can make the fault within limits. Compared to traditional power distribution subsystem, distributed power distribution subsystem has advantages in flexibility, weight, automation, reliability, operability and maintainability [4, 5].

Figure 5 shows typical distributed power distribution subsystem which contains two-stage distribution structure. Main bus distribution unit receive the generated high voltage power bus and distribute it to several load distribution units. Its main function is power flow and diffluence, which accomplished by high power SSPC (HPSSPC). Each HPSSPC is corresponding to a load distribution unit. Load distribution unit is placed nearby the load which is consisted with several low power switches SSPC (LPSSPC). Each LPSSPC is corresponding to a load.

The SSPC (Solid State Power Controller) is based on MOSFET, which is a solid state device contains the conversion function of the relay and the circuit protection function of the breaker. SSPC plays an important role in the new generation space power distribution system. Compared with the traditional switch with mechanical contact, SSPC has many advantages such as no contact, no electric arc, no electronic hash, quick response, low EMI, long life, high reliability, easy to long distance control and so on. Figure 6 shows typical structure of SSPC.SSPC drives MOSFET working in cutoff region or saturated region to make electric circuit break or connect [6]. SSPC contains five main function circuits: driving circuit, status detection circuit, short-circuit protection circuit, I^2t protection circuit and insulation circuit. MOSFET ON or OFF is controlled by driving circuit. Signals such as current, voltage, temperature and switch status is collected by status detection circuit. Short-circuit protection circuit's function is to trip immediately when the

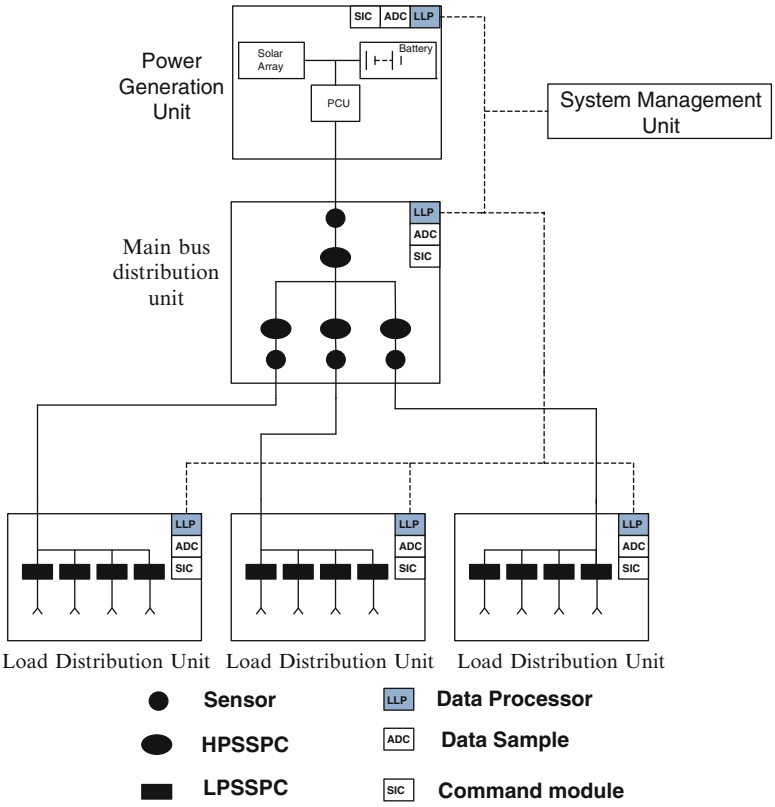

Fig. 5 Distributed power distribution system

current exceed the limitation. I^2t protection circuit is to realize the heat protection in the over-current status. Insulation circuit makes the control circuit and the power circuit insulate.

Following shows some test results of distributed power distribution system, such as Short-circuit protection, I^2T Protection and loads characteristic analysis.

3.1 Short-Circuit Protection and I^2T Protection

SSPC contains short-circuit protection functions which will detect and trip on short circuit failure in the load or wiring, and the protection function can distinguish between the normal surge and the abnormal electric arc. This will make sure the SSPC work rightly.

The mechanism of short-circuit protection design is as follows: A sensing resistance is cascaded in the power line, so the voltage drop on the resistance can

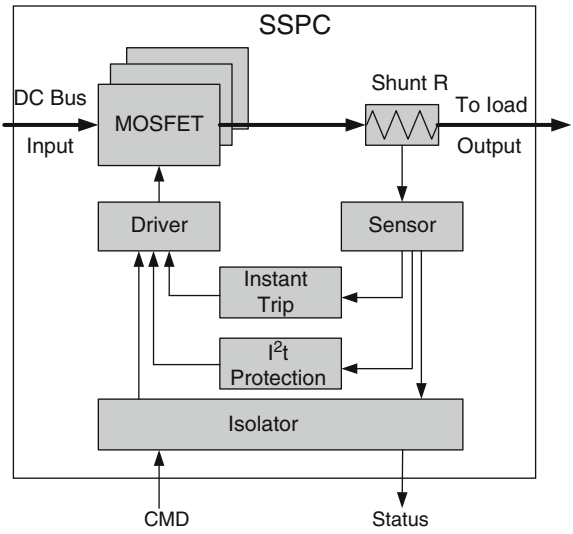

Fig. 6 SSPC structure

represent the load current. The voltage signal is been send to the comparator. The comparator is a decision mechanism. If the load current enlarges suddenly, the voltage signal will exceeds the threshold value and the drive circuit will pull down the Vgs of MOSFET, which will make SSPC "OFF". The whole process can be less than 100 us. The experiment result is as following Fig. 7. Channel 1 is Vds of MOSFET and channel 2 is the load current. It shows that when the short-circuit appears, the load current rising quickly, and the SSPC trip time is about 35 us.

When the load current is greater than the rated value, but does not reach the instant trip level, the SSPC will carry on the I^2T protection like fuse. The I^2T show the relationship between the load current and the trip delay time. By identify the over-current, SSPC will calculate different trip delay time. The more the over current is, the less the trip time is.

The I^2T trip curve is designed according to extremely anti- time limit curve of IEC60255-3.Its protection domain is 120–400 % of the rate current. The relationship between over current and trip time is as above Fig. 8 (between the upper limit curve and the lower limit curve). It can be seen that the SSPC I^2t protection Function work rightly.

3.2 Loads Characteristic Analysis

The SSPC is a no-contact switch. Surge-current will be produced when SSPC is turned on especially in capacitive loads and spike-voltage will be induced between the drain and source of MOSFET in inductive loads when the switch is turned off. In order to reduce the surge-current and spike-voltage, the advantages of solid-state device should be utilized fully to control turn-on and turn-off time of the MOSFET.

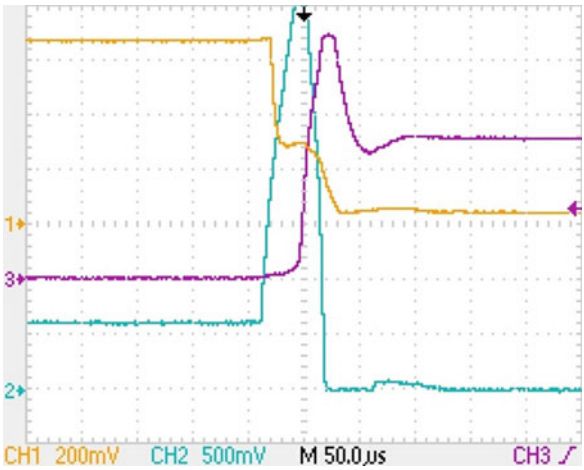

Fig. 7 SSPC normal and over-current protect curve

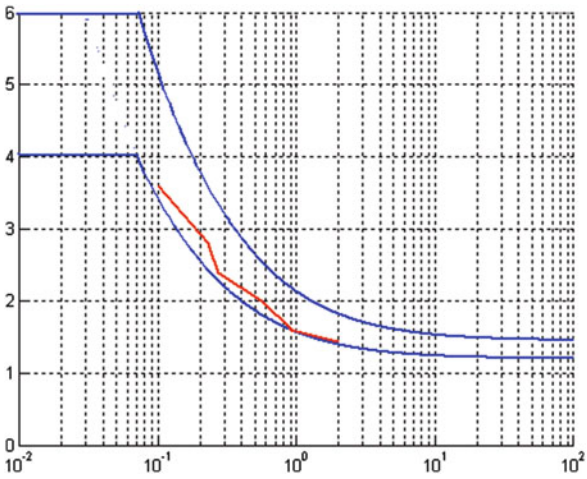

Fig. 8 SSPC I2t protection curves

The soft-starting and soft-turning-off of solid-state switch means, when the solid-state switch is on or off, load current rise and fall with smaller change rate and at last reach the stable state.

Capacitive loads, such as the input filters in equipment being controlled, draw large surge currents when turned on rapidly. Even small capacitors will draw more than the three-per-unit trip current. In operation the SSPC appears not to turn on.

Turn-on of a 100 µF capacitive load at 100 V is shown in Fig. 9 (left). The surge-current with capacitive loads when SSPC is turned on is:

$$I_D = c\frac{du_c}{dt} = 100 \times 10^{-6} \times \frac{100}{400 \times 10^{-6}} = 25 \text{ A}$$

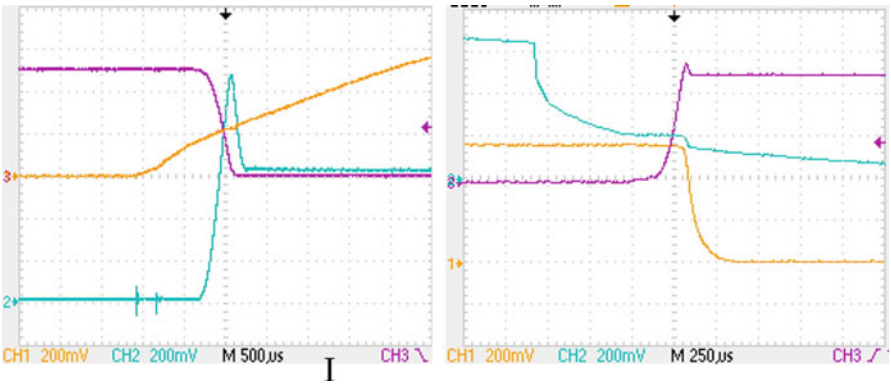

Fig. 9 The turning-on wave form of capacitive/inductive loads. Load current ID at 5A/division; sweep, 500 µs/division

The turning-on wave form shows that the turn-on time is about 400 µs. The current ramped to the 25-A trip point, where the SSPC opened.

If SSPC carrying 100 A in a circuit with an inductance of 20 pH is opened in 5 ps, a transient voltage of 400 V will be generated (Ldi/dt). Few MOSFET's with high enough voltage ratings to handle this magnitude of surge voltage are available. Something must be done to limit the rate of change of current in inductive loads and prevent the generation of large spike voltages that would damage the MOSFET's. Slowing the turnoff time to 50 ps decreased the spike voltage generated to 40 V, which can be more readily handled. The energy stored in the inductor should safely dissipate during the slow turnoff period.

Figure 9 (right) shows the wave form of ID, UDS and UGS in the turning-off process of 4.8 mH inductive loads. It is can be seen from the wave form that the fall time of the load current is 250 µs and the spike-voltage is suppressed completely.

4 Distributed Voltage-Convert System

In the distributed power system, all the converters were designed independently, when those converters were connected in the same system, the affect between the converters, series parallel, would make the system instability or stability degraded.

The stability of the DC distributed power system could be analyzed and evaluated, by the way of input impedance (Z_i) and output impedance (Z_o) measure and Nyquist Plot of Z_o/Z_i. The Z_i and Z_o would directly affect the Gain and Phase margins and dynamic characteristic of the distributed power system. When the output impedance (Z_o) of the front stage converter was known, and the Gain and Phase margins were decided, we could design the input impedance (Z_i) of the next stage converters. Then, the Gain and Phase margins of the PDS could be designed and controlled, the stability of all the PDS could be ensured [7].

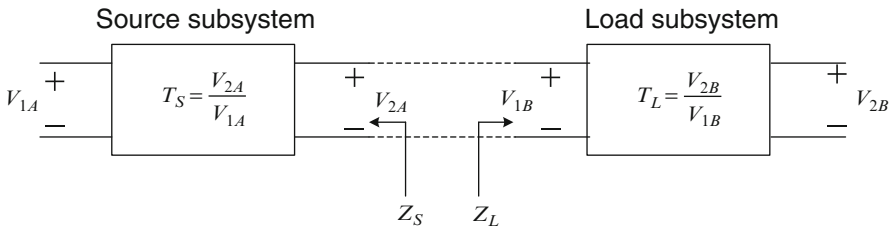

Fig. 10 Interface between source and load subsystem

A power system could be divided into two part, source subsystem and load subsystem, the source system with output impedance Zs and the load system with input impedance Z_L, as shown in Fig. 10. T_s and T_L are transfer functions of the source system and load system respectively, T_{SL} is the transfer function of this power system [8, 9].

$$T_{SL} = \frac{T_S T_L}{1 + (Z_S/Z_L)} \tag{1}$$

$Z_S/Z_L = T_M$ is the loop gain of this power system, T_M could be use to evaluated stability of the interface between source and load of the power system. If $|Z_L| > |Z_S|$ at all frequencies, the interface is guaranteed stable. In those frequencies $|Z_L| < |Z_S|$, if the phases and magnitudes of Z_S and Z_L meet some condition, the system is guaranteed stable too. Such as, When guaranteed gain margin is GM (6 dB usually), guaranteed phase margin is PM (60°usually), the system is stable, if $|Z_L|$-$|Z_S| >$ GM in all frequencies. And, the system is stable too, in those frequencies $|Z_L|$-$|Z_S| <$ GM, if the Phases of Z_S and Z_L meet the requirement of formula (2).

$$180^\circ - PM < \angle Z_S - \angle Z_L < 180^\circ + PM \tag{2}$$

The main factor, which affects the distributed power system stability, is impedance matching. The factors, which affect the impedance matching of power system, are the input filter circuit, control mode, output filter capacitor, and so on.

For example, in a space power system, the front stage converter (source) and the next stage converter (load), all Use the forward topology, the DC voltage ripple of the interface of the source and the load converter would be affected by the input filter of the load, Fig. 11 show the ripples in the interface, when use different input filter circuit. The input filter affected the stability of the system obviously.

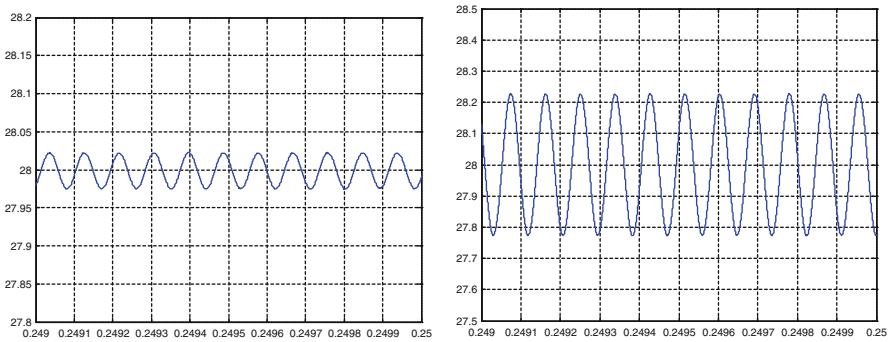

Fig. 11 Ripple in the interface of source and load (*Left*: L = 60uH/C = 3.3uF; *Right*: L = 6uH and C = 33uF)

5 Conclusion

This paper presents the key character of space distributed power system and focuses on the distributed power generation technology, distributed power distribution technology and distributed voltage-convert technology. For distributed power generation technology, the paper presents the power bus characteristics when separate power systems work together; For distributed power distribution technology, the paper presents its key component SSPC and its main function; For distributed voltage-convert technology, the paper gives the distributed system stability solution. The related research results of this paper are meaningful in the future research of space distributed power system.

References

1. Shijun Ma, Guojing Han (2001) Satellite power supply technology. China Astronautic Publishing House, Beijing, China, pp 376–391
2. Lei Yu, Jun Sun, Cheng'an Wan (2008) The research on the power utility technology of multi-spacecrafts. In: 59th International Astronautical Congress, Glasgow, UK, pp IAC-08.C3.2.2
3. Sturman JC (1985) High-voltage, high-power solid-state remote power controllers for aerospace applications. NASA Technical Paper 2437
4. Lei Yu, Deying Yi, Liang Ren, Xiaoyu Meng, Dianrui Zhang (2010) Research on several key problems of SSPC in advanced space power distribution system. In: 61th international astronautical congress, Prague, Czech Republic, pp IAC-10.C3.2.7
5. Xian-cheng Zheng, Xiao-bin Zhang, Zhao-hui Gao (2008) Study of novel solid-state power distribution technology for spacecrafts application. Acta Astronaut 29:1431–1434

6. Li-jing Weng, Li Wang, Zhi-qiaing Wang (2003) Analysis and implementation of inverse-time characteristic for solid state relay. Electr Pow Sci Eng 4(4):50–53
7. Wildrick CM, Lee FC (1995) A method of defining the load impedance specification for a stable distributed power system. Power Electr IEEE 10(3):280–285
8. Kamiar KJ (1995) Verification of space station secondary power system stability using design of experiment, NASATM- 1998–206531
9. Gholdston EW, Karimi KJ, Lee FC et al (1996) Stability of large DC power systems using switching converters, with application to the international space station. In: 31st inter society energy conversion engineering conference, IEEE 1, Ann Arbor, USA, pp 166–171

Configuration of the Wind Farm Reactive Power Compensation

Fei Guo, Zengping Wang, Tao Zheng, and Jing Li

Abstract This paper analyzes the influencing factors to the wind farm's capacity of reactive power compensation, providing the reactive power calculation formulas of transformer, aerial cables and two main wind turbines, and estimates reactive power of different types of wind farms. Comparing four common reactive power compensation devices used in wind farms, the selection of device and method of the wind farm reactive power compensation are recommended, and its developing trend is also pointed out.

Keywords Wind farm • Reactive power compensation • SVC • SVG

1 Introduction

Wind power energy is a kind of promising renewable energy, but the non-determinacy of the wind's speed and direction makes it transmitted to the grid unstable, and grid-integration of wind power has been a significant problem to the power system. To keep the vibration within required range, reactive power compensation is needed, which has three main functions to the wind farm: (1) Increase the power factor and static voltage stability; (2) Supply reactive power consumed in the generator's transient process to increase the capability of LVRT; (3) Optimize power flow, reducing the grid loss [1–3].

F. Guo (✉) • Z. Wang • T. Zheng • J. Li
State Key Laboratory of Alternate Electrical Power System with Renewable Energy Sources, North China Electric Power University, Beijing, China
e-mail: olivia_guofei@126.com

W. Wang (ed.), *Mechatronics and Automatic Control Systems*, Lecture Notes in Electrical Engineering 237, DOI 10.1007/978-3-319-01273-5_48,

2 Reactive Power Characteristics of Wind Farm

Wind farm electrical system consists of wind generators, box-type substation, collecting power lines and transformers, which are all high inductive devices and the reactive power characteristics of them should be analyzed [4, 5].

2.1 Net Components of Wind Farm

The transmission lines includes two categories, i.e. overhead lines and cable lines, whose reactive power consumed all mainly comes from the parallel susceptance and series reactor, as Eq. 1 shows. It's estimated that: When the wind speed is low and the system has light load, the charging power of transmission lines is large and the system is capacitive, inductive reactive power compensation is needed. On the contrary, capacitive reactive power is needed to compensate for the transformers and transmission lines.

$$\begin{aligned}\Delta Q &= \Delta Q_L + \Delta Q_B = (P+Q)X/U_1 - (U_1+U_2)\mathrm{B}/2 \\ &= 3I^2X - (U_1+U_2)B/2\end{aligned} \tag{1}$$

ΔQ, ΔQ_L are the reactive power loss of transmission line and reactance; ΔQ_B is the charging power of transmission line; P & Q are the active and reactive power transmitted on the lines; U_1 & U_2 are the voltages of the line's two terminals; I is the current flows through the line; X is the line's reactance; B is the line's susceptance.

The transformer's reactive power loss consists of the winding loss in normal operation and the iron-core loss in non-load operation, as Eq. 2 shows. And the latter always exist whatever the operation type is.

$$\Delta Q_T = \Delta Q_0 + \Delta Q_S(S^2/S_{N2}) = (I_{0\%}/100)S_N + (U_{0\%}/100)S_N(S^2/S_{N2}) \tag{2}$$

ΔQ_T is the reactive power loss of transformer; ΔQ_o is the excitation loss; ΔQ_s is the leakage loss (reactive power loss of load);S is the apparent power; S_N is the rated capacity of transformer; $I_0\%$ is the no-load current percentage; $U_s\%$ is the short circuit impedance percentage.

2.2 Typical Wind Generators

DFIG is based on the ordinary winding asynchronous induction motor, which adds with the converter and its control system connected between the rotor and stator of the generator. In the two-phase synchronous revolution coordinate system (dq), the stator flux is oriented to d-axis to analyze the power characteristics of DFIG.

$$Q_S = u_{sq} i_{sd} - u_{sd} i_{sq} = U_s i_{sd} = \frac{-U_s}{L_s}(\psi_s - L_o i_{rd}) \tag{3}$$

From Eq. 3, when U_s fixed, Qs can be controlled by i_{rd}. Its reactive properties are similar to the synchronous generator. However, when the grid's voltage drops sizably, the crowbar of the rotor's control circuit will be activated to short the rotor side converter. Then the wind generator will works as motor. Then the grid side converter cannot satisfy the reactive power requirement. Considering that DFIG doesn't need reactive power from the grid in normal operation, the suggested installing reactive compensation is 20–30 % of the total installed capacity.

Direct drive wind generator is composed of multi-polar low-speed PMSG which is driven directly by wind wheels. It converts the power energy by power conversion circuit and gets connected into the grid. PMSG has good capability of capacitance compensation and low voltage ride through. It's getting increasing attention for its better grid compatibility. In the dq coordinate system, the stator output reactive power of PMSG has the similar expression with DFIG:

$$Q_s = \frac{3}{2}(\omega_s L_s i_s^2 + \omega_s \psi i_{sd}) \tag{4}$$

Q_s is decided by i_{sd}, i.e. PMSG can control the reactive power by the rotor side converter. In normal operation and when failure happens in the wind farm, PMSG doesn't need to absorb reactive power from the grid. But the reactive power loss of transformers and transmission lines should be considered. For the wind farm with all PMSGs, the suggested installing reactive compensation is 10–20 % of the total installed capacity.

3 Reactive Power Compensation Principles of Wind Farm

3.1 V-Q Relationship of Wind Power Plant

Single machine-infinite bus system is used to analyze the characteristics of wind farm's V-Q in this paper, as shown in Fig. 1.

The wind turbine in Fig. 1 stands for the whole wind farm, P_g and Q_g – power transmitted into the power system; Q_{gc} – reactive power compensation of the connecting point bus; Z – the impedance of the equivalent transmission line between wind farms and infinite grid; U_2 – the node voltage of the infinite system.

The voltage difference between the wind farm and the infinite system is:

$$\dot{U}_1 - \dot{U}_2 = Z\dot{I} = Z\left(\frac{S_2}{U_2}\right)^* = Z\left(\frac{S_2^*}{U_2^*}\right) \tag{5}$$

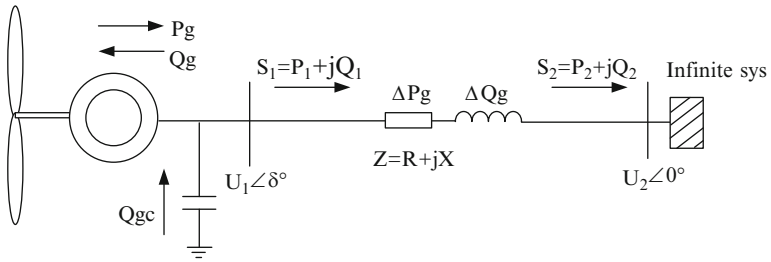

Fig. 1 Single machine-infinite bus system of wind farm

Assuming the phase angle of $\dot{U}_2$ is 0, we will get:

$$U_1 \approx \frac{Q_2 X + P_2 R}{U_2} + U_2 \tag{6}$$

In the infinite system, U_2 does not change with the rating of wind farms. Z can be determined after the grid planning. Therefore, the voltage of the connecting point bus is totally determined by the active power and reactive power, injected by the wind farm and equivalent line as a system into the infinite system.

Through a series of load flow calculation, V-Q relationship is achieved, i.e. V-Q curve, to test the robustness of the power system. Since wind turbines based on different types of generators differ in reactive characteristics, wind farms have variable influences on the system voltage stability.

3.2 Improvement of Reactive Power to Voltage Stability

The improvement of reactive power compensation to the voltage stability embodies in the improvement to static voltage stability and transient voltage stability. When the active power P is constant, the feature of static reactive voltage embodies in the V-Q curve. The features of V-Q curve mainly reflect the small interference stability of the connecting point voltage of the wind farm [6].

When short circuit occurs in the gird or disconnection fault happens, the connecting point bus voltage will suddenly drop. From Eqs. 1 and 2, the voltage reduction results in the reduction of active power output by asynchronous generator, while the mechanical torque input by wind turbine does not actually reduce. The generator will speed up or slow down driven by unbalanced torque, then it will increase its absorbed reactive power, and the bus voltage will further drop, while the active power continues reducing. Finally the whole system will collapse because of over-speeding.

4 Selection of Wind Farm's Reactive Power Compensation Plan

4.1 Reactive Power Compensation Capacity Configuration

The mathematical optimization model of the optimal reactive power compensation uses load flow constraint equation, controlled variable constraint equation and state variable constraint equation as restraint conditions, the total system network loss as the objective function. The model calculates the reactive power compensation capacity which accords with load flow distribution, satisfies boundary limits of the voltage and power, and also of the minimum network loss [7, 8]. There are two research thoughts of such nonlinear programming problems with constraints: (1) Transform nonlinear problems into linear problems; (2) Transform problems with constraints into problems without constraints. In the practical engineering, it usually uses the voltage balance of the grid interconnection side to determine the capacity of reactive power compensation.

4.2 Reactive Power Compensation Device

The main measures for reactive power compensation of wind farms are parallel capacitor (PC), Static Var Compensator (SVC), Static Var Generator (SVG) and Controllable Shunt Reactor (CSR). The means of PC will not be discussed here.

1. Static Var Compensator (SVC)
   The common SVC consists of Thyristor Controlled Reactor (TCR), Thyristor Switched Capacitor (TSC) and filter. The common advantages of different SVCs are their low costs, while the disadvantages are they contain many passive devices, which take much space; the work range is narrow; reactive power drops faster with voltage decrease; SVC itself has no inhibition to harmonics, while produces large amount of low order harmonics with the distortion of current waveforms, which requires extra filters.
2. Static Var Generator (SVG)
   Static Var Generator (SVG) can be divided into voltage-type and current-type according to the energy storage devices (capacitance or inductance) that equipped on the DC-side. Most SVGs in use are voltage-type as discussed in this paper. SVG can adjust the capacity and property of the output reactive power by controlling the output voltage of the inventor. Therefore,SVG can be equal to continuously adjustable capacitor or reactor.

   Compared with other devices, SVG has many advantages: (1) The operation range is an approximate rectangular with equal widths up & down; (2) Controlled by PWM, and responses faster; (3) The regulation of reactive power is not

achieved by controlling the values of capacitive or inductive reactance, so the system resonance does not exist and the device volume is reduced greatly.

3. Controllable Shunt Reactor (CSR)
   Common types of CSR are high-leakage inductance transformer type CRS (T-CSR) and magnetic-valve type CSR (M-CSR, or MCR). TCSR adjusts the capacity of the reactor by changing the low voltage winding's conduction state of the high short-circuit impedance transformer. MCR changes the reactor value by adjusting the core saturation. It has simple structures and low cost, but responses more slowly than CSR.

4.3 Selection of Reactive Compensation Device

Among all the devices discussed above, fixed capacitors have not been commonly used. The following part focuses on the comparison of the features of three main dynamic reactive power compensation devices, as Table 1 shows.

1. Selection according to the response time and whether the dynamic adjustment is supported
   Different types of wind generator, different sizes of installation and the degree of the local power grid strength (the size of the system short circuit capacity) will affect the wind farm's response speed to reactive power compensation, thus affecting the selection of reactive power compensation devices.
   In general, for large-capacity wind farms, where the grid short circuit capacity are small, voltage fluctuations caused by wind speed vibration are relatively large. When short circuit fault or short-term fault occurs, the wind farm may all get out of operation and it will cause the whole area's voltage collapse. Wind farms like this should be able to support reactive power dynamically, i.e. the dynamic reactive power compensation device (SVC & SVG) are needed. On the contrary, automatically switching capacitor or MCR can satisfy the reactive power requirements of small wind farms.
2. Selection according to the construction costs (Table 2)
   Almost every newly built wind farm require dynamic reactive power compensation device, however these devices are very expensive. Considering the cost of floor coverage and maintenance, etc., it's required that the wind farms of high cost to reasonably and scientifically compare and select reactive power compensation methods.

4.4 Selection of Reactive Power Compensation Method

There are two main methods of wind farm reactive power compensation, centralized compensation and distributed compensation.

Table 1 Comparison of features of three main reactive power compensation

Device	SVC	SVG	MCR
Area	Large	Small (30 % ~ 50 % of SVC)	Medium
Adjustable range	Linear scale: 0–100 %	Linear (Larger than MCR & TCR, especially when the voltage is low)	Linear scale: 0–100 %
Voltage level	6–220 kV	Limited	6–800 kV
Reactive power output	Continuous	Continuous	Continuous
	Inductive/ capacitive	Inductive/capacitive	Inductive
Response time	$\leq$20 ms	$\leq$5 ms	$\geq$100 ms
Linearity	Good	Good	Nonlinearity
Harmonic	5th & 7th are large (need additional filtering device)	Small	Small
Harmonic suppression	Not able	Can filter 13th and lower harmonic	
Control flexibility	Good	Good	Good
Fluctuations suppression	Yes	Yes	Yes
Phase adjustment	Yes	Yes	Yes
Running loss rate (%)	0.5–0.7	0.75–2.25	$<$1.5
Reliability (failure rate)	Reliable, easy to happen resonant amplification	Technology is not mature, low reliability; Less easy to resonance; no over compensation and reactive anti- send	Reliable

Table 2 Cost comparison of three main reactive power compensation device

Device	SVC	SVG	MCR
Useful time (year)	$>$20	10 ~ 15	$>$20
Cost of device	Medium, 150-200yuan/ kvar, (Imported equipment cost high and replacement cycle is long)	High, sets for pricing, 10 kV,0-30Mvar, 300-320yuan/kvar	Low, Price vary with the response time 80 ~ 150yuan/kvar
Maintenance expense	Easy to maintain, low operating costs	Easy to maintain	Easy to maintain
Application	Widely used	Not widely used yet	Widely used

Centralized compensation means to install compensation devices centrally at the output substation of the wind farms, in which the surging inrush is large and may cause damage to the electric equipment. And this will influence the whole wind farm's power factor and the substation's voltage level. Besides, it can only compensate the overall reactive power, but cannot solve the V-Q balance of the wind farm's internal network.

While distributed compensation means to select several compensation points which have the best performance in the reasonable scope of investment by mathematical or intelligent algorithm, and compensate locally, then the internal loss of wind farm gets decreased and the voltage quality gets improved. It also has the advantage that the compensation points may communicate and cooperate with each other, then the chance of under/over compensation gets decreased, and the compensation result will get optimized.

5 Conclusion

1. For large wind farms or the ones in the major hub point of the power system, it needs to determine the reactive power compensation capacity of the wind farm booster station by flow calculation. For small wind farms or the ones at the grid's end, the compensation can be estimated in the condition of less information. For wind farm based on DFIG, compensation is 20–30 % of the total installed capacity; and for the one based on PMSG, 10–20 %.
2. The selection of compensation devices: Considering the aspects of response speed, whether the dynamic reactive power compensation is supported and the construction costs: For the small wind farms or the ones at the end of the grid, FC or MCR are considerable; for large wind farms or the ones in the major hub point of the power system, SVC or SVG are preferred.
3. The selection of compensation methods: For the wind farms which influence the power system little, with simple topology and can islanded operate when separated from the grid, centralized compensation is considered; For large wind farms, especially off-shore wind farms, distributed compensation is considered.

References

1. Wen Buying, Jiang Yuewen, Chen Chong (2008) Reactive power compensation optimization for grid connected wind farm. Electr Power Autom Equip 28(5):42–46
2. Zhu Xueling, Zhang Yang, Gao Kun, et al. (2009) Research on the compensation of reactive power for wind farms. Power Syst Prot Control 37(16): 68–72, 76
3. Liu Qihui, Wang Zhiming (2011) Reactive power generation mechanism and characteristic of double frequency wind power generator. Proc CSEE 31(3):82–89

4. Lei Yazhou, Wang Weisheng, Yin Yonghua (2001) An optimization method for determining wind power penetration limit in power system under static security constraints. Proc CSEE 21 (6):25–28
5. Karki R, Billinton R (2001) Reliability/Cost implications of PV and wind energy utilization in small isolated power systems. IEEE Trans Energy Convers 16(4):368–373
6. Sun Tao, Wang Weisheng, Dai Huizhu, Yang Yihan (2003) Voltage fluctuation and flicker caused by wind power generation. Pow Syst Technol 12(27):62–66
7. Zhao Jianbiao (2010) Discuss on SVC equipment to improve the electric power quality of wind farm. Xinjiang Electr Power Thechnol 2:51–53
8. Xiang Zhen, Xie Da, Gong Jinxia et al (2008) Dynamic characteristics analysis of STATCOM for reactive compensation in wind farm. Autom Electr Power Syst 32(9):92–95

Design and Implementation of an Embedded Intelligent Reader

Lijing Tong, Yifan Li, Huiqun Zhao, Guoliang Zhan, and Quanyao Peng

Abstract This paper designs and realizes a new kind of embedded intelligent reader based on image processing, OCR (Optical Character Recognition) and TTS (Text To Speech) technology. This machine can help the blind and visually impaired people read paper document, and improve the quality of their life. The reader mentioned in this paper uses the embedded system design, and its advantages are small volume, convenient carrying and so on. This machine can obtain printed text information with the help of its built-in camera sensor. Then, after the handling of the software of image processing, TTS, OCR to process word recognition and speech synthesis, a speech can be output. This system considers the needs of the visually impaired fully and uses voice navigation and One-Key-OK"s" humankind design. As the system test shows, the reader can get the information written in a flat paper effectively, and its accuracy rate of speech reading is above 95 %.

Keywords Intelligent reader • Embedded system • Character recognition speech synthesis

1 Introduction

According to the report of U.S. NFB, only 10 % people of 1.3 million blind can read Braille and only 10 % visually impaired children are learning Braille [1]. In our country, the basic approach for blind to get information is still the Braille books and audio books. But only a few blind can understand the Braille, and the electronic products, take audio book and radio for example, just have single functions. There is too much limitation for blind to communicate with others by using these ways. It can't meet the needs of blind who desire independent access to information [2, 3]. Therefore,

L. Tong (✉) • Y. Li • H. Zhao • G. Zhan • Q. Peng
College of Information Engineering, North China University of Technology, Beijing, China
e-mail: tong_lijing@163.com

W. Wang (ed.), *Mechatronics and Automatic Control Systems*, Lecture Notes in Electrical Engineering 237, DOI 10.1007/978-3-319-01273-5_49,

we made this portable machine for blind reader which is based on image processing [4], character recognizing, and TTS (Text To Speech) technology [5]. It can take a photo of the paper printed text images, and then, translate it into data information which can be edited with the help of OCR (Optical Character Recognition) [6], after all of above, the use of TTS makes the information into a speech output. This machine has own battery, can be available offline and support storage of audio books. The product can solve the problem mentioned above perfectly.

2 Hardware Design of the System

Embedded intelligent reader is a blind-oriented intelligent reading device. The proposed hardware structure design is shown as Fig. 1.

The CPU of the embedded intelligent reader is S3C6410 controller. The memory of the reader is the SDRAM. In the Embedded intelligent reader, there is also some FLASH to saves the system start-up programs. Some CF/SD/MMC cards are devised for user to store the information too, and its capacity can reach 4G.

The built-in camera has an image sensor with five million pixels and a high resolution camera lens.

The RSA232 serial port is devised to receive the data sent by GPS module. The battery can keep the embedded intelligent reader on working for 6 and 12 h if you choose the standby mode.

The paper-fixed device is a peripheral device. The device, which is designed for placing book paper, intends to prevent placing paper so obliquely to influence reading effect.

We design a special One-Key-Ok key for visually impaired one. At the same time we provide the function control keyboard. The designed function of each key describes as Table 1.

3 Software Design of the System

The mainly structure of embedded intelligent reader software structure is described as Fig. 2.

Each module's specific function is described as follows.

(a) Data acquisition module: The function of data acquisition is dealing and obtaining the image information. What's more, it contains page layout correction module and page layout analysis module; wherein, the first one is used to correct the error which is produced by perspective distortion and skew distortion during the process of getting picture by camera [7]. The layout analysis module is used to isolate text, graphics and tables in the image [8].

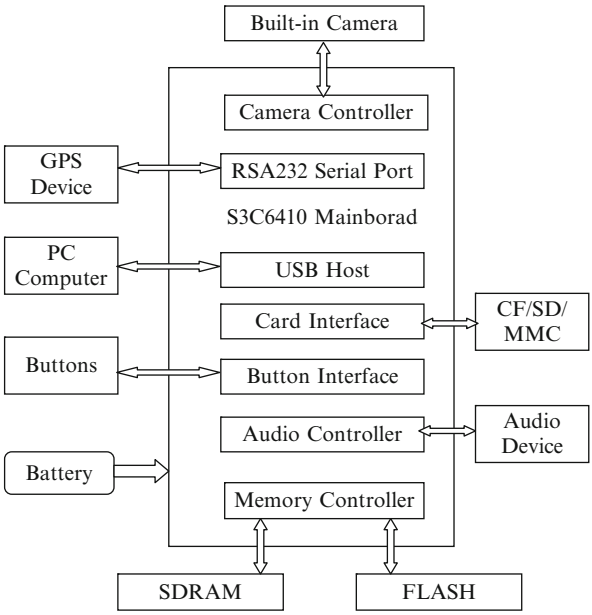

Fig. 1 The proposed hardware structure design

Table 1 Key function design

Key label	Key name	Key function
●	System starting	It completes system power-up and initialization function
▼	Reading starting	The reader transforms character information to voice
‖	Reading pausing	This button stops reading, or continues reading
+/-	Volume controlling	This button adjusts the volume, when the reader is reading
~	Reading sound selection	This button completes male and female voices choosing
↑	Accelerating speed	This button accelerates the voice reading speed
↓	Slowing speed	This button slows down the voice reading speed
⊙	Returning	This button changes the current state to the ready state
■	Confirming	This button completes the function of the voice prompt
◇	Taking pictures	This button realizes the photo taking and stores pictures

(b) Character recognition module: It uses OCR recognition software to do the character recognition. If the result is not meaningful, the image will be rotated [9] and does recognition again.
(c) Speech synthesis module: Speech synthesis module uses speech synthesis module of TTS, translates the received text information into speech signal, and then send the result to the pronunciation module [10].
(d) Pronunciation module: This module includes voice modulation module and a voice output module.
(e) Storage module: The storage module's main function is caching the image data and text data produced during the system operation.

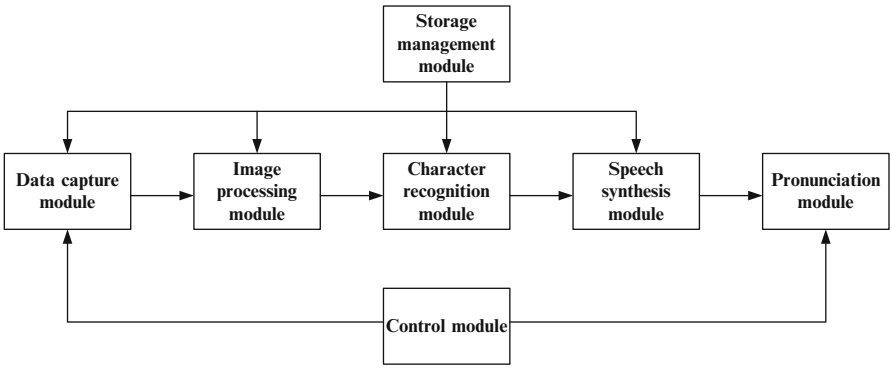

Fig. 2 The proposed software module design

(f) Control module: The control module's main function is responding to a user control commands.
(g) Image processing module: This module does some image processing before OCR and will be introduced in Sect. 4.

4 Humanized Design of the System

Given that most users are blinds, embedded intelligent reader has the function of voice navigation [11]. Embedded intelligent reader also has the One-Key-Ok function. When user puts a book in the paper-fixed device, and presses the OK button, the reader fulfills the image processing and reads the text of the documents automatically. The software design of One-Key-Ok is shown in Fig. 3.

(a) Capture image: Drives the built-in camera to capture image when user presses down the OK button,
(b) Gray-scale optimization: Does gray optimization, and translate the color images into gray ones [12]. Normally the gray transforming equation is as follows:

$$H = 0.299R + 0.587G + 0.114B \tag{1}$$

Because the time consuming is large, we devised a quick approximate algorithm for the gray scale transforming:

$$0.299R \approx H(R >> 2) + H(R >> 4) \tag{2}$$

$$0.587G \approx H(G >> 1) + H(G >> 4) \tag{3}$$

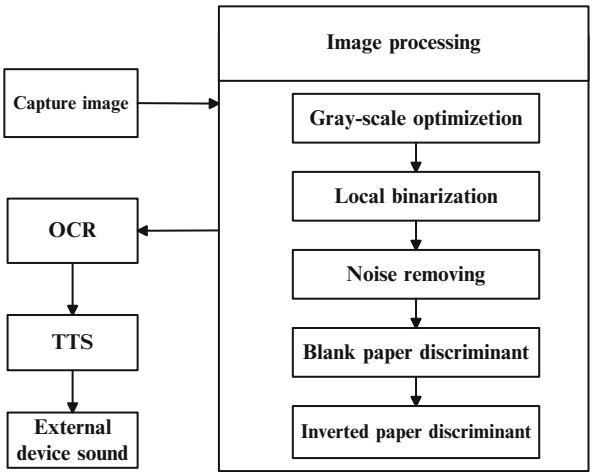

Fig. 3 The proposed One-Key-Ok function design

$$0.114\mathrm{B} \approx \mathrm{H}(\mathrm{B} >> 3) \tag{4}$$

Here "≫" means right shift. For example, "H(R≫2)" means shifting the red color value 2 bits to the right. Then the total gray value is calculated by:

$$\mathrm{H} \approx \mathrm{H}(\mathrm{R} >> 2) + \mathrm{H}(\mathrm{R} >> 4) + \mathrm{H}(\mathrm{G} >> 1) + \mathrm{H}(\mathrm{G} >> 4) + \mathrm{H}(\mathrm{B} >> 3) \tag{5}$$

(c) Local binarization: Does local binarization to the captured images, and change gray images to binary ones [13]. For a pixel, we take into account the N*N windows centered with the pixel. In the window, we calculate the mean value $\psi(x, y)$ and the mean square deviation $\varphi(x, y)$ firstly. If the $\varphi(x, y) < 0.9$, we think the window is the background. So the binarization of the pixel is 255. Otherwise, we take the Eq. 6 to calculate the threshold for the binarization.

$$f(x, y) = \psi(x, y) - 0.2\phi(x, y) \tag{6}$$

(d) Noise removing: Does noise removing for binary images to remove noise in the binarized image.
(e) Blank paper identification: Does blank-paper test for images, and there will be a voice warning if the paper is blank. Here we can use the binarization results to do the identification. Because there are normally still some black noise pixels remain, if the number of the black pixels is no more than 1 % of the total number of the pixels in the image, we identify this paper is a blank paper.
(f) Inverted paper identification: Does inverted paper test, and there will be a voice warning if the paper is inverted.
(g) OCR: it will process the preprocessed images and translate it into text documents.
(h) TTS: Does speech synthesis for the text recognized by OCR.
(i) External device sound: Reads the synthesized speech out by TTS.

5 System Implementation and Performance Testing

We implemented the embedded intelligent reader based on the designs of the hardware system, the software system, and the humanized design. The implemented embedded intelligent reader is shown as Fig. 4.

A large number of tests are conducted in our implemented embedded intelligent reader (with the configuration of the 600 MHz CPU and 256 M memory). The tests show that the flat paper documents can be read effectively and the reader can obtain more than 95 % recognition rate.

We also test the effect of the quick approximate algorithm for the gray scale transforming. The time consuming of Eq. 1 is 9 s. After we take the Eq. 5 to substitute Eq. 1, the time consuming is 450 ms.

In these tests, we also find that the flatness of the paper has a higher influence to character recognition. Three typical kinds of paper are tested. Their comparison results are listed as follows in Table 2.

The results shows: when the paper is flat, the recognition time is about 33 s and the recognition rate is about 99 %. When the paper is warped partly, the recognition time will be about 37 s and the recognition rate is about 73 %. When most of the paper is warped, the recognition time is about 38 s and the recognition rate is about 69 %.

These experiment results show that the performance of the intelligent reader is stable. For ideal images, the reader has a high recognition and its processing time is about 33 s. Meanwhile, it shows the external factors have a great influence to the intelligent reader's character recognition, especially when the paper is warped. It will have a lower recognition and longer processing time when the paper is warped. From this point of view, finding a new algorithm to process the distorted document image is very necessary.

Fig. 4 Implemented embedded intelligent reader

Table 2 Recognition rate and speed tests

Classification	Recognition rate (%)	Recognition speed (s)
The flat paper page	99	33
The paper with a large distortion in the spine	73	37
The paper with a large distortion in the surface of the page	69	38

6 Conclusion

In this paper, we designed and realized an embedded intelligent reader for blind people. With the help of the embedded system design approach, OCR, TTS and image processing technology, the reader can recognize printed document paper after taking photo, and change it to voice. This research provided a fine solution for intelligent reader. The experimental results prove that the reader can obtain good speaking results for thinner books, magazines and a single sheet of paper. Its recognition rate can be more than 95 %.

Acknowledgements This research is funded by the Funding Project for Academic Human Resources Development (PHR201107107, PHR20110865) in Institutions of Higher Learning under the Jurisdiction of Beijing Municipality, and the 11th 5 year Key Technology R&D Program (2009BAI71B02) of China.

References

1. Chun J, Zhao Y, Xue XJ (2010) Research on talking book library and its construction mode. Libr Info Serv 54(23):106–110 (In Chinese)
2. Chen Q, Li X, Jiang QX (2007) Development of reader for blinds based on embedded platform. Chin J Rehabil Theory Pract 13(4):344–345 (In Chinese)
3. Hairuman IFB, Foong OM (2011) OCR signage recognition with skew & slant correction for visually impaired people. In: Proceedings of the 2011 11th international conference on hybrid intelligent systems, IEEE Computer Society, Malacca, Malaysia, pp 306–310
4. Yang SY (2005) Introduction of an example program framework. VC++ image processing programming design. Tsinghua University Press, Beijing, pp 336–341 (In Chinese)
5. Cai RZM, Cai ZJ (2011) Study on the text analysis and processing for Tibetan TTS. In: Proceedings of the 4th international conference on intelligent networks and intelligent systems, IEEE Computer Society, Kunming, China, pp 229–231
6. Beg A, Ahmed F, Campbell P (2010) Hybrid OCR techniques for cursive script languages–a review and applications. In: Proceedings of the second international conference on computational intelligence, communication systems and networks, IEEE Computer Society, Liverpool, United Kingdom, pp 101–105
7. Wang HZ, Li MJ, Zhang LW (2011) The distortion correction of large view wide-angle lens for image mosaic based on OpenCV. In: Proceedings of 2011 international conference on Mechatronic Science, Electric Engineering and Computer (MEC), IEEE Computer Society, Jilin, China, pp 1074–1077

8. Behin H, Ebrahimi A, Ebrahimi S (2010) Incorporated preprocessing and physical layout analysis of a binary document image using a two stage classification. In: Proceedings of 2010 international conference on computer and communication engineering, IEEE Computer Society, Kuala Lumpur, Malaysia, pp 1–5
9. Yalniz IZ, Manmatha R (2011) A fast alignment scheme for automatic OCR evaluation of books. In: Proceedings of the 2011 international conference on document analysis and recognition. IEEE Computer Society, Beijing, China, pp 754–758
10. Yu ZL, Yue DJ, Zu YQ, Chen GL (2010) Word intelligibility testing and TTS system improvement. In: Proceedings of the IEEE 10th international conference on signal processing, IEEE Computer Society, Beijing, China, pp 593–596
11. Sun YQ, Zhou Y, Zhao QW, Yan YH, Wu X (2009) One fuzzy retrieval algorithm for speech navigation system. In: Proceedings of the international conference on bioMedical information engineering. IEEE Computer Society, Sanya, Hainan, China, pp 85–89
12. Su B, Lu SJ, Tan CL (2011) Combination of document image binarization techniques. In: Proceedings of 2011 international conference on document analysis and recognition. IEEE Computer Society, Beijing, China, pp 22–26
13. Zong L, Wu YH (2009) A parallel matching algorithm based on image gray scale. In: Proceedings of the international joint conference on computational sciences and optimization. IEEE Computer Society, Sanya, Hainan, China, pp 109–111

Modeling of High Throughput Screening Systems

Danjing Li, Xiaobin Li, Heng Wan, Bing Xu, and Jianhua Wang

Abstract In this paper we propose a max-plus algebra modeling, which guarantees non-negative order models for any predetermined optimal schedule of high throughput screening systems. Often for such systems, some events in previous batches are expected to happen after certain events in later batches. Therefore there are negative order system matrices in the corresponding models. With a straightforward re-indexing process, the proposed modeling avoids searching and calculating of transformation matrix and thus derives non-negative order models directly and quickly.

Keywords High throughput screening systems • Max-plus algebra • Modeling

1 Introduction

High throughput screening (HTS) systems [1] are used in fields of biology, chemistry and especially in pharmaceutical industries to automatically identify biochemical and/or chemical compounds. In a very short time, HTS processes are able to automatically screen thousands of substances. In such processes, hundreds of substances are aggregated within one batch. A large number of batches have to pass through resources (e.g., incubators, pipettes) to finish all activities or work steps.

In order to compare many different batches of an assay, it is often required that each batch follows an identical time scheme. In other words, HTS systems are operated in a strictly cyclic way. Although cyclic operation is sometimes also

D. Li (✉) • X. Li • H. Wan • B. Xu • J. Wang
School of Electrical and Electronic Engineering, Shanghai Institute of Technology, Shanghai, China
e-mail: skya_22@sina.com

W. Wang (ed.), *Mechatronics and Automatic Control Systems*, Lecture Notes in Electrical Engineering 237, DOI 10.1007/978-3-319-01273-5_50,

applied to other discrete event system (DES) applications such as manufacturing or chemical engineering, the HTS scheduling problem and its control still differ from problems of those systems [2]. For example, there may be upper and/or lower time bounds for batch time scheme. Especially, in HTS systems, resources may be shared by several batches and may be revisited several times by the same batch. Moreover, there are no buffers between the resources. Mayer, Raisch and colleagues proposed a method to determine the globally optimal schedules for such systems [1, 2]. With max-plus algebra, it is then possible to model the predetermined optimal schedule to perform further system analysis and control.

Often for such optimal schedules of HTS systems, some events in previous batches are expected to occur after certain events of later batches. This results in negative order system matrices in the corresponding models. By introducing the γ transformation [3, 4], the existing negative order system matrices could be eliminated with the help of some certain transformation matrix $\mathscr{T}$.

However, in this paper, instead of searching for the corresponding transformation matrix $\mathscr{T}$, we especially discuss a straightforward re-indexing process to model predetermined schedules for HTS systems. For a predetermined HTS optimal schedule, by appropriately re-indexing the events of the considered system, the improved modeling avoids searching and calculating of transformation matrix $\mathscr{T}$. Therefore, the proposed modeling derives non-negative order model directly and quickly.

This paper is structured as follows. Section 2 briefly describes the basic ideas of max-plus algebra. Illustrated with an HTS application presented in Mayer and Raisch [2], the specifications for high throughput screening systems and the modeling of predetermined time schedules with max-plus algebra are explained in Sect. 3. In Sect. 4, an improved modeling idea avoiding negative order system matrices is provided. Conclusions and suggestions for future work are included in Sect. 5.

2 Max-Plus Algebra

Max-plus algebra [3] is a convenient tool to model and analyze timed DES. The DES timing often involves maximum and addition operations. The equations describing the behavior of the system are nonlinear in the conventional algebra, but are linear in the sense of max-plus algebra. Max-plus algebra is the set $\mathbb{R}_{max} = \mathbb{R} \cup \{-\infty\}$, endowed with two operations: *addition* $\oplus$ and *multiplication* $\otimes$. Addition $\oplus$ is defined to be the maximum of two elements in conventional algebra, while multiplication $\otimes$ is defined to be conventional addition, i.e., $\forall a, b \in \mathbb{R}_{max}$:

$$a \oplus b := \max(a, b), \tag{1}$$

$$a \otimes b := a + b. \tag{2}$$

As in conventional algebra, the multiplication symbol is sometimes omitted and $a \otimes b$ is written as $a\ b$. The additive identity (neutral element of addition) in max-plus algebra is $-\infty$, also denoted as ε. The multiplicative identity (neutral element of multiplication) in max-plus algebra is 0, also denoted as e:

$$\forall a \in \mathbb{R}_{max}, a \oplus \varepsilon = \varepsilon \oplus a = a. \tag{3}$$

$$\forall a \in \mathbb{R}_{max}, a \otimes e = e \otimes a = a. \tag{4}$$

Matrix addition in max-plus algebra is defined as:

$$C_{ij} = (A \oplus B)_{ij} = A_{ij} \oplus B_{ij}, \quad A, B, C \in \mathbb{R}_{max}^{p \times q}, \tag{5}$$

while the definition of matrix multiplication in max-plus algebra is:

$$C_{ij} = (A \otimes B)_{ij} = \bigoplus_{k=1}^{m} A_{ik} \otimes B_{kj} = \max_{k} (A_{ik} + B_{kj}), \tag{6}$$

where $A \in \mathbb{R}_{max}^{l \times m}$, $B \in \mathbb{R}_{max}^{m \times n}$, $C \in \mathbb{R}_{max}^{l \times n}$. The *identity matrix* in max-plus algebra is denoted as I, for $i = j$, $I_{i\ j} = e$, for $i \neq j$, $I_{i\ j} = \varepsilon$. The *null matrix* in max-plus algebra is N, $N_{ij} = -\infty$.

Normally, the max-plus algebra model for a noncyclic deterministic DES system has the form of:

$$X = A_0 \otimes X \oplus B \otimes u, \tag{7}$$

$$Y = C \otimes X. \tag{8}$$

System state x_i denotes the earliest possible event time (EPET) of event i, ($i = 1, \quad \cdots \quad n$). $[A_0]_{ij}$, the element of system matrix A_0 represents the minimum time needed from the occurring of event j to the happening of event i. u_i and y_i correspond to earliest happening time instants of certain input and output events respectively. For such a deterministic DES system (which should be implementable), the above implicit model can be transferred into an explicit max-plus algebra model:

$$X = A_0^* \otimes B \otimes u, \tag{9}$$

$$Y = C \otimes X, \tag{10}$$

where

$$A_0^* = [A_0^{n-1} \oplus \cdots \oplus A_0 \oplus I]. \tag{11}$$

3 Modeling of High Throughput Screening Systems

The time scheme for a single batch is determined according to requirements specified by users. An HTS process contains several resources. A single batch has to pass through resources in a fixed sequence to finish corresponding activities. It may also revisit a resource several times. Here we assume that each resource has capacity one, so once a resource is allocated by a batch, it is not possible for other batches to occupy the resource.

To maximize the throughput of an HTS system, usually several batches are operated concurrently to make better use of system resources and the system operation is in a cyclicly repeated fashion. In the following, we first show the modeling for a single batch time scheme.

3.1 Modeling of Single-Batch Time Scheme

For the HTS application discussed in Mayer and Raisch [2], considering the operation requirements, the desired time scheme for a single batch is shown in Fig. 1. For this HTS process, a batch has to finish six activities on a total of three resources: activity 1 to activity 4 allocate resource 1 while activity 5 and activity 6 occupy resource 2 and resource 3 respectively. In other words, resource 1 is revisited by a single batch. The six activities are performed in the following order: activity 1 → activity 5 → activity 2 → activity 3 → activity 6 → activity 4. The starting time (or the ending time) of activity i is not necessarily the entering time o_i (or the leaving time r_i) of the corresponding batch on the resource because there may exist either pre-processing or post-processing time requirements.

For this single batch time scheme, the corresponding precedence graph is shown in Fig. 2. x_i is the earliest possible event time of starting event i (or ending event) for a certain activity. To reduce the complexity of the system model, some entering events and leaving events are omitted from the graph, once x_i is determined, the occurring time of its corresponding entering event (or leaving event) could be easily obtained.

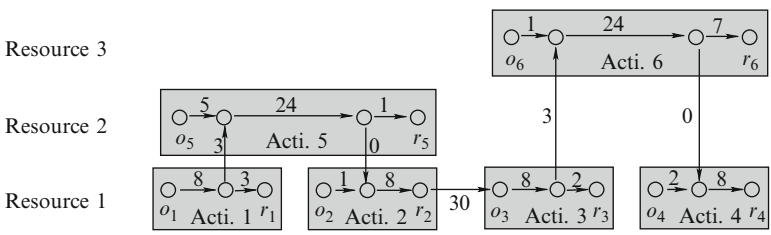

Fig. 1 Time scheme for a single batch

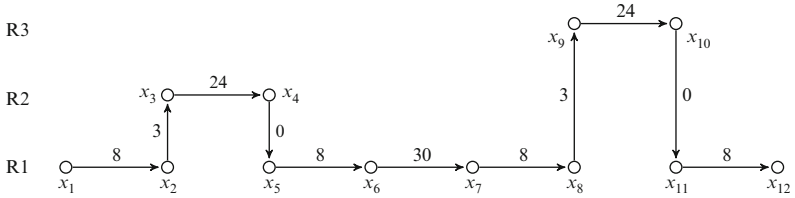

Fig. 2 Precedence graph for a single batch scheme

Since in Fig. 2, all events belong to a same batch, the arcs connecting events are called zero order arcs. $[A_0]_{ij}$, the element of zero order system matrix A_0 is the weight of the arc connecting from event j to event i, specifically, $[A_0]_{2,1} = [A_0]_{6,5} = [A_0]_{8,7} = [A_0]_{12,11} = 8$, $[A_0]_{4,3} = [A_0]_{10,9} = 24$, $[A_0]_{3,2} = [A_0]_{9,8} = 3$, $[A_0]_{5,4} = [A_0]_{11,10} = e$, $[A_0]_{7,6} = 30$, and for all other (i, j), $[A_0]_{ij} = \varepsilon$, i.e., there is no time constraint from event j to event i.

3.2 *Modeling of Cyclicly Repeated HTS*

To maximize the throughput of an HTS plant, obviously it is not optimal to operate the first activity of a single batch always after all activities of its previous batch have been finished. On the contrary, at a certain time instant, several different batches could occupy different resources simultaneously. As represented by a Gantt chart shown in Fig. 3, the optimal schedule derived in Mayer and Raisch [2] is an example of the better use of system resources. Different batches pass through resource 3 (and resource 2 as well) sequentially. Therefore, for resource 3, as shown in Fig. 4, i.e., the corresponding precedence graph for the optimal schedule, there is a first order arc (marked with one small slash " / ") connecting from x_{10} to x_9. The arc represents the fact that the starting event 9 of a later batch $\rho + 1$ happens after the ending event 10 of a previous batch ρ.

On resource 1, according to Fig. 3, different batches share the resource in the following way: the first activity of batch ρ follows the second activity of batch $\rho - 1$ and then is followed by the fourth activity of batch $\rho - 3$ and this activity is then followed by the third activity of batch $\rho - 2$. Correspondingly in Fig. 4, for instance, the negative order arc (marked with three small circles " ∘ ") connecting x_2 and x_{11} ensures the first activity of batch ρ happen before the fourth activity of batch $\rho - 3$. Furthermore, the fourth order arc connecting x_{12} and x_1 always ensures the fourth activity of batch ρ happen before the first activity of batch $\rho + 4$. Compared with Fig. 2, the additional arcs in Fig. 4 ensure safe resource sharing.

Based on Fig. 4, the max-plus algebra model for the optimal schedule shown in Fig. 3 then can be represented as:

$$X(\rho) = \bigoplus_{m=-3}^{4} \left(A_m \otimes X(\rho - m) \right) \oplus Bu, \tag{12}$$

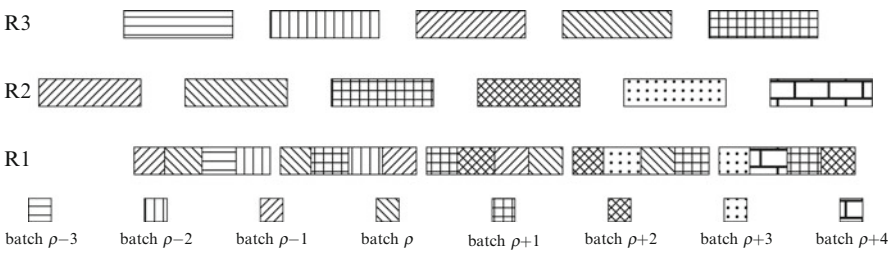

Fig. 3 Gantt chart of the optimal schedule for batches

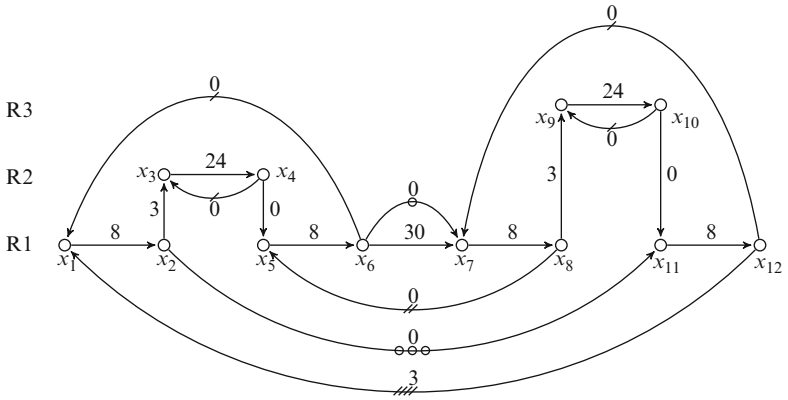

Fig. 4 Precedence graph for the optimal schedule with negative order arcs

$$Y(\rho) = C \otimes X(\rho), \tag{13}$$

where the element of the precedence matrix $[A_m]_{ij}$ is the weight of the m-th order arc connecting from event j of a batch $\rho - m$ to event i of a batch ρ. Specifically, the elements for non-zero order precedence matrices $[A_m]_{ij}, m \neq 0$ are: $[A_{-3}]_{11,2} = 0$, $[A_{-1}]_{7,6} = 0$, $[A_1]_{1,6} = [A_1]_{7,12} = [A_1]_{3,4} = [A_1]_{9,10} = 0$, $[A_2]_{5,8} = 0$, $[A_4]_{1,12} = 3$, for $m = -3, \cdots -1, \cdots 4$ and all other (i, j), $[A_m]_{ij} = \varepsilon$.

With the existence of negative order system matrices, the implicit model (12) is acasual in terms of batches. Unlike the noncyclic case described at the end of Sect. 2, the corresponding explicit model cannot be derived directly from (12). For analysis and control of general DES models with negative order system matrices, one possible solution is to transform the acasual model into a casual one first, with the help of γ transformation and an appropriate transformation matrix $\mathscr{T}$ [4, 5]. In the next section, we propose an easy and fast way, in which γ transformation and the searching for $\mathscr{T}$ are not involved, to model the original system without negative order system matrices directly.

4 Improved Modeling of HTS Systems

In the above derived model (12), with the existing of A_m, $m < 0$, the states for batch ρ, i.e., $X(\rho)$ depends on the states of later batches ($\rho - m$), which is acausal with respect to batch index ρ. To facilitate further analysis and control, it is preferred that HTS systems are modeled so that there are no precedence matrices A_m, $m < 0$.

The sequence of batches performed on resource 3 (or resource 2) is casual, the acasual parts of the system matrices resulted from the acasual visiting sequence of batches on resource 1. However, on resource 1, for each individual activity, as demonstrated in Table 1, the sequence of batches is also casual. For example, after batch $\rho - 1$ finishes activity 2, the next batch to perform activity 2 is batch ρ, then batch $\rho + 1$ and so on.

Therefore, instead of considering all six activities of one single batch, if we appropriately choose and include six different activities from several batches into one group, which is called a "cycle" in Table 1, the resulted system model with new indexing is casual with respect to cycle index.

Suppose for each resource i, the number of its related activities is N_{ri}. In the new indexing system, each cycle is also ensured to contain N_{ri} activities related to resource i. Since only resource 1 is revisited and four out of six activities revisit resource 1, for this HTS system, $N_{r1} = 4, N_{r2} = N_{r3} = 1$. The maximum number of activities performed on resources is

$$N_{mr} = \max_i (N_{ri}) = N_{r1} = 4.$$

For each resource i, we choose N_{ri} activities in such a way that they are consecutive (i.e., no other activity interrupting them) in the Gantt chart. The first resource considered is always the one which has the maximum number of activities, i.e., $N_{ri} = N_{mr}$. Here it is resource 1. Although for a predetermined schedule, the performing order of N_{ri} activities on a resource i is fixed (e.g., for resource 1, the performing order is activity 2 $\rightarrow$ activity 1 $\rightarrow$ activity 4 $\rightarrow$ activity 3 $\rightarrow$ activity 2), there are different options for the selection of N_{ri} activities. As long as the selected N_{ri} activities are consecutive in the Gantt chart, there is no constraint on batch indices of activities. In Table 1, for resource 1, the following N_{mr}, i.e., four activities are included into cycle k: activity 2 of batch ρ, activity 1 of batch $\rho + 1$, activity 4 of

Table 1 Re-indexing events with cycle index

R3	Acti.6	$x_9 \rightarrow x_{10}$	$\rho - 3$	$\rho - 2$	$\rho - 1$	ρ	$\rho + 1$
R2	Acti.5	$x_3 \rightarrow x_4$	ρ	$\rho + 1$	$\rho + 2$	$\rho + 3$	$\rho + 4$
R1	Acti.2	$x_5 \rightarrow x_6$	$\rho - 1$	ρ	$\rho + 1$	$\rho + 2$	$\rho + 3$
	Acti.1	$x_1 \rightarrow x_2$	ρ	$\rho + 1$	$\rho + 2$	$\rho + 3$	$\rho + 4$
	Acti.4	$x_{11} \rightarrow x_{12}$	$\rho - 3$	$\rho - 2$	$\rho - 1$	ρ	$\rho + 1$
	Acti.3	$x_7 \rightarrow x_8$	$\rho - 2$	$\rho - 1$	ρ	$\rho + 1$	$\rho + 2$
Cycle			$k - 1$	k	$k + 1$	$k + 2$	$k + 3$

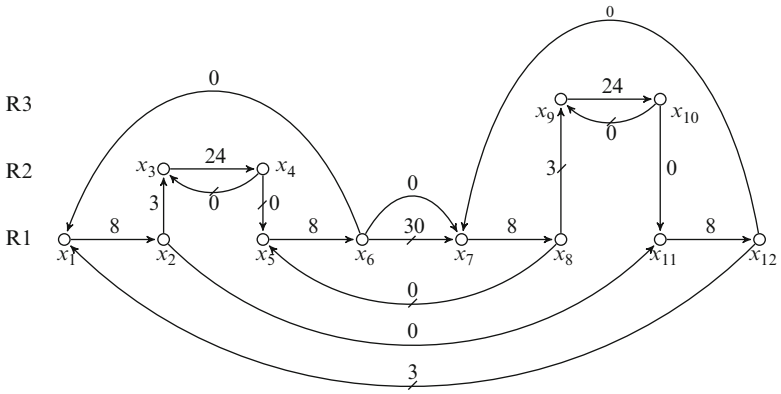

Fig. 5 Precedence graph for the optimal schedule without negative order arcs

batch $\rho - 2$, activity 3 of batch $\rho - 1$. Instead of activity 3 of batch $\rho - 1$, for example, another possible selection could be: activity 3 of batch $\rho - 2$, which is also consecutive with the other three activities.

Once the first N_{mr} activities have been decided to form a cycle k, for each of the rest resources, its corresponding N_{ri} activities (which are consecutive in the Gantt chart if $N_{ri} > 1$) are selected from the ones occurring right before or right after any of the first N_{mr} activities, if not simultaneously. Normally, they have same batch indices as those of the first N_{mr} activities, for there are no buffers between resources, e.g., for resource 2 and resource 3, cycle k contains activity 6 of batch $\rho - 2$ and activity 5 of batch $\rho + 1$. Among all these six activities which belong to different batches, activity $1 \sim 4$ relate to resource 1, since they are all indexed with cycle k, no negative order system matrices are needed in the new model.

On the other hand, activities used to be in one single batch now could belong to different cycles. For example, in Table 1, activity 2 and activity 5 of batch ρ are indexed with cycle k and cycle $k - 1$ respectively, the zero order arc connecting from x_4 to x_5 in Fig. 4 now should be of first order, as shown in Fig. 5, i.e., the corresponding precedence graph for the new model. With the cycle indexing shown in Table 1, this precedence graph devoid of negative order arcs can be derived directly from the Gantt chart shown in Fig. 3. It can be seen from Table 1 that based on Fig. 4, if we perform the following procedure, we also get Fig. 5: decrease the batch index of $x_1 \sim x_4$ by one batch and denote it with the new cycle index (i.e., $\rho + 1 \rightarrow k$), furthermore, increase the batch indices of $x_7 \sim x_8$ and $x_9 \sim x_{12}$ by one batch and two batches (i.e., $\rho - 1 \rightarrow k$ and $\rho - 2 \rightarrow k$) respectively, and finally remain the batch index of the rest x_i (i.e., $\rho \rightarrow k$).

Figure 5 consists of zero order arcs and first order arcs. Thus the new model contains only A_0 and A_1:

$$X(k) = A_0 X(k) \oplus A_1 X(k-1) \oplus Bu, \tag{14}$$

$$Y(k) = C \otimes X(k). \tag{15}$$

Of course, here A_0, A_1, B and C are different from the ones in (12) and (13), e.g., now $[A_0]_{5,4} = \varepsilon$ while $[A_1]_{5,4} = e$. Furthermore, as the noncyclic case, the implicit model of (14) and (15) can be transformed into the following explicit model:

$$X(k) = A_0^* \otimes A_1 \otimes X(k-1) \oplus A_0^* \otimes B \otimes u, \tag{16}$$

$$Y(k) = C \otimes X(k), \tag{17}$$

For any predetermined implementable schedule of an HTS system, regardless of the number of revisited resources and the number of activities performed on such resources, the improved modeling guarantees non-negative order precedence matrices. With model (16) and (17), it is straightforward and easy to perform system analysis, simulation and control.

5 Conclusion

This contribution proposed an improved max-plus algebra modeling for predetermined optimal schedules of a class of specific DES systems, i.e., high throughput screening systems. For an HTS plant, resources could be revisited by one single batch and also are shared by several batches. Normally, the resulted model contains negative order system matrices and therefore is not convenient for further system analysis and control. With a straightforward re-indexing process, the proposed modeling guarantees non-negative order system matrices.

With the derived non-negative order model of the predetermined optimal schedule, it is then possible for an online supervisory control to ensure safe running of the HTS system. For the control framework, one aspect that will be considered in the future is how the throughput can be increased under disruptive environments.

Acknowledgements This work is partially supported by the Key Project of Shanghai Science and Technology Commission (Grant No. 11510502700) and the Innovation Project of Shanghai Municipal Education Commission (Grant No. 12ZZ189).

References

1. Mayer E, Haus U-U, Raisch J, Weismantel R (2008) Throughput-optimal sequences for cyclically operated plants[J]. Discret Event Dyn Syst 18:355–383
2. Mayer E, Raisch J (2004) Time-optimal scheduling for high throughput screening processes using cyclic discrete event models[J]. Math Comput Simul 66:181–191

3. Baccelli F, Cohen G, Olsder GJ, Quadrat J-P (1992) Synchronization and linearity: an algebra for discrete event systems[M]. Wiley, New York
4. Geyer F (2004) Analyse und optimierung zyklischer ereignisdiskreter systeme mit reihenfolgealternativen[D]. Diplomarbeit, IFAT, Otto-von-Guericke-Universität Magdeburg, Magdeburg
5. Li D (2008) A hierarchical control structure for a class of timed discrete event systems[M]. PhD thesis, Fachgebiet Regelungssysteme, Technische Universität Berlin, Berlin

Power Management Strategy of Low Voltage DC Micro Grid

Ming Lei, Yue Guo, and Kai Ding

Abstract In order to improve the efficiency and safety of the utilization of user-invested small scale renewable distributed generation (RDG), a structure of multi level DC micro grid based on the load classification, and corresponding stabilizing strategy were proposed in this paper. The methods of load classification and multi-level grid are introduced to design the structure of DC micro grid. Three flexible operational modes of the structure and corresponding stabilizing strategy in grid mode based on the calculation of real-time status of user-level micro grids were discussed. A minimum test bench with two users was established, and a LabVIEW-based control system consists of supervisory terminal and main controller was designed for test and illustration. The results showed that the system can track the changes of status such as varying the loads and irradiance, and keep the bus voltage of the micro grid within a pre-set range.

Keywords Photovoltaic • DC micro grid • Power management • Distributed power resource

1 Introduction

In recent years, modern industries are exhausting the fossil energy, such as crude oil, coal, and natural gas, and the consuming of fossil energy will result in severe environmental problems. In this case, the renewable distributed generations (RDG), with PV arrays and wind turbines as the representatives [1, 2], are playing a more important role in the global energy market.

As we know, small-scale standalone RDG systems are inefficient, and connecting the RDGs directly to the distribution grid, however, will degrade the

M. Lei (✉) • Y. Guo • K. Ding
Electric Power Research Institute, Hubei Electric Power Company, Wuhan, China
e-mail: hbeptriyf@126.com

W. Wang (ed.), *Mechatronics and Automatic Control Systems*, Lecture Notes in Electrical Engineering 237, DOI 10.1007/978-3-319-01273-5_51,

stability and quality of power supply due to the unreliability and unpredictability characteristics of renewable energy. Thus, connecting the small-scaled distributed RDGs to a node with local loads and energy storage devices, to form a micro grid system [3] becomes a commonly used approach to improve the efficiency of the renewable energy and reduce the dependence of fossil energy [4].

The commonly used structures of micro grids are single-leveled, which confined the utilization of RDGs to one specific operational mode. If the requirements of such mode cannot be satisfied, the whole system will be out of service.

Micro grid can be classified as AC micro grid and DC micro grid [1]. In low-voltage cases, the DC micro grids are more efficient, less complicated, and safer than AC micro grids as described in [1, 2].

Therefore, in this paper, a multi-level DC micro grid structure designed for low-voltage DC micro grid connecting user-invested RDGs and household appliances together, and the flexible operational modes of this structure were proposed, and related stabilizing strategy in grid mode was discussed. The test results verified the feasibility and the performance of this strategy.

2 Multi Level DC Micro Grid Structure

2.1 Structure Introduction

The proposed structure of DC micro grid is shown in Fig. 1. The micro grid consists of a community-level micro grid and several user-level micro grids, the former is a bus that connects all the user-level micro grids together, and the latter are double-bus structures serving as intermediates of municipal distribution grid, community-level micro grid and the users' appliances.

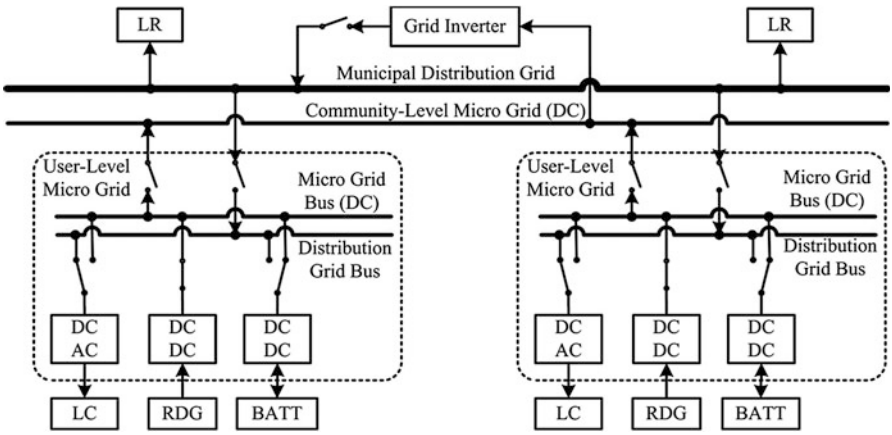

Fig. 1 Multi level structure of DC micro grid

Users' appliances include RDGs, loads, and batteries (BATTs). The loads can be classified as regular loads (LRs) and compatible loads (LCs), while the LRs refer to the loads that require high power quality and reliability, such as air conditioner, and the LCs refer to the loads that are more compatible with various sorts of power supply, such as electronic digital appliances.

Distributed grid bus and micro grid bus are connected separately to municipal distribution grid and community-level micro grid via breakers.

LCs and BATTs are connected to the double bus via DC/AC inverters, DC/DC charge/discharge controllers and switches, while the RDGs are connected only to the micro grid bus via DC/DC stabilizers and breakers. LRs are plugged directly into distribution grid to acquire high-quality power.

The one-way power transmission from community-level micro grid to distribution micro grid can be implemented via grid inverter and breaker. The transmission only occurs when the output of inverter meets the synchronization requirements of distribution grid.

2.2 Operational Modes

There are three operational modes of the above mentioned micro grid structure as followed:

1. Standalone mode: users may choose to isolate the user-level micro grid from the community level micro grid, and local controller operates the micro grid. If the RDG is not available, LC can be instantly switched to distribution grid bus.
2. Grid mode: if majority of the LCs are in service, users may choose to join the community level micro grid and share the power with other users. All the RDGs, LCs, and BATTs are connected to micro grid bus. The distribution bus is serving as backup power.
3. Feedback mode: if few LCs are in service, the system will decide to feedback the energy to distribution grid, the grid inverter converts the DC power to AC power and adjust to meet the synchronization requirements, while the LCs are connected to distribution grid to acquire the AC power.

2.3 Components Description

As shown in Fig. 1, the main parts to build a micro grid are converters and switches, which are described as followed:

1. DC/DC regulators and charge/discharge controllers are utilized in the middle of DC micro grid bus and RDGs/BATTs, to ensure the output power to the bus keep a certain voltage. Buck and Boost structure are commonly used in the DC/DC voltage conversion devices [5].

2. DC/AC inverters are utilized to convert DC power from DC micro grid bus to AC power to serve the household appliances.
3. Switches in the DC micro grid are SPST and SPDT, which are controlled by system controller. Relays are usually used in automated micro grid systems.

3 DC Micro Grid Stabilizing Strategy

Although the DC/DC stabilizer is capable of clamping the voltage of micro grid bus within a certain range, as described in Sect. 2, the output power of RDGs, which is mainly depend on weather conditions, cannot be as easily controlled as traditional power plant. Thus, the switches of LCs and RDGs should be adjusted dynamically.

The strategy is described in Fig. 2, all the status data of user-level micro grids, including voltage U_{bus}, load current I_L, and power current I_G, are firstly collected and organized periodically to form a node list, which is real-time updated. Then the output power of RDG P_{Gi} and the power of load P_{Li} of each node can be calculated as Eq. 1.

$$P_{Gi} = U_{bus} \times I_{Gi}; P_{Li} = U_{bus} \times I_{Li} \tag{1}$$

If the power of RDGs in the micro grid is insufficient to supply all the LCs, the output voltage of DC/DC stabilizer will drop down according to the voltage regulation [6] and MPPT algorithm [7]; the deviation of bus voltage from the pre-set value ΔU_{bus} is used to estimate the power shortage P_S, as described in Eq. 2.

$$P_S = \left(U'_{bus} - U_{bus}\right) \times \sum I_{Li} = \Delta U_{bus} \times \sum I_{Li} \tag{2}$$

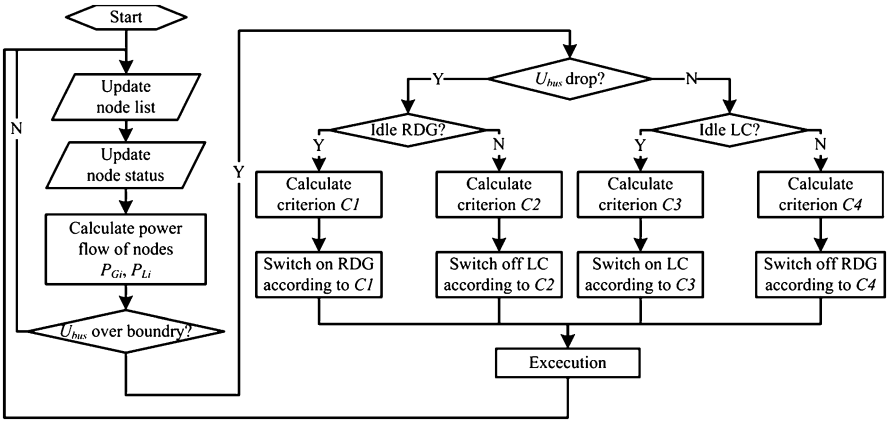

Fig. 2 Flowchart of the stabilizing strategy

The strategy traverses the node list for appropriate idle RDG to activate according to criterion C1 in Eq. 3, which means the power output of chosen RDG P_{Gc}, which can be estimated as Eq. 4, minimally outnumbers P_m. If all the RDGs in the list are activated, the system determines appropriate LC to be switched off according to criterion C2 in Eq. 5 similar to Eq. 3.

$$C1 = MIN(P_{Gc} - P_S) \tag{3}$$

$$P_{Gc} = U_{mppt} \times I_{mppt} \times \eta \tag{4}$$

$$C2 = MIN(P_S - P_{Li}) \tag{5}$$

If there is an excess of power supply in the micro grid, a voltage rise will be detected by the system. Similarly, the power residue P_R is calculated, as described in Eq. 6.

$$P_R = \left(U'_{bus} - U_{bus}\right) \times \sum I_{Li} = \Delta U_{bus} \times \sum I_{Li} \tag{6}$$

Then the strategy traverses the node list for appropriate idle LC to plug in, according to criterion C3 in Eq. 7, which means the power residue minimally outnumbers the power consuming of chosen LC P_{Lc}, which can be estimated as the apparent power of the LC as in Eq. 8. If there is no idle LC, an appropriate RDG is to be chosen to be switched off according to criterion C4 in Eq. 9.

$$C3 = MIN(P_R - P_{Lc}) \tag{7}$$

$$P_{Gc} = U_{ac} \times I_{ac} \tag{8}$$

$$C4 = MIN(P_{Gi} - P_R) \tag{9}$$

4 Simulation Test System Design

The minimum test bench consists of two users with PV arrays, DC/DC regulators, relays and control system. In this test bench, paralleled DC bulbs and single phase off-grid inverters are used as DC loads. The components used in the system are listed in Table 1. The interface of the test system is shown in Fig. 3.

The control system is designed based on the platform of LabVIEW. Compact RIO modules are used to sample the status data of each user node, including analog statuses U_{bus}, I_L, I_G, I_{ac}, etc., digital statuses of the relays, and sensor statuses of irradiance and temperature. The implementation of the strategy is in the module of LabVIEW.

Table 1 Components parameters

Device type	Parameters	Remarks
PV module	Peak power P = 40Wp Short circuit current Is = 2.56 A Open circuit voltage Vo = 21.5 V MPPT voltage Vp = 17.5 V (25 °C) MPPT current Ip = 2.33A (25 °C)	User A & B
DC/DC regulator	MPPT enable Voltage regulation VR = 5 % Convert efficiency η = 90 % Preset min bus voltage V_{min} = 9.6 V Preset max bus voltage V_{max} = 10.4 V	User A & B
Loads	DC bulbs Single phase inverters	User A & B
Relay	Operate voltage Vop = 5 V	User A & B

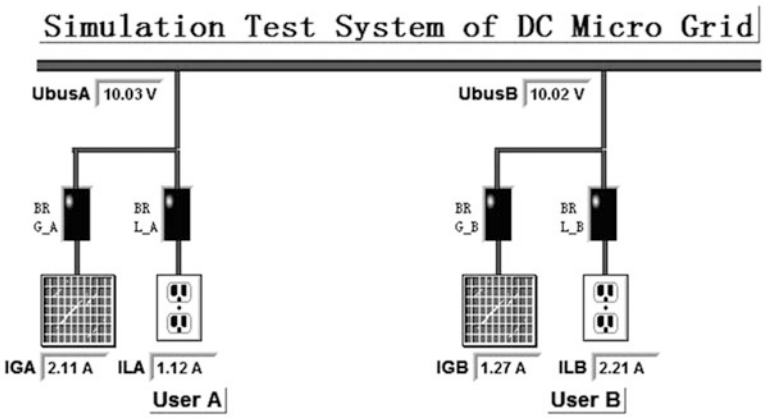

Fig. 3 Interface of simulation test system

The DC/DC regulator of user A is assigned to be the voltage anchor, the output voltage is the reference of U_{bus}, and the counterpart of user B use the MPPT to supply the maximum power to the micro grid. The irradiance to PV arrays is varied to simulate the situation of weather condition. The loads that connected to DC power adaptor are plugged or unplugged to simulate the variation of LCs.

Initially, all the switches in the test bench are OFF state, the RDGs and loads are not connected to the bus. Then the strategy is enabled, the RDG of user B is chosen by the system to be put in service, and then the load of user A is plugged in to pull the bus voltage that over the upper limit back to the preset range, as shown in Fig. 4a.

Since the load of user A is gradually increased, the output power of MPPT could not satisfy all the loads, the bus voltage is pulled below the lower limit, as shown in

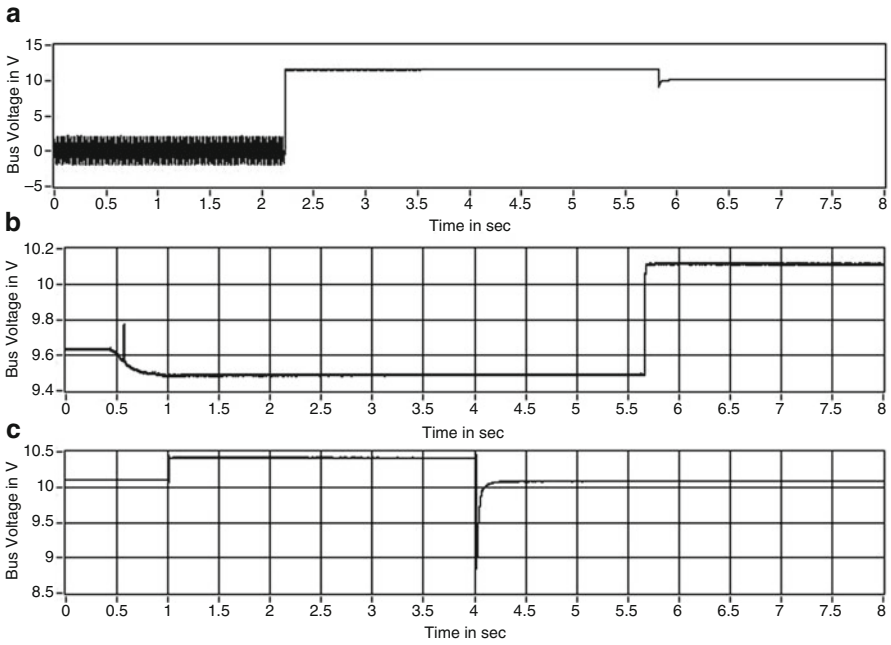

Fig. 4 Simulation results

Fig. 4b, since all the RDGs are in service, the load of user B is chosen to be switched off the micro grid, and the bus voltage is back in range.

Then part of the load of user A is cut off from the micro grid, as shown in Fig. 4c, the bus voltage is over range, load of user B is chosen to be plugged in to pull the bus voltage back in range.

5 Conclusion

Renewable distributed energy is a good solution to the world energy shortage situation. In order to solve the inefficiency and instability problem in the renewable energy utilization, a kind of multi level structure of DC micro grid based on the load classification, with three flexible operational modes that can be altered aiming at the best cost-effective goal, was proposed in this paper. A corresponding strategy that manages the power of the DC micro grid was also proposed, and implemented on the platform of LabVIEW. A simulation test bench with PV arrays, DC/DC regulators, and DC loads was established to test the performance of the efficiency. The results showed that the strategy can work effectively in maintaining the DC micro grid stable.

References

1. Lasseter RH, Paigi P (2004) Microgrid: a conceptual solution. In: 35th annual IEEE power electronics specialists conference, IEEE, Aachen, Germany, pp 4285–4290
2. Xu She, Srdjan Lukic, Alex Q. Huang (2010) DC zonal micro-grid architecture and control. In: 36th annual conference on IEEE industrial electronics society, IEEE, Glendale, USA, pp 2988–2993
3. Stan Mark Kaplan, Fred Sissine (2009) Smart grid: modernizing electric power transmission and distribution. The Capitol Net Inc, Alexandria, USA, pp 412–414
4. Beatriz Cancino, Eduardo Galvez, Pedro Roth, Alexis Bonneschky (2001) Introducing photovoltaic systems into homes in rural chile. IEEE Technol Soc Mag 79(1):29–36
5. Kakigano H, Miura Y, Ise T, Uchida R (2006) DC voltage control of the DC Micro-grid for super high quality distribution. In: 37th annual IEEE power electronics specialists conference, IEEE, Jeju, Korea, pp 1–7
6. Lee J, Han B, Seo Y (2011) Operational analysis of DC micro-grid using detailed model of distributed generation. In: 8th international conference on power electronics, IEEE, Jeju, Korea, pp 248–255
7. Wei Jiang, Yu Zhang (2011) Load sharing techniques in hybrid power systems for DC microgrids. In: Power and energy engineering conference (APPEEC), 2011 Asia-Pacific, IEEE, pp 1–4

Manipulation of Pneumatic Components in Microfluidic Chips by Circuit Based on Single-Chip Microcomputer

Xiaona Sun

Abstract In order to control and drive the pneumatic components in the microfluidic chips for the complicated manipulation of the fluid in the microchannels, a control system based single-chip microcomputer is introduced in this paper. This system could provide an integrated approach to control several pneumatic components in the microfluidic chips simultaneously by the circuit design and programming. The microchannels, micro valves and micropumps integrated in one chip could be controlled by the system through press keys and solenoid valves. The fluid in the microchannels is selected or driven with the actions of the micro components. The pulsatile characterization of the fluid driven by the system is also analyzed. This circuit can make it easy to control the fluid in the microfluidic chips in a simple and robust way. And it could extend to different microfluidic platforms for complicated applications.

Keywords Microfluidic chips • Single-chip microcomputer • Microfluidic control • Micro valves

1 Introduction

Microfluidic chips have been an attractive platform for biochemical application since they appeared in the 1980s, because of their characterizations of miniaturization, integration, automation, process controllability, regent saving et al. [1, 2]. They are fabricated by micro-electro-mechanical systems (MEMS) and equipped with channel networks of micro or nano scale, where all the manipulations and reactions performed.

X. Sun (✉)
School of Electrical and Electronic Engineering, Shanghai Institute of Technology, Shanghai, China
e-mail: nataliesun@sit.edu.cn

W. Wang (ed.), *Mechatronics and Automatic Control Systems*, Lecture Notes in Electrical Engineering 237, DOI 10.1007/978-3-319-01273-5_52,

The fluid in these microchannels is the key element in the application of microfluidic chips because all the information is contained there. So it is important to explore technologies to control the fluid in the microfluidic chips, such as peristaltic pumps, syringes, electric field and so on. However, these technologies are limited by the fact that they do not consider the integration with microfluidic chips.

With the development of microfabrication, it prefers to use the microstructures integrated in the chips to control the fluid, such as micro valves and micro pumps [3]. They can control the fluid more precisely and flexible. The more complex the experiments are, the more valves and pumps they need [4]. So it is a challenge to operate these components accurately. And the structures of the microfluidic vary according to different applications. But there is not a universal platform for these requests. In this paper, we introduce a control unit based on single-chip microcomputer for the manipulation of the microvalves and micropumps integrated in the microfluidic chips. Single-chip microcomputers worked as the programmable units have been widely used for control and information processing. Here, the specially designed circuit board includes independent keys, which were used to control the corresponded microstructure to drive the microfluidic inside the chip. This system is of good stability and maneuverability. And it is also easy to upgrade to control more units or perform other actions for different systems and applications. The characteristics of the fluidic driven by the pneumatic components in the microchannels is also analyzed.

2 System Design

2.1 Working Principle

Pneumatic microvalves and micropumps fabricated by soft lithography are simple and robust ways to move fluids in the microfluidic chips [5]. They consist of several microchambers connected in series. When the air is compressed into or released from these chambers sequentially, the thin film between microchamber and microchannel is deformed to drive fluids. These pneumatic devices are requested to be manipulated separately and continuously at different working frequency. So it needs a control unit to manipulate these components. The circuit based on a single-chip microcomputer will satisfy this requirement easily. Each pneumatic device corresponds to a button, which can send a command to the single-chip microcomputer. The control unit can be extended to different kinds of platforms for the manipulation of fluids in the microchannels.

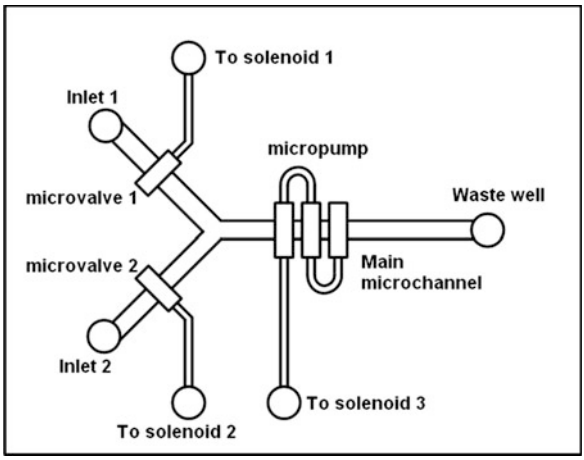

Fig. 1 Schematic illustration of the Y-shaped microfluidic chip

2.2 System Architecture

The system consists of two parts: one is the microfluidic chip with microchannels, micropumps and microvalves fabricated by MEMS technology; and the other is the control unit based on single-chip microcomputer for the manipulation of the pneumatic device in the microfluidic chip.

The microfluidic chip is the classical *Y*-shape microchannel structure as shown in Fig. 1. There are two inlet wells to load different reagents and an outlet well to storage waste reagent. In order to choose different reagent to flow into the main microchannel, a pneumatic microvalve locates on each inlet microchannel. On the main microchannel, a pneumatic micropump locates there to move fluid in the whole chip.

There are three separated pneumatic components that need to be controlled to charge or release air. Each of the pneumatic component is connected a nitrogen cylinder by a three-way solenoid valve. If the solenoid is energized, the compressed air flows into the corresponded microchamber in the chip. And if it is not energized, the microchamber connects with the atmosphere, and then the compressed air flows out from the chip. In particular, the micropump needs to repeat the process continuously to make the fluids flow in the chip. So the corresponded solenoid valve should be driven by a continuous pulse signal. In order to satisfy these requirements, we develop a general platform for easy and reliable manipulation of the pneumatic components.

The platform is a control circuit, which use a sing-chip microcomputer, STC90C516RD + (Hongjing Technology, Guangdong), as the control unit. Because the microcomputer is low power device, it can't drive solenoid valve directly. So we use a ULN2003 chip and electric relay to solve the problem, which also can isolate the disturbance for these electronic components. Then the orders from the keys can transfer to the solenoid valve through the single-chip

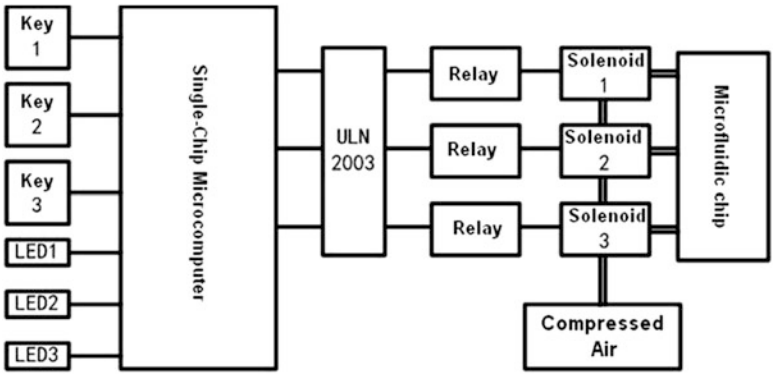

Fig. 2 Schematic illustration of the system architecture of the control unit

microcomputer. And the system architecture is shown in Fig. 2. The LEDs indicate the working states of different pneumatic components in the microfluidic chip.

3 Experiments

3.1 Microfluidic Chip Fabrication

The microfluidic chip is fabricated by well established photolithography and micromolding methods [6]. According the design, the chip consists of three layers, the upper polydimethylsiloxane (PDMS) layer for pneumatic micropumps and microvalves, the middle PDMS layer for fluid circulation and cell culture, and the bottom glass layer for bonding. First, two SU-8 structures are fabricated on silicon wafers, one is the Y-shape microchannel, and the other is the pneumatic microchambers. Then the well mixed PDMS is poured on the master and cured in an oven. Then the PDMS layers with embossed surface pattern are peeled off and cut down to size. And the inlets and outlets for the fluids are punched out by sharpened blunt-tip needles. Then the two layers of PDMS are bonded by an oxygen plasma treatment. In the end, the glass substrate is bonded with these PDMS layers to form the sealed microchannels.

3.2 System Programming

According to the system architecture, the single-chip microcontroller should be configured by the program. It continuously processes the information from the keys and generates output commands to the relevant solenoid valve by the ULN2003 and

the electric relay to choose the inlet and drive the fluids flow in the microchannels. And the LEDs also indicate the work status of each component. All the programs are written by C language, and then stimulated and compiled in Keil C. Finally, the compiled program is downloaded to the STC90C516RD + single-chip microcontroller through the serial port of the computer. Then the microcontroller can identify the different keys. When the key 1 or key 2 is pressed, the solenoid 1 or solenoid 2 will be turned on or off. The compressed air is charged into the microvalves to cut off the fluid or the air is release to restore the flow. Because the fluid flow in the microchannel must be driven be the continuous charging and releasing air in the micropump, the signal from the microcontroller for the selonoid is the pulse signal. And the working frequency can be easily changed in the program to drive the fluid flow in the different flow rate. When the key 3 is pressed, the solenoid 3 will turned off or turned on and off continuously by the electronic pulse signals from the microcontroller, while the LED3 is dark or blinking at a certain frequency.

4 Results

4.1 Fluidic Drive and Flow Rate Analysis

The Y-shape microfluidic chip can be worked as a mixer or a selector. We can press key 1 or key 2 to activate the microvalves on the inlet channels to select one reagent into the main microchannel. We also cannot activate any microvalves to select both of the reagents. Then we press the key 3 to activate the pneumatic micropump to drive the fluids flow in the microchannel. The LED 3 will blink at the same frequency with the pulse signal. So it is easy to control the component integrated in the microfluidic and indicate their working state separately. Although the control unit is very simple, it can also be extend to control more devices. Only a part of the pins of the microcontroller are used, the free pins can be used for more solenoids and keys. The program is easily be modified for the complex control.

Pneumatic micropumps have been efficient driving equipments in the microfluidic chips. Because the volume driven by the micropump is definite in one working cycle, the pumping performance is dependent on the working frequency. We measure the flow rate in the microchannel with the working frequency between 0 and 3.0 Hz. Their relationship is shown in Fig. 3. The pressure of the compressed air is 0.1 MPa. The flow rate at 2 Hz is about 5 nL/s. The flow rate driven by the pump in the microchannel increases with the working frequency becomes higher. But it is not entirely linear relationship as shown in the figure. With the frequency increases, the growth of the flow rate is become lower. This is relevant to the properties of the PDMS. The PDMS is flexible material, and it takes a certain amount of time to regenerate the deformation. The interval between the two pulses becomes short with the frequency increase, which is not enough to completely regeneration. This may contribute to the lower flow rate growth. If the

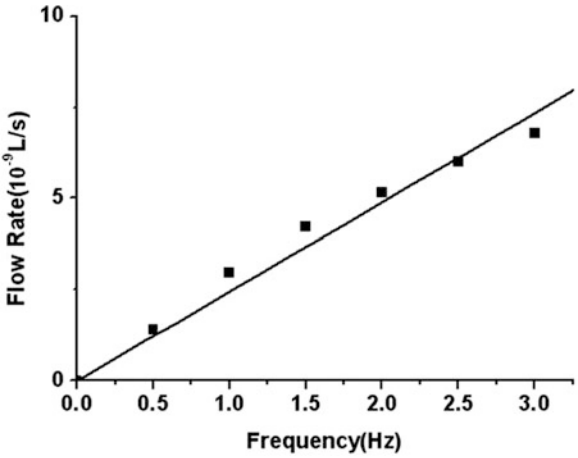

Fig. 3 Relationship between the flow rate and working frequency of the pneumatic micropump

working frequency becomes higher, the flow rate is not inexorably going up. We must adjust the frequency on the solenoid to meet the conditions of flow rate for analysis. This can be easily achieved by the control unit, which is an advantage of the system.

4.2 Flow State Analysis

The control unit based on the single-chip microcomputer works well to drive the fluid in the microfluidic chips. But the fluids flow driven by the pneumatic micropump show different feature in the microchannel. The flow state is not uniform velocity, not the same as the fluids driven by the syringes. The flow shows pulsatile characterization in the microchannel. In order to analyze the flow feature, we infuse the medium with suspending cells. The cells can flow with the fluids and indicate the flow feature. The motion tack of the cells following the fluids is shown in Fig. 4, and the working frequency is 1Hz. Before working, the cell locates at the zero point. As shown in the figure, in each cycle it moves forward and backward. But the forward distance is longer than the backward distance, the cell is moving forward. The pulsatile characterization is resulted in the working principle of the pneumatic micropump. In a cycle the microchambers of the pump are activated by charging and releasing compressed air. On a micro level, it doesn't work in a steady state. This instability is indicated by the fluids in the microchannel. Except the fluids flowing, the pulsatile shows the advantage in some fields. For example, it improves the efficiency of the mixer. And it also can simulate the situation inside the blood vessel.

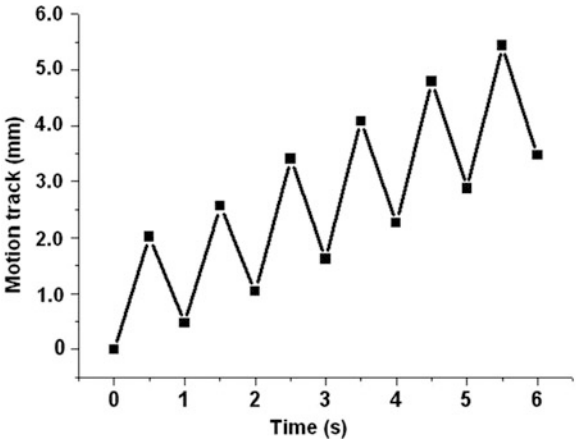

Fig. 4 Cell motion tack with the flow driven by the micropump

5 Conclusion

This paper introduced a control unit based on a single-chip microcomputer for the manipulation of the fluid in the microfluidic chips. It can be used to control the pneumatic micropumps and microvalves assembled in a Y-shaped microfluidic chip. It shows the characterizations of convenience and stability. Especially, the control unit is a universal platform for the manipulations of the pneumatic component in the microfluidic chips. It can be easily extended to other microfludic platforms by updating the program downloaded in the single-chip microcomputer. The flow rates in the microchannel and their relationship with the working frequency were analyzed as well. In some frequency range, they showed a linear relationship. We also study the flow state driven by the pneumatic micropump, which shows pulsatile motion state. This additional feather shows potential values in the future applications.

Acknowledgements This work was supported by grants from Science and Technology Commission of Shanghai Municipality (Grant No. 11510502700), Shanghai Municipal Education Commission (Grant No. 12ZZ189).

References

1. Reyes DR, Iossifidis D, Auroux PA et al (2002) Micro total analysis systems. 1. Introduction, theory, and technology. Anal Chem 74(12):2623–2636
2. Whitesides GM (2006) The origins and the future of microfluidics. Nature 442(7101):368–373
3. Unger MA, Hou-Pu Chou, Todd Thorsen et al (2000) Monolithic microfabricated valves and pumps by multilayer soft lithography. Science 288(5463):113–116
4. Wang CH, Lee GB (2005) Automatic bio-sampling chips integrated with micro-pumps and micro-valves for disease detection. Biosens Bioelectron 21(3):419–425

5. Chen CT, Lee GB (2006) Formation of microdroplets in liquids utilizing active pneumatic choppers on a microfluidic chip. J Microelectromech Syst 15(6):1492–1498
6. Sia SK, Whiteside GM (2003) Microfluidic devices fabricated in poly(dimethylsiloxane) for biological studies. Electrophoresis 24(21):3563–3576

A Summary of Line Selection in Single Phase Earth Fault System

Zhixia Zhang and Xiao Liu

Abstract Single-phase-to-earth fault is the most common fault in distribution network. To perfect the existing fault line selection methods and enhance their accuracy in small current grounding system, research on the accuracy of selecting fault feeder has been conducted by many experts in relay protection field. This paper analyzes those common methods on selecting fault line in phase-to-ground system, and summarizes their advantages and shortages. Through systematically analyzing, some new study directions about the accuracy of fault feeder selection are advanced to improve the safe power supply level. This paper may have guiding significance for further fault line selection study.

Keywords Distribution network • Single-phase-to-earth fault • Line selection methods

1 Introduction

About 80 % of distribution networks in China are neutral non-effectively grounding system [1]. When phase-to-earth fault occurs, the short-circuit current is too small to constitute low impedance circuit [2]. Such a system is called small current neutral grounding power system [3]. During fault time, the value of fault phase-voltage almost drops to zero while the healthy value rise to the value of line voltage [4, 5]. Rose phase-voltages are potential threats to grid insulation. The fault line must be found and removed as soon as possible. A lot of research on this problem was done by many experts in recent years and some useful methods were put forward too.

Z. Zhang (✉) • X. Liu
Shenyang Agricultural University, Shenyang, China
e-mail: syzzx7@163.com

W. Wang (ed.), *Mechatronics and Automatic Control Systems*, Lecture Notes in Electrical Engineering 237, DOI 10.1007/978-3-319-01273-5_53,

2 Research Situation

Lots of researchers have presented a good deal of methods on fault line selection as there is a single-phase-to-earth fault in non-effective neutral grounding system since the nineteenth century. These methods can be divided into two basic types: steady line selection method and transient line selection method [6].

2.1 Steady-State Detection Method

Steady-state method requires steady-state information of fault current signal and fault voltage signal. Nowadays, steady-state method commonly includes residual incremental method, injection method, comparing amplitude and phase of zero-sequence current method.

2.1.1 Residual Incremental Method

The amplitude and phase of zero-sequence current in fault line are closely related to the compensation of arc suppression coil in the case of single permanent phase earth fault. The damping size of arc suppression coil must be changed to judge the active component change of zero-sequence currents in all lines. The line whose zero-sequence current changed is the fault line. This method can realize fault line selection by detecting changes of zero-sequence current when compensation-degree was changed. a current or voltage time threshold can be set up before fault happens. When the ground fault duration exceeds the set threshold, the fault can be considered as a permanent ground fault [1].

This method can eliminate the influence of Current Transformer (CT), and is useful to select fault feeder. But in isolated neutral system and high impedance neutral system this method is non-effective.

2.1.2 Injection Method

A current signal whose frequency is between n time and n + 1 time of industrial frequency is injected into the grid when phase-to-earth fault occurs. The injected signal flows into the earth along the fault line. Using signal detection and signal tracking, fault selection and location can be realized [7]. The schematic of injection method is shown in Fig. 1.

The line which the injected signal flows into is selected as the fault line. But in this method, the intensity of the injected signal is limited by the voltage transformer capacity. If the grounding resistance is too large, the capacitance of fault lines' will influence the accuracy of fault feeder selection. When intermittent arc grounding

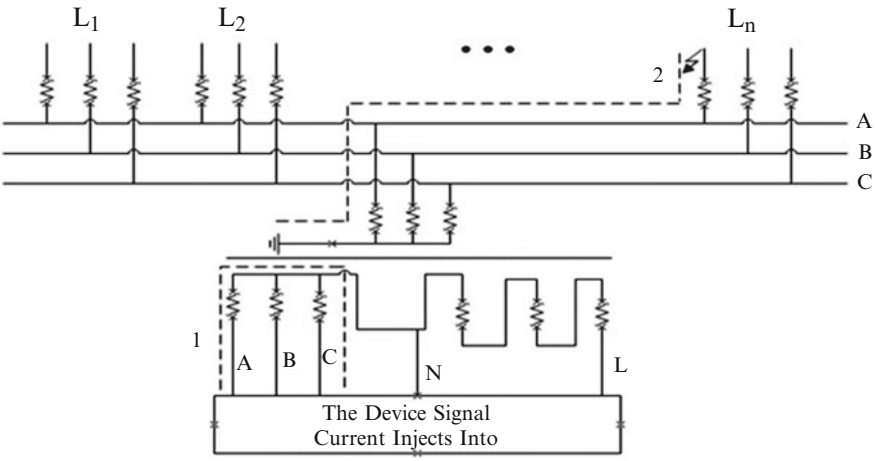

Fig. 1 The schematic of injection method

fault occurs, the detection is not very good because of the ever-changing injected signal [8].

Besides, an additional detecting system is needed which is used to offer the injecting current signal in this method, which may increase the testing cost.

2.1.3 Method of Comparing Amplitude and Phase of Zero-Sequence Current

In this method, several zero-sequence currents with large amplitude need to be collected. Compared the phases of these currents, the line who has opposite phase with others may have fault. If there isn't such a line, then the faulty part is in bus line [1]. This method can make up the deficiency of comparing amplitude or phase respectively but it can't eliminate the wrongly selected rate fundamentally [6]. When single-phase-to-earth fault occurs in system through arc suppression coil, zero-sequence current is changed because of the compensation of arc suppression coil. Amplitude of zero-sequence current in fault line is usually smaller than that in non-fault line at this time. And the phase of fault line is same to non-fault line. The main shortage of this method is it may result in false selection when feeders are short or feeders are earthed through large resistance.

2.1.4 Harmonic Method

The method of comparing amplitudes and phases of zero-sequence currents is not adaptive in neutral earthed via arc extinguishing coil system.

There are lots of harmonic signals in fault current. The most abundant among them is the fifth harmonic current [9]. The compensation offers by arc suppression coil has great influence on zero-sequence current but little on five harmonic. Based on these two factors, the harmonic method can be applied to fault line selection. The amplitude of five harmonic current is large relatively and its phase is opposite in fault line compared with non-fault line [10].

As the five harmonic current is less than fundamental harmonic in zero-sequence current. In order to improve sensitivity of selection, the sums of squares of 3, 5, and 7 harmonic amplitudes in all lines can be compared [11]. In addition, we must to seek an effective method to obtain five harmonic current accurately.

2.2 Transient-State Detection Methods

The transient-state detection methods can select fault feeder by using momentary voltage and current signal. The most famous method is wavelet method.

2.2.1 Wavelet Method

As wavelet analysis has good localizing peculiarity and multi-solution feature in time and frequency domain [12], it is used to analysis transient signals to collect amplitude and phase of zero-sequence current. And it can reflect the relationship of frequency and time domain of transient signals. The wavelet transformation can be applied to obtained fault signals after wavelet transformation of transient zero-sequence current. The difficulty of wavelet method is to choose wavelet decomposition scale and primary function. The choice usually lack of theoretical bases [13].

With the widespread use of nonlinear electrical load such as power electronic equipment in power distribution network, harmonic content in network is greatly increased, which may have great influence on the accuracy of fault line selection. Although lots of research on wavelet method in theory has been done, the application of research achievement is poor.

2.2.2 Method of First-Half Wave

The basic condition of first half wave method is an assumption that the single phase-to-earth fault occurs at the maximum of fault phase voltage [14]. It is acknowledged that the capacitance of fault phase discharges to fault point through fault line. The first half wave of fault line short-circuit current has different direction with normal lines'. This method can detect unstable earthed fault whose polarity relationship exists for a relatively short time. This method requires a high data-sampling rate. Large amount of data is easily affected by some factors, like transmission line parameters, fault initial angles, and so on.

Because of the non-mutation current in arc suppression coil, this method can only be used in non-resonant system. Besides, when the fault occurs nearby zero value of phase-voltage, the transient component current is very small, which may elicit misjudgment of polarity.

2.2.3 Method of Transient Energy of Zero Sequence Current

The integration of 0 model instantaneous power is 0 model energy function. In contrast with correct lines, the amplitude of energy function of the fault line is the biggest and the function polarity is inverse [15]. The fault line selection can be realized from the theory above. However, the biggest defect of transient energy of zero sequence current method is a poor proportion of active component in transient current. This method can't make full use of the information provided by transient signal. The detection sensitivity is low [16].

3 Influence Factors of Accurate Selection

Theories about fault line selection mentioned above are very mature. Those methods can be applied to various kinds of devices which are accurate theoretically but actually they don't perfect in the practical application [17]. There are some reasons shown as follow.

3.1 Different Device Has Different Influence on Fault Line Selection

The influence of devices characteristics on selection's characteristics was summarized up in three aspects.

3.1.1 Different Neutral Grounding Mode

In neutral non-grounding system [18], high impedance neutral system and coil of arc extinction neutral grounding system have extremely different characteristics [19]. For example, earthed current is compensated when neutral grounded system adopts coil of arc earthed way. The earthed current in isolated neutral system is different. That is harmful to extract characteristics of signal [19].

3.1.2 The Unbalance Current's Impacts

The offset voltage resulted from the unbalance parameters of three phases naturally produces unbalance current which is mutable. When single phase earthed fault occurs, not only zero current but unbalance current can be detected. Selection may have mistake if the unbalance current is too large [20].

3.1.3 The Influence of Transformers

The loss of CT excitation current is zero and the current in primary side is equal to secondary side current in amplitude and phase in an ideal state. Actually they are not equal accurately for the existence of excitation current [20].

3.2 The Modelling of Single Phase-Ground Fault Is Difficult

There are types of fault generally summarized as stable ground fault and unstable fault. Stable ground faults include metal ground fault, low resistance ground fault, and high resistance fault. Unstable faults consist of transient arc-ground fault, and unstable arc-ground fault. Therefore, the circumstance is very complex. The modeling which is suitable to all kinds of single phase-ground fault is difficult [3].

4 Future Research Directions

4.1 New Harmonic Method

Compared with traditional harmonic method, new harmonic method adopts effective digital filter or modified phase-locked loop to extract frequency range of harmonic with the highest energy. This method avoids false selection caused by drawing single harmonic frequency [21].

4.2 Mathematical Morphology Method

The mathematical morphology is a nonlinear filtering method based on set theory and integral geometry. Its basic principle is measurement and extraction of structural correspondence in signals and rejection of irrelevant structure through structure element [22]. This kind of measurement and extraction can realize signal analysis and identification [23]. When the single phase earthed fault occurs, this

method can be used to dispose zero-sequence fault currents, like filtering harmonic component, noise, shift [24]. After that, effective fault information can be obtained and fault line can be distinguished by using appropriate algorithm.

4.3 Multi-source Data Fusion Algorithm

With the development of power system, single route selection theory can't satisfy with the demand of system with abnormal complex fault types and variable mode of operations. A technique with a variety of new selection criterions and modern information fusion is essential to improve the robustness and precision of line selection devices [25].

Although there are many multi-source data fusion algorithms, like extension theory [26], neural network and fuzzy theory [27], these methods only stay in theory research levels and have great distance to practical application.

5 Conclusion

From the analysis above, every method has its superiority and shortage. Selection methods based on steady component are usually low-sensitivity, susceptible to electric arc, and lack versatility. Other methods based on transient component are susceptible to harmonic interference and fault occurrence time. Some methods cannot make full use of fault signal. Seeking an universal selection method which may adapt to all kinds of power system or overcoming the shortage of a present selecting method should be studied.

References

1. Liang Rui, Wang Chonglin (2010) Based on fault type comprehensive fault line selection of single-phase base. China Mining University, Xuzhou
2. Jia Qingquan (2007) The ineffective route network grounding protection technology. National Defence Industry Press, Beijing, pp 80–85
3. Cheng Changpeng (2004) Ground wire selection and fault locating with ungrounded neutral. Northeast Electr Power Technol 5(6):6–10
4. Lou Shuqing, Liu Aihua (2009) Small current neutral grounding system fault line selection method. Jiangxi Electr Power 1(33):38–41
5. Li Peng, Yang Qisun (2004) Based on DSP technology of small current locate single-phase grounding device. Electr Power Autom Equip 3(3):51–52
6. Zhang Xinhui (2008) Prony algorithm based on small current grounding fault line selection technology. Shandong University, Jinan

7. Cusido J, Rosero J, Romera L (2006) New techniques for fault detection analysis by injecting additional frequency test. In: Instrumentation and measurement technology conference, IEEE, Sorrento, Italy, pp 2087–2090
8. Mou Longhua, Meng Qinghai (2003) Power supply security technology. China Machine Press, Beijing, pp 56–65
9. Xu Weixing (2010) Research on fault line selection in small current grounded system based on evidence theory. Henan University, Zhengzhou
10. Cheng Zhiliang, Fan Chunjv (2006) Line selection in small current grounded system based on 5 times of harmonic mutations. Proc CSU-EPSA 10(5):37–41
11. Qi Zheng, Yang Yihan (2004) The technology analysis of earth fault protection in non-solid grounded system. Autom Electr Power Syst 14(28):1–5
12. Wu Ling, Sun Ying (2003) Application of continuous wavelet transform to select the fault line of single-phase earth faults in non-solid earthed power system. Relay 31(11):20–24
13. Gong Linchun, Huang Zhixiong (2008) Research of simulating the small current neutral grounding systems fault line selectio10n based on wavelet packets. Comput Eng Sci 3:103–105
14. Shao Baozhu, Song Dan, Wang Youyin (2008) Fault line selection of single-phase grounding in low current grounding system. Northeast Electr Power Technol 10(8):23–26
15. He Benteng, Hu Weixian (1998) A new principle to detect the grounded line in a neutral point indirectly grounded power system based on the energy function. J Zhejiang Univ 32(4):451–457
16. Zhu Dan, Cai Xu (2004) Improved energy function to detect the grounded line in neutral point indirectly grounded network. Power Syst Prot Control 32(10):44–48
17. Mou Longhua (2000) Grounding protection and fault point positioning. China Mining University Press, Xuzhou, pp 30–45
18. Liang R, Xue X, Li X (2009) Peterson coils based on changing magnetic coupling to control reactance and its application. AJEEE Aust J Electr Electron Eng 6(2):205–212
19. Dewadasa M, Ghosh A, Ledwich G (2011) Fault isolation in distributed generation connected distribution networks. Gener Trans Distrib IET 10(5):1053–1061
20. Shu Hongchun (2008) Fault line selection of distribution power system. China Machine Press, Beijing, pp 50–70
21. Zhuang Rufeng (2007) The current situation and development tendency of fault line selection devices. Electr Eng Appl 1:11–14
22. Zeng Jiyong, Ding Hongfa, Duan Xianzhong (2005) A harmonic detect method based on mathematical morphology method. Autom Electr Power Syst 29(6):55–59
23. Debayle J, Pinoli JC (2005) Multi Scale image filtering and segmentation by means of adaptive neighborhood mathematical morphology. Image Process 3(11):537–540
24. Chen Weihua (2009) Single line to ground fault line selection in non-direct ground power system based on mathematical morphology method. Central China Electr Power 22(4):4–8
25. Li Cailin, Zhong Yi, Huang Zhichao (2011) The methods for single phase-to-ground faulty line selection in distribution network. J Guilin Univ Electron Technol 31(5):391–395
26. Shu Hongehun, Peng Shixin, Li Bin et al (2008) Fault line detecting approach to hybrid feeders consisting of power cables and over head lines in distribution network using extenics. Trans China Electro Tech Soc 23(11):146–153
27. Mu Daqing, Mo Jingjun (2007) Discussion of fuzzy comprehensive evaluation application on earth fault line selection. Power Syst Prot Control 35(13):1–5

Micro-grid Environmental Economic Dispatch Using Improved Linearly Decreasing Weight Particle Swarm Optimization

Gujing Han, Yunhong Xia, and Wuzhi Min

Abstract Comparing with large power grid, micro-grid is quite different in operation method, energy strategy, power source type, load characteristics, power quality constraints and so on. These make its environmental economic dispatch technically difficult. Based on the improved linearly decreasing weight particle swarm optimization, this paper makes an exploratory study on the environmental economic dispatch of a simplified micro-grid which consists of photovoltaic generation, wind turbine, micro gas turbine, fuel cell, battery and electric loads. A mathematical model is built, which includes fuel cost, operation cost, maintenance cost and emission cost. Given several related constraint conditions, the model could be effectively solved by the improved WPSO. Different objective functions were carried out by computer simulation in three energy management operation policies between micro-grid and large power grid. The results showed the improved algorithm were theoretically correct and practically feasible.

Keywords Environmental economic dispatch • Weight particle swarm optimization • Power generation cost • Emission cost

1 Introduction

Protecting environment, reducing emission and making full use of renewable energy and new energy are the inevitable choices to achieve persistent development for China. As effective complement and strong support to the large power grid, micro-grid is getting more and more attention, for being environmentally friendly and low construction cost [1]. It integrates generators, loads, energy storage and control equipments to a single control unit. Comparing with large power grid,

G. Han (✉) • Y. Xia • W. Min
School of Electronic and Electrical Engineering, Wuhan Textile University, Wuhan, China
e-mail: gjhan@wtu.edu.cn

W. Wang (ed.), *Mechatronics and Automatic Control Systems*, Lecture Notes in Electrical Engineering 237, DOI 10.1007/978-3-319-01273-5_54,

micro-grid has much difference in operation method, energy strategy, power source type, load characteristics, power quality constraints and so on, which makes its environmental economic dispatch technical difficult [2]. This paper made some exploratory research on such problem. On grid-connected condition, considering the power supply cost of the micro-grid, environmental economic dispatch model was built for the lowest cost with a variety of constraints and solved by the improved weight particle swarm optimization(WPSO) algorithm. Different objective functions were carried out by computer simulation in three energy management operation policies between micro-grid and large power grid. The results showed the improved algorithm were theoretically correct and practically feasible.

2 Simplified Micro-grid

A simplified micro-grid structure is shown in Fig. 1. It consists of photovoltaic generation (PV), wind turbine (WT), micro gas turbine (MT), fuel cell (FC), battery and electric load. The simplified structure directly reflects the relationship between supply and demand within the micro-grid. Based on this structure, the following analysis and calculation will be carried out for micro-grid environmental economic dispatch.

3 The Objective Function for Environmental Economic Dispatch

Environmental economic dispatch of the micro-grid is to reasonably and effectively arrange the output of all micro power sources under the condition of load demand and the lowest cost generation and emission cost [2, 3]. This paper does not consider the cost of energy storage equipment. The objective functions are as follows.

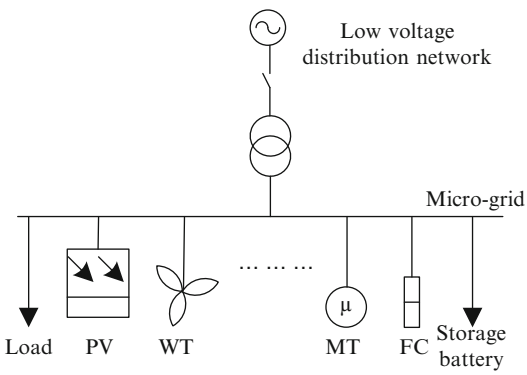

Fig. 1 Simplified structure of the micro-grid

$$\min F = \rho \cdot C_{\text{gen}} + \omega \cdot C_{\text{emission}} + \sum_{t=1}^{24} \left(C_{\text{buy}}(P_{\text{grid}}^t) - C_{\text{sell}}(P_{\text{grid}}^t) \right) \tag{1}$$

$$C_{\text{gen}} = \sum_{t=1}^{T} \left(\sum_{i=1}^{N} \left(C_{f,i}(P_i^t) + C_{\text{OM},i}(P_i^t) \right) \right) \tag{2}$$

Where, ρ and ω respectively represent the proportion of power generation cost and the emission cost. C_{gen} is micro-grid power generation cost and C_{emission} is micro-grid emission cost. T is the scheduling cycle of the micro-grid, commonly choosing 24 h. N is the total number of micro power sources which can be scheduled. $C_{f,i}(P_i^t)$ are the fuel cost of several micro power sources, and $C_{\text{OM},i}(P_i^t)$ is the operation and maintenance cost of them.

Photovoltaic cells and wind power are natural without consumption of primary energy, so their fuel costs are zero. However, Fuel cells and micro turbines consume fossil-fuel energy, and there is significant relationship between their fuel costs and their work efficiency [4]. The fuel cost of fuel cells and micro turbines is as Eq. 3.

$$C_{\text{fuel}} = (C_{\text{nl}}/L) \cdot \sum_{j} P_j/\eta_j \tag{3}$$

Where, C_{nl} is the natural gas price (RMB/m3). L is the natural gas low-hot value, taken as 9.7 kWh/m^3. P_j is the output power within the time period. η_j is the efficiency within the time period j. The operation and maintenance cost of micro power sources can be expressed as Eq. 4.

$$C_{\text{OM}} = \sum_{i=1}^{N} k_{\text{OM},i} \cdot P_i \tag{4}$$

Where, $k_{\text{OM},i}$ is operation and maintenance coefficient of the micro power source. P_i is the output power of the micro power source. And the emission cost is as Eq. 5.

$$C_{\text{emission}} = \sum_{t=1}^{T} \sum_{j=1}^{3} \alpha_j \cdot \left(\sum_{i=1}^{N} \beta_{ij} \cdot P_i^t \right) \tag{5}$$

Where, j represents the total number of pollutant, and the pollutants include NO_x、SO_2、CO_2. α_j is the processing price of the pollutant j. β_{ij} is the emission factor of the pollutant j when micro power source i output P_i^t.

3.1 Power Balance Constraint

$$P_{\mathrm{L}}^{t} + P_{\mathrm{loss}}^{t} = P_{\mathrm{WT}}^{t} + P_{\mathrm{PV}}^{t} + P_{\mathrm{MT}}^{t} + P_{\mathrm{FC}}^{t} \tag{6}$$

Where, P_{L}^{t} is the load at time interval t. P_{loss}^{t} is the loss at time interval t. P_{WT}^{t} P_{FC}^{t} P_{PV}^{t} and P_{MT}^{t} respectively represent the output power of WT, FC, PV and MT.

3.2 Inequality Constraints

Inequality constraints contain upper and lower constraint of the micro source power, emission constraint, and physical interaction power constraints between micro grid and the large power grid.

Upper and lower constraint of the source power is as Eq. 7

$$P_{i}^{t,\min} \leq P_{i}^{t} \leq P_{i}^{t,\max} \tag{7}$$

Where, $P_{i}^{t,\min}$ $P_{i}^{t,\max}$ respectively represent the lower and upper constraint of the power of micro source i.

And emission constraints can be expressed as Eqs. 8, 9, and 10 [5].

$$\sum_{i=1}^{N} \beta_{i,\mathrm{co_2}} \cdot P_{i}^{t} \leq L_{\mathrm{co_2}} \tag{8}$$

$$\sum_{i=1}^{N} \beta_{i,\mathrm{so_2}} \cdot P_{i}^{t} \leq L_{\mathrm{so_2}} \tag{9}$$

$$\sum_{i=1}^{N} \beta_{i,\mathrm{NO_x}} \cdot P_{i}^{t} \leq L_{\mathrm{NO_x}} \tag{10}$$

Where, L_{CO2}, L_{SO2}, L_{NOx} respectively represent the emission limit of CO_2, SO_2 NO_x in control region. The limit of power interaction between micro grid and the main grid is as Eq. 11

$$P_{\mathrm{grid}}^{\min} \leq P_{\mathrm{grid}}^{t} \leq P_{\mathrm{grid}}^{\max} \tag{11}$$

4 Operation Policies

The output power of WT and PV are taken use in priority for environmental reason. Then, considering the dispatching order of other micro power sources and whether there is power interaction between micro grid and the large power grid, there could be three operation policies.

1. Use FC and MT in priority to meet the micro grid load. If they cannot meet the load, power should be purchased from the large power grid and micro-grid does not output power.
2. FC, MT and the large power grid participate in system optimization together and power can be also purchased from the large power grid but no power output to it.
3. FC, MT and the large power grid participate in system optimization together. Micro grid can purchase power from the large power grid when the power generation of micro grid is lower. Besides, micro grid can sell power to the large power grid.

5 Solution by the Improved Weight Particle Swarm Optimization Algorithm

In particle swarm algorithm (PSO), inertia weight is one of the most important parameters. For PSO algorithm is easy to precocious and later is easy to oscillation near the global optimal solution, linearly decreasing weight particle swarm optimization algorithm can be used, and the modified formula is as Eq. 12 [6].

$$\omega = \omega_{\max} - \frac{t \times (\omega_{\max} - \omega_{\min})}{t_{\max}} \tag{12}$$

Where, ω is inertia weight. $\omega_{\max}$ and $\omega_{\min}$ are maximum and minimum weight. t is the number of iterations, and $t_{\max}$ indicates the maximum number of iterations.

In micro grid, micro source output range is commonly from 0 to rated value and can be continuously adjustable. Therefore, the unit commitment problem in the micro grid can be simplified. The economic dispatch cannot consider the unit start and stop. In this paper, the micro-power output active power in each time interval. P_i^t is the random generation of the unit output among $[0, P_i^{t,\max}]$. 0 represents that unit i turns off. And when P_i^t exceeds the upper limit, it equals its upper limit [7]. For Eqs. 6, 8, 9, and 10, a mixed penalty function can make them equivalent in the objective function (1). The modified objective function can be expressed as Eq. 13.

$$\min F' = F + r_k \sum_{i=1}^{m} \frac{1}{g_i(x)} + \frac{2}{\sqrt{r_k}} \sum_{j=1}^{n} [h_j(x)]^2 \tag{13}$$

Where, $g_j(x)$ are inequality constraints, and $h_j(x)$ are equality constraints.

6 Example Analysis

6.1 System Parameters

In the simplified micro-grid system as Fig. 1, the standby power battery neither charges nor discharges. Penalty price and emission factors of pollutants are shown in Table 1 [4]. Table 2 are parameters of different scheduling micro sources. Table 3 is physical power limits transferred between the micro-grid and the main grid in different operation policies. The 24 h forecast curves of the photovoltaic and wind turbine and 24 h forecast curve of load are referred from [8], shown in Figs. 2 and 3.

6.2 Results and Analysis

Computer simulation is based on MATLAB 7.10, and the computation cycle is 24 h. The current price of natural gas in Wuhan is 2.53 yuan/m^3. Ignoring grid loss, the relevant parameter values set for PSO are as follows. The size of the particle swarm is 20. The maximum number of iterations is 200. $\omega_{\max} = 0.9$, $\omega_{\min} = 0.4$. Power purchase price and sale price are both 0.6 yuan in RMB.

6.2.1 ρ:ω = 1:1 in Different Operation Policies

When $\rho : \omega = 1 : 1$ was set in Eq. 1, Figs. 4, 5, and 6 showed the different results in the three different operation policies. Figure 4 was for the first policy. It could be seen that FC was used in priority, because the total cost of FC was lower than MT. During 18–20 time intervals, which were peak hours, micro-grid could not meet the load demand, so it needed to purchase power from the large power grid. Figure 5 was for the second policy, and FC was still used in priority. Because the total cost of MT was higher than the large power grid, the power purchased from the

Table 1 Penalty price and emission factors of pollution emissions

Emission type	α_j (*RMB*/kg)	β_{MT} (kg/kWh)	β_{FC} (kg/kWh)	β_{PV} (kg/kWh)	β_{WT} (kg/kWh)
NO_x	62.946	0.00003	0.00044	0	0
SO_2	14.842	0.000006	0.000008	0	0
CO_2	0.210	0.001078	0.001596	0	0

Table 2 Parameters of different scheduled micro sources

Control strategy	Operation and maintenance coefficient (*RMB*/kg)	The upper limit (kW)	The lower limit (kW)
MT	0.088	30	0
FC	0.0293	40	0

Table 3 Physical power limits

Control strategy	1	2	3
$P_{\text{grid}}^{\min}$/kW	0	0	−20
$P_{\text{grid}}^{\max}$/kW	40	40	40

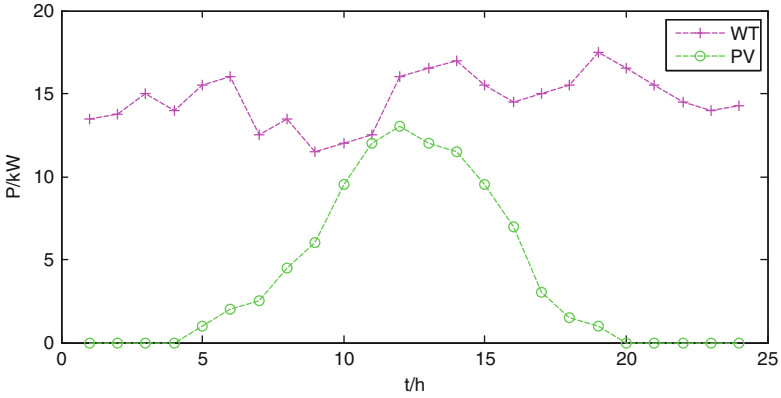

Fig. 2 Forecast curves of PV and WT

grid was used in priority. And MT couldn't be used at all. Figure 6 was for the third policy. At 1–5 time intervals, FC output was full-fat. There remained surplus power which could be sole to the large power grid to obtain certain benefits, and MT did not used at all.

6.2.2 Different Optimization Goals

In policy 3, optimization results with different ρ and ω were shown in Figs. 7 and 8. When $\rho : \omega = 0 : 1$ was set in Eq. 1, the optimization result was to obtain the lowest value in Eq. 5. From Fig. 7, it could be seen that the emission cost of FC was higher than MT. Meanwhile, the purchase cost from the large power grid was higher than the emission costs of FC and MT. So, it was in priority to dispatch MT and FC. After meeting the load demand, the remained surplus power could be sole to the main grid to obtain certain benefits. But it could not exceed energy interaction limit between micro grid and the large power grid, such as 1–6 time intervals and 12–14 time intervals. When $\rho : \omega = 1 : 0$ was set, the results was shown in Fig. 8, and it was similar to Fig. 6 that FC was dispatched in priority.

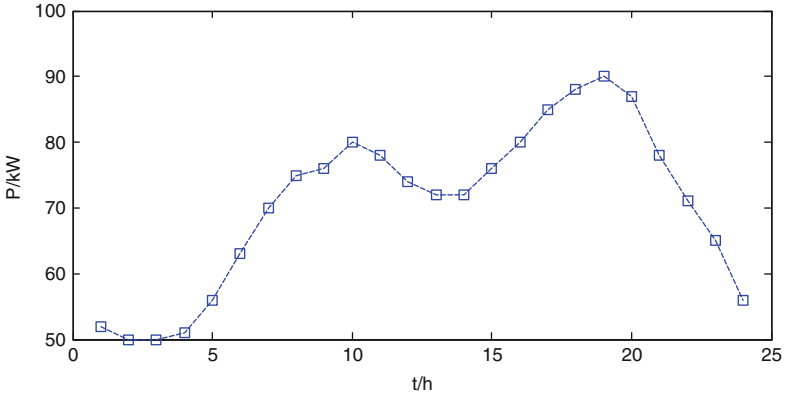

Fig. 3 Forecast curve of load

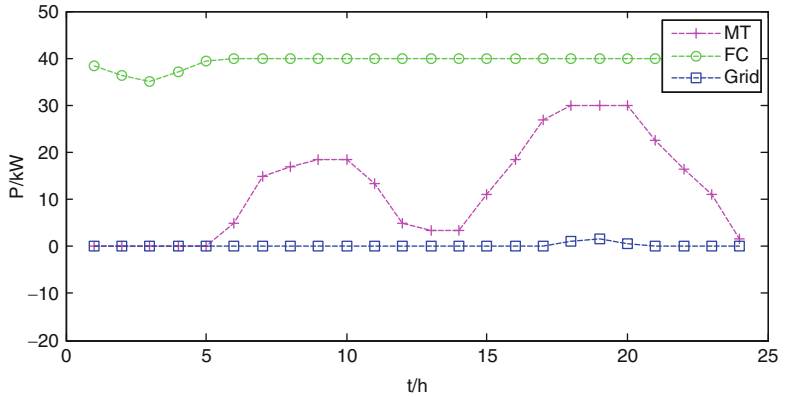

Fig. 4 In policy 1

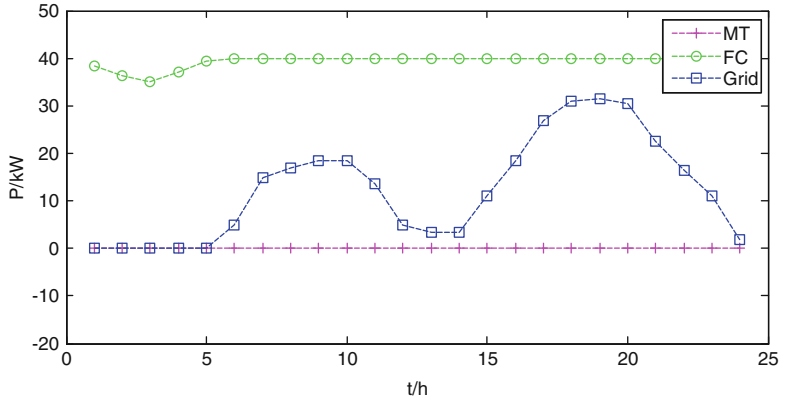

Fig. 5 In policy 2

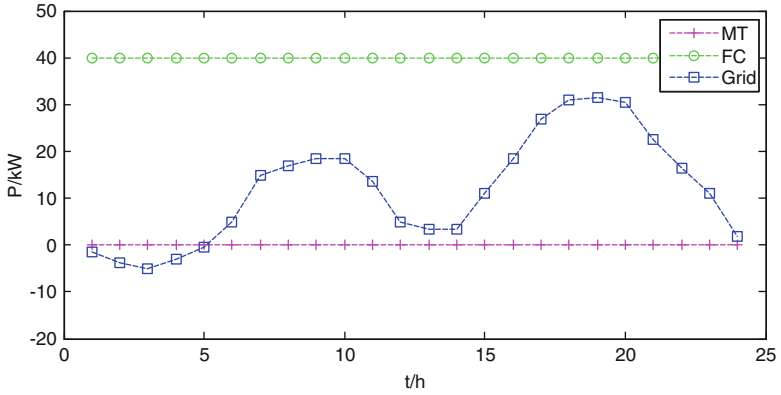

Fig. 6 In policy 3

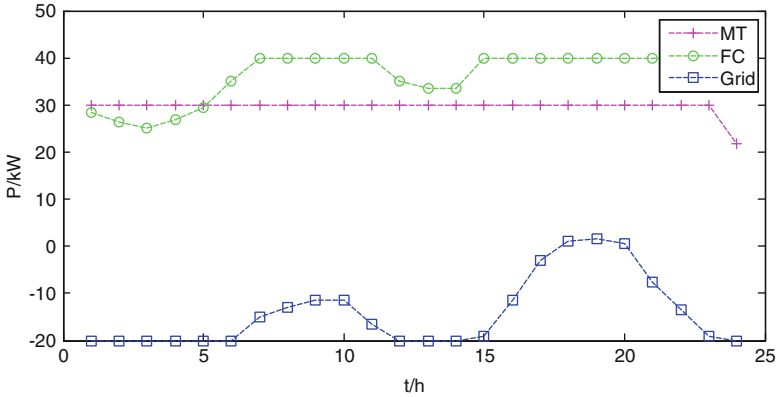

Fig. 7 $\rho : \omega = 0 : 1$

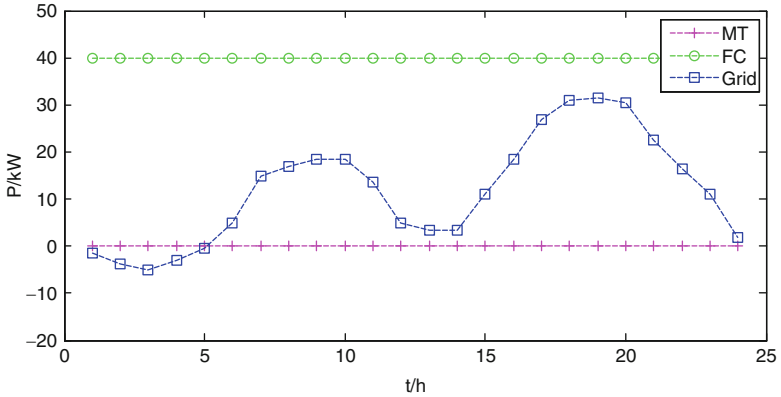

Fig. 8 $\rho : \omega = 1 : 0$

7 Conclusion

This paper analyzed the micro-grid connected with large gird in different operation policies. For typical cases in micro-grid environmental economic dispatch, three operation policies were proposed. Besides, for one typical operation policy, two optimization goals were realized by WPSO. Computer simulation results showed that optimized by WPSO through different control policies, different micro sources could be reasonably dispatched, and micro-grid could be made more environment-friendly and more economical to run.

References

1. Chen Dawei, Zhu Guiping (2010) Optimal load distribution of micro-grid. Autom Electr Power Syst 34(20):45–49, In Chinese
2. Lu Zongxiang, Wang Caixia (2007) Micro-grid research. Autom Electr Power Syst 31 (19):100–107, In Chinese
3. Hou Guoyan, Wang Biao (2011) Environmental economic dispatch of micro-grid in network. Sichuan Electr Power Technol 34(5):80–83, In Chinese
4. Bhuvaneswari R, Edrington CS, Cartes DA, Subramanian S (2009) Online economic environmental optimization of a micro-grid using an improved fast evolutionary programming technique. In: North American Power Symposium (NAPS). IEEE conference publicationsis, Starkville, MS, USA, pp 1–6
5. Yang Peipei, Ai Xin, Cui Mingyong, Lei Zhili (2009) Based on the particle swarm optimization the economic operation analysis of the micro-grid with a variety of functional systems. Power Syst Technol 33(20):38–42, In Chinese
6. Gong Chun, Wang Zhenglin (2012) Proficient in MATLAB optimization. Publishing House of Electronics Industry, Beijing, pp 201–241
7. Xi Peng, Li Peng (2011) Based on improve particle swarm optimization the study of micro-grid economic load allocation. Power Syst Technol 35(10):7–10, In Chinese
8. Chen C, Duan S, Cai T, Liu B, Hu G (2011) Smart energy management system for optimal micro grid economic operation. IET Renew Power Gener 5(3):258–267

Comparative Study of Grey Forecasting Model and ARMA Model on Beijing Electricity Consumption Forecasting

Wenyan Guo, Xiaoliu Shen, Xinke Ma, Li Ma, and Ting Cao

Abstract With the rapid development of the national economy, the power consumption is increasing. It is of great significance that how to make an accurate prediction of electricity consumption. Through the prediction model, the energy structure can be adjusted and the energy policies can be made to guide power consumption. In this paper, the Beijing electricity consumption is forecasted with Grey Prediction model and ARMA model based on the real data over years. Next these two models are compared. It can be seen from the comparison that the GM is more suitable for the prediction of electricity consumption and the prediction accuracy can be increased to 98.2 %. Based on the theoretical study, Beijing electricity consumption is well forecasted to support the government decision making.

Keywords ARMA • GM • Electricity consumption

1 Introduction

After china enters into the industrialization, energy-intensive industry grows quickly and energy consumption increases rapidly, so china has become the first major energy producer and the second energy consumer. In China the electric power enterprise is the main energy consumers as well as the ones which discharge the most pollutant. The electricity industry has always been the basic industry of our country's national economic development for a long time, it is also the important indicator of checking national energy consumption [1]. Thus, we should coordinate

W. Guo (✉) • X. Shen • X. Ma • L. Ma • T. Cao
School of Control and Computer Engineering, North China Electric Power University, Beijing, China
e-mail: guowenyanking@163.com

W. Wang (ed.), *Mechatronics and Automatic Control Systems*, Lecture Notes in Electrical Engineering 237, DOI 10.1007/978-3-319-01273-5_55,

the relationship among electricity supply, electricity demand and economic growth and we also should do the research of electricity power consumption forecasting well to avoid blocking the economic growth because of the future electricity power shortage or surplus under the form of our country's rapid economic growth. The objective of this paper is to forecast the Beijing electric power demand with two different models and do a contrast.

The electric demand forecasting has always been widely focused by most scholars. The frequently-used forecasting models are as follows: Grey Forecasting Model(GM) and ARMA Model (Auto Regressive integrated Moving Average). In this paper, to compare the two model's accuracies of electric power demand forecasting, based on the electric consumption data in a 20-year between 1991 and 2010, the model used are $GM(1,1)$ Grey Forecasting Model and $ARMA$,then the results from the established models are compared, and finally it finds the most suitable model for electric power demand forecast [2].

2 Grey Forecast Model

2.1 Construction of Grey Prediction Model

In the grey system theory, the model of description of continuous change of inside, using less or uncertain data to present the system behavior characteristics, it is called the grey model (GM). It is a dynamic model based on pseudo differential equation, which can describe system characteristics and development trends. Its extrapolating performance is superior to the statistical regression equations, and it does not require the sample data have a larger capacity and meet a certain statistical distribution [3].

The specific model construction is as follows [4]:

1. Get Original Sequence: $X^{(1)} = \sum_{1}^{m} X^{(0)}m$. $X^{(1)}$ is the orginal sequence, $X^{(0)}m$ is the accumulative sequence.
2. Get u and a: Based on $X^{(1)}$ and LSM, the a and u in the model can be determined, that is to say, from $\begin{bmatrix} a \\ u \end{bmatrix} = (B^T B)^{-1} B^T Y$, then get the value of a and u.
3. Get B and Y: Based on

$$B = \begin{bmatrix} -\frac{1}{2}\left[X^{(1)}(1) + X^{(1)}(2)\right], 1 \\ -\frac{1}{2}\left[X^{(1)}(2) + X^{(1)}(3)\right], 1 \\ \cdots\cdots \\ -\frac{1}{2}\left[X^{(1)}(n-1) + X^{(1)}(n)\right], 1 \end{bmatrix}, \quad Y = \begin{bmatrix} X^{(0)}(2) \\ X^{(0)}(3) \\ \cdots \\ X^{(0)}(n) \end{bmatrix}$$

4. Construct Accumulative Sequence:

$$X^{(1)}(k+1) = \left(X^{(0)}(1) - \frac{u}{a}\right)e^{-ak} + \frac{u}{a}$$

5. Analyze Model.
6. Predict according to the GM.

2.2 Empirical Analysis

Now, according to the step of modeling, the empirical analysis result is as follows.

1. Get Original Sequence: According to the raw data $X^{(0)}$ of Beijing Statistical Yearbook 1991–2010 annual electricity consumption and the data sequence after a summation $X^{(1)}$:

   $X^{(0)}$ = (1,613,977, 1,759,611, 1,924,978, 2,054,504, 2,225,922, 2,443,709, 2,636,078, 2,762,080, 2,972,629, 3,844,266, 3,999,415, 4,399,637, 4,676,056, 5,131,804, 5,705,364, 6,115,719, 6,670,089, 6,897,189, 7,391,465, 8,099,000).

   Then the result of $X^{(1)}$ can be found:

   $X^{(1)}$ = (1,613,977, 3,373,588, 5,298,566, 7,353,070, 9,578,992, 12,022,701, 14,658,779, 17,420,859, 20,393,488, 4,237,754, 28,237,169, 32,636,806, 37,312,862, 42,444,666, 48,150,030, 54,265,749, 60,935,838, 67,833,027, 75,224,492, 83,323,492).

2. Get u and a: According to the least square method, we will find the parameter values $a = -0.08462$, $u = 1{,}611{,}064.16$.
3. Get GM:

$$\begin{aligned} &X^{(1)}(k+1) \\ &= (X^{(0)}(1) - u/a)e^{(-ak)} + u/a \\ &= (1,613,977 + 19038159.2761)e^{-19038159.2761k} + 19038159.2761 \end{aligned}$$

4. Result: Computing the absolute error and relative error between annual electricity consumption and predictive value in Beijing from 1991 to 2010 (Table 1).
5. Result Analysis: According to the relative error of the residuals, we can find that the average relative error is 1.68 % and the prediction accuracy is 98.32 %. Forecasting data is as shown in Fig. 1.

Table 1 The absolute error and relative error of Beijing electricity consumption

Years	Actual value	Predictive value	Absolute error	Relative error
1991	1,613,977	1,613,977	0	0
1992	1,759,611	1,823,719.604	−64,108.60436	−0.036433396
1993	1,924,978	1,984,766.053	−59,788.05257	−0.031059084
1994	2,054,504	2,160,033.962	−105,529.9625	−0.051365177
1995	2,225,922	2,350,779.183	−124,857.1828	−0.056092344
1996	2,443,709	2,558,368.462	−114,659.4619	−0.04692026
1997	2,636,078	2,784,289.241	−148,211.241	−0.056224149
1998	2,762,080	3,030,160.312	−268,080.3124	−0.097057403
1999	2,972,629	3,297,743.418	−325,114.4182	−0.109369322
2000	3,844,266	3,588,955.874	255,310.126	0.066413231
2001	3,999,415	3,905,884.307	93,530.69307	0.023386093
2002	4,399,637	4,250,799.607	148,837.3929	0.033829471
2003	4,676,056	4,626,173.199	49,882.80083	0.010667708
2004	5,131,804	5,034,694.751	97,109.24918	0.018923024
2005	5,705,364	5,479,291.445	226,072.5549	0.039624563
2006	6,115,719	5,963,148.955	152,570.0453	0.024947197
2007	6,670,089	6,489,734.268	180,354.7319	0.027039329
2008	6,897,189	7,062,820.532	−165,631.5316	−0.024014353
2009	7,391,465	7,686,514.085	−295,049.0853	−0.039917538
2010	8,099,000	8,365,283.886	−266,283.8861	−0.032878613

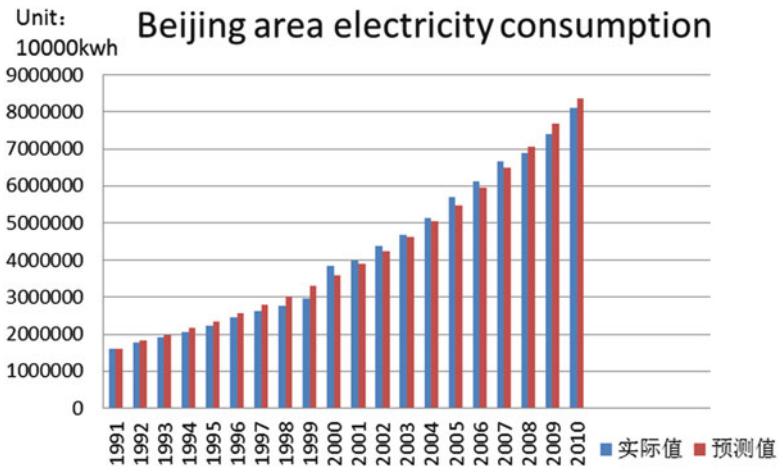

Fig. 1 The data of Beijing 1991–2010 forecasting electricity consumption

3 ARMA Model

3.1 Construction of ARMA Model

ARMA model is the important research method on time series forecasting, it is mixed by autoregressive model (AR model) and sliding average model. In this model, the prediction index is regarded as a random sequence with time change, the dependency relations with this set of random variables is embodied the continuity of original data. The time series is approximately regarded as a zero mean stationary series, in this situation, the condition of ARMA model construction is met. If this condition can't be met, the difference method can be taken to make the random fluctuating item as far as possible approach zero mean stationary time series [5].The ARMA (p, q) is as follows:

$$\mathrm{y(t)} = -\sum_{i=1}^{p} \phi_k * y(t-i) + \sum_{j=1}^{q} \theta_j * \alpha(t-j) + \alpha(t) \tag{1}$$

In this equation, p and q are the order number of autoregressive part and sliding average part respectively; (i = 1,2...p) is the coefficient of autoregressive part, (j = 1,2...q) is the coefficient of sliding average part, $\phi_i(i = 1, 2, 3, ..., p)$, $\theta_j(j = 1, 2, 3, ..., q), \alpha_t \sim N(0, \sigma_\alpha^2)$. To determine the unknown parameters, firstly, we must get the order of the model. In this paper, it mainly analyzes the Beijing city electric power consumption using SAS software. According to the auto correlation and partial autocorrelation functions, we can get the specific form of ARMA model.

3.2 Empirical Analysis

1. Actual Data: Sequential chart based on Beijing electricity consumption over the years: From the Fig. 2, we find that the time sequence is not smooth, so the data must be processed to meet the conditions. The method used is method of least squares, finally we can get the autocorrelation function and partial autocorrelation function.
2. Autocorrelations: From the Tables 2 and 3, we find the data processed by second-order difference is stationary. From the Table 4, the p value is 1, q value is 2, BIC(1,2) = 24.38823 is smallest, so the model ARMA(1,2) is selected.
3. Result Analysis: Set the confidence degree is 95 %, the prediction curve is shown in Fig. 2. From the prediction figure, we find that the fitting degree of predictive value and actual value is high in a small interval.

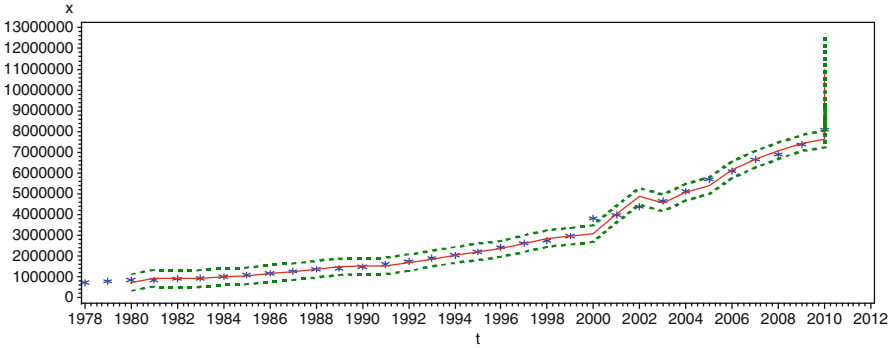

Fig. 2 Predictive curve (the fitting degree is 95 %)

Table 2 Autocorrelations

Lag	Covariance	Correlation	-1 9 8 7 6 5 4 3 2 1 0 1 2 3 4 5 6 7 8 9 1	Std Error
0	1.2532E11	1.00000	**********	0
1	9.51367E10	0.75915	**********	0.179605
2	7.78556 E10	0.62125	**********	0.263513
3	7.58234 E10	0.60504	**********	0.307148
4	7.29565 E10	0.58216	**********	0.343449
5	6.62918 E10	0.52898	**********	0.373928
6	4.82312 E10	0.38486	********	0.397335
7	3.67818 E10	0.29350	******	0.409184
8	2.38158 E10	0.19004	****	0.415920
9	2.30948E10	0.18429	****	0.418711
10	1.09337 E10	0.08725	**	0.421320
11	-1.3391 E10	-0.10685	**	0.421902
12	-1.6911 E10	-0.13494	***	0.422774

4 The Prediction Model of GM(1, 1)-ARMA(p, q)

From the above, we can know that Beijing's electric power demand is forecasted by GM and ARMA model separately and the results are compared. Figures 1 and 2 show the actual consumption value and predicted value in Beijing over the years. The conclusion can be gotten that with the changing of the time series, the actual and predictive values of GM have a higher similarity, and the prediction accuracy of GM can be up to 98.2 %. Therefore, to establish gray prediction model can objectively reflect the dynamic trend of electricity consumption in Beijing, and

Table 3 Inverse autocorrelations

Lag	Correlation	-1 9 8 7 6 5 4 3 2 1 0 1 2 3 4 5 6 7 8 9 1
1	-0.46108	. ********* .
2	0.13000	. . *** .
3	-0.09659	. . ** .
4	0.01251	. .
5	-0.14635	. . *** .
6	0.11770	. . ** .
7	-0.16776	. . *** .
8	0.18640	. . **** .
9	-0.10573	. . ** .
10	-0.10897	. . ** .
11	0.21136	. . **** .
12	-0.05030	. . * .

Table 4 Minimum information criterion

Lags	MA0	MA1	MA2	MA3	MA4
AR0	25.40699	25.28611	25.35714	25.29863	25.22052
AR1	24.44172	24.5278	24.38823	24.49417	24.58308
AR2	24.55248	24.47504	24.49502	24.51476	24.62199
AR3	24.42988	24.48035	24.5911	24.61607	24.6908
AR4	24.50162	24.57038	24.6251	24.72277	24.50527

Error series model: AR(4)
Minimum table value:BIC(1,2) = 24.38823

ARMA model for steady trend forecast. Meanwhile, electricity demand time series for both to contain deterministic dynamic trends contain random fluctuations in non-stationary time series.

First, through gray theory we can get the GM model from the historical data trend items of the electricity demands, second, getting time series analysis of the data after removing the trend term, and establish the ARMA model, finally, combining the above two models constitute a combined model for forecasting electricity demand. Then we can get the GM (1, 1)-ARMA (p, q) prediction model as follows:

$$X(t) = [1 - \exp(\alpha)] * \left[\left(X^{(0)}(1) - \frac{u}{a}\right)e^{-ak}\right] \exp[-\alpha(k-1)] - \sum_{i=1}^{p} \phi_k * y(t-i) + \sum_{j=1}^{q} \theta_j * \alpha(t-j) + \alpha(t) \quad (2)$$

In the formula, the first part is gray model GM (1, 1) of the development trend items, the after three parts are ARMA (p, q) model of Random fluctuation items, The formula has considered the time sequence of certainty trends and random fluctuations characteristic, therefore it has a better fitting prediction accuracy.

5 Conclusion

This paper mainly studied Beijing's demand of electricity through the GM model and the ARMA model for those years. However, the annual electricity demand of time series contains both deterministic dynamic trend and randomness fluctuations in non-stationary time series. ARMA is one of the most sophisticated statistical analysis methods of stationary random sequence, and the grey system theory is a dynamic trend in forecasting theory. Therefore, the next step is to combine these two models to constitute a combination of model, after research achieving more accurate prediction analysis. Therefore, the next step is to combine these two models, which may generate more accurate prediction analysis in the power industry.

Acknowledgements The work described in this paper was supported by: (1) Beijing Natural Science Foundation (Project Number: 9122021), (2) Beijing Municipal Commission of Education (Project Name: Research of Beijing energy industry comprehensive risk management system model and decision support platform).

References

1. Chen hui Liu (1987) Power system load forecasting theory and method. Harbin Institute of Technology Press, Harbin, pp 11–18
2. Kaigui Xie, Chunyan Li, Jiaqi Zhou (2002) Load combinations based on neural network prediction model. Chin Soc Electr Eng 22(7):85–89
3. Yangyong Guo (1996) The on gray time sequence combination of and its in the mine of predicting water influx. Hydrogeol Eng Geol 36(6):36–39, in Chinese
4. Julong Deng (1987) The basic methods of gray system. Huazhong Institute of Technology Press, Wuhan, pp 54–57
5. Toyoda J, Che NM, Inoue Y (1970) An application of state estimation to short-term forecasting. IEEE Trans on PAS 89:1678–1688

Design and Realization on Evolvable Circuit Self-Repair

Jianan Lou, Chuantao Li, Jianhua Yu, and Jie Chu

Abstract This study exploits and tests the circuit self-repairing based on the evolution technology using Virtual Reconfigurable Circuit technology in order to further improve the viability of electronic system under a severe environment. First of all, this paper builds a gate circuit model for the digital circuit evolution and designs a binary chromosome encoding according to Virtual Reconfigurable Circuit technology. Afterwards, it puts forwards the working process to realize circuit self-repair and discusses ways to diagnose and repair circuit faults. In the simulation that a single particle in the space burns the logic gate in the DC brushless motor control circuit, common SA faults are produced, leading to abnormal operation of the motor. Finally, by means of online evolution method, the motor may rotate again by skipping wrong units. This experiment demonstrates that the evolution method may effectively solve SA faults in circuits, thus improving the reliability of circuits.

Keywords Evolvable circuit • Self-repairing • Virtual reconfigurable circuit • Chromosome encoding

1 Introduction

As the electronic technology develops rapidly, it becomes increasingly complex, accompanied by a larger error rate. For example, in the application field of space technology, such high-energy particles as X-ray in the space may seriously affect its performance and reliability in the core control parts of an on-orbit spacecraft. In September 1988 and September 1990, China launched two polar orbiting meteorological satellites of FY-1A and FY-1B successively, both of which were out of order respectively after they have operated normally for 3 days and 165 days due to

J. Lou • C. Li (✉) • J. Yu • J. Chu
Mechanical Engineering College, Shijiazhuang, China
e-mail: lichuantao614@126.com

W. Wang (ed.), *Mechatronics and Automatic Control Systems*, Lecture Notes in Electrical Engineering 237, DOI 10.1007/978-3-319-01273-5_56,

the space particle bombardment on the on-board control system. Besides, technicians could not repair them at site, which, however, may be solved by the evolvable hardware technology.

Upon the completion of traditional electronic equipments, their inner structures and functions may not be easily changed and self-repairing may not be realized in case of faults. However, the evolvable hardware provides a technology used in the self-repairing of the electronic system. Thompson and others from Britain put forward an idea of using genetic algorithm to reconfigure a system with a fault and recover it. With the genetic algorithm, they conducted on-line self-diagnosis and self-repairing on the full adder and double-digit multiplier, etc. [1]. Researchers of U.S. Jet Propulsion Laboratory conducted self-repairing experiment on the half-wave rectifier under 300 K Rad TID (Total Ionizing Dose), −196 °C, 280 °C, and other extreme environments by the use of a stand-alone board-level evolvable system [2, 3].

There are some papers show about circuits self-repair [1], which is an assumption of the fault self-repairing of the logic door. There also some papers well introduced the circuit self-adaption to the temperature [2, 3]. This paper simulates very common SA faults which produced during a single particle in the space burning the logic door in DC brushless motor controller circuit, and aiming at the electronic commutation circuit of DC brushless motor, realizes a circuit failure self-repairing method combining evolution and rapid reconfiguration based on the circuit model of VRC.

2 Realization of Circuit Evolution

The early evolvable hardware technology was mainly software simulation. There is also outer evolution. In other words, the circuit is evolved by PC and the elite circuit is loaded in the film, which is called outer evolution. The outer evolution has distinctive birth defects in designing the adaptive circuit. For example, with the embedded development, the circuit module often operates independently from PC, but the evolution of outer evolvable circuit must be provided with one set of PC loaded with windows XP and the development software of FPGA. Therefore, the evolution way of the outer evolvable circuit limits the application of the evolvable hardware technology in the circuit self-adaption. This paper evolves the rotor commutate of the brushless DC motor by loading Microblaze [4] and VRC matrix in FPGA. The chromosome encoding of circuit dynamically generated through evolution algorithm may selectively use the logic unit in VRC matrix, making every PE unit in PE matrix become a dynamic backup unit [5, 6]. Therefore, compared with the traditional circuit, the circuit designed in VRC matrix has some distinctive characteristics, which are just analyzed and researched in this thesis.

Figure 1 is the experiment platform of the design. Its main chip is XC3S500E including 9,312 Slices of Spartan 3E series. PS21353-G is a motor control chip, of which the auxiliary signal conditioning circuit completes the power supply and

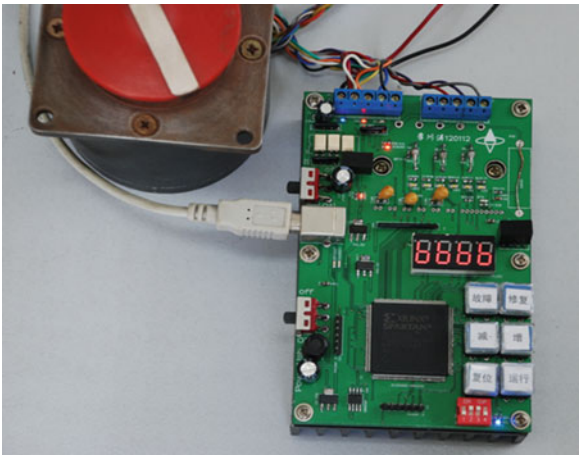

Fig. 1 Motor evolution mother board based on Spartan3E FPGA

commutation of the DC brushless motor. MP25P80 FLASH chip of a third party is designed on the board, ensuring that FPGA may run automatically upon being electrified. In addition, USB chip is added on the board in order to supervise the operating condition of the board. In this way, while the evolution algorithm analysis is conducted by the use of the board, only a USB cable may complete the power supply to the board and computer communication, which is extremely convenient for debugging.

Any digital combinational logic circuit may be realized by some basic logic units such as AND, NOR or OR gate circuits. There are a large quantity of basic logic units in Spartan3E such as LUT (Look-up Table) and every LUT may realize the logic function of any four (or less than four) input. Corresponding logic circuits may be realized through interconnection between units. The LUT in FPGA is compared to a neuron and lines between LUT is compared to axons between neurons, then a similar feed forward neural network circuit model shown in Fig. 1 is built on FPGA.

Compared with the multi-layer feed forward neural network, units in the circuit model realize the digital logic treatment function and the link weights between nodes in different layers reflect the link relation of nodes, in which '1' represents link and '0' represents link failure, but not reflect the link weight values. The circuit encoding is the first procedure to evolve a circuit, which first express the topological structure of a circuit in mathematic language and then evolve the circuit by the use of the evolution algorithm. The circuit encoding not only decides the individual chromosome arrangement pattern, but also decides the decoding method of commutating the genotype of an individual in the search space to a phenotype in the solution space. Figure 3 shows a unit in Row H1 shown in Fig. 2. In the design, there are four functional units: when FunChose is 00, it represents AND gate; when FunChose is 01, it represents OR gate; when FunChose is 10, it represents NAND gate; when FunChose is 11, it neither represents NOR gate (Fig. 3).

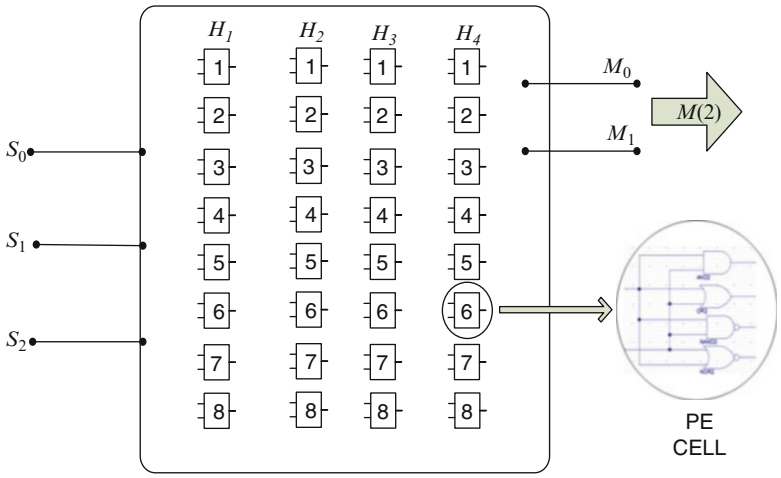

Fig. 2 Multi-layer feed forward neural network circuit model

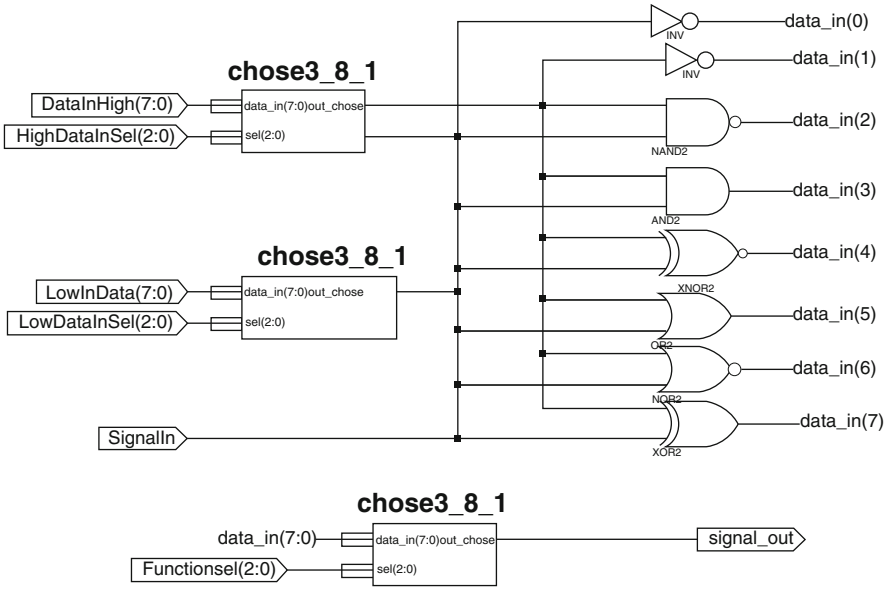

Fig. 3 PE unit model

Every PE (Programmable Element) unit also needs two input signals and the input signals are selected from a one-of-eight multichannel selector, i.e. determined by HighDatainSel = "000" represents selecting 0st signal, "001" represents selecting 2st signal. . ."111" represents selecting seven signal.

Every PE unit has two three-bit one-of-eight signal selection units. In this way, every PE unit has a chromosome encoding with the bit length of 2 + 3 + 3 = 8. As shown in Fig. 2, the encoding length of a matrix of 8*4 PE units is 8*8*4 = 256 bits. However, in order to improve the evolution speed, the design adopts circuit self-growth evolution mode simulating the creature growth mode, which is also called layered evolution.

The commutation table of the motor rotor is a 3-input and 6-output logic conversion table. However, a large number of experiments demonstrate that the PE matrix units from 8*4 bits to 8*7 bits may not easily evolve the motor commutation table. Therefore, the self-growth evolution way only evolves 3-input and 2-output for any matrix shown in Fig. 2. Such three circuits constitute a motor commutation circuit. There into, the three position signals of the three circuits are not linked together and output signals are also independent. Therefore, the chromosome encoding length of such genetic algorithm is 3*256 = 768 bits, which means that the target circuit may be found in 2^{768} possibilities by the use of the genetic algorithm.

The genetic algorithm adopts a common (1 + λ) evolution strategy in the design of evolvable circuit by VRC in the world. With multiple experimental trials, we find that the combination of "roulette" selection and "roulette" selection parent and the evolution strategy of the "immune" operator splendidly balances the contradiction between the diversity of the population and the algorithm convergence speed, achieves good effects, and improves (1 + λ) evolution algorithm.

$$fitness = \sum_{i=1}^{m} \sum_{j=1}^{n} \mathbf{C}(i,j), \mathbf{C} = \overline{\mathbf{X} \oplus \mathbf{M}} \tag{1}$$

In Eq. 1 formula, X is the corresponding simulation output matrix of the individual and M is a standard output matrix.

3 Operating Process of The Circuit Self-Repairing and Analysis on the Experimental Result

There are two running modes for a circuit board including the operating mode and fault self-adaption mode. Under the operating mode, while the circuit is electrified, the serial FLASH chip will automatically configure FPGA and Microblaze loaded in FPGA will take out the chromosome encoding of VRC from a specific address of FLASH and rapidly configure VRC unit upon running, and then the motor will operate. When a circuit cannot operate in case of TID (Total Ionizing Dose), SEU (Signal Event Upset), and SEB (Signal Event Tran-Silent), etc., the circuit enters the fault self-adaption model. Under such a model, Microblaze soft core in FPGA re-configures VRC matrix of fault units and avoids the fault logic gates by the use of the genetic algorithm, thus realizing the circuit self-repairing.

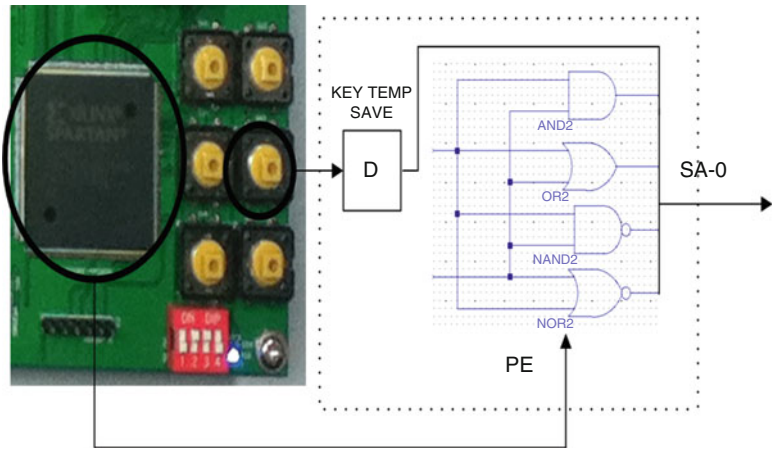

Fig. 4 Button inject SA-0 fault to FPGA inside circuits

This thesis researches the experiment of logic gate damage and self-repairing of PE units in the first row of the matrix constituted by 8*4 PE units of VRC. The commonest fault in the digital circuit is SA faults, which refers to that the node outputs a fixed logic value for whatever inputs. In references [7, 8], the problem of the reliability of SA fault model is analyzed. SA fault may be caused by the accumulation of faults in FPGA or that the single particle in the space burns the logic gate unit in FPGA. SA faults include [7, 8], SA-0 (stuck-at-0) and SA-1 (stuck-at-1) and this thesis inputs SA-0 faults on PE unit in the first row.

In this thesis, assuming there is a fault on a logic gate in a PE unit, the whole PE unit may not run normally. This thesis tests 0 logic gate to 6 logic gates of faults in the first row, and every fault mode is represented by PE0 ~ PE6 respectively (Fig. 4).

This experiment saves the input of the button through D flip-flop and leads the input to the output of PE unit, thus mandatorily lowering down the output of PE unit and producing SA-0 fault. Parameters adopted by the genetic algorithm: the population scale is 10, the rate of variation is 0.02, the crossover rate is 0.3, and the maximum evolution generation is 100,000. According to the damaged number of PE units in the first row, seven different fault modes are designed. The evolution algorithm needs a mass of random number seeds. A seed of key shall be given to the function of strand ((unsigned) key) in the initialized population and correspondingly there is an evolution generation on a key. Every fault adopts 100 different random number seeds. In other words, 100 experiments are conducted on every fault. Every evolution is conducted for about 10 min and the statistic result of evolution is shown in Table 1.

The experimental results demonstrate that a correct solution in the VRC evolution with Microblaze core may be found within 1,00,000 generations, which successfully proves the good fault tolerance of the algorithm. The reason why PE6 mode circuit cannot evolve a correct unit to avoid the fault is that when

Table 1 Statistics on repaired generations of different fault modes

Fault modes	PE_0	PE_1	PE_2	PE_3	PE_4	PE_5	PE_6
Minimum	341	304	243	502	903	2,027	100,000
Maximum	4,718	6,740	8,518	15,103	26,665	43,605	100,000
Average	1,978	2,172	3,275	3,664	6,801	14,091	100,000

there are six damaged PE units in the first row, the three-input of the circuit changes to be two input through the input signals of two PE units, in which there is no any unit to transmit all input information to PE units in the second layer. Therefore, a correct circuit may not be evolved. PE5 may evolve a correct circuit, which just proves the strong search capacity of the evolution algorithm. Therefore, this circuit design effectively improves the drawback of one unchangeable design of the traditional circuit design, making a circuit avoid fault units in case of a fault and realizing functional self-repairing.

4 Conclusion

The evolvable hardware method based on VRC designed a multi-layer feed forward neural network model and introduced the chromosome encoding way of this experimental board and evolution model in details. Besides, it tested the effectiveness of this model circuit by the evolution the commutation table circuit of the motor rotor. Related fault test data demonstrated that this method may realize the circuit self-repairing in a timely way. However, this experiment focused on narrating a method and thought instead of a large scale circuit evolution. Next, the intellectual evolution of large-scale circuit may be studied. In other words, the evolvable hardware will be applied to the electromagnetic bionics.

References

1. Thompson A (1996) Evolutionary techniques for fault tolerance. In: Proceedings of the UKACC international conference on control, LNCS. 1802, South West England, UK, pp 121–132
2. Stoica A, Keymeulen D, Zebulum R et al (2006) Reconfigurable electronics for extreme environments. In: Higuchi T, Liu Y, Yao X (eds) Evolvable hardware. Springer Science + Business Media, LLC, New York, pp 91–96
3. Zebulum R, Keymeulen D, Ramesham R et al (2006) Characterization and synthesis of circuits at extreme low temperatures. In: Higuchi T, Liu Y, Yao X (eds) Evolvable hardware. Springer Science + Business Media, LLC, New York, pp 113–142
4. Xilinx Microblaze IP core (2003). http:/www.xilinx.com
5. Kola J, Keane M, Streeter M (2003) What's AI done for me lately? Genetic programming's human-competitive results. IEEE Intell Syst 18(3):25–31
6. Keane M, Koza J, Streeter M (2002) Automatic synthesis using genetic programming of an improved general-purpose controller for industrially representative plants. In: Stoica A (ed)

Proceedings of the 2002 NASA/DOD conference on evolvable hardware, LNCS, Washington DC, USA, pp 113–122
7. Choudhury MR, Mohanram K (2007) Accurate and scalable reliability analysis of logic circuits. In: Proceedings of design automation and test in Europe (DATE), LNCS, Yokohama, Japan, pp 1454–1459
8. Choudhury MR, Mohanram K (2009) Reliability analysis of logic circuits. IEEE Trans Comput Aided Des Integr Circ Syst 28(3):321–336

Design and Application of Solar Power Supply System

Pengfei Liu, Xiaoqian Lu, and Xueyan Bai

Abstract In order to reduce the loss of power transmission and distribution and save electricity, this paper discusses the mechanism of solar photovoltaic power generation and photovoltaic system maximum power tracking point Principle in depth and adopt disturbance observation method to realize the most power tracing and design an intelligent power supply system, whose main power is solar panels and batteries, and the backup power is city power. These power supplies are switched on different conditions. Practical application shows that: the voltage and current outputted by this intelligent power supply system are pretty good. In a word, this design realize the concept of low carbon green.

Keywords Solar power • Micro systems • Solar panel

1 Introduction

Widely distributed and inexhaustible energy, solar energy resources is renewable, which is free from the restriction of geography, elevation and other factors. Solar power generation does not consume non-renewable resources such as oil, coal and natural gas. The electric power generation process does not discharge any hazardous material including greenhouse gases and this process has features such as no pollution and no noise. Developing solar energy and using renewable energy have become the key role in solving the world energy crisis.

P. Liu (✉)
School of Mechanical Engineering, Beijing Vocational College of Electronic Science, Beijing, China
e-mail: liupengfeibj@163.com

X. Lu • X. Bai
College of Electrical & Power Engineering, Taiyuan University of Technology, Taiyuan, China
e-mail: luxiaoqian880210@163.com; baixueyan0705@163.com

W. Wang (ed.), *Mechatronics and Automatic Control Systems*, Lecture Notes in Electrical Engineering 237, DOI 10.1007/978-3-319-01273-5_57,

Solar photovoltaic as a new form of energy [1] has made great development in recent years. In regions with abundant light supply but short of electricity. Solar power may be used to meet the needs of electricity. This paper on one hand describes the concept and practice of the system, on the other hand improves the awareness of energy conservation which provides an idea for building a society with green environmental protection.

2 The Mechanism of Solar Power

2.1 Photovoltaic Effect Principle

The principle of solar photovoltaic is the photovoltaic effect. Photovoltaic effect refers to the fact that through using of solar cell's photo galvanic effect, making the radiant energy of sunlight directly into electricity. Figure 1 shows the detailed principle of this process: after absorbing light, some special semiconductor materials produce a pair of separate positive and negative charges which generate an outside current field. Then the current flows to the battery negative terminal through the load from the bottom of the battery of crystalline silicon.

2.2 Photovoltaic System Maximum Power Tracking Point Principle

Photovoltaic array output characteristic has nonlinear characteristic, and its output is affected by sunshine intensity, environment temperature and load condition.

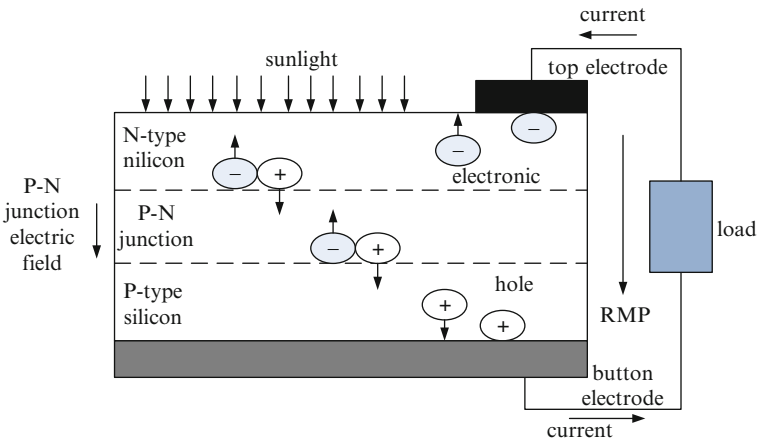

Fig. 1 Principle of photovoltaic effect diagram

Photovoltaic array can work in different output voltage under certain sunshine intensity and environment temperature. But only in one value, the output power of Photovoltaic array can achieve maximum, then its working point reach the highest point of the output power voltage curve, called the maximum power point (MPP, maximum power point). Thus, to improve the efficiency of the photovoltaic power generation system [2], an important way is to adjust photovoltaic array working point in real-time – making the working near to the maximum power point, this process is called MPPT (maximum power point tracking).

One of the main disadvantages of Photovoltaic power generation system is that its cost is too high, and its low efficiency of the solar cell photoelectric conversion. Generally speaking, the efficiency of polycrystalline silicon solar cell photoelectric conversion is about 12–14 %. In order to solve these problems, on the one hand, we must develop photoelectric material who with low price and high efficiency of energy conversion, on the other hand is that: realize the high power output of the solar cell through controlling grid inverter. At present, there are certain degree of research on MPPT [3] control technology at home and abroad, such as persistence voltage tracking method (CVT), disturbance observation (P&O), incremental conductance method and so on. Through the actual test and verify, the disturbance observation method can realize the most power tracing successfully.

Perturbation and observation principle is that disturb output voltage value (U + Δu), then measure the power change. Compared with the no disturbance power value, if the power value increases, it means the disturbance in the right direction, moving in the same direction (+ Δu). If the power value decrease, moving in the opposite direction (− Δu).

Connect Access database in VB6.0, write the convenient VB operation interface for users, just as the following Fig. 2 shows.

The text box in the upper-left corner is voltage output, click command1, no matter how much of the voltage, the power can achieve maximum 75.983 W. The other text boxes of the frame are intermediate variable, can be set to invisible, and finally to simplify as Fig. 3.

3 The Design of Photovoltaic Power Supply System

3.1 Design Proposal

Solar photovoltaic power generation system mainly consists of the solar cell module, batteries, solar controller and automatic switching device just as Fig. 4 shows. The system which consists of these electronic components, is installed and maintained conveniently and the operation is stable and reliable. During the day, solar panels [3, 4] will turn the luminous energy into electricity which will be stored in

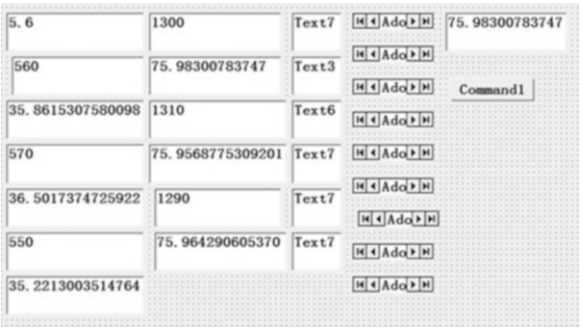

Fig. 2 Disturbance observation in the VB operation interface

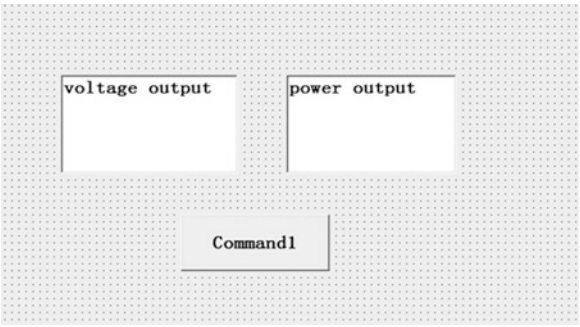

Fig. 3 Operation interface

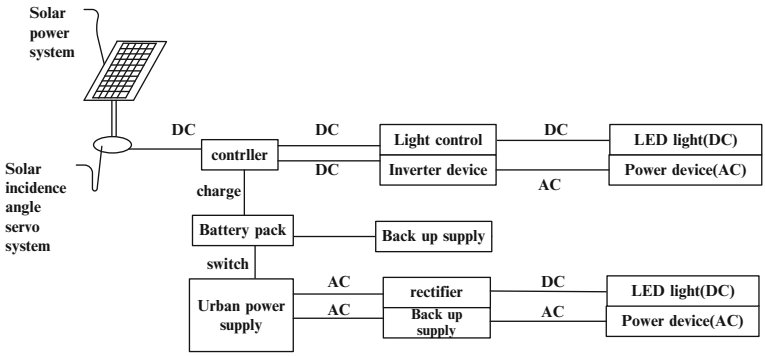

Fig. 4 The diagram of the solar power system

the battery. The night, it will be released from the battery and supply power for indoor. If the system detects battery power is not enough and solar panels output voltage is insufficient, it will switch to the city electric power.

Solar cells as a main power produce electrical energy. Storage battery as a storage device store up the excess of energy and supply power at night. Solar controller link solar panels and battery and control them. Three ways of power are controlled by a switching device, which works according to their respective voltages.

3.2 Equipment Selection

3.2.1 Solar Panels

Solar panels [4] are equipped with the biaxial movable tracking system. The Horizontal rotation angle of the equipment is 360° and the vertical one is 90°. Rotation is driven by an external battery panels and the position of the sun is tracked by light sensors and built-in controller as Fig. 5 shows.

3.2.2 Controller

Since the voltage of Solar panels is unstable owing to factors sun light intensity changes, loads and temperature, solar controller [5] is particularly important as the core of the whole system. This controller provides continued direct current (DC) for load and controls battery charging and discharging by adopting PWM control technique. When the voltage of solar panels below the storage battery's, the controller removes the solar panel system and offers power to the load by battery as Fig. 6 shows.

Fig. 5 Double axes tracking system the actual fig

Fig. 6 Controller

3.3 Setting up System

The system employs 16 pieces of Solar Module [6] whose nominal voltage is 12 V, nominal power is 100 W and total power is 1.6 kW. Storage battery employing Lead-acid batteries(nominal voltage is 12 V, capacity is 200 Ah) and Lithium Battery matches with Solar Module. The Power Capacity of Control Inverter is 2.2 kW, while the input DC value is 12 V and the AC output is 220 V. The conversion efficiency is more than 80 %. Figure 7 shows the overall power supply system and the equipment of the system selected on the bases of given parameters.

4 The Analysis of Application

Measured on the power supply platform, the results indicate, during the day with sufficient sunshine, the open-circuit voltage of Solar panels is 21 V(fluctuate for 1 V); And the working voltage is 12.8 V, slightly above the voltage of the battery, and solar panels charge battery up through the controller. Until after 5 PM, as light intensity weakens largely, this moment the output voltage of the solar panels changes obviously. When it stays down to the battery voltage, the solar panels has voltage but no current output. Then it will be removed from system temporarily and the battery will turn to supply power. And the load voltage would still maintain at 12 V. According to the measured data, we can draw the voltage、current and power of solar panels changes with time curves in the system, as Fig. 8 shows.

For solar controller, through the record of the experiment, it is known that no matter how solar panels output voltage change, the output voltage of the controller

Fig. 7 Actual building system

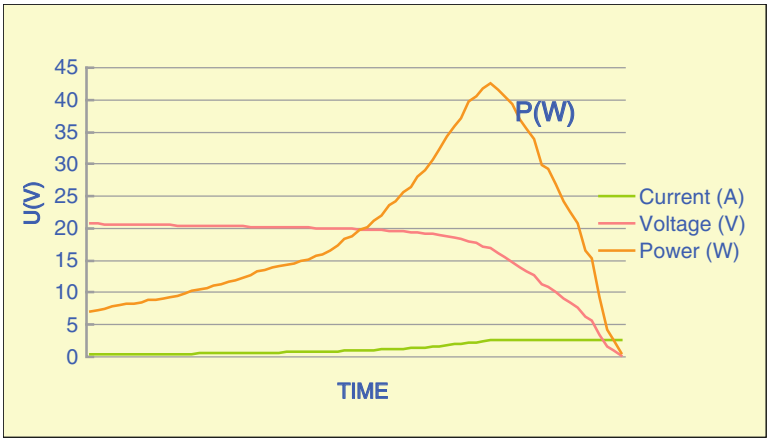

Fig. 8 Solar panels working voltage, current and power changes with time

and output current is constant, not affected by external light intensity, temperature conditions and other factors influence.

Thus, the solar panels can maintain a more stable output level and voltage fluctuation is not large during the day. But the short circuit current changes greatly. However, the intensity of light is not sufficient when the sun set, which make the battery plate output voltage decrease obviously. Solar energy controller can improve this situation and provide a stable power supply environment.

5 Conclusion

Our research on solar system is in a bottleneck stage. Compared with the traditional power, the up-front investment of solar photovoltaic power generation is more, and subsequent economic benefit is very good. Developing micro commonly used solar photovoltaic power generation systems can reduce the loss of power transmission and distribution and save electricity. Solar photovoltaic power generation systems have the maintenance operation cost and a high degree of automation. And in protecting the environment and reducing carbon emissions, it has irreplaceable function and broad development prospects.

References

1. Yan HM, Zhou ZZ, Lu HY (2009) Photovoltaic industry and market investigation. In: 1st international conference on sustainable power generation and supply'09, IEEE conference publications, Nanjing, China, pp 1–4
2. Zheng GP, Yang W (2012) Research on energy conversion model of solar photovoltaic power generation system. Adv Mater Res 429:222–228
3. Chen P, Ren SB, Wen WH, Wang HT (2011) Hybrid dynamic modeling and MPPT control for photovoltaic power generation system. In: Proceedings – 3rd international conference on measuring technology and mechatronics automation, computer science, vol 2, Shanghai, China, pp 336–339
4. Xu XL, Liu LQ, Zuo YB (2010) A study on all-weather flexible auto-tracking control strategy of high-efficiency solar concentrating photovoltaic power generation system. In: Proceedings – 2010 2nd WRI global congress on intelligent systems, IEEE conference publications, vol 2, Wuhan, China, pp 375–378
5. Abdullah SM, Muslih IM, Abu.Husain W (2010) National grid, diesel, and photovoltaic power generation systems in Jordan: an engineering and economical evaluation. Energy Source 5(4):370–383
6. Attaviriyanupap P, Tokuhara K, Itaya N, Marmiroli M, Tsukamoto Y, Kojima Y (2011) Estimation of photovoltaic power generation output based on solar irradiation and frequency classification. In: 2011 I.E. PES innovative smart grid technologies, IEEE conference publications, vol 2, Perth. WA, Australia, pp 1–7

Emergency DC Power Support in Parallel AC/DC Power System

Xiangqiang Liu, Huifan Xie, Haijun Wang, Zhaoshuo Wang, and Jinzhuang Lv

Abstract Emergency DC Power Support (EDCPS for short) is an economical and practical emergency control measure to enhance the transient stability in parallel AC/DC power system and deserves further research. In this paper some research issues related to EDCPS in parallel AC/DC system are presented, including the mechanism of how EDCPS enhances transient stability in multi-machine system, the optimization of EDCPS strategy parameters and the effect of load characteristics on EDCPS strategy. As for online prediction control, an online preconceive calculation and real-time matching EDCPS control framework for China Sothern Power Gird is put forward, and as for time control for EDCPS, the optimal sequence time control theory is introduced, so is auto-disturbance rejection control theory. And finally the limitation for EDCPS is brought forward, and how to own a quick starting-time and quick DC power changing-rate deserves further research.

Keywords Parallel AC/DC system • Emergency DC power support • Online prediction control • Time-optimal control theory • Auto-disturbance rejection control theory

1 Introduction

With the complete implement of power supply strategy of "Nationwide Network Connection, Power Transmitted from West to East and Mutual Supply South and North", more and more HVDC projects will be put into practice in China network, and HVDC will lead a dominant role in that proposed power supply strategy.

X. Liu (✉) • H. Xie (✉)
Extra High Voltage Transmission Company of China Southern Power Grid, Guangzhou, China
e-mail: liuxiangqiang@ehv.csg.cn; xiehuifanscut@163.com

H. Wang • Z. Wang • J. Lv
Extra High Voltage Transmission Company of China Southern Power Grid, Guangzhou, 510663, China

W. Wang (ed.), *Mechatronics and Automatic Control Systems*, Lecture Notes in Electrical Engineering 237, DOI 10.1007/978-3-319-01273-5_58,

Since it has a large transmission capacity and what's more, with 1.1 times' longtime overload-ability and 1.5 times' overload-ability for 3 s, HVDC can enhance transient stability after heavy disturbance in parallel AC/DC power grid. HVDC can quickly modulate both active and reactive power in a large scale, and when there exits heavy disturbance, those available HVDC systems can rapidly modulate active power into AC systems and finally compensate the power unbalance between the sending and receiving network, which is named Emergency DC Power Support [1, 2] (EDCPS for short), accordingly better last-low-voltage level or voltage vibrating conditions. EDCPS owns a great deal advantages, such as rapidity, reliability and great capacity, thence for the time being EDCPS has been an economical and practical emergency control measure and therefore deserves further research.

2 Study on Mechanism of Emergency DC Power Support

EEAC [3] is introduced to explain the mechanism of how EDCPS enhances transient stability by heavy disturbance in AC/DC power grid. After heavy disturbance, all generators in power grid can be divided into two groups, namely severely disturbed group (S group) and remnant group (R group), and then the whole system can be equaled into two-machine-unstable model. Considering that it is an unstable model of S group relative to R group, the whole system can be further equaled into One-Machine-Infinite-Bus system. In One-Machine-Infinite-Bus system, the DC power should be increased to make increasing area smaller than decreasing area, which will enhance transient stability, as illustrated in Fig. 1, and during the angle-swing-back course, DC power should be reduced to make increasing area smaller than decreasing area, which will better transient stability during swing-back course [5], as illustrated in Fig. 2.

3 Study on Emergency DC Power Support Strategies

Deep study has been done on Emergency DC Power Support Strategy, including the HVDC power support starting-time, the power support increment, the rising-rate and the lasting-time. The Yun-guang UHVDC Emergency DC Power Support Strategy in China Southern Power Grid of year 2010 is studied by PSD-BPA simulation tool, which is useful for power flow calculation and transient stability analysis. Study results show [4] that: DC power increment should be appropriate, bigger increment leads to bigger reactive power consumption, resulting in unfavorable effect on voltage recovery, while the power angle stability is enhanced; support starting- time should be proper, advanced start causes bigger reactive power consumption while delayed start may not provide enough accelerating area, as

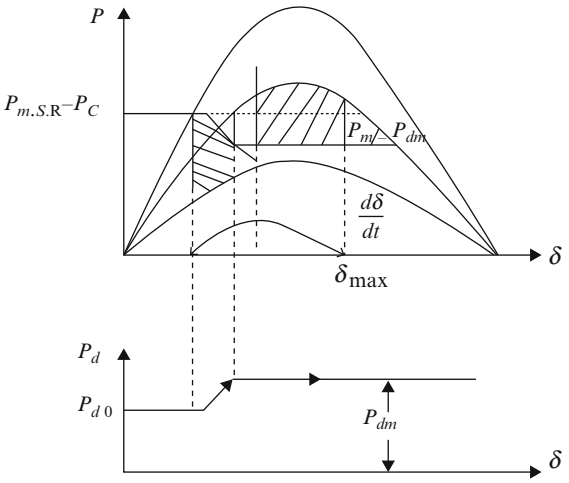

Fig. 1 Swing-up course

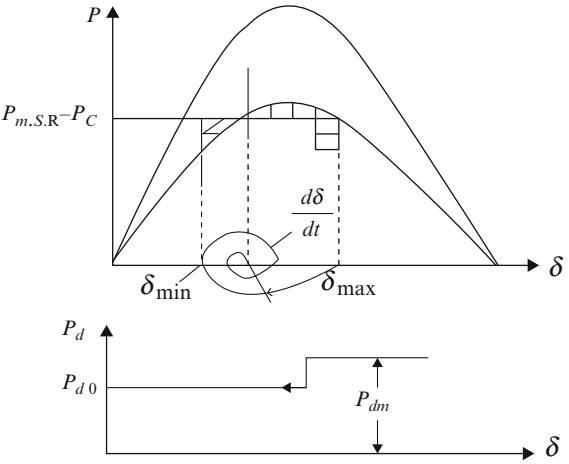

Fig. 2 Swing-back course

shown in Fig. 3; rising rate should not be too fast, otherwise reactive power consumption will increase and phase conversion voltage stability decrease; an appropriate DC power decrement during the swing-down of OMIB system power angle will enhance transient stability. After heavy disturbance, Emergency DC Power Support Strategy will take both angle stability and voltage stability into account, the HVDC power support starting-time, the power support increment, the rising-rate and the lasting-time all should be optimized.

Influence of load model on the Emergency DC Power Support Strategy is well analyzed. The impact of ZIP load (including constant -active-power-load, constant-current-load and constant-impedance-load), IM load (dynamic induction motor model), load composition, and load location of the specific CSG network on the EDCPS performance following large disturbances are studied by FASTEST tool,

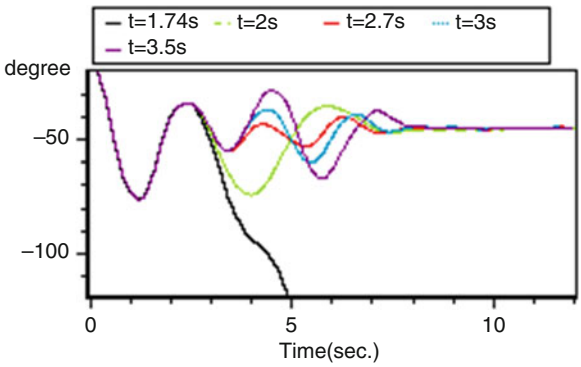

Fig. 3 Angle curve of Pinghai generator

which is useful for transient security quantitative analysis [5]. It is found that following a large disturbance, IM load absorbs more active power than ZIP load and the influence of the sending-end IM load on the post-fault EDCPS power-angel stability is completely opposite to that of receiving-end load. The sending-end loads are helpful to enhance the system stability. In the case that the sending-end load is smaller than the receiving-end load, synthesis load tends to deteriorate the post-fault EDCPS effect, and the active power support needs to be increased or provided in good advance.

IM model low-voltage response characteristic will deteriorate the EDCPS effect. Low voltage causes IM slip-ratio to increase, rotor equivalent resistance to decrease and stator current to increase so greatly that the absorbed reactive power increases too, which ultimately leads to low voltage because of lack of reactive power. In view of EEAC, the maximal value of electromagnetic power decreases and will reflect in the Power-Angel characteristic chart, which shows that the accelerating area increases and decreasing area decreases, and it is necessary for DC power to be increased to make accelerating area smaller and decreasing area bigger. What's more, the EDCPS starting-time should be appropriate, neither too early nor too late. If EDCPS starts too late, it can't provide enough decreasing area, and if EDCPS starts too early during voltage-dropping period, it will leads much more fluctuant to inverter commutation voltage and under the function of Voltage Depend Current Limiter Unit the actual DC power increment will be delayed and even be held back to drop. Figure 4 shows actual Yunnan-Guangdong UHVDC power by different Guangdong IM load proportions, with the function of Voltage Depend Current Limiter Unit the actual DC power can't reach the expected value 3,750 MW and after near 0.5 s the DC power drops to lower than 2,500 MW. It is easy to come to a conclusion from Fig. 4 that the bigger IM model proportions in Guangdong power grid the worse the power system stability.

Longer study reveals that with a timely EDCPS, an appropriate DC power rise and the corresponding rising rate in the first two up-swing courses, and with a suitable drop and the corresponding dropping rate in the first two back-swing courses, the transient stability is well imp roved. Moreover, by using the genetic-taboo searching algorithm, the modulation parameters are well optimized. Thus,

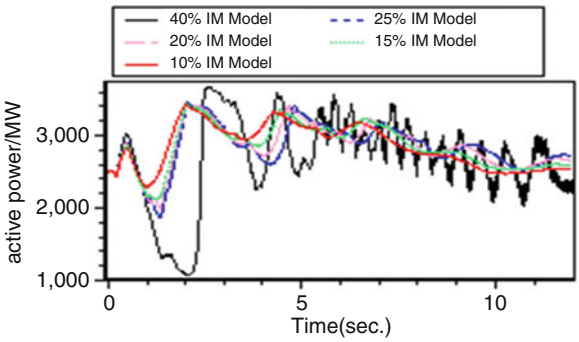

Fig. 4 Y/G DC power under different dynamic load proportions

according to the pre-set key power flow or the real-time power flow as well as the preconceive accident sets in the energy management system, the transient stability parameters of some serious preconceive accident sets can be calculated off line or on line in a certain operation mode. Case study indicates that the proposed EDCPS strategy effectively improves the transient stability of the power system.

4 Emergency DC Power Support Strategies Online Prediction Control

For emergency control framework of Online Preconceive Calculation and Real-time Matching, an Online Preconceive Calculation and Real-time Matching EDCPS Strategy [6] is put forward based on Integrated Extended Equal Area Criterion. The post-fault generators are firstly divided into two generator groups, namely severely disturbed group and remnant group, and then that proposed two groups are equated into One Machine Infinite Bus System. EDCPS strategies, including EDCPS starting-time, DC power rising-amount, rising and dropping ratio, are optimized by Enumeration Method with transient angle stability margin and transient voltage-drop acceptable margin as the objective index. EDCPS table can be made online in less than 5 min with the real-time data from Energy Management System (EMS for short).

Emergency DC Power Support function can quickly modulate available DC power when heavy fault occurs in parallel AC lines or other HVDC systems, and finally enhances transient stability with short-time DC overload capacity. Therefore, how to implement online EDCPS prediction by Wide Area Measurement System (WAMS for short) signals is of great significance and deserves to be researched. An online EDCPS prediction model based on WAMS signals is established for EDCPS online prediction control, and a newly structured Multi-resolution Analysis Orthogonal Wavelet Neural Network (MAOWNN for short) is constructed and applied to ECDPS prediction. The rotor speed and its corresponding changing-rate signals from generators near the available HVDC

converter station are mapped by IEEAC as the characteristics signals for MAOWNN input, as formulas (1a and 1b), and the output of MAOWNN is the DC power rising-amount and its corresponding ratio. Adopting orthogonal scaling function as activation function, the proposed MAOWNN can converge fast and ensure the uniqueness of approximating function expression. Simulation results show that based on dimension-reduced principal components the MAOWNN can accurately give the controlled quantity of EDCPS.

$$\begin{cases} X = [X_1, X_2, \ldots X_n, X_\Sigma, \dot{X}_\Sigma] \\ X_n = \omega_{sa.n}^1, \omega_{sa.n}^2, \cdots, \omega_{sa.n}^k \\ X_\Sigma = \omega_{sa.\Sigma}^1, \omega_{sa.\Sigma}^2, \cdots, \omega_{sa.\Sigma}^k \end{cases} \tag{1a}$$

$$\begin{cases} \delta_{sa} = \sum_{i \in s} M_i \delta_i / \sum_{i \in s} M_i - \sum_{j \in a} M_j \delta_j / \sum_{j \in a} M_j \\ \omega_{sa} = \sum_{i \in s} M_i \omega_i / \sum_{i \in s} M_i - \sum_{j \in a} M_j \omega_j / \sum_{j \in a} M_j \\ \dot{\omega}_{sa} = \sum_{i \in s} M_i \dot{\omega}_i / \sum_{i \in s} M_i - \sum_{j \in a} M_j \dot{\omega}_j / \sum_{j \in a} M_j \end{cases} \tag{1b}$$

Where, s is the severely disturbed generator group near rectifier station, a is the remnant generator group neat inverter station, and k is the sampling points.

And the output of the DC power rising-amount and its corresponding ratio are shown as the following formula (2)

$$\begin{cases} \Delta P_d, \ \Delta P_d \in [0, 0.3, 0.5] \text{p.u.} \\ V_d, \ V_d \in [0, 999] MW / \min \end{cases} \tag{2}$$

5 Advanced Control Technology on Emergency DC Power Support

Advanced control technology is introduced to Emergency DC Power Support for better angle stability and voltage stability, and Time-optimal Control Theory [7] (TOC for short) is applied successfully.

Based on the equivalent-two-machine-two-area AC/DC parallel system, a TOC plane for second-order oscillation system is deduced, as shown in Fig. 5, and a TOC strategy for quickly suppressing inter-zone disturbance is proposed.

The second-order oscillation system TOC rule for an equivalent two-machine-two-area power system is deduced to determine when to raise DC power and when to drop DC power to quickly suppress disturbance, the rule is given in formula (3). Firstly TOC theory drives system state to a post-fault equilibrium point and Linear

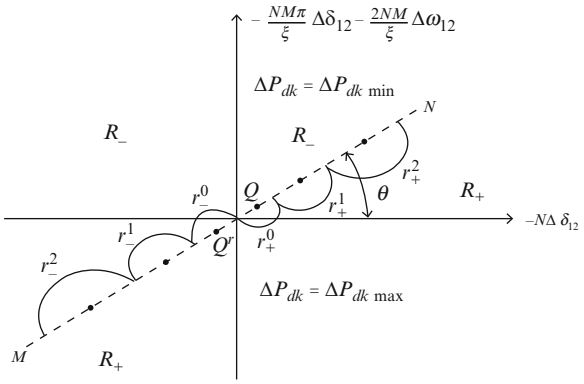

Fig. 5 Optimal switching curve plane

Quadratic Optimal Control (LQOC for short) theory is used to fix state in that equilibrium point. Switching curve is improved to avoid DC power jump-changing and to eliminate high-frequency nonlinear chattering and overshoot, and an optimal DC power control amount is calculated for fewest switching control. The proposed TOC strategy can well combine with the practical DC Emergency Run-up and Run-back control function effectively and quickly suppress inter-zone oscillation after first angle swing [8].

$$\Delta P_{dc}=\begin{cases}\Delta P_{dc.\max},\ \ if\left(-N\Delta\delta_{12},-\dfrac{NM\eta}{\xi}\Delta\delta_{12}-\dfrac{2NM}{\xi}\Delta\omega_{12}\right)\in R^+\cup r^+\\ \Delta P_{dc.\min},\ \ if\left(-N\Delta\delta_{12},-\dfrac{NM\eta}{\xi}\Delta\delta_{12}-\dfrac{2NM}{\xi}\Delta\omega_{12}\right)\in R^-\cup r^-\\ r^+=\underset{k=0}{\overset{\infty}{\cup}}r_+^k;r^-=\underset{k=0}{\overset{\infty}{\cup}}r_-^k\end{cases}\tag{3}$$

Where, $\Delta P_{dc.\max}$ and $\Delta P_{dc.\min}$ are respectively the max DC power rising-amount and the max DC power decreasing-amount, and with the range $0<\Delta P_{dc.\max}\le 0.5, -0.5\le\Delta P_{dc.\min}\le 0$.

Auto-disturbance Rejection Control (ADRC for short) owns high adaptability and robustness and is also introduced.

Based on Time-optimal Control Theory and Auto-Disturbance Rejection Control theory [9] (ADRC for short), a new EDCPS control rule for quickly suppress disturbance in parallel AC/DC network is designed with WAMS signals.

TOC theory is introduced to drive and fix system state to a post-fault new equilibrium point which based on Integrated Extended Equal Area Criterion can be approached on-line with WAMS signals, and finally Auto-disturbance Rejection Control theory is introduced to trace the virtual control input. Simulation results of six-machine-dual-infeed three-area system show that the proposed EDCPSCS can take advantage of quick DC power modulation and short-time overload capability to provide emergency control and power support and has a better control effect than that of traditional linear DC power modulation. ADRC owns characteristics of high

adaptability and robustness in disturbance and model uncertainty, moreover, control effect aimed at the new equilibrium point is better than that aimed at the original one [10].

6 Limitations and Difficulty of Emergency DC Power Support

HVDC owns 1.1 times' long-time overload-ability and 1.5 times' overload-ability for 3 s and can enhance transient stability after heavy disturbance in parallel AC/DC power grid. EDCPS owns a great deal of advantages, such as rapidity, reliability and great capacity, thence for the time being EDCPS has been an economical and practical emergency control measure. But there still exists some limitation and difficulty for EDCPS in practical HVDC. For example, firstly, the starting-time is not as quick as assumed because of AC filter's slow action; secondly, the DC power rising-rate and DC power decreasing-rate are lower than assumed, the max rates of HVDC power changing-rate in China Sothern Power Gird are both 999 MW per minute, and suck slow active power support makes no effect in transient stability. Hence how to own a quick starting-time and quick DC power changing-rate deserves further research.

References

1. Xu Zhen, Gao Huimin, Yang Jingpin (2004) Effect of HVDC emergent power modulation in South China power system. High Volt Eng 30(11):24–26
2. Yang Weidong, Xue Yusheng (2003) Emergency DC power support to AC power system in the South China power grid. Autom Electr Power Syst 27(17):68–72
3. Xue Y, Van Cutsem T, Ribbens-Pavella M (1988) A simple direct method for fast transient stability assessment of large power system. IEEE Trans PWRS 3(2):400–412
4. Xie Huifan, Zhang Yao, Xia Chengjun (2008) Study of UHV emergency DC power support strategy. Electr Power Autom Equip 28(8):1–8
5. Xie Huifan, Zhang Yao, Xia Chengjun et al (2008) Influence of load model on UHVDC emergency DC power support strategy. In: DRPT Conference, IEEE, Nanjing, China, pp 1992–1996
6. Xie Huifan, Zhang Yao, Nie Shulin et al (2009) Wide-area EDCPS online prediction based on orthogonal wavelet neural network. Power Autom Equip 29(11):82–86
7. Zhang Hongrong, Wang Qing (2006) Optimal control theory and its applications. Higher education Press, Beijing
8. Xie Huifan, Zhang Yao, Deng Quanshuai et al (2009) Emergency DC power control strategy for quickly suppressing inter-zone disturbance based on time-optimal control theory. Control Theory Appl 26(11):1267–1272
9. Han Jingqing (1998) Adaptive auto-disturbance rejection control and its applications. Contro1 Decis 13(1):19–23
10. Xie Huifan, Zhang Yao et al (2009) Emergency DC power support control based on time-optimal control and auto-disturbance rejection control. Trans China Electr Soc 24(12):145–153

Application of Soft Switching Technology in Inverter and Its Influence on Electromagnetic Interference

Yinghua Yang, Honglin Gao, Xinhua Wang, Jinfei Tang, Jialiang Li, and Yu Tian

Abstract This paper analyzes the electromagnetic interference (EMI) source and spread path of traditional PWM inverter. To reduce the EMI it puts forward a new soft switching PWM inverter, and expounds the inverter's working principle. It applies soft switching technology to traditional inverter. It measures the turn-on voltage spike and the EMI conductive noise of AC inverter system through experiment. It also analyzes and compares under hard switching condition and soft switching condition respectively. It proves that soft switching inverter can reduce EMI effectively.

Keywords Soft switching • Inverter • EMI • Noise spectrum

1 Introduction

At present, switching frequency of the traditional PWM inverter becomes higher and higher. The higher frequency makes inverter output more pulses during per period, so the equivalent voltage wave closes to sine wave much more. Then it can reduce harmonic output and improve speed regulation performance.

However, the traditional inverter runs under hard switching condition, namely the switches of inverter turn on and turn off under non-zero voltage switching (NZVS) condition or non-zero current switching (NZCS) condition. It causes problems such as switching loss, diode reverse recovery, inductive turn-off, capacitive turn-on and electromagnetic interference (EMI) [1]. When the inverter is working, it causes EMI to other devices, which get more severe with higher

Y. Yang (✉) • H. Gao • X. Wang • J. Tang
Navy Submarine Academy, Qingdao, China
e-mail: flymarsyang@sina.com

J. Li • Y. Tian
Military Delegate Office of 8357 Research Institute, Tianjin, China

W. Wang (ed.), *Mechatronics and Automatic Control Systems*, Lecture Notes in Electrical Engineering 237, DOI 10.1007/978-3-319-01273-5_59,

frequency. It involves mighty conductive EMI caused by high *du*/*dt* and *di*/*dt* of power devices. It also causes great electromagnetic radiation, which can cause mistake to itself and EMI to other equipments and affect their performance.

2 Electromagnetic Interference Source and Spread Route of PWM Inverter

In motor drive system high *du*/*dt* and *di*/*dt* occur with performance of power device because of PWM modulation. Harmonic waves of the voltage and current range from several *kHz* to hundreds of *MHz*. These high frequency factors shape leaking current through parasitical capacity and common impedance and produce conductive EMI. There are two spread routes of leaking current of motor drive system. One is coupling of the parasitical capacity between power electronic device and radiator, the other is coupling of the distributive capacity between motor winding and stator enclosure. Coupling of the distributive capacity between cable and the earth should be taken into account if the inverter output cable is very long. The return route of leaking current is mainly neutral point grounding wire of system transformer. The EMI spread route of motor PWM drive system is shown in Fig. 1 [2, 3]. In Fig. 1 *C*sg is the distributive capacity between motor winding and stator enclosure; *C*lg is the distributive capacity between cable and the earth; *C*ll is the distributive capacity between cables. In addition, there is parasitical capacity between power electronic device and radiator. The dashed line is differential mode current route and the dotted line represents common mode current route.

3 The Novel Soft Switching Inverter

The effective method to overcome shortcomings of traditional PWM inverter is soft switching technology. Soft switching involves zero voltage switching (ZVS) and zero current switching (ZCS) [4–6]. The switch turns on and off under ZVS or ZCS condition, which can restrict turn-on *di*/*dt* and turn-off *du*/*dt*, so as to reduce EMI.

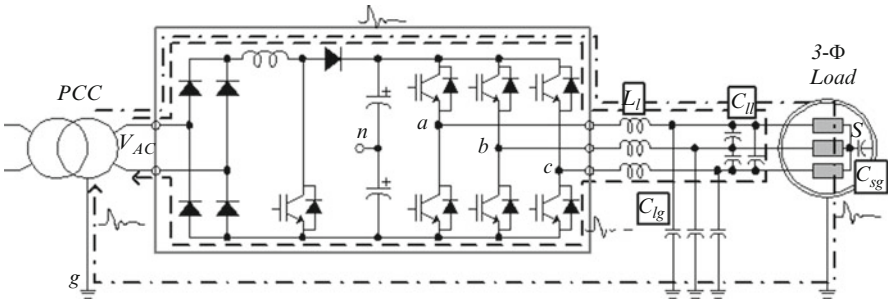

Fig. 1 EMI spread route of motor PWM drive system

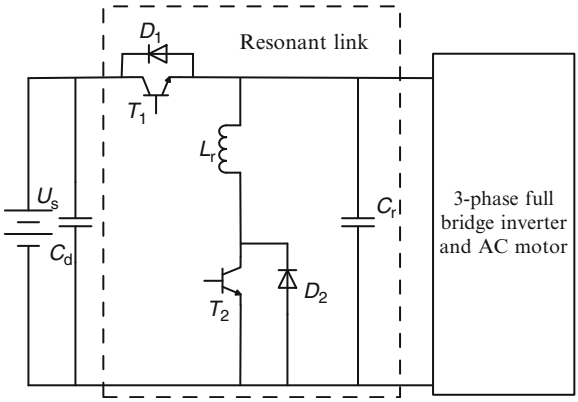

Fig. 2 Topology of novel PRDCLI

The paper puts forward a new parallel resonant DC link inverter (PRDCLI), Fig. 2 is the topology. The circuit includes auxiliary resonant link, inverter circuit and AC motor. The auxiliary switch $T1$, diode $D1$, auxiliary switch $T2$, diode $D2$, resonant inductance Lr and resonant capacitance Cr constitutes the auxiliary circuit. The resonant inductance Lr and resonant capacitance Cr compose of resonant link circuit. The resonant link causes periodic ZVS grooves on DC side. It provides soft switching condition for power devices $S1$~$S6$ of the 3-phase full bridge inverter.

The advantage of the new inverter is all the switching devices operate under soft switching condition. Switch $T1$ turns on and turns off under ZVS condition, Switch $T2$ turns on under ZCS condition and turns off under ZVS condition. It brings no extra voltage and current stress to the main switches. The circuit is simple and easy to control. It can make voltage of DC side descend to zero and hold for a needed time for inverter PWM modulation and soft switching operation. Voltage of Cr descends to zero when the main switches turn on.

4 Experimental Result and Analysis

The experimental parameters are: DC voltage $Us = 200\ V$, resonant inductance $Lr = 1\ \mu H$, resonant capacity $Cr = 3.8\ \mu F$, inverter frequency $f = 10\ kHz$, resonant frequency $f' = 80\ kHz$. The experiments are carried through under hard switching condition and soft switching condition respectively.

4.1 Improving of Turn-On Peak of Inverter Switch

Figure 3 is voltage waves of main switches under hard switching (a) and soft switching (b). Figure 3 proves that with resonant link the turn-on du/dt peak of main switch is improved greatly. The max turn-on du/dt peak of main switch

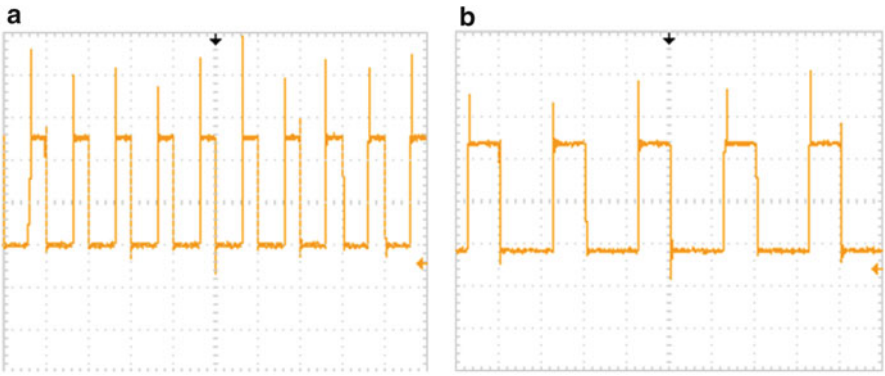

Fig. 3 Waveforms of device switch voltage under hard switching and soft switching situation

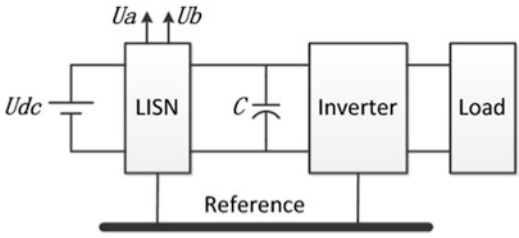

Fig. 4 EMI measurement system

reduces from *200 V* under hard switching to *140 V* under soft switching condition, the reducing amplitude is beyond 30 %. So it can reduce EMI greatly.

4.2 EMI Experimental Result and Analysis

Conductive EMI can be measured through linear impedance steady net (LISN). The EMI measurement system is shown in Fig. 4 [7]. The equivalent circuit of LISN is shown in Fig. 5. Noise voltage *U*a and *U*b are the output of LISN, which are fed to spectrum analyzer. We can use FFT function of spectrum analyser to analyse *U*a or *U*b and get EMI spectrum. We measure noise voltage of hard switching inverter and soft switching inverter under the same condition, and feed them to Tektronix TDS1012B-SC scope. We use the scope's FFT function to analyze noise voltage and get EMI spectrum.

Figure 6 shows the EMI noise spectrum of hard switching inverter and soft switching inverter.

The paper Compares Fig. 6a with Fig. 6b, it shows that during most of the frequencies the soft switching inverter reduces EMI noise greatly. It is because in soft switching inverter all the main switches perform under ZVS condition, it reduces the switching du/dt and di/dt. And the auxiliary switches $T1$ and $T2$ operate

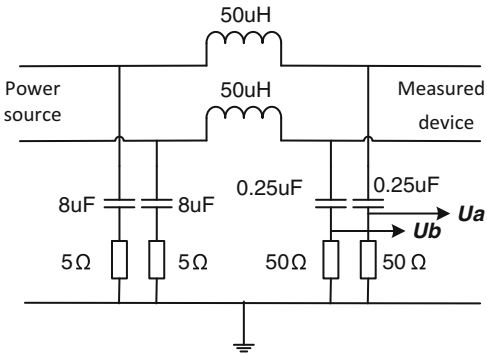

Fig. 5 Equivalent circuit of LISN

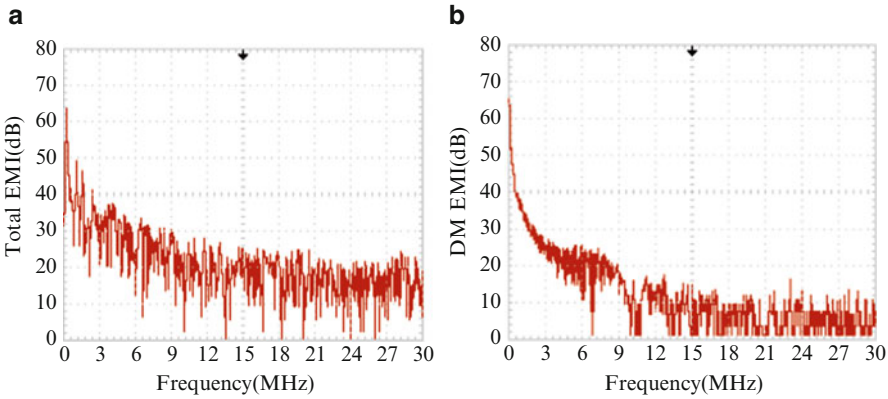

Fig. 6 EMI noise spectrum of hard switching inverter and soft switching inverter

under soft switching too. The auxiliary switch $T1$ turns on and turns off under ZVS condition. The auxiliary switch $T2$ turns on under ZCS condition and turns off under ZVS condition.

The comparison shows that soft switching inverter can immensely reduces conductive noise of traditional hard switching inverter. And then it can reduce the EMI to other equipment, so as to ensure the system perform safely and normally.

4.3 Comparison with the Related Works

Figure 7 shows the EMI noise spectrum of the new switching inverter and the related works.

The paper also compares Fig. 7a with Fig. 7b, it shows that during most of the frequencies the new soft switching inverter can reduces EMI noise more than the

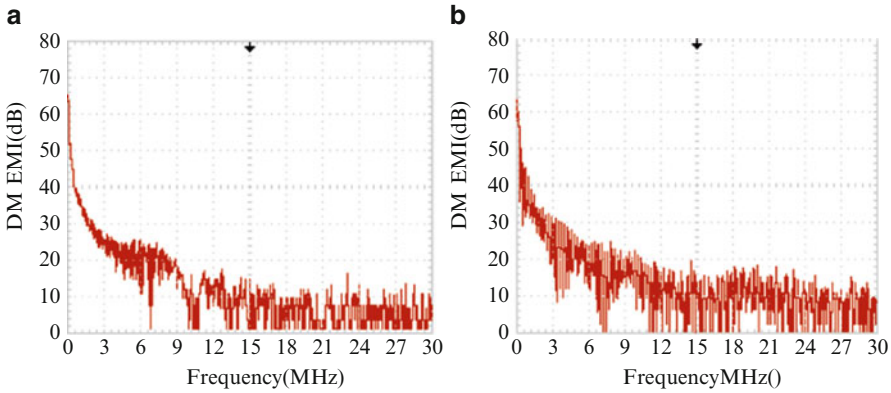

Fig. 7 EMI noise spectrum of the proposed switching inverter and the related works

related works. It is because in the new soft switching inverter all the switches operate under soft switching condition, it can reduce the switching *du*/*dt* and *di*/*dt* greatly. But the auxiliary switches of the related works do not operate under soft switching condition, it brings more EMI. So it proves that the new soft switching inverter is more advanced than other related works.

5 Conclusion

The paper presents a new soft switching inverter to reduce EMI of traditional hard switching inverter. It measures the turn-on voltage spike and the EMI conductive noise of AC inverter system. It also analyzes and compares the EMI noise spectrum under hard switching and soft switching condition. It also compares the EMI noise spectrum with other related works. Finally it proves the new soft switching inverter can reduce effectively EMI. The soft switching inverter is feasible and positive.

References

1. Son YC, Sul SK (2002) Conducted EMI in PWM inverter for household electric appliance [J]. IEEE Trans Ind Appl 38(5):1370–1379
2. Zhao D, Ferreira JA, Polinder H et al (2006) Investigation of EMI noise transfer characteristic of variable speed drive system[C]. In: SPEEDAM 2006 international symposium on power electronics, electrical drives, automation and motion, pp 603–608
3. Lai JS, Huang X, Pepa E et al (2003) Inverter EMI modelling and simulation methodologies [C]. Conference Rec. of IEEE IECON Annual Meeting, Roanoke, pp 736–744
4. Santolaria A, Balcells J, Gonzalez S et al (2003) Evaluation of switching frequency modulation in EMI emissions reduction applied to power converters[C]. In: Industrial electronics society, 2003. IECON'03. The 29th annual conference of the IEEE, vol 3. pp 2306–2311

5. Rahkala M, Suntio T, Kalliomaki K (2002) Effects of switching frequency modulation on EMI performance of a converter using spread spectrum approach[C]. In: Applied power electronics conference and exposition, 2002. APEC 2002. Seventeenth annual IEEE, vol 1. pp 93–99
6. González D, Gago J, Balcells J (2003) New simplified method for the simulation of conducted EMI generated by switched power converters[J]. IEEE Trans Ind Electr 50(6):1078–1084
7. Archambeault B, Pratapneni S, Wittwer DC et al (2008) A proposed set of specific standard EMC problems to help engineers evaluate EMC modelling tools. IBM, Dell Computer Corp., Intel Corp., IEEE EMC Society TC9 [DB/OL]. http://www.ewh.Ieee.org/cmte/tc9/summary/summary.html

A Summary of Harmonic Detection in Electricity Distribution Based on the Instantaneous Power Theory

Zhi-xia Zhang, Chang-liang Liu, Xin-yu Zhang, and Funaki Tsuyoshi

Abstract In order to prove that the Instantaneous power theory can be applied to the power quality research field, applications of the harmonic detection method based on the instantaneous power theory in three-phase four-wire electricity distribution and single-phase electricity distribution were discussed. Moreover, basic approaches of the instantaneous power, pq method and $i_p - i_q$ method were introduced. Simulations about pq method and $i_p - i_q$ method were built by the MATLAB software to confirm the validity of the method. The harmonic detection method based on instantaneous power theory in three-phase four-wire electricity distribution and single-phase electricity distribution was easy to implement, and harmonic current can be detected accurately and real-time in the case of voltage distortion or frequency changes.

Keywords Harmonics • Instantaneous power theory • Current detection • Low-pass filter • Electricity distribution

1 Introduction

In modern power system, because of increasing using nonlinear loads, especially power electronic devices, a large number of harmonics and reactive current [1] inject into the grid, causing problems that voltage flicker, the frequency changes, three-phase imbalance, which will affect power quality, transmission efficiency and equipment safety. The harmonics and reactive power compensation have received increasing attention. Currently, an important trend of harmonic suppression is to use active power filter (APF). APF can track the frequency and amplitude of the grid current which are parameters of making a compensation, and its compensation

Z.-x. Zhang (✉) • C.-l. Liu • X.-y. Zhang • F. Tsuyoshi
Shenyang Agricultural University, Shenyang, China
e-mail: syzzx7@163.com

W. Wang (ed.), *Mechatronics and Automatic Control Systems*, Lecture Notes in Electrical Engineering 237, DOI 10.1007/978-3-319-01273-5_60,

characteristic cannot affected by network impedance, so it plays an important role in harmonic suppression. Its principle is that harmonic current is detected from compensation object by the compensation device on the purpose of generating compensation current which compare with the harmonic current, its size is equal but the polarity is reverse, consequently, grid current only contains the fundamental component. How to extract the harmonic current accurately and real-time from the grid in the harmonic detection is the big key. The APF compensation characteristics depend on the algorithm about extracting harmonic current from the grid. Among harmonic detection algorithms, which is the most widely used in APF is the detection method based on the "instantaneous power theory". This paper described the application of the harmonic detection method based on the instantaneous power theory in three-phase electricity distribution and single-phase electricity distribution.

2 Instantaneous Power Theory Basis

Akagi Thai, Japanese scholar in 1983 [2], proposed the instantaneous power theory in the three-phase circuit firstly, which is also known as *pq* theory. In 1990s, Wang Zhao-an, a professor in Xi'an JiaoTong University, completed instantaneous current definition of the instantaneous power theory. The instantaneous power theory is based on the definition of the instantaneous active power p and instantaneous reactive power q [3]. Instantaneous active power p(instantaneous reactive power q) is the product of voltage vector e and instantaneous active current i_p (instantaneous reactive current i_q), and then a matrix form of formula can be written to arrive at the coefficient matrix.

Suppose the three-phase currents in the grid are the i_{abc}. Equation 1 is the currents transform formula, the voltages transform is same as the currents.

$$\begin{bmatrix} i_\alpha \\ i_\beta \end{bmatrix} = \sqrt{\frac{2}{3}} \begin{bmatrix} 1 & -\frac{1}{2} & -\frac{1}{2} \\ 0 & \frac{\sqrt{3}}{2} & -\frac{\sqrt{3}}{2} \end{bmatrix} \begin{bmatrix} i_a \\ i_b \\ i_c \end{bmatrix} \tag{1}$$

The traditional active power and reactive power are defined in the average concept or phasor concept which can only apply to the case when the voltage and current are sine-wave. However, the concept of instantaneous power theory, is defined on the basis of the instantaneous value which not only applies to sine wave, also applies to non-sine wave and any other transition processes. It can be seen from all of the above definition of the concept of instantaneous power theory that the new theory is very similar with the traditional theory in form and can be treated like the promotion and extension of the traditional theory. Based on this theory, the two detection methods named *pq* detection method and $i_p - i_q$ detection method can be drawn to calculate the harmonics of three-phase circuit.

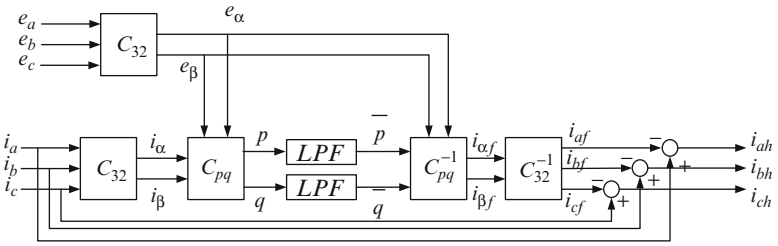

Fig. 1 *pq* detection method principle block

2.1 *pq* Detection Method

The *pq* detection principle is that the current (voltage) is converted from matrix transformation of three-phase to two-phase reference frame.

Through the operator matrix, three-phase active power p and the three-phase reactive power q can be drawn, through low-pass filter, the DC component of p and q will be lefted. After getting the fundamental component of the current through the matrix operations, fundamental active current in three-phase reference frame can be drawn from the two-phase to three-phase transformation. Then the three-phase harmonic current i_{ah}, i_{bh}, i_{ch} can be obtained by original current subtracting from the fundamental grid current. Figure 1 shows its principle block.

Where the matrix C_{pq} is

$$C_{pq} = \begin{bmatrix} v_\alpha & v_\beta \\ v_\beta & -v_\alpha \end{bmatrix} \tag{2}$$

2.2 i_p–i_q Detection Method

i_p–i_q detection principle is that active current i_p and reactive current i_q can be obtained by multiplying the current in two-phase reference frame by matrix C, which is gained from the first-order phase-locked loop [4] by a phase voltage. Fundamental active current in three-phase can be obtained through the LPF and two-phase to three-phase transformation, then the three-phase current harmonic currents i_{ah}, i_{bh}, i_{ch} can be gained by the original current subtracting from the fundamental active current. Figure 2 shows the principle block. It can be seen from the above theory, *pq* detection method requires the detection of three-phase currents and voltages, its service condition is that three-phase grid voltage cannot distort, otherwise, the harmonic current cannot be detection accurately and real-time. i_p–i_q detection method is the improvement of *pq* detection method. It only

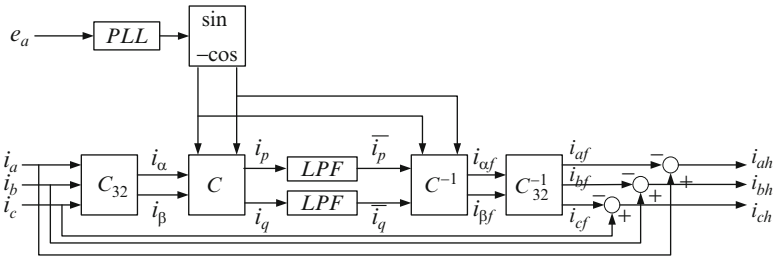

Fig. 2 i_p−i_q detection method principle block

needs the phase information of a phase voltage, but does not need all of three-phase voltages, therefore harmonic current can be detected accurately under the voltage distortion.

Where matrix C is

$$C = \begin{bmatrix} \sin \omega t & -\cos \omega t \\ -\cos \omega t & -\sin \omega t \end{bmatrix} \tag{3}$$

2.3 Simulation

Based on the above principle, Matlab/Simulink toolbox is used to build a simulation model. Take *pq* detection method for example. The settings of simulation are that AC voltage 220v, 50Hz, three-phase symmetric linear load and distortion current is generated by the rectifier bridge. Figure 3 shows A-phase result which are A-phase voltage v_a, current i_a, fundamental current i_{af} and harmonic current i_{ah} respectively.

Simulation model of i_p−i_q is built based on its principle block. Using the phase-lock loop to track phase information, and rest of i_p−i_q simulation model is similar to *pq* model. Parameter settings are the same. In the same condition, its simulation result is also shown as Fig. 3.

3 Application in Three-Phase Four-Wire Electricity Distribution and Single-Phase Electricity Distribution

3.1 Application in Three-Phase Four-Wire Electricity Distribution

At present, China's low-voltage distribution system mainly uses three-phase four-wire power system, such as factories, residential and urban power systems. Therefore, the compensation strategy of the harmonic current detection method in the

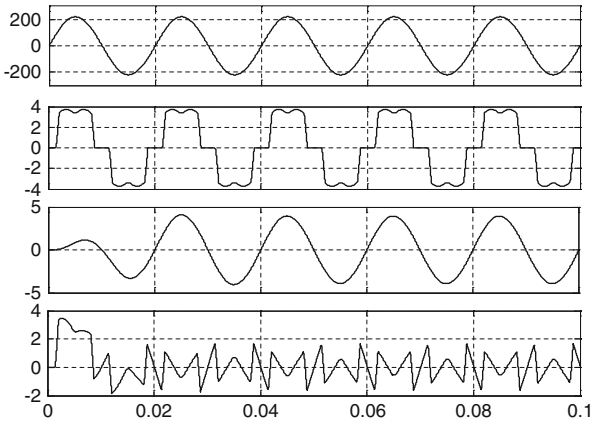

Fig. 3 Result of simulation of *pq* detection method

three-phase four-wire electricity distribution has an important practical significance. Harmonic detection based on instantaneous power theory cannot be used in three-phase four-wire electricity distribution originally, because three-phase current contains zero-sequence component(i_0).A simple solution is to remove zero-sequence component, afterward detecting harmonic current. In three-phase four-wire electricity distribution, three-phase currents contain the zero-sequence components equal, and its values are one-third of sum of three-phase currents, as the following Eq. 4 shows,

$$i_{a0} = i_{b0} = i_{c0} = (i_a + i_b + i_c)/3 \tag{4}$$

After the zero-sequence components are subtracted from three-phase currents respectively, the traditional detection based on instantaneous power theory can be used. The principle block is shown in Fig. 4 (Take $i_p{-}i_q$ method for example).

3.2 Application in Single-Phase Electricity Distribution

Harmonic detection method also cannot be used in single-phase electricity distribution, because single-phase circuit only has one phase current and one phase voltage. Transformation is a necessary process if the harmonic detection method want to be used.

One solution method is the single-phase current or voltage decomposition method, which is based on three-phase voltage phase relationship that differ 120° respectively [5]. Assume v and i are single-phase voltage and single-phase current respectively in the single circuit, lagging v_s 120° and 240° can structure v_b and v_c, make i_s the same treatment. Consequently, the pq detection method or $i_p{-}i_q$ detection method can be used. Because of the advantages of the $i_p{-}i_q$ method, the new detection method under $i_p{-}i_q$ detection method is taken into consideration. Its principle block is shown in Fig. 5.

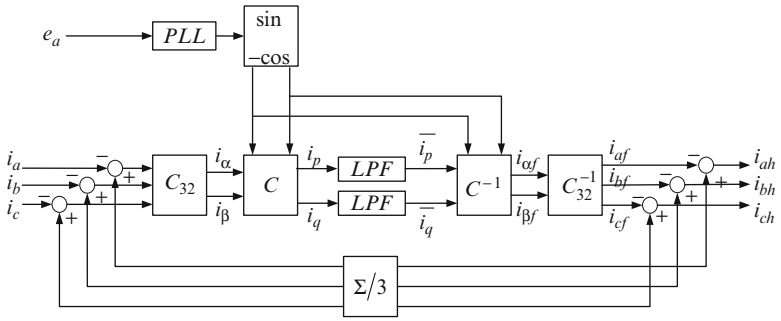

Fig. 4 Principle of i_p−i_q detection method in four-wire circuit

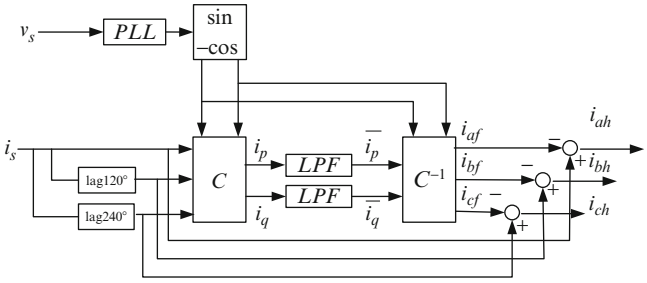

Fig. 5 Decomposition method under i_p−i_q detection method

Another solution method is to construct two-phase reference frame current (voltage) directly from the single-phase current (voltage) [6]. The method is that taking i_s is i_α and taking i_s lagged 90° is i_β. Harmonic current also can be detected by this method real-time and accurately. It is similar to the first method but is more easier than it. The characteristic of this approach is easy to implement.

It has theoretically testified that two methods mentioned above are effective. Figure 6 shows the second method's principle block. At present, many scholars, professional and technical personnel has make in-depth and meticulous research about harmonic detection in theory and in fact, initially realized, but still not perfect [7].

4 Conclusion

According to the above analysis results, in the situation of three-phase imbalanced and voltage distortion, i_p−i_q detection method can calculate the harmonic current of the power grid real-time and accurately, while the result of the traditional pq detection method has error, because voltage in the grid with distortion is not involved in the i_p−i_q detection method. Therefore, i_p−i_q detection method can be

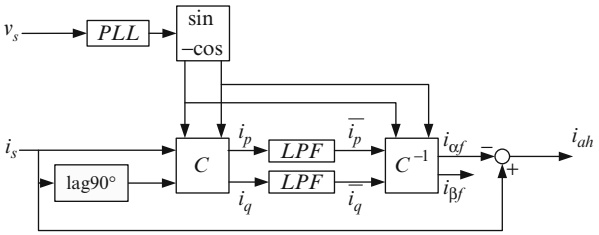

Fig. 6 The second method under $i_p - i_q$ detection method

applied in the grid parameters measurement technology more widely. Even though harmonic detection method based on instantaneous power theory was originally supposed to be applied for the three-phase three-wire circuit, in three-phase four-wire electricity distribution, the detection method can be used when the zero-sequence component is removed from the grid current. Regarding to single-phase electricity distribution, in accordance with single-phase voltage and current, it can construct the corresponding three-phase system (or construct orthogonal variables in two-phase reference frame directly) and consequently, the harmonic current detection methods also can be applicable.

References

1. Akagi H (1994) Trends in active power line conditioners[J]. IEEE Trans Power Electr 9 (3):263–268
2. Sun Shu-guang, Wang Jing-qin, Shi Shun-quan (2008) Study on real-time detection of harmonics and reactive currents in single phase circuit [J]. Electr Meas Instrum 45(505):4–7
3. Aredes M, Hafner J, Heumann K (1997) Three-phase four-wire shunt active filter control strategies[J]. IEEE Trans Power Electr 12(2):311–318
4. Zhang Zhi-xia, Piao Zai-lin, Guo Dan, Xie Ying (2012) A kind of phase-locked loop for power system[J]. Trans China Electrotech Soc 27(2):250–254, 222
5. Ma Xue-li (2007) A method of harmonic current detection for single-phase circuit[D]. Tianjin University, Tianjin
6. Li Ya (2011) Study of the real-time harmonic and reactive current detection in single-phase circuit[J]. J Electr Power 26(1):22–25
7. Huang Ling, Liu Ji, Cao Bin (2001) A method of harmonic current detection based on the instantaneous reactive-power theory[J]. J Harin Univ Sci Technol 6(4):103–106

Reduce-Size Dual-Polarized Microstrip Antenna

Yong Cheng and ZhenYa Wang

Abstract This study proposes a new design of dual linearly polarized microstrip (patch) antenna which uses a set of slits and slots to effectively reduce the area of patch compared with the conventional, dual linearly polarized square patch. The proposed antenna was simulated by using EM simulator IE3D. The antenna is designed on inexpensive FR4 substrate. Simulated results show that at the same operates frequency the proposed antenna is more than 50 % smaller compared to a conventional dual-polarized square patch. Isolation between the port1 and the port2 is lower than 35dB. Additionally, the cross-polarization level of the proposed compact dual-polarized is better than -30dB in the E- and H-plane patterns.

Keywords Compact microstrip antenna • Dual-polarized radiation

1 Introduction

Microstip antennas are widely used in the wireless communications, because of its compact size, low prices and. To achieve circularly polarization, a microstrip line is used to feed a square ring patch [1] and a inverted L slit is embedded in the ground plane to excite two orthogonal vectors [2]. Meandering probes feed the patch to obtain dual-polarized performance [3]. A novel microstrip dual-polarized antenna is excited by a hook shaped probe [4] and other excites method [5] are reported. In this article, some symmetrical slits and slots are embedded in the radiation patch to make the size of the antenna be reduced significantly while excited the excellent dual-polarized radiation for the operating frequency. Two probe feeds are used to excite two line polarizations.

Y. Cheng (✉) • Z. Wang
College of Electronics Science and Engineering, Jiangsu Key Laboratory of Wireless Communications, Nanjing University of Posts and Telecommunications, Nanjing, China
e-mail: chengy@njupt.edu.cn

W. Wang (ed.), *Mechatronics and Automatic Control Systems*, Lecture Notes in Electrical Engineering 237, DOI 10.1007/978-3-319-01273-5_61,

2 Antenna Design

A novel antenna with the addition of slits and slots is described in this section. The side length of the square radiating patch is L which is 28.5 mm. The substrate of the antenna is FR4 with thickness 1.6 mm and relative permittivity 4.4. The width of the slits and slots are all 1 mm. The antenna is fabricated on rectangles of FR4 substrate of dimensions: 60.00 × 60.00 × 1.6 (length × width × thickness in millimeter). The geometry of the antenna is shown as Fig. 1. The antenna is fed by two coaxial probes. dp = 5.9 mm represents the location of the two feeding points away from the antenna center.

The proposed design, optimized for a resonant frequency of 1.72 GHz. Each slit has length of y1 = 11.65 mm and the cross slot has length of y3 = 10.0 mm. The other four slots are the same and have length of x1 = 9.23 mm and y2 = 4.57 mm, and they are at a distance of 5.25 mm away from the patch edge (x2 = 5.25 mm). The combination of slits and slots effectively increases the length of the current streamlines. Consequently the fundamental frequency is lower than for a conventional microstrip antenna without slits and slots. Therefore the size of the proposed antenna can be reduced than the conventional design at the same operating frequency.

3 Simulated Results and Discussion

Antennas A1, A2, A3 are three kinds of prototype with the same dimension but different dp (the position of the feeding point). Reference antenna A is a corresponding antenna without slits and slots. All of the antennas have the same

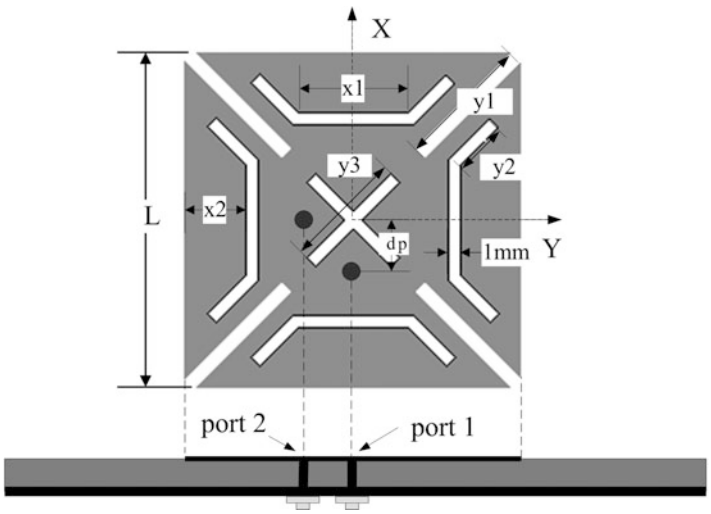

Fig. 1 Geometry of the antenna

Table 1 Antenna parameters and performances

	dp (mm)	x1 (mm)	x2 (mm)	y1 (mm)	y2 (mm)	y3 (mm)	L (mm)	Fr (MHz)	BW (%)
Antenna A1	5.7	9.23	5.25	11.65	4.57	10.0	28.5	1,715	1.46
Antenna A2	5.9	9.23	5.25	11.65	4.57	10.0	28.5	1,720	1.51
Antenna A3	6.1	9.23	5.25	11.65	4.57	10.0	28.5	1,722	1.50
Reference A	5.9	0	0	0	0	0	0	2,434	2.42

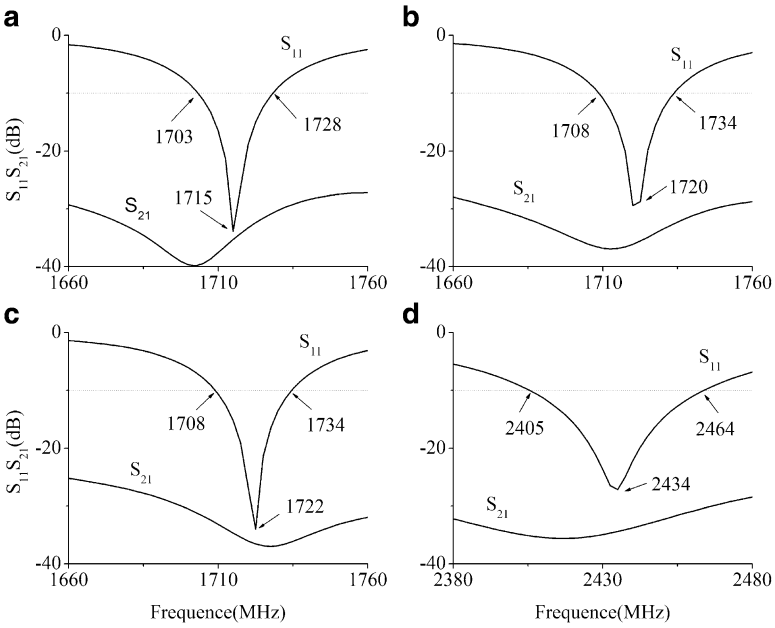

Fig. 2 Simulated S_{11} and S_{21} versus frequency; (**a**) A1.(**b**) A2. (**c**) A3. (**d**) Reference A

size. The four antennas are studied to compare their performances. The Table 1 shows the parameters of the slits and slots and the dual-polarized bandwidths. Figure 2 presents the S_{11} and S_{21} versus frequency.

As the Fig. 2 shows, it is obviously that the obtained resonant frequency of antenna A2 is much lower than that of the reference A. The resonant frequency of antenna A2 is 1,720 MHz. That is lower about 29 % compared to the operating frequency of reference A,2,434 MHz. It is observed that the variations of S_{11} are not sensitive to the feed position dp. It moved from 5.7 mm (antenna A1) to 6.1 mm (antenna A3). However, the isolation between the port1 and the port2 changes greatly versus frequency with a small variation in the probe feeding position. Finally, it should be noted that as the resonant frequency decreases, the operating impedance bandwidth decreases. Figure 3 shows the radiation patterns of antenna

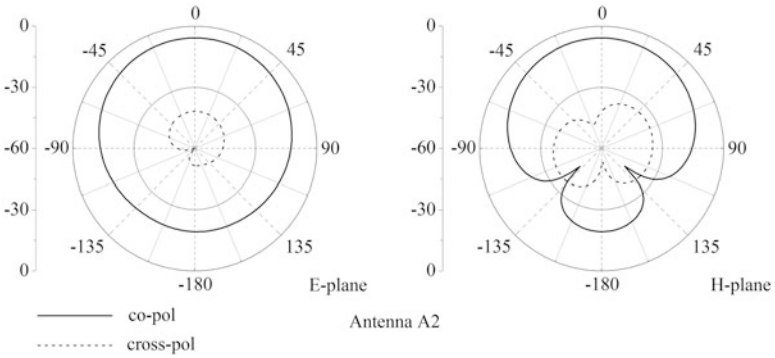

Fig. 3 Co-polarization and cross-polarization radiation patterns of antenna A2

Table 2 Antenna parameters and performances

	dp (mm)	x1 (mm)	x2 (mm)	y1 (mm)	y2 (mm)	y3 (mm)	L (mm)	Fr (MHz)	BW (%)
Antenna A2	5.9	9.23	5.25	11.65	4.57	10.0	28.5	1,720	1.51
Reference B	9.1	0	0	0	0	0	40.55	1,720	2.2

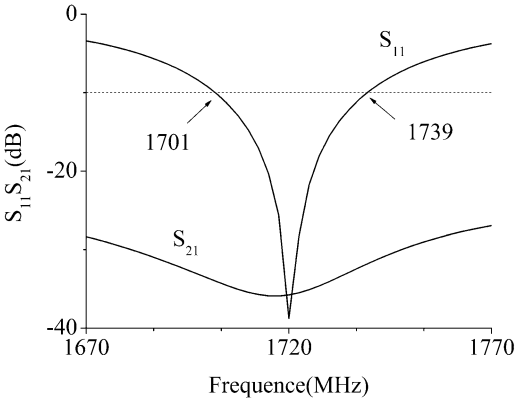

Fig. 4 Simulated S_{11} and S_{21} of reference B: L = 40.55 mm

A2 at 1,720 MHz. The excitation is fed from port1. The cross-polarization levels of antenna A2 in the E- and H-planes are both better than −30 dB.

To see the size merit of the design more clearly, we simulate another antenna Reference B, a conventional, dual linearly polarized square patch without slits and slots, and the fundamental resonant frequency is 1.72 GHz which is same as Antenna A2. The parameters and performances of Antenna A2 and Reference B are given in Table 2. For the same resonant frequency, the proposed design A2 with slits and slots has side dimensions of L = 28.5 mm, whereas Reference B had dimensions of 40.55 mm. Hence, Antenna A2 has achieved the 50 % size reduction comparing the reference antenna. Figure 4 presents the S_{11} and S_{21} versus frequency of antenna Reference B.

4 Measurements

After studying the antenna detailly by using EM software, a prototype of the antenna is fabricated. The photo of the antenna is shown in Fig. 5. The antenna is fed by two probes. The characteristics of the two input ports are measured using vector network analyzer 8720ET. The results are shown in Fig. 6. The center frequency is 1,718 MHz and the bandwidth (below −10 dB) is 27 MHz. Relative bandwidth is 1.57 %.

The isolation between the port1 and port2 is measured and shown in Fig. 7. At the center frequency, the isolation is below −30 dB.

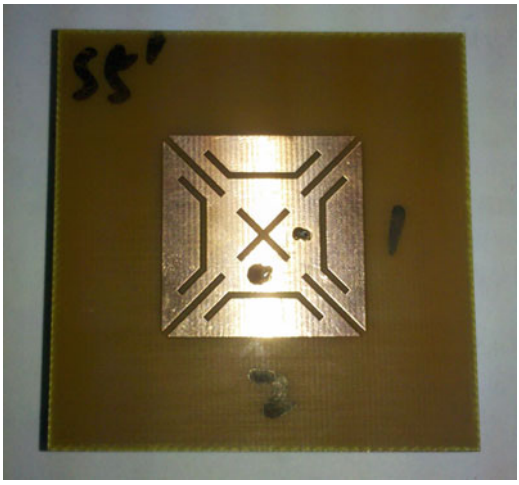

Fig. 5 The photo of the antenna

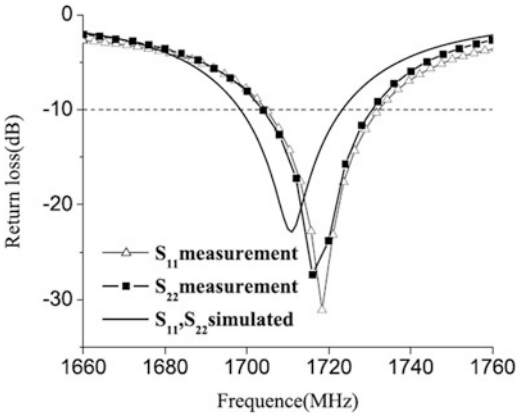

Fig. 6 The return loss of the antenna

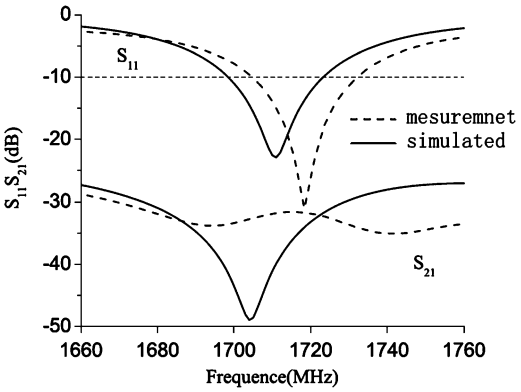

Fig. 7 The isolation between port1 and port2

5 Conclusion

In this paper, a novel, microstrip patch antenna which has compact size, dual-polarization is investigated. By embedding some slits and slots in the square radiating patch to change the electrical current that the resonant frequencies of the two linear polarizations can be lowed. In the proposed design, the cross polarization level is lower than−30 dB and the size of the antenna can be reduced of 50 %.

Acknowledgements This work was supported by National Science and Technology Major Project under granted no. 2012ZX03001028-005 and Research Project of Nanjing University of Posts and Telecommunications (208035)

References

1. Hua-Ming Chen, Yang-Kai Wang, Yi-Fang Lin, Che-Yen Lin, Shan-Cheng Pan (2009) Microstrip-fed circularly polarized square-ring patch antenna for GPS applications. IEEE Trans Antennas Propag 57(4):1264–1267
2. Christina F. Jou, Jin-Wei Wu, Chien-Jen Wang (2009) Novel broadband monopole antennas with dual-band circular polarization. IEEE Trans Antennas Propag 57(4):1027–1034
3. Hau-Wah Lai, Kwai-Man Luk (2007) Dual polarized patch antenna fed by meandering probes. IEEE Trans Antennas Propag 55(9):2625–2627
4. Kenny Seungwoo Ryu, Ahmed A. Kishk (2008) Wideband dual-polarized microstrip patch excited by hook shaped probes. IEEE Trans Antennas Propag 56(12):3645–3649
5. Gosalia K, Lazzi G (2003) Reduced size, dual-polarized microstrip patch antenna for wireless communications. IEEE Trans Antennas Propag 51(9):2182–2186

Grain Logistics Management Information System Based on Short Message Service Technology

Feng Wang, Zhaohui Xu, Tong Zhen, Xiaoming Zhang, and Meng Zhang

Abstract For grain logistics information's real-time transmission and management, a method of using smart phone as a client terminal is proposed and a relevant grain logistics management information system based on SMS technique designed. The grain logistics information can be transmitted between the smart phone and the database server by means of SMS and windows service. And the real-time monitoring of grain logistics can be realized in virtue of the platform of management information system. This system realized such functions as collecting grain logistics information, distributing scheduling information and monitoring the grain vehicle location information. Test results showed that the grain logistics information can be collected and managed conveniently and effectively with our system.

Keywords Grain logistics • Short message service • Windows service

1 Introduction

Grain is a special commodity which has close relationship to national economy and the people's livelihood [1]. The production, circulation, processing and sale of grain play an important role in the national economy and social development.

F. Wang (✉) • T. Zhen
Henan University of Technology, Zhengzhou, China

Key Laboratory of Grain Information Technology & Control, Ministry of Education, Zhengzhou, China
e-mail: wfmail@sina.com

Z. Xu
Key Laboratory of Grain Information Technology & Control, Ministry of Education, Zhengzhou, China

X. Zhang • M. Zhang
Henan University of Technology, Zhengzhou, China

W. Wang (ed.), *Mechatronics and Automatic Control Systems*, Lecture Notes in Electrical Engineering 237, DOI 10.1007/978-3-319-01273-5_62,

The modern food logistics system building is the key link to guarantee our country's food security. Short messaging service (SMS) technology has the advantages of GSM (Global System for Mobile Communications) network of the high efficiency of spectrum, safety, high stability, large capacity, wide covering range and strong anti-noise ability advantages [2]. Its application to the grain logistics management information businesses can provide data support for the grain logistics management, and then the real-time transmission and management of grain logistics information can be achieved.

2 System Design

2.1 System Architecture

The smart phone is used as user terminal on platform of the development grain logistics management information system, and the application software is developed on it to realize the information transmission between the user terminals and management information system platform. To complete the whole system function, the SMS cats, communication server and database components are needed. The system architecture is shown in Fig. 1.

Smart phone interact information with communication server and database through SMS cats and the platform of management information system operate the database directly [3, 4]. The system has features of low coupling and is expandable.

2.2 The Main Functional Modules of the System

The system functional module structure is shown in Fig. 2. The platform of management information system realize the functions of delivering grain scheduling information, managing grain operation information and monitoring the grain

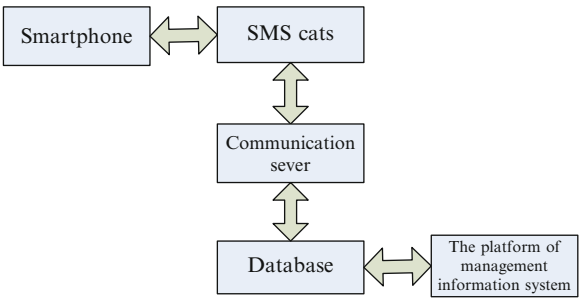

Fig. 1 System architecture

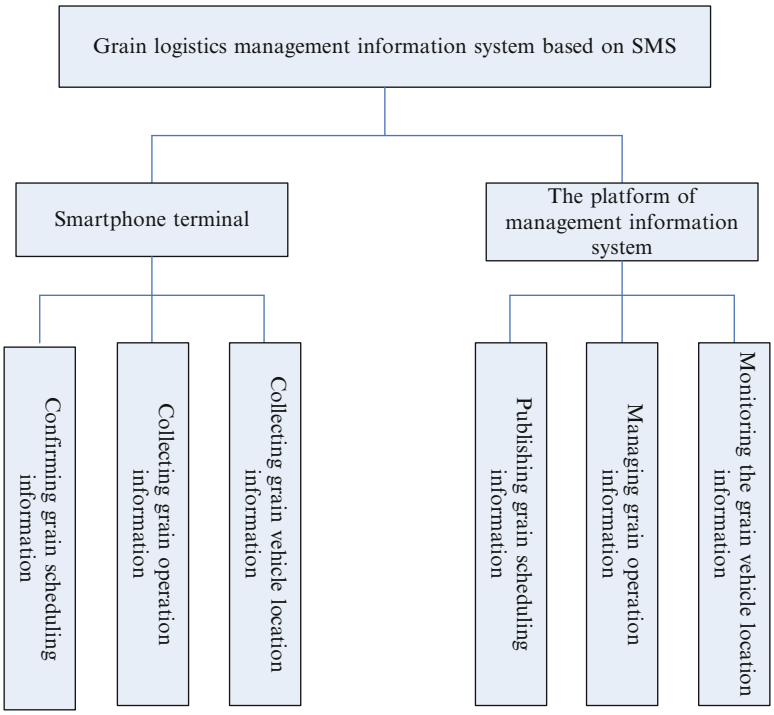

Fig. 2 System structure

vehicle location information, etc; the smart phone system realize the functions of confirming grain scheduling information, collecting grain operation information and grain vehicle location information, etc.

3 Key Techniques of the System

3.1 Smart Phone Terminal

3.1.1 SMS Processing Flow

In this paper, the windows mobile smart phone terminal with GPS functional module is selected. It can receive, process and send grain logistics information. After the enablement of smart phone terminal system, the application program calls Windows CE Mail Application Programming Interface (hereinafter referred to as CEMAPI) through the "platform invocation services" to read specific grain scheduling message (hereinafter referred to as the "specific message") from message inbox automatically, analysis and abstract the mobile phone number, transportation

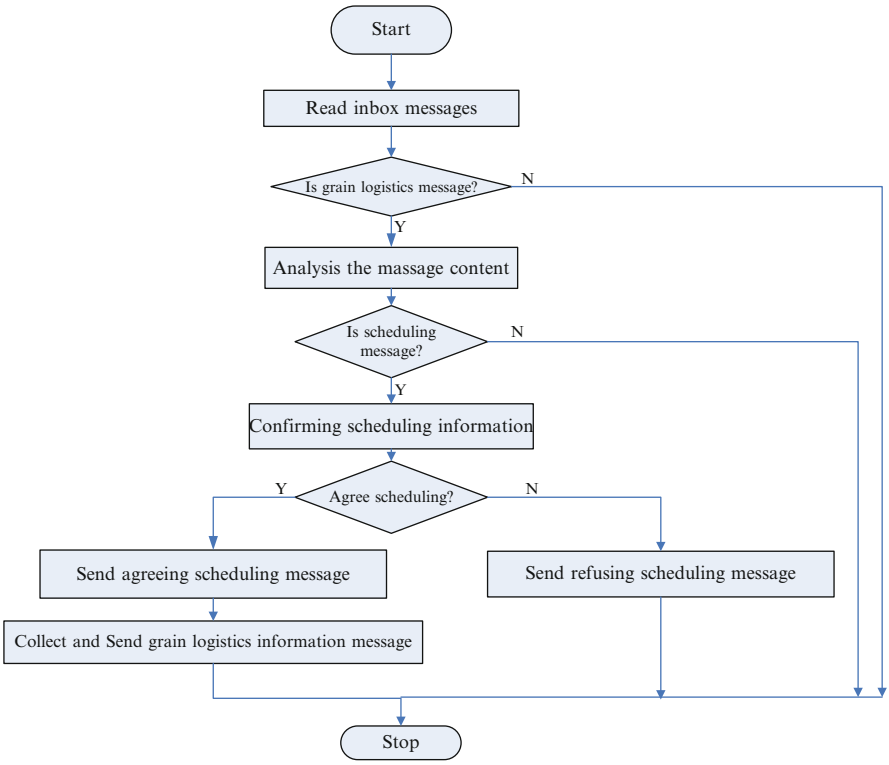

Fig. 3 Flow chart of the SMS handling of smart phone

contract number and GPS sending time interval corresponding to the message,then confirm scheduling information, collect data related to grain logistics, and finally, complete the sending of grain logistics data. The SMS processing flow chart is shown in Fig. 3.

3.1.2 Reading and Analysing the Specific Message from Inbox

The application program uses CEMAPI to realize reading specific messages from inbox automatically, and the specific steps are as follows. Firstly, analysis and get session object which the IMAPISession access. Secondly, abstract short message's IMsgStore store object. Thirdly, abstract IMAPIFolder directory objects of the inbox. Finally, get IMessage object, and compare the attribute of sender to contact list members to judge whether the message is sent by the platform of management information. If so, after reading message content to data table named DataGrid, the application program analysis the message content based on message agreement, get the transportation contract number and GPS sending time interval, transfer them

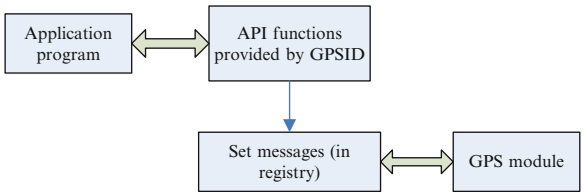

Fig. 4 Schematic diagram of obtaining the GPS information

and then show them to respective relevant interface of the application program automatically. Users only need simply input loading, unloading, weighing and other few necessary information.

3.1.3 Obtaining Grain Vehicle GPS Information

The smart phone's GPS module transfer text format data made by NMEA (National Marine Electronics Association) through the serial port. Using GPSID (GPS Intermediate Driver) to analysis NMEA grammar can obtain GPS information which contains longitude, latitude, speed and time. The schematic diagram is shown in Fig. 4.

In Fig. 4, GPSID is a device driver located between the application program and interface layer of the GPS module [5], and it packages the serial port operation, making the developed applications access GPS module directly without through serial port, instead, access API functions provided by it, and then it access GPS module.

3.1.4 The Grain Logistics Message Agreement

The types of information sent by mobile phone including the confirmation scheduling, loading and unloading good's weight and vehicle' GPS information. To distinguish them, the judgment information type's marks are added as follows: confirmation scheduling = 1, loading information = 2, unloading information = 3, vehicle's GPS information = 4. The symbol "/" is used to demarcate each field of grain logistics message content. Various kinds of message agreement content format are as follows:

1. 1/transportation contract number/[agree with scheduling or disagree];
2. 2/transportation contract number/the longitude of loading place/the latitude of loading place/gross weight after loading;
3. 3/transportation contract number/the longitude of unloading place/the latitude of unloading place/weight after unloading;
4. 4/transportation contract number/the longitude of transportation vehicle/the latitude of transportation vehicle.

For example, a grain unloading message is as follows:

3#04#86136********#3/2010041501/113.544305/34.831813333333/30#10-4-1514:30:12

In this message, '3/2010041501/113.544305/34.831813333333/30' is unloading information, including fields of flag bits, transportation contract number, the longitude of unloading place, the latitude of unloading place and weighting unloading, etc.

3.2 Communication Server

The communications server adopts windows service technology and multi-thread mechanism to realize the sending and receiving of the grain logistics SMS through calling the dynamic link libraries of SMS cats. The sending SMS thread and receiving SMS thread should be opened. When these two threads use the serial communication of SMS cat, it uses the thread synchronization mechanism. The process of sending SMS thread is described as follows.

A queue is used to storage outgoing SMS messages. It should be judged whether the queue has outgoing messages. When there are messages in the queue, reading them one by one and calling the SMS sending function in the dynamic link libraries of SMS cat to send messages. If send successfully, add messages to sending successful table; otherwise, add messages to sending failed table. When the queue is empty, continue to cycle and judge whether the queue has outgoing messages.

The process of receiving SMS thread is described as follows. The new SMS discrimination function in the dynamic link libraries of SMS cat is used to judge whether the system has received a new SMS. If a new message received, the receiving message function in dynamic link libraries to read the new message is called. The message's legality is determined. If the SMS is legal, then add the messages to receiving SMS table and delete the received messages in the SIM card. Otherwise, delete the received SMS in the SIM card directly. Then go to begin and determine whether the system has received a new SMS. The flow chart is showed in Fig. 5.

3.3 Database Server Message Processing

The smart phone and the platform of management information system realize data transmission through interaction with database respectively.

The platform of management information system generates the scheduling information according to the transportation contract table and the vehicle information table in database, and inserts it into the outgoing messages table in database. If the outgoing messages table has new message inserted, the platform uses trigger to call user-defined communication client for data transmission, and then in Windows

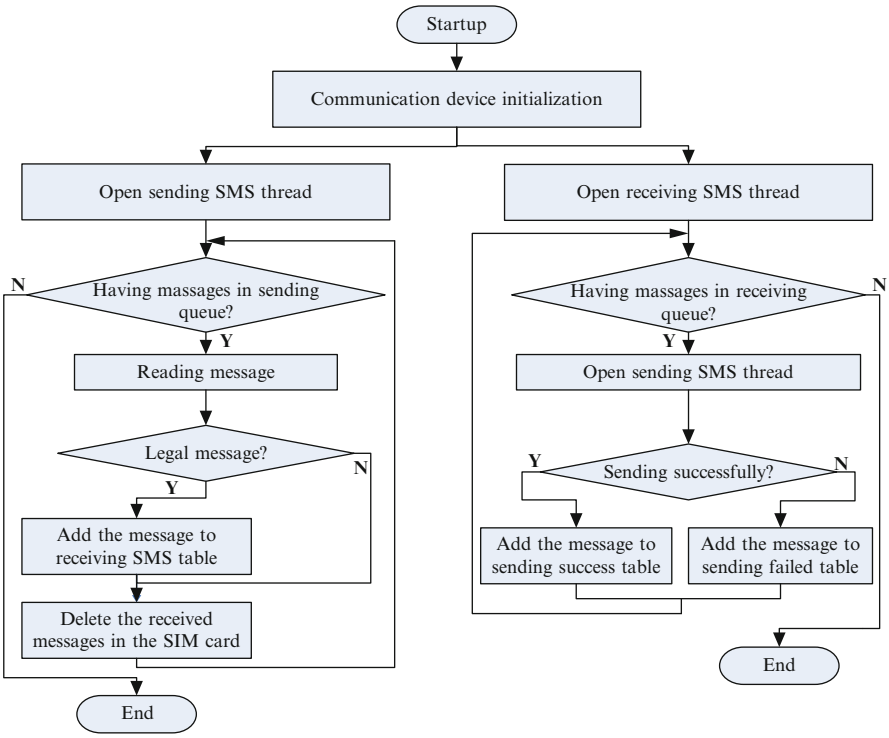

Fig. 5 Flow chart of the SMS handling of windows service

server use TCP protocol communication technology and multi-thread processing mechanism to receive the data from communication client, and put data into the outgoing message queue one by one, so as to realize that the database changes will be automatically notified by communication server.

The grain logistics messages database insert the receiving SMS table through SMS cats and communication server. SQL Server Service Broker is used to create conversation, and exchange messages between the target and the initiator; SqlDependency is used to provide SQL query statement of setting rules to SQL Server Service Broker for subscribing query notification. When the data in database change, OnChange events will be triggered automatically by SqlDependency to inform the application program, so as to achieve the purpose that the system data or cache be updated automatically.

3.4 The Platform of Management Information System

The messages sent by the platform of management information system include grain scheduling information and grain vehicle GPS information. Considering the convenience of receiving message function of using smart phone operating system

and understanding the message content for mobile phone users, we added the information type's judgment marks, "scheduling instruction" or "GPS instruction". The symbol "*" is used to demarcate each field of grain logistics message content.

The formats of grain logistics message content in platform are as follows:

1. Scheduling instruction * transportation contract number. . . * scheduling content;
2. GPS instruction * transportation contract number. . . * time interval (minutes).

4 Test Results and Conclusions

The functions of the system were tested by the Grain Trading Logistics Market in Henan Province, China. It's a large special enterprise involves with grain's purchase, sale and logistics. Test results showed that the grain logistics information can be collected and managed conveniently and effectively with the system.

SMS technology's application to the grain logistics management information businesses can provide key data support for the grain logistics management. And the real-time transmission and management of grain logistics information can be achieved.

References

1. Yang Xinting, Qian Jianping, Fan Beilei et al (2011) Establishment of intelligent distribution system applying in logistics process traceability for agricultural product[J]. Trans Chin Soc Agric Mach 42(5):125–130 (In Chinese)
2. Wang Guofeng (2006) Building up the grain logistics system in China[J]. J Chin Cereals Oils Assoc 21(5):139–143 (In Chinese)
3. Ju Ronghui, Shen Zuorui (2004) Greenhouse ecosystem health calling system using short message[J]. Trans CSAE 20(3):226–228 (In Chinese)
4. Zhou Guox iang, Zhou Jun, Miao Yubin et al (2005) Development and application on GSM based monitoring system for digital agriculture. Trans CSAE[J] 21(6):87–91 (In Chinese)
5. Li Hongfeng, Wang Jinlun, Du Jiang (2004) On-line monitoring system based on SMS and application server [J]. Comput Eng 30(5):167–169 (In Chinese)

Pricing Strategies for Reverse Supply Chain of Electronic Waste Based on Game Theory

Huali Sun, Feng Hong, and Yaofeng Xue

Abstract The pricing strategies of the reverse supply chain system of electronic waste (e-waste) consisted of recyclers and processors are proposed. The trapezoidal fuzzy membership functions are used to describe the uncertainty of the recycling price. The amount of recycling e-waste, the recycling price and the profits of recyclers and processors in cooperation and non-cooperation game decisions are presented. The simulated results show that the cooperation, the elasticity coefficients of price, the remanufactured rate, the recycling cost, the re-manufacturing cost and the government subsidy for non-recycled e-waste will affect the recycling price, the amount of recycling e-waste and the profits of recyclers and processors directly. The results in this paper can provide good guidance and reference for the operation of the e-waste reverse supply chain system.

Keywords Electronic waste • Reverse supply chain • Price decision • Trapezoidal fuzzy number • Game theory

1 Introduction

The electronic waste (e-waste) refers to all kinds of electronic products which nearly reach the end of their life cycle, such as the computer waste, the communication equipment waste, the household appliance waste, the electronic instrument and meter waste. The e-waste contains a large number of harmful materials such as

H. Sun • F. Hong
Management School, Shanghai University, Shanghai, China

Y. Xue (✉)
Shanghai Engineering Research Center of Digital Educational Equipment, East China Normal University, Shanghai, China
e-mail: yaofeng.xue@163.com

W. Wang (ed.), *Mechatronics and Automatic Control Systems*, Lecture Notes in Electrical Engineering 237, DOI 10.1007/978-3-319-01273-5_63,

lead, cadmium and mercury. If the harmful materials are processed improperly, they will seriously threaten the natural environment and human life. At the same time, e-waste contains precious metals such as gold, silver and platinum. These precious metals have economic value by being processed effectively. Therefore, the reverse supply chain of e-waste plays an important role in the environmental protection, reducing the consumption of resources and achieving sustainable development. However, the market of the reverse supply chain of e-waste in China is still lacking of a reasonable pricing mechanism.

In recent years, many scholars studied the reverse supply chain pricing [1, 2]. E-waste is more valuable than other wastes, and its recycling pricing is more complex. There is little work for e-waste reverse supply chain pricing. Wang (2006) discussed the pricing problem of e-waste reverse supply chain with three recycling models, including the national investment model, industry alliance model and manufacturer model. The results show that the manufacturer model of recycling system can obtain the maximal profit at the lowest price in competition [3]. Mitra (2007) analyzed the pricing problem of the mobile phone waste in India with achieving the maximum value of the revenue function. She considered that different recycling products in quality will lead to different prices [4]. Sun developed the pricing strategy of the close-loop supply chain of e-waste between the single manufacturer and the single distributor. A Stackelberg game model and a cooperation game model were formulated in which the manufacturer is leader and the distributor is follower [5]. Cao built a three-level reverse supply chain model of e-waste which consists of manufacturers, repair centers and retailers. The model achieves the Stackelberg equilibrium and the optimal solution of cooperation mechanism by using the game theory. This paper studies the reverse supply chain consisted of recyclers and processors of e-waste. In view of the uncertainty of e-waste recycling in quality, the trapezoidal fuzzy membership functions describing the uncertainty of the recycling prices are proposed. The parameters standing for harmless processing cost and the government subsidies are added to the recycling pricing model. After discussing the recycling pricing strategies, some practical suggestions are presented.

2 Problem Description

2.1 Model Assumptions and Symbol Descriptions

It assumes that, in the reverse supply chain including single recycler and single processor of e-waste, the recycler recycles e-waste from customers, and processor must purchase all e-waste from recycler. The processor classifies the e-waste into different grades by quality. The irreplaceable products will be processed harmlessly and the replaceable products will be re-manufactured in order to return the market. The market information is known completely. The e-waste recycler and processor

are independent decision makers. Their decision objectives are to achieve the maximum value of their own profit. At the same time, the government provides economic subsidies for harmless treatment of e-waste.

Here are symbol descriptions of model:

p_0 denotes a unit sale price of re-manufactured products re-manufactured by processor. $\tilde{p}_r$ denotes a unit fuzzy recycling price of e-waste recycled by processor from recycler. According to the trapezoidal fuzzy number [6] $\tilde{p}_r = (\sigma p_r - L, \sigma p_r, p_r, p_r + R)$,where R, L, σ are values with regard to experiences; p_r is a decision variable for the recycling price of the good quality of e-waste by processor; σp_r is the recycling price of bad quality of e-waste. In addition, $0 < \sigma < 1$. c_r denotes a unit recycling cost of e-waste processor. c'_r denotes a unit re-manufacturing cost of e-waste processor. ψ denotes the transfer recycling price of e-waste recycler. $\tilde{p}_h = (1-\psi)\tilde{p}_r$ denotes a unit fuzzy recycling price of e-waste by recycler. $\tilde{p}_h = ((1-\psi)\sigma p_r - (1-\psi)L, (1-\psi)\sigma p_r, (1-\psi)p_r, (1-\psi)p_r + (1-\psi)R)$, where p_h is a decision variable of e-waste recycler. c_h denotes a unit recycling cost of recycler. c'_h denotes a unit management cost of recycler. $\tilde{D}$ denotes the recycling quantity of e-waste, $\tilde{D} = d(\tilde{p}_h)^k, (d > 0, k > 1)$,d is the conversion factor, k is the elastic coefficient of price. t denotes a unit cost of harmless processing for irreplaceable e-waste by processor. The total processing cost is $T = t(1-\eta)D = t(1-\eta)dp_h^k$, where η is the re-manufactured rate. θ denotes a unit subsidy for irreplaceable e-waste products; the total subsidies are $\theta(1-\eta)dp_h^k$, and the total subsidies are less than the total processing costs of non-value e-waste. $\tilde{\pi}_r$ denotes the fuzzy profit for processor. $\tilde{\pi}_h$ denotes the fuzzy profit of recycler. $\tilde{\pi}$ denotes the fuzzy profit of the supply chain system, $\tilde{\pi} = \tilde{\pi}_r + \tilde{\pi}_h$.

2.2 Estimation Values of $\tilde{\pi}_r$, $\tilde{\pi}_h$ and $\tilde{\pi}$

According to trapezoidal fuzzy number [6] and let $\Delta = \frac{R-L}{4}$, the estimation values of $\tilde{\pi}_r$, $\tilde{\pi}_h$ and $\tilde{\pi}$ are as follows respectively:

$$\begin{aligned} E(\tilde{\pi}_r) = &\left[p_0 - \left(\frac{1+\sigma}{2}p_r + \Delta\right) - c_r - c'_r\right] d(1-\psi)^k \cdot \left(\frac{1+\sigma}{2}p_r + \Delta\right)^k \\ &+ (\theta - t)(1-\eta)d(1-\psi)^k \cdot \left(\frac{1+\sigma}{2}p_r + \Delta\right)^k \end{aligned} \tag{1}$$

$$E(\tilde{\pi}_h) = \left[\left(\frac{1+\sigma}{2}p_r + \Delta\right)\psi - c_h - c'_h\right] d(1-\psi)^k \cdot \left(\frac{1+\sigma}{2}p_r + \Delta\right)^k \tag{2}$$

$$E(\tilde{\pi}) = \left[p_0 - c_r - c'_r - c_h - c'_h - (1-\psi)\left(\frac{1+\sigma}{2}p_r + \Delta\right) + (\theta - t)(1-\eta)\right] d(1-\psi)^k \left(\frac{1+\sigma}{2}p_r + \Delta\right)^k \tag{3}$$

(p_r, ψ) is the pricing strategy. Thus, the following lemma can be proved:

Lemma *when*

$$\frac{2(k-1)}{(1+\sigma)(k+1)}[p_0 - c_r - c'_r + (\theta - t)(1-\eta)] - \frac{2\Delta}{1+\sigma} + \frac{4(c_h + c'_h)}{(1+\sigma)(k+1)} < p_r < \frac{2}{1+\sigma}(p_0 - c_r - c'_r - \Delta),$$

$$\frac{c_h + c'_h}{\frac{1+\sigma}{2}p_r + \Delta} < \psi < \frac{2}{k+1} + \frac{(k-1)(c_h + c'_h)}{(k+1)\left(\frac{1+\sigma}{2}p_r + \Delta\right)},$$

$E(\tilde{\pi}_r)$ is the lower convex function of p_r; $E(\tilde{\pi}_h)$ is the lower convex function of ψ; $E(\tilde{\pi})$ is the lower convex function on (p_r, ψ);F and (p_r, ψ) is the set of pricing strategies.

$$F = \left\{(p_r, \psi) \middle| \begin{array}{l} \frac{2(k-1)}{(1+\sigma)(k+1)}[p_0 - c_r - c'_r + (\theta - t)(1-\eta)] \\ + \frac{4(c_h + c'_h)}{(1+\sigma)(k+1)} - \frac{2\Delta}{1+\sigma} < p_r < \frac{2}{1+\sigma}(p_0 - c_r - c'_r - \Delta), \\ \frac{c_h + c'_h}{\frac{1+\sigma}{2}p_r + \Delta} < \psi < \frac{2}{k+1} + \frac{(k-1)(c_h + c'_h)}{(k+1)\left(\frac{1+\sigma}{2}p_r + \Delta\right)} \end{array}\right\} \tag{4}$$

Lemma shows that, when $(p_r, \psi) \notin F$, both parties have no benefit, or the fuzzy estimation values of the profit of processor, the profit of recycler and the total profit of the supply chain will reduce due to the reduced recycling amount. Therefore, both parties make pricing decisions in F, which is called a feasible set.

3 Non-cooperation Game Model for Pricing

In the non-cooperation game theory [7], the processor is the leader and the recycler is the follower. It is a typical Stackelberg game model. Thus, we can formulated the following decision model:

$$MaxE(\tilde{\pi}_r) = \left[p_0 - \left(\frac{1+\sigma}{2}p_r + \Delta\right) - c_r - c'_r + (\theta - t)(1-\eta)\right] \cdot d(1-\psi)^k \left(\frac{1+\sigma}{2}p_r + \Delta\right)^k \tag{5}$$

$$s.t.MaxE(\tilde{\pi}_h) = \left[\left(\frac{1+\sigma}{2}p_r + \Delta\right)\psi - c_h - c'_h\right] d(1-\psi)^k \cdot \left(\frac{1+\sigma}{2}p_r + \Delta\right)^k \tag{6}$$

Estimation the recycling price of e-waste by recycler:

$$E(\tilde{p}_h)^* = \frac{k^2}{(k+1)^2}[p_0 - c_r - c'_r - c_h - c'_h + (\theta - t)(1-\eta)] \tag{7}$$

Estimation the profit of processor:

$$E(\tilde{\pi}_r)^* = d\frac{k^{2k}}{(k+1)^{2k+1}}[p_0 - c_r - c'_r - c_h - c'_h + (\theta - t)(1-\eta)]^{k+1} \tag{8}$$

Estimation the profit of recycler:

$$E(\tilde{\pi}_h)^* = d\frac{k^{2k+1}}{(k+1)^{2k+2}}[p_0 - c_r - c'_r - c_h - c'_h + (\theta - t)(1-\eta)]^{k+1} \tag{9}$$

Estimation the profit of the supply chain system:

$$E(\tilde{\pi})^* = d(2k+1)\frac{k^{2k}}{(k+1)^{2k+2}}[p_0 - c_r - c'_r - c_h\text{-}c'_h + (\theta - t)(1-\eta)]^{k+1} \tag{10}$$

4 Cooperation Game Model for Pricing

In cooperation decision model, there is a cooperation between processor and recycler. Both parties work together to achieve the maximal profit, we can formulate the following decision model:

$$MaxE(\tilde{\pi}) = \left[p_0 - c_r - c'_r - c_h - c'_h - (1-\psi)\left(\frac{1+\sigma}{2}p_r + \Delta\right) + (\theta - t)(1-\eta)\right] d(1-\psi)^k \left(\frac{1+\sigma}{2}p_r + \Delta\right)^k; \quad s.t(p,\psi) \in R \tag{11}$$

The solution set is:

$$F = \{(\bar{p}_r, \bar{\psi}) | (1-\psi)\left(\frac{1+\sigma}{2} p_r + \Delta\right) = \frac{k}{k+1} \cdot [p_0 - c_r - c'_r - c_h - c'_h + (\theta - t)(1-\eta)]\} \tag{12}$$

$$E(\tilde{p}_h)^* = \frac{k}{k+1}[p_0 - c_r - c'_r - c_h - c'_h + (\theta - t)(1-\eta)] \tag{13}$$

$$E(\tilde{\pi})^* = \frac{dk^k}{(k+1)^{k+1}}[p_0 - c_r - c'_r - c_h - c'_h + (\theta - t)(1-\eta)]^{k+1} \tag{14}$$

By comparing the results of the two decision models, several conclusions are summarized:

(a) In the non-cooperation decision model, the profit of processors is higher than that of recycler.
(b) In the cooperation decision model, the recycling price, the recycling amount and the system profit of recycler are higher than that of processor.
(c) The relationship of government subsidies for the recycling price and the recycling profit is positive growth in both decision models. Thus, the profits of recycler and processor will increase, when the government subsidies, the recycling prices and the recycling amount increase. Conversely, the profits of recycler and processor will decrease, when the recycling prices decrease and the recycling amount reduces.
(d) In both decision models, the profit of processors will decrease, when the recycling price and the re-manufactured cost increase and the sale price of re-manufactured products decrease, and vice versa.

5 Numerical Simulations

In order to analyze how the elasticity coefficient of price and the re-manufactured rate will affect the recycling price, the recycling amount and the profits of both parties in both decision models, the numerical simulation of an example is presented. In this example, p_0 =300, c_r =50, c'_r =10, t =10, θ =5, c_h =5, c'_h =5, d =20. All of the units are Yuan (the Chinese Currency Unit) per unit. The value of k ranges among 0~1. The recycling price, the recycling amount and the profits of both parties on the condition of $\eta = 0.2$ and $\eta = 0.8$ are compared. The relevant information is shown in Figs. 1, 2, and 3.

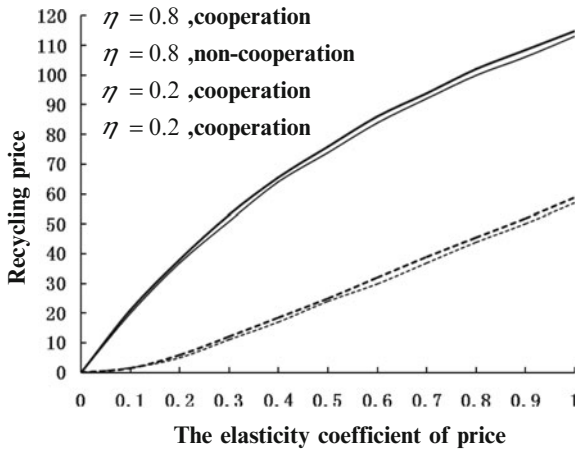

Fig. 1 Effect of elasticity coefficient on recycling price

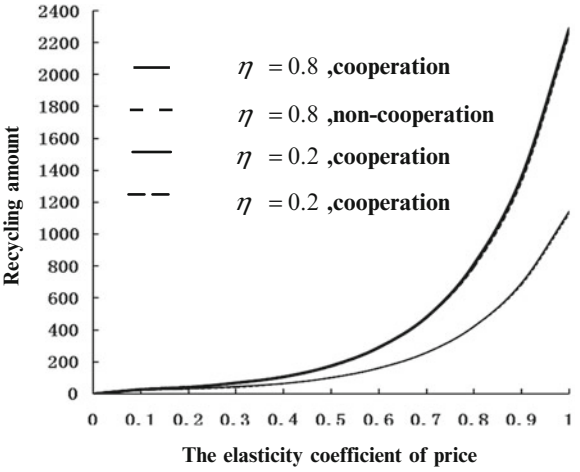

Fig. 2 Effect of elasticity coefficient on recycling amount

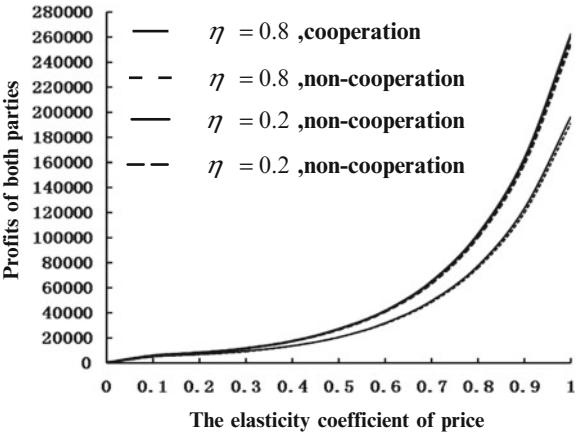

Fig. 3 Effect of elasticity coefficient on recycling d profit

From the Figs. 1, 2, and 3, we can reach the following conclusions:

(a) The recycling price will increase with the elasticity coefficient of price. With the same elasticity coefficient of price, the recycling price in cooperation model is higher than that in non-cooperation model. In addition, the recycling price in cooperation model grows faster than that in non-cooperation mode.
(b) The recycling amount will increase with the elasticity coefficient of price. With the same elasticity coefficient of price, the recycling amount in cooperation model is larger than that in non-cooperation model.
(c) The profits of e-waste recycler and processor will increase with the elasticity coefficient of price. With the same elasticity coefficient of price, the profits of e-waste recycler and processor in cooperation model are larger than that in non-cooperation model.
(d) The margin of the recycling price, the recycling amount and the profits of both parties between the two decision models will increase with the elasticity coefficient of price. With the same elasticity coefficient of price, the increase of profits in cooperation model is larger than that in non-cooperation model.

6 Conclusion

The paper discussed that in non-cooperation decision and cooperation decision models, e-waste recycler and processor make their equilibrium recycling price based on their own maximal profits. The results show that, in order to gain more profit, the recycler should cooperate or reduce the recycling and re-manufacturing costs of e-waste or improve the recycling quality of e-waste (the re-manufactured rate). For the e-waste with lower quality (the re-manufactured rate is low), the government should provide more supportive measures to e-waste processor, increase the capital investment and improve the financial subsidies to the recycling processor. The research results are also instructive for other reverse supply chain.

Acknowledgements This work was supported by the Humanity Social Science Research Project of Ministry of Education of P. R. China (Grant No. 10YJC630213), the Key Innovation Project of Shanghai Municipal Education Commission (Grant No. 12ZS094).

References

1. Gu qiaolun, Ji jianhua (2006) The pricing strategy research of reverse supply chain based on the fuzzy recycling price [J]. Inf Control 35(4):417–422
2. He chunchi, Wang chenghan, He yajing (2008) Ordering and pricing decisions in a two-echelon supply chain with asymmetric demand information [J]. Eur J Oper Res 190(2):509–525
3. Wang fahong, Da qingli (2006) The decision analysis of electronic industry in re-manufactured reverse logistics model [J]. Chin J Manage Sci 14(6):44–49

4. Mitra S (2007) Revenue management for remanufactured products [J]. Int J Manage Sci 35 (5):553–562
5. Sun Jing, Ge xinquan (2009) The recycling pricing strategy research of e-waste [J]. J Beijing Inf Sci Technol Univ 24(3):13–16
6. Wang jinxia (2009) The decision method of multiple attribute group based on the trapezoid fuzzy number [D]. HeFei: Master Dissertation of HeFei University of Technology
7. Zhang weiying (1996) The game theory and information economics[M]. Shanghai people's Publishing House, Shanghai, pp 154–156

A Novel Wide Area Protection Zone Division and Main Station Selection Method

Tong Wang

Abstract In order to address the problems of protection zone-division and main station-selection of the regional wide area protection system, a new protection zone-division scheme for regional wide area protection system is proposed in this paper. In this scheme, protection zone-division principles of the main station selection, overlapping coverage and most coverage of the regional wide area protection system are firstly discussed on the basis of degree priority of the power law statistical characteristic of the network topology. Then, based on the above principles, original main stations of protection zones are determined and the cut of the alternative main stations of protection zones are selected sequentially by searching from the original main stations as the starting point with three logical lengths. Finally, the circular grid-formed and overlapping coverage protection zone-division is formed. Test results of IEEE-39 test system and an actual 68 bus system in North America power system show that divided protection zones are clear and meet the principle of overlapping coverage. Also, main station is set reasonably and not need to be optimized manually. Furthermore, the protection zone-division searching method which is simple is feasible and more applicable for practical use.

Keywords Regional wide area protection • Circular grid formed protection zone • Overlapping coverage zone-division principle • Degree priority • Power law statistical characteristic

T. Wang (✉)
State Key Laboratory for Alternate Electrical Power System with Renewable Energy Sources, North China Electric Power University, Beijing, China
e-mail: hdmajing@yahoo.com.cn

W. Wang (ed.), *Mechatronics and Automatic Control Systems*, Lecture Notes in Electrical Engineering 237, DOI 10.1007/978-3-319-01273-5_64,

1 Introduction

The increasingly complex and gradually flexible structure of grid has caused it difficulty to the traditional protection scheme merely on the basis of local statistics. The contradiction between selectivity and sensitivity is becoming more and more obvious [1, 2]. So it is imperative to focus on wide area protection system multipoint communication of power system [2].

There are three main ways divided by the composition of wide area protection system: the distributed wide area protection system, the substation wide spread protection system and the regional wide area protection system. A kind of distributed wide area protection system based on intelligent electronic device (IED) is constructed, determined the principle of division on protecting scope [3]. On that basis, one based on longitudinal comparison principle is proposed to overcome the faults resulted from some refuse operation of IED [4]. However, the communication structure and logic of the distributed wide area protection is so intricate that it is hard to achieve the large regional protective functionality flexibly. Therefore, a kind of substation wide spread protection system is proposed [5]. This system used direction comparison principle to judge fault component taking some situation into account such as the refuse operation of main protection, breaker failure and the disappearing of the adjacent substation direct current. Meanwhile the system put bus and converter into protection can promote the adaptability of the electrical wiring of the main forms. On that basis, a three layers fault-tolerant algorithm is proposed [6], much enhanced the performance of the substation wide area protection system. Considering that the actual communication competence and DMU (decision making unit) data handling capacity, a regional wide area protection system is proposed collecting direction information in area of each substation lines protection devices quick judged the lines faults and make the operation decision. The concept of area protection is proposed, with an area protection system constructed being able to cooperate work with main protection and backup protection. On that basis, double DMU in area protection architecture is raised [7], solved the protection system mal-operation caused by communication factors, enhanced fault-tolerant performance of the relay protection.

In accordance with the problems of protection zone-division and main station-selection of the regional wide area protection system, a new protection zone-division scheme for regional wide area protection system is proposed [8, 9] in this paper. This paper mainly studied protection zone-division principle and searching method on the basis of degree priority of the power law statistical characteristic of the network topology. Test results of IEEE-39 test system and an actual 68 bus system in North America power system show that divided protection zones are clear and meet the principle of overlapping coverage. Also, main station is set reasonable and not need to be optimized manually. Furthermore, the protection zone-division searching method which is simple is feasible and more suitable for being into practice.

2 Regional Wide Area Protection System Operation Mode

Regional wide area protection system can work with traditional main protection and backup protection provided a new kind of protection system. The specific contents of the operation mode are summarized as follows:

Divided the power system into several protection zone, each zone composed of a main station and several sub-station. In each substation of the protection zone, every IED in charge of collecting the information of analog quantity and state quantity at the relay location and uploading the information to MCU of the substation via process layer bus and station layer bus (main control unit) sent as GOOSE/GSSE packets. MCU of each sub-station used ATM communication technology to upload the message to the DMU of their zone main station. The DMU of the main station judged the fault component according to the summarizing message, formulated protect strategy and sent trip signals as GOOSE packets when fault occurs. MCU of each sub-station selected related IED and carried out protection function according to the trip signals combined with the wiring form.

3 The Zone-Division Principles of Regional Wide Area Protection System

3.1 The Principle of Main Station Selection

3.1.1 Principle of Degree Priority

Defining substation degree as the numbers of the lines directly linked with. The result of statistic character of electrical power system demonstrated multi-IEEE test system and the average degree of Sino-US actual power system substation range from 2 to 3 following a power-law distribution. These substations are almost high voltage grade or hubs even though the substations with higher degree held a very small proportion. So the degree can reflect the importance of the substation to some extent. Considering line personnel, communication facilities, protection devices and other factors, these substations are prior to main station selection.

3.1.2 The Principle That Borderline Network Stations Are Not Suitable for Using as Main Stations

Defining the borderline network stations as the substations with degree one. A borderline network station may only be step-up station or step-down station end radial network under normal network topology structure. These substations with low voltage located on the beginning and the end of power system grid will finally

become unmanned substations. Use these substations as main stations create small scope of protection, low equipment utilization rate and the developing direction in want of more line personnel against power system. So the borderline network stations are not suitable for using as main station on the basis of practical engineering application.

3.1.3 The Principle That Any Two Main Stations Are Nonadjacent

In the architecture of regional wide area protection, there will be too many overlapping coverage protection zone that makes the whole grid holds excessive protection zones if any two main stations are adjacent. Thus it will cause a series of troubles, for instance, increasing line personnel, high construction cost, more maintenance charge and pressure build-up of communication system.

3.2 Principle of Overlapping Coverage

The protection scope of regional wide area protection system can cover all the components, that is to say, any station or bus will be divided in a specific protection zone. Therefore overlapped area of two adjacent zones includes at least one station. What's more, because the directly lined lines will lose protection when DC source of the overlapped station is off, so overlapped area of two adjacent zones includes at least one line. It is called principle of overlapping coverage. This principle ensured the integrity of the whole grid protection scope.

3.3 Principle of Most Coverage

A few main stations and their protection zone can be defined by principle of degree priority in the power system. Besides, it is imperative to use less protection zone to coverage the whole grid. Think of the protection radius of regional wide area protection system and principle of overlapping coverage, searching should start from defined main stations, outward with three logical length to determine the set of alternative main stations. When the alternative main stations with the highest degree are not unique, choose the one overlapping coverage with the most zones that is called principle of most coverage.

It needs to point out that the above zone-division principles are suitable for any electrical power system. The paper show the simple electrical network in Fig. 1, introduced the principle of protection zone-division. Supposed that B1 is the main station, so its protection scope V1 includes: lines L1, L2, stations B1, B2, B3. Because the zone-division of regional wide area protection should meet all the

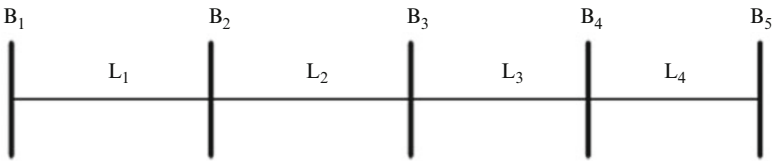

Fig. 1 Sketch map of protection zones of limited wide area protection system

principles of zone-division, the only two modes if this network zone-division protection are:

Mode 1: station B4 is the main station, B2, B3 and B5 are sub-stations. This protection zone V2 includes: lines L2, L3 and L4, stations B2, B3, B4 and B5.

Mode 2: station B3 is the main station, B1, B2, B4 and B5 are sub-stations. This protection zone V2 includes: lines L1, L2, L3 and L4, stations B1, B2, B3, B4 and B5.

4 Example Analysis

When the status of substation network is changed locally, the existing methods need to re-read the substation network status to detect the connectivity. The advantage of tracking algorithm for substation network topology analysis is tracking local changing of the network timely and needn't to re-read the substation network status. Whereas it's disadvantage is taking plenty of time to estimate the network status for the first time. And the calculation speed is not as fast as expectation. The improved tracking algorithm is easy to put into practice and fast. Especially there are only three steps for calculation when the network nodes are connected, which improved the speed of the network state estimation tremendously.

This paper used IEEE-39 node system as test system. Its undirected network topological graph is shown in Fig. 2.

Calculated the degree of all the test stations in the system, selected the station B16 with highest degree as the main station. Searching outward started with the main station B16, determined the set of waiting main stations {B3, B4, B13, B14, B18, B20, B22, B23, B26, B27} and selected B26 as the main station. Searching outward started with B26, determined the set of waiting main stations {B1, B2, B3, B18} and selected B2 as the main station. Searching outward started with B2, get the set of waiting main stations {B4, B5, B9, B14, B18, B39}.

Now the degree of all waiting main stations less than the degree of B6, so selected B6 as the main station. Searching outward started with B6, determined the set of waiting main stations {B4, B8, B9, B10, B12, B13, B14} and selected B4 as the main station. Searching outward started with B4, get the set of waiting main stations {B8, B9, B10, B12, B13} and selected B13 as the main station. Searching outward started with B13, get the waiting main stations set is empty.

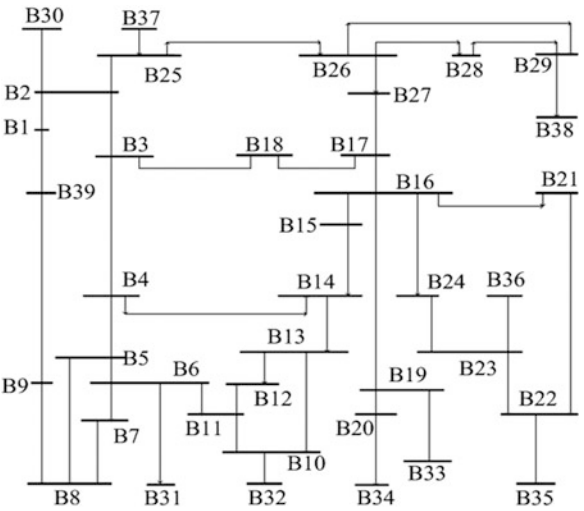

Fig. 2 Undirected topological graph of IEEE-39 bus system

Table 1 Protection zones of IEEE-39 node system

Zone number	Main station	Sub-station
V1	B2	B1, B3, B4, B9, B18, B25, B26, B30, B37, B39
V2	B4	B2, B3, B5, B6, B8, B13, B14, B15, B18
V3	B6	B4, B5, B7, B8, B10, B11, B12, B31
V4	B9	B1, B5, B7, B8, B39
V5	B13	B4, B10, B11, B12, B14, B15, B32
V6	B16	B14, B15, B17, B18, B19, B20, B21, B22, B23, B24, B27, B33
V7	B18	B2, B3, B4, B16, B17, B27
V8	B20	B16, B19, B33, B34
V9	B22	B16, B21, B23, B24, B35, B36
V10	B26	B2, B17, B25, B27, B28, B29, B37, B38

Now the degree of all waiting main stations less than the degree of B6, so selected B6 as the main station. Searching outward started with B6, determined the set of waiting main stations {B4, B8, B9, B10, B12, B13, B14} and selected B4 as the main station. Searching outward started with B4, get the set of waiting main stations {B8, B9, B10, B12, B13} and selected B13 as the main station. Searching outward started with B13, get the waiting main stations set is empty.

Put all the possible remaining stations into set {B8, B9, B18, B20, B22, B23, B39} and determined B9 and B18 as the main stations. Searching outward started with B9 and B18, the set of waiting main stations is empty. Put all the possible remaining stations into set {B20, B22, B23} and determined B22 as the main station. Searching outward started with B22, the set of waiting main stations is empty. Put all the possible remaining stations into set {B20}, determined B20 as the main station. Now that the searching flow is over. The results of zone-division list in Table 1.

It can be inferred from Table 1, the whole system has been divided into 10 protection zones, each zones set a main station. Because each line can achieve its main protection and backup protection through a main station working independently, so it's no need to communicate among the main stations with low communication pressure. Besides, there are many advantages that the selected main station covered all hub substations in the whole grid, follow the principle of overlapping coverage, reasonable setting, practical and suitable for being into practice.

5 Conclusion

This paper proposed a new protection zone-division scheme for wide area protection system. It has the following characteristics:

1. It proposed a new circular grid-formed and overlapping coverage protection zone division scheme based on power law statistical characteristic with degree priority, and established a sound searching method of protection zone-division.
2. Divided protection zones are clear and meet the principle of overlapping coverage. Also, main station is set reasonably and not need to be optimized manually.
3. The searching method is simple, practical, accords with actual engineering and suitable for any power system.

Acknowledgements Project Supported by The National Basic Research Program of China (973 Program) (2012CB215200); National Natural Science Foundation of China (50907021, 50837002); The "111" Project (B08013); The Chinese University Scientific Fund Project (11MG01, 09QX64); The Project Sponsored by the Scientific Research Foundation for the Returned Overseas Chinese Scholars, State Education Ministry ([2011] No. 1139); Hebei Natural Science Foundation (E2012502034); Electric Power Youth Science and Technology Creativity Foundation of CSEE ([2012] No. 46).

References

1. Yin Yonghua, Guo Jianbo, Zhao Jianjun (2003) Preliminary analysis of large scale blackout in interconnect North America power grid. Power Syst Technol 27(10):8–11
2. Hu Xuehao (2003) Rethinking and enlightenment of large scope blackout in interconnected North America power grid. Power Syst Technol 27(9):2–6
3. Su Sheng, Li KK, Chan WL (2005) An expert system for wide area protection system protection zone selection. Power Syst Technol 29(3):55–58
4. Cong Wei, Pan Zhencun, Zhao Jianguo (2006) A wide area relaying protection algorithm based on longitudinal comparison principle. Proc Chinese Soc Electr Eng 26(21):8–14
5. Cong Wei, Pan Zhencun, Zhao Jianguo (2006) A wide area protective relaying system based on current differential protection principle. Power Syst Technol 30(5):91–96
6. Zhang Baohui, Zhou Liangcai (2009) Centralized substation backup protection. Electr Power Autom Equip 29(6):1–5

7. Zhang Baohui, Zhou Liangcai, Wang Chenggen (2010) Wide area backup protection algorithm with fault-tolerance performance. Autom Electr Power Syst 34(5):66–71
8. Wu Kecheng, Lin Xiangning, Lu Wenjun (2007) Principle and realization of the hierarchical region protection system for power system. Autom Electr Power Syst 31(3):72–77
9. Wang Yang, Yin Xianggen, Zhao Yijun (2008) Regional power network intelligent protection based on genetic algorithm. Autom Electr Power Syst 32(17):40–45

Part IV
Control Theory and Application

Monte Carlo Based Predictive Method for Determining Work Envelope of Spacesuit in EVA Operation

Huaiji Si, Qianfang Liao, and Wanxin Zhang

Abstract Astronauts worn spacesuit manipulate objects in the extravehicular environment is strikingly different from that on the ground. A critical issue addressed in planning for Extra-Vehicular Activity (EVA) and evaluating EVA worksites is whether the astronaut can reach and comfortably work in the designed worksite or not. In this paper, a 9-DOF arm model of spacesuit is established, Monte Carlo based computer simulation and predictive method are researched and the arm workspace is predicted by the limitations of spacesuit joint angles. The prediction result is verified by a Articulated Arm Coordinate Measuring Machines (AACMM). This method provides a basis for planning EVA tasks of space suit and further study of mobility of space suit.

Keywords Monte Carlo • Work envelope • Spacesuit • Mobility • Extravehicular activity

1 Introduction

A spacesuit for EVA is a small space craft with complicated life support systems, which can to keep astronauts alive in the harsh environment (vacuum and extreme temperature) of outer space [1]. A critical issue addressed in planning for EVA and evaluating EVA worksites is whether the astronaut can reach and comfortably work in the designed worksite. Reaching envelope is the boundary of the space that a person can reach and the work envelope is a subset of the reach envelope, in which a person can work comfortably [2]. These two types of envelopes depend not only on the size but also the flexibility of the individual. Work envelope analysis that

H. Si (✉) • Q. Liao • W. Zhang
National Key Laboratory of Human Factors Engineering, Astronaut Center of China, Beijing 100094, China
e-mail: sihuaiji@126.com

W. Wang (ed.), *Mechatronics and Automatic Control Systems*, Lecture Notes in Electrical Engineering 237, DOI 10.1007/978-3-319-01273-5_65,

incorporates the mechanics of the space suit and ergonomics of the astronauts is a useful method for both assessing potential worksite locations and evaluating the functional significance of modifications to space suit mobility and visibility [3].

The microgravity environment and spacesuits constrain astronauts' body motions in significant and complicated ways make EVA operations strikingly different from those performed on the ground [4]. Since the cost of experimenting in microgravity is high and underwater training lead to motions inappropriate for microgravity. Traditional computational methods used inverse kinematic method with simplified model to avoid the complicated calculation, which were adopted by researchers to simulate in the ground [5]. In this article, a prediction method based on Monte Carlo using a 9 DOF kinematic arm model was present and the result was agreed well with the experiment.

2 Monte Carlo Predictive Model

2.1 Human Upper Limb and Spacesuit Arm

When an astronaut wearing a spacesuit to move his body to manipulate objects, he must do extra work every time as bending the joint and maintain a force to keep the joint bent, which is strikingly different from operates on the ground. All movable upper limbs joints of human wearing spacesuit are as shown in Fig. 1, in which three glenohumeral joints (abduction-adduction, flexion-extension, and rotation), elbow extension joint, elbow abduction joint, wrist extension and wrist abduction are included. All joints are sequenced by the spacesuit joints. Generally, a 7-DOF arm model without acromioclavicular joints is adopted to construct upper-limb kinematics model. Acromioclavicular joints have rather small motion limits, their existence greatly enlarge motion limits of upper limbs. In this paper, a 9-DOF model including acromioclavicular joints is applied, so as to make workspace of mobility better approximate that of real human body wearing spacesuit. As many researchers have done, the Denavit-Hartenberg convention is used to compute segment parameters of the upper limbs of spacesuit. Parameters of transform matrix between different coordinate systems with DH parameters are shown in Table 1.

$$ {}^{i-1}_{i}T = \begin{bmatrix} c\theta_i & -s\theta_i & 0 & a_{i-1} \\ s\theta_i c\alpha_{i-1} & c\theta_i c\alpha_{i-1} & -s\alpha_{i-1} & -s\alpha_{i-1} d_i \\ s\theta_i s\alpha_{i-1} & c\theta_i s\alpha_{i-1} & c\alpha_{i-1} & c\alpha_{i-1} d_i \\ 0 & 0 & 0 & 1 \end{bmatrix} \tag{1} $$

By replacing parameters in Table 1 with the transform matrix in Eq. 1, kinematics model of spacesuit arm can be obtained.

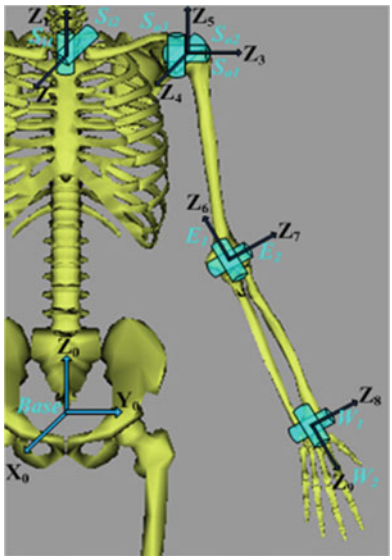

Fig. 1 Kinematic model of human upper left limb by the sequence of spacesuit joints

Table 1 DH Parameters for spacesuit-human arm

Num	Joint	α_{i-1}	a_{i-1}	d_i	θ_i
1	S_{i1}	0°	0	L_1	$\theta_1(90°)$
2	S_{i2}	90°	0	0	$\theta_2(-90°)$
3	S_{o1}	−90°	0	L_2	$\theta_3(0°)$
4	S_{o2}	90°	0	0	$\theta_4(90°)$
5	S_{o3}	−90°	0	0	$\theta_5(90°)$
6	E_1	0°	0	$-L_3$	$\theta_6(-180°)$
7	E_2	−90°	0	0	$\theta_7(90°)$
8	W_1	0°	L_4	0	$\theta_8(180°)$
9	W_2	−90°	0	0	$\theta_9(-90°)$
End	Palm	−90°	0	$-L_5$	−90°

$$ {}^{0}_{end}T = {}^{0}_{1}T^{1}_{2}T^{2}_{3}T \ldots {}^{8}_{9}T^{9}_{end}T = \begin{bmatrix} n_x & o_x & a_x & p_x \\ n_y & o_y & a_y & p_y \\ n_z & o_z & a_z & p_z \\ 0 & 0 & 0 & 1 \end{bmatrix} \tag{2} $$

Obviously, the model is rather complex, and it is impossible to accomplish by inverse kinematics analysis method. In this paper, forward kinematics analysis method based on Monte Carlo is applied.

To supply enough oxygen for respiration, a spacesuit using pure oxygen must have a pressure of about 32.4 kPa (240 Tor, 4.7 psi), which means an astronaut move his body to operate objects need extra effort to bend the limbs, resisting a soft pressure garment's natural tendency to stiffen against the vacuum.

Compared with human arm joints angular limits, EVA spacesuit has smaller angular limits due to manufacturing process and limitation of joints. Thus, it will be

unreliable to determine workspace of spacesuit by mobility of human arm. Some originally achievable attitudes can no longer be achieved, and some originally reachable areas can no longer be reached, since astronauts are limited and affected by spacesuit when he bends joints.

2.2 Monte Carlo Predictive Method

Reachable workspace is defined as W_R, that is the maximum mobility limits of arms' ends, or volume that reachable points of arms' ends take. According to kinematics definition, W_R can be regarded as mapping from joints space variables to reachable workspace, and can be expressed as:

$$W_R = \{p(q) : q \in Q\} \subset \mathbf{R}^3 \tag{3}$$

In Eq. 3, where in $p(q) : Q \rightarrow \mathbf{R}^3$ represents a position component of kinematics mapping positive solution, q represents generalized joints variables, Q represents joints workspace, W_R represents reachable workspace and $\mathbf{R}^3$ the whole three-dimensional space.

According to mapping relationship of forward kinematics, a certain number of random quantities in accord with demand of joints' changes are assigned to joints' variables by uniform distribution, in order to obtain a graph made up by random points of reachable workspace, which forms Monte Carlo workspace. Decision method of Monte Carlo workspace has following steps:

Step1. According to space-coordinate point cloud acquired by kinematics equations, firstly identical numbers of random quantities are assigned to nine joints' variables (θ_i, $i = 1$ to 9) within their value ranges on the basis of the mapping relationship of each joint's variable and arm's reachable workspace. Then the nine joints' variables are mapped to workspace by kinematics equation to form three-dimensional "nephogram". But this nephogram cannot be observed or analyzed, and needs further processing in the following steps.

Step2. Divide series of strata of the nephogram according to the height, extract boundaries on different strata, and connect extracted boundaries by sequence to form boundary lines. The Monte Carlo workspace and Curve shown in Fig. 2 is acquired by kinematics model of spacesuit and spacesuit angular limits.

Step3. Boundary lines acquired in Step2 is reachable workspace envelop of spacesuit, that is maximum limits actually reached by spacesuit arm. The final workspace is obtained by combining reachable workspace with visible workspace. Visibility of points in reachable workspace can be obtained on the basis of mesh generation method and successive judgment of each point's visibility. Visible points' reachable points are the workspace of spacesuit. Visibility analysis of reachable workspace envelop is shown in Fig. 3 and the final maximum workspace envelop is shown in Fig. 4.

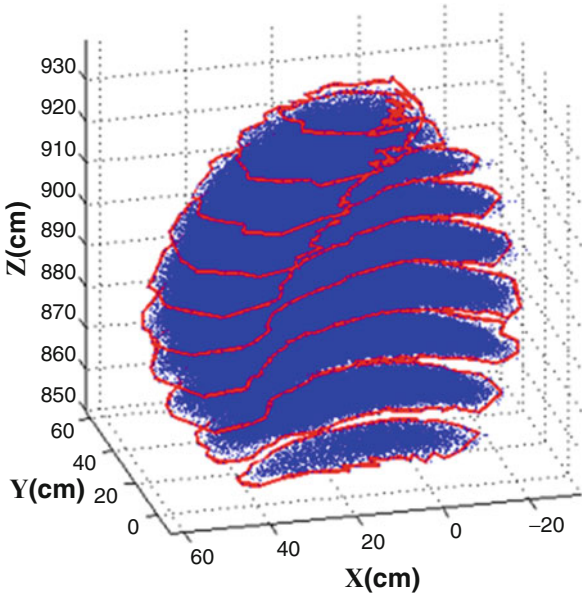

Fig. 2 Reach envelope with Monte Carlo predictive method

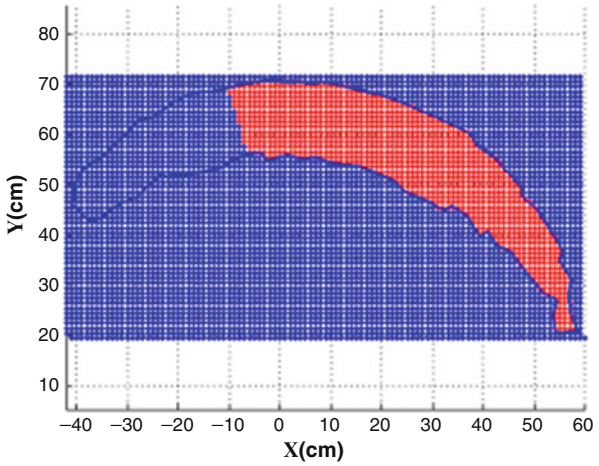

Fig. 3 Dividing reach envelope by visible (*red*) or not (*blue*)

Work envelope and reach envelope was distinguished by the visibility of points, which were shown in Fig. 3.

This model can clearly report the region of left hand, right hand and both hands. And the volumes of the operation regions are accurately calculated. The measurement provides a reliable support in the spacesuit engineering design. The shape and size of work envelop calculate by this method was shown in Fig. 4.

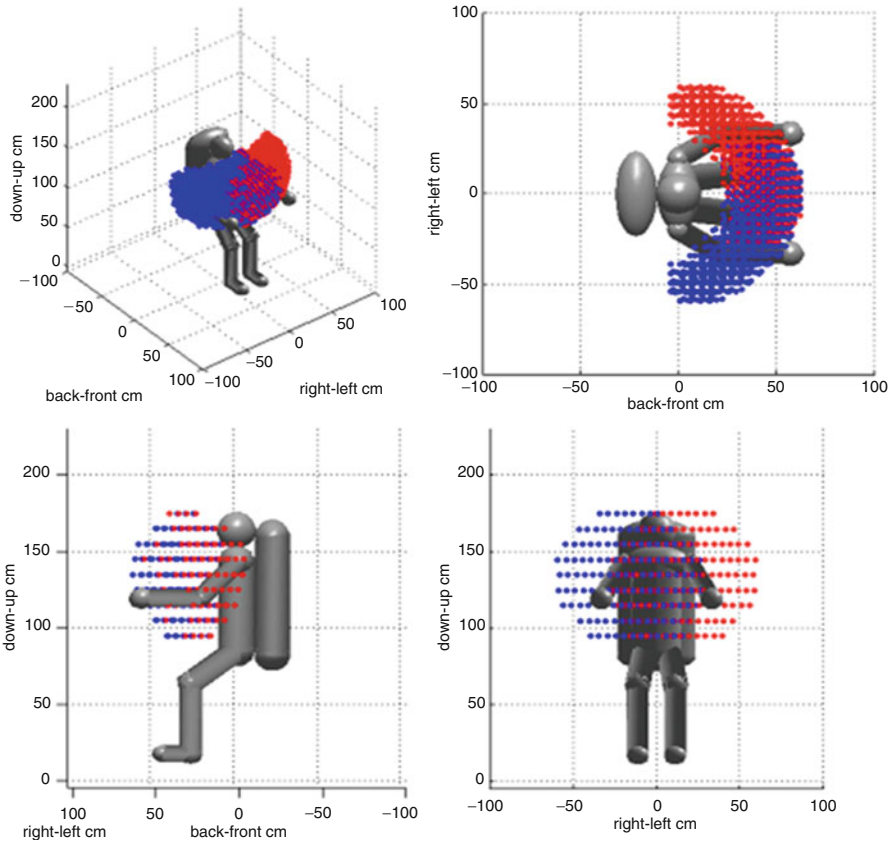

Fig. 4 Simulation of work envelope of spacesuit (*blue* for *right hand* and *red* for *left hand*)

3 Experimental

For the verification of the Predictive Model, a mechanical manipulator has been developed to measure the mobility and work envelope of astronaut wearing spacesuit. The measuring arm was designed combining the advantages of perpendicular ACMM which includes four rotation mechanical arms in horizontal plate and elevation device. Interface of test routine is shown in Fig. 5.

During reach envelop testing process, two subjects (male youth) wearing spacesuit respectively to operate the test handle moving in a horizontal plane. The motion path was recorded by testing routine, which is shown in Fig. 6. When a horizontal plane test was finished, height of test handle can be adjusted by lift to another horizontal plane. By testing motion path in each horizontal plane, the reach envelope can be calculated with reverse engineering method.

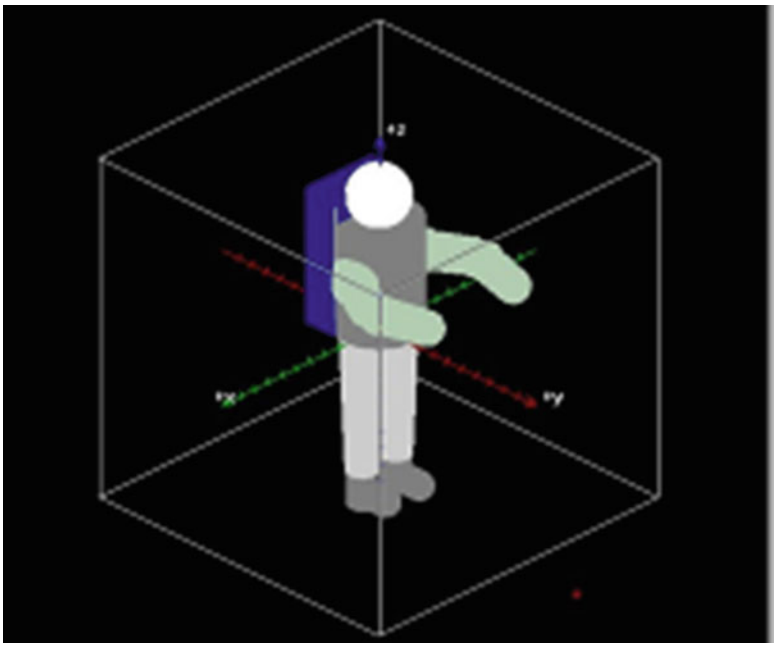

Fig. 5 Interface of spacesuit work envelope testing system

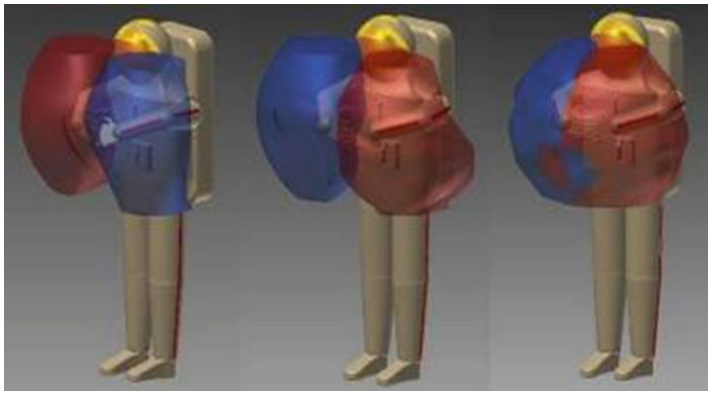

Fig. 6 Compared with experimental work envelope (*left* and *mid*) and simulation work envelope (*right*)

Experiments were performed to verify the Monte Carlo method simulation result, which were shown in Fig. 6. Compared with experiment result, the simulation result was similarity of shape and volume differ within 5 %, which prove the method meet the project need.

4 Conclusion

In this paper, a predictive method is used to determine work envelope of astronaut wearing spacesuit during EVA operating which considered the influence of spacesuit and human upper limbs. Monte Carlo based work envelope predictive model was established with kinematic model of human upper limbs by considering the sequence of spacesuit joints. A mechanical testing system was developed to verify the model. Different individuals wearing different spacesuit operated the manipulator to test the reach and visible envelope. Testing results and computational results were compared to verify the model.

The results of the project serve as a stepping stone for further research in this area, the availability of spacesuit-arm model, predictive model, and testing system will allow us to implement different modify and control methods to analyze the effect on the spacesuit's mobility performance.

References

1. Schmidt PB (2001) An investigation of space suit mobility with applications to EVA operations. Doctoral dissertation, Massachusetts Institute of Technology
2. Stirling L, Willcox K, Newman D (2010) Development of a computational model for astronaut reorientation. J Biomech 43:2309–2314
3. Judnick D, Newman D, Hoffman J (2007) Modeling and testing of a mechanical counterpressure bio-suit system. In: Proceedings of the international conference on environmental systems, Massachusetts Institute of Technology, Chicago, pp 87–112
4. Xu WF, Li LT (2007) Workspace analysis of space 3R robot. J Astronaut 28(5):1389–1394
5. Frazer A (2003) Modeling human-spacesuit interactions. Master's thesis, Massachusetts Institute of Technology, Cambridge, pp 43–51

Reduced Thrust Take-Off of Large Passenger Aircraft Based on Derate Method

Xinmin Wang, Haitao Yin, Yi Zheng, and Rong Xie

Abstract As the actual take-off weight of the aircraft is less than the maximum take-off weight, the technology which use thrust less than maximum take-off thrust for take-off is called reduced thrust take-off. Derate Method is one of the methods. In this paper, the principle of reduced thrust take-off is analyzed, and process and limitation are studied, and principle and application conditions of Derate Method are analyzed. At last, the vertical control law of Derate Method Reduced Thrust Take-off is designed and simulated to a large commercial aircraft. The results show that, under the safe flight condition, Derate Method reduced thrust take-off reduces fuel consumption effectually and is very meaningful to improve economic.

Keywords Reduced thrust takeoff • Derate method • Aircraft engine

1 Introduction

During the flight of the large commercial aircraft, the take-off stage is one of the most important stage in the whole flight. It not only directly affects flight safety, but also has significant influence on the engine performance. Research further reducing the operating costs of airlines on the basis of meeting safety performance of take-off is an important issue faced by Civil Aviation [1–3].

Civil Aviation large transport aircraft mostly use the Reduced Thrust Take-off technology. Reduced Thrust Take-off is that aircraft use thrust less than normal engine thrust to take off on the premise to ensure the flight safety [4, 5].

X. Wang • H. Yin • Y. Zheng • R. Xie (✉)
School of Automation, Northwestern Polytechnical University, Xi'an, China
e-mail: Yinhaitao198691@163.com

W. Wang (ed.), *Mechatronics and Automatic Control Systems*, Lecture Notes in Electrical Engineering 237, DOI 10.1007/978-3-319-01273-5_66,

This paper first describes the principle of Reduced Thrust Take-off, and then introduces the principle of Derate Method, and the example is simulated at last. Necessity to implement Reduced Thrust Take-off in large aircraft is analyzed with quantitative data.

2 Principle of Reduced Thrust Take-Off

Reduced Thrust Take-off (known as flexible thrust take-off) is that aircraft use thrust less than normal engine thrust to take off on the premise to ensure the flight safety (meet to the requirements of the appropriate regulations).

2.1 Process of Reduced Thrust Take-Off

The take-off process of the aircraft is shown as Fig. 1. In the process of take-off, ground acceleration stage is from loosing brake to lifting the front wheel; take-off decision speed V_1 is reached at some point of that stage; take-off cannot be interrupted when V_1 is reached. The speed when lifting the front wheel refers to as V_R, pilots should keep the nose about 8° in this stage until aircraft leave the ground. Then aircraft needs to accelerate to take-off safety speed. After climbing, the aircraft usually keeps speed $(V_2 + 10kn)$ before it reaches enough height [6].

When the weight of the aircraft is less than weight limited by airport length, V_1, V_2 and V_R will be reached in advance. Thus the aircraft will take-off without the whole runway and Reduced Thrust Take-off can be used by excess runway. And it is possible to implement Reduced Thrust Take-off.

2.2 Restriction of Reduced Thrust Take-Off

The lighter weight of the aircraft is, the larger climb gradient is, and the higher flight altitude is. The greater thrust is, the larger climb gradient is [7]. The aircraft cannot

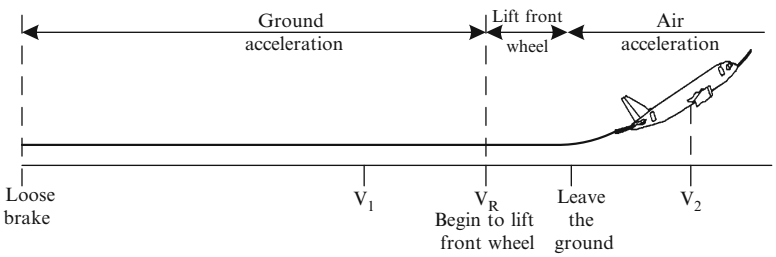

Fig. 1 Longitudinal sectional view of take-off

take off safely when the thrust of the engine cannot satisfy the minimum climb gradient.

Now we analyze the relationship of the take-off weight and thrust by the climb gradient [7]. As angle of attack α and angle of incidence of engine φ_T is very small, we can get,

$$F - D - mg \sin\theta - m\frac{dV}{dt} = 0 \tag{1}$$

By Eq. 1 and definition of rate of climb (r/c) we can obtain,

$$r/c = V \sin\theta = \frac{(F-D)V}{mg} - \frac{V}{g}\frac{dV}{dt}$$

By the definition of the climb gradient (C.G), we gen formula of C.G,

$$C.G = \frac{r/c}{V} = \frac{\frac{F}{mg} - \frac{C_D}{C_L}}{1 + \frac{V}{g}\frac{dV}{dh}} \tag{2}$$

In formula (2), F is thrust of engine, D is air resistance, m is take-off weight, V is take-off speed, θ is pitch angle, C_L is lift coefficient, C_D is drag coefficient. With given conditions of take-off, the greater the take-off weight is, the smaller the climb gradient is. The minimum available climb gradient provided by American Airlines Management Regulations (FAR-25) limits the maximum take-off weight. Equation 2 shows that, when lift coefficient and drag coefficient are dug out and take-off speed is determined, we can determine the relationship of thrust and take-off weight.

3 Derate Method

The essence of Derate Method is engine is regarded as a smaller power engine. The thrust of take-off must not exceed the maximum thrust of the virtual small power engine.

Figure 2 is variation of engine thrust dependent on temperature which aircraft take off with whole thrust and different levels of Derate Method. In general engine set two derating thrust level, TO1 and TO2. Each level has its restriction. The maximum thrust will decrease when derate level is selected in take-off. As Derate Method determines the take-off performance, take-off performance chart corresponded to power must be used. Derate Method have no operating limitation. It can be used under any circumstances provided aircraft performance is allowed.

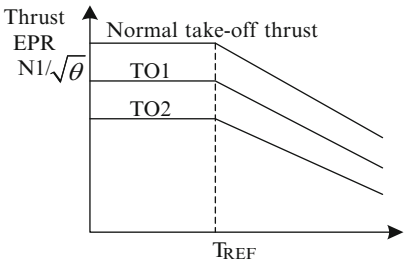

Fig. 2 The principle of Derate method

Different derate level usually corresponds to fixed reduced thrust, and specific data reduced by each airline may also be different (TO1 is 10 % and TO2 is 20 % in China Southern Airlines) [6]. And not all type can use Derate Method. Currently, all of types of Boeing can use Derate Method, and only can A319, A321, A330 and A340 use Derate Method in Airbus. There are six levels in A330 and A340. And thrust reduced is 4 %, 8 %, 12 %, 16 %, 20 % and 24 %. It cannot be used on other types.

4 Establishment of Fight and Propulsion Comprehensive Model

Establishing fight and propulsion comprehensive system requires that thrust provided by engine and thrust needed by plane is balance. So we can get general expression of state-space equation of the fight and propulsion comprehensive system [8],

$$\begin{cases} \dot{X} = AX + BU \\ Y = CX + DU \end{cases}. \tag{3}$$

In Eq. 3,

$$X = \left[X_p, X_e\right]^T = [V, \alpha, \theta, q, n_l, n_h]^T,\ Y = \left[Y_p, Y_e\right]^T = [V, \alpha, \theta, q, n_l, n_h, F]^T,$$
$$U = \left[U_p, U_e\right]^T = \left[\delta_e, m_f, A_e\right]^T$$

$$A = \begin{bmatrix} -0.0069 & 6.5191 & -9.8000 & 0 & 0.0007 & 0 & 0 \\ -0.0003 & -0.6105 & 0 & 1 & 0 & 0 & 0 \\ 0 & 0 & 0 & 1 & 0 & 0 & 0 \\ 0.0027 & -2.3540 & 0 & -0.4970 & 0 & 0 & 0 \\ 0 & 240 & 240 & 0 & 0 & 0 & 0 \\ 0 & 0 & 0 & 0 & -2.3410 & -3.5730 & 0.6720 \\ -0.0318 & 0 & 0 & 0 & -3.2410 & 0.3370 & -3.4920 \end{bmatrix},$$

$$B = \begin{bmatrix} 0.3504 & 0.0003 & 0 \\ -0.0251 & 0 & 0 \\ 0 & 0 & 0 \\ -1.8867 & 0 & 0 \\ 0 & 0 & 0 \\ 0 & 0.4960 & 0.6690 \\ 0 & 0.6360 & 3.6040 \end{bmatrix} C = \begin{bmatrix} 1 & 0 & 0 & 0 & 0 & 0 & 0 \\ 0 & 1 & 0 & 0 & 0 & 0 & 0 \\ 0 & 0 & 1 & 0 & 0 & 0 & 0 \\ 0 & 0 & 0 & 1 & 0 & 0 & 0 \\ 0 & 0 & 0 & 0 & 1 & 0 & 0 \\ 0 & 0 & 0 & 0 & 0 & 1 & 0 \\ 0 & 0 & 0 & 0 & 0 & 0 & 1 \\ 0.3950 & 0 & 0 & 0 & 67.3260 & 3.8357 & 1.3573 \end{bmatrix},$$

$$D = \begin{bmatrix} 0 & 0 & 0 \\ 0 & 0 & 0 \\ 0 & 0 & 0 \\ 0 & 0 & 0 \\ 0 & 0 & 0 \\ 0 & 0 & 0 \\ 0 & 0 & 0 \\ 0 & 29.8606 & -0.5174 \end{bmatrix}$$

5 Simulation Example

5.1 Structure and Processes of Simulation

Vertical Derate Method control law is taken to design and simulate to a large passenger aircraft. The given aircraft is equipped with four turbofan engines; the maximum thrust of single engine is 84.48 kN; the maximum thrust of aircraft is

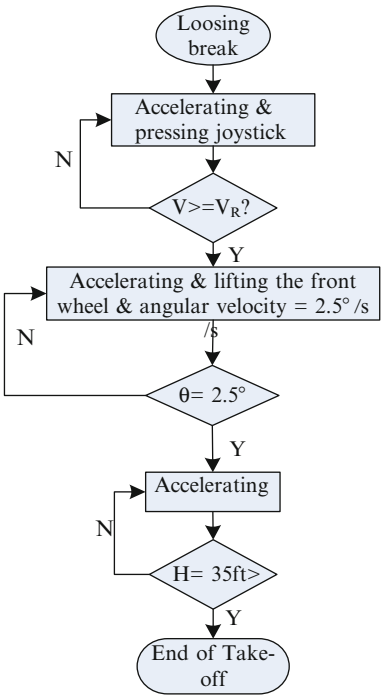

Fig. 3 Simulation process of take-off

320.8 kN. Speed of lifting the front wheel is read as $V_R = 69.72m/s$, and Take-off Safety Speed is $V_2 = 72.5m/s$ [7]. Simulation process is shown as Fig. 3.

The aircraft takes off from loosing brake. First, press the joystick; when speed reaches to the speed of lifting the front wheel V_R, aircraft lifts the front wheel with the pitch angular rate of $2.5^{\circ}/s$ and prepares to take off; pitch angle maintains to 7.5° at last and continues to climb. The take-off stage ends when the altitude reaches to 35 ft (10.7 m).

Now we make simulation with Derate Method take-off. Derate Method is set as two levels by the rules of a airline. TO1 is set as 10 %, and TO2 is set as 20 %. The structure of longitudinal take-off combining of aircraft and engine is shown as Fig. 4, which aircraft model is controlled with PID and engine model is controlled with Optimal Servo.

5.2 Simulation Results

The model is simulated by MATLAB 7.8. Responses of speed, altitude, distance rolling and fuel quantity of the full thrust and Derate Method is show as Figs. 5, 6, 7, and 8.

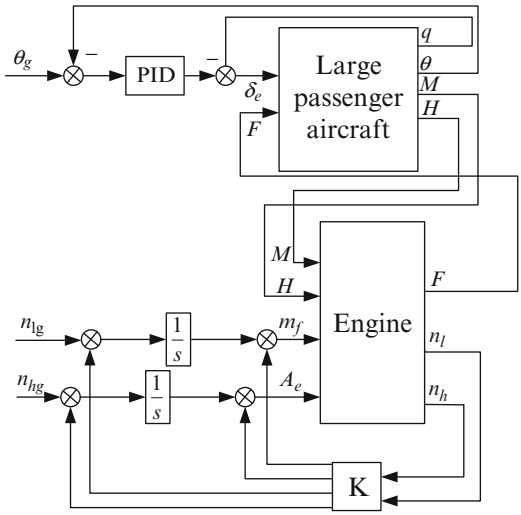

Fig. 4 Control structure of take-off

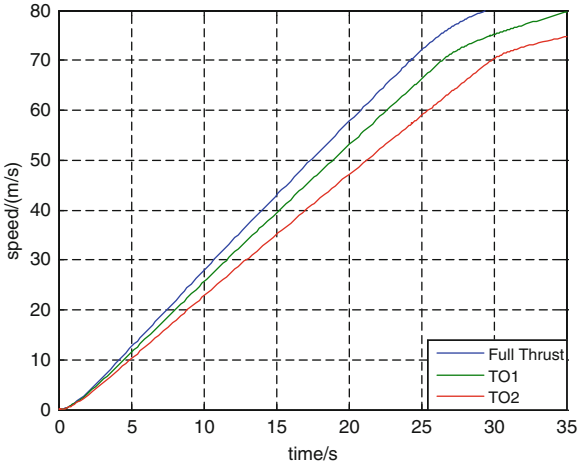

Fig. 5 Speed response

As shown from Figs. 5, 6, 7, and 8, time of TO1 and TO2 are respectively 28.77 and 31.95 s; speed of them are respectively 73.81 and 72.6 m/s; distance of them are 928 and 1052 m; fuel quantity of them are 265 and 262 kg. Compared Derate Method with full thrust, take-off time of TO1 is prolonged 4.05 %, and distance is increased 5.82 %, and fuel is reduced 4.35 %, take-off speed is $V = 73.81 > V_2$. Take-off time of TO2 is prolonged 15.55 %, and distance is increased 19.95 %, and fuel is reduced 5.07 %, take-off speed is $V = 72.6 > V_2$. Simulation results show that, as length of runway allowing, using Derate Method can ensure the security of take-off, and reduce fuel consumption greatly, and has a significant role in improving economic efficiency.

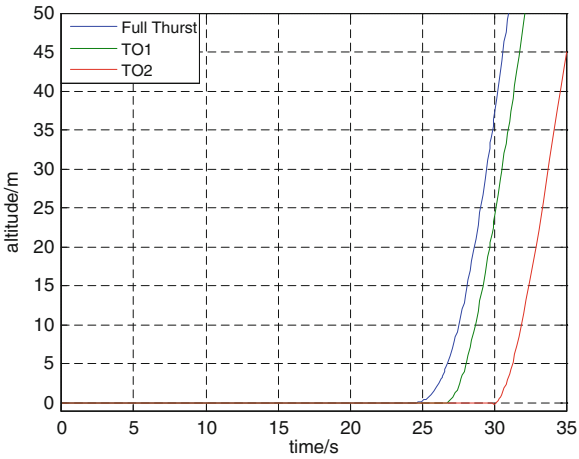

Fig. 6 Altitude response

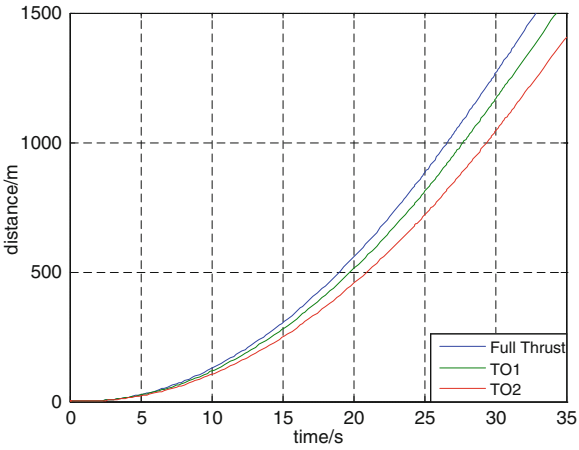

Fig. 7 Distance response

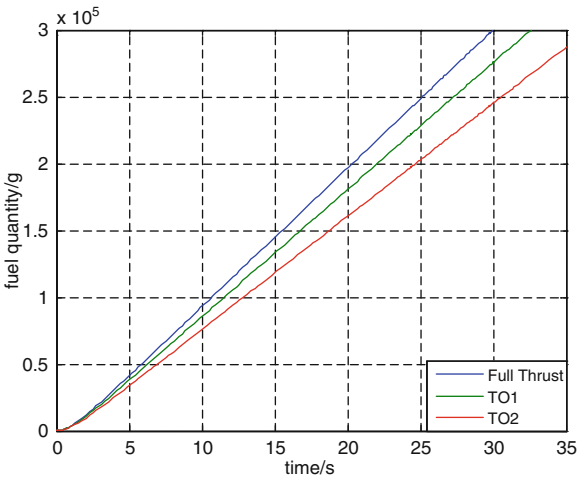

Fig. 8 Fuel quantity response

6 Conclusion

In this paper, the simulation is proved that Derate Method can reduce fuel consumption and transportation costs. Derate Method can also reduce in-flight shutdown rate and unscheduled engine removal rate, and improve safety standard of airlines. So it is necessary to study and spread Reduced Thrust Take-off.

References

1. Tingyu Zhao (2005) Necessity analysis of reduced-thrust taking-off of turbofan engines. Tianjin J Civil Aviat Univ China 23(3):6–8 (In Chinese)
2. Yong Wu (2005) An analysis of CFM56-5B Derated takeoff & flex takeoff. Beijing China Civil Aviat 1(49):73 (In Chinese)
3. Tingyu Zhao (2005) Principle of assumed temperature reduced thrust takeoff. Chengdu J Southwest Jiaotong Univ 40(5):677–679 (In Chinese)
4. Chmiela B, Sozanska M, Cwajna J (2012) Identification and evaluation of freckles in directionally solidified casting made of PWA 1426 nickel-based superalloy. USA Arch Metall Mater 57(2):559–564
5. Ao Liangzhong (2012) Thrust lever angle signal processing of an aircraft engine. In: Proceedings – 2012 international conference on computer science and electronics engineering, ICCSEE 2012, Los Alamitos, CA, USA, pp 613–616
6. Xiaoming Liu, Tingyu Zhao, Xiaohang Wen et al (2009) Reduced-thrust takeoff technique applied to passenger airplanes. Xi'an Flight Dynam 27(3):83–85 (In Chinese)
7. Tongjun Tian (2002) The integrated flight/propulsion H_∞ controller design[D]. Northwestern Polytechnical University, Xi'an, pp 19–22 (In Chinese)
8. Zhihuai Chen, Runping Gu, Junjie Liu (2006) Aircraft performance engineering[M]. Ordnance Industry Press, Beijing, pp 49–55 (In Chinese)

Permanent Magnet Synchronous Motor Feedback Linearization Vector Control

Hehua Wang and Xiaohe Liu

Abstract In order to solve the control problem of a class multiple-input multiple-output nonlinear system, the feedback linearization method is introduced. By calculating the output variables of Lie derivative, the appropriate coordinate transform and nonlinear state feedback are obtained, then through the coordinate transformation and state feedback, the input-output linearization is realized and the system decoupling is achieved. According to the system's linear model, the actual control rate is designed. For illustration, a multiple-input multiple-output nonlinear system example is utilized to show the feasibility of the feedback linearization in solving the permanent magnet synchronous motor, and then combines with the vector control method. Using MatLab7.6/Simulink to build modular and simulation verifies the effectiveness of the algorithm. Empirical results show that the feedback linearization is a better method to handle nonlinear system. From the simulation results we can be obtained that the feedback linearization vector control method has a good control effect.

Keywords Feedback linearization • Vector control • Effectiveness

1 Introduction

In recent years, with the high performance permanent magnet material technology, power electronics technology and microelectronics technology growing fast. Make permanent magnet synchronous motor be characterized by small volume, high efficiency, and the advantages of small losses. The PMSM plays an increasingly important role in small power motion control system. With the deepening of vector control theory and automatic control principle, the permanent magnet synchronous

H. Wang (✉) • X. Liu
Beijing Information Science & Technology University, Beijing, China
e-mail: wanghehua1985@126.com; liuxiaohe551026@163.com

W. Wang (ed.), *Mechatronics and Automatic Control Systems*, Lecture Notes in Electrical Engineering 237, DOI 10.1007/978-3-319-01273-5_67,

motor control system has developed rapidly. As a nonlinear system, the precise control methods have been studied by many scholars, among which the one based on differential geometry feedback linearization has achieved a big development. People have successfully solved the many problems about motor control with it, and got a good control effect. Such as the PMSM control systems based on SVPWM [1], the designs of PMSM in the vector control system, which has a good control effect for PMSM [2], and research the application feedback linearization in PMSM [3].

2 Description of Problem

For the following n-order multi-variable nonlinear system, using state space form to describe as follow types of equations:

$$\begin{aligned} \dot{x} &= f(x) + \sum_{i=1}^{m} g_i(x)u_i \\ y_1 &= h_1(x) \\ &\cdots \\ y_m &= h_m(x) \end{aligned} \tag{1}$$

Here $f(x), g_1(x), \cdots, g_m(x)$ is n-dimensional smooth vector function; $h_1(x), \cdots, h_m(x)$ is a scalar function. These equations can be more compact form:

$$\begin{aligned} \dot{x} &= f(x) + g(x)u \\ y &= h(x) \end{aligned} \tag{2}$$

Here $g(x) = (g_1(x), \cdots, g_m(x))$ is $n \times m$ order matrix; $h(x) = (h_1(x), \cdots, h_m(x))^T$ is m-dimensional column vector. Given the definition of the relation degree:

1. $L_{g_i} L_f^k h_i(x) = 0$;
2. The m-dimensional square $A(x)$ is singular at x_0.

$$A(x) = \begin{pmatrix} L_{g_1} L_f^{r_1 - 1} h_1(x) & \cdots & L_{g_m} L_f^{r_1 - 1} h_1(x) \\ L_{g_1} L_f^{r_2 - 1} h_2(x) & \cdots & L_{g_m} L_f^{r_2 - 1} h_2(x) \\ L_{g_1} L_f^{r_m - 1} h_m(x) & \cdots & L_{g_m} L_f^{r_m - 1} h_m(x) \end{pmatrix}$$

Here $L_{gi} L_f^k h_i(x) = \frac{\partial L_f^k h_i(x)}{\partial x} g_i(x), L_f^k h_i(x) = \frac{\partial L_f^{k-1}}{\partial x} f(x), \quad L_f h(x) = \frac{\partial h(x)}{\partial x} f(x), \quad$ the $L_f h(x)$ can also be written in the form of $(x), f(x) >$ that is Lie bracket, they $L_f h(x)$ can also be defined as the derivative of $h(x)$ along the vector field $f(x)$. The formula $L_g L_f h(x) = \frac{\partial L_f h(x)}{\partial x} g(x)$ is the derivative of $h(x)$ along the vector field $f(x)$, and then along the vector field $g(x)$.

The relation degree vector is $\{r_1, \cdots, r_m\}$, the relation degree is $r = r_1 + \cdots r_m$. Now we discuss system feedback linearization problem.

1. If $r = r_1 + \cdots + r_m \leq n$, for any $1 \leq i \leq m$ meets:

$$\begin{aligned} \phi_1(x) &= h_1(x) \\ \phi_2(x) &= L_f h_2(x) \\ &\cdots \\ \phi_i(x) &= L_f^i h_i(x) \end{aligned} \tag{3}$$

   Here $L_f^i h_i(x) = \frac{\partial L_f^{i-1} h_{i-1}(x)}{\partial x} f(x)$, $L_f h_1(x) = \frac{\partial h_1(x)}{\partial x} f(x)$.

   When $r = r_1 + \cdots + r_m$ is strictly less than n, so can find $n - r$ functions $\phi_{r+1}(x), \cdots, \phi_n(x)$, which make mapping $\Phi(x) = (\phi_1^1(x), \cdots, \phi_{r_1}^1(x), \cdots, \phi_1^m(x), \cdots, \phi_{r_m}^m(x), \phi_{r+1}(x), \cdots, \phi_n(x))^T$ have a nonsingular Jacobian matrix at x_0, so the mapping is equivalent to a local coordinate transformation at a neighborhood of x_0.

   The values of these additional functions can be arbitrary chose according to the following condition:

   $L_{g_j} \phi_i(x) = \frac{\partial \phi_i(x)}{\partial x} g_j(x) = 0$, For any x within a field of x_0, $r + 1 \leq i \leq n$ and $1 \leq j \leq m$.

2. When $r = r_1 + r_2 + \cdots + r_m$ is strictly equal to n, so can find out a set of functions: $\phi_k^i(x) = L_f^{k-1} h_i(x)$, $1 \leq k \leq r_i$, $1 \leq i \leq m$. We can define $\phi_k^i(x)$ as a local coordinate transformation in a neighborhood of x_0. By the local coordinate transformation, the system can use this form of m-group equations described under the new coordinate, making $z_i = \phi_i(x) = L_f^{i-1} h(x)$.

$$\begin{cases} \dot{z}_1 = z_2 \\ \dot{z}_2 = z_3 \\ \vdots \\ \dot{z}_{r-1} = z_r \\ \dot{z}_r = L_f^r h(x) \end{cases} \tag{4}$$

   By the above-mentioned transforms, z is selected as a new variable, the system becomes a linear system.

3 Mathematical Model of AC PMSM and Simulation

3.1 Mathematical Model of AC PMSM

The stators of Ac permanent magnet synchronous motor (PMSM) and general electric excitation three-phase synchronous motor are similar, if the permanent

magnet produces the induced electromotive force and the excitation coil generates induced electromotive force are the same, also to be the sine wave. The mathematical models of PMSM and electric excitation synchronous motor are the same. Some assumptions are made as follows:

1. Magnetic saturation, eddy current loss and hysteresis loss are neglected
2. Oversight space harmonic, three-phase winding symmetry, the air gap magnetic field is sine distribution
3. Three-phase power supply voltage balance

Based on the above assumptions, the mathematical model of PMSM under *d-q* coordinate system is [4]:

$$\begin{bmatrix} \dot{i}_d \\ \dot{i}_q \\ \dot{\omega} \end{bmatrix} = \begin{bmatrix} -\dfrac{R}{L} & P_n\omega & 0 \\ -P_n\omega & -\dfrac{R}{L} & -\dfrac{P_n\varphi_f}{L} \\ 0 & \dfrac{3P_n\varphi_f}{2L} & -\dfrac{B}{J} \end{bmatrix} \begin{bmatrix} i_d \\ i_q \\ \omega \end{bmatrix} + \begin{bmatrix} \dfrac{u_d}{L} \\ \dfrac{u_q}{L} \\ -\dfrac{T_L}{J} \end{bmatrix} \tag{5}$$

Here i_d, i_q denote d-q reference current, u_d, u_q denote d-q equivalent voltage, R is stator resistance, P_n denotes the number of pole pairs, L is equivalent inductance, ω is rotor speed, T_L represents load torque, J is the moment of inertia, B denotes the friction coefficient, φ_f represents the magnetic flux. Then Eq. 5 can be written in the form of affine nonlinear systems standards:

$$\dot{x} = f(x) + g_1(x)u_d + g_2(x)u_q \tag{6}$$

Here $x = [i_d, i_q, \omega]^T, g_1(x) = [\frac{1}{L}, 0, 0]^T, \quad g_2(x) = [0, \frac{1}{L}, 0]^T, \quad f(x) = \begin{bmatrix} -\frac{R}{L}i_d + P_n\omega i_q \\ -\frac{R}{L}i_q - P_n\omega i_d - \frac{P_n\varphi_f}{L}\omega \\ \frac{3P_n\varphi_f}{2J}i_q - \frac{B}{J}\omega - \frac{T_L}{J} \end{bmatrix}$. In order to make the system into linear system can make the following transformation, choosing ω, i_d as the output of the system, defining new output variables:

$$\begin{cases} z_1 = h_1(x) = \omega \\ z_2 = L_f h_1(x) \\ z_3 = h_2(x) = i_d \end{cases} \tag{7}$$

State equation of the system under new coordinate system as follows:

$$\begin{cases} \dot{z}_1 = z_2 \\ \dot{z}_2 = L_f^2 h_1(x) + L_{g1} L_f h_1(x) u_d + L_{g2} L_f h_1(x) u_q \\ \dot{z}_3 = L_f h_2(x) + L_{g1} h_2(x) u_d + L_{g2} h_2(x) u_q \end{cases}. \tag{8}$$

The system can be feedback linearized because it contains three inputs, three outputs and its relation degree vector is {1, 1, 1}. That means the sum of vectors is equal to the rank of the system. So the system can be described as exact feedback linearization and won't appear zero dynamics problems, selecting the new variables:

$$\begin{cases} \dot{z}_1 = z_2 \\ \dot{z}_2 = \nu_1 \\ \dot{z}_3 = \nu_2 \end{cases} \tag{9}$$

This system has become a linear system. We can select v_1 and v_2 as the control variables of the system. According to linear system poles configuration theory and state feedback, we can achieve the linear design of the system [5].

$$\begin{aligned} v_1 &= -k_1(y_1 - y_{1ref}) - k_2 \dot{y}_1 = -k_1(\omega - \omega_{ref}) - k_2 \dot{\omega} \\ v_2 &= -k_3(y_3 - y_{3ref}) = -k_3(i_d - i_{dref}) \end{aligned} \tag{10}$$

Let v_1 and v_2 be the control variables of system, so the actual control variables of the system are u_d u_q.

$$\begin{aligned} u_q &= \frac{2JL}{3P\varphi_f}\left[\frac{3P\varphi_f}{2JL}\left(\frac{R}{L} i_q + P\omega i_d + \frac{P\varphi_f}{L}\omega\right) + \frac{B}{J}\left(\frac{3P\varphi_f}{2J} i_q - \frac{B}{J}\omega - \frac{T_L}{J}\right) + v_1\right] \\ u_d &= L\left(\frac{R}{L} i_d - P\omega i_q + v_2\right) \end{aligned} \tag{11}$$

3.2 Simulation Module Introduction

According to the established mathematical model and feedback linearization of knowledge, and the knowledge of the motor control [4], we can get the system control diagram as follows the Fig. 1. Depending on the Eq. 10, we can know that the P controller can be used in the comparison between i_d and i_{dref}, the comparison between ω and ω_{ref} can use the PI controller.

In the MATLAB7.6/Simulink environment, set up its simulated modules based on the system control diagram. The following will describe a few of the more important in the simulated model.

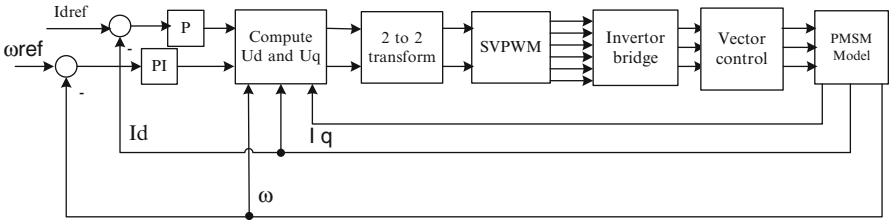

Fig. 1 Block diagram of the control system

Fig. 2 Abc2alfa-beta module

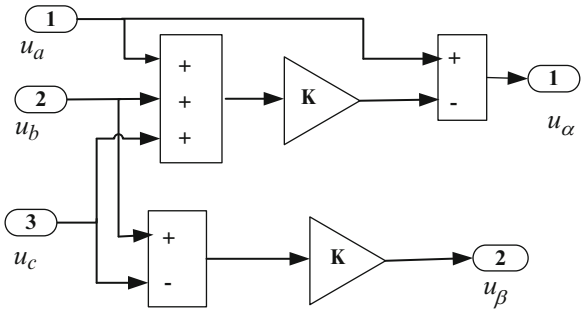

Fig. 3 Alfa-beta2dq module

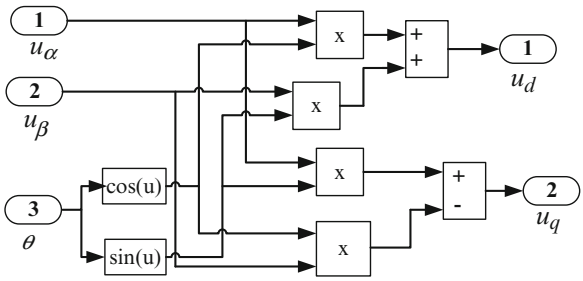

1. Vector control module

The basic thought of vector control is that through three to two transformation make two phases stationary coordinate system of the alternating current i_α, i_β equivalent to three-phase static coordinate system of the stator alternating current i_a, i_b, i_c. Then after rotor field orientation rotation transformation, letting i_α, i_β equivalent into two phases rotating coordinate system of the current i_d, i_q, i_d equivalents to DC motor of the excitation current, i_q equivalents to DC motor armature current. Realize vector control need two modules [6]: abc2*alfa* − *beta* and *alfa* − *beta*2*dq* transformation modules. As shown Figs. 2 and 3:

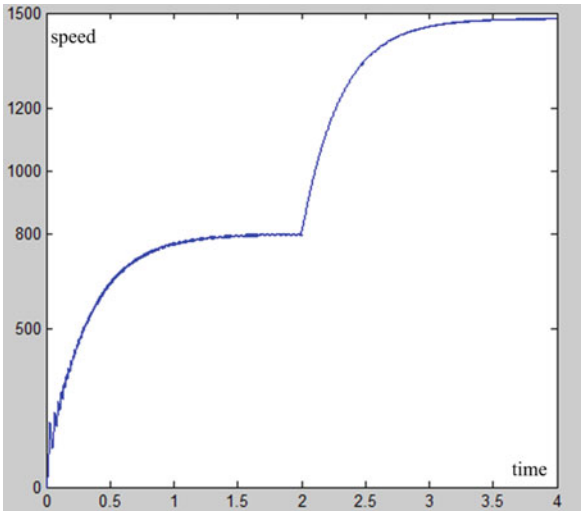

Fig. 4 Speed variation

3.3 Simulation Results Analysis

According to the above each simulation module, In the MATLAB7.6/Simulink environment, the PMSM parameter is set as follows: $R = 4.2\ \Omega$, $L = 0.0153$ H, $\varphi_f = 0.175\ Wb$, $J = 0.0021$ kg * m^2, $P_n = 3$, $B = 0.006$ Nm.Sec/rad. At first, given the reference ω_{ref} is 800 rad/s, after two seconds the reference ω_{ref} is 1,500 rad/s, the simulated results as follows. The speed variation is Fig. 4:

From the Fig. 4 we can clearly see that the system will soon be able to track the reference ω_{ref}, and no overshoot and steady state error. It can be known from the simulated result that the system responds rapidly and has good robust stability.

At the same time we can get phase current i_q change curve Fig. 5. We can clearly see that the phase current i_q soon enters a stable state and the change of the reference ω_{ref} will cause the current change of i_q. We can know that different sizes of ω_{ref} disturbance to i_q is not the same, but the phase current i_q can be able to quickly run in the stable state.

From the above the simulated result we can know that feedback linearization vector control method has a good control effect. The system responds rapidly and has good robust stability. We also know that the system can quickly run in the stable state, the response is fast, almost no steady-state error.

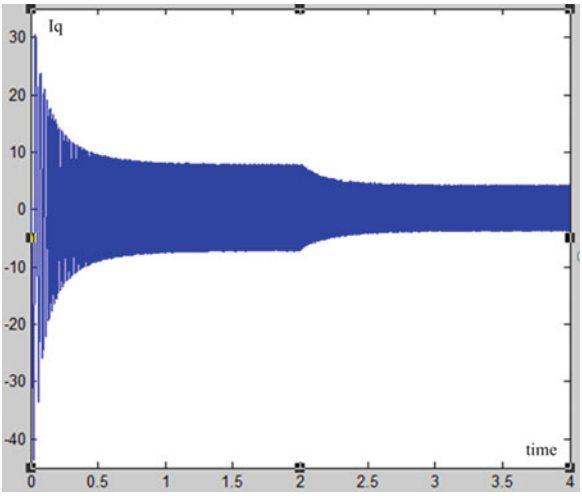

Fig. 5 Phase current Iq variation

4 Conclusion

This paper described the Feedback linearization vector control of PMSM, using the MATLAB7.6/Simulink to construct the system of the simulated model. The simulated result shows that the system runs smoothly, with good dynamic performance; the feedback linearization vector control method has a good control effect; the designed system responds rapidly and has good robust stability, which will provide useful reference to the PMSM control system design and analysis later.

References

1. Dong SY, Sun SH (2010) Modeling and simulation of PMSM control system based on SVPWM. Mod Electron Tech 18(329):188–191
2. Wu B (2008) Modeling and simulation of PMSM vector control system based on MATLAB/Simulink & SimPower systems. Electro-Mech Eng 24(3):57–59
3. Liu DL, Zhao GY (2006) Speed tracking control of PMSM based on direct feedback linearization. Electr Drive Autom Control 28(2):8–10
4. Kou BQ, Cheng SK (2008) Ac servo motor and control. China Machine Press, Beijing, pp 112–115
5. Wang CY (2009) Modern control technology for electric machines. China Machine Press, Beijing, pp 56–70
6. Zhang XF, Wang J, Chen XY, Li YJ (2011) MATLAB mechanical and electrical control system technology and application. Tsinghua University Press, Beijing, pp 98–105

Design and Simulation of Image Compensation Control System

Chan Tan and Lei Ding

Abstract Image compensation is a key to high resolution imaging. This paper designs and simulates an image compensation control system based on swing pointing mirror. The principle of pointing mirror compensation is presented and the mathematical model of pointing mirror's driving motor is established. Based on this model, a high accurate controller which consists of current loop and velocity loop is designed and simulated. Considering that there is disadvantage of traditional speed PID controller in dynamic performance, which is speed overshoot, the speed loop adopts pseudo derivative feed-forward (PDFF) controller. Theoretical analysis and simulation results show that the designed image compensation control system has good characteristic in following performance, dynamic response and noise resistance.

Keywords Image compensation control • Swing pointing mirror • PDFF controller

1 Introduction

If there is relative motion between camera and aim during exposure time, the target image recorded in detectors is moved and blur. So it is necessary to compensate image shift due to the limitation of MTF (Modulation Transfer Function). In order to resolve the image motion, many methods have been proposed, including mechanical compensation [1], electronic compensation such as TDI (Time Delay Integration) CCD and whole frame transfer CCD [2], optical compensation such as optical joint correlators [3, 4] and swing mirror, and software compensation [5] etc.

C. Tan (✉) • L. Ding
Key Laboratory of Infrared System Detection and Imaging Technology, Shanghai Institute of Technical Physics, Chinese Academy of Sciences, Shanghai, China
e-mail: helen367@126.com

W. Wang (ed.), *Mechatronics and Automatic Control Systems*, Lecture Notes in Electrical Engineering 237, DOI 10.1007/978-3-319-01273-5_68,

However, mechanical compensation is only applied in film camera, and electronic compensation based on TDI CCD merely achieves one-dimension compensation, and optical joint correlator is strict to the environment, while compensation based on swing mirror could not only compensate forward image shift but also pitching and yawing image shift.

To achieve the compensation, the swing pointing mirror has to swing at certain speed during satellite's forward flight, and due to its extreme low compensation speed, the servo system of pointing mirror must be stable and high accuracy. Because PMSM have excellent speed adjustment performance and high efficiency which is fit for high-powered close-loop control system and small torque ripple. So this paper chooses PMSM as swing pointing mirror's driving motor.

Firstly, this paper gives the principle and calculation of swing pointing mirror compensation, and then establishes mathematical model of PMSM. Based on this model, a high accurate controller is designed including current loop and speed loop. Besides, in order to reduce speed overshoot, the speed loop adopts PDFF controller. Theoretical analysis and simulation results show that the designed image compensation control system has good characteristic in following performance, dynamic response and noise resistance.

2 Swing Mirror-Based Image Compensation Control System

2.1 Principle of Swing Pointing Mirror Compensation

The principle of pointing mirror compensation is shown in Fig. 1 [6].

It can be seen that before compensation, with the forward flight of the camera, the aim's image is moved and blur on CCD plane. After compensation, when the camera is flying forward, the mirror is swing at certain speed, by whose lead the aim

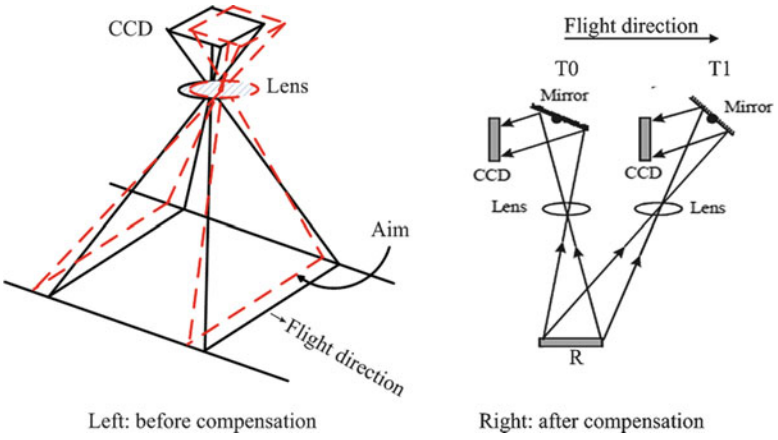

Fig. 1 Pointing mirror compensation principle chart

images on CCD, in other words, CCD camera "sees" the same aim at time T0 and T1, thus the image's residence time increase. In a word, the purpose of pointing mirror compensation is to make sure CCD camera imaging the same aim for several continuous times with the pointing mirror swing on its axis at certain speed, thus increase the resident time of CCD camera.

2.2 *Calculation of Swing Speed of Compensation Pointing Mirror*

All detail analysis and calculation of motion compensation speed could be seen in reference [7], here just gives the final calculation formula shown as follows.

$$\omega_m = \frac{K-1}{2K} \frac{H\sqrt{R^2-(R+H)^2\sin^2 2\theta_m}\cos 2\theta_m}{\left[(R+H)\cos 2\theta_m - \sqrt{R^2-(R+H)^2\sin^2 2\theta_m}\right]^2}\Omega \tag{1}$$

Where ωm is pointing mirror's angle speed, θm is pointing mirror's pointing angle, H is orbit height, R is the earth radius, Ω is satellite's angle speed and K is multiple of CCD camera's residence time. The relationship between ωm and θm in different orbit height H and different K is shown in Fig. 2.

It can be seen that with the increase of orbit height, the compensation speed becomes lower. Even when the orbit height is 100 Km, the largest compensation speed is 2° per second, which needs the servo control system to be highly stable and accurate. This paper chooses PMSM as compensation mirror's driving motor due to its high accuracy in closed-loop control system.

3 Mathematical Model of PMSM

The mathematical model of PMSM in d-q synchronous rotating coordinate is shown as follows [8]:

$$\begin{gathered}
\frac{d}{dt}i_d = \frac{1}{L_d}U_d - \frac{R}{L_d}i_d + \frac{L_q}{L_d}P_n\omega_r i_q \\
\frac{d}{dt}i_q = \frac{1}{L_q}U_q - \frac{R}{L_q}i_q - \frac{L_d}{L_q}P_n\omega_r i_d - \frac{\psi_f}{L_q}P_n\omega_r \\
\psi_q = L_q i_q \\
\psi_d = L_d i_d + \psi_f \\
T_e = 1.5P_n[\psi_f i_q + (L_q - L_d)i_d i_q] \\
J\frac{d\omega_r}{dt} = T_e - B\omega_r - T_l
\end{gathered} \tag{2}$$

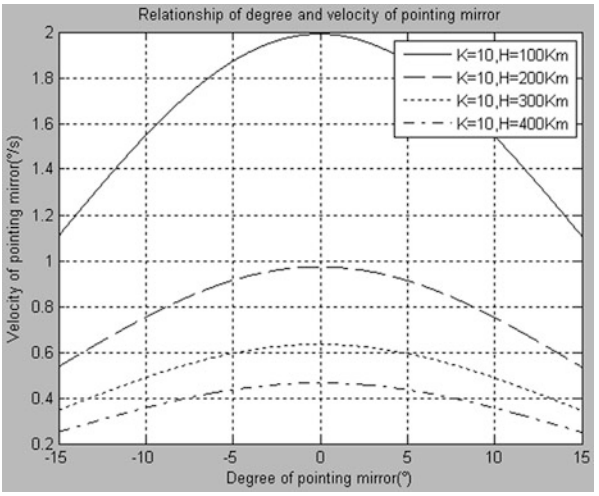

Fig. 2 Relationship of pointing mirror's speed to its angle

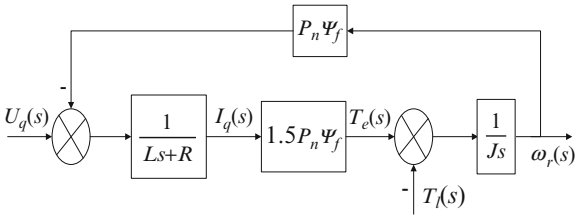

Fig. 3 Control diagram of PMSM

Where Ud and Uq is d-axis and q-axis stator voltage respectively, id and iq is d-axis and q-axis stator current respectively, ψd and ψq is d-axis and q-axis stator magnet linkage respectively, ψf is magnetomotive, R is stator resistance, ωr is rotator angle speed, Te is magnet torque, Tl is load torque, J is rotary inertia and B is friction coefficient. The control diagram of PMSM, which is shown in Fig. 3, could be achieved by transforming the mathematical model of PMSM into Laplace form.

There are many control methods of PMSM and the most widely used control strategy is field orientated control. When id is equal to zero, the motor could gain the largest torque, which is space vector control method [9]. Thus the control structure of PMSM is shown in Fig. 4, where GASR and GACR is speed and current PID adjustor respectively. Especially, when the pointing mirror performs the function of image compensation, the input is compensation speed calculated in second part, so the control structure of PMSM is just speed loop and current loop. In next part, this paper will discuss how to design speed and current PID adjustor.

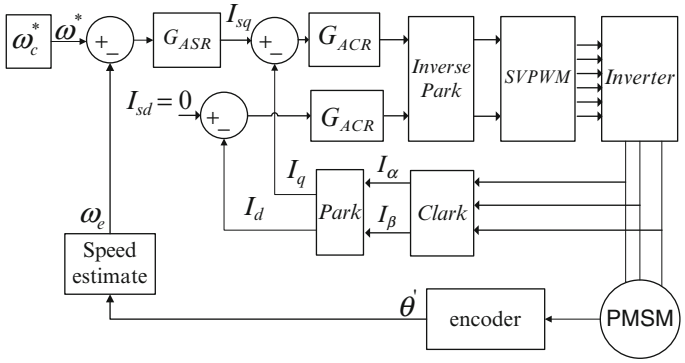

Fig. 4 Control structure of PMSM

4 Design of PID Controller

To design multiple loop system, outer loop sees inner loop as a whole element, and according to practice experience, when the bandwidth of inner loop is over five times of outer loop's, the inner loop could be seen as first-order inertial element.

4.1 Current Loop Controller

As the inner most loop, current loop must have the characteristic of fast following to the change of input voltage and excellent noise resistance, no matter when the pointing mirror performs orientation or compensation. According to the model of PMSM, the motor armature is equivalent to a first-order inertial loop with time constant Tm = L/R, and the PWM inverter is also a first-order inertial loop with time constant Ti, so the control object of current loop is two first-order inertial elements, whose transfer function is as follows:

$$G_{iobj} = \frac{1}{(Ls+R)(T_i s+1)} \tag{3}$$

According to the design method in engineering, the system should be adjusted into I-system, and the controller has an integrating element and a proportional element [10], thus the controller's transfer function is shown in Eq. 4,

$$G_{ACR}(s) = K_{ip}\frac{\tau_i s+1}{\tau_i s} \tag{4}$$

Where Kip is the proportional coefficient and τi is integrating time constant. Making τi = L/R and KI = Kip/Rτi, the current loop's open-loop transfer function is

$$G_i(s) = K_I \frac{1}{s(T_i s + 1)} \tag{5}$$

To consider dynamic response and overshoot, make KI * Ti = 0.5. Supposing the motor's inductance L = 8.5 mH, and resistance R = 6.42 Ω, using MATLAB/SIMULINK to simulate the current loop, and the result shows that the −3 dB bandwidth is 3.37 KHz and the gain in low frequency band is smooth, which approaches the first-order inertial element, besides, the step response is stable at 1.8 ms and no overshoot. Moreover, the amplitude of noise response is 2.8 % of input noise, and decreases to zero in 10 ms. So the designed current loop satisfies the characteristic in fast response, no overshoot and strong noise resistance.

4.2 Speed Loop Controller

From above discussion, the current loop is similar to first-order inertial element, and it could be seen as an element of speed loop. Besides, according to Fig. 3, the current loop and the integrated element Kt/Js constitute the control object of speed loop. In general, the system should be adjusted into II-system, however, this kind of system always has large overshoot, which is not tolerable in image compensation because as long as the mirror's speed deviates the compensation speed shown in Fig. 2, the compensation loses its function. To resolve this problem, speed differential negative feedback is introduced; nevertheless, speed differential would introduce noise, even though some of the noise could be eliminated by filter, while the filter would lead to phase delay, limiting system's performance improvement. Thus, this paper adopts a pseudo derivative feed-forward controller, which has a gain adjustable feed-forward channel, and changing this gain could improve dynamic response and decrease overshoot. Use MATLAB/SIMULINK to build the simulation model as Fig. 5, where Kvfr is gain constant of feed-forward channel, τs is integration time constant and KS is proportional coefficient, and GACR is the current loop above designed.

So the speed loop's close-loop transfer function is shown in Eq. 6.

$$H_s = \frac{K_{vfr} K_t K_s K_I \tau_s s + K_t K_s K_I}{J\tau_s s^3 + J\tau_s K_I s^2 + K_t K_s K_I \tau_s s + K_t K_s K_I} \tag{6}$$

When Kvfr = 0.6, τs = 0.025 and KS = 14, use MATLAB to analyze the transfer function, and the result shows that −3 dB bandwidth of speed loop is

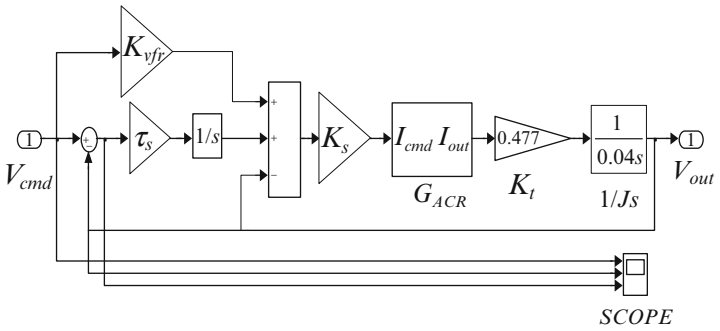

Fig. 5 Simulation model of speed loop

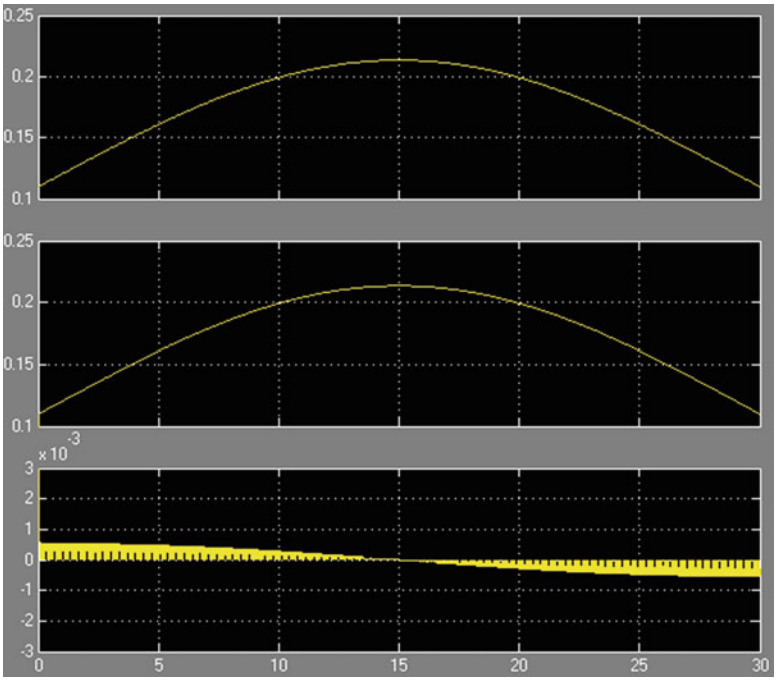

Fig. 6 Speed loop's response to input compensation speed (from up to down: input, output, error)

101 Hz and the step response is stable at 0.06 s and no overshoot. Furthermore, the speed loop's step noise response is only 5 % of input and decreases to zero in 0.1 s.

Besides, use SIMULINK to see how the speed loop's following performance is and the result is shown in Fig. 6. It can be seen that the speed loop follow the input compensation speed very well and the follow error is less than 0.001, thus the designed speed loop satisfy the requirements.

5 Conclusion

This paper designs and simulates an image compensation control system based on pointing mirror driven by PMSM. The principle and calculation of pointing mirror compensation is given firstly and then the mathematical model and control structure of PMSM is established. Finally, based on this model, a high accurate controller including current loop and speed loop is designed and simulated, the simulation results show that the designed controller has good performance in fast response, no overshoot and noise resistance.

References

1. Gu Song, Yan Yong, Xu Kai et al (2011) Design of motion compensation mechanism of satellite remote sensing camera. Proc SPIE 8196:81961Z-1–81961Z-8
2. Wang De-jiang, Kuang Hai-peng, Cai Xi-chang et al (2008) Digital implementation of forward motion compensation in TDI-CCD panoramic aerial camera. Opt Precis Eng 16:2465–2471 (In Chinese)
3. Tchernykh V, Dyblenko S, Janschek K, Seifart K, Harnisch B (2004) Airborne test results for a smart Pushbroom imaging system with optoelectronic image correction. Proc SPIE 5234:550–559
4. Janschek K, Tchernykh V, Dyblenko S, Flandin G, Harnisch B (2004) Compensation of focal plane image motion perturbations with optical correlator in feedback loop. Proc SPIE 5570:280–288
5. Liu Ming (2005) Research on detection and compensation technology of forward image motion in aerial photography based on image restoration. Ph.D. thesis, Graduate School of Chinese Academy of Sciences (In Chinese)
6. Lv Peng, Tang Yuanhe et al (2007) Study CCD image motion for remote sensing detection. Proc SPIE 6279:62795S-1–62795S-7
7. Xie Ren-Biao (2009) The research of aerospace low-speed high accuracy scanning-controlling technology. Ph.D. thesis, Graduate School of Chinese Academy of Sciences (In Chinese)
8. Zhang Yu (2010) The research of image compensation and control of space staring imaging. Ph.D. thesis, Graduate School of Chinese Academy of Sciences (In Chinese)
9. Chen Rong (2004) The research of PMSM servo system. Ph.D. thesis, Nanjing University of Aeronautics and Asnautics (In Chinese)
10. Chen Boshi (2003) Electrical towage automatic control system. China Machine Press, Beijing, pp 59–80 (In Chinese)

μ-Method for Robust Stability of Active Aeroelastic Wing with Multiple Control Surfaces

Fu-hu Liu, Xiao-ping Ma, and Zi-jian Zhang

Abstract μ-method for robust stability of an active aeroelastic wing section with leading and tailing edge control surface is developed. Robust system is constructed to account for the uncertainty parameters associated with the variable structural damping and the nonlinear structural stiffness. The nominal and robust stability margins, critical flutter airspeeds and frequencies are computed to analyze the aeroelastic and aeroservoelastic robust stability in the μ-framework. The analysis process shows μ method for robust stability analysis of aeroservoelastic system with uncertainties is effective. The simulation results indicated that uncertain perturbation reduces stability margin of system. The aeroservoelastic system increases flutter speed and critical dynamic pressure to the aeroelastic (openloop) system, specifically increases in flutter speed is 12 % when leading edge flap activated and 32 % when both leading and trailing edge flap activated. The system tends to stabilize more quickly and trailing edge flap deflects smaller by using both the leading and trailing edge control surfaces simultaneously.

Keywords Robust stability • Aeroservoelastic • Uncertain perturbation

1 Introduction

For the active aeroelastic wing [1], researchers have focused much attention on active flutter suppression (AFS). Great progress has been made since active control technology has been further developing. However, few literatures have been written about AFS on an active aeroelastic wing with multiple control surfaces. Platanitis

F.-h. Liu (✉)
Northwestern Polytechnical University, Xi'an, China
e-mail: liufuhu2008@163.com

X.-p. Ma • Z.-j. Zhang
UAV Research Institute, Northwestern Polytechnical University, Xi'an, China

W. Wang (ed.), *Mechatronics and Automatic Control Systems*, Lecture Notes in Electrical Engineering 237, DOI 10.1007/978-3-319-01273-5_69,

and Strganac [2] used feedback linearization and adaptive control method for the suppression of limit-cycle oscillations (LCO) of a typical wing section with leading and trailing edge control surfaces. It is compared with the study of the wing with only trailing edge control surface, which investigated by Jeffry and Thomas [3] using full-state feedback control law. The result shows that globally stabilizing control may be achieved by using two control surfaces.

Uncertainty is an important issue to its stability for the modern control system. Therefore, robust stability has been put forward. It means the systems with uncertainty can keep stable. Aeroservoelastic (ASE) system considers the interaction of aeroelastic (AE) system and servoactuators. Aeroservoelastic stability has been a necessary condition for safety of air vehicles flight. In the classical control systems analysis of aeroservoelastic stability, the precision magnitude and phase stability margin can be reduced from Nyquist method, which is for single-input-single-output (SISO) system. For multi-input and multi-output (MIMO) system stability analysis, it is a well-known and practically effective technique to use minimum single value method. However, it cannot analyze robust stability for the system with parametric uncertainties. The result of minimum single value method is deficient because it only considering unparametric uncertainties, such as additive perturbation and multiplicative perturbation. Therefore, so many researchers examined μ-method in their analysis to solve this problem. Livne indicated that the uncertainties are one of the important effects in future aeroelasticity research [4]. Lind and Brenner at the NASA Dryden Flight Research Center combining μ-method and flight test data for the estimation of robust flutter and aeroservoelastic margins of F/A-18 research aircraft, and which improve safety of flight test [5, 6]. Lind suggested a match point solution method for a robust flutter prediction. He analyzed the variation of the air vehicles flutter speed in terms of the altitude [7]. Borglund suggested a μ-k method for a robust aeroelastic stability analysis [8]. It proves that μ-method for robust flutter and analysis is more practicable.

In this paper, a typical wing section with leading and trailing edge control surfaces is concerned with the structural and dynamic pressure uncertainty. We construct uncertain AE and ASE system. Furthermore, robust stability for uncertain system is analyzes with μ-method. Herein, robust stability of active aeroelastic wing with multiple control surfaces is studied.

2 Structured Singular Value μ-Method

Standard $\boldsymbol{P} - \boldsymbol{\Delta}$ configuration shown in Fig. 1, where $\boldsymbol{P}$ is the plant of a system, and $\boldsymbol{\Delta}$ is structured matrix of perturbations. For $\boldsymbol{P} \in C^{n\times n}$ and a known structure of $\boldsymbol{\Delta}$,

$$\boldsymbol{\Delta} = [\mathrm{diag}(\delta_1 \mathrm{I}_{r1}, \ldots \delta_s \mathrm{I}_{rs}, \Delta_1, \ldots \Delta_f) : \delta_i \in C, \Delta_j \in C^{m_j \times m_j}] \tag{1}$$

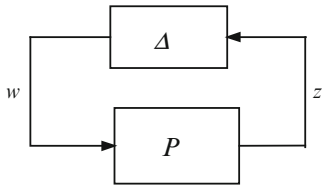

Fig. 1 $\boldsymbol{P}-\boldsymbol{\Delta}$ block diagram for robust stability analysis

Note the structured perturbation $\boldsymbol{\Delta}$ is a block diagonal matrix, where $\sum_{i=1}^{s} r_i + \sum_{j=1}^{f} m_j = n$ with n is the dimension of the block $\boldsymbol{\Delta}$.

The structure singular value μ is defined by

$$\mu_{\Delta}(\boldsymbol{P}) = \left(\min\{\sigma_{\max}(\boldsymbol{\Delta}) : \boldsymbol{\Delta} \in \text{-}\boldsymbol{\Delta}, \det(\boldsymbol{I} - \boldsymbol{P}\Delta) = 0\}\right)^{-1} \tag{2}$$

and unless $\boldsymbol{I} - \boldsymbol{P}\Delta$ is not singular for any $\boldsymbol{\Delta} \in \text{-}\boldsymbol{\Delta}$, then $\mu_{\Delta}(\boldsymbol{P}) = 0$ [9].

It is obvious that the structured singular value μ denotes a measure of the smallest destabilizing perturbation. The robust stability result with regard to structured uncertainty is given as follow.

Robust stability theorem [10]: Let the nominal feedback system be stable and let $\gamma > 0$ be an uncertainty bound, i.e. $\|\Delta\|_{\infty} \leq \gamma$. The perturbed system of Fig. 1 is robustly stable, with respect to $\boldsymbol{\Delta}$, if and only if $\mu_{\Delta}(\boldsymbol{P}) < 1/\gamma$.

Generally we assume the set of $\boldsymbol{\Delta}$ is bounded to unity $\|\Delta\|_{\infty} \leq 1$, the robust stability condition is then $\mu_{\Delta}(\boldsymbol{P}) < 1$.

3 System Model

3.1 A Typical Wing Section

A typical wing section with both a leading and trailing edge control surface is shown in Fig. 2, where b is semichord of the wing, a is nondimensional distance from the midchord to the elastic axis, h is plunge displacement, α is pitch angle, β and γ are trailing and leading edge flap deflection, x_{α} is nondimensional distance between the elastic axis and the center of mass, K_h is structural stiffness in plunge, K_{α} is structural stiffness in pitch.

The wing has four degrees of freedom, and the frequency dynamics of the control surfaces are far higher the dynamics of the primary system. Thus the motion of the system, with two degrees of freedom pitch and plunge, may be described by

$$\begin{bmatrix} m_t & m_w x_{\alpha} b \\ m_w x_{\alpha} b & I_{\alpha} \end{bmatrix} \begin{bmatrix} \ddot{h} \\ \ddot{\alpha} \end{bmatrix} + \begin{bmatrix} C_h & 0 \\ 0 & C_{\alpha} \end{bmatrix} \begin{bmatrix} \dot{h} \\ \dot{\alpha} \end{bmatrix} + \begin{bmatrix} K_h & 0 \\ 0 & K_{\alpha} \end{bmatrix} \begin{bmatrix} h \\ \alpha \end{bmatrix} = \begin{bmatrix} -L \\ M \end{bmatrix} \tag{3}$$

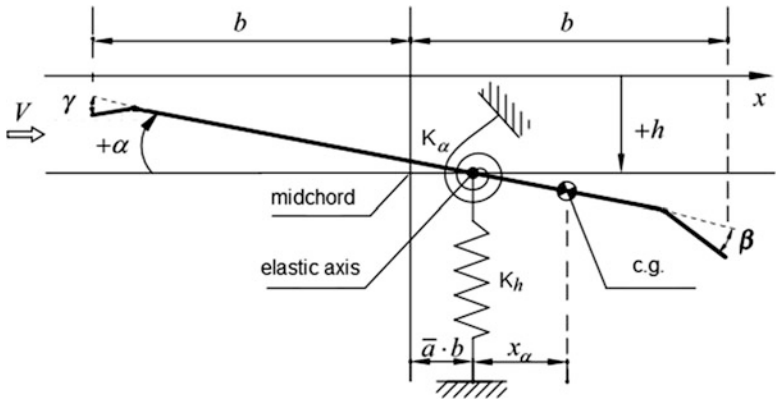

Fig. 2 The wing section with two degrees of freedom with multiple control surfaces

where m_t is total mass of the pitch-plunge system, m_w is total mass of the wing plus mount mass, I_α is total mass moment of inertia about the elastic axis. C_h and C_α are structural damping coefficients in plunge and in pitch. The lift L and moment M are quasi-steady aerodynamic forces and moments with leading and trailing edge have been based on Theodorsen's theory and Fung's theory [11]

$$L = q\left(2bs_pC_{L\alpha}[\alpha + (\dot{h}/V) + (0.5 - a)b(\dot{\alpha}/V)] + 2bs_pC_{L\beta}\beta + 2bs_pC_{L\gamma}\gamma\right) \quad (4)$$

$$M = q\left(2b^2s_pC_{m\alpha}[\alpha + (\dot{h}/V) + (0.5 - a)b(\dot{\alpha}/V)] + 2b^2s_pC_{m\beta}\beta + 2b^2s_pC_{m\gamma}\gamma\right) \quad (5)$$

where s_p is wing span, q is dynamic pressure, $q = \frac{1}{2}\rho V^2$, ρ is air density, V is velocity, $C_{L\alpha}$, $C_{L\beta}$ and $C_{L\gamma}$ are lift coefficient per angle of attack, trailing edge flap deflection and leading edge flap deflection, $C_{m\alpha}$, $C_{m\beta}$ and $C_{m\gamma}$ are moment coefficient per angle of attack, trailing edge flap deflection and leading edge flap deflection.

3.2 Nominal AE Systems

To compute stability margin, the unsteady dynamic pressure can be modeled as the nominal dynamic and perturbation associate with unsteady dynamic pressure

$$q = q_{nom} + \delta_q \quad (6)$$

where δ_q is the perturbation of unsteady dynamic pressure, $\delta_q \in R$.

In order to construct μ framework, we let

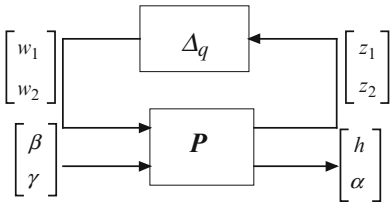

Fig. 3 Nominal AE system block diagram

$$z_1 = \left(2bs_pC_{L\alpha}[\alpha + (\dot{h}/V) + (0.5 - a)b(\dot{\alpha}/V)] + 2bs_pC_{L\beta}\beta + 2bs_pC_{L\gamma}\gamma\right) \tag{7}$$

$$z_2 = \left(2b^2s_pC_{m\alpha}[\alpha + (\dot{h}/V) + (0.5 - a)b(\dot{\alpha}/V)] + 2b^2s_pC_{m\beta}\beta + 2b^2s_pC_{m\gamma}\gamma\right) \tag{8}$$

$$w_1 = \delta_1 z_1 \tag{9}$$

$$w_2 = \delta_2 z_2 \tag{10}$$

where $\delta_1 = \delta_2 = \delta_q$.

Combining Eqs. 4, 5, 6, 7, 8, 9, and 10, the aerodynamic loads are reformulated

$$\begin{aligned} L = q_{nom}(&2bs_pC_{L\alpha}\left[\alpha + \left(\dot{h}/V\right) + (0.5 - a)b(\dot{\alpha}/V)\right] \\ &+ 2bs_pC_{L\beta}\beta + 2bs_pC_{L\gamma}\gamma) + w_1 \end{aligned} \tag{11}$$

$$\begin{aligned} M = q_{nom}\big(&2b^2s_pC_{m\alpha}\left[\alpha + \left(\dot{h}/V\right) + (0.5 - a)b(\dot{\alpha}/V)\right] \\ &+ 2b^2s_pC_{m\beta}\beta + 2b^2s_pC_{m\gamma}\gamma) + w_2 \end{aligned} \tag{12}$$

Combining Eqs. 3, 4, 5, 6, 7, 8, 9, and 10 we obtain nominal system is shown in Fig. 3, where $\boldsymbol{\Delta}_q = diag(\delta_1, \delta_2)$.

3.3 Robust AE and ASE Systems

Robust system is the nominal system considers structure perturbation. The structural damping coefficient due to variable damping can be defined as

$$C_h = C_{hnom} + W_3\delta_3 = C_{hnom}(1 + e_3\delta_3) \tag{13}$$

$$C_\alpha = C_{\alpha nom} + W_4\delta_4 = C_{\alpha nom}(1 + e_4\delta_4) \tag{14}$$

where δ_3 and δ_4 are perturbation to the structural damping coefficient in plunge C_{hnom} and in pitch $C_{\alpha nom}$, $\delta_3, \delta_4 \in R$ and $|\delta_3| \leq 1$, $|\delta_4| \leq 1$; W_3 and W_4 are the weighting on perturbation to the structural damping coefficient in plunge C_{hnom} and

in pitch $C_{\alpha nom}$, $W_3, W_4 \in R$; e_3 and e_4 are weighted modeling error on the structural damping coefficient in plunge C_{hnom} and in pitch $C_{\alpha nom}$, and $|e_3| \leq 1$, $|e_4| \leq 1$;

Similar the structural stiffness coefficient with perturbation can be defined as

$$K_h = K_{hnom} + W_5\delta_6 = K_{hnom}(1 + e_5\delta_5) \tag{15}$$

$$K_\alpha = K_{\alpha nom} + W_6\delta_6 = K_{\alpha nom}(1 + e_6\delta_6) \tag{16}$$

where δ_5 and δ_6 are perturbation to the structural stiffness coefficient in plunge K_{hnom} and in pitch $K_{\alpha nom}$, $\delta_5, \delta_6 \in R$ and $|\delta_5| \leq 1, |\delta_6| \leq 1$; W_5 and W_6 are the weighting on perturbation to the structural stiffness coefficient in plunge K_{hnom} and in pitch $K_{\alpha nom}$, $W_5, W_6 \in R$; e_5 and e_6 are weighted modeling error on the structural damping coefficient in plunge K_{hnom} and in pitch $K_{\alpha nom}$, and $|e_5| \leq 1$, $|e_6| \leq 1$;

In order to construct μ framework, we let

$$\begin{bmatrix} z_3 \\ z_4 \\ z_5 \\ z_6 \end{bmatrix} = \begin{bmatrix} W_3 & & & \\ & W_4 & & \\ & & W_5 & \\ & & & W_6 \end{bmatrix} \begin{bmatrix} \dot{h} \\ \dot{\alpha} \\ h \\ \dot{\alpha} \end{bmatrix} \tag{17}$$

$$\begin{bmatrix} w_3 \\ w_4 \\ w_5 \\ w_6 \end{bmatrix} = \begin{bmatrix} \delta_3 & & & \\ & \delta_4 & & \\ & & \delta_5 & \\ & & & \delta_6 \end{bmatrix} \begin{bmatrix} z_3 \\ z_4 \\ z_5 \\ z_6 \end{bmatrix} = \boldsymbol{\Delta}_p \begin{bmatrix} z_3 \\ z_4 \\ z_5 \\ z_6 \end{bmatrix} \tag{18}$$

where $\boldsymbol{\Delta}_p$ is the perturbation block, $\boldsymbol{\Delta}_p = \mathrm{diag}(\delta_3, \delta_4, \delta_5, \delta_6)$ and $\left\|\boldsymbol{\Delta}_p\right\|_\infty \leq 1$.

Combining Eqs. 2, 17, and 18, the motion of the system are reformulated

$$\begin{cases} m_t\ddot{h} + S_\alpha\ddot{\alpha} + C_{hnom}\dot{h} + K_{hnom}h + w_3 + w_5 = -L \\ S_\alpha\ddot{h} + I_\alpha\ddot{\alpha} + C_{\alpha nom}\dot{\alpha} + K_{\alpha nom}\alpha + w_4 + w_6 = M \end{cases}. \tag{19}$$

The robust AE system block diagram can be constructed as shown in Fig. 4, where $[\boldsymbol{w}_i] = diag(w_3, w_4, w_5, w_6)$, $[\boldsymbol{z}_i] = diag(z_3, z_4, z_5, z_6)$.

The robust ASE system block diagram is constructed by adding two servocontrols to the robust AE system. The transfer functions for trailing edge flap $\boldsymbol{K}_\beta$ and leading edge flap $\boldsymbol{K}_\gamma$ can be defined as

$$\boldsymbol{K} = \frac{\delta(s)}{\delta_c(s)} = \frac{k}{(1/\omega^2)s^2 + (2\zeta/\omega)s + 1} \tag{20}$$

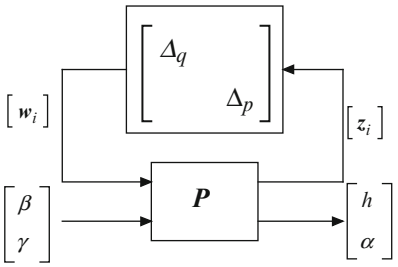

Fig. 4 Robust AE system block diagram

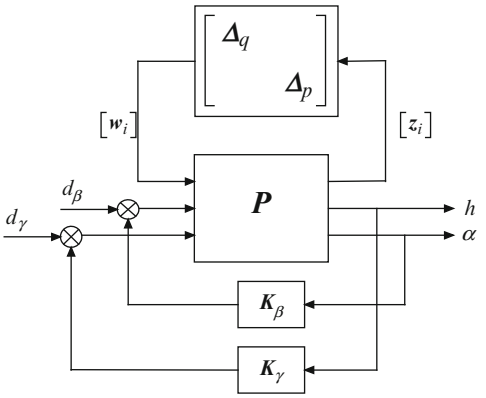

Fig. 5 Robust ASE system block diagram

where δ is the deflection of the control surface, δ_c is the input deflection command of the control surface, k is the gain of servoactuators, ω is frequency of servoactuators, ζ is damp ratio of servoactuators.

In this paper, based on characteristic of the trailing edge flap and leading edge flap, servoactuators parameters are $\omega_\beta = \omega_\gamma = 50Hz$, $\xi_\beta = \xi_\gamma = 0.5$, $k_\beta = -1.02$, $k_\gamma = 23.4$. The robust ASE system block diagram shown in Fig. 5, where d_β and d_γ are additional inputs of trailing and leading edge flap deflections.

3.4 State-Space Model

For the robust stability analysis, the uncertainty system should be constructed as state-space model form. Let $\boldsymbol{X}_s = [h \quad \alpha]^{\mathrm{T}}$ and combining Eq. 19 and Fig. 4, the motion of the system are reformulated in matrix form

$$\begin{cases} \boldsymbol{M}_s\ddot{\boldsymbol{X}}_s = (\boldsymbol{C}_a - \boldsymbol{C}_s)\dot{\boldsymbol{X}}_s + (\boldsymbol{K}_a - \boldsymbol{K}_s)\boldsymbol{X}_s + \boldsymbol{B}_a\boldsymbol{u} \\ [z_i] = \boldsymbol{C}_z\left[\boldsymbol{X}_s \quad \dot{\boldsymbol{X}}_s\right]^{\mathrm{T}} + \boldsymbol{D}_z[\beta \quad \gamma]^{\mathrm{T}} \end{cases}. \tag{21}$$

where $\boldsymbol{u} = [w_1 \quad w_2 \quad w_3 \quad w_4 \quad w_5 \quad w_6 \quad \beta \quad \gamma]$,

$$\boldsymbol{M}_s = \begin{bmatrix} m_t & m_w x_\alpha b \\ m_w x_\alpha b & I_\alpha \end{bmatrix}, \boldsymbol{C}_s = \begin{bmatrix} C_{hnom} & 0 \\ 0 & C_{\alpha nom} \end{bmatrix}, \boldsymbol{K}_s = \begin{bmatrix} K_{hnom} & 0 \\ 0 & K_{\alpha nom} \end{bmatrix}$$

$$\boldsymbol{C}_a = q_{nom} \begin{bmatrix} -2bs_p C_{L\alpha}(1/V) & -2b^2 s_p C_{L\alpha}(0.5-a)(1/V) \\ 2b^2 s_p C_{m\alpha}(1/V) & 2b^3 s_p C_{m\alpha}(0.5-a)(1/V) \end{bmatrix},$$

$$\boldsymbol{K}_a = \begin{bmatrix} 0 & -q_{nom} 2bs_p C_{L\alpha} \\ 0 & q_{nom} 2b^2 s_p C_{m\alpha} \end{bmatrix},$$

$$\boldsymbol{B}_a = \begin{bmatrix} -1 & 0 & -1 & 0 & -1 & 0 & -q_{nom} 2bs_p C_{L\beta} & -q_{nom} 2bs_p C_{L\gamma} \\ 0 & 1 & 0 & -1 & 0 & -1 & q_{nom} 2b^2 s_p C_{m\beta} & q_{nom} 2b^2 s_p C_{m\gamma} \end{bmatrix},$$

$$\boldsymbol{C}_z = \begin{bmatrix} 0 & 2bs_p C_{L\alpha} & 2bs_p C_{L\alpha}(1/V) & 2b^2 s_p C_{L\alpha}(0.5-a)(1/V) \\ 0 & 2b^2 s_p C_{m\alpha} & 2b^2 s_p C_{m\alpha}(1/V) & 2b^3 s_p C_{m\alpha}(0.5-a)(1/V) \\ 0 & 0 & W_3 & 0 \\ 0 & 0 & 0 & W_4 \\ W_5 & 0 & 0 & 0 \\ 0 & W_6 & 0 & 0 \end{bmatrix},$$

$$\boldsymbol{D}_z = \begin{bmatrix} 2bs_p C_{L\beta} & 2bs_p C_{L\gamma} \\ 2b^2 s_p C_{m\beta} & 2b^2 s_p C_{m\gamma} \end{bmatrix}$$

Then defining the state variables $\boldsymbol{x} = [h \quad \alpha \quad \dot{h} \quad \dot{\alpha}]^{\mathrm{T}}$, one obtains the state-space form of the openloop AE system, which represent $\boldsymbol{P}$ in Fig. 5

$$\begin{cases} \dot{\boldsymbol{x}} = \boldsymbol{A}\boldsymbol{x} + \boldsymbol{B}\boldsymbol{u} \\ \boldsymbol{y} = \boldsymbol{C}\boldsymbol{x} + \boldsymbol{D}\boldsymbol{u} \end{cases} \tag{22}$$

where output $\boldsymbol{y} = [z_1 \quad z_2 \quad z_3 \quad z_4 \quad z_5 \quad z_6 \quad h \quad \alpha]^{\mathrm{T}}$, input $\boldsymbol{u} = [w_1 \quad w_2 \quad w_3 \quad w_4 \quad w_5 \quad w_6 \quad \beta \quad \gamma]$,

$$\boldsymbol{A} = \begin{bmatrix} \boldsymbol{0}_{2\times 2} & \boldsymbol{I}_{2\times 2} \\ \boldsymbol{M}_s^{-1}\boldsymbol{K} & \boldsymbol{M}_s^{-1}\boldsymbol{C} \end{bmatrix}, \boldsymbol{B} = \begin{bmatrix} \boldsymbol{0}_{2\times 8} \\ \boldsymbol{M}_s^{-1}\boldsymbol{B}_a \end{bmatrix}, \boldsymbol{C} = \begin{bmatrix} \boldsymbol{C}_z \\ \boldsymbol{I}_{2\times 2} \quad \boldsymbol{0}_{2\times 2} \end{bmatrix}, \boldsymbol{D} = \begin{bmatrix} \boldsymbol{0}_{2\times 6} & \boldsymbol{D}_z \\ \boldsymbol{0}_{6\times 6} & \boldsymbol{0}_{6\times 2} \end{bmatrix},$$

$$\boldsymbol{K} = \boldsymbol{K}_a - \boldsymbol{K}_s, \ \boldsymbol{C} = \boldsymbol{C}_a - \boldsymbol{C}_s.$$

4 Simulation Results and Discussion

Platanitis and Strganac give a wing section with training and leading edge flaps, and we use the parameters of this wing [2]. The wing in experiments occur flutter at 13 m/s for openloop AE system [2]. Therefore, in this research, the systems are simulated at nominal speed 13 m/s. Let the system initial state variables are $x = [0.01\ 0.1\ 0\ 0]^T$ and perturbation parameters are $e_3 = e_4 = 0.4$, $e_5 = e_6 = 0.05$. Both system modeling of analysis and the computation are code with MATLAB μ-Analysis and Synthesis Toolbox [12]. The iteration flow chart of stability margin is shown in Fig. 6, which include AE system, ASE system, nominal system and robust system.

The concerned parameters in this study are flutter speed V_F, flutter frequency f_F, critical dynamic pressures q_{cr}, and stability margins $\delta_{q\max}$. $\delta_{q\max}$ is the maximum of dynamic pressure perturbation stabilize system, and $q_{cr} = q_{nom} + \delta_{q\max}$. Figure 7 shows the iteration process of μ value for robust AE system. The iteration is not interrupt until $\mu < 1$. When system reach critical stable structured singular value μ curves are shown in Fig. 7, where ASE (one flap) represents the ASE system with the leading edge flap, and ASE (two flaps) denotes the ASE system with both the leading and trailing edge flap. The computation results are presented as in Table 1.

By above figure, frequency versus structured singular value $\mu = 1$ means flutter frequency. Robust AE system f_F =9.69 rad/s, robust ASE system with leading edge flap f_F =13.80 rad/s, robust ASE system with both leading and trailing edge flap f_F =13.01 rad/s (Fig. 8).

From table above, we observe that stability margin of system. Flutter frequency is identical to Fig. 7. Uncertain perturbation reduces stability margin of system. The decrease in stability margin is 69 % for AE system, 64 % for ASE system (one flap)

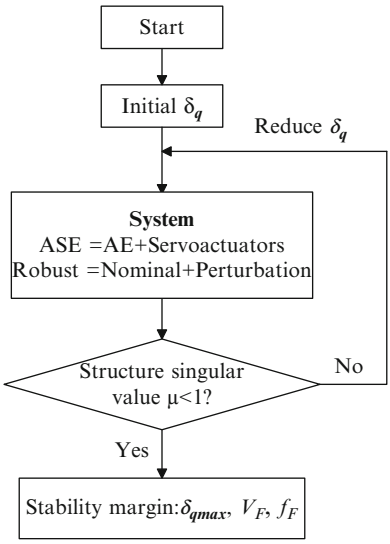

Fig. 6 Iteration flow chart of stability margin

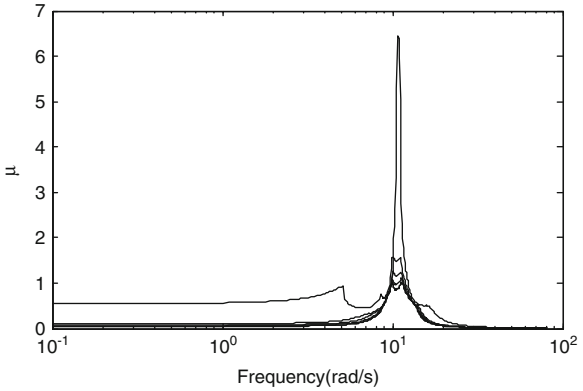

Fig. 7 Iteration process of μ value for robust AE system

Table 1 Computation results of system at V = 13 m/s

System model	Type	V_F (m/s)	f_F (Hz)	$\delta_{q\max}$ (N/m^2)
AE	Nominal	13.9752	1.7264	16.1133
	Robust	13.3062	1.5425	4.93345
ASE (one flap)	Nominal	17.9044	2.1274	92.8345
	Robust	14.9529	2.1971	33.4359
ASE (two flaps)	Nominal	22.5324	1.9675	207.458
	Robust	17.6148	2.0724	86.5338

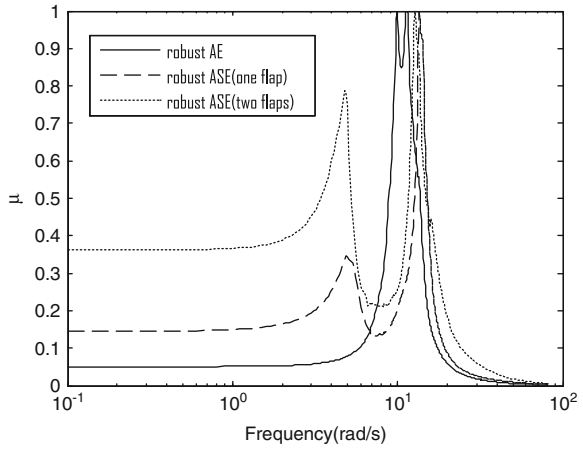

Fig. 8 AE system structured singular value μcurves

and 58 % for ASE system (two flaps). The ASE system increases flutter speed and critical dynamic pressure to the AE (openloop) system, specifically increases in flutter speed is 12 % when leading edge flap activated and 32 % when both leading and trailing edge flap activated. By using both the leading and trailing edge control surfaces are more effective on flutter suppression.

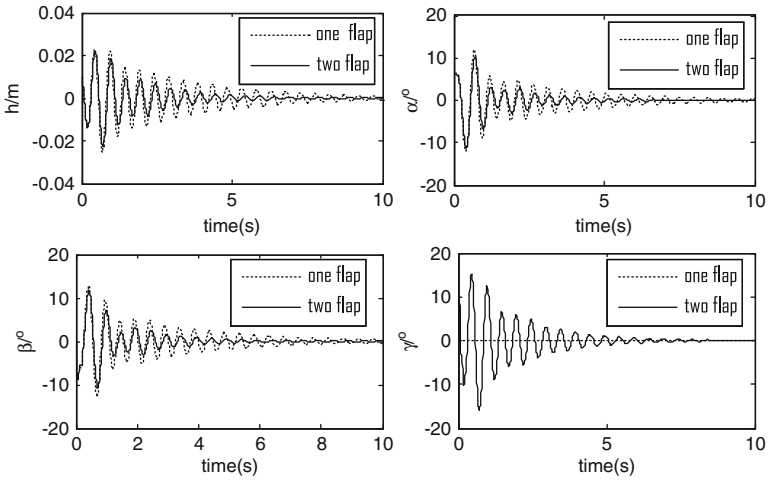

Fig. 9 Time response of robust ASE system with single control surface and multiple control surfaces at V = 14.5 m/s

Figure 9 shows time response of ASE system with only leading edge flap (dotted line) and ASE system with both leading and trailing edge flaps (solid lines). Examining time response process of plunge, pitch and control surface, one notes that the system tended to stabilized more quickly and trailing edge flap deflects smaller by using both the leading and trailing edge control surfaces simultaneously.

5 Conclusion

μ-method for robust stability of an active aeroelastic wing section with leading and tailing edge control surface is developed. Nominal AE system with dynamic pressure perturbation is established. Robust AE system is constructed to account for the uncertainty parameters associated with the variable structural damping and the nonlinear structural stiffness. Robust ASE system is constructed by adding two servocontrols to the robust AE system. The nominal and robust stability margins, critical flutter airspeeds and frequencies are computed. We investigate the aeroelastic and aeroservoelastic robust stability in the μ-framework.

The analysis process shows μ method for robust stability analysis of aeroservoelastic system with uncertainties is effective. The simulation results indicated that uncertain perturbation reduces stability margin of system. The ASE system increase flutter speed and critical dynamic pressure to the AE (openloop) system. The system tends to stabilized more quickly and trailing edge flap deflects smaller by using both the leading and trailing edge control surfaces simultaneously.

References

1. Perry B III, Cole SR, Miller GD (1995) Summary of an active flexible wing program. J Aircr 32(1):10–15
2. Platanitis G, Strganac TW (2004) Control of a nonlinear wing section using leading- and trailing-edge surfaces. J Guid Control Dynam 27(1):52–58
3. Block JJ, Strganac TW (1998) Applied active control for a nonlinear aeroelastic structure. J Guid Control Dynam 21(6):838–845
4. Livne E (2003) Future of airplane aeroelasticity. J Aircr 40(6):1066–1092
5. Lind R, Brenner M (1997) Robust flutter margins of an F/A-18 aircraft from aeroelastic flight data. J Guid Control Dynam 20(3):597–604
6. Lind R, Brenner M (1998) Incorporating flighting data into a robust aeroelastic model. J Aircr 35(3):470–477
7. Lind R (2002) Match-point solutions for robust flutter analysis. J Aircr 39(1):91–99
8. Borglund D (2004) The μ-k method for robust flutter solutions. J Aircr 41(5):1209–1216
9. Gu DW, Hr. Petkov P, Konstantinov MM (2005) Robust control design with MATLAB. Springer-Verlag London Ltd, London, pp 71–73
10. Doyle JC (1982) Analysis of feedback systems with structured uncertainties. IEEE Proc-Part D 129:242–250
11. Buttrill CS, Bacon BJ, Heeg J, Houck JA, Wood DV (1996) Aeroservoelastic simulation of an active flexible wing tunnel model. NASA technical paper 3510, pp 11–13
12. Balas GJ, Doyle JC, Glover K, Packard A, Smith R (2004) μ-analysis and synthesis toolbox user's guide. The Math Works, Natick, MA, USA, pp 299–316

Nonlinear Flight Controller Design Using Combined Hierarchy-Structured Dynamic Inversion and Constrained Model Predictive Control

Chao Wang, Shengxiu Zhang, and Chao Zhang

Abstract In order to account for hard limits on state and actuator range, a nonlinear flight control method combined hierarchy-structured dynamic inversion (HSDI) and constrained model predictive control (MPC) was proposed for a researched unmanned aircraft (RUA). First, the HSDI control law linearizes the nonlinear dynamic model of the aircraft. Then, constrained MPC is designed in accordance with Pseudo-linear system to guarantees HSDI and determines online constrained optimal inputs. Finally, the robust performance of the combined controller is improved by employing on-line identification for uncertainties based on adaptive estimation approaches. The nonlinear model was updated with adaptive parameter T-S fuzzy model to improve the fidelity of the model used for controller synthesis. Simulation results show satisfactory performance of the presented controller for attitude command tracking control, and the robustness to parameters variations and the disturbance rejection are successfully accomplished.

Keywords Flight control • Hierarchy-structured dynamic inversion • Constrained model predictive control • T-S fuzzy model • Adaptive parameter approximation

1 Introduction

New nonlinear guidance and control laws will command and execute agile flight with rapid manoeuvring capability, large thrust, and closer approach to stall boundaries for fast deceleration and rapid turning than previously possible. Such performance improvements expand the operational regime of UAVs. Nevertheless, because of dynamic constraints such as limited manoeuvrability, minimum turn radius for the specified airspeed, and actuator saturation, the physical

C. Wang • S. Zhang (✉) • C. Zhang
Precise Guidance and Simulation Lab, Xi'an Research Institute of Hi-Tech, Xi'an, China
e-mail: Dieche1218@sina.com

W. Wang (ed.), *Mechatronics and Automatic Control Systems*, Lecture Notes in Electrical Engineering 237, DOI 10.1007/978-3-319-01273-5_70,

impossibility of applying unlimited control signals makes actuator saturation a ubiquitous problem in control systems. A known approach to this task is the treatment of the flight control as a nonlinear model predictive control (NMPC) problem [1–3]. However, this is computationally demanding due to the nonlinearities that have to be considered. Whenever the computational power of the onboard computer is limited, a straight forward NMPC implementation becomes very difficult, or even impossible. One alternative approach is to linearize the nonlinear system on-line using Feedback Linearization (FBL) which can be combined with linear, discrete-time MPC. Van Soest has done this, for example, including only input constraints [4]. Guemghar has also taken state constraints into account, and there the principle of Time Scale Separation (TSS) is used [5]. Nevertheless, uncertainties and disturbances have not been discussed in above literatures.

In this paper, the combination of hierarchy-structured dynamic inversion (HSDI) control and constrained model predictive control (MPC) is applied to track the reference attitude angles for a RUA, which is modeled to be nonlinear with hard limits on state and actuator range. Combining HSDI with MPC gives the best of both worlds: HSDI allows application of the simple linear discrete model predictive control concept; MPC provides explicit constraint handling as part of the optimization process. In order to deal with uncertainties and disturbances, this paper therefore improves the nominal combined controller by employing on-line identification for uncertainties using T-S fuzzy model. The nonlinear model developed based on first principle theory was updated with adaptive parameter T-S fuzzy model to improve the fidelity of the model used for controller synthesis. An online adaptation algorithm for the parameter matrixes of T-S fuzzy model is designed.

The paper is organized as follows: In the next section, the RUA nonlinear dynamic is given. On-line estimator for uncertainties based on adaptive parameter T-S fuzzy model is introduced in Sect. 3. Sect. 4 designs the combined controller and the constraint mapping algorithms. The simulation results are shown in Sect. 5. Finally, Sect. 6 draws the conclusions.

2 Research Unmanned Aircraft Model

Let $\boldsymbol{x}_1 = [\alpha \quad \beta \quad \mu]^{\mathrm{T}}$, $\boldsymbol{x}_2 = [p \quad q \quad r]^{\mathrm{T}}$ and control input $\boldsymbol{u} = [\delta_a \quad \delta_e \quad \delta_r]^{\mathrm{T}}$. Where α, β and μ respectively denote angle of attack, sideslip angle and conical rotation angle; p, q and r respectively denote roll, pitch, and yaw rates about the body axes; δ_a, δ_e and δ_r denote deflections of aileron, elevator and rudder, respectively. Based on the assumption of the flat Earth and constant mass properties [6], the general nonlinear 6DOF dynamic of the RUA with uncertainties and disturbances can be written as [7]:

$$\begin{aligned}\dot{\boldsymbol{x}}_1 &= \boldsymbol{f}_{1n}(\boldsymbol{x}_1) + \boldsymbol{g}_{1n}(\boldsymbol{x}_1)\boldsymbol{x}_2 + \boldsymbol{h}_{1n}(\boldsymbol{x}_1)\boldsymbol{u} + \boldsymbol{\Delta}_1 \\ \dot{\boldsymbol{x}}_2 &= \boldsymbol{f}_{2n}(\boldsymbol{x}_1, \boldsymbol{x}_2) + \boldsymbol{g}_{2n}(\boldsymbol{x}_1)\boldsymbol{u} + \boldsymbol{\Delta}_2\end{aligned} \tag{1}$$

Where subscript n is added to indicate the nominal situation; The functions $\boldsymbol{f}_{1n}$, $\boldsymbol{f}_{2n}$, $\boldsymbol{g}_{1n}$, $\boldsymbol{g}_{2n}$ and $\boldsymbol{h}_{1n}$ for each controller design are given by Cao [7]; $\boldsymbol{\Delta}_1 = [\Delta_\alpha \quad \Delta_\beta \quad \Delta_\mu]^T$ and $\boldsymbol{\Delta}_2 = [\Delta_p \quad \Delta_q \quad \Delta_r]^T$ are lumped disturbances. With assumptions 2 in Cao [7] (which implies that $\boldsymbol{h}_{1n}\boldsymbol{u} \approx 0$) and given a specific sampling time T_s, we have a discrete-time MIMO affine nonlinear system:

$$\begin{aligned}\boldsymbol{x}_1(k+1) &= \boldsymbol{f}_{1n}(k) + \boldsymbol{g}_{1n}(k)\boldsymbol{x}_2(k) + \boldsymbol{\Delta}_1(k) \\ \boldsymbol{x}_2(k+1) &= \boldsymbol{f}_{2n}(k) + \boldsymbol{g}_{2n}(k)\boldsymbol{u}(k) + \boldsymbol{\Delta}_2(k)\end{aligned} \tag{2}$$

3 On-line Identification for Uncertainties

In the system (2), there are some unknown uncertainties $\Delta\boldsymbol{f}_i(\cdot)$ and $\Delta\boldsymbol{g}_i(\cdot)$ and disturbances $\boldsymbol{d}_i$. They are combined to form an unknown nonlinear function $\boldsymbol{\Delta}_i$ as follows:

$$\begin{aligned}\boldsymbol{\Delta}_1(k) &= \Delta\boldsymbol{f}_1(k) + \Delta\boldsymbol{g}_1(k)\boldsymbol{x}_2(k) + \boldsymbol{d}_1(k) \\ \boldsymbol{\Delta}_2(k) &= \Delta\boldsymbol{f}_2(k) + \Delta\boldsymbol{g}_2(k)\boldsymbol{u}(k) + \boldsymbol{d}_2(k)\end{aligned} \tag{3}$$

To identify $\boldsymbol{\Delta}_i(k)\ i = 1, 2$, T-S fuzzy model is applied. The *j-th* fuzzy rule can be described as:

$$\begin{aligned}&R^j : IF\ x_1(k) is F_1^j\ and \cdots x_n(k) is F_n^j\ and\ u_1(k) is F_{n+1}^j\ and \cdots u_n(k) is F_{2n}^j \\ &\quad THEN\ \ \hat{\boldsymbol{\Delta}}_i(k) = \hat{\boldsymbol{A}}^j(k)\boldsymbol{x}(k) + \hat{\boldsymbol{B}}^j(k)\boldsymbol{u}(k)\end{aligned} \tag{4}$$

Where $\boldsymbol{x}(k) = [x_1(k), x_2(k), \cdots, x_n(k)]^T \in \Re^n$ is the state vector, $\boldsymbol{u}(k) = [u_1(k), u_2(k), \cdots, u_n(k)]^T \in \Re^n$ is control input.

Applying some commonly used defuzzification strategies, system (3) becomes:

$$\hat{\boldsymbol{\Delta}}_i(k) = \sum_{j=1}^{r} w^j [\hat{\boldsymbol{A}}^j(k)\boldsymbol{x}(k) + \hat{\boldsymbol{B}}^j(k)\boldsymbol{u}(k)] \tag{5}$$

Where $w^j = \prod_{l=1}^{2n} \mu_{F_j^i}(z_j) \Big/ \sum_{j=1}^{r} \prod_{l=1}^{2n} \mu_{F_l^j}(z_l)., j = 1, 2, \cdots r$, $\mu_{F_l^j}(z_l)$ is the value of the membership function, $z_l = [\boldsymbol{x}(k) \quad \boldsymbol{u}(k)]^T$.

By choosing the following parameter adaptation law:

$$\begin{aligned}\hat{\boldsymbol{A}}^j(k) &= \hat{\boldsymbol{A}}^j(k-1) - \gamma_a w^j [\boldsymbol{A}_s \boldsymbol{e}(k)]^T \boldsymbol{P}\boldsymbol{x}(k) \\ \hat{\boldsymbol{B}}^j(k) &= \hat{\boldsymbol{B}}^j(k-1) - \gamma_b w^j [\boldsymbol{A}_s \boldsymbol{e}(k)]^T \boldsymbol{P}\boldsymbol{u}(k)\end{aligned} \tag{6}$$

And according to a standard Lyapunov theorem extension [8], the tracking error vector for the state variables $\boldsymbol{e}(k)$ is bounded above by ε defined in Eq. 7. Therefore, the adaptive law Eq. 6 permits the adaptation of T-S fuzzy model parameters.

$$\left\{\boldsymbol{e}(k) : \|\boldsymbol{e}(k)\| < \varepsilon = \rho\sqrt{\lambda_{\max}(\boldsymbol{P})/\kappa}\right\} \tag{7}$$

Where γ_a, γ_b is a gain in adaptive law; $\lambda_{\max}(\boldsymbol{P})$ is the largest singular value of $\boldsymbol{P}$; ρ is a positive constant.

The T-S fuzzy model of the $\boldsymbol{\Delta}_i(k),\ i = 1, 2$ is identified and validated, as explained above. Using Eq. 5, system (2) can be rewritten as:

$$\begin{aligned}\boldsymbol{x}_1(k+1) &= \boldsymbol{f}_1(k) + \boldsymbol{g}_1(k)\boldsymbol{x}_2(k) \\ \boldsymbol{x}_2(k+1) &= \boldsymbol{f}_2(k) + \boldsymbol{g}_2(k)\boldsymbol{u}(k)\end{aligned} \tag{8}$$

Where $\boldsymbol{f}_1(k) = \boldsymbol{f}_{1n}(k) + \sum_{j=1}^{r} w_1^j \hat{\boldsymbol{A}}_1^j(k)\boldsymbol{x}_1(k)$, $\boldsymbol{g}_1(k) = \boldsymbol{g}_{1n}(k) + \sum_{j=1}^{r} w_1^j \hat{\boldsymbol{B}}_1^j(k)$; $\boldsymbol{f}_2(k) = \boldsymbol{f}_{2n}(k) + \sum_{j=1}^{r} w_2^j \hat{\boldsymbol{A}}_2^j(k)\boldsymbol{x}_2(k)$, $\boldsymbol{g}_2(k) = \boldsymbol{g}_{2n}(k) + \sum_{j=1}^{r} w_2^j \hat{\boldsymbol{B}}_2^j(k)$.

4 The Controller Architecture

This section provides the theory of both HSDI and MPC and discusses in-depth the interconnection issues that arise from this combination. Figure 1 provides an overview of how MPC and NDI are to be combined in each subsystem.

4.1 Hierarchy-Structured Dynamic Inversion

An HSDI-based flight control law is developed in such a way that a general fixed-wing aircraft system is decomposed into subsystems according to the time scales inherent in the dynamics and nonlinear dynamic inversion (NDI) is applied to each subsystem. In each subsystem, the slow variables are controlled by taking the fast variables as fictitious control input. HSDI therefore features a simple nested structure of the first order NDI controllers. Thus, considering the two time scales nonlinear system (8), inner-loop and outer-loop controllers are designed by NDI. Control law in each loop of the system is given by:

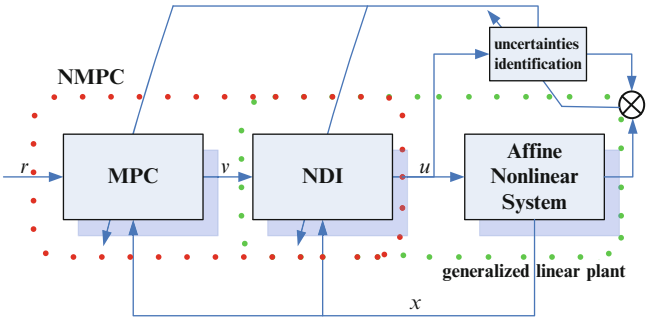

Fig. 1 MPC+NDI control concept. The input to the MPC controller is the reference and current system state, the output is a virtual control input which is mapped by the NDI control law to the input signal of the system

$$\boldsymbol{x}_{2c}(k) = \boldsymbol{g}_1^{-1}(k)[-\boldsymbol{f}_1(k) + \boldsymbol{v}_1] \tag{9}$$

$$\boldsymbol{u}(k) = \boldsymbol{g}_2^{-1}(k)[-\boldsymbol{f}_2(k) + \boldsymbol{v}_2] \tag{10}$$

Nonlinear control of the "inner loop" (i.e., rate loops) and the "outer loop" (i.e., attitude loops) is accomplished via HSDI. This yields a discrete-time linear system with inputs that are subject to state-dependent constraints. Instead of employing a simple HSDI design which has the possibility of generating extremely large control inputs, the feedback-linearized system is regulated with a linear model predictive controller with explicit constraint handling capability.

4.2 Constrained Model Predictive Control

The closed-loop systems with HSDI controllers (9) and (10) are defined as:

$$\boldsymbol{x}_1(k+1) = \boldsymbol{v}_1(k) \tag{11}$$

$$\boldsymbol{x}_2(k+1) = \boldsymbol{v}_2(k) \tag{12}$$

Equations 11 and 12 represent the basic models for the MPC design in this section. The designs of outer loop's MPC_1 and inner loop's MPC_2 are identical, only the design of MPC_2 is discussed here. The basis of MPC controller is an optimization problem. Therefore, the task of the controller has to be translated into a Performance Index (PI). Optimization of this PI leads to an optimal input sequence. The goal of the inner loop controller is to track the reference trajectory commanded by the outer loop controller as good as possible and since this trajectory is defined in terms of angular rates, the PI is based on the error between the

actual measured angular rates and the reference angular rates. The PI needs to be minimized is defined as:

$$J = \sum_{i=1}^{N_p} \boldsymbol{e}(k+i|k)^T \boldsymbol{Q} \boldsymbol{e}(k+i|k) \tag{13}$$

Where $\boldsymbol{e}(k+i|k) = \hat{\boldsymbol{x}}_2(k+i|k) - \boldsymbol{x}_{2c}(k+i|k)$, $\boldsymbol{Q} \geq 0$ is the weighting matrix of tracking error, and $\hat{\boldsymbol{x}}_2(k+i|k)$ is the predicted value of $\boldsymbol{x}_2(k+i)$ at time k.

Using relationship (12), the control variable $\boldsymbol{u}$ is replaced by the intermediate variable $\boldsymbol{v}_2$, the PI (13) of the standard MPC is transformed as follows:

$$J = (\bar{\boldsymbol{x}}_2 - \bar{\boldsymbol{x}}_{2c})^T \bar{\boldsymbol{Q}} (\bar{\boldsymbol{x}}_2 - \bar{\boldsymbol{x}}_{2c}) = (\bar{\boldsymbol{v}}_2 - \bar{\boldsymbol{x}}_{2c})^T \bar{\boldsymbol{Q}} (\bar{\boldsymbol{v}}_2 - \bar{\boldsymbol{x}}_{2c}) = \bar{\boldsymbol{v}}_2^T \bar{\boldsymbol{Q}} \bar{\boldsymbol{v}}_2 - 2\bar{\boldsymbol{x}}_{2c}^T \bar{\boldsymbol{Q}} \bar{\boldsymbol{v}}_2 \tag{14}$$

Where $\bar{\boldsymbol{x}}_2 = [\boldsymbol{x}_2(k+1|k), \cdots, \boldsymbol{x}_2(k+N_p|k]^T$; $\bar{\boldsymbol{x}}_{2c} = [\boldsymbol{x}_{2c}(k+1|k), \cdots, \boldsymbol{x}_{2c}(k+N_p|k)]^T$; $\bar{\boldsymbol{u}} = [\boldsymbol{u}(k|k), \cdots, \boldsymbol{u}(k+N_p-1|k)]^T$; $\bar{\boldsymbol{v}}_2 = [\boldsymbol{v}_2(k|k), \cdots, \boldsymbol{v}_2(k+N_p-1|k)]^T$; $\bar{\boldsymbol{Q}} = \boldsymbol{I}_{N_p} \otimes \boldsymbol{Q}$; $\boldsymbol{I}_{N_p}$ is an identity matrix of size N_p, and the operator $\otimes$ indicates the Kronecker product of two matrices.

The PI to be minimized on every sampling instant k is a quadratic criterion on $\bar{\boldsymbol{v}}_2$. In this case, fast and reliable quadratic program (QP) optimization routines can be used to find the solution of $\bar{\boldsymbol{v}}_2$. The QP can take any kind of constraint into account, provided it is linear. Due to the NDI controller the actual inputs and states are not directly 'visible' for the MPC controller and the constraints on the actual inputs and states have to be converted by the NDI control law, which is called the constraint mapping. Below first the input constraint mapping will be explained followed by the state constraint mapping.

4.3 Constraint Mapping

Both input and state constraints are considered. The input constraints are defined as aerodynamic control surface deflections, all the control surface deflections are limited to ±25 deg. State constraints are defined in terms of maximum and minimum allowed deviations of the body angular rates p, q and r, and the aerodynamic angles α, β and μ, the magnitudes of the state constraints are given in Table 1.

4.3.1 Input Constraint Mapping

Consider the vectors of upper and lower bounds on $\boldsymbol{u}$:

Table 1 State constraints

Attitude angle	Amplitude range/°	Angular rate	Amplitude range/°
α	$-10 \sim +15$	p	$-80 \sim +80$
β	$-5 \sim +5$	q	$-30 \sim +30$
μ	$-60 \sim +60$	r	$-15 \sim +15$

$$\underbrace{\begin{bmatrix} -\boldsymbol{I}_n & \boldsymbol{I}_n \end{bmatrix}^T}_{\boldsymbol{M}} \boldsymbol{u} \leq \underbrace{\begin{bmatrix} -\boldsymbol{u}_{\min} & \boldsymbol{u}_{\max} \end{bmatrix}^T}_{\boldsymbol{b}_u} \tag{15}$$

The implementation of the NDI scheme maps the input vector of $\boldsymbol{u}$ into the predictive controller's output $\boldsymbol{v}_2$ through the inverse of the NDI law (16), thus the original set of linear inequality constraints $\boldsymbol{u}$ in Eq. 15 is transformed into a new set of non-linear inequality constraints in $\boldsymbol{v}_2$.

$$\boldsymbol{v}_2(k) = \boldsymbol{f}_2(k) + \boldsymbol{g}_2(k)\boldsymbol{u}(k) \tag{16}$$

Expanding Eqs. 15 and 16 over the control horizon as follows:

$$\underbrace{(\boldsymbol{I}_{N_p} \otimes \boldsymbol{M})}_{\bar{\boldsymbol{M}}} \bar{\boldsymbol{u}}(k) \leq \underbrace{[11 \cdots 1]^T \otimes \boldsymbol{b}_u}_{\bar{\boldsymbol{b}}_u} \tag{17}$$

$$\bar{\boldsymbol{v}}_2 = \underbrace{\begin{bmatrix} \boldsymbol{f}_2(k) \\ \vdots \\ \boldsymbol{f}_2(k+N_p-1) \end{bmatrix}}_{\boldsymbol{\Phi}} + \underbrace{\begin{bmatrix} \boldsymbol{g}_2(k) & 0 & \cdots & 0 \\ \vdots & \vdots & \ddots & \vdots \\ 0 & 0 & \cdots & \boldsymbol{g}_2(k+N_p-1) \end{bmatrix}}_{\boldsymbol{\Theta}} \bar{\mathbf{u}} \tag{18}$$

Equation 17 can be substituted for $\boldsymbol{u}$ in Eq. 18. This results in the following expression:

$$\bar{\boldsymbol{M}}_1 \bar{\boldsymbol{v}}_2 \leq \bar{\boldsymbol{b}}_1 \tag{19}$$

Where $\bar{\boldsymbol{M}}_1 = \bar{\boldsymbol{M}}\boldsymbol{\Theta}^{-1}$, $\bar{\boldsymbol{b}}_1 = \bar{\boldsymbol{b}}_u - \bar{\boldsymbol{M}}\boldsymbol{\Theta}^{-1}\boldsymbol{\Phi}$.

Expression Eq. 19 clearly shows the problem of the constraint mapping, the inequality constraint is not only depending on the state $\boldsymbol{x}(k)$, but also on the future state $\boldsymbol{x}(k+i)$. However, the future state $\boldsymbol{x}(k+i)$ is not known until the MPC problem is solved. To address this problem, we present constant constraint mapping. The inequality constraint for time k of Eq. 19 is valid for the entire control horizon; that is, $\hat{\boldsymbol{x}}(k+i) = \boldsymbol{x}(k)$. Thus, matrix $\boldsymbol{\Theta} \approx \boldsymbol{I}_{N_p} \otimes \boldsymbol{g}(k)$, $\boldsymbol{\Phi} \approx [11 \cdots 1]^T \boldsymbol{f}(k)$.

The reason for using constant constraint mapping can be explained as follows: the constraints on $\boldsymbol{v}_2(k)$ depend on the actual measured state, only the constraints on $\boldsymbol{v}_2(k+i)$ for $i = 1 : N_p - 1$ are approximations. Therefore, the implemented inputs

$\boldsymbol{v}_2(k)$ are feasible to satisfy the original input constraints at time k. The actual implemented input is not affected by the approximation.

4.3.2 State Constraint Mapping

With the state bound defined as:

$$\underbrace{\begin{bmatrix} -\boldsymbol{I}_n & \boldsymbol{I}_n \end{bmatrix}^T}_{\boldsymbol{M}} \boldsymbol{u} \leq \underbrace{\begin{bmatrix} -\boldsymbol{x}_{2\min} & \boldsymbol{x}_{2\max} \end{bmatrix}^T}_{\boldsymbol{b}_s} \tag{20}$$

And the state space model as Eq. 12. For each $i = 1 : N_p - 1$, the state constraints are transformed into input constraints, resulting in the inequality constraint

$$\bar{\boldsymbol{M}}_2 \bar{\boldsymbol{v}}_2 \leq \bar{\boldsymbol{b}}_2 \tag{21}$$

Where $\bar{\boldsymbol{M}}_2 = \bar{\boldsymbol{M}}$, $\bar{\boldsymbol{b}}_2 = [11 \cdots 1]^T \otimes \boldsymbol{b}_s$.

Together with Eqs. 19 and 21 forms the final inequality constraint used in the optimization of $\boldsymbol{v}_2(k)$.

$$\bar{\boldsymbol{M}}_v \bar{\boldsymbol{v}}_2 \leq \bar{\boldsymbol{b}}_v \tag{22}$$

Where $\bar{\boldsymbol{M}}_v = \begin{bmatrix} \bar{\boldsymbol{M}}_1 & \bar{\boldsymbol{M}}_2 \end{bmatrix}^T$, $\bar{\boldsymbol{b}}_v = \begin{bmatrix} \bar{\boldsymbol{b}}_1 & \bar{\boldsymbol{b}}_2 \end{bmatrix}^T$.

Now, using the NDI and the constraint mapping, the constrained control problem in the original nonlinear system is transformed into the intermediate variables. With this formulation, the nonlinear predictive control problem is solved using a standard quadratic programming (QP). It is much less computationally intensive to solve a MPC problem of the following form:

$$\begin{aligned} \min_{\boldsymbol{v}} J &= \bar{\boldsymbol{v}}_2^T \bar{\boldsymbol{Q}} \bar{\boldsymbol{v}}_2 - 2\bar{\boldsymbol{x}}_{2c}^T \bar{\boldsymbol{Q}} \bar{\boldsymbol{v}}_2 \\ s.t. \quad & \bar{\boldsymbol{M}}_v \bar{\boldsymbol{v}}_2 \leq \bar{\boldsymbol{b}}_v \end{aligned} \tag{23}$$

The MPC_2 controller calculates the optimal inputs $\boldsymbol{v}_2(k)$ based on the reference trajectory in terms p_c, q_c, r_c and $\boldsymbol{x}_2(k)$. The continuous time input $\boldsymbol{v}_2(k)$ is defined by a zero-order hold function on $\boldsymbol{v}_2(k)$. Based on $\boldsymbol{v}_2(k)$ and $\boldsymbol{x}_2(k)$ and aerodynamic data, the combined controller calculates the reference tracking input $\boldsymbol{u}(t)$, which is the actual input to the RUA.

5 Simulation Results

The proposed controller was tested on the GNC simulation platform. The guidance commands had been calculated to get the vehicle follows the trajectory. The controller is evaluated on tracking performance and robustness. The parameters considered for the MPC are T_s, N_p, N_c and $\boldsymbol{Q}$. The sample time T_s is set at 0.1 s resulted in a satisfying tradeoff between computation speed and tracking performance. The prediction horizon is set at 3 s ($N_p = 30$), with a corresponding control horizon of 2 s (N_c =20). Two simulation scenarios have been carried out to verify the proposed controller in different way, one of which presented in this section is aims at pointing out the explicit constraint handling capabilities enabled by the constrained MPC+HSDI approach. The other aims at demonstrating the improved robustness characteristics of the constrained MPC+HSDI with adaptive parameter T-S fuzzy model.

5.1 MPC+HSDI Versus HSDI

To demonstrate the effective constraint handling capability of the combined formulation, The constrained MPC+HSDI control concept is numerically evaluated and compared with HSDI control design by flown a relatively aggressive attitude reference command. The results of both controllers are starting with the case without uncertainties. See Fig. 2. The blue curve in Fig. 2 shows that the performance of the constrained MPC+HSDI controller is able to keep the vehicle stable and behaved well by tracking the desired references effectively. The inputs and states all change in the given constraint domains. The red curve in Fig. 2 displays the control effect of the HSDI controller. The results show that the closed-loop system is not stable during the conical rotation maneuver. As demonstrated in Fig. 2c, the saturation of ailerons and rudders plays an important role. As a result of saturation, HSDI cannot be accomplished, resulting in large tracking errors.

5.2 Robust MPC+HSDI Versus Nominal MPC+HSDI

To demonstrate the robustness of the combined formulation with adaptive parameter T-S fuzzy model, uncertainty is introduced into model parameters. The simulation presented here assumes that there are +30 % and −30 % uncertainties in the aerodynamic coefficients and aerodynamic moment coefficients respectively. Besides, the disturbance moments upon the RUA are both selected as $\sin(\pi t)[\,0.05 \quad 0.01 \quad 0.05\,]^T$. In approximating $\boldsymbol{\Delta}_1$ and $\boldsymbol{\Delta}_2$, the inner and outer loop adaptive parameter T-S fuzzy models are applied. For outer-loop, five fuzzy sets are defined for $\boldsymbol{x}_1$ and three fuzzy sets for $\boldsymbol{x}_{2c}$; for inner-loop, three fuzzy sets are

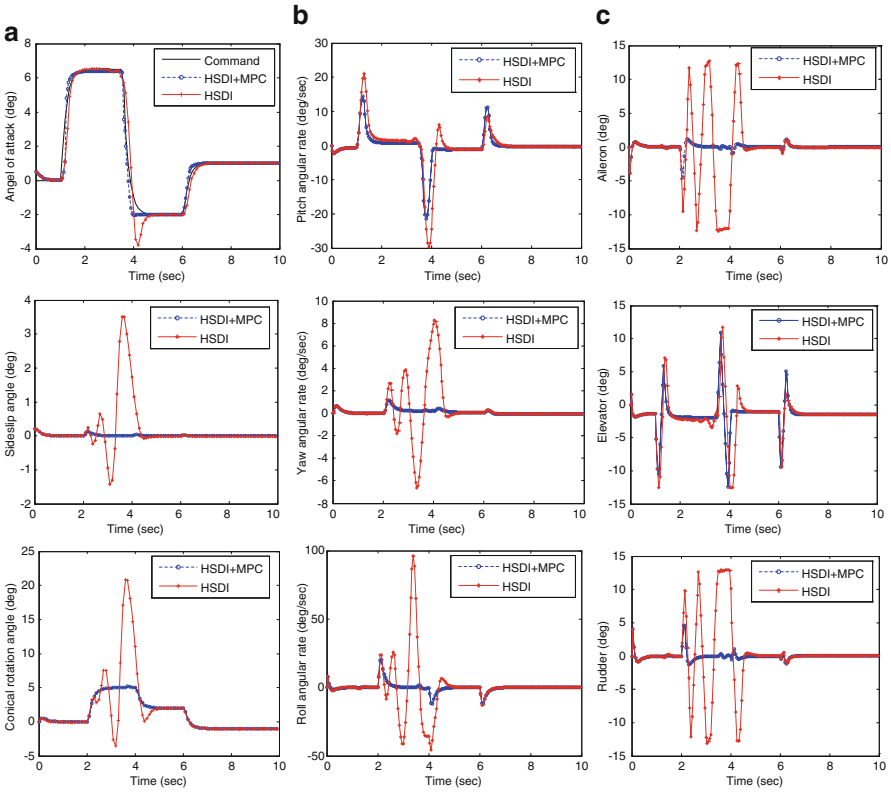

Fig. 2 Tracking performance comparison between the constrained MPC+HSDI and HSDI, (**a**) response of angle commands tracking, (**b**) time histories of body angular rates, (**c**) time histories of control surface deflections

defined for $\boldsymbol{x}_2$ and five fuzzy sets for $\boldsymbol{u}$. All adjustable parameters are initialized to 0.01 to represent the initial absence of knowledge about the uncertainties, where the gain of adaptive law $\gamma_a = 1$ and $\gamma_b = 0.5$ are used.

In the first case, we assume that no parameter adaptation law is applied. The blue curve in Fig. 3a shows the tracking performance when uncertainties of aerodynamic parameter and disturbances are considered by adopting the nominal constrained MPC +HSDI method, it can be seen that the overshoot is large and has side-effects like the steady state error. The control results may be worse if uncertainties became much bigger.

In order to improve the control effects in control system, Eq. 6 is applied to update the estimated parameters in the second case. The red curve in Fig. 3a show that the angle of attack, sideslip angle and conical rotation angle commands tracking is quite good for the constrained MPC+HSDI controller with adaptive parameter T-S fuzzy model despite the unknown nonlinear function, the addition of adaptive parameter T-S fuzzy model compensating controllers makes a significant improvement for tracking performance in each channel. The approximation performance for Δ_β and Δ_q are shown in Fig. 4.

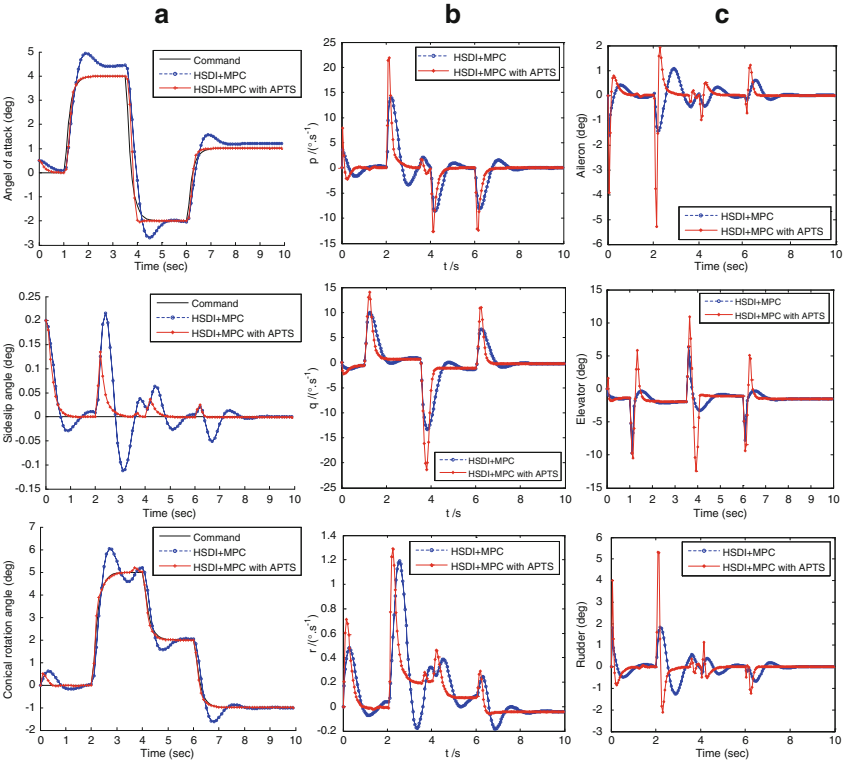

Fig. 3 Tracking performance comparison between the robust constrained MPC+HSDI and nominal constrained MPC+HSDI, (**a**) response of angle commands tracking, (**b**) time histories of body angular rates, (**c**) time histories of control surface deflections

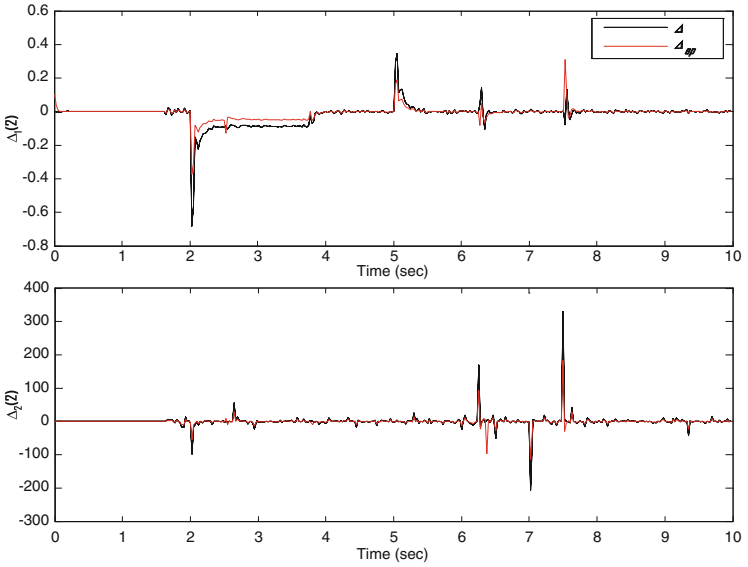

Fig. 4 Approximation performance of the T-S fuzzy model for $\boldsymbol{\Delta}_{\beta}$ and $\boldsymbol{\Delta}_{q}$, *dash line* $\boldsymbol{\Delta}$ is the actual value and *solid line* $\boldsymbol{\Delta}_{ap}$ is the approximation

6 Conclusion

The nonlinear fight control algorithm based on hierarchy-structured dynamic inversion and constraint model predictive control presented in this paper provides a real-time feasible solution to attitude command tracking of a RUA with constrained dynamical behavior. Better results are obtained when compared with the HSDI. Simulation show that constrained MPC+HSDI is superior to HSDI, with respect to both tracking performance and control behavior. Furthermore, when the performance of the constrained MPC+HSDI control law deteriorates much under strong uncertainties, on-line identification for uncertainties using adaptive parameter T-S fuzzy model is combined with the controller design for its capability of canceling out the negative effects of uncertainties and disturbances. The simulation results show that the robust controller indeed has improved robustness characteristics compared to a nominal constrained MPC+HSDI controller, while constraints on the input and states are satisfied.

References

1. Breger L, How JP (2006) Nonlinear model predictive control technique for unmaned air vehicles. J Guid, Control Dyn 29(5):1179–1188
2. Bhattacharya R, Balas GJ, Kaya A, Packard A (2002) Nonlinear receding horizon control of F-16 aircraft. J Guid, Control, Dyn 25(5):924–931
3. WANG XG, Liang M (2011) Simulation and analysis of nonlinear model predictive control for guided projectile attitude. J Nanjing Univ Sci Technol 01:66–71 (In Chinese)
4. van Soest WR, Chu QP, Mulder JA (2006) Combined feedback linearization and constrained model predictive control for entry flight. J Guid Control Dyn 29(2):427–434
5. Guemghar K, Srinivasan B, Mullhaupt P (2005) Analysis of cascade structure with predictive control and feedback linearisation. J Control Theory Appl 152(3):317–324
6. Stevens BL, Lewis FL (2003) Aircraft control and simulation [M], 2nd edn. Wiley, New York, pp 88–106
7. Cao L, Zhang S, Yan S, Li X (2011) Flight controller design using adaptive parameter approximation block backstepping. Acta Aeronauti Astronaut Sin 32(12):2256–2267 (In Chinese)
8. Qi R, Brdys MA (2008) Stable indirect adaptive control based on discrete-time t-s fuzzy model. J Fuzzy Sets Syst 159(8):900–925

Cooperative Multitasking Software Design for Gas Pressure Control Based on Embedded Microcontroller System

Pubin Wang and Longxiang Lou

Abstract In order to control the pressure of coal gas fed to thermal treatment furnaces, a multitasking design method base on the RTX51 Tiny is used in this paper. The control system's hardware was mainly made up of microcontroller, analog, digital and serial interfaces. According to the features of control process and the hardware's performance, the system's software was divided into control task, manual task, display task, alarm task and command task. By running in cooperative multitasking manner, the five tasks handle various functions of the system. For illustration, each task's code structure is provided, and the task scheduling is explained. It is shown by application that the system satisfies the control requirements. With the advantages of multitasking software framework, simple hardware architecture, low cost and reliability, the design method we mentioned is valuable for developing embedded microcontroller control systems.

Keywords Cooperative multitasking • Gas pressure control • Embedded microcontroller • RTX51 Tiny

1 Introduction

One mechanical equipment manufacturing company has several thermal treatment furnaces, which use coal gas as fuel to heating iron and steel parts. The heat treatment processes for many parts often maintain above 10 h. During so long

P. Wang (✉)
School of Mechanical Engineering & Automation, University of Science and Technology Liaoning, Anshan, China
e-mail: wangpubin@126.com

L. Lou
Shengzhou Airflow Pipeline Co. Ltd, Shengzhou, China
e-mail: lou.longxiang@163.com

W. Wang (ed.), *Mechatronics and Automatic Control Systems*, Lecture Notes in Electrical Engineering 237, DOI 10.1007/978-3-319-01273-5_71,

heating durations, the temperature control systems of those furnaces need the coal gas pressure steady or fluctuation less. But the pressure of the coal gas which was supplied by another company are rise or fall every now and then, sometimes the variable ranges were even too high. Operators had to adjust the coal gas main pipe valve manually to decrease the outlet pressure. In order to make the quality of thermal treatment products even better, coal gas pressure control system was required. For this purpose, a coal gas pressure control system was designed. In that system, a microcontroller was used as the core, and the real time operation system RTX51 Tiny was used as software kernel.

2 Hardware Composition

The main framework of the control system is shown in Fig. 1. A buttery valve was fixed on the coal gas main pipe. The inlet and outlet differential pressure sensors were fitted both sides of the valve. When coal gas moves through the main pipe, two differential pressure transducers convert the input and output gas pressures to normal voltages. Two TLC549 A/D converter chips change those two analog voltages to digital values for the microcontroller reading. After averaging the digital values, the AT89S52 microcontroller executes control routine and puts the result to TLC5615 D/A converter chip, which converts the digital value to analog voltage and sends it to an electric actuator connected to the buttery valve. Finally, the actuator drives the buttery valve rotate between 0° and 90° so as to adjust the coal gas outlet pressure within a preset range.

The hardware also includes some parallel interfaces for manual operations. In order to reduce misoperations, only a few buttons and switches were used in the system, keyboard was not assigned. Several LEDs and seven segment displays (7-SEGs) are used to display system running states and the real time pressures. In addition, by RS485 serial interface, the microcontroller can communicate with the factory's host computer, which performs the works of sending commands and receiving history data.

3 Software Design

There are several actions and operations in the control system. Some of them are periodic, such as sampling, real time control computing, reporting data to the host computer with serial communication interface and displaying messages. Manual operations and receiving command information from the host computer are stochastic. So it is reasonable to use real time operation system in control software design [1]. We selected RTX51 Tiny as the software development platform.

Real time applications are composed of one or more tasks that perform specific operations [2]. We can take some sequence operations to one task. As we

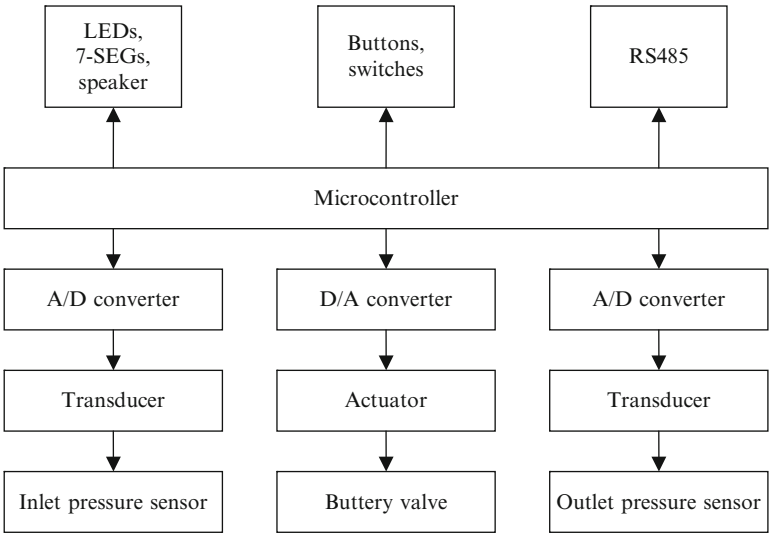

Fig. 1 Framework of system structure

mentioned above, from reading A/D converter values to driving the buttery valve waggling, the procedure is ordinal, thus all operations of that procedure can be assigned in one task. Another manner of planning task is according to hardware functions. For example, manual task is related to buttons and switches digital input interfaces, display task is related to LEDs and 7-SEGs digital output interfaces, command task is depended on the RS485 serial interface. In the end, the whole software includes five tasks, shown in Fig. 2.

3.1 Manual Task, Display Task and Alarm Task

The manual task scans manual inputs and deals with them. A few buttons were assigned to perform manual operations. One reset button was used to clear alarm state and make the system return to initial state. A shift button was used to display preset pressure or set point value. Two buttons were assigned to turn the preset pressure value increasing and decreasing manually.

The control system has two running modes: automatic mode and manual mode. In automatic mode, the buttery valve's swing is adjusted by control program automatically. While in manual mode, the buttery valve's movement is driven directly by pushing manual operation buttons on the control panel. A mode select switch was set to choose one of the two modes.

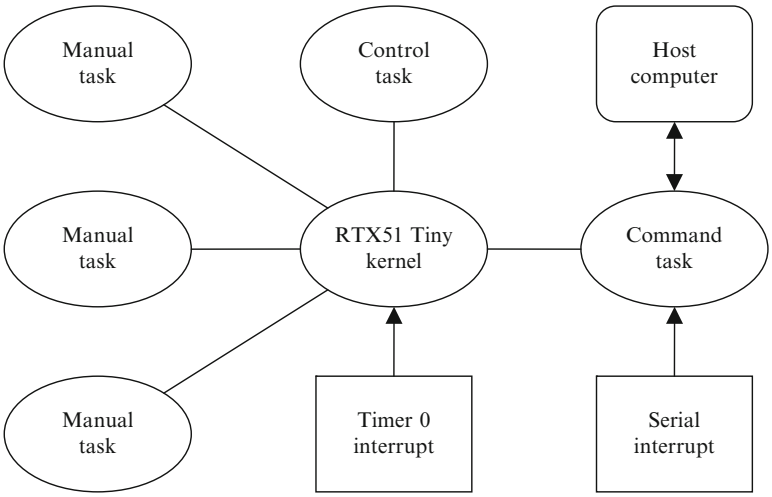

Fig. 2 Software structure

The code structure of manual task is shown as follows:

```
void manual_task (void) _task_ 3 {
while (1) {
if(shiftKEY==HIT && incKEY==HIT)setVAL++;
if(shiftKEY==HIT && decKEY==HIT)setVAL-;
if(RESET_BUTTON==HIT)reload_args( );
run_mode=(MODE_SLCT==ON) ?
AUTOMATIC_MODE : MANUAL_MODE;
os_wait (K_TMO, MANUAL_TICKS, 0); }
}
```

Several large scale 7-SEG chips were used to display real time control variables for the convenience of the operator's observation. The inlet and outlet pressures are displayed commonly. When the shift button is pushed, it can display current preset pressure.

The code structure of display task is shown as follows:

```
void display (void) _task_ 1 {
while (1){
if (shiftKEY==HIT) display_normal( );else display_set
point( );
os_wait (K_TMO, DISPLAY_TICKS, 0); }
}
```

The main function of alarm task is to check if the inlet and/or outlet pressures are out of their preset limits. If those situations occur, it should be noticed and the operator notified. The alarm task is responsible for this.

The code structure of alarm task is shown as follows:

```
void alarm_task (void) _task_ 2 {
while (1) {
alarmLED = realVAL > alarmVAL ? ON:OFF;
alarmBEEP = realVAL > alarmVAL ? ON:OFF;
os_wait (K_TMO, LED_BLINK_TICKS, 0);alarmLED = OFF;
os_wait (K_TMO, LED_BLINK_TICKS, 0); }
}
```

3.2 Control Task

This task runs the gas pressure control loop periodically. The process includes a series of steps as follows: getting the gas inlet and outlet pressure digital values from A/D converters, and several samples are required for filtering typically (sampling); in order to attenuate noise and external disturbance effects, using averaging those digital values or other calculating and filtering methods to get an estimative result (filtering) [3]; calling control computing routine to work out the digital output value (computing); if the system is running in automatic mode, sending the result to D/A converter to convert it to an analog voltage so as to driving the butterfly valve swing (output). Otherwise, the program goes to next loop directly. The code structure of control task is shown as follows:

```
void control (void) _task_ 0 {
init_serial_port ( );
os_create_task (1);os_create_task (2);os_create_task (3);
os_create_task (4);
while (1) {
for(unsigned char i = 0;i < NUMBER_OF_SAMPLING;i++){
get_inlet_pressure( );get_outlet_pressure( );
os_wait (K_TMO,SAMPLING_TICKS , 0);}
filtering( );
control_computing( );
if(Automatic_mode==1)dac_output( );
os_wait (K_TMO,CONTROL_TICKS , 0); }
}
```

3.3 Command Task

This task receives the host computer's commands with the microcontroller serial port and executes them. The commands that sent form host computer include setting control arguments and pressure ranges, reading them, and telling

microcontroller report real time data, such as inlet, outlet and preset pressures. The serial interface data receiving is performed by serial interrupt routine, which is independent of RTX51 Tiny kernel.

The code structure of command task is shown as follows:

```
void serial (void) interrupt 4 using 2 {
unsigned char c = SBUF;RI = 0;
if(SM2==1){if(c==STATION_ID){SM2=0; rcvinx=0;}}
else{rcvbuf[rcvinx] = c;
     if(rcvinx<BUF_LENGTH-1)rcvinx++;
if(c=='\r')
isr_send_signal(COMMAND);}
}
void command (void) _task_ 4 {
while (1) {
  os_wait (K_SIG, 0, 0);
unsigned char cmd = rcvbuf[0];
SM2=1;
os_clear_signal(COMMAND);
switch(cmd){
case 'A': set_alarmVAL( ); break;
case 'P': set_presetVAL( ); break;
case 'R': report_data( ); break;
/*other commands.....*/
default:break;}
}
}
```

4 Task Scheduling

RTX51 Tiny supports cooperative multitasking, which was used in our software design. By setting the TIMESHARING variable to 0 in the 'Conf_tny.A51' file, task switches are only performed when the running task voluntarily gives up control of the processor [4]. For example, when the function of os_wait (K_TMO, n, 0) is called, the running task will gives up CPU an interval of n ticks at least, in which task switches are performed.

RTX51 Tiny maintains each task in exactly one state (Running, Ready, Waiting, Deleted, or Time-Out). Only one task at a time may be in the Running State. Figure 3 shows the chart of the five tasks' switching sequences. The state '1' indicates a task is in the Running state, while state '0' indicates a task is in one of the other states, or we can say it is idle. In Fig. 3a, the grid interval is 5 s. Due to the execution period of a task is far less than the grid interval, it appears a vertical line. In Fig. 3b, the grid interval is 1 s, so the running states of control task and command task appear two pulses. The control task cycle was set as 30 s, and each cycle

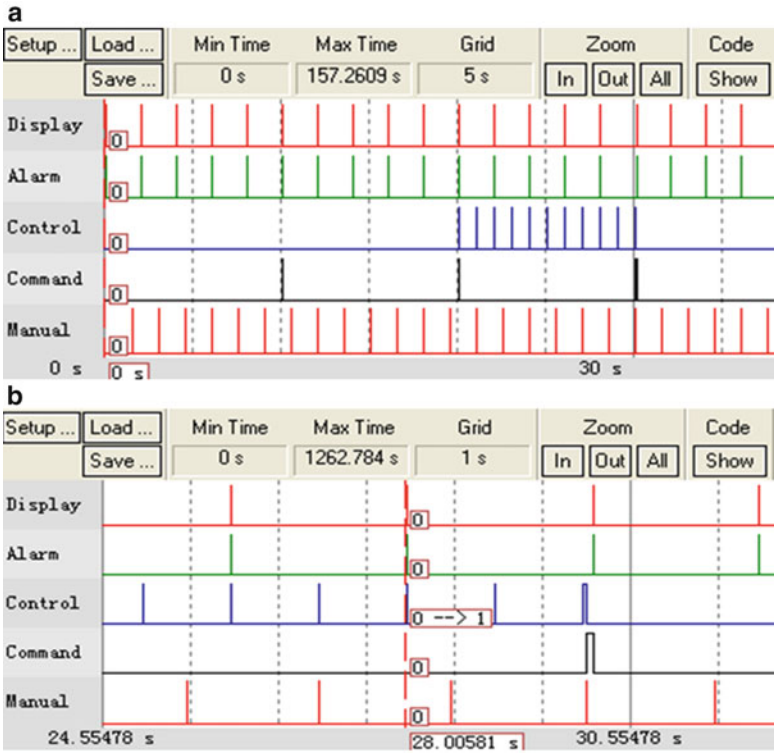

Fig. 3 Chart of task switching

includes 11 times sampling. The command task cycle was set as 10 s for sending data to the host computer. The cycles of display task and alarm task were set as 2 s, and the cycle of manual task was set as 150 milliseconds.

Limited to the electric actuator's action frequency, 10 times per minute maximally, the control task execution cycle should be set not less than 30 s. Furthermore, the on-the-spot tests shown that even that cycle was set as 60 s, the control system could meet the requirement of the factory's actual production process effectively. This means that rapid response would not be needed for the gas pressure control system. Therefore, the processor has enough time to run other tasks in so long control period. Figure 3 shows that other tasks were inserted ceaselessly during one control task execution cycle of 0–30 s, and all tasks were executed seemingly at the same time.

If tasks work cooperatively, the os_wait function or the os_switch_task function must be called somewhere in each task. These functions signal RTX51 Tiny to switch to another task. If one task consumes much CPU time, it will deprive other task's execution. For example, if the display task is always in the Running state, then other tasks will have no opportunity to run. In fact, the cycle of a typical

periodic task consists of action time and idle time. Why a running task state shown in Fig. 3 looks like a vertical line? The reason is that its action time is very smaller than its idle time. By calling the os_weit function during its idle time, a task will gives up CPU an interval. Thus, if every task has enough idle time, the task scheduling would be performed effectively. Such a situation was shown in Fig. 3a. With RTX51 Tiny, task-level response is still non-deterministic [5]. As we mentioned above, responsiveness is not important for the gas pressure control system. Thus, cooperative multitasking kernel is a reasonable selection.

A cooperative multitasking kernel does not interrupt a task unless the task itself calls a certain procedure. Thus, a function or a program in a running task will not be broken by other tasks. This feature ensures that the function of control_computing in the control task can be executed simultaneously. Compared with round-robin system, the stability of control system has been improved.

5 Conclusion

Based on the RTX51 Tiny and microcontroller hardware, a real time multitask control system has been build. It is indicated by practical application that the system has good stability and reliability. The thermal treatment product quality has been improved. With cooperative multitasking kernel, though the system's task-level response is non-deterministic, but it can meet the requirement for the gas pressure control system. RTX51 Tiny is a very small system, so the gas pressure control software has the feathers of low cost and small code size. In the control software, many fixed interval operations were arranged in their related task. That makes the control program simple and realistic. By assigning several operations in one task, the system's task number was reduced and the task switching efficiency was improved.

References

1. Wayne Wolf (2008) Computers as components: principles of embedded computing system design, 2nd edn. Elsevier, Burlington, pp 290–302
2. Daniel D Gajski, Samar Abdi, Andreas Gerstlauer, Gunar Schirner (2009) Embedded system design modeling, synthesis and verification. Springer Science+Business Media, New York, USA, pp 173–176
3. Yongwei LU (2007) System of temperature control based on RTX51 Tiny. Mod Electron Tech 15:133–135 (In Chinese)
4. Kai Qian, David den Haring, Li Cao (2009) Embedded software development with C. Springer Science+Business Media, New York, USA, pp 145–146
5. Jean J Labrosse (2000) Embedded system building blocks, complete and ready-to-use modules in C, 2nd edn. Miller Freeman, Lawrence, Kansas, USA, pp 67–68

Robust H_∞ Filtering for Uncertain Switched Systems Under Asynchronous

Guihua Li and Jun Cheng

Abstract This paper investigated the problem of robust H_∞ filtering for uncertain switched systems with asynchronous switching and average dwell time. The asynchronous switching concerned in this paper represents that the switching instants of the presented controllers are lag behind those of the considered subsystems. Based on the Lyapunov function approach and average dwell time technique, sufficient conditions of the robust H_∞ filter are derived. Finally, an example is also given to illustrate the advantages and effectiveness of the theoretical results.

Keywords Switched neutral systems • Asynchronous switching • Exponential stability • Linear matrix inequality • Average dwell time

1 Introduction

The H_∞ filter problem has been a wide range of discussed over the past a few decades and its applications in all kinds of areas, for example signal estimation, signal processing, pattern recognition and communications, control application as well as some other practical control systems. During the last few years, the H_∞ filtering technique was first proposed in [1], which has been received much attentions and it is very important to investigate for many others [2, 3]. A great number of useful results have showed up for analyzing the H_∞ filtering conditions

G. Li
School of Computer Science, Civil Aviation Flight University of China, Guanghan, China
e-mail: lighua4519@163.com

J. Cheng (✉)
School of Automation Engineering, University of Electronic Science and Technology of China, Chengdu, China
e-mail: jcheng6819@126.com

W. Wang (ed.), *Mechatronics and Automatic Control Systems*, Lecture Notes in Electrical Engineering 237, DOI 10.1007/978-3-319-01273-5_72,

with delay-dependent [4, 5]. However, time delays is very important which always encountered in many practical systems such as electronics, hydraulic or networked control systems and so on [5, 6]. Therefore, it is important to investigate H_∞ filtering issues with the time-varying delays.

It has nothing to do that the aforementioned results are based on the average assumption that, in practice, the filter switching instants is simultaneous with those of the system. The controller switching signal is not match the proposed system switching signal precisely and inevitably exists the asynchronous switching. In real world, during the filter and the system in actual operation, there exists asynchronous switching, which means that, the real switching instants of the filter lag behind or exceed those of the proposed system, which may lead to performance of the systems deteriorated. In fact, during many chemical and mechanical systems, it has been shown the necessity of taking the asynchronous switching into consideration in efficient controller design. There are extensively results about asynchronous switching presented on control synthesis have been proposed [7–9]. However, to the best of authors' knowledge, the problem of asynchronous switching filter design for switched systems has not been fully considered, this motivated us to do this study.

In this paper, the problem of robust H_∞ filtering for uncertain switched systems with asynchronous switching has been proposed. The dwell time approach is utilized for the stability analysis and controller design, then the design asynchronous switching of the filters for switched systems is also developed. At last, a numerical example is provided to illustrate the effectiveness of proposed design approach.

2 Preliminaries

In this paper, we consider the following

$$\begin{cases} \dot{x}(t) = A_{\sigma(t)}(t)x(t) + A_{h\sigma(t)}(t)x(t-\tau_1(t)) + A_{\tau\sigma(t)}(t)x(t-\tau_2(t)) + B_{\sigma(t)}\omega(t), \\ y(t) = C_{\sigma(t)}(t)x(t) + C_{d\sigma(t)}(t)x(t-\tau_1(t)) + D_{\sigma(t)}\omega(t), \\ z(t) = L_{\sigma(t)}(t)x(t), \\ x_{t_0} = x(t_0+\theta) = \varphi(t), \dot{x}_{t_0} = \dot{x}(t_0+\theta) = \phi(t), \theta \in [-\max\{\tau_1, \tau_2\}, 0]. \end{cases} \tag{1}$$

Where $x(t) \in R^n$ is the state of the system, $\omega(t) \in R^{\mathrm{p}}$ is the noise input, $\mathrm{y}(t) \in R^{\mathrm{m}}$ is the measurement vector, $z(t) \in R^{\mathrm{q}}$ is the signal to be estimated. Switching signal $\sigma(t)$ is a piecewise constant function of time t, and takes values in a finite set $\mathrm{P} = \{1, 2, \ldots r\}, r > 1$ denotes the number of subsystems. $\sigma(t) = i \in P$ means the i th subsystem is active. $\mathrm{A}_i(t), \mathrm{A}_{hi}(t), \mathrm{A}_{\tau i}(t), \mathrm{C}_i(t),$ and $\mathrm{C}_{di}(t)$ are uncertain real-valued appropriate dimensions matrices. $\mathrm{B}_i(t), \mathrm{D}_i(t)$ are known real constant matrices.

Without loss of generality, we assume that the uncertain real-valued matrices satisfying the following relations:

$$A_i(t) = A_i + \Delta A_i, A_{hi}(t) = A_{hi} + \Delta A_{hi}, A_{\tau i}(t) = A_{\tau i} + \Delta A_{\tau i}, \mathrm{C}_i(t) = C_i + \Delta C_i,$$

$$\begin{aligned} C_{di}(t) &= C_{di} + \Delta C_{di}, \mathrm{F}_i^{\mathrm{T}}(t)\mathrm{F}_i(t) \le I, [\Delta A_i, \Delta A_{hi}, \Delta A_{\tau i}, \Delta C_i, \Delta C_{di}] \\ &= M_i F_i(t)[N_{1i}, N_{2i}, N_{3i}, N_{4i}, N_{5i}], \end{aligned}$$

Where $\mathrm{A}_i, \mathrm{A}_{hi}, \mathrm{A}_{\tau i}, \mathrm{C}_i, \mathrm{C}_{\mathrm{d}i}, \mathrm{N}_{1i}, \mathrm{N}_{2i}, \mathrm{N}_{3i}, \mathrm{N}_{4i}, \mathrm{N}_{5i},$ are known real constant matrices with appropriate dimensions and $\mathrm{F}_i(t)$ is unknown time-varying matrix. $\tau_1(\mathrm{t})$ and $\tau_2(\mathrm{t})$ denote the time-varying delay which satisfy

$$0 \le \tau_1(t) \le \tau_1, 0 \le \tau_2(t) \le \tau_2, \dot{\tau}_1(t) \le d_1 \le \infty, \dot{\tau}_2(t) \le d_2 \le \infty,$$

For known constants τ_1, τ_2, d_1, d_2.

In this paper, the switching signal $\sigma(t)$ considered is time-dependent, that is $\sigma(t)$: $\{(t_0, \sigma(t_0)), (t_1, \sigma(t_1)), \ldots, (t_k, \sigma(t_k))\}$, where t_0 is the initial instant and in this paper we denote t_{k} represent the kth switching instant. For simplicity, $\sigma_f(t)$ is given to denote the filter switching signal, which can be written as

$$\sigma_f(t) : \{(t_0, \sigma_f(t_0)), (t_1 + \Delta_1, \sigma_f(t_1 + \Delta_1)), \ldots, (t_k + \Delta_k, \sigma_f(t_k + \Delta_k))\}$$

where $\sigma_f(t_0) = \sigma(t_0), \sigma_f(t_k + \Delta_k) = \sigma(t_k), \Delta_k > 0$ or $\Delta_k < 0$ denotes the period that the filter switching instants exceed or lag behind those of the system. In the whole paper we consider the case of $\Delta_k > 0$.

It is always assumed that, during the switching instant $t_{\mathrm{k}-1}$, the ith subsystem is activated and at the switching instant t_{k} the jth subsystem is activated. Thanks to asynchronous switching, the filter switching instant reacting to jth subsystem is $t_{\mathrm{k}} + \Delta_k$, there must exists at least a matched period during the time interval $[t_{\mathrm{k}-1} + \Delta_{k-1}, t_{\mathrm{k}})$, then we can obtain a mismatched period correspond at time interval $[t_{\mathrm{k}}, t_{\mathrm{k}} + \Delta_k)$.

In this paper, we assume the filtering problem considered in this paper is to design a filter with the following structure

$$\begin{cases} \dot{x_f}(t) = A_{f\sigma_f(t)}(t)x_f(t) + B_{f\sigma(t)}y(t), \\ z_f(t) = L_{f\sigma_f(t)}(t)x_f(t), \end{cases} \tag{2}$$

Where $A_{f\sigma_f(t)}, B_{f\sigma_f(t)}, L_{f\sigma_f(t)}$ are filtering matrices which needed to be determined later, $x_f(t) \in R^n$ is the filter state, $z_f(t) \in R^q$ is the output of the filter. Denote

$$\eta(t) = [x^{\mathrm{T}}(t), x_f{}^{\mathrm{T}}(t)]^{\mathrm{T}}, \overline{z} = z(t) - z_f(t), A_{ei}(t) = \begin{bmatrix} A_i(t)0 \\ B_{fi}C_i(t) \quad A_{fi} \end{bmatrix},$$

$$B_{ei}(t) = \begin{bmatrix} A_{hi}(t) \\ B_{fi}C_{di}(t) \end{bmatrix}$$

$$C_{ei}(t) = \begin{bmatrix} A_{\tau i}(t) \\ 0 \end{bmatrix}, D_{ei}(t) = \begin{bmatrix} B_i(t) \\ B_{fi}D_i \end{bmatrix}, L_{ei} = [L_i \quad -L_{fi}], A_{eij}(t) = \begin{bmatrix} A_f(t) & 0 \\ B_{fi}C_j(t) & A_{fi} \end{bmatrix},$$

$$\mathrm{B}_{eij}(t) = \begin{bmatrix} A_{hj}(t) \\ B_{fi}C_{dj}(t) \end{bmatrix}, C_{eij}(t) = \begin{bmatrix} A_{\tau j}(t) \\ 0 \end{bmatrix}, D_{eij}(t) = \begin{bmatrix} B_j \\ B_{fi}D_j \end{bmatrix}, L_{eij} = [L_j \quad -L_{fi}]$$

When $t \in [t_0, t_1) \cup [t_{k-1} + \Delta_{k-1}, t_k), k = 2, 3, \ldots,$ that is to say when the proposed switched system runs at the matched period, then we have the filtering error system as follows

$$\Sigma \begin{cases} \dot{\eta}(t) = A_{ei}\eta(t) + B_{ei}\eta(t - \tau_1(t)) + C_{ei}\dot{\eta}(t - \tau_2(t)) + D_{ei}\omega(t), \\ \overline{z}(t) = L_{ei}\eta(t), \end{cases} \tag{3}$$

When $t \in [t_k, t_k + \Delta_k), k = 1, 2, \ldots,$ that is to say when the proposed switched system runs at the mismatched period, then we have the filtering error system as follows

$$\Sigma^1 \begin{cases} \dot{\eta}(t) = A_{eij}\eta(t) + B_{eij}\eta(t - \tau_1(t)) + C_{eij}\dot{\eta}(t - \tau_2(t)) + D_{eij}\omega(t), \\ \overline{z}(t) = L_{eij}\eta(t) \end{cases} \tag{4}$$

In this paper, during $[t_0, t]$, let $\mathrm{T}^+(t_0, t)$ represents the total matched period and $\mathrm{T}^-(t_0, t)$ represents the total mismatched period, respectively.

Definition 1.[7] For given a switching signal $\sigma(t)$, the trajectory of the given filtering error system (3) and (4) satisfies $\|x(t)\| \leq \alpha\|x(t_0)\|e^{-\beta(t-t_0)}$, then filtering error system (3) and (4) are said to be exponential stability, where $\alpha > 0, \beta > 0$ and $t \geq t_0$.

Definition 2.[9] For given scalars $T_2 > T_1 \geq 0$, let $N_\sigma(T_1, T_2)$ denote the switching number of $\sigma(t)$ during (T_1, T_2). If $N_\sigma(T_1, T_2) \leq N_0 + \frac{(T_2 - T_2)}{T_a}$ holds for $N_0 \geq 0$ and $T_a > 0$, then N_0 and T_a are called chattering bound and average dwell time, respectively. Moreover, assume $N_0 = 0$ for simplicity as extensively in the literature.

Lemma 1. Suppose $0 < h_m < h_M$, and $x(t) \in R^n$, for any positive matrix $Q \in R^{n\times n}$, then

$$-(h_M - h_m)\int_{t-h_M}^{t-h_m} x^{\mathrm{T}}(s)Q\dot{x}(s)ds \le \begin{bmatrix} x(t-h_m) \\ x(t-h_M) \end{bmatrix}^{\mathrm{T}} \begin{bmatrix} -Q & Q \\ * & -Q \end{bmatrix} \begin{bmatrix} x(t-h_m) \\ x(t-h_M) \end{bmatrix}.$$

3 Main Results

Theorem 1 *For given scalars $\alpha > 0, \beta > 0$, then the system (3) and (4) is exponentially stable, if there exists positive-definite symmetric matrices $P_i, P_{ij}, Q_i, Q_{ij}, R_i, R_{ij}$, such that the following LMIs hold:*

$$\Xi_{1i} = \begin{bmatrix} \Xi_{1,1}^1 & P_iB_{ei} + H_ie^{-\alpha\tau_1} & P_iC_{ei} & P_iD_{ei} & A_{ei}^{\mathrm{T}}R_i & \tau_2A_{ei}^{\mathrm{T}}H_i \\ * & \Xi_{2,2}^1 & 0 & 0 & B_{ei}^{\mathrm{T}}R_i & \tau_2B_{ei}^{\mathrm{T}}H_i \\ * & * & -(1-d_2)e^{-\alpha\tau_2}R_i & 0 & C_{ei}^{\mathrm{T}}R_i & \tau_2C_{ei}^{\mathrm{T}}H_i \\ * & * & * & -\gamma^2I & D_{ei}^{\mathrm{T}}R_i & \tau_2D_{ei}^{\mathrm{T}}H_i \\ * & * & * & * & -R_i & 0 \\ * & * & * & * & * & -H_i \end{bmatrix} < 0 \tag{5}$$

$$\Xi_{2i} = \begin{bmatrix} \Xi_{1,1}^2 & P_{ij}B_{eij} + H_{ij}e^{-\alpha\tau_1} & P_{ij}C_{eij} & P_{ij}D_{eij} & A_{eij}^{\mathrm{T}}R_{ij} & \tau_2A_{eij}^{\mathrm{T}}H_{ij} \\ * & \Xi_{2,2}^2 & 0 & 0 & B_{eij}^{\mathrm{T}}R_{ij} & \tau_2B_{eij}^{\mathrm{T}}H_{ij} \\ * & * & -(1-d_2)e^{-\alpha\tau_2}R_{ij} & 0 & C_{eij}^{\mathrm{T}}R_{ij} & \tau_2C_{eij}^{\mathrm{T}}H_{ij} \\ * & * & * & -\gamma^2I & D_{eij}^{\mathrm{T}}R_{ij} & \tau_2D_{eij}^{\mathrm{T}}H_{ij} \\ * & * & * & * & -R_{ij} & 0 \\ * & * & * & * & * & -H_{ij} \end{bmatrix} < 0 \tag{6}$$

Where $\Xi_{1,1}^1 = P_iA_{ei} + A_{ei}^{\mathrm{T}}P_i + \alpha P_i + Q_i + L_{ei}^{\mathrm{T}}L_{ei} - H_ie^{-\alpha\tau_1}, \Xi_{2,2}^1 = -(1-d_1)e^{-\alpha\tau_1}$ $Q_i - H_ie^{-\alpha\tau_1}\Xi_{1,1}^2 = P_{ij}A_{eij} + A_{eij}^{\mathrm{T}}P_{ij} + \alpha P_{ij} + Q_{ij} + L_{eij}^{\mathrm{T}}L_{eij} - H_{ij}e^{-\alpha\tau_1}, \Xi_{2,2}^2 = -(1-$ $d_1)e^{-\alpha\tau_1}Q_{ij} - H_{ij}e^{-\alpha\tau_1}$

In this situation, the average dwell time of switching signal satisfies

$$T_a^* = \frac{\ln\mu_2\mu_1}{\kappa}, \frac{T^+(t_0,t)}{T^-(t_0,t)} \ge \frac{\beta+\kappa}{\alpha-\kappa}, 0 \le \kappa < \alpha$$

system (3) and (4) is exponential stability with an H_∞ weighted level γ, where $\mu \geq 1$ satisfying that

$$P_j \leq \mu_1 P_{ij}, P_{ij} \leq \mu_2 P_j, Q_j \leq \mu_1 Q_{ij}, Q_{ij} \leq \mu_2 Q_j, R_j \leq \mu_1 R_{ij}, R_{ij} \leq \mu_2 R_j,$$
$$H_j \leq \mu_1 H_{ij}, H_{ij} \leq \mu_2 H_j, \forall i \neq j, i, j \in P$$

Theorem 2 *For given scalars* $\alpha > 0, \beta > 0, P_i = \begin{bmatrix} P_{1i} & 0 \\ 0 & P_{2i} \end{bmatrix}, P_{ij} = \begin{bmatrix} P_{1ij} & 0 \\ 0 & P_{2ij} \end{bmatrix}$, *then the system (3) and (4) is exponential stability with a performance* H_∞ *level* γ *for any average dwell time of switching signal and (7) and (8), such that the following LMIs hold:*

$$\begin{bmatrix} \Pi^1_{1i} & \Pi^1_{2i} \\ * & \Pi^1_{3i} \end{bmatrix} < 0, \tag{7}$$

$$\begin{bmatrix} \Pi^2_{1i} & \Pi^2_{2i} \\ * & \Pi^2_{3i} \end{bmatrix} < 0, \tag{8}$$

Where

$$\Pi^1_{1i} = \begin{bmatrix} \Pi^1_{1,1} & \Pi^1_{1,2} & \Pi^1_{1,3} & P_{1i}A_{\tau i} & P_{1i}B_i & A_i^{\mathrm{T}}R_i & \tau_2 A_i^{\mathrm{T}}H_i \\ * & \Pi^1_{2,2} & X_{2i}C_{di} & 0 & X_{2i}D_i & 0 & 0 \\ * & * & \Pi^1_{3,3} & 0 & 0 & A_{hi}^{\mathrm{T}}R_i & \tau_2 A_{hi}^{\mathrm{T}}H_i \\ * & * & * & \Pi^1_{4,4} & 0 & A_{\tau i}^{\mathrm{T}}R_i & \tau_2 A_{\tau i}^{\mathrm{T}}H_i \\ * & * & * & * & -\gamma^2 I & B_i^{\mathrm{T}}R_i & \tau_2 B_i^{\mathrm{T}}H_i \\ * & * & * & * & * & -R_i & 0 \\ * & * & * & * & * & * & -H_i \end{bmatrix},$$

$$\Pi^1_{2i} = \begin{bmatrix} \varepsilon_{1i}P_{1i}M_i & N_{1i}^{\mathrm{T}} & \varepsilon_{2i}N_{1i}^{\mathrm{T}} & 0 & 0 & 0 & \varepsilon_{4i}N_{4ii}^{\mathrm{T}} & 0 \\ 0 & 0 & 0 & 0 & \varepsilon_{3i}X_{2i}M_i & 0 & 0 & X_{2i}M_i \\ 0 & N_{2i}^{\mathrm{T}} & \varepsilon_{2i}N_{2i}^{\mathrm{T}} & 0 & 0 & N_{5i}^{\mathrm{T}} & 0 & 0 \\ 0 & N_{3i}^{\mathrm{T}} & \varepsilon_{2i}N_{3i}^{\mathrm{T}} & 0 & 0 & 0 & 0 & 0 \\ 0 & 0 & 0 & 0 & 0 & 0 & 0 & 0 \\ 0 & 0 & 0 & R_iM_i & 0 & 0 & 0 & 0 \\ 0 & 0 & 0 & \tau_1 H_iM_i & 0 & 0 & 0 & 0 \end{bmatrix},$$

$$\Pi^1_{3i} = \begin{bmatrix} -\varepsilon_{1i}I & 0 & 0 & 0 & 0 & 0 & 0 & 0 \\ * & -\varepsilon_{1i}I & 0 & 0 & 0 & 0 & 0 & 0 \\ * & * & -\varepsilon_{2i}I & 0 & 0 & 0 & 0 & 0 \\ * & * & * & -\varepsilon_{2i}I & 0 & 0 & 0 & 0 \\ * & * & * & * & -\varepsilon_{3i}I & 0 & 0 & 0 \\ * & * & * & * & * & -\varepsilon_{3i}I & 0 & 0 \\ * & * & * & * & * & * & -\varepsilon_{4i}I & 0 \\ * & * & * & * & * & * & * & -\varepsilon_{4i}I \end{bmatrix},$$

$$\Pi_{1i}^2 = \begin{bmatrix} \Pi_{1,1}^2 & \Pi_{1,2}^2 & \Pi_{1,3}^2 & P_{1ij}A_{\tau ij} & P_{1ij}B_j & A_j^{\mathrm{T}}R_{ij} & \tau_2 A_j^{\mathrm{T}}H_{ij} \\ * & \Pi_{2,2}^2 & \Pi_{2,3}^2 & 0 & \Pi_{2,5}^2 & 0 & 0 \\ * & * & \Pi_{3,3}^2 & 0 & 0 & A_{hj}^{\mathrm{T}}R_{ij} & \tau_2 A_{hj}^{\mathrm{T}}H_{ij} \\ * & * & * & \Pi_{4,4}^2 & 0 & A_{\tau j}^{\mathrm{T}}R_{ij} & \tau_2 A_{\tau j}^{\mathrm{T}}H_{ij} \\ * & * & * & * & -\gamma^2 I & B_j^{\mathrm{T}}R_{ij} & \tau_2 B_j^{\mathrm{T}}H_{ij} \\ * & * & * & * & * & -R_{ij} & 0 \\ * & * & * & * & * & * & -H_{ij} \end{bmatrix},$$

$$\Pi_{2i}^2 = \begin{bmatrix} \varepsilon_{1ij}P_{1ij}M_j & N_{1j}^{\mathrm{T}} & \varepsilon_{2ij}N_{1j}^{\mathrm{T}} & 0 & 0 & 0 & \varepsilon_{4ij}N_{4j}^{\mathrm{T}} & 0 \\ 0 & 0 & 0 & 0 & \varepsilon_{3ij}P_{2ij}P_{2i}^{-1}X_{2i}M_j & 0 & 0 & P_{2ij}P_{2i}^{-1}X_{2i}M_j \\ 0 & N_{2j}^{\mathrm{T}} & \varepsilon_{2ij}N_{2j}^{\mathrm{T}} & 0 & 0 & N_{5j}^{\mathrm{T}} & 0 & 0 \\ 0 & N_{3j}^{\mathrm{T}} & \varepsilon_{2ij}N_{3j}^{\mathrm{T}} & 0 & 0 & 0 & 0 & 0 \\ 0 & 0 & 0 & 0 & 0 & 0 & 0 & 0 \\ 0 & 0 & 0 & R_{ij}M_j & 0 & 0 & 0 & 0 \\ 0 & 0 & 0 & \tau_1 H_{ij}M_j & 0 & 0 & 0 & 0 \end{bmatrix},$$

$$\Pi_{3i}^2 = \begin{bmatrix} -\varepsilon_{1ij}I & 0 & 0 & 0 & 0 & 0 & 0 & 0 \\ * & -\varepsilon_{1ij}I & 0 & 0 & 0 & 0 & 0 & 0 \\ * & * & -\varepsilon_{2ij}I & 0 & 0 & 0 & 0 & 0 \\ * & * & * & -\varepsilon_{2ij}I & 0 & 0 & 0 & 0 \\ * & * & * & * & -\varepsilon_{3ij}I & 0 & 0 & 0 \\ * & * & * & * & * & -\varepsilon_{3ij}I & 0 & 0 \\ * & * & * & * & * & * & -\varepsilon_{4ij}I & 0 \\ * & * & * & * & * & * & * & -\varepsilon_{4ij}I \end{bmatrix}$$

With

$$\Pi_{1,1}^1 = P_{1i}A_i + A_i^{\mathrm{T}}P_{1i} + \alpha P_{1i} + Q_i + L_i^{\mathrm{T}}L_i - H_i e^{-\alpha\tau_2}, \Pi_{1,2}^1 = C_i^{\mathrm{T}}X_{2i}^{\mathrm{T}} - L_i^{\mathrm{T}}X_{3i},$$

$$\Pi_{1,3}^1 = P_{1i}A_{hi} + H_i e^{-\alpha\tau_2}, \Pi_{2,2}^1 = X_{1i}^{\mathrm{T}} + X_{1i} + \alpha P_{2i} - X_{3i}^{\mathrm{T}}X_{3i},$$

$$\Pi_{3,3}^1 = -(1-d_1)e^{-\alpha\tau_2}Q_i - H_i e^{-\alpha\tau_2}, \Pi_{4,4}^1 = -(1-d_2)e^{-\alpha\tau_2}R_i,$$

$$\begin{aligned} \Pi_{1,1}^2 &= P_{1ij}A_j + A_j^{\mathrm{T}}P_{1ij} - \beta P_{1ij} + Q_{ij} + L_j^{\mathrm{T}}L_j - H_{ij}e^{\beta\tau_1}, \Pi_{1,2}^2 \\ &= C_j^{\mathrm{T}}X_{2i}^{\mathrm{T}}P_{2i}^{-1}P_{2ij} - L_j^{\mathrm{T}}X_{3i}, \end{aligned}$$

$$\Pi_{1,3}^2 = P_{1ij}A_{hj} + H_{ij}e^{\beta\tau_2}, \Pi_{2,3}^2 = P_{2ij}P_{2i}^{-1}X_{2i}C_{dj}, \Pi_{2,5}^2 = P_{2ij}P_{2i}^{-1}X_{2i}D_j,$$

$$\Pi_{2,2}^2 = P_{2ij}P_{2i}^{-1}X_{1i} + X_{1i}^{\mathrm{T}}P_{2i}^{-1}P_{2ij} - \beta P_{2ij} - X_{3i}^{\mathrm{T}}X_{3i},$$

$$\Pi_{3,3}^2 = -(1-d_1)e^{\beta\tau_1}Q_{ij} - H_{ij}e^{\beta\tau_2}, \Pi_{4,4}^2 = -(1-d_2)e^{\beta\tau_2}R_{ij}$$

What's more, a design filter of the system (2) is

$$A_{fi} = P_{2i}^{-1} X_{1i}, B_{fi} = P_{2i}^{-1} X_{2i}, L_{fi} = X_{3i}.$$

Remark 1 It is pointed that the linear matrix inequalities (5), (6), (7) and (8) are dependent on each other. Moreover, we can obtain the feasible solutions through fixed parameter appropriately.

4 Conclusion

This paper is investigated with the problem of robust H_∞ filtering for uncertain switched systems with asynchronous switching, based on the average dwell time technology, the obtained sufficient conditions of a linear filter to ensure the filtering error system is exponential stability.

Acknowledgements The authors would like to give thankful to referees for their valuable suggestions and comments. This work was supported by the Fundamental Research Funds for the Scientific Research Fund for Ph.D. Talents Introduction of CAFUC (Grant No. J2010-46).

References

1. Elsayed A, Grimble M (1989) A new approach to the H_∞ design of optimal digital linear filters. IMA J Math Control Inf 6(2):233–251
2. Karimi H, Zapateiro M, Luo N (2010) A linear matrix inequality approach to robust fault detection filter design of linear systems with mixed time-varying delays and nonlinear perturbations. J Frankl Inst 347(6):957–973
3. Liu J, Hu S, Tian E (2011) A novel method of H_∞ filter design for time-varying delay systems. Int J Innov Comput, Inf Control 7(3):1299–1310
4. Xu S, Chen T (2004) An LMI approach to the H_∞ filter design for uncertain systems with distributed delays. IEEE Trans Circuit Syst 51(4):195–201
5. Yue D, Han Q, Peng C (2004) State feedback controller design of networked control systems. IEEE Trans Circuit Syst 51(11):640–644
6. Yue D, Han Q, Lam J (2005) Network-based robust H_∞ control of systems with uncertainty. Automatica 41(6):999–10007
7. Xiang Z, Wang R (2009) Robust stabilization of switched nonlinear systems with time-varying delays under asynchronous switching. Proc Inst Mech Eng, Part I: J Syst Control Eng 223:1111–1128
8. Zhang L, Shi P (2009) Stability, L2-gain and asynchronous control of discrete-time switched systems with average dwell time. IEEE Trans Autom Control 54:2193–2200
9. Zhang L, Gao H (2010) Asynchronously switched control of switched linear systems with average dwell time. Automatica 46(5):953–958

A Kind of Adaptive Backstepping Sliding Model Controller Design for Hypersonic Reentry Vehicle

Congchao Yao, Xinmin Wang, Yao Huang, and Yuyan Cao

Abstract In order to solve a class of hypersonic vehicle nonlinear multi-input and multi-output (MIMO) systems control problem, a new kind of adaptive controller is designed in this paper. Backstepping is used to build the control law. To ensure the stability of each uncertain subsystem in each step, a virtual zero-order controller is given in sliding surface design, which can guarantee the robustness. A second-order filter is utilized to replace virtual input to avoid the huge computation complexity in multi-step derivatives. The effectiveness of the control law is verified by simulation even under deep uncertainty. The results suggest the feasibility of this method.

Keywords Hypersonic vehicle • Sliding model control • Backstepping control • Adaptive control

1 Introduction

Hypersonic vehicle (HSV) is one kind of aircraft with large envelope. Their special high-speed and complex environments require much more challenges on design of flight control system [1, 2].

Backstepping is considered as an effective method to design flight control system [3, 4]. To achieve global regulation or tracking, the stabilizing controller is designed step by step. Adaptive control methods such as robust, neural network are used based on it [5–7]. Dynamic surface control (DSC) method was first proposed by Swaroop [8, 9]. Calculating expansion can be caused by multi-step derivatives. To avoid this problem, a first-order low-pass filter is introduced to estimate the virtual control law [10].

C. Yao (✉) • X. Wang • Y. Huang • Y. Cao
School of Automation, Northwestern Polytechnical University, Xi'an, China
e-mail: yaocongchao@126.com

W. Wang (ed.), *Mechatronics and Automatic Control Systems*, Lecture Notes in Electrical Engineering 237, DOI 10.1007/978-3-319-01273-5_73,

Based on the results before, this paper includes the following works: (1) A new kind of adaptive backstepping controller is designed based on dynamic surface technology; (2) A second-order filter is proposed to avoid the "calculating expansion" by instead of virtual control input, which can estimate the measurement noise and time derivative effectively.

2 Problem Statement

To solve the control problem of a general hypersonic vehicle, which is a strict-feedback affine nonlinear uncertain MIMO system, the vehicle can be described as follows:

$$\begin{cases} \dot{x}_1 = f_1(x_1) + g_1(x_1)x_2 + \Delta_1 \\ \dot{x}_2 = f_2(x_2) + g_2(x_2)u + \Delta_2 \\ y = x_1 \end{cases} \tag{1}$$

where $x_1 = [\alpha, \beta, \mu]^T$ are angle of attack, sideslip angle and roll angle, respectively. $x_2 = [p, q, r]^T$ are roll rate, pitch rate and yaw rate, respectively. $u = [L, M, N]^T$ are roll, pitch, yaw control torque caused by aerodynamic control surfaces. Define Δ_1 and Δ_2 as follows:

$$\begin{cases} \Delta_1 = \Delta f_1(x_1) + \Delta g_1(x_1)x_2 + d_1 \\ \Delta_2 = \Delta f_2(x_2) + \Delta g_2(x_2)u + d_2 \end{cases} \tag{2}$$

where d_1 and d_2 are external disturbances. Δ_1 and Δ_2 are parameters and modeling uncertainties.

Because of the existence of the uncertainties, we should design the effective control law to make sure that the system outputs can track the desired trajectory y_d.

3 Design Adaptive Backstepping Sliding Model Control Law

3.1 Definition and Assumption

In order to design the control law, first of all, one definition and three assumptions are given as follows:

Definition 1 *The* Frobenius *norm for a matrix A is defined as* $\|A\| = \sqrt{tr(A^T A)}$.

Assumption 1 The desired trajectories y_d are bounded and continuously differentiable. And so are their first derivatives.

Assumption 2 The inverses of $g_1(x_1)$ and $g_2(x_2)$ are existent.

Assumption 3 The uncertainty terms Δ_1 and Δ_2 are bounded.

3.2 Design Control Law

According to Eq. 1, the virtual feedback errors z_1 and z_2 are defined as bellow respectively:

$$\begin{cases} z_1 = y_1 - y_{1d} = x_1 - x_{1d} \\ z_2 = x_2 - \alpha_1 \end{cases} \tag{3}$$

First Step: according to Eqs. 1 and 3, the differential of z_1 is expressed as

$$\dot{z}_1 = f_1(x_1) + g_1(x_1)z_2 + g_1(x_1)\alpha_1 + \Delta_s \tag{4}$$

Define the second-order sliding mode filter as following:

$$\begin{aligned} \dot{q}_1 &= -\frac{1}{l_1}(q_1 - \alpha_{1d}) - g_1^T(x_1)z_1 - \lambda_1 \frac{2}{\pi}\arctan(q_1 - \alpha_{1d}) \\ \dot{q}_2 &= -\frac{1}{l_2}(q_2 - \dot{q}_1) - z_2 - \lambda_2 \frac{2}{\pi}\arctan(q_2 - \dot{q}_1) \end{aligned} \tag{5}$$

There α_{1d} is the expected virtual control input. And $q_1 = \alpha_1$.

Lyapunov function V_1 and the virtual control input α_{1d} are defined as

$$V_1 = \frac{1}{2}z_1^T z_1 + \frac{1}{2}(\alpha_1 - \alpha_{1d})^T(\alpha_1 - \alpha_{1d}) \tag{6}$$

$$\alpha_{1d} = g_1^{-1}(x_1)[-f_1(x_1) - k_1 z_1 + \dot{y}_d - \gamma_1 \frac{2}{\pi}\arctan(z_1)] \tag{7}$$

Omitting the negative definite term of $\dot{V}_1$, which is the differentiation of V_1, the follow express can be gotten:

$$\begin{aligned} \dot{V}_1 \le & -\left\|z_1^T\right\| g_1(x_1)\|z_2\| - \Psi_1 \left\|z_1^T\right\|\left(\eta_1 \frac{2}{\pi}\arctan(\|z_1\|) - 1\right) \\ & -\left\|(\alpha_1 - \alpha_{1d})^T\right\| \varpi_1 \left(\rho_1 \frac{2}{\pi}\arctan(\|\alpha_1 - \alpha_{1d}\|) - 1\right) \end{aligned} \tag{8}$$

where $\varpi_1 = \dot{\alpha}_{1d\max}$ and $\Psi_1 = \varepsilon_{1\max}$. Select switch gains as:

$$\gamma_1 = \eta_1 \psi_1, \quad \lambda_1 = \rho_1 \varpi_1 \qquad (\eta_1, \rho_1 > 1) \tag{9}$$

The following conditions which are used to guarantee all factors on the right side of Eq. 8 negative, should be satisfied to make $\dot{V}_1 < 0$.

$$\|z_1\| > \tan\left(\frac{\pi}{2\eta_1}\right) \tag{10}$$

$$\|\boldsymbol{q}_2 - \dot{\boldsymbol{q}}_1\| > \tan\left(\frac{\pi}{2\rho_1}\right) \tag{11}$$

Also, if the conditions bellow can be guaranteed, the boundedness can be ensured:

$$\|z_1\| \leq c_1 \tan\left(\frac{\pi}{2\eta_1}\right), c_1 > 1 \tag{12}$$

$$\|\boldsymbol{q}_2 - \dot{\boldsymbol{q}}_1\| \leq \tau_1 \tan\left(\frac{\pi}{2\rho_1}\right), \tau_1 > 1 \tag{13}$$

Second Step: Lyapunov function V_2 and actual control input $\boldsymbol{u}$ are defined as

$$V_2 = V_1 + \frac{1}{2}\boldsymbol{z}_2^T\boldsymbol{z}_2 + \frac{1}{2}\left(\boldsymbol{q}_2 - \dot{\boldsymbol{q}}_1\right)^T\left(\boldsymbol{q}_2 - \dot{\boldsymbol{q}}_1\right) \tag{14}$$

$$\boldsymbol{u} = \boldsymbol{g}_2^{-1}(\boldsymbol{x}_2)(-\boldsymbol{f}_2(\boldsymbol{x}_2) - \boldsymbol{k}_2 z_2 - \boldsymbol{g}_1^T(\boldsymbol{x}_1)z_1 + \boldsymbol{q}_2 - \gamma_2 \frac{2}{\pi}\arctan(z_2)) \tag{15}$$

Omitting the negative definite term of $\dot{V}_1$, which is the differentiation of V_1, the follow express can be gotten:

$$\dot{V}_2 \leq -\Psi_2\left\|\boldsymbol{z}_2^T\right\|\left(\eta_2\frac{2}{\pi}\arctan(\|\boldsymbol{z}_2\|) - 1\right) - \left\|\left(\boldsymbol{q}_2 - \dot{\boldsymbol{q}}_1\right)^T\right\|\varpi_2\left(\rho_2\frac{2}{\pi}\arctan(\|\boldsymbol{q}_2 - \dot{\boldsymbol{q}}_1\|) - 1\right) \tag{16}$$

where $\varpi_2 = \ddot{\boldsymbol{q}}_{1\max}$ and $\Psi_2 = \varepsilon_{2\max}$. Select switch gains as:

$$\gamma_2 = \eta_2\psi_2, \quad \lambda_2 = \rho_2\varpi_2 \quad (\eta_1, \rho_1 > 1) \tag{17}$$

Also we need to satisfy the following conditions to keep all the right side factors of Eq. 16 negative, so that $\dot{V}_2 < 0$ and the stability of the system can be ensured:

$$\|z_2\| > \tan\left(\frac{\pi}{2\eta_2}\right) \tag{18}$$

$$\|\boldsymbol{q}_2 - \dot{\boldsymbol{q}}_1\| > \tan\left(\frac{\pi}{2\rho_2}\right) \tag{19}$$

Also, if the conditions bellow can be guaranteed, the boundedness can be ensured:

$$\|z_2\| \leq c_2 \tan\left(\frac{\pi}{2\eta_2}\right), c_2 > 1 \tag{20}$$

$$\|q_2 - \dot{q}_1\| \leq \tau_2 \tan\left(\frac{\pi}{2\rho_2}\right), \tau_2 > 1 \tag{21}$$

4 Simulation

4.1 Equation of a Hypersonic Vehicle

In order to demonstrate the effectiveness of the control law, simulation is studied. The hypersonic vehicle six degree-of-freedom (DOF) equations are based on the Winged-Cone model provided by NASA Langley Research Center [11, 12]. Based on singular perturbation theory, affine nonlinear model can be obtained as follows:

$$\begin{cases} \dot{\boldsymbol{\Omega}} = \boldsymbol{f}_s + \boldsymbol{g}_{s1}\boldsymbol{\omega} + \boldsymbol{g}_{s2}\boldsymbol{\delta}_C \\ \dot{\omega} = \boldsymbol{f}_f + \boldsymbol{g}_f \boldsymbol{M}_C \end{cases} \tag{22}$$

where $\boldsymbol{\Omega} = [\alpha, \beta, \mu]^T$ are angle of attack, sideslip angle and roll angle, respectively, and $\boldsymbol{\omega} = [p, q, r]^T$ are roll rate, pitch rate and yaw rate, respectively. $\boldsymbol{M}_C = [l_{ctrl}, m_{ctrl}, n_{ctrl}]^T$ are roll control torque, pitch control torque and yaw control torque, respectively. They are generated by both aerodynamic control surfaces and thrusts. And $\boldsymbol{f}_s = [f_\alpha, f_\beta, f_\mu]^T, \boldsymbol{f}_f = [f_p, f_q, f_r]^T$.

$$\begin{aligned} f_\alpha &= \frac{1}{MV\cos\beta}\left[-\hat{q}SC_{L,\alpha} + Mg\cos\gamma\cos\mu - T_x\sin\alpha\right] \\ f_\beta &= \frac{1}{MV}\left[\hat{q}SC_{Y,\beta}\beta\cos\beta + Mg\cos\gamma\sin\mu - T_x\sin\beta\cos\alpha\right] \\ f_\mu &= -\frac{g}{V}\cos\gamma\cos\mu\tan\beta + \frac{1}{MV}\hat{q}SC_{Y,\beta}\beta\tan\gamma\cos\mu\cos\beta \\ &\quad + \frac{T_x}{MV}\left[\sin\alpha(\tan\gamma\sin\mu + \tan\beta) - \cos\alpha\tan\gamma\cos\mu\sin\beta\right] \\ &\quad + \frac{1}{MV}\hat{q}SC_{L,\alpha}(\tan\gamma\sin\mu + \tan\beta) \end{aligned} \tag{23}$$

$$\boldsymbol{g}_{s1} = \begin{bmatrix} -\tan\beta\cos\alpha & 1 & -\tan\beta\sin\alpha \\ \sin\alpha & 0 & -\cos\alpha \\ \sec\beta\cos\alpha & 0 & \sec\beta\sin\alpha \end{bmatrix} \tag{24}$$

$$\begin{aligned} f_p &= I_{xx}^{-1}\left[l_{aero} - qr(I_{zz} - I_{yy})\right] \\ f_q &= I_{yy}^{-1}\left[m_{aero} - rp(I_{zz} - I_{yy})\right] \\ f_r &= I_{zz}^{-1}\left[n_{aero} - pq(I_{zz} - I_{yy})\right] \end{aligned} \tag{25}$$

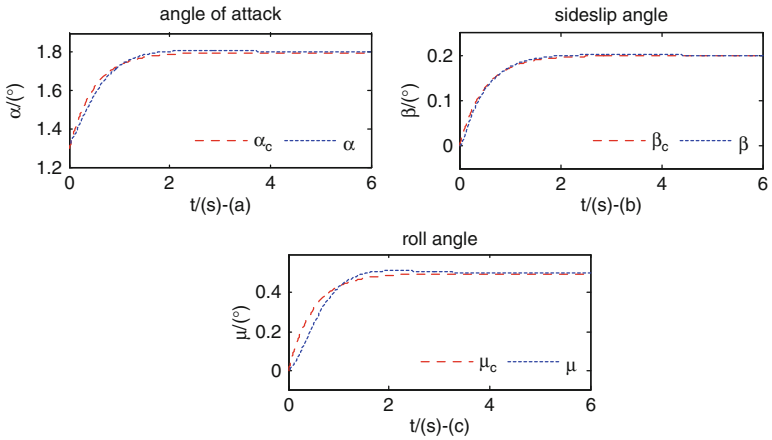

Fig. 1 Responses of attitudes with no uncertainty

$$g_f = diag\{ I_{xx}^{-1} \quad I_{yy}^{-1} \quad I_{zz}^{-1} \} \tag{26}$$

Where, L is lift force and Y is side force; m is the quality; V is aircraft speed; γ is the flight path angle; T_x, T_y, T_z are the three thrusts. $l_{aero}, m_{aero}, n_{aero}$ are the rolling, pitching and yawing moment, respectively, when deflections of control surfaces are zero.

4.2 Numerical Simulation

The simulation is done under the condition of 15 Mach and 33.5 km. m is 65,530 kg. The I_{xx}, I_{yy}, I_{zz} are 9.15 $\times$ 105 kg $\cdot$ m2. 9.49 $\times$ 106, 9.49 $\times$ 106 kg $\cdot$ m2, respectively. Transfer function of the actuator is assumed as $50/(s + 50)$. Deflections of control surfaces are limited in the range of $\pm 30°$, while the thrust vectors are $\pm$ 15°. The initial values of attitudes are $\alpha_0 = 1.3°, \beta_0 = \mu_0 = 0°$, and the desired trajectories are $\alpha_c = 1.8°, \beta_c = 0.2°, \mu_c = 0.5°$. Choose the parameters $\eta = \rho = 1.4$, $l = 0.001$, and $k_1 = 4, k_2 = 4.7$. By Simulating, performances of the attitudes α, β, μ are shown in Figs. 1 and 2.

From Fig. 1 it's easy to see that the desired trajectories can be tracked in nearly 2 s. The tracking trajectory is smooth with few overshoots.

It can also be gotten From Fig. 2 that desired ideal trajectories can be tracked in less than four seconds when model parameters have uncertainty of 40 %. The controller also has better performance. Although a few overshoots exist, which are caused by the uncertainty, the overshoots are limited in 5 %. And the purposes designed are achieved.

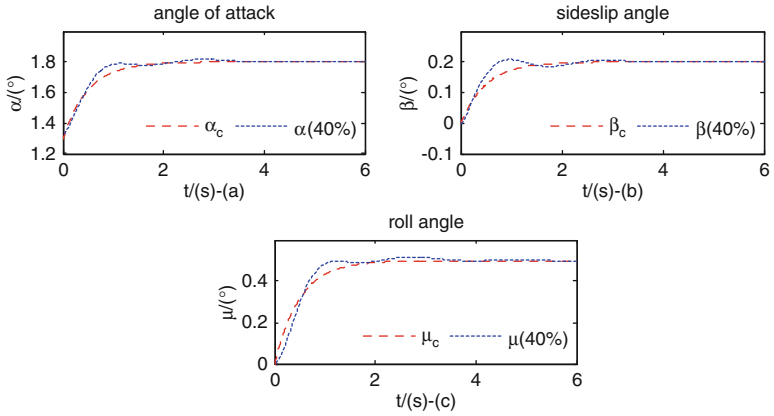

Fig. 2 Responses of attitudes with 40 % uncertainty existing

5 Conclusion

High level of technology is required in HSV reentry flight control system design. The problems of adaptive backstepping control of MIMO system have been discussed in this article. Based on dynamic surface and backstepping technology, Lyapunov function is defined to guarantee system stability. In high supersonic condition, simulation of trajectory tracking is done. The uncertainty is also discussed. The results display strong robustness of the controller.

Acknowledgements This research is financially supported by Foundation of the New Teachers from Northwestern Polytechnical University (No. 11GH0322). The authors are also wish to give thanks to Dr. Wang and Dr. Huang who give great ideas during the HSV FCS design.

References

1. Calise AJ, Buschek H (1992) Research in robust control for hypersonic vehicles. Progress report No.1 to NASA Langley Research Center. NAG-1-1451
2. Hall CE, Gallaher MW, Hendrix ND (1998) X-33 attitude control system design for ascent, transition, and entry flight regimes. NASA Marshall Space Flight Center. AIAA-98-4411
3. Kokotovic PV (2002) The joy of feedback: nonlinear and adaptive. IEEE Control Syst Mag 12 (7):266–285
4. Lian BH, Bang H, Hurtado JE (2004) Adaptive backstepping control based autopilot design for reentry vehicle. In: Proceedings of AIAA guidance, navigation, and control conference and exhibit, AIAA, pp 2004–5328
5. Jagannathan S, Lewis FL (2000) Robust backstepping control of a class of nonlinear systems using fuzzy logic. Inf Sci 133(3/4):223–240

6. Kim KS, Kim Y (2003) Robust backstepping control for slew maneuver using nonlinear tracking function. IEEE Trans Control Syst Technol 11(6):822–829
7. Zhang T, Ge SS, Hang CC (2000) Adaptive neural network control for strict-feedback nonlinear systems using backstepping design. Automatica 36(12):1835–1846
8. Swaroop D, Gerdes JC, Yip PP et al (1997) Dynamic surface control of nonlinear systems. In: Proceedings of the American control conference. IEEE, vol 5, Los Alamitos, CA, pp 3028–3034
9. Swaroop D, Hedrick JK, Yip PP et al (2000) Dynamic surface control for a class of nonlinear systems. IEEE Trans Autom Control 45(10):1893–1899
10. Wang D, Huang J (2005) Neural network-based adaptive dynamic surface control for a class of uncertain nonlinear systems in strict-feedback form. IEEE Trans Neural Netw 16(1):195–202
11. Shaughnessy JD, Pinckney SZ, McMinn JD (1991) Hypersonic vehicle simulation model: winged-cone configuration, NASA TM2102610, pp 1–15
12. Keshmiri S, Colgren R (2005) Development of an aerodynamic database for a generic hypersonic air vehicle. In: Proceedings of AIAA guidance, navigation, and control conference and exhibit, AIAA, San Francisco, CA, USA, pp 2005–6257

Design of Smith Auto Disturbance Rejection Controller for Aero-engine

Fang-Zheng Luo, Shi-Ying Zhang, Min Chen, and Yu Hu

Abstract In order to suppress many strong disturbances while aero-engine is working at steady-state, Auto Disturbance Rejection Control (ADRC) for aero-engine rotor speed was studied in this paper. By analyzing characteristics of the controlled object and making full use of Smith predictor, the two-order Smith-ADRC Controller instead of directly using three-order controller was designed which could avoid the shortcoming of tuning a large number of parameters and effectively compensate time delay of the controlled object. The simulation results show that the designed two-order Smith-ADRC controller can effectively suppress instantaneous and random disturbance, and can be suitable for aero-engine control.

Keywords Aero-engine • Speed control • Smith-ADRC controller • Time delay • Disturbance

1 Introduction

In most time of working process, aero-engine works in cruising state, therefore, the cruising state control called steady-state control is the emphasis of engine control. At this stage, the control law keeping the rotor speed constant is generally used. In practical engineering application, PID control algorithm, which is simple and easily tuned, is usually selected. However, PID control algorithm is only a linear adjustment method based on error feedback signal, which is difficultly used to control the nonlinear objects. Advantages and disadvantages of PID control algorithm were deeply analyzed [1, 2], then ADRC controller was further proposed to hopefully replace PID control algorithm. ADRC controller with strong robustness is a controller that basically not relied on mathematical model of the object and can

F.-Z. Luo (✉) • S.-Y. Zhang • M. Chen • Y. Hu
Xi'an Research Institute of Hi-Tech, Xi'an, China
e-mail: 857962178@qq.com

W. Wang (ed.), *Mechatronics and Automatic Control Systems*, Lecture Notes in Electrical Engineering 237, DOI 10.1007/978-3-319-01273-5_74,

effectively exploit the non-linear function. The controller has been widely exploited since it was proposed [3], while the algorithm of the controller is so complex that research and application was seldom developed in the aero-engine field. The problem of turbo-shaft engine torque disturbed was solved by using ADRC controller [4, 5], and the design of decoupling engine multivariable by using ADRC controller was achieved [6]. ADRC controller was used to control the two-order system of turbofan engine, which obtaining better result than using PID controller [7]. However, at this stage, there is no literature about ADRC controller applied in this situation, in which aero-engine model considering the model of actuating mechanism and delay characteristic of engine working process. To solve the problem, the model of actuating mechanism and the influence of delay characteristic in engine working process were considered. In this paper, taking the high-pressure rotor speed as the control variable, ADRC control of engine steady-state process was studied.

2 Selections of Mathematical Model and Control Scheme

With the change of flight altitude and speed, the model of aero-engine is time-varying. In the field of aero-engine control, the basic mathematical model is non-linear model, which is established based on the structure and thermodynamics characteristics of turbofan engine. However, the solving process of nonlinear model in aero-engine is so complex that it cannot satisfy real-time control. In engineering application, the simplified model can be gotten by using the linearization method. Based on operating characteristics of a certain type of turbofan engine, engine high-pressure speed-fuel control system was regard as the controlled object. Near the steady-state point ($H = 0, Ma = 0, n\% = 85\%$), the simplified engine mathematical model is

$$G_p(s) = \frac{s + 5.38}{s^2 + 8.46s + 16.72} \tag{1}$$

The mathematical model of actuating mechanism can be approximately seen as [7]:

$$G_v(s) = \frac{1}{0.3s + 1} \tag{2}$$

The mathematical model of system delay characteristic (delay time is 0.1 s) :

$$G_\tau = e^{-0.1s} \tag{3}$$

The controlled object transfer function could be assembled by these three-part series. Actually, it is a three-order delay model.

$$G(s) = \frac{s + 5.38}{0.3s^3 + 3.538s^2 + 13.48s + 16.72} e^{-0.1s} \tag{4}$$

Generally speaking, while selecting the control scheme, the order of the controlled object transfer function should be same to that of the controller [8]. However, if selecting three-order controller to control three-order system, there are a large number of parameters needing to be tuned. Therefore, it is can be considered that using the two-order controller which has been maturely studied at this stage. Through simulation examples, it was shown that three-order object could be well controlled by using two-order ADRC controller [9]. The method that using two-order ADRC controller to control three-order delay object is also certainly described [8]. However, for the object studying in this paper, there is no specific description to design the controller. In this paper, the control scheme is that engine three-order delay object was controlled by the two-order ADRC controller. By adjusting the parameters, making full use of the strong self-adaption of ADRC controller, the three-order control object could be regard as a two-order object to control. System delay characteristics could be compensated by Smith-predictor.

3 Design of Controller

The principle of ADRC controller is described [1]. Figure 1 shows the basic structure of ADRC controller. Where r is input signal, r_1 is transient process, r_2 is differential signal, u is control variable, ω is disturbance, y is system output.

In Fig. 1, ADRC controller is mainly composed by three parts: tracking-differentiator (TD), nonlinear state error feedback control law (NLSEF) and extended state observer (ESO). TD is used to track input signal and produce an approximate differential signal for original input signal. ESO is designed to estimate extended state of system. NLSEF is introduced to compose margin of error in a nonlinear way and gain control variable. For two-order system, input–output relationship is directly manifested as two-order differential equations. While $u(t)$ is defined as system control variable, $y(t)$ as output variable, control algorithm of

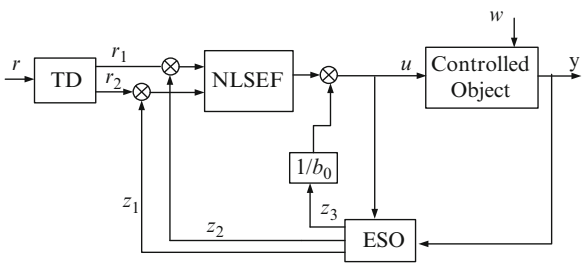

Fig. 1 The basic structure of ADRC controller

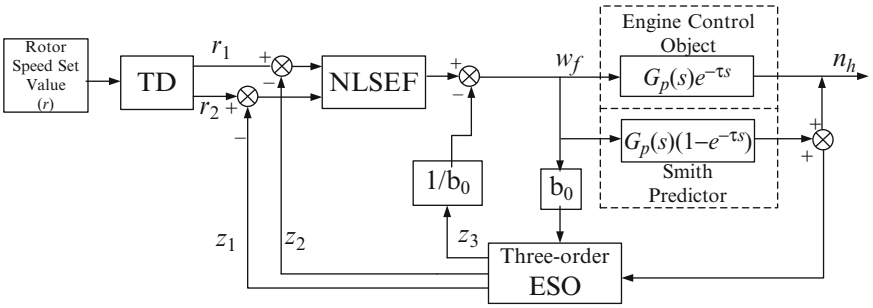

Fig. 2 Engine two-order Smith-ADRC control system

this system is expressed by Eq. 5. In Eq. 5, $fst(\bullet)$ and $fal(\bullet)$ are nonlinear functions, $r, h, \beta_1, \beta_2, \beta_3, \alpha_1, \alpha_2, \alpha_3, \alpha_4, \alpha_5, \delta_1, \delta_2, k_1, k_2$ are all undetermined coefficients, b is input variable magnification coefficient of the controlled object transfer function. Due to space limitation, specific meanings of related functions and parameters can been seen in other references [7, 8].

$$\begin{cases} TD: \dot{r}_1 = r_2 \\ \dot{r}_2 = fst(r_1, r_2, r(t), r, h) \end{cases} \begin{cases} ESO: \varepsilon = z_1(t) - y(t) \\ \dot{z}_1 = z_2 - \beta_1 \cdot fal(\varepsilon, \alpha_1, \delta_1) \\ \dot{z}_2 = z_3 - \beta_2 \cdot fal(\varepsilon, \alpha_2, \delta_1) + bu(t) \\ \dot{z}_3 = -\beta_3 \cdot fal(\varepsilon, \alpha_3, \delta_1) \end{cases}$$
$$\begin{cases} NLSEF: e_1 = r_1 - z_1, e_2 = r_2 - z_2 \\ u_0 = k_1 \cdot fal(e_1, \alpha_4, \delta_2) + k_2 \cdot fal(e_2, \alpha_5, \delta_2) \\ u = u_0 - \dfrac{z_3}{b} \end{cases} \tag{5}$$

Combining the parameter tuning methods and practical experience [1, 7, 8], the parameters can be tuned as follows:

TD: system transition time($t_0 = 0.1s$), amplitude of tracking signal($d = 1$),speed factor($r = 4$); filter factor(h) is equal to emulating time of system, $h = 0.001$.
ESO: according experience, $\alpha_1 = 0.5$, $\alpha_2 = 0.25$, $\alpha_3 = 0.1$; band width ($\omega_0 = 15$ rad/s), $\beta_1 = 45$, $\beta_1 = 675$, $\beta_1 = 3375$.
NLSEF: according experience, $\alpha_4 = 0.5$, $\alpha_5 = 1.5$; the controlled model, $b_0 = 3.3$, $\xi = 1$; according to system band width, $k_1 = 225$, $k_2 = 30$.

To compensate the delay characteristics of the system, Smith predictor could be added to the ADRC controller. The basic principle of Smith Predictor is that import a suitable feedback element to the controller. The delayed controlled variable can be reflected in the controller in advance, which can counteract the influence of time delay [10].

Based on the analysis above, the two-order Smith-ADRC system could be designed in Fig. 2.

4 Results and Analysis

Setting a square wave as the speed tracking signal and applying a Gaussian white noise signal ($\mu = 0$, $\sigma^2 = 1$) to the controlled object, the mentioned above tuned parameters was use to simulate. Simulation results could be seen in Figs. 3 and 4.

In Fig. 3, under initial tuning parameters, system tracking response is stable in square wave band, settling time was equal to 0.937 s ($ts = 0.937s$). The applied noise could be well suppressed by the controller, which has a good tracking

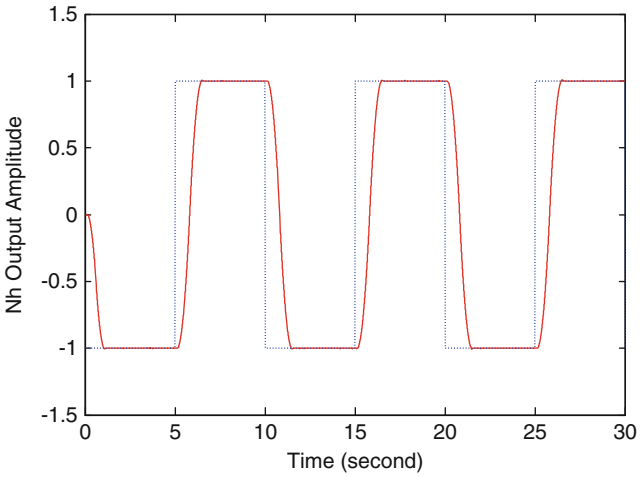

Fig. 3 $r = 4$, system tracking response curve

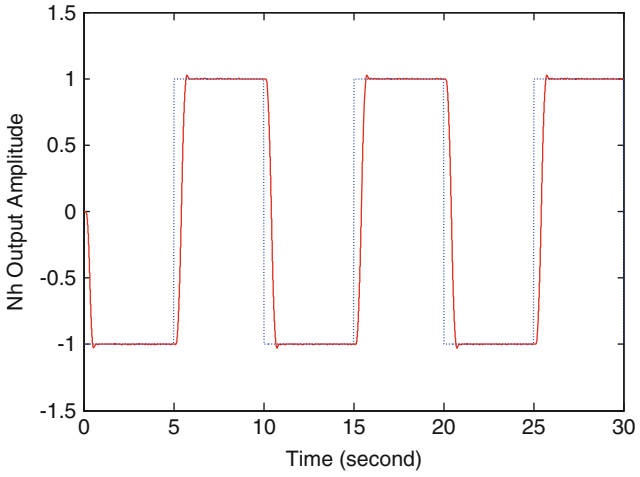

Fig. 4 $r = 20$, system tracking response curve

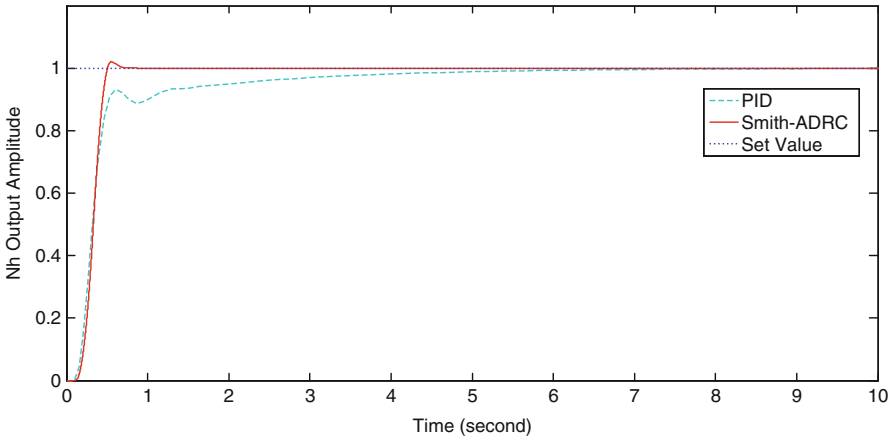

Fig. 5 The comparison of two control methods step response

performance. While adjusting speed factor (r), the shorter setting time could be obtained (Fig. 4). In Fig. 4, increasing r to 20 ($r = 20$), settling time reduced to 0.47 s ($ts = 0.47s$). However, if there was no Smith predictor, oscillation could emerge in system simulation curve. The simulation result shows that Smith predictor can effectively compensate the system time delay.

For engine speed PID and two-order Smith-ADRC control circuits, respectively applying a step signal, without adding disturbance, step responses of control system were displayed in Fig. 5.

Where the adoptive parameters of PID controller were $k_p = 10.22$, $k_i = 5.8$, $k_d = 1.41$. The as seen in Fig. 5, respectively using PID and ADRC controllers to control the system, the obtained response characteristics were similar. However, better tracking performance could be obtained by ADRC controller. Using ADRC controller, it just took 0.4678 s for system to obtain permissible steady-state error, and overshoot was just 2 %.

Simulation results shown that although the system did not use the above tuning parameters or given controlled object, the designed controller all had good control performance. From simulation results, it is also clear that the designed controller with strong robustness and adaptability is not just suitable for the specific object.

4.1 Robustness of Controller

For a controller, the ability, that adjusting the controller's parameters in a certain range has no influence on tracking the set value, is called robustness. For the designed controller, keeping other parameters unchanged, adjusting the speed factor (r) within a wide range, the simulation results shown that while r was less than 10,000, overshoot could be controlled within $\pm 5\,\%$.

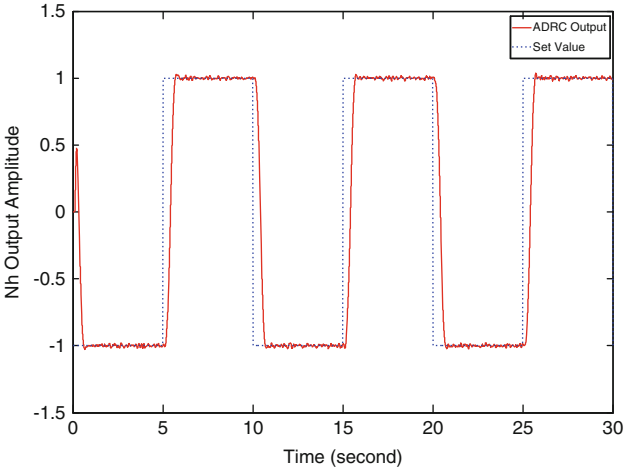

Fig. 6 Applying Gaussian white noise ($\mu = 100$, $\sigma^2 = 200$),speed tracking response curve

While adjusting these parameters (β_1, β_2, β_3, k_1, k_2), except the contracted parameters in most of literatures, good curves could be obtained. It is proved that the controller has strong robustness. Compared with PID controller, although the ADRC controller has more parameters needing to be tuned, these parameters can be easily tuned within a wide range.

4.2 Anti-interference Performance of Controller

Increasing intensity of Gaussian white noise signal applied to system, average value was adjusted to 100 ($\mu = 100$), variance was adjusted to 200 ($\sigma^2 = 200$), system tracking curve was displayed in Fig. 6. If applying a white noise with power of 10 ($P = 10$), system simulation curve was displayed in Fig. 7.

Figure 6 shows that Gaussian white noise could be well suppressed by the system. In Fig. 7, while applying a white noise with power of 10, oscillation of high-pressure rotor was within ± 0.2. Therefore, the white noise of high-power could be also well suppressed.

For chronological disturbance, the designed controller also has strong anti-interference capability. After system working into steady-state, at the 6 s of simulation time, applying a tunable pulse signal with amplitude of A to system, the experiment is used to obtain the responses while the two systems undergoing instantaneous shock. Duration time of the pulse signal was 0.001 s, system response curve could be seen in Figs. 8 and 9.

In Fig. 8, for PID control circuit, while undergoing instantaneous shock which was 180 times amplitude of input signal, the response of high-pressure rotor output

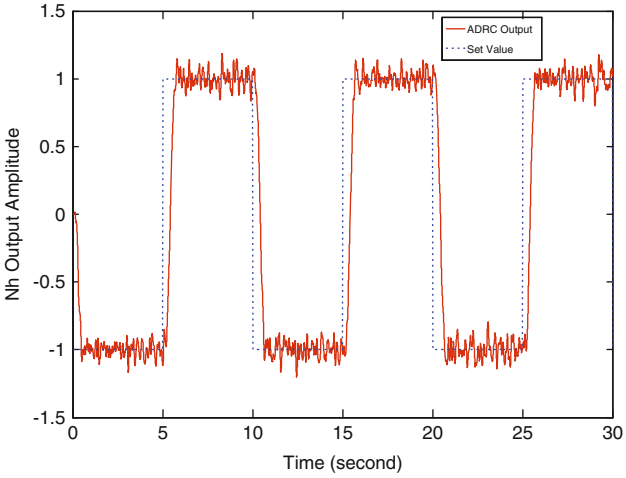

Fig. 7 Applying white noise ($P = 10$), speed tracking response curve

Fig. 8 The simulation result of PID control system after undergoing instantaneous shock

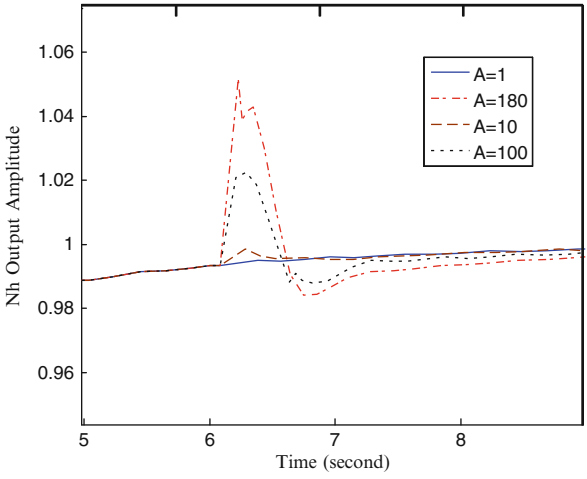

signal was less than 1.06 times. However, for Smith-ADRC control circuit, while undergoing instantaneous shock which was 1,000 times amplitude of input signal, the response of high-pressure rotor output signal was less than 1.08 times (Fig. 9). The results show that ADRC control circuit has stronger shock resistance than PID control circuit, and ADRC control circuit can be faster entering steady-state than PID control circuit after undergoing instantaneous shock.

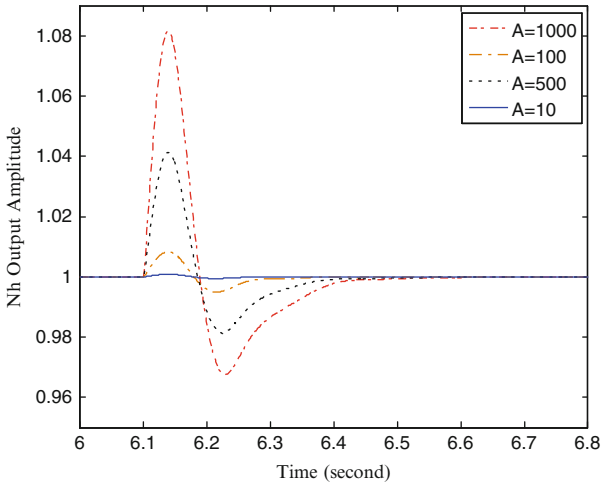

Fig. 9 The simulation result of Smith-ADRC control system after undergoing instantaneous shock

5 Conclusion

In the paper, by taking the mathematical model of three-order time delay speed-fuel control system as the control object, a two-order Smith-ADRC controller was designed, which realized the control of aero-engine steady-state. From the simulation results, although the algorithm of ADRC controller is more complex, parameters tuning are more accurate than PID engineering tuning, and the ADRC controller has a strong anti-interference ability. Two-order Smith-ADRC controller, which can avoid many shortcomings than three-order controller and effectively overcome the time delay of system, is a new controller suitable for aero-engine control.

References

1. Jing-Qing Han (2007) Auto disturbances rejection control technique. Front Sci 1(1):24–31
2. Fan-Dong Meng (2009) Study of design and application for the active disturbance rejection controller. Dissertation, Harbin University of Science and Technology, Harbin
3. Zhao-Jing Zhang (2007) Parameter adjustments of auto-disturbance rejection control systems. Dissertation, Southern Yangtze University, Wuxi
4. Hai-Bo Zhang, Jian-Guo Sun, Li-Guo Sun (2010) Design and application of a disturbance rejection rotor speed control method for turbo-shaft engines. J Aerosp Power 25(4):943–950
5. Hai-Bo Zhang, Li-Guo Sun, Jian-Guo Sun (2010) Robust disturbance rejection control design for integrated helicopter system/turbo-shaft engine. Acta Aeronaut Et Astronaut Sinica 31 (5):883–892
6. Hai-Bo Zhang, Jian-Kang Wang, Ri-Xian Wang et al (2012) Design of an active disturbance rejection decoupling multivariable control scheme for aero-engine. J Propuls Technol 33 (1):78–83

7. Shu-Qing Li, Sheng-Xiu Zhang, Yi-Nan Liu et al (2012) Simple design and application of auto disturbance rejection controller for aeroengine. Aeroengine 38(3):46–48
8. Xiao-Mei Yao (2002) Two-order ADRC control for general industrial plants. Control Eng China 9(5):59–62
9. Li-Ming Zhang (2009) Research on application of active disturbance rejection technology to AUVheading control. Dissertation, Harbin Engineering University, Harbin
10. Ke Xu (2004) Distributed control systems for aero-engines. Dissertation, Nanjing University of Aeronautics and Astronautics, Nanjing

Asynchronous Motor Vector Control System Based on Space Vector Pulse Width Modulation

YingZhan Hu and SuNa Guo

Abstract In order to improve the control result of asynchronous motor with power supplied by battery, the voltage vector control technology is used to respectively control the asynchronous motor excitation current and the torque current by measuring and controlling the vector of asynchronous motor stator current according to the principle of field oriented. The method to realize the algorithm of the voltage space vector pulse width modulation is introduced in detail, and the simulation model of three-phase asynchronous motor is built. The algorithm is simulated. The results show that the algorithm is reasonable, the control performance is better and application requirements of control for AC motor with power supplied by battery is satisfied.

Keywords Voltage space vector pulse width modulation • Asynchronous motor • Vector control • Simulation

1 Introduction

Space vector pulse width modulation (SVPWM) technique is to control the switching of the inverter in the way of controlling three-phase motor stator to generate the tracking circular rotating field with power supplied by Voltage Source Inverter. This control strategy could improve the utilization of the voltage on the DC side, make the calculation easy [1], reduce the switching loss and thus reduce motor harmonic losses, lower the torque ripple, is especially for the situation with power supplied by battery such as electric vehicles.

Vector control theory develops on the electric machine unification theory, electromechanical energy conversion and coordinate transformation theory, and it

Y. Hu (✉) • S. Guo
Department of Electrical Engineering, Henan Polytechnic Institute, Nanyang, China
e-mail: huyz168@163.com

W. Wang (ed.), *Mechatronics and Automatic Control Systems*, Lecture Notes in Electrical Engineering 237, DOI 10.1007/978-3-319-01273-5_75,

has features such as advanced, novelty and practical etc. It makes induction motor-model become a DC motor-model by the coordinate transformation, decompose the stator current into two DC parts which are orientated towards the rotator magnetic field,control them so as to realize the decouple of magnetic flux and torque and achieve the DC motor effect.

2 Principle of SVPWM

The main circuit structure of the typical three-phase voltage source inverter is shown in Fig. 1 [2, 3].

There are two switching devices on each bridge arm. PWM control is to adjust the average current by adjusting the switch-off time of each bridge arm. The switching rule of the six switching devices must obey the following rules:

1. The numbers of switching devices in the open state and in the off state must be three at any time;
2. The two switching devices of the same bridge arm is controlled by complementary drive signals, and cannot be shoot-through.

The space vector pulse width modulation (SVPWM) is to convert the input voltage of three-phase inverter to the space voltage vector and approximate the voltage circle by using the eight space vectors formed by different switching states of the inverter, and then form the SVPWM trigger wave. The position and size of eight voltage space vectors is shown in Fig. 2 [4].

There are six nonzero vectors U_x (x = 1, 2, 3, 4, 5, 6) and two zero vectors (U_0, U_7) in Fig. 2, The switching states corresponding to the upper bridge of inverter are marked in small brackets after the vector under the action of each vector. "1" indicates the on-state, and "0" indicates the off-state. Each of the six nonzero voltage vectors magnitude is $2U_d/3$, and their phase angle difference is $\pi/3$. The complex plane is divided into six fan-shaped regions, and they are identified as 1, 2, 3, 4, 5, 6 in this paper. In any fan-shaped region, the voltage vector U^* can be made up of the adjacent space voltage vectors (U_x, $U_{x\pm60}$). The corresponding basic space vector constitute instantaneous command is the purpose of voltage space vector technology. The average input voltage is made equal to the command voltage U^*

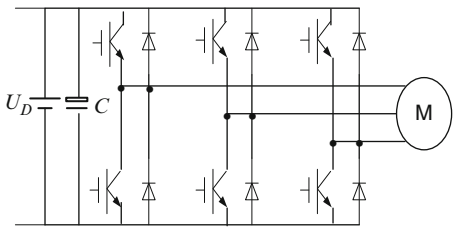

Fig. 1 Three-phase power inverter

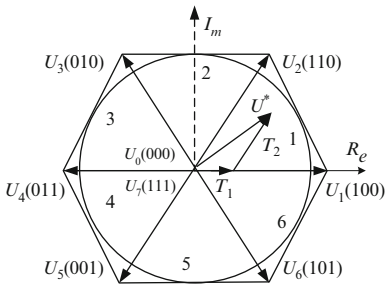

Fig. 2 The space vector and switching state

during the pulse period T .so that the space voltage vector trajectory approaches a round.

In other words, in arbitrarily small cycle time T, the output of the inverter is the same as the average instructions voltage, such as Eq. 1.

$$\frac{1}{T}\int_{nT}^{(n+1)T} U^*(t)dt = \frac{1}{T}(T_1U_x + T_2U_{X\pm60}) \tag{1}$$

T_1, T_2 respectively is the action time of U_x, $U_{x\pm60}$. If the sum of T_1 and T_2 is less than the pulse period T, the zero vector(U_0, U_7)will be used to fill up the remaining time of period T [5] . When the end of the flux vector is stationary under the action of zero vector, and the original rotation frequency of the flux has been changed. As a result, Variable frequency is realized [2, 6].

3 Asynchronous Motor Vector Control System Based on SVPWM

In this system, three-phase windings of Asynchronous Motor adopt Y-connected without zero line, then $i_a + i_b + i_c = 0$ or $i_c = -i_a - i_b$. The diagram of rotor field oriented control system for induction motor based on SVPWM is shown in Fig. 3.

This control system is composed of the outer loop speed control and the inner loop current control. The speed control loop is the speed command value ω_{ref} given by the user compared with the speed feedback signal ω_2 of the optical encoder on the motor shaft, and its deviation is adjusted through the speed PI regulator, and output the torque current component used as the command value of inner torque regulator loop, then compare with the three-phase stator current signal i_q after the Clarke and Park transformations detected by the hall current sensor, then the stator torque voltage component ν_q^* in rotating frame is obtained after the torque PI regulator. In the current control loop, the excitation component command value i_{dref} (zero) compared with the signal i_q which is the three-phase stator current signal after the Clarke and Park transformations detected by the hall current sensor, voltage excitation component $\nu^*{}_d$ of the stator in rotating frame will been obtained

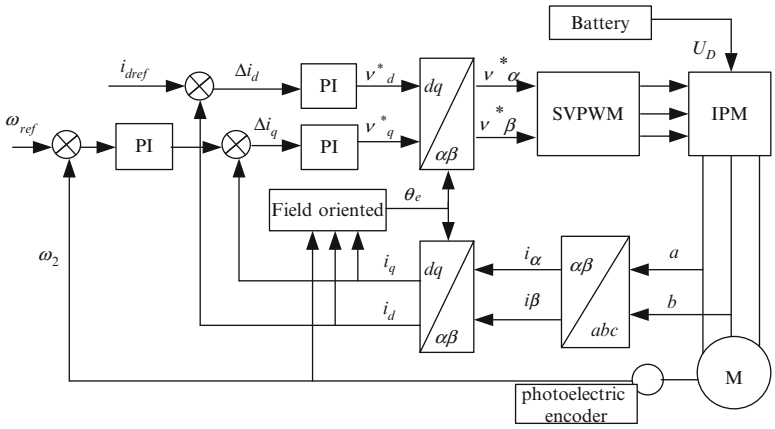

Fig. 3 The diagram of rotor field oriented control system for induction motor based on SVPWM

after the torque PI regulator. Then we can transform v_d^* and v_q^* to the two-phase stationary stator frame by the anti-Park transformation, obtain the two voltage components $v^*{}_\alpha$ and $v^*{}_\beta$ which have the same frame with the inverter voltage space vector. Finally, it uses the space vector pulse width modulation to generate the PWM waveform of the inverter switch on-state. On-state inverter switching PWM waveform is generated by the use of the technique of space vector pulse width modulation [7, 8].

4 The Implementation of SVPWM Algorithm

*4.1 Determine the Sector of Space Voltage Vector U**

The command value of space vector voltage U^* is determined by the two voltage components $v^*{}_\alpha$ and $v^*{}_\beta$ acquired by coordinate transformation. But it can be synthesized by adjacent space voltage vectors of a sector only by acquiring the sector. The period of a wave is divided into six intervals according to three-phase voltages with an angle width (60°), and the zero-crossing of voltage is used as the beginning and the end of sector. The sector can be determined by two-phase voltage and another with the opposite sign, as follows [9]:

1. Segment 1 $v_a^* > 0, v_b^* < 0, v_c^* > 0$;
2. Segment 2 $v_a^* > 0, v_b^* < 0, v_c^* < 0$;
3. Segment 3 $v_a^* > 0, v_b^* > 0, v_c^* < 0$;
4. Segment 4 $v_a^* < 0, v_b^* > 0, v_c^* < 0$;
5. Segment 5 $v_a^* < 0, v_b^* > 0, v_c^* > 0$;
6. Segment 6 $v_a^* < 0, v_b^* < 0, v_c^* > 0$.

Table 1 The relationship of sector and P

P value	1	2	3	4	5	6
Sector number	2	6	1	4	3	5

Of course, anti-Clarke transformation should been done before above as follows:

$$\begin{aligned} v_a^* &= v_\beta^* \\ v_b^* &= -\frac{\sqrt{3}}{2}v_\alpha^* - \frac{1}{2}v_\beta^* \\ v_c^* &= \frac{\sqrt{3}}{2}v_\alpha^* - \frac{1}{2}v_\beta^* \end{aligned} \tag{2}$$

Making $P = 4sign(v_b^*) + 2sign(v_c^*) + sign(v_a^*)$, and looking up Table 1 to determine the number of sectors.

4.2 Action Time of the Adjacent Switching Vector

Making

$$\begin{aligned} X &= \sqrt{3}kv_\alpha^* \\ Y &= \frac{\sqrt{3}k}{2}v_\beta^* + \frac{3}{2}kv_\alpha^* \\ Z &= \frac{\sqrt{3}k}{2}v_\beta^* - \frac{3}{2}kv_\alpha^* \end{aligned} \tag{3}$$

There is $k = T/U_d$ in Eq. 3.
The values of T_1, T_2 is defined according to the different values of P as Table 2.
If $T_1 + T_2$, then amended T_1, T_2 as follows method:

$$T_1 = \frac{T_1}{T_1 + T_2}T,\ T_2 = \frac{T_2}{T_1 + T_2}T$$

The values of T_1, T_2 in the right hand side of the equal sign is based on Table 2, the left hand of the equal sign is corrected value. Assume

$$\begin{cases} T_a = (T - T_1 - T_2)/2 \\ T_b = T_a + T_1/2 \\ T_c = T \end{cases}. \tag{4}$$

Table 2 Assignment table of T_1, T_2

P value	1	2	3	4	5	6
T1	Z	Y	−Z	−X	X	−Y
T2	Y	−X	X	Z	−Y	−Z

Table 3 T_a,T_b,T_c corresponding to three-phase *a*,*b*,*c* in all sectors

	Sector number					
	1	2	3	4	5	6
Phase a	Ta	Tb	Tc	Tc	Tb	Ta
Phase b	Tb	Ta	Ta	Tb	Tc	Tc
Phase c	Tc	Tc	Tb	Ta	Ta	Tb

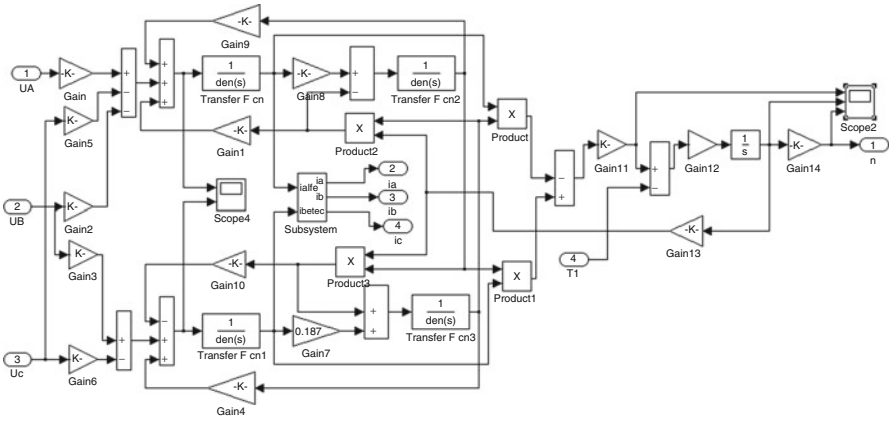

Fig. 4 The simulation model of three-phase induction motor

T_a,T_b,T_c corresponding to three-phase are defined in Table 3. T_a,T_b,T_c are the values to generate PWM waveforms by Comparing with the triangular wave. SVPWM wave is modulated to control the inverter, then to control the motor.

5 Simulation of Motor Vector Control System

The simulation model of three-phase induction motor is shown in Fig. 4, and this model is based on the three-phase induction motor YTSP90L-4.

The Motor parameters: rated power: 1.5 kw, rated voltage: 380 V, rated current:4.0 A, rated frequency: 50 Hz, $R_1 = 0.07\ \Omega$, the self-inductance of stator L1 = 0.066 mH, $R_2 = 0.052\ \Omega$, the self-inductance of rotor L_2=0.101 mH, The mutual inductance $L_m = 2.108$ mH, Number of pole pairs $n_p = 2$.

As this algorithm above, a simulink model of the rotor flux oriented induction motor vector control system with simulink is built, shown in Fig. 5.

Figures 6 and 7 are respectively for the motor three-phase speed and the three-phase current waveform. From the figure we can see, the motor is operated steady

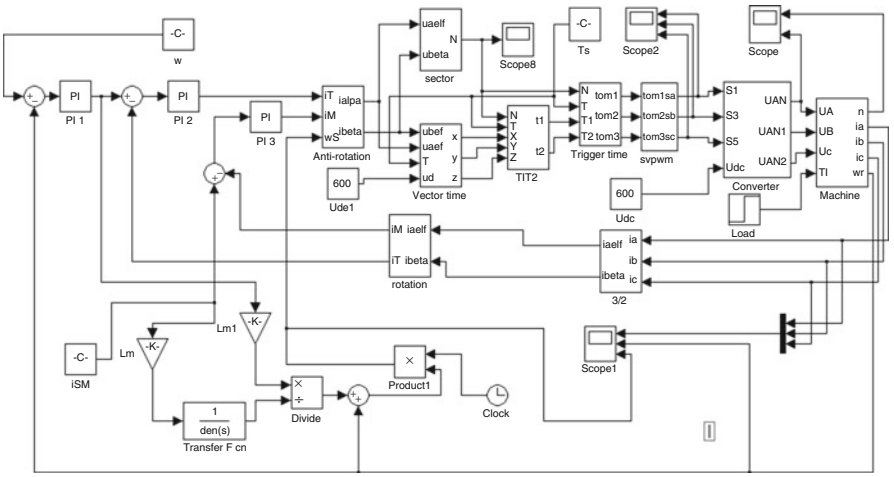

Fig. 5 The simulink model of system

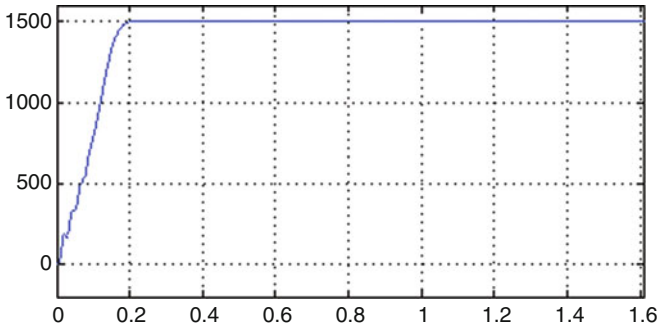

Fig. 6 The waveform of three-phase motor speed (*left*)

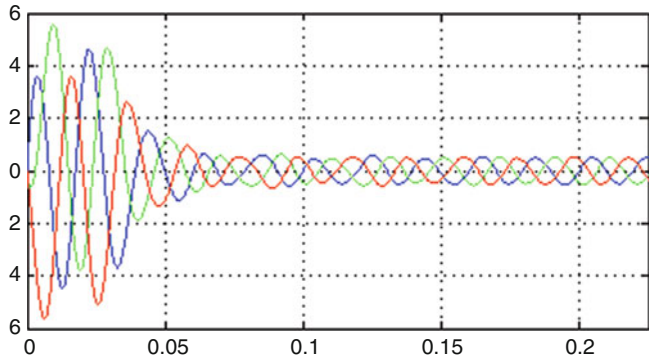

Fig. 7 The waveform of three-phase induction motor stator current (*right*)

and smoothly when the reference speed is 1,500 r/min, and the overshoot is small with fast response. The current harmonic is low. The control results are satisfactory.

6 Conclusion

On the basis of theoretical analysis, the MATLAB simulation model of asynchronous motor vector control system based on SVPWM was realized. The simulation results verified that the algorithm was correct and scientific and the properties of the control systems were fine, and it could satisfy the control requirements of the AC motor with power supplied by battery. The preparations can be made for the realization of control circuit with the core of DSP, SOPC and so on.

References

1. Ag. Wu, Chz. Piao, Rg. Yang (2011) SVPWM simplified algorithm and dead zone compensation. Power Electron 45(7):72–74 (in Chinese)
2. Li J (2012) Implementation of SVPWM control technology for asynchronous motor based on DSP. Min Process Equip 40(3):100–105 (in Chinese)
3. Shr. Huang, Rk. Hao, Zhu J (2010) SVPWM control technology implementation of induction motor based on DSP. Electr Driv Autom Control 32(5):19–22 (in Chinese)
4. Xl. Wen, Xg. Yin, Zhe Z (2009) Unified space vector PWM implementation method for three-phase inverters. Trans China Electrotech Soc 24(10):87–93, in Chinese
5. Yq. Xue, Liu B (2010) Analysis of zero state vector distribution based on space vector PWM. Electr Mach Control 14(8):93–97 (in Chinese)
6. Jc. Fang, Yz. Ling (2006) Simulation of the vector control system with SVPWM for asynchronous motors. Tech Autom Appl 25(9):54–56 (in Chinese)
7. Fl. Shen, Yk. Man, Jh. Wang (2011) The research on space vector control of induction motor system based on rotor field orientation. 2011 Chinese Control and Decision Conference (CCDC2011). IEEE conference Publications, Los Alamitos, CA, USA, pp 3400–3403
8. Qs. Yu. (2010) Study on the SVPWM vector control system for asynchronous motor [D]. Chongqing University, Chongqing, pp 7–34 (in Chinese)
9. Zheng Z, Hj. Tao (2006) Studying of control algorithm for fast space vector PWM. Electr Appl 25(8):38–40 (in Chinese)

Design of Direct Current Subsynchronous Damping Controller (SSDC)

Shiwu Xiao, Xiaojuan Kang, Jianhui Liu, and Xianglong Chen

Abstract First, this article analyzes the basic principles of supplementary subsynchronous damping controller (SSDC) inhibiting SSO caused by the DC control system. Second, based on the principle of phase compensation, a multi-mode SSDC is designed in accordance with the maximum phase compensation method. Third, test signal method is used to analyze SSDC's compensation role in improving the system electrical damping. Finally, the availability of SSDC designed in this paper is simulated and verified in an actual power system model.

Keywords DC transmission • Subsynchronous oscillation • Phase compensation • Test signal method • Electrical damping characteristics

1 Introduction

1.1 Mechanism Analysis of SSO Caused by DC Control System

Interaction of high voltage direct current (HVDC) systems and turbine-generator units may produce subsynchronous oscillation (SSO) to endanger the safe and stable operation of the grid and units. The world's first HVDC causing SSO of turbine-generator unit was found in the debugging of the Square Butte HVDC Transmission Project in 1977 [1]. Rapid control of the HVDC transmission system can cause SSO problem of the system under certain conditions (Fig. 1).

S. Xiao • X. Kang (✉) • J. Liu • X. Chen
School of Electrical & Electronics Engineering, North China Electric Power University, Beijing, China
e-mail: kangxiaojuan_2006@126.com

W. Wang (ed.), *Mechatronics and Automatic Control Systems*, Lecture Notes in Electrical Engineering 237, DOI 10.1007/978-3-319-01273-5_76,

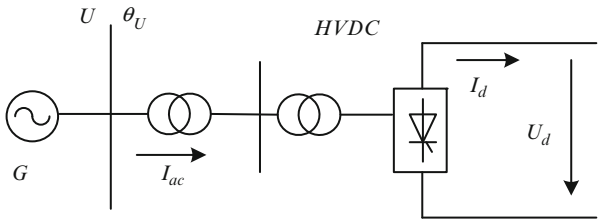

Fig. 1 SSO's occurrence schematic

The tiny rotor mechanical perturbation $\Delta\delta = A\sin\mu t$ on the generator strongly coupled with the rectifier station, it will cause the terminal voltage (the rectifier station AC bus voltage $U\angle\theta_U$ in this case) amplitude and phase perturbation ΔU and $\Delta\theta_U$. Among them, $\Delta\theta_U$ makes the same size deviation for the rectifier station trigger angle and expected firing angle, resulting in a perturbation in the DC bus voltage U_d; terminal voltage amplitude perturbation ΔU, also will cause the perturbation of DC bus voltage U_d. The perturbation of U_d would lead to perturbation ΔI_d (and ΔP_d), DC constant current (constant power) control attempting to prevent perturbation of I_d (P_d), which cannot ultimately completely eliminate ΔI_d (ΔP_d), resulting in perturbation of the generator electromagnetic torque ΔT_e. Once the phase is appropriate, this ΔT_e will help to increase the initial mechanical disturbance $\Delta\delta$, namely the electrical damping becomes negative, once it is stronger than the showing mechanical damping in the corresponding shaft frequency, the situation that DC control system causes instability of shaft torsional oscillation will appear, i.e., SSO caused by the DC control system [2].

1.2 The Principle of SSDC Inhibition to DC SSO

The method, using supplementary subsynchronous oscillation damping controller (SSDC) to solve the SSO problems caused by HVDC is mentioned in the EPRI's research report "HVDC System Control for Damping Subsynchronous Oscillation" [3]. This method has been used in many DC projects. The basic principle of the SSDC is to provide positive electrical damping in the subsynchronous frequency range of the turbine-generator shaft [4].

From the mechanism analysis of DC rapid control system causing SSO, the direct cause of the instable shaft torsional vibration is the phase angle difference between generator speed offset $\Delta\omega$ and the electromagnetic torque variation ΔT_e exceeds 90° after the disturbance, which produces an electrical negative damping to help increase the occurrence probability of SSO, as shown in Fig. 2. SSDC usually selects signals can reflect the severity of the generator shaft torsional oscillation as inputs. For example, generator speed deviation is selected as input signal. After the proportion and phase-shift link of SSDC, its output signal through the Constant Current Control loop to provide an additional electromagnetic torque $\Delta T_e^{'}$, and makes the phase angle difference between $\Delta\omega$ and the vector synthesized by ΔT_e

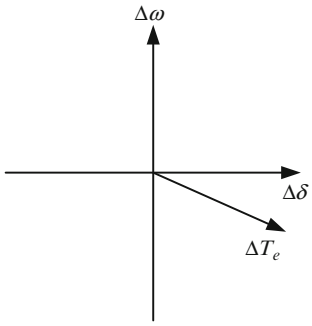

Fig. 2 The relationship of electromagnetic torque and rotation speed after disturbance

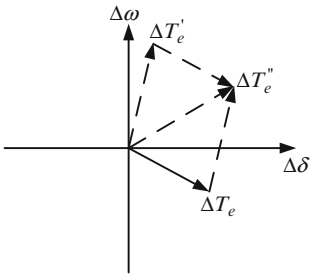

Fig. 3 Synthetic torque of additional electromagnetic torque and the original electromagnetic torque

and $\Delta T_e^{'}$ smaller than 90°, Therefore, the system eventually will have a positive damping torque, as shown in Fig. 3. In order to ensure to get the maximum damping effect, additional electromagnetic torque $\Delta T_e^{'}$ should be provided and $\Delta T_e^{'}$ should be in the same phase with $\Delta\omega$.

2 System Model

For islanding operation mode of Suizhong power plant, the SSO problem is most serious. So system model for SSO study is established under this operation mode, shown in Fig. 4. The dynamic response of the speed governor is ignored. DC system using a unipolar 12-pulse structure, the converter valves are triggered at equal intervals, the rectifier side of the DC system uses constant current control mode while the inverter side uses the constant extinction angle control mode [5]. A detailed block diagram of the constant current controller is shown in Fig. 5, the DC current deviation ΔI_d is adjusted by the Proportional Integral (PI) component to output the trigger angle signal α, in which parameters of PI control component are K = 1.0, T = 0.005 s, βmax = 3.054 rad (175°), βmin = 0.52 rad (30°).

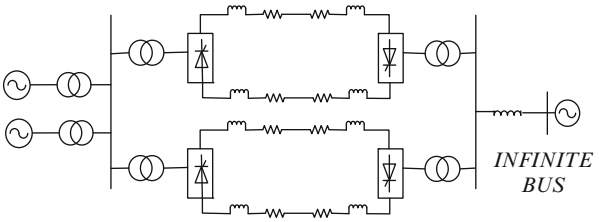

Fig. 4 System simulation model

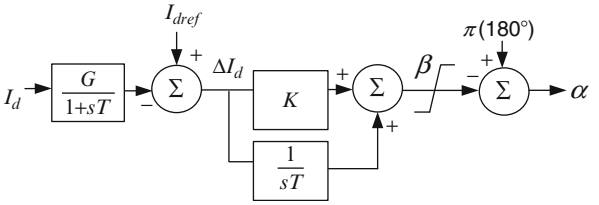

Fig. 5 Structure of constant current controller

3 The Optimized Design of SSDC

Design methods of SSDC control element can be either the broadband design method or the narrowband design method. In the narrowband design method, narrow-band filters are designed respectively according to several torsional vibration characteristic frequencies of steam turbine with SSO risks, SSO inhibition effect is designed for different torsional vibration modal frequencies. This method requires knowing exact shaft characteristic frequencies of the generator sets, and the designed SSDC link can significantly improve the electrical damping in the specified shaft modal frequency. The disadvantage of this method is additional negative damping may be produced near the specified frequency for units. The broadband design approach is to design a band-pass filter in a frequency range and the band contains characteristic frequencies may which exist SSO risks of the unit, so the electrical damping can be improved in the whole band. Compared with the narrowband design method, additional damping provided by the broadband design method is relatively small, but its advantage is SSDC can play a role in a very wide frequency range [6].

The research system in this article has three characteristic frequencies in the subsynchronous frequency range (see Part IV of this article), and the characteristic frequency of mode 2 is closer to the characteristic frequency of mode 3. If the narrow-band method is adopt to design the SSDC, the controller design will be complex and it is hard to ensure that the designed controller can provide additional positive damping for units in the entire sub-synchronous frequency range, hence, broadband method is applied to design SSDC in this paper.

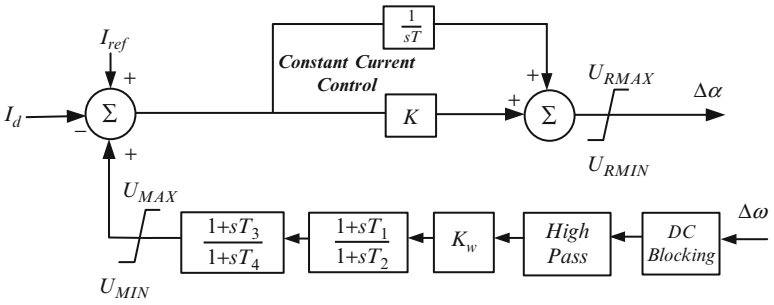

Fig. 6 SSDC structure diagram

3.1 Determine the Phase Compensation Parameters

SSDC can modulate both the current reference value and the firing angle to provide the positive electrical damping in the subsynchronous frequency range to achieve the purpose of inhibition of synchronous oscillation [7]. And they both can play a good inhibitory effect on the SSO in the case of rational design. In this design, the generator speed deviation is used as input signal of SSDC and SSDC's output signal is the current reference value input signal of the constant current controller in the rectifier side.

Figure 6 shows the structure diagram of SSDC. SSDC's basic principle is that providing positive damping for the turbine-generator units in the subsynchronous frequency range, so it should contains the DC blocking element, the high pass filter element, amplification element, phase compensation elements and limiting element.

The SSDC parameter to be determined most difficultly is the time constants of the phase shift aspects, the compensated phase of shift aspects is determined according to the phase of the current reference value input signal of the constant current controller lagging behind the electromagnetic torque which can be measured in the time domain simulation. This phase can be easily got by the test signal method, the detailed steps are as follows: First, based on the simulation system shown in Fig. 4, put a series of small-signal oscillating current ΔI_0 processed by the DC blocking link of SSDC and low-pass filter in the current reference areas of the DC constant current regulator (containing different frequency components, the frequency range is 7–40Hz), when the system run to steady state, measure the generator electromagnetic torque and get the corresponding output response ΔT_e; then, analyze ΔI_0 and ΔT_e in the public cycle with Fourier decomposition, the phase difference between the electromagnetic torque and the test signal under different frequencies can be calculated in turn, the calculated results are shown in Fig. 7.

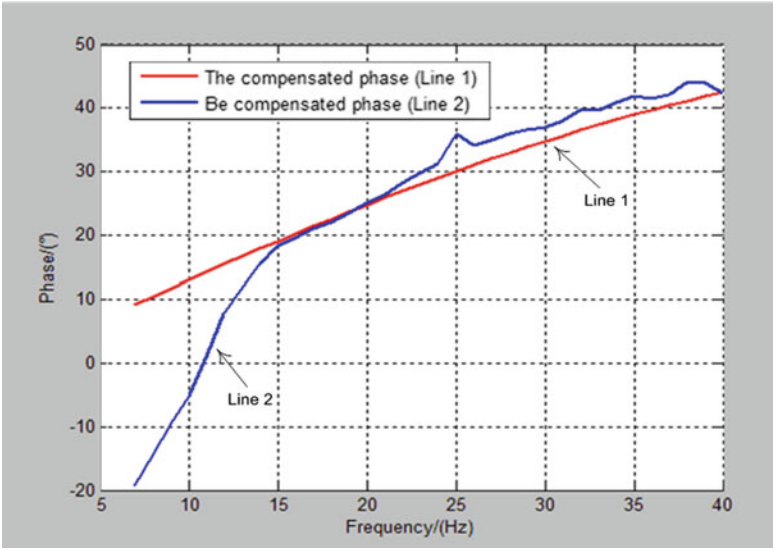

Fig. 7 Be compensated phase and the compensated phase of SSDC's phase shift links

Use two lead links to fit the curve of be compensated phase and then time constants can be calculated out as T1 = T3 = 0.002828, T2 = T4 = 0.001. The lead compensation phases in accordance with fitting function are shown in Fig. 7.

3.2 Determine the Phase Compensation Parameters

Shaft using a single rigid block model, test signal method is applied to simulate the study system, analyze the SSDC effect on SSO electric damping characteristics of the generator set. Curves of generating units' electrical damping coefficient De in the subsynchronous frequency range in different circumstances: without SSDC, SSDC amplification gain Kw = 1 and SSDC amplification Kw = 5 can be obtained respectively, as shown in Fig. 8.

We can see from Fig. 8, electrical damping within the entire synchronization band significantly increases when SSDC is applied, the band width corresponding to the system negative electrical damping is greatly reduced, which helps to avoid the SSO occurrence. The greater controller magnification is, the more beneficial to the SSO inhibition. But taking it into account that applying SSDC should not change the system stability, So the controller magnification should not be selected too large.

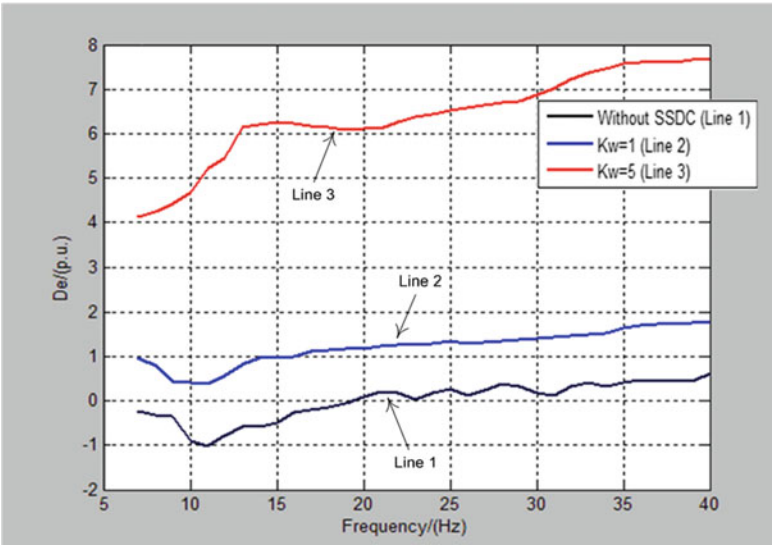

Fig. 8 The influence of magnification Kw on the electrical damping coefficient De

4 Simulation Results

Time-domain simulation of the power system shown in Fig. 4 is conducted with electromagnetic transient simulation software PSCAD/EMTDC. The Suizhong generator shaft using the multi-rigid-body model, the shaft consists of the high-pressure cylinder (HP), the medium-pressure cylinder (IP), the low-pressure cylinder A (LPA), the low-pressure cylinder B (LPB) and the generator (GEN5), totally five concentrated mass blocks. The shaft contains four torsional vibration modes, the torsional vibration frequencies are 13.39, 23.30, 26.74 and 53.89Hz. Observe the electrical damping characteristics curve without SSDC in Fig. 8, we can find that the shaft torsional vibration under the frequency of mode 1 is highly likely to occur when there is no SSDC applied.

The SSDC has a complete control structure and the amplification gain Kw is taken as 5. Observe the changes of modal generator speed differences after the system disturbance when there is no SSDC or not by time-domain simulation. Simulation results are shown in Figs. 9 and 10. A single phase to ground fault is applied in 4.3 s moment in the AC bus of the rectifier side, the fault duration is 0.1 s. Seen from Fig. 9, When the SSDC controller is not applied, the modal 1 generator speed difference is divergent, illustrates the SSO is unstable. Seen from Fig. 10, When the SSDC controller is applied, the modal 1 generator speed difference is decaying rapidly after fault, demonstrates that SSDC can damp the shaft torsional vibration effectively. This conclusion is consistent with the analysis results of the electrical damping characteristics and verifies the validity of SSDC.

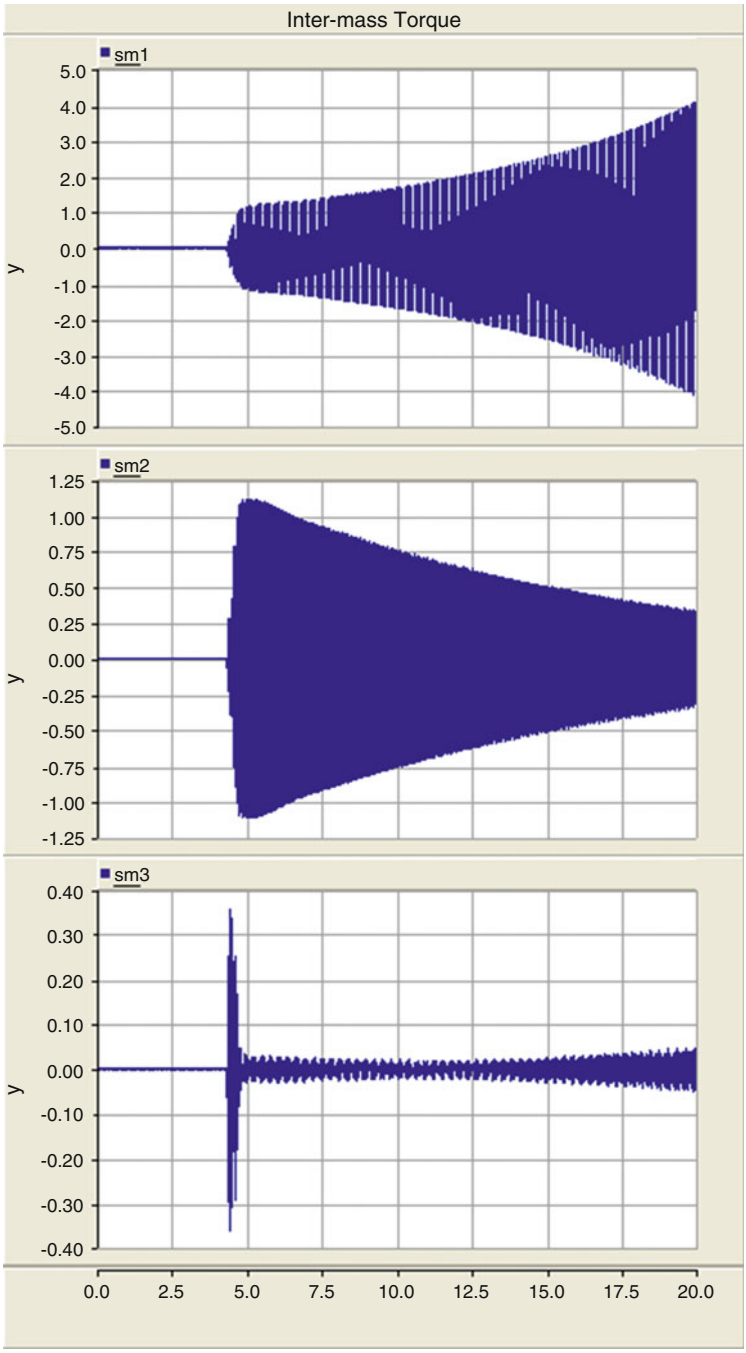

Fig. 9 Speed differences before SSDC is applied

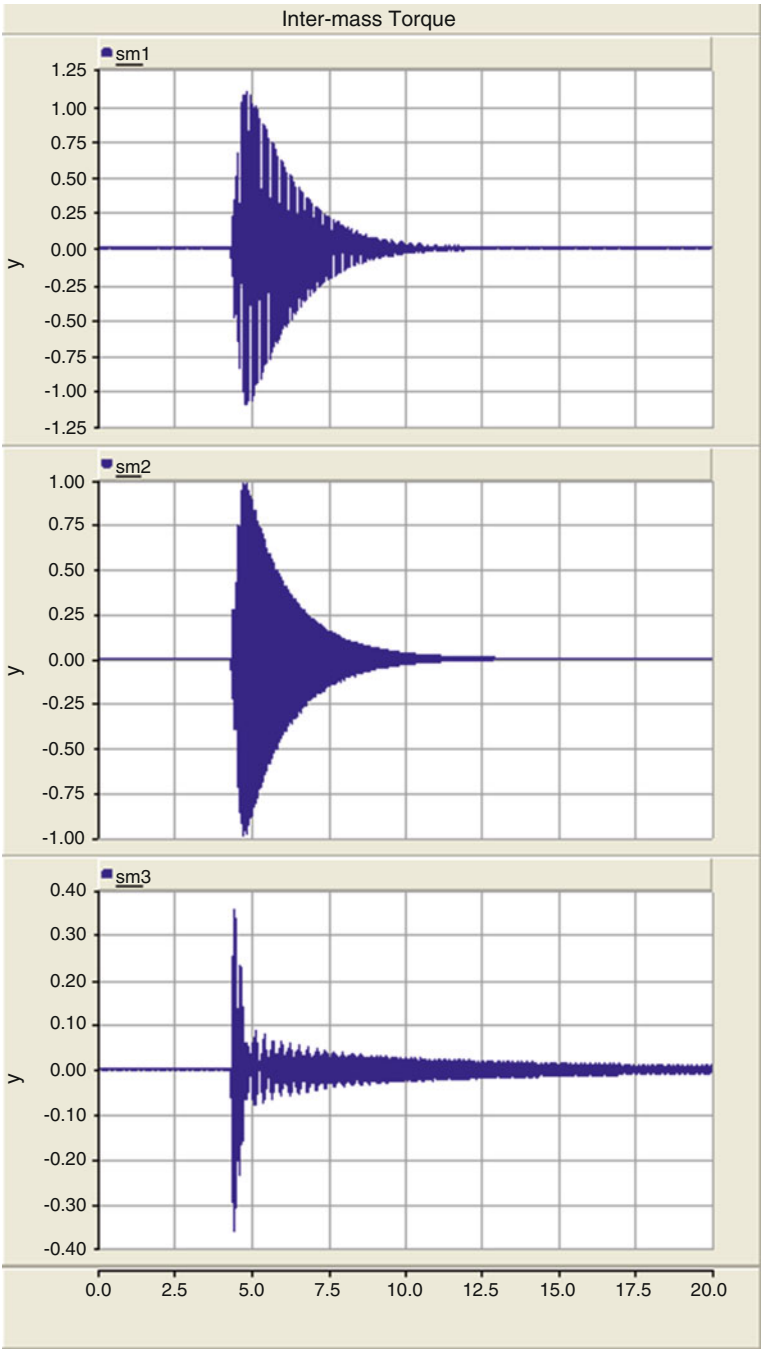

Fig. 10 Speed differences after SSDC is applied

5 Conclusion

This article designed SSDC is accordance with the broadband design method based on the phase compensation principle. The test signal method was used to analyze the electrical damping characteristics before and after the SSDC is applied. Analysis results demonstrated that the designed SSDC has the ability to significantly increase the electrical damping in the subsynchronous frequency range. Time-domain simulation results also verify the effectiveness of the designed SSDC.

Acknowledgements Thanks to the crew of the subsynchronous resonance (SSR) & subsynchronous oscillation (SSO) research team of North China Electric Power University.

References

1. Bahrnlan M, Larsen EV, Piwko RJ et al (1980) Experience with HVDC-turbine-generator torsional interaction at Square Butte [J]. IEEE Trans Power Appar Syst 99(3):966–975
2. Ni YX, Chen SS, Zhang BL (2002) Dynamic power system theory and analysis [M]. Tsinghua University Press, Beijing, pp 304–309 (In Chinese)
3. EPRI EL-2708 (1982) HVDC system control for damping subsynchronous oscillation. Project 1425–1 final report
4. Gao BF, Zhao CY, Xiao XN et al (2010) Design and Implementation of SSDC for HVDC. High Volt Eng 36(2):501–506 (In Chinese)
5. Xu Z (2004) AC-DC power system dynamic behavior analysis [M]. Mechanical Industry Press, Beijing, pp 34–59 (In Chinese)
6. Thomas R, Pertti J (2010) On feasibility of SSDC to improve the effect of HVDC on subsynchronous damping on several lower range torsional oscillation modes. In: Power and Energy Society General Meeting, Minneapolis, pp 1–8
7. Zhang F, Xu Z (2008) A method to design a subsynchronous damping controller for HVDC transmission system[J]. Power Syst Technol 32(11):13–17 (In Chinese)

Three Current-Mode Wien-Bridge Oscillators Using Single Modified Current Controlled Current Differencing Transconductance Amplifier

Yongan Li

Abstract In order to obtain new current-mode Wien-bridge oscillators using single modified current controlled current differencing transconductance amplifier (MCCCDTA) as the active element, according to the terminal relations of MCCCDTA as well as the basic structure of current-mode Wien-bridge oscillator, three new current-mode Wien-bridge oscillators are presented. The canonical number in proposed oscillators was used for component quantity and the condition and frequency of oscillation can be controlled electronically by means of adjusting bias currents of the MCCCDTA. The oscillators provide current output from high output impedance terminals. Finally, frequency error for one of the proposed oscillators is analyzed. The computer simulation results are given to verify the realizability of the derived circuits.

Keywords Wien-bridge oscillator • Error analysis • Current-mode circuit • MCCCDTA

1 Introduction

Several Wien-bridge oscillator structures made use of different design methods have been reported [1–3]. Although the oscillators based on voltage feedback operation amplifiers (VFAs), current feedback operation amplifiers (CFAs), and second generation current conveyors (CCIIs) possess simple structure, they lack the electronic adjustability. While the oscillators using operation tranconductance amplifiers (OTAs) have good electronic adjustability, they undergo complex structure and a number of active components. The quadrature and multiphase oscillators

Y. Li (✉)
Department of Electronics and Information Engineering,
Shaanxi Institute of International Trade & Commerce, Xianyang, China
e-mail: lya6189@sohu.com

W. Wang (ed.), *Mechatronics and Automatic Control Systems*, Lecture Notes in Electrical Engineering 237, DOI 10.1007/978-3-319-01273-5_77,

employing current differencing transconductance amplifiers (CDTAs) have also been reported [4, 5]. They not only provide the independent electronic control between the oscillation frequency and the oscillation condition by tuning the bias current of the CDTA, but also possess high out impedances and low input impedances. However, because of the parasitic resistances at input ports, the circuits using CDTA must make use of some external passive resistors. This makes it not suitable for integrated circuits due to take up too much chip area.

Recently, a current controlled current differencing tranconductance amplifier, CCCDTA, has been popularized [6, 7]. As using an input bias current can control its parasitic resistances at two current input ports, the circuits using CCCDTAs are superior to ones using CDTAs. The universal biquad filters and sinusoidal oscillators [6, 7] have supported this viewpoint well.

In this paper, three Wien-bridge oscillators using MCCCDTA [7] are given. They use only one MCCCDTA, two capacitors, and one resistor or resistor less, and are easy to be integrated. The condition for oscillation and oscillation frequency can be varied through controlling bias currents of the MCCCDTA. The outputs of the circuit have high output impedances; the circuit has a low sensitivity. Finally, frequency error for one of the proposed oscillators is analyzed and the results of the circuit simulation are in agreement with theoretical anticipations.

2 Circuit Description

2.1 Three Wien-Bridge Oscillators Using MCCCDTA

According to the terminal relation of MCCCDTA as well as Fig. 2a in [7], three Wien-bridge oscillators using MCCCDTA is given in Fig. 1.

Figure 1a shows the class A oscillator using MCCCDTA. The oscillator consists of one grounded capacitor, one floating capacitors, and one current-controlled current amplifier with the gain $I_{B1}/8I_{B0}$. The parasitic resistance R_p is used as R_1 in the series and parallel RC networks, and the second-stage OTA in MCCCDTA is used as R_2, $R_2 = 1/g_m = 2V_T/I_{B2}$.

Figure 1b shows the class B oscillator using MCCCDTA. The oscillator consists of one grounded capacitor, one floating capacitors, one grounded resistor, and one current-controlled current amplifier. Z-Copy CCCDTA and second-stage OTA in the MCCCDTA are served as the current-controlled current amplifier with the gain I_{B2}/I_{B1}. The parasitic resistance R_p is served as R_1 in the series and parallel RC networks.

Figure 1c shows the class C oscillator using MCCCDTA. The oscillator uses one grounded resistor and two capacitors, one of the ground, the other floating. The parasitic resistance R_p is used as R_1 in the series and parallel RC networks, and second-stage OTA in the MCCCDTA is used as R_2 in ones. Z-Copy CCCDTA is used as current-controlled current amplifier with the gain $R_{Z1}I_{B1}/2V_T$.

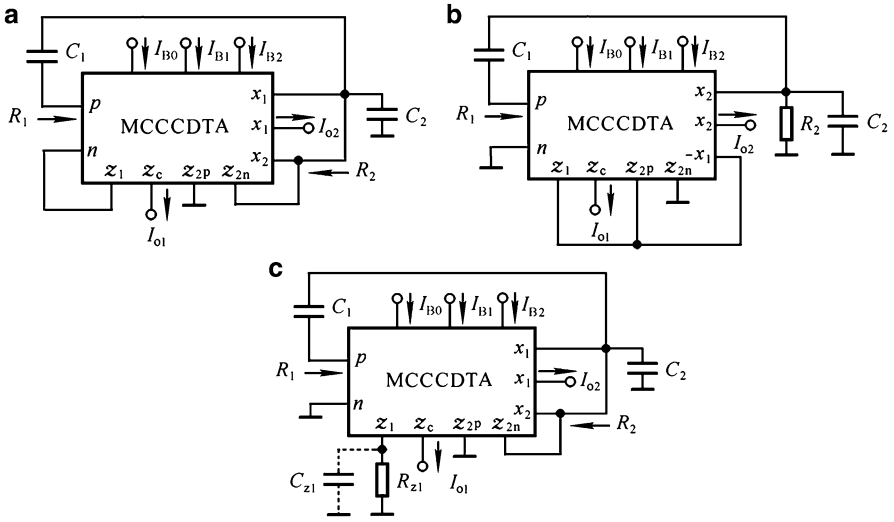

Fig. 1 (**a**) Class A oscillator, (**b**) class B oscillator, (**c**) class C oscillator

Table 1 Oscillation conditions, oscillation frequencies and current ratio of the proposed circuits

Number	Oscillation conditions	Oscillation frequencies	Current ratio	Remarks
A	$I_{B1} \geq 24I_{B0} = 6I_B$	$f_o = I_B/4\pi V_T C$	$I_{o1}/I_{o2} = 1/3$	$I_B = I_{B2} = 4I_{B0}$
B	$I_{B2} \geq 3I_{B1}$	$f_o = 1/2\pi C\sqrt{R_2 V_T/2I_{B0}}$	$I_{o1}/I_{o2} = 1/3$	
C	$I_{B1} \geq 6V_T/R_{z1}$	$f_o = I_B/4\pi V_T C$	$I_{o1}/I_{o2} = 1/3$	$I_B = I_{B2} = 4I_{B0}$

If $C_1 = C_2$, and $R_1 = R_2$, using Eqs. 5, 6, and 7 in [7], the conditions for oscillation, the frequencies of oscillation and the current ratio for three circuits can be given, respectively, as shown in Table 1.

From Table 1, for class A, if $I_B = I_{B2} = 4I_{B0}$, the frequency of oscillation, f_o, varies with bias current, I_B, whereas the oscillation condition separately varies with bias current, I_{B1}. It is clearly shown that both the condition for oscillation and f_o cannot be varied independently by controlling the bias currents.

For class B, f_o can vary with I_{B0} without affecting the condition of oscillation, which can also vary with I_{B1} or I_{B2} without affecting f_o. This means that the oscillation condition and f_o can be varied electronically and independently. However, the adjusting law for f_o is nonlinear.

For class C, if $I_B = I_{B2} = 4I_{B0}$, f_o can be turned electronically and linearly by adjusting I_B without affecting the condition for oscillation, which can also be tuned electronically and linearly by adjusting I_{B1} without affecting f_o. This means that the circuit provides the attractive feature in independent linear current control of f_o and the oscillation condition.

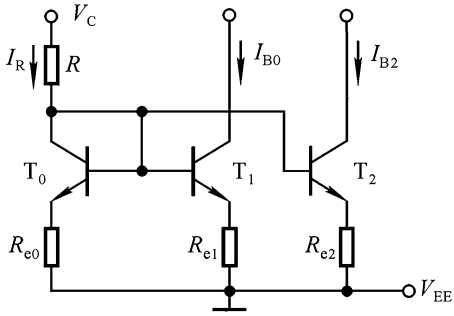

Fig. 2 Multi-transistor proportion current mirror

2.2 Adjustment Circuit for the Bias Currents

$4I_{B0}$ and I_{B2} can be varied together by a multi-transistor proportion current mirror, as shown in Fig. 2. Assuming that all transistors are matched and Early voltage is infinite, The relationship between each load current and the reference current can be written as follows:

$$I_R = \frac{V_C - V_{EE} - V_{BE}}{R + R_{e0}}, \tag{1}$$

$$I_{B0} = \frac{R_{e0}}{R_{e1}} I_R, \quad I_{B2} = \frac{R_{e0}}{R_{e2}} I_R. \tag{2}$$

Assuming $R_{e1} = 4R_{e2}$, from (2), we obtain $I_B = I_{B2} = 4I_{B0}$. It is natural that if the circuit parameters R_{e0}, R_{e1}, R_{e2}, V_{EE}, and V_{BE} are available, the load currents, I_{B2} and $4I_{B0}$, can be raised or lowered simultaneously by changing an external control voltage, V_C.

3 Non-ideal Analysis

Since the adjustment rule about the oscillation condition and frequency in Fig. 1c are non-interactive and independent, we only study non-ideal analysis for Fig. 1c. The parasitic capacitances emerging at terminal x_1 can be absorbed into the external capacitor, as they are shunt with the external one. Since the parasitic capacitors at terminal p and n can be neglected, we only take into account parasitic capacitance appearing at terminal z. It is clear that this parasitic capacitance, C_{z1}, is shunt with the external resistor. Again, analyzing the circuit in Fig. 1c produces the following the modified gain of the current-controlled current amplifier

$$A_i = \frac{g_{m1} R_z}{1 + sR_z C_{z1}} = \frac{GB}{s + GB/A_0}. \tag{3}$$

Here, A_0 is DC gain, $GB = g_{m1}/C_{z1}$, it represents the gain-bandwidth of the current-controlled current amplifier. Thus, the finite GB has changed the amplifier from the ideal current amplifier to a first-order low-pass filter. Considering (3), $C_1 = C_2$, and $R_1 = R_2$, we can get the modified characteristic equation:

$$s^3 + s^2 a_2 + s a_1 + a = 0. \tag{4}$$

Here, $a_2 = \frac{GB}{A_0} + \frac{3}{RC}$, $a_1 = \frac{GB}{RC}(\frac{3}{A_0} - 1) + \frac{1}{R^2C^2}$, $a_0 = \frac{GB}{A_0} + \frac{1}{R^2C^2}$.

In order to made the circuit to oscillate, the coefficients must satisfy $a_2 a_1 = a_0$. Hence,

$$\left(\frac{GB}{A_0} + \frac{3}{RC}\right)\left[\frac{GB}{RC}\left(\frac{3}{A_0} - 1\right) + \frac{1}{R^2C^2}\right] = \frac{GB}{A_0 R^2 C^2}. \tag{5}$$

Let $A_0 = 3 + \Delta A$ and simplify:

$$(GBRC)^2 \Delta A + 3(3 + \Delta K)(GBRC)\Delta A - 3(3 + \Delta A)^2 = 0. \tag{6}$$

As long as $GBRC >> 9$, $|\Delta A| << 3$, the above equation reduces to

$$\Delta A = \frac{27}{(GBRC)^2} = 27\left(\frac{\omega_o}{GB}\right)^2. \tag{7}$$

Hence, the critical value of the gain must be set higher than for the ideal case to sustain oscillations. The higher the frequency of oscillation, the higher is the required gain for oscillation. Consequently, unless additional circuitry is used the oscillator will drop out of oscillation as the frequency is changed to a higher value.

Using $\omega_{om} = (a_0/a_2)^{0.5}$, we can obtain the modified frequency of oscillation [8]:

$$\omega_{om} = \frac{\omega_o}{\sqrt{1 + 3A_0\omega_o/GB}} \approx \omega_o(1 - 9\omega_o/2GB). \tag{8}$$

The deviation for oscillation frequency is

$$\frac{\Delta f}{f_o} \approx -\frac{9\omega_o}{2GB}. \tag{9}$$

Hence, if A_0 is adjusted to the critical value, the higher f_o, the higher becomes $|\Delta f_o/f_o|$.

4 Simulation Results

In order to confirm the performances of the proposed circuit, the circuit model for the MCCCDTA [7] is constructed on transistor QNL and QPL by ELECTRONICS WORKBENCH 5.0 software (EWB5.0), and then Fig. 1c is created. Finally, the circuit of Fig. 1c is simulated with parameters: $V_{CC} = 1.5$ V, $V_{EE} = -1.5$ V, $C_1 = C_2 = 1$ nF, $R_{z1} = 1\text{k}\Omega$, $I_B = I_{B2} = 4I_{B0} = 250$ μA, and $I_{B1} = 156$ μA. Theoretically, the circuit will oscillate when $I_{B1} = 156$ μA, as mentioned in Table 1. However, in practical behavior, I_{B1} must be 160 μA. It is slightly higher than 156 μA to sustain oscillation, as mentioned in (5). The simulation result is shown in Fig. 3. It goes without saying that the circuit really realizes a sinusoidal oscillation. Using Table 1 can get the design value: f_o =765.556 kHz and using the pointer in EWB5.0 can obtain the actual value: $f_{om} = 571.429$ kHz, so the deviation for f_o is (571.429–765.556)/765.556 = −25.36 %. The error results from the parasitic capacitance emerging at terminal z_1. Using the frequency analysis in EWB5.0, we receive the parasitic capacitance $C_{z1} = 0.03006$ nF. Substituting these data into (6) gives that the theoretical expected value for relative error is −21.09 %.

To illustrate the tuning characteristic of f_o by adjusting I_B, letting $C_1 = C_2 = 1$ nF, $R_{z1} = 1\text{k}\Omega$ $I_B = I_{B2} = 4I_{B0} = 125$ μA, and $I_{B1} = 158$ μA, we obtain the simulation result shown in Fig. 4. Similarly, the deviation for f_o is (308.642–382.778)/382.778 = −19.37 %, $C_{z1} = 0.04502$ nF, and the theoretical expected value for relative error is −16 %.

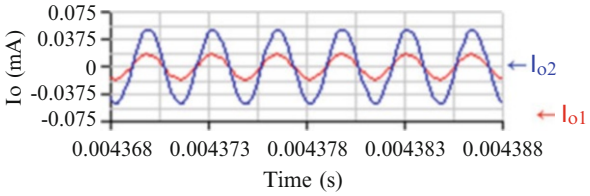

Fig. 3 Waveforms for the circuit of Fig. 1c with IB = IB2 = 4IB0 = 250 μA, C1 = C2 = 1 nF, and IB1 = 160 μA

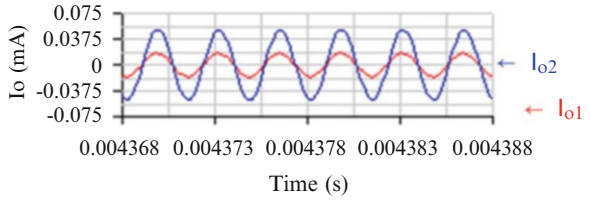

Fig. 4 Waveforms for the circuit of Fig. 1c with IB = IB2 = 4IB0 = 125 μA, C1 = C2 = 1 nF, and IB1 = 158 μA

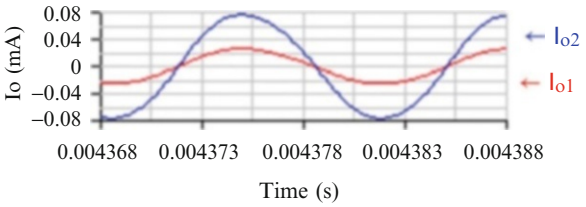

Fig. 5 Waveforms for the circuit of Fig. 1c with IB = IB2 = 4IB0 = 250 μA, C1 = C2 = 10 nF, and IB1 = 156 μA

It is seen that the deviation will be increased when the design value for f_o increases. By setting $C_1 = C_2 = 10$ nF, $R_{z1} = 1\text{k}\Omega$ $I_B = I_{B2} = 4I_{B0} = 250$ μA, and $I_{B1} = 156$ μA, the simulation result is given in Fig. 5. In like manner, the deviation for f_o is (76.3359–76.5556)/76.5556 = −0.29 %, $C_{Z1} = 0.03$ nF, and the theoretical expected value for relative error is −2.1 %. It is noted that the circuit simulation results are basically consistent with theory.

When $I_B = I_{B2} = 4I_{B0} = 250$ μA, $C_1 = C_2 = 10$ nF, and $I_{B1} = 156$ μA, the total harmonic distortion of the circuit THD ≈ 1.75 %. The oscillations growing exponentially in amplitude cause the distortion while the OTA and the current mirror in MCCCDTA come near to their saturation regions. The oscillator can maintain output signal with low distortion.

5 Conclusion

Based on the traditional Wien-bridge oscillator, three classes for current-mode Wien-bridge oscillator employing single MCCCDTA are provided, which furnish two current outputs from high output impedance terminals and enjoy low passive and active sensitivities and are canonic in component count. The oscillation condition and frequency of class C oscillator can be tuned linearly and independently by means of controlling bias currents of the MCCCDTA. The main disadvantage of the circuit is that f_o is dependent on temperature. In additional, there is a floating capacitor. Therefore, further research is needed.

References

1. Boutin N (1983) Two new single op-amp RC bridge T oscillator circuits. IEE Proc G Electron Circuits Syst 130(5):222–224
2. Sena R, Kumar BA (1989) Linearly tunable Wien bridge oscillator realised with operational transconductance amplifiers. Electron Lett 25(1):19–21
3. Soliman AM (2010) Generation of CCII and ICCII based Wien oscillators using nodal admittance matrix expansion. AEU-Int J Electron Commun 64(10):971–977
4. Jaikla W et al (2008) A simple current-mode quadrature oscillator using single CDTA. Radioengineering 17(4):33–40

5. Li YA (2010) Electronically tunable current-mode quadrature oscillator using single MCDTA. Radioengineering 19(4):667–671
6. Siripruchyanun M, Jaikla W (2008) CMOS current-controlled current differencing transconductance amplifier and applications to analog signal processing. AEU-Int J Electron Commun 62(4):277–287
7. Li YA (2012) A new single MCCCDTA based Wien-bridge oscillator with AGC. AEU-Int J Electron Commun 66(2):153–156
8. Budak A (1991) Passive and active network analysis and synthesis. Waveland Press, Boston, pp 461–462

Improved Phase-Locked Loop Based on the Load Peak Current Comparison Frequency Tracking Technology

Bingxin Qi, Hui Zhu, Yonglong Peng, and Yabin Li

Abstract Considering that the induction heating power supply controlled by pulse density modulation operated in the free resonance state, it was impossible to precisely detect a very small amount of load current, a conventional PLL (Phase-Locked Loop) circuit does not work properly, so a improved PLL frequency tracking control technology is presented in this paper. When the power stage decreased the discharge power into 1–10 % of the full power, the S/H (Sample and Hold) circuit and the PCD (Peak Current Detector) were used to guarantee the inverter working at the vicinity of the resonant frequency. The output signal from PCD opened and closed the S/H to drive the VCO (voltage-controlled oscillator), and a selected load peak current reference value was compared with the actual load peak current to control the PCD. Finally the control strategy is verified by using the Matlab / Simulink simulation results, the power stage can always work in the state of zero current and zero voltage switching and the phase-locked failure is avoid.

Keywords Induction heating power supply • Pulse density modulation • Frequency tracking control • Improved phase-locked loop

1 Introduction

Induction heating technology is developed in the direction of high-power and high frequency. Different heating process such as smelting, diathermy, annealing and hardening have special requirements for the power and frequency, and then leads to a variety of power conditioning and frequency tracking control method. According to the adjustment link, the power modulation method can be divided into rectifier regulation, DC side control and inverter power regulation [1, 2].

B. Qi (✉) • H. Zhu • Y. Peng • Y. Li
North China Electric Power University, Baoding, China
e-mail: qbingxin@163.com

W. Wang (ed.), *Mechatronics and Automatic Control Systems*, Lecture Notes in Electrical Engineering 237, DOI 10.1007/978-3-319-01273-5_78,

The inverter side power regulation in line with different control ways can be divided into pulse frequency regulation [3], pulse phase shift modulation [4] and pulse density modulation. Power switching devices using the pulse frequency regulation and pulse phase shift modulation method [5, 6] will work incessantly in the non-zero current and non-zero voltage switching state, it will lead to the increase of switching losses and electromagnetic noise interference [7]. In addition, the pulse frequency regulation and pulse phase shift modulation will change the phase between output voltage and current during regulating the output power, thus affecting the performance of the frequency tracking controller or phase-locked loop controller [8]. The pulse density modulation proposed in literature [9] adopt a reasonable choice of pulse sequence to realize a greater adjustment range in the output power and ensure that the inverter always operating in a quasi- resonance state, thus achieving zero current and zero voltage switching. However, the restoration from the free resonance state to the output power state needs to re-lock the operating frequency of the inverter, which could easily lead to the system out of control.

To avoid phase lock failure after the end of the pulse density modulation period, a improved phase-locked loop control scheme based on the load peak current is proposed in this paper, when the induction heating power supply changes from the powering state to a free resonance state and again returned to the powering state, according to the sampling hold circuit, two different reference current values are analyzed and calculated, a current selection scheme corresponding to the minimum pulse density value is proposed, the simulation results verified the feasibility of the proposed scheme.

2 The Principle of Pulse Density Modulation

According to the main circuit structure shown in Fig. 1, the equation can be expressed as follows:

$$\mathrm{L}\frac{di_o}{dt}+\frac{1}{\mathrm{C}}\int i_o dt+\mathrm{r}i_o=\frac{4\mathrm{U_d}}{\pi}\sin\omega t \tag{1}$$

Only considering the fundamental voltage component added to the load when the load circuit is at the resonance state. Where, $\omega = \omega r = 1/(LC)1/2$, assume that $2\omega rL/r = 2Q >> 1$, Q represents the quality factor of the resonant circuit, so load current can be given:

$$i_o=\frac{4\mathrm{U_d}}{\pi\mathrm{r}}(1-\mathrm{e}^{-\frac{r}{2L}t})\sin\omega t \tag{2}$$

Although the load resonant circuit is a second order system, however, Fig. 2 shows that the envelope line of the load resonant current is fist-order response, and

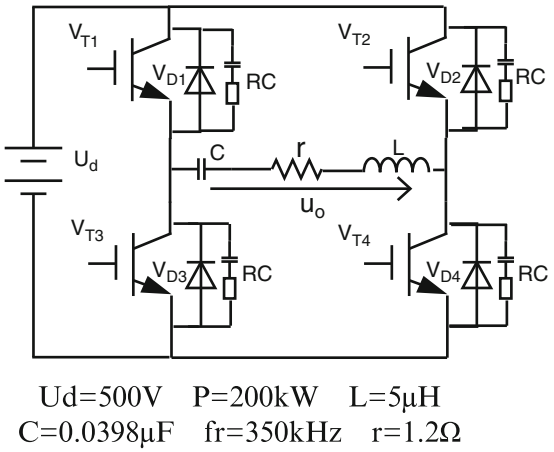

Fig. 1 The main circuit of series resonant inverter

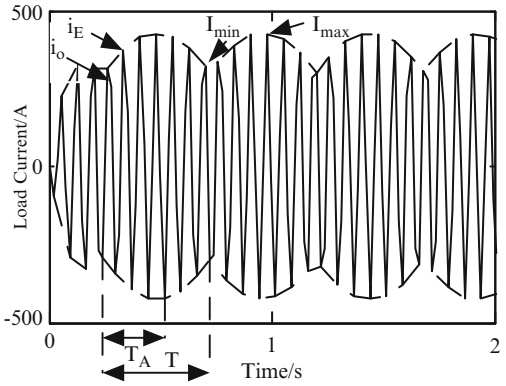

Fig. 2 The load current modulated by pulse density

the time constant $\tau = 2\,L/r$, then the envelope line of the resonant current iE can be expressed as:

$$\begin{cases} i_E(t) = \hat{I}(1 - e^{-\frac{t}{\tau}}) + I_{min}e^{-\frac{t}{\tau}}(0 \le t \le T_A) \\ i_E(t) = I_{max}e^{-\frac{t-T_A}{\tau}}(T_A \le t \le T) \end{cases}. \tag{3}$$

Where:

$$I_{min} = \hat{I}\frac{e^{\frac{T_A}{\tau}} - 1}{e^{\frac{T}{\tau}} - 1} \tag{4}$$

$$I_{max} = \hat{I}\frac{1 - e^{-\frac{T_A}{\tau}}}{1 - e^{-\frac{T}{\tau}}} \tag{5}$$

$\hat{I}$ is the current when the modulation ratio is $D = T_A/T = 1$.

3 Improved Phase-Locked Loop Control Based on the Load Peak Current Comparison

This paper uses the load current comparison control method, introduces the load peak current detection section and compares the load current with the preset reference current value, when the peak current is higher than the set reference value, the sample hold circuit works at the state of sampling, the frequency tracking circuit still operating in the normal phase-locked loop, however, when the peak current detection value is lower than the reference current, sample and hold circuit will no longer receive the output signal of the filter, but keep the signal in the last moment before the state transition to drive the VCO continue working, the control principle is shown in Fig. 3.

However, induction heating surface treatment sometimes needs to reduce the output power to 10 % of the rated power or even lower, namely, when the pulse density modulation ratio decreases, the output load current will be small, according to present resolution and accuracy, the peak current detector have been unable to accurately detect such a small current, thus the frequency tracking circuit will not function properly. So how to select the appropriate current reference value ensure that the frequency tracking control circuit to work properly must be solved.

Further analysis, consider the main circuit parameters shown in Fig. 1, the load quality factor $Q = 10$, the difference of the maximum peak current Imax and the minimum peak current Imin is shown in Fig. 4.

Noted from Fig. 4 that when $D > 0.1$, the difference between the maximum value Imax and the minimum value Imin increases as the modulation ratio significantly increases, when $D = 0.5$ the difference is the maximum, the performance of the phase-locked loop frequency tracking control circuit in the small fluctuations of the sampled signals is much better than the larger signal fluctuations, the smaller the signal fluctuations, the higher the resolution of the phase-locked loop, the more sensitive to changes in the signal phase, while for the large disturbance is not sensitive, which leads to the judgment delay, even in some cases beyond its phase capture range leads to lock failure.

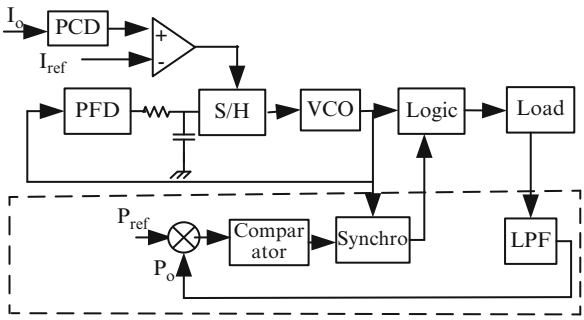

Fig. 3 The frequency tracking circuit based on load peak current detection

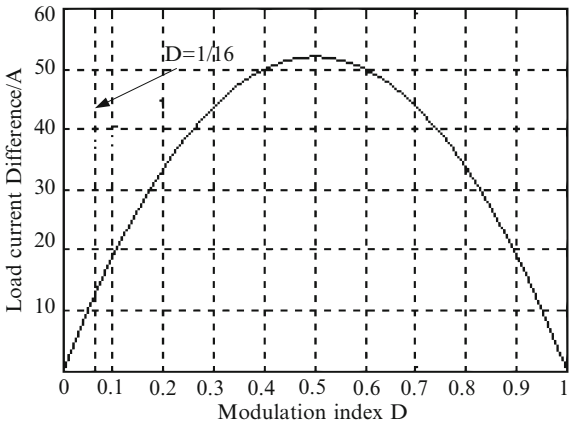

Fig. 4 Load current difference Q = 10

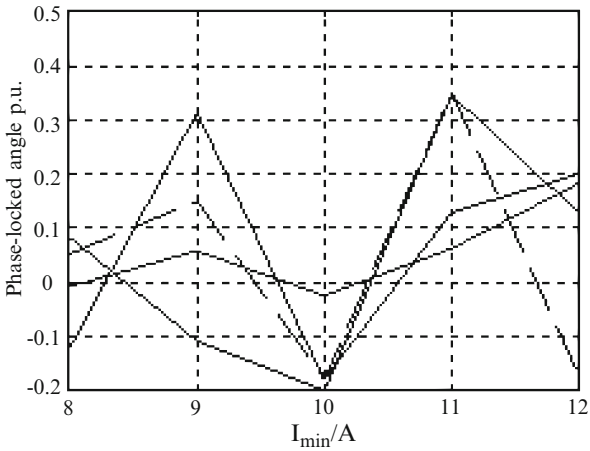

Fig. 5 Phase-locked angle as a function of minimum current

Based on the above analysis, D = 1/16 as the lower bound and 1 ‰ as the gain, infinitely approaching to D = 0.1, the function relationship of the phase-locked angle and the corresponding minimum current of the peak current Imin ranging from D = 1/16 to D = 0.1 is obtained, as shown in Fig. 5.

It can be reduced that when the phase-locked angle is a very small inductive angle ranging from 0 to 0.1, Imin can be equal to 9.5, 10.5, 11.5A. Then the optimal peak current reference value selection scheme will be obtained by simulation analysis.

4 Simulation Analysis

A single phase series resonant inverter model is built by utilizing the Matlab/Simulink tools, main circuit parameter is shown in Fig. 1, DC source voltage is $U_d = 500$ V, the resonant load parameters are $L = 5$ μH ,$C = 0.0398$ μF, $r = 1.2\Omega$, the rated power is $P = 200$ kW, the resonant frequency is $f_r = 350$ kHz, RC snubber parameters are $R = 11.5\Omega$,$C = 2200$ pF, the main circuit lead inductance is $L_s = 0.01$ μH, the output power control using pulse density modulation.

Adopting improved phase-locked loop control based on the peak load current comparison, phase-locked switching process is analyzed as follows. Under the condition that the DC voltage Ud = 500 V is invariable, regulating the DC side current achieves the purpose of adjusting the output power, Fig. 6 shows that when DC current reduced from 90A to 40A the corresponding output load current and voltage waveform.

1. When the peak load current comparison control is not considered, the pulse density modulation ratio D = 1: 2 corresponding to the condition that the output power decrease, the output voltage and current waveforms are shown in Fig. 7, the phase-lock tracking control circuit output waveform is shown in Fig. 8.

   In Fig. 7, at the free resonance state, the load power flows through the RC snubber and anti-paralleled diode, then the phase angle selection must be accurate, and can predict the phase-locked position angle in the next pulse density modulation cycle, when the modulation ratio is 1: 2 or even smaller, as shown in Fig. 8, the inductive angle is so large that a voltage spike is produced

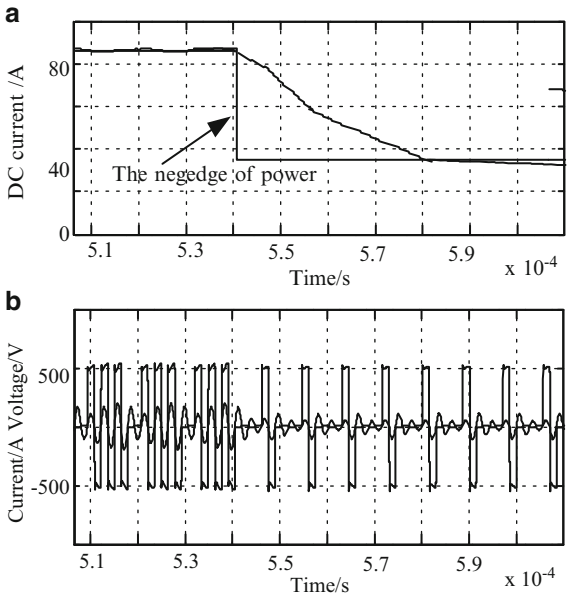

Fig. 6 The output voltage and current when power decrease

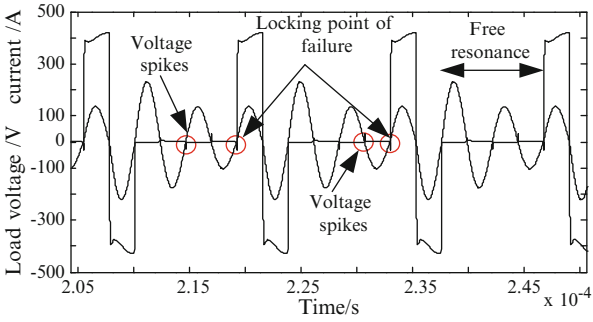

Fig. 7 The output voltage and current when D = 1:2

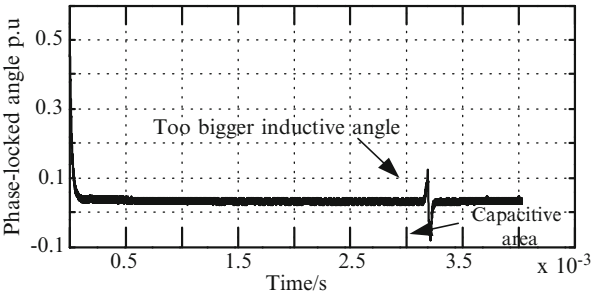

Fig. 8 The change of phase-locked angle when modulation index D decrease

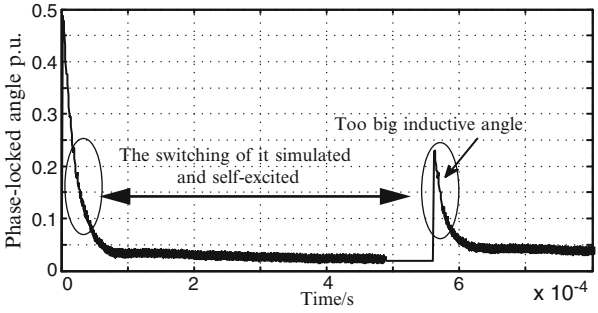

Fig. 9 Added to sample and hold device phased-locked angle

during the free resonance state, the switch loss increases, which leads to the power loss increasing, even at the beginning of the next modulation period, entering the capacitive area, causing the phase lock failure and then burning power electronic devices.

2. Considering the load current comparison control, the pulse density modulation ratio is D = 0.3 or even lower values, we can consider a limit state, when D = 1/16, the corresponding pulse density modulation minimum value is calculated by the formula (6) that Iref = 7.95A, the phase control angle is shown in Fig. 9.

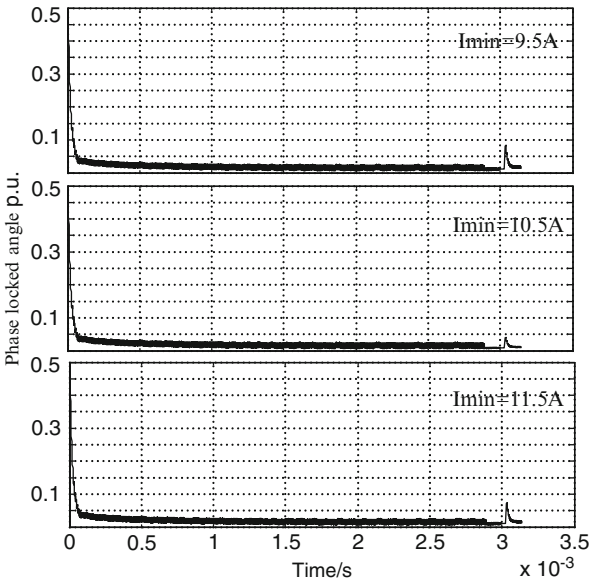

Fig. 10 Phase-locked angle corresponding to selected three current value

Figure 9 shows, set Iref = 7.95A as the peak current reference value, when the load current works at the free resonance state, the sampling hold circuit works at the hold state, keep the lock phase signal in the last moment before the state transition to drive the VCO to generate the control pulses, as the linear part shown in the graph; but when changes from the free resonance state back to the powering state, if switching phase-locked state at the minimum current reference value Iref = 7.95A, as shown in Fig. 9, a large inductive angle running at an initial state can be observed, repeating the separate-excitation turns to self-excitation process when the inverter startup, at that time the separate-excitation control circuit has stopped the work, which shows the frequency tracking control circuit is out of control, turns into the "free resonance" state, at this time any external electromagnetic disturbance or fault will cause this condition amplifying, switching devices loss increasing even being burned.

According to the above analysis, when the frequency tracking control circuit turns from the powering state to the free resonance state, set a small load current as the reference value of the peak current comparison to ensure reliable work, a load current value is also calculated as the peak current reference value when changes free resonance state back to the powering state to further improve the phase-locked loop load resonant frequency tracking speed. According to the analysis of 3.2 and phase angle and the minimum current Imin distribution relationship in Fig. 5, select Iref = 9.5, 10.5, 11.5A respectively, the corresponding phase angle experimental waveforms are shown in Fig. 10. The Imin = 10.5A is the most appropriate peak current reference value when changing from the free resonance state back into the powering state.

5 Conclusion

In order to meet the requirement of switching frequency constant when the output power drops below 10 % of the rated power in the heating process, an improved phase-locked loop control method based on the load peak current comparison is proposed in this paper. Adding the sampling hold device to the existing phase-locked loop circuit without changing the capture range and accuracy condition, furtherly improving the tracking speed of the phase-locked loop on the load resonant frequency even the load current is quite small, which ensures the inverter switching devices continue working at zero voltage and zero current switching state when switching between the free resonance state and the powering state. Compared with the traditional phase-locked loop control, the proposed control method can further reduce the power loss of power switching devices and improve the operating efficiency of equipment.

References

1. Fujita H, Akagi H (1996) Pulse density modulated power control of a 4 kW, 450 kHz voltage-source inverter for induction melting applications. IEEE Trans Ind Appl 32(2):279–286
2. Hong Lv, Yushui Huang, Zhongchao Zhang (2003) The PWM-PFM control method of induction heating power supply. Power Electron Technol 37(1):8–11
3. Hong Mao, Zhaolin Wu, Zhencheng Hou (1998) Induction heating power supply zero phase difference frequency tracking control circuit. Power Electron Technol 32(2):69–72 (In Chinese)
4. Jun Yang (2004) Research on the IGBT super audio frequency induction heating power supply phase tracking. Tsinghua University, Beijing
5. Liqiao Wang, Yushui Huang, Changyong Wang, Zhongchao Zhang (2001) Research on induction heating power supply based on a novel phase-shifted control. Power Electron Technol 35(1):3–4 (In Chinese)
6. Tianming Pan (1996) Modern induction heating device. Metallurgical Industry Press, Beijing, pp 125–196
7. Tianming Pan (1983) Power frequency and medium frequency induction furnace. Metallurgical Industry Press, Beijing, pp 68–89
8. Yabin Li, Yonglong Peng, Heming Li (2006) The optimal ZVS control of series resonant inverter. Power Electron Technol 40(3):14–16 (In Chinese)
9. Zonggang Qi, Peng Liu, Huiming Chen (2003) Research on power modulation for induction heating[J]. Heat treatment metals (China) 2003(7):54–57 (In Chinese)

Optimization of Low-Thrust Orbit Transfer

Zhaohua Qin, Min Xu, and Xiaomin An

Abstract A Gauss pseudospectral method is used to optimize the interplanetary low-thrust orbit transfer. The Gauss pseudospectral method is utilized to parameterize the orbit transfer. In order to solve the large-scale parameters multi-constraints optimization problem, the sequential quadratic programming (SQP) is used. Then, the optimization method is demonstrated on an Earth-Mars low-thrust orbit transfer application by the solar electric propulsion. The numerical results show that the method is effective and rapid in finding the optimal orbit transfer and does not require particular initial guesses.

Keywords Orbit transfer • Low-thrust • Fast optimization • Gauss pseudospectral

1 Introduction

Historically, the methods to optimize interplanetary low-thrust orbit transfer can be divided into two categories: one is called indirect methods and the other is direct methods [1, 2]. The two-point boundary-value problem can be solved by indirect methods. However, direct methods turn optimal control problem into nonlinear programming problem (NLP) [3–5].

In this paper, we research a method for optimal orbit transfer called the Gauss pseudospectral method. The complicated orbit transfer optimization problem is translated into a large-scale parameters optimization problem with multi-constraints. Thus the NLP can be solved numerically by the SQP.

Z. Qin (✉) • M. Xu • X. An
College of Astronautics Northwestern Polytechnical University, Xian, China
e-mail: xinixn812@163.com

W. Wang (ed.), *Mechatronics and Automatic Control Systems*, Lecture Notes in Electrical Engineering 237, DOI 10.1007/978-3-319-01273-5_79,

2 The Optimization of Low-Thrust Orbit Transfer

The motion of the low-thrust spacecraft around the sun is described by the Cartesian coordinates:

$$\begin{cases} \dot{\boldsymbol{r}} = \boldsymbol{v} \\ \dot{\boldsymbol{v}} = -\mu \boldsymbol{r}/r^3 + \frac{T}{m}\boldsymbol{u} \\ \dot{m} = -\frac{T}{I_{sp} g_0} \end{cases}. \tag{1}$$

Where $m = m_0 - |\dot{m}|t$. m is the spacecraft mass, m_0 is its initial mass, $|\dot{m}|$ is the engine fuel consumption of seconds, T is the engine thrust equal to $2\eta P_0 / (I_{sp} g_0 r^2)$, t is the flight time. P_0 is its input power in 1 AU, I_{sp} is its specific impulse, and g_0 is the gravitational acceleration. $\boldsymbol{u} = [u_x, u_y, u_z]$ is defined as the unit vector of the thrust.

With the engine continuously working, the optimal-fuel performance index is evaluated at:

$$J_1 = -(m_0 - \int_{t_0}^{t_1} \dot{m} dt) = -m_1 \tag{2}$$

The optimal-time performance index is evaluated at:

$$J_2 = \int_{t_0}^{t_1} dt = t_1 - t_0 \tag{3}$$

In order to make full use of the advantages of the low-thrust propulsion system, we presume the launch of the spacecraft energy be zero, $C_3 = 0$, the trajectory musts satisfy the initial and final boundary conditions:

$$\begin{cases} \boldsymbol{E}_1[\boldsymbol{x}(t_0), t_0] = \boldsymbol{x}(t_0) - \boldsymbol{x}_1(t_0) = \boldsymbol{0} \\ \boldsymbol{E}_2[\boldsymbol{x}(t_1), t_1] = \boldsymbol{x}(t_1) - \boldsymbol{x}_2(t_1) = \boldsymbol{0} \end{cases} \tag{4}$$

During the transfer, the thrust vector direction must satisfy the following conditions:

$$C[\boldsymbol{u}(t), t] = u_x^2 + u_y^2 + u_z^2 = 1 \tag{5}$$

The optimal parameter is defined as:

$$\boldsymbol{Z} = [t_0, t_1, \boldsymbol{x}(t), \boldsymbol{u}(t)]^T \tag{6}$$

With the description of the problem, the parameter of the optimal problem concludes the discrete-time variable, the continuous trajectory and control variables. But the continuous variable cannot be recalibrated directly, and it must be processed and then the adjustable discrete variables can be obtained.

It is noted that it can transform the problem from the time interval $\kappa \in [-1, 1]$ to the time interval $t \in [t_0, t_1]$:

$$\kappa = -1 + \frac{2(t - t_0)}{t_1 - t} \tag{7}$$

Orthogonal collocation of the dynamics is performed at the Legendre-Gauss (LG) points in the Gauss pseudospectral method. The state can be approximated by Lagrange interpolating polynomials L,

$$\boldsymbol{x}(\kappa) \approx \boldsymbol{X}(\kappa) = \sum_{i=0}^{N} \boldsymbol{X}(\kappa_i) L_i(\kappa) \tag{8}$$

Where $L_i(\kappa)$ are defined as

$$L_i(\kappa) = \prod_{j=0, j \neq i}^{N} \frac{\kappa - \kappa_j}{\kappa_i - \kappa_j}, i = 0, \ldots, N \tag{9}$$

Additionally, the control can be approximated by Lagrange interpolating polynomials L^* as

$$\boldsymbol{u}(\kappa) \approx \boldsymbol{U}(\kappa) = \sum_{i=1}^{N} \boldsymbol{U}(\kappa_i) L_i^*(\kappa) \tag{10}$$

Where

$$L_i^*(\kappa) = \prod_{j=1, j \neq i}^{N} \frac{\kappa - \kappa_j}{\kappa_i - \kappa_j}, i = 1, \ldots, N \tag{11}$$

Note that the approximation for the control is not the only allowable control approximation, but it has produced very good results when compared with other control approximations.

Base on the differential expression of Eq. 8, we can obtain

$$\dot{\boldsymbol{x}}(\kappa) \approx \dot{\boldsymbol{X}}(\kappa) = \sum_{i=1}^{N} \boldsymbol{X}(\kappa_i) \dot{L}_i(\kappa) \tag{12}$$

Each Lagrange polynomial derivative in the LG points can be expressed as a differential approximation matrix, $\boldsymbol{P}$, whose elements are determined offline as follows:

$$P_{ki} = \dot{L}_i(\kappa_k) = \sum_{l=0}^{N} \frac{\prod_{j=0, j\neq i,l}^{N} (\kappa - \kappa_j)}{\prod_{j=0, j\neq i}^{N} (\kappa_i - \kappa_j)} \tag{13}$$

Then the dynamic constraint is as follows:

$$\begin{aligned} &\boldsymbol{F}(\boldsymbol{X}_k, \boldsymbol{U}_k, \kappa_k; t_0, t_1) \\ &= \sum_{i=0}^{N} D_{ki} \boldsymbol{X}_i - \frac{t_1 - t_0}{2} \boldsymbol{f}(\boldsymbol{X}_k, \boldsymbol{U}_k, \kappa_k) = 0 \end{aligned} \tag{14}$$

Where $\boldsymbol{X}_k \equiv \boldsymbol{X}(\kappa_k), \boldsymbol{U}_k \equiv \boldsymbol{U}(\kappa_k)$. Then we can define additional variables in the discretization as follows:

$$\begin{cases} \boldsymbol{X}_0 \equiv \boldsymbol{X}(-1) \\ \boldsymbol{X}_1 \equiv \boldsymbol{X}_0 + \frac{t_1 - t_0}{2} \sum_{k=1}^{N} w_k \boldsymbol{f}(\boldsymbol{X}_k, \boldsymbol{U}_k, \kappa_k; t_0, t_1) \end{cases}. \tag{15}$$

Where $\boldsymbol{X}_1$ is defined in terms of $\boldsymbol{X}_k$ and $\boldsymbol{U}_k$,$\boldsymbol{f}$ is the variable of the Eq. 1, and w_k are the Gauss weights, $w_k = \int_{-1}^{1} \prod_{i=1, i\neq k}^{N} \frac{\kappa - \kappa_i}{\kappa_k - \kappa_i} d\kappa, k = 1, \ldots, N$.

Finally, it is noted that discontinuities in the state or control can be effectively dealt with by dividing the trajectory into phases, where the dynamics are transcribed at each phase and connected together with the additional phase interface constraints. This procedure has been applied to many fields.

Thus, the interplanetary low-thrust optimization problem can be converted to parameters of the constraint optimization problem. The optimal parameter concludes the launch time, the fair time and the variable of the state and control to each node.

$$\boldsymbol{Z}_1 = [\boldsymbol{X}_0^T, \boldsymbol{X}_1^T, \ldots, \boldsymbol{X}_f^T, \boldsymbol{U}_1^T, \boldsymbol{U}_2^T, \ldots, \boldsymbol{U}_N^T, t_0, t_1]^T \tag{16}$$

The problem is transcribed to the NLP, and it is solved by using the solver of the SQP.

3 Results

An Earth-Mars direct transfer is presented. Its parameters: the solar array power at 1 AU P_0 is 6.5 kW, the constant I_{sp} is 3,100 s, the engine efficiency is 0.65, and the initial spacecraft mass is 1,200 kg. And it uses the astrosphere calendar, DE405, and the Matlab programming environment on a 3.06 GHz Pentium 4 PC.

The launch time window is from January 1, 2014 to December 31, 2014, and the maximum duration is 500 days. The optimal variable and the restriction equation solutions to N = 29 are 291 and 240. The NLP has been used to solve the TOMLABT version of the NLP solver SNOPT [6].

The optimal result is shown in Figs. 1, 2, 3, and 4.

The optimization solution concludes the launch time is April 10, 2014, the flight time is 306.6370 days, the remaining mass is 912.3415 kg, the iterative process is 52 steps and the computing time is 58.467 s.

The optimization result is good, which shows that the method can get the optimal transfer trajectory rapidly and accurately.

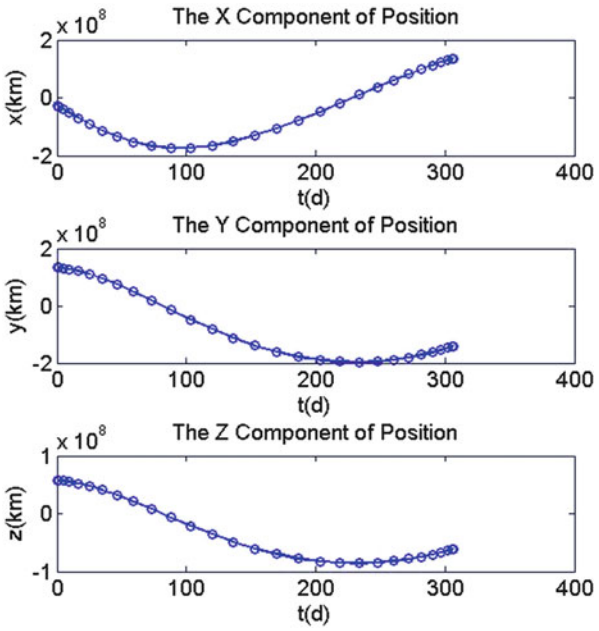

Fig. 1 Optimal position vector

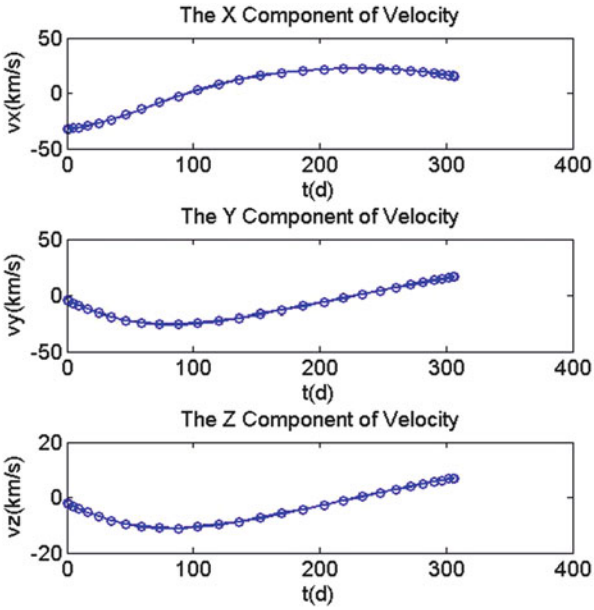

Fig. 2 Optimal velocity vector

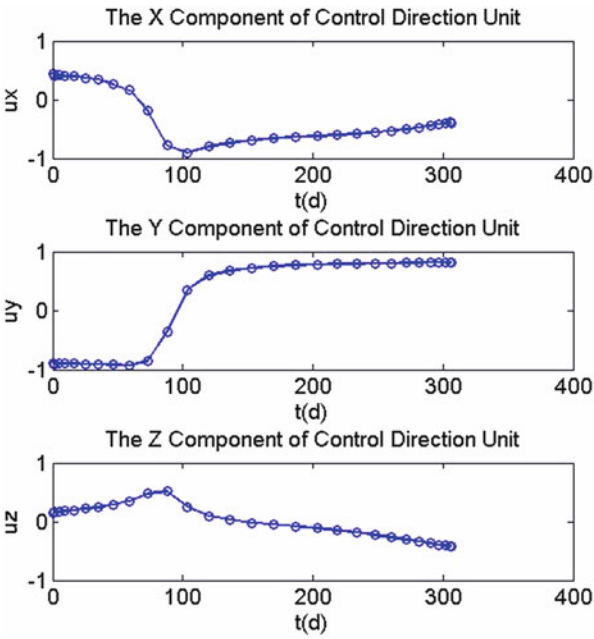

Fig. 3 Optimal control steering

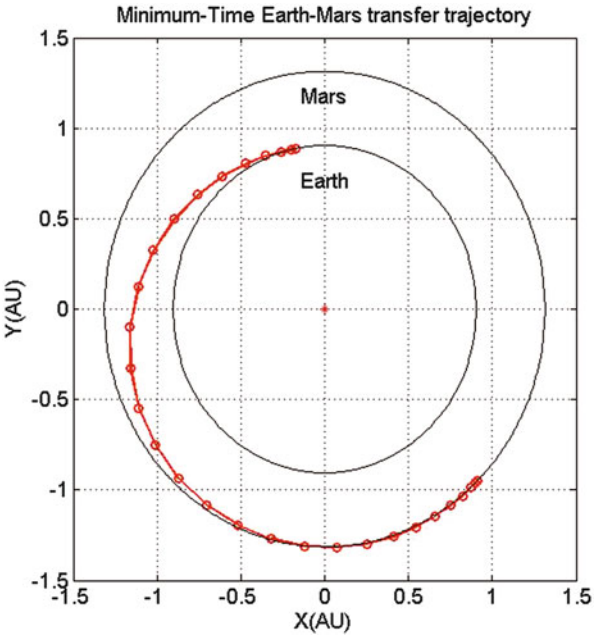

Fig. 4 Optimal Earth-Mars direct transfers

4 Conclusion

This paper studies the rapid optimization of orbit transfer which bases on Gauss pseudospectral method. In the optimal transfer, the method turns the transfer optimal control problem into the NLP, and avoids the huge compute capacity, the real-time identification, the sensitivity to guess value and so on. The results obtained in this paper show that the optimization method adopted for the optimization of the interplanetary low-thrust orbit transfer demands less accurate initial guesses and has good search capability with high accuracy.

References

1. Gao Yang (2003) Advances in low-thrust trajectory optimization and flight mechanics. University of Missouri-Columbia, Columbia
2. Enright PJ, Conway BA (1991) Optimal finite-thrust spacecraft trajectories using collocation and nonlinear programming. J Guid 14(5):981–985
3. Ren Yuan, Cui Pingyuan, Luan Enjie (2007) An earth-mars low-thrust trajectory design based on hybrid method. J Harbin Inst Technol 39(3):359–362
4. Kluever CA, Oleson SR (1998) Direct approach for computing near-optimal low-thrust earth-orbit transfers. J Spacecraft Rockets 35(4):509–515
5. Benson D (2005) A Gauss pseudospectral transcription for optimal control. Massachusetts Institute of Technology, Boston
6. Gill PE, Murray W, Saunders MA (2002) SNOPT: an SQP algorithm for large scale constrained optimization. SIAM J Optim 12(4):979–1006

Self-Healing Control Method Based on Hybrid Control Theory

Qiang Zhao, Meng Zhou, and XinQian Wu

Abstract Due to the overall optimum ability, the hybrid power control technology is particularly useful for self-healing control for the grid. Based on the study of hybrid control theory, this article introduced the WAMS-based (wide area measurement system) real-time information platform to the physical layer of hybrid power control model and applied the modified model into self-healing control. Meanwhile, based on the modified model, the article established an easily-attainable self-healing control model, and produced solutions to some key problems. Since the real-time information alternative to the traditional observer, the self-healing control system based on the modified hybrid power control technology is suitable for the self-healing of large power grid because it is simple, overall optimum and easy to extend.

Keywords Power control • Self-healing control • WAMS • Event-driven

1 Introduction

In recent years, with the constant increase of the demand of grid stability and power supply quality with the mankind, the research on smart grid is intensifying constantly. Although the definition of smart grid remains controversial, however, overall, the smart grid should have the following characteristics [1, 2]: self-healing, interactive, optimization, integration, compatible. Self-healing is not only an important safeguard to ensure automated stable operation of the grid, but also an important symbol of the smart grid. So how to achieve self-healing of the grid has become the focus of the smart grid.

Q. Zhao • M. Zhou (✉) • X. Wu
School of Control and Computer Engineering, North China Electric Power University, Beijing, China
e-mail: zhaoqiang@ncepu.edu.cn; Shenghuo1988@hotmail.com; happyskywxq@qq.com

W. Wang (ed.), *Mechatronics and Automatic Control Systems*, Lecture Notes in Electrical Engineering 237, DOI 10.1007/978-3-319-01273-5_80,

The existing study of self-healing often emphasis on the reality grid with corresponding characteristics, and then look for a self-healing control method solution which is suitable to this grid, such as reference [3]. These control methods can be implemented on the local grid self-healing controlling, however, they cannot be applied to the overall grid for lacking of compatibility and expandability. Self-healing grid control covers a lot of fields of new technology and new progress, such as automatic control, relay protection, computers and software, Applied Mathematics. It is an integrated software and intelligent device control technology.

As a system composite in parallel or serial of continuous component and discrete component, the hybrid system [4] is well suited for the control of multi-objective large modern power system. At present, hybrid control theory has been successfully used in the construction of the grid voltage control system, and received a good effect.

This paper analyzed the basic conditions of self-healing, modified the theory of hybrid power control, and introduced the concept of hybrid control to grid self-healing control. Based on the modified theory, grid self-healing system model was established.

2 Hybrid Power Control Theory and Its Improvement

The hybrid system [4] contains both discrete behavior (behavior with state and output) and continuous behavior. So how do describe discrete and continuous dynamic characteristics and mutual relations correct and unified has become a research focus on the modeling of hybrid systems. Hybrid power control theory [5], which made use of the concept of the event generator, compare the value of continuous variables in the grid or the value of these variables as independent variables "event function" with the prior defined criteria. Whether the incident consistent or inconsistent, an event will occur.

Based on the WAMS grid real-time information platform, this paper introduces hybrid power system model underlying as an alternative to traditional observer, so that the model of the controlled layer has the capabilities recording network real-time information, and then pass the data have been processed by the real-time data transmission channel to level of decision-making and decision makers only judge event and issue a directive. Improved hybrid power control model has a more cleared structure, while the introduction of WAMS can enhance the real-time of closed-loop control and the entire process of the controlled layer.

In Fig. 1, $u(t)$ represent for the bottom of the power components of the original continuity-based closed-loop control; $x(t)$ represent for the continuous change of the dynamic power system variables; $y(t)$ is the underlying power system state output variables in continuous time; Γ is the formation of discrete events; A is the event used for display; $u_D(t)$ represents for collection operational control inspired by the events.

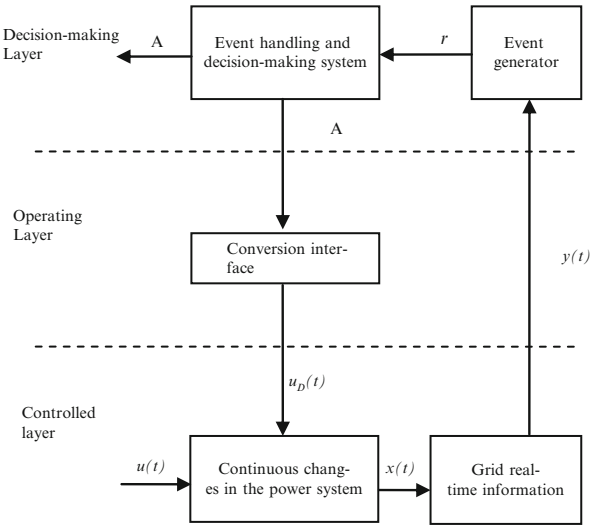

Fig. 1 Modified hybrid power system model

In summary, the hybrid power control system is a collection of continuous process of regulation and discrete scheduling decision-making process, and can achieve the power system multi-goal drive superior purpose, it suited for self-healing control of power systems well, while improved hybrid power control model allows control has better real-time visibility.

3 The System Model for a Self-Healing Grid Based on Hybrid Power Control Theory

This paper adopts this definition for self-healing: to the slight disturbance of the system from the outside and inside, the system should have a good preventive function, timely detection, diagnosis, remove the disturbance; to the fault which cannot be avoided, system should be maintained sustained and stable operation of the power system. Its purpose is on the foundation of less cutting load even not cutting load, to cut off the fault circuit, analysis the fault, alarm the fault, and manually repair the fault.

Based on the above definition of self-healing systems, combined with a hybrid power system control theory, this paper presents a grid self-healing system model, as shown below (Fig. 2).

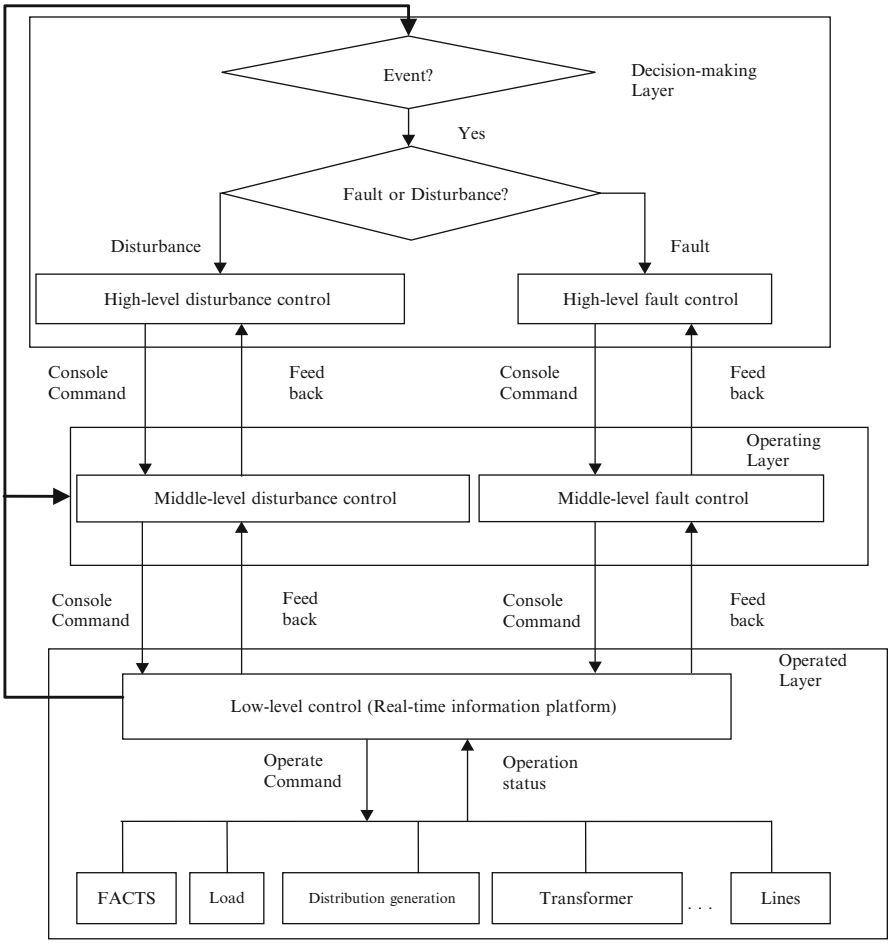

Fig. 2 Grid self-healing system model

3.1 The Task and Design of Decision-Making Layer

First of all, the decision-making layer of the hybrid self-healing control system receive real-time data from the information platform on the bottom of the power system; then accord the definition of the event to judge the formation of the event. The decision-making layer accord node voltage, current, active power, reactive power and other power system real-time parameters, to develop the grid status eligibility standard, and take the failed state of the network parameters as the event; when judge to have the event, the decision-making layer accord the real-time data and the feedback of the operation layer, to determine whether or not this event is disturbance or fault. Finally, the decision-making layer issues a control instruction to the operating layer, to mobilize disturbance middle-layer control or fault

middle-layer control. At the same time, the decision-making layer under take the task of the event display, failure notification and other human-computer interaction function.

3.2 The Task and Design of Operating Layer

The operating layer of the hybrid self-healing control system must establish the real-time database, the perturbation model, and the fault control module. First of all, the operation layer of the hybrid self-healing control system receive high-level control commands from the decision-making layer to start the disturbance middle-level control or fault middle-level control, then based on the data transfer from the underlying power system information platform, detail analysis the type of disturbance or fault to give the optimal control program which can correct the disturbance or cut off the fault line and adapt to the current system. Finally, the program formed the instructions to send to the controlled layer, and receive the feedback from the controlled layer. At the same time, the operating layer undertake the task of display optimize control programs, perform and other human-computer interaction function.

3.3 The Task and Design of Controlled Layer

The controlled layer of hybrid self-healing control system is composed of two parts. The one part is the underlying physical grid which contained power plants, substations, FACTS devices and other existing protection devices. The other part is the real-time power system platform based-on the WAMS. The real-time power system platform receive the power system optimization or protection programs from the Operating layer, then send operating instructions to the transformers, power system protection devices, and feedback the implementation to the Operating layer. At the same time, the real-time power system platform also under take the task of real-time record, showing power system operating conditions.

According to the above model, the hybrid self-healing control system can be a brief description of the process as follows: the power system information platform on the bottom record the real-time grid status, upload and synchronization it to the Decision-making layer and Operating layer through the data communication channel. Decision-making layer through the grid state judge whether there is event occurred. If the event occurred, then judge whether it is fault or disturbance, send a control instruction to the operating layer. Operating layer make a specific optimization or fault solutions by the real-time grid data, then send it to controlled layer in the form of a document. Finally the power system information platform control the physical network. In summary, the hybrid self-healing control mechanism is simple, and can achieve the global optimization of the power system, the global sharing of data to fully enhance the automation degree of self-healing power system.

4 Realization of Grid Self-Healing Hybrid Control

The grid of self-healing hybrid control system model according to text, to achieve the grid self-healing, first of all, a clear definition of "event" is needed; second, we need to achieve the control of disturbances and faults, At the same time, the solution should be to ensure the optimal solution; Finally, The real-time and global of overall healing process should be to ensure. The following will detail the key of implementation and necessary technology of the self-healing hybrid control.

4.1 Definition of "Event"

It can be said that the guiding ideology of the grid self-healing system based on hybrid control is defining the grid state which doesn't meet the requirement as "events", then excitation control action by the "event", so how to define the "event" becomes the focus of hybrid self-healing control. Any aspect of the grid state which does not meet the requirements should be regarded as the "event", in other words, for the all real-time network parameters recorded by controlled layer power system, we should define the dissatisfied ones as the "event". The grid has the following important parameters: Power system frequency, harmonics; node voltage of the power system, the amplitude of line current, phase angle; inputs and outputs of node active and reactive power; generators, temperature of power transformers and other hardware state. The above parameters have a certain range of security, that is, the threshold; the state which exceeds or below the threshold is defined as "events". With reactive power of a node for example, the constraint conditions:

$$Q_{Gimin} \leq Q_{Gi} \leq Q_{Gimax} \tag{1}$$

Q_{Gi}, Q_{Gimin}, Q_{Gimax} are for the reactive power and its upper and lower limits of node i. In this example, "$Q_{Gimin}-Q_{Gi}>0$" and "$Q_{Gimax}-Q_{Gi}<0$" are defined as "events".

"Event set" take the union of the "event" set, in the running grid, once the "incident" occurred, the decision-making control is excited.

4.2 Concrete Realization of Disturbance Control and Fault-Controlled

In recent years, study for disturbance control and fault control of the power system emerges continually, this system use the failure to control and optimal control based on wide area measurement to construct the control layer of hybrid power operation of self-healing.

Wide area measurement technique based on GPS can measure the node voltage magnitude and phase angle directly and has good value in the power system state estimation, fault location and positioning, power system reactive power and voltage optimization, etc. For the failure of the power system control, cutting off the fault line and determining the location of the point of failure is particularly important.

4.3 Real-time and Localized of Self-Healing Control

Due to the complexity of the structure of the grid, it is very easy to cause a chain reaction leading to the large-scale collapse of the power grid, so real-time is required in the grid self-healing control. In this paper, the hybrid self-healing control, take full use of the WAMS systems' advantage of rapid processing of real-time data of the grid ensuring the good liquid of the control process and procedure. The decision-making layer of Self-healing control based on the hybrid control can achieve the global control of the grid. Regarding all the disturbances as "events", when expansion the physical structure of the power grid, we can cover the new physical structure as long as adding a new event definitions without having to re-deploy the software system, this thinking has a good flexibility.

5 Conclusion

This article discussed the possibility of applying hybrid control theory into the grid self-healing control, established a grid self-healing control system based on hybrid control theory and gave the key technology required by concrete realization. Overall, the basic idea of hybrid grid self-healing control is "event driven", regarding the grid state which does not meet the needs as "incident", using discrete event to drive the disturbance control or failure of control. The advantages show in the simplicity in its concept, global optimization, easiness to expand and applicability to global healing of large power grids.

References

1. Wenliang Zhang, Zhuangzhi Liu, Mingjun Wang (2009) Research status and development trend of smart grid. Power Syst Technol 33(13):1–11 (In Chinese)
2. U.S. Department of Energy Office of Electricity Delivery and Energy Reliability, National Energy Technology Laboratory. (2009). Systems view of the Modern Grid, EB/OL. httP://www.netl.doe.gov/moderngrid
3. BR Williams, TD John (2008) System and method for a self-healing grid using demand side management techniques and energy storage. U.S.A., US7389189B2
4. Galan S, Barton PI (1988) Dynamic optimization of hybrid systems. Comput Chem Eng 22:183–190
5. Hu Wei, Lu Qiang (2005) Hybrid power control system and its application. Trans China Electrotech Soc 20(2):11–16

PMSM Sensorless Vector Control System Based on Single Shunt Current Sensing

Hongyan Ma

Abstract To reduce the cost and volume of permanent magnet synchronous motor (PMSM) drive system fed by pulse width modulation (PWM) inverter, this paper presents a single shunt current sensing with rotor-position sensorless control method of PMSM vector control system. The reference voltage of space vector pulse width modulation (SVPWM) inverter is researched to implement the requirements by AC-link phase current reconstruction with single shunt current sensing. By model reference adaptive system (MRAS), speed estimation method is investigated to satisfy rotor-position sensorless control. Simulations are tested on a PMSM vector control system fed by SVPWM inverter. Simulation results demonstrate the feasibleness and the effectiveness of the single shunt current sensing with MRAS sensorless control method.

Keywords Single shunt current sensing • MRAS sensorless • PMSM • PWM inverter

1 Introduction

For permanent magnet synchronous motor (PMSM) having many advantages such as high ratio of torque to weight and high efficiency, PMSM vector control systems, which supplied by pulse width modulation voltage source inverters (PWM-VSI), are widely used in many applications [1]. High performances PMSM vector control systems depended on the precise information of AC-link currents by AC-link current sensors and the rotor position by mechanical sensor. To reduce the cost and volume of inverter, no current sensors control methods based on a single shunt current sensing to reconstruct three phase AC currents have been proposed by

H. Ma (✉)
Department of Electrical Engineering, Beijing University of Civil Engineering and Architecture, Beijing, China
e-mail: m_hy71@163.com

W. Wang (ed.), *Mechatronics and Automatic Control Systems*, Lecture Notes in Electrical Engineering 237, DOI 10.1007/978-3-319-01273-5_81,

researchers [2–4]. The sensorless rotor-position estimation methods like the Extended Kalman Filter (EKF) algorithm combining with single shunt sensing and the model reference adaptive method combining with no AC-link current sensor have been developed [5, 6].

In sensorless AC drive systems, the practical rotor position/speed estimation method is based on model reference adaptive system (MRAS). In this paper, single shunt current sensing with the MRAS sensorless method is researched in PMSM vector control systems supplied by space vector PWM voltage source inverter (SVPVM-VSI). The validity and feasibility of the researched method are verified by simulation results of PMSM vector control systems supplied by three phase voltage source inverter.

2 Single Shunt Current Reconstruction Based on DC-Link

Single shunt current sensing control scheme is reconstructed the AC-link currents by the measured DC-link current values with single shunt. The voltage vector diagram of SVPWM-VSI shown as Fig. 1, there are six sectors in the voltage vector diagram of SVPWM and six active voltage vectors ($\boldsymbol{V}_1 \sim \boldsymbol{V}_6$) and two zero vectors $\boldsymbol{V}_0$ (000) and $\boldsymbol{V}_7$ (111). The reference voltage vector $\boldsymbol{V}_r$ located in sector 1 is only studied in follows.

In sector 1, the reference voltage vector $\boldsymbol{V}_r$ is synthesized by the two adjacent active voltage vectors $\boldsymbol{V}_1$, $\boldsymbol{V}_2$. In the linear modulation range, conventional seven segment SVPWM signals distribution strategy which is to synthesize $\boldsymbol{V}_r$ by using two adjacent non-zero vectors and one zero vector in one sampling period $\boldsymbol{T}_s$ is applied, $\boldsymbol{V}_r$ is given as

$$\boldsymbol{V}_r = \frac{T_1}{T_s}\boldsymbol{V}_1 + \frac{T_2}{T_s}\boldsymbol{V}_2 \tag{1}$$

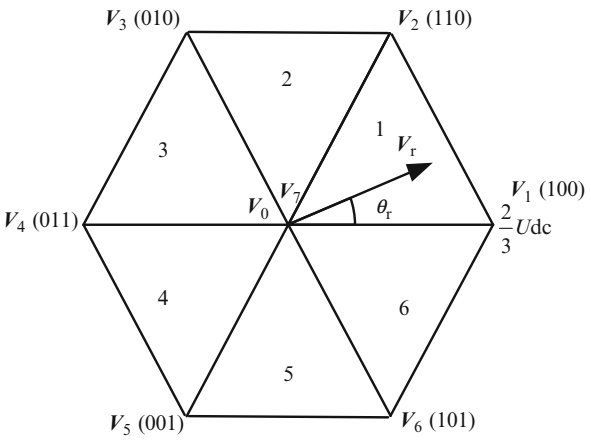

Fig. 1 The voltage vector diagram of SVPWM-VSI

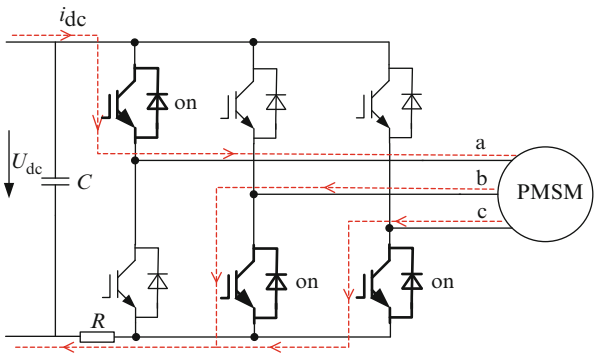

Fig. 2 No AC-link current sensor control in sector 1

Table 1 Voltage vectors and measured phase currents by i_{dc}

Voltage vector	i_{dc}	Voltage vector	i_{dc}
$\boldsymbol{V}_0(000)$	0	$\boldsymbol{V}_4(011)$	$-i_a$
$\boldsymbol{V}_1(100)$	$+i_a$	$\boldsymbol{V}_5(001)$	$+i_c$
$\boldsymbol{V}_2(110)$	$-i_c$	$\boldsymbol{V}_6(101)$	$-i_b$
$\boldsymbol{V}_3(010)$	$+i_b$	$\boldsymbol{V}_7(111)$	0

$\boldsymbol{T}_1$ and $\boldsymbol{T}_2$ are the on-durations of the switching state vectors $\boldsymbol{V}_1$ and $\boldsymbol{V}_2$. They can be calculated as

$$\begin{cases} T_1 = \sqrt{3} T_s \dfrac{|\boldsymbol{V}_r|}{U_{dc}} \sin\theta_r \\ T_2 = \sqrt{3} T_s \dfrac{|\boldsymbol{V}_r|}{U_{dc}} \sin(\pi/3 - \theta_r) \end{cases} \tag{2}$$

Where U_{dc} is DC-link voltage, θ_r is the angle of $\boldsymbol{V}_r$.

The on-duration of zero vector T_0 can be obtained as

$$T_0 = T_s - T_1 - T_2 \tag{3}$$

Used an active voltage vector to PMSM, AC-link phase current is measured by the DC-link current i_{dc}. In Fig. 2, by detecting i_{dc} as active vector $\boldsymbol{V}_1$ employed, a-phase current i_a of the motor is achieved; as zero vectors employed, i_{dc} equals zero, then the phase current is not measured. In each control period, two phase currents achieved by the DC-link current i_{dc}, the third phase current is determined by the zero sum of three-phase currents.

As shown in Table 1, the applied voltage vector employed, the responding phase current is measured from the DC-link current i_{dc}.

In practice, using single shunt sensing to reconstruct the AC-link phase current, the precision of reconstructed AC-link phase current is determined by the DC-link current. In order to achieve a dependable DC-link current i_{dc}, the minimum sampling time T_{min} has to be less than the operation period of applied active vector.

3 Sensorless PMSM Vector Control

3.1 PMSM Mathematical Model

In the d-q rotor reference frame, PMSM mathematical model of is given by the following equations.

$$\begin{cases} u_{\mathrm{d}} = \mathrm{p}\psi_{\mathrm{d}} - \psi_{\mathrm{q}}\omega + Ri_{\mathrm{d}} \\ u_{\mathrm{q}} = \mathrm{p}\psi_{\mathrm{q}} - \psi_{\mathrm{d}}\omega + Ri_{\mathrm{q}} \end{cases} \tag{4}$$

$$\begin{cases} \psi_{\mathrm{d}} = L_{\mathrm{d}}i_{\mathrm{d}} + \psi_{\mathrm{r}} \\ \psi_{\mathrm{q}} = L_{\mathrm{q}}i_{\mathrm{q}} \end{cases} \tag{5}$$

$$T_{\mathrm{em}} = p_{\mathrm{n}}\left(i_{\mathrm{q}}\psi_{\mathrm{d}} - i_{\mathrm{d}}\psi_{\mathrm{q}}\right) \tag{6}$$

Where u_{d} and u_{q} stand d-q axis voltages, i_{d} and i_{q} express d-q axis currents, ψ_{d} and ψ_{q} denote d-q axis flux linkages, R is stator resistance, L_{d} and L_{q} are d-q axis inductances, ψ_{r} is the permanent magnetic flux, T_{em} and T_{L} are electrical torque and load torque, p_{n} is numbers of pole pairs of the motor, p is d/dt, ω stands for the rotor speed that is equal to $p\theta$, θ is the actual rotor position.

3.2 Speed Estimation Method Based on MARS

In MRAS method, the current equation of PMSM is chosen as the adjustable model and the actual PMSM as reference model. The error between currents of the adjustable model and the currents of the actual PMSM is used to calculate motor speed.

In the rotating d-q reference frame, the PMSM stator current equations are

$$\frac{\mathrm{d}}{\mathrm{d}t}\begin{bmatrix} i_{\mathrm{d}} \\ i_{\mathrm{q}} \end{bmatrix} = \begin{bmatrix} -\dfrac{R}{L_{\mathrm{d}}} & \dfrac{L_{\mathrm{q}}}{L_{\mathrm{d}}}\omega \\ -\dfrac{L_{\mathrm{d}}}{L_{\mathrm{q}}}\omega & -\dfrac{R}{L_{\mathrm{q}}} \end{bmatrix}\begin{bmatrix} i_{\mathrm{d}} \\ i_{\mathrm{q}} \end{bmatrix} + \begin{bmatrix} \dfrac{u_{\mathrm{d}}}{L_{\mathrm{d}}} - \dfrac{\omega\psi_{\mathrm{r}}}{L_{\mathrm{q}}} + \dfrac{u_{\mathrm{q}}}{L_{\mathrm{q}}} \end{bmatrix} \tag{7}$$

Considering the convenience of stability analysis, the system matrix A is written as

$$\boldsymbol{A} = \begin{bmatrix} -\dfrac{R}{L_{\mathrm{d}}} & \dfrac{L_{\mathrm{q}}}{L_{\mathrm{d}}}\omega \\ -\dfrac{L_{\mathrm{d}}}{L_{\mathrm{q}}}\omega & -\dfrac{R}{L_{\mathrm{q}}} \end{bmatrix} \tag{8}$$

Let $i_{\mathrm{d}}^{'} = i_{\mathrm{d}} + \frac{\psi_{\mathrm{r}}}{L_{\mathrm{d}}}, i_{\mathrm{q}}^{'} = i_{\mathrm{q}}, u_{\mathrm{d}}^{'} = \frac{u_{\mathrm{d}}}{L_{\mathrm{d}}} + \frac{R\psi_{\mathrm{r}}}{L_{\mathrm{d}}^2}, u_{\mathrm{q}}^{'} = \frac{u_{\mathrm{q}}}{L_{\mathrm{q}}}$. Then the simple reference model form is obtained as

$$\frac{\mathrm{d}}{\mathrm{d}t}\boldsymbol{i}^{'} = \boldsymbol{A}\boldsymbol{i}^{'} + \boldsymbol{u}^{'} \tag{9}$$

Speed estimation process described as follows.

The simple parallel connection adjustable model form is

$$\frac{\mathrm{d}}{\mathrm{d}t}\hat{\boldsymbol{i}}^{'} = \hat{\boldsymbol{A}}\hat{\boldsymbol{i}}^{'} + \boldsymbol{u}^{'} \tag{10}$$

The state variables error is

$$e = \boldsymbol{i}^{'} - \hat{\boldsymbol{i}}^{'} \tag{11}$$

The parallel connection model is

$$\begin{cases} \dfrac{\mathrm{d}}{\mathrm{d}t}\boldsymbol{e} = \boldsymbol{A}\boldsymbol{e} \\ \boldsymbol{v} = \boldsymbol{D}\boldsymbol{e} \end{cases} \tag{12}$$

If $\boldsymbol{D} = \boldsymbol{I}$, then $\boldsymbol{v} = \boldsymbol{e}$.

By the Popov super stability theory, the estimation equation of $\hat{\omega}$ can be obtained as

$$\hat{\omega} = \int_0^t k_1(i_{\mathrm{d}}{}'\hat{i}_{\mathrm{q}}{}' - i_{\mathrm{q}}{}'\hat{i}_{\mathrm{d}}{}')\mathrm{d}\tau + k_2(i_{\mathrm{d}}{}'\hat{i}_{\mathrm{q}}{}' - i_{\mathrm{q}}{}'\hat{i}_{\mathrm{q}}{}') + \hat{\omega}(0) \tag{13}$$

Where, $k_1 \geq 0, k_2 \geq 0$.

Replacing $i_{\mathrm{d}}{}', i_{\mathrm{q}}{}'$ with $i_{\mathrm{d}}, i_{\mathrm{q}}$, the estimated speed is obtained as

$$\begin{aligned} \hat{\omega} = \int_0^t k_1[i_{\mathrm{d}}\hat{i}_{\mathrm{q}} - i_{\mathrm{q}}\hat{i}_{\mathrm{d}} - \frac{\psi_{\mathrm{r}}}{L_{\mathrm{d}}}(i_{\mathrm{q}} - \hat{i}_{\mathrm{q}})]\mathrm{d}\tau + k_2[i_{\mathrm{d}}\hat{i}_{\mathrm{q}} - i_{\mathrm{q}}\hat{i}_{\mathrm{d}} - \frac{\psi_{\mathrm{r}}}{L_{\mathrm{d}}}(i_{\mathrm{q}} - \hat{i}_{\mathrm{q}})] \\ + \hat{\omega}(0) \end{aligned} \tag{14}$$

Where, $\hat{i}_{\mathrm{d}}$ and $\hat{i}_{\mathrm{q}}$ are determined by the adjustable model, i_{d} and i_{q} are achieved by the transformation of the reconstructed three-phase stator currents with single shunt current sensing control method.

Integrating the estimated speed, the rotor position is

$$\hat{\theta} = \int_0^t \hat{\omega}\mathrm{d}t \tag{15}$$

4 Simulation Study

In order to prove the feasibleness and effectiveness of single shunt current sensing with MRAS sensorless method, the diagram of PMSM vector control system is built in Fig. 3. Conventional vector control technique such as $i_d = 0$ is applied to the PMSM drive system.

The simulation parameters are shown in Table 2. The dead time effect is not considered in simulation.

Figure 4 shows the speed curve. The speed steady-state error between the motor speed and the reference speed 1,500 rpm is very small. The motor has good performance under this control strategy. Figure 5 shows PMSM stator current. The phase current can concord with the reconstruction current. Figure 6 shows

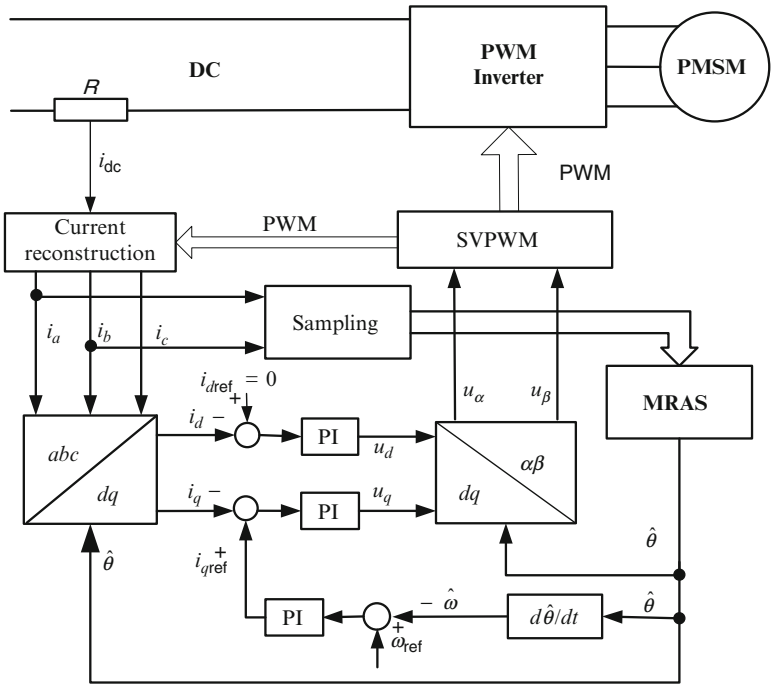

Fig. 3 Block diagram of single shunt current sensing with MRAS sensorless PMSM vector control system

Table 2 The simulation parameters of the motor

Parameter	Value	Parameter	Value
L_d/mH	7.418	L_q/mH	12.285
R/Ω	0.618	ψ_r/V/(rad/s)	0.1128
p_n	2	T_L/Nm	1.5

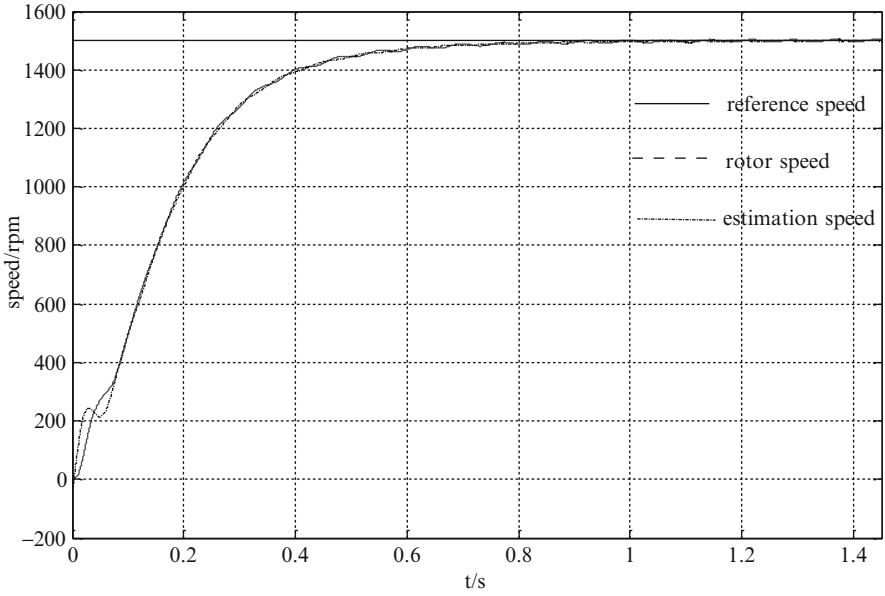

Fig. 4 Speed response curve

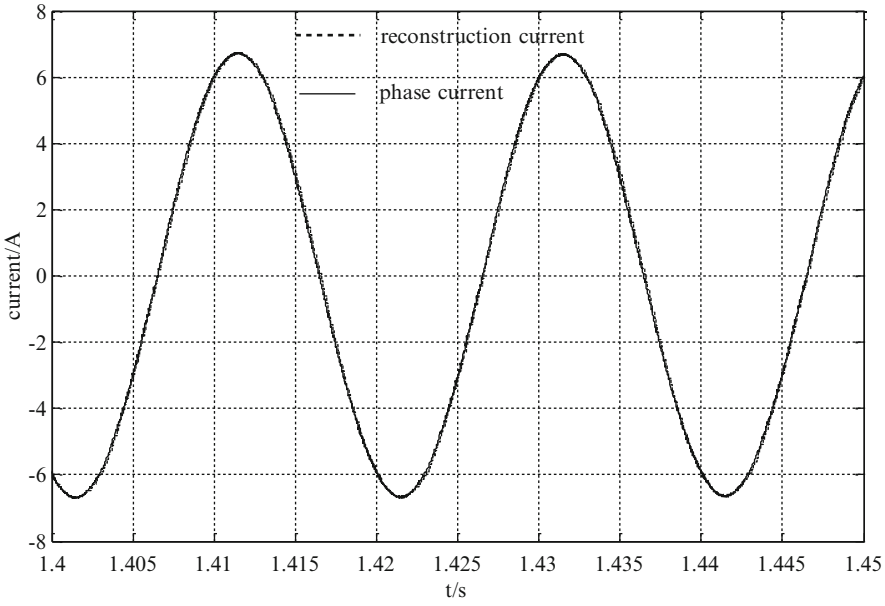

Fig. 5 Waveforms of AC-link phase current

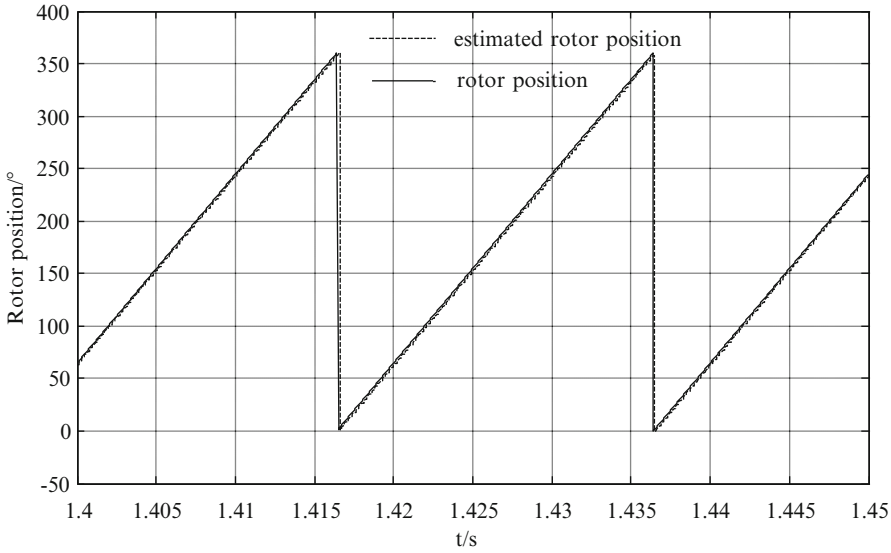

Fig. 6 Waveforms of rotor position

the waveform of rotor position. The real rotor position can concord with the estimated rotor position by MRAS method and reconstructed AC-link phase current.

This verifies that the single shunt current sensing with MRAS sensorless control method is effective in PMSM vector control.

5 Conclusion

In this paper, single shunt current sensing control combined with MRAS sensorless scheme was used for PWM-VSI fed PMSM vector control system. The MRAS sensorless control used the reconstructed AC-link phase currents to estimate rotor position. Simulations demonstrated that, in PWM-VSI fed PMSM vector control, the method that is using single shunt current sensing with rotor position sensorless control based on MRAS method, is valid and feasible.

Acknowledgements The author thanks the financial support by Beijing Municipal Commission of Education of China (PHR201108211) and MOHURD project (2011-k8-3).

References

1. Mohamed B (2005) Implementation and experimental investigation of sensorless speed control with initial rotor position estimation for interior permanent magnet synchronous motor drive. IEEE Trans Power Electron 20(6):1413–1422
2. Liu Yan, Shao Cheng (2007) Reconstruction strategies for phase currents in three phase voltage-source PWM inverters. Info Control 36(4):506–513 (In Chinese)
3. Chu Jianbo, Hu Yuwen et al (2010) Phase current sampling reconstruction for inverter. Trans China Electrotech Soc 25(1):111–117 (In Chinese)
4. Blaabjerg F, Pedersen JK et al (1997) Single current sensor technique in the DC link of three-phase PWM-VS inverters: a review and a novel solution. IEEE Trans Ind Appl 33 (5):1241–1253
5. Yuan Xibo, Li Yongdong, Feng Lichao (2009) Low cost sensorless control of PMSM for air-conditioner compressor application. Electr Drive 39(5):15–19 (In Chinese)
6. Sun Kai, Huang Lipei (2010) Sensorless over-modulation control of PMSM-compressor systems. J Tsinghua Univ (Sci Technol) 50(1):18–22 (In Chinese)

Wind Power System Simulation of Switch Control

Yuehua Huang, Guangxu Li, and Huanhuan Li

Abstract In order to find a balance between energy efficiency and reliability of wind power generation system, this paper presents a switch control strategy. This paper establishes a wind power system simulation model by controlling the electromagnetic torque in the Matlab/Simulink environment. The electromagnetic torque consists of three parts: the equivalent control quantity u_{eq}, the changing high-frequency part u_N and the additional low-frequency part u_{Nf}. The u_{eq} can make the system close to the optimal operating point, and u_N、u_{Nf} make the system operate stably around the optimal operating point. The simulation results show that: the actual speed can track the best speed very well, and the fluctuation range of the electromagnetic torque is very small. This switching control strategy can effectively improve the efficiency of wind power generation system and reduce fatigue load, and it solves the problem of imbalance between energy efficiency and reliability.

Keywords Wind power • Switch control • Matlab/simulink • Torque

1 Introduction

With the rapid development of modern industry, the useful conventional energy sources on Earth become more and more scarce. In order to achieve sustainable development of energy, many countries are trying to develop new energy and renewable energy. Among them, wind energy has many advantages, it has wide distribution, large reserves, and it can be developed and used effectively [1]. As a new type of renewable energy, wind power is the fastest-growing energy in the global.

Y. Huang • G. Li (✉) • H. Li
Institute of Electrical and new energy, Three Gorges University, Yichang, China
e-mail: lgxonly@sina.com

W. Wang (ed.), *Mechatronics and Automatic Control Systems*, Lecture Notes in Electrical Engineering 237, DOI 10.1007/978-3-319-01273-5_82,

Wind power has following characteristics: good environment, mature technology and strong feasibility, and it is used more and more widely in the world [2]. Wind energy is safe, clean and inexhaustible, and it is different from fossil fuels. This local resource is permanent, and it can give us long-term stable supply of energy. At the same time, it does not produce carbon emissions.

In the case of a certain wind turbine speed, the greater the wind speed, the greater the output power of wind turbine. For a certain wind speed, there is always a existence of biggest power point. Only when the wind turbine works in the optimum tip speed ratio, the system can output the maximum power [3]. The wind speed often changes, so the wind turbine tip speed ratio also changes, which makes the wind turbine deviate from the best working condition, and affects the energy conversion efficiency of wind turbines. In order to ensure the best conversion of energy, we should make the system run in optimal condition. To achieve this goal, this article uses the switch control strategy to make the tip speed ratio close to the optimal tip speed ratio condition, which can realize the biggest energy conversion of wind power generation system.

2 Analysis of Wind Turbine Characteristics

Bates theory shows that the wind turbine power absorbed from the air is [4]:

$$P = \frac{\rho}{2} C_p A V^3 \tag{1}$$

In this formula, P is useful output power for the wind turbine, the unit is W; ρ is air density, the unit is kg/m^3;A is wind turbine swept area, the unit is m^2; V is wind speed, the unit is m/s; Cp is wind energy utilization factor. We can see from Eq. 1, for a certain wind speed, the greater the wind energy utilization factor Cp, the greater the useful power of wind turbine. Wind energy utilization factor Cp and wind turbine tip speed ratio λare related, λ is operating parameter of the wind turbine:

$$\lambda = \frac{r\Omega}{V} \tag{2}$$

In this formula: Ω is angular frequency of the wind turbine, the unit is rad/s; r is radius of the wind turbine, the unit is m; For the wind turbine, λ determines the size of the Cp, the relationship between them is curve of the parabolic relationship.

3 The Establishment of the Wind Model

Wind energy is kinetic energy generated by flowing air of the Earth's surface [5]. It is a natural phenomenon on earth, the size of wind energy depends on wind speed and air density, the wind speed and direction are constantly changing with strong randomness in the flowing process. Wind model is shown in Fig. 1, and wind direction is not considered. The purpose of the wind model is describing the randomness of wind, and the wind model is set up by the white noise generator and the shaping filters. The white noise generator generates random signals, and the effect of the shaping filters is filtering. Transfer Fcn 1, Transfer Fcn 2 and Transfer Fcn 3 are all shaping filters, and 7 is the average value of wind speed. Wind velocity waveform is shown in Fig. 2. We can see from the Fig. 2, simulation time is 60 s, and wind speed changes between 6 and 8 m/s.

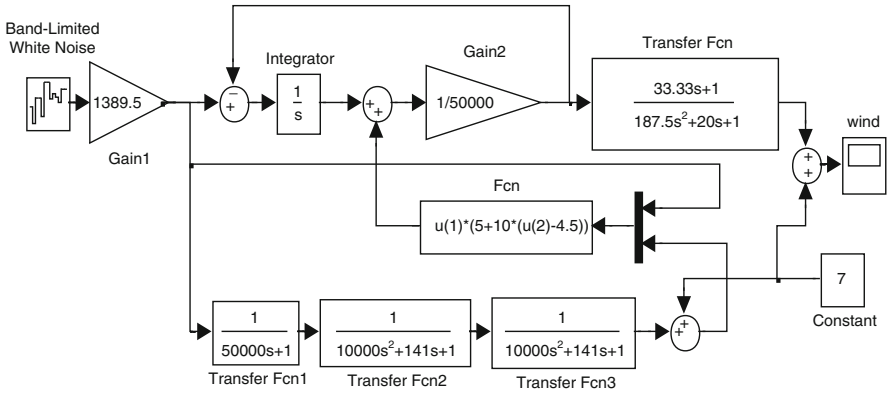

Fig. 1 Wind speed model diagram

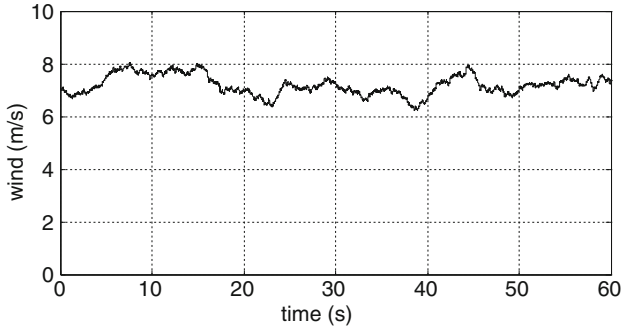

Fig. 2 Wind speed waveform diagram

4 Wind Power System Model

The wind power system model in this article is mainly constituted by the wind, the aerodynamic model, the transmission and the generator model [6]. The role of the aerodynamic model is effectively converting wind energy into useful mechanical energy; the role of the transmission is passing the rotational motion of the wind wheel to the generator, it uses gearbox as the mechanical transmission structure, in this way, the speed of wind wheel can adapt to the needs of generator, which can help generator operate normally. The role of the generator model is generating electricity, the purpose of the model is to convert the mechanical energy transmitted by chain transmission to electricity; the power terminal of the generator is connected to the public grid, in this case, electrical energy is transferred to the power grid. The entire wind power generation system is an organic entity, the various sub-parts must have higher compatibility, which can achieve the efficient conversion of wind energy. The wind power system model is shown in Fig. 3. The whole system is made up by four sections, they are wind model, aerodynamic model, transmission model, and the generator model.

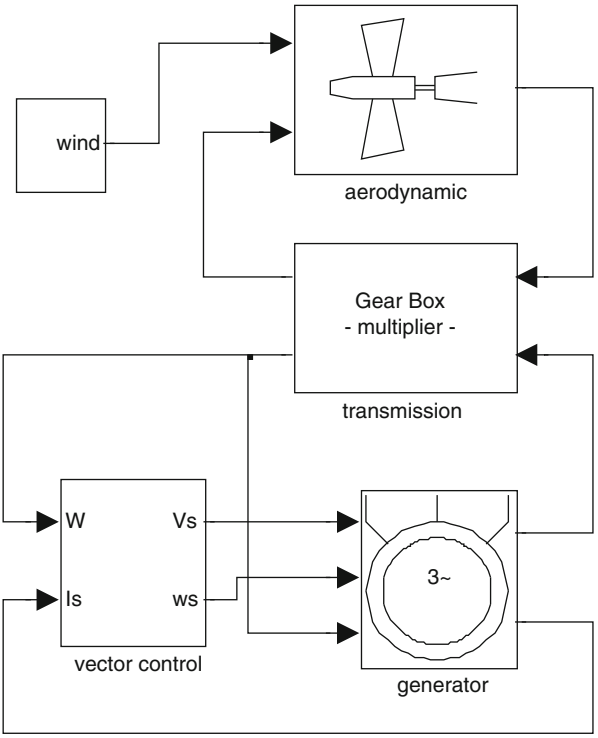

Fig. 3 Wind power system model diagram

5 The Establishment of Switch Control Model

In order to make wind power generation system have the biggest energy conversion efficiency, the paper uses the torque which is relative to the steady-state operating point to control generator, this method can achieve the target. This paper has presented a switch control strategy, the structure of the strategy is shown in Fig. 4.

The control strategy of Fig. 4 shows the steady-state torque reference value U, it consists of three parts:

$$U = Ueq + Un + Unf \tag{3}$$

In this formula, the equivalent control quantity Ueq is a steady-state part which is relative to the optimal operation point, its value is proportional to the square of low-frequency wind speed v_s^2, that is

$$Ueq = Cv_s^2 \tag{4}$$

U_n is the changing high-frequency part, it changes between the two values $+\beta$ and $-\beta$,among them, $\beta > 0$,

$$Un = \beta \bullet \mathrm{sgn}[\sigma(t)] \tag{5}$$

Ueq drives the system to run in the optimal operating point, the role of U_n is to maintain stability of system which is running around the optimal operating point. Unf is received by filtering Un, and it is proportional to the average of Un.

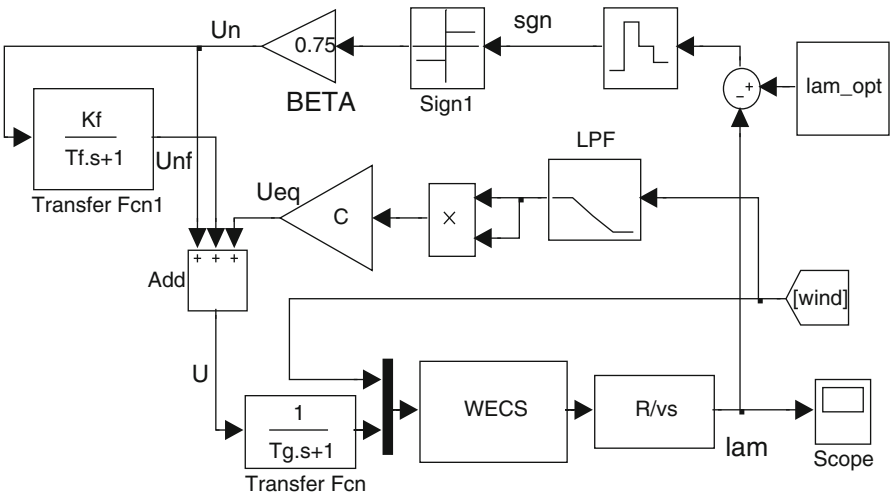

Fig. 4 Switch controller structure diagram

In Fig. 4, lam is tip speed ratio λ, lam_opt is optimal tip speed ratio λ_{opt}, *Ueq* is obtained by wind speed V, *Un* is obtained by λ and λ_{opt}, *Unf* is obtained by filtering, U is obtained by these three values, then we can control the tip speed ratio λ by adjusting U. This control strategy can make tip speed ratio λ close to the optimal value λ_{opt}. The tip speed ratio λ is used to aerodynamic model in Fig. 3,in this case, the whole system can run stably, the output power is the maximum of wind turbine power.

6 Analysis of Simulation Results

The wind power generation system based on switch control strategy is simulated with Matlab/Simulink. The simulation parameters are as follows: $\beta = 3$ N.m, C = 0.25, air density p = 1.25 kg/m^3, efficiency $\eta = 0.95$, optimal tip speed ratio $\lambda_{opt} = 7$, biggest wind energy utilization factor $C_{pmax} = 0.47$, length of wind turbine blade R = 3.1m, drive ratio i = 6.6, low speed shaft inertia J1 = 3.6 kg.m^2, stator resistance Rs = 1.366 Ω, rotor resistance Rr = 1.63 mΩ, stator inductance Ls = 0.172H, rator inductance Ls = 0.162H, mutual inductance Lm = 0.151H, the simulation time is 60 s.

We can see from Fig. 5, the tip speed ratio only has a small amplitude oscillation nearby the optimal value 7, the oscillation amplitude is very small, which explain that the wind turbine can keep a very good tip speed ratio during operation process. Wind energy utilization factor waveform is shown in Fig. 6, wind energy utilization factor is proportional to output power, which can directly reflect the size of the output power. Wind energy utilization coefficient and tip speed ratio have close relationship, when the tip speed ratio is the optimal tip speed ratio, wind energy utilization factor is the biggest wind energy utilization factor, the largest wind energy utilization coefficient of this article is 0.476,

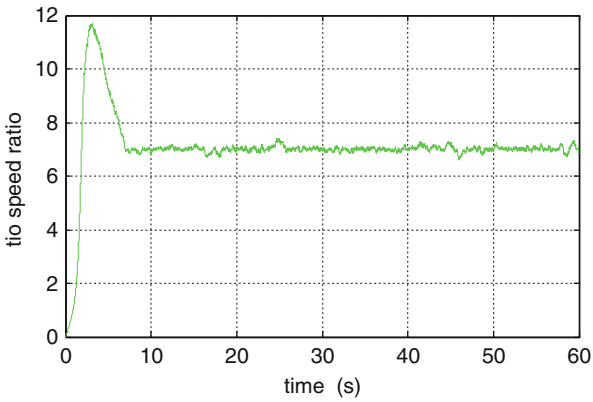

Fig. 5 Tip speed ratio waveforms diagram

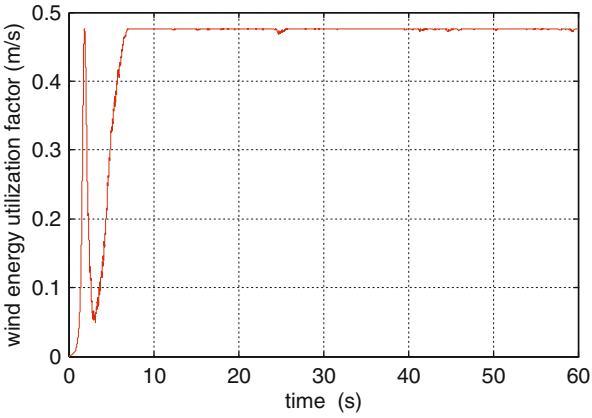

Fig. 6 Wind energy utilization factor waveforms diagram

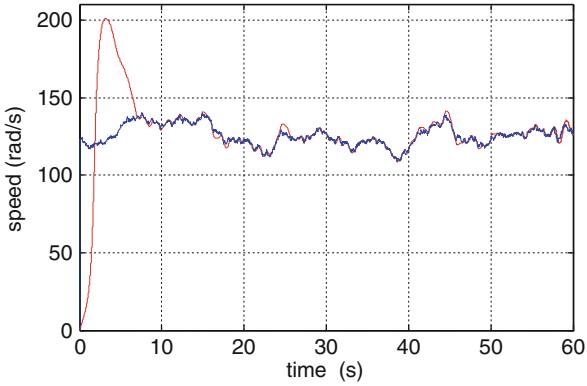

Fig. 7 Wind turbine speed waveforms diagram

the Cp of Fig. 6 has been near the biggest wind energy utilization coefficient 0.47, the amplitude of fluctuation is very small, therefore, the final output power is the maximum of wind turbine power. The speed simulation waveform is shown in Fig. 7, blue curve represents the optimum rotational speed of the wind wheel, the red curve represents the actual speed of the wind wheel. We can see that the trace of actual speed has been very close to the trace of optimum rotational speed, when the optimum rotational speed increases, the actual speed increases relatively; when the optimum rotational speed reduces, the actual speed also reduces relatively; it can track the optimum speed well. You can explain, in the actual generation process, the wind turbine can achieve maximum power transfer successfully. The waveform of electromagnetic torque is shown in Fig. 8, we can see from Fig. 8 that the amplitude and frequency of the electromagnetic torque pulsation are very small, so the system can reduce the mechanical fatigue.

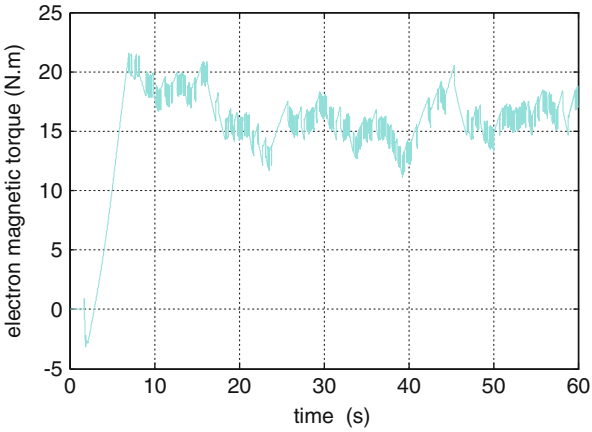

Fig. 8 Electromagnetic torque waveforms diagram

7 Conclusion

This paper establishes a wind power system simulation model by using Matlab/Simulink simulation software, and uses switch control technology to simulate the wind power generation system. Simulation results show that tip speed ratio and wind energy utilization factor curve are in the vicinity of the best value, and the actual speed can track the best speed well. It shows that the wind turbine can get the maximum energy conversion efficiency. In addition, the fluctuation range of the electromagnetic torque is very small, which can reduce mechanical fatigue of the wind power system. It can be concluded that the switch control strategy used in this paper is feasible and effective, and the system can achieve balance between energy efficiency and reliability. The global energy crisis and environmental crisis have become more and more serious, wind power industry has made rapid development, the biggest power point tracking has also become a hot topic of wind power research, and the simulation results in this paper provide a reference for analyzing the efficiency of wind turbines.

References

1. Chen Yidong, Yang Yulin, Wang Liqiao (2010) Maximum power point tracking technology and simulation analysis for wind power generation. High Voltage Engineering 36(5):1322–1326
2. Li Chuantong (2005) New energy and renewable energy technologies. Southeast University Press, Nanjing, China, pp 2–5
3. Li Shaowu (2011) Research on MPPT control algorithm of small- sized wind energy conversion system. Journal of Hubei University for Nationalities 29(2):192–193
4. Huang Jincheng, Yang Ping (2011) An optimize maximum power point tracking algorithm for small scale wind power generator. Electr Mach Control Appl 38(3):44–48
5. Zheng Ping (2010) Maximum power point tracing in 20kw wind power system. Beijing University of Chemical Technology, Beijing
6. Jin Xin (2007) Application of simulation in analysis of performance of wind turbine. J Chongqing Univ 19(24):2823–2836

Simulation of Variable-Depth Motion Control for the High-Speed Underwater Vehicle

Tao Bai and Yuntao Han

Abstract In order to solve the problem of variable-depth motion control of underwater high-speed vehicle, cavitator-fins joint control method and mathematical model simulation analysis method were used in this paper. First, improvement to the model of high-speed underwater vehicle, according to the analysis of relationship between supercavity shape and force for vehicle; Secondly, linearization the motion equations used by state variable feedback exact linearization method and then used pole placement for design controller. Third, use MATLAB/SIMULINK software to design simulation model of high-speed underwater vehicle. The simulations reveal that this controller is proved to be effective. The cavitator-fins joint control method can effectively solve a class of the variable-depth control of high-speed underwater vehicle.

Keywords High-speed underwater vehicle • Supercavity • Variable-depth motion control • Simulation study

1 Introduction

Supercavitation can provide possibility for lessen viscous drag, so that reduction by maintaining a stable single vaporized water bubble around the vehicle, it can making extend the velocity range of the underwater vehicle. However, supercavitation involves complicated hydrodynamic dynamics, that the vehicle experiences strong nonlinear forces and the system dynamics presents challenges for stabilization and maneuver control of the vehicle.

T. Bai (✉) • Y. Han
College of Automation, Harbin Engineering University, Harbin, China
e-mail: baitao812@126.com

W. Wang (ed.), *Mechatronics and Automatic Control Systems*, Lecture Notes in Electrical Engineering 237, DOI 10.1007/978-3-319-01273-5_83,

Savchenko proposed several stable motion modes of the supercavitation vehicle in the different speed ranges [1] and some related control problem with supercavitation vehicle [2]. Bálint Vanek used low-level longitudinal model to study the control characteristics of the supercavitation vehicle [3, 4].

This paper is devoted to the motion model improvement and design controller for the high-speed underwater vehicle in the longitudinal axis. First, improve motion model of high-speed underwater vehicle on vertical plane; Second, linearization transformation of the nonlinear movement equations based on state variable feedback exact linearization method. Third, design controller for supercavitation vehicle by cavitator-fins joint control method and pole placement. Finally, simulation was performed by using Matlab/Simulink, then discussed about the simulation results.

2 Model Improvement for Supercavitating Vehicle

2.1 Analysis on Supercavity Shape

The cavity entirely enveloping the moving body, which are filled by the water vapor, so it was called "supercavitating". Based on the general theory of similarity of hydrodynamic, the cavitation number σ is the most important independent dimensionless parameters in the similarity criteria of the supercavitating flows, σ may be calculated by formulae [1]:

$$\sigma = \frac{2(p_\infty - p_c)}{\rho V^2} \tag{1}$$

The p_∞ is simply the hydrostatic pressure at the operating depth of the vehicle; p_c is the pressure in cavity; ρ is the fluid density; V is velocity of the vehicle in undisturbed flow.

In the case of the low cavitation numbers ($\sigma < 0.1$), the semi-empirical relations can be derived for shape of supercavity to disk cavitator (Fig. 1).

$$R_c = R_n\sqrt{\frac{c_x}{0.9\sigma}} \quad x_1 = D_n \quad L_c = D_n\frac{2\sqrt{c_{x0}}}{\sigma} \tag{2}$$

The R_c and L_c are the mid-section radius and the length of the supercavity; D_n is the cavitator diameter; c_x is the cavitation drag coefficient; c_{x0} is the cavitatin drag coefficient when $\sigma = 0$. The G.V. Logvinovich's formula [1] is most elementary for compute the shape of axisymmetric and steady cavity, shapes of the part I and part II of the cavity are calculated by different formulae [2].

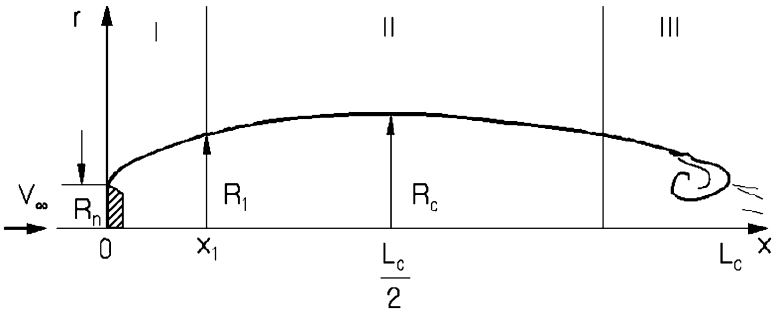

Fig. 1 Shape of the steady axisymmetric cavities

$$\begin{cases} R(x) = R_n\left(1 + \dfrac{3x}{R_n}\right)^{\frac{1}{3}}. & x \le x_1 \\ R(x) = R_c\sqrt{1 - \left(1 - \dfrac{R_1^2}{R_c^2}\right)\left(1 - 2\dfrac{x - x_1}{L - 2x_1}\right)^2}. & x \ge x_1 \end{cases} \tag{3}$$

2.2 Force Analysis of High-Speed Underwater Vehicle

When vehicles travel at high-speed in underwater, cavitator is contact with water is located front of vehicles. Cavitator can rotate around its axis into a certain angle to produce supercavitation and provide lift for vehicle. The aft plan force have periodic impact on cavity up or down wall in the vertical plane [3] (Fig. 2).

The vehicle can be seen as one rigid body, its reference coordinate is the body coordinate, its reference point O is gravity centre on vehicle, there are five forces acting on the body, the gravity, thrust force, cavitator, fins forces, and planning which is not always present.

Lift force acting on cavitator can be approximated as:

$$F_c = \frac{1}{2}\pi\rho R_n^2 V^2 C_x \alpha_c = C_l \alpha_c \tag{4}$$

Force acting on fins can be expressed as:

$$F_f = nC_l\alpha_f \tag{5}$$

The parameter n is the effectiveness of surfaces in provided lift, it is a function of fins effectiveness relative to the cavitator effectiveness. In both force equations, the angle-of-attack terms are assumed to be small so that small angle approximations

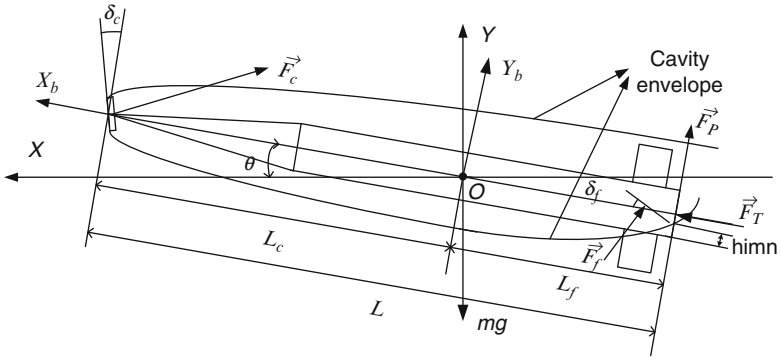

Fig. 2 Schematic of geometry and force of supercavitating vehicle

apply to trigonometric functions. The fins effectiveness n = 0.5 in the whole proposed for Dzielski's model.

The planning force is provided by interaction of vehicle aft and cavity wall. If the diameter of cavity at the planning location is R_c, then the planning force can be approximated as Eq. 6 in small immersion angle:

$$F_{plane} = -\rho R^2 \pi V^2 \left(1 - (R'/(h' + R'))^2\right) \left(\frac{1 + h'}{1 + 2h'}\right) \alpha_p \tag{6}$$

Where, R' denotes the normalized distance from cavity radius to vehicle radius, h' is the immersion depth and α_p is the immersion angle.

Due to the existence of vehicle aft planning force, the system has nonlinear terms, hence the mathematic model of vehicle longitudinal motion is expressed as the affine nonlinear systems [4]:

$$\begin{aligned} \dot{\boldsymbol{x}} &= \boldsymbol{f}(\boldsymbol{x}) + \boldsymbol{G}(\boldsymbol{x})u \\ \boldsymbol{y} &= \boldsymbol{H}(\boldsymbol{x}) \end{aligned} \tag{7}$$

Where $\boldsymbol{x} \in R^4$, $\boldsymbol{u} \in R^2$, $\boldsymbol{y} \in R^2$, $f(x)$ is four dimensions full smooth vector field; and $\boldsymbol{G}(\boldsymbol{x})$ is 4 × 2 dimension full smooth matrix.

$$\begin{aligned} \boldsymbol{H}(\boldsymbol{X}) &= [h_1(x), h_2(x)]^{\mathrm{T}} = [x_1, x_3]^{\mathrm{T}} \, \boldsymbol{x} = [x_1 \;\; x_2 \;\; x_3 \;\; x_4]^{\mathrm{T}} = \left[y, V_y, \omega_z, \theta\right]^{\mathrm{T}} \boldsymbol{y} \\ &= [y_1 \;\; y_2]^{\mathrm{T}} \end{aligned} \tag{8}$$

$$\begin{aligned} \boldsymbol{f}(\boldsymbol{X}) &= [f_1 \;\; f_2 \;\; f_3 \;\; f_4]^{\mathrm{T}} \\ &= \begin{bmatrix} x_2 - Vx_4 \\ \dfrac{(C_1 - C_2)}{(MV)} x_2 + \dfrac{(C_1 L_c - C_2 L_f)}{(MV)} x_4 + g \\ \dfrac{(-C_1 L_c + C_2 L_f)}{(I_{yy} V)} x_2 + \dfrac{(C_1 L_c^2 - C_2 L_f^2)}{(I_{yy} V)} x_4 \\ x_3 \end{bmatrix} + \begin{bmatrix} 0 \\ \dfrac{C_p}{M} \\ -\dfrac{C_p}{I_{yy}} L_f \\ 0 \end{bmatrix} F_{plane} \end{aligned} \tag{9}$$

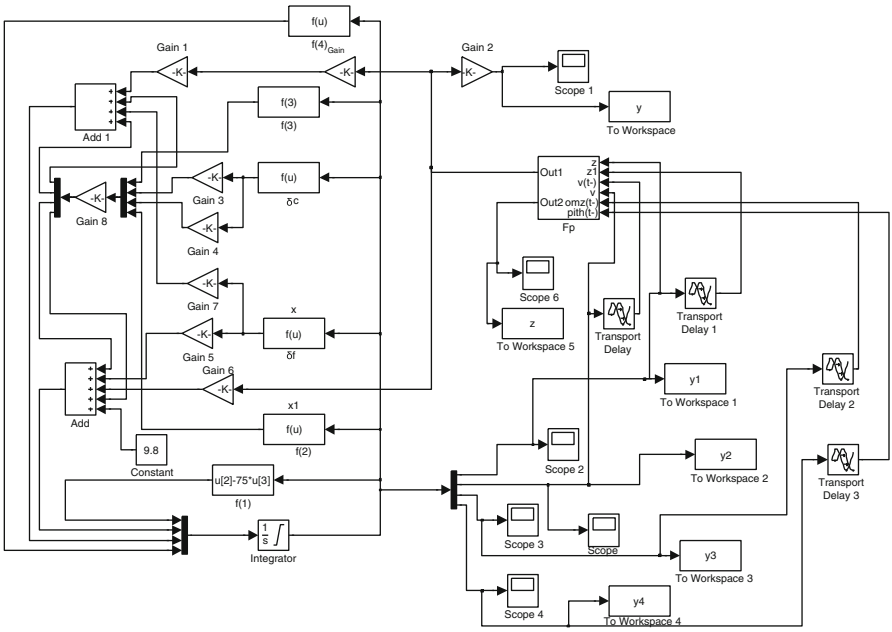

Fig. 3 Simulation model of high-speed underwater vehicle

$$\begin{aligned} \boldsymbol{G}(\boldsymbol{x}) &= [g_1 \quad g_2\ ] \\ \boldsymbol{u} &= [u_1 \quad u_2]^{\mathrm{T}} = [\delta_c, \delta_f]^{\mathrm{T}} \end{aligned} \tag{10}$$

Where

$$g_1(x) = \begin{bmatrix} g_{11} \\ g_{12} \\ g_{13} \\ g_{14} \end{bmatrix} = \begin{bmatrix} 0 \\ C_1/M \\ -C_1 L_c/I_{yy} \\ 0 \end{bmatrix}, g_2(x) = \begin{bmatrix} g_{21} \\ g_{22} \\ g_{23} \\ g_{24} \end{bmatrix} = \begin{bmatrix} 0 \\ C_2/M \\ -C_2 L_c/I_{yy} \\ 0 \end{bmatrix} \tag{11}$$

The simulation model of high-speed underwater vehicle is established by MATLAB/SIMULINK (Fig. 3).

3 Design Controller of High-Speed Underwater Vehicle

3.1 Model Linearization

Based on differential geometry theory, first verify whether or meet the conditions of state variable feedback exact linearization for the affine nonlinear system (9). If a matrix $g(X_0)$ rank is m, then state-space exact linearization problem is solvable, if and only if [5]:

- For each $0 \leq i \leq$ n $-$ 1, distribution G_i dimension is invariant near the X_0.
- Distribution G_{n_1} have dimension n.
- For each 0 $\leq$ i $\leq$ n $-$ 2, the distribution G_i is involution.

In the system (9), $G_0 = \text{span}\{g_1, g_2\}$ in neighborhood X_0 has dimension $m = 2$, because $[g_1, g_2]\,(x) = 0$ and $rank(g_1, g_2) = rank(g_1, g2, [g_1, g_2])$, so distribution G_0 is involution.

Calculation of the dimensions of distribution G_1, G_2, G_3, so G_1, G_2 is involution. G_3 is 4, that equal to n.

Based on the above calculation, the multi-input affine nonlinear Eq. 9 satisfied the conditions for exact linearization, could transformed into linear and control system based on feedback and appropriate coordinate transformation.

3.2 Control System Design

Based on above calculation and analysis, that in the neighborhood U of X0 have m = 2, so λm (x) is smooth real output functions. The Eq. 9 is considered as multiple-input multiple-output (MIMO) affine nonlinear system [6]:

Assumption that output functions are: $\lambda_1(x) = x_1$, $\lambda_2(x) = x_4$.

$$\begin{cases} \dot{z}_1 = \dot{x}_1 = f_1(x) = z_2 \\ \dot{z}_2 = f_2(x) - Vf_4(x) = v_1 \\ \dot{z}_3 = \dot{x}_4 = f_4(x) = z_4 \\ \dot{z}_4 = f_3(x) = v_2 \end{cases} \tag{12}$$

So chosen output functions λm (x) is meet conditions, because $A(x)$ is nonsingular matrix in $X0$. Coordinate transform: $z_1 = x_1$; $z_2 = x_2 - V\ x_4$; $z_3 = x_4$; $z_4 = x_3$. Let input of system: $\dot{z}_2 = v_1$; $\dot{z}_4 = v_2$.

Design a control law be used by MIMO pole placement method and coordinate transforming, and obtained controller Eq. 13.

$$u = \begin{bmatrix} \delta_c \\ \delta_f \end{bmatrix} = \begin{bmatrix} k_{11} & k_{12} & k_{13} & k_{14} \\ k_{21} & k_{22} & k_{23} & k_{24} \end{bmatrix} \begin{bmatrix} x_1 \\ x_2 \\ x_3 \\ x_4 \end{bmatrix} \tag{13}$$

4 Numerical Simulation

The following conditions to ensure the cavity integrated and the vehicle moved stably:

- Immersion depth $h < R/6$, R is vehicle radius.
- $0.02 < \sigma < 0.036$.
- θ, δ_c, δ_f is not more than 15 ° (0.26 rad).

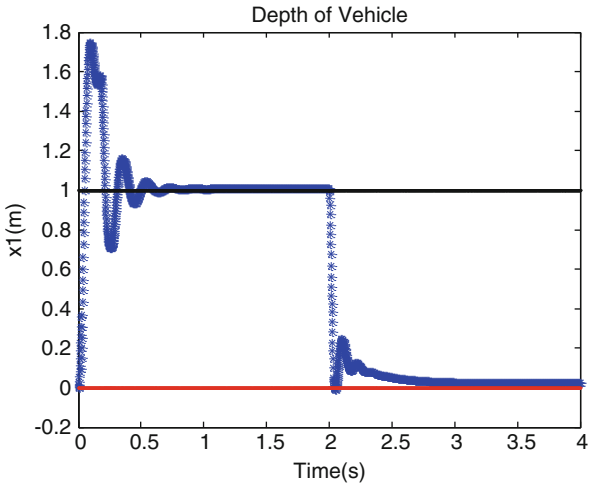

Fig. 4 Simulation to variable-depth motion of vehicle

Parameters of vehicle in simulation model follow:

Depth objective: $y_1 = 1$ m, $y_2 = 0$ m; Gravitational acceleration g = 9.8; Density ratio (water) m = 2; Vehicle mass $M = 22.7$ kg; Vehicle length L = 1.8 m; efficiency coefficient n = 0.5; Cavitator radius $R_n = 0.0191$(m); Vehicle radius R = 0.0508(m); Velocity V = 75(m/s); Drag coefficient $C_x = 0.82$.

Motion simulations of vehicle are performed in Matlab/Simulink, all parameters is respect to the above setup. The move is a variable-depth motion: the horizontal speed is 75 m/s, while the vehicle moves down 1 m under only cavitator control, then cavitator-fins joint control to returns to continue its straight path as seen in Fig. 4. The cavitator-fins joint control method can ensure vehicle moving stably in different depth.

In Fig. 5, θ, δ_c, δ_f is not more than 0.26 rad, the immersion depth not more than 0.008 m in most of the time, which satisfy control demand, meet the requirement for the vehicle stable motion control.

Based on analysis of the simulations result, it can be seen that both of the different depth control via the cavitator-fins joint control are efficacious and the motion stability can be ensured for supercavitation vehicle. Consequently, the control method and algorithm in paper is simple and well implemented.

5 Conclusion

Through the motion analysis to high-speed underwater vehicle, conclusions are achieved as the following: the improved system longitudinal motion model, it accords with the real motion law of the high-speed underwater vehicle. It can be seen from the simulations result, that the vehicle depth can quickly track settings point, the controller designed has good tracking performance. At the same time,

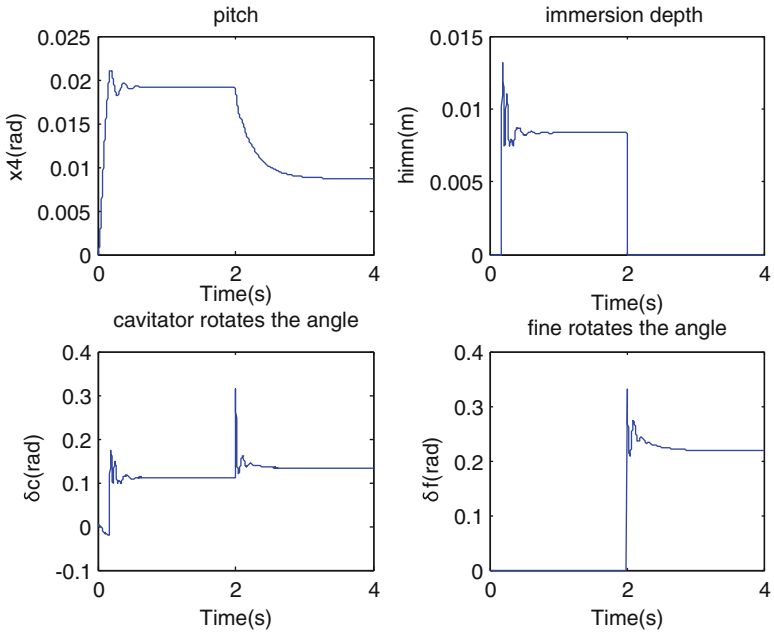

Fig. 5 Schematic diagram of parameter variation

when vehicle is controlled by the designed controller, all state variables return to steady-state value after changing in the allowed range, that can meet the control requirements of system. It is verified that suitable controller can successfully to eliminate motion oscillations and strengthen the stability of the system of high-speed underwater vehicle.

Acknowledgements The work was supported by "the Fundamental Research Funds for the Central Universities" No. HEUCF041212, HEUCFR1211, and "Province in Heilongjiang youth science fund" No. QC2011C031.

References

1. Savchenko Yu N (2001) Control of supercavitation flow and stability of supercavitating motion of bodies, vol 13, VKI special course on supercavitating flows, Brussels. RTO-AVT and VKI. RTO-EN-010, Brussels, pp 212–221
2. Savchenko Yu N (2001) Control of supercavitating motion of bodies, vol 11, VKI special course on supercavitating flows. RTO-AVT and VKI. RTO-EN-010, Brussels, pp 313–329
3. Vanek B, Bokor J, Balas G (2006) Theoretical aspects of high-speed supercavitation vehicle control. In: Proceedings of the 2006 American control conference, IEEE, Minneapolis, pp 5263–5268

4. Vanek B, Bokor J, Balas GJ (2007) Longitudinal motion control of a high-speed supercavitation vehicle. J Vib Control 13(2):159–184
5. Isidori A (1995) Nonlinear control system, 3rd edn. Springer, London, pp 101–112
6. Yuan Lei, Wu Han-song (2010) Multiple sliding mode adaptive fuzzy controller for nonlinear marine autopilot systems. Trans Intell Syst 5(4):308–312

A Low Power Received Signal Strength Indicator for Short Distance Receiver

Qianqian Lei, Erhu Zhao, Min Lin, and Yin Shi

Abstract A low power received signal strength indicator (RSSI) with limiter amplifier (LA) and an integrated automatic gain control (AGC) loop are fabricated in SMIC 0.13 μm technology for short distance receiver. The proposed limiter achieves minimum power dissipation which uses six-stage amplifier architecture. The RSSI has larger than 58 dB dynamic linear range, and the linearity error of the RSSI is less than 1 dB with the input power of limiter chain from −65 to −8 dBm. The voltage of RSSI output is from 0.13 to 0.98 V, the slope of output curve is 14.65 mV/dB, and the RSSI consumes 1.5 mA under 1.2 V supply voltage. By the proposed AGC loop, the receiver senses the input signal strength automatically and modifies the low noise amplifier (LNA) gain in order to make the strength of the output signal stable.

Keywords Limiter • RSSI • AGC

1 Introduction

System of wireless communication, propagation loss or multi-path fading causes the strength of the received signal to change several decades in the receiver. The variation of magnitude increases the loading of dynamic range, which makes the receiver synchronization mechanism complicated. In order to ease the proposed problem, at the last stage of intermediate frequency (IF) processor, the control mechanism of the signal magnitude needs to be provided, which is used to make the constant output signal for being demodulated further.

Q. Lei (✉) • E. Zhao
Department of physics, Xi'an Polytechnic University, Xi'an, China
e-mail: leiqianqian@163.com

M. Lin • Y. Shi
Suzhou-CAS Semiconductors Integrated Technology Research Center, Suzhou, China

W. Wang (ed.), *Mechatronics and Automatic Control Systems*, Lecture Notes in Electrical Engineering 237, DOI 10.1007/978-3-319-01273-5_84,

Generally, magnitude control circuit has two types, namely LA and AGC. An AGC is configured as a closed loop structure which consists of a variable gain amplifier and a detector of magnitude to adjust the receiver gain [1, 2] However, a limiter amplifier is made of a gain stages chain saturates the input scope to a constant value, which is an open-loop structure. With less current dissipation, LA can achieve a very larger dynamic range, so the LA is broadly used than an AGC in wireless transceiver. Besides, the RSSI is generally realized in logarithmic-linear form which is used to show the strength of the received signal.

This paper is organized as follows: System requirements and circuit architecture designs are depicted in Sect. 2. Detailed circuit design of the RSSI, LA and comparator are presented in Sect. 3. Measurement results are supplied in Sects. 4 and 5 gives conclusion, finally.

2 System Requirements and Circuit Architecture

Figure 1 shows the AGC loop architecture which is mainly composed of RSSI, LA, comparator, FSM (Finite State Machine) circuit and voltage generator. From Fig. 1, the LA amplifies the input signal to provide a signal of constant amplitude. RSSI circuit indicates the strength of the received signal is employed, be compared with the given voltages V_{IH} and V_{IL}, the RSSI output voltage can generate corresponding values, then, the FSM circuit produces a DC control voltage to change the low noise amplifier (LNA) gain according the compared results. Using this feedback loop, the system can automatically sense the receiver input signal strength and change the LNA gain to maintain constant strength of limiter output.

The RSSI characteristic can be seen in Fig. 2a and the state diagram of LNA gain can be seen in Fig. 2b. The principle of LNA gain tuning can be described as follows: When the input signal of LNA is larger enough, the LNA circuit should work under the set of low gain mode finally. However, if LNA works on the state of high gain initially, the control word of LNA is 11. On the basis of the larger input signal, the RSSI can output a smaller voltage which is compared with the first low reference voltage V_{AL} and exports a new product to vary the state of FSM, and the new state 10 through the loop feedback to the control port to vary the LNA gain, the LNA works under the gain state of moderate at present. On this state, if the output of RSSI is also a smaller voltage compared with second reference voltage V_{BL}, then, the present state will be changed by FSM, and new control word 01 should be supplied to LNA circuit to make the circuit works on the state of low gain, which forces the AGC loop to stability. On the other hand, if the input signal is smaller enough, using the same feedback and comparison process, the AGC loop can force LNA working on the state of high gain at last.

The block diagram of logarithmic amplifiers and limiters is proposed in Fig. 3. While the limiter input signal is very small, all limiter stages provide full gains. If A is each stage gain and n is stage numbers, thus, the overall gain of the chain becomes A^n. When input signal of chain raises and achieves a special level, the

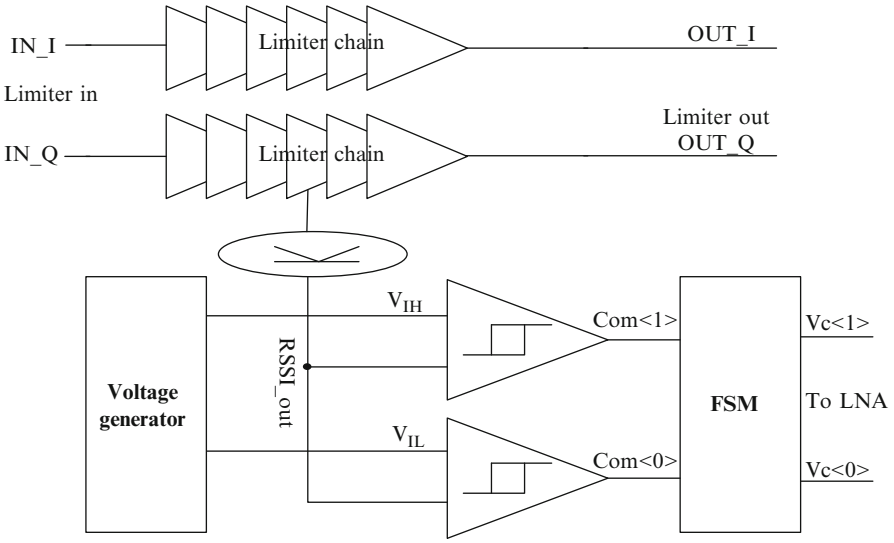

Fig. 1 The system architecture of AGC loop

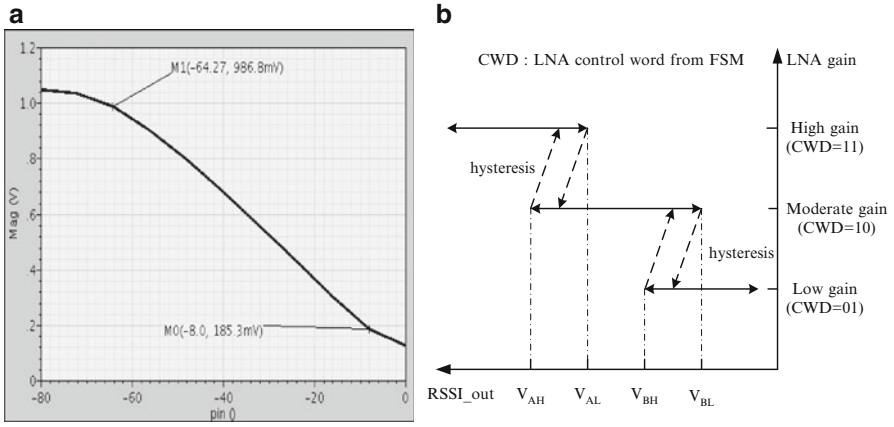

The characteristic of RSSI The state diagram of LNA gain

Fig. 2 (**a**) The characteristic of RSSI (**b**) The state diagram of LNA gain

end stage of the limiter chain starts to clip, so the full gain of the chain converts A^{n-1}. As increasing of the LNA input signal, more limiter gain stages clip. While the LNA input rises farther, every limiter stages clip, finally, so the gain of limiter chain turns one. Thus, the strength of RSSI input determines all gain piece wisely.

Also, the proposed amplifiers chain in Fig. 3 can extract the RSSI information. The input stage of rectifiers are carried out to transform voltage into current signal at every stage node, thus, each current of rectifier is summed and transformed into

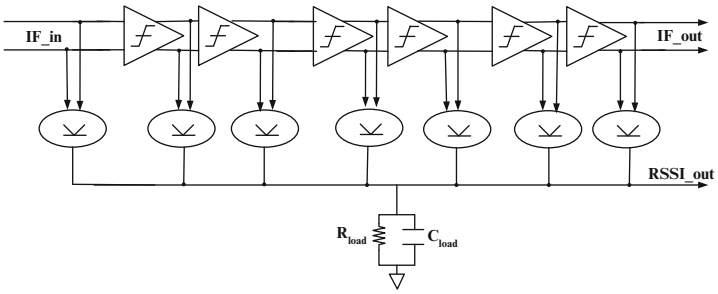

Fig. 3 Block diagram of RSSI

voltage with a resistor R_{load}. And AC component can be filtered by paralleled capacitor C_{load} and resistor R_{load}.

In order to achieve gain, allowable errors, bandwidth as well as low power consumption, it is significant to select the number of stages in the limiter and RSSI design. Increasing the limiter chain stage numbers, there are more poles are generated from every LA, and the bandwidth of the chain will reduce [3, 4]. Furthermore, if the stage number is six or seven, the chain obtains minimum power consumption with the overall bandwidth is 10 MHz and overall gain is 60 dB.

3 Circuit Designs

Figure 4 shows the individual LA circuit, the limiter uses current mirrors to eliminate the load transistors body effect [4]. The circuit configuration can use in low supply voltage. As can be seen in Fig. 4, if the size of transistors M_{3-4} and M_{7-8} has the same values, and the input transistors have the identical bias current. So, the amplifier gain can be given as

$$A_V = \frac{g_{M1}}{g_{M5}} = \frac{\sqrt{(W_1/L_1)}}{\sqrt{(W_5/L_5)}} \tag{1}$$

From Eq. 1, we can see the gain of the limiter amplifier circuit is determined by the transistor ratio, so, the amplifier gain is insensitive to thermal variations and process during prospered design.

Figure 5 shows the rectifier circuit [5]. The rectified signals are generated from differential pairs with unbalanced source-coupled. And one differential pair size is k times as big as the other differential pair size.

The rectifier current I_{out} can be shown as

$$I_{out} = (I_2 + I_3) - (I_1 + I_4) \tag{2}$$

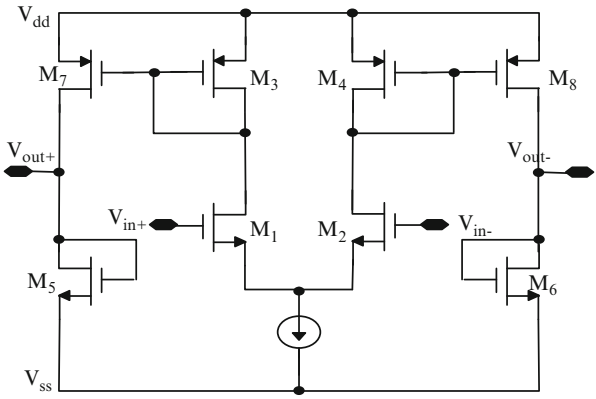

Fig. 4 The limier gain cell

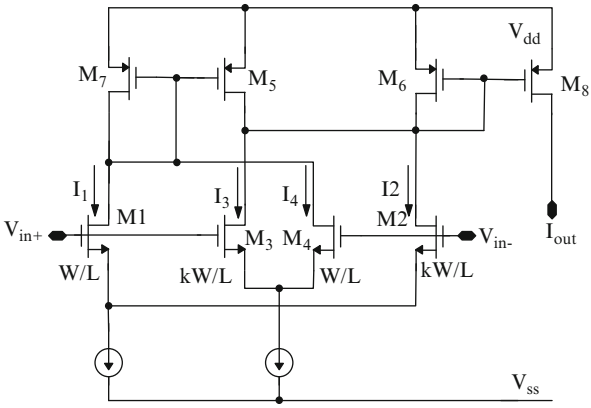

Fig. 5 The rectifier cell

As the input voltage of rectifier has no differential, the larger size transistor M_2, M_3 current will be K-times bigger than the current of smaller size transistor M_1, M_4. As input voltage is very small, the M_2 and M_3 is flowed by most of current. As a result, the current I_{out} will achieve maximum value based on Eq. 2, because the current flow into M_6 and M_8 which is the right side current mirror is larger than the current mirror (M_5 and M_7) of the left side. At the same time, the current I_{out} will decrease, when the input voltage differential increases.

As input voltage of the schematic in Fig. 5 increases, transistors M_1 and M_4 begin to get the current flow into the left side current mirror. Thus, the current of the right side decreases, thus, the input voltage determines the output current. When the input of the differential is large enough, the current flowing into M_{2-4} or M_{1-3} equivalent to the maximum tail currents, and the output current I_{out} will be nearly zero. The proposed rectifier can be uses in lower application because it has only three transistors stacked.

From Fig. 3, we can see each FWR current at output is summed and filtered to a filter which is a first-order passive LPF. We use internal capacitor and resistor as the passive LPF, and use variable resistors to adjust the filter bandwidth and RSSI linear slope.

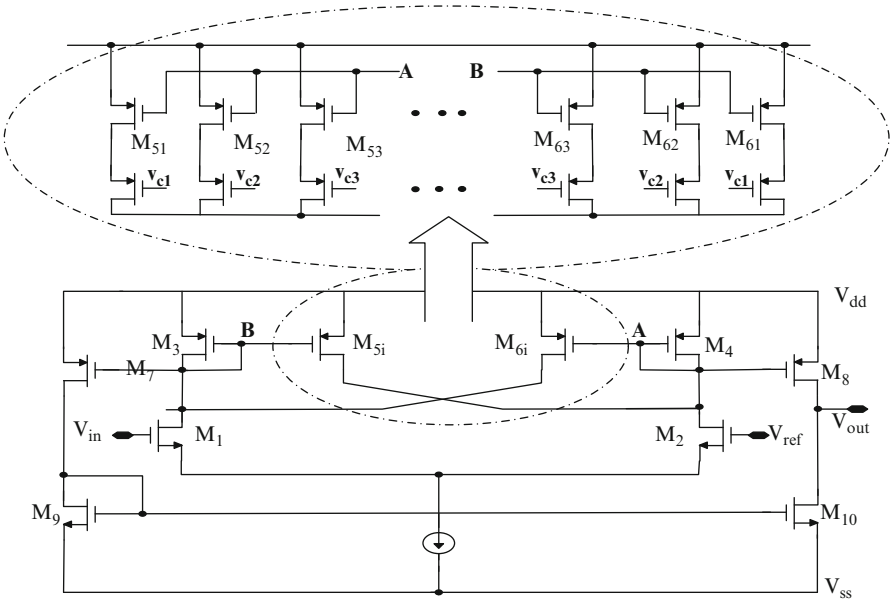

Fig. 6 Schematic of comparator with hysteresis

Figure 6 shows the schematic of comparator circuit which is used to transform the output voltage of RSSI into binary data. Considering the output of RSSI is not a very clean voltage, so we need a comparator with hysteresis. From Fig. 6, we can see the comparator contains a differential source-coupled pair and a differential to single ended converter. The hysteresis of this circuit is

$$V_H = 2 \times \sqrt{\frac{I_0}{k(W/L)_1}} \frac{\sqrt{\alpha} - 1}{\sqrt{1+\alpha}} \tag{3}$$

From the Eq. 3, we can see the comparator hysteresis is dependent on transistors size W/L, voltages of V_{GS} and V_{TH}, so, if the circuit process or supply voltage or temperature (PVT) has changed, the hysteresis of proposed comparator is also varied. In order to compensate the variation, we use control word of three bits to realize changeable hysteresis. Figure 6 gives the realization circuit of variable hysteresis in the dashed line.

4 Measurement Results

The proposed LA and RSSI with internal AGC loop have been implemented in SMIC 0.13 μm technology under $V_{DD} = 1.2$ V, the total power is 1.8 mW (without LNA). The die micrograph of the proposed circuit is shown in Fig. 7, and the die area with pads is 0.4 mm^2.

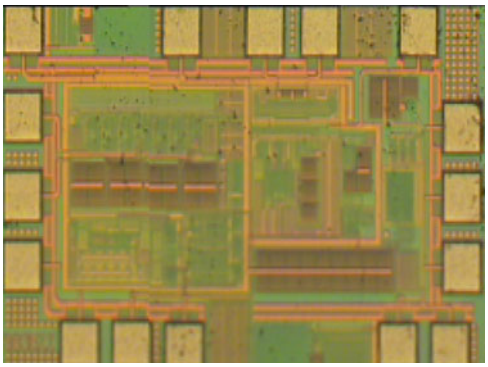

Fig. 7 Die photograph of the proposed RSSI with AGC loop

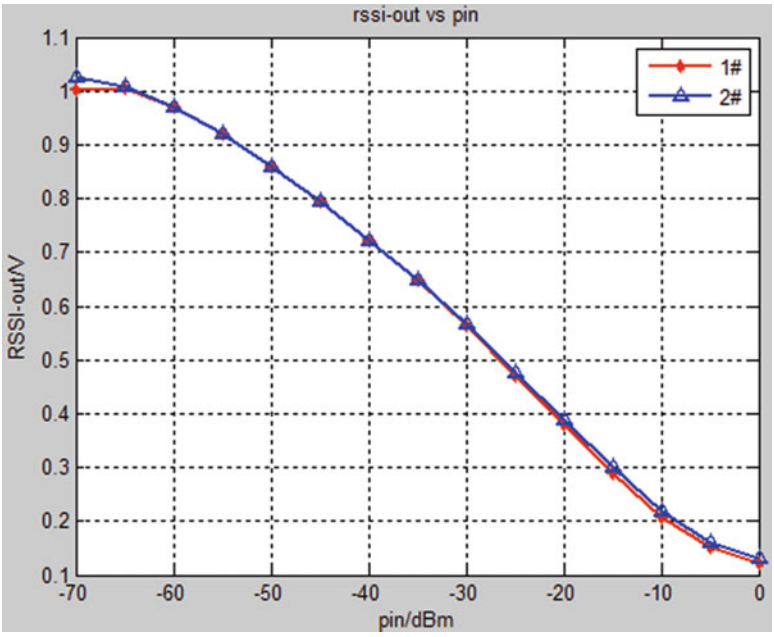

Fig. 8 The characteristic of RSSI

The characteristic of RSSI is tested with 22 Kohm load resistance and 10 pF internal capacitance. We use variable load resistance to achieve the desired value. Figure 8 gives the tested RSSI transfer functions which is graphed with two randomly chips. From Fig. 8, we can seen the linear scope of RSSI is about 58 dB, the linearity error is less than 1 dB, the linear voltage of RSSI is from 0.13 to 0.98 V, and the slope of linear range is achieved as 14.65 mV/dB.

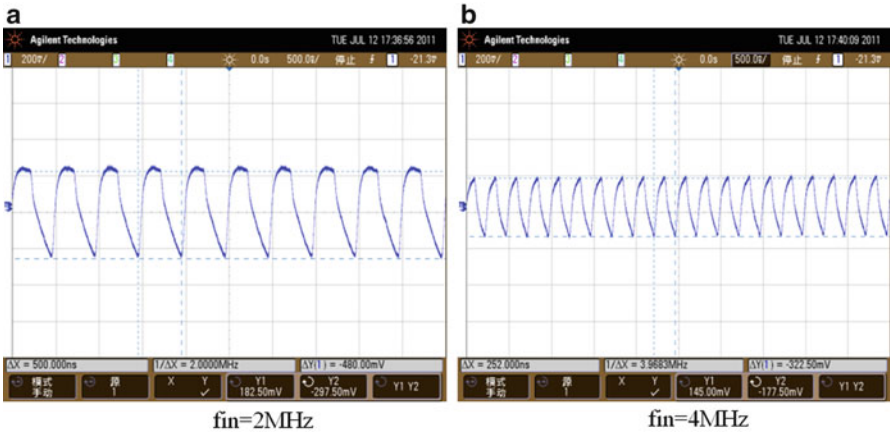

Fig. 9 Measured limiter outputs (**a**) fin = 2 MHz, (**b**) fin = 4 MHz

Table 1 The overall performance of the proposed RSSI

Parameters	Values
Technology	SMIC 0.13 μm technology
Die areas	0.4 mm^2
Output of limiter	480 mV
output voltage of RSSI	0.13~0.98 V
Linearity range	58 dB
Error of RSSI	<1 dB
Slop of RSSI	14.65 mV/dB
Variation of RSSI with temperature	30~40 mV
Supply voltage	1.2 V
Two path currents	1.5 mA

Figure 9 shows the limiter tested outputs under the 4 and 2 MHz frequencies of. As can be seen from Fig. 9, as increasing of frequency, the severely distortion of output waves. In our simulation, the limiter output wave does not have distortion at 4 MHz. The reason is that we use 2 pF capacitance as the simulated load, but use 10 p ~ 20 pF capacitance as the tested load, which distortion the output. The measured limiter output is 480 mVpp. And the measurement results of the proposed RSSI is listed in Table 1.

5 Conclusion

A larger dynamic range lower power RSSI with integrated AGC loop is presented in this paper. The proposed RSSI with AGC loop can automatically control the LNA gain to make stable output. Tested results prove that the proposed RSSI linear range

is larger than 58 dB, the output of the limiter peak to peak is 480 mV. Without the front-end LNA, the total loop with two paths consumes 1.5 mA under the 1.2 V supply voltage.

Acknowledgements This work was supported by the Doctoral Scientific Starting Research from the Xi'an Polytechnic University (Grant No. BS1209), and also was supported by Scientific Research Program Funded by Shaanxi Provincial Education Department (Grant No. 12JK0546) and (Grant No. 12JK0981).

References

1. Alegre JP, Calvo B, Celma S (2008) A high performance CMOS feedforward AGC circuit for wideband wireless receivers. In: IEEE international symposium on industrial electronics, Cambridge, UK, pp 1657–1661
2. Jeon O, Fox RM, Myers BA (2006) Analog AGC circuitry for a CMOS WLAN receiver. IEEE J Solid State Circ 41(10):2291–2300
3. Huang P-C, Chen Y-H, Wang C-K (2000) A 2-V 10.7MHz CMOS limiting amplifier/RSSI. IEEE J Solid State Circ 35(10):1474–1480
4. Wu C-P, Tsao H-W (2005) A 110MHz 84-dB CMOS programmable gain amplifier with integrated RSSI function. IEEE J Solid State Circ 40(6):1249–1258
5. Kimura K (1993) A CMOS logarithmic IF amplifier with unbalanced source-coupled pairs. IEEE J Solid State Circ 28(1):78–83

Ship Shaft Generator Control Based on Dynamic Recurrent Neural Network Self-Tuning PID

Ming Sun

Abstract Dynamic recurrent neural network (DRNN) self-tuning PID is proposed to control the unknown dynamic nonlinear function that includes nonlinearity, parameter uncertainty, load disturbance, etc. This control scheme is applied to the hardware-in-the-loop ship shaft generator (SSG) system; it can be mainly utilized to test and verify a real SSG control system on a simulating plant. The performance of DRNN self-tuning PID controller is shown assuming that the measurements available are the AC circuit voltage and current. This controller was also compared with a conventional PID controller for SSG. Simulation and experiment results show that the DRNN self-tuning PID controller is modified to track a desired reference signal.

Keywords Marine power station • Ship shaft generator • Self-tuning PID • DRNN

1 Introduction

Marine main engines (ME) are widely used in ocean-going ships, due to their high efficiency [1]. Optimization methodologies have been introduced into the ocean-going ships. An attractive option for ocean-going ships consists of electricity producing units, such as the ship shaft – generator (SSG) and the exhaust-gas turbo-generator (TG). The SSG is coaxially connected with ME and makes use of residual power of ME and raises its efficiency and economy. The application of SSG significantly reduces the fuel consumption and forms an effective energy-saving strategy [2]. A doubly fed induction generator was developed for a stand alone shaft alternator supplying constant frequency power to more effectively utilize the SSG to save energy [3].

M. Sun (✉)
Qingdao Ocean Shipping Mariners College, Research Center of Marine Energy Efficiency and Emission Reduction, Qingdao, China
e-mail: sunming@coscoqmc.com.cn

W. Wang (ed.), *Mechatronics and Automatic Control Systems*, Lecture Notes in Electrical Engineering 237, DOI 10.1007/978-3-319-01273-5_85,

PID controllers have dominated control applications for marine power station, although there has been considerable research achievements in the application of advanced controllers [4]. SSG processes have nonlinearity in the system dynamics in a wide operating range and DRNN self-tuning PID control strategies have been investigated in [5]. DRNN can evaluate online the unknown dynamic nonlinear functions that include nonlinearity, parameter uncertainty, load disturbance et al. [6]. Adaptive laws of the adjustable parameters and the evaluation error bounds of DRNN are formulated based on Lyapunov stability theory and a stable adaptive controller is synthesized [4, 6].

In this paper, the SSG of static frequency converter type is introduced, which includes a Thyristor inverter and converter, first used to direct current and then to alternate current at a constant frequency [7]. The mathematical model of the variable speed constant frequency SSG is used to develop a stator flux oriented vector control for a stand-alone system that maintains the output voltage constant [8]. Double self-tuning PID controller gives good stability and transient behavior and the SSG can supply the entire range of power demands while keeping a constant voltage and frequency for variations in both load and speed.

2 Description of the Ship Shaft Generator

The ship shaft generator system is shown as follows [9], which consists of SG (shaft generator), SC (synchronous condenser), PM (run-up motor), FM (fan motor), DCL (DC reactor), ACL (AC reactor), TH1 (thyristor converter), TH2 (thyristor inverter), ACB (air circuit breaker), MCCB (model case circuit breaker), BT (battery) and AVR (automatic voltage regulator).

In Fig. 1, SG is driven by the ME, which takes ME as its prime mover and makes full use of the remaining power of the ME. There is typical thyristor SSG system in Fig. 1, in which voltage, frequency and power can be automatically adjusted to ensure the power system voltage and frequency with high accuracy, while its energy saving effect is more prominent, it is widely used in ocean-going vessels.

3 Control Function

PID1 controller is the current controller, while PID2 controller is the frequency controller. The control circuit droops the frequency instruction signal with the increase of the output power, providing drooping characteristics of the power and eliminating any trouble for parallel running. Function generator is margin angle constant controller. The fire angle of the inverter side thyristor is normally set to approx. 140 (constant). However, while the inverter current increases, the voltage drops due to the revolution of the converter, and the overlap angle enlarges due to

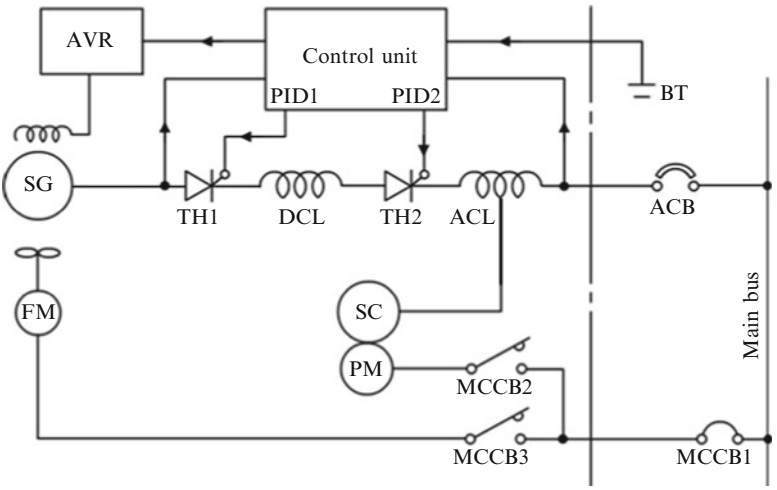

Fig. 1 The skeleton diagram for ship shaft generator system

the increase in S/G revolution, causing the reduction of the margin angle. This circuit, therefore, is to provide the signal to keep this margin angle constant.

The discrete-time PID of the following form:

$$u(k) = K_{\mathrm{p}}(k)x_1(k) + K_{\mathrm{i}}(k)x_2(k) + K_{\mathrm{d}}x_3(k) \tag{1}$$

Where $x_1(k) = e(k), x_2(k) = \sum_{i=1}^{k} (e(i) \times T), x_3(k) = \frac{e(k)-e(k-1)}{T}$. $e(k)$ is the process tracking error defined as $e(k) = y_{\mathrm{d}}(k) - y(k)$. $y_{\mathrm{d}}(k)$ is the desired trajectory, T is the sampling time, (K_{p1}, K_{i1}, K_{d1}) and (K_{p2}, K_{i2}, K_{d2}) are PID1 and PID2 controller parameter matrices, respectively.

A parameter vector $\theta_{\mathrm{pid}}(k)$ is formulated as

$$\theta_{\mathrm{pid}}(k) = \begin{bmatrix} [\,k_{\mathrm{p1}}(k) & k_{\mathrm{i1}}(k) & k_{\mathrm{d1}}(k)\,]^{\mathrm{T}} \\ [\,k_{\mathrm{p2}}(k) & k_{\mathrm{i2}}(k) & k_{\mathrm{d2}}(k)\,]^{\mathrm{T}} \end{bmatrix} \tag{2}$$

The PID self-tuning algorithm is defined as

$$\theta_{\mathrm{pid}}(i+1) = \theta_{\mathrm{pid}}(i) + \Delta\theta_{\mathrm{pid}}(i) = \theta_{\mathrm{pid}}(i) + K_{\mathrm{pid}}(i)e(i) \tag{3}$$

Where i is the iteration steps, $K_{\mathrm{pid}}i$) is the gain matrix and is designed as

$$K_{\mathrm{pid}}(i) = \frac{1-\varepsilon}{\varepsilon}\left[\frac{\partial y(i)}{\partial\theta_{\mathrm{pid}}(i)}\right]^{\mathrm{T}}\left\{\frac{\partial y(i)}{\partial\theta_{\mathrm{pid}}(i)}\left[\frac{\partial y(i)}{\partial\theta_{\mathrm{pid}}(i)}\right]^{\mathrm{T}}\right\}^{-1} \tag{4}$$

ε is a positive constant and defined as a discrete-time Lyapunov function $V(i) = \varepsilon e(i)^{\mathrm{T}} e(i) > 0$.

$K_{\mathrm{p}}(k)$, $K_{\mathrm{i}}(k)$ and $K_{\mathrm{d}}(k)$ tuned by DRNN is designed as

$$E(k) = \frac{1}{2}(e(k))^2 \tag{5}$$

$$K_{\mathrm{p}}(k) = K_{\mathrm{p}}(k-1) - \eta_{\mathrm{p}} \frac{\partial E}{\partial K_{\mathrm{p}}} = K_{\mathrm{p}}(k-1) + \eta_{\mathrm{p}} e \frac{\partial y}{\partial u} x_1(k) \tag{6a}$$

$$K_{\mathrm{i}}(k) = K_{\mathrm{i}}(k-1) - \eta_{\mathrm{i}} \frac{\partial E}{\partial K_{\mathrm{i}}} = K_{\mathrm{i}}(k-1) + \eta_{\mathrm{i}} e \frac{\partial y}{\partial u} x_2(k) \tag{6b}$$

$$K_{\mathrm{d}}(k) = K_{\mathrm{d}}(k-1) - \eta_{\mathrm{d}} \frac{\partial E}{\partial K_{\mathrm{d}}} = K_{\mathrm{d}}(k-1) + \eta_{\mathrm{d}} e \frac{\partial y}{\partial u} x_3(k) \tag{6c}$$

$\eta_{\mathrm{p}}, \eta_{\mathrm{i}}$ and η_{d} are the learning rates of proportional, integral and derivative, respectively.

$$\frac{\partial y}{\partial u} \approx \frac{\partial y_{\mathrm{DRNN}}}{\partial u} = \sum_j \omega_j^{\mathrm{o}} f'(S_j) \omega_{ij}^{\mathrm{I}} \tag{7}$$

$$\omega_j^{\mathrm{o}}(k) = \omega_j^{\mathrm{o}}(k-1) + \eta_{\mathrm{out}} \Delta\omega_j^{\mathrm{o}}(k) + \alpha\left(\omega_j^{\mathrm{o}}(k-1) - \omega_j^{\mathrm{o}}(k-2)\right) \tag{8a}$$

$$\omega_{ij}^{\mathrm{I}}(k) = \omega_{ij}^{\mathrm{I}}(k-1) + \eta_{\mathrm{in}} \Delta\omega_{ij}^{\mathrm{I}}(k) + \alpha\left(\omega_{ij}^{\mathrm{I}}(k-1) - \omega_{ij}^{\mathrm{I}}(k-2)\right) \tag{8b}$$

$$f(x) = (1 - e^{-x})/(1 + e^{x}) \tag{8c}$$

Where η_{in} and η_{out} are the learning rates of DRNN input layer and output layer, respectively, α is the inertia coefficient. S is the hyperbolic functions of recurrent layer neural networks. w^{I} is the NN weight vector of input layer, w^{o} is the NN weight vector between recurrent layer and output layer.

4 Modeling of SSG

Suppose the SSG is connected to an infinite bus, then SSG rotating at a synchronous speed ωs and capable of absorbing or delivering any amount of energy, the SSG can be modeled by the following equations

$$\zeta \ddot{\delta}_{\mathrm{m}} + \xi \dot{\delta}_{\mathrm{m}} + P_{\mathrm{g}} = P_{\mathrm{m}} \tag{9}$$

$$T'_{\mathrm{D0}}\left|\dot{E}'_{\mathrm{a}}\right| = -\frac{X_{\mathrm{D}}}{X'_{\mathrm{D}}}|E'_{\mathrm{a}}| - \left(\frac{X'_{\mathrm{D}} - X_{\mathrm{D}}}{X'_{\mathrm{D}}}\right)|V_{\infty}|\cos(\delta_{\mathrm{m}}) + E_{\mathrm{fD}} \tag{10}$$

Where $\delta_{\mathrm{m}} = \angle E'_{\mathrm{a}} - \angle V_{\infty}$ is the SSG power angle with reference to the infinite bus, $\omega = \dot{\delta}_{\mathrm{m}}$ is the rotor angular speed, E'_{a} – transient voltage, ζ – inertia constant, ξ – damping constant, P_{m} is the constant mechanical power supplied by the ME, and T'_{D0} – transient time constant. X_{D} (= x_{D} + x_{L}) is the augmented reactance, x_{D} – the direct axis reactance and x_{L} – the line reactance, X'_{D} – the transient augmented reactance, V_{∞} – the infinite bus voltage. P_{g} is the generated power while E_{fD} is the field excitation voltage given by

$$P_{\mathrm{g}} = \frac{1}{X'_{\mathrm{D}}}|E'_{\mathrm{a}}||V_{\infty}|\sin(\delta_{\mathrm{m}}) + \frac{1}{2}\left(\frac{1}{X_{\mathrm{Q}}} - \frac{1}{X'_{\mathrm{D}}}\right)|V_{\infty}|^2\sin(2\delta_{\mathrm{m}}) \tag{11}$$

$$E_{\mathrm{fD}} = \frac{\omega_{\mathrm{s}} M_{\mathrm{f}}}{\sqrt{2} r_{\mathrm{f}}} v_{\mathrm{f}} \tag{12}$$

Where v_{f} is the field excitation voltage, X_{Q} is the quadrature axis augmented reactance, M_{f} is the mutual inductance between stator and rotor windings, r_{f} is the field resistance.

SSG model can be rewritten as

$$\dot{\delta}_{\mathrm{m}} = \omega - \omega_{\mathrm{s}} \tag{13}$$

$$\dot{\omega} = \frac{P_{\mathrm{m}}}{\zeta} - \frac{|V_{\infty}|}{\zeta X'_{\mathrm{D}}}|E'_{\mathrm{a}}|\sin(\delta_{\mathrm{m}}) - \frac{1}{2}\frac{|V_{\infty}|^2}{\zeta}\left(\frac{1}{X_{\mathrm{Q}}} - \frac{1}{X'_{\mathrm{D}}}\right)\cos(\delta_{\mathrm{m}})\sin(\delta_{\mathrm{m}}) - \frac{\xi}{\zeta}(\omega - \omega_{\mathrm{s}}) \tag{14}$$

$$\left|\dot{E}'_{\mathrm{a}}\right| = -\frac{X_{\mathrm{D}}}{T'_{\mathrm{D0}}X'_{\mathrm{D}}}|E'_{\mathrm{a}}| - \left(\frac{X'_{\mathrm{D}} - X_{\mathrm{D}}}{T'_{\mathrm{D0}}X'_{\mathrm{D}}}\right)|V_{\infty}| + \frac{E_{\mathrm{fd}}}{T'_{\mathrm{D0}}} \tag{15}$$

$$\dot{\psi}_{D} = -\frac{\omega_{\mathrm{s}} R_{s}}{X'_{\mathrm{D}}}\psi_{\mathrm{D}} + \omega\psi_{\mathrm{Q}} + \frac{\omega_{\mathrm{s}} R_{s}}{X'_{\mathrm{D}}}E'_{Q} + \omega_{\mathrm{s}} V\sin(\delta_{\mathrm{m}}) \tag{16}$$

$$\dot{\psi}_{\mathrm{Q}} = -\omega\psi_{\mathrm{D}} - \frac{\omega_{\mathrm{s}} R_{\mathrm{s}}}{X'_{\mathrm{D}}}\psi_{\mathrm{Q}} + \omega_{\mathrm{s}} V\cos(\delta_{\mathrm{m}}) \tag{17}$$

Where ψ_{D} and ψ_{Q} are the direct and quadrature-axes stator flux linkages, respectively, R_{s} is an equivalent transmission line resistance.

Suppose the above parameters are constant limited in only equilibrium point and are bounded, in other cases, they are time-variant [10, 11].

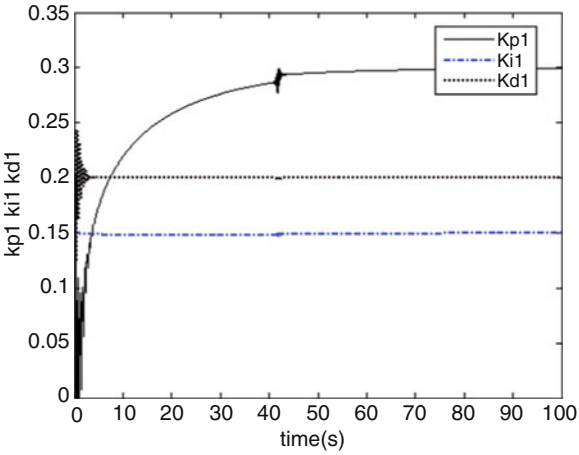

Fig. 2 Step response with PID1 controller parameters

5 Experiments and Results

PID controller is based on DRNN self-tuning algorithm, its parameters are originally obtained as follows: NN input $I = \{u(k-1), y(k), 1.0\}, \eta_{in} = 0.4, \eta_{out} = 0.4$, $\alpha = 0.04$, w^o and w^I are random numbers and its span is $[-1,1]$. Initial $K_p = 20$, $T_I = 4$ s, $T_D = 1.75$ s, $\varepsilon = 0.6$; $\eta_{p1} = 0.5$, $\eta_{d1} = 0.3$, $\eta_{i1} = 0.001$; $\eta_{p2} = 0.5$, $\eta_{d2} = 0.3$, $\eta_{i2} = 0.0001$. Sampling time $T = 0.1$ s. Step response results of K_p, K_i and K_d shown in Figs. 2 and 3.

The SSG process controlled by the developed DRNN self-tuning PID control and the fixed parameter PID control is made as follows, the tracking performance for a process is shown in Figs. 4 and 5.

In Fig. 4, it can be seen that the performance of the DRNN self-tuning PID is superior to the fixed parameter PID. In Fig. 5, the SSG hardware-in-the–loop system is detailed in [10, 11], it is able to track the desired reference signals with minimum error. The effects of parameters, such as ε, α and η on the SSG control model, will compensate for the PID parameters variation through DRNN self-tuning. Hence, DRNN self-tuning PID multivariable control has a fast response, adaptive ability, strong anti-disturbance capability.

6 Conclusion

In this paper, a DRNN self-tuning PID control was proposed for SSG system with unknown dynamic state. As the DRNN self-tuning algorithm of the PID was derived using the Lyapunov method, convergence of the model tracking error was guaranteed stable and maintained minimum. Therefore, the DRNN self-tuning PID controller can exert adaptive compensation effect for the system parameter

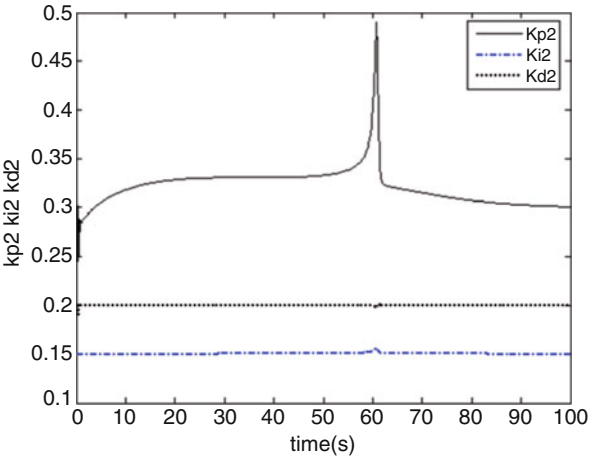

Fig. 3 Step response with PID2 controller parameters

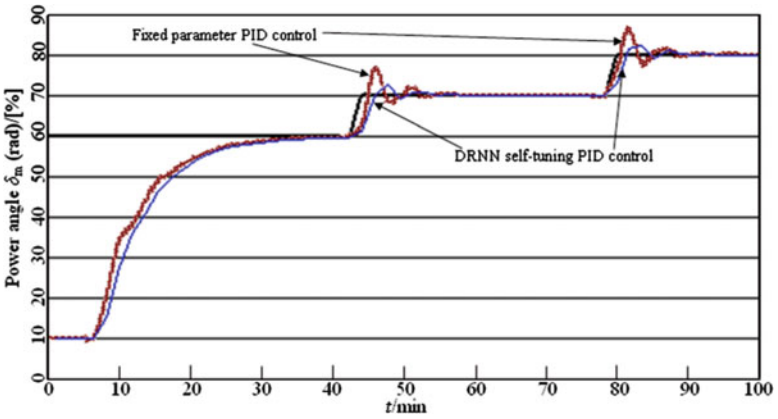

Fig. 4 Process response with PID controller

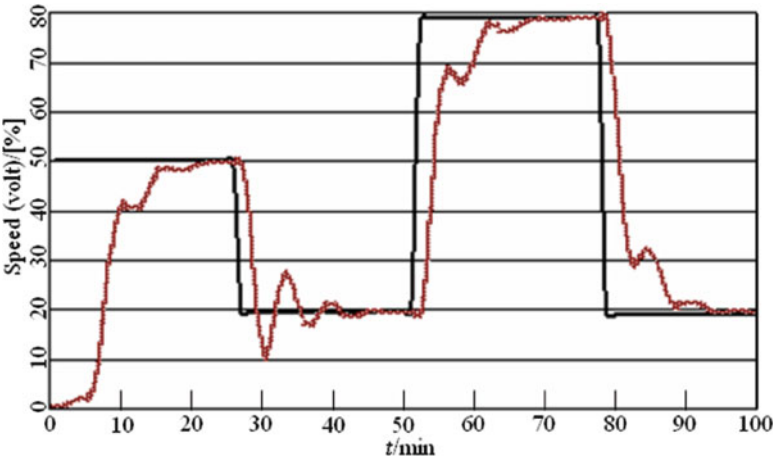

Fig. 5 Hardware-in-the-loop system speed response

uncertainty and disturbance, and SSG system is capable of robustness and good tracking performance. The developed controller is applied to the improvement of hardware-in-the-loop SSG system. The features described above were verified by the simulation results.

Acknowledgements This work was supported by the National Natural Science Foundation of China (51179102).

References

1. Lamaris VT, Hountalas DT (2010) A general purpose diagnostic technique for marine diesel engines-application on the main propulsion and auxiliary diesel units of a marine vessel. Energy Convers Manage 51(4):740–753
2. Gui-chen Zhang, Jie Ma (2011) A general purpose diagnostic technique for marine diesel engines-application on the main propulsion and auxiliary diesel units of a marine vessel. J Harbin Inst Technol 43(11):682–687 (In Chinese)
3. Peng Ling, Li Yong Dong et al (2009) Vector control of a doubly fed induction generator for stand-alone shaft generator systems. J Tsinghua Univ (Sci Tech) 49(7):938–942 (In Chinese)
4. Yu DL, Chang TK, Yu DW (2007) A stable self-learning PID control for multivariable time varying systems. Control Eng Pract 15(12):1577–1587
5. Wei-der Chang, Jun-juh Yan (2005) Adaptive robust PID controller design based on a sliding mode for uncertain chaotic systems. Chaos Soliton Fract 26(1):167–175
6. You-wang Zhang, Wei-hua Gui, Quan-ming Zhao (2005) Adaptive electro-hydraulic position tracking system based on dynamic recurrent fuzzy neural network. Control Theory Appl 22 (4):551–556 (In Chinese)
7. Gui-chen Zhang (2010) Application of energy-feedback and energy-saving technology based on SINAMICS in the marine shaft generating. Ship Eng 32(2):43–46 (In Chinese)
8. De Leon-Morales J, Busawon K, Acha-Daza S (2001) A robust observer-based controller for synchronous generators. Elec Power Energy Syst 23(3):195–211
9. Gui-chen Zhang (2012) Modern marine power station. Dalian Maritime University Press, Dalian, p 144 (In Chinese)
10. Gui-chen Zhang (2012) Hardware-in-the-loop for on-line identification of SSP driving motor. Lect Notes Elec Eng 135(31):251–256
11. Saleem A, Issa R, Tutunji T (2010) Hardware-in-the-loop for on-line identification and control of three-phase squirrel cage induction motors. Simul Model Pract Theory 18(3):277–290

Control System Design and Simulation of Microelectromechanical Hybrid Gyroscope

Haiyan Xue, Bo Yang, and Shourong Wang

Abstract In order to achieve the closed-loop control of those microelectromechanical hybrid gyroscopes with large open-loop zero outputs, a self-tuning control system is designed. Firstly, the gyroscope tuning principle is illustrated and the dynamic system is presented. Next, the whole open-loop system is analyzed and the tuning simulation is performed. The tuning simulation results confirm the feasibility of the tuning principle. Finally, the self-tuning control system is designed. The scheme of the closed-loop system is constructed and the corresponding simulation is carried out. The self-tuning simulation results indicate that the closed-loop system can lock the positions of the rotors, showing that the self-tuning control system is feasible.

Keywords Microelectromechanical hybrid gyroscope • Tuning • Self-tuning control • Closed-loop system

1 Introduction

Microelectromechanical hybrid gyroscope evolves on the basis of the dynamically tuning technology and the silicon micro-machined technology [1, 2]. It is featured in the theoretical accuracy of 0.005 °/h, as accurate as Dynamically Tuned Gyroscope (DTG), and the smaller volume compared to the silicon micro-gyroscope [3, 4]. By means of the dynamically tuning technology, the classical decoupling control system can theoretically achieve the closed-loop control on the hybrid gyroscope [5, 6]. However, since the structure design and the assembly technology of the gyroscope is still not imperfect, zero outputs of some gyroscopes are large in

H. Xue • B. Yang (✉) • S. Wang
Key Laboratory of Micro-inertial Instrument and Advanced Navigation Technology of Ministry of Education, Southeast University, Nanjing, China
e-mail: yangbo20022002@163.com

W. Wang (ed.), *Mechatronics and Automatic Control Systems*, Lecture Notes in Electrical Engineering 237, DOI 10.1007/978-3-319-01273-5_86,

open-loop mode, which makes the integrators saturation in the decoupling network. As a result, the decoupling control system is difficult to achieve the closed-loop control of gyroscopes [7, 8]. It's necessary to seek an innovative method to control these gyroscopes steadily.

2 The Dynamic Analysis of Microelectromechanical Hybrid Gyroscope

The schematic of microelectromechanical hybrid gyroscope is shown in Fig. 1. Traditionally, the tuning in the DTG is achieved by adjusting its stiffness coefficient of torsion bars, the gimbal inertia moment and the motor's speed. However, the rotor structure is not easy to be adjusted repeatedly by means of the bulk silicon process. Besides, the gimbal negative stiffness coefficient is only 10^{-3} times of the torsion bar. In this way, a high speed motor which can be accurately adjusted is required in the hybrid gyroscope. But this is difficult to realize. At the same time, in order to make full use of the static electricity feedback of the silicon micro mechanical structure, a preload voltage is exerted on torque feedback electrodes in the hybrid gyroscope, generating the electrostatic torque compensate stiffness moment of torsion bars. Referring to the dynamics equations of DTG, the hybrid gyroscope dynamics equations can be deducted [9, 10]:

$$\begin{aligned} J\ddot{\beta} + \delta\dot{\beta} + (\Delta K - K_C)\beta + H\dot{\alpha} + \lambda\alpha &= M_{fx} - J\ddot{\varphi}_x - H\dot{\varphi}_y \\ J\ddot{\alpha} + \delta\dot{\alpha} + (\Delta K - K_C)\alpha - H\dot{\beta} - \lambda\beta &= M_{fy} - J\ddot{\varphi}_y + H\dot{\varphi}_x \end{aligned} \tag{1}$$

Where, $\Delta K = K_{\mathrm{p}} - K_{\mathrm{N}}$. K_{p} is the stiffness coefficient of torsion bars. K_{N} is the negative stiffness coefficient of gimbals. K_{C} is the electric stiffness coefficient. J is the inertia moment of gyroscope spindle, H is the rotation angular momentum of gyroscope. α, $\dot{\alpha}$, $\ddot{\alpha}$, β, $\dot{\beta}$, $\ddot{\beta}$ are angles, angular velocities, angular accelerations of gyroscope spindle in the oy-axis and the ox-axis of the shell coordinate. $\varphi_x, \dot{\varphi}_x, \ddot{\varphi}_x, \varphi_y$, $\dot{\varphi}_y$, $\ddot{\varphi}_y$ are angles, angular velocities, angular accelerations of the gyroscope shell in ox-axis and oy-axis of inertial space. $M_{\mathrm{fx}}, M_{\mathrm{fy}}$ are feedback torques exerted on the

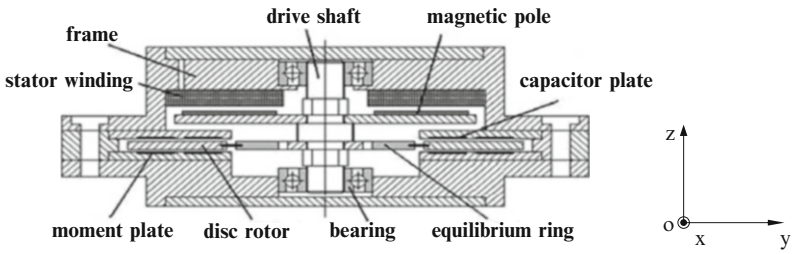

Fig. 1 Schematic diagram of microelectromechanical hybrid gyroscope

ox-axis and the oy-axis of the shell coordinate. λ is the orthogonal damping elasticity coefficient, $\lambda = (\delta + D)\dot{\theta}$. δ is the viscous damping coefficient of flexible torsion bar. D is the damping coefficient of rotor rotation axis. The Laplace transformation of Eq. 1 is as follows:

$$\begin{bmatrix} \beta \\ \alpha \end{bmatrix} = \begin{bmatrix} G_{11} & G_{12} \\ G_{21} & G_{22} \end{bmatrix} \begin{bmatrix} M_{fx} \\ M_{fy} \end{bmatrix} - \begin{bmatrix} C_{11} & C_{12} \\ C_{21} & C_{22} \end{bmatrix} \begin{bmatrix} \varphi_x \\ \varphi_y \end{bmatrix} \tag{2}$$

Where,

$$\begin{bmatrix} G_{11} & G_{12} \\ G_{21} & G_{22} \end{bmatrix} = \begin{bmatrix} [Js^2 + \delta s + (\Delta K - K_C)]/\Delta(s) & -(Hs + \lambda)/\Delta(s) \\ (Hs + \lambda)/\Delta(s) & [Js^2 + \delta s + (\Delta K - K_C)]/\Delta(s) \end{bmatrix} \tag{3}$$

$$\begin{bmatrix} C_{11} & C_{12} \\ C_{21} & C_{22} \end{bmatrix} = \begin{bmatrix} z_1(s)/\Delta(s) & z_2(s)/\Delta(s) \\ -z_2(s)/\Delta(s) & z_1(s)/\Delta(s) \end{bmatrix} \tag{4}$$

$$z_1(s) = J^2 s^4 + J\delta s^3 + (J(\Delta K - K_C) + H^2)s^2 + H\lambda s$$

$$z_2(s) = (H\delta - J\lambda)s^2 + H(\Delta K - K_C)s$$

$$\begin{aligned} \Delta(s) = {} & J^2 s^4 + 2J\delta s^3 + (\delta^2 + 2J(\Delta K - K_C) + H^2)s^2 \\ & + (2\delta(\Delta K - K_C) + 2H\lambda)s + (\Delta K - K_C)^2 + \lambda^2 \end{aligned}$$

Where, G_{11} and G_{22} indicate the damping effects on the inertia axis. G_{12} and G_{21} show the damping effects on the orthogonal axis. In the closed-loop state, C_{11}, C_{12}, C_{21} and C_{22} also have damping effects on outputs. Neglecting damping effects, C_{12} and C_{21} characterize the precession of the microelectromechanical hybrid gyroscope, C_{11} and C_{22} show the rigid body characteristic.

3 Microelectromechanical Hybrid Gyroscope Tuning Principle

The hybrid gyroscope structure diagram is shown in Fig. 2 [11]. The upper and lower discs are fixed electrode plates. These electrodes are divided into the inner and outer rings. The inner ring is a detecting electrode and the outer ring is a torque feedback electrode. The intermediate disc is a silicon structure rotor module. The rotor module consists of the inner ring, gimbals, the rotor and torsion bars. In Fig. 2, V_o is the preload voltage, V_f is the feedback voltage in closed-loop condition, V_1 is the carrier voltage, I_{out1} and I_{out2} are the detecting signal outputs of the inner rings.

On one hand, by applying a proper preload voltage on the torque feedback electrodes, the electric stiffness moment is generated to balance the stiffness

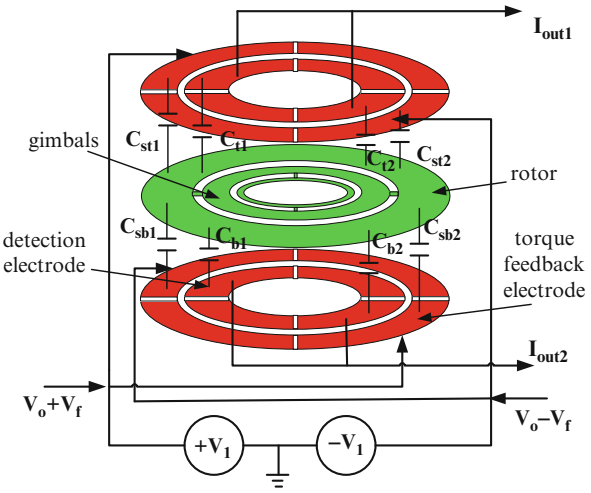

Fig. 2 The structure diagram of microelectromechanical hybrid gyroscope

moment of torsion bars. On the other hand, the feedback voltage balances the Coriolis torque caused by the angular velocity.

When applying $V_o + V_f, V_o - V_f$ on two normal torque feedback electrodes of y axis, The total moment, made up of the generated electrostatic torque and the torque component in y-axis of the shell coordinates from inside to rotor, is as follows:

$$T_y^{'} + M_y = -(\Delta K - K_C)\alpha + \delta\beta\dot{\theta} + K_{VF}V_f \tag{5}$$

Where the electric stiffness coefficient is $K_C = \varepsilon_s\gamma(R^4{}_M - r^4{}_M)V^2{}_o/d^3$. ε_s is the dielectric constant in air. γ is the single feedback electrode angle. R_M and r_M are outer and inner radiuses of the force feedback electrodes. d is mounting distance between rotor and electrodes.

Thus, a proper preload voltage is exerted to make $\Delta K - K_C = 0$. When the gyroscope is tuned, the preload voltage is as follows:

$$V_o = \sqrt{\Delta K d^3 / \varepsilon_s \gamma (R_1^4 - r_M^4)} \tag{6}$$

Because $\Delta K = 6.858 \times 10^{-4}$ N · m/rad, $d = 40 \times 10^{-6}$ m, $\varepsilon_s = 8.86 \times 10^{-12}$, $\gamma = 1.309$ rad, $R_M = 10 \times 10^{-3}$ m, $r_M = 7.05 \times 10^{-3}$ m, the tuning voltage is $V_o = 25.77$ V.

4 Microelectromechanical Hybrid Gyroscope Open-Loop System Analysis and Simulation

In open-loop condition, ignoring the external disturbances and the gyro nutation, the steady-state solutions of hybrid gyroscope dynamic equations are as follows:

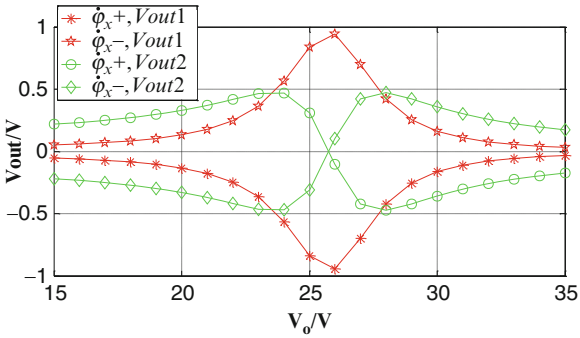

Fig. 3 Hybrid gyroscope open-loop system simulation diagram with variable preload voltage

$$\begin{aligned}\alpha^* &= \frac{H\dot{\varphi}_x(\Delta K - K_C) - \lambda H\dot{\varphi}_y}{\lambda^2 + (\Delta K - K_C)^2} \\ \beta^* &= \frac{-H\dot{\varphi}_y(\Delta K - K_C) - \lambda H\dot{\varphi}_x}{\lambda^2 + (\Delta K - K_C)^2}\end{aligned} \tag{7}$$

When $\delta = 1 \times 10^{-7}$, $D = 5 \times 10^{-9}$, angular rate input of y axis $\dot{\varphi}_y = 0$, angular rate inputs of x axis $\dot{\varphi}_x = 1\ ^\circ$/s and $\dot{\varphi}_x = -1\ ^\circ$/s, considering the angle-capacitor transforming coefficients $K_{\beta C}$ and the capacitor-voltage transforming coefficients K_{CV}, the inertia axis output voltage *Vout1* and orthogonal axis output voltage *Vout2* are shown as Fig. 3.

From the simulation of variable preload voltages, it is evident that the tuning voltage is 25.77 V which is accordant with the calculation in the upper segment. At the tuning point, the output of the inertia axis reaches a maximum value and the output of the orthogonal axis is zero. Two axis outputs can be obviously distinguished. When off the tuning point, effected by the torsion bars rigidity, the outputs of two axes get closer and closer, and even crossed.

5 Closed-Loop Control System Design and Simulation

The cross-coupling component is expected not to exist in the gyro rotor's output. In other words, the input angular velocities along their own measuring axis have a one-to-one relationship with their corresponding outputs, and won't affect each other. However, confined by the mechanical structure, the cross-coupling between the two measuring axes is inevitable. Since the zero outputs of some gyros are large, the integrator in the decoupling network tends to saturate, which restricts the application of whole decoupling control system. Thereby, the system is designed to be self-turned only.

When the gyroscope works in the tuning state, ignoring the damping, the open-loop transfer functions of the inertia axis and the quadrature axis are respectively as follows:

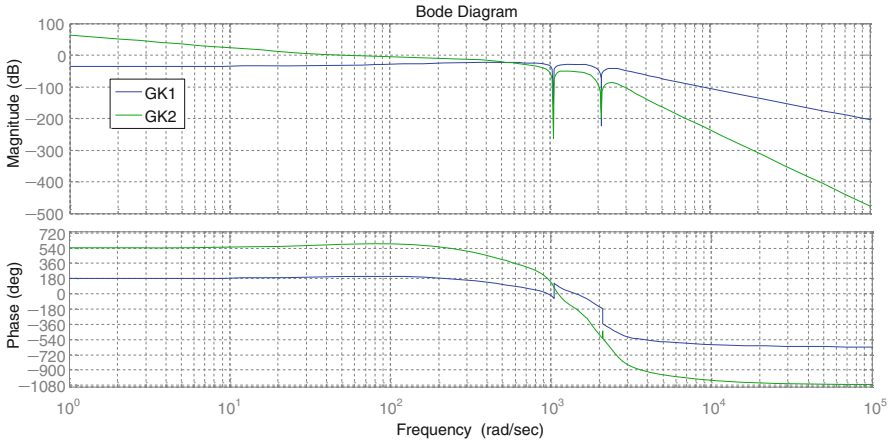

Fig. 4 Open-loop Bode diagram of hybrid gyroscope with self-tuning element

$$G'_{K1} = K_{\beta C} K_{CV} K_{VF} \Big/ \left\{ J[s^2 + (H/J)^2] \right\} \tag{8}$$

$$G'_{K2} = K_{\beta C}^2 K_{CV}^2 K_{VF}^2 H^2 \Big/ \left\{ J^2 s[s^2 + (H/J)^2] \right\}^2 \tag{9}$$

Where, K_{VF} is the torque feedback coefficient. Considering adopting the band-stop filter to eliminate the motor disturbance and nutation, the system with the proper configuration of zeros and poles should be fast, accurate and steady in response. The open-loop transfer functions are as follows:

$$G_{K1} = \frac{2.4456 K_{\beta C} K_{CV} K_{VF} (1/60\ \mathrm{s} + 1)}{J[s^2 + (H/J)^2](1/1,500\ \mathrm{s} + 1)(1/1,500\ \mathrm{s} + 1)} \tag{10}$$

$$G_{K2} = \frac{5.9811 K_{\beta C}^2 K_{CV}^2 K_{VF}^2 H^2 (1/60\ \mathrm{s} + 1)^2}{\left\{ J^2 s[s^2 + (H/J)^2](1/1,500\ \mathrm{s} + 1)(1/1,500\ \mathrm{s} + 1) \right\}^2} \tag{11}$$

The Bode diagram of the open-loop system is shown in Fig. 4. It can be seen from the diagram that when the inertia axis amplitude is under 0 dB, the intermediate region of the precession axis is gentle. The crossover frequency is 48 rad/s. The amplitude margin is 10.4 dB and the phase margin is 45°. The system can lock the rotor position quickly, accurately and stably.

Based on the design of the self-tuning system, the closed-loop system block diagram is built, as Fig. 5. Where, k is the self-tuning element (1/60 s + 1)/((1/1,500 s + 1)(1/1,500 s + 1)), $k_x = k_{\beta C} \times k_{cv}$, k_l is the low pass filter and band-stop filter.

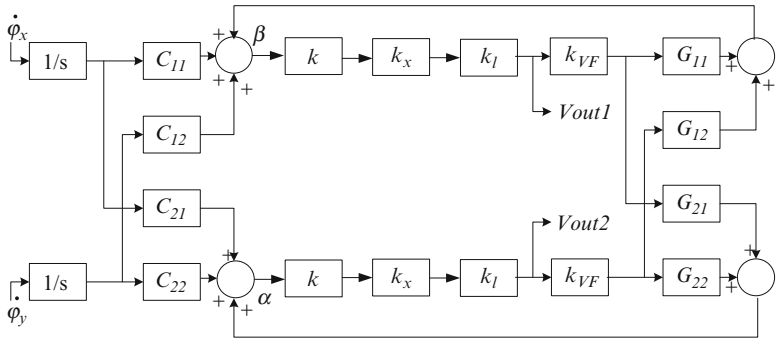

Fig. 5 Hybrid gyroscope closed-loop system block diagram

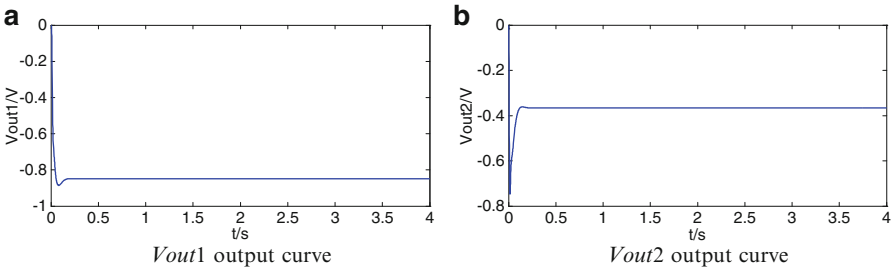

Fig. 6 When $\dot{\phi}_x = 0°/s$ and $\dot{\phi}_y = 1°/s$, the system outputs (**a**) *Vout*1 output curve, (**b**) *Vout*2 output curve

Considering the damping, the tuning voltage is utilized in the system. When $\dot{\phi}_x = 0°/s$, $\dot{\phi}_y = 1°/s$, *V*out1 and *V*out2 are shown in Fig. 6. From the graph, the system realizes the closed-loop control for the gyroscope. Due to the effect of damping, the response time is 0.15 s. The output of the orthogonal axis not only tracks the input angular velocity but also is affected by the damping. The response amplitude is 0.85 V. The output of the inertia axis is 0.37 V under the effect of damping. It should be explained that the damping coefficients of microelectromechanical hybrid gyroscope are the valuations in reference to DTG.

6 Conclusion

This paper introduces a microelectromechanical hybrid gyroscope dynamic model. It briefly illustrates the tuning principle, deduces the corresponding tuning voltage, analyzes the open-loop system and performs the tuning simulation. In view of the large open-loop zero outputs of some gyroscopes, in order to avoid saturation failure of the integrators in the traditional decoupling control system, the self-tuning control

system is designed. The simulation results indicate that the self-tuning control system is feasible. When considering damping, the closed-loop system realizes the locking function in controlling the rotor position, but the outputs are coupled under the effect of damping. It is necessary to further probe how to eliminate the damping effect.

References

1. Jenkins LJ, Hopkins RE, Kumar K et al (2003) Hybrid wafer gyroscope. US Patent 6615681
2. Arif SM, Raghunandan PS, Andhra TA et al (2003) A novel method to measure the decay frequency of a dynamically tuned gyroscope flexure. Meas Sci Technol 14:2081–2088
3. Ren Wang, Peng Cheng, Fei Xie et al (2011) A multiple-beam tuning-fork gyroscope with high quality factors. Sensor Actuator A 166:22–33
4. Dong Y, Kraft M, Hedenstierna N et al (2008) Microgyroscope control system using a high-order band-pass continuous-time sigma-delta modulator. Sensor Actuator A 145–146:299–305
5. Jin Woo Songa, Jang Gyu Leea, Taesam Kang (2002) Digital rebalance loop design for a dynamically tuned gyroscope using H2 methodology. Control Eng Pract 10:1127–1140
6. Yen-Cheng Chen, M'Closkey RT, Tuan A et al (2005) A control and signal processing integrated circuit for the JPL-Boeing micromachined gyroscopes. IEEE Trans Control Syst Technol 13:286–300
7. Acar C, Shkel AM (2005) An approach for increasing drive-mode bandwidth of MEMS vibratory gyroscopes. J Microelectromech Syst 14:520–528
8. Xu Guoping, Weifeng Tian, Zhihua Jin et al (2007) Temperature drift modelling and compensation for a dynamically tuned gyroscope by combining WT and SVM method. Meas Sci Technol 18:1425–1432
9. Bailin Zhou (2002) Design and manufacturing of dynamically tuned gyroscope. Southeast University press, Nanjing, pp 30–35 (In Chinese)
10. Shie Lin et al (1983) Dynamically tuned gyroscope. National Defense Industry Press, Beijing, pp 40–47 (In Chinese)
11. Bo Yang, Shourong Wang, Kunyu Li et al (2009) System design and simulation of microelectromechanical hybrid gyroscope. J Southeast Univ 39(5):951–955 (In Chinese)

Part V
Data Mining and Application

New Detection Technology Based on the Theory of Eddy Current Loss

Yafei Si and Jianxin Chen

Abstract The equivalent resistance of eddy current power losses was proposed in the paper as characteristic parameter of metal target information, which was in direct proportion with sixth power of detection distance. Using the method of pulse width modulation for detection coil and by detecting the change of coil's free-wheeling process, the equivalent resistance of eddy current losses could be measured. It could not only determine the distance but also eliminate environmental interference and improve anti-jamming capability by measuring area difference of coil's freewheeling process between whether there is a target. Target signal detection circuit was designed and target properties measurement results were given.

Keywords Magnetic induction • Eddy current • Detection equivalent resistance

1 Introduction

The electromagnetism detection technology is applied to many fields such as industry, agriculture and national defence [1]. Since the magnetism detection technology is not interfered by cloud, fog, dust and smog in wars and has high sensibility, it is gradually applied to many related products. The theory of the magnetism detection technology is based on Fluxgate Magnetic Technology, Reluctance Technology and Magnetic Film Technology [2]. There is already a paper which investigates a method using vector impedance characteristics of the metal target to detect the changes of probe coil impedance vector when the target approaches [3]. Since we are supposed to detect the changes of voltage with the same direction and different direction while detecting the impedance vector, it is difficult to apply this method to the products. This paper proposes a method based

Y. Si (✉) • J. Chen
Beijing University of Technology, Beijing, China
e-mail: debby.1992@yahoo.com.cn; chjx@bjut.edu.cn

W. Wang (ed.), *Mechatronics and Automatic Control Systems*, Lecture Notes in Electrical Engineering 237, DOI 10.1007/978-3-319-01273-5_87,

on the eddy current power target: The equivalent resistance of the target eddy current power is used as the characteristics of the target amount of information detection. By applying this method, we are able to detect a circuit in a more simple way. This method has a high anti-interference ability also. The result of the intersection of the detector and the target is given in the paper.

2 Researches on the Theory of the Magnetic Sensor Section Heading

A metal conductor is placed next to a detection coil, and when the alternating current passes through the coil, space around the coil will produce an alternating magnetic field H_1. The metal conductor in magnetic field will produce an eddy and an alternating magnetic field H_2. H_1 and H_2 are in different direction. Since the reaction of magnetic field H_2 will reduce the magnetic flux of the detection coil, which means we can detect the induced EMF produced by eddy current magnetic field in the detection coil or the effective impedance of the detection coil will change. The essence of studying the impact of metal target against the detector is to investigate the distribution of the eddy on the surface of metal. Since the working fluency is between 102 and 105 Hz, circuit size is much smaller than operating wavelength, electromagnetic field distribution and the current changes in the distribution at the same time is quasi-static electromagnetic field. The eddy current magnetic field induces by the metal surface follows the equations below [4]:

$$\nabla^2 H(x, y, t) = \mu\sigma \frac{\partial H(x, y, t)}{\partial t} \tag{1}$$

μ stands for the permeability of the metal target. σ stands for the electrical conductivity of the metal target. Equation 1 is called the electromagnetic penetration equation. Eddy current loss power P_w is [5]:

$$P_w \propto \sum_{m=1}^{\infty} \sum_{n=1}^{\infty} J^2{}_{mn} \propto {H_0}^2 \propto \frac{1}{l^6} \tag{2}$$

H_0 is the alternating magnetic field produced by detection coil. L is the distance between the detection coil and the target.

Magnetic sensor is also called magnetic probe, which is made by the core of the probe and some coils. The core of the probe is rolled by Fe-Co-based amorphous ribbons. The profile is shown in Fig. 1. Figure 2 is the circuit diagram of the metal target.

The detection coil in Fig. 1 is regarded as the collector load of transistor T in the Fig. 2. Resistance R_1 and diode D are used as the freewheeling of detection coil B. U_i is a square wave excitation signal with frequency f and duty cycle δ. As the

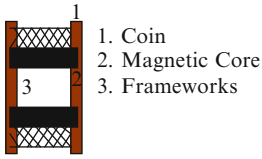

Fig. 1 Section of detection coin

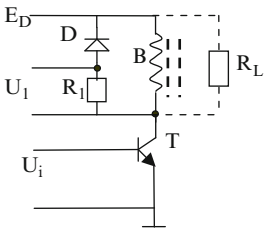

Fig. 2 Detection current of iron

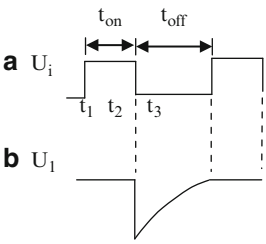

Fig. 3 Detection signal wave

waveform 3a shows, it is used to drive the base of transistor T. U_1 is the voltage waveform of freewheeling resistor R_1 produced by the freewheeling current of the detection coil B during the transistor turns off (Fig. 3b). R_l is an introduction physical element. It equals the resistance lead by the eddy current loss when the target appears.

Take the oscillation cycle as an example to investigate its working principle. U_i is the PWM(Pulse-Width Modulation) signal produced by oscillator. Its period is $T = T_{on} + T_{off}$ and the duty cycle is $\delta = t_{on}/(t_{on} + t_{off})$. From Fig. 3 we can know that $t_{on} = t_2 - t_1$, $t_{off} = t_3 - t_2$. During $t_1 \sim t_2$, the base of transistor is driven, the transistor turns on, the DC E_D initiates detection coil through transistor T and the current in the coil increases. The transistor turns off in t_2. From Lenz's Law we know that reverse voltage will be produced in both sides of the detection coil. The reverse voltage releases the magnetic energy stored during detection coil turns on via the freewheeling R_1 and D. And after freewheeling process, the core flux will return to zero to ensure that the core will work normally during next period. When the transistor turns on, it actually means to put a battery at both sides of the detection coil. According to the circuit theory, the maximum current in the detection coil is determined by the equation below.

$$i_{L\max} = \frac{1}{L}\int_{t_1}^{t_2} E_D dt = \frac{E_D}{L}(t_2 - t_1) = \frac{E_D}{L} t_{on}$$

L stands for the inductance of the detection coil. E_D stands for the battery's voltage. t_{on} stands for the conduction time.

During $t_2 \sim t_3$, the transistor turns off and the freewheeling is conducted. The current in freewheeling is determined by the equation below

$$i = i_{L\max} e^{-\frac{t}{\tau_1}} = \frac{E_D}{L} t_{on} e^{-\frac{t}{\tau_1}} \tag{3}$$

$\tau_1 = \frac{L}{R_1}$ is the time constant (we ignore the resistance of the diode). R_1 is the resistance of the freewheeling. U_1 (t) (the voltage of R_1) is

$$U_1(t) = i \cdot R_1 = i_{L\max} \cdot R_1 \cdot e^{-\frac{t}{\tau_1}} = \frac{E_D R_1}{L} \cdot t_{on} \cdot e^{-\frac{t}{\tau_1}} \tag{4}$$

It equals the equation $U_1(t) = U_{1\max} \cdot e^{-\frac{t}{\tau_1}}$.

In the equation above, $U_{1\max} = \frac{E_D R_1}{L} \cdot t_{0n}$, which is the highest reverse voltage of the freewheeling. But actually, the reverse peak of the detection coil is much higher than when the transistor turns off due to the impact of the distribution of the capacitance and the disclosure of the magnetism. To guarantee the safety of the transistor, we use some method such as connecting two voltage regulator tubes and two varistors in different direction in order to limit the maximum voltage to an extent which is a little bit higher than $U_{1\max}$. If the external factors have no influence, the initiation and the freewheeling process of the detection coil and the changes of the current and the voltage due to the time follow Figs. 3 and 4.

During t_{on}, the battery will provide energy P_{on} to the detection coil when the metal target accesses to the detector. P_{on} is made up of two parts: one is the excitation power P_{on1} produced by the detection coil, the other is the power of eddy current loss produced by the target. Since P_{on} is provided by the battery, and $P_{on1} > P_{on2}$, it is difficult to distinguish the energy of the eddy current loss from the whole energy during the positive half cycle of the detector generation.

However, in the negative cycle of the detector (during t_{off}), we use the energy stored in the detection coil instead of the energy provided by the DC battery to guarantee the continuation of the currency. Then we can equal the value of the eddy current loss provided by the freewheeling current on the surface of the target to the power provided by resistance R_L hang in parallel at both sides of the detection coil. If U stands for the voltage produced by the detection coil in the freewheeling process, the eddy current loss equals to:

$$P_w = \frac{U^2}{R_L} \tag{5}$$

Compared Eq. 2 with Eq. 5, the eddy current loss of the target and the distance follow the equation below:

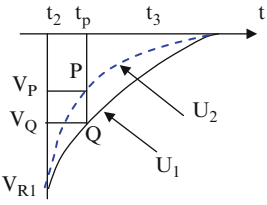

Fig. 4 Voltage wave of loop current

$$R_L \propto l^6 \tag{6}$$

If we ignore the resistance of the diode when it is conducted, the resistance of the freewheeling equals to the resistance of R_1 and R_L in parallel. The time constant of the freewheeling changes and the freewheeling voltage is:

$$U_2 = U_{1\max} \cdot e^{-\frac{t}{\tau_2}} \tag{7}$$

In the equation above, $\tau_2 = \frac{R_1+R_L}{R_1R_L}L$.

Figure 4 is used to describe Eqs. 4 and 7. Solid curve represents freewheeling decay U_1, which is without the metal target. Virtual curve represents the freewheeling decay U_2 that is with the metal target. We select a moment t_p from t_2 to t_3, the points of intersection of the two curves and t_p are P and Q. In t_p, the difference of the freewheeling voltage of whether there is the target near the detection is:

$$\Delta U = U_Q - U_P = U_1 - U_2 = U_{1\max}\left(e^{-\frac{t_p}{\tau_1}} - e^{-\frac{t_p}{\tau_2}}\right)$$

After using Taylor series expansion, the equation is:

$$\Delta U = U_{1\max}t_p\frac{\tau_2-\tau_1}{\tau_2\tau_1} \approx U_{1\max}t_p\frac{L}{{\tau_1}^2}\left(\frac{R_1+R_2}{R_1R_2}-\frac{1}{R_1}\right) = U_{1\max}\frac{t_p}{{\tau_1}^2}\cdot\frac{L}{R_L}$$

Taking Eq. 6 into account,

$$\Delta U \propto \frac{1}{l^6} \tag{8}$$

The theory indicates the target position by measuring the scale factor of the equation above or adopting the multi-probe measurement system. However, due to the constant changes of the signal, it is difficult to measure all the voltage and do the calculation. Therefore, in the real situation, we are supposed to find a new way.

After analyzing the information in Fig. 4, we can find that the area surrounded by curve U_1 and U_2 is the time integral of ΔU. It means the change of freewheeling area is:

$$\Delta S_{\Delta U \Delta t} = \int_{t_2}^{t_3} \Delta U dt_p = \int_{t_2}^{t_3} \left(U_{1\max} \frac{L}{R_L} \cdot \frac{t_p}{{\tau_1}^2} \right) dt_p = \frac{U_{1\max} L}{2{\tau_1}^2} \cdot \frac{{t_3}^2 - {t_2}^2}{R_L} \tag{9}$$

Taking Eq. 6 in to account, Eq. 9 changes into:

$$\Delta S_{\Delta U \Delta t} \propto \frac{U_{1\max} L}{2{\tau_1}^2} \cdot \frac{{t_3}^2 - {t_2}^3}{l^6} \propto \frac{U_{1\max} L}{l^6} \tag{10}$$

According to Eq. 4, $U_{1\max} = \frac{E_D R_1}{L} \cdot t_{0n}$. U_{1max} is the highest reverse voltage of the freewheeling branch. Put U_{1max} into above equation, then

$$\Delta S_{\Delta U \Delta t} = K \cdot \frac{E_D R_1 t_{on}}{l^6} \tag{11}$$

K is a coefficient, which can be got by the experiment.

Equation 11 is called Target Detection Equation, which shows the difference of the freewheeling curve area between whether there is the target near the detection or not is proportional to the voltage E_D supplied by the power, the resistor R_1 of the freewheeling circuit and the oscillation pulse width ton. But R_1 and ton are limited by other factors. Since R_1 has a direct effect on the radiation field of the detection coil during the transistor turns off, it is not a good way to improve the detection sensitivity by increasing R_1. Besides, it is also a bad way to improve the detection ability by improving the pulse width ton since the pulse width is inversely proportional to the working frequency.

According to the theory and the experiment, raising battery voltage E_D is the most efficient way to increase detection range. This conclusion can be drawn from Eq. 11. Besides, when the voltage of working battery rises, the electromagnetic energy that detection coil radiates increase and the eddy current loss increases. Therefore, the detection range increases as well.

3 The Target Signal Detection Principle

Figure 5 is a circuit principle diagram based on the theory of eddy current loss. The circuit consists of three parts: PWM pulse width modulation oscillator; detection coil, reference coil and comparator. The working principle is analyzed below.

If there is no metal target around the detection coil, the detection coil and the reference coil output the same waves, and the comparator outputs zero. When a metal target exists around the detection coil, according to Eq. 11, the detection coil and the reference coil output different waves. This signal goes through the comparator and is output as the target signal after being filtered by the filter circuit. When the ferromagnetic metal targets go through the detection area at a certain speed along the X direction as Fig. 6 shows, we suppose the maximum detection range of

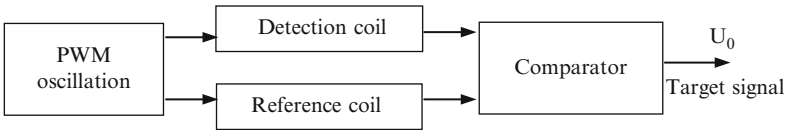

Fig. 5 Target signal detecting electrical principle of detector

the detector is $r_{max.}$ Detection zone is a circle of radius r_{max}, and the detector is at the center point O. In t_1, the target moves to point A and starts to enter the target zone. In t_m, the target moves to point C, the nearest position from the detection. In t_2, the target goes through point B and then, leaves the target zone. During the intersection of the bomb project, the target waveform output by detector circuit is shown as Fig. 7. According to Fig. 7, detection range is the closest in t_m, and the maximum signal is U_{0max}.

4 Measurements of Target Characteristics

4.1 Target Characteristics in Different Frequency

After analyzing the experimental results, we can know that the sensitivity of detector is related to working frequency. Take ferromagnetic metal targets as the example, it has the highest sensitivity under the frequency ranging from 5.0 to 6.5 kHz, and 5.565 kHz is the best.

4.2 Target Characteristics in Different Detection Range

Figure 8 shows the response waveform of detector and ferromagnetic metal targets (the size is $4 \times 100 \times 150$ mm/A_3) in different intersection distance. It shows that as the detection range raises, the margin of response waveform decreases. And when the intersection distance is close to a certain degree, there will be no response of the detector.

4.3 Target Characteristics in Different Transmit Power

The theory above shows that it is practical to increase detection range by raising the working voltage of detector. To confirm this conclusion, we make the response waveform of one detection target in the same detection range and in two different voltages. Figure 9a shows the detection waveform in the excitation parameters 6 V/23 mA.

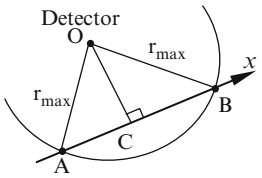

Fig. 6 Detector output wave to target

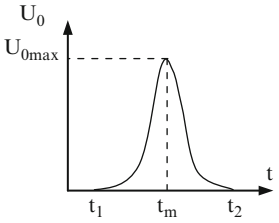

Fig. 7 Test wave of target

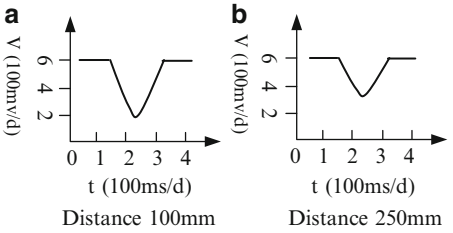

Fig. 8 Detector output wave to target

The peak of waveform is 500 mV × 1.5 = 750 mV. Figure 9b shows the detection waveform in the excitation parameters 9 V/61 mA. The peak of waveform is 500 mv × 3.4 = 1,700 mv. The consequence conforms that rising transmit power of the detector can increase detection range.

5 Conclusion

The paper proposes the characteristic quantity based on the theory that regarding target eddy current loss as the detection of target information from the perspective of conservation of energy, and introduces the concept of target loss equivalent resistance and derive the result that equivalent resistance is proportion with six power of detection distance. By using pulse width modulation excitation coil detection method and detecting the changes of freewheeling process in the coil, the equivalent resistance can be measured by the eddy current loss. It can not only determine the distance, but also exclude environmental interference. As the experimental data shows, the best detection frequency is 5.565 kHz and raising excitation voltage can increase detection range.

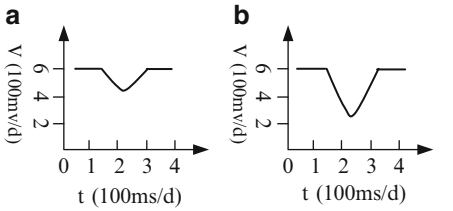

Excitation voltage 6v Excitation voltage 9v

Fig. 9 Detector output wave to target

References

1. Aderin ME, Burch IA (1998) Countermine: hand held and vehicle mounted mine detection. Deflection of abandoned land mines, 1998 second international conference. IEE Conference Publication, Dera Chertsey, pp 198–202
2. Kildishev AV, Nyenhuis JA (1999) Application of magnetic signature processing to magnetic center primpointing in marine vehicles. OCEANS'99MTS/IEEE 3:1532–1536
3. Si Huaiji, Cui Zhanzhong, Zhang Yanmei (2005) Study of electronmagnetic fuze detection principle. J Beijing Inst Technol 25(1):79–82 (in Chinese)
4. Feng Cizhang (1985) Static electromagnetic field. Xi'an Jiaotong University Press, Xi'an, pp 73–75 (in Chinese)
5. Si Huaiji (2005) Research on technology of magnetic detection based on the theory of the eddy current loss. School of Mechatronics Engineering, Beijing Institute of Technology, Beijing (in Chinese)

Pedestrian Detection Based on Road Surface Extraction in Pedestrian Protection System

Hao Heng and Huilin Xiong

Abstract Pedestrian protection system (PPS) in the advanced driver assistance system (ADAS) to improve traffic safety, has become an important research area. The major challenge in PPS is to develop a reliable on-board pedestrian detection system. Compared to the pedestrian detection on static images, on-board pedestrian detection is facing some new difficulties, such as high real-time demand, wide range of illumination variation and so on. In order to deal with these challenges, we presented a method in this paper by combining the road surface extraction technique and the histogram of oriented gradient (HOG) feature based classification, so that the search regions are only limited within the extracted road surface. Experiment results show that this method can remarkably reduce the false alarm rate, improve the detection speed, and significantly improve the small pedestrian detection rate.

Keywords Pedestrian detection • Road surface extraction • Histogram of oriented gradients • Support vector machine

1 Introduction

Road accidents have become the main cause of road traffic casualties over the last century. In the recent decade, researchers have turned their attention to the more intelligent on-board systems, aiming to avoid accidents or reduce the severity of accidents. For example, the intelligent on-board systems can remind the driver of a potential dangerous situation, assist him/her in taking action immediately to avoid the accident. These systems are usually referred to as advanced driver assistance systems (ADAS).

H. Heng (✉) • H. Xiong
Department of Automation, Shanghai Jiao Tong University, and Key Laboratory of System Control and Information Processing, Ministry of Education of China, Shanghai, China
e-mail: haoheng@outlook.com

W. Wang (ed.), *Mechatronics and Automatic Control Systems*, Lecture Notes in Electrical Engineering 237, DOI 10.1007/978-3-319-01273-5_88,

In this paper, we focus on the pedestrian detection, which is the most important part of the pedestrian protection system (PPS). Accident statistics indicate that 70 % vehicle-to-pedestrian accidents occur in front of vehicle; therefore, using a forward-facing on-board camera to capture the driving scenarios is necessary.

In recent years, a number of methods have been proposed to tackle these problems. Papageorgiou and Poggio [1] employed Haar features in combination with a polynomial support vector machine (SVM) classifier to detect pedestrians. Tran and Forsyth [2] used local histograms of gradients and local PCA of gradients as features to establish a model of human body. Dalal and Triggs [3] employed histograms of oriented gradients (HOG) features in combination with SVM classifier to detect pedestrian and achieved good performances. Felzenszwalb [4] presented a flexible part model by adding the position of parts of the body as a latent variable into the SVM learning algorithm. Wu and Nevatia [5] proposed a system to automatically construct tree hierarchies for the problem of multi-view pedestrian detection. They use a boosting framework in combination with edge-let features. Dollár [6] presented an approach that automatically learns flexible parts from training data and uses a boosting framework with wavelet features.

We employ a road extraction technique as foreground segmentation, together with HOG feature-based classification to detect pedestrian. The rest of this paper is organized as follows. Section 2 introduces the algorithm that used to extract road surface in the illumination invariant color space. Section 3 describes pedestrian detection in the extracted ROIs. The experiment results are presented in Sects. 4 and 5 is the conclusion.

2 Road Surface Extraction

2.1 Theory Introduction

Finlayson showed that if an object has Lambertian surfaces and is imaged by three narrow band sensors under Planckian illumination (*PLN*), it is possible to convert the RGB color image into a shadow free gray scale image, on which the influence of lighting variations could be greatly reduced [7]. This theory is derived from the physics behind color formation in the presence of a Planckian light source, Lambertian surface, and narrow band camera sensors. Experiment results show that this theory holds even for real world situation.

Experiment results show that this theory holds even for real world situation. Figure 1 shows the process of computing a shadow free image I from a given color RGB image I_{RGB}. Let R, G and B be the standard color channels, $r = \log(R/G)$ and $b = \log(B/G)$ are the corresponding log-chromaticity values by using the G as the normalizing channel. Then, different colors under different illuminations form the parallel lines in the log-chromaticity space. There is a line, donated by l_θ in Fig. 1, being orthogonal to these parallel lines. On l_θ the same color with different

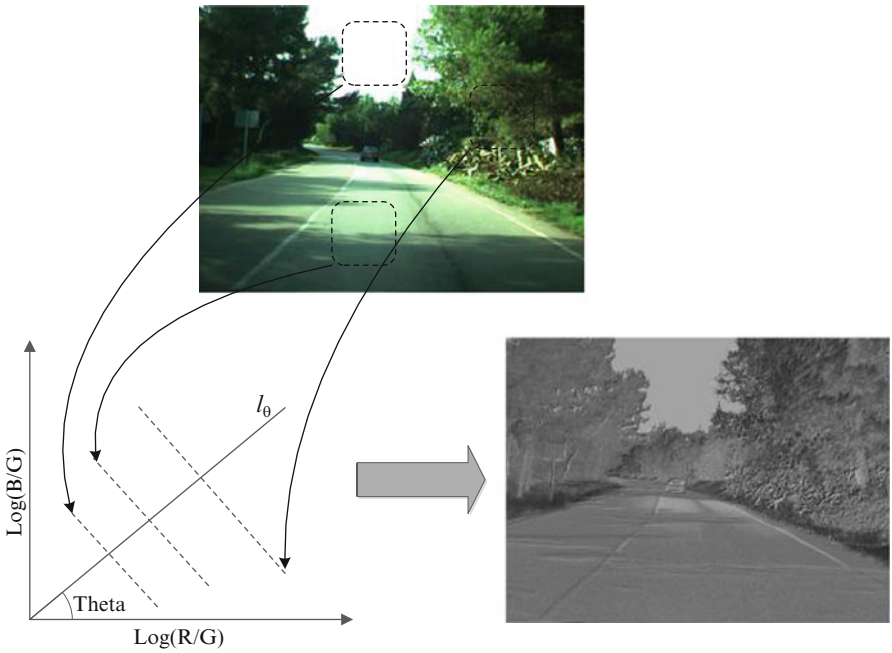

Fig. 1 Obtain the shadow free *gray-scale* image

illuminations is represented by the same point, and moving along l_θ means changing the chromaticity. In other words, l_θ is a gray level axis, where each gray level corresponds to a surface chromaticity. Therefore, projection χ' onto l_θ can remove the influence of illumination variations.

2.2 Camera Calibration

According to the theory above, obtaining the direction (θ) of l_θ is crucial. In fact, θ is a parameter of the camera sensor, independents to the lighting condition or the surface material. So, a calibration process for a given camera can be computed offline and just needs to be done once.

Different to the ways [8, 9] for calibrating the camera parameter θ, in this paper, we present a new standard-deviation based calibration algorithm. The idea behind our calibration is pretty simple, with a wrong θ, the similar chromaticity values of I_{RGB} will scatter with a large value of the standard-deviation, denoted by *Var*; on the other hand, with the right θ, the similar chromaticity values of I_{RGB} will reach the minimal value of *Var*. Hence, the minimal value of *Var* is expected. The algorithm is summarized below:

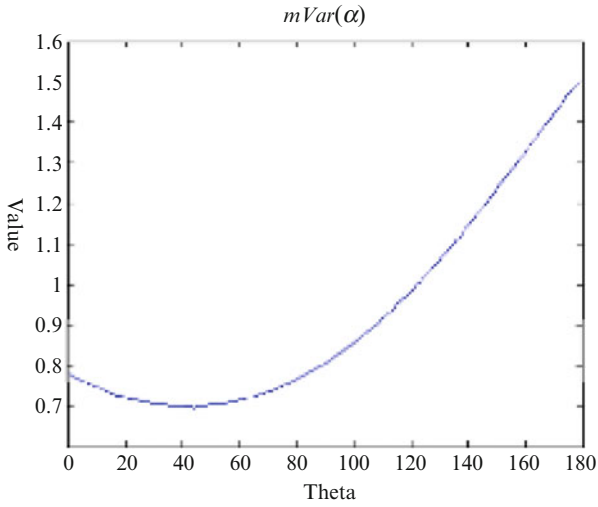

Fig. 2 The value of $mVar(\alpha)$ changes according to θ

1. Select K images $\{I^1_{RGB}, \cdots, I^K_{RGB}\}$ from the database together with their pre-annotated road region images $\{I^1_{road}, \cdots, I^K_{road}\}$.
2. Select an image, I^k_{RGB}, and its corresponding I^k_{road}. Initialize the projection angle $\alpha = 0°$.
3. Projecting the log-chromaticity pixel values of I^k_{RGB} onto l_α to obtain a grayscale image I_α, and extract the road surface image I_{road} from I_α using I^k_{road}.
4. Compute the standard deviation $Var^k(\alpha)$, using the pixels whose gray values are in the $[0.05, 0.95]$ range of I_{road}.
5. Calculate the standard deviation values for I^k_{RGB} as steps 3–5 with $\alpha \in [0°, 1°, \cdots, 179°]$.
6. Repeat steps 2–6 for each image. $k \in [1, 2, \cdots K]$.
7. For each discrete value of α, calculate the average value of $Var^k(\alpha)$ with $mVar(\alpha) = \frac{1}{K}\sum_{k=1}^{K} Var^k(\alpha)$.
8. Then the value of the parameter θ is chosen as $\theta = \arg\min_{\alpha} mVar(\alpha)$.

Figure 2 shows the curve of $mVar(\alpha)$ using the same database as Finlayson [8] used, from which we calibrate the camera parameter θ to be 44°. The value of θ obtained by our calibration algorithm is the same as Finlayson's. However, our algorithm is more stable and robust.

2.3 Road Detection Algorithm

The shadow free gray-scale image I can be calculated by θ. According to the illuminant invariant property of I, pixels are of the similar gray values, even in

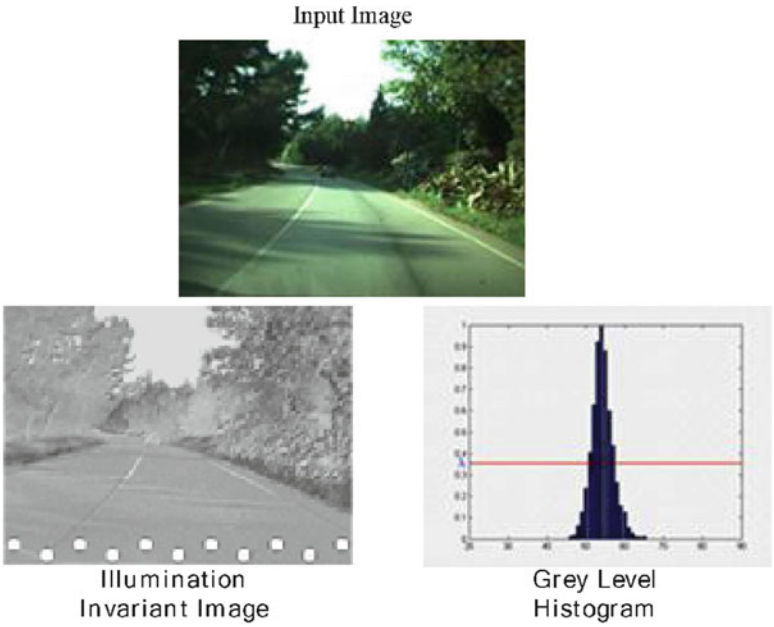

Fig. 3 Obtain the *gray-level* distribution of road surface

shadow regions. Based on this property of this illuminant invariant image I, we extract the road surface by employing a statistic technique and the flood-fill based morphological processing.

We employ a conditional function $p(I(p)|road)$ to decide whether a gray value, $I(p)$, belongs to road or not. A pre-defined threshold, λ, is introduced to eliminate the influence of the tiny variants of the road pixels and other interference factors. Our experiments find that $\lambda = 0.35$ can lead to a better performance.

$$\begin{cases} I(p)\ belongs\ to\ road, & if\ p(I(p)|road) \geq \lambda \\ I(p)\ doesn't\ belong\ to\ road, & otherwise \end{cases} \tag{1}$$

The conditional probability, $p(I(p)|road)$, can be estimated using a set of "seeds", which are a number of small square blocks on I, usually located at the bottom of the image (see Fig. 3). The regions that the seeds located are assumed to be on the road, since they correspond to the nearest front of the vehicle. In this paper, we select 11 small square blocks in size of 9×9 at the bottom of I (see Fig. 3), to estimate $p(I(p)|road)$.

Our road detection algorithm can be summarized as follows:

1. Compute the illuminant invariant gray-scale image, I, from I_{RGB} using the calibrated parameter, θ.
2. Estimate $p(I(p)|road)$ from the normalized histogram of the selected "seed" blocks using threshold λ, and then get the initial road pixels according (10).

3. From each seed, using the Flood-fill method to generate a coarse road surface.
4. Use a morphological operation to fill some small holes on the road surface.

3 Pedestrian Detection

After the road detection, we treat the extracted road surface as foreground, on which a series of parallel rectangular boxes are placed. These rectangular boxes are viewed as our ROI regions, on which the pedestrian searching is performed. The heights of these ROIs are established using the distance information and the pinhole imaging model.

To detect the small pedestrian effectively, we resize these ROIs to a unified scale so that the small pedestrian, which is far from the cameras, will be enlarge, and this could substantially improve the detection rate of small pedestrian. Figure 4 shows the procedure of resizing the ROIs. In our experiments, we resize all the heights of ROIs to 128 pixels. Another advantage of resizing ROIs is that, in pedestrian detection on each ROI, we do not need to perform a time-consuming search of targets in different sizes, which is the conventional way to detect the targets.

Then, on each ROI, we use the HOG features [4] and a linear support vector machine (SVM) classifier to detect pedestrian.

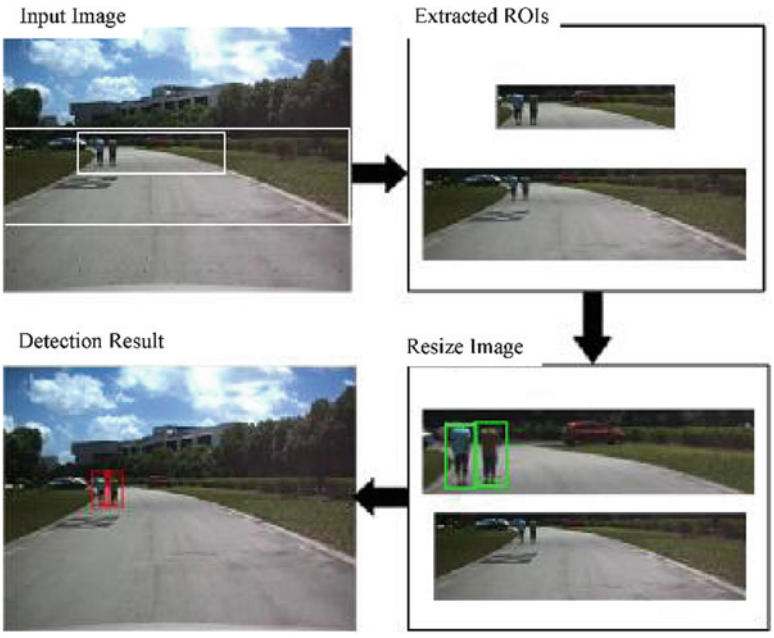

Fig. 4 Extract ROIs based on road surface, and then resize them

4 Experiment Results

We tested our algorithm on a public available dataset, CVC-02 Pedestrian Dataset,[1] and a video dataset collected by ourselves. We select four sequences (the third, fifth, sixth and tenth) of 1,173 frames with 2,347 pedestrian from CVC-02 and 1,026 frames with 2,148 pedestrian from our dataset.

In our experiment, the HOG features of the ROIs are sent to the 64×128 size based SVM classifier to detect pedestrians. We use detection rate, false alarm rate and detection time to evaluate and compare the performances of our method and the conventional sliding window based searching approach.

Figure 5 shows part of detection results on three video frames. Table 1 gives the statistic results concerning the detection rate, false alarm rate and detection time per frame (in seconds) on the testing video data. We can see that:

- The 64×128 HOG detector works well for the large pedestrians; however, it often misses the small pedestrians.
- The 32×64 HOG detector performs well in detecting small and large targets; however, it tends to produce many false alarms.

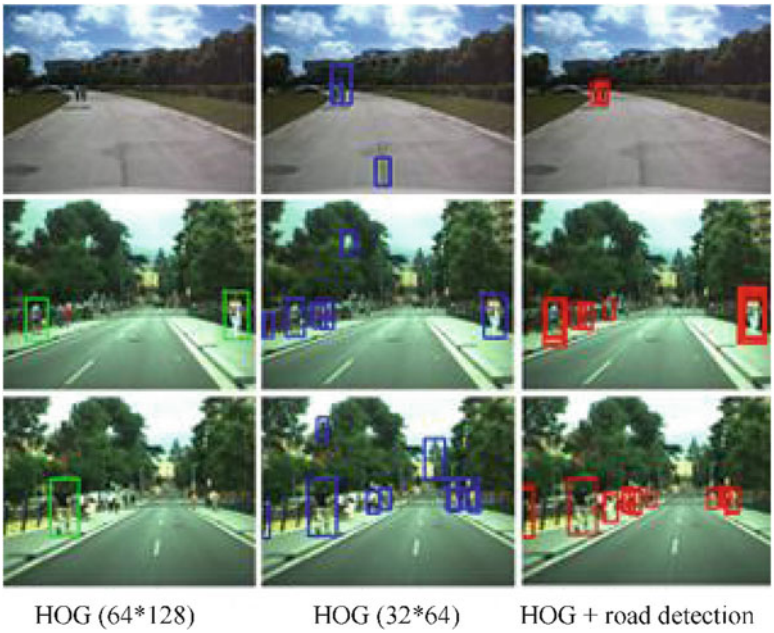

Fig. 5 Part of experiment result images

[1] CVC-02 dataset: http://www.cvc.uab.es/adas/site/

Table 1 The statistical results of experiment

Experiment result	HOG (64 × 128)	HOG (32 × 64)	HOG + road detection
Detection rate	36.14 %	79.08 %	77.82 %
False alarm rate	15.24 %	78.12 %	7.76 %
Detection time (s)	3.23	18.89	1.52

- Our method presents the best performance, either in detecting small targets or large targets with a low false alarm rate. Meanwhile, the proposed method works faster than the other two detectors.

5 Conclusion

In this paper, we have presented a method by combining the road surface extraction technique with the HOG feature based classification. Experiment results have shown that this method can remarkably reduce the false rate, improve the detection speed, and significantly improve the small pedestrian detection rate.

References

1. Papageorgiou C, Poggio T (2000) A trainable system for object detection. Int J Comput Vision 38:15–33
2. Tran D, Forsyth D (2007) Configuration estimates improve pedestrian finding. Adv Neural Inform Process 644:1529–1536
3. Dalal N, Triggs B (2005) Histogram of oriented gradient for human detection. Comput Vision Pattern Recogn 1:886–893
4. Felzenszwalb P, McAllester D, Ramanan D (2008) A discriminatively trained, multi-scale, deformable part model. Computer vision and pattern recognition, Chicago, pp 1–8
5. Wu B, Nevatia R (2007) Cluster boosted tree classifier for multi-view, multi-pose object detection. In: International conference on computer vision, Los Angeles, pp 1–8
6. Dollár P, Babenko B, Belongie S, Perona P (2008) Multiple component learning for object detection. In: European conference on computer vision, vol 5303, Marseille, France, pp 211–224
7. Finlayson G, Hordley S, Lu C, Drew M (2006) On the removal of shadows from images. IEEE Trans Pattern Anal Mach Intell 28:59–68
8. Finlayson G, Hordley S, Drew M (2002) Removing shadows from images. In: Proceedings European conference on computer vision, Comenhagen, Denmark, pp 129–132
9. Alvarez JMA, Ĺopez AM (2011) Road detection based on illuminant invariance. IEEE Trans Intell Transport Syst 12(1):184–193

Methods on Reliability Analysis of Friction Coefficient Test Instrument

Tianrong Zhu, Xizhu Tao, Xinsheng Xu, and Tianhong Yan

Abstract In order to analyze the reliability of instrument with the consideration of experiment data shortage or even no, reliability element method is proposed in this paper. The reliability indexes corresponding to serial system and parallel system are investigated respectively. The steady-state availability and the reliability degree are introduced as the key reliability index for friction test instrument based on the analysis of the function and structure characteristics of its. In addition, the reliability diagram of sliding friction test instrument is constructed. A program module based on MATLAB is developed to calculate the reliability index effectively. Finally, an example was given out to verify the feasibility of methods mentions above.

Keywords Reliability index • Reliability element method • Steady-state availability • Degree of reliability • Sliding friction test instrument

1 Introduction

With the rapid development of manufacturing technologies for test instrument, the accuracy and veracity of test instrument has been improved significantly. As we all know a product which is going to be produced in batch should ensure its quality [1]. Nowadays, the quality characteristics of product, besides accuracy and reliability, also include reliability, safety and economy and so on [2–4].

Friction tester is a kind of instrument used to measure the friction coefficient between the conveyor and the armrest of elevator [5]. The reliability analysis of

T. Zhu • X. Tao • X. Xu (✉)
Institute of Industrial Engineering, China Jiliang University, Hangzhou, China
e-mail: zhu_tianrong@163.com; taoxizhu008@126.com; lionkingxxs@cjlu.edu.cn

T. Yan
Institute of Mechatronics Engineering, China Jiliang University, Hangzhou, China
e-mail: thyan@cjlu.edu.cn

W. Wang (ed.), *Mechatronics and Automatic Control Systems*, Lecture Notes in Electrical Engineering 237, DOI 10.1007/978-3-319-01273-5_89,

friction test instrument is to obtain the primary information of the reliability index of it. Furthermore, it is to find out that the defect or weak link of it as well as the parts that affect its reliability. Thereupon, these can provide evidences to improve the friction test instrument itself. In reliability engineering, the reliability analysis of system equipment, based on large amount of experiment data, is to use the mathematical theories such as probability and statistics to investigate the exact reliability index [6]. And on the basis of this, the reliability of system equipment can be evaluated in the end. However, it always leads to low assessment accuracy when experiment data of equipment itself is little or even no [7]. Obviously, it cannot meet the analysis requirement of some instrument products. In engineering practice, an instrument always consists of a lot of components. And the reliability level of instrument depends on the reliability of components constituting instrument [8]. The reliability model of instrument can be constructed by analyzing the functional diagram of the instrument.

2 Reliability Index and Its Calculation

Usually, the reliability level of instrument is the comprehensive reflection by several parameters (namely reliability index). The reliability is a kind of statistical index, and it can be used to analyze the reliability of instrument quantitatively.

In general, the reliability index of instrument consists of many types of elements including degree of reliability, failure rate, cumulative failure probability, mean repair time, reliable life, and steady-state availability and so on. In this work, the degree of reliability and steady-state availability are used as the key reliability index of friction test instrument with the consideration of the function characteristics and the structure features of friction test instrument.

2.1 Reliability Calculation of Friction Test Instrument

Steady-state availability A is an important index to measure the degree of reliability $R(t)$ of friction test instrument. It refers to the probability of friction test instrument keeping its stability normal function in long-term work. And the degree of reliability refers to the probability of friction test instrument fulfilling the specified function under the stipulated conditions within prescribed period. The state transferring process of instrument is a kind of Markov random process when the life and the repair time of all components constituting instrument are all exponential distribution [9]. Otherwise it is non-Markovian stochastic process. To the large complex instrument consisting of many components, the steady-state availability can be calculated through two steps. The first step is to calculate the component failure rate and component repair rate respectively, and the second step is to

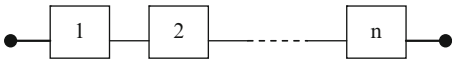

Fig. 1 The component structure of serial system

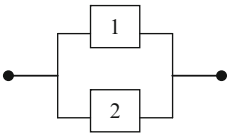

Fig. 2 The component structure of parallel system

calculate the degree of availability of the whole instrument based on the logic constraint relationships among components constituting instrument.

Based on stochastic process theory, the steady-state availability A and the degree of reliability $R(t)$ of each component is as the following respectively.

$$A = \frac{\mu}{\mu + \lambda}, \quad R(t) = P(T) \tag{1}$$

Where λ is the failure rate of components, μ is the repair rate of components, T is the life of instrument, and t is specified time.

- For the serial system consisting of n components and repair equipment illustrated in Fig. 1, the parameters of reliability index are as follows.

$$\lambda_s = \sum_{i=1}^{n} \lambda_i \tag{2}$$

$$\mu_s = \sum_{i=1}^{n} \lambda_i \Big/ \sum_{i=1}^{n} \frac{\lambda_i}{\mu_i} \tag{3}$$

$$R_S(t) = \prod_{i=1}^{n} e^{-\lambda_i t} \tag{4}$$

Where λ_i is the failure rate of the ith component, μ_i is the repair rate of the ith component, and $R_i(t)$ is the degree of reliability of the ith component. The exponential form of $R_i(t)$ indicates that it obey Markov distribution.

- For the parallel system consisting of two different components and a repair equipment illustrated in Fig. 2, the parameters of reliability index are as the following respectively.

$$\lambda_s = \frac{\mu_1\pi_3 + \mu_2\pi_2}{\pi_0 + \pi_1 + \pi_2} \tag{5}$$

$$\mu_s = \frac{\mu_1\pi_3 + \mu_2\pi_4}{\pi_3 + \pi_4} \tag{6}$$

$$R_s(t) = 1 - \prod_{i=1}^{n}[1 - e^{-\lambda_i t}] \tag{7}$$

Where π_0, π_1, π_2, π_3, and π_4 are the steady-state distribution of components respectively.

$$\pi_1 = \frac{\lambda_2(\lambda_1 + \lambda_2 + \mu_1)}{\lambda_1\mu_1 + \lambda_2\mu_2 + \mu_1\mu_2}\pi_0 \tag{8}$$

$$\pi_2 = \frac{\lambda_1(\lambda_1 + \lambda_2 + \mu_2)}{\lambda_1\mu_1 + \lambda_2\mu_2 + \mu_1\mu_2}\pi_0 \tag{9}$$

$$\pi_3 = \frac{\lambda_1\lambda_2(\lambda_1 + \lambda_2 + \mu_2)}{\mu_1(\lambda_1\mu_1 + \lambda_2\mu_2 + \mu_1\mu_2)}\pi_0 \tag{10}$$

$$\pi_4 = \frac{\lambda_1\lambda_2(\lambda_1 + \lambda_2 + \mu_1)}{\mu_2(\lambda_1\mu_1 + \lambda_2\mu_2 + \mu_1\mu_2)}\pi_0 \tag{11}$$

$$\pi_0 = \frac{\psi}{(\lambda_1\mu_2(\lambda_2 + \mu_1) + \lambda_2\mu_1(\lambda_1 + \mu_2)) \times (\lambda_1 + \lambda_2 + \mu_1) + \psi} \tag{12}$$

$$\psi = u_1u_2(\lambda_1u_1 + \lambda_2u_2 + u_1u_2)$$

It can be seen that the calculation models of the degree of reliability $R(t)$ are different for different instrument systems. However, the steady-state availability of the whole instrument and the steady-state availability of single component are the same at calculation models. They are all expressed as follows.

$$A_s = \frac{\mu_s}{\mu_s + \lambda_s} \tag{13}$$

Where λ_s is the failure rate of the whole instrument, and μ_s is the repair rate of the whole instrument.

2.2 Reliability Analysis Method of Friction Test Instrument

The experiment data concerning friction test instrument is little or even no in practice. It would lead to very low assessment accuracy if only use the data of

instrument itself. As a result, reliability unit method is adopted to calculate the reliability index of instrument in this work. The analysis processes are as follows.

- Analyzing the functions structure of instrument and drawing its diagram of reliability. The reliability association among components is described based on the diagram of reliability.
- Calculating the failure rate and repair rate of a single component. On the basis of these, the steady-state availability of its would be calculated.
- According to the logic structure among components such as parallel or serial, and selecting reliability unit method, the reliability index of the whole instrument can be calculated by using unit reliability.

3 Reliability Model of Sliding Friction Test Instrument

The sliding friction test instrument illustrated in Fig. 3 is a kind of pin disc structure which was developed by our research team. It is used to measure the sliding friction coefficient between conveyor belt and armrest of elevator. This sliding friction test instrument is designed with the consideration of different friction conditions. It can show friction coefficient in time and implement measure online.

3.1 Functional Structure of Friction Test Instrument

3.1.1 Sliding Friction Device

This device is mainly composed of test platform, main shaft, loading mechanism, motor, and reducer and so on. All these are used to simulate the mechanical equilibrium when friction is generated between specimens. Based on these, the

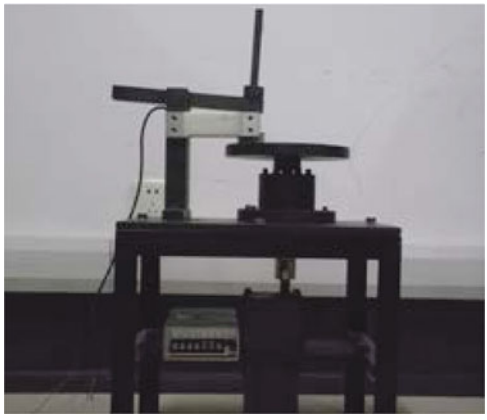

Fig. 3 The pin disc sliding friction test instrument

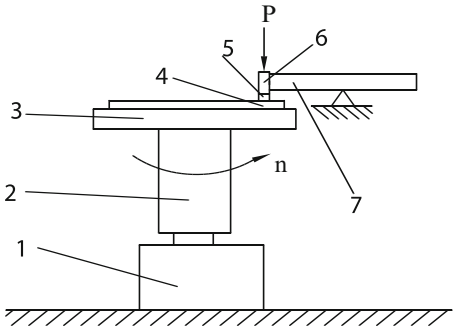

Fig. 4 Working principle diagram of sliding friction device (*1* – motor; *2* – axis; *3* – Test bench; *4* – down-specimen; *5* – up-specimen; *6* – round pin; *7* – support)

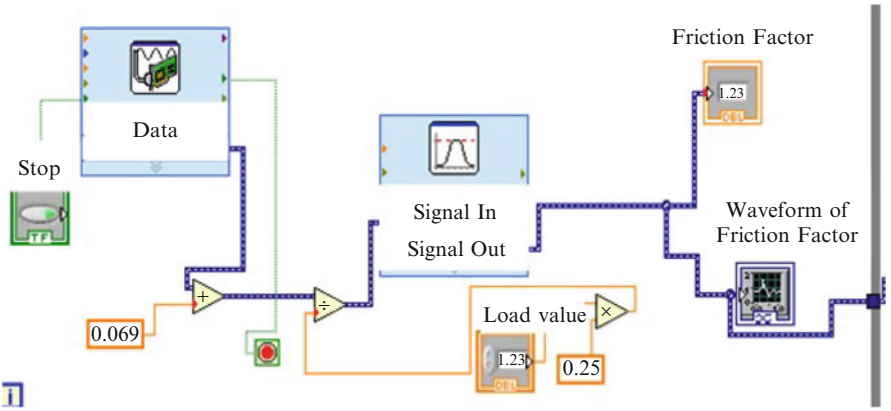

Fig. 5 The test program diagram of friction factor

acquisition environment of friction value is constructed. The working principle is presented in Fig. 4.

3.1.2 Signal Acquisition System

Signal acquisition system makes analog signal into signal forms that computer can read. It consists of sensor, amplifier and data acquisition card.

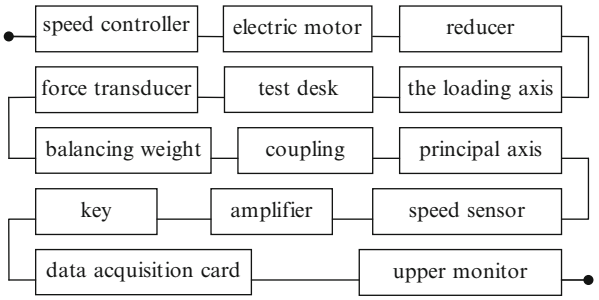

Fig. 6 Reliability diagram of friction test instrument

Table 1 The list of parameter distribution of failure time parameters and the working time parameters of each component

Number	Name	Failure rate	Repair rate
1	Speed controller	0.00903	0.8903
2	Electric motor	0.01026	0.9029
3	Reducer	0.00891	0.8894
4	Balancing weight	0.00073	0.6491
5	The loading axis	0.00513	0.8675
6	Force transducer	0.00729	0.8853
7	Coupling	0.00627	0.8768
8	Principal axis	0.01104	0.9113
9	Key	0.00187	0.7186
10	Speed sensor	0.00774	0.8879
11	Amplifier	0.00682	0.8779
12	Data acquisition card	0.00701	0.8842
13	Upper monitor	0.00145	0.8391
14	Test desk	0.00132	0.8087

3.1.3 Computer Control System

Computer control system use software such as LabView to compile the PC software. This environment provides control method to process data. And then a automatic measure process would be implemented. This computer control system can display the curve of friction coefficient after experiment finish as well as save and read experiment data (Fig. 5).

3.2 Reliability Diagram of Friction Test instrument

After analyzing the function and structure of friction test instrument, the reliability diagram of friction test instrument are obtained shown in Fig. 6.

4 Experiments and Applications

4.1 Component Parameter Description of Friction Test instrument

It can be seen that this friction test instrument is a kind of serial system composed of many components. Table 1 gives out the failure time parameter and working time parameter of each component according to historical data. Its reliability index can be calculated based on formulas (2), (3), (4), and (5) mentioned above.

4.2 Reliability Index Calculation Based on MATLAB

In order to calculate the reliability index of friction test instrument introduced in Sect. 2.2, a software module was developed based on MATLAB. Based on this MATLAB program module, the steady-state availability of friction test instrument, after plugging the experiment data of friction test instrument into formulas above, can be obtained which is 0.912.

5 Conclusion

Aiming at the facts of experiment data shortage or even no, reliability element method was proposed to analyze the reliability of friction test instrument namely steady-state availability. And a program module was developed based on MATLAB to calculate these reliability indexes efficiently. The methods presented in this paper not only reduce the amount of calculation, but also increase the accuracy of reliability index. It is an effective way to analyze the reliability issues of customized instrument.

References

1. Liu p (2008) Base of reliability engineering. China Metrology Publishing House, Beijing, pp 35–46, In Chinese
2. Cao JH, Cheng K (2012) A mathematical introduction to reliability. Higher Education Press, Beijing, pp 117–132, In Chinese
3. Zhang S, He MG (2012) Reliability analysis method of handling system of specialized bulk cargo terminal. Logist Eng Manag 4(32):60–62
4. Li Y (2002) Reliability analysis of several Markov repairable system. Nanjing University of Aeronautics and Astronautics, Nanjing, pp 31–69, In Chinese

5. Shi HL (2012) Development of pin-on-disc sliding friction coefficient tester. China Jiliang University, Hangzhou, pp 13–56, In Chinese
6. Kang R, Wang ZL (2005) Framework of theory and technique of reliability of system engineering. Chin J Aeronaut 26(5):633–636, In Chinese
7. Cheng ZJ, Guo B (2006) System availability analysis under repair strategy opportunity. Pract Underst Math 36(10):137–140
8. Mi J (2006) Limiting availability of system with non-identical lifetime distributions and none-identical repair time distributions. Stat Probab Lett 76(7):729–736
9. Cao JH, Chen K (2012) Introduction of reliability mathematics. Higher Education Press, Beijing, pp 126–141, In Chinese

Design and Implementation of a New Power Transducer of Switch Machine

Yanli Wang and Bin Li

Abstract The design and implementation of an on-line monitoring system which can improve anti-interferences and stability of the railway switch machine in the railway industry is illustrated in this paper. The on-line monitoring system can detect three-phase electrical power by collecting the current and power of railway switch throughout its startup and working periods. This scheme adopts the multi-parameter power collecting chip ATT7022A to collect and process data, and uses the 485 bus line to implement communication between C8051F410 and PC. Field practice shows that the system possesses advantages of high-precision, low-energy consumption, and high reliability.

Keywords Switch machine • Power transducer • Online monitoring • Fieldbus

1 Introduction

Railway switch is one of important railway electrical signal devices. Generally, it is used to change the switch of railway tracks and indicate the switch's position at cross ways. It plays a crucial role in improving efficiency and ensuring the transportation safety of railway [1].

When a train arrives, it is crucial that whether the railway switch can switch on time and reliably or not for the safety of train running. However, there are some disadvantages in the present railway switch products, such as easy to reset, weak anti-interferences, instability. Therefore, designing a product with high anti-interferences and stabilities is very important. This paper demonstrates a new power transducer, which can improve the performance of the railway switch machine. The system includes fieldbus, sensor, computer network, and data communicational technologies.

Y. Wang (✉) • B. Li
Henan Technical College of Construction, Zhengzhou, China
e-mail: yanli1015@sina.com

W. Wang (ed.), *Mechatronics and Automatic Control Systems*, Lecture Notes in Electrical Engineering 237, DOI 10.1007/978-3-319-01273-5_90,

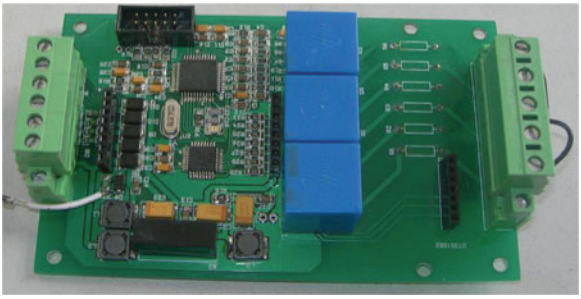

Fig. 1 Photo of prototype

The prototype is shown in Fig. 1. As adoption of high reliable isolation technology in the whole system, the system's security, stability, anti-interferences capability, and reliability have been improved greatly. From the test results of the prototype, one can see that the switch power sensor has stable performance, superior anti-lightning strike and anti-electromagnetic interference capabilities. Consequently, the maintenance and management works would achieve a new level if the system is applied in the railway widely.

2 The Whole System Design Scheme

The system is used to complete the on-line monitoring for three-phase motor power of industrial occasions, which mainly includes lower single chip micyoco (SCM) system, upper measurement, control software and the corresponding buffer circuit. The design includes systematic function, the overall structure design, and selection of upper computer communication mode, peripheral circuit design, and systematic anti-interference and so on. In terms of hardware design, we choose the C8051F410 SCM produced by the American Silabs company as the main controller micro programmed control unit (MCU) [2]. The signal acquisition and processing are completed by precise multi-function dedicated energy metering chip ATT7022A. The signal processing results are delivered to MCU by serial peripheral interface (SPI) of ATT7022A, and the MCU communicates with upper computer are completed through RS485. Hardware design program is shown in Fig. 2.

3 System Hardware Design

Data acquisition is completed by the corresponding transducer. Therefore, system designs must satisfy and match test requirement. We adopt special isolate modules (voltage and current transducer) to isolate and convert the measured AC voltage (current) into the Ac current (voltage) maintaining the same frequency and phase. Because that the current transducer connects two sides of the large current or

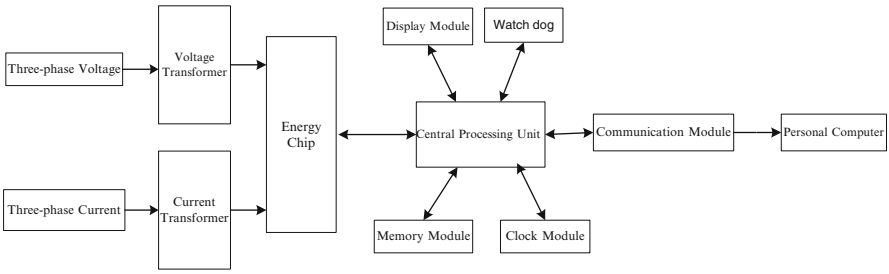

Fig. 2 Design program of hardware

current rectifier (the maximum input current required by the design is 10 A and the effective value of the maximum input sinusoidal signal offered to ATT7022 is 1 V), the linear current mutual inductor, with work function range 0–10 A and specification 5 A/2.5 mA is chosen.

The required input voltage (0–500 V) and current (0–10 A) are simulation signals, but the computer can only process the digital signal. So the collected simulation signal needs to be changed into digital signal (A/D change). For the same reason, when the control signal which comes from the computer drives the external device, the digital signal must be changed into simulation signal (D/A change), and then is magnified to control the electrical machine. By comparison, we select ATT7022A produced by Zhuhai Juli integrated circuit Design Company as sigma-delta ADC. ATT7022A is a digital signal processor (DSP) inserted with high velocity compute component, and it can be used to high accurate electrical gauging of three phase multi-parameter system. It includes six sigma-deltas ADC, reference voltage circuit and all of power, energy, effective value, power factor, frequency and digital signal dispose circuits. Consequently, it can gauge effective power, ineffective power, apparent power, and apparent current, effective voltage both each phase and mixed phase, which fully satisfies the development standard of the switch machine power transducer.

The main control module of C8051F410 is adopted as CPU to finish compute, storage, manifestation and communication of data. Combined with anti-interference circuit, the main control module possesses high ability in anti-interference, integration and system expansion. C8051F410 is a kind of fully integrated system-on-chip mixture signal MCP systems with low power consumption [3]. The functions of power on reset, VDD monitor, watchdog and clock oscillator in the system-on-chip system C8051F410 can work independently at the factory temperature (−40–80 °C).

Three-phase voltage outputted from the main control circuit converts into the output current of 4–20 mA through filter rectification of circuit. The circuit diagram is shown in Fig. 3.

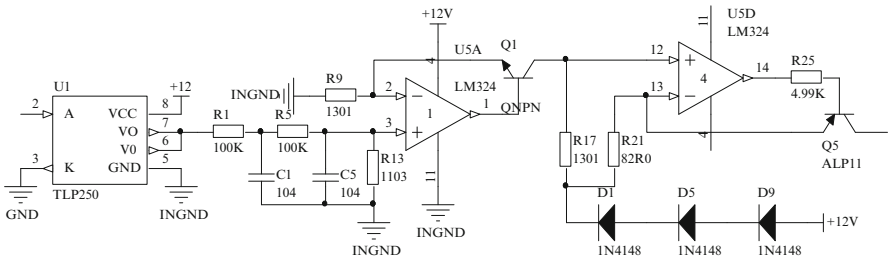

Fig. 3 Circuit diagram of current source

4 The Anti-interference Design of the Data Adoption System

Data acquisition system is usually applied at the complicated work site, with various kinds of interferences. Due to internal or external interferences, there will be interference signals in the measured voltage and current. As the main interferences of the electrical net are high-order harmonic, low pass filter was adopted at the output of mutual inductor to dispose high order wave with frequency higher than 50 Hz. Consequently, the wave shape has been ameliorated. To guard the stability of AC power supply, voltage-stability source between the electrical net and the mutual inductor was adopted to increase the anti-interferences of the system, which mainly contains isolation, wave filter technologies. For the isolation part, electromagnetic coupling of isolated magnify are used to isolate and transmit the captured message (after A/D change) before entering data gathering system [4]. Then the signal (after A/D change) is isolated by photo-coupler, and then inputted to the total line of the computer using photo coupling component. RC filter is used to dispose interference of the power frequency signal at 50 Hz.

5 System Software Design

The lower computer is mainly used to collect, manage and send the gathered data to the control room by RS-485 total line transmission [5]. For the overall design, the system is divided into main program and many sub modules. In the programming process, every module should be as independent as possible to compile, modify and debug software to reduce error easily. With the recycle property, the development time is reduced greatly. Besides, because the modules read in internal memory only if they are used, the occupation of the system resources and the running of the program space are reduced, and thus the running speed is enhanced greatly.

The upper machine mainly completes the following functions: communicate with the RS-485 serial module of master; receive, dispose, analyze and compute the data; manifest multi-switch machine real-time waveform; inquire history data and

so on. Firstly, programs receive the data package transferred from lower machine and unpack the data package according to the custom format. Secondly, after analyzing and computing the data, the programs compress and store the data into data bank for inquiry. If any debugging appears, it will give alarms and present debugging information. The program can display the power variation of multiple switch machines in the form of wave shape on the displayer.

6 Communication Method and Debugging Results

RS-485 communication interface is adopted to achieve remote data transmission in the system. Doublet RS-485 communication method is chosen to control the center machine to achieve the connectivity of multi-smart nodes and delivery of the remote data in the design. The system of main machine serial port uses RS-232 treaty. And the isolated RS-485/232 converter is chosen to complete the level conversion which needed in the program. The subject of the whole system includes three parts: front smart nodes, central monitor, and analyzing and diagnosing work station of the central controller [6].

The switch machine power transducer have been debugged at spot, and the debugging precision achieves the design requirement of 0.5 level (the basic cite error at any point of the linear measurement scope is less than 0.5 % of the output standard). On the other hand, the transducer functions required in the design are checked. The on-spot debugging shows that the system has high reliability, high anti-interference ability and can be applied to the railway line. The switch machine power transducer can provide technique guarantees for the steady and safety of train running. The linearity of test results is shown in Fig. 4. The linearity of the power transducer can meet the design requirement.

7 Conclusion

The design and implementation of an on-line monitoring system in the railway industry was illustrated in this paper. The multi-parameter power collection chip ATT7022A, with advantages of high precision (achieved 0.5 level), convenient function expansion and easy to achieve of software, is adopted in system, which simplifies the hardware and software structures. This system has many advantages as follows. The hardware electrical circuit C8051F410 mixed signal MCU is adopted as the control core, which decreases the power loss and volume of the system, but enhances the ability of real-time control. The switch machine distributed monitor system model based on RS-485 bus line technique is provided, which can enhance the efficiency of the management work in the railway equipment.

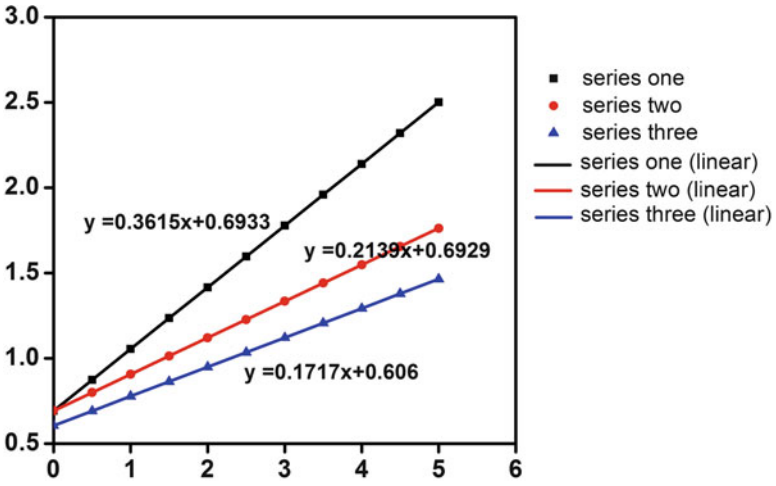

Fig. 4 The linearity of test results

According to the above design, the power switch machine was produced successfully. After adjusting of software, the output DC simulation signal achieves 4–20 mA. This system possesses advantages of high reliability, high anti-interference and can be applied to the railway line, which can supply technique guarantees for the steady and safety of train running.

References

1. Igarashi Y (2006) Development of monitoring system for electric switch machine. QR RTRI 47:78–82
2. Li G, Lin L (2002) Compatible with the 8051 high-performance, high-speed microcontroller the C8051FXXX. Beijing University of Aeronautics and Astronautics press, Beijing, pp 10–50, In Chinese
3. Xia L, Huang L, Jiang M (2006) Application of high speed system-on-chip MCU C8051F in experiment and leaching. Chin J Electron Device 4:1354–1358, In Chinese
4. Wang Z, Sun Y (2010) A new type AC/DC/AC converter for contactless power transfer system. Trans China Electrotech Soc 25:84–89, In Chinese
5. Qin P, Lin Y (2007) Simulation study of cargo oil handling system based on RS485 standard. J Syst Simul 19:5827–5831, In Chinese
6. Tian S (2001) Construction machinery condition monitoring and fault diagnosis. Constr Mach 32:26–30

Data Model Research of Subdivision Cell Template Based on EMD Model

Delan Xiong and Qingzhou Xu

Abstract Aiming at solving the problems of vast data, complex operation, and time consuming processing for remote sensing image, subdivision cell template was proposed based on Global Subdivision Grid (GSG). Subdivision cell template can realize a high level abstraction and generalization for remote sensing image. Based on a kind of GSG model of the Extended Model Based on Mapping Division (EMD), this paper discussed the model and structure of subdivision cell template, and put forward some new ideas for remote sensing image template processing. The relate experiment shows, this study might help improve remote sensing image processing speed, reduce repeated handling of huge amounts of image data, and expand practical application of remote sensing.

Keywords GSG • EMD • Remote sensing image • Subdivision cell template

1 Introduction

With the rapid development of modern science and technology, the acquisition and application of spatial information resources get more and more attention. As a real-time, rich-information and covering a wide range of spatial information resources, remote sensing image has become an important foundation data in many military and civilian areas [1]. In recent years, much kind of remote sensing image data have appeared and expanded rapidly. But in many practical fields, we need to think of the compatibility, timeliness, accuracy, and reliability of these data. At the same time, processing speed has become the bottleneck of remote sensing applications [2]. Therefore, it needs to develop a more efficient theory and technology system to organize and manage global spatial information.

D. Xiong (✉) • Q. Xu
International School of Education, Xuchang University, Xuchang, China
e-mail: xiongdelan@aliyun.com

W. Wang (ed.), *Mechatronics and Automatic Control Systems*, Lecture Notes in Electrical Engineering 237, DOI 10.1007/978-3-319-01273-5_91,

Global Subdivision Grid (GSG) provides a new way to build a global, multi-resolution level of open geospatial data organization framework [3]. Based on space partition organizational framework, the earth is divided into levels of regular, hierarchical, discrete cells. It will achieve rapidly storage, extraction and analysis of a worldwide mass data. In this paper, a kind of GSG model of EMD is introduced [4]. Then we propose the concept of subdivision cell template, and deeply discuss its application in remote sensing image processing. Some useful experiments and application demonstration will be done for testing.

2 Aerospace Information Subdivision Framework of EMD

2.1 EMD Method of Subdivision

In support of national 973 projects, Aerospace Information Engineering Research Center of Peking University proposed a set of multi-level geospatial framework, namely the Extended Model Based on Mapping Division (EMD) [5, 6]. The EMD mode can integrate the advantages of various global subdivision models in the world. The main idea of the EMD model is: using regular polyhedron to divide in the high-latitude regions, while using equal latitude and longitude grid to divide in low-latitude regions. The specific subdivision methods are as follows:

- First level subdivision. One divided cell is from south latitude 88° to the South Pole, marked as by 0. The other cell is from north latitude 88° to the North Pole, marked as 21. There are two latitude belts if we divide the surface of the earth from north latitude 88° to south latitude 88° through the equator. Each latitude belt can divide into ten longitude belts with width of 36° initially from west longitude 180°. So there are 20 subdivision cells, each one covers a range of 88° × 36°. These cells are orderly marked as 1, 2,…, 20. Therefore, the first level subdivision can get 22 cells, as shown in Fig. 1a.
- Second and Third level subdivision. Each first subdivision is divided into four equal second level subdivision cells. Each one has latitude difference of 44° and longitude difference of 18°. These cells are coded by 0, 1, 2 and 3. Then, each second subdivision cell is further divided into 33 third subdivision cells. Each one covers a range of 11° × 6°. They are shown in Fig. 1b.
- More than Fourth level subdivision. Subdivisions from the fourth to sixth level are divided according to mapping division rules. They are corresponding to 1:50000, 1:25000 and 1:10000 map respectively. From seventh level, subdivisions are recursively carried on by quadtree method with equal latitude difference and longitude difference.
- Pole Subdivision. The South Pole and North Pole were divided regular polyhedron division. Detail subdivision method was introduced in Ref. [5].

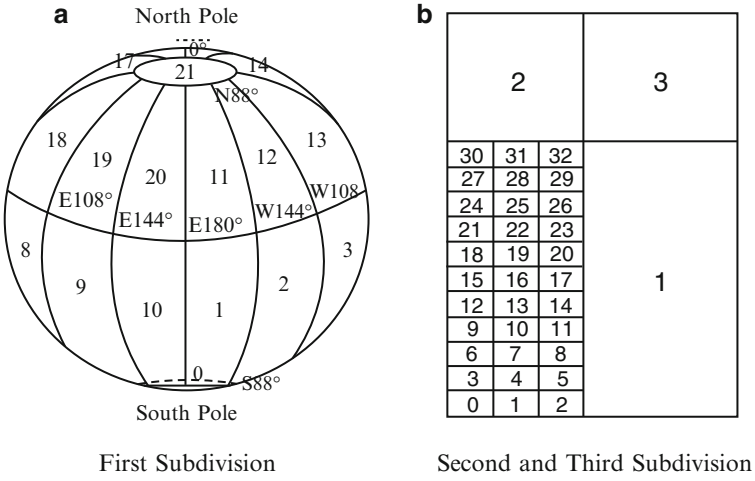

Fig. 1 Subdivision method of EMD model

2.2 The Advantages of EMD Model

Compared with the other method of subdivision, the EMD model has many advantages [7].

- The EMD model can provide a unified geospatial framework for various types of spatial data. Remote sensing image can be described in structure style using EMD model, which will improve expression ability of target.
- The EMD model can realize multi-scale representation of spatial data. All levels of subdivision cells form a strict hierarchy system, which can meet data requirements of different scales. Certain level subdivision cell has a unique correspondence with the cells in its upper level and lower level cells.
- The EMD model provides a unified spatial information integration services. Practice has proved that index of location is the basic approach to organize and use spatial data. EMD model can make spatial data of different levels and different regions have spatial logical relationships, just like a bridge.
- The practicality of EMD model. This model has a simple and clear correspondence with existing spatial data and coordinate expression Existing massive spatial data can be organized by this system easily.

3 Subdivision Cell Template Based on EMD Model

3.1 Subdivision Cell Template

GSG is a larger-scale hierarchical open spatial data management framework. It researches on how to subdivide the Earth into a series of cells with same area and similar shape. Subdivision cell is a multi-scale, discrete segmentation unit. It can be

Type	Item	Description
Cell Information	ID	Coding of subdivision cell
	Level	Subdivition level
	Area	the area of cell
	Length	the length of cell
	Location	Geographical region of cell
	Curvature	the average curvature of cell
Template Type	Name	the type name of subdivision template
	Application	Application goal of template
	Data Format	Metadata format for template
	Data Type	Data type and requirement of template
	File Interface	Data file and data processing algorithm interface
Image Data	Resolution	the resolution of remote sensing image
	Projection-type	Remote sensing plat and projection type
	Coordinate Information	Main coordinate value in image
	Entity Feature	Geometrical feature of main entity in image

Fig. 2 Main structure of subdivision cell template

expressed by an only digital or character encoding in the world [4]. It corresponds to a real region in the earth surface through subdivision. It has advantages of global, multi-resolution, well proportioned spatial location. Subdivision cell template is a standard data sample of remote sensing image corresponding to appointed region of certain subdivision cell. It contains data sets of spatial characteristics, geographic features and control points information of subdivision cell. Subdivision cell template inherits the advantages of subdivision cell, and establishes a correlation between the abstract model and specific remote sensing image. It will provide a good condition to organize, manage, process remote sensing image.

Subdivision cell template is composed of cell information, template type and image data. The main items are as shown in Fig. 2. Here, cell information contains detail subdivision cell information, such as coding, level, shape, size, spatial position, projection transformation and so on. Template type contains a variety of the template metadata, which is corresponding to specific subdivision processing algorithm. The template can be created by the template management module. Template data contains standard remote sensing image information according to certain subdivision cell. It not only includes resolution, coordinate information of remote sensing image, but also includes the color, texture, shape feature of spatial entity.

3.2 Modeling Process for Subdivision Cell Template

Constructing model for subdivision cell template is the key of remote sensing image processing. Hierarchical strategy and partition method are the main idea in construct data for subdivision cell template [8]. Modeling process can be described as following.

- Determine the number of layers for original remote sensing images. Firstly, make the original highest resolution images as the bottom resource. Then, determine relate layer number of other resolution image data based on multiplying power relationship.
- There are two kind methods to construct template. One is using existing image data correspond to appropriate layer. The other is circularly resample original data and generates other layer data.
- When meet a termination condition, it will stop creating new layer. Otherwise, creating new layer until the data amount of image is less than a image block.

Hierarchical strategy can be adjusted flexibly according to the situation of the data source. There is a greater flexibility in establishing image pyramid for multi-source data. The goal is as far as possible to ensure the accuracy of the image, reduce the data calculation, and improve processing speed.

Partition method is to improve I/O access efficiency of image data. Generally, the block of $2^n \times 2^n$ pixels is selected as the standard image data size [9].

4 Subdivision Cell Template Applications in Remote Sensing Image Processing

4.1 Subdivision Cell Template Processing Idea

Subdivision cell template can be fit for massive remote sensing image information, and improve processing speed of data. According to specific subdivision model, the subdivision cell has outstanding feature in size and shape. We can select several continuous subdivision cells as research object. Thinking of different application requirements, the high resolution and orthogonal projected remote sensing image of typical hot area can be selected. Then, subdivision cell template should be established through standardized processing. Subdivision cell template processing task includes image segmentation, feature extraction, manual annotation. The processing flow can be described by Fig. 3.

4.2 Application Demo for Remote sensing image

Based on EMD model, we have research on shape, feature and coding of subdivision cell in certain level. Then, we constructed the corresponding subdivision template of remote sensing image. An initial prototype system for subdivision template of remote sensing image processing system was developed [10]. The simple demonstration system was developed in Windows Server 2003. At present,

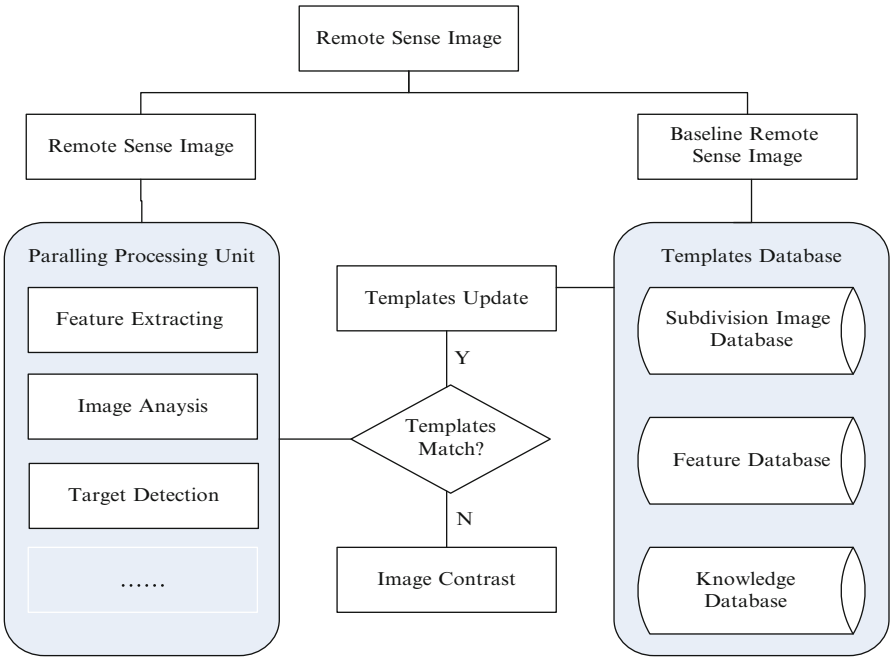

Fig. 3 Subdivision cell template processing framework

it used SQL Server 2005 to manage remote sensing data. And basic interface was designed and developed by VC++.

Preliminarily, we selected several high-resolution remote sensing images of tourist attractions, and create subdivision template manually. At present, basic functions such as image browsing, template view and feature retrieval according to the specified conditions were completed. A kind of operation is shown as Fig. 4. You can select retrieve mode (such as image subject), and input the keywords (such as Henan AND tourism AND spa). Then, the search results will be shown. You can get more information of image and template by clicking the related buttons.

At present, the system has completed of basic functions testing in single computer environment. Preliminary tests showed that the system have highly-targeted, high practicability, high retrieval efficiency and good expandability. More functions would be further developed.

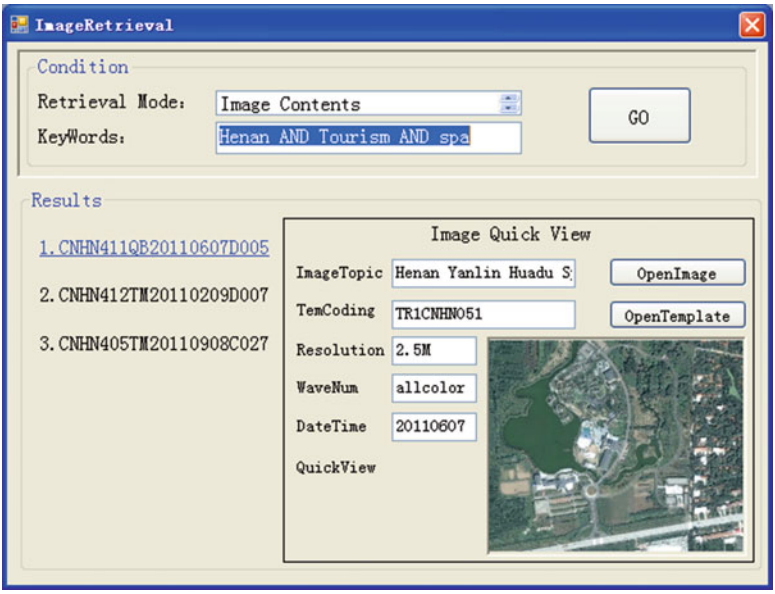

Fig. 4 Subdivision cell template and image retrieve interface

5 Conclusion

Remote sensing images have been widely used in various fields such as military reconnaissance, disaster forecasting, and environmental monitoring. Now the sensing images data is increasing, and its application requirement is expanding. The collection, organization, management and sharing of remote sensing data have become the most prominent problem to be solved for data producers and users.

The global subdivision model of EMD divides the Earth into cells at levels. Combining with the features and advantages of subdivision cell, this paper put forward the concept of subdivision template and proposed to construct subdivision cell template of remote sensing image. This method can be done gradually by level, by batches, and by cell region. With the increase of subdivision cell template, parallel processing technique would be adopted to improve processing efficiency and sharing service. This study might have significance for extending application fields of remote sensing image. It will open many practical applications of GSG, and enhance the value of spatial data.

Acknowledgements This work is supported by the Science and Technology Research Project of Henan Province under Grant No. 112102210079, and Third Young Backbone Teacher Support Program of Xuchang University.

References

1. LI De-ren (2005) On generalized and specialized spatial information grid. J Remote Sens 9 (5):513–520
2. Goodchild M (2000) Discrete global grids for digital earth. In: International conference on discrete global grids, Santa Barbara Press, California, pp 1271–1288
3. Sahr K, White D, Kimmerling A (2003) Geodesic discrete global grid systems. Cartogr Geogr Info Sci 30(2):121–134
4. CHENG Chengqi, GUAN Li (2010) The global subdivision grid based on extended mapping division and its address coding. Acta Geodaeticaet Cartographica Sinica 39(3):295–30
5. SONG Shu-hua, CHENG Cheng-qi, GUAN Li et al (2008) Analysis on global geodata partitioning models. Geogr Geo-Info Sci 24(5):11–15
6. GUAN Li, LU Xuefeng (2012) Properties analysis of geospatial subdivision grid framework for spatial data organization. Acta Scientiarum Naturalium Universitatis Pekinensis 48 (1):123–132
7. CHENG Cheng-qi, ZHANG En-dong, WAN Yuan-wei et al (2010) Research on remote sensing image subdivision pyramid. Geogr Geo-Info Sci 26(1):19–23
8. CHENG Qi-min (2011) Remote sensing image retrieve technology. Wuhan University Press, Wuhan, pp 123–127
9. Plaza A, Plaza J, Valencia D (2007) Impact of platform heterogeneity on the design of parallel algorithms for morphological processing of high-dimensional image data. J Supercomput 40 (1):87–107
10. DU Gen-yuan, MIAO Fang, GUO Xi-rong (2010) A novel network service mode of spatial information and its prototype system. Adv Mater Res 12(5):108–111, 319

A Spatial Architecture Model of Internet of Things Based on Triangular Pyramid

Weidong Fang, Lianhai Shan, Zhidong Shi, Guoqing Jia, and Xin Wang

Abstract In This paper, a novel spatial architecture model is proposed for the Internet of Things (IoT) based on triangular pyramid. Under the support of generic technologies, this spatial architecture model is composed of "Sensing and Controlling", "Ubiquitous Transmission" and "Diversified Requirements and Applications". The proposed architecture model may not only achieve effective convergence of technology, but also simplify the heterogeneous network and facilitate the application design of IoT. So, the current application situation of IoT is introduced first, and the architecture of IoT is then analyzed. Secondly, the spatial architecture model is proposed and some relevant compositions are discussed. Finally, the application prospect is described.

Keywords Internet of things • Architecture • Triangular pyramid

W. Fang • Z. Shi
School of Communication and Information Engineering, Shanghai University, Shanghai, China

L. Shan (✉)
Shanghai Internet of Things Co., Ltd, Shanghai, China
e-mail: shanlianhai@163.com

G. Jia
College of Physics and Electronic Information Engineering, Qinghai University for Nationalities, Xining, China

X. Wang
Changchun Institute of Engineering Technology, Changchun, China

W. Wang (ed.), *Mechatronics and Automatic Control Systems*, Lecture Notes in Electrical Engineering 237, DOI 10.1007/978-3-319-01273-5_92,

1 Introduction

The Internet of Things (IoT) is an advanced multi-disciplinary research field nowadays. It is considered to be one of the most important technologies which have enormous influence in the twenty-first century. In 2005, ITU defined IoT as [1], "The connectivity for anything by embedding mobile transceivers into a wide array of additional gadgets and everybody items, enabling new forms of communication between people and things, and between things themselves." Actually, the IoT could sense, collect and monitor all kinds of information in real-time through various integrated micro-sensor, processing information by embedded systems, and converging information through self-organizing multi-hop relay communication networks. The IoT would transfer this information to the user's terminal to complete various applications and achieve the "ubiquitous computing" goal.

Currently, the IoT is gradually applied in various fields. K.H. Su focused and summarized the relationship between "smart city" and "digital city" [2]. A municipal solid waste recycling management information platform was proposed [3]. The application of "smart community" and "community security management" was depicted respectively [4, 5]. In terms of people's lives, G.X. Yang investigated security and defense system for home based on IoT [6], Y.G. Li researched the reinforcement of communication security of the intelligent home [7]. Of course, there are other application fields, such as "Logistics Industry", "Electronic Commerce" and so on.

Although the applications have a bright future, the IoT is an ongoing research and development work. At present, there is no IoT system of ITU strict definition and objective architecture. In this paper, we will introduce the current research status of IoT architecture. For assuring the objectivity and rationality of assumption, we will propose our novel architecture based on the understanding to IoT, and then put forward key technologies involved with this architecture.

2 Related Works

It is very heterogeneous for each joint of IoT from sense, transmission to application. The future needs to be taken openly and expansive network system architecture for achieving interconnection, interaction and interoperability of information.

2.1 Architecture of IoT Based on Technology

At present, the mainly research describing the architecture of IoT is divided into two types. One is based on the high-level architecture of Ubiquitous Sensor Networks (USN) in Y.2221 of ITU [8]; the other refers to the OSI model.

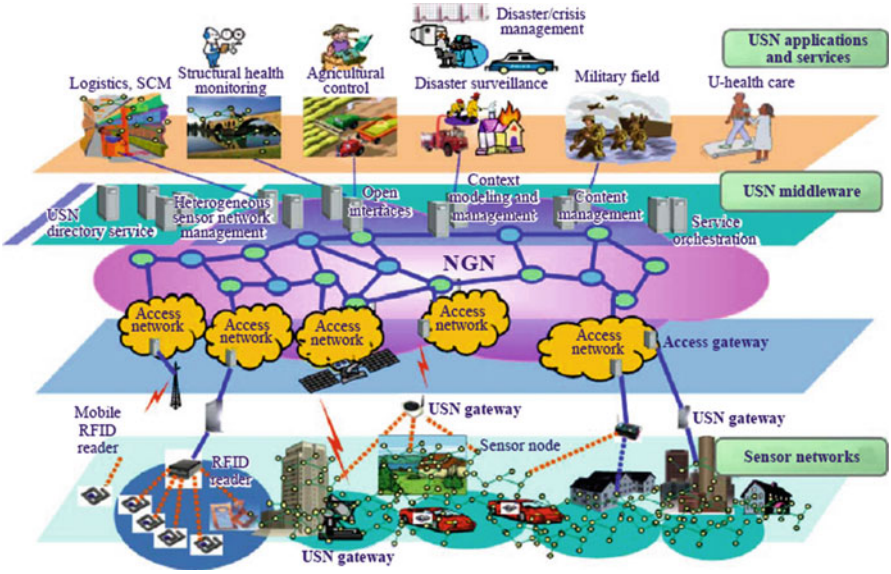

Fig. 1 An overview of USN with related technical areas

The architecture is divided into four layers based on oriented applications and services of the USN in Fig. 1. It includes the underlying sensor network, access networks, USN middleware, USN applications and services from bottom to up.

Another architecture that refers to OSI model is divided into three layers by using hierarchical design. It includes the Perception Layer, the Network layer and the Application Layer. Although the architecture ignores the network heterogeneity, it is cursory and flat. This architecture's layer is divided more from the application's point of view, mentioned less for the interface between the layers (data interface or physical interface) and scalability.

In fact, there is no specialized research for IoT in the ITU's technology roadmap, but take the communication between persons and things, things and things as the IoT's important function, which is adopted by ITU.

2.2 Architecture of IoT Based on Application

There are three types of IoT's architectures based on application, which include Radio Frequency IDentification (RFID), WSN and Machine-to-Machine (M2M).

1. Base on RFID
   The electronic tags that change "things" into intelligent objects may be the most flexible in the three types of systems architecture, tagging mobile and

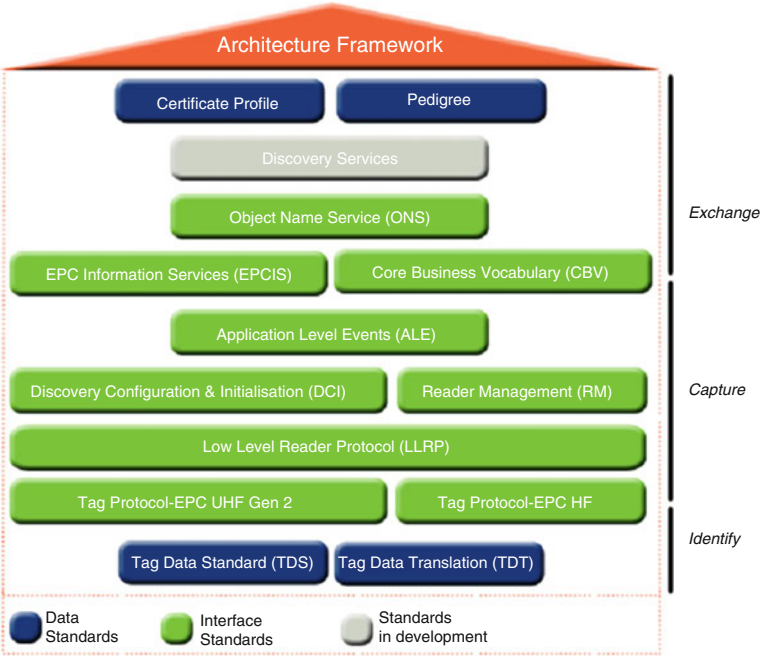

Fig. 2 EPCGlobal standard architectures

non-mobile assets are their major application for tracking and management. Prof. E. Fleisch believes that RFID, just like punch card, keyboard and barcode, is a data entry method, belongs to a scope of IoT.

In the coding, the Auto-ID Centre proposed EPCGlobal system for all electronic encoding; RFID is just a carrier of encoding. It proposed five technical components of the Auto-ID system in Fig. 2, including an EPC (electronic product code) tag, RFID reader, ALE Middleware for information filtering and gathering, EPCIS (EPC Information Service) and EPCIS Discovery Service.

2. Based on WSN

WSN is composed of a set of "autonomy" wireless sensor nodes in free space, which collaborate to complete the monitoring of specific environmental conditions, such as temperature, humidity, and so on. It is self-organizing or self-configuring network, including Mesh Networks and Mobile Ad-hoc Network.

Although WSN is still a hot spot in the research field, there is seldom a success case in the industrial field. This is because, the research on WSN focus on sub-layer of network mostly. According to its current development, we think the WSN has certain distance from the IoT of real sense, because it is inadequate for research on the issue of its level. On the other hand, some researchers of WSN are so high on wireless technology that they ignore the combination of using field bus in perception aspect and using long distance wireless communication in the transmission, which have achieved the goal of large scale application from the practicability and commerce popularization.

3. Based on M2M
   Generally speaking, the concepts and architecture of M2M cover a wide range, including the part of the contents of the EPCGlobal and WSN, also covering both wired and wireless communication.

   Similarly, the development of M2M lacks standardized specification and unified system architecture. Although there is some attempt (such as oBIX and oMIX), the unified specification has not yet formed, there is still a long way to go.

   In contrast, the technical architectures of WSN and M2M have not yet fully been raised to the IoT's ONS/PML technology system height. We believe that it should refer to ONS/PML technology system on the road towards the IoT.

3 Novel Architecture Profile

The architecture is the most important prerequisite for the guidance of the system design. In addition, the design of the architecture will determine the IoT's technical details, application patterns and trends.

We have followed the research methods used by ITU for architecture of IoT. Firstly, we abstracted its applications and scenarios, which are the basis of the design and verification of its architecture; then put forwards the general principles and requirements. At last, we proposed a common architecture and the functional structure models in Fig. 3.

We know that the objective of common architecture is the development of the functional methodology and general model. So, we propose the spatial architecture model of IoT based on triangular pyramid differs from the traditional form. This architecture consists of four parts: 'Sense and Control', 'Ubiquitous Transmission', 'Diversified Services and Applications' and 'Generic Technologies', in which 'Generic Technologies' are the bases for above mention.

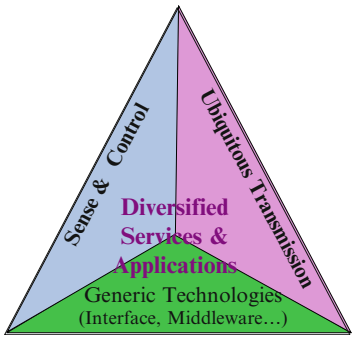

Fig. 3 A spatial architecture model of internet of things

1. Sense and Control
   The technology of things sensed and controlled is also called information things technology. It belongs to the interface technology between the physical world and network world. In a wide sense, it translates the analog into the digital, which would be used. According to the instruction, it could perform some operation.

   The connotation of this technology is very extensive. It includes the Cyber Physical System (CPS) [9]. Some researchers who study on CPS usually take the embedded systems as the basic technology between real-world and network systems in the U.S.A. Other researchers think that RFID, Near Field Communication and WSN constitute the basic technology to connect the real world and the digital world in Europe. This difference derived from the different research point of view.
2. Ubiquitous Transmission
   The ubiquitous transmission means information can be reached anywhere, not just the end to end. This transmission should have the high efficiency, low latency and QoS guarantee. The ubiquitous transmission relates to the network of self-management capability. On the other hand, it extended to "Any time, any place, to connect to any things, to transmit any type of information".

   From a macro perspective, Internet to carry transmission of thing's information is no longer Internet of traditional sense. It must ensure that the information about the query things has a time stamp and space markings, and instructions to manipulate things must be the instructions of the time and space semantics. All of these require the Internet to carry transmission of thing's information has the clock system and the coordinate system associated with the physical world,
3. Diversified Services and Applications
   The IoT is embracing the people and things of the modern society, so the applications and services involve various industries. Its applications can be divided into several categories. The transportation and logistics classes include the logistics management, automatic toll collection based on personal identification, and electronic navigation map. The applications of medical classes are composed of the tracking of medical objects, perception of physical symptoms, as well as a database system. The personal and social classes are composed of real-time interaction between people and networks, finding missing items. The application of the future class is not yet available in the current deployment of the conditions, including the robot taxi, smart city; and so on. These applications are various services, which include multimedia services and data services. Of course, these services could be divided into narrow-band services and wideband services from the aspect of bandwidth.
4. Generic Technologies
   In general, the generic technology is a class of technology that may be widely used in many areas in the future, It's R & D results can be shared, and profoundly impact one or more industries and enterprises. As a major part of the spatial architecture model of IoT based triangular pyramid, the generic technologies play an important role from cognizing and sensing the ambient world to

diversified services and applications. These generic technologies could not only solve the heterogeneity of the network, but also promote the convergence of multiple technologies. The generic technologies of IoT include middleware, interface and information process, but not limited to these items.

4 Associated with Cloud Computing

In 2008, the concept of cloud computing was proposed by Google, caused widespread concern in the industry. Forester Research gave cloud computing a definition: A standardized IT capability (services, software, or infrastructure) delivered in pay-per-use, self-service way [10]. We believe that cloud computing is the combination of information processing, storage and operations based on cooperation. The main source of information is the massive data, which mostly comes from the ambient world.

In the traditional sense, the association of cloud computing and the IoT is vague. However, through the proposed architecture in this paper, they both could conveniently be associated by 'Generic Technologies'. This is due to that some technical features are not only owned by the two, and some events are but also driven jointly.

Many associated technologies combined with novel architecture of IoT and cloud computing, we focus on the pre-processing technology of massive data in IoT. At present, with the expansion of the scale of the IoT's applications, the amount of data that is generated by perceived information is growing exponentially. On the other hand, the perceptual characteristics of the sensor node, just as multi-point sensing a common target, as well as a single-point sensing multi-target, would cause the deviation and redundant of the information within a certain range. In addition, in the process of information transmission, especially the transmission process in the self-organizing multi-hop network, part of the data loss caused by dirty data – in the data of source system (data perception and transmission in IoT), the size of the data is not within the given range, or the data is meaningless for the actual services, or data format is illegal, as well as there are non-standard coding and vague logic of service. These dirty data would reduce the operating efficiency of the system, or even cause system collapse. In order to solve the above-mentioned issues, some measurements should be taken:

- Date filtering or data cleaning based on variable constraint for 'Sense and Control';
- Data aggregation based on distributed multi-source for 'Ubiquitous Transmission';
- Data reduction based on the feature of the perceived target for 'Diversified Services and Applications'.

5 Conclusion

There are some arguments about the research and development of IoT. One is whether it has its own technology architecture. Someone holds passive attitudes. They claim that it has just been the integration of existing technologies. However, others hold opposite opinions. In this paper, the novel architecture pro-posed ensures to provide guidance for how to define the functional structure of an IoT. The guidance includes how to divide into the appropriate feature set and how to define the reference point between the feature set corresponding to the physical realization and interface definition. Meanwhile, it is believed that although the IoT possesses features of computer, communication, network and control, the simple integration of these technologies cannot constitute a flexible and efficient IoT. Based on the convergence of above mentioned technology, the IoT forms own technical architecture through further research, development and application.

In accordance with the ITU point of view, "Interconnect Any Thing" is the expansion of capacity, services and applications of the NGN. Therefore, it is recommended that the IoT should be applied to NGN's research scope and be implemented in the NGN technology development roadmap. We should further study the functional architecture of the IoT and specific configuration model.

Acknowledgements This work is partially supported by the Science and Technology Innovation Program of Shanghai (12DZ2250200, 12511503300), and the Tianjin University – Qinghai University for nationalities Independent Innovation Fund Projects.

References

1. ITU internet reports: the internet of things (2005)
2. Su KH, Li J, Fu HB (2011) Smart city and the applications. In: Proceeding IEEE ICECC, Ningbo, China, pp 1028–1031
3. Chen T, Li X (2010) Municipal solid waste recycle management information platform based on internet of things technology. In: Proceeding IEEE MINES, Nanjing, China, pp 729–732
4. Li X, Lu RX, Liang XH, Shen XM (2011) Smart community: an internet of things application. IEEE Commun Mag 49:68–75
5. Liu JH, Yang L (2011) Application of internet of things in the community security management. In: Proceeding IEEE CICSyN, Bali, Indonesia, pp 314–318
6. Yang GX, Li FJ (2010) Investigation of security and defense system for home based on internet of things. In: Proceeding IEEE WISM, Nanjing, China, pp 8–12
7. Li YG, Jiang MF (2011) The reinforcement of communication security of the internet of things in the field of intelligent home through the use of middleware. In: Proceeding IEEE KAM, Sanya, China, pp 254–257
8. ITU. T. Recommendation Y.2221 (2010) Requirements for support of ubiquitous sensor network (USN) applications and services in the NGN environment
9. Atxori L, Iera A, Morabito G (2010) The internet of things: a survey. Comput Netw 54:2787–2805
10. http://www.forrester.com/Cloud-Computing

Design and Realization of Fault Monitor Module

Dongmei Zhao, Huanhuan Dong, and Xiang Xue

Abstract Fault monitor module is designed for power grid fault diagnosis and recovery system. It sets interface with dispatching automation platform to get real-time operating data. In order to solve the problem – "Data are flooding but useful fault information is lack and fuzzy", this paper analyzed and processed the upload of data in fault condition. It uses semantic analysis and logical analysis to delete interference, integrate some other messages and do some complement. With the more reliable and clear messages to identify the condition, it can avoid the fault diagnosis mistakenly start through fault identification functional module. It uses fast network topology analysis (using depth-first method search whole net and dynamic topology tracking the net changes) to monitor real-time data changes of the power grid running state. The whole program is divided into several separate threads to improve the efficiency. The application result shows that it improves the diagnosis and the recovery can be more accurate, more efficient and faster.

Keywords Monitor • Interface • Fast topology analysis • Multi-thread • Fault identify

1 Introduction

Modern grid becomes bigger and the harm caused by fault is more and more serious. At the same time, users' requirements are also rising about continuous power and its quality. Grid is developing toward the direction of building a strong and smart grid, trying to realize it's self-healing and self-adaptive. In other word it means when simple or complex fault happens to grid, the automation system can

D. Zhao • H. Dong (✉) • X. Xue
School of Electrical and Electronic Engineering, North China Electric Power University, Beijing, China
e-mail: dong.huanhuan@163.com

W. Wang (ed.), *Mechatronics and Automatic Control Systems*, Lecture Notes in Electrical Engineering 237, DOI 10.1007/978-3-319-01273-5_93,

accurately and rapidly identify the fault zone to determine the true fault element, then to restore power to the users in blackout region with the faster speed and optimal path. Therefore, fast and accurate fault diagnosis and recovery system is significant to the stable and reliable operation of the power grid.

Fault diagnosis and recovery methods are all based on the gathered fault messages. Without the fault messages, the fault diagnosis and recovery system is just like bricks without straw, so fault messages analysis and processing is necessary and essential. We establish the monitor module to receive real-time information collected by the dispatching automation platform, and then to classify and select from the information to make network topology analysis in this paper. It can provide reliable and useful fault information and coordinate the execution order of the program.

2 The Overall Program Design

The monitor module has several sub-modules: data interface, alarm information identification, fast network topology analysis, the system self-test, multi-thread management. The whole system's function block diagram has shown in Fig. 1.

2.1 Data Interface

It connects SCADA/EMS to get the static and dynamic data for fault processing. The static data includes device model, topology information and some secondary device configuration information. We can get the static data from CIM. Dynamic data are real-time operation messages. It can provide grid operating information. We can get real-time operating codes and translate them into information that can be directly and easily used by following program based on the 104 rules.

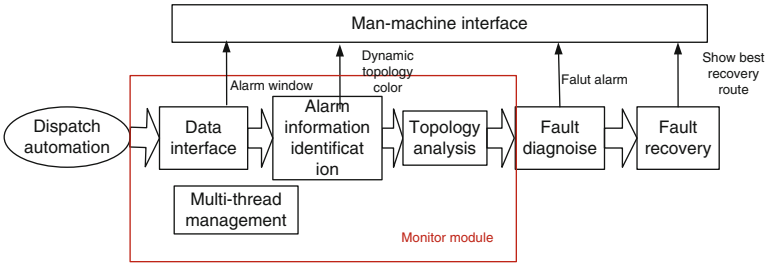

Fig. 1 Fault diagnosis and recovery system monitor module functional diagram

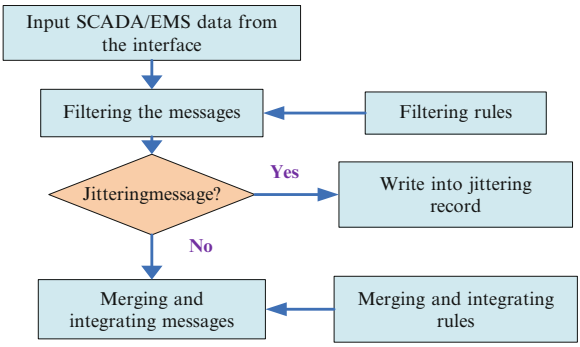

Fig. 2 Fault messages pre-treatments flow chart

Alarm information window includes the new alarms fault diagnosis system getting data last time till it getting data this time(suppose the time interval flag is t). With testing many times, t equaling 10 sends is suitable for getting fault messages.

2.2 Fault Messages Pre-treatment

There are plenty of fault messages, but many of them are redundant and useless. The messages are incomplete inconsistency and possibly they are got not at the same time. All of these will lead the interface to miss some of the troubleshooting critical information, so the messages pre-treatments are necessary [1] (Fig. 2).

2.2.1 Filter

In order to highlight main information, we can filtering some alarm messages which contains some special keywords, for example, the alarm messages including words like “DC panel”, “fault recorder” and so on. What is more, we can provide the editing functions such as add, delete, modify keywords to enhance the adaptability [2].

2.2.2 Anti-shaking

The jitter messages do great harm to fault diagnosis, so the rules of judge and deal with jitter messages are developed to ensure that jitter messages are written into jitter record table and being prevented from uploading.

2.2.3 Messages Merging

Based on message merging logic, the messages which have the same semantic content or extension meaning should be merged. E.g. some important components that have dual-microprocessor-based relay protection and the two sets of protection device may act and send messages at the same time. To merge the messages according to the logic, then choose the most suitable one for display.

2.2.4 Comprehensive

Most of the protection signals, such as over current protection, differential protection, and overload protection are all have a fixed protection tripping objects. We can integrate the related fault messages into one message according to the directly relationship between the relay signals and breaker tripping messages.

2.2.5 Dealing with the Mistake Messages and Omitted Messages

According to action logical relationship between the relay protection and circuit breakers, and considering some auxiliary secondary signals at the same time, it can do in-depth analysis of the protection signals to see the possibility of errors in logic or to see whether missing some circuit breaker tripping messages that should be uploaded. After these are done, it can suggest the possibly mistake messages and the omitted messages, and directly delete the insignificant ones [3, 4].

2.3 Fault Identification

The fault diagnosis and recovery program isn't running when grid is operating well. It starts only when fault happens, so fault identification is important to start diagnosis program. The fault criterion is made with the necessary fault information of relay protection, circuit breakers and so on.

$D = \{d_1,d_2,\ldots,d_i\}$ is a collection of all devices, including generators, transformers, buses, lines. $P = \{p1,p2,\ldots pj\}$ is a collection of all relay protections. $B = \{b_1,b_2,\ldots,b_k\}$ is a collection of all breakers.

Relationship $\Re$ is defined as follows:

$$\Re = \{(p,b)|\text{p move contributes to } bmove, \text{p} \in \text{P}, b \in \text{B}\} \quad (1)$$

If p and b have the relationship as Eq. 1, we can say p and b are relations.

For $\text{p} \in \text{P}$, the related breakers are $B(p)$

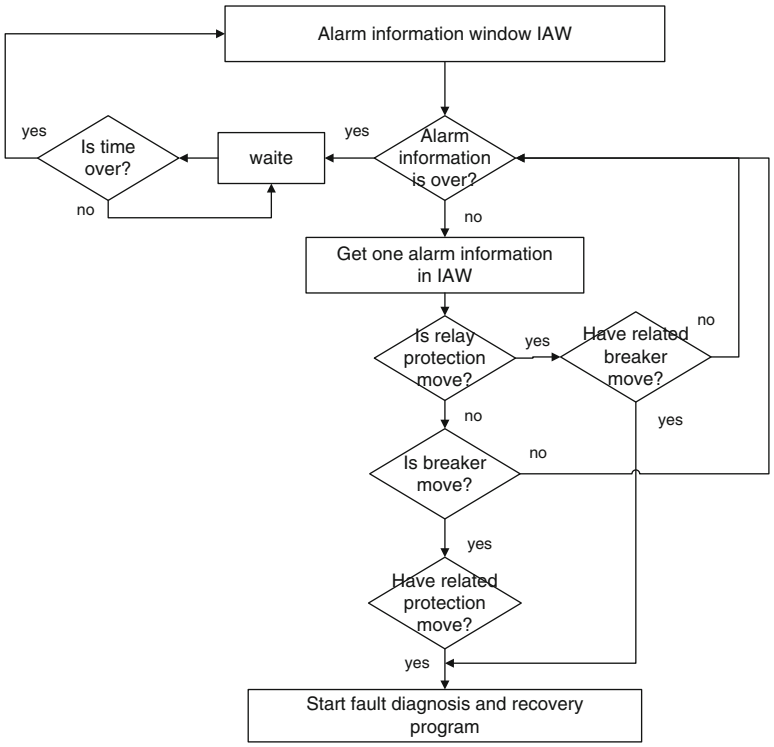

Fig. 3 Fault identification flow chart

$$\mathrm{B}(p) = \{b | p \Re b, b \in B\} \tag{2}$$

For $b \in B$, the related protections are $P(b)$

$$P(b) = \{p | p \Re b, p \in P\} \tag{3}$$

If there is protection p ∈ P arising, and at the same time there is related breaker move-information $b \in B$, it tips fault happen [5]. The detailed identification process is shown in Fig. 3.

2.4 Fast Network Topology Analysis

2.4.1 Network Topology Analysis

The information of connecting relationship of the devices and the real-time status of switches which comes from the interface are important data for topology analysis.

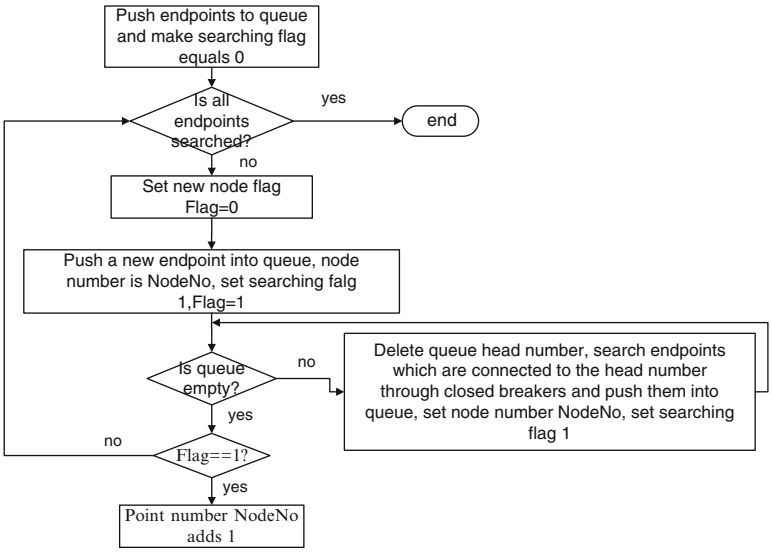

Fig. 4 Topology nodes analysis

If the switching device is closed then the two endpoints of it can integrate into one node. Check all the switching devices with this method to form the endpoints-nodetable. The detailed analysis process is shown in Fig. 4.

After that, integrating lines transformers and other impedance devices' two nodes into one subsystem. The method is similar with topology nodes analysis above.

The subsystem has power and load representing that it is operating well. Otherwise, it is an island that is isolated from the grid. In order to ensure the timeliness of the online application, it needs real-time information to update current grid dynamic topology and to provide the relations between devices for the whole program.

2.4.2 Dynamic Topology Tracking

Partial network topology tracking is essential for improving the speed. It directly focuses on the move zone and analyzes the partial zone based on the breakers movement [6]. Figure 5 is the flowing chart.

1. Are the breaker's two endpoints still belonging to one node? If the answer is yes, the track is over; If answer is no, to start searching from breaker's one endpoint based on closed neighbor breakers, set their node number MaxNodeNum+1 (MaxNodeNum is the max node number before the breaker opens).
2. Are the breaker's left and right nodes still belonging to one system? If answer is yes, the track is over; otherwise, to start searching from the new node based on impendence devices, set their system number MaxSysNum+1(MaxSysNum is the max system number before the breaker opens) (Fig. 6).

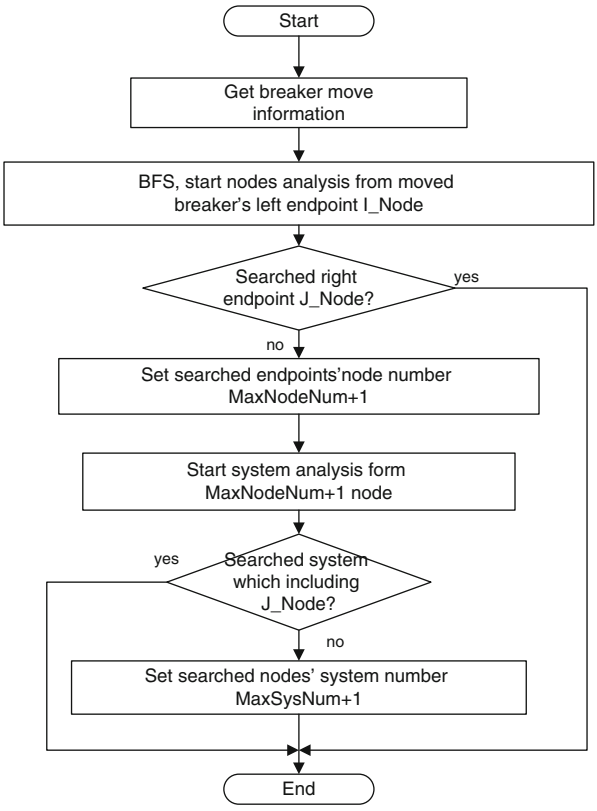

Fig. 5 Dynamic topology tracking when breaker opens

2.5 Multi-thread Management

Multi-thread management sub-module sets separate threads to improve the running efficiency as multi-thread technology aloud several threads running at the same time. It also sets their running prior to decide which one running first when crash happens.

Prior I: fault identification function starts the online fault diagnosis and recovery program has the first position, its running cannot be disturbed by other threads. Other threads are all hang.

Prior II: data interface is an always running thread, and it is listening for data transmission request all the time.

Prior III: users' request from man – machine interface such as electrical devices' parameter adding, deleting or changes and so on.

In a word, multi-thread management can solve threads' crash and order the sequence of their running. The thread which has the higher prior could obtain more CPU running time and recourse.

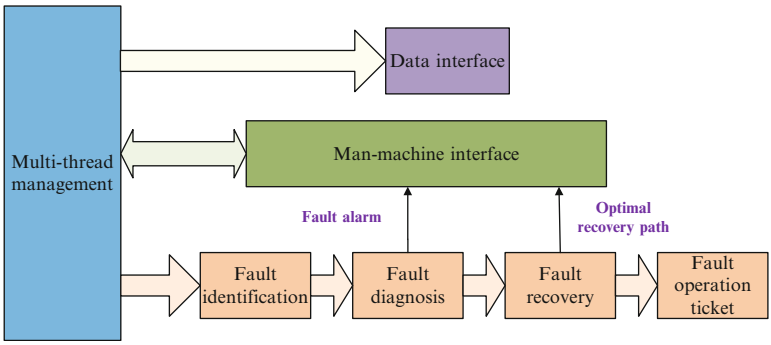

Fig. 6 Multi-thread management module functional block diagram

3 Software Testing

Due to the low probability of fault in the grid, it designs the study states fault simulation to test effectiveness and practicality of the software. Using the alarm information that read from the database to set fault condition to test the software, the results show that the software running smoothly and the diagnostic result and recovery path are correct and reasonable. We apply it to a regional power grid's fault diagnosis and recovery system to see that it could read real-time data, give warning tips when it accepts exceptional messages. It has high reliability and meets the development requirements of the system's function.

4 Conclusion

Monitor module is a data provider for fault diagnosis and recovery system, and it is also the entire system's manager and commander. It controls the priority order of the system program's implementation and trigger conditions, etc., keeps coordination of the various program modules and avoids conflicts. In advancing the process of fault diagnosis and recovery system utility, full attention must be paid to the collection and collation of the fault information, including the pretreatment of the fault information for building underlying data and extracting diagnostic knowledge for fault diagnosis.

References

1. Ding Jian, Bai Xiao-min, Zhao Wei (2007) Fault information analysis and diagnosis method of power system based on complex event processing technology. Proc CSEE 27(28):40–45, In Chinese
2. Guo Jin-zhi (2003) Study on the on-line intelligent fault diagnosis of power transmission network. North China Electric Power University, Beijing, pp 6–14, In Chinese
3. Liu Dao-bing, Gu Xue-ping, Zhao Jie-qiong (2010) Practical research of fault restoration for the regional power grid. Power Syst Prot Control 38(21):48–52, In Chinese
4. Zhou W (2008) Research and development of power grid intelligent alarm information processing system. North China Electric Power University, Beijing, pp 1–38, In Chinese
5. Liu Dao-bing (2012) Modeling and solving of a complete analytic model for fault diagnosis of power systems. North China Electric Power University, Beijing, pp 18–62, In Chinese
6. Chen Jiong (2008) Research on the method of automatically generate topology in the grid operator decision-making system. Nanjing Normal University, Nanjing, pp 30–40, In Chinese

Dynamical System Identification of Complex Nonlinear System Based on Phase Space Topological Features

Lei Nie, Zhaocheng Yang, Jin Yang, and Weidong Jiang

Abstract Dynamical system identification of complex nonlinear system can be regarded as parameter estimation task of uncovering the nature of the system, which is of much importance for many engineering applications. Sea clutter is one kind of complex nonlinear system, which has intrinsic complexity and high nonstationarity. Therefore, it is difficult to detect marine targets due to the low Signal-Noise-Ratio (SNR) and low Signal-Clutter-Ratio(SCR). To improve the performance of marine target detection in, a method to discover fundamental geometric structures from high-dimensional and multivariable data sets is proposed. The method can improve the target detection performance and its main novelty lies in phase space reconstruction and topological features extraction, based on the dynamical system identification scheme and topological data analysis (TDA) techniques. Experiments with measured sea-clutter data demonstrate the performance of the method proposed in this work.

Keywords System identification • Pattern discovery • Sea clutter

1 Introduction

Robust marine target detection [1] and adequate sea clutter modelling [2, 3] are significant capabilities in utilizing the modern maritime surveillance radar, which has high-resolution and broadband [4, 5]. The massive data of radar echo provide more possibilities as well as more difficulties in knowledge extraction.

L. Nie (✉) • Z. Yang • J. Yang • W. Jiang
School of Electronic Science and Engineering, National University of Defense Technology, Changsha, China
e-mail: Nielei@Nudt.Edu.cn

W. Wang (ed.), *Mechatronics and Automatic Control Systems*, Lecture Notes in Electrical Engineering 237, DOI 10.1007/978-3-319-01273-5_94,

Recent years, Topological Data Analysis (TDA) methods [6] are being developed for data sets on which the natural structure is not a metric, but rather a partial order [7, 8]. By extracting global geometrical structures from lower dimension expression, this non-parametric approach is proved to be an effective tool for massive data analysis [9]. The primary processes applied in TDA are described as several common steps [10].

To implement TDA methods on the datasets of measured sea-clutter, the transformation from original data to point cloud data (PCD) must be made. The global geometrical features are extracted from PCD and are certain presentation for the original data. The hidden structures and properties consist in the sea-clutter represented as digital form time series.

In real world most systems are doubtless nonlinear and non-stationary systems. A prerequisite for the representation of nonlinear and non-stationary data is to find the adequate adaptive basis. It is advisable to apply TDA methods on sea-clutter, the typical complex system of practical radar clutter environment.

2 Nonlinear Dynamical System Identification

Devote to reconstruct dynamical systems from measured data, system identification can be regard as a general term to provide mathematical tools and algorithms representation. The field of system identification is well developed for linear systems. In fact, all physical systems are nonlinear to an extent and exhibit a variety of complex dynamic behavior, so nonlinear dynamical system identification is of great importance. To deal with the curse of dimensionality and insufficiency of priori knowledge, nonlinear dynamical system identification have to consider efficient method capable of dimension reduction and knowledge discovery, like TDA mentioned above. It is obvious that there is no particular representation of nonlinear systems which can be regarded as the best for all applications, however, it seems that system identification is in many aspects simpler and more convenient to implement.

As is shown in Fig. 1, A general implementation procedure to estimate a nonlinear model can be described as follows:

1. *Select the model structure*
2. *Split the observed data into two parts: an estimation data set and a validation dataset.*
3. *Select the input and output lag spaces nu and ny and the input time delayed.*
4. *Train a number of nonlinear models by using the estimation data set*
5. *For each of these models, use validation data to compute the value of the criterion.*
6. *Select the one which minimizes the fit on the validation data as the final model.*

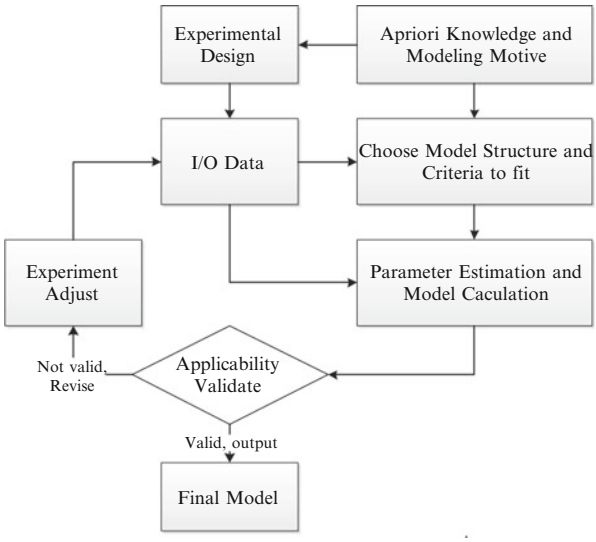

Fig. 1 The common implementation procedure of system identification

3 Topological Features Extraction

Discovering hidden patterns or structures is of significant importance to study complex systems. Actually, the description of pattern or structural knowledge can be classified into many kinds according to the research area and application objective. The topological structure and invariant are what we focused in this work.

Pattern recognition [4] and most related works is about methods of supervised learning and unsupervised learning. Usually, the patterns to be classified are groups of measurements or observations. Data or patterns classification take advantages of priori knowledge, or ulteriorly statistical information, whereas, pattern discovery takes advantages of using domain-specific knowledge, processes the data by reverse-engineering method, and aims to acquire the certain patterns which are able to character the complex system effectively. The patterns include topological structure, topological invariants, and manifold characteristics, et al. (Fig. 2)

As a novel approach of studying the inner structure and sub-structure of complex systems, pattern discovery use less theoretical assumption but provide more practically useful knowledge. It can be considered as the extension of pattern recognition and machine learning. Up to now, the idea of pattern discovery illustrates considerable superiorities through the integration with nonlinear dynamics, dimension reduction, statistical manifolds, and topological analysis.

The classical statistical and non-statistical models based on the amplitude statistics of sea clutter are extensively studied for many years. Topological methods under pattern discovery scheme, which are natural to be applied in this direction, is suitable to see through the instinct complexity by extract structural information and topological invariants, simply because geometry can be regarded as the study of distance functions.

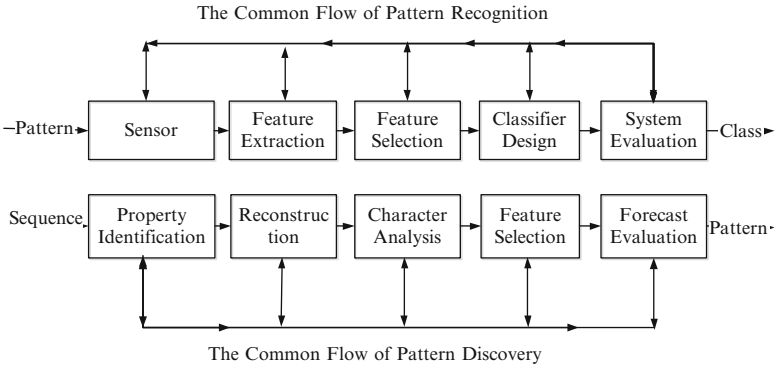

Fig. 2 Pattern discovery and pattern recognition comparison

Currently, the geometrical and topological methods for structural analysis of the data are being pursued in the three allied fields of computer science, mathematics and statistics.

Although each field has their own particular approach and questions of interest, there are still lots of similarities among all three fields. Taking advantages of geometry and topology methods, novel and effective methods could be proposed, among which TDA is a typical tool. In this work, the method based on TDA is implemented by the following steps:

1. Locate the critical points in the dataset
2. De-noise, convenient for the structural pattern extraction
3. According to proximity parameter, replace the data points with a family of indexed simplicial complexes
4. Through algebraic topology and especially persistent homology, analyze topological features
5. In the form of Betti number, get the representation of the persistent homology.

In order to utilize the topological structural patterns in the dynamical system identification, a distance function based on the coherence function could be defined to evaluate the "closeness" of two processes:

$$d(X_i, X_j) \triangleq \left[\frac{1}{T}\int_0^T \left(1 - C_{X_i X_j}(f)\right)\right]^{1/2} \tag{1}$$

Where $C(f)$ is coherence function of the two processes. The topological invariants then provide efficient parameters to evaluate if there exist significant differences between the reconstructed dynamical systems.

4 Experiments and Conclusion

Experimental sea-clutter data used in this work are provided with McMaster University IPIX radar. This radar is located at OHGR, Dartmouth, Canada, on a cliff facing the Atlantic Ocean. It is fully coherent X-band radar with several advanced features [2]: dual-polarized, coherent with an antenna beam width of 1″, built-in calibration equipment, and digital control system.

The antenna of this radar points along with a fixed direction, and the radar works at dwelling mode of operation. Only a piece of the ocean surface is illuminated, and the sea clutter features completely depends on the sea surface's motion modality.

The experimental results are given on the measured sea clutter data of the data set #17 and #18. Experiments on correlative datasets, for instance, #19, #28, #26, #283, #300, and most other datasets, bring similar results and conclusions.

The sea clutter time series can be reconstructed to get a set of vectors which are m-dimensional, and these vectors consist in the reconstructed phase space. To deal with effective structural features extraction in these vectors, Topological Data Analysis methods could be utilized (Fig. 3).

Figure 4 demonstrates the three dimensional phase space portrait of sea clutter datasets #17 and #18. It is notable that the distributions are severely imposed by the target. Based on these distribution patterns, the topological structures could be acquired by implementing dimension reduction methods and topological transformations.

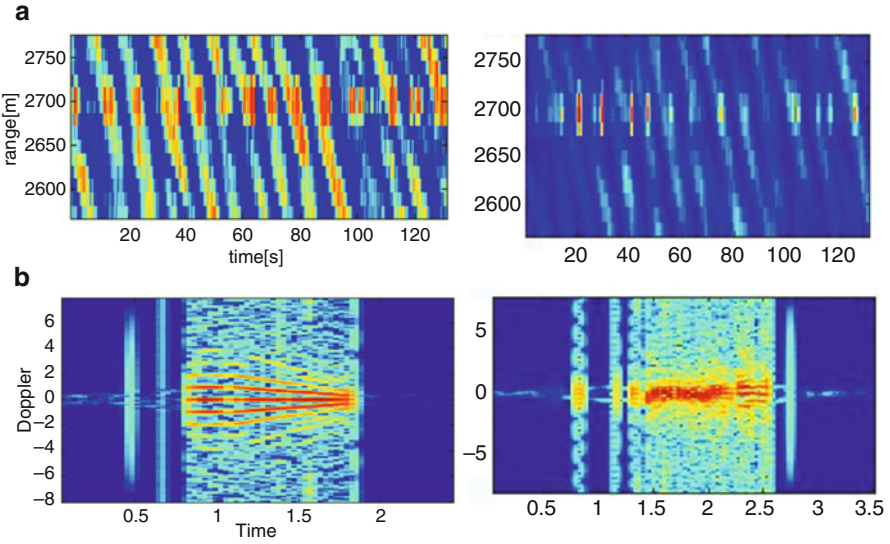

Fig. 3 The sea-clutter data of #17(*left*) and #18(*right*): (**a**) range profiles; (**b**) range bin 9 time-doppler imaging

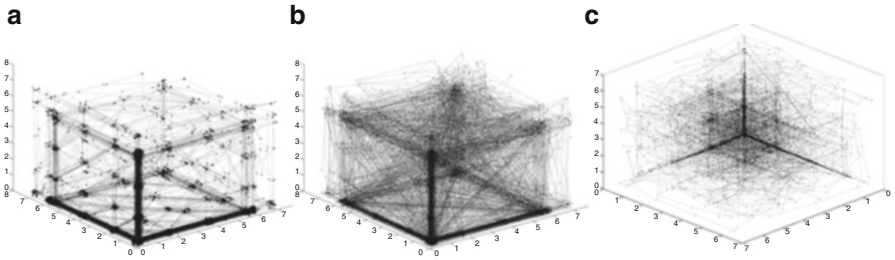

Fig. 4 (**a**) #17 No.14 bin 3-D phase space portrait of sea clutter data set; (**b**) #17 No.9 bin 3-D phase space portrait of sea clutter data set (**c**) #18 No.5 bin 3-D phase space portrait of sea clutter data set

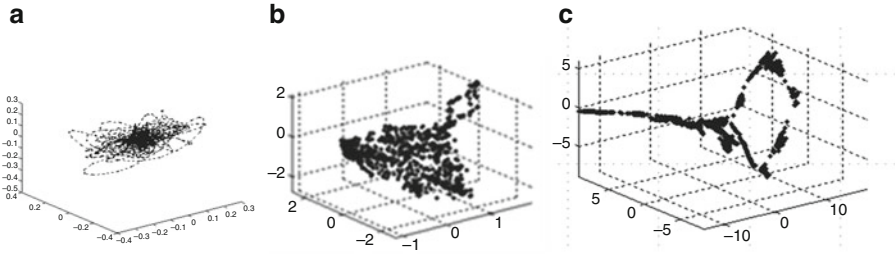

Fig 5 (**a**) #17 No.14 bin phase space topological structures; (**b**) #17 No.9 bin phase space topological structures; (**c**) phase space structural features simplified by TDA

As is shown in Fig. 5a, b and more obvious in Fig. 5c, the No. 9 range bin which contains the marine target illustrates a prominent topological structure compared with the other range bins. Furthermore, the topological structural patterns can be utilized in nonlinear dynamical system identification.

Knowledge discovery and system identification on sea clutter, which are typically massive, high-dimensional and multivariable, are undoubtedly valuable as well as full of challenge. A nonlinear dynamical system identification scheme based on the topological pattern discovery was proposed in this work, aiming to provide useful knowledge for corresponding complex sea clutter modeling and addressing analysis problem. Through the method proposed in this work, the target detection performance in the sea clutter can be improved significantly. Based on the dynamical system identification scheme and topological data analysis techniques, the method may help find ways through complex sea clutter data. Experiments with measured sea-clutter data demonstrate the performance of the method proposed in this work.

References

1. Xie N, Leung H, Chan H (2003) A multiple-model prediction approach for sea clutter modelling. IEEE Trans Geosci Remote Sensing 41:1491–1502
2. Haykin S, Bakker R, Currie BW (2002) Uncovering nonlinear dynamics-the case study of sea clutter. Proc IEEE 90:860–881
3. Totir F et al (2008) Advanced sea clutter models and their usefulness for target detection. MTA Rev Xviii(3):1–17
4. Duda RO, Hart PE, Stork DG (2001) Pattern classification, 2nd edn. Wiley, New York. ISBN 0-471-05669-3
5. Goodwin GC, Payne RL (1977) Dynamic system identification: experiment design and data analysis. Academic, New York, pp 171–172
6. Collins A, Zomorodian A, Carlsson G, Guibas L (2004) A barcode shape descriptor for curve point cloud data, eurographics symposium on point-based graphics, vol 28. Zürich, pp 881–894
7. Edelsbrunner H, Letscher D, Zomorodian A (2000) Topological persistence and simplification. FOCS ’00 Proceedings of the 41st Annual Symposium on Foundations of Computer Science, IEEE Computer Society, Washington DC, USA, pp 454–463
8. Yao Y, Sun J, Huang X et al (2009) Topological methods for exploring low-density states in biomolecular folding pathways[J]. The Journal of chemical physics 130:144115
9. Robins V, Abernethy J, Rooney N (2003) Topology and intelligent data analysis. Springer, Berlin/Heidelberg, pp 111–122
10. Group S, Carlsson G (2009) Topology and data. Bull Am Math Soc 46(2):255–308

Field Programmable Gate Array Configuration Monitoring Technology for Space-Based Systems

Longxu Jin, Jin Li, and Yinan Wu

Abstract In order to solve the problem of field programmable gate array (FPGA) configuration failure after the Satellite TDI CCD camera power-up, a FPGA configuration process monitoring system was designed. First, this paper describes the core monitoring circuit in the FPGA configuration monitoring system. Then the design ideas of software are proposed for the monitoring system. Finally, the experiments were performed in the monitoring system. Experiment results showed that the proposed FPGA configuration monitoring system can timely monitor exception occurred in FPGA configuration process and can analyze the error origins and can configure successfully the FPGA applications. The FPGA configuration successful rate reaches 98.2 % after using this system. The monitor system can improve the reliability of FPGA configuration and solve the problem of FPGA configuration failure.

Keywords Space camera • Field programmable gate array configuration • Monitor state machine

1 Introduction

The Field Programmable Gate Array (FPGA) devices based on SRAM have been widely used in the Satellite TDI CCD camera these days [1, 2]. They are volatile devices- they do not retain their configuration when power is removed [3]. To ensure a FPGA system operating properly, people must reinitialize the CCLs inside the device each time power is cycled, that is the ICR (In-Circuit Re-configurability) [4, 5]. However, configuration failure often occurs in the current space and aviation FPGA system. Once FPGA configuration failure occurred, people have to make the

L. Jin (✉) • J. Li • Y. Wu
Changchun Institute of Optics, Fine Mechanics and Physics, Chinese Academy of Sciences, Changchun, China
e-mail: 1458312813@126.com

W. Wang (ed.), *Mechatronics and Automatic Control Systems*, Lecture Notes in Electrical Engineering 237, DOI 10.1007/978-3-319-01273-5_95,

Satellite TDI CCD camera system re-power up. Under the satellite environment, the power-up operation is very trouble in the Satellite TDI CCD camera [6].

To ensure Satellite TDI CCD camera operating properly under the satellite environment, the traditional design method overcoming FPGA configuration failure is watchdog technology. When the power-off controller discovers a watchdog alarming, the power-off controller makes the camera power up again. This method need to design a dedicated power-off controller, watchdog monitor and a separate power supply system. And it has brought a lot of trouble in the Satellite TDI CCD camera design. So it is necessary that a FPGA configuration process monitoring system was designed in the FPGA module. On the one hand, the new design does not require additional power supply system, watchdog monitor and the controller that controls the Satellite CCD camera power-off; On the other hand, when the Satellite TDI CCD Camera after a one-time power-up, FPGA configuration is successful. And the FPGA system runs at normal state. Meanwhile, the monitoring system can make FPGA reconfigure successfully a bit-stream again when it is notified to reconfigure a bit-stream by FPGA. In addition, the monitoring system can analyze and monitor the FPGA configuration process. Once a FPGA configuration fault is detected by the monitoring system, the reconfiguration process begins during the Satellite TDI CCD Camera power up.

Take Xilinx's Virtex-IIPro family FPGA as an example, A FPGA configuration process monitoring system was designed in this paper. And the external system was designed to verify the feasibility and superiority of the new design method. The design can satisfy the Satellite TDI CCD camera requirements of high success rate and reliability in configuring the FPGA application, and improve the success rate of the FPGA configuration.

2 The Scheme of FPGA Configuration Monitoring System

Figure 1 illustrates the total block diagram of FPGA configuration monitoring system. The system contains a FPGA sub-system, power-off subsystem, communication module, and data transmission subsystem and host computer. The FPGA subsystem is mainly composed of two circuits which contain two same FPGA and FLASH devices. One has the FPGA configuration monitoring circuit, the other don't have the circuit. The two Flash devices separately load the configuration data into the corresponding SRAM-based FPGA devices after power-up when the Power-off subsystem has operated. If a FPGA configuration failure occurs, the FPGA sub-system sent configuration failure information to the communication module. And according to an instruction receiving, communication module issues a corresponding command to the power-off system, and the power-off system disconnects the power of the FPGA device configuration failure. In addition, the FPGA configuration information is transmitted by the communication module, and is stored in the host computer. After the FPGA configuration successful, application displays in the host computer through the data transmission module. If the two

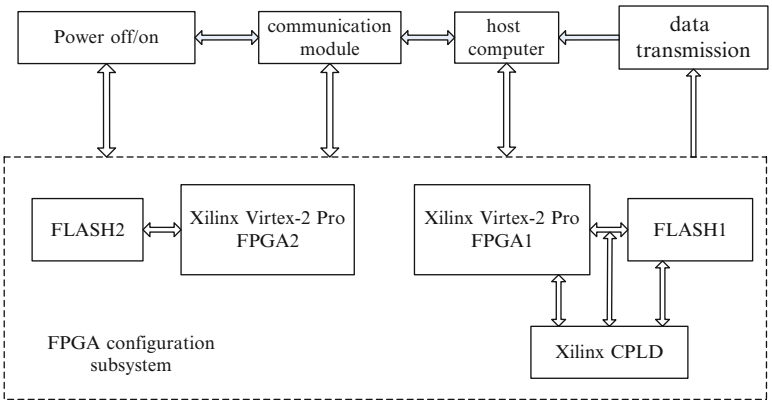

Fig. 1 Block diagram of configuration monitoring system

FPGA devices can successfully configure a bit-stream file, the power-off system is notified by the communication module, and the whole system starts the next configuration experiment. The host computer can inject the number of configuration experiments parameters into the communication module. The FPGA configuration process monitoring is completed by a CPLD device.

3 The Hardware Circuit and Soft Design of FPGA Configuration Monitoring System

The FPGA configuration monitoring system design is used for verifying feasibility and superiority of the monitoring circuit in FPGA configuration process. Therefore, the core of the FPGA configuration system is monitoring circuit. In order to monitor entire FPGA configuration process and real-timely reflect configuration information, data re-configuration is needed under power-up situation when configuration failure happens. As the result, circuit design requirements are:

1. The device used for monitoring FPGA configuration process should guarantee its configuration data won't lose when powered off. And it can quickly and reliably enter operation state at every power-up.
2. In order to real-timely monitor FPGA configuration process, FPGA, configuration memory and monitoring process need to work in the same clock.
3. FPGA, configuration memory and monitoring process should be in the same scan chain.

Figure 2 is a concise circuit diagram which is used for monitoring FPGA configuration process. XC2VP40-6FG676 chip produced by Xilinx has powerful processing property. It is selected as FPGA of this circuit. XCF16P-VQ44C produced by Xilinx is selected as configuration memory and XC2C64A chip in

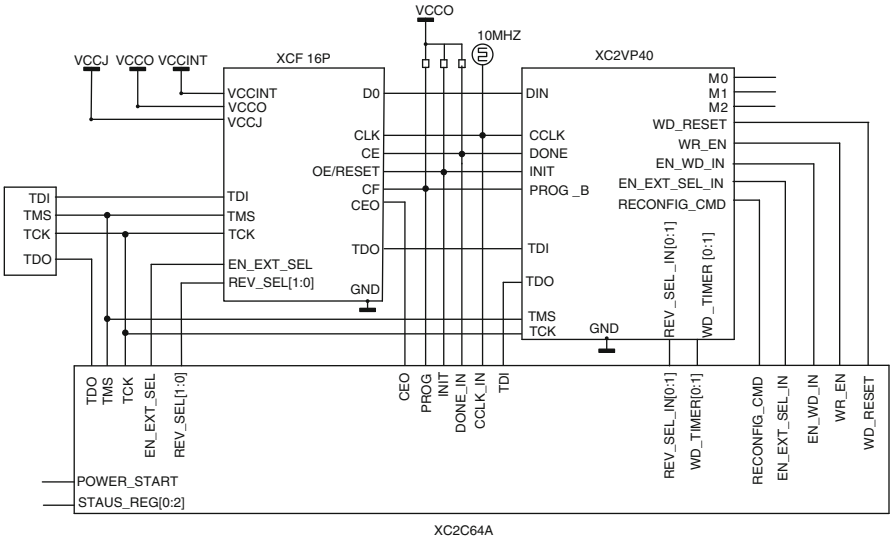

Fig. 2 FPGA configuration monitoring circuit

CoolRuner-II family produced by Xilinx is selected as monitor CPLD. XC2C64A chip is non-volatile device [7], so configuration memory is not needed and configuration data won't lose when powered off. The three devices in configuration monitor circuit are in the same scan chain and the configuration data are accordingly downloaded to chips by the same JTAG. In order that configuration clock and monitor operate in the same clock, slave serial configuration mode must be selected in FPGA and FLASH. As the processor which monitors FPGA configuration process, CPLD is used to control storage location of the FPGA bit-stream in FLASH, monitor configuration process, analyze failure reasons, re-configure configuration data when a configuration failure occurs, re-configure configuration data when FPGA re-configuration order is received and monitor whether the FPGA user program operating normally and so on. Furthermore, the method has been used for the FPGA configuration monitor soft [8].

4 Experiment Studying

Figure 3 illustrates tested simulation results which contain Configuration passing, CRC checksum failure, Missing synchronization word and watchdog alarm through Xilinx ISE 10.1 software. From the Fig. 3, a conclusion that the monitor state machine can handle various configuration failure problems during the FPGA configuration process can be drawn. When the state machine detecting configuration failure, it enables FPGA to reconfigure data until the configuration data is

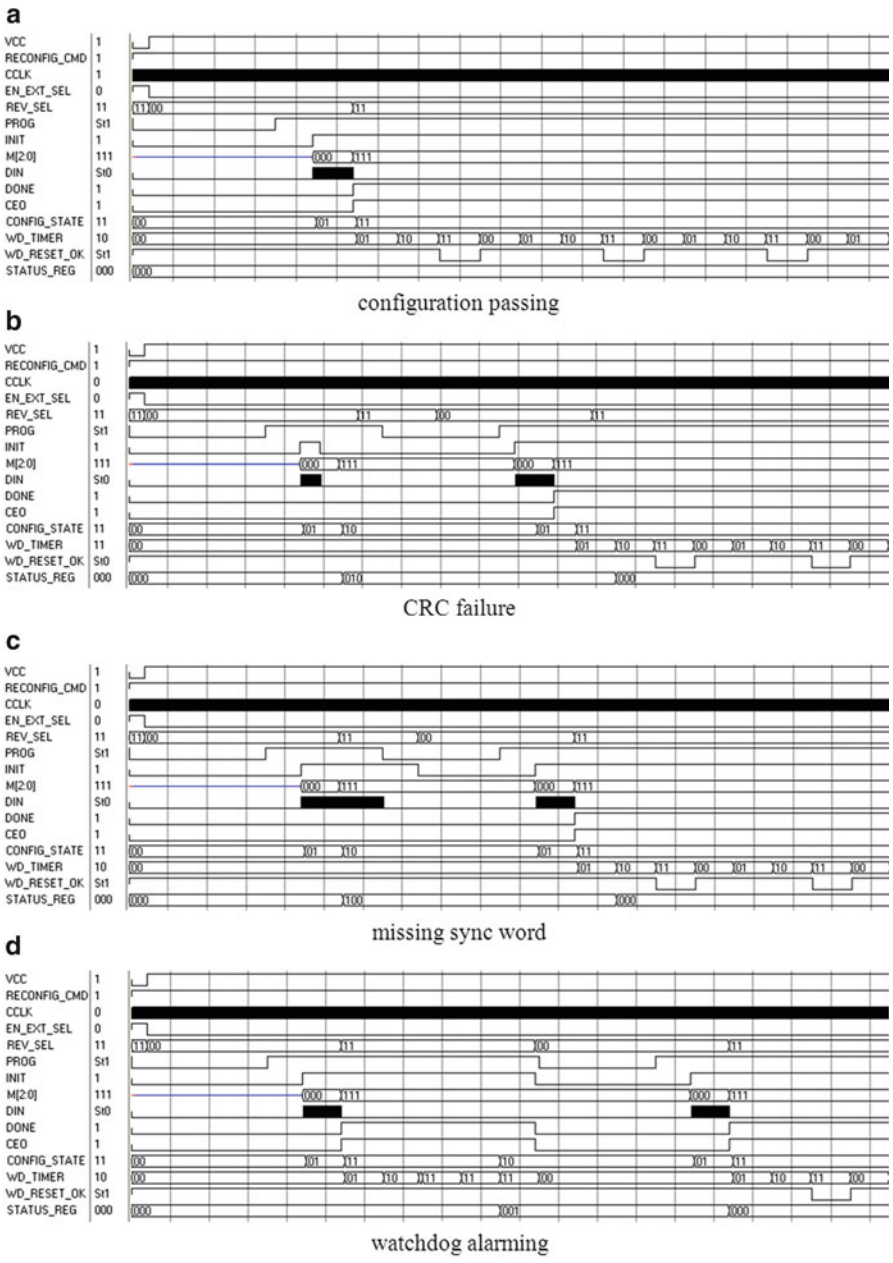

Fig. 3 Diagram of state machine simulation (**a**) configuration passing (**b**) CRC failure (**c**) missing sync word (**d**) watchdog alarming

Table 1 Statistics of configuration failure times per 100 times with different boards

Board number	Un-using monitor system	Using monitor system
1	3	1
2	7	0
3	0	0
4	9	2
5	2	0
6	7	3
7	4	1
8	8	2
9	5	2

successfully configured. At the same time, configuration registers can accurately reflect the results of the entire configuration process.

Up to now, the simulation result indicates that the design mentioned in this paper is correct. Then after FPGA configuration monitoring system designed power-up, PC computer through Xilinx ISE 10.1 software makes IMPACT software and circuit board communication. And the software scans the devices on circuit board, can find XC2VP40, XC2C64A, XCF16P in the same scan chain. In the same chain, different formats application can be downloaded into the corresponding device. Meanwhile, after the host computer injecting parameters into the power-off system, FPGA configuration experiment begin, and the configuration information is recorded. The experimental results show that the configuration causes from the actual device operation consistent with that shown Fig. 3. This shows the design mentioned in the paper is feasibility. We test the performance of configuration of nine blocks of circuit board. The test results are shown in Table 1 using the monitoring system and Table 1 un-using the monitoring system. The experimental data is analyzed by a binomial distribution formula. The formula is

$$f_X(x) = P[X = k] = \frac{n!}{k!(n-k)!} p^k (1-p)^{n-k} \tag{1}$$

where n is the total number of configuration test, p is the probability of configuration passing, 1-p is the probability of configuration failure, x is the number of configuration passing in n configuration tests. From the Eq. 1, the experimental data were processed using MATLAB. The result processed shows that the configuration failure rate using traditional FPGA configuration method is 5 %, while 1.2 % using the monitoring system. This shows the new design greatly improves the configuration success rate, which reaches 98.8 %. This shows the new design greatly improves the configuration success rate, and fully is able to meet the requirements of Satellite TDI CCD cameras.

Table 2 Statistics of configuration failure average times per 100 times with different configuration rate

Configuration rate/MHz	Un-using monitor system	Using monitor system
1	0	0
5	1	0
10	1	0
15	3	0
20	4	0
25	7	1
30	7	1
35	9	2
40	10	2
45	12	2
50	13	3
55	16	3

In addition, the author tests the performance of configuration of nine blocks of circuit board at different configuration rate using the method proposed by this paper when working temperature is +20 °C. The test results are shown in Table 2. From Table 2, the probability of FPGA configuration success is 98 % under configuration rate low 40 MHz, which is the requirement of space camera. Therefore, the method proposed by this paper meets fully the application of space camera.

5 Conclusion

Based on the TDI CCD cameras requirements of the high success rate and reliability of FPGA configuration, the FPGA configuration monitoring system mentioned in the paper was designed. The feasibility and superiority of the system designed was verified through tens of thousands of test. The results show that, FPGA configuration monitoring system can overcome a variety of failure problems in the FPGA configuration process in practice; the FPGA configuration successful rate is up to 98.2 % after using this system. Compared with the traditional methods of FPGA configuration, the new design made configuration success rate to increase by 3.8 %. It can satisfy the satellite camera requirements of high success rate and reliability in configuring the FPGA application.

References

1. Li Jin, Jin Longxu et al (2012) Application of ADV212 to the large field of view multispectral TDICCD space camera. Spectrosc Spect Anal 32(6):1700–1707
2. Li Jin, Jin Longxu et al (2012) Reliability of space image recorder based on NAND flash memory. Opt Prec Eng 20(5):1090–1101

3. Cheng Ming, Bi Liheng, Yang Xiaoguang (2007) Using CPLD and flash memory to configure FPGA. Control Autom 23(20):171–173
4. Zhou Wei, He Jianying, Nie Jugeng (2006) Implementation of the programming and configuring of CPLD and FPGA. Comput Digit Eng 34(1):100–102
5. Mao Jianhui, Hei Yong Wu, Qiao Shushan (2008) A of new scheme of multi-mode configuring FPGA devices. Microcomput Info 24(2):179–181
6. Li Jin, Lv Zengming et al (2012) Error correction technology for CCD image using high speed optical fiber transmission. Optics Precis Eng 20(11):2549–2558
7. Li Yamchun (2008) Fast dynamic reconfiguratuion of FPGA based on CPLD. Telecommun Eng 48(7):87–89
8. Li Jin, Li Guoning et al (2010) Design of FPGA configuration monitoring system. Chin J Liq Cryst Disp 25(6):851–857

HVS-Inspired, Parallel, and Hierarchical Traffic Scene Classification Framework

Wengang Feng

Abstract In order to quickly, accurately, and efficiently classify traffic scene based on the image semantics, a bionic, parallel, and hierarchical scene classification framework is presented in this paper. Based on the perception as defined by the human visual system (HVS), the model is built. At first, an image pyramid was used to present both the global scene and local patches containing specific objects. Secondly, codebooks were built, which satisfy both long stare and short saccade similar to those of humans. Next, the visual words by generative and discriminative methods were trained respectively, which obtain the initial scene categories based on the potential semantics using the bag-of-words model. Then, a neural network was used to simulate a human decision process. This led to the final scene category. Experiments showed that the parallel, hierarchical image representation and classification model obtained superior results in terms of accuracy.

Keywords Image pyramid • Visual codebook • Generative method • Discriminative method • Neural network

1 Introduction

Scene classification [1–3] plays an important role in efficient image resource management and automatic image classification and is very important in computer vision and pattern recognition domain as well as content-based retrieval. The goal of a computer vision system is to build a model of the real world that allows a user

W. Feng (✉)
Police Intelligence Department, Public Security Intelligence Research Center, Chinese People's Public Security University, Beijing, China
e-mail: wengang.feng@gmail.com

W. Wang (ed.), *Mechatronics and Automatic Control Systems*, Lecture Notes in Electrical Engineering 237, DOI 10.1007/978-3-319-01273-5_96,

to interact with it. The ultimate goal is to allow a computer to "see" the world in a manner similar to the biological visual system. First it must build the framework then realize cognition and inference. The goal of this research is to allow images to be quickly, accurately, and efficiently classified based on the image semantics.

In cognitive theory [4], the majority of research on scene classification has focused on the roles of either low level visual feature cues or high-level factors such as object-, semantic-level cues, or behavioral task demands. However, the latest research in cognitive neuroscience found the partial separation scanning the global scene relocate to new areas, as well as evidence to support the existence of small amplitude, the importance of "correct" image browser glanced natural cycle. So both global features and local features are good visual feature candidates for targets on which the eyes fixate. They should be used together for scene modeling, in a parallel fashion.

The perception in the human visual system follows a hierarchical model in which the information of scale space is not changed by altering the scale [5]. Humans can recognize one scene in a very short time because they have a large and complex scene dataset in the brain. The model needed to classify a scene has been trained sufficiently to fit most situations. Based on cognitive neuroscience, we propose a novel parallel, hierarchical scene classification framework that has superior results for scene recognition.

2 Traffic Scene Classification Framework

In the training step, there are five stages: First, each one image will be presented as 21 images (patches) in three layers using an image pyramid. Second, we will build codebooks, and third, each visual word extracted from one image patch is trained in a generative way using pLSA model. Each training patch is then represented by z-vectors ($p(z|d)$) where z is a topic and d is an image. Fourth, the z-vectors obtained from last step are subjected to discriminative training. Finally, we use neural network to get the final classification category on the 21 patches scene categories. The approach simulates human's decision process based on local and global visual perception.

The test step also proceeds in five stages. The difference is that the test image is projected onto the learning during the training period by the vector spanned simplex. This is used in learning the expectation maximization (EM) to run in a similar manner, but now, only in the z vector updating steps with other learned vector fixed in each of M step. As a result, the test image is represented by the z-vector. Then test the multi-class image classification discriminant classification (Fig. 1).

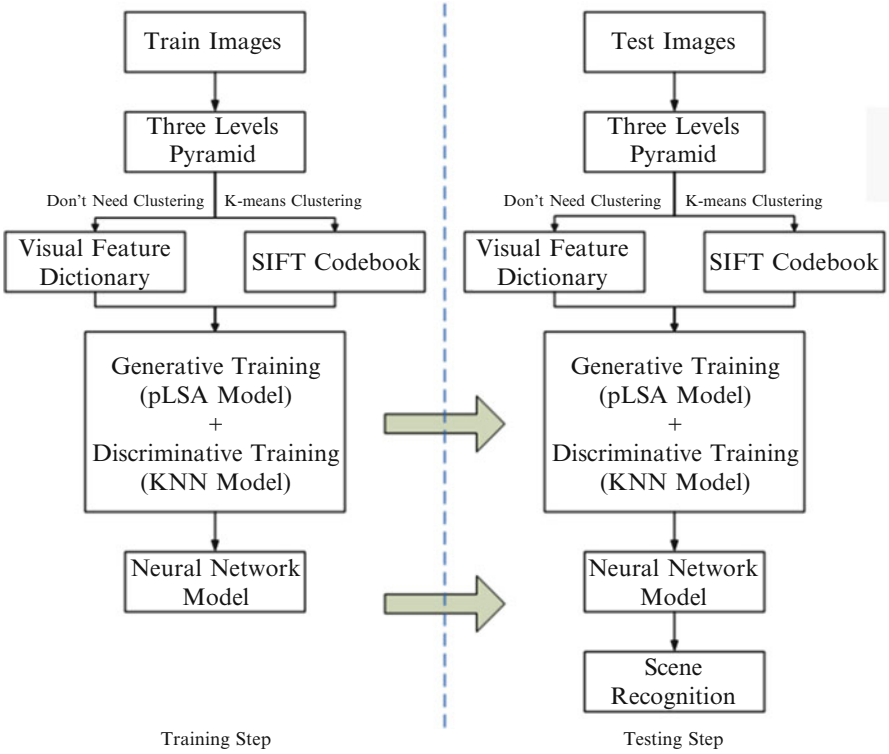

Fig. 1 Flowchart of the algorithm

2.1 Image Pyramid

On the basis, the image is further divided into a planar sequence, $I_k = \{I_i^k\}_{i=1}^{4^{k+1}}$, where I_i^k is the image content of the subscript area R_i^k in the image I.

$$I_i^k = \left\{I_{x,y}, (x,y) \in R_i^k\right\}_{i=1}^{4^{k+1}} \tag{1}$$

Where R is the subscript matrix of the image I, and R_i^k is the subscript set of the i-th patch of the k-th layer in the pyramid. Here we use three layers as shown in Fig. 2: (Where (X, Y) is the pixel resolution of image I.)

$$R = \left\{R_i^k\right\}_{i=1}^{4^{k+1}}, R = \{(x,y)|x = 1,\ldots,X, y = 1,\ldots,Y\} \tag{2}$$

Here we use a three-layer pyramid: The first layer is the original image; the second layer has four grids, which means each patch is a quarter of the original image; the last layer has 16 grids, which is one sixteenth of the original image.

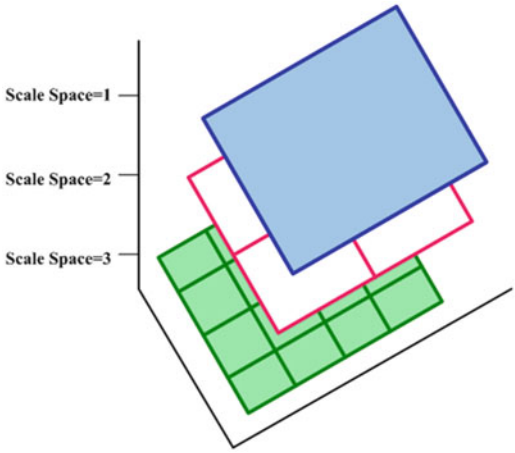

Fig. 2 Image scale space

2.2 *Feature Extraction*

In the framework, first an input image is separated into three layers and 21 patches by an image pyramid. We treat each patch from the original image as one independent image. For each patch we extract two types of features to build codebooks used in the experiments of Sect. 4. First, we have the so-called "clustering codebook," which are SIFT [6] (scale- invariant feature transformer) features. The SIFT feature is highly distinctive, shown to provide robust property of affine distortion, image scale and rotation, in the three-dimensional views of the changes, noise, and lighting changes.

We also use a non-clustering codebook combination of color, texture, and fractal characteristics. The description of all colors can be extracted image or image region. The structure of the color distribution and spatial color structure histogram. Texture descriptors can extract the image or image area. There are five common texture descriptors: left, right, upper, lower, and the internal boundary of the texture histogram, which describes the spatial distribution of the image of the local structure. Complex and irregular fractal dimension can be represented by the image, we can use the histogram of the global and the local fractal dimension.

2.3 *Generative Model Training*

Probabilistic Latent Semantic Analysis (pLSA) is a generative model from statistical text literature [7]. The model is applied to images by using a visual analog of words, formed by clustering and non-clustering codebooks (as described in Sect. 2.2). pLSA is appropriate here because it provides a correct statistical model for clustering in the case of multiple object categories per image.

In detail, each image is modeled as a mixture of Z topics, and each topic is a distribution over the vocabulary of words. More formally, we have a set of images

$D = d_1, \ldots, d_N$, each modeled as a histogram of word counts over a vocabulary of $W = w_1, \ldots w_V$. The corpus of images is represented by a co-occurrence matrix of size $V \times N$, with entry $n(w, d)$ listing the number of times the words w occurred in an image d. Image d has N_d words in total.

The key values used or obtained from training via pLSA are probabilities. $p(d_j)$ denotes the probability of observing a particular image d_j. $p(w_i|z_k)$ signifies the probability of a specific word conditioned on the unobserved topic variable z_k. Finally, $p(z_k|d_j)$ expresses an image specific probability distribution over the latent variable space. Based on these, we can express the specific pLSA model for the problem. First, an image d_j is selected with the probability $p(d_j)$; second, a latent topic z_k is picked with the probability $p(z_k|d_j)$; finally, a word w_i is generated with the probability $p(w_i|z_k)$. It is the probability of the latent variable, $p(w_i|z_k)$, for which we must solve.

$$p(w, d) = \sum_{z=1}^{Z} p(w, d, z) = \sum_{z=1}^{Z} p(d)p(w|z)p(z|d) \tag{3}$$

2.4 Discriminative Model Training

For a discriminative model, one needs only the conditional probabilities of the target labels, $p(z|d)$. For each patch, we now have a vector for each image whose cardinality equals the number of the topics, $\langle p(z_1|d), p(z_2|d), \ldots, p(z_n|d)\rangle$. Two discriminative models are used, one to obtain the best estimate of the label (and its probability) for each patch and one to obtain the best label for the overall scene.

To obtain the single-estimate probability and label for one patch we use KNN over an R^2 -space, in which the training set is embedded, KNN where $k = 7$ is used to select the best label. The probability is estimated as the average probability over neighbors having similar labels. The probability is used in the next step.

2.5 Neural Network Model Training

Radial basis function (RBF) networks [7] typically have three layers: an input layer, a hidden layer, and a linear output layer. The hidden layer consists embeds an RBF activation function, each having stronger responses when the N inputs are nearer the mean. The output, y, is a weighted sum of the hidden neurons,

$$y = \sum_{i=1}^{S} \alpha_i \rho(\|x - c_i\|) \tag{4}$$

Where S is the number of neurons in the hidden layer, c_i is the center vector of neuron i, α_i are the weights of the neuron, and β_i is the response of hidden neuron:

$$\rho(\|x - c_i\|) = \exp\left[-\beta_i \|x - c_i\|^2\right] \tag{5}$$

Here, we set the initial value of weights, i, but in the training, all weights are changed to optimum values. The norm is taken to be the Euclidean distance.

The number of inputs, N, is 21 – one for each patch. The value of the input is the value $p(z|w, d)$ instantiated by the KNN step described earlier. There is one output, y, from which a Z-way decision is extracted by Z − 1 thresholds.

3 Experiments

In this section, we present the traffic scene classification results of our approach, and comparing it with pLSA model [7]. Our set of experiments was divided into three scene categorical datasets. The first one involved day-time, night-time, and twilight-time. The second one included fog, rain, snow, and sunny traffic scenes. And the last one was to consisted of free-flow, light-congestion and heavy congestion traffic scenes. This database contained 200 images per category. The images were of medium resolution, i.e., about 500 × 330 pixels.

Why does the proposed framework obtain the more accurate results? As opposed contrast to pLSA model, the proposed framework uses the image pyramid to connect the global and local semantic information, and get better choice depending on the discriminative model. Simultaneously comparing with the image pyramid-SVM model, the proposed frame work has generative model training. Besides such advantages, choosing the different visual words and using neural network upgrade the performance of the proposed framework.

We investigated three aspects: the visual found (1) locally extracted from the image measurement functions, ranging from the number 40–100,000. Constant descriptor records, canceled unexpected lighting, viewpoint or scale differences. To capture the complexity of the world, we extracted descriptors including texture, spirit, SIFT and color, in of visual global and local, then extract the image and patch within each pyramid. (2) visual vocabulary of semantics – this is not verbal, but the gradient image of a general description of a detail, the patch every word every place. We only summarize the most significant points, wherein semantic scene category learned set of images corresponds to, and then using the determined object class, and (3) the model into a semantic concept of visual words. In fact, it is assigned a probability at the same time all the concepts. These possibilities are used to rank the concept of existing image (Fig. 3).

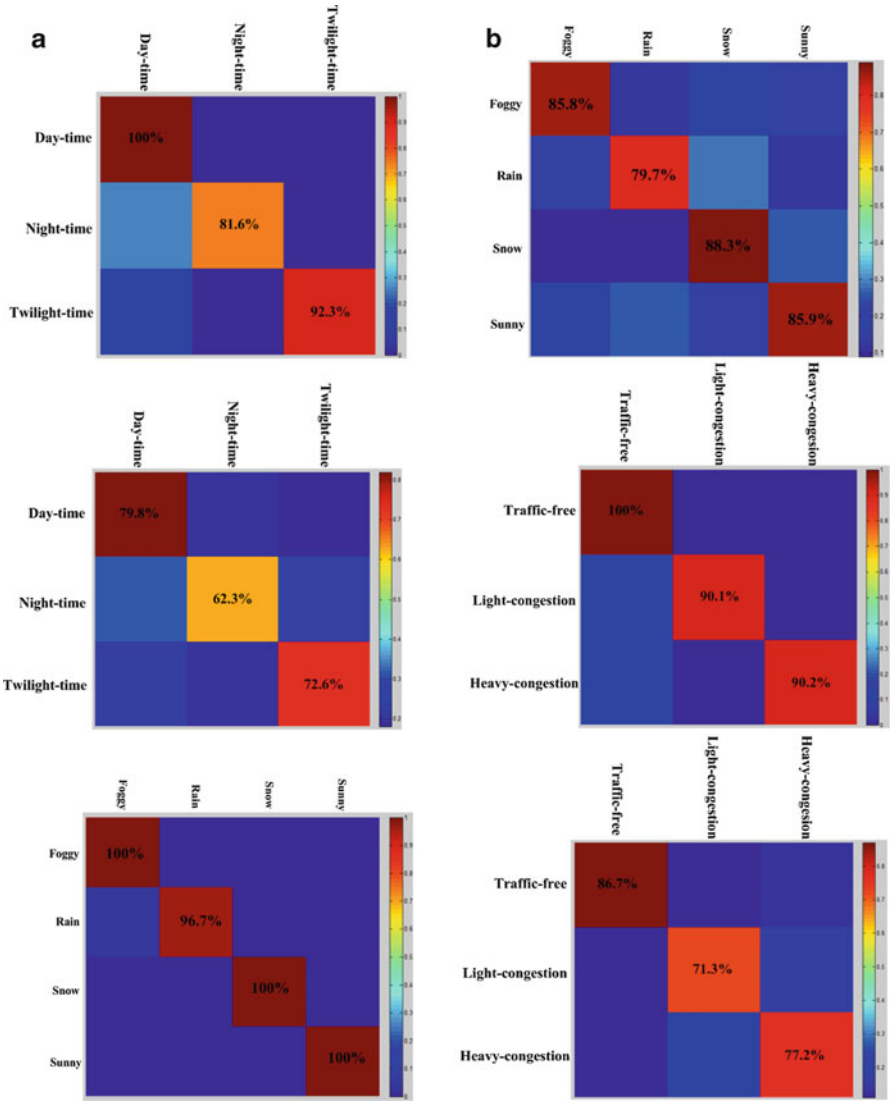

Fig. 3 Confusion matrix for traffic scene categories, (**a**) the result of our method; (**b**) the result of the baseline pLSA method

4 Conclusion

This paper proposed an HSV-inspired, parallel, hierarchical traffic scene classification framework, which can recognize the traffic scene category, enabling it to be possible that the most efficient vehicle tracking can be automatically selected and traffic surveillance algorithms for the conditions can be obtained. The model is able

to obtain semantic information from global and local manners despite using coarse features. The image pyramid was used to acquire the information at scales to emulate human perception. This study also built different codebooks to simulate long stare and short saccade to imitate human vision. Besides, generative method, discriminative method, and neural network were used here to train the visual words to get the semantic information from images to simulate human beings visual system. Finally a traffic scene classification result depending on the generic framework could be obtained as well.

References

1. Lazebnik S, Schmid C, Ponce J (2006) Beyond bags of features: spatial pyramid matching for recognizing natural scene categories. In: Proceedings of the IEEE conference on computer vision and pattern recognition, New York, USA, pp 1–8
2. Rasiwasia N, Vasconcelos N (2009) Holistic context modeling using semantic co-occurrences. In: Proceedings of the IEEE conference on computer vision and pattern recognition, Miami, USA, pp 1–7
3. Malisiewicz T, Efros AA (2008) Recognition by association via learning per-exemplar distances. In: Proceeding of the IEEE conference on computer vision and pattern recognition, Anchorage, USA, pp 1–8
4. Torralba A, Sinha P (2001) Recognizing indoor scenes. Technical report, Boston, MIT AI lab
5. Siagian C, Itti L (2007) Rapid biologically-inspired scene classification using features shared with visual attention. IEEE Trans pattern anal mach learn 29(2):300–312
6. Agarwal A, Triggs B (2008) Multilevel image coding with hyperfeatures. Int J Comput Vis 78(2):15–27
7. Haykin S (1994) Neural networks. Prentice-Hall, Upper Saddle River

Analysis and Application on Reactive Power Compensation Online Monitoring System of 10 kV Power Distribution Network

Yan-jun Shen and Jin-liang Jiang

Abstract Data shows that the reactive power compensation devices break down frequently in 10 kV power distribution network. But the failure cannot be discovered in a short time, so lots of manpower and resources are wasted. This paper proposes one method which uses the JST-C20 series Low-voltage Intelligent Capacitors to solve the problem and formulates the reactive power optimization plan for several typical lines based on the reactive power compensation optimization computation. Finally, the article analyzed the validity of this method on voltage quality improvement, energy saving, on-line monitoring and fault diagnosis.

Keywords Low-voltage intelligent capacitor • Reactive power compensation • Online monitoring system • Fault diagnosis

1 Introduction

Lots of manpower and resources has been put into the routine line patrol work in Jiangmen Power Supply Bureau. They discovered the high failure rate of the dynamic reactive power compensation devices and controllers, such as the abnormal phenomenon when the capacitors are using or exiting, the burning events of the capacitors and so on. It leads to that the operational state of the device cannot be uploaded to the main station, and the flowing of information cannot be realized. Now, the reactive power compensation devices belong to Jiangmen Power Supply Bureau is lack of the function of online monitoring and fault diagnosing. Because of the large amount of the compensation points, the failure capacitors cannot be

Y.-j. Shen (✉)
School of Electric Power, South China University of Technology, Guangzhou, China
e-mail: syjzb.2007@163.com

J.-l. Jiang
School of Business Administration, South China University of Technology, Guangzhou, China

W. Wang (ed.), *Mechatronics and Automatic Control Systems*, Lecture Notes in Electrical Engineering 237, DOI 10.1007/978-3-319-01273-5_97,

repaired timely. It is not only harmful to the user's normal using of electricity and the quality service of Jiangmen Power Supply Bureau, but also is a waste of the manpower and resources [1, 2].

Therefore, it is a useful method to use a new generation of intelligent low voltage reactive power compensation device which can achieve the following functions, including reactive power compensation, on-line monitoring, fault diagnosis, alarming and other functions to solve the problem discovered in Jiangme Power Supply Bureau.

2 Introduction of the Advanced Low-Voltage Intelligent Capacitor

The reactive power compensation device selected in the paper is a new generation of intelligent product which is based on power measuring technology, computer technology and modern mobile communication technology. It meets the need of the network users of the Power Supply Bureau at the county level. The Low-voltage Intelligent Capacitor consists of a CPU control unit, thyristor composite switch, protector, two (△ type) or one (Y type) low self-healing power capacitors [3]. It uses the advanced GPRS/CDMA public wireless communication technology to achieve the function of reactive power compensation, on-line monitoring and fault diagnosis. The system of the low-voltage intelligent capacitor can be divided into three layers, including the layer of terminal equipment, layer of communication network, layer of the main station, shown in Fig. 1.

1. The terminal device layer which is installed in the distribution room includes intelligent capacitors and the communication management unit. When it is compensating the reactive power, it can also collect the information and monitor the device's operational state, record and analyze the operating data and movement time. Most importantly, it can send out alarming signal and store the running information when the equipment works in an abnormal condition.

   The communication management unit has the function of the communicating, managing and storing. It connects the intelligent capacitor with the GPRS network, and stores the operating information at the same time.
2. Communications network layer is not only the GPRS public network, but also is the bridge between the main station and terminal equipment. It transmits the information of the terminal equipment to the main station, and issues the control commands of the main station to the terminal equipment.
3. The main station is mainly responsible for dealing with the data and alarming information coming from the terminal device layer, and dealing with the historical data, issuing various types of control commands to the terminal device layer.

Following are the details of the three major functions of the low-voltage intelligent capacitor.

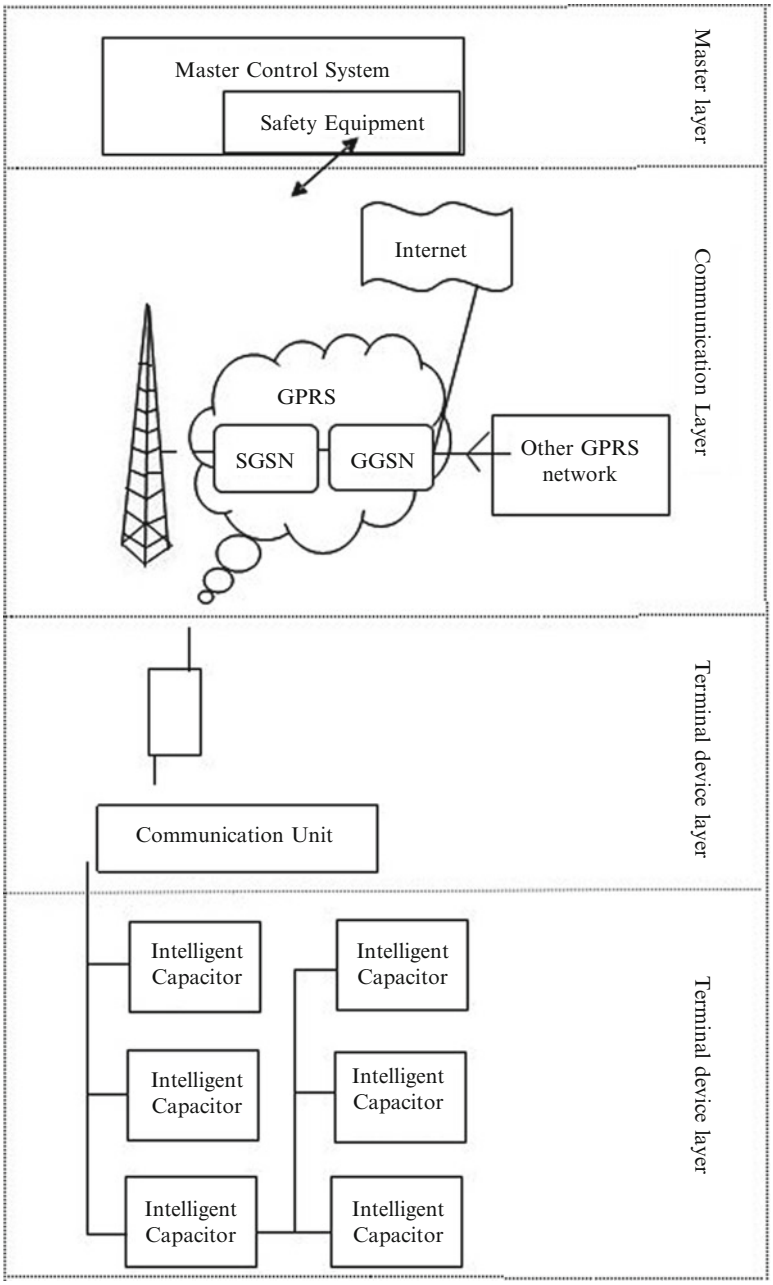

Fig. 1 System architecture of low-voltage intelligent capacitor

2.1 Reactive Power Compensation Function

The low-voltage intelligent capacitor calculates the system's voltage, current, active power, reactive power and power factor according to the three-phase voltage and three-phase current of the system. It can also make the decision to input or quit the capacitors so as to realize real-time reactive power compensation function based on the reactive power and power factor. Following are the characteristics [4]:

1. The switching switch is composed by relay, zero trigger turn-on circuit; thyristor protection circuit. It can reach the purpose of inputting capacitors when the voltage is zero and quitting the capacitors when the current is zero.
2. The power switch has the characteristics of responding quickly and operating frequently, micro-power, controlling Common and phase compensation easily, lower failure rate, longer working life.

2.2 Online Monitoring Function

The online monitoring system of the low-voltage intelligent capacitor chooses GPRS as the method to realize data communication and the public GSM network as the carrier. It is supplemented by the line of RS485 and infrared. The system regards the large users, public distribution transformer and household as the main controlled and management objects. It can realize the electric power online monitoring, controlling and managing form power lines to power users [5]. Following are the characteristics:

1. Input the accounting information of the distribution transformer intelligently.
2. The man–machine interface is simple, graphics and the charts are rich.
3. Because of the online monitoring function on voltage, it can monitor the running configuration state of the low-voltage intelligent capacitor in real time.
4. Provide the statistical information of operating conditions of the transformer and the comprehensive data for users to analysis the economic operation of the transformer.
5. Follow the standard database designing principles and provide strongly technical guaranty for the application integration system of the power supply enterprises.
6. The system has powerful data mining capabilities.
7. The system has self-diagnosis function, maintenance-free function and a variety of statistical analysis functions.
8. The network system is safe and reliable composed by routers, hardware firewall or dedicated network security isolation device.

2.3 Fault Diagnosis and Alarming Function

The low-voltage intelligent capacitor judges whether the device is over voltage, under-voltage or lack of phase according to monitoring the system's voltage. It can also discover abnormal operating conditions of the capacitors such as short-circuit, over-current or overload. Above is the stage of fault diagnosis. If it diagnosed the fault, the capacitor will send the information to communication unit. After the communication unit stores the electrical parameters before and after the accident, the alarming signal will be reported to the main station. With the acceptance of the main station, it can remind the low-voltage intelligent capacitor of the alarming, then save and record the information.

3 Practical Application and Analysis of Low-Voltage Capacitor

According to the operating data of Jiangmen power distribution network and the field investigation, this paper puts forward a plan to make the low-voltage intelligent capacitors into use in Jiangmen, and analyzes the effectiveness of the program on reactive power compensation, on-line monitoring and fault diagnosis. To some extent, it fills the blank of the practical application on online monitoring function of reactive power compensation equipment of power distribution network.

3.1 Determining the Point and Capacity of Reactive Power Compensation

This paper chooses two typical lines of 10 kV power distribution network in Jiangmen to complete reactive power optimization calculations based on the software of energy saving of power distribution network (PSAS). As follows: the total length of A line is 15.698 km, the number of its public transformer is 17, the total capacity is 2,600 kVA, the number of the dedicated transformer is18, the total capacity is 8610kVA; the total length of B line is 13.69 km, the number of the public transformer is 9, the total capacity is 2,364 kV.A, the number of the dedicated transformer is 59, the total capacity is 11,650 kVA.

According to the simulation results of PSAS and the operational characteristics of the grid of Jiangmen, the project selects three points for reactive power compensation named A, B and C in B line, the original capacity of the three points above are 0 kvar, 90 kvar and 210 kvar, and the added capacity are 200 kvar, 190 kvar and 210 kvar; The project also selects one point for reactive power compensation named D in A line, the original capacity of the D point is 210 kvar, the added capacity is 790 kvar.

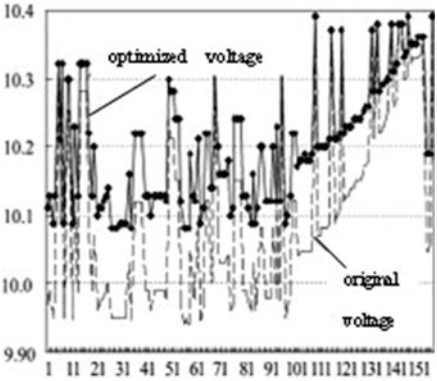

Fig. 2 Voltage contrast before and after optimization on A line

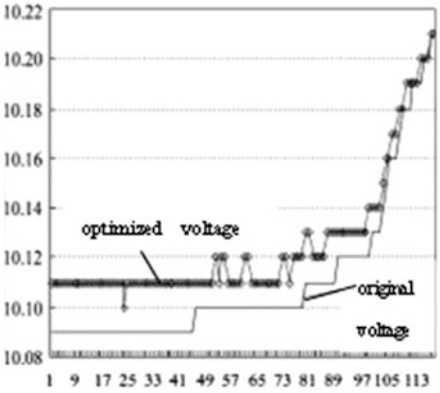

Fig. 3 Voltage contrast before and after optimization on B line

3.2 Realizing the Function of Real-Time Reactive Power Compensation Function

After inputting the corresponding capacity of reactive power compensation on the four points selected above, this paper compares the original voltage with the optimized voltage on A line and B line, shown in the Figs. 2 and 3.

According to the results above, this paper draws the following conclusions: the original node voltage on A line and B line is generally lower than the voltage before the reactive power compensation. After inputting the corresponding capacity of reactive power compensation on the four points selected above, not only the voltage quality has been improved significantly, but also the line losses and loss expenses are both cut down, shown in the Table 1

As is shown in the Table 1 above, the line loss and Loss costs of A line and B line are both reduced after applying the corresponding capacity of reactive power compensation.

Table 1 Comprehensive results of reactive power compensation on A and B line

	A line		B line	
	Original data	Optimal dat	Original data	Optimal data
Total active power of power supply/kW	1103.15	1104.02	1512.54	1506.35
The total supply of reactive power and reactive/kvar	692.36	585.13	1096.15	446.31
Total active power loss	36.49	37.52	71.68	66.45
Total reactive power loss	11.54	11.89	21.65	21.91
Loss costs/Million	3.39	3.42	4.76	4.56
Power factor	0.85	0.88	0.81	0.96

After installed the low-voltage intelligent capacitors in the actual compensation points, on one side the Reactive power compensation function has been realized, on the other side the power factor has been improved. The results proved the Practicality and economy of the low-voltage intelligent capacitor in reactive power compensation.

3.3 Realizing the On-line Monitoring Function

The low-voltage intelligent capacitors installed in A line and B line are equipped with a Four-in-one terminal system so as to realize its function, including collecting the voltage, current, active power and reactive power automatically, and also monitor harmonic wave. It can also upload the capacitors' operating condition parameters and real-time information to realize the on-line monitoring function accurately.

3.4 Realizing the Fault Diagnosis and Alarming Function

Because of the fault diagnosis function, the low-voltage intelligent reactive power compensation device can monitor the fault conditions including over voltage, under-voltage, short circuit, over-current, over harmonic wave, phases unbalance, over-temperature.

It can also carry on reactive power compensation control algorithm based on the picked parameters to make the decision to input or quit the single intelligent capacitor.

4 Conclusion

1. The advanced low-voltage intelligent reactive power compensation device used in Jiangmen Power Supply Bureau can carry on a variety of settings based on the actual requirements. It can complete the task of picking and controlling data, on-line monitoring the related electricity information so as to realize the functions including monitoring, controlling, managing the electricity consumption from the line to the user. It can also monitor the distribution transformer, measure remotely, monitor voltage and reactive power compensation and so on.
2. The fact proved that the advanced low-voltage intelligent reactive power compensation device installed in Jiangmen Power Supply Bureau has brought good results. On one hand, because of the real-time reactive power compensation function not only the voltage quality has been improved, but also the users' satisfaction has been enhanced greatly. On the other hand, the devices online monitoring function and its fault diagnosis and alarming function can help the workers to find out and repair the failure capacitors without delay. In one word, the advanced reactive power compensation device help guarantee the grid running safely and reliably, saving a lot of manpower and material resources.

References

1. ZHANG Yong-jun, REN Zhen (2005) Readjusting cost of dynamic optimal reactive power dispatch of power systems. Autom Electr Power Syst 29(2):34–38
2. ZHANG Yong-jun, YU Yue, REN Zhen, LI Bang-feng (2004) Research on dynamic modeling for reactive power optimization under real-time circumstance. Power Syst Technol 28(12):12–15
3. Wang Pei, Raghuveer MR, Mcdermid W et al (2001) A digital technique for the on-line measurement of dissipation factor and capacitance. IEEE Trans Dielectr Electr Insul 8(2):228–232
4. Allan D, Blundell M, Boyd K et al (1992) New techniques for monitoring the insulation quality of in-service HV apparatus. IEEE Trans Electr Insul 27(3):578–581
5. Moore PJ, Carranza RD, Tohns AT (1996) Model system test on a new numeric method of power system frequency measurement. IEEE Trans Power Deliv 11(2):696–701

Histogram Modification Data Hiding Using Chaotic Sequence

Xiaobo Li and Quan Zhou

Abstract In order to solve the security problem of data hiding with obvious detectable traces to attacker, a histogram modification data hiding scheme using chaotic sequence is presented. This algorithm modifies a cover image histogram by using a chaotic sequence to conceal the embedding process, and then secret information can be embedded into the modified image with encrypted trace. Experimental results show that the algorithm can achieve sound invisibility and large embedding capacity while guaranteeing high security. With the proposed scheme, the hiding trace of secret data is concealed. Even though the attacker detects the existence of hidden message under stego-image, the secret message cannot be extracted without private keys.

Keywords Data hiding • Histogram modification • Chaotic sequence • Embedding capacity

1 Introduction

With the development of internet and demand of users, image, video and multimedia data transmission in the internet increased rapidly over the last few years. Therefore, data security becomes more and more important. Data hiding [1] is a data security technique to undetectably insert secret message into a cover media to create a stego medium such that the existence of hidden information will not be detected by attacker. At the receive end, the hidden information can be extracted correctly by legal users. i.e., it provides a safer and securer data communication manner.

X. Li (✉) • Q. Zhou
Key Laboratory of Space Microwave Technology, China Academy of Space Technology, Xi'an, China
e-mail: lxb619@126.com

W. Wang (ed.), *Mechatronics and Automatic Control Systems*, Lecture Notes in Electrical Engineering 237, DOI 10.1007/978-3-319-01273-5_98,

A number of data hiding methods were proposed. There are three general types: spatial domain methods [2], frequency domain methods [3] and compression domain methods [4]. Spatial domain data hiding manner mixes secret data into the distributed pixels directly. A commonly used method, called the least significant bit (LSB) [5] method, is a simple spatial domain data hiding method by replacing the least significant bit of cover image pixels to embed secret bits. For the frequency domain manner, firstly, the cover image pixels must be transformed into frequency coefficients by using a frequency transform method such as the discrete cosine transformation (DCT) [6] and discrete wavelet transformation (DWT) [7]. Later, the secret data are embedded by modifying the relative coefficients in the frequency-form image. Finally, stego image can be obtained by utilizing corresponding inverse transform. The compression domain method means that the secret message are embedded into the compression codes, such as block truncation coding (BTC)-based [8] scheme and side match vector quantization (SMVQ)-based [9] scheme, and so on.

The desires of good data hiding schemes are high security and low image distortion as well as large payload. However, despite claiming good imperceptibility in previous schemes mentioned above, it leaves obvious detectable traces to attacker inevitably. In other words, once the attacker realizes there is a hidden information under stego-image, the secret data would be extracted possibly. To further reinforce the security of data hiding, we develop a novel histogram modification data hiding scheme by using chaotic sequence to control the embedding procedure. With this scheme, the hiding trace of secret message is concealed. Even though the attacker detects the existence of hidden message under stego image, the secret message cannot be extracted without private keys. Furthermore, the proposed scheme has nice image quality and high payload.

The rest of this paper is organized as follows. The proposed data hiding method is presented in Sect. 2. In Sect. 3, the experimental results of our method are demonstrated. Finally, the conclusions of paper are presented in Sect. 4.

2 Proposed Scheme

In this section, the proposed data hiding scheme will be presented. The proposed algorithm has the merits of high security and low image distortion as well as large embedding capacity. To enhance the security, we utilize chaotic sequence to conceal the histogram modification trace. Figure 1 shows an example of the embedding process. Figure 1a shows an image block of size 4×4 and histogram of the image block. Consider a binary chaotic sequence as “0110001111010110”. There is a one-to-one relationship between pixels in image block and bits of chaotic sequence. Before embedding, the image block is scanned by raster-scan order. Once an even pixel value is encountered, if the corresponding bit of chaotic sequence is “1” the pixel is added by “1”, else it is kept intact. On the contrary, once an odd pixel value is encountered, if the corresponding bit of chaotic sequence is “0” the

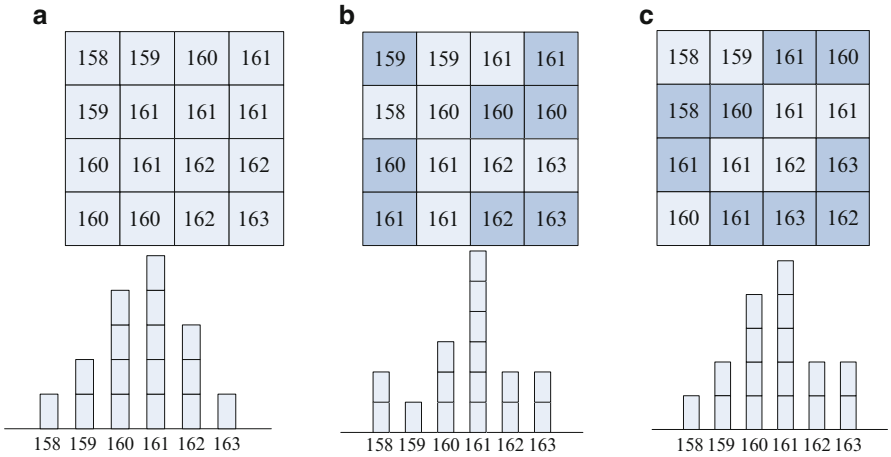

Fig. 1 An example of the embedding process : (**a**) original image block and histogram;(**b**) modified image block and histogram; (**c**) embedded image block and histogram

pixel is decremented by "1", else it is kept intact. The result of modifying operation by using chaotic sequence as shown in Fig. 1b. Suppose that the payload data is the stream of "100100111001011". To embed the stream of data, the modified image block is scanned in the same scan order once again. Whenever the same chaotic sequence '0' is encountered, we sequentially check the bit of payload data. If the payload data bit is "1" the pixel is added by "1", else it is kept intact. When the chaotic sequence "1" is encountered, if the corresponding payload data bit is "1" the pixel is decremented by "1", otherwise it is not changed. As a result, the embedded image block is obtained as shown in Fig. 1c. Data extraction is actually the reverse of the embedding process. Note that the number of payload data bits that can be hidden into an image and the number of pixels associated with the image are equal. The detail algorithm is shown as below.

2.1 Embedding Process

Assume that the cover image X of size $M \times N$ is an 8-bit grayscale image. Denote the pixel value as $X(i,j)$, where (i,j) indicates the location in the original image. We select logistic map [10] to generate chaotic sequence, as shown in formula (1):

$$l_{n+1} = \alpha \cdot l_n(1 - l_n) \tag{1}$$

Where α is bifurcation parameter, and $l_n \in (0,1)$, $n = 0,1,2\cdots$. When $3.5699456\cdots < \mu \leq 4$, the logistic map is in chaotic state. In this paper, the parameter α and initial value l_0 are used as private keys.

Step1: Select parameter α and initialize value l_0, chaotic sequences S_k can be obtained by

$$S_k = \begin{cases} 0 & if \quad 0 < l_n < 0.5 \\ 1 & if \quad 0.5 \leq l_n < 1 \end{cases} \tag{2}$$

Where $k = 1, 2, \ldots, M \times N$, $n = 0, 1, \ldots, (M \times N) - 1$.

Step2: Scan the whole image in a given order, modify the pixel value $X(i,j)$ by

$$Y(i,j) = \begin{cases} X(i,j) & if \quad S_k = 0 \& R_{i,j} = 0 \\ X(i,j) - 1 & if \quad S_k = 0 \& R_{i,j} = 1 \\ X(i,j) & if \quad S_k = 1 \& R_{i,j} = 1 \\ X(i,j) + 1 & if \quad S_k = 1 \& R_{i,j} = 0 \end{cases} \tag{3}$$

Where $R_{i,j} = rem(X(i,j), 2)$ is the remainder of pixel value $X(i,j)$ and integer 2, $Y(i,j)$ is modified value of pixel $X(i,j)$, $1 \leq i \leq M$, $1 \leq j \leq N$, and $k = 1, 2, \ldots, M \times N$.

Step3: Scan the whole image in the same order in step2, and modify $Y(i,j)$ according to the secret message B.

$$Z(i,j) = \begin{cases} Y(i,j) + B & if \quad S_k = 0 \\ Y(i,j) - B & if \quad S_k = 1 \end{cases} \tag{4}$$

Where S_k is the same chaotic sequences in step2, $k = 1, 2, \ldots, M \times N$. B is a binary sequence, and $B \in \{0, 1\}$.

Finally, the final stego image Z with the embedded secret information is constructed.

2.2 Extraction Process

The secret information extraction process is similar with the embedding process exception the image is stego image. The extraction process is described as follows:

Step1: Generate chaotic sequences S_k by utilizing private keys α and l_0.

Step2: Scan the whole stego image Z in the same order as during the embedding. Extract message B by

$$B = \begin{cases} 0 & if \quad S_k = 0 \& R_{i,j} = 0 \\ 1 & if \quad S_k = 0 \& R_{i,j} = 1 \\ 0 & if \quad S_k = 1 \& R_{i,j} = 1 \\ 1 & if \quad S_k = 1 \& R_{i,j} = 0 \end{cases} \tag{5}$$

Where $R_{i,j} = rem(Z(i,j), 2)$ is the remainder of pixel value $Z(i,j)$ and integer 2, $1 \leq i \leq M$, $1 \leq j \leq N$, and $k = 1, 2, \ldots, M \times N$.

Thus, the secret message hidden in the stego image are obtained.

3 Results and Discussions

We select four 8-bits grayscale images of size 512 × 512 to evaluate the performance of the proposed scheme, as shown in Fig. 2. These natural images, "Lena", "Baboon", "Boat", and "Pepper", are selected from CVG-UGR image database [11]. To evaluate the visual quality of stego image, we use the function of peak-signal-to-noise-ratio (PSNR), which is defined as in

$$PSNR(dB) = 10 \times \log_{10}\left(\frac{255^2 \times M \times N}{\sum_{i=1}^{M}\sum_{j=1}^{N}(X(i,j) - Z(i,j))^2}\right) \tag{6}$$

Where, X and Z denote the original cover image and stego image, M and N denote the width and height of the cover image, respectively.

The results of four test images for embedding are listed in Table 1, which shows the embedded capacity and PSNR of the stego image. From the Table 1 it is seen that the values of PSNR of four test images are all greater than 51 dB. The embedding capacity of four test images are 262,144 bits, i.e. 1 bpp (bits per pixel). This demonstrates that our proposed algorithm can achieve nice invisibility and large embedding capacity.

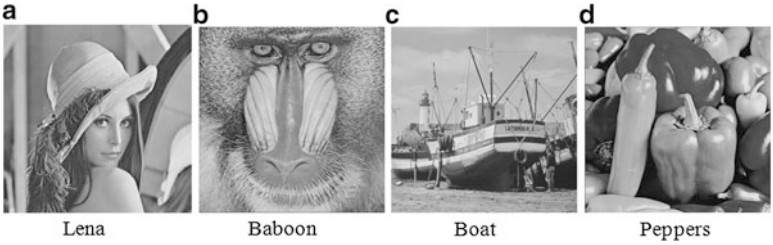

Fig. 2 Original cover images (**a**) Lena (**b**) Baboon (**c**) Boat (**d**) Peppers

Table 1 Embedding capacity and distortion for test images

Test images	Capacity (bits)	PSNR (dB)	Key
Lena	262,144	51.13	Yes
Baboon	262,144	51.13	Yes
Boat	262,144	51.14	Yes
Peppers	262,144	51.13	Yes

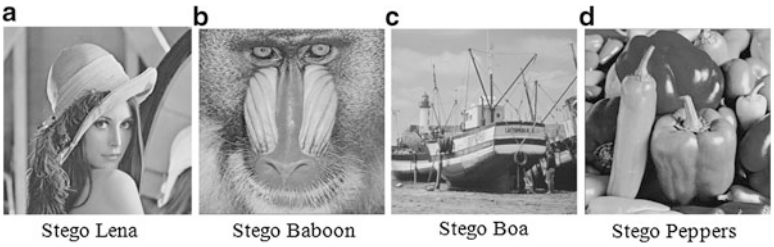

Fig. 3 The stego images (**a**) Stego Lena (**b**) Stego Baboon (**c**) Stego Boa (**d**) Stego Peppers

Figure 3 shows the visual quality of stego images when embedding same secret data with length of 262,144 bits. The visual differences cannot be detected by the Human Vision System (HVS) between the stego images and the corresponding original cover images. This is the most important desire for data hiding application.

Figure 4 shows the histogram distribution of Lena image after embedding data by using LSB method and our proposed method, respectively. Figure 4a is the histogram of original Lena image. Figure 4b is the histogram of stego image obtained from applying the classical LSB data hiding approach. From Fig. 4b, the histogram of stego image has changed obviously. it leaves detectable traces to attacker inevitably. In other words, once the attacker realizes there is a hidden information under stego image, the secret data would be extracted possibly by analysing the distribution of histogram of the stego image. Figure 4c is the histogram of stego image obtained from applying our proposed data hiding method. With reference to Fig. 4c we can clearly see that there is almost no change on histogram between stego image and original image. i.e., the attacker cannot detect the changes done for data hiding.

The result of security test for our proposed method is showed in Fig. 5. Figure 5a is a secret binary image with size 512×512. We embed this secret binary image into cover image by applying our proposed embedding process with private keys, and then extract the hidden information under stego image by applying our proposed extraction process with wrong keys. Finally, the extracted image is shown in the Fig. 5b. From the Fig. 5b it is seen that the extracted image is similar to white noise image, which demonstrates the extracted image varies sensitively with the variances of the private keys.

4 Conclusion

This paper put up a histogram modification data hiding method using chaotic sequences for increasing the security. The secret message is embedded at different histogram modification traces, which are encrypted by private keys. Even though the attacker detects the existence of hidden message under stego image, the secret message cannot be extracted without private keys. Experimental results

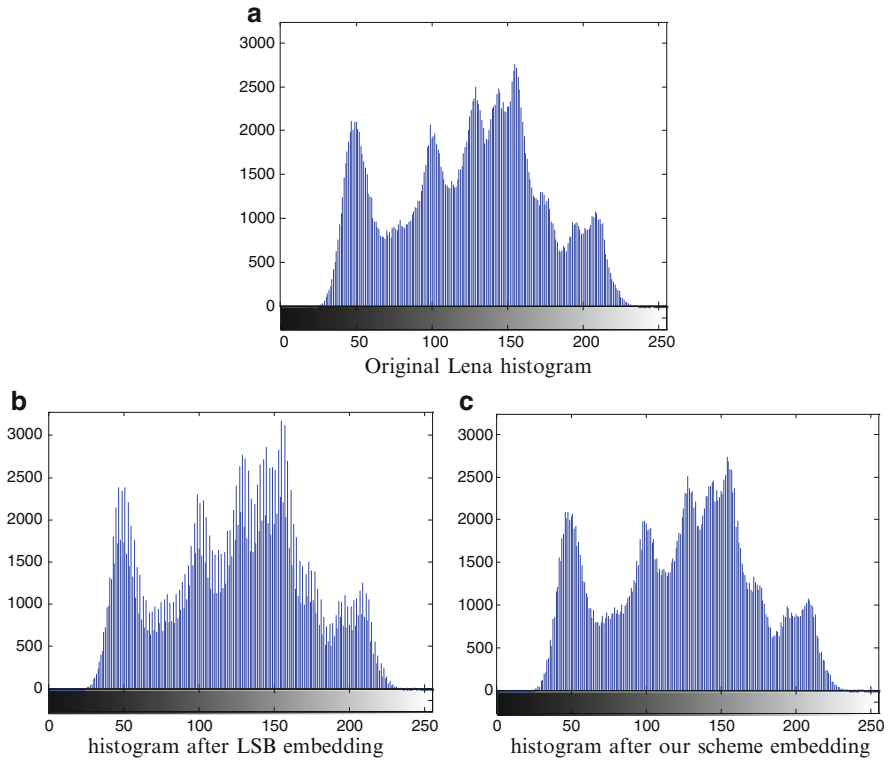

Fig. 4 The original Lena histograms and the stego image histograms with different embedding methods (**a**) original Lena histogram, (**b**) histogram after LSB embedding (**c**) histogram after our scheme embedding

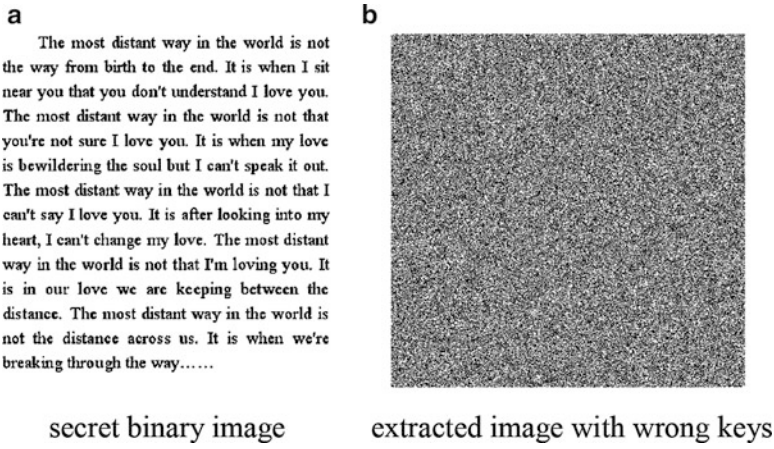

Fig. 5 Security test (**a**) secret binary image (**b**) extracted image with wrong keys

demonstrated that the proposed data hiding scheme can provide higher security while keeping low distortion and large embedding payload. Besides, the embedding process of the proposed scheme just deals with the scanning, adding, and subtracting operations that the computation complexity of this scheme is also very small. It is expected that the proposed scheme having high security can be deployed for extensive application fields.

References

1. Petitcolas FAP, Anderson RJ, Kuhn MG (1999) Information hiding-a survey. Proc IEEE 87 (7):1062–1078
2. Wu DC, Tsai WH (2000) Spatial-domain image hiding using image differencing. IEE Proc Vis Image Signal Process 147(1):29–37
3. Bao P, Ma X (2005) Image adaptive watermarking using wavelet domain singular value decomposition. IEEE Trans Circuits Syst Video Technol 15(1):96–102
4. Chuang JC, Chang CC (2006) Using a simple and fast image compression algorithm to hide secret information. Int J Comput Appl 28(4):329–333
5. Chan CK, Cheng LM (2004) Hiding data in images by simple LSB substitution. Pattern Recog 37(3):469–474
6. Singh S, Siddiqui TJ, Singh R et al (2011) DCT-domain robust data hiding using chaotic sequence. In: International conference on multimedia, signal processing and communication technologies, IEEE Press, Aligarh, India, pp 300–303
7. Huang HY, Chang SH (2010) A lossless data hiding based on discrete Haar wavelet transform. In: IEEE 10th international conference on Computer and Information Technology (CIT), IEEE Press, Bradford, England, pp 1554–1559
8. Chang CC, Lin CY, Fan YH (2008) Lossless data hiding for color images based on block truncation coding. Pattern Recog 41(7):2347–2357
9. Lee JD, Chiou YH, Guo JM (2010) Reversible data hiding based on histogram modification of SMVQ indices. IEEE Trans Info Forensics Secur 5(4): 638–648
10. Sun Y, Wang GY (2011) An image encryption scheme based on modified logistic map. International workshop on Chaos-Fractals Theories and Applications(IWCFTA), IEEE Press, Hangzhou, China, pp 179–182
11. CVG-UGR Image Database: http://decsai.ugr.es/cvg/dbimagenes/index.php

A Family of Functions for Generating Colorful Patterns with Mixed Symmetries from Dynamical Systems

Jian Lu, Yuru Zou, Guangyi Tu, and Haiyan Wu

Abstract This paper investigates generating artistic patterns with mixed symmetry by means of dynamical systems. First, a new family of functions is introduced to produce colorful patterns with cyclic/dihedral symmetries and some crystallographic symmetries. Successively, two functions with distinct symmetries are applied to create patterns having mixed symmetries in different planar regions with the aid of a mixing technique. The method might provide a novel approach for automatically generating a great variety of artistic patterns.

Keywords Crystallographic groups • Cyclic group • Dihedral group • Mixed symmetry

1 Introduction

The fact that the attractors arising from the iteration of functions in the plane that are designed to have symmetry has been the subject of much recent study. Carter et al. [1] explored the construction of the families of functions which can be used to create chaotic attractors with symmetries of the frieze and wallpaper groups. Field and Golubitsky [2] investigated how to generate chaotic attractors with cyclic, dihedral and some of the planar crystallographic symmetries. In addition, Carter [3] illustrated two functions of the plane that have distinct symmetries intertwined using a sinew function to produce a function of three variable having different symmetries in different regions of space. Dumont et al [4] studied the evolution of families of attractors that change from one symmetry type to another. Dumont and Reiter [5] further discussed the chaotic attractors with symmetries that are close to forbidden and their associated functions. The methods of coloring the chaotic

J. Lu • Y. Zou (✉) • G. Tu • H. Wu
College of Mathematics and Computational Science, Shenzhen University, Shenzhen, China
e-mail: yrzou@163.com

W. Wang (ed.), *Mechatronics and Automatic Control Systems*, Lecture Notes in Electrical Engineering 237, DOI 10.1007/978-3-319-01273-5_99,

attractors mentioned above are based on the point-hitting frequency. And always suppose that the attractor has a Sinai-Ruelle-Bowen (SRB) measure [6, 7].

In this paper, different from Dumont et al.'s work constructing attractors with evolving symmetry or forbidden symmetry, we first present an effective method to generate artistic patterns with cyclic/dihedral symmetry or some wallpaper symmetries from dynamical systems. Furthermore, the colorful patterns with mixed symmetry are investigated by using a mixing technique from dynamical systems. The presented method is based on our previous work [8, 9] and can be used to create a great variety of artistic patterns.

2 Planar Symmetry Groups

A mapping $g : \mathbf{R}^2 \to \mathbf{R}^2$ is said to be *equivariant* with respect to a symmetry group if $g \circ \gamma = \gamma \circ g$ for all elements γ of the group. The discrete planar symmetry groups are well known to consist of the identity, cyclic and dihedral groups, 7 frieze groups and 17 crystallographic groups. Cyclic and dihedral groups are subgroups of permutation groups. The cyclic group, C_n, is generated by n-fold rotations about a single point. A mapping with C_n symmetry should be equivariant with respect to

$$S_n = \begin{pmatrix} \cos 2\pi/n & -\sin 2\pi/n \\ \sin 2\pi/n & \cos 2\pi/n \end{pmatrix}$$

The dihedral group, D_n, contains n-fold rotations as well as a reflection through a line passing through the point of rotation. A mapping with D_n symmetry should be equivariant with respect to S_n and

$$M = \begin{pmatrix} 1 & 0 \\ 0 & -1 \end{pmatrix}$$

The crystallographic groups are characterized by two independent translations, which give rise to a lattice. In addition, the crystallographic groups may contain rotations of order two, three, four and six. Together with reflections and glide reflections, there are a total of 17 crystallographic groups. For instance, the $p31m$ symmetry group contains third-fold rotations and mirrors about y-axis as well as two independent translations. Since a lattice does not map to itself by third turns, we can take $u_0 = 2\pi(1, 0)$ and $u_1 = 2\pi(-\frac{1}{2}, \frac{\sqrt{3}}{2})$ as the generators of the lattice L. Connecting vertices in this lattice produces a regular tiling of the plane that is called a hexagonal lattice. The vectors $v_0 = (1, -\frac{1}{\sqrt{3}})$ and $v_1 = (0, -\frac{2}{\sqrt{3}})$ form a basis for the dual lattice L^*. The generators of $p31m$ include $\delta(x, y) = (x, -y)$ and $\delta(x, y) = (-\frac{1}{2}x - \frac{\sqrt{3}}{2}y, \frac{\sqrt{3}}{2}x - \frac{1}{2}y)$.

The theory of which polynomials have cyclic and dihedral symmetries is discussed in Field and Golubitsky [1]. Carter et al. [2] investigated a family of crystallographic functions using trigonometric functions. In traditional methods [1, 2], all these equivariant mappings are applied to create chaotic attractors with different planar symmetries. In next section, we will present another new family of functions for creating colorful patterns with cyclic/dihedral symmetries and some wallpaper symmetries. The construction of these equivariant functions is based on the theory introduced by Dumont and Reiter [5] for creating attractors with forbidden symmetry.

3 New Symmetric Functions

Suppose $g : \mathbf{R}^2 \to \mathbf{R}^2$ being an arbitrary function and G being a finite group on $\mathbf{R}^2$, then [10],

$$F(\vec{x}) = \sum_{\gamma \in G} \gamma^{-1}(g(\gamma(\vec{x}))) \tag{1}$$

is equivariant with respect to G, where $\vec{x} \doteq (x, y) \in \mathbf{R}^2$. In fact, it is easy to verify that for any $\sigma \in G$, $F(\sigma(\vec{x})) = \sum_{\gamma \in G} \sigma(\gamma\sigma)^{-1}(g(\gamma\sigma(\vec{x}))) = \sigma(F(\vec{x}))$. So, various functions can be used for creating cyclic or dihedral symmetry provided that the group G is C_n or D_n [10]. In the method here, according to lattice theory, we will discuss a family of functions that can be used to generate cyclic and dihedral patterns as well as some specific crystallographic patterns, such as $p3$, $p31$m, $p4$, $p4$m, $p6$, $p6$m etc. We first consider a lattice L in $\mathbf{R}^2$ along with a dual lattice L^*, which implies that $\vec{\alpha} \bullet \vec{\beta}$ is an integer for any vectors $\vec{\alpha} \in L$ and $\vec{\beta} \in L^*$. Thus, $\sin(\vec{\beta} \cdot (\vec{x} + \vec{\alpha})) = \sin(\vec{\beta} \cdot \vec{x})$, if $\vec{\beta} \in 2\pi L^*$, and likewise for cosine. This means that $\vec{a}\sin(\vec{\beta} \cdot \vec{x}) + \vec{b}\cos(\vec{\beta} \cdot \vec{x}) + \vec{c}\sin(\vec{\beta} \cdot \vec{x})\cos(\vec{\beta} \cdot \vec{x}) \bmod L$ is equivariant with respect to the translations L, where $\vec{a}, \vec{b}$ and $\vec{c}$ are constant vectors and $\vec{a}, \vec{b}, \vec{c} \in \mathbf{R}^2$.In practical use, $\vec{a}, \vec{b}, \vec{c}$ are produced randomly. Based on this analysis, similar to Dumont and Reiter [5], we can construct a new equivariant function g with respect to the translational symmetries of L and

$$g(\vec{x}) = \sum_{\vec{\beta} \in \Omega} (\vec{a}\sin(\vec{\beta} \cdot \vec{x}) + \vec{b}\cos(\vec{\beta} \cdot \vec{x}) + \vec{c}\sin(\vec{\beta} \cdot \vec{x})\cos(\vec{\beta} \cdot \vec{x})) \bmod L \tag{2}$$

Note that even if we take a function of the form $F_g(\vec{x})$ in Eq. 1 with g having the form in Eq. 2, $F_g(\vec{x})$ has the symmetry of G and may not take the symmetry of the lattice. Naturally, if we define the function

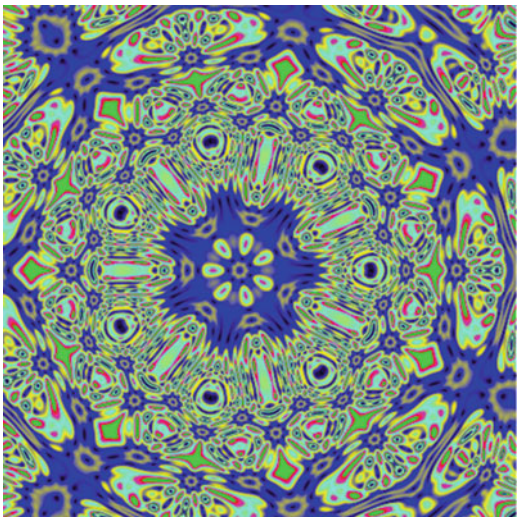

Fig. 1 A pattern with D_7 symmetry

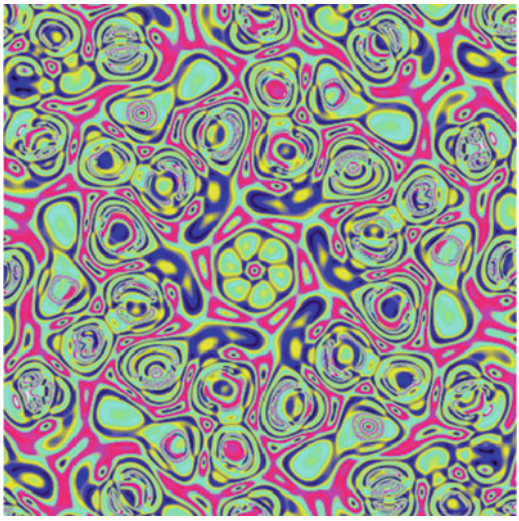

Fig. 2 A pattern with C_6 symmetry

$$\tilde{F}_g(\vec{x}) = F_g(\vec{x}) \bmod L \tag{3}$$

and the group G can map the lattice L back onto itself, then the desired symmetries of $F_g(\vec{x}) \bmod L$ are obtained [5].

Combining with the above equivariant functions $F_g(\vec{x})$ or $\tilde{F}_g(\vec{x})$, colorful pattern with specific planar symmetries can be created by using invariant mapping from dynamical systems. For instance, Figs. 1, 2, and 3 are generated by using Eq. 1. Figure 4 is created by using Eq. 3.

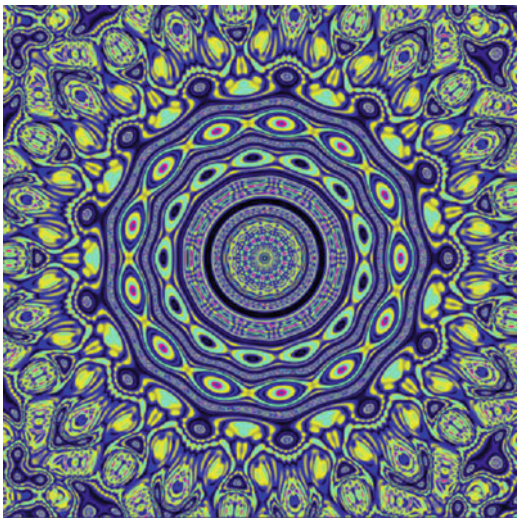

Fig. 3 A pattern with D_{13} symmetry

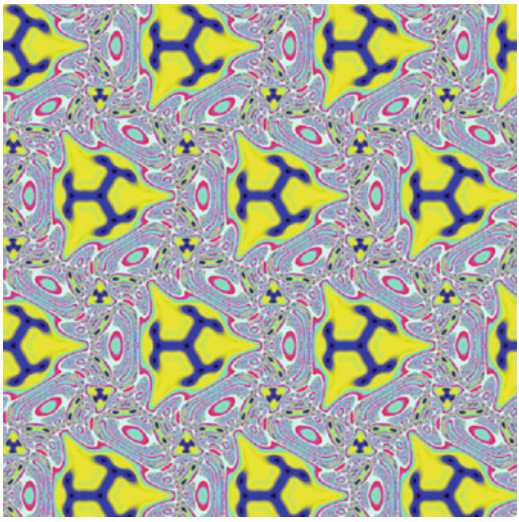

Fig. 4 A pattern with $p31m$ symmetry

4 Colorful Patterns with Mixed Symmetry

Our construction of mixed symmetric patterns utilizes two functions with symmetry in the plane intertwined and connected via stochastic scheme. Let $F_1(\vec{x})$ and $F_2(\vec{x})$ be two desired symmetric functions. In order to mix the two symmetries visually, we need to consider a smooth transition by following function

$$F(\vec{x}) = \lambda(\vec{x})F_1(\vec{x}) + (1 - \lambda(\vec{x}))F_2(\vec{x}) \tag{4}$$

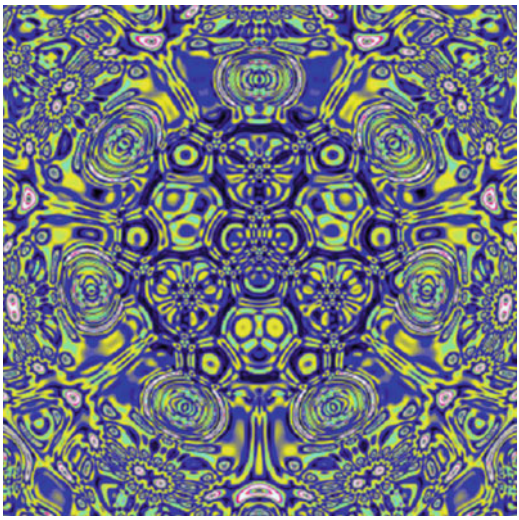

Fig. 5 A mixed symmetric pattern with dominated D_7 outer symmetry and dominated D_3 inner symmetry

Note that, when $\lambda(\vec{x}) \equiv 1$, the function is $F_1(z)$, and when $\lambda(\vec{x}) \equiv 0$, the function is $F_2(z)$. The values of $\lambda(\vec{x})$ between 0 and 1 show the intermediate steps for intertwining between one symmetry and the other symmetry. Suppose a disc region Ω is defined by $\Omega = \{(x, y)^T \in R^2 | \sqrt{x^2 + y^2} \leq r\}$ where r is a constant and $r \in R$. Here, we proposed two methods for constructing mixed symmetry. One simple method is introduced by defining $\lambda(x, y)$ as

$$\lambda(x, y) = \begin{cases} \lambda_1 & (x, y) \in \Omega \\ \lambda_2 & otherwise. \end{cases} \tag{5}$$

where λ_1 and λ_2 is constant and $\lambda_1, \lambda_2 \in [0, 1]$. Equation 5 implies that if $\lambda_1 \gg 0.5$, the symmetries in region Ω is dominated by $F_1(x, y)$; conversely, the symmetries in region Ω is dominated by $F_2(x, y)$ if $\lambda_2 \gg 0.5$. For example, we take $\lambda_1 = 0.1$ and $\lambda_2 = 0.9$ to create the mixed symmetric pattern with dominated D_7 outer symmetry and dominated D_3 inner symmetry, as shown in Fig. 5.

The other method is implemented by defining $\lambda(x, y)$ as

$$\lambda(x, y) = \begin{cases} \left(\dfrac{\sqrt{x^2 + y^2}}{r} \right)^5 & (x, y) \in \Omega \\ 1 & otherwise \end{cases} \tag{6}$$

Equation 6 means that the mixed symmetry is gradually transformed from $F_2(x, y)$ to $F_1(x, y)$ in the region Ω and the symmetry is dominated solely by $F_1(x, y)$. For instance, the mixed symmetric pattern with dominated D_9 outer

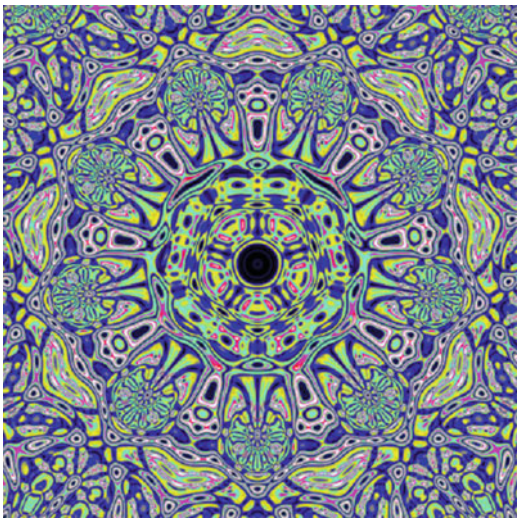

Fig. 6 A mixed symmetric pattern with dominated D_9 outer symmetry and dominated D_5 inner symmetry

symmetry and dominated D_3 inner symmetry shown in Fig. 5 is created by using Eq. 6.

Let $\psi(X)$ a symmetry group of a certain subset of the plane, namely X. A mapping $f : \mathbb{R}^2 \to \mathbb{R}$ is said to be *invariant* with respect to a symmetry group if $f \circ \gamma = f$ for all elements γ of the group. Since the crystallographic symmetries contain two translations in nonparallel directions, we only need to design the invariant functions on a period parallelogram. In other words, f need not be invariant with respect to $\gamma(x, y) = (x + T, y + T')$, where T, T' is the translation period. So, It can directly verify that $f(x, y)$ is invariant for C_n/D_n and crystallographic symmetries if $f(x, y) = h \circ v(x, y)$, where $v(x, y) = x^2 + y^2$ and $h : \mathbb{R} \to \mathbb{R}$ is any real function [10]. For example, we take $f(x, y) = v(x, y) + |\cos(v(x, y))| + 0.15v^3(x, y) + 12v(x, y)$ to generate the images in Figs. 1, 2, and 5; and take $f(x, y) = |\sin(v(x, y)) + \cos(h^3(x, y))| + 10v(x, y)$ and $f(x, y) = |6\sin(v^3(x, y)) + 2\tan(v^3(x, y))|$ to create the image in Figs. 3, 4, and 6. Here, Figs. 1, 2, 3, and 4 are patterns with D_7, C_7, D_{13} and $p31m$ symmetries, respectively. It is worth noting that Fig. 4 is also a D_3 symmetric pattern. Figure 5 is a mixed symmetric pattern with dominated D_7 outer symmetry and dominated D_3 inner symmetry; Fig. 6 is a mixed symmetric pattern with dominated D_9 outer symmetry and dominated D_5 inner symmetry.

5 Color Scheme

Suppose that the scope for generating patterns is denoted by U; f is a invariant function and $f(x, y) \geq 0$; F is equivariant with respect to planar symmetry groups as described above; M is a given positive integer and τ is a positive real number.

For each point $p(x, y)$ in displaying area U, the equivariant mapping F is determined by the position of p. Calculate the f-values $\{f(F^j(p))\}_{j=1}^{J}$ of the orbit $\{F^j(p)\}_{j=1}^{J}$ of p under F where F^j s the j-th iteration of F. Once $f(F^j(p)) < \tau$ for some $j \leq J$, the iteration exits and then we take $\hat{F}(p) = \frac{F(f^j(p))}{\tau}$, which is used to color the pixel p. Otherwise, $\hat{F}(p)$ is defined as $\hat{F}(p) = 0$ and the pixel p is colored black. Since $\hat{F}$ is a symmetric density function on X, the group symmetrically placed pixels can get the same color with the same density. Outstanding features of this color method appear in Lu et al.'s work [9].

6 Conclusion

This paper introduced a new family of functions to create artistic images with mixed symmetry. Specially, two functions with different symmetries were investigated and integrated for constructing mixing symmetric images in displaying regions by using a mixing technique. The generated symmetric patterns verified the validity of this method.

Acknowledgements The authors were supported by NSFC #61003178, #10926142, #11201312, #61272252, #11071150, Shenzhen MSTP #JC2011051 70615A and #JC201005280508A.

References

1. Carter NC, Eagles RL, Hahn AC, Grimes CA (1998) Chaotic attractors with discrete planar symmetries. Chaos Soliton Fract 12:2031–2054
2. Field M, Golubitsky M (1992) Symmetry in chaos. Oxford University Press, New York, pp 89–101
3. Carter NC (1997) Attractors with duelling symmetry. Comput Graph 21:263–271
4. Dumont JP, Heiss FJ, Jones KC et al (1999) Chaotic attractors and evolving planar symmetry. Comput Graph 23:613–619
5. Dumont JP, Reiter CA (1998) Chaotic attractors near forbidden symmetry. Chaos Soliton Fract 11:1287–1298
6. Field M (2001) Designer chaos. Comput Aided Des 33:349–365
7. Robinson C (1994) Dynamical systems. CRC Press, Boca Raton, pp 351–356
8. Lu J, Ye ZX, Zou YR (2007) Automatic generation of colorful patterns with wallpaper symmetries for dynamics. Vis Comput 23:445–449
9. Lu J, Zou YR, Li WX (2011) Colorful patterns with discrete planar symmetries from dynamical systems. Fractals 18:35–43
10. Jones KC, Reiter CA (2000) Chaotic attractors with cyclic symmetry revisited. Comput Graph 24:271–282

Automatic Calibration Research of the Modulation Parameters for the Digital Communications

Kai Wang, Zhi Li, Ming-zhao Li, Chong-quan Zhu, Qiang Ye, and Juan Lu

Abstract Calibration of the modulation quality as an important parameter of wireless communication, it played a vital role in the performance of wireless com-munications test. We proposed a auto-calibration method of digital modulation parameters of a digital mobile communication tester, against the unstable modulation parameters and high error rate of manually test, what's more, analyzed the uncertainty of the measurement results. The experiment results showed that the automatic test method was precision, high stability, and practical.

Keywords Digital mobile communications integrated tester • Automatic calibration • Digital modulation

1 Introduction

TD-SCDMA (Time Division-Synchronous Code Division Multiple Access), the first complete mobile communication technology standards of the Chinese telecommunications industry for centuries, and got the full support of the China Communications Standards Association (CWTS) and 3GPP international organizations, was one of the technical specifications by ITU formally released the third generation mobile communications space interface to of the modulation quality of the main parameters of the digital communications tester, also an important part of the conformance testing of TD-SCDMA terminal, the main measure of the modulation error generated by the modulator and RF devices quality of the modulated signal.

K. Wang • Z. Li • M.-z. Li (✉) • C.-q. Zhu • J. Lu
Shenzhen Academy of Metrology and Quality Inspection, Shenzhen, China
e-mail: smqlmz@163.com

Q. Ye
College of Information and Engineering, China Jiliang University, Hangzhou, China

W. Wang (ed.), *Mechatronics and Automatic Control Systems*, Lecture Notes in Electrical Engineering 237, DOI 10.1007/978-3-319-01273-5_100,

The GPIB (General-Purpose Interface Bus)-based automated test system was a product of the combination of computer technology and automated testing techniques and now widely used in many fields [1]. E5515C wireless communications test instrument of Angilent under the Visual Basic environment called the GPIB DLL send SCPI commands to control the E5515C, and accomplished TD-SCDMA standard digital modulation quality parameters of the automatic calibration, and introduced an automatic calibration method of a wireless communication tester.

2 System Model

In this paper, the system model was divided into two parts of the hardware and software systems to introduce:

First, the automatic measurement system was consist of a E4445A spectrum analyzer with vector signal analysis function, computers, and GPIB interface card and Angilent 8960 digital communications tester, system hardware block diagram shown in Fig. 1.

The automatic measurement system was consist of Angilent 8960 Series E5515C digital communications, E4445A spectrum analyzer with a vector signal

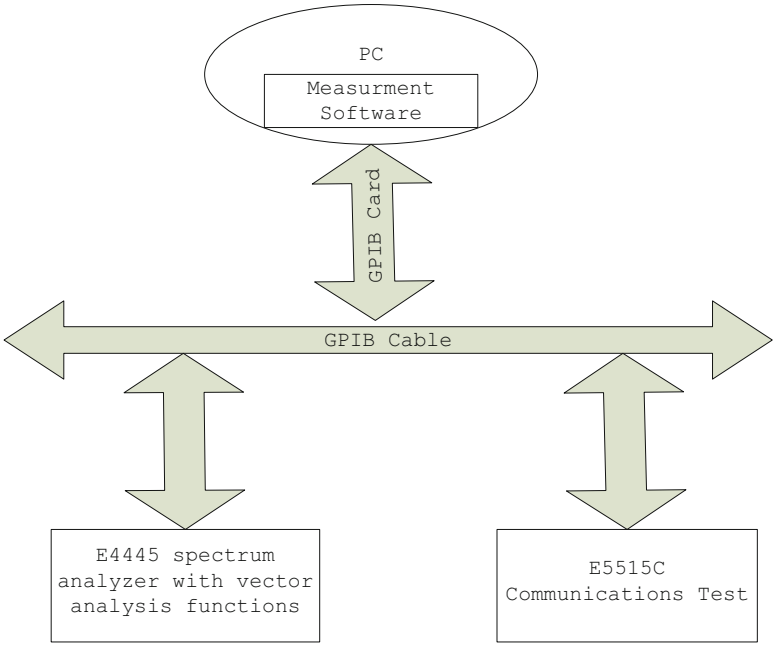

Fig. 1 System hardware framework

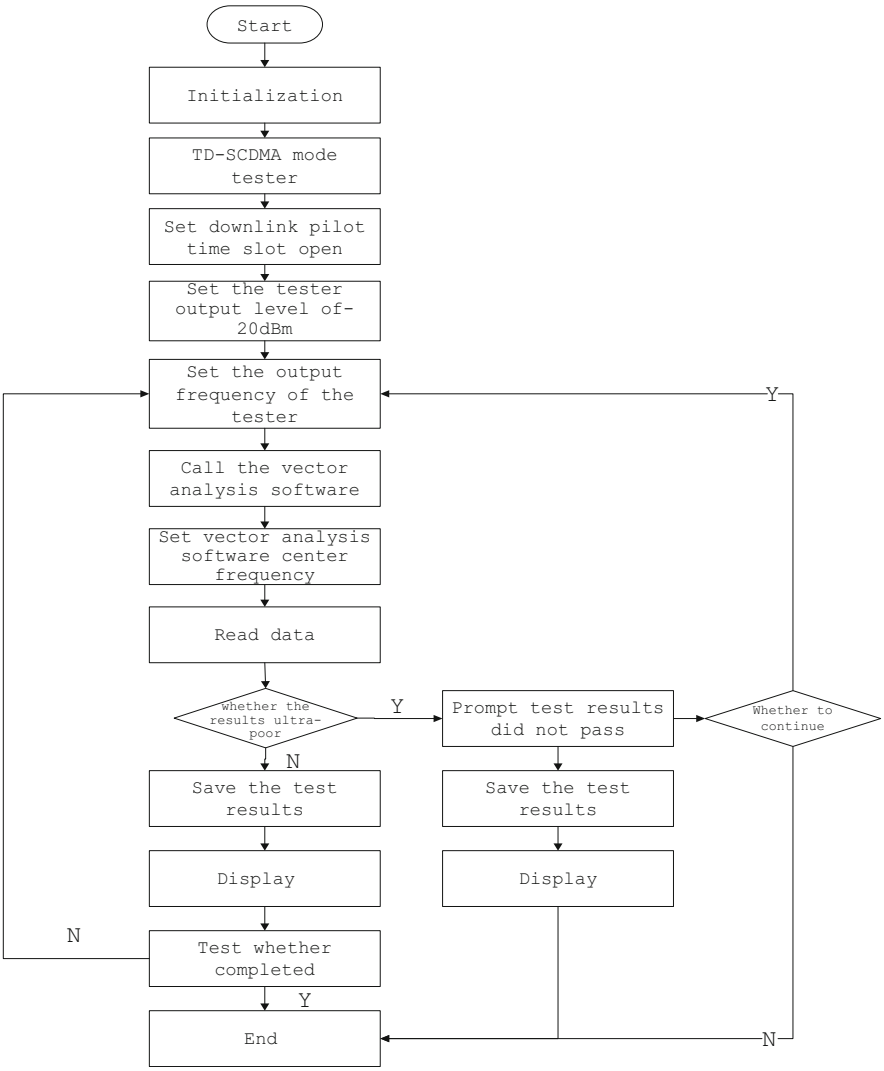

Fig. 2 Software flow chart

analyzer function, computers, GPIB interface card and cable. The system took computer as the core, connected the GPIB interface card, the standard and the measured instrument with GPIB cables. Computer sent SCPI command to control and management standards and the measured instrument, and accomplished data transmission and processing [2].

Secondly, the software system was the core part of the whole system, the realization of the process shown in Fig. 2.

Software sent commands to initialize the instrument, the tester was set to TD-SCDMA standard, and set the modulation signal of the tester for the downlink, at the same time, vector analysis software was also needed to set to a downlink demodulation, then, the tester would be able to output the TD-SCDMA modulated signals. Tester output level too large or too small would lead vector analysis software would not be able to demodulate, so the modulated signal was typically set to -20dBm. The vector analysis of the EVM software demodulation fluctuate, in order to reduce its error, returned average results of 20 groups.

The software system was the core part of the whole system, in order to achieve the data acquisition and analysis, under VB environment, Communication between the standard device and the gpib32 of the dll library in GPIB interface card the gpib32 of the dll library were connected through the IEEE-488. The E5515C tester issued TD-SCDMA modulated signals, relying on the modulation signal Angilent 89600 vector analysis software to analyze, re-used testing software to make data processing and judgment, the final test results showed in the test software interface and deposited to ACCCESS database [3].

3 System Performance Analysis

ATS (Automatic Testing Systems) was a system, which could automatically measure, data process, and display or output the test results in an appropriate manner with people rarely participate or not participate in. Compared with manual testing, automated testing could save time, improve labor productivity and product quality, which had an important role in production, research and defense [4].

TD-SCDMA combine code division multiple access, time division multiple access frequency division multiple access as one, had a class of noise and autocorrelation characteristics. There were two general methods of measurement such as these signals: the appropriate amount of margin of error by using the CDMA waveform quality RHO and WCDMA EVM.RHO and EVM reflected the overall quality of the modulation was a composite indicator for CDMA [5].

TD-SCDMA system used QPSK modulation, which was a fly constant envelope modulation, there were errors in the amplitude, phase error and frequency difference did not adequately reflect the raised accuracy, therefore, needed a indicator comprehensive measured the error of the signal amplitude and phase. The error vector could clearly reflect the degree of damage of the signal, so the error vector magnitude parameters proposed [6]. EVM measurements of the vector difference between the actual signal waveforms with the theoretical reference signal, was the ratio of RMS error vector magnitude and the reference signal amplitude. EVM was a measure of the overall quality of the modulated signal, if you want to further analyze modulation quality factors were also needed to measure the code domain error [7].

Basis JJF1204-2008 TD-SCDMA digital mobile communications test instrument calibration specification, took direct measurement.

According to the method used, the measured output tester modulation error was expressed as the formula (1):

$$\Delta R = R_X - R_N \tag{1}$$

According to the formula (2):

$$u_c^2(\Delta R) = \sum \left(\partial f / \partial R_i\right)^2 u^2(R_i) \tag{2}$$

Variance as formula (3):

$$u_c^2 = c^2(R_X) \cdot u^2(R_X) + c^2(R_N) \cdot u^2(R_N) \tag{3}$$

Propagation coefficient as formula (4) and (5):

$$c(R_X) = \partial f / \partial R_X = 1 \tag{4}$$

$$c(R_N) = \partial f / \partial R_N = -1 \tag{5}$$

Select spectrum analyzer E4445A with vector analysis software 89601A spectrum as standard instrument, 8960 Mobile Phone Tester as measured instrument to do uncertainty evaluation [8].

Under reference conditions, use E4445A spectrum analysis instrument with TD-SCDMA Digital demodulation functions on the 8960 Mobile Phone Tester TD-SCDMA output digitally modulated signals of the EVM measurement repeated 10 times.

Standard deviation expressed as formula (6):

$$S = \sqrt{\frac{\sum_{i=1}^{n} \left(R_i - \overline{R}\right)^2}{(n-1)}} \tag{6}$$

Calculated by the data in the experimental, we can get standard uncertainty of measurement results from (6):

$$u_1 = S = 0.02\%$$

Standard uncertainty components expressed as formula (7):

$$u_2 = a_2 / k_2 \tag{7}$$

Check technical manuals that the E4445A measurement EVM value of the maximum allowable error was ± 1.00 %, $a_2 = 1.00$ %. Assumed that the

components were uniformly distributed, $k_2 = \sqrt{3}$. we could get the standard uncertainty components from formula (7):

$$u_2 = a_2/k_2 = \frac{1.00\%}{\sqrt{3}} = 0.58\%$$

The above component was independent and unrelated, we could get the combined standard uncertainty from formula (3):

$$u_c = \sqrt{u_1^2 + u_2^2} = 0.58\%$$

Taken to contain factor k = 2, the expanded uncertainty was:

$$U = k \cdot u_c = 1.2\%$$

4 Test Results Analysis

After testing, draw curve of the test results automatically at same frequency and different temperatures, and the contrast curve of the same frequency of manual testing and automated testing at same temperature. Shown in Fig. 3, at different temperatures, the same frequency point of the automatic measurement of EVM value fluctuations, but very smooth, showed that the stability of the system under different circumstances.

Shown in Fig. 4, at the same temperature, the contrast curve of the same frequency, manual testing and automated test showed that the accuracy of the automated testing. Thus, the automatic test method was reliable, high stability, and practical.

5 Conclusion

In this paper, the automatic calibration method for TD-SCDMA standard digital modulation quality parameters compared to manual testing, greatly improved the speed of measurement and saved the time of measurement. Meanwhile, repeated measurements after averaging that significantly improved the accuracy of measurement. The research of TD-SCDMA standard digital modulation quality parameters auto-calibration method, provided a good reference for automatic calibration of other standard digital modulation quality parameters, with the rise of 4G networks, the next step would research LTE standard calibration method, so as to realizing the automatic calibration of the LTE standard digital modulation quality parameters.

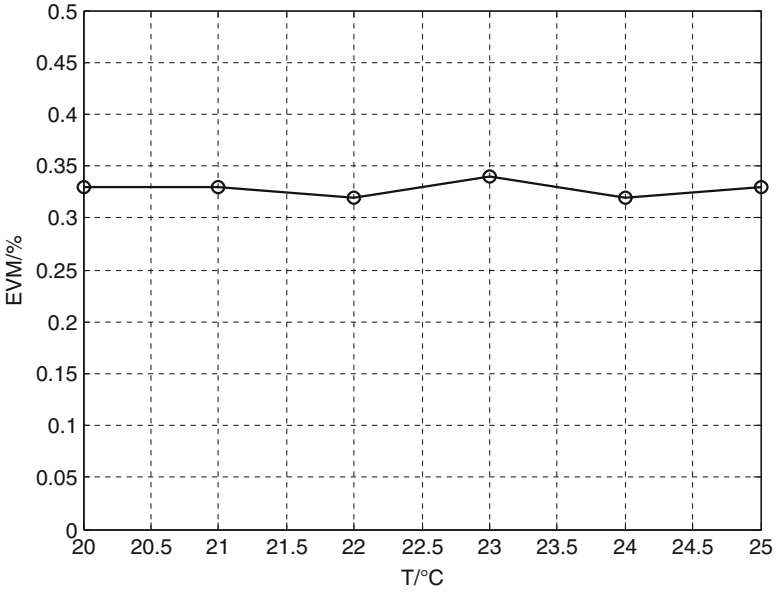

Fig. 3 EVM curve of the automatic measurement at different temperature

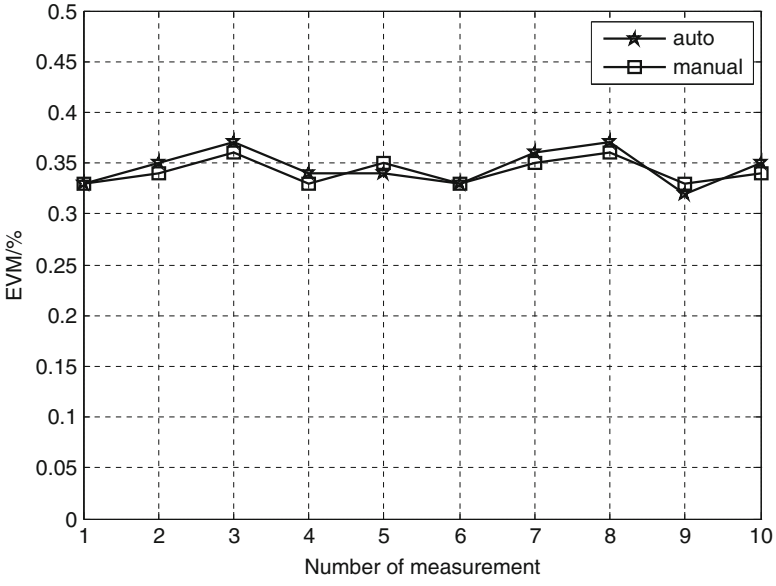

Fig. 4 The comparison of the manual and automatic measurement, under the same conditions

References

1. Qing JI (2007) Modern metering communications. Realize the GPIB-based automated test system with VB. 13(5):19–21
2. Qiu Hai Bo, Zhan Zhi Qiang, Zhao Ji Xiang et al (2011) China Institute of Metrology. The E5515C tester 1xEV-DO standard digital modulation parameter calibration. 22(2):139–143
3. Fan Xiu Li, Zheng Jian Hong, Chen Li et al (2005) TD-SCDMA, EVM testing and analysis. Journal of Chongqing College of Post and Telecom (Natural Science Edition) 17(2):156–159
4. Nassery A, Ozev S, Verhelst M et al (2011) Extraction of EVM from Transmitter system parameters. European Test Symposium (ETS), IEEE 33(5):75–80
5. Indrawati, Murugesan S, Raman M (2010) 3G mobile multimedia services (MMS) utilization in Indonesia: an exploratory research. Technol Soc (ISTAS) 21(5):145–155
6. Zhu Z, Zhang H, Shen L (2010) The application of structure arrays and files in the SCPI parsing system. Intell Comput Technol Autom (ICICTA) 15(6):710–713
7. Dasnurkar S (2009) Hybrid BiST solution for analog to digital converters with low-cost automatic test equipment compatibility. Circuit Syst ISCAS 14(7):9–12
8. Ross WA (2003) The impact of next generation test technology on aviation maintenance. IEEE Autotestcon 22(5):2–9

Adaptive Matching Interface Technology Based on Field: Programmable Gate Array

Xuejiao Zhao, Xiao Yan, and Kaiyu Qin

Abstract In order to handle the error happened when FPGA (Field-Programmable Gate Array) reads the data from the ultra-fast ADC. We studied and developed an adaptive matching interface based on the internal resources of FPGA. It can solve the problems occurred in high-speed reading of data between the FPGA and ADC. Based on the Xilinx Virtex-5 chip, guided by the phase-locked loop theory, and take advantage of the internal IP CORE of the Virtex-5, this study tried to construct a model which is able to predict and revise the phase of datas between the FPGA and ADC as well as to align the phase and read datas accurately. The model was designed to correct the error of phase matching which is caused by the delay time after the data entering into the internal FPGA chips and it can't be predicted while it was programming. Tests showed that the adaptive matching interface can totally apply to the adaptive reading of signal whose input rate is 0–250 MHz, and it can solve the problems happening in data reading between FGPA and ADC effectively by same peripheral devices.

Keywords FPGA • Adaptive • ADC interface matching • ISEDERS • Deserializer

1 Introduction

In recent years, Digital signal processing speed improved fast, also including the digital conversion chip. However, with the development of the ADC module speed, there are some new problems on using FPGA to read the ADC output data.

X. Zhao (✉) • X. Yan • K. Qin
Institute of Astronautics & Aeronautics, University of Electronic Science and technology of China, Chengdu, China
e-mail: 106906195@qq.com

W. Wang (ed.), *Mechatronics and Automatic Control Systems*, Lecture Notes in Electrical Engineering 237, DOI 10.1007/978-3-319-01273-5_101,

Especially in each FPGA synthesis process, ADC module output data matches to FPGA internal D flip-flop in the correct phase difficultly after entering different routes with its clock, because the internal wiring is different, device delay, input pin delay [1]. Thus it often leads to large amounts of data read errors. Even in the case that the clock frequency is variable, the relative phase relationship will still change with the frequency [2].

The traditional method is to constraint wiring before comprehension [2], or to calculate the wiring delay with graph theory and to modify the wiring considering the device delay after comprehension [3]. Each FPGA integrated wiring is different, so this method must modify delay values each time comprehension. But with the increase of the chip number, operability seriously decline. So it urgently needs adaptive matched interface that can be apply to most of the FPGA chips.

2 The Analysis of Data Read Principle and Traditional Method

2.1 Data Read Principle

For example, the 14-bit analog-digital converted chip ADC9642 of ADI company, shown in Fig. 1. There are seven output pins in the rising edge of DCO clock with seven even-numbered bit outputted. In the falling edge of DCO clock with seven odd-numbered bit outputted, and the sampling rate are 250 MSPS.

The 14-bit parallel ADC standard path of reading is shown in Fig. 2. Now take read of lowest bit D0/D1 in the seven-channel data for instance. Signal output from the ADC, with the arrival to the internal FPGA via pins.

$$DCO\_cycle = \frac{1}{Sample\_rate} \tag{1}$$

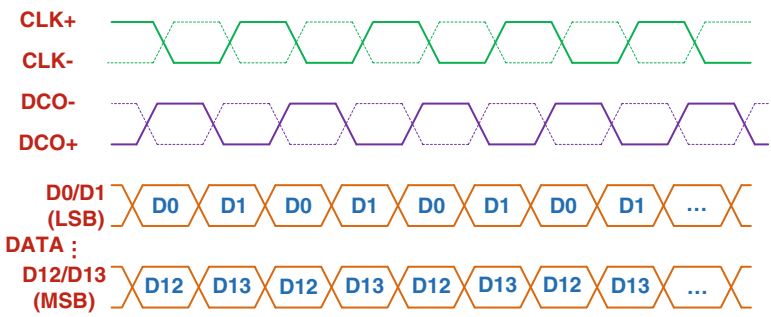

Fig. 1 The timing diagram of 14-bit high speed ADC

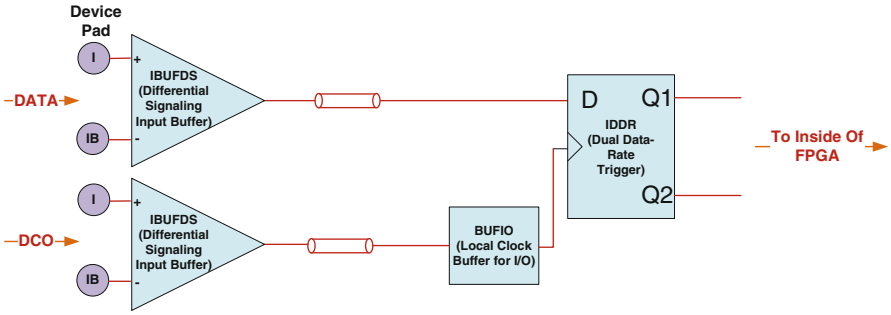

Fig. 2 The internal transmission path of DATA and DCO of FPGA

Known by the result of formula (1), the cycle of the DCO-outputting is 4ns, the delay of one device in the FPGA is about 4.5ns [4]. So, when the DCO and DATA get through the two paths with difference in devices and transmission line length to reach Dual D flip-flop within the FPGA, the initial phase relationship between DCO and DATA signals has lost [4]. But dual d flip-flop is still reading D0 and output to Q1 in accordance with the rising edge, falling edge to read the D1 and output to Q2, leading to a large number of errors in reading data. What is worse, wiring is different in each integration. When the routing path delay is just an integer multiple of the cycle after wiring, if its phase can align, then it is read correctly, otherwise it is wrong.

2.2 Traditional Method

2.2.1 Wiring Constrained

With proposition by some methods, as wiring delay can be calculated based on graph theory, we can adjust the wiring in accordance with its delay in after routing and adjust its delay to an integer multiple of the cycle [3].

Though this method has high accuracy, the actual operation is quite difficult in the actual work. For the difference in each wiring, calculation and adjustment to the wiring delay is necessary each time. Not only increase the workload in debug, but also wiring adjustment is required for each product while in mass production. Obviously, the feasibility of this method is not very high.

2.2.2 Constant Delay Time

It is suggested that after the DCO is read via the input buffer [5], the DCO get through the clock buffer and the module which can generate fixed delay, then get into the double D flip-flop to use a fixed waveform to help its “training”.

According to the effect of the output to modify the delay value of the fixed – delay module, until a delay value which make the output relatively stable is get.

In the same chip, each wiring is not very different, which can make the chip work in a safer range. But different FPGA chips differ much, it is impossible to use the same delay value to help the delay compensation [4]. Although this method is simple and feasible, but its portability is poor and the delay value is only an estimate with low accuracy.

2.2.3 Data Training

A way to send data in the training is proposed in the literature [6], solutions are proposed which apply to this problem according to the principle, whose internal link structure is similar to the fixed delay program. What the difference is that the ADC chip send a series of fixed data to the FPGA within a fixed period of time, the ASCII code sequence order of ABCD for instance. Within this period of time, FPGA compare the received data with local data, adjust the fixed delay if some differences occur, and will not stop the adjustment until the same training data is consistent with local data.

This method is accurate, but which is based on the cooperation between ADC and FPGA with each other. For the stabilization time of FPGA is not definite, the time of ADC sending a fixed sequence is difficult to accurately control, and will increase the turn-on time of the system. And the portability of this method is poor.

3 Implementation of Technology of Adaptive Interface Matching

3.1 Clock Interface of DCO

Again, take the ADC9642 LSB D0/D1 port and DCO as an example. As shown in Fig. 3, DATA and DCO pass through pad and input buffer, and then to ISEDERS front-end. The production process of the FPGA can guarantee that the delay time in this distance of DATA as well as DCO, so before entering ISEDERS input interface, the DATA and DCO are strictly in phase matching.

3.1.1 Description of Matching Interface of DCO

After entering the ISEDERS, DCO passes through the delay module of ISEDERS, then to BUFIO (clock-driver). Sample the input DCO with the output clock of BUFIO as the sampling clock of the ISEDERS. BUFR (clock frequency divider)

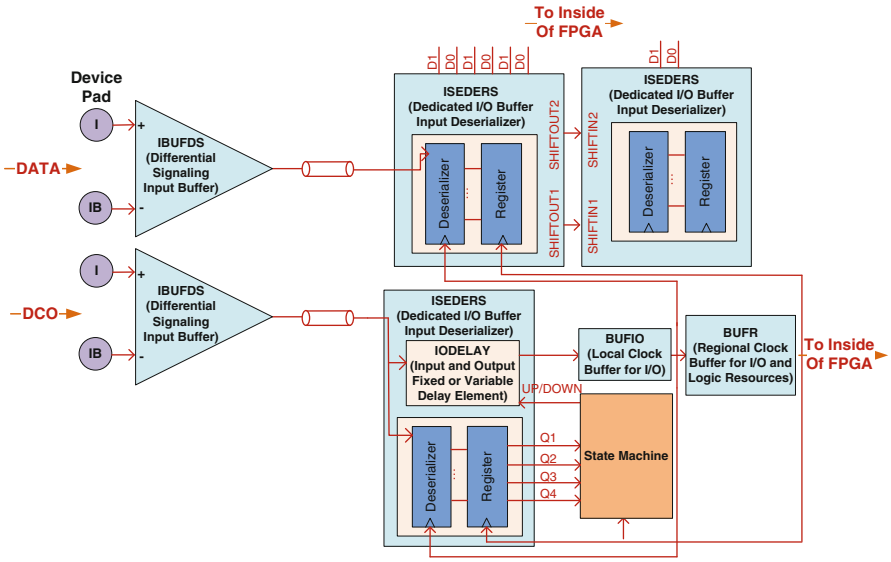

Fig. 3 Adaptive interface matching of ADC in FPGA

divide the input signal of BUFIO into four, then use to ISEDERS register as output clock and trigger clock of state machine [4]. ISEDERS works in SDR state, which is used to make sure that the sampling only happens at the positive edge of clock.

3.1.2 Operation of State Machine

The state machine is divided into five states.

STATE1: When use the output clock of BUFIO to sample the input clock of ISEDERS, if taken to a low level, the output sampling values of Q1, Q2, Q3, Q4 in Fig. 4 are all 0 s, we should increase the IODELAY TAP at that time, after that the sampling point will move to the right. Repeat testing until the output sampling values of Q1, Q2, Q3, Q4 are not 0 s, then stop increasing the IODELAY TAP and reduce 2 TAPS, so that the two clock edges align more accurately.

STATE2: When use the output clock of BUFIO to sample the input clock of ISEDERS, if taken to a high level, the output sampling values of Q1, Q2, Q3, Q4 in Fig. 5 are all 1 s. We should reduce the IODELAY TAP at that time, after that the sampling point will move to the left. Repeat testing until the output sampling values of Q1,Q2,Q3,Q4 are not 1 s, then stop reducing the IODELAY TAP and increase 2 TAPS, so that the two clock edges align more accurately.

STATE3: When use the output clock of BUFIO to sample the input clock of ISEDERS, if taken to a edge, the output sampling values of Q1, Q2, Q3, Q4 in Fig. 6 are neither all 0 s nor all 1 s we should increase or reduce the IODELAY TAP

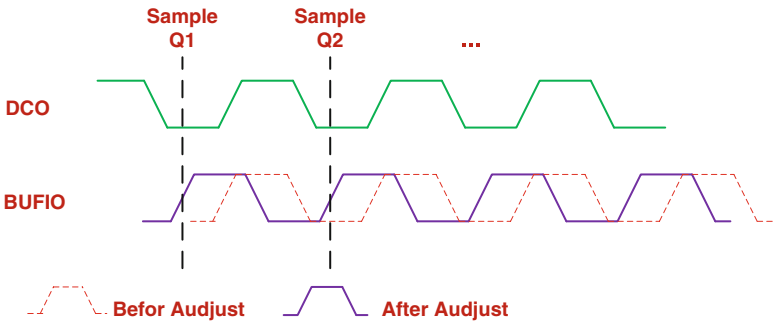

Fig. 4 Sampling to low level

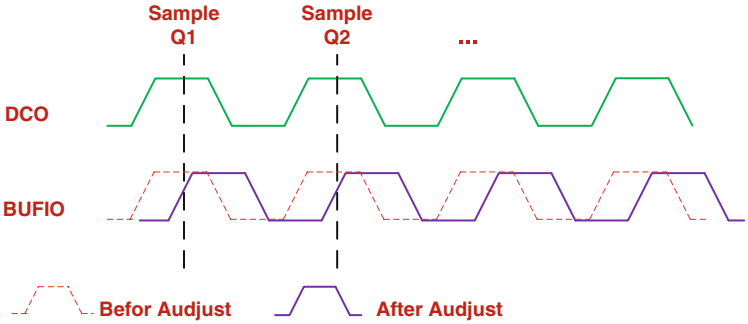

Fig. 5 Sampling to high level

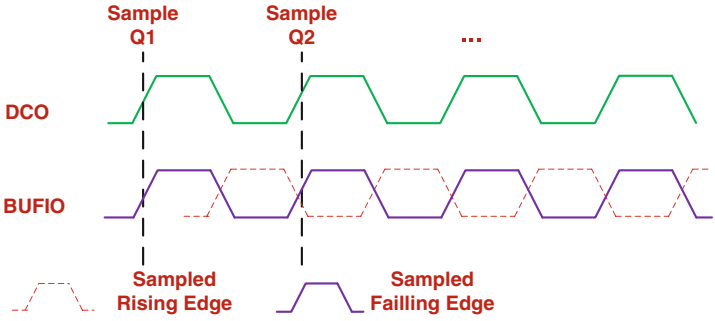

Fig. 6 Sampling to edge

at that time continuously. Repeat testing until the output sampling values of Q1, Q2, Q3, Q4 are all 0 s or all 1 s, then stop to go into the STATE1 or STATE1 for further operation.

STATE4: When the cycle is greater than 4.9 ns and less than 10 ns, it would not yet encountered electrical level conversion of Q1, Q2, Q3, Q4 although the 32 TAPS is full filled, the TAP will go back to 0 to re-start to accumulate automatically, and the

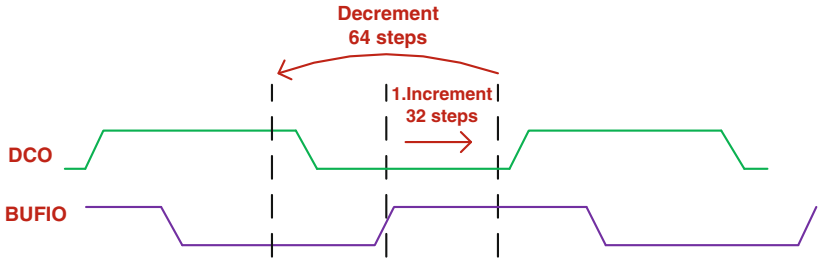

Fig. 7 The level converse when 32 TAP is full filled and went back to 0

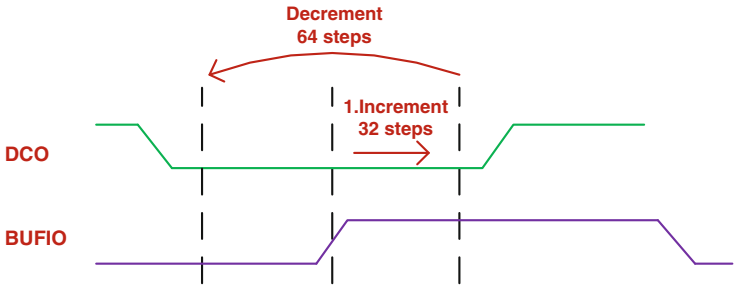

Fig. 8 The level do not converse when 32 TAP is full filled and went back to 0

electrical level will converse at that time. We can accumulate the TAPS which we increase at first. When the level conversion occurs and the value of accumulated register is 32, we can't see this situation as matching to edge acquiescently, instead we should go into STATE1 or STATE2 for a further operation according to the new level (Fig. 7).

STATE5: When the cycle is greater than 10 ns, the electrical level conversion of Q1, Q2, Q3, Q4 will not happen not only when the 32 TAPS is full filled, but also when the TAP go back to 0 to re-start to accumulate automatically. If you start to experience high level, increase the delay TAPS to the maximum. If you start to experience low level, reduce the delay TAPS to the minimum. Because when the cycle is greater than 10 ns, the impact of delay time of lines and devices to the matching of data and DCO is limited, so the approximate treatment is enough (Fig. 8).

3.2 DATA Interface of DCO

After the step 3.1, the sampling clock of ISEDERS of DATA route can use the clock which was adjusted. Because ISEDERS work in the DDR (sampling happen at both positive edge and negative edge) pattern [6], data wide should be set to 6, so to the output wide. Then we should use two ISEDERS cascade. As shown in Fig. 9, it's an

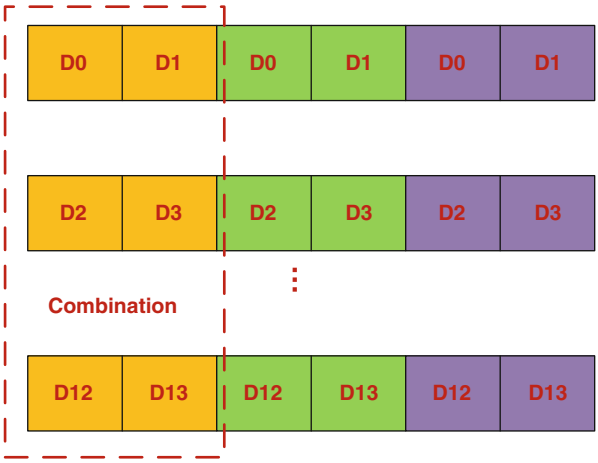

Fig. 9 The combination of output data

output data of a quarter of the frequency of the cycle, each line include six output data of a DATA route [7]. To combine each line of the two data which are shown in Fig. 9, we will gain a 14-bit data.

4 Output Effect of Experimental Platform

As shown in Fig. 10, before using the matching techniques described in this paper, the output effect is very poor and the wave contains too much ripples almost lose the original appearance of sine wave when putting the normal sine wave to the input port of the ADC. The phase of the DATA and DCO do not match, so the odd and even bit of DATA have reversed. After using adaptive ADC interface matching technique, the output effect is very perfect, as shown in Fig. 11 distinctly.

5 Conclusion

This technical structure and related software were confirmed completely in the real-time spectrum analyzer of Institute of Astronautics & Aeronautics UESTC (University of Electronic Science and Technology of China), which can work stably. The output effect is sound, and the error rate is reduced greatly after the simulation data is converted by the ADC and continued to input into FPGA. And it can run for quite a long time without any mistakes. This method can be used for other general engineering practices, and also it has certain reference value for other types of optimization of FPGA system.

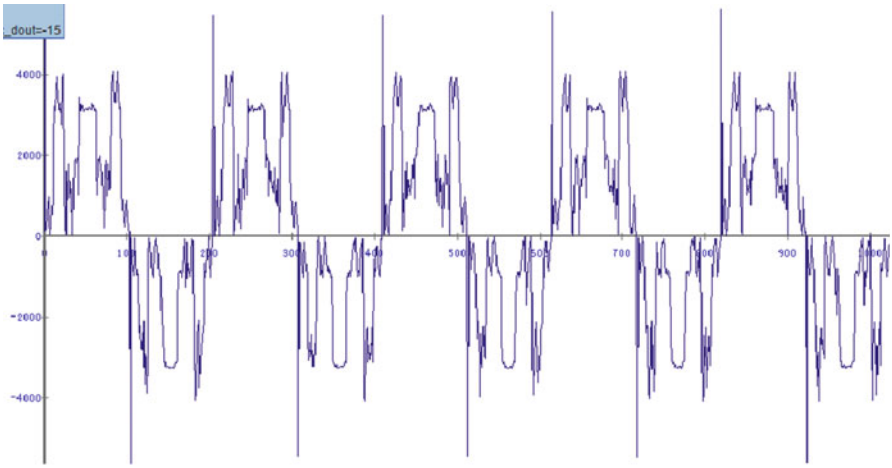

Fig. 10 The output wave before the using of matching techniques

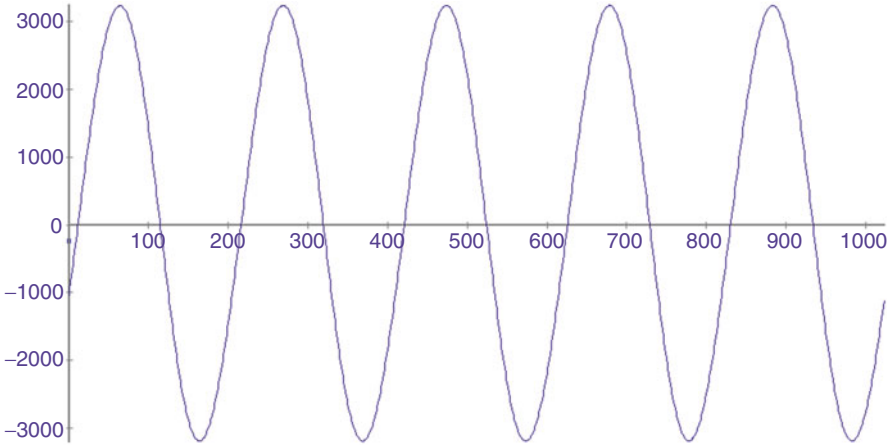

Fig. 11 The output wave after the using of matching techniques

References

1. Betz V (1998) Architecture and CAD for speed and area optimization of FPGAs[M]. Ph.D. thesis, National Library of Canada, University of Toronto
2. Guoxing Zhang, Junfeng Gao (2007) Adaptive synchronizer based on FPGA. Appl Integr Circ 348(06):63–65
3. Wang Chun-zao, Zhang Han-fu, Shi Liang (2007) The optimized design of routing switch and wire segment of FPGA. Electron Pack 52:27–29
4. Defossez M (2008) An interface for Texas instruments analog-to-digital converters with serial LVDS outputs, XAPP866 (v3.0). Available for download from http://www.xilinx.com. 7th Apr 2008

5. Betz V, Rose J (1999) FPGA routing architecture: segmentation and buffering to optimize speed and density[R]. In: FPGA '99 Proceedings of the 1999 ACM/SIGDA seventh international symposium on Field programmable gate arrays, Ann Arbor, Michigan, USA, pp 59–68
6. Luo Zhi nian, Li Si, Zhang Wenjun (2007) Improved frame synchronization algorithm for IEEE 802.11a. Comput Eng Appl 43(32):31–32
7. Wu GuangMing, Chang YaoWen (1999) Quasi-universal switch matrices for FDP design. IEEE Trans Comput 48(10):1107–1109

Power Grid Fundamental Signal Detection Based on an Adaptive Notch Filter

Zhi-xia Zhang, Xin-yu Zhang, Chang-liang Liu, and Tsuyoshi Funaki

Abstract In order to detect the power grid fundamental signal in the polluted environment, a new adaptive notch filter (ANF) algorithm is used in this paper. A prominent advantage of the algorithm is that it does not require a phase-locked loop (PLL) for the synchronization, but it can track the change of fundamental component automatically by adjusting its own parameters, γ and ζ. Empirical results show that the algorithm is simple and can offer a high degree of immunity and insensitivity to voltage mutations, harmonics, three-phase unbalanced and other types of pollution that exist in the grid signal. The ANF algorithm can accurately extract the real-time power grid fundamental signal in the polluted environment.

Keywords ANF • Fundamental signal estimation • Distributed generation (DG)

1 Introduction

With the development of distributed generation technology, the distributed generation technology is one of the important directions of energy technology development in the future. However, some problems of the grid voltage, such as, voltage swells/sags, phase shifts, frequency shifts and three-phase voltage unbalance etc. are often happen for grid-connected. These problems affect the detection of frequency, phase and amplitude of fundamental positive sequence voltage. Therefore, it is of an important significance to implement steady, accurate and real-time extraction of the fundamental component in grid [1–3].

At present, a variety of algorithms to detect the power grid fundamental signal were proposed by many domestic and foreign scholars. These algorithms can be

Z.-x. Zhang (✉) • X.-y. Zhang • C.-l. Liu • T. Funaki
Shenyang Agricultural University, Shenyang, China
e-mail: syzzx7@163.com

W. Wang (ed.), *Mechatronics and Automatic Control Systems*, Lecture Notes in Electrical Engineering 237, DOI 10.1007/978-3-319-01273-5_102,

mainly summarized into the following three stages. The first detection stage is based on a simple sinusoidal signal model. The primary methods in this stage are voltage zero-crossing method and maximum algorithm. The structural simplicity of this algorithm makes it desirable from the standpoint of implementation in both software and hardware environments. However, these methods ignore all harmonics and noises. Therefore, these two methods cannot be applied to detect the power grid fundamental signal in the polluted environment. The second detection stage is based on a cycle signal model. The primary method in this stage is the discrete Fourier transform (DFT). In fact, grid is in a dynamic state, and sometimes the fundamental frequency is changing. Therefore, there are spectral leakage and fence effect. The last detection stage is based on a complex signal model. The primary methods in this stage are wavelet transform, neural network, PLL based on *d-q* transformation and Kalman filtering. The characteristic of wavelet transform and neural network methods are large calculative volume and poor real-time. The cutoff frequency of low-pass filter in PLL is set relatively low in order to achieve good filtering, however, the low cutoff frequency will affect the dynamic characteristics of detection system. The Kalman filtering belongs to IIR filter and has unsure group delay, thus it is difficult to accurately calculate the phase angle of phasor [4–6].

This paper presents an ANF algorithm in order to settle this problems which are mentioned above. A prominent advantage of the algorithm is that it does not require a phase-locked loop (PLL) for the synchronization, but it can track the change of fundamental component automatically by adjusting its own parameters, γ and ζ. Therefore, ANF algorithm is real-time and accurate.

2 Synchronization Technique Based on ANF

2.1 ANF

An ideal notch filter whose frequency response is characterized by a unit gain at all frequencies except at a particular frequency, at which its gain is zero. This structure cannot make the particular frequency of signal pass, while the rest of frequency of signal can be passed completely. This particular frequency is called notch frequency. ANF can automatically adjust the notch frequency by tracking the change of signal frequency, which makes it possible that ANF can estimate fundamental component of voltage signal.

Very often, when a sinusoidal signal is contaminated, it can be modeled by [7]

$$y(t) = \sum_{k=1}^{\infty} A_k \sin \phi_k(t) + A_0 + n(t) \tag{1}$$

Where $f_k = \omega_k t + \varphi_k$ is phase angle of the k, A_k is amplitude of the k (k = 1, 2, ...), A_0 is the dc component, $n(t)$ is the noise. ϕ_k and A_k is typically unknown parameters. Estimating the unknown parameters is the key in this study.

The dynamic behavior of the ANF is characterized by the following set of differential equations:

$$\begin{cases} \ddot{x} + \theta^2 x = 2\zeta\theta e(t) \\ \dot{\theta} = -\gamma x\theta e(t) \\ e(t) = y(t) - \dot{x} \end{cases} \tag{2}$$

Where x is the state variable, θ is the estimated frequency, ζ and γ are adjustable positive parameters that determine the estimation accuracy and the convergence speed of ANF.

For a single sinusoid, $y(t) = A_1 \sin(\omega_1 t + \varphi_1)$. This ANF has a unique periodic orbit located at [2, 8, 9]

$$\mathrm{O} = \begin{pmatrix} \bar{x} \\ \dot{\bar{x}} \\ \bar{\theta} \end{pmatrix} = \begin{pmatrix} -A_1 \cos(\omega_1 t + \varphi_1) \\ A_1\omega_1 \sin(\omega_1 t + \varphi_1) \\ \omega_1 \end{pmatrix} \tag{3}$$

The third entry is the estimated frequency, ω_1. Dynamic equations in (2) are stable, which means that the proposed ANF is stable. We proceed with a discussion on the stability of the Eq. 2, and it can be rewritten as

$$\dot{\theta} \approx -\frac{\gamma}{2\zeta} x^2(\theta^2 - {\omega_1}^2) \tag{4}$$

That is, it is stable in the process of approaching periodic orbit O.

2.2 ANF Block Diagram

Figure 1 shows the schematic structure of ANF. At Eqs. 2 and 3, reveals that ANF is composed of adders, multipliers and integrators. The structure has two independent design parameters, γ and ζ. Parameters γ determines the adaptation speed. Parameters ζ determines the depth of the notch. However, increasing one of the parameters will affect the other factor. Therefore, A tradeoff between the accuracy and convergence speed can be carried out by adjusting design parameters, γ and ζ.

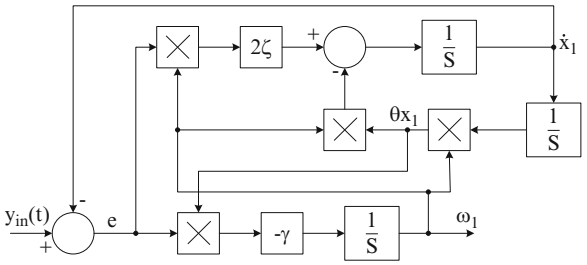

Fig. 1 Block diagram of ANF

3 Simulation Analyses

Under the Matlab7.6.0/Simulink, that uses the proposed algorithm to establish system simulation model and make an analysis. The parameters of ANF can set to $\zeta = 0.75$ *and* $\gamma = 800$. The initial condition for the integrator that outputs the frequency, ω, is set to $2\pi 50$ rad/s. The initial conditions for all other integrators are set to zero.

3.1 ANF Performance Evaluation

Figure 2 shows the tracking performance of ANF (there only gives the tracking characteristics of ANF on amplitude). Where, (a), (b), (c) are the input signal, the amplitude of input signal, and the error between input signal and extraction signal, respectively. At $t = 2$ *s*, the amplitude of input signal jumps from *1pu* to *0.75pu* [10]. The fast response and accurate performance of ANF can be seen from the Fig. 2.

3.2 Positive and Negative Sequence Extraction

In the abc frame, a three-phase voltage signal *u(t)* can be decomposed into $u(t) = u^{+}(t) + u^{-}(t) + u^{0}(t)$. Where, $u^{+}(t)$, $u^{-}(t)$ and $u^{0}(t)$ are positive, negative, and zero-sequence components, respectively. Its sequence components can be decomposed as follows [11, 12]:

$$\begin{cases} u^{+}(t) = T_2 X_1(t) + T_1 X_2(t) \\ u^{-}(t) = T_2 X_1(t) - T_1 X_2(t) \\ u^{0}(t) = (I - 2T_2) X_1(t) \end{cases} \tag{5}$$

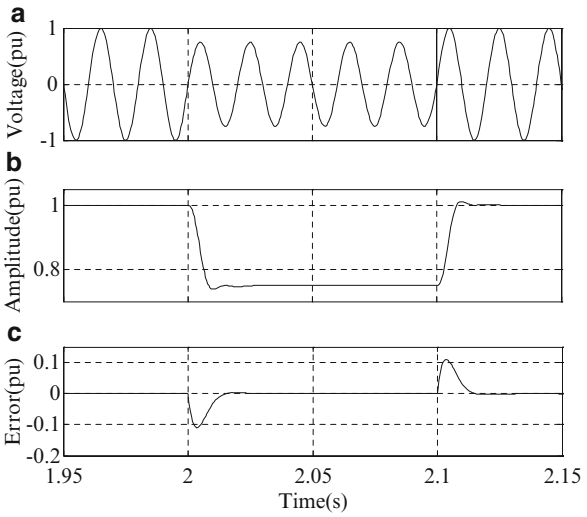

Fig. 2 Tracking performance of ANF

Where, $X_1(t)$ and $X_2(t)$ are the fundamental components of the input signal and its 90° phase shift, respectively. I is a 3×3 identity matrix, T_1 and T_2 are 3×3 matrixes. As follows:

$$T_1 = \frac{1}{2\sqrt{3}} \begin{pmatrix} 0 & 1 & -1 \\ -1 & 0 & 1 \\ 1 & -1 & 0 \end{pmatrix} \tag{6}$$

$$T_2 = \frac{1}{3} \begin{pmatrix} 1 & -0.5 & -0.5 \\ -0.5 & 1 & -0.5 \\ -0.5 & -0.5 & 1 \end{pmatrix} \tag{7}$$

From the above, the positive-sequence and negative sequence extractor unit can be comprised of three ANFs and simple arithmetic operators. ANFs adaptively extract the fundamental voltages and their 90° phase shift. That is, $X_1(t)$ and $X_2(t)$.

The simulation results are shown in Fig. 3.

Under Matlab/Simulink, that uses electronic components to set up a signal model which can produce polluted signal (Fig. 3a). The positive, negative components of fundamental signal can be extracted after those treatments. It can be seen from the Fig. 3 that the system will be able to accurately extract the positive sequence and negative sequence components of fundamental signal after two cycles (Fig. 3b, c).

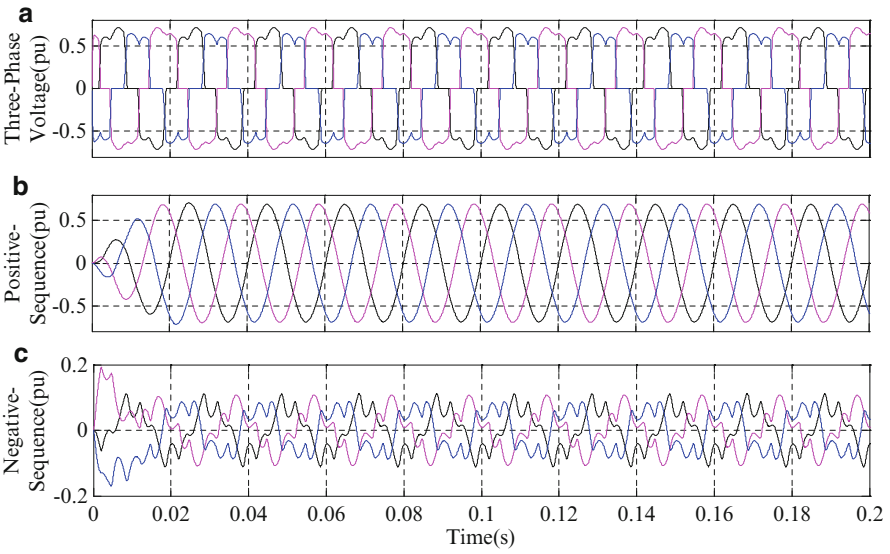

Fig. 3 Extract the fundamental positive, negative sequence component

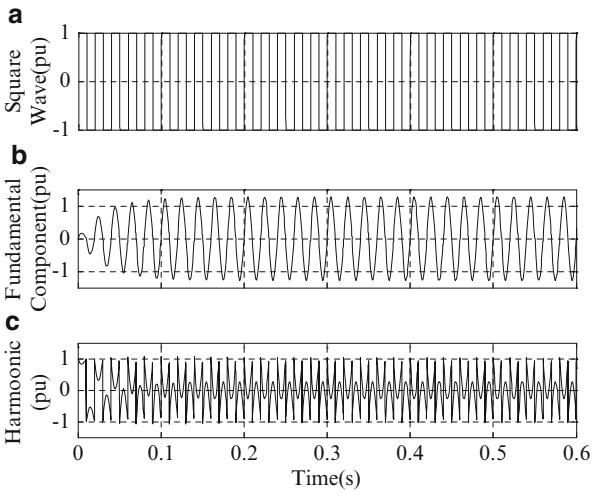

Fig. 4 Extraction of the square wave

3.3 Harmonic Extraction

In this section, a square wave as an example. The fundamental signal can be extracted by ANF, the simulation results are shown in Fig. 4.

Under Matlab/Simulink, a square wave signal can be generated by M-File. Then, a simulation model is established to extract the fundamental signal. It can be seen from the Fig. 4 that the system can effectively isolate from its fundamental and total

harmonic distortion components, and output their values after five cycles. The M-File of square wave signal can be rewritten as

```
clear all;
t=(0:0.0001:10)';
for c=1:500
for m=(200*(c-1)+1):(200*c-100); u1(m)=1; end;
for m=(200*(c-1)+1+100):(200*c); u1(m)=-1; end; end;
u1(100001)=1;u=u1';plot(t',u');axis([0  10  -1.5  1.5]);
grid on;
```

4 Conclusion

In this paper, a series of simulation examples illustrated that the rapidity and accuracy of ANF in extracting the fundamental component in the polluted environment. A prominent advantage of the approach is that it does not require a PLL for the synchronization, but it can accurately extract the fundamental component in real-time grid by adjusting its own parameters. In the three-phase unbalanced system, the positive sequence component and negative sequence component can be extracted by ANF, and in the harmonic pollution environment, the fundamental and harmonic distortion components can be extracted by ANF. The principle of this algorithm is reliable and simple, so it has a high practical value.

References

1. Chu Zhao-bi (2009) Adaptive notch filter-based time-frequency analysis of signals in power system[D]. Hefei University of Technology, Hefei
2. Chu Zhao-bi, Zhang Chong-wei, Feng Xiao-ying (2010) Adaptive notch filter-based frequency and amplitude estimation. Acta Automat Sin 36(1):60–66
3. Zou San-hong, Pei Wei, Qi Zhi-ping (2010) Common interface for interconnection between distributed generation and microgrid. Autom Elec Power Syst 34(3):91–95
4. Mai Rui-kun, He Zheng-you, He Wen et al (2010) Adaptive frequency tracking algorithm for power systems. Proc CSEE 30(16):73–78
5. Zhang Shi-ping, Zhao Yong-ping, Zhang Shao-qing et al (2003) A novel approach to measurement of power system frequency using adaptive notch filter. Proc CSEE 23(7):81–83
6. Zhang Zhi-xia, Piao Zai-lin, Guo Dan, Xie Ying (2012) A kind of phase-locked loop for power system. Trans China Electrotech Soc 27(2):250–254, 222
7. Mojiri M, Karimi-Ghartemani M, Bakhshai A (2007) Estimation of power system frequency using an adaptive notch filter. IEEE Trans Instrum Meas 56(6):2470–2477
8. Mojiri M, Bakhshai AR (2007) Estimation of n frequencies using adaptive notch filter. IEEE Trans Circ Syst 54(4):338–342
9. Mojiri M, Bakhshai AR (2004) An adaptive notch filter for frequency estimation of a periodic signal. IEEE Trans Autom Control 49(2):314–318

10. Zhang Bin, Zhang Dong-lai (2011) Adaptive fundamental component extraction and frequency tracking algorithm for power systems. Proc CSEE 31(25):81–89
11. Karimi-Ghartemani M, Iravani MR (2004) A method for synchronization of power electronic converters in polluted and variable-frequency environments. IEEE Trans Power Syst 19 (3):1263–1270
12. Du Xiong, Wang Li-ping, Li Shan-hu et al (2012) A voltage synchronization method with adaptive frequency response. Proc CSEE 32(4):115–121

The Precise Electric Energy Measurement Method Based on Modified Compound Simpson Integration

Min Zhang, Huayong Wei, and Weimin Feng

Abstract In time domain the asynchronous sampling is easy realized in hardware, but it leads to measurement error in energy measurement. Modified compound Simpson integral method is proposed to reduce the error. The computing formula is deduced. Ideal signals and distortion signals are simulated. Simulating results show the proposed integral method has the highest precision, compared with previous method, the precision is improved dramatically. The results also show the sampling rate has little influence on the measurement accuracy. So the new algorithm is practical and is easy realized by DSP.

Keywords Asynchronous sampling • Leakage error • Modified compound Simpson integral method • Electric energy measurement

1 Introduction

With the far-ranging use of non-linear components in electric and electronic devices, the electrical harmonic pollution has deteriorated the power quality in electrical power networks significantly. The harmonic distortion of voltage and current greatly affects on the accuracy of electric energy measurement [1]. In order to improve the measurement accuracy, many methods have been proposed. These methods measure the energy in time domain or in frequency domain. In time domain the precise measurement methods are used such as Newton-Cotes integration algorithm [2] and Compound Trapezoidal [3]; the error caused by window

M. Zhang (✉) • H. Wei
Xinyang Power Supply Company, Henan, China
e-mail: peidiandianlan@yahoo.cn

W. Feng
College of Electric and Information Engineering, Zhenzhou University of Light Industry, Zhengzhou, China

W. Wang (ed.), *Mechatronics and Automatic Control Systems*, Lecture Notes in Electrical Engineering 237, DOI 10.1007/978-3-319-01273-5_103,

function is corrected in time domain [4]. The time domain methods are low processing time and easy applicability for digital signal processors, but are very sensitive to the presence of harmonic and inter-harmonic components [4]. The frequency domain methods use DFT to obtain the harmonics amplitude and phase angle, then the power is calculated according to harmonics respectively. The data is smoothed by window function, then reduce the leakage effects [5]; an overview of active power measurement has been made and a new method is proposed infrequency domain [6]; a new decomposition of voltage, current and power is presented to improve the accuracy [7]. In order to improve the accuracy of electric energy measurements of harmonic in the complex industrial environment, the wavelet packets decomposition and reconstruction algorithm are employed [8].

At present, the electric energy measurements are mainly based on the synchronized sampling of signals. The synchronized sampling is realized by using PLL (Phase Locked Loop) [4]. However, synchronized sampling is not normally provided for in practical applications. So the electric energy measurement based on synchronous sampling has larger measurement error. In order to improve the measurement precision, some error compensation algorithms are presented according to the asynchronous sampling [3, 5, 9]. In this paper, Modified Compound Simpson Integration algorithm is proposed to improve the energy metering accuracy.

2 Algorithm Principle

A periodic signal $f(t)$, T is the fundamental cycle time and the fundamental frequency is $f = 1/T$. According to the Nyquist sampling theorem, if the maximum frequency component of the signal is $f_{\max}$, the sampling rate f_s must be higher than $2f_{\max}$. N points are sampled in one fundamental cycle, so the interval of ideal synchronous sampling $\Delta T = T/N$. But the synchronous samplings are difficult to realize because of harmonics and noise pollution. If the sampling rate f_s is fixed, so sampling time is $T_s = 1/f_s$. The ratio of the fundamental cycle T and T_s can be expressed as: $T = T_s(N + \Delta)$ $(0 \leq \Delta < 1)$. Where N is integers and Δ is a fraction. In order to improve the measurement accuracy, Δ must be calculated precisely.

An asynchronous sampling is shown in Fig. 1. $f_0(N)$ and $f_1(N)$ are the last sampling values of the first and second cycle respectively; $f_1(0)$ and $f_2(0)$ are the first sampling values of the first and second cycle respectively. From the picture can be seen: $f_0(N)$ and $f_1(0)$ are opposite sign, so $f_0(N)^* f_1(0) \leq 0$. There is a zero between $f_0(N)$ and $f_1(0)$. Likewise, $f_2(0)^* f_1(N) \leq 0$, there is always a zero between $f_1(N)$ and $f_2(0)$. According to the value of several points, the value of $\triangle$ can be calculated.

If the sampling frequency f_s is high, the sampling time-interval T_s between $f_0(N)$ and $f_1(0)$ is very small, the connection of the two points can be approximated as a straight line. In the second cycle, according to linear interpolation, the time delay Y_s can be calculated which is the time interval between the starting point of this cycle and $f_1(0)$. Y_s can be expressed as:

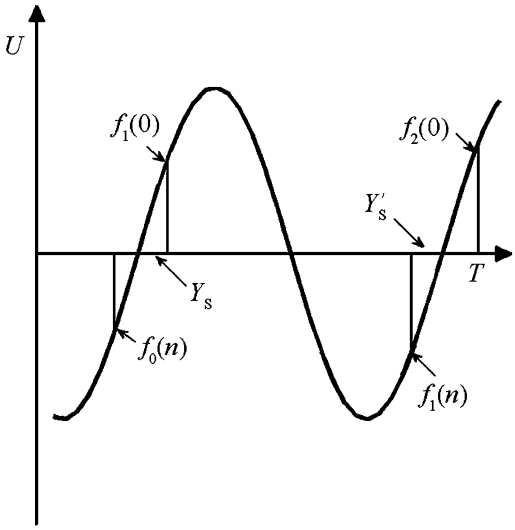

Fig. 1 Schematic of sampling error of asynchronous

$$Y_s = \Delta_1 {}^* T_s = \frac{f_1(0)}{f_1(0) - f_0(N)} {}^* T_s \tag{1}$$

Similarly, the time interval $Y_s{}'$ between $f_1(N)$ and the ending point of this cycle can be expressed as:

$$Y_s{}' = \Delta_2 {}^* T_s = \frac{-f_1(N)}{f_2(0) - f_1(N)} {}^* T_s \tag{2}$$

So: $\Delta = \Delta_1 + \Delta_2$.

In order to improve the accuracy, The Compound Trapezoidal is used in [3], the formula has been given in the paper, and we do not write it here.

The compound Simpson integration is also a useful method in improving measurement accuracy, it can be expressed as:

$$\begin{aligned} S_n = \frac{1}{T}\int_0^T f(t)dt = \frac{1}{T}\sum_{k=0}^{n/2-1}\int_{2k^*\Delta T}^{(2k+2)\Delta T} f(t)dt = \frac{1}{T}\sum_{k=0}^{n/2-1}\frac{1}{3}(f(2k^*\Delta T) + 4f((2k+1)^*\Delta T) \\ + f((2k+2)^*\Delta T))^*\Delta T \approx \tfrac{1}{3^*n}[f(0) + f(n^*\Delta T) + 2\sum_{k=1}^{n/2-1} f(2k^*\Delta T) \\ + 4\sum_{k=0}^{n/2-1} f((2i+1)^*\Delta T)] \end{aligned} \tag{3}$$

In practice, the frequency of power system is always fluctuated with time. If the sampling frequency is fixed, the signals are asynchronous sampling. Then the fraction Δ will bring leakage error. In order to reduce the leakage error, the modified compound Simpson integration is presented. It is shown as below:

$$\begin{aligned} S_{nm} &= \frac{1}{T}\int_0^T f(t)dt = \frac{1}{T}\left[\sum_{k=0}^{N/2-1}\int_{2k^*T_s}^{(2k+2)T_s} f(t)dt + \int_{N^*T_s}^{(N+\Delta)^*T_s} f(t)dt\right] \\ &\approx \frac{1}{T}\left[\frac{1}{6}\sum_{k=0}^{N/2-1}(f(2k^*T_s)+4^*f((2k+1)^*T_s)+f((2k+2)^*T_s))^*2^*T_s\right. \\ &\quad \left.+\frac{1}{2}{}^*\Delta^*(f(N^*T_s)+f((N+\Delta)^*T_s)^*T_s\right] \\ &= \frac{1}{6^*(N+\Delta)}\left[2^*(f(0)+f(N^*T_s)+2\sum_{k=1}^{N/2-1} f(2^*k^*T_s)\right. \\ &\quad \left.+4\sum_{k=0}^{N/2-1} f((2^*k+1)^*T_s))+3^*\Delta^*(f(N^*T_s)+f(0))\right] \end{aligned} \tag{4}$$

3 Simulation and Result Analysis

The input sinusoidal voltage and current are:

$$u(t) = \sqrt{2}V_p \sin(2\pi ft) \tag{5a}$$

$$i(t) = \sqrt{2}I_p \sin(2\pi ft + \alpha) \tag{5b}$$

The average (active) power is:

$$P = \frac{1}{T}\int_0^T u(t)^*i(t)dt = \frac{V_p{}^*I_p}{T}\int_0^T [\cos\alpha - \cos(4\pi ft - \alpha)]dt \tag{6}$$

The active power is calculated by the three methods (Compound Trapezoidal integration, Compound Simpson integration and Modified compound Simpson integration are aforementioned). All the simulating programs are written in C# language and are simulated in personal computer. The simulating time is 10 cycles.

Table 1 The simulating results of sinusoidal signal (f = 49.8 Hz)

Delay Y_s	Compound Trapezoidal integration (%)	Compound Simpson integration (%)	Modified compound Simpson integration (%)
0	0.418582	0.418916	8.806647×10^{-5}
0.3 T_s	0.398320	0.398638	8.380354×10^{-5}
0.5 T_s	0.384621	0.384928	8.092129×10^{-5}

3.1 Sinusoidal Signal

Given the input voltage $u(t) = 220^* \sin(2\pi ft)$.

The current waveform $i(t) = 20^* \sin(2\pi ft + \theta)$.

Where f is the fundamental frequency, $f = 49.8Hz$, $\theta = \pi/3$. The sampling frequency is $f_s = 6400Hz$. The input average power is 1,100 W per cycle.

Table 1 shows the results of the three different methods. From the table we can see Compound Trapezoidal integration and Compound Simpson integration almost have the same accuracy. But compared with the Modified compound Simpson integration, these two methods bring larger error, the error rate maintains at 0.385 %. While the results of proposed method show that the computation errors are very small and are all under 10^{-6}. The results illustrate the proposed method improve the precision dramatically. It means that the method can be used to design the high-precision power measurement equipment. From the table we can see also, if Ys are taken into account (Ys is the interval between the sampling start time and the origination time of the signals), the computation errors of these three methods have little changed and are at least of a similar order of magnitude. So, when discussing these three methods, Ys can be taken no account of.

3.2 Non-sinusoidal Signal

In the electrical power system, the input voltage and current generally include some harmonic waves. So the input voltage and current waveforms are non-sinusoidal and are same as [3]:

$$u(t) = 220^* \sin(2\pi ft) - 20^* \sin\left(2\pi f + \frac{\pi}{3}\right) + 2.5^* \sin\left(6\pi f + \frac{\pi}{3}\right) + 2.5^* \sin\left(10\pi f + \frac{\pi}{3}\right) + 2.5^* \sin\left(14\pi f + \frac{\pi}{6}\right) \tag{7a}$$

$$i(t) = 20^* \sin\left(2\pi f + \frac{\pi}{3}\right) + 2.5^* \sin\left(6\pi f + \frac{\pi}{6}\right) + 2.5^* \sin(10\pi f) + 2.5^* \sin\left(14\pi f + \frac{\pi}{6}\right) \tag{7b}$$

Table 2 The simulating results of non-sinusoidal signal (f = 49.8 Hz)

Delay Y_s	Compound Trapezoidal integration (%)	Compound Simpson integration (%)	Modified compound Simpson integration (%)
0	0.551523	0.553543	5.452108×10^{-4}
0.3 Ts	0.526144	0.528120	5.331358×10^{-4}
0.5 Ts	0.508808	0.510752	5.246681×10^{-4}

Table 3 The simulating results of non-sinusoidal signal (f = 50.2 Hz, Ys = 0.3 Ts)

Sampling rate	Compound Trapezoidal integration(%)	Compound Simpson integration(%)	Modified compound Simpson integration(%)
1.6 kHz	0.612635	0.684873	7.6663699×10^{-3}
3.2 kHz	0. 580093	0. 589462	7.7982671×10^{-4}
6.4 kHz	0. 529072	0. 524328	4.9546879×10^{-4}

Where f is the fundamental frequency and f_s is the sampling frequency, $f_s = 6400Hz$. The real input average power is 909.375 w. The simulating results are shown in Table 2.

The simulation results of Table 2 are similar to Table 1. The Modified compound Simpson integration is more precise than other two methods, while Compound Trapezoidal integration and Compound Simpson integration have the same accuracy. But compared with the results of Table 1, the harmonics have great affluence on the measurement accuracy of the modified compound Simpson integration, an order-of-magnitude has been decreased. Because the Compound Trapezoidal integration and Compound Simpson integration have lower precision, the results of the two methods have been affected little. Similarly to ideal signals, the delay Ys has little affected on measurement.

The signals have been simulated with three different sampling rates, the signal frequency is $f = 50.2$ Hz. All the results are shown in Table 3. We can see that the bigger the sampling rate is, the higher the precision of all integration methods is. Among these integrations, the precision of Modified Compound Simpson integration is highest. We can also see that at sampling rate 3.2 and 6.4 kHz, the error of the proposed method is below 10^{-6}. The results illustrate this method is fitted in lower sampling rate.

In the last, the active power of non-ideal signals is test in a DSP Development Board, all the sampling date are input the DSP and calculate by the Modified Compound Simpson Integration. The experimental results illustrate the proposed method is effective.

4 Conclusion

The modified compound Simpson integration has been proposed to improve measurement accuracy under asynchronous sampling. The computing formulas are deduced. Ideal signals and distortion signals are simulated and the results are compared with other methods. The results show the proposed method has the highest precision in different frequency of signals; the delay sampling time has little influence on measurement accuracy. Different sampling rate has also been simulated; the results show when the sampling rate is high to some extent, increasing the sampling rate has little influence on the accuracy. Simulation and experimental results show that the modified compound Simpson integration improves the accuracy of energy measurement dramatically. So the proposed method has the characteristics of generality, less calculation, high velocity and high efficiency and can be used in DSP easily.

References

1. Kusˇljevic´ MD, Tomic´ JJ, Marcˇetic DP (2009) Active power measurement algorithm for power system signals under non-sinusoidal conditions and wide-range frequency deviations. IET Gener Transm Distrib 3(1):57–65
2. Yi LQ, Song HN (2010) The application of compound Newton-cotes integral algorithm to energy measurement. Electr Meas Instrum 47(10):15–19 (In Chinese)
3. Feng WM, Shi BS, Wu ZJ (2011) The electric energy measurement method based on modified trapezoidal integral. In: International conference on electronics, communications and control, Ningbo, China, pp 2914–2917
4. Novotny M, Sedlacek M (2009) Measurement of active power by time-domain signal processing. Measurement 42(8):1139–1152
5. Agrez D (2008) Power measurement in the non-coherent sampling. Measurement 41:230–235
6. Sedlacek M, Stoudek Z (2011) Active power measurements–an overview and a comparison of DSP algorithms by noncoherent sampling. Metrol Meas Syst XVIII(2):173–184
7. Ortiz A, Ma˜nana M, Renedo CJ (2011) A new approach to frequency domain power measurement based on distortion responsibility. Electr Power Syst Res 81:202–208
8. Teng Zhaosheng, Luo Zhikun, Sun Chuanqi et al (2010) Harmonic energy measurement based on wavelet packet decomposition and reconstruction algorithm. Trans China Electrotech Soc 25 (8):200–206 (In Chinese)
9. Nyarko D, Stromsmoe KA (1991) Analysis of truncation errors in asynchronous sampling of periodic signals. In: Proceedings of the 34th Midwest symposium on circuits and systems, Monterey, vol 2, pp 1117–1120

A Frequency Reconfigurable Microstrip Patch Antenna

Yong Cheng, ZhenYa Wang, XuWen Liu, and HongBo Zhu

Abstract A novel microstrip antenna with the frequency reconfiguration characteristic is proposed in this article. A U-slot has been introduced in the square patch. The slot is switched on and off by using three PIN diodes, which realizes the frequency reconfiguration characteristics. The antenna has been studied with Zeland's IE3D, simulated return loss and radiation results are proposed in this article. As the results show, from 3.85 to 7.05 GHz, the antenna can operate at six different frequencies with similar radiation patterns. The antenna has 2 dB gain flatness with the maximum gain being 5 dBi over the whole range. The conclusion that radiation performance within the operating bandwidth of the antenna is stable can be obtained.

Keywords Frequency • Reconfigurable • Antenna microstrip antenna • PIN diode

1 Introduction

Frequency reconfigurable antennas have the advantages of compact size, multiband capability. As the same time, the shape of the radiation patterns of the antennas must maintain unchanged when the operating frequencies are switched from one band to the other. Various methods have been reported in the literature to achieve reconfigurable antennas such as using PIN switches tuning the antenna [1], varying the ground plane electrical length [2] supporting a patch antenna or changing the

Y. Cheng (✉) • Z. Wang • X. Liu • H. Zhu
College of Electronics Science and Engineering, Jiangsu Key Laboratory of Wireless Communications, Nanjing University of Posts and Telecommunications, Nanjing, China
e-mail: chengy@njupt.edu.cn

W. Wang (ed.), *Mechatronics and Automatic Control Systems*, Lecture Notes in Electrical Engineering 237, DOI 10.1007/978-3-319-01273-5_104,

induced electric current distribution [3]. The reconfigurable operating frequencies [4] obtained by switching different feeding location. Several reconfigurable antenna designs [5, 6] has been reported for the flexibility of integrating electronic switches.

In this article, a frequency reconfigurable microstrip patch antenna is investigated. The reconfiguration has been carried by etched a U-slot into the patch. The frequency characteristic has been realized by switching three PIN diodes on the slot on and off configurations. The geometrics of the antenna and the results will be explained in next sections. The full-wave electromagnetic simulation and analysis for the proposed antenna has been performed using Zeland's IE3D, which is based on the Method of Moments (MoM). Return loss, radiation pattern and the gain of the antenna are simulated and the results are presented. The antenna shows similar pattern and flat gain at different operating frequencies.

2 Design of the Antenna

The geometry and coordination of the antenna is shown in Fig. 1. It is a microstrip patch antenna with a U-slot. The antenna has been designed on a PCB with the relative permittivity of the dielectric substrate is 2.2, loss tanδ is 0.001, thickness h = 3 mm and surface area is A × B. To obtain the configurable frequency characteristic, Three PIN diodes has been used as switches. PIN diode1, 2 and

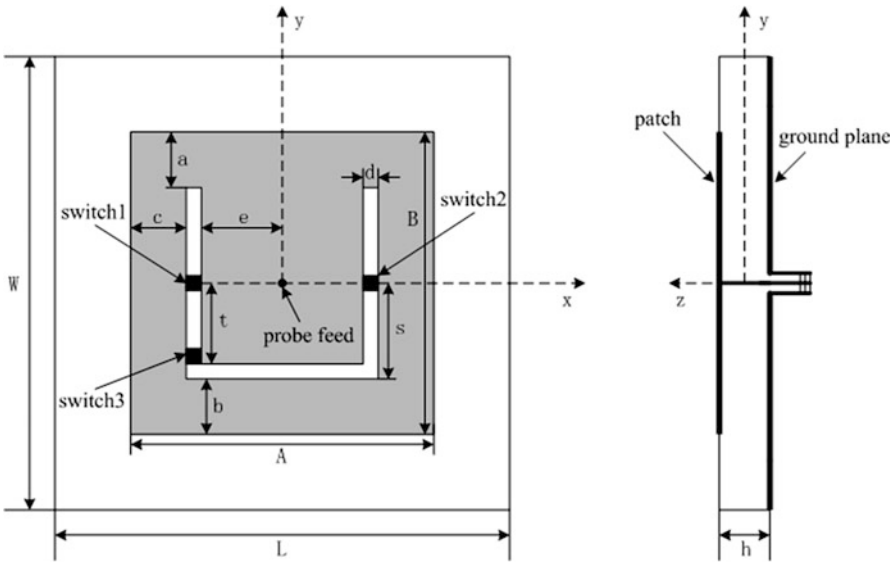

Fig. 1 Geometry of the proposed reconfigurable antenna

Table 1 Dimension parameters (mm)

L	30	c	4
W	30	d	0.5
A	20	e	5.5
B	20	t	5.5
a	4	s	6
b	4	h	3

PIN diode3 have been inserted the gap between the side and the center part of the patch. By switching the diodes on and off, the resonating frequencies of the antenna have been controlled. A coaxial probe is used to feed the antenna at the center of the patch. Detail dimension parameters of the antenna are shown in Table 1.

3 Results of Simulation

The return loss of the proposed antenna has been simulated with IE3D at five switch configurations as shown in Table 2. The simulation results for different cases of switches combinations is shown in Fig. 2

From Fig. 2, the operating frequency have been controlled by the switches configurations. At case1, the three switches are all on, the resonating frequency of the antenna is 5.05 GHz; When switch1 is on while the others are off, the resonating frequency of the antenna is 5.5 GHz; When switch1 and switch2 are both on, switch3 is off, the antenna resonates at 3.85 and 6.1 GHz;When switch1 and switch3 are both on, switch2 is off, the antenna resonates at 5.95 GHz; When the three switches are all off, the antenna operates at 7.05 GHz. In the above six bands, the return loss of the antenna is less 15 dB as shown in Table 2.

Then, the E-plane and H-plane radiation patterns of the antenna at six frequencies have been simulated and shown in Figs. 3, 4, 5, 6, 7 and 8, respectively. As the results show, the radiation patterns of the antenna are similar at the six frequencies. That performance is very important for a frequency reconfigurable antenna.

Finally, the maximum gain of the proposed antenna also has been simulated from 3.85 to 7.05 GHz, and the result is shown in Fig. 9. It is seen that the average maximum gain of the antenna is about 5 dBi, and the antenna has 2 dB gain flatness from 3.85 to 7.05 GHz. From the simulated results of the radiation patterns and gain, it can be obtained the conclusion that the proposed antenna has stable performance within the whole operating frequency range.

Table 2 Operating frequency bands and bandwidth for different cases

Case	Switch1	Switch2	Switch3	Center frequency (GHz)	Bandwidth
Case1	Off	Off	Off	5.05	4.952–5.115(3.24 %)
Case2	On	Off	Off	5.5	5.405–5.572(3.04 %)
Case3	On	On	Off	3.85/6.1	3.844–3.895(1.32 %)/ 6.06–6.147(1.43 %)
Case4	On	Off	On	5.95	5.882–6.024(2.39 %)
Case5	On	On	On	7.05	6.954–7.115(2.29 %)

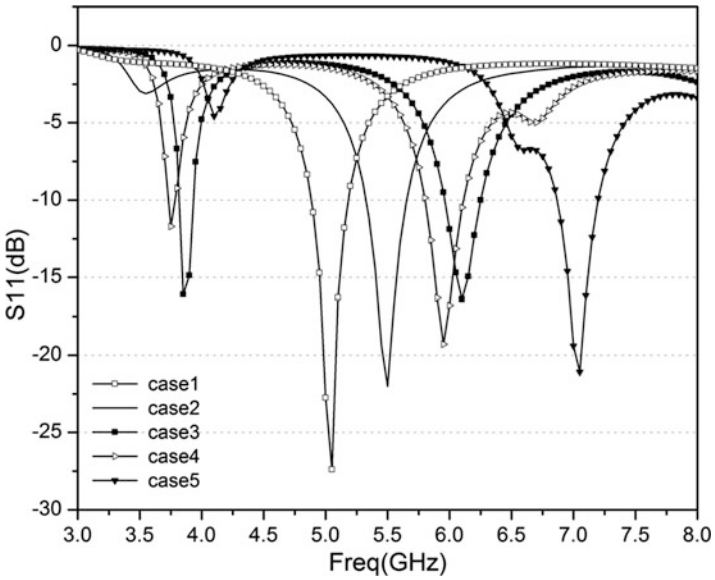

Fig. 2 S_{11} for different cases

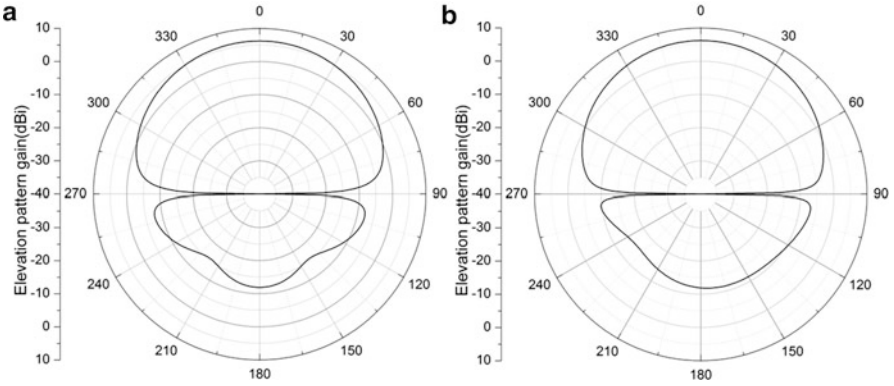

Fig. 3 Radiation pattern at 3.85 GHz (**a**) H plane (**b**) E plane

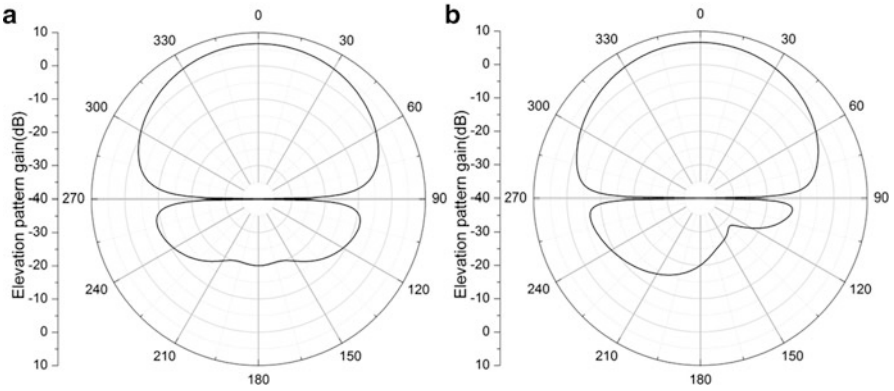

Fig. 4 Radiation pattern at 5.05 GHz (**a**) H plane (**b**) E plane

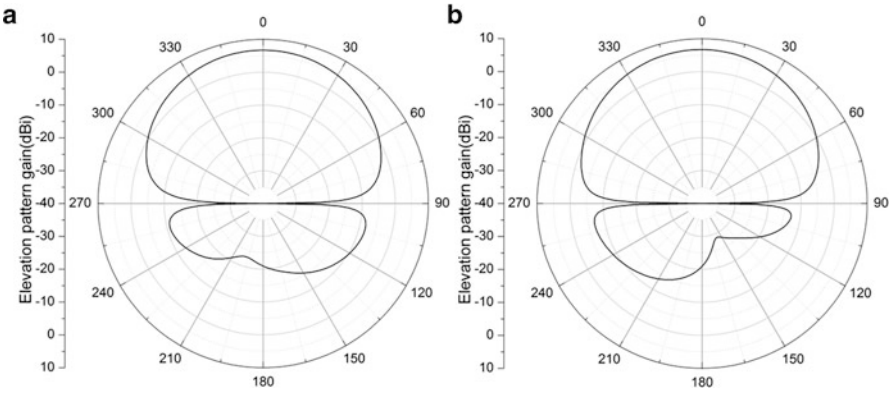

Fig. 5 Radiation pattern at 5.5 GHz (**a**) H plane (**b**) E plane

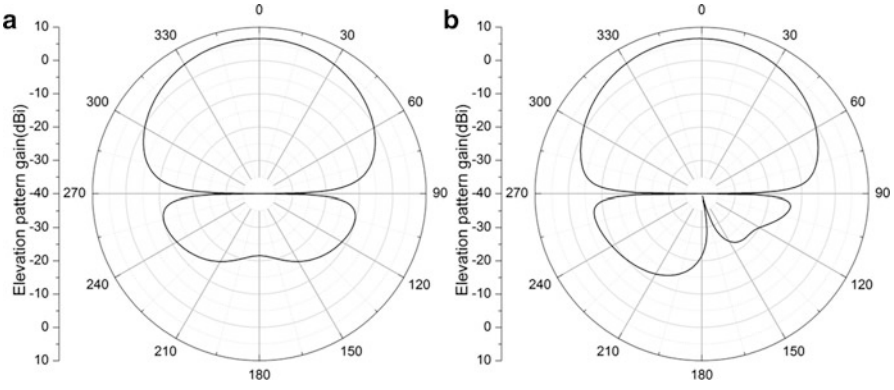

Fig. 6 Radiation pattern at 5.95 GHz (**a**) H plane (**b**) E plane

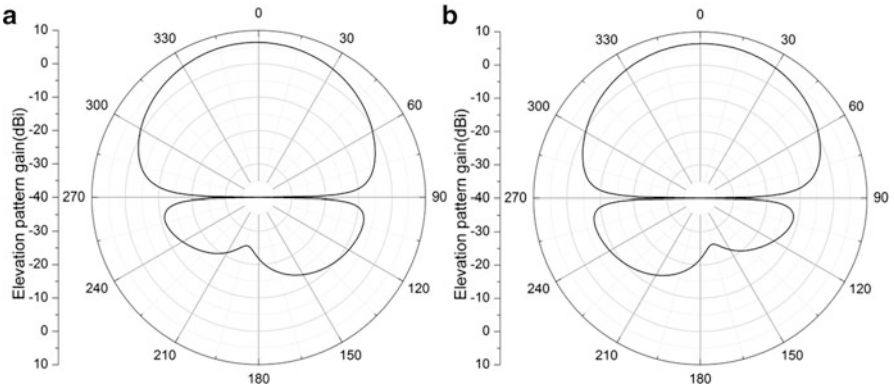

Fig. 7 Radiation pattern at 6.1 GHz (**a**) H plane (**b**) E plane

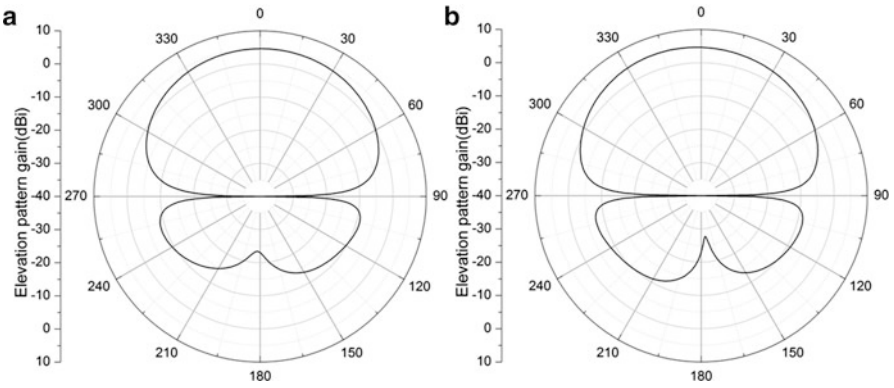

Fig. 8 Radiation pattern at 7.05 GHz (**a**) H plane (**b**) E plane

4 Conclusion

Design concept of microstrip patch etched U- slot antenna with three PIN diodes switches has been proposed in this article. The radiation performances of the antenna have been studied by using EM software and presented in this paper. As the results show that the proposed antenna has advantages such as reconfigurable frequency, stable radiation patterns, flat gain, compact size, etc., so it can be used for other wireless communications system.

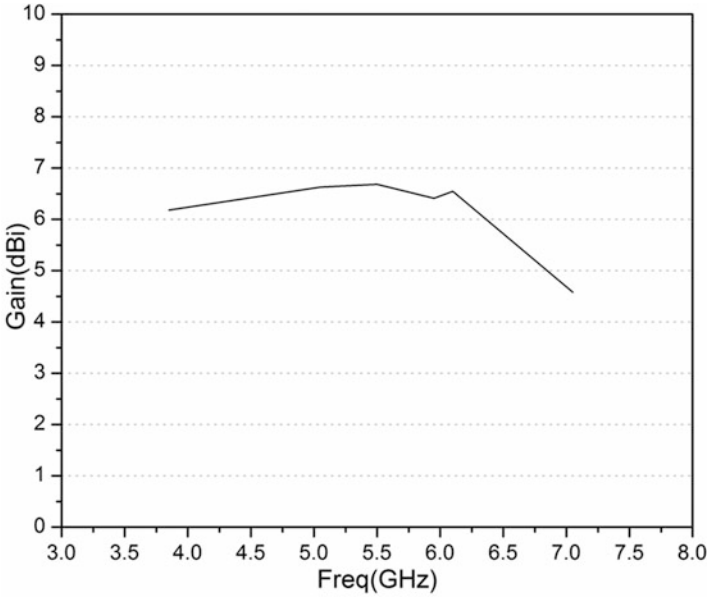

Fig. 9 Gain of proposed antenna

Acknowledgements This work was supported by National Science and Technology Major Project under granted no. 2012ZX03001028-005 and Research Project of Nanjing University of Posts and Telecommunications (208035)

References

1. Sheta AF, Mahmoud SF (2008) A widely tunable compact patch antenna. IEEE Anten Wirel Propag Lett 7:40–42
2. Byun SB, Lee JA, Lim JH, Yun TY (2007) Reconfigurable ground-slotted patch antenna using PIN diode switching. ETRI J 29(6):832–834
3. Lai ML, Wu TY, Hsieh JC, Wang CH, Jeng SK (2009) Design of reconfigurable antennas based on an L-shape slot and PIN diodes for compact wireless devices. IET Microw Anten Propag 3(1):47–54
4. Mak ACK, Rowel CR, Murch RD, Mak CL (2007) Reconfigurable multiband antenna design for wireless communication devices. IEEE Trans Anten Propag 55(7):1919–1928
5. Peroulis D, Sarabandi K, Katehi LPB (2005) Design of reconfigurable slot antennas. IEEE Trans Anten Propag 53(2):645–654
6. Li H, Xiong J, Yu Y, He S (2010) A simple compact reconfigurable slot antenna with a very wide tuning range. IEEE Trans Anten Propag 58(11):3725–3728

Electricity Consumption Prediction Based on Non-stationary Time Series GM (1, 1) Model and Its Application in Power Engineering

Xiaojia Wang

Abstract The construction of smart grid will comprehensively enhance the intelligent level of every step in the power grid of our country. The data prediction ability determines the quality of smart grid. This paper addresses situations in which the prediction accuracy of the Grey Model (GM (1, 1) model) is high for non-negative smooth monotonic sequences but inadequately low for non-stationary sequences, and isolates the trending sequence from the non-stationary time series using a numerical filtering algorithm, which is then used to make predictions. Numerical examples demonstrate that this method can improve the prediction accuracy of the GM (1, 1) model.

Keywords Non-stationary time series • Numerical filtering algorithm • GM (1, 1) model • Prediction

1 Introduction

With the continuous progress of social economy, power industry has been developing rapidly, and the network scale of power grid system is expanding constantly. On the basis of conventional power grid, the concept of smart grid is presented. Smart grid is based on physical power grid and implements optimal allocation of electric power by applying advanced modern technology in various fields.

Data prediction ability determines the quality of smart grid. As for electricity consumption, low prediction will cause power cut due to lack of allocated electricity, while high prediction will bring unnecessary generation cost and energy waste.

X. Wang (✉)
China Key Lab of Process Optimization and Intelligent Decision-making, Hefei University of Technology, Hefei, China
e-mail: tonysun800@sina.com

W. Wang (ed.), *Mechatronics and Automatic Control Systems*, Lecture Notes in Electrical Engineering 237, DOI 10.1007/978-3-319-01273-5_105,

Therefore, it is essential to predict the electricity consumption accurately. One of the commonest electricity consumption prediction models is grey model- GM (1, 1) [1]. GM (1, 1) model can play a greater role in data forecast of smart grid. By use of its theory, prediction data accuracy can be improved to meet the requirement for data with high quality in smart grid.

After 20 years of development, grey system theory has been widely applied in many areas, including social science and economics. Deng [1]created the grey system theory and system described the principle of grey system, the applications of grey system in many different fields, such as science and economy; Wang, Yang and Wang [2]used cubic spline formula to improve the background value, and constructed a novel grey forecasting model, they used this new model to forecast electricity consumption and obtained high predict accuracy; Hsu and Wang [3, 4] applied the grey prediction model to the global integrated circuit industry and obtained a good prediction effect; Shen, Chung and Chen [5] introduced a novel application of grey system theory to information security, expanded the application field of grey system; Chang and Tsai [6] used neural network adaptation to support vector regression grey model, obtained effect forecasting results, the grey system and artificial intelligence method are combined well; Chen [7] combined the grey system with Bernoulli model, constructed a new grey forecasting model NGBM (1, 1), use this NGBM (1, 1) model to forecast the foreign exchange rates of Taiwan's major trading partners, and receive good effect; Huang [8] use a hybrid grey model to forecast the stock market also achieved good results. But the GM (1, 1) model is ineffective in predicting non-stationary time series, however, mainly because the sequence computed by the GM (1, 1) model is monotonic and because the inverted sequence is also monotonic. Based on these previous studies, this paper aims to find the appropriate treatment to turn a non-stationary sequence into a sequence suitable for the GM (1, 1) model and then to create the GM (1, 1) model to improve modelling and prediction accuracy.

The remainder of the paper is organized as follows: Sect. 2 present some preliminaries of this work, and in Sect. 3 we give the main results of construction process of the prediction model, the data simulation and accuracy comparison are in Sect. 4, finally, we make a conclusion for this paper in Sect. 5.

2 Preliminaries

In this section, we firstly give some preliminaries.

Definition 2.1 Given the time series $\{x_t\},\ t = 1, 2, \cdots, n$, if

$$Bx_t \triangleq x_{t-1} \tag{1}$$

then B is denoted as the backward shift operator of the time series $\{x_t\}$. B^{-1} is denoted as forward shift operator.

Definition 2.2 Compute the d-order differential for non-stationary time series $\{x_t\}$, $(t = 1, 2, \cdots, n)$, which results in the following differential sequence:

$$\nabla^d x_t = (1 - B)^d x_t = \sum_{i=0}^{d} (-1)^i C_d^i x_{t-i},\ t = 1, 2, \cdots, n,\ t \geq d + 1 \tag{2}$$

C_d^i denotes the coefficients of the binomial $(1 - B)^d$, and there exist i combinations of set d.

$$C_d^i = \frac{d!}{i!(d - i)!} \tag{3}$$

Definition 2.3 If B is the backward shift operator of time series $\{x_t\}$, then the following expression is the binomial of B:

$$F(B) = \sum_{j=0}^{n} (-1)^j C_d^j (B^j + B^{-j}),\ j = 0, 1, \cdots n \tag{4}$$

3 Main Results

If $\{x_t\}$ is a known non-stationary sequence according to the following numerical filtering algorithm:

$$x_t = T_t + S_t + \varepsilon_t,\ t = 1, 2, \cdots, n \tag{5}$$

S_t represents the periodic sequence (i.e., the seasonal component, where the specified interval is 12) denoted as $\{S_t\}$. T_t represents the aggregation of all trends (i.e., the trend component) other than $\{S_t\}$, which is denoted as $\{T_t\}$. ε_t represents the stationary random sequence (i.e., the irregular component), which is denoted as $\{\varepsilon_t\}$.

Rewriting Eq. 6 results in the following:

$$\varepsilon_t = x_t - T_t + S_t,\ t = 1, 2, \cdots, n \tag{6}$$

If the periodic sequence $\{S_t\}$ and the trend aggregation sequence $\{T_t\}$ are decomposed, we can eventually compute the trending stationary random sequence $\{\varepsilon_t\}$ from the non-stationary sequence $\{x_t\}$. The following steps demonstrate the computation:

Step 1: Multiply the binomial $F_1(B)$ for B with $\{x_t\}$, resulting in sequence $\{\tilde{T}_t\}$, which roughly estimates sequence $\{T_t\}$:

$$\tilde{T}_t = F_1(B)x_t,\ t = 1, 2, \cdots, n \tag{7}$$

Step 2: Multiply the binomial $F_2(B)$ for B with sequence $\{x_t - \tilde{T}_t\}$, resulting in sequence $\{\tilde{S}_t\}$, which roughly estimates sequence $\{S_t\}$:

$$\tilde{S}_t = F_2(B)[x_t - \tilde{T}_t],\ t = 1, 2, \cdots, n \tag{8}$$

Step 3: Multiply the binomial $F_3(B)$ for B with sequence $\{x_t - \tilde{S}_t\}$, resulting in T_t:

$$T_t = F_3(B)[x_t - \tilde{S}_t],\ t = 1, 2, \cdots, n \tag{9}$$

Step 4: Multiply the binomial $F_4(B)$ for B with sequence $\{x_t - T_t\}$, resulting in S_t:

$$S_t = F_4(B)[x_t - T_t],\ t = 1, 2, \cdots, n \tag{10}$$

Step 5: Compute $\varepsilon_t = x_t - T_t + S_t$, resulting in the trending stationary random sequence $\{\varepsilon_t\}$, $t = 1, 2, \cdots, n$.

From definition 2.3, we can obtain the binomials for B shown in Eqs. 7 through 10:

$$F_1(B) = \frac{1}{24}\left[\sum_{j=-6}^{5} B^j + \sum_{j=-5}^{6} B^j\right] \tag{11}$$

$$F_2(B) = \frac{1}{9}\left[\sum_{j=0}^{2} B^{12j} + \sum_{j=-1}^{1} B^{12j} + \sum_{j=-2}^{0} B^{12j}\right] \tag{12}$$

$$\begin{aligned} F_3(B) = {} & 0.24 + 0.214(B + B^{-1}) + 0.147(B^2 + B^{-2}) \\ & + 0.066(B^3 + B^{-3}) - 0.028(B^5 + B^{-5}) - 0.019(B^6 + B^{-6}) \end{aligned} \tag{13}$$

$$F_4(B) = 0.2 + 0.2(B^{12} + B^{-12}) + 0.13(B^{24} + B^{-24}) + 0.07(B^{36} + B^{-36}) \tag{14}$$

If $\{x_t\}$ is a non-stationary sequence, it can be transformed into a trending stationary random sequence using numerical filtering. The transformed sequence is denoted as:

$$f : x_t \to y_t,\ t = 1, 2, \cdots, n \tag{15}$$

$\{y_t\}$ represents the transformed sequence; f represents the rules of relevant numerical filtering transformation, as shown in Step 1 through Step 4. This paper use GM (1, 1) prediction model forecasting series $\{y_t\}$, can effectively suppress the influence of both high and low frequency noise in the sequence information from the non-stationary sequence, effectively improve the prediction accuracy

Next, we introduce the modelling mechanism of GM (1, 1) model.

Assume that $X^{(0)} = \{x^{(0)}(1), x^{(0)}(2), \cdots, x^{(0)}(n)\}$ is the original series. Applying accumulated generating operation, it can be getting that:

$$X^{(1)} = \{x^{(1)}(1), x^{(1)}(2), \cdots, x^{(1)}(n)\}$$

where $X^{(1)}(k) = \sum_{i=1}^{k} x^{(0)}(i) \quad (k = 1, 2, \cdots, n)$. $X^{(1)}(k)$ is called accumulated generating operation of $X^{(0)}(k)$ denoted as 1-AGO.

The first order linear ordinary differential equation expressed as

$$\frac{dx^{(1)}}{dt} + ax^{(1)} = b \tag{16}$$

is called whitened differential equation of GM(1, 1), of which the difference form is:

$$x^{(0)}(k) + az^{(1)}(k) = b \tag{17}$$

Where a, b are parameters to be identified. a is called developing coefficient, and b is called grey input. Solve it using least square method and obtain:

$$[a, b]^T = (B^T B)^{-1} B^T Y_n \tag{18}$$

Where

$$Y_n = [x^{(0)}(2), x^{(0)}(3), \cdots, x^{(0)}(n)]^T, \; B = \begin{bmatrix} -z^{(1)}(2) & 1 \\ -z^{(1)}(3) & 1 \\ \vdots & \vdots \\ -z^{(1)}(n) & 1 \end{bmatrix} \tag{19}$$

In Eq. 19, the background value is formulated as

$$z^{(1)}(k+1) = \frac{1}{2}[x^{(1)}(k) + x^{(1)}(k+1)] \; k = 1, 2, \ldots, n-1 \tag{20}$$

The discrete solution of Eq. 16 is:

$$\hat{x}^{(1)}(k+1) = \left(x^{(0)}(1) - \frac{b}{a}\right) \cdot e^{-ak} + \frac{b}{a} \tag{21}$$

The reduction value is:

$$\hat{x}^{(0)}(k+1) = \hat{x}^{(1)}(k+1) - \hat{x}^{(1)}(k) = (1 - e^{a})\left(x^{(0)}(1) - \frac{b}{a}\right) \cdot e^{-ak} \tag{22}$$

Where $k = 1, 2, \cdots, n$.

4 Data Simulation and Accuracy Comparison

Now using the GM (1, 1) prediction model based on non-stationary time series treatment process to forecasting the electricity consumption and C# program to realize the forecast data. Figure 1 shows the smoothing processing results and Table 1 shows the calculated results. (Unit: 10^7 kwh) 1 (Fig. 2).

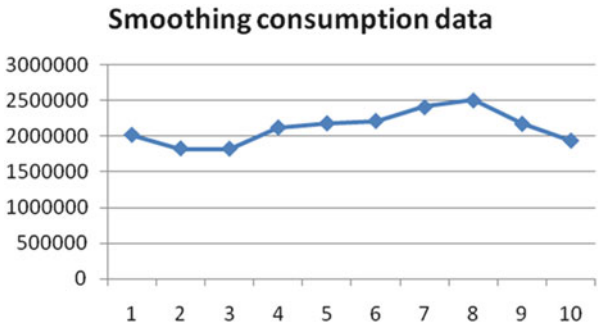

Fig. 1 Smoothing processing result

Table 1 Prediction results of smoothing data

Smoothing data	Forecast value	RE (%)
2,015,064	2,165,983	7.48
1,822,061	1,977,702	8.54
1,818,564	2,014,071	10.75
2,119,474	2,051,108	3.22
2,178,475	2,088,827	4.11
2,212,318	2,127,239	3.84
2,406,550	2,166,357	9.98
2,503,051	2,206,195	11.85
2,170,697	2,246,765	3.50
1,932,446	2,188,082	13.22

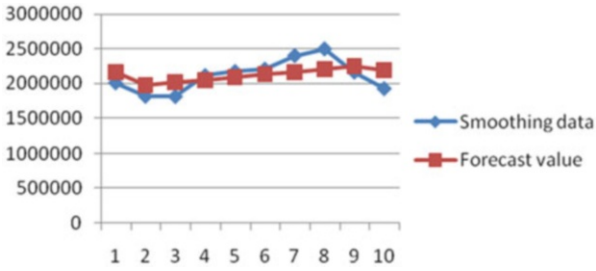

Fig. 2 Comparison chart of prediction accuracy

5 Conclusion and Future Work

This paper introduced a new thought to make electricity consumption prediction. The simulation example showed a stronger applicability that the smoothing processing for non-stationary time series effectively suppress the influence of both high and low frequency noise in the sequence information from the non-stationary sequence. And then by using the GM (1, 1) model to forecast the series obtained above, which is close to the real situation of power data, the forecasting accuracy can be really improved, and it will work more effectively in the smart grid and other practical applications. After exploring the GM (1, 1) model, this paper further extended the other new prediction model, such as the use of the artificial intelligent method.

Acknowledgements This research was partially supported by National Natural Science Foundation of China, grant No.71101041, National 863 Project, grant No. 2011AA05A116, Foundation of Higher School Outstanding Talents Grant No. 2012SQRL009 and National Innovative Experiment Program No.111035954.

References

1. Deng julong (1985) Gray system: social and economics[M]. National Defence Industry Press, Beijing, pp 24–76
2. Wang xiaojia, Yang shanlin, Wang haijiang et al (2010) Dynamic GM(1,1) model based on cubic spline for electricity consumption prediction in smart grid. China Commun 7(4):83–88
3. Hsu liChang (2003) Applying the gray prediction model to the global integrated circuit industry. Technol Forecast Soc Change 70(6):563–574
4. Hsu lichang, Wang chaohung (2009) Forecasting integrated circuit output using multivariate gray model and gray relational analysis. Expert Syst Appl 36(5):1403–1409
5. Shen VRL, Chung yufang, Chen teshong (2009) A novel application of gray system theory to information security (Part I). Comput Stand Inter 31(1):277–281

6. Chang baorong, Hsiu Fen Tsai (2008) Forecast approach using neural network adaptation to support vector regression gray model and generalized auto-regressive conditional heteroscedasticity. Expert Syst Appl 34(2):925–934
7. Chenchun, Chen honglong, Chen shuopei (2008) Forecasting of foreign exchange rates of Taiwan's major trading partners by novel nonlinear gray Bernoulli model NGBM(1, 1). Commun Nonlinear Sci Numer Simul 13:1194–1204
8. Huang kuangYu, Jane CJ (2009) A hybrid model for stock market forecasting and portfolio selection based on ARX, gray system and RS theories. Expert Syst Appl 36(5):5387–5392

Electricity Load Forecasting in Smart Grid Based on Residual GM (1, 1) Model

Jianxin Shen, Haijiang Wang, and Shanlin Yang

Abstract The construction of smart grid has put forward higher requirements on deployment accuracy of the energy. Power generation and electricity sectors have carried out more accurate data analysis and forecasting. In this context, a residual GM (1, 1) model is proposed. This model can overcome the lack of traditional grey model and make accurate forecasting of electricity consumption in smart grid. Finally, numerical examples demonstrate that this method can efficiently improve the prediction accuracy.

Keywords Smart grid • Electricity load forecasting • Residual GM (1, 1) model

1 Introduction

Compared with the traditional power grid, smart grid is characterized by environmental protection, safety, efficiency, etc. Particularly, it assists decision-making, which is useful to the optimal allocation of power resource. Data of every terminal in power grid can be controlled real timely by advanced communication facilities in smart grid. According to the forecasting of electricity consumption, smart grid allocates electricity to make a balance between supply and demand of electricity, which realizes optimizing the usage of power energy. Prediction of too much electricity consumption will cause excess power generation and distribution. While prediction of too little electricity consumption will bring power cut due to lack of power supply, then arouse economic losses and social unrest. Therefore, it is of great significance to predict the power consumption accurately. That is to say, the prediction accuracy of electricity consumption determines the quality of smart grid.

J. Shen • H. Wang (✉) • S. Yang
Key Lab of Process Optimization and Intelligent Decision-making,
Hefei University of Technology, Hefei, China
e-mail: tonysun800@sina.com

W. Wang (ed.), *Mechatronics and Automatic Control Systems*, Lecture Notes in Electrical Engineering 237, DOI 10.1007/978-3-319-01273-5_106,

Data prediction ability determines the quality of smart grid. As for electricity consumption, low prediction will cause power cut due to lack of allocated electricity, while high prediction will bring unnecessary generation cost and energy waste. Therefore, it is essential to predict the electricity consumption accurately. One of the commonest electricity consumption prediction models is grey model- GM (1, 1) [1]. GM (1, 1) model can play a greater role in data forecast of smart grid. By use of its theory, prediction data accuracy can be improved to meet the requirement for data with high quality in smart grid.

After 20 years of development, grey system theory has been widely applied in many areas, including social science and economics. Deng [1]created the grey system theory and system described the principle of grey system, the applications of grey system in many different fields, such as science and economy; Wang, Yang and Wang [2]used cubic spline formula to improve the background value, and constructed a novel grey forecasting model, they used this new model to forecast electricity consumption and obtained high predict accuracy; Hsu and Wang [3, 4] applied the grey prediction model to the global integrated circuit industry and obtained a good prediction effect; Shen, Chung and Chen [5] introduced a novel application of grey system theory to information security, expanded the application field of grey system; Chang and Tsai [6] used neural network adaptation to support vector regression grey model, obtained effect forecasting results, the grey system and artificial intelligence method are combined well; Chen [7] combined the grey system with Bernoulli model, constructed a new grey forecasting model NGBM (1, 1), use this NGBM (1, 1) model to forecast the foreign exchange rates of Taiwan's major trading partners, and receive good effect; Huang [8] use a hybrid grey model to forecast the stock market also achieved good results. But the GM (1, 1) model is ineffective in predicting non-stationary time series, however, mainly because the sequence computed by the GM (1, 1) model is monotonic and because the inverted sequence is also monotonic. Based on these previous studies, this paper aims to find the appropriate treatment to turn a non-stationary sequence into a sequence suitable for the GM (1, 1) model and then to create the GM (1, 1) model to improve modelling and prediction accuracy.

The remainder of the paper is organized as follows: Sect. 1 present some preliminaries of this work, and in Sect. 2 we give the main results of construction process of the prediction model, the data simulation and accuracy comparison are in Sect. 3, finally, we make a conclusion for this paper in Sect. 4.

2 Main Results

In this section, we firstly introduce the modeling mechanism of traditional GM (1, 1) model, then, introduce the building process of residual GM (1, 1) forecasting model [9].

Assume that $X^{(0)} = \{x^{(0)}(1), x^{(0)}(2), \cdots, x^{(0)}(n)\}$ is the original series. Applying accumulated generating operation, it can be get that:

$$X^{(1)} = \{x^{(1)}(1), x^{(1)}(2), \cdots, x^{(1)}(n)\} \tag{1}$$

where $X^{(1)}(k) = \sum_{i=1}^{k} x^{(0)}(i) \quad (k = 1, 2, \cdots, n)$. $X^{(1)}(k)$ is called accumulated generating operation of $X^{(0)}(k)$ denoted as 1-AGO.

The first order linear ordinary differential equation expressed as

$$\frac{dx^{(1)}}{dt} + ax^{(1)} = b \tag{2}$$

is called whitened differential equation of GM (1, 1), of which the difference form is:

$$x^{(0)}(k) + az^{(1)}(k) = b \tag{3}$$

where a, b are parameters to be identified. a is called developing coefficient, and b is called grey input. Solve it using least square method and obtain:

$$[a, b]^T = (B^T B)^{-1} B^T Y_n \tag{4}$$

$$Y_n = [x^{(0)}(2), x^{(0)}(3), \cdots, x^{(0)}(n)]^T, \; B = \begin{bmatrix} -z^{(1)}(2) & 1 \\ -z^{(1)}(3) & 1 \\ \vdots & \vdots \\ -z^{(1)}(n) & 1 \end{bmatrix} \tag{5}$$

In Eq. 3, the background value is formulated as

$$z^{(1)}(k+1) = \frac{1}{2}[x^{(1)}(k) + x^{(1)}(k+1)] \; k = 1, 2, \ldots, n-1 \tag{6}$$

The discrete solution of Eq. 2 is:

$$\hat{x}^{(1)}(k+1) = (x^{(0)}(1) - \frac{b}{a}) \cdot e^{-ak} + \frac{b}{a} \tag{7}$$

The reduction value is:

$$\hat{x}^{(0)}(k+1) = \hat{x}^{(1)}(k+1) - \hat{x}^{(1)}(k) = (1 - e^{a})(x^{(0)}(1) - \frac{b}{a}) \cdot e^{-ak} \tag{8}$$

Where $k = 1, 2, \cdots, n$.

To further improve the accuracy of the model, we establish the GM (1, 1) model using the residual sequence

$$q^{(0)}(k) = \{z^{(0)}(k) - \hat{z}^{(0)}(k)\} \tag{9}$$

Considering most residual sequences include both positive and negative elements, we needed to process the data by dividing the sequence by the aggregate of the negative elements and thus yielding new sequences $q_1^{(0)}, q_2^{(0)}$. We can then establish the GM (1, 1) models separately with new residual sequences. The improved prediction model is shown as follows [10–12]:

$$\begin{aligned}\hat{x}^{(1)}(k+1) = (x_1^{(0)}(1) - \frac{b}{a})e^{-ak} + \frac{b}{a} - \delta(k - i_1)(q_1^{(0)}(1) - \frac{b_1}{a_1})e^{-a_1 k} \\ + \frac{b_1}{a_1} + \delta(k - i_2)(q_2^{(0)}(1) - \frac{b_2}{a_2})e^{-a_2 k} + \frac{b_2}{a_2}\end{aligned} \tag{10}$$

Where

$$\delta(k - i) = \begin{cases} 1, & k > i \\ 0, & k < i \end{cases} \tag{11}$$

3 Data Simulation and Accuracy Comparison

Now using the residual GM (1, 1) model forecasting the electricity consumption and C# program to realize the forecast data. Next, we also apply the traditional GM (1, 1) model for comparison purposes. First, we give the trends of original data in Fig. 1. Secondly, the comparison results are show in Table 1 and Fig. 2.

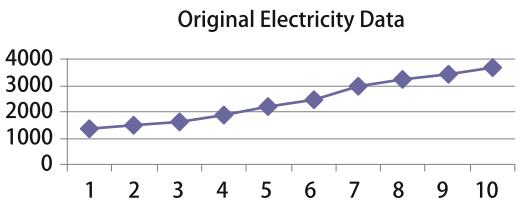

Fig. 1 Trends of original electricity load data

Table 1 Prediction and relative error comparison

Original data	Research model	RE(%)	Traditional GM model	RE(%)
1,346.62	1,283.549	4.68	1,435.28	6.58
1,468.25	1,404.6689	4.33	1,553.87	5.83
1,638.62	1,560.8704	4.74	1,740.65	6.22
1,889.12	1,877.8124	0.59	1,949.87	3.21
2,176.13	2,263.1869	4.00	2,184.24	0.37
2,468.85	2,660.8946	7.77	2,446.78	0.89
2,936.82	3,072.6476	4.62	2,740.87	6.67
3,245.84	3,192.2110	1.65	3,070.32	5.40
3,426.85	3,247.8194	5.22	3,439.37	0.36
3,659.53	3,611.2760	1.31	3,852.77	5.28

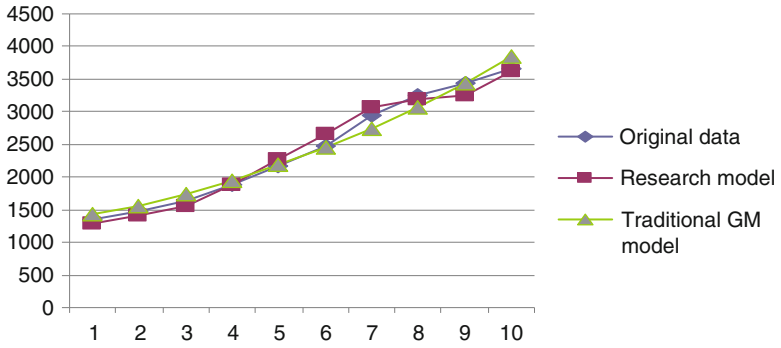

Fig. 2 Comparison chart of prediction accuracy

4 Conclusion and Future Work

This paper introduced a residual GM (1, 1) model to forecast the electricity load. Simulation example shows that the residual GM (1, 1) model can more accurately make prediction than the traditional GM (1, 1) method. The result showed that the proposed method can be effective for electricity load forecasting in smart grid.

Acknowledgements This research was partially supported by National Natural Science Foundation of China, grant No. 71101041, National 863 Project, grant No. 2011AA05A116, Foundation of Higher School Outstanding Talents Grant No. 2012SQRL009 and National Innovative Experiment Program No. 111035954.

References

1. Deng julong (1985) Gray system: social and economics[M]. National Defence Industry Press, Beijing, pp 24–76
2. Wang xiaojia, Yang shanlin, Wang haijiang (2010) Dynamic GM(1,1) model based on cubic spline for electricity consumption prediction in smart grid. China Commun 7(4):83–88
3. Hsu liChang (2003) Applying the gray prediction model to the global integrated circuit industry. Technol Forecast Soc Change 70(6):563–574
4. Hsu lichang, Wang chaohung (2009) Forecasting integrated circuit output using multivariate gray model and gray relational analysis. Expert Syst Appl 36(5):1403–1409
5. Shen VRL, Chung yufang, Chen teshong (2009) A novel application of gray system theory to information security(Part I). Comput Stand Inter 31(1):277–281
6. Chang baorong, Hsiu Fen Tsai (2008) Forecast approach using neural network adaptation to support vector regression gray model and generalized auto-regressive conditional heteroscedasticity. Expert Syst Appl 34(2):925–934
7. Chenchun, Chen honglong, Chen shuopei (2008) Forecasting of foreign exchange rates of Taiwan's major trading partners by novel nonlinear gray Bernoulli model NGBM(1,1). Commun Nonlinear Sci Numer Simul 13:1194–1204
8. Huang kuangYu, Jane CJ (2009) A hybrid model for stock market forecasting and portfolio selection based on ARX, gray system and RS theories. Expert Syst Appl 36(5):5387–5392
9. Mao mingzi, Chirwa EC (2006) Application of gray model GM(1, 1) to vehicle fatality risk estimation. Technol Forecast Soc Change 73(5):588–605
10. Li DC, Chang CJ, Chen WC, Chen CC (2011) An extended gray forecasting model for omnidirectional forecasting considering data gap difference. Appl Math Model 35:5051–5058
11. Tien TL (2009) The deterministic gray dynamic model with convolution integral DGDMC (1, n). Math Pract Theory 33:3498–3510
12. Xie naiming, Liu sifeng (2009) Discrete gray forecasting model and its optimization. Appl Math Model 33:1173–1186

Electricity Consumption Forecasting Based on a Class of New GM (1, 1) Model

Mei Yao and Xiaojia Wang

Abstract In recent years, with the development of society and the progress of science and technology, the GM (1, 1) model has been widely applied in economy, management, industry, control, social development plan, etc. But the GM (1, 1) model in the application process has encountered a low accuracy of predictions. Therefore, the improvement and optimization research of GM (1, 1) model is an important issue. In order to improve the prediction accuracy of GM (1, 1) model, it is necessary to consider reconstructing the background value of the model, which can improve the quality of the forecasting model. This paper discusses the improved GM (1, 1) model. The improved model has better prediction accuracy. It is used to forecast the society electricity consumption in eastern China, and the specific numerical examples demonstrate that this method can improve the simulation and the prediction accuracy.

Keywords GM (1,1) model • Background value • Electricity consumption prediction

1 Introduction

Since professor Deng JuLong in the early 1980s puts forward the gray system theory [1], after three decades of development, this theory has been widely applied in economy, management, industry, control, social development plan, etc., and has achieved many good results. GM (1, 1) model is the one core contents of gray

M. Yao (✉)
School of Mathematics, Hefei University of Technology, Hefei, China
e-mail: ymwalzn@163.com

X. Wang
Key Lab of Process Optimization and Intelligent Decision-making, Hefei University of Technology, Hefei, China

W. Wang (ed.), *Mechatronics and Automatic Control Systems*, Lecture Notes in Electrical Engineering 237, DOI 10.1007/978-3-319-01273-5_107,

system theory [2, 3]. The value of its application is to be reflected in an increasing number of areas [4–6].

GM (1, 1) model in the application process has encountered a low accuracy of predictions, therefore, in recent years, the improvement and optimization research of GM (1, 1) model has been the concern of many scholars [7–9]. Through the observation, the author found that these improvements can be divided into the following three types: (1) the improvement of the model parameter estimation methods; (2) the reconstruction of the model background value; (3) the improvement of the model initial conditions. Because of the iterative nature of the model GM (1,1), type (1) and type (3) eventually can be attributed to the reconstruction of the background value, so the type (2) that is the reconstruction of the model background value, has great significance. Therefore, the background value construction method will directly affect the accuracy and applicability of the model. Based on the comprehensive analysis of existing research literature, we make use of the improved method of optimized background value in GM (1, 1) model to forecast the society electricity consumption in eastern China. The results show that compared with the traditional gray GM (1, 1) model, the improved GM (1, 1) model has higher precision of the simulation.

2 Establishment of Mathematical Model

2.1 Modeling Ideas of the Traditional GM (1, 1) Model

Suppose that $X^{(0)} = \{x^{(0)}(1), x^{(0)}(2), \cdots, x^{(0)}(n)\}$ is the original sequence, and it can get through once cumulation:

$$X^{(1)} = \{x^{(1)}(1), x^{(1)}(2), \cdots, x^{(1)}(n)\}$$

Where $x^{(1)}(k) = \sum_{i=1}^{k} x^{(0)}(i)$ $(k = 1, 2, \cdots, n)$, we define $X^{(1)}(k)$ as a cumulative sequence of $X^{(0)}(k)$,then $X^{(1)}(k)$ is called $1 - AGO$.

An order linear differential equations

$$\frac{dx^{(1)}}{dt} + ax^{(1)} = b \tag{1}$$

is called as the winterization differential equation of the grey GM (1, 1) model (Gray differential equation)

$$x^{(0)}(k) + az^{(1)}(k) = b \tag{2}$$

Where a, b are parameters to be identified, and a is called the development coefficient, b is called the grey action. By means of the least square method,

We have

$$[a, b]^T = (B^T B)^{-1} B^T Y_n \tag{3}$$

Where: $Y_n = [x^{(0)}(2), x^{(0)}(3), \cdots, x^{(0)}(n)]^T$

$$B = \begin{bmatrix} -z^{(1)}(2) & 1 \\ -z^{(1)}(3) & 1 \\ \vdots & \vdots \\ -z^{(1)}(n) & 1 \end{bmatrix} \tag{4}$$

In formula (4), the background value

$$z^{(1)}(k+1) = \frac{1}{2}[x^{(1)}(k) + x^{(1)}(k+1)] \quad k = 1, 2, \cdots, n-1. \tag{5}$$

The discrete solution of the Eq. 1 as follows:

$$\hat{x}^{(1)}(k+1) = (x^{(0)}(1) - \frac{b}{a}) \cdot e^{-ak} + \frac{b}{a} \tag{6}$$

Then the original value as follows:

$$\hat{x}^{(0)}(k+1) = \hat{x}^{(1)}(k+1) - \hat{x}^{(1)}(k) = (1 - e^{a})(x^{(0)}(1) - \frac{b}{a}) \cdot e^{-ak} \tag{7}$$

Where $k = 0, 1, 2, \cdots, n-1$.

2.2 *Establishment of Improved GM (1, 1) Model*

The improved GM (1, 1) model is based on the reconstruction of the model background value. By formula (6), we find the simulation and prediction precision of the GM (1, 1) model depends on the constants a and b, but a and b depend on the value of the original sequence and structure form of the background value. Therefore the structure formula of background value $Z^{(1)}(k)$ is one of the key factors which lead to the simulation error $\varepsilon^{(0)}(k) = \hat{x}^{(1)}(k) - x^{(1)}(k)$ and the suitability of the GM (1, 1) model.

We can have integral calculation on both sides of the system (1):

$$\int_{k-1}^{k} \frac{dx^{(1)}}{dt} dt + a \int_{k-1}^{k} x^{(1)} dt = b$$

Thus, we get

$$x^{(1)}(k) - x^{(1)}(k-1) + a \int_{k-1}^{k} x^{(1)}(t) dt = b$$

$$x^{(0)}(k) + a \int_{k-1}^{k} x^{(1)}(t) dt = b \tag{8}$$

By formula (2), the background value as follows:

$$z^{(1)}(k) = \int_{k-1}^{k} x^{(1)}(t) dt (k = 2, 3, \cdots n) \tag{9}$$

Set $x^{(1)}(t) = Be^{At}$,
Where A and B are constants to be determined with

$$x^{(1)}(k) = Be^{Ak}, (k = 1, 2, \cdots, n) \tag{10}$$

Generate $x^{(1)}(t) = Be^{At}$ into formula (9), we get

$$z^{(1)}(k) = \int_{k-1}^{k} Be^{At} dt = \frac{1}{A}(Be^{Ak} - Be^{A(k-1)}) = \frac{1}{A}(x^{(1)}(k) - x^{(1)}(k-1)) \tag{11}$$

Since

$$\frac{x^{(1)}(k)}{x^{(1)}(k-1)} = \frac{Be^{Ak}}{Be^{A(k-1)}} = e^{A}$$

We have

$$A = \ln x^{(1)}(k) - \ln x^{(1)}(k-1) \tag{12}$$

Generate formula (12) into formula (11), we have

$$z^{(1)}(k) = \frac{x^{(1)}(k) - x^{(1)}(k-1)}{\ln x^{(1)}(k) - \ln x^{(1)}(k-1)}, (k = 2, 3, \cdots, n) \tag{13}$$

Generate formula (13) into formula (4), we get forecasting formulas of improved GM (1, 1) model

$$\hat{x}^{*(0)}(k+1) = \hat{x}^{(1)}(k+1) - \hat{x}^{(1)}(k) = (1-e^{a})(x^{(0)}(1) - \frac{b}{a}) \cdot e^{-ak} \qquad (14)$$

Thus we get the background value formula after optimized reconstruction.

3 Application Examples

Electricity as a special commodity has two main characteristics: the instantaneous characteristics of production, transmission and consumption.

The characteristics of electricity cannot be stored, which determines the demand for electricity is closely related to economic development. Because of the long construction period of the electricity, it is important to carry out its early warning systems in order to avoid its impact on social stability and the investment environment. The forecast methods of electricity consumption are GM (1, 1) model, multiple regression analysis, the exponential regression ARMA model, etc.

We select the monthly society electricity consumption of East China and record them as original data. We use the optimization method of background value and the traditional GM (1, 1) model to predict and comparatively analyze. The forecast scheme uses the data of the first 8 months to predict the data after the following 2 months. The calculated results show in Table 1.

From Table 1, using the optimization method of background value to carry out the forecast, the average relative error is 7.88 %, the forecasting accuracy has

Table 1 Contrast of the optimum one to the traditional GM (1, 1) about the prediction

		The optimum GM (1,1) model		Traditional GM (1,1) model	
Monthly	Original data	Model data	Relative error (%)	Model data	Relative error
1	2,140,773	2,312,850	8.0	149,475	30.2
2	1,503,399	1,909,487	27.0	1,991,297	32.5
3	2,133,739	2,069,753	2.9	2,013,600	5.6
4	2,105,210	2,078,968	1.2	2,036,153	3.3
5	2,251,740	2,145,116	4.7	2,058,958	8.6
6	2,172,995	2,092,433	3.7	2,082,019	4.2
7	2,640,204	2,240,846	15.1	2,105,338	20.3
8	2,365,997	2,290,378	3.2	2,128,918	10.1
9	1,975,497	2,141,057	8.3	2,152,763	8.9
10	1,999,394	2,092,908	4.7	2,176,874	15.2
Average relative		7.88		13.89	

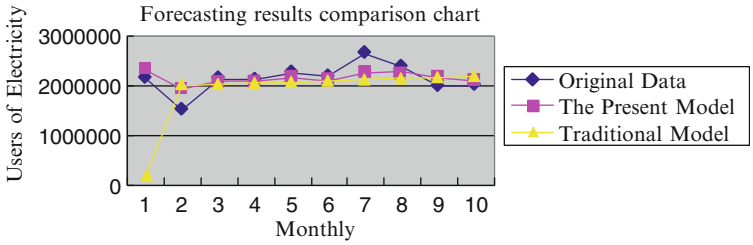

Fig. 1 Forecasting results comparison chart

greatly improved compared to the traditional GM (1, 1) method. It proves that the background value reconstruction is a key factor to affect the prediction accuracy and applicability and it also shows that the proposed method is effective.

The following is the figure of the Table 1 (Fig. 1).

4 Conclusion

By using gray system theory model, the GM (1, 1) model can overcome the weakness of related data and avoid the influence of the artificial factor. In this paper, the simulation results of the improved gray prediction model were closer to the practical value, prediction error was small and the model accuracy was better. This suggested prediction accuracy of improved gray prediction model was higher than the traditional gray prediction model. It verified the reliability and validity of the method presented in this paper.

Acknowledgements This research was partially supported by National Natural Science Foundation of China, grant No. 71101041, National 863 Project, grant No. 2011AA05A116, Foundation of Higher School Outstanding Talents Grant No. 2012SQRL009, the Youth Development Foundation of Hefei University of Technology, Grant No. 2013HGXJ0227 and National Innovative Experiment Program No. 111035954.

References

1. Deng Julong (1985) Gray system[M]. National Defence Industry Press, Beijing, pp 18–40
2. Liu Sifeng, Guo Tianbang, Dang Yaoguo (1999) Gray system theory and its application [M]. Science Press, Beijing, pp 60–72
3. Luo Dang, Liu Sifeng, Dang Yaoguo (2003) The optimization of Grey Model GM (1, 1). Eng Sci 5(8):50–53
4. Wang Xiaojia, Yang Shanlin, Haijiang Wang et al (2010) Dynamic GM (1, 1) model based on cubic spline for electricity consumption prediction in smart grid. China Commun 7(4):83–88

5. Xiaojia Wang, Shanlin Yang (2009) On delay-dependent stability for a class of neutral systems. In: Proceedings-5th international conference on wireless communications, networking and mobile computing, WiCOM 2009. IEEE Computer Society, Piscataway, pp 1–3
6. Xiaojia Wang, Shanlin Yang (2010) Electricity demand forecasting based on threepoint Gaussian quadrature and its application in smart grid. In: Proceedings-6th international conference on wireless communications, networking and mobile computing, WiCOM 2010. IEEE Computer Society, Piscataway, pp 1–3
7. Wang Xiaojia, Yang Shanlin, Hou Liqiang et al (2010) Simulation of orthogonalization prediction based on Grey Markov chain for electricity consumption. J Syst Simul 22(10):2253–2256
8. Xiaojia Wang (2011) Application research on electricity demand forecasting based on Gaussian quadrature formula. Procedia Eng 15:5574–5578
9. Wang Xiaojia, Shen Jianxin, Yang Shanlin (2010) Application research on Gaussian orthogonal interpolation method for electricity consumption forecasting of smart grid. Power Syst Prot Control 38(21):141–145

Spectral Visibility of High-Altitude Balloon by the Ground-Based Detection

Xiaoping Du, Yu Zhang, and Dexian Zeng

Abstract In order to determine the visible spectral region of the target, the paper made the analysis of the high-altitude balloon by the ground-based detection. By using the atmospheric transporting model (MODTRAN), the paper calculated the background noise intensity at the probe point and the brightness of the background of the target in the different time. And by using the reverse Monte-Carlo method, the paper calculated the scattering radiance of the high-altitude balloon the ground-based probe point received. After calculating the ratio of the signal to the noise, the paper made the analysis of the visibility of the target. The results show that, during the ground-based detection, with the smaller detecting angle or the greater solar zenith angle of the target, the signal to noise ratio can be higher when the target's location and the detecting altitude are both fixed. This study is beneficial to the determination of the threshold of detection equipment and the choice of spectral bands.

Keywords High-altitude balloon • Ground-based detection • Reverse Monte-Carlo method • Scattering characteristics • Signal to noise ratio • Spectrum • MODTRAN

1 Introduction

The high-altitude balloon is a non-powered aircraft which works in the stratosphere. With 30 years' development, average flying height of the high-altitude balloon can be 40–50 km. Having the features such that the experimental cost is low, the flight organizing is convenient and the testing cycle is short, the high-altitude balloon

X. Du (✉) • Y. Zhang • D. Zeng
The Academy of Equipment, Beijing, China
e-mail: dxp8600@163.com; xlrui522@163.com

W. Wang (ed.), *Mechatronics and Automatic Control Systems*, Lecture Notes in Electrical Engineering 237, DOI 10.1007/978-3-319-01273-5_108,

has been used in the ground-based remote sensing, the atmospheric physics and the military. Thus carrying out the research of the recognition technology on the detection of high-altitude balloon should bring great value.

Due to the small radar scattering cross section the high-altitude balloon has, spectral detection technology is widely used as a sophisticated means of detection [1]. The paper used the ground-based detecting means to conduct the research of the high-altitude balloon. After completing the geometric modeling and determination of the spectral reflectance of the coating material, the paper calculated the scattering properties of the target on the visible spectrum by using the reverse Monte-Carlo method, and made the analysis of the spectral visibility of the target.

2 Analysis of the Radiance of the Background Lights

When the time to start observing, such condition must be met that the scattering intensity should be higher than the noise intensity entering the detector on the period of spectrum being used [2].

Generally speaking, the target-scattering lights can be divided into the direct sunlight and varieties of lights which have multiple scattering effects. To make the illustration conveniently, the upward scattering lights are all named as ground-lights, and the downward scattering lights, excepting the direct sunlight, are all named as sky-lights. Usually, people use the background radiation whose incident zenith angle is 45° instead of the average radiance of the sky-lights, and use the background radiation whose incident zenith angle is 135° instead of the average radiance of the ground-lights when conducting the engineering calculation [3, 4]. In the form of noise, the radiance of the sky-lights of the detector will enter the pupil surface if the detector is below the target in the altitude. Throughout the environment of exploration, the solar zenith angle and the solar azimuth of the target or the detector will both change as long as the time changes, which is mean that the radiance of the scattered light of the target and the intensity of the noise of the detector will change correspondingly.

For the target located in the atmosphere, apparently, the ground-lights and the sky-lights both exist. But for the reception of the detector which is below the target, the sky-lights of the target can be ignored because that although the under surface of the target can receive the sky-lights when the solar zenith angle of the target takes some angles, but comparing with the ground-lights, the reflected energy is too small to reach the detector. Although the direct sunlight is downward, but the reflected energy is so high that cannot be ignored.

Generally, the scattered lights of the target include the ground-lights and the direct sunlight at the location of the target. The ground-lights include the upward scattering sunlight, the upward atmospheric path radiation, the black-body radiation of the earth's surface and the reflected lights by the earth's surface for various atmospheric background lights. The sky-lights include the downward scattering sunlight, the downward atmospheric path radiation.

The energy of every kind of radiation is related with the latitude, season, time and atmospheric physical state. By using the atmospheric transporting model (MODTRAN), the paper calculated the background noise intensity at the different situation.

3 The Modeling of the Scattering Property of the Target

This section calculated the radiance, scattered from the target, the detector received by using the reverse Monte-Carlo method (RMC). RMC assumes that the detector emits lights in the field of view of the target. Only the light which can reach the target is useful for the follow-up recursive calculation on the light's energy. Obviously, this process is the reverse one of the real ray-casting. In details, RMC assumes that the energy of the light is from the black-body radiation of the target if the light is been absorbed by the target, and assumes that the energy of the light is from the background light scattered by the target if the light is scattered into the environment by the target [5–7]. Ultimately, the statistics for each light can be obtained.

The paper named the lights having no contact with the target as the invalid ones, and named the lights having intersection with the target as the effective ones. Ultimately some lights are absorbed by the target, the others are scattered into the environment. The light's energy will be gradually decreasing if it is multiply scattered. Given the actual situation of the spectral reflectance of the target coating material, the scattering times can be set to downsize the simulation scale. Figure 1 shows the transmission of energy between two surface elements in the vacuum.

In Fig. 1, dS is the area of the surface element of the target, dS' is the area of the surface element of the detector's pupil surface, dΩ is the solid angle of the detector to the target, r is the length the line of centers of two surface elements, n is the normal line of the surface element of the target, n' is the normal line of the surface element of the detector, θ' is the included angle between n' and the line of centers of two surface elements.

The paper assumed that the change of the energy of the light being scattered is only relevant to the material's spectral reflectivity named as $\rho(\lambda)$. The spectral radiant flux named as $d\Phi'(\lambda)$ received by dS' can be expressed as

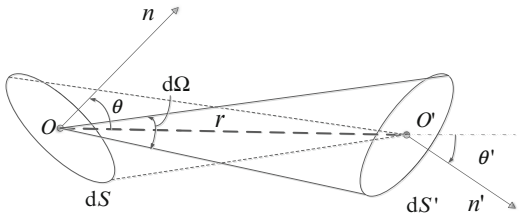

Fig. 1 The transmission of energy between two surface elements

$$\mathrm{d}\Phi'(\lambda) = \rho(\lambda) \cdot L_{\mathrm{back}}(\lambda)\mathrm{d}\Omega\mathrm{d}S\cos\theta = \rho(\lambda) \cdot L_{\mathrm{back}}(\lambda) \cdot \frac{\mathrm{d}S'\cos\theta'}{r^2}\mathrm{d}S\cos\theta \tag{1}$$

Here λ is the wavelength in microns and $L_{\mathrm{back}}(\lambda)$ is the spectral radiance of the light scattered by the target. Thus the spectral irradiance named as $\mathrm{d}E(\lambda)$ received by $\mathrm{d}S'$ can be deduced as

$$\mathrm{d}E(\lambda) = \frac{\mathrm{d}\Phi'(\lambda)}{\mathrm{d}S'} = \frac{\rho(\lambda) \cdot L_{\mathrm{back}}(\lambda)\mathrm{d}S\cos\theta\cos\theta'}{r^2} \tag{2}$$

Avoiding calculating complicated angle factor, that the multiplication of $\cos\theta$ can be replaced of the ratio of the amount of different lights is one of the advantages of RMC's. So it means that

$$\sum \mathrm{d}S\cos\theta = \frac{1}{N} \cdot [\sum_{a_1=1}^{S_{\mathrm{sca\_}1}} S_{a_1} + \sum_{a_2=1}^{S_{\mathrm{sca\_}2}} S_{a_2} + \cdots + \sum_{a_n=1}^{S_{\mathrm{sca\_}n}} S_{a_n}] \tag{3}$$

where n is the scattering times, S_{a_n} is the area of the surface element from which the light numbered a_n is scattered into the environment ultimately, $S_{\mathrm{sca\_}n}$ is the quantity of the lights whose scattering times are n.

Due to the presence of the scattering phenomenon, the energy of the light will change in different degree, so the above equation should be amended as

$$\sum \mathrm{d}S\cos\theta = \frac{1}{N} \cdot [\sum_{a_1=1}^{S_{\mathrm{sca\_}1}} S_{a_1} + \rho(\lambda)\sum_{a_2=1}^{S_{\mathrm{sca\_}2}} S_{a_2} + \cdots + \rho(\lambda)^n \sum_{a_n=1}^{S_{\mathrm{sca\_}n}} S_{a_n}] \tag{4}$$

Considering the presence of the invalid light, the above equation should be amended again, which is showed as

$$\sum \mathrm{d}S\cos\theta = \frac{1}{N - S_{\mathrm{sca\_}0}} \cdot [\sum_{a_1=1}^{S_{\mathrm{sca\_}1}} S_{a_1} + \rho(\lambda)\sum_{a_2=1}^{S_{\mathrm{sca\_}2}} S_{a_2} + \cdots + \rho(\lambda)^n \sum_{a_n=1}^{S_{\mathrm{sca\_}n}} S_{a_n}] \tag{5}$$

Thus for the entire target, the radiance named as $L(\lambda)$ received by the detector can be deduced as

$$L(\lambda) = \frac{\tau(\lambda) \cdot \rho(\lambda) \cdot L_{\mathrm{back}}(\lambda) \cdot \cos\theta'}{N - S_{\mathrm{sca\_}0}} \cdot [\sum_{a_1=1}^{S_{\mathrm{sca\_}1}} S_{a_1} + \rho(\lambda)\sum_{a_2=1}^{S_{\mathrm{sca\_}2}} S_{a_2} + \cdots + \rho(\lambda)^n \sum_{a_n=1}^{S_{\mathrm{sca\_}n}} S_{a_n}] \tag{6}$$

Where $\tau(\lambda)$ is the atmospheric spectral transmittance of the optical path from the target to the detector, N is the quantity of the lights the detector emits, and θ', also named as the detecting angle, here is the included angle between the normal line of the detector's pupil surface and the line from the target to the detector [8–10].

4 Simulations and Analysis

4.1 The Geometrical Model and the Coating Material of the Target

Taking the background of the research into account, the paper set the typical high-altitude balloon as the research target. Based on the software (3ds MAX), the paper completed its finite element modeling and exported its triangular mesh data. Figure 2 shows the Geometric model of the target.

The coating material made of the high-pressure polyethylene after its hot pressing welding has good properties of low temperature and tensile strength. Using the spectrometer, the paper made the determination of the spectral reflectance of the material being set as PVC. The bands range is set from 0.38 to 0.78 in microns. Figure 3 shows the curves of the spectral reflectance of the material after calibration by the whiteboard.

4.2 The Process and the Results of the Simulation

The location of the target is set to the urban area of Beijing (E 116.6° N 39.9°) and the vertical height from the surface is set to 40 km. The value of detecting angle determined the locations of the ground-based detectors. After analyzing the latitude

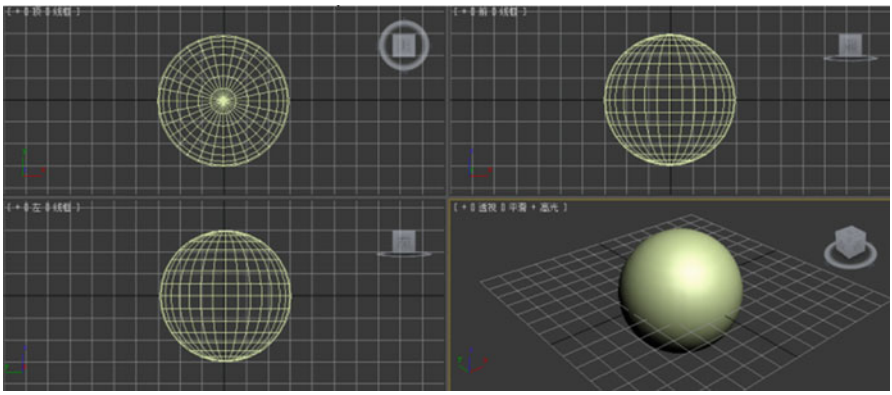

Fig. 2 The geometric model of the target

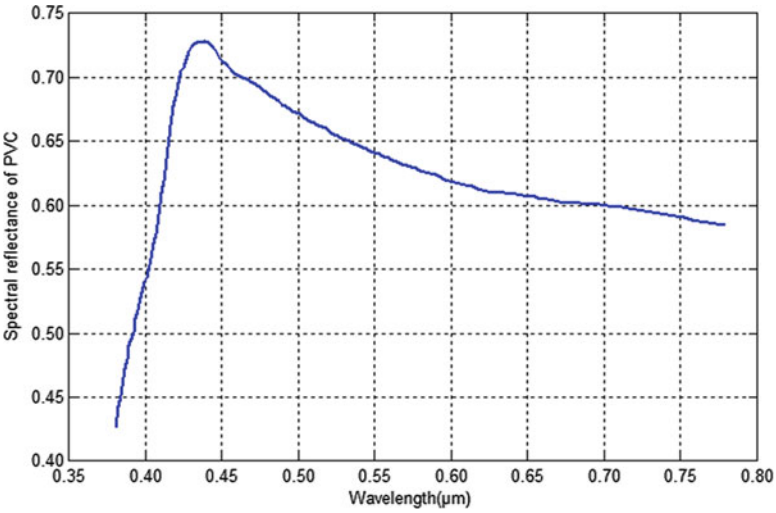

Fig. 3 The curves of the spectral reflectance of the material

and longitude of various districts and counties of China, the paper determined three typical positions. These three locations respectively were Tongzhou (E 116.65°, N 39.92°, $\theta' = 28.38°$), Changping (E 116.23°, N 40.22°, $\theta' = 44.13°$) and Pinggu (E 117.12°, N 40.13°, $\theta' = 59.35°$).

During the observation, the main difficulty lies in the low contrast and the SNR caused by the strong radiance of the background lights. Here SNR is expressed as the ratio of the radiance of the lights scattered by the target to the brightness of the background noise of the detector [11]. For simulation, time was set to May 4, 2012. The model of atmosphere was set as U.S. 1976 standard, the model of the aerosol was rural, and the visibility was 23 km [12].

4.2.1 When Time Is Changing, SNR of the Same Detecting Point

Setting the detecting point as Tongzhou District, Fig. 4 shows the curves of the SNR of Tongzhou at different time when the solar zenith angle of the target were 35°,45°, 55°and 75° respectively.

Figure 4 shows that, with the adding of the solar zenith angle, the curve shows an increasing tendency. If the SNR is fixed, the start point of the visible area on the spectrum moves forward with the increasing of the solar zenith angle.

4.2.2 When Time Is Fixed, SNR of Different Detecting Point

When the solar zenith angle of the target is 75°, the solar zenith angle of each detector were 74.82°(Tongzhou), 75.16° (Changping) and 74.47°(Pinggu). Figure 5 shows the curves of the SNR of different detecting points at the same time.

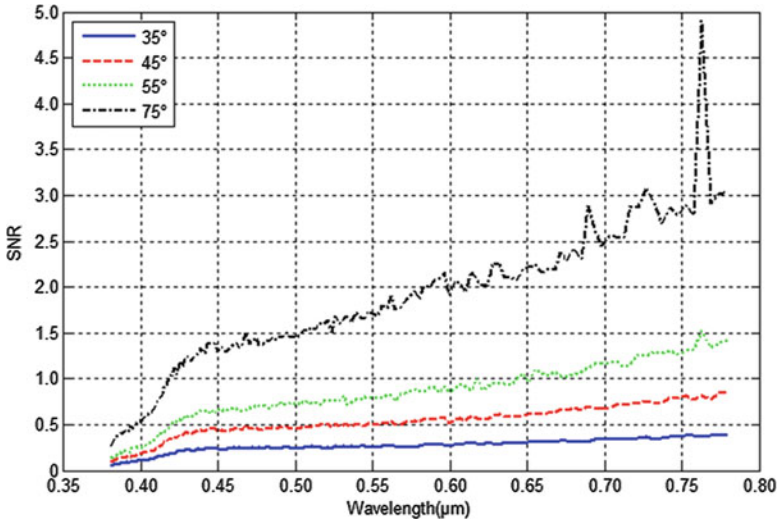

Fig. 4 The curves of the SNR of Tongzhou at different time

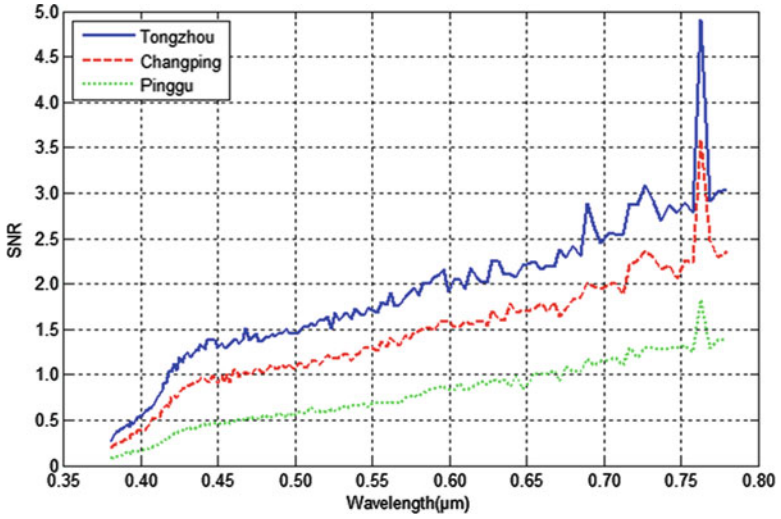

Fig. 5 The curves of the SNR of different detecting points at the same time

Figure 5 shows that with the adding of the detecting angle, the curve shows a decreasing tendency. If the SNR is fixed, the start point of the visible area on the spectrum moves backward with the increasing of the detecting angle.

5 Conclusion

By using the reverse Monte-Carlo method, the paper calculated the scattering radiance of the high-altitude balloon the ground-based probe point received and made the comparison with the background noise intensity at the probe point in different time and the brightness of the background of the target at different times. The following conclusions can be inferred:

(a) When the detecting point is fixed, with the increasing of the solar zenith angle of the target, SNR showed an upward trend on the whole. And when the SNR value is the same, with the increasing of the solar zenith angle of the target, the visible area of the spectrum will move forward.
(b) When the detecting time is fixed, with the increasing of the detecting angle, SNR showed a downward trend on the whole. And when the SNR value is the same, with the increasing of the solar zenith angle of the target, the visible area of the spectrum will move backward.

References

1. Zhou Linghui (2008) Simulation and identification of the spectral properties of space targets [D]. Master dissertation of the Huazhong University of Science and Technology, Wuhan, (In Chinese)
2. Li Daoyong, Wang Zengyu, Zhang Yanqun (2005) The visual conditions of properties of the light scattered by the space targets. Opt Optoelectron Technol 3(5):5–8 (In Chinese)
3. Wu Zhensen, Liu Anan (2002) Scattering of solar and atmospheric background radiation from a target. Int J IR Mill Waves 23(6):907–917
4. Li Daoyong, Wang Yunqiang, Gong Yanjun (2004) The properties of the light scattered by the space targets. J Yantai Univ 17(3):183–187 (In Chinese)
5. Shan Yong, Zhang Jingzhou, Guo Rongwei (2008) Numerical computation and analysis of the infrared radiation characteristic of missile scarfskin. J Aerosp Power 23(2):251–255 (In Chinese)
6. Lv Jianwei, Wang Qiang (2009) Numerical calculation and analysis of infrared radiation characteristics from aircraft skin by using RMC method. Infrared Laser Eng 38(2):232–237 (In Chinese)
7. Liu Gang, Riqitai E, Zhu Xijuan (2011) Simulation of infrared radiation characteristics of cruise missile skin by backward Monte Carlo method. Sci Technol Eng 11(5):1012–1017
8. Li Liangchao, Niu Wubin, Wu Zhensen (2011) Parallel calculation for scattering of background infrared irradiation from aerial complex targets. Syst Eng Electron 33(12):2573–2576 (In Chinese)
9. Yang Yufeng, Wu Zhensen, Cao Yunhua (2011) Scattering characteristics of complex background infrared radiation from a non-lambertian target. Infrared Laser Eng 40(5):800–804 (In Chinese)
10. Shu Rui, Zhou Yanping, Tao Kunyu (2006) The study of infrared spectrum of spacetarget. Opt Tech 32(2):196–199 (In Chinese)

11. Chen Yuheng, Zhou Jiankang, Chen Xinhua (2009) Calculation of SNR of a satellite CCD camera based on MODTRAN. Infrared Laser Eng 38(5):910–914 (In Chinese)
12. Mao Kebiao, Tan Zhihao (2004) The transmission model of atmospheric radiation and the computation of transmittance of MODTRAN. Geomat Spat Inf Technol 27(4):1–3 (In Chinese)

Part VI
Sensing Control Theory

A Novel Demodulation Method for Fiber Optic Interferometer Sensor Using 3 × 3 Coupler

Haiyan Xu and Zhongde Qiao

Abstract Fiber optic inetrferometric sensors have advantages of high sensitivity and can be employed to measure very small disturbance. In this paper, a novel demodulation method of fiber optic interferometer sensor is presented, which is based on the 3 × 3 coupler to demodulate the phase shift. By employing two output signals of the 3 × 3 coupler, it can eliminate the insensitive areas. The optical structure and the demodulation algorithm are easy to deploy, compared with the PGC (phase generated carrier) technique and other 3 × 3 coupler based demodulators. This algorithm can effectively overcome the phase distortion caused by the instability of the light output power. The simulation and experiment demonstrate that the high demodulate precision has been achieved.

Keywords Fiber optic sensor • Interferometer • 3 × 3 coupler

1 Introduction

Recently, distributed fiber-optic sensor is available for many applications, such as intruder detection, moving vehicle location, and oil pipeline leakage monitoring. The most distinguished techniques for distributed sensing involve the use of the optical time domain reflectometer (OTDR) [1, 2] and fiber-optic interferometer sensors [3, 4]. The optical fiber interferometer has been widely used in the physical measurement because of its high sensitivity, such as the sound of water, strain, magnetic field, current and acceleration. Double-beam interferometer is the main development direction for the interferometer sensors [5].

H. Xu (✉)
Jiangsu Key Laboratory of Power Transmission and Distribution Equipment Technology, Hohai University, Changzhou 213002, China
e-mail: xhyjstu@hotmail.com

Z. Qiao
Changzhou Ruize Microelectronics Co. Ltd, Changzhou, China

W. Wang (ed.), *Mechatronics and Automatic Control Systems*, Lecture Notes in Electrical Engineering 237, DOI 10.1007/978-3-319-01273-5_109,

However, the photo detector can only respond to changes in light intensity, after the interference of light received by the photo detector of interference items, we need to use different methods to demodulate the phase signal. The demodulator methods are generally divided into phase generated carrier (PGC) [6] and the passive homodyne demodulation technique with a 3 × 3 coupler.

The main drawback of the PGC technology is the use of low-pass filter which ignore the higher order Bessel function, and results in the serious distortion of the demodulation. Dynamic range of the phase generated carrier has been restricted with the limited carrier frequency. When using the externally modulated carrier, the optical path is more complicated. A demodulation scheme utilizing a 3 × 3 coupler has the advantage of passive detection and low cost as it requires no phase or frequency modulation in the reference arm or of the laser source, and so there are no active components in the optical domain. There are basically three methods for demodulation with a 3 × 3 coupler: in the first one two of the three outputs are used to obtain the required 90° phase difference from their sum and difference and these form the inputs to a differentiating cross-multiplying demodulator [7], the method needs a dc offset in the circuit to eliminate the dc component resulting from summing up the two inputs, therefore when the light power in the interferometer changes, the circuit will become unbalanced; whereas in the second one, all three outputs are utilized symmetrically in an analog processing algorithm to obtain the demodulated time-changing phase difference [8], However, if the 3 × 3 coupler is not symmetric, the symmetric method will face rather serious problems; Whereas in the third one, an asymmetric 3 × 3 coupler demodulate method is proposed, but the demodulation process is more complex because of the gain control factor [9],so it is difficult to apply to the practical engineering.

In this paper, we present a new demodulation method which requires only two interference signals with a certain initial phase. The method can effectively overcome the phase distortion caused by the instability of the light output power. As compared to the PGC technique and past 3 × 3 coupler based demodulator, the method has no phase carrier, no filters, no calibration, no need for uniform splitting ratio of coupler, the optical structure and the demodulation algorithm are all simple. The demodulator method we proposed here can meet the requirements of practical application, which has a certain practical significance.

2 Theoretical Analysis

2.1 Signal Acquisition

We can achieve two AC output signals with constant phase difference when using a 3 × 3 coupler to construct the interferometer. The two outputs of the photodiodes are given by:

$$\begin{cases} I_1(\mathrm{t}) = A^{'}(t) + A(t)\cos(\Delta\varphi(t) + \phi) \\ I_2(\mathrm{t}) = B^{'}(t) + B(t)\cos(\Delta\varphi(t) - \phi) \end{cases} \tag{1}$$

Where $\Delta\varphi(t)$ is the phase difference of the interferometer at its output, which is a function of time containing the information on the quantity to be measured; and A、B、$A^{'}$、$B^{'}$ are dependent on the optical power of system input; ϕ is the constant, for a symmetric 3 × 3 coupler, we have $\phi = 2\pi/3$, and for an asymmetric 3 × 3 coupler, we can also achieve the value of ϕ. Use the two outputs signals from the 3 × 3 coupler, the phase shift to be measured can be recovered.

After removing the DC components, the following equations are met:

$\Delta\varphi(t) = 0, I_1(t) = I_2(t) = 0$. According to the symmetry character of the 3 × 3 coupler, there is

$A^{'}(t) = -A(t)\cos\phi, B^{'}(t) = -B(t)\cos\phi$, then we can rewrite Eq. 1 as:

$$\begin{cases} I_1(\mathrm{t}) = A(t)\cos(\Delta\varphi(t) + \phi) - A(t)\cos\phi \\ I_2(\mathrm{t}) = B(t)\cos(\Delta\varphi(t) - \phi) - B(t)\cos\phi \end{cases} \tag{2}$$

Discretized the signals in Eq. 2, suppose the sampling time interval is Δ, then $t = n\Delta$ (n = 0,1,2.....), therefore

$$\begin{cases} I_1(n) = A(n)\cos(\Delta\varphi(n) + \phi) - A(n)\cos\phi \\ I_2(n) = B(n)\cos(\Delta\varphi(n) - \phi) - B(n)\cos\phi \end{cases} \tag{3}$$

2.2 DC Components Calculation

For simplicity, we only analysis the signal of $I_1(n)$, because of the amplitude of the signals is big enough, that is, the dynamic range of $\varphi(n)$ exceeds one cycle, the maxim and minimum of Eq. 3 is:

$$Max(I_1(n)) = A(n)(1 - \cos\phi) \tag{4}$$

$$Min(I_1(n)) = -A(n)(1 + \cos\phi) \tag{5}$$

so

$$A(n)\cos\phi = -\frac{Max(I_1(n)) + Min(I_1(n))}{2} \tag{6}$$

Similarly

$$B(n)\cos\phi = -\frac{Max(I_2(n)) + Min(I_2(n))}{2} \tag{7}$$

Substituting Eqs. 6 and 7 into Eq. 3, we can have

$$I_1(n) - \frac{Max(I_1(n)) + Min(I_1(n))}{2} = A(n)\cos(\Delta\varphi(n) + \phi) \tag{8}$$

$$I_2(n) - \frac{Max(I_2(n)) + Min(I_2(n))}{2} = B(n)\cos(\Delta\varphi(n) - \phi) \tag{9}$$

2.3 Normalization

We need to normalize the signals considering the amplitude difference of the two signals. Equation 4 subtract Eq. 5, can be expressed as

$$A(n) = \frac{Max(I_1(n)) - Min(I_1(n))}{2} \tag{10}$$

Similarly, $B(n)$ can be expressed as

$$B(n) = \frac{Max(I_2(n)) - Min(I_2(n))}{2} \tag{11}$$

By substituting Eqs. 10 and 11 into Eqs. 8 and 9, we get the normalized signal

$$I_1^{'}(n) = C(n)\cos[\Delta\varphi(n) + \phi] = 2\left(\frac{I_1(n) - Min(I_1(n))}{Max(I_1(n)) - Min(I_1(n))}\right) - 1 \tag{12}$$

$$I_2^{'}(n) = C(n)\cos[\Delta\varphi(n) - \phi] = 2\left(\frac{I_2(n) - Min(I_2(n))}{Max(I_2(n)) - Min(I_2(n))}\right) - 1 \tag{13}$$

Where $C(n)$ is a normalization factor. Ideally, $C(n)$ =1. During the actual experimental tests, due to systematic errors, each point corresponding to the C is vary, we can obtain the corresponding C according each set of experimental data (see Eq. 16).

2.4 Demodulation Algorithm

For simplicity, by add and subtract the two signals of Eqs. 12 and 13, there is

$$I_+(n) = I_1^{'}(n) + I_2^{'}(n) = 2C(n)\cos\phi\cos\Delta\varphi(n) \tag{14}$$

$$I_-(n) = I_1^{'}(n) - I_2^{'}(n) = 2C(n)\sin\phi\sin\Delta\varphi(n) \tag{15}$$

According to the above two equations, $C(n)$ can be denoted as:

$$C(n) = \sqrt{\left(\frac{I_1^{'}(n) + I_2^{'}(n)}{2\cos\phi}\right)^2 + \left(\frac{I_1^{'}(n) - I_2^{'}(n)}{2\sin\phi}\right)^2} \tag{16}$$

From the amplitude ratio of Eqs. 14 and 15, it can be shown that $\Delta\varphi(n)$ can also be expressed as in one cycle:

$$\Delta\varphi(n) = \tan^{-1}\left(\frac{I_-(n)}{I_+(n)} / \tan\phi\right) \tag{17}$$

Then need to further expansion of the phase to complete the automatic accumulation function of the signal over one cycle. For an arbitrary n, subtract $\varphi(n)$ and $\varphi(n-1)$, k = k − 1 while the value more than $\pi/2$; k = k + 1 while the value less than $-\pi/2$. $\Delta\varphi(n)$ can be rewrite as

$$\Delta\varphi(n) = k\pi + \tan^{-1}\left(\frac{I_-(n)}{I_+(n)} / \tan\phi\right) \tag{18}$$

The phase difference $\Delta\varphi(n)$ can be achieved through software technology with the above algorithm. For a symmetric 3 × 3 coupler, $\phi = 2\pi/3$, as the coupler is an asymmetric, according to Eqs. 14 and 15:

$$\tan\phi = \frac{I_{-A}(n)}{I_{+A}(n)} \tag{19}$$

Where subscript A denotes the amplitude of $I_-(n)$ and $I_+(n)$, by substituting Eq. 19 into Eq. 18, the demodulation signal can be achieved.

3 Simulation and Experimental

3.1 Simulation

To verify the correctness of the demodulation algorithm, the single-frequency sinusoidal signal is used. Make the amplitude of $\Delta\varphi(t)$ is 2.8 V, the frequency of $\Delta\varphi(t)$ is 5 kHz, the sample frequency is 500 kHz, according to the Eq. 3, the

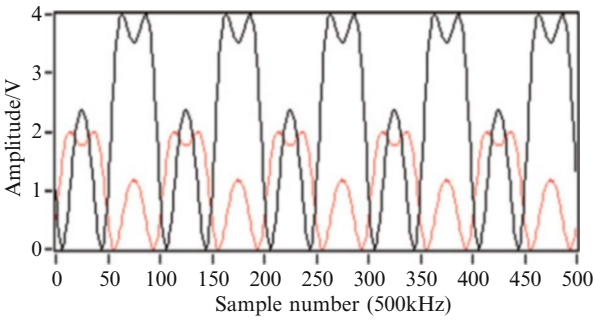

Fig. 1 Time sequences before demodulation

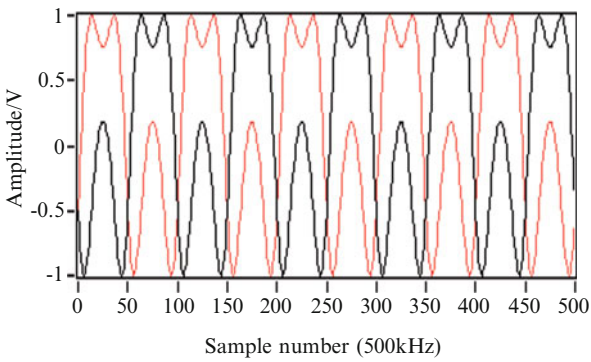

Fig. 2 Time sequences normalized

waveform of the two interference signals is shown in Fig. 1. The normalized signal which acquired according to the Eqs. 12 and 13 is shown in Fig. 2.

Figure 3 shows the demodulate signal which acquired by the demodulation algorithm that we proposed. The curve of the demodulation signal is relatively smooth. It reflects the original signal correctly. From the error curve (shown in Fig. 4), we can see that the error function presents a regular change along with the time, and the absolute error is less than ± 0.00017 V, the accuracy is relative higher. Construct the different analog signals with different frequencies and amplitudes, the signals can be demodulated correctly with the algorithm we proposed.

3.2 Experimental

To verify the feasibility of the demodulation algorithm, we utilized the fiber optic interferometer sensor to construct the experiment system. The schematic diagram of the distributed fiber-optic interferometer sensor is shown in Fig. 5. It includes a continuous wave super luminescent laser diode (SLD) source (40 nm bandwidth with a central wavelength of 1,310 nm and the output power is 5 mw), one isolator, one 3×3 fiber coupler, one symmetric 2×2 fiber coupler, one delay coil (Ld $=$ 2 km), one Faraday rotation mirror, two photo-detectors (PD1 and PD2), one sensing fiber cable, D is the position of the disturbance acting at the sensing fiber.

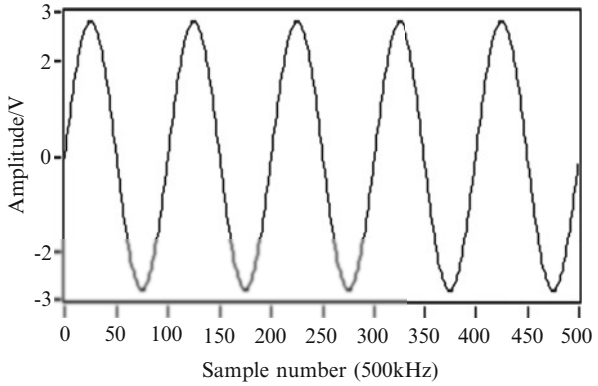

Fig. 3 Time sequences after demodulation

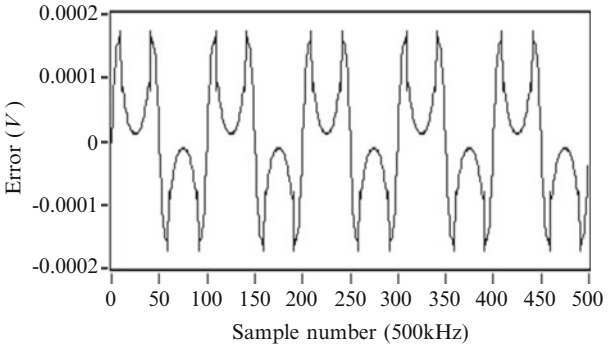

Fig. 4 Error of the demodulation signal

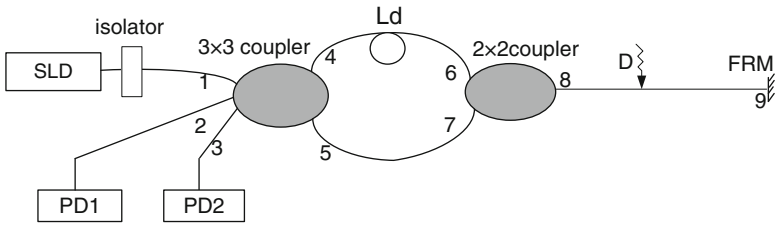

Fig. 5 The structure of optic fiber interferometer sensor

The two counter propagating beams can stably interfere at 3 × 3 coupler. The two beams have a delay 2nLd/c of the arrival time at the sensing section, which causes asymmetric phase shifts between the two counter propagating waves when a perturbation occurs. Intensity variation is converted to an electrical signal at the PD. The purpose of the demodulation is to acquire the external disturbance signals $\Delta\varphi(t)$ from the two phase modulation signals. The signals arrived at PD1 and PD2 can be expressed as:

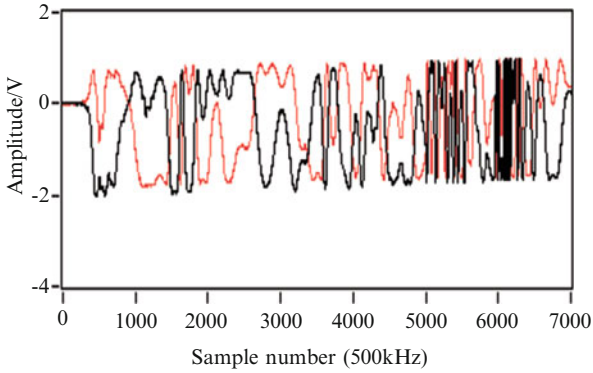

Fig. 6 The two signals of PD1 and PD2

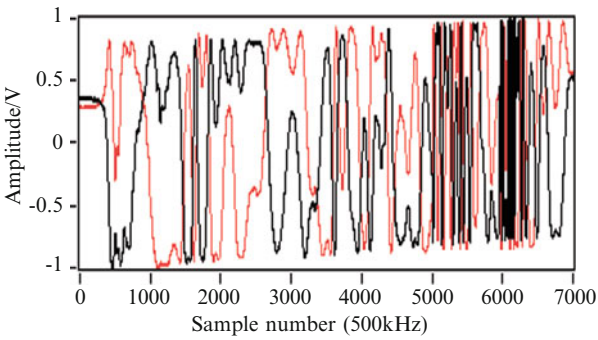

Fig. 7 The normalized signals of PD1 and PD2

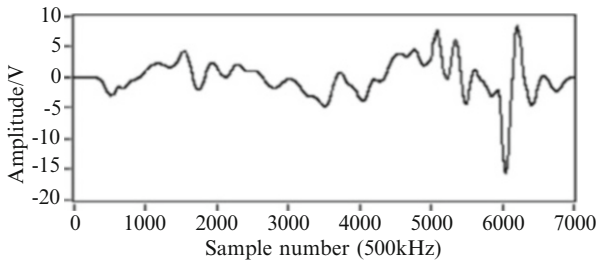

Fig. 8 The demodulation signal

$$I_1(\mathrm{t}) = A + B\cos(\Delta\varphi(t) + \phi) \tag{20}$$

$$I_2(\mathrm{t}) = A + B\cos(\Delta\varphi(t) - \phi) \tag{21}$$

The two outputs of PDs acquired by a 16 bits acquisition card (the sampling rate is 500 kbps) according to Eqs. 3 and 5 is shown in Fig. 6. After normalization, signals of IP1 and IP2 are shown in Fig. 7. The demodulation signal of IP1 and IP2 is shown in Fig. 8. Figures 6, 7, and 8 shows that the disturbance signal can be demodulated according to the method we proposed.

4 Conclusion

From the above theoretical analysis, simulation and experiment, it is shown that the phase modulated signal can be demodulated with the two interferometer signals. The main features of the method are as follows : Firstly, the output phase difference of the two signals can be arbitrary(except for theπ); secondly, there is no need for uniform splitting ratio of 3×3 coupler (this overcome the drawback of the demodulation method based on the 3×3 coupler symmetry); thirdly, simple mathematical operations without complicated operations of the integral and the operations of the differential. The method we discussed overcomes the phase distortion caused by the instability of the light output power effectively and it has the high precision which can meet the practical applications.

Acknowledgements This paper is supported by "the Fundamental Research Funds for the Central Universities (2012B03814)" and "the National Natural Sciences Foundation of China (Grant No. 61273170)".

References

1. Parker TR, Farhadiroushan M, Handerek VA (1997) A fully distributed simultaneous strain and temperature sensor using spontaneous Brillouin backscatter. IEEE Photon Technol Lett 9:979–981
2. Fernandes N, Gossner K, Krisch H (2010) Low power signal processing for demodulation of wide dynamic range of interferometric optical fibre sensor signals. In: Proceeding SPIE 7653, Fourth European workshop on optical fibre sensors, Porto, Portugal, 765328
3. Hoffman PR, Kuzyk MG (2004) Position determination of an acoustic burst along a Sagnac interferometer. J Lightw Technol 22:494–498
4. Russell SJ, Brady KRC, Dakin JP (2001) Real-time location of multiple time-varying strain perturbations, acting over a 40-km fiber section, using a novel dual-Sagnac interferometer. J Lightw Technol 19:205–213
5. Xu HY, Xu Q, Xiao Q, Jia B (2010) Disturbance detection in distributed fiber-optic sensor using time delay estimation. Acta Opt Sinica 30:1603–1607
6. Danbridge A, Tveten AB, Giallorenzi TG (1982) Homodyne demodulation scheme for fiber optic sensors using phase generated carrier. IEEE Trans Microw Theory Tech 30:1635–1641
7. Koo KP, Tveten AB, Dandridge A (1982) Passive stabilization scheme for fiber interferometers using 3×3 fiber directional couplers. Appl Phy Lett 41:616–618
8. Jiang Y, Lou M, Wang HW (1998) Software demodulation for 3×3 coupler based fiber optic interferometer. Acta Photon Sinica 27:152–155
9. Xu Y, Li YQ, Jiang Y (2011) Application of 3×3 coupler based Mach-Zehnder interferometer in delamination patch detection in composite. NDT E Int 44:469–476

High Resolution Radar Target Recognition Based on Distributed Glint

Baoguo Li, Zongfeng Qi, Ying Zhou, and Jing Lei

Abstract To solve the problem of aspect angle sensitivity of range profile while used in radar target recognition, the concept "distributed glint" is presented for high resolution radar. The detailed deducing procedure of "distributed glint" is given through theoretical analysis. A new target recognition strategy based on range profile and distributed glint is proposed. Computer simulation proves that this method can greatly enhance the performance of recognition strategy based on range profile.

Keywords High resolution radar • Target recognition • Distributed glint

1 Introduction

Range profile, which is the projection of a target's backscattering on the radar line of sight, has been shown to be highly discriminative of target features. However, while used as the feature for radar target recognition, the main drawback of range profile is its aspect sensitivity, mainly caused by the interference of different

B. Li (✉)
The State Key Laboratory of Complex Electromagnetic Environmental Effects on Electronics & Information System of China, Luoyang, China

School of Electronic Science and Engineering, National University of Defense Technology, Changsha, China
e-mail: laglbg322@yahoo.com.cn

Z. Qi • Y. Zhou
The State Key Laboratory of Complex Electromagnetic Environmental Effects on Electronics & Information System of China, Luoyang, China

J. Lei
School of Electronic Science and Engineering, National University of Defense Technology, Changsha, China

W. Wang (ed.), *Mechatronics and Automatic Control Systems*, Lecture Notes in Electrical Engineering 237, DOI 10.1007/978-3-319-01273-5_110,

scattering centers, which seriously degraded the performance of various kinds of target recognition methods exploiting range profile. To fully characterize the target, a larger number of range profiles at densely spaced aspect angles must be stored as templates [1]. The interference of different scattering centers is the main cause of target's angular scintillation (also called "glint"). Glint is harmful for tracking radar, and so engineers usually wish to suppress it [2]. Glint is a typical radar target characteristic signal. The most often used is linear glint offset, which means the deviation range, caused by glint. From target's glint, one can know some information about its physical structure. This leads us to consider using glint to enhance the target recognition performance. In this paper, the concept "distributed glint" is presented and a target recognition strategy using both distributed glint and range profile simultaneously is introduced. Computer simulation is performed to validate the efficiency of this method. The remainder of the paper is organized as follows. In section II, the concept of "distributed glint" is proposed and the detailed forming procedure is deduced through theoretical analysis. In section III, we give out a target recognition method using range profile and "distributed glint" simultaneously. Section IV gives out the simulation results of the above method. In section V, some conclusions and the forthcoming work are given.

2 Distributed Glint

For high resolution radar, range profile indicates the local RCS characteristic within each range cell. If the linear glint offset of each range cell is jointed together, the "distributed glint" is formed. Distributed glint can be induced through phase gradient method. Here we use a simplified multi-scatterers target model as Fig. 1 to illustrate the forming procedure of "distributed glint" [3]. In Fig. 1, target is represented by N statistically independent scattering centers; each scattering center is restricted within a cubic of L meters long. Radar transmits single carrier rectangular pulses as

$$s_0(t) = rect\left(\frac{t}{T_1}\right)\exp(-j2\pi f_0 t) \tag{1}$$

Where T_1 is the pulse width, f_0 is the signal's center frequency. Let R_k, a_k be each scattering centers' range from radar in radar's line of sight (LOS) direction and echo amplitude, respectively. Target's centroid is at the origin of the coordinates. So the echo signal can be expressed as

$$s(t) = \sum_{k=1}^{N} a_k rect\left(\frac{t - 2R_k/c}{T_1}\right)\exp(-j2\pi f_0(t - 2R_k/c)) \tag{2}$$

Fig. 1 Target model

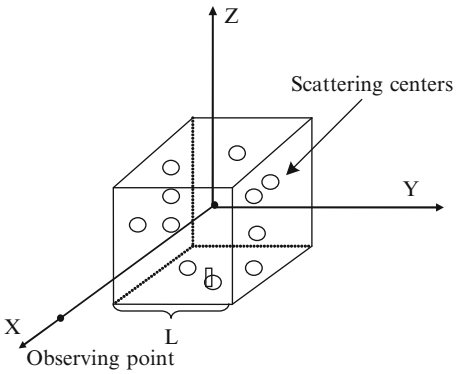

Remove the carrier, we get

$$s_1(t) = \sum_{k=1}^{N} a_k rect\left(\frac{t - 2R_k/c}{T_1}\right) \exp(j4\pi f_0 R_k/c) \tag{3}$$

Sampling $s_1(t)$ inside the range gate, the result is

$$s_1(n) = \sum_{k=1}^{N} a_k rect\left(\frac{t_0 + nt_s - 2R_k/c}{T_1}\right) \exp(j4\pi f_0 R_k/c) \tag{4}$$

Where $n = 1, 2, \ldots, M$, and M, t_s, t_0 denote the total number of sampling points, sampling interval and initial sampling instant, respectively. Letting $b(n,k) = rect\left(\frac{t_0+nt_s-2R_k/c}{T_1}\right)$ and $\varphi_k = (4\pi f_0/c)R_k$, we can get:

$$s_1(n) = |s_1(n)| \exp(j\varphi_E(n)) \tag{5}$$

$$\varphi_E(n) = \tan^{-1}\left[\sum_{k=1}^{N} a_k b(n,k) \sin\varphi_k / \sum_{k=1}^{N} a_k b(n,k) \cos\varphi_k\right] \tag{6}$$

The linear glint offset can be derived using phase gradient method [3]. The fluctuations of the normal to the phase front are determined by the gradient of φ_E, i.e.

$$\nabla\varphi_E = \frac{\partial\varphi_E}{\partial x} i_x + \frac{\partial\varphi_E}{\partial y} i_y + \frac{\partial\varphi_E}{\partial z} i_z \tag{7}$$

Where i_x, i_y and i_z are the unit vector components in the LOS coordinates.

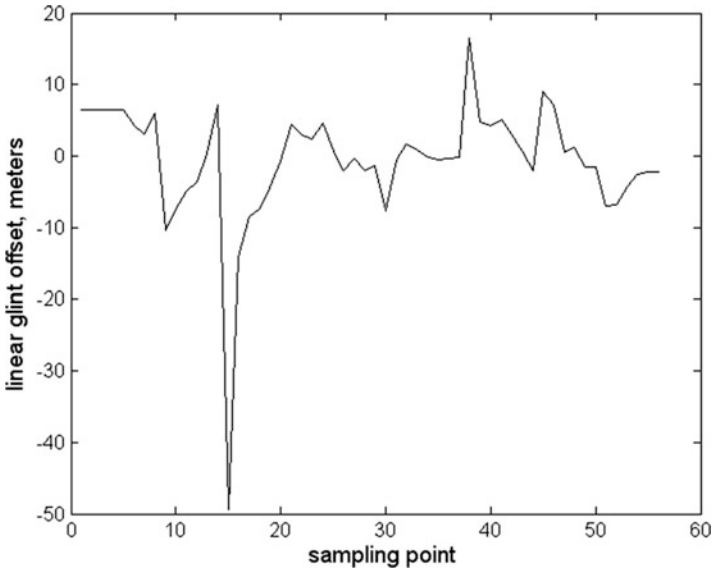

Fig. 2 Plot of a target's distributed glint

Take y direction as an example, the linear glint offset for each sampling point is as follows [2].

$$g_y(n) = \frac{\sum_{k=1}^{N}\sum_{l=1}^{N} a_k b(n,k) a_l b(n,l) y_l \cos(\varphi_k - \varphi_l)}{\sum_{k=1}^{N}\sum_{l=1}^{N} a_k b(n,k) a_l b(n,l) \cos(\varphi_k - \varphi_l)} \tag{8}$$

Here y_l is the scatter coordinate of y direction. Equation 8 shows how to compute the distributed glint of a target. Figure 2 is a plot of a target's distributed glint. In reality, it is impossible to know the accurate coordinate of each scatters.

In real battlefield environment, target is often noncooperative. For high resolution radar, distributed glint can be extracted from radar echoes as follows. Firstly, target can be separated into many range cells, for each range cell, the range and deviation angle can be computed, linear glint is the product of these two entries. From radar echoes, we can only get the absolute angle of each range cell, which subtracts the angle of range cell centroid is the deviation angle. So the key technologies lie in the estimation of range cell centroid. There are many methods to estimate the centroid, such as frequency diversity plus amplitude weighting [4], and it is not the emphasis of this paper. We lay the emphasis on the application of distributed glint.

3 Distributed Glint Based Target Recognition

It's well known that target glint (usually referred to linear glint offset) and target RCS (radar cross section) are not correlated, but the absolute value of target glint and target RCS are weakly negative-correlated [4]. The latter is the base of amplitude weighting glint suppressing algorithms and the former determines that glint can be used for target recognition. Since glint is not correlated with RCS, it must contain target structure information that RCS does not contain certainly. For high resolution radar, glint corresponds to distributed glint and RCS corresponds to range profile. So we propose a target recognition strategy based on distributed glint and range profile for high resolution radar.

In the recognition phase we have to select a suitable decision rule to compare the feature vector of an unknown target with feature vectors of known targets in the data base. Here we use the Matching-score rule introduced in Ref. [5]. The proposed recognition algorithm goes as follows:

Step 1: Construct the data base comprising the feature templates of M preselected targets at aspects of interest. These feature templates include range profiles, distributed glint in elevation direction and distributed glint in azimuth direction. Denote them by $g_i^r(\theta,\varphi), g_i^e(\theta,\varphi), g_i^a(\theta,\varphi)$, for each target i at aspect (θ,φ). The templates step angle obeys the criterion that the range motion of the scattering centers should not exceed a resolution cell if the target aspect changes an increment size.

Step 2: Calculate the normalized average correlation coefficients (ANCC) of three types of templates in the data base, respectively. Denote them by $\alpha_r, \alpha_e, \alpha_a$. These coefficients are stored as the fusion coefficients for future use.

Step 3: Fetch the input feature vector of an unknown target at a certain aspect, including range profiles, distributed glint in elevation direction and distributed glint in azimuth direction, and calculate the correlation coefficients with three types of feature templates at all aspects in the data base. Denote them by m_r, m_e, m_a, respectively.

Step 4: Use the fusion coefficients derived in step 2 to calculate the fusion matching-score of three types of features. The procedure can be expressed as $m_f = \alpha_r m_r + \alpha_e m_e + \alpha_a m_a$, where m_f is the fusion matching score.

Step 5: Identify the unknown target with one which has the maximum fusion matching score, m_f.

4 Simulations

Four simulated targets are chosen as the known targets. Target model is shown as Fig. 1. They each are combined with 80 scattering centers. All scattering centers are restricted within a cubic which is 20 m long. The coordinates of each scattering

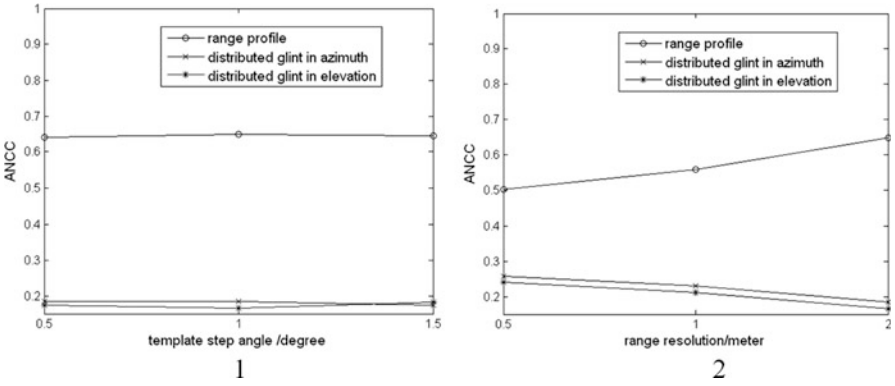

Fig. 3 ANCC of templates in the data base (1): constant range resolution 2 m, different step angle (2): constant step angle 1°, different range resolution

centers are uniformly randomly generated and then remain constant while aspect changes, the same is with each scattering centers' amplitude. The aspects region of interest is $(0, \pi/10)$. The transmitted radar signal's center frequency is 35 GHz. The range profile and distributed glint are supposed to have been aligned according to the center of the target already.

For range profile and distributed glint templates, ANCC indicate the similar degree of two consecutive templates. So the aspect sensitivity of each template can be characterized by ANCC. From Fig. 3 we can see that distributed glint is more aspect sensitive than range profile, so distributed glint can only be used to enhance the performance of target recognition based on range profile as an assistant feature. It is also shown from Fig. 3 that range resolution is the main factor that influences ANCC rather than the step angle.

Computer simulation is made to validate the performance of seven recognition methods based on three single feature and some combinations of each feature. The result is shown in Fig. 4. Seven recognition methods are symbolized by character "a" to "g" in the x-coordinate of Fig. 4, the relations are as follows:

a — only use range profile;
b — only use distributed glint in azimuth direction;
c — only use distributed glint in elevation direction;
d — combination of a and b (maximum fusion matching score);
e — combination of a and c (maximum fusion matching score);
f — combination of a, b and c (maximum fusion matching score);
g — combination of a, b and c (using vote rule);

It is seen from Fig. 4(1) that for all kinds of recognition methods, under constant range resolution, average recognition rate decreases when step angle increases, and vice versa. From Fig. 4(2) we can see that for all kinds of recognition methods, under constant step angle, average recognition rate decreases when range resolution

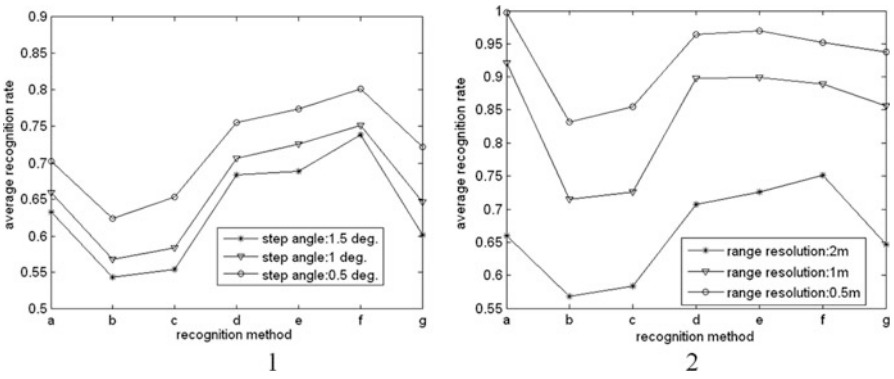

Fig. 4 Average recognition rate of each recognition method (1): constant range resolution 2 m, different step angle (2): constant step angle 1°,, different range resolution

decreases, and vice versa. The performance of method (a) is superior to method (b) and (c) under various conditions. This proves that distributed glint can only be used as an assistant feature of range profile for its much more serious aspect sensitivity than range profile. We can also see that the performance of fusion recognition methods (d, e, f) is far superior to that of recognition method using single range profile feature when range resolution is relatively low (such as 2 m in the simulation). When range resolution is relatively high (such as 1 and 0.5 m in the simulation), the fusion methods' recognition performance is nearly equivalent to that of the recognition method using single range profile feature. This phenomenon can be interpreted as: when range resolution is low, each range cell of the target contains many scattering centers, so distributed glint contains enough information about target's structure and it will enhance the performance of recognition method using single range profile. On the other hand, when range resolution is high, almost every scattering center is separated into different range cell, distributed glint contains many range cells of zero value and it does not contain enough information about target's structure.

5 Conclusion

In this paper, we proposed a new concept of "distributed glint" and discussed the application of this new target feature in radar target recognition. Through computer simulation, we see that target distributed glint can explicitly enhance the performance of target recognition based on target range profile. In real engineering applications, the accuracy of distributed glint directly affected the performance of target recognition method we proposed. How to improve the estimation accuracy of range cell centroid is the most critical problem, and this is the emphasis of our future work.

Acknowledgements The authors are with the State Key Laboratory of Complex Electromagnetic Environmental Effects on Electronics & Information System of China and the School of Electronic Science and Engineering, National University of Defense Technology. This work was supported by the fund of "The State Key Laboratory of Complex Electromagnetic Environmental Effects on Electronics & Information System, China (No.CEMEE2012K0303B)" and "National Natural Science Foundation of China (No.61101074, 61101097)".

References

1. Xuejun Liao, Zheng Bao (1998) Circularly integrated bispectra: novel shift invariant features for high-resolution radar target recognition. Electron Lett 34(19):1879–1880
2. Dongtao Zhao, Hao Wang (2010) Glint suppression based high resolution radar angle tracking. Electron Sci Tech 23(11):67–69
3. Sandhu GS, Saylor AV (1985) A real-time statistical radar target model. IEEE Trans A E S 21(4):490–507
4. Hong Cheng Yin, Pei Kang Huang (2008) Further comparison between two concepts of radar target angular glint. IEEE Trans Aerosp Electron Syst 44(1):372–380
5. Hsueh-Jyh Li, Sheng-Hui Yang (1993) Using range profiles as feature vectors to identify aerospace objects. IEEE Trans Antennas Propag 41(3):261–268

A Differential Capacitive Viscometric Sensor for Continuous Glucose Monitoring

Zhijun Yang, Meng Wang, Youdun Bai, and Xin Chen

Abstract The development of glucose micro sensors for clinical use is driven by the aim of automatic blood glucose normalization in diabetic patients. An improved affinity viscometric sensor for continuous glucose monitoring (CGM) is presented by using a micro-electro-mechanical system (MEMS) with a differential capacitor. A numerical model using Reynolds equation is used to simulate the dynamic response under different viscosities, and the relationship between capacitance and viscosity is revealed. Compared to the previous version presented by Columbia University, the sensor designed in this paper has enhanced the capacitor by introducing a differential capacitance, which also avoided volume changes of the air and polymer solution chambers during the vibration, increasing the linear range of the sensor. In addition, the simulation results show that the sensor can be driven by a Gaussian Pulse resulting in a significant power saving, when compared to a sinusoidal excitation.

Keywords Continuous glucose monitoring • Biosensor • Differential capacitance • Viscometer

1 Introduction

The development of glucose sensors for clinical use is driven by the aim of blood glucose normalization in diabetic patients [1]. Close monitoring of daily blood sugar levels reduces the risk of diabetes-related complications by allowing timely identification and correction of hyperglycemia as well as hypoglycemia, a condition that typically results from excessive insulin uptake.

Z. Yang (✉) • M. Wang • Y. Bai • X. Chen
School of Electromechanical Engineering, Guangdong University of Technology, Guangzhou, China
e-mail: yangzj@gdut.edu.cn

W. Wang (ed.), *Mechatronics and Automatic Control Systems*, Lecture Notes in Electrical Engineering 237, DOI 10.1007/978-3-319-01273-5_111,

This can be most effectively achieved by continuous glucose monitoring (CGM), which involves continuous measurements of physiological glucose levels.

There are two types of CGM devices that have been developed. The first one is an electrochemical method, including enzymatic or non-enzymatic reactions [2]. Electrochemical methods are capable of sensitive and specific glucose detection. However, the irreversible consumption of glucose in the electrochemical detection induces a potential change in the equilibrium glucose concentration in the tissue and thus affects the actual measured glucose level. In addition, the rate of glucose consumption is diffusion limited [3]. This lack of reliability has been severely hindering CGM applications in relation to practical diabetes management.

Another type of CGM is a physical method, in which the glucose is not consumed. More importantly, affinity sensing is considerably more stable, as the deposition of biological material on the implanted sensor surface results only in an increased equilibrium time, without any changes in the measurement accuracy. A widely used affinity sensing technique is based on concanavalin A (Con A), whose specific binding to glucose can be detected via methods such as fluorescence [4, 5] and viscosity [6]. The integration of capacitive detection within the MEMS affinity glucose sensor [7]represents a major improvement to the previously reported devices [6]. This viscosity change causes variations in the viscous damping on the magnetically driven vibration of a flexible diaphragm, whose deflection results in changes of the capacitance between two electrodes, one of which is embedded in the diaphragm. Thus, the capacitance change can be measured to detect the damped diaphragm vibration and further determine the interstitial fluid glucose concentration. However, the tension of the membrane changes with the compression of the trapped air, so the amplitude of vibration cannot be too large (less than 1 μm) in order to keep a linear relationship, such that the capacitance and its changes are very small [8].

In this paper, we introduce a relatively rigid silicon beam supported by a Parylene diaphragm in the middle, the magnetic force is applied to beam on the capacitor side, causing the beam to vibrate in a seesaw manner. The movement of the beam causes the diaphragm to deform in a seesaw manner "ᔓ ᔕ", avoiding any change in the overall volume of the air chamber and consequent change in the diaphragm tension. The damping forces caused by the movement of the membrane affect the beam's motion, further increasing the sensitivity of the sensor. In addition, the simulation results show that the sensor can be driven by a Gaussian Pulse resulting in a significant power saving when compared to a sinusoidal excitation, and the sensitivity can be adjusted by the clearance between the beam and walls.

2 Principle and Design

The affinity glucose sensor is based on a relatively rigid beam that is supported in the middle of a parylene membrane between two micro-chambers. The structure of the glucose sensor is shown in Fig. 1. In the figure, one end of the beam is situated inside a polymer solution micro-chamber, which is filled with the solution of a biocompatible polymer that binds specifically and reversibly with the glucose, and

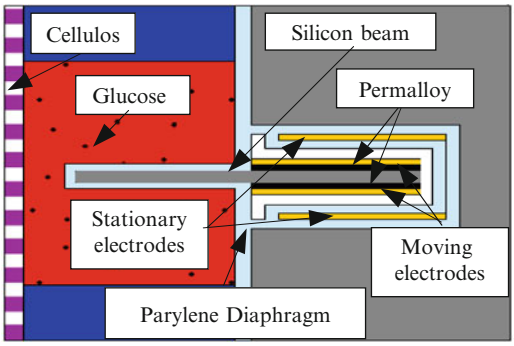

Fig. 1 The structure of the designed glucose sensor

is sealed by a cellulose acetate semi-permeable membrane, which allows the glucose to permeate into and out of the chamber while keeping the glucose-sensitive polymer from escaping. The silicon beam is coated by a parylene film to avoid direct contact with the polymer solution.

The other end of the beam is located inside a micro air chamber and is coated with a Permalloy layer so that it can be excited by a magnetic force. The moving electrodes are situated on the beam, together with stationary electrodes on the chamber walls to form the differential capacitor. The differential capacitor is more sensitive to the vibration of the moving electrode of the capacitor [9].

The beam is excited by the microcoils that cause the Parylene membrane bending vibration. The electrodes on the beam are insulated by the Parylene to avoid direct contact with the polymer solution.

3 Modelling and Simulation

In order to investigate behavior of the presented glucose sensor, a multiphysics model has been developed using Reynolds equation for thin film lubrication, combining structural mechanics, fluid dynamics and electrostatic analysis, to analyze the vibration of the Parylene diaphragm and beam structure, and the capacitance of the differential capacitor. The parameters are shown is Fig. 2, and the detailed values are listed in Table 1.

The materials used are silicon, Parylene C, Permalloy (80 %Ni, 20 %Fe). The prestress of the Parylene diaphragm is set at $35MPa$. The material properties for polymer solution with the mass density $1000kg/m^3$.and the viscosity values studied are 10, 20, 30, 40 and 50 cP. The mass density and viscosity of air is $1.293kg/m^3$, and $17.9 \times 10^{-6}Pa \cdot s$, respectively.

The fluid type can be determined by the relaxation time, where the relaxation time can be estimated according to the properties of the polymer solution. It is not known exactly what the fluid characteristic the polymer is, the possible characteristics are rigid rod, free draining and non free draining [10]. It has been proved that no matter what kind of molecular type it is, the relaxation frequency is

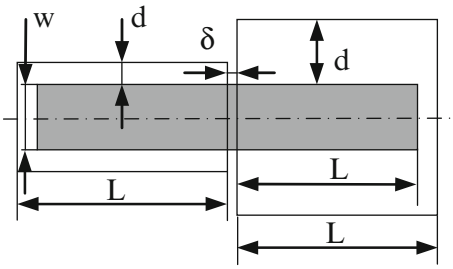

Fig. 2 The original parameters of the model

Table 1 Dimensions of the sensor

Parameters	Value (μm)	Parameters	Value (μm)
Thickness of Parylene diaphragm (δ)	10	The length of air chamber (L_a)	1,000
Width of silicon beam (w)	1,000	Thickness of silicon beam (δ_s)	50
The length of Silicon beam in both sides (L)	900	Clearance between silicon beam and air chamber (d_a)	10
The length of polymer solution chamber (L_s)	1,000	Clearance between beam and solution chamber (d_s)	10

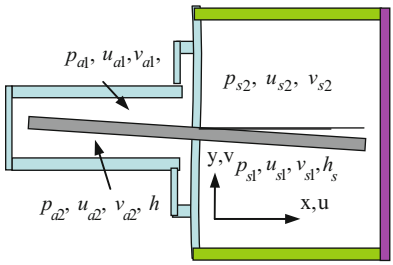

Fig. 3 The vibration shape of the beam structure

much higher than excitation frequency, so the fluid can be recognized as Newtonian fluid [8].

The velocity of the fluid

$$v < A\omega = 10^{-5}m \times 1000s^{-1} = 10^{-2}m/s \tag{1}$$

where ω and A are the circular frequency and amplitude of the response, respectively. The velocity of the fluid v is only $2.6 \times 10^{-5}Ma$, much less than $0.3Ma$, so the fluids are incompressible.

For the parylene diaphragm and silicon beam structure, the vibration (shown in Fig. 3) can be equivalent as

$$I\ddot{\theta} + c\dot{\theta} + k\theta = M_{ext} \tag{2}$$

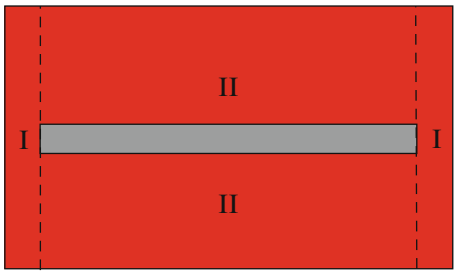

Fig. 4 Different flow in the glucose sensor

where I, c and k are the inertial, damping and stiffness, respectively. θ is the rotation of the membrane, and M_{ext} is the excitation moment caused by the magnetic force and interacted fluid flow pressure.

The length of beam is 900 μm, if the maximum displacement is 60 μm, the rotation of the parylene diaphragm is atan(60/900) = 3.81°, which is within the linear vibration of the diaphragm. The damping force of membrane is much smaller than that caused by polymer solution, can be neglected for simplicity.

Once the excitation moment M_{ext} is known, it is easy to solve Eq. 2. However, the flow inside micro-chambers are complicated, the pressure of the fluid flow is hard to get. Fortunately, if we divided the flow domain into sections I and II (shown in Fig. 4), and assume that the fluid is incompressible, the volume flow between two sections II all passes through the gap between the tip of beam and the wall of chamber as it is much wider than the gap between the sides of the beam and the chamber walls. The length of beams are much longer than the thickness, it can be seen that section I is oscillatory flow, and section II is squeezed film flow.

According to thin film lubrication theory, the fluid inside micro-chamber can be described by Reynolds equation [11].

$$\nabla \cdot \left[\left(\frac{\rho_i h_{ij}^3}{\mu} \right) \nabla p_{ij} \right] = 12 \frac{\partial (\rho_i h_{ij})}{\partial t} + 6 \nabla \cdot (\rho_i h_{ij} u_{ij}) \tag{3}$$

where ∇ represent the gradient operator, and ρ, h, μ, p and t are mass density, thickness, viscosity, pressure and time, respectively. The subscript $i = a, s; j = 1, 2$, a means air, s means polymer solution.

$$h_{ij}(x) = a_i \pm x_i \sin(\theta) \tag{4}$$

$$u_{ij}(x) = x_i \dot{\theta} \cos(\theta) \tag{5}$$

$$v_{ij}(x) = x_i \dot{\theta} \sin(\theta) \tag{6}$$

Where x is the distance starts from the membrane, u and v are the horizontal and vertical velocity, respectively. In addition, there still exists shear forces between the edges of the beam and the walls.

For the section I, the flow is a typical Stokes' second law problem [12], the shear force f_e is

$$f_e = \mu_i \frac{\partial v_i}{\partial d_i} \tag{7}$$

For the tip edge, assume that the fluid volume change all passes through the clearance between the tip and the wall. The volume change ΔV is

$$\Delta V_i = \pi L_i^2 w \cdot \frac{\theta}{2\pi} = \frac{1}{2} L_i^2 w\theta \tag{8}$$

The volume flow rate between the tip and the wall is

$$\dot{V}_i = \frac{\Delta \dot{V}_i}{w(L_i - L\cos(\theta))} = \frac{1}{2} \frac{L_i^2 \dot{\theta}}{L_i - L\cos(\theta)} \tag{9}$$

Therefore, the shear force between the tip and the wall ft is

$$f_t = \mu_i \frac{\partial v_i}{\partial r_i} = \mu_i \frac{L_i \dot{\theta} + \dot{V}_i}{L_i - L\cos(\theta)} \tag{10}$$

The electric force of the capacitor f_e is

$$F_e = \frac{\varepsilon A (\Delta V)^2}{2h_a^2} \tag{11}$$

where ε is relative permittivity of air. Therefore, the total moment of the vibrating structure is

$$M_{ext} = \int_0^L (p_{i1} - p_{i2}) w x dx + 2\int_0^L x f_e dx + w f_t L\cos\theta + \frac{1}{2} f_m L \tag{12}$$

where f_m is the total magnetic force applied to the beam.

The capacitance of the differential capacitor is

$$C = \int_0^L \frac{\varepsilon w}{4\pi k h_{a1}(x)} dx - \int_0^L \frac{\varepsilon w}{4\pi k h_{a2}(x)} dx \tag{13}$$

C is capacitance, k is electrostatic constant $k = 9.0 \times 10^9 N \cdot m^2 / coulomb^2$.

4 Results and Discussions

The vibration of the beam diaphragm structure is shown in Fig. 3. It can be seen that the main vibration is the bending of the diaphragm, which enable the volume of both air chamber and solution chamber to remain constant.

Assumed that the excitation force is sinusoidal function, the displacement response is shown in Fig. 5. The relationship between viscosity and capacitance is almost linear (Fig. 6), and the sensitivity is $-3 \times 10^{-8} pF/cp$.

However, the continuous excitation would cost too much energy. In order to save energy, the exciting force is a Gaussian pulse instead of sinusoidal function, the excitation magnetic forces with magnitude of $0.9\mu N$ in total.

The displacement response of a point at the tip of the silicon beam at air chamber side under different viscosities 10, 20, 30, 40 and 50 cP are shown in Fig. 7. It can be seen that the displacements are decreasing with viscosities.

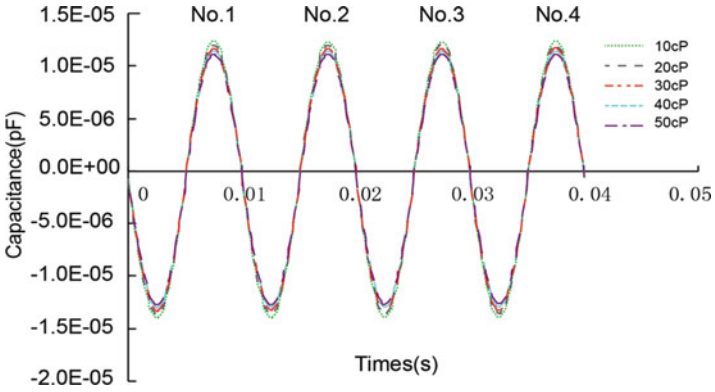

Fig. 5 The displacement response of sinusoidal excitation

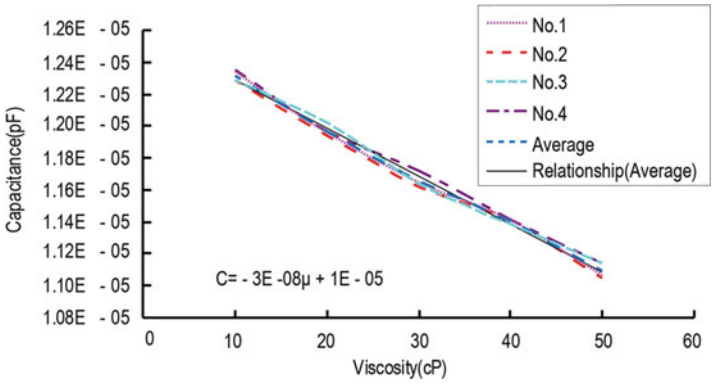

Fig. 6 The relationship between amplitude and viscosities

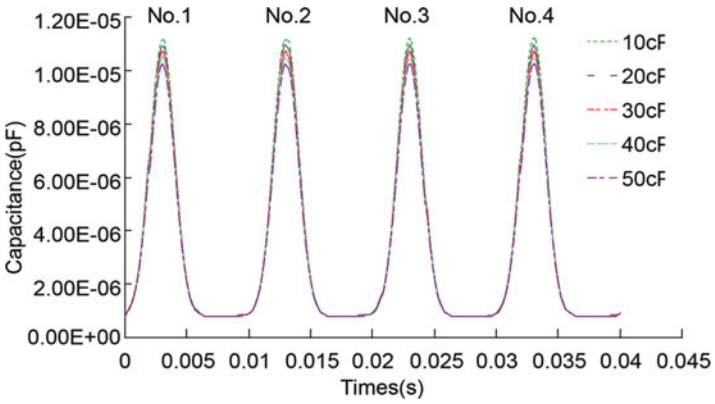

Fig. 7 The displacement response of Gaussian pulses with different viscosities (Original)

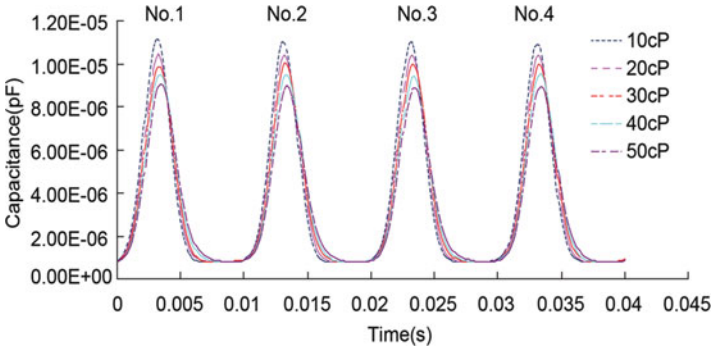

Fig. 8 The displacement response of Gaussian pulses with different viscosities (Improved)

The relationship between amplitude and viscosities is almost linear, the sensitivity is $-2 \times 10^{-8} pF/cp$, and the error is within 0.5 %.

From Eq. 7, one can see that the clearances d_a and d_s are very important to the damping forces. We increase the clearance in the air chamber to $d_a = 50\mu m$, while decreasing the one in the polymer solution chamber to $d_s = 10\mu m$. The results are shown in Fig. 8, the relationship between amplitude and viscosities is linear and the sensitivity is $-4 \times 10^{-8} pF/cp$. As a result, the sensitivity is doubled.

When the capacitance is measured, the dynamic viscosity of the polymer solution can be calculated by

$$\mu = -2.5 \times 10^7 C - 250 \tag{14}$$

using the relationship between viscosity and glucose concentration [7], the glucose concentration can be easily detected.

The relationship has been estimated by Eq. 14, and the results of the original design and improved design show that the relative error of the improved design are within 0.341 %, which is much low than original design (0.945 %).

5 Conclusion

This paper presents an improved differential capacitance based viscometer glucose sensor. The operating principle is the vibration of a compound micro beam and pre-stressed membrane structure which is excited by Gaussian pulse. The vibration amplitude can be changed according to viscosity of the polymer solution. The sensitivity of the viscosity can be adjusted by the clearance between the beam and the walls. The relationship between vibration amplitude and viscosity is almost the same as sinusoidal excitation. Therefore a Gaussian pulse may be used as the exciting force, significantly reducing the power consumption of the sensor and enable a longer battery life.

Acknowledgements This work is supported by Natural Science Foundation of China (U1134004, 50905033), Guangdong Innovative Research Team Program (201001G0104781202), The National Basic Research Program of China (2011CB013100-G, National key technology support program (2012BAF12B10), Specialized Research Fund for the Doctoral Program of Higher Education of China (20094420120001)

References

1. Clark HR, Barbari TA (1999) Modeling the response time of an in vivo glucose affinity sensor. Biotechnol Prog 15:259–266
2. MiniMed Paradigm (2006) REAL-time insulin pump and continuous glucose monitoring system[P]. Medtronic MiniMed, San Antonio
3. Tracey Neithercott (2011) Continuous glucose monitoring system[J]. Diabetes Forecast 64:44–46
4. Schultz JS, Mansouri S et al (1982) Affinity sensor – a new technique for developing implantable sensors for glucose and other metabolites[J]. Diabetes Care 5(3):245–253
5. Schultz J, Sims G (1979) Affinity sensors for individual metabolites[J]. Biotechnol Bioeng Symp 9:65–71
6. Zhao yongjun, Li siqi et al (2007) A MEMS viscometric sensor device for continuous glucose monitoring[J]. J Micromech Microeng 17(12):2528–2537
7. Huang xian, Li siqi et al (2009) A capacitive MEMS viscometric sensor for affinity detection of glucose[J]. J Microelectromech Syst 18(6):1246–1254
8. Yang zhijun, Robert Kelley et al (2011) A numerical investigation of a capacitive viscometer with fluid–structure interaction using equivalent modeling[C]. Adv Mater Res Adv Mater Process, PTS 1–3(311–313):2423–2429
9. Lotters JC, Olthuis W et al (1999) A sensitive differential capacitance to voltage converter for sensor applications[J]. IEEE Trans Instrum Meas 48(1):89–96

10. Block H, North AM (1970) Dielectric relaxation in polymer solutions, advances in molecular relaxation processes. Elsevier Publishing Company, Amsterdam – Printed in the Netherlands, pp 309–374
11. Sherman FS (1990) Viscous flow[M]. McGraw-Hill Higher Education, New York, pp 746–747
12. Batchelor GK (1998) An introduction to fluid dynamics[M]. Cambridge University Press, New York, pp 302–303

An Improved Secure Routing Protocol Based on Clustering for Wireless Sensor Networks

Lin Chen and Long Chen

Abstract The security and efficiency are essential primary points for Wireless Sensor Networks (WSNs) when designing routing strategy. This paper proposes a secure routing solution based on LEACH protocol and clustering method in which system security is integrated into sensor node and clusters are changed dynamically and periodically according to node mobility, and it is different with the traditional encryption mechanism by using key clustering homemade management to reach the overall security. The simulation results show that the proposed secure routing protocol improve the survivability of node more efficiently in a harsh sensor network environment. Through clustering management dynamically, the immunity of WSNs has been enhanced, and it can be concluded that this routing protocol improved the network security effectively.

Keywords Wireless sensor network • Routing protocol • Security • LEACH

1 Introduction

A wireless Sensor Networks (WSNs) is an ad hoc wireless telecommunication network which embodies a number of tiny, low-powered sensor nodes densely or sparsely deployed in the area of interest to accomplish a particular mission like habitat monitoring, agricultural farming, battlefield surveillance etc. [1]. The extensive rise of using WSNs in diverse applications such as hostile, unattended, and inaccessible environments, have mandated the users to be more assured about the security and efficiency compared to the survivability. As long as security schemes

L. Chen (✉) • L. Chen
College of Computer Science, Yangtze University, Jinzhou, China
e-mail: chenlin@yangtzeu.edu.cn

W. Wang (ed.), *Mechatronics and Automatic Control Systems*, Lecture Notes in Electrical Engineering 237, DOI 10.1007/978-3-319-01273-5_112,

provide confidentiality, authentication, and integrity, which are critical for such applications, a secure and survivable infrastructure is always desired. Network survivability has been defined as the ability of the network to fulfill its mission in the presence of attacks and/or failures in a timely mode [2]. In such hostile environments, the information exchanged between two communicating parties might include highly sensitive data that must be safeguarded, therefore security investigation and efficient routing strategy for WSNs have been a continuous research hot topic in the recent decades [3].

LEACH (Low Energy Adaptive Clustering Hierarchy) is a classical and hierarchical routing protocol which is based on the idea of clustering to lengthen the network lifetime and forward data reliably, but LEACH protocol is not secure enough to against all kinds of network threats, so it has no ability to resist some attacks in network layer. Therefore, a variety of improved routing protocols based on LEACH are investigated to improve security of WSNs, such as RLEACH protocol which is based on LEACH and embed encryption and authentication technologies to prevent unauthorized node to participate in route creating and data transmission works. However, it is vulnerable to a number of security attacks including jamming, spoofing and replay, the reason is that the LEACH protocol is a cluster-based protocol and rely on their Cluster Heads(CHs) for routing to a great extent, and some attacks involving CHs are most dangerous, if a attacker intrude networks successful and become a CH in cluster-based networks, it can stage attacks such as sink hole and data selective forwarding, to disrupt the WSNs network, the intruder may also leave the routing alone and try to inject bogus sensor data into the network to destroy the normal work [4].

A Homemade Low Energy Adaptive Clustering Hierarchy (HLEACH) protocol for WSNs is proposed to strengthen sensor node security in this paper. HLEACH is different with traditional encryption mechanism using KEY management which consumes considerable network and computing resources. In order to resolve the problem about KEY management, HLEACH protocol adopts distributed method between each clusters to reduce resource management consumption and improve routing efficiency, and during nodes migrating randomly, the KEY of the sensor nodes will change dynamically according to cluster, if one node is captured, the entire network security will not been affected.

2 The LEACH Protocol and Vulnerabilities

2.1 The LEACH Protocol Description

The LEACH protocol consists of three steps to create cluster and cluster membership.

In the first step, every node may decide probabilistically whether or not to become a CH for the current round or period. These candidate CH nodes will

broadcast a message advertising this fact, and nodes at some extend can receive these broadcasting messages. In this step, the CSMA-MAC protocol is used to avoid channel collision.

In the cluster joining step, the remaining nodes select a cluster to join based on the largest received signal strength from a candidate CH, and send a join request message using CSMA-MAC to this candidate CH to show their intentions. At the end of this step, distributed clusters geographically will emerge, and membership between the CH and its receivers will also generate in a period.

Once a CH receive all the join requests, the confirmating step starts with the CH broadcasting a confirmation message that includes a time slot schedule to be used by their cluster members for communication during the steady state phase.

After the clusters are set up, the network will be a steady state phase, where actual communication between sensor nodes, CHs and the BS(base station) will take place. Each node knows when it is turn to transmit their sampling data in their environment according to the time slot schedule. The CHs collect messages from all their cluster members, and aggregate these data according some aggregating strategies, then send the aggregating results to the BS.

2.2 Security Vulnerabilities

Like most routing protocols for WSNs, LEACH does not take into account the security and is also vulnerable to a number of network attacks. In contrast to more conventional multi-hops transmitting schemes, member nodes around the CHs and BS are especially attractive for some attackers, but CHs in LEACH communicate directly with the BS, may be anywhere geographically in the network, and can change dynamically from round to round. All these characteristics make it harder for an adversary to identify CHs, so the dynamic CHs strategically are more important nodes to avoid network attack. Because LEACH is a cluster-based protocol, relying on the CHs fundamentally for data aggregation and routing, attacks involving CHs are the most dangerous.

LEACH routing protocol may extend the entire network life cycle, but not get a good improvement in terms of security. Because KEY management is an effective method to identify illegal nodes, and the dynamic CHs also make attackers harder to separate CHs and cluster members, the two ideas can be employed to improve WSNs' security. Therefore, in order to further improve the security, the proposed HLEACH uses dynamic changeable CHs and KEY encryption management to check the validity of each node in the identity authentication phase [5, 6].

3 The Proposed HLEACH Protocol

The setup of the proposed HLEACH protocol consists of four steps: the choice of Cluster Head nodes (CHs), CHs broadcasting, CHs identity authentication and cluster internal management.

1. Choice phase of CHs. The CHs choice of HLEACH protocol is same as that of the LEACH protocol. The choice of CHs is based on the node number in network, the total number of CHs and node distributed geographically. In this choice procedure, each candidate generates a value between 0 and 1 randomly, if this value is lower than a certain threshold, it will become a CHs and then enter the next phase.
2. CHs broadcasting message phase. After a candidate CH becomes a CH, it will broadcast this fact in the whole network through the radio, and other sensor nodes in a certain radius range in the network decide whether or not to join this clusters based on the signal strength of the received information, if the node decide to join in, then it will notify the appropriate CH, in a stable state a cluster will be established. Finally, the CHs allocate the interval of transmitting data for each node in the cluster.
3. CHs identity authentication phase. This step will ensure whether that CH is a legitimate node, and to make sure that the legitimacy of the CH has a crucial role in WSN security. Each node in the WSNs has an unique ID distributed by the base station, when a new node joins into in a cluster, it should get a ID form the BS, if a node become CH in the first phase, it should report its own ID to the BS, and the other nodes in the cluster can also receive this report messages and save the ID. Then the BS will validate this ID, if the ID verification is successful, the BS will send a broadcast message to all sensor nodes and notify that the CH is legitimate. In the same time the BS sends a public KEY to this CH, this public KEY will be used between CHs to ensure the security of information transmitting.
4. Cluster internal management phase. CHs notify its ID to every node in the cluster through the radio. The nodes use the CH's ID as the KEY to send messages, there are many encryption algorithms which may be used, in our simulation the DES encryption algorithm is adopted.

Figure 1 shows the relationship between KEYs and nodes, letter N delegate sensor node, A and B are the ID of CHs, C is the public KEY. The left side of Fig. 1 shows that when the nodes send the message to the CH which the KEY is CH's ID-A, the right side of Fig. 1 shows that when the nodes send the message to the CH which the key is CH's ID-B. When the CH sends a message to the BS or other CHs which the KEY is the public key-C.

In the stable phase, the nodes sample data and transmit them to the CH. The CHs collect data send by all their cluster members, and aggregate these data, and then send the result data to the BS. The steady state phase lasts much longer compared with the setup phase. The network will be restarted to establish the cluster and transmit sampling data in the next cycle repeatedly.

Fig. 1 Key distribution

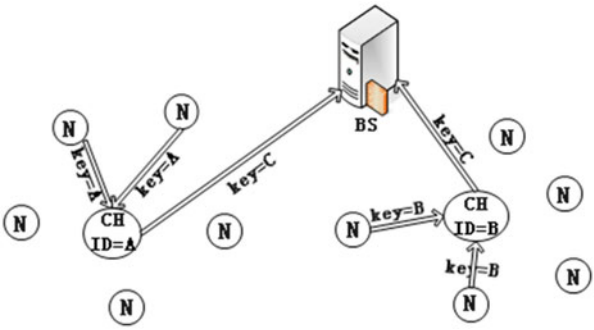

4 Performance Evaluation

In order to evaluate the performance of HLEACH protocol, NS2 simulation tools are used as experiment platform with 50 nodes and 2 malicious nodes in 1,200 × 1,200 range, simulation time is 1,000 s. In simulation procedure, two different parameters are adopted to measure performance.

Memory consumption: WSNs has some applications in memory, but sensor nodes have a tiny memory volume and can't hold a bigger memory, the lack of memory has always been a difficult problem in WSNs.

Network lifetime: Sensor node power supply is battery powered and is always a central point of the research. There are a lot of programs to save energy consumption. The life cycle is one of the most important indicators to measure the feasibility of a protocol.

The following figures show the performance curve which interference by malicious nodes.

Figure 2 shows the memory consumption of each node in the network, although HLEACH protocol embedded encryption mechanism, when the network was attacked, its memory consumption is significantly less than that of LEACH protocol. Figure 3 shows the node lifetime of HLEACH is reduced in the case of attack. The improved agreement to extend the life cycle of WSNs, it also proved that the improved protocol is feasible.

5 Conclusions and Future Work

WSNs is a low cost, fast ad hoc networks of anti-survivability characteristics and is applied strong and widely in many areas of military, industrial, etc. and needs a secure solution to solve many common challenging problems. The security is a prerequisite of a new technology application. In this paper, HLEACH is proposed to

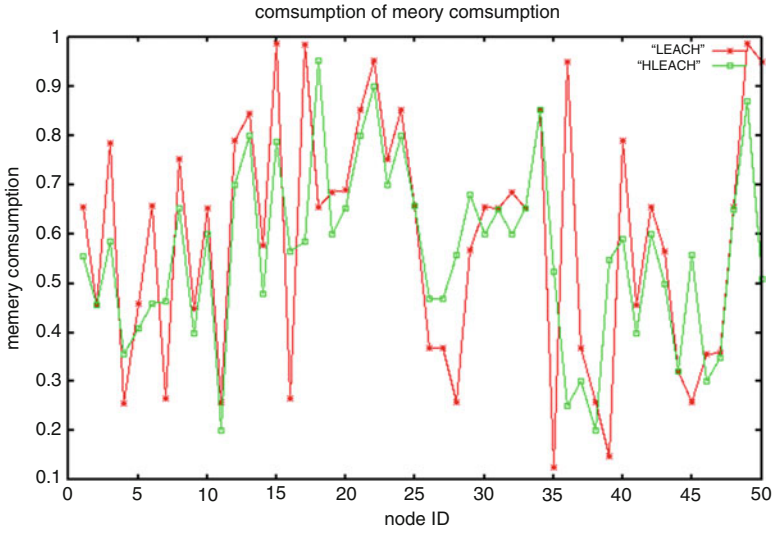

Fig. 2 Analysis of network memory

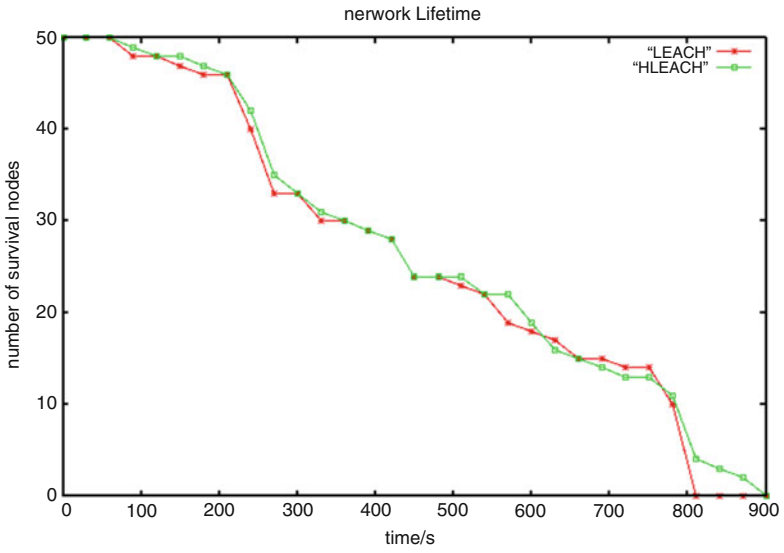

Fig. 3 Analysis of network lifetime

improve routing protocol on the basis of the LEACH protocol, which transmits the information through the sub-cluster autonomy and multi-channel, it can prevent some network attacks. But it adds a certain amount of memory and energy consumption, which is a gap of this paper, and it also needs further improvement.

Acknowledgements This work is supported by the Hubei Natural Science Foundation. I would like to show my deepest gratitude to this organization, without its support we will not finish this paper very smoothly.

References

1. Karlof C, Wagner D (2003) Secure routing in wireless sensor networks: attacks and countermeasures. Elsevier's Ad Hoc Networks Journal, Special Issue on Sensor Network Applications and Protocols 1:293–315
2. Jing Dengrichard, Shivakant, Mishra (2006) Decorelating wireless sensor network traffic to inhibit traffic analysis attacks. Special Issue of Elsevier Journal of Pervasive and Mobile Computing Journal (PMC)on Security in Wireless Mobile Computing Systems 2(2):159–186
3. Zhu S, Setia S, Jajodia S (2003) LEAP: efficient security mechanisms for large-scale distributed sensor networks. In: Proceedings of the 10th ACM conference on computer and communication security, ACM Press, Washington DC, USA, pp 62–72
4. Heinzelman WB, Chandrakasan A, Balakrishanan H (2002) An application-specific protocol architecture for wireless microsensor networks. IEEE Trans Wirel Commun 1(4):660–670
5. Akkaya K, Younis M (2004) Energy-aware routing of delay-constrained data in wireless sensor networks. J Commun Syst 17(6):663–687
6. Przydatek B, Song D, Perrig A (2003) SIA:Secure information aggregation in sensor networks. In: ACM SenSys 2003, Los Angeles, CA, USA, pp 175–192

Spatiotemporal Dynamics of Normalized Difference Vegetation Index in China Based on Remote Sensing Images

Yaping Zhang and Xu Chen

Abstract Based on 17 phases of Normalized Difference Vegetation Index and climate images obtained from 1982 to 1998, the paper analyzed normalized difference vegetation index trends, spatial distribution and their relationships with climate and human activity. The results indicate that at the national scale, the increases of monthly and seasonal NDVI correspond mainly to climate changes. However, corresponding mainly to human activities, the significant spatiotemporal heterogeneity of NDVI trends is found at the regional scale. Therefore, a set of policies must be established to ensure the ecological conservation and restoration, especially in ecological sensitivity areas.

Keywords NDVI • Spatiotemporal dynamics • Time-series

1 Introduction

Normalized Difference Vegetation Index (NDVI) is a general biophysical parameter that correlates with photosynthetic activity of vegetation. It is calculated as NDVI = (CH2 − CH1)/(CH2 + CH1), where CH1 and CH2 represent radiances from channels 1 (0.58–0.68 mm) and 2 (0.725–1.10 mm) of the AVHRR, respectively. Although NDVI does not provide land cover type directly, it provides an indication of the 'greenness' of the vegetation [1]. Therefore, a time series of NDVI values can separate different land cover types based on their phenology, or seasonal

Y. Zhang (✉)
School of Information Science and Technology, Yunnan Normal University, Kunming, China
e-mail: zhangyp.cs@gmail.com

X. Chen
Computer & Information Science Department, Southwest Forestry University, Kunming, China

W. Wang (ed.), *Mechatronics and Automatic Control Systems*, Lecture Notes in Electrical Engineering 237, DOI 10.1007/978-3-319-01273-5_113,

signals [2], and have significantly improved our understanding of intra and inter-annual variations in vegetation from a regional to global scale [3]. Based on AVHRR data, numerous regional to global scale vegetation studies have been done. For example, using AVHRR NDVI time series data from regional to global scale, the changes of vegetation phenology could be analysed [4–7]. By intercomparing climatic variables such as rainfall and air temperature with long term time series analysis of AVHRR NDVI, the geo-biophysical causes of vegetation greenness or NPP changes could be revealed [8, 9]. Furthermore, combination with other geophysical parameters like albedo, continental scale trends of NDVI could be analyzed associated with environmental changes [10].

China has a large climate range because of its geographic size. This causes the country to have diverse and species-rich vegetation types, from the tropical to subarctic/alpine and from rain forest to desert. Since the late 1980s, land use patterns in China have been changed dramatically along with urbanization and loss of cultivated. In the late twentieth century and early twenty-first century, China has undergone a rapid socio-economic development, and a series of development strategies, including "Western Development", "Revitalization of Northeast", "Rising of Central China" and so on have been implemented across the nation. Meanwhile, the modification of industrial structure and acceleration of industrialization have resulted in remarkable changes and modifications in the spatial distribution of China's land use too [11]. The urbanization and large scale land use change over the last two decades in China have attracted international attention to analyze the impacts, driving forces, and future trends [12]. So, paying more attention to land cover monitoring and land use planning is necessary in china for protecting natural environment and ecosystem effectively [13]. In this paper, we used the NDVI and climate data from 1982 to 1998, together with information on land use to explore the variations of monthly, seasonal and annual NDVI and their relationships with climate and human activity.

2 Data and Method

2.1 Data

NDVI data used in this study were derived from the NOAA/AVHRR Land data set, produced by the Global Inventory Monitoring and Modeling Studies (GIMMS) group. Its spatial resolution was 8×8 km^2 with 15-day intervals, between January 1982 and December 1998 [14–16]. Annual mean air temperature and precipitation data at 1×1 km^2 resolution were compiled from the 1982–1998 temperature/precipitation database of China. DEM was derived from GTOPO30 that USGS distributes to the public through the Internet. And the 1:1,000,000 Land Use Map of China in 1980s was derived from sharing infrastructure of Earth system science.

2.2 Methodology

All data were aggregated to grid cells at 8 × 8 km^2 resolution, as done for the NDVI data sets. And then, the mask, geometric correction, coordination transformation, and other processes were carried out with ArcGIS 9.3. The mean-value iteration filter (MVI) [17], as a simple method, was used to reduce the noise and reconstruct high quality NDVI time-series. By using the maximum NDVI value in each month, season and year [18], we produced month, seasonal and annual NDVI data set to reduce residual atmospheric and bidirectional effect. Finally, the mean of NDVI, temperature and precipitation, the highest temperature and the lowest temperature, as well as aspect and slope were calculated for analysis.

3 Results

3.1 National Scale

From 1982 to 1998, annual NDVI did not appear the trend ($r^2 = 0.123$, $p = 0.169$), and the correlation between annual mean NDVI and climatic factors was not significant. But the significant increase trends of NDVI could be seen for spring and autumn. The largest NDVI increase ($r^2 = 0.533$, $p = 0.001$) was in spring, with a magnitude of 17.7 % over the 17 years and a trend of 0.00211 $year^{-1}$ (the 17-year averaged NDVI is 0.3111). The other increase of NDVI ($r^2 = 0.355$, $p = 0.012$) for autumn was 7.21 % with a trend of 0.001126 $year^{-1}$. Despite the pronounced NDVI increases in two seasons, there were several large fluctuations in the NDVI trends. For example, seasonal NDVI was large in 1987 and 1990 but small in 1991 and 1995 for spring and autumn respectively (Fig. 1a).

As everyone knows, the magnitude of monthly NDVI and its change over time are important indicators of the contribution of vegetation activity in different months to annual plant growth total [16]. In China, except November and December, the positive values of monthly NDVI trends indicated that NDVI had increased throughout the year almost over the 17-year study period (Fig. 1b). The monthly NDVI trends for May and September increased significantly. The largest monthly NDVI increase ($r^2 = 0.531$, $p = 0.001$) was in May, with a magnitude of 19.96 % over the 17 years and a trend of 0.0022 $year^{-1}$ (the 17-year averaged NDVI is 0.3047). The increase ($r^2 = 0.358$, $p = 0.011$) for September was 8.14 % with a trend of 0.001243 $year^{-1}$. But monthly NDVI got to maximum value in August and was rather small from December through March (Fig. 1b). The plant growth peak occurred in the middle of growing season (summer), while the largest NDVI increase appeared in the early growing season (spring). This means that the trends and patterns of monthly and seasonal NDVI are likely coupled with climate patterns and moisture availability [16].

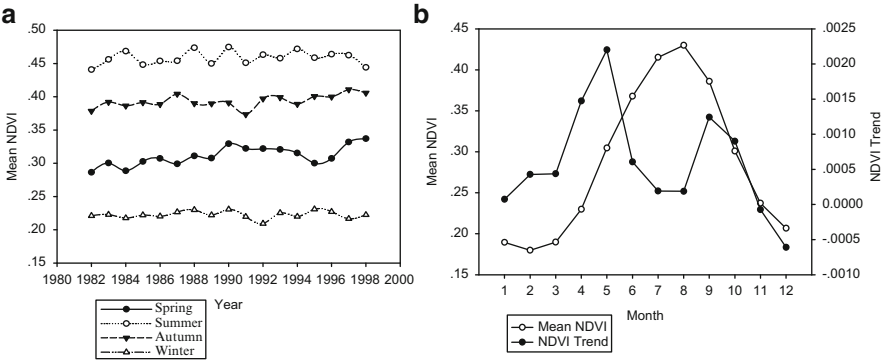

Fig. 1 Seasonal and monthly NDVI change in China (**a**) seasonal NDVI (**b**) monthly NDVI

Table 1 Land use types transformation matrix from 1980s to 2000 (10^4 km^2)

	2000						
1980s	Farm	Forest	Grass	Water	Urban	Unused	Total
Farm	167.69	4.03	3.80	0.34	0.66	0.62	177.15
Forest	2.62	245.88	6.20	0.09	0.08	0.53	255.40
Grass	3.81	6.52	275.48	0.51	0.026	18.15	304.48
Water	0.36	0.13	0.98	11.04	0.10	0.58	13.20
Urban	0.064	0.01	0	0.01	1.17	0.01	1.25
Unused	0.79	1.27	12.62	0.91	0.03	176.51	192.13
Total	175.34	257.84	299.08	12.89	2.07	196.40	943.62
I rate	−1.02 %	0.95 %	−1.77 %	−2.38 %	64.80 %	2.22 %	

3.2 Regional Scale

From 1982 to 1998, annual NDVI did not show the apparent trend at the national scale. But the spatial heterogeneity was found in the North China Plain, hilly and plain areas of Central China, Yangtze River deltas and Pearl River deltas, because of landuse changed significantly in these areas. Table 1 gave the main characteristics of the change in land cover types over the period 1980s–2000.

The areas of forestland, urban land and unused land increased; urban land had the greatest rate of increase, which was 64.8 % during the period. The areas of farmland, grassland and water area decreased; water area had the biggest rate of decrease, which was 2.38 % during the period. At the provincial scale, the provincial NDVI trends for Inner Mongolia ($r^2 = 0.235$, $p = 0.049$), Shanxi ($r^2 = 0.378$, $p = 0.009$), Xinjiang ($r^2 = 0.339$, $p = 0.014$) and Ningxia ($r^2 = 0.292$, $p = 0.025$) increased significantly. The largest provincial NDVI increase was in Ningxia, with a magnitude of 42.59 % over the 17 years and a trend of 0.002943 $year^{-1}$ (the 17-year averaged NDVI was 0.323). The increase for Inner Mongolia, Shanxi and Xinjiang were 7.22 %, 10.76 %, and 17.61 % with a trend of

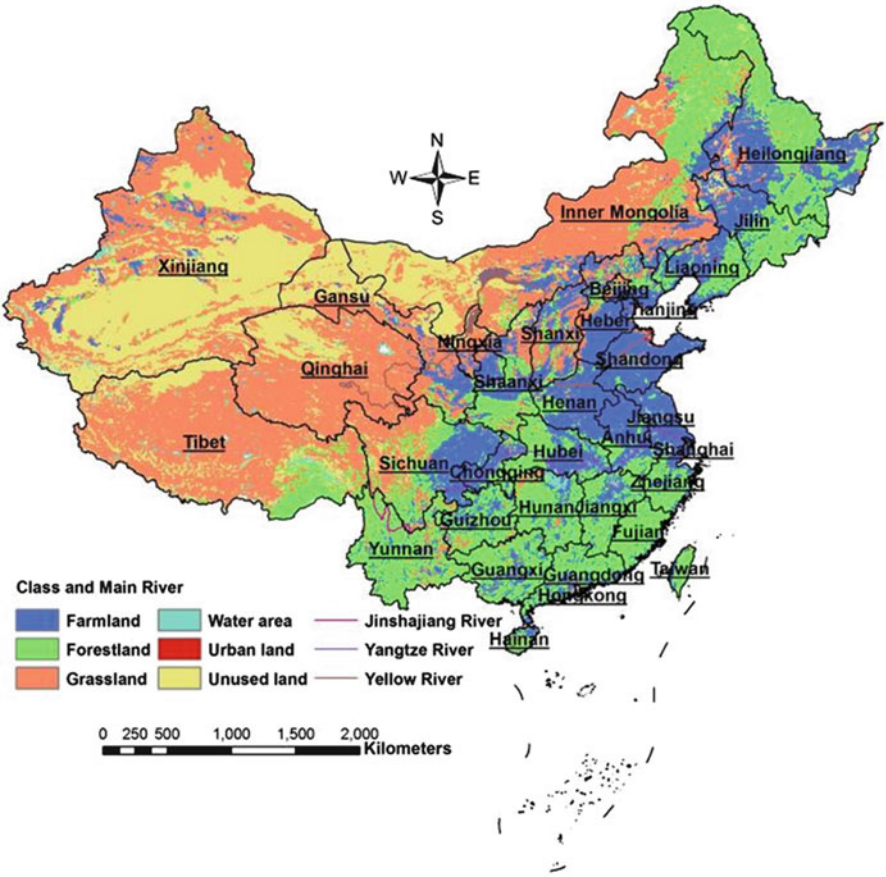

Fig. 2 Land use map of China

0.001908 year^{-1}, 0.002613 year^{-1}, and 0.001322 year^{-1}, respectively. But because a rapid urbanization had taken place over the past 20 years, there was significantly decrease in Guangdong ($r^2 = 0.27$, $p = 0.032$), with a trend of -0.001845 year^{-1}.

3.3 Land Use Scale

In this paper, the land use/cover types of Land Use Map of China were classified as: Farmland, Forestland, Grassland, Water Area, Urban Land and Unused Land, based on the land use/cover categories proposed by the Chinese Academy of Sciences (Fig. 2). If we assumed the locations of land covers were not change, annual NDVI and its trends showed spatial heterogeneity at land cover scale (Table 2). This is very similar to annual NDVI and its trend over the past 17 years at the provincial

Table 2 NDVI regression analysis from 1982 to 1998 in Landuse scale

Landuse	N	Reg coef	T	P	R	I rate
Farmland	17	0.001482	2.003	0.064	0.459	0.064469
Forestland	17	−0.000373	−0.671	0.512	0.171	−0.02506
Grassland	17	0.001004	1.807	0.091	0.423	0.053312
Water area	17	0.001295	2.259	0.039	0.504	0.121757
Urban land	17	−0.000344	−0.389	0.703	0.100	0.046945
Unused land	17	0.000606	1.720	0.106	0.406	0.105325

scale. Especially, the annual NDVI trends increased significantly for water area ($r^2 = 0.254$, $p = 0.039$) with a magnitude of 12.18 % over the 17 years and a trend of 0.001295 $year^{-1}$. This means that the trends and patterns of regional NDVI are likely associated with climate patterns and human activities.

4 Conclusion

By using the NDVI and climate data set from 1982 to 1998, together with information on land use, the variations of monthly, seasonal and annual NDVI and their relationships with climate and human activity were analyzed. The results indicated that both increase of monthly and seasonal NDVI at the national scale corresponded mainly to climate changes. It suggests that climate change is playing an important role at the national scale for the patterns of NDVI trends. But a large spatial and temporal heterogeneity of NDVI trends at the regional scale corresponded mainly to human activities. It suggests that human activities are playing an important role at the regional scale for the patterns of NDVI trends, besides some sensitive areas with climate changes.

Human activities have exerted a large effect on the spatiotemporal patterns of NDVI trends in some regions. So, it is necessary to establish a set of policies to ensure the ecological conservation and restoration, especially in ecological sensitivity areas.

Acknowledgements This work was financially supported by applied basic research projects of Yunnan Province (2010CD047) and (2011FZ140).

References

1. Sellers PJ (1985) Canopy reflectance, photosynthesis, and transpiration. Int J Remote Sens 6:1335–1372
2. Lenney MP, Woodcock CE, Collins JB (1996) The status of agricultural lands in Egypt: the use of multitemporal NDVI features derived from Landsat TM. Remote Sens Environ 56:8–20

3. Fensholt R, Rasmussen K, Nielsen TT, Mbow C (2009) Evaluation of earth observation based long term vegetation trends – intercomparing NDVI time series trend analysis consistency of Sahel from AVHRR GIMMS, Terra MODIS and SPOT VGT data. Remote Sens Environ 113:1886–1898
4. Anyamba A, Tucker CJ (2005) Analysis of Sahelian vegetation dynamics using NOAA AVHRR NDVI data from 1981 to 2003. J Arid Environ 63:596–614
5. Jeyaseelan AT, Roy PS, Young SS (2007) Persistent changes in NDVI between 1982 and 2003 over India using AVHRR GIMMS (Global Inventory Modeling and Mapping Studies) data. Int J Remote Sens 28(21):4927–4946
6. Stöckli R, Vidale PL (2004) European plant phenology and climate as seen in a 20- year AVHRR land surface parameters data set. Int J Remote Sen 25(17):3303–3330
7. Heumann BW, Seaquist JW, Eklundh L, Jonsson P (2007) AVHRR derived phenological change in the Sahel and Soudan, Africa, 1982–2005. Remote Sens Environ 108(4):385–392
8. Xiao J, Moody A (2005) Geographic distribution of global greening trends and their climatic correlates: 1982 to 1998. Int J Remote Sens 26(11):2371–2390
9. Hickler T, Eklundh L, Seaquist J, Smith B, Ardö J, Olsson L, Sykes MT, Sjöström M (2005) Precipitation controls Sahel greening trend. Geophys Res Lett 32:L21415
10. Govaerts YM, Lattanzio A (2008) Estimation of surface albedo increase during the eighties Sahel drought from Meteosat observations. Global Planet Change 64:139–145
11. Liu J, Zhang Z, Xu X (2010) Spatial patterns and driving forces of land use change in China during the early 21st century. J Geogr Sci 20:483–494
12. Zhang J, Zhang Y (2007) Remote sensing research issues of the National Land Use Change Program of China. ISPRS J Photogramm Remote Sens 62:461–472
13. Chen X, Tateishi R, Wang C (1999) Development of a 1-km landcover dataset of China using AVHRR data. ISPRS J Photogramm Remote Sens 54:305–316
14. Tucker CJ, Slayback DA, Pinzon JE (2001) Higher northern latitude NDVI and growing season trends from 1982 to 1999. Int J Biometeorol 45:184–190
15. Zhou LM, Tucker CJ, Kaufmann RK (2001) Variations in northern vegetation activity inferred from satellite data of vegetation index during 1981 to 1999. J Geophys Res 106:069–083
16. Piao S, Fang J, Zhou L, Guo Q, Henderson M, Ji W, Li Y, Tao S (2003) Interannual variations of monthly and seasonal normalized difference vegetation index (NDVI) in China from 1982 to 1999. J Geophys Res 108:4401
17. Ma M, Veroustraete F (2006) Reconstructing pathfinder AVHRR land NDVI timeseries data for the Northwest of China. Adv Space Res 37:835–840
18. Holben BN (1986) Characteristics of maximum value composite images from temporal AVHRR data. Int J Remote Sens 7:1417–1434

Part VII
Signal Processing and Control

The Application of Digital Filtering in Fault Diagnosis System for Large Blower

Changfei Sun, Yong Han, Zhishan Duan, and Yingge Xu

Abstract The analog signals that gathered from engineering test are often mixed with noises which will produce many adverse effects and greatly reduce the system operation speed. These useless and harmful signals can be got rid of by the digital filter. In the real-time monitoring and diagnosis system for the No. six blast furnace blower in The ChangZhi Steel Ltd, the Butterworth analog filter is converted into a digital filter, which can filter those useless and harmful signals. In order to confirm the validity of this digital filter, the high-pass digital filter in this real-time monitoring and diagnosis system is analyzed. The results show that the high-pass digital filter can effectively remove the unwanted signals under 5 Hz. Obviously, the digital filter can effectively remove the useless ingredients and harmful ingredients of the signals, and the system's operation speed can be greatly increased.

Keywords Fault diagnosis system • Filter • Digital filter

1 Introduction

For the influence of the factors of work environment and instrument, the analog signal that extracted from engineering test is often mixed with noise, even the signal is covered by noise. After A/D transformation, the quantization noise of the A/D converter is added into the discrete time signal besides the original noise. Many troubles for the subsequent judgment and diagnostic work are produced for the existing noise, so false-negatives, incorrect diagnosis are appeared in the system. In addition, not all of the signals have to be useful during fault diagnosis, which even reduce the speed of calculation. So the harmful signal must be deleted before data processing [1].

C. Sun (✉) • Y. Han • Z. Duan • Y. Xu
School of Mechanical and Electrical Engineering, Xi'an University of Architecture and Technology, Xi'an, China
e-mail: sunchangfei27@163.com

W. Wang (ed.), *Mechatronics and Automatic Control Systems*, Lecture Notes in Electrical Engineering 237, DOI 10.1007/978-3-319-01273-5_114,

Due to the higher vibration frequency of the blast furnace blower, some low frequency components which is under 5 Hz should be filtered out in order to improve the operation efficiency.

2 Digital Filter

Digital filter can filter out some unnecessary frequency components in signal by some numerical calculations. Digital filter is one of important contents in digital signal processing. Because of the operation way in digital filtering, it has the characteristics of high precision, high stability, using large scale integrated circuit, small volume, light weight, realizing flexible without requiring impedance matching [2]. In the real time monitoring and diagnosis system, the digital filtering method is taken.

The numerical calculation method is used in the digital filter to achieve the purpose of filter, so by following some certain algorithms, the software is established. In addition, at present many kinds of special digital signal processing chip are developed, which is easy to make the design of the digital filter [3].

3 The Design of Digital Filter

Digital filter is divided into infinity impulse response digital filter and finite impulse response digital filter, respectively called IIR filter and FIR filter. In this real-time monitoring and diagnosis system IIR filter is used.

Digital filter can be described by a N order difference equations

$$y(n) = \sum_{i=0}^{M} b_i x(n-i) - \sum_{k=1}^{N} a_k y(n-k) \tag{1}$$

its corresponding function is

$$H(z) = \frac{\sum_{i=0}^{M} b_i z^{-i}}{1 + \sum_{k=1}^{N} a_k z^{-k}} \tag{2}$$

The task of designing is finding a group of coefficients (a_k, b_i) according to the prescribed technical index, and making the function of the filter meet technical index.

There are many design methods for digital filter, the most commonly used one is designing digital filter from simulation filter, because the theory and design method of simulation filter have developed very mature. There are several kinds of typical simulation filter for choice, such as Butterworth filter, Chebyshev filter, Cauer filter, Bessel filter, etc. [4]. The Design method of digital filter is designing a simulation low-pass filter $H_a(s)$ according to the technical requirement, then the low-pass filter $H_a(s)$ is converted into a needed digital filters by converting the frequency. Frequency can be converted in the analog domain, also can be converted in the digital domain. so there are two conversion methods. The first method is to design low-pass filter in the simulation domain, then convert the frequency in the simulation domain, and convert it into a needed simulation filter. Then switch it from the s plane to the z plane to obtain the required digital filter. The second method is to switch the simulation low-pass filter from the s plane to the z plane to get digital low-pass filter, and then convert the frequency in the digital domain to get a desired digital filter [5].

4 The Application of Digital Filter

But the first method will cause the distortion of the frequency response, so it's not appropriate for the design of the high-pass filter and the band elimination filter. The second method is very trouble and inconvenient. So In this real-time monitoring and diagnosis system the high-pass filter is obtained by normalizing a simulation low-pass filter to a desired digital filter directly. The design method of the IIR digital filter is converting a Butterworth low-pass analog filter into a high-pass digital filter.

The technical parameters of this filter are: The cut-off frequency of the band pass filter is $f_p = 5$ Hz, the cut-off frequency of the stop band filter is $f_s = 1$ Hz, Sampling frequency is $f = 2500$ Hz, The maximum attenuation of passband is 3 dB, the minimum attenuation of stopband is 18 dB Resistance with inner minimum attenuation is 18 dB, Frequency characteristics as shown in Fig. 1 shows.

Firstly the boundary of frequency for equivalent high-pass digital filter is calculated

$$\omega_p = 2\pi f_p T = 2\pi \bullet 5/2500 = 0.004\pi \text{ rad} \tag{3}$$

$$\omega_s = 2\pi f_s T = 2\pi \bullet 1/2500 = 0.0008\pi \text{ rad} \tag{4}$$

From the above formula, the cut-off frequency of the band pass filter Ω_p and the cut-off frequency of the stop band filter Ω_s of the analog low-pass filter is calculated.

$$\Omega_p = \frac{1}{2}\Omega_c^2 T ctg\frac{1}{2}\omega_p \tag{5}$$

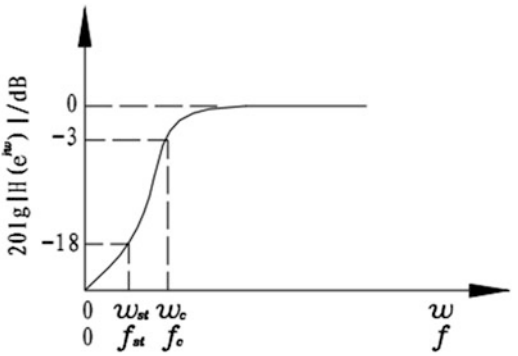

Fig. 1 Characteristics of the required digital filter's frequency

$$\Omega_s = \frac{1}{2}\Omega_c^2 T ctg\frac{1}{2}\omega_s \tag{6}$$

The requirement is Low-pass filter $|\Omega| < \Omega_p$, Attenuation is not more than 3 dB, $\Omega_s < |\Omega|$, Attenuation than 18 dB.

According to the above index, the simulation low-pass filter is designed.

$$\Omega_s/\Omega_p = \frac{\frac{1}{2}\Omega_c^2 T ctg\frac{\omega_s}{2}}{\frac{1}{2}\Omega_c^2 T ctg\frac{\omega_p}{2}} = \frac{ctg\frac{\omega_s}{2}}{ctg\frac{\omega_p}{2}} = \frac{ctg0.0004\pi}{ctg0.002\pi} = 5 \tag{7}$$

The basic parameters of Butterworth filter are:

$$N = -\frac{\lg k}{\lg \lambda} \tag{8}$$

$$k = \sqrt{\frac{10^{0.1a_p} - 1}{10^{0.1a_s} - 1}} = \sqrt{\frac{10^{0.3} - 1}{10^{1.8} - 1}} = 0.1257 \tag{9}$$

$$\lambda = \frac{\Omega_s}{\Omega_p} = 5 \tag{10}$$

$$N = -\frac{\lg 0.1257}{\lg 5} = 1.3 \tag{11}$$

so $N = 2$

According to $N = 2$, after looking up the table, transmission function for the second order normalized simulation low-pass filter is

$$A(p) = \frac{1}{p^2 + \sqrt{2}p + 1} \tag{12}$$

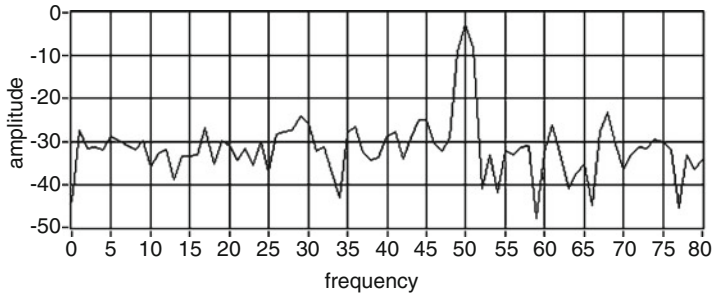

Fig. 2 The signal of a phase stator current of a electromotor

$$\because\ \Omega_p = \frac{1}{2}\Omega_c^2 T ctg\frac{1}{2}\omega_p = \Omega_c \tag{13}$$

$$\therefore\ \Omega_c = \Omega_p = \frac{2}{T} tg\frac{\omega_p}{2} \tag{14}$$

$$\begin{aligned}\therefore\ p = G(z^{-1}) &= \frac{1}{2}\Omega_c T\frac{1+z^{-1}}{1-z^{-1}} \\ &= \frac{T}{2}\cdot\frac{2}{T} tg\frac{\omega_p}{2}\frac{1+z^{-1}}{1-z^{-1}} \\ &= tg\frac{\omega_p}{2}\frac{1+z^{-1}}{1-z^{-1}} = 0.0063\frac{1+z^{-1}}{1-z^{-1}}\end{aligned} \tag{15}$$

$$\begin{aligned}H(z) = A(p)\Big|p = G(z^{-1}) &= 0.0063\frac{1+z^{-1}}{1-z^{-1}} \\ &= \frac{0.991 - 1.982z^{-1} + 0.991z^{-2}}{1 - 1.982z^{-1} + 0.982z^{-2}}\end{aligned} \tag{16}$$

From the second order IIR digital filter system function, the second order difference equation for the designed digital filter is

$$\begin{aligned}y(n) = {} & 0.991x(n) - 1.982x(n-1) + 0.991x(n-2) + 1.982y(n-1) \\ & - 0.982y(n-2)\end{aligned} \tag{17}$$

According to the above formulas program a filtering procedure, so the digital filter is achieved.

The signal shown in Fig. 2 is a phase stator current of an electromotor gathered by us, it can be filtered by this digital filter, the result is shown in Fig. 3. Compare Fig. 2 with Fig. 3, a conclusion can be drawn that the signal which frequency is below 5 Hz can be filtered out by this digital filter.

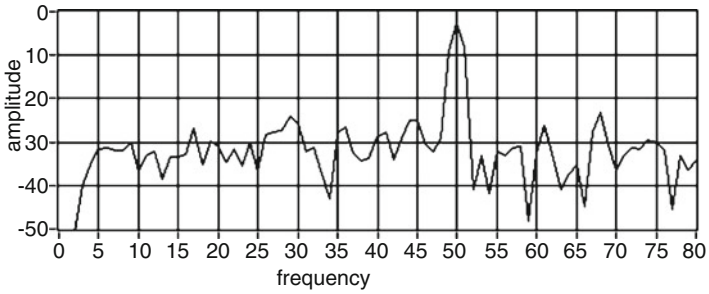

Fig. 3 The signal in Fig. 2 filtered by the digital filter

5 Conclusion

The results show that the high-pass digital filter can effectively remove the unwanted signals under 5 Hz. Obviously, the digital filter can effectively remove the useless ingredients and harmful ingredients of the signals, and the system's operation speed can be greatly increased.

As a consequence, a digital filtering is effective in the real-time monitoring and diagnosis system. The Butterworth analog filter can be converted into a digital filter, which can filter those useless and harmful signals and increase the operation speed of the diagnosis system.

References

1. Peiqing Cheng (2002) Digital signal processing tutorial. Tsinghua University Press, Beijing, pp 42–43
2. Mitchell JS (1990) The analysis and monitoring of mechanical fault. Machinery Industry Press, Beijing, pp 65–68
3. Jianhua Leng (2002) Digital signal processing. Defense industry press, Beijing, pp 52–55
4. Lichen Gu (2000) Mechanical signal processing and application. Shaanxi science and technology press, Xi'an, pp 62–65
5. Yong He (2003) The development of real-time monitoring and diagnosis system in rotating machine[D]. Xi'an University of Architecture & Technology, Xi'an

Performance Analysis on ST-ASLC with Wide-Band Interference

Xingcheng Li and Shouguo Yang

Abstract In order to find the relationship between the cancellation ratio with the wide interference and the delay lines, auxiliary channels and interference bandwidth. And we also would like to draw a quantification conclusion about the performance of ST-ASLC (Space Time Adaptive Side-lobe Canceller). Firstly, We will derive the ST-ASLC (Space Time Adaptive Side-lobe Canceller) processing models with wide-band interference in this article, and we also will derive the interference covariance and correlation matrix with amplitude and phase errors between the main and auxiliary channels; Secondly, based on the interference cancellation ratio, we will explain the performance influence of the auxiliary channels, delay time and delay lines number with simulation results. Finally, we will summarize the law about the ST-ASLC performance with wide interference as follows: the wider the interference bandwidth is, the lower the ASLC cancellation ratio will be; Auxiliary channels and delay lines increasing can improve the ASLC system's interference cancellation ratio, however, multi-auxiliary-channels system is better than the single channel system which has the same channels number of delay lines.

Keywords ST-ASLC • Wide-band interference • Space filter response • Cancellation ratio

X. Li (✉)
School of Air and Missile Defense, Air Force Engineering University, Xi'an, China
e-mail: lixingcheng2008@sina.com.cn

S. Yang
School of Air and Missile Defense, Air Force Engineering University, Xi'an, China

School of Electronic and Information, Northwestern Polytechnical University, Xi'an, China

W. Wang (ed.), *Mechatronics and Automatic Control Systems*, Lecture Notes in Electrical Engineering 237, DOI 10.1007/978-3-319-01273-5_115,

1 Introduction

Under wide-band interference, different frequency component of interference has different delay in each antenna unit of radar side-lobe cancellation arrays, and the main and auxiliary channels have different responses to the interfering signals with different frequency components. Therefore, the wide-band interference (relative to the array) will lead to the mismatched amplitude and phase of ASLC, and it may result in the degradation of the interfering cancellation performance of ASLC system [1]. There is a widespread concern on improving the performance of ASLC system under wide-band interference. If the center frequency and band width of the wide-band interference are f_0 and Δf, and the incident angle is θ_0, which can be viewed as a group of sine-wave signals with different frequency, it can be equalized by the continuous-wave signals with f_0 which are incident simultaneously from several directions. The equivalent angle dispersion of the wide-band interference can be expressed as [2]

$$\frac{\Delta f}{f_0} = \frac{\Delta \sin\theta}{\sin\theta_0} \tag{1}$$

As for the single-frequency incident wave, the optimum weights of ASLC depend on the incident angle. For one incident angle has the corresponding optimum weights, the optimum processing of the wide-band interference should have a group of optimum weights correspondingly. The wide-band interference will occupy ASLC system a large number of degrees of freedom (DOF) and lower its efficiency. To improve the interference cancellation performance of ASLC under wide-band interference, the most direct method is to reduce the bandwidth of the received interference, which can be fulfilled by using sub-band filter banks processing or fast Fourier transform(FFT) to obtain the multi-path signals divided according to the frequency [3, 4], and subsequently constructing independent adaptive array processing for each sub-band. Another method is to add delay lines in each auxiliary channel to add DOF, which can control the antenna's frequency response more profitably; this is space time adaptive side-lobe cancellation [5, 7]. It has been proved that these two methods have the same cancellation performance when the numbers of delay lines equal to the sub-band and delay time of each delay line equals to the sampling period of sub-band [6].

In this paper, the mathematical model of ST-ASLC with amplitude and phase error under wide-band interference is presented, and the performance is fully analyzed. Finally, the significant conclusions are presented.

2 ST-ASLC Processing Models

A ST-ASLC system with M auxiliary channels is shown in Fig. 1, each auxiliary channel has K delay lines. The signals of auxiliary channels can be expressed as

$$X = \begin{bmatrix} X_1 \\ \vdots \\ X_M \end{bmatrix} \tag{2}$$

Where $X_m = \begin{bmatrix} x_{m1} & x_{m2} & \cdots & x_{mK} \end{bmatrix}^T$, the system's weights are

$$W = \begin{bmatrix} W_1 \\ \vdots \\ W_M \end{bmatrix} \tag{3}$$

Where $W_m = \begin{bmatrix} w_{m1} & w_{m2} & \cdots & w_{mK} \end{bmatrix}^T$.

Suppose that the interference signal's spectrum response is flat in the entire bandwidth. The center frequency and bandwidth of the interference signal are f_0 and Δf respectively. Then when the interference signal comes from θ, and the delay time of delay lines $\Delta = T_\mathrm{d}$, the Kth line's interference signal in the Mth auxiliary channel is

$$x_{mk} = G_a J[t - (k-1)T_d - (m-1)T] + n[t - (k-1)T_d] \tag{4}$$

Where $m = 1, \bullet\bullet\bullet, M, k = 1, \bullet\bullet\bullet, K$. T_d is the delay time of delay lines. G_a is the auxiliary antenna's gain (for all the auxiliary antennas).

$$T = \left(\frac{d}{c}\right) sin\theta = \frac{\xi \sin\theta}{f_0} \quad \text{and} \quad \xi = \frac{d}{\lambda} \tag{5}$$

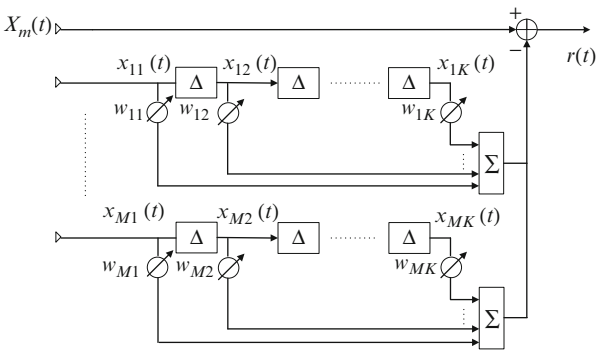

Fig. 1 Space-time ASLC processing system

T is the time delay between auxiliary antennas. The interference covariance matrix and correlation matrix are respectively

$$\boldsymbol{M} = E\left(\boldsymbol{X}^*\boldsymbol{X}^T\right) = \begin{pmatrix} \boldsymbol{M}_{11} & \cdots & \boldsymbol{M}_{1M} \\ \vdots & \ddots & \vdots \\ \boldsymbol{M}_{M1} & \cdots & \boldsymbol{M}_{MM} \end{pmatrix} \boldsymbol{R} = E(X^*X_M) = \begin{bmatrix} \boldsymbol{R}_1 \\ \vdots \\ \boldsymbol{R}_M \end{bmatrix} \tag{6}$$

Where $\boldsymbol{M}_{mn}$ and R_m are respectively $K \times K$, $K \times 1$ dimension matrix. X_M represents the signal samplings of the main channel.

According to the expresses above, $\boldsymbol{M}_{mn}$ and $\boldsymbol{R}_m$ are given by

$$\left(\boldsymbol{M}_{mn}\right)_{pq} = G_a^2 P_j e^{j2\pi f_0[(p-q)T_d+(m-n)T]} \sin c[\Delta f((p-q)T_d + (m-n)T)] \tag{7}$$

$$\left(\boldsymbol{R}_m\right)_q = G_m G_a P_j e^{j2\pi f_0[(q-1)T_d+mT]} \sin c[\Delta f((q-1)T_d + mT)] \tag{8}$$

Where $p, q = 1, \cdots, K$, P_j is the interference power. G_m is the main antenna gain in the interference direction.

Suppose that $T_d = rT_{90}$, $T_{90} = 1/(4f_0)$ is the required unit delay time, and

$$\Delta f T_d = \frac{rB}{4},\ B = \frac{\Delta f}{f_0},\ \Delta f T = B\xi \sin\theta \tag{9}$$

$$\left(\boldsymbol{M}_{mn}\right)_{pq} = G_a^2 P_j e^{j2\pi\left[(p-q)\frac{r}{4}+(m-n)\xi\sin\theta\right]} \sin c\left[(p-q)\frac{Br}{4} + (m-n)B\xi\sin\theta\right] \tag{10}$$

$$\left(\boldsymbol{R}_m\right)_q = G_m G_a P_j e^{j2\pi\left[(q-1)\frac{r}{4}+m\xi\sin\theta\right]} \sin c\left[(q-1)\frac{Br}{4} + mB\xi\sin\theta\right] \tag{11}$$

Taking the amplitude and phase error into account, let b_m ($m = 1$, •••, M) be the Mth channel's maximum phase shift and a_m ($m = 1$, •••, M) be the Mth channel's maximum fluctuation amplitude. The interference covariance and correlation matrix can be derived as [8]

$$\begin{aligned} \left(\boldsymbol{M}_{mn}^i\right)_{pq} &= G_a^2 P_j e^{j2\pi\left[(p-q)\frac{r}{4}+(m-n)\xi\sin\theta\right]} \\ &\quad \times \frac{\sin c(\kappa)}{\sqrt{1+a_m^2/2}\sqrt{1+a_n^2/2}} \begin{pmatrix} 1 + \dfrac{a_m a_n}{2} + \dfrac{a_m a_n \kappa^2}{2(\kappa^2-4)} \\ -\dfrac{a_m\kappa^2 + a_n\kappa^2}{\kappa^2-1} \end{pmatrix} \end{aligned} \tag{12}$$

$$\left(\boldsymbol{R}_m^i\right)_q = G_m G_a P_j e^{j2\pi\left[(q-1)\frac{r}{4}+m\xi\sin\theta\right]} \frac{\sin c\left(\kappa'\right)}{\sqrt{1+a_m^2/2}} \left(1 - \frac{a_m \kappa'^2}{\kappa'^2 - 1}\right) \tag{13}$$

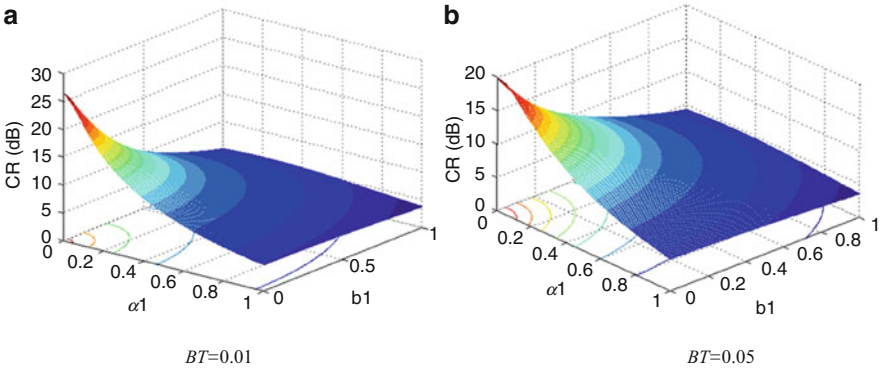

Fig. 2 ST-ASLC system CR with amplitude and phase error (**a**) $BT = 0.01$ (**b**) $BT = 0.05$

Where

$$\kappa = (p-q)\frac{Br}{4} + (m-n)B\xi\sin\theta + \frac{b_m - b_n}{\pi},\ \kappa' = (q-1)\frac{Br}{4} + mB\xi\sin\theta + \frac{b_m}{\pi} \tag{14}$$

In the following Fig. 2, suppose that the main channel is base channel, ASLC has only one auxiliary channel, and there are no delay lines in each channel, we named it channel 1. When the amplitude and phase error is considering, the cancellation ratio is descending when this error becomes larger. So the real equipment must have a good amplitude and phase characteristic corresponding, which must be strict to 0–0.12 with amplitude and 10^0 with phase, this is also equal to the engineering experiencing value in our exercise.

The optimum weights of ASLC system are $\boldsymbol{W}_{opt} = \boldsymbol{M}^{-1}\boldsymbol{R}$, the interference cancellation ratio (CR, Cancellation Ratio) is defined as the ratio between system output interference-to-noise power ratio in case of no auxiliary channels and auxiliary channels.

Without considering the expected signal, CR is

$$CR = \frac{E\left\{|X_M|^2\right\}}{E\left\{\left|X_M - \boldsymbol{W}^T\boldsymbol{X}\right|^2\right\}} = \frac{E\left\{|X_M|^2\right\}}{E\left\{|X_M|^2\right\} - \boldsymbol{W}^T\boldsymbol{R}^*} = \frac{E\left\{|X_M|^2\right\}}{E\left\{|X_M|^2\right\} - \boldsymbol{R}^H\boldsymbol{M}^{-1}\boldsymbol{R}} \tag{15}$$

The main antenna's gain in interference band is G_m, and the auxiliary antennas' gain is G_a. The system has M auxiliary channels. Here the spatial filtering output response of ST-ASLC system is

$$H(e^{j\varphi}) = \begin{bmatrix} 1 & \frac{G_a}{G_m}\boldsymbol{W}_{opt}^H \end{bmatrix}\begin{bmatrix} 1 \\ \boldsymbol{S}_a' \end{bmatrix} = 1 + \frac{G_a}{G_m}\boldsymbol{W}_{opt}^H\boldsymbol{S}_a' \tag{16}$$

Where

$$S_a^{'} = [e^{j\varphi}(1, e^{j2\pi\frac{f}{4f_0}r}, \cdots e^{j2\pi\frac{f}{4f_0}(K-1)r}), \ldots, e^{jM\varphi}(1, e^{j2\pi\frac{f}{4f_0}r}, \cdots e^{j2\pi\frac{f}{4f_0}(K-1)r})]^T, \varphi = 2\pi\frac{d}{\lambda_0}\sin\theta\frac{f}{f_0} \tag{17}$$

3 Simulations

Suppose that an ASLC system has three auxiliary channels, the interference comes from the direction of 8^0, JNR = 30 dB, SNR = 30 dB, the equivalent distance between main and auxiliary antennas' phase center is 40 times of the wavelength (the actual number is larger), and the main and auxiliary channels are isometric and linear arrays. a_i and b_i are normal distribution random numbers whose means are both 0 and variances are 0.12 and 10^0 respectively. The simulation runs 100 times and then calculates the average. Figure 3 shows the curves of interference cancellation ratio with interference bandwidth for single-auxiliary-channel and three-auxiliary-channels ASLC systems when $r = 1$. Apparently, the wider the interference bandwidth is, the smaller the interference cancellation ratio will be.

Figure 4 shows the relation between delay lines and interference cancellation ratio when $r = 1$ and $B = 0.05$. The more the delay lines are, the higher the interference cancellation ratio will be. But the more the delay lines are, the more complex the system will be, and the more the amount of calculation is. The amount of weights has a direction ratio with $(KM)^3$ [9]. So we must choose the right amount of delay lines for the balance between the improved interference cancellation ratio and the amount of calculation.

Figure 5 shows the relation between delay time and interference cancellation ratio when $K = 10$, $B = 0.05$. We can see that the changes of the delay time have

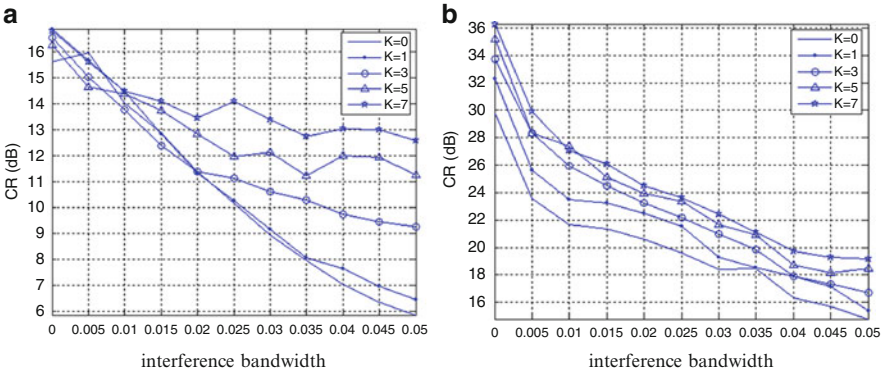

Fig. 3 ST-ASLC system CR with interference bandwidth (**a**) ($r = 1, M = 1$) (**b**) ($r = 1, M = 3$)

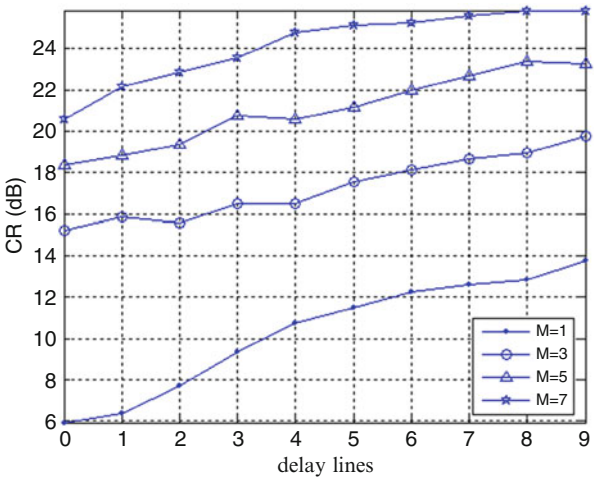

Fig. 4 CR with delay lines ($r = 1, B = 0.05$)

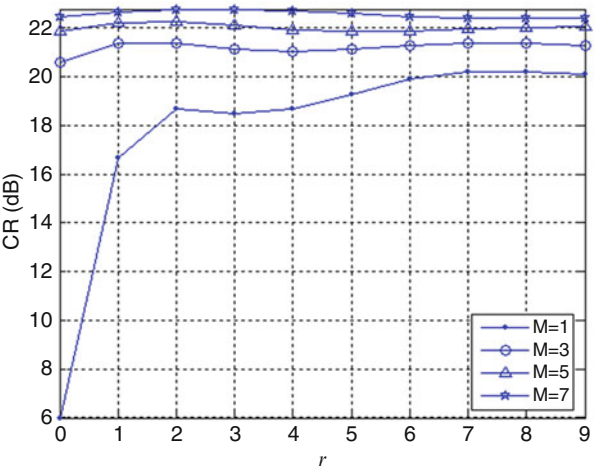

Fig. 5 CR with r ($K = 10$, $B = 0.05$)

little effect on interference cancellation ratio. But there exists an optimal delay time ratio. Actually; we should choose the optimal r according to different ASLC structures, different delay lines and different interference bandwidth. Figure 6 shows the ST-ASLC system's spatial filtering amplitude response. We can see that the notch of single-auxiliary-channel spatial filtering amplitude response is significantly widened. This is the essential reason for improving the performance of ASLC under wide-band interference by the delay lines.

Under no amplitude and phase error conditions, Fig. 7 shows the changing curves of ASLC system's CR with auxiliary channels. Figure 8 gives the changing curves of single –auxiliary-channel ST-ASLC system's CR with delay lines. We can see that adding auxiliary channels and increasing delay lines have the same effect as for the single-auxiliary-channel ASLC system.

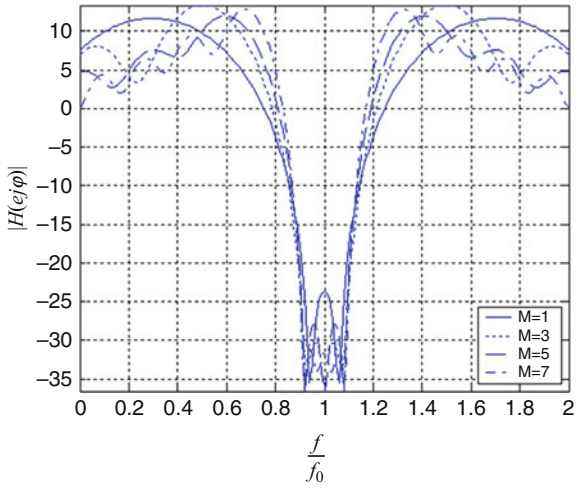

Fig. 6 ST-ASLC spatial filtering response under wide-band interference ($K = 4, r = 1$)

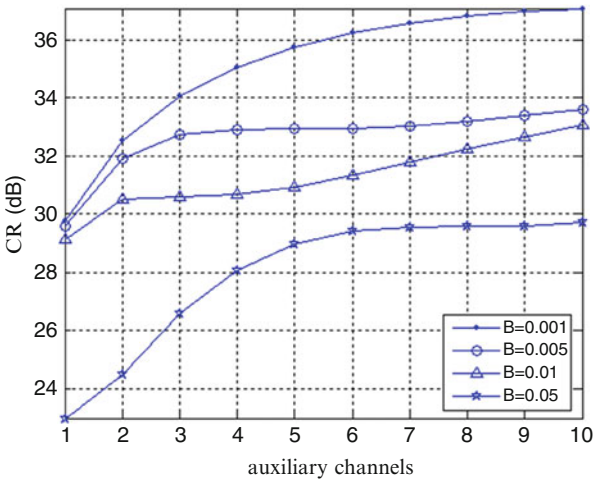

Fig. 7 ASLC CR with auxiliary channels

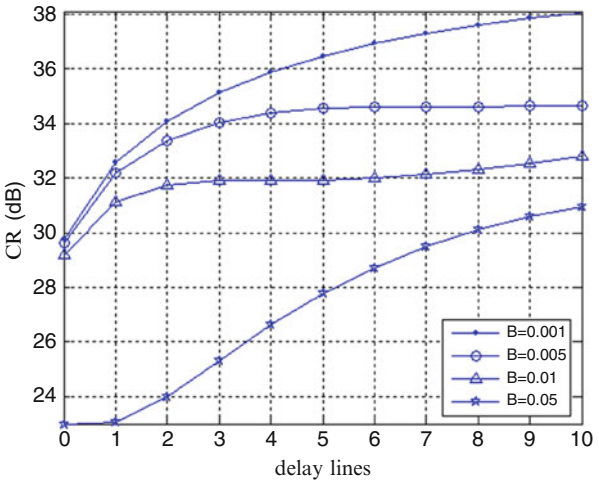

Fig. 8 ST-ASLC CR with delay lines ($r = 1, M = 1$)

4 Conclusion

Through the theory analysis and simulations above, conclusions can be drawn as follows:

Wide-band interference can reduce the single-channel ASLC system's interference cancellation performance. The wider the interference bandwidth is, the lower the single-channel ASLC cancellation ratio is. Or in other words, nearly the single-auxiliary-channel ASLC system doesn't have the anti-jamming ability under wide-band interference. For example, single-auxiliary-channel ASLC interference cancellation ratio is only 6 dB when $B = 0.05$.

Auxiliary channels and delay lines increasing can both improve the system's interference cancellation ratio. When there are no amplitude and phase errors, increasing the delay lines and the auxiliary channels have the same effect as for the single-auxiliary-channel system. Multi-auxiliary-channel system will be better than the same delay lines single channel system when the channel numbers are equal to the delay lines'.

The advantages of increasing the auxiliary channels lies in improving the system's degrees of freedom and eliminating multiple interferences while it has the disadvantages of high costs and expensive expenses. The biggest advantage of increasing the delay lines is low cost. But it is unable to work with multiple interferences.

References

1. Xingcheng Li, Yong-shun Zhang (2008) Analysis of ASLC performance under wide-band jamming [J]. Mod Radar 3:34–36 (In Chinese)
2. Yaohuan Gong (2003) Adaptive filtering [M], 2nd edn. Electronic Industry Press, Beijing, p 7 (In Chinese)
3. Steinhardt AO et al (2000) Sub-band STAP processing [A]. 1th IEEE sensor array and multi-channel signal processing workshop [C], IEEE Press, New York, pp 1–6
4. Zhang Y et al (2001) Adaptive array processing for multi-path fading mitigation via exploitation of filter banks [J]. IEEE Trans Antenna Propag 49(4):505–516
5. Compton RT Jr (1988) The relationship between tapped delay line and FFT processing in adaptive array [J]. IEEE Trans Antenna Propag 36(1):15–26
6. Wisler DJ et al (1988) The development of a base-band cross-pol canceller [A]. IEEE ICC 88 [C]. 3, 1349–1354
7. Xingcheng Ling (2008) Research on electronic interference techniques of ASLC system [D]. Doctoral Dissertation of Air Force Engineering University (In Chinese)
8. Jun Jiang, Xingcheng Li, Wei-Hua Ren (2009) Performance analysis of ASLC with amplitude and phase error [J]. Electron Opt Control 3:34–36 (In Chinese)
9. Sien-chang, Charies Liu et al (1997) Wideband and wide angle side-lobe cancellation technique [P]. US Patent 3202990, 29 Jul 1997

Velocity Error Analysis of INS-Aided Satellite Receiver Third-Order Loop Based on Discrete Model

Dong-feng Song, Bing Luo, Xiao-ping Hu, An-cheng Wang, Pu-hua Wang, and Kang-hua Tang

Abstract Traditionally, continuous model is usually applied to analyze the velocity error of INS-aided GNSS receiver. However, the actual implemented system is discrete. In consequence, the analysis results based on continuous model are iffy. Aimed at this problem, this paper establishes a discrete model of INS-aided third-order carrier loop according to the actual system. Then, the velocity error caused by discretization is investigated and the error mechanism is analyzed. Analysis and simulation results show that the delay of aiding information is the main error source of INS aided GNSS receiver in high dynamic scene. To improve the dynamic performance of INS-aided carrier loop efficiently, the delay of aiding information should be shortened as much as possible.

Keywords INS-aided • High dynamic • Discrete model

1 Introduction

Third-order PLL (Phase Locked Loop) is often used in a GNSS (Global Navigation Satellite System) receiver's tracking loop. The effects of noise increase with increasing loop bandwidth, while dynamic tracking errors increase with decreasing loop bandwidth [1]. So in high dynamic scene, the tracking loop is often out of lock due to a great Doppler frequency shift. But the tracking loop aided by INS velocity information can adapt to the high dynamic scene and has a better dynamic performance [2, 3]. The continuous model and transfer function of INS-aided tracking loop in complex frequency domain are given, and the simulation results based on continuous model show a remarkable improvement in dynamic performance [4].

D.-f. Song • B. Luo (✉) • X.-p. Hu • A.-c. Wang • P.-h. Wang • K.-h. Tang
College of Mechatronics and Automation, National University of Defense Technology, Changsha, China
e-mail: ruobing@nudt.edu.cn

W. Wang (ed.), *Mechatronics and Automatic Control Systems*, Lecture Notes in Electrical Engineering 237, DOI 10.1007/978-3-319-01273-5_116,

Most references have built continuous model in complex frequency domain and proved the advantages of INS-aided loop using continuous model. But the continuous model cannot reflect the actual quantitative velocity error in a specific dynamic scene. In this paper, the discrete simulation model of INS-aided third-order carrier loop with the reference of actual system in z domain is gradually established and theoretical analysis of the velocity error is given. The whole paper is organized as follow: (1) Introduction; (2) The establishment of the continuous third-order carrier PLL model and the INS-aided carrier PLL model; (3) Building up the third-order carrier PLL discrete model and INS-aided PLL model in z domain based on the actual GNSS receiver's loop; (4) Calculating the velocity errors of aforementioned four models in a specific high dynamic scene and comparing corresponding results; (5) The mechanism analysis on discrete INS-aided carrier loop velocity error; (6) Conclusion.

2 Continuous Third-Order Carrier PLL Model and INS-Aided Model

Third-order PLL is a basic part of GNSS receiver's carrier loop and determines the dynamic performance of the loop. The research of the third-order carrier PLL model in complex frequency domain is very important.

2.1 Model 1: Continuous Model of Third-Order PLL in Complex Frequency Domain

Third-order PLL is sensitive to jerk signal and stays stable while noise bandwidth is equal to or below 18 Hz. The third-order PLL model is established using Matlab/Simulink tool as shown in Fig. 1.

In Fig. 1, NCO means Numerical Controlled Oscillator and NCO is usually modeled as an integrator. With the help of formula (1), the third-order loop parameters $k_3 = 12079.21, k_2 = 579.10, k_1 = 55.07$ are calculated when $B_n = 18Hz$ [5].

$$k_3 = {w_0}^3, k_2 = 1.1{w_0}^2, k_2 = 2.4w_0, B_n = 0.7845w_0 \tag{1}$$

The closed-loop transfer function is:

$$\frac{\hat{\varphi}}{\varphi} = \frac{k_1 s^2 + k_2 s + k_3}{s^3 + k_1 s^2 + k_2 s + k_3} \tag{2}$$

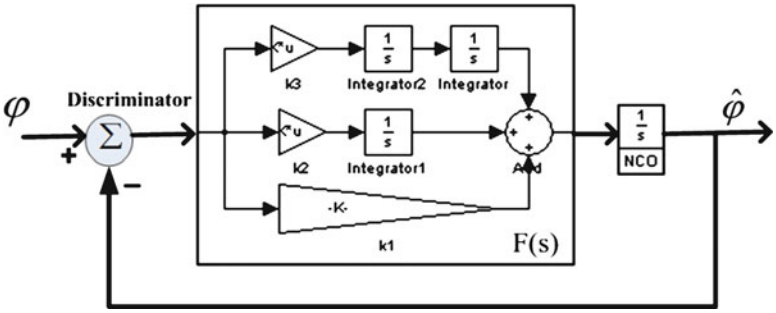

Fig. 1 The third-order PLL model

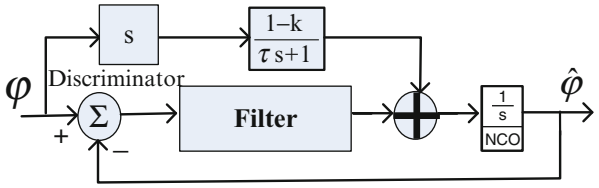

Fig. 2 INS-aided PLL model

2.2 *Model 2: Continuous Model of INS-Aided Third-Order PLL in Complex Frequency Domain*

INS's velocity information is used to aid PLL. We can establish the INS-aided model shown in Fig. 2, where $\frac{1-k}{\tau s+1}$ represents the aided velocity error, k represents velocity scaling error and τ represents constant delay time.

The transfer function of INS-aided carrier loop is inferred:

$$\frac{\hat{\varphi}}{\varphi} = \frac{(1-k+k_1\tau)s^3 + (k_1+k_2\tau)s^2 + (k_2+k_3\tau)s + k_3}{\tau s^4 + (1+k_1\tau)s^3 + (k_1+k_2\tau)s^2 + (k_2+k_3\tau)s + k_3} \tag{3}$$

In most cases, k has little effect on the performance of the loop, so it is set to 0; the output rate of inertial device is usually 200 Hz, and the output rate of inertial navigation solution information is often 100 Hz while using two-sample method navigation-solution. INS velocity information changes every 10 ms, so τ is set to 0.01 s.

3 Discrete Third-Order Carrier PLL Model and INS-Aided Model

GNSS receiver is a discrete control system, so establishing the discrete model of carrier loop is very necessary. And only the discrete model can reflect the correct velocity information of receiver's carrier loop.

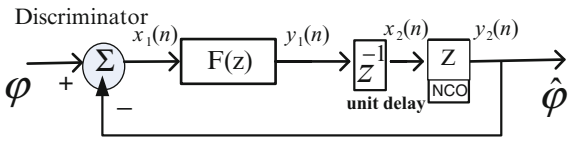

Fig. 3 Discrete third-order PLL model

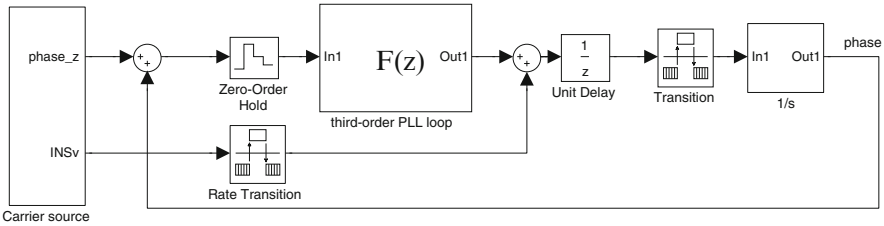

Fig. 4 INS-aided third-order PLL discrete model

3.1 Model 3: Discrete Model of Third-Order PLL in z Domain

In a discrete model in z domain, the analog integrator is often replaced by a rectangular digital integrator. Thus the third-order PLL is modeled as $F(z)$ which is shown in Fig. 3. Noting that third-order PLL's input sequence is $x_1(n)$, and the output sequence is $y_1(n)$. We can work out the third-order loop transfer function as follow ($T_1 = 1$ms):

$$\frac{Y_1(z)}{X_1(z)} = \frac{k_1 z^{-2} - (2k_1 + k_2 T_1) z^{-1} + (k_1 + k_2 T_1 + k_3 {T_1}^2)}{z^{-2} - 2z^{-1} + 1} \tag{4}$$

In the design of actual receiver, the control quantity of the current period cannot immediately act on the plant. There exists a one-control-period delay as z^{-1} shown in Fig. 3. The receiver's IF sampling frequency is in the order of 10^6, so we set NCO Sequence $x_2(n)$, $y_2(n)$ update rate to 0.1 MHz. This two-period model is shown in Fig. 3.

3.2 Model 4: Discrete Model of INS-Aided Third-Order PLL in z Domain

For the actual INS information rate being 100 Hz, we must establish a three-period model in Matlab/Simulink environment. And the INS information update period is equal to τ in Fig. 2. We use the correct INS velocity to aid third-order PLL directly, which means setting k in Fig. 2 to zero. Thus this discrete model's parameters are the same with those in Fig. 2 (Fig. 4).

4 Simulations Results in a Specific High Dynamic Scene

Third-order PLL is sensitive to jerk signal and the steady-state error is 0 when acceleration signal exists. So we should test the models in a high dynamic scene with both jerk and acceleration signals.

4.1 Simulation Scene

We set a high dynamic scene which includes jerk signal and acceleration signal: the track stays 10 g/s from 0 to 10 s, then the track stays 100 g from 10 to 20 s. At last, the track stays -10 g/s during 20 ~ 30 s. This scene is shown in Fig. 5:

4.2 The Simulation Results of the Different Models

Figures 6, 7, 8, and 9 show velocity error in the dynamic scene in Fig. 5.

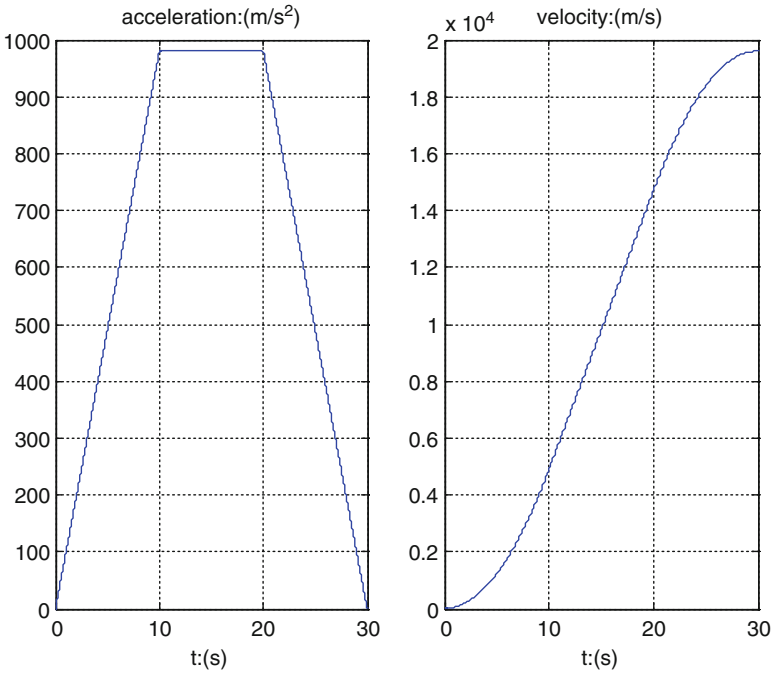

Fig. 5 Acceleration and speed change curve of the high dynamic scene

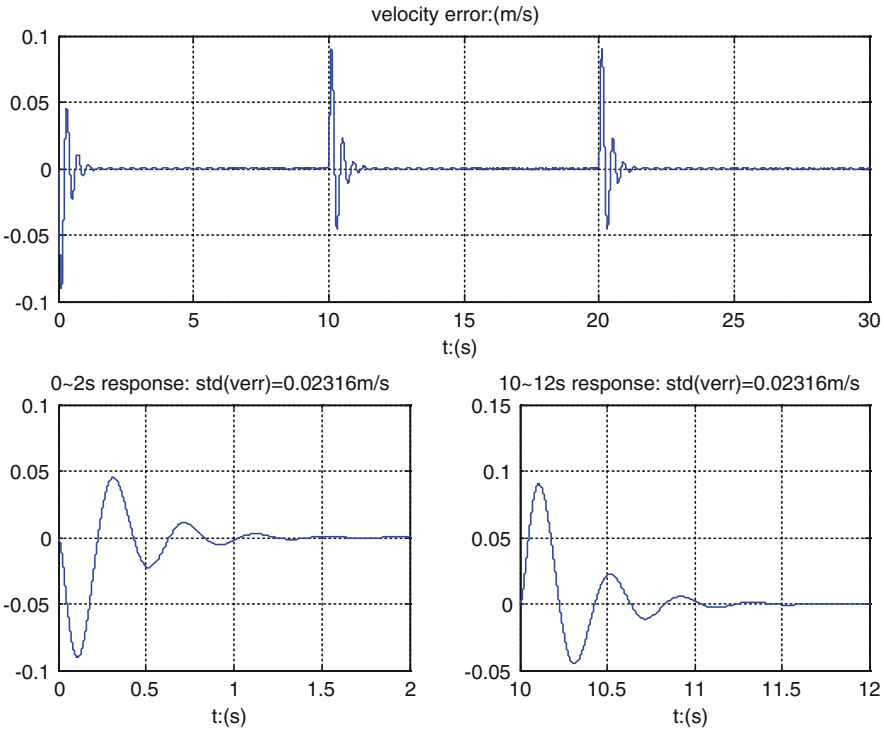

Fig. 6 Velocity error of Model 1

The features of these four figures are concluded in Table 1. The simulation steady-state errors in jerk and acceleration scene of Model 1 and Model 2 are the same with theoretic error. And the shock amplitudes of Model 2 are much smaller than that of Model 1, which proves the theoretic advantage of INS-aided loop. But the features of Model 3 and Model 4 are much worse than that of Model 1 and Model 2. As Model 3 and Model 4 are more similar to actual system, the continuous model of carrier loop and INS-aided carrier loop cannot reflect the velocity error of actual system. At the same time, Figs. 8 and 9 give more details of velocity error.

5 The Mechanism Analysis on Velocity Error of Model 4

Model 3 is the discrete system of Model 1 and while Model 4 is the discrete system of Model 2. We should draw some comparison figures to show the difference between them so as to get the reason of the bigger velocity error. In actual GNSS receiver, the period of carrier loop is usually 1 ms, which cannot be shortened because of the limitation of CPU speed. Thus the research of how to use the INS

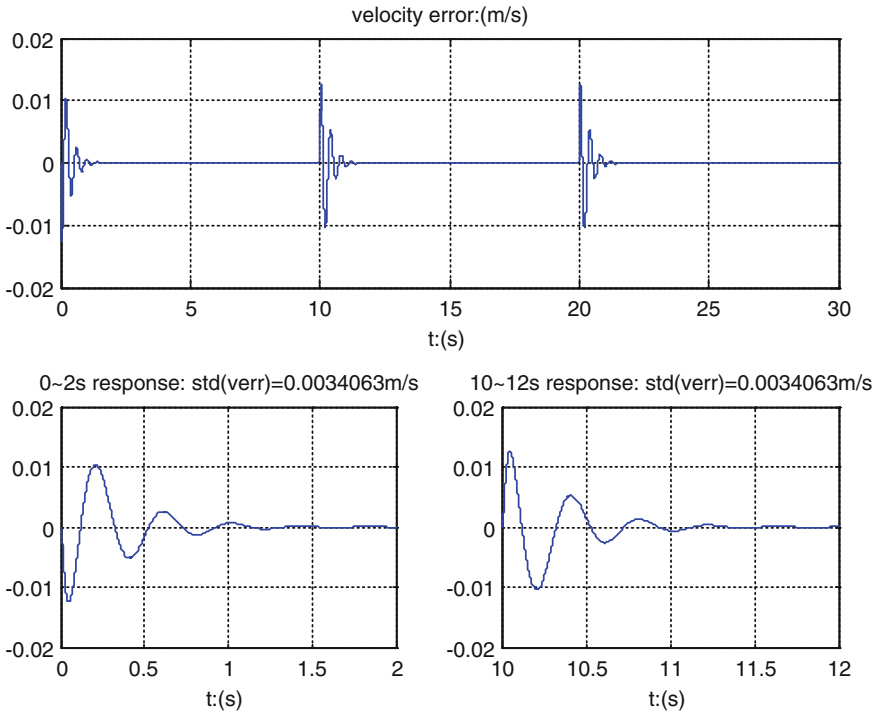

Fig. 7 Velocity error of Model 2

information properly to decrease velocity error is very important. Normally, the aided velocity error at k + 1 time is consists of three parts shown in Eq. 5.

$$\delta\vec{v}_{rx,k+1} = \delta\vec{v}_{rx,k} + \vec{a}_{rx,k}\tau + \vec{j}_{rx,k}\tau^2/2 \tag{5}$$

Where, $\delta \boldsymbol{v}_{rx,k}$ is velocity error at k time, $\boldsymbol{a}_{rx,k}$ is acceleration at k time, $\boldsymbol{j}_{rx,k}$ is jerk at k time. At time of 15 s, $\delta \boldsymbol{v}_{rx,k} = 0, \boldsymbol{j}_{rx,k} = 0$. From Fig. 10, at time of 15 s there exists a sudden change with the aided velocity shown in Eq. 6.

$$\Delta V = \vec{a}_{rx,k}\tau \tag{6}$$

Thus, $\Delta V = \vec{a}_{rx,k}\tau$ is the source of the shocking velocity error of INS-aided carrier loop. And the shocking amplitude depends on the features of NCO and third-order PLL. Figure 11 shows the state trajectory of the velocity error during the whole scene. We can see the velocity error's shocking period is the same as aided velocity's changing period.

To suppress velocity error, the sudden change of ΔV must be decreased, which means that τ should be decreased. If $\tau = 0$, it means the INS information update rate is 1 kHz as carrier loop, and simulation results shows that the velocity error will be

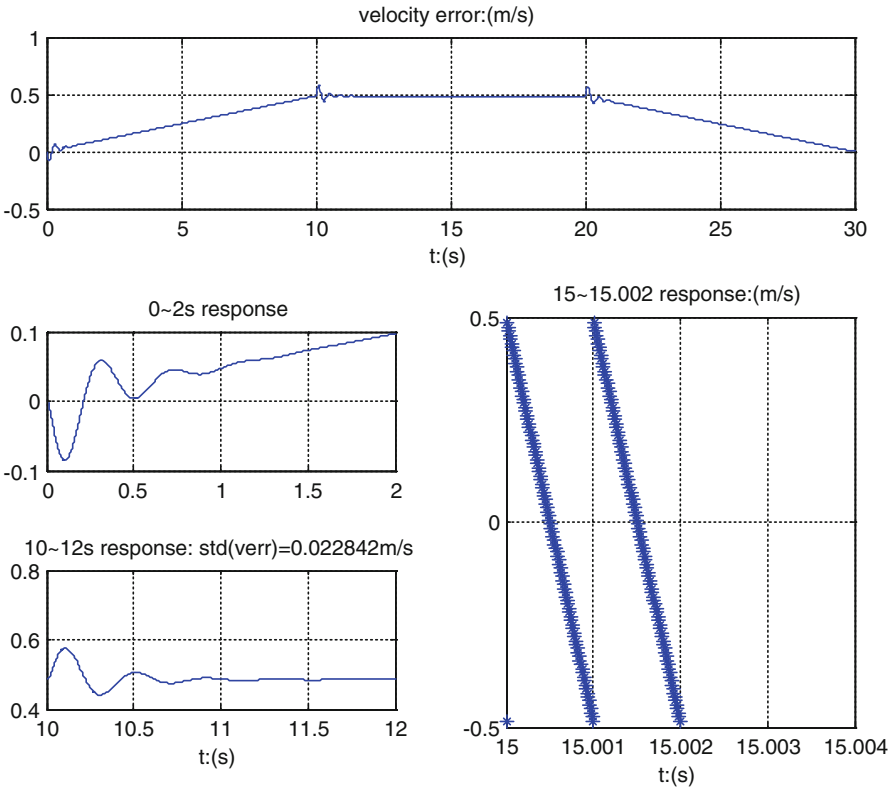

Fig. 8 Velocity error of Model 3

0 just like Model 2. But INS's update rate cannot be as fast as carrier loop because of the limitation of INS device. To decrease τ, Yong Luo [6] uses interpolation and extrapolation method.

6 Conclusion

This paper introduces how to establish the discrete model of INS-aided third-order carrier loop and puts forward the analysis of velocity error of discrete model in a specific high dynamic scene. To decrease velocity error, τ should be decreased. This conclusion guides us to decrease the INS delay time as the most efficient method to improve the dynamic performance of carrier loop. Only when τ is short enough, could, INS information help to improve the loop.

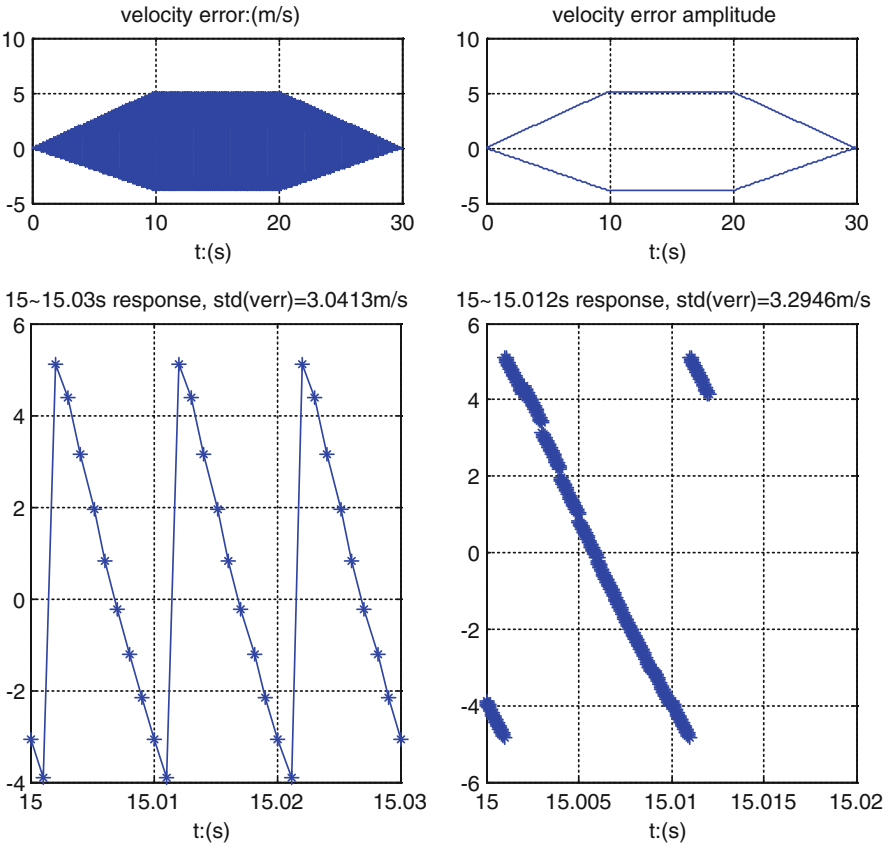

Fig. 9 Velocity error of Model 4

Table 1 Simulation results comparison

Time	0 ~ 10 s (Jerk)		10 ~ 20 s (Acceleration)	
Item	Shocking amplitude(m)	Steady-state error(m)	Shocking amplitude(m)	Steady-state error(m)
Model 1	−0.09 ~ 0.045	0	−0.045 ~ +0.09	0
Model 2	−0.012 ~ +0.01	0	−0.01 ~ +0.012	0
Model 3	−0.08 ~ +0.06	Increase	−0.44 ~ +0.57	0.48
Model 4	Increase	Shocking increase	−3.9 ~ +5.1	Shocking

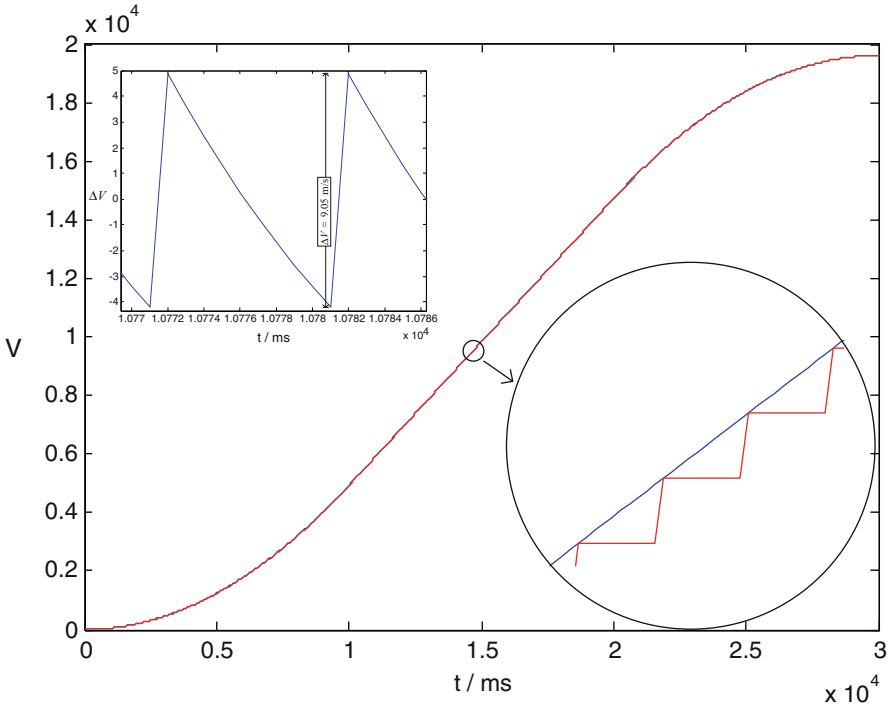

Fig. 10 The error between aided velocity and real velocity

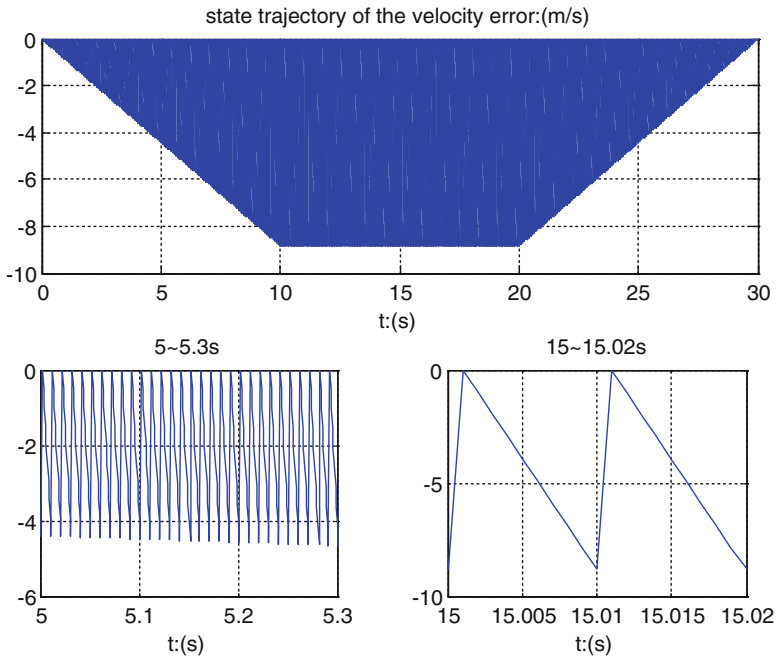

Fig. 11 State trajectory of the velocity error

References

1. Lian-yang Han (2009) Research on high dynamic INS aided GPS carrier tracking algorithm. Aerosp Control 27(3):65–71 (In Chinese)
2. Schmidt GL, Phillips RE (2003) INS/GPS integration architecture performance comparisons [R]. Navigation sensors and integration technology, RTO-EN-SET-064. NATO, London, pp 127–132
3. Xiu-feng He, Jian-ye Liu, Xin Yuan (1996) Performance analysis of GPS receiver aided by velocity signal provide by inertial system. Aerosp Control 4:40–46 (In Chinese)
4. Zhong-qing Yu, Jie Zhang, Gong Cheng (2008) Research on GNSS receiver tracking loop using inertial velocity. Wirel Commun Technol 1:34–36, 41 (In Chinese)
5. Kaplan ED (2002) Understanding GPS principles and applications[M]. Artech House, Boston, pp 185–187
6. Yong Luo, Wen-qi Wu, Xiao-feng He, Yao Guo (2011) Doppler interpolation method based on extrapolation and CIC filter. J Chin Inert Technol 19(2):64–68 (In Chinese)

Data-Processing for Ultrasonic Phased Array of Austenitic Stainless Steel Based on Wavelet Transform

Xiaoling Liao, Qiang Wang, and Tianhong Yan

Abstract In order to suppress the large number scattering signal echoes caused by the coarse grain structure which is tend to cover up the defect signal, resulting in the defect misjudgment in the detection of austenitic stainless steel material by ultrasonic phased array, the wavelet transform was applied to deal with the experimental data. By introducing the theory of wavelet transform and based on the study of ultrasonic testing characteristics of austenitic stainless steel welds, ultrasonic phased array testing were performed in an austenitic stainless steel welds test block, a real-time S-scan detection image was chosen for quantitative analysis from an UT acquisition system. The experimental results show that the wavelet transform can enhance the signal-to-noise ratio of the austenitic stainless steel ultrasonic phased array inspection effectively and help identify the location of defects. The researches demonstrate that this method achieves the defect measurement for the 90 mm thick of austenitic stainless steels.

Keywords Ultrasonic phased array • Ultrasonic testing • Austenitic stainless steel welds • Wavelet transform

1 Introduction

Austenitic stainless steel is a face-centered cubic crystal structure of the iron-based alloys, it has been widely applied in harsh environments, especially in the field of aerospace and nuclear industry for its non-magnetic, high toughness and excellent plasticity performance.

X. Liao • Q. Wang (✉)
College of Quality and Safety Engineering, China Jiliang University, Hangzhou, China
e-mail: qiangwang@cjlu.edu.cn

T. Yan
College of Mechanical and Electrical Engineering, China Jiliang University, Hangzhou, China

W. Wang (ed.), *Mechatronics and Automatic Control Systems*, Lecture Notes in Electrical Engineering 237, DOI 10.1007/978-3-319-01273-5_117,

Ultrasonic phased array system for non-destructive testing (NDT) has been used increasingly in recent years. Compared with conventional single element transducers, the ultrasonic phased array can perform multiple inspections without the need of reconfiguration.

Due to the imperfect welding technology, grain noise usually appears in NDT ultrasonic phased array testing, which caused by unresolvable reflectors and the defects tend to locate in austenitic stainless steel welds and lead security issues. This noise can be suppressed by certain de-noising algorithms, such as band pass filter, low pass filter and wavelet de-noising algorithm.

In order to satisfy the security requirements in these fields, non-destructive tested for these material is necessary. In addition, more and more researches were done to take effective measurements to suppress the noise in the ultrasonic. Several acoustic and ultrasonic testing techniques are trying to be used to work for the inspection such as acoustic emission, guided waves and phased array [1]. Among these techniques, phased array is good at checking for degradation in thick wall coarse-grain materials like austenitic stainless steel [2–4].

Because of some key advantages over Fourier analysis, wavelet analysis has been widely utilized in signal estimation, classification and compression. Wavelet transform cut up data into different frequency component, and reconstruct the useful components by thresholding policy. Also with its multi-resolution characteristics, it is widely used in ultrasonic signal de-noising processing to improve the signal-to-noise ratio [5].

In this paper, conventional ultrasonic testing problems are analyzed combined with the principle of phased array [6, 7], and wavelet transform is made through the ultrasonic phased array testing experiment on defects in the depths of 40 mm in the austenitic stainless steel block. The choice of the mother wavelet is also discussed in this paper [8]. Choosing the appropriate wavelet based on the correlation coefficient and denoising has been applied.

2 Experimental Studies

2.1 Experimental Instruments and Method

Pulse-echo method was chosen and Omniscan MX2 detector by Olympus was employed in this experiment. Detection parameters are shown in Table 1. The probe has 64 array elements but only 16 of them simultaneous excitation, its frequency is 5 MHz and oil was used as the coupling agent in this experiment. Besides, the S-scan angle is 40–70° and the defect in the depth of 40 mm is the main defect we detect.

In order to simulate the defects, we made a test block. The material of the test block is 304 and it is 90 mm thick. Five side–drilled holes with a diameter of 2 mm were machined in the block (Fig. 1). Three of them are in the austenitic stainless

Table 1 Detection parameters

Probe model	Wedge model	Scan style
5L64-A12	SA12-N55S	S Scan 40–70°

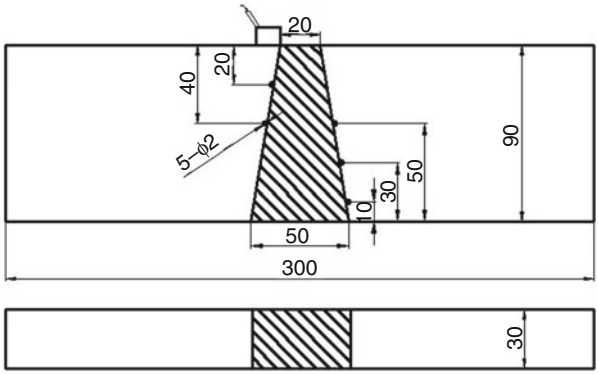

Fig. 1 The structure and size parameters of the test block

steel and their depths are 10, 30 and 50 mm. Two of them are in the austenitic stainless steel welds and their depths are 20 and 40 mm. The probe radiate by refraction through a Plexiglas wedge and produces transverse waves.

2.2 Wavelet Transform

In many applications in signal and image processing the observed data are influenced by noise. An important question in this text is how to estimate the underlying "clear" signal from the noisy observations.

Wavelet transform (WT) based methods is useful for analyzing signals. In overcoming the problems associated with Fourier transform methods, they analyze the signals in time – frequency domain. So the information regarding both the time-domain and frequency-domain are available. Choosing a wavelet member from a wavelet family is at best a trial-and error method.

The Wavelet transform Ws(a, b) of a signal x(t) is given by [9].

$$Ws(a,b) = \int_{-\infty}^{\infty} x(t)\psi\left(\frac{t-b}{a}\right)dt \tag{1}$$

Where $\psi(.)$ is the mother wavelet and a, b are the dilatation and translation coefficients respectively.

Based on the principle of suppressing the noise signal, Wavelet transform procedures can be summarized as (i) wavelet transform of the noisy register; (ii) pruning and/or thresholding of the coefficients in the trans-formed domain; (iii) reconstruction of the de-noised signal by inverse transform [10].

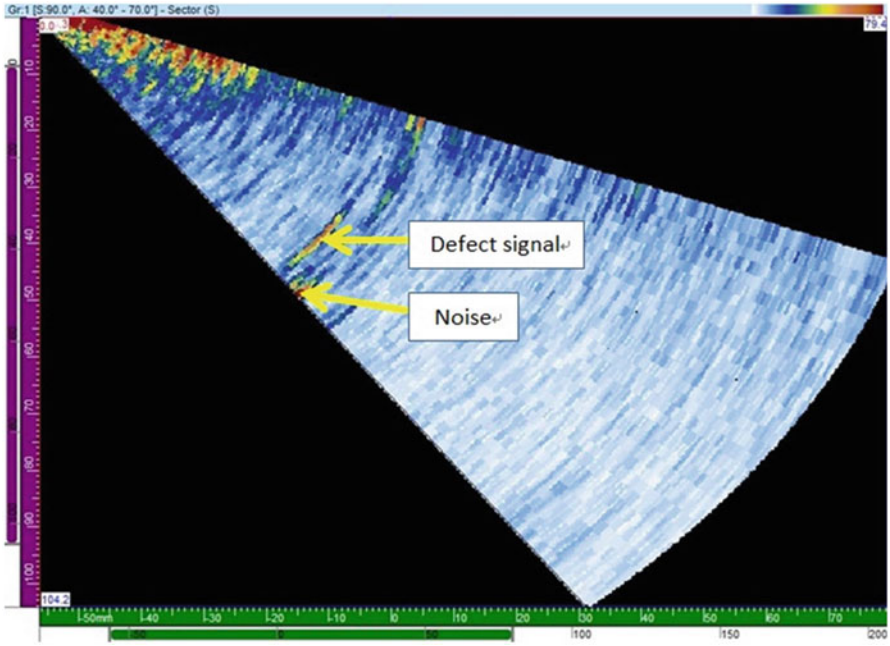

Fig. 2 The test result of the defect in 40 mm depth

According to recently researches, in the detection of ultrasonic echo waves on both time and frequency domains, different kinds of mother wavelet in the Symlet family displays different features. So the mother wavelet of Sym8 was selected in this paper.

2.3 Experimental Data Analysis

To conduct a quantitative analysis, the data of the ultrasonic S-scan image in angle 45° was extracted. In addition, the signal amplitude is expressed by percentage of the total image height in this paper.

As shown in the S-scan images obtained from UT acquisition system (Fig. 2), due to the effects of noise and attenuation caused by coarse grain structure, the signal-to-noise ratio of defect signal has become quite low, defect in 45 mm was caused by instrument(Marked in Fig. 2).

In Fig. 3, it presents the analysis results of ultrasonic plot data after wavelet transform. The mother wavelet in this paper was sym8, and the 3rd-order wavelet, the 5th-order wavelet and 8th-order wavelet was used to process the plot. Comparing the Fig. 3a–d, it's clear that the wavelet transform can suppress the grain

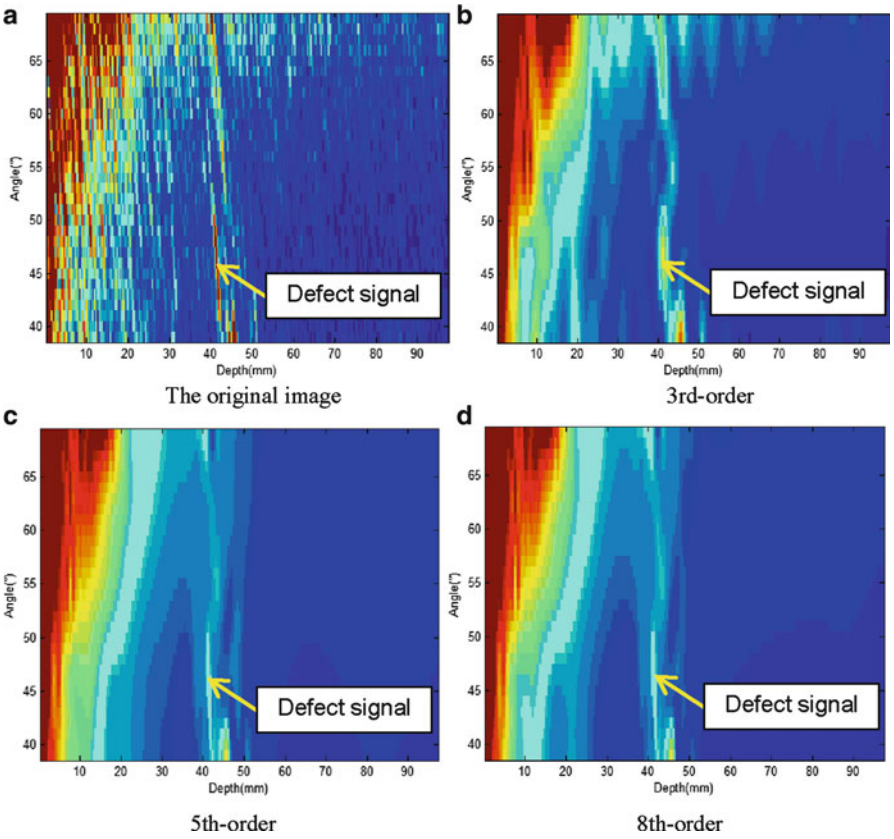

Fig. 3 The effect of transform with mother wavelet sym8 for (**a**) the original plot and (**b**) 3rd-order wavelet transform and (**c**) 5th-order wavelet transform and (**d**) 8th-order wavelet transform

noise well. Particularly, the 3rd-order wavelet transform displays the satisfied performance in suppressing grain noise.

Almost all the depth of noise has been attenuated effectively, and the noise signal curve is very smooth. But the defect in 45 mm caused by instrument is still retain. However, to some extent, it also reduce the useful signal.

3 Conclusion

In this paper we discuss the noise models and the different approaches of processing the noise in the domain of various wavelet transforms. In particular, we focus on how the wavelet transforms with different order affect the processing results. Furthermore, we state three different orders wavelet processing images to discuss the impact.

Wavelet transform approach is presented for analyzing noisy signals. The adopted method shows that the wavelet transform can be effectively applied to austenitic stainless steel measurement.

1. The wavelet de-noising analysis can suppress the grain noise of ultrasonic phased array systems with 64 linear piezoelectric elements for NDT effectively. It can suppress the noise amplitude, smooth the signal curve, and retain the backwall echo signal, though it also can reduce the helpful signal.
2. Ultrasonic phased array technology can effectively detect the defects of austenitic stainless steel. But to the welds' detection, the SNR is low, so in order to increase the defect detection rate, mathematical methods is needed to improve the SNR of deep defects.
3. To coarse grained material and anisotropic structure like austenitic and austenitic welds, the path of the ultrasonic wave would change but the change is irregular.

Acknowledgements This work is supported by Key Program of Science and Technology Planning Project of Zhejiang Province, China under Grant 2011C11079.

References

1. Song S-J, Shin HJ, Jang YH (2002) Development of an ultra sonic phased array system for non destructive tests of nuclear power plant components. Nucl Eng Des 214:151–161
2. Steve M, Jean-Louis G, Olivier R et al (2004) Application of phased array techniques to coarse grain components inspection. Ultrasonics 42:791–796
3. Chassignole B, El Guerjouma R, Ploix M-A et al (2010) Ultrasonic and structural characterization of anisotropic austenitic stainless steel welds: towards a higher reliability in ultrasonic non-destructive testing. NDT&E Int 43:273–282
4. Dong H, Qiang W, Kun X et al (2012) Ultrasonic phased array for the circumferential welds safety inspection of urea reactor. Procedia Eng 43:459–463
5. Grosse CU, Finck F, Kurz JH et al (2004) Improvements of AE technique using wavelet algorithms, coherence functions and automatic data analysis. Constr Build Mater 18:203–213
6. Ruiju H, Lester W, Schmerr J (2009) Characterization of the system functions of ultrasonic linear phased array inspection systems. Ultrasonics 49:219–225
7. Mendelsohn Y, Wiener-Avnear E (2002) Simulations of circular 2D phase-array ultrasonic imaging transducers. Ultrasonics 39:657–666
8. Kun X, Qiang W, Dong H (2012) Post signal processing of ultrasonic phased array inspection data for non-destructive testing. Procedia Eng 43:419–424
9. Rodríguez MA, San JL, Lázaro JC et al (2004) Ultrasonic flaw detection in NDE of highly scattering materials using wavelet and Wigner–Ville transform processing. Ultrasonics 42:847–851
10. Sgarbi M, Colla V, Cateni S et al (2012) Pre-processing of data coming from a laser-EMAT system for non-destructive testing of steel slabs. ISA Trans 51:181–188

The Non-stationary Signal of Time-Frequency Analysis Based on Fractional Fourier Transform and Wigner-Hough Transform

Jun Han, Qian Wang, and Kaiyu Qin

Abstract In order to solve the problem of non-stationary signal analysis, a time-frequency analysis method is introduced in this paper. By comparing with several common time-frequency analysis techniques, this paper proposes a non-stationary signal time-frequency analysis based on the fractional Fourier transform (FRFT) and the Wigner-Hough transform. The simulation results indicate that the FRFT combined with Wigner-Hough transform is a useful method to perform high-resolution non-stationary signal analysis.

Keywords Time-frequency analysis • Fractional Fourier transform • Wigner-Hough transform

1 Introduction

The study of non-stationary signal in both the time and frequency domains simultaneously is very important. It is encountered commonly in many research areas such as radar and sonar analysis, signal detection and parameter estimation, image processing, and fault diagnosis etc. The practical motivation for time–frequency analysis is that classical Fourier analysis assumes that the signal is infinite in time or periodic, while the signal in practice is short duration, and has substantially changed over their duration. This is poorly represented by traditional methods, which motivates time–frequency analysis. One of the most basic forms of time-frequency analysis is the short-time Fourier transform (STFT). In the continuous-time case, the function required to be transformed is multiplied by a window function which is

J. Han (✉) • Q. Wang • K. Qin
Astronautics & Aeronautics institute, University of Electronic Science and Technology of China, Chengdu, China
e-mail: hanjun192835@126.com

W. Wang (ed.), *Mechatronics and Automatic Control Systems*, Lecture Notes in Electrical Engineering 237, DOI 10.1007/978-3-319-01273-5_118,

nonzero for only a short period of time. The Fourier transform (a one-dimensional function) of the resulting signal is taken as the window is slid along the time axis, resulting in a two-dimensional representation of the signal [1, 2]. The main advantage of this method is its easiness in implementation by using the fast Fourier transform. Since it is a linear time-frequency representation, the crucial drawback of this method is that windowing the signal leads to a tradeoff in time resolution and frequency resolution. At the same time, the rectangular window is often used in the short time Fourier transform, this approach has more serious boundary effects. So we often need to use other more complex window function which adds the complexity of the calculation [3]. Compared with the short time Fourier transform, the Wigner-Ville (WVD) distribution is one of commonly used bilinearity time-frequency distribution. It has many superior properties, especially to the single component of the non-stationary signal analysis. However, due to the bilinearity time-frequency distribution of WVD, the WVD for multi-component of the non-stationary signals will lead to serious cross terms which degrade the energy accumulation [4].

The fractional Fourier transform (FRFT) is one family of linear transformations generalizing the Fourier transform. It can be thought of as the Fourier transform to the n-th power, where n need not be an integer — thus, it can transform a function to any intermediate domain between time and frequency. Its applications range from filter design and signal analysis to phase retrieval and pattern recognition. Moreover, it has been applied to different applications such as high resolution SAR imaging; sonar signal processing, blind source separation [5]. The FRFT can make the signal of time-frequency analysis have more choices. Wigner-Hough transform is a shape-matching technique proposed by Hough in 1962, it can test the detected image of the parametric curves in the parameter space and coalesce the formation with the corresponding curve parameters about the peak point, and get the image of each curve parameter [6]. For discrete limited image, the idea of the Hough transform is quantified the parameter space which made by all possible line parameters into a finite number of parameters table. In application, we first transform signal with the Wigner-Ville, then transform signal with the Hough, and now we get the Wigner-Hough transform.

2 The Relationship Between the FRFT and Other Time-Frequency Analysis

The FRFT can be understood as rotation of the signal for arbitrary α -angle in the time-frequency plain [7]. The FRFT can be defined by Eq. 1:

$$X_p(u) \stackrel{def}{=} \{F^{\alpha}[x(t)]\}(u) = \int_{-\infty}^{+\infty} x(t)K_p(t,u)\mathrm{d}t \tag{1}$$

The transform kernel $K_p(t,u)$ is:

$$K_p(t,u) \stackrel{def}{=} \begin{cases} \sqrt{\frac{1-j\cot\alpha}{2\pi}} \exp\left[j\frac{t^2+u^2}{\cot}\alpha - jut\csc\alpha\right], \alpha \neq n\pi \\ \delta(t-u), \alpha = 2n\pi \\ \delta(t+u), \alpha = (2n+1)\pi \end{cases}$$

Where p and α are the order of FRFT and the rotation angle, $\alpha = p\frac{\pi}{2}$. The energy of the white noise was uniformly distributed in the whole time-frequency plane. The probability of energy accumulation is very small in the fractional Fourier domain. The energy of linear frequency modulation signal (LFM) is accumulated in the fractional Fourier domain. We can estimate the initial frequency and chirp rate of the LFM signals through the location of the energy accumulation in the two-dimensional fractional plane. So that, we can complete the parameters estimate. The FRFT has very close contact with other time-frequency analysis methods.

2.1 Relationship Between the FRFT and WVD

The WVD of signal $x(t)$ can be defined as follows: Set $x(t)$ for a continuous time signal, The WVD can be expressed by Eq. 2:

$$X(t,\omega) = \int_{-\infty}^{\infty} x\left(t+\frac{\tau}{2}\right)x^*\left(t-\frac{\tau}{2}\right)e^{-j\omega\tau}d\tau \tag{2}$$

Substitute $\tau = \frac{\tau}{2} + t$ into the above Eq. 2, we can get Eq. 3:

$$X(t,\omega) = 2e^{2j\omega t}x^*(2t-\tau)e^{-2j\omega\tau}d\tau \tag{3}$$

Use the FRFT motion properties, we can express $x^*\left(t-\frac{\tau}{2}\right)$ as follows:

$$X^*\left(t-\frac{\tau}{2}\right) = \int_{-\infty}^{\infty} X_{\alpha-z+2t\cos\alpha}e^{-j2t^2\sin\alpha+j2zt\sin\alpha}K_\alpha(\tau,z)dz \tag{4}$$

So, we get Eq. 5:

$$X(t,\omega) = 2e^{2j\omega t}\int_{-\infty}^{\infty} X_\alpha^*(-z+2t\cos\alpha)* \\ e^{-j2t^2\sin\alpha\cos\alpha+j2z\sin\alpha}\int_{-\infty}^{\infty} x(\tau)e^{-2j\omega\tau}K_\alpha(\tau,z)d\tau \tag{5}$$

We can get Eq. 6 from use the frequency shift properties of the FRFT [8].

$$X(t,\omega) = 2e^{2j\omega t} \int_{-\infty}^{\infty} X_p(z + 2\omega \sin\alpha) \\ X_p^*(-z + 2t\cos\alpha) e^{-j2\left(t^2+\omega^2\right)\sin\alpha + 2jz\sin\alpha - 2jzt\omega\cos\alpha} dz \tag{6}$$

Substitute $\varepsilon = z + 2\omega \sin\alpha$ into the above Eq. 6, we can get Eq. 7:

$$X(t,\tau) = 2e^{2j\omega t} \int_{-\infty}^{\infty} X_p(\varepsilon) X_p^*(-\varepsilon + 2t\cos\alpha + 2\omega\sin\alpha) * \\ \exp\begin{pmatrix} 2j\left(\omega^2 - t^2\right)\sin\alpha\cos\alpha + \\ 2j\varepsilon(t\sin\alpha - \omega\cos\alpha) - 4j\omega t\sin^2\alpha \end{pmatrix} d\varepsilon \tag{7}$$

This expression is the WVD in the (t,ω) coordinate system. We would like to change to a new coordinate system (u,v) According to the following formula coordinates $\begin{cases} u = t\cos\alpha + \omega\sin\alpha \\ v = -t\sin\alpha + \omega\cos\alpha \end{cases}$ we transform (t,ω) into (u,v), and after simplification, then Eq. 7 can be written as Eq. 8:

$$X(t,\omega) = 2e^{2juv} \int_{-\infty}^{\infty} X_\alpha(\varepsilon) X_\alpha * (2u - \varepsilon) e^{-2jv\varepsilon} d\varepsilon \tag{8}$$

From the above discussion, the right side of equation is the WVD of $X(u)$. So we can see that, in considering the significance of the axis of rotation, the WVD of $X(u)$ is same with the WVD of $x(t)$.

2.2 *Relationship Between FRFT and Wigner-Hough Transform*

The Wigner-Hough transform is a straight line integral projective transformation. S. Kay and G.F. Boudreax-Bartels firstly applied Hough transform to the WVD [6]. The transform, often called Radon-Wigner transform (RWT) or Wigner-Hough transform (WHT), have been used to facilitate the analysis and synthesis of the non-stationary signals[8]. To the given finite energy signal $x(t)$, we define the Wigner-Hough transform domain to the mapping of the parameter field of (f,g), then The Wigner-Hough transform can be defined as Eq. 9:

$$WHT_x(f,g) = \int_{-\infty}^{\infty} \int x\left(t+\frac{\tau}{2}\right)x^*\left(t-\frac{\tau}{2}\right) * e^{-j2\pi(f+gt)\tau} d\tau dt \tag{9}$$

Compared with the WVD, the Wigner-Hough transform has the advantage of noise suppression and suppress cross terms. The modulus square of the signal $x(t)$, P order FRFT transform is just the Wigner-Hough transform on the α direction [9]. Use of this relationship, many properties of the Wigner-Hough can be applieddirectly in the FRFT transform [10]. Meanwhile, the Wigner-Hough combined with the FRFT will achieve better results in the time-frequency analysis.

3 Simulation Results

In the simulation, the non-stationary signal which consists of the two transient signals of different positions is analyzed. The simulation conditions were as follows: Signal 1 is the product of a Gaussian amplitude modulated signal whose signal points are 128, time center is 45 and a constant frequency modulation signal whose normalized frequency f_0 is 0.25. Signal 2 is the product of a Gaussian amplitude modulated signal whose signal points are 128, time center is 85 and a constant frequency modulation signal whose normalized frequency f_0 is 0.25. The simulation signal is sum of signal 1 and signal 2.

Figure 1 shows the time-domain waveform of non-stationary signals, which consists of two components. Figure 2 shows the STFT with the window function of the 65-point hamming window. This time the frequency resolution is better, but the two components of the signal can't be distinguished on the timeline. The signal was analyzed with the WVD and the time-frequency diagrams are shown in Fig. 3, we can clearly see that signal exists cross-connection interference item. We first transform signal with the Wigner-Ville, then transform signal with the Hough, and now we get the Wigner-Hough transform, Fig. 4 shows the signal's Wigner-Hough

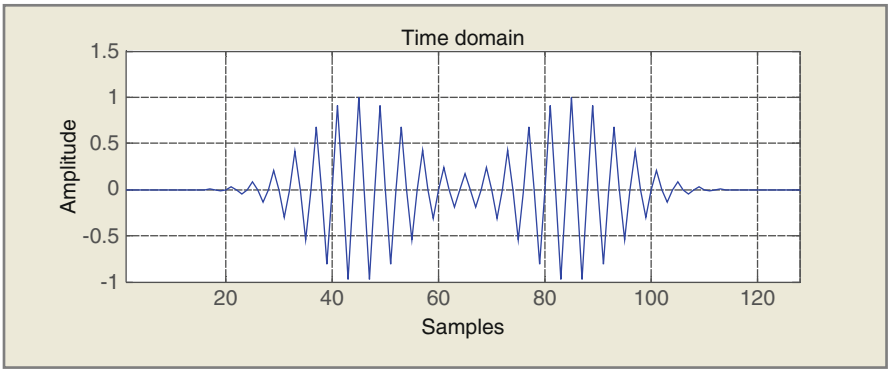

Fig. 1 Time domain waveform of the simulation signal

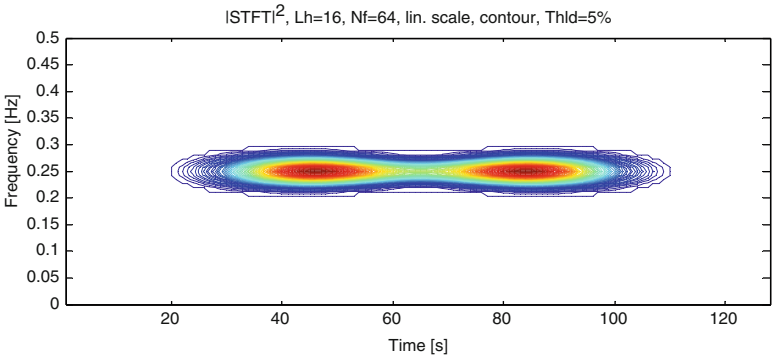

Fig. 2 The simulation signal's time-frequency graph about STFT

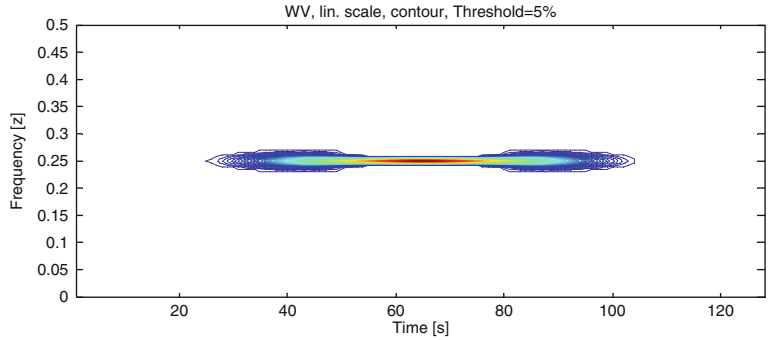

Fig. 3 The time-frequency graph about Wigner-Ville

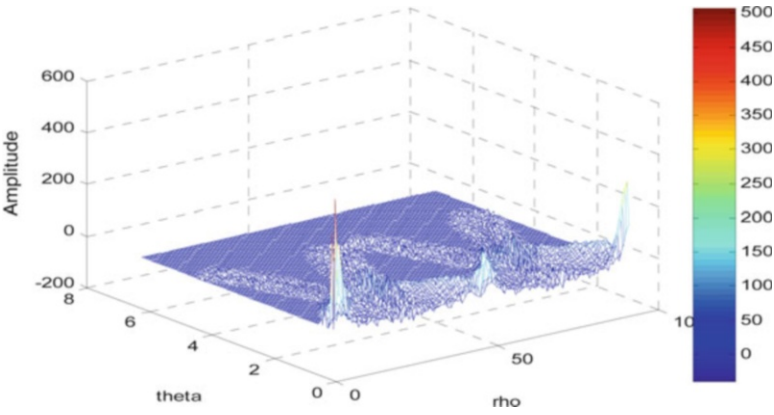

Fig. 4 The time-frequency graph about Wigner-Hough

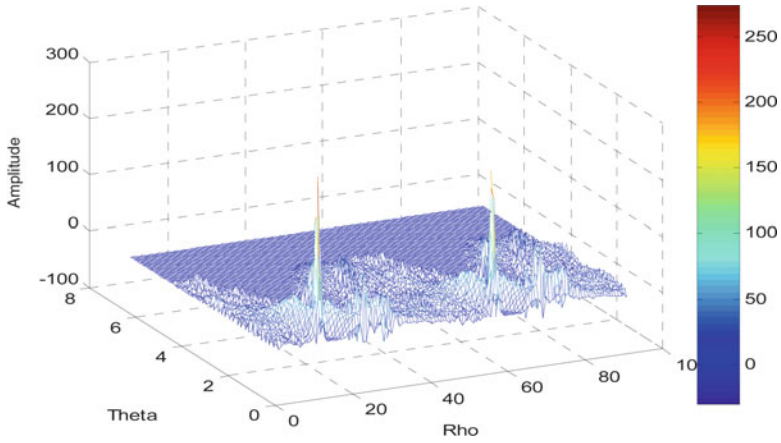

Fig. 5 The time-frequency graph about the FRFT and WVD

transform. We can see there are two peaks in the (ρ, θ) plane, which corresponds to the simulation signal. Although the Wigner-Hough transform do good for suppress the cross terms, but still not enough obviously.

In this paper, firstly, I take the FRFT to the simulation signal, the simulation signal in the original coordinate system (t, ω) counter-clockwise α angles, and then transform it with Wigner-Hough. The results showed in Fig. 5. We can see more clearly that signal in (ρ, θ) plane has two peaks, and the peaks in the middle of the three-dimensional time-frequency graph.

4 Conclusion

In conclusion, the combination of FRFT and the Wigner-Hough transform provides a method for the time-frequency analysis. This paper firstly took the FRFT to the simulation signal by setting the $K_p(t, u)$, and then transformed it with Wigner-Hough. The results showed that the method not only detected the signal components in the non-stationary signals well, but also easily observed and estimated the instantaneous frequency of the analysis signal, and restored the phase information. This advantage enables the method to be quite useful in time-frequency analysis.

References

1. Qian SE, Chen DP (1996) Joint time-frequency analysis, methods and applications. Prentice Hall PTR, New York, pp 15–67
2. Amein AS, Soraghan JJ (2007) The fractional Fourier transform and its application to high resolution SAR imaging. In: IEEE Proceedings of geoscience and remote sensing. IEEE Computer Society, Barcelona, Spain, pp 5174–5177
3. Barbu M, Kaminsky EJ, Trahan RE (2005) Fractional Fourier transform for sonar signal processing. In: IEEE Proceedings of OCEANS. IEEE Computer Society, Washington DC, USA, pp 1630–1635
4. Deng L (1999) Wavelet denoising of chirp-like signals in the Fourier domain. In: Proceedings of the IEEE international symposium on circuits and system. IEEE Computer Society, Orlando, Florida, USA, pp 540–543
5. Kay S, Boudreax-Bartels GF (1985) On the optimality of the Wigner distribution for detection. In: Proceedings of the IEEE ICASSP-85. IEEE Computer Society, Orlando, Florida, USA, pp 1017–1021
6. Barbarossa S (1995) Analysis of multicomponent LFM signals by a combined Wigner-Hough transform. IEEE Trans Signal Process 43(6):1511–1515
7. Capus C, Brown K (2003) Short-term fractional Fourier methods for the time-frequency representation of chirp signals. J Acoust Soc Am 113(6):3253–3263
8. Boashash B (1992) Estimating and interpreting the instantaneous frequency of a signal-part2: fundamentals. Proc IEEE 80(4):540–568
9. Allen JB (1977) A unified approach to short-time Fourier analysis and synthesis. Proc IEEE 65(11):1558–1564
10. Pei S, Min-Hung Yeh, Tzyy-Liang Luo (1999) Fractional Fourier series expansion for finite signals and dual extension to discrete-time fractional Fourier transform. IEEE Trans Signal Process 47(10):2883–2888

Weakness in a Serverless Authentication Protocol for Radio Frequency Identification

Miaolei Deng, Weidong Yang, and Weijun Zhu

Abstract The design of secure authentication protocols for radio frequency identification (RFID) system is still a quite challenging problem. Many authentication protocols for RFID have been proposed, but most have weaknesses or flaws. We analyze the security of a serverless RFID authentication protocol which recently been presented by Hoque et al. The protocol was expected to safeguard both RFID tag and RFID reader against major attacks, and RFID server is not needed in the protocol. However, our security analysis shows that the authentication protocol is vulnerable to attack of data desynchronization. This attack destroys the availability of the protocol. Furthermore, improvement to overcome the security vulnerability of the protocol was presented.

Keywords RFID • Authentication protocols • Security • Attack

1 Introduction

Radio frequency identification (RFID) has been widely applied, and has the advantages of automatic object recognition. RFID can be used in a great variety of applications such as stock security, supply chain management, retail inventory control, access control or product tracking. In an RFID system, the cost of the tags is low, which implies that the tags have very limited computational capabilities and storage. General -purpose security protocols cannot be applied directly to the RFID system [1].

M. Deng • W. Yang
College of Information Science and Engineering, Henan University of Technology, Zhengzhou, China
e-mail: dmlei2003 @163.com

W. Zhu (✉)
School of Information Engineering, Zhengzhou University, Zhengzhou, China
e-mail: zhuweijun76@163.com

W. Wang (ed.), *Mechatronics and Automatic Control Systems*, Lecture Notes in Electrical Engineering 237, DOI 10.1007/978-3-319-01273-5_119,

With the wide application of RFID systems, the security of the transmissions between the readers and the tags has received additional consideration [2]. So far, many RFID authentication protocols [3–5]have been put forward to protect RFID communications. These protocols have used the "backend database" (also known as server) model. Three parties are contained in this model, that is, the RFID tag, the RFID reader, and the backend database (or server). The backend database will return the information of the RFID tag to the RFID reader when the backend database verifies the tag and reader. This is possible because the backend database has knowledge of all the tag secrets as well as tag data. However, a prominent weakness of the backend database model is that an always reliable connection between the backend database and the RFID reader is needed. In addition, having a backend database creates a single point of failure, which may result in denial of service attacks [6].

To solve the problems, some authentication protocols have been presented which provide mutual authentication between the tag and the reader without the need for a constant backend database [7–9]. Recently, Hoque et al. suggest a serverless, untraceable authentication and forward secure protocol for RFID tags [10]. Hoque's authentication protocol safeguards both reader and tag against attacks as often as possible without the intervention of server (i.e. backend database). However, our security analysis shows that the authentication protocol is vulnerable to attacks of data desynchronization. This attack destroys the availability of the protocol. Furthermore, the improved serverless RFID authentication protocol is proposed, and it can withstand the attack of data desynchronization.

2 Hoque's Authentication Protocol

Usually, an RFID system comprises the RFID reader, R, the RFID tag, T, and the backend database. Nevertheless, Hoque's RFID system is a serverless system. Therefore, Hoque's serverless RFID system mainly contains two parties, one is a set of RFID tags and the other is the RFID reader R. In addition, a certification authority CA is encompassed in the RFID system to authorize readers to tags.

2.1 Notation and Assumption

In the system, all tags and readers have knowledge of a function $M(.)$ and a pseudorandom number generator $P(.)$. $P(.)$ is a low cost random number generator which applies to the RFID system. $M(.)$ is assumed as an one way hash function. An RFID reader R has a contact list L and a unique identifier r. L and r are obtained from a CA by R. In addition, each tag T includes a unique secret t and a unique identifier id. Subscripts are utilized to describe a particular T or R and their variables. The contact list L_i has the following shape,

Fig. 1 Hoque's RFID authentication protocol

(1) $R_i \rightarrow T_j$: $request, rand_i$
(2) T_j : $n_j = P(seed_{Tj} \oplus (rand_i \| rand_j))$
(3) $R_i \leftarrow T_j$: $n_j, rand_j$
(4) R_i : $n_i = rand_i$
(5) for all m from 1 to n //run through list L_i
(6) Let $n_m = P(seed_m \oplus (rand_i \| rand_j))$
(7) if $(n_m == n_j)$ then
(8) Let $s = M(seed_m)$
(9) $n_i = P(s)$
(10) $seed_m = M(s)$
(11) $R_i \rightarrow T_j : n_i$
(12) T_j : Let $k = M(seed_{Tj})$
(13) Let $a = P(k)$
(14) if $(a == n_i)$ then
(15) $seed_{Tj} = M(k)$
(16) else
(17) *Reader is not authorized or is an adversary*

$$L_i = \begin{cases} seed_1 & \vdots & id_1 \\ \dots & \vdots & \dots \\ seed_n & \vdots & id_n \end{cases}$$

where, for $1 \leq j \leq n$, $seed_j$ is initialized by $seed_j = h(r_i \| t_j)$. The initial $seed_j$ is given by CA and stored in R_i's nonvolatile memory. An adversary is denoted as Q.

2.2 RFID Authentication Protocol

Hoque's authentication protocol is shown in Fig. 1.

3 Vulnerability of Hoque's Protocol

Hoque et al. analyzed their proposed RFID authentication protocol and deemed that their protocol is secure. They claimed that the RFID protocol can provide privacy protection and withstand tracking attack, cloning attack, denial of service (DoS) attack, physical attack, and eavesdropping attack.

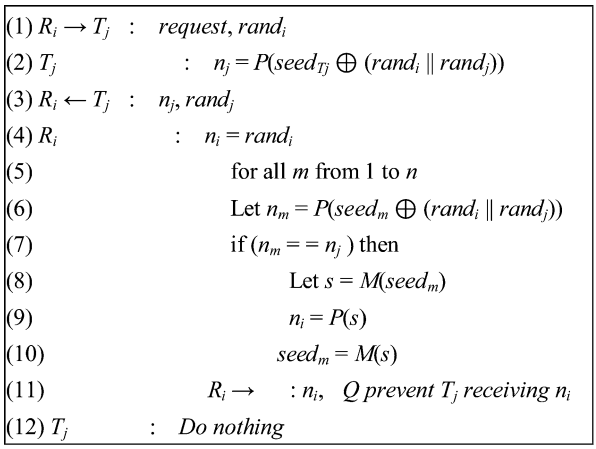

Fig. 2 Data desynchronization attack

However, the RFID protocol cannot offer any protection against data desynchronization attack: an adversary Q can easily force an honest tag to fall out of desynchronization with the reader so that it can no longer authenticate itself successfully. The attack can be described as follows (Fig. 2).

In the attack, the adversary Q easily destroys the desynchronization of the $seed_{Tj}$ updating between the reader and the tag. In line (11), Q can interrupt the message n_i from the tag T_j to the reader R_i. Thus, the reader R_i has refreshed the secret $seed_{Tj}$ while the tag T_j will not. Therefore, the shared secret between the tag T_j and the reader T_j may not be identical, which will threw the RFID system into confusion. After a successful data desynchronization attack, because Q makes the reader R_i and the valid tag T_j share the different secrets, R_i will not be authorized by T_j and T_i will not be authorized by R_j yet. The attack destroys the availability of the protocol.

4 The Anti-desynchronization RFID Protocol

We are trying to improve Hoque's RFID authentication protocol and provide an anti-desynchronization authentication protocol in this section.

4.1 Improvement of Hoque's Authentication Protocol

The reader ought to keep the history of the entire seed update in order to settle the data desynchronization attack issue. That is, the reader should keep not only the current records but also the previous records of the seed update process. When the reader cannot authenticate an honest tag because of the data desynchronization attack, it uses the old shared seed again to accomplish the authentication.

In particular, the RFID reader R_i stores contact list L_i and an identifier r_i in its nonvolatile memory. The contact list L_i comprises information about the RFID tags that R_i can access to and each tag contains the current seed $seed_j$, the previous seed $seed_{jp}$ and a unique identifier id. Thus L_i will have the following shape after authenticating itself to CA,

$$L_i = \begin{cases} seed_{1p}, seed_1 & \vdots & id_1 \\ \cdots & \vdots & \cdots \\ seed_{np}, seed_n & \vdots & id_n \end{cases}$$

In a general authentication process, the current seed of T_j, $seed_{Tj}$, will be utilized to accomplish the mutual authentication between the reader and the tag. Nevertheless, if the reader fails to look up the current seed for the desynchronization of the shared secret, it may use the previous seed to complete the authentication. Thus the improved protocol is shown in Fig. 3.

4.2 Security Analysis

The improved RFID protocol is analyzed in this section to estimate whether the protocol satisfies the security requirements or not. Similar to the original Hoque's authentication protocol, the improved protocol can also guarantee the privacy of the RFID tag, and resist the tracking attack, cloning attack, denial of service attack, eavesdropping attack and physical attack. The detailed analysis of security in this respect is overleapt and the similar analysis can be seen in Hoque's paper [10].

The adversary can impede the communication between a tag and a reader, which can threw the RFID system into confusion as before, but the desynchronization resistant mechanism that discussed just now makes the authentication protocol also meet the requirement of desynchronization resistance.

The improved protocol is also forward security. The protocol conceals the information utilized for updating the seed. The seed updating is performed whenever the authentication is successful, therefore future security compromised on an RFID tag will not disclose data previously transmitted.

4.3 Performance Evaluations

A wide adoption of RFID technology requires the RFID protocols not only to be secure, but to be practical and efficient. We analyze the improved RFID protocol by estimating its storage cost and computation cost.

Fig. 3 The improved RFID authentication protocol

(1) $R_i \rightarrow T_j$: $request, rand_i$
(2) T_j : $n_j = P(seed_{Tj} \oplus (rand_i \| rand_j))$
(3) $R_i \leftarrow T_j$: $n_j, rand_j$
(4) R_i : $n_i = rand_i$
(5) for all m from 1 to n
(6) Let $n_m = P(seed_m \oplus (rand_i \| rand_j))$
(7) if $(n_m == n_j)$ then
(8) Let $s = M(seed_m)$
(9) $n_i = P(s)$
(10) $seed_m = M(s)$
(11) $R_i \rightarrow T_j : n_i$
(12) else Let $n_m = P(seed_{mp} \oplus (rand_i \| rand_j))$
(13) if $(n_m == n_j)$ then
(14) Let $s = M(seed_{mp})$
(15) $n_i = P(s)$
(16) $seed_m = M(s)$
(17) $R_i \rightarrow T_j : n_i$
(18) T_j : Let $k = M(seed_{Tj})$
(19) Let $a = P(k)$
(20) if $(a == n_i)$ then
(21) $seed_{Tj} = M(k)$
(22) else
(23) *Reader is not authorized or is an adversary*

An RFID tag in improved scheme just stores its one seed for its only one authorized RFID reader. Certainly a tag still requires other memory space for communication and computation. However, computation in the improved protocol only contains hash operation and only one value utilized as authentication needs to be stored, so the required memory space is very limited.

The computation load of RFID tags in the improved protocol is also rather light-weight. The improved authentication protocol contains two hash functions, $M(.)$ and $h(\cdot, \cdot)$. The tag T_j will get $h(r_i \| t_j)$ as $seed_{Tj}$ from CA, that is, the hash functions, $h(\cdot, \cdot)$ is computed by CA. Therefore the cost of the protocol may be determined based on the computation of $M(.)$ function. According to the improved RFID authentication protocol described above, it can be seen that $M(.)$ is computed twice, first in line (18) and second in line (21). Therefore, the cost for the protocol

is little higher than other protocols [3–5] that require the tag to execute only one hash function. In our scheme, the additional hash functions can avoid disclosing the tag secret to the reader and also permit the protocol to be serverless.

5 Conclusion

Designing of a secure authentication solution for low-cost RFID tags is still an open and challenging problem. In this paper the cryptanalysis of a recent lightweight RFID authentication protocol is proposed. The RFID authentication protocol is vulnerable to attack of data desynchronization. The proposed attack could have been avoided by following a desynchronization resistant mechanism for designing RFID protocols. The improved RFID authentication protocol is forward security, and satisfies the security requirements, such as privacy protection, tracking attack resistance, cloning and physical attack resistance. The improved protocol is light-weight and suitable for the low-cost RFID environment.

Acknowledgements This work is supported by China Postdoctoral Science Foundation (2012M511588), Ph.D. Programs Foundation of Henan University of Technology (2013BS007) and National Natural Science Foundation of China under Grant No. U1204608.

References

1. Chai Q (2012) Design and analysis of security schemes for low-cost RFID systems[D]. Doctor dissertation of Waterloo University, Waterloo
2. Jules A (2006) RFID security and privacy: a research survey. IEEE J Sel Areas Commun 24 (2):381–394
3. Lee YK, Batina L, Singele D (2010) Low-cost untraceable authentication protocols for RFID systems[C]. In: Proceedings of the 3rd ACM conference on wireless network security, ACM Press, New Jersey, pp 55–64
4. Deng Miaolei, Ma Jianfeng, Zhou Lihua (2009) Design of anonymous authentication protocol for RFID. J Commun. 30(6):24–31 (in Chinese)
5. Moessner M, Khan GN (2012) Secure authentication scheme for passive C1G2 RFID tags. Comput Netw 56(1):272–286
6. Duc DN, Kim K (2011) Defending RFID authentication protocols against DoS attacks. Comput Commun 34(3):1196–1211
7. Tan CC, Sheng B, Li Q (2007) Serverless search and authentication protocols for RFID[C]. In: Proceedings of the 5th annual IEEE international conference on pervasive computing and communications, IEEE Press, New York, pp 34–41
8. Ahamed SI, Rahman F, Hoque E (2008) S3PR: secure serverless search protocols for RFID [C]. In: International conference on information security and assurance, IEEE Press, Busan, pp 187–192
9. Deng Miaolei, Wang Yulei, Qiu Gang et al (2009) Authentication protocol for RFID without back-end database. J Beijing Univ Posts Telecommun 32(2):68–71 (in Chinese)
10. Hoque ME, Rahman F, Ahamed SI et al (2010) Enhancing privacy and security of RFID system with serverless authentication and search protocols in pervasive environments. Wirel Pers Commun 55:65–79

The Radar Images Smooth Rolling

Peng Gao

Abstract The main problem of achieving the radar images rolling demo is how to achieve the goal of smooth rolling. The problem was mainly caused by the high computational load for image processing and low computing efficiency. In order to solve this problem, a complete solution is brought up in this paper. In this solution, the computational load is reduced by compressing the raw format radar images. A new compression method for RAW format radar image is raised. The image processing time is reduced by choosing the right gray equilibrium and Image Mosaic method. In this paper, a new gray equilibrium method is raised based on the histogram equalization method. And the gray correlation matching algorithm with iterative search method based image pyramid is used to splice images. Moreover, the calculation efficiency is increased by using two threads for control data reading and processing. The parallelization between CPU and I/O can be achieved. Meanwhile, the parallel computing ability of Multi-core CPU can also be used. The solution has proved the efficiency by detailed description and examples. The high resolution radar images can be rolled smoothly with less calculation and memory consumption and have satisfactory image quality. So this solution can effectively achieve the goal of smooth rolling.

Keywords Radar image • Roll • Compression • Gray equilibrium • Multi-threaded

1 Introduction

Usually the radar images showed to uses and audiences are static [1], such as paper image and electronic image. But if showed the continuous images in same strip, the method of static display is difficult to promises continuous experience.

P. Gao (✉)
Master, Center for Earth Observation and Digital Earth Chinese Academy of Sciences, Institute of Remote Sensing and Digital Earth Chinese Academy of Sciences, Beijing, China
e-mail: foree@foxmail.com

W. Wang (ed.), *Mechatronics and Automatic Control Systems*, Lecture Notes in Electrical Engineering 237, DOI 10.1007/978-3-319-01273-5_120,

By comparison, showing these images in rolling way is much better. For achieving these images rolling demo, there are many problems need to be solved in the process of achieving the images smooth rolling, one of the most critical is how to achieve the goal of smooth rolling. By now, there is no complete solution for solving radar images smooth rolling and the related issues. So In this paper, a complete solution is brought up and proved the efficiency by detailed description and examples.

The radar image for this solution is the most common RAW format. The 16-bit integer RAW high resolution radar image will be used in this paper. This type of images always has huge volume. This will lead to a huge amount of calculation and Further influence the computing efficiency. So compressing the radar image is very necessary. At present there have been many research results for radar image compression [2–4], but no specific to RAW format radar image. In this paper, through the analysis of the characteristics of this kind of image, a new data progressing algorithm is raised. Using this algorithm, the 16-bit image can be compressed to 8-bit. This will reduce the computation time effectively.

Grey equilibrium is also the implementation steps for RAW format image rolling demo. Because of most of the gray details in RAW image are in low gray level, the image without gray equilibrium show black or with odd light spot. Even after image compression processing, the image are still dull. So the grey equilibrium processing are essential for raising the image visual effect. Because of the process need a number of calculations, the choice of the equilibrium method concerns the image quality and smooth roll. In this paper, a new method come is raised based on the histogram equalization method [5]. This method takes the same calculation as histogram equalization but better processing effects. So using this method will put less pressure on smooth rolling.

The RAW images do not just need gray equilibrium, but also need image mosaic processing. It's also time-consuming. Because the images in the same strip are overlapped in a small area near and along the vertical direction near the boundary, we can choose the gray correlation matching algorithms [6]. Through the pyramid iterative search strategy [7], the gray correlation matching algorithms will spend much less calculated. The images are in rolling, so the stitching precision can only be required no visual differences for users. By verification, this method can reach the stitching precision.

Besides, a novel double thread scheduling method is used to control the image processing, read, and display in this solution. Combining multi-threading parallel computing [8] thoughts, this method realizes the parallel operation between the CPU and I/O, also realizes the multi-thread parallel computing. It's useful for increasing the calculation efficiency and the image rolling smoothly.

To sum up, in order to achieve the goal of the radar images smooth rolling, meet the image quality requirements and user experience, much research is developed aimed at data compression, gray equilibrium, image mosaic and multi-threading control. As a result, many effective methods are brought up.

2 Solution

The solution stated above, mainly includes three aspects: image processing, image mosaic and multithreading control. The image processing includes image compression and gray equilibrium. Images are calculated and displayed by the two threads. Their functions are alternative during the image rolling. Figure 1 is the flow chart for this solution. From now on, we will introduce the three mainly aspects by combining the flow chart above.

2.1 Multithreaded Control

As shown in Fig. 1, the whole process of calculation and display are completed in two threads. But in Fig. 1 the flow chart shows the flow when the program has run a period of time and the two threads are stability alternative. It's subtle differences with the flow at the beginning of the program running. Combined with the flow chart, I will introduce the processing from initial rolling to steady rolling.

At the beginning of the program, the thread-1 read two images once. This is different with the Fig. 1. After reading, It will be checked whether the thread-1

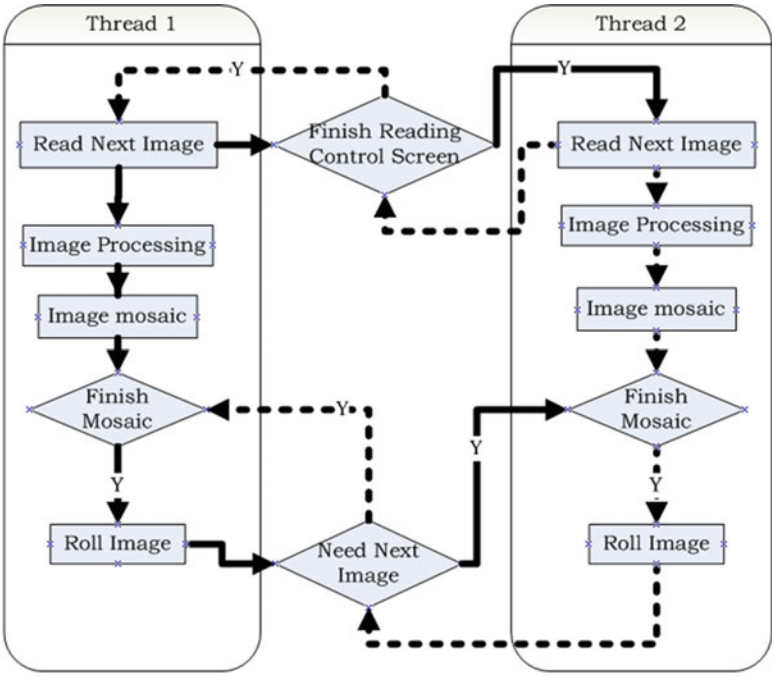

Fig. 1 Solution flow chart

controls the screen display. If so, continue; if not, wait. Because the program is just in the initial state, no one control the screen display. So thread-1 continues. Then the thread-1 notifies the thread-2 to read next image. At the same time, the thread-1 begins to compress image and equilibrate the gray. After these, the two images will be spliced. Then, it will be checked whether the screen need display new image. Usually, it will happen when the old image has showed completely.

After thread-1 has finished the image reading, the thread-2 will be noticed to read next image. After the thread-2 finished reading, the same notice will be sent to thread-1 from thread-2. If thread-1 is controlling the screen display, and the image is still rolling, the notice will be suspended. When the new image is needed, thread-1 will release the old image memory, and begins to deal with the notice which has be suspended.

When thread-2 receives the request for show next image from thread-1, it will be checked whether the image processing and image mosaic has finished. If so, control the screen and show new image; if not, wait until they finish. Now the thread-1 has worked as the thread-2 before, reading and process image in background. In proportion, thread-2 becomes the controller instead of thread-1. From now on, the images will roll continuous as the Fig. 1.

Above is the basic flow that two threads control the screen display alternately in order to achieve the goal of the image rolling demo. When finish themselves rolling task, each thread release the right of controlling screen and image memory, then begins to read next image. In this way, there are always no more than two images in memory. Moreover, in the process of image rolling, the two threads will not be destroyed and new thread or variables will not be created, so the total used memory will not increase.

Besides, when a thread is reading data, the other is always processing data or displaying images. So they will never ask for the I/O control at the same time, As a result, the I/O and CPU will work in parallel. If the time for reading is short, it will be appear that the two threads are using CPU in the same time. On a dual core processor platform, it will take full advantage of parallel computing ability of CPU. Fortunately, the multi-core processor has become the mainstream. These designs above are all for avoiding the stumble rolling when the images roll at high speed.

Unfortunately, because of the runtime environment and data size differs from each other, the maximum speed is not unfixed with smooth rolling. Through the analysis of the flow, we can find out the most likely scenario which causes the rolling suspend is that the time for reading and processing image is too long, so that image mosaic has not finished when the screen require a new image. So, we will introduce the appropriate method for processing and splice image.

2.2 Image Processing

In this paper, the 16-bit integer radar image is used. It's 16,384 $\times$ 16,384 pixels and 512 MB. If such large data is immediately used to gray equilibrium or image mosaic

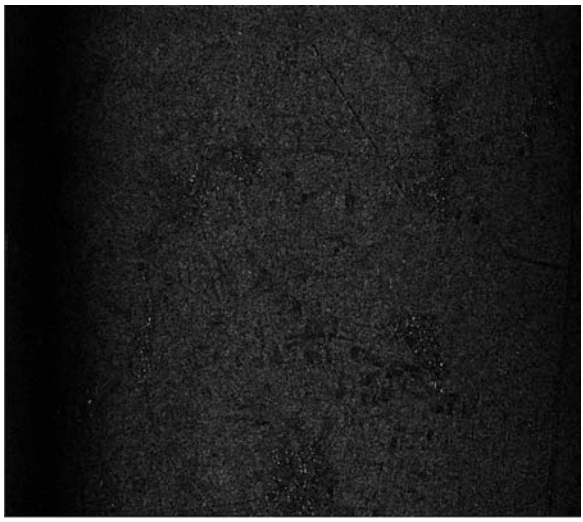

Fig. 2 The image after compressing

or display on screen, the efficiency will be very low. The time can't meet the requirements that the smooth rolling need short processing time. So before using the image data, it must be compressed firstly.

A light and shade moderate RAW image will be a black image browsed directly. So the image doesn't list here. The reason is that the main nonzero grays are mostly in the low gray level. For most RAW image, the higher 6–7 bit of gray value are mostly 0, the nonzero gray bit are almost in front 12 bits, the last 4 bits are always 0. Moreover, the first bit are always 0. So all these bits which are always 0, can be compressed and omitted.

Due to the limitation of the human eye, the small gray variance of too much light or dark pixels is difficult to distinguish, but is easier distinguished for middle tone. So the middle tone should be kept while compressing image data. The low 1-bit or 2-bit should be compressed. For the reason that the most screen can only show the 8-bit gray image, the 16-bit RAW image can be compressed to 8-bit without influencing the effect for screen display. Through the above analysis, the compression method in this paper is that the high six bits and low two bits will be ignored, only the middle eight bits will be reserved. Using this method, the image data will be compressed to half size.

The image compressed is showed in Fig. 2. As shown, the image isn't wholly dark, and already shows some gray details. So the data compression can be regarded as gray equilibrium.

Although the visual effect in Fig. 2 has been improved greatly than raw image, it's still dull and difficult to differ ground information. The reason for this is that most gray are still in the low level. So farther gray equilibrium need to be introduced to image processing.

At present there have been many method for image equilibrium [9], such as time domain enhancement technology. For radar image, many methods can be used,

Fig. 3 The image after image equilibrium

such as wavelet transform, histogram equalization, histogram specification and so on. The image smooth rolling required the time for image compression should not vary long, so the method which is high-computational is not suitable. The histogram equalization is the fastest method, but its treatment effect is unsatisfactory. This method remarks the middle gray and weakens the boundary gray, so the image shows too much white. Unfortunately, the most important ground characteristics in radar image are showed by high and low gray. So use the original histogram equalization method will lose many ground characteristics. In order to avoid such, the original histogram equalization should be changed to weaken middle tone little, and enhance the boundary tone.

A new simple but effective gray equilibrium has been raised in this paper. Calculating image histogram is the first step, how many pixels in each gray level (0–255) will be known. Than find the minimum gray level 'Min' in which the first pixel appears from level 0 to level 255. In the same way, find the maximum gray level 'Max' in which the first pixel appears from level 255 to 0. Than choose the gray level, to which the total pixels are first exceed 5.5 % of the whole image from 'Min' level, as the 'NewMin'. Also in the same way, choose the gray level, to which the total pixels are fist exceed 5.5 % of the whole image from 'Max' level, as the 'NewMax'. In the end, scan all pixel. If its grey level is less than or equal to 'NewMin', set its grey level as 0; if its grey level is more than or equal to 'NewMax', set its grey level as 255; the rest will be set as '(original level – 'NewMin') * 255/('NewMax'–'NewMin')'.

The image processed in this way will be shown as Fig. 3. Compare with Fig. 2, the image after gray equilibrium is much better. The difference between the new method and original histogram equalization is that the new method save the pixel gray level which belongs to 5.5 % of the whole pixels in the highest level and 5.5 % of the whole pixels in lowest level, at the same time, weaken the middle gray level.

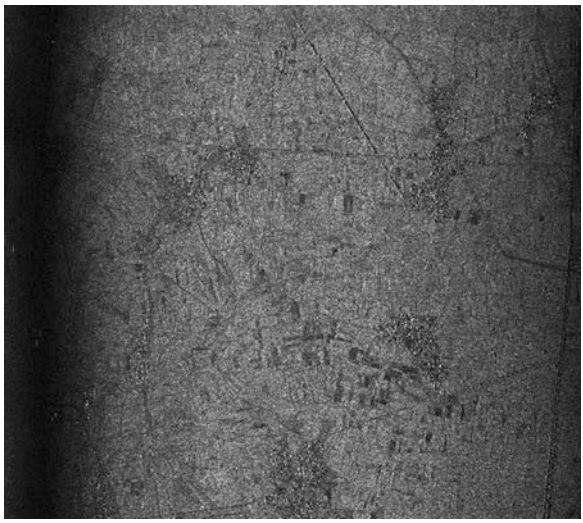

Fig. 4 The image after mean processing

Though enlarged the image, we can see many speckle noise in the image, in this paper, the easiest mean processing is used to remove the noise. Compare Fig. 4 with Fig. 3, although the mean processing is sample but works well. In view of the requirement that smooth rolling needs speed data processing, other more complex method will not be considered, even they may have better treatment effect.

2.3 Image Mosaic

At present image mosaic algorithm [10] has already been very mature. The three main types are the mosaic algorithm based on region gray level correlation calculation, the mosaic algorithm based on attribute correlation, and the mosaic algorithm based on similar interpretation.

Because of the images are always rolling, the requirement for image mosaic precision is not very high, but for the image processing speed is high. The image mosaic for the image in same trip is always along the vertical direction, and the overlapping regions are small in the boundary region of image. So the mosaic complexity is low and the calculation is little. For these feature, the mosaic algorithm based on region gray level correlation calculation is very suitable. The characteristics of this method are simple and well registration performance while there are not large deformations, and also good adaptability. The image data used for this method should keep the original gray, so the data after compressing is suitable. The iterative search method based image pyramid has been used for this mosaic algorithm in this paper. In this method, the rectification begins from the lowest level, and set the level as the center for next level rectification, until up to original image level (the pyramid bottom). In this way, the calculation will be reduced.

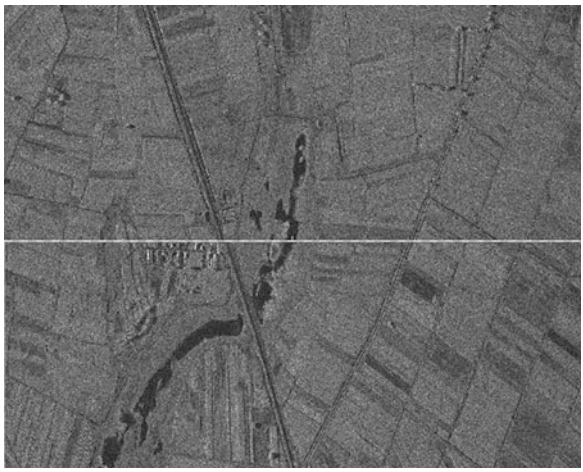

Fig. 5 The image after mosaic

Figure 5 is the partial close-up of mosaic image of the adjacent image. The mosaic effect is satisfactory. Even there are small offset, but it's difficult to find during the image rolling. So the mosaic algorithm based on region gray level correlation calculation can meet the requirements of smooth rolling and mosaic effect. Though description all respect of this solution combining with the demonstrations, the solution has been proved to be effective for solving the problem of radar images smooth rolling.

3 Conclusion

A new solution has been raised for radar image rolling demo in this paper. The solution has been proved to be effective by detailed description and demonstrations. It not only has applicative value, but also is instructive and meaning full to the related project. Moreover, a new method for image compression and an improved method for gray equilibrium, have been raised aiming at the features of radar image and the combining requirement of image smooth rolling. Although these methods have strong pertinence, they will work well in other projects with some modifications.

References

1. Zhang Xin (2011) Radar image display and processing[D]. Dalian Maritime University, Dalian
2. Dong Pengshu, Zhange Chaowei, Jin Jiagen, Xie Youcai (2009) Compression and implementation of high resolution radar signals[J]. Syst Eng Electron 31(1):54–56
3. Pan Shoudao, Zhu Jie (2012) The research of a new radar image compression method based on BAQ algorithm[J]. Electron Meas Technol 35(2):65–68

4. Wang Renlong (2009) The research on radar image compression based on wavelet transform [D]. Harbin Engineering University, Harbin
5. Gonzalez RC, Woods RE (2003) Digital image processing[M], 2nd edn. Prentice Hall, London, p 793
6. Zhang Hongbing (2009) Research on algorithm of remote sensing image mosaics[J]. Xidian University, Xi'an
7. Jenkinson M, Smith S (2001) A global optimization method for robust affine registration of brain images[J]. Med Image Anal 5(2):143–156
8. Andrews GR (2002) Foundations of multithreaded, parallel, and distributed programming [M]. Addison Wesley, New Jersey, p 664
9. Guo Hongyan (2010) Research on synthetic aperture radar image enhancement and detection technology[D]. University of Electronic Science and Technology of China, Sichuan
10. Zhou Juntai (2011) Studies of technologies and methods on image mosaic[D]. Hunan University of Technology, Hunan

Index of Volume 1

W. Wang (ed.), *Mechatronics and Automatic Control Systems*, Lecture Notes in Electrical Engineering 237, DOI 10.1007/978-3-319-01273-5,

Index of Volume 2

W. Wang (ed.), *Mechatronics and Automatic Control Systems*, Lecture Notes in Electrical Engineering 237, DOI 10.1007/978-3-319-01273-5,